GSI Report 2015-1
December 2015

SCIENTIFIC REPORT 2014

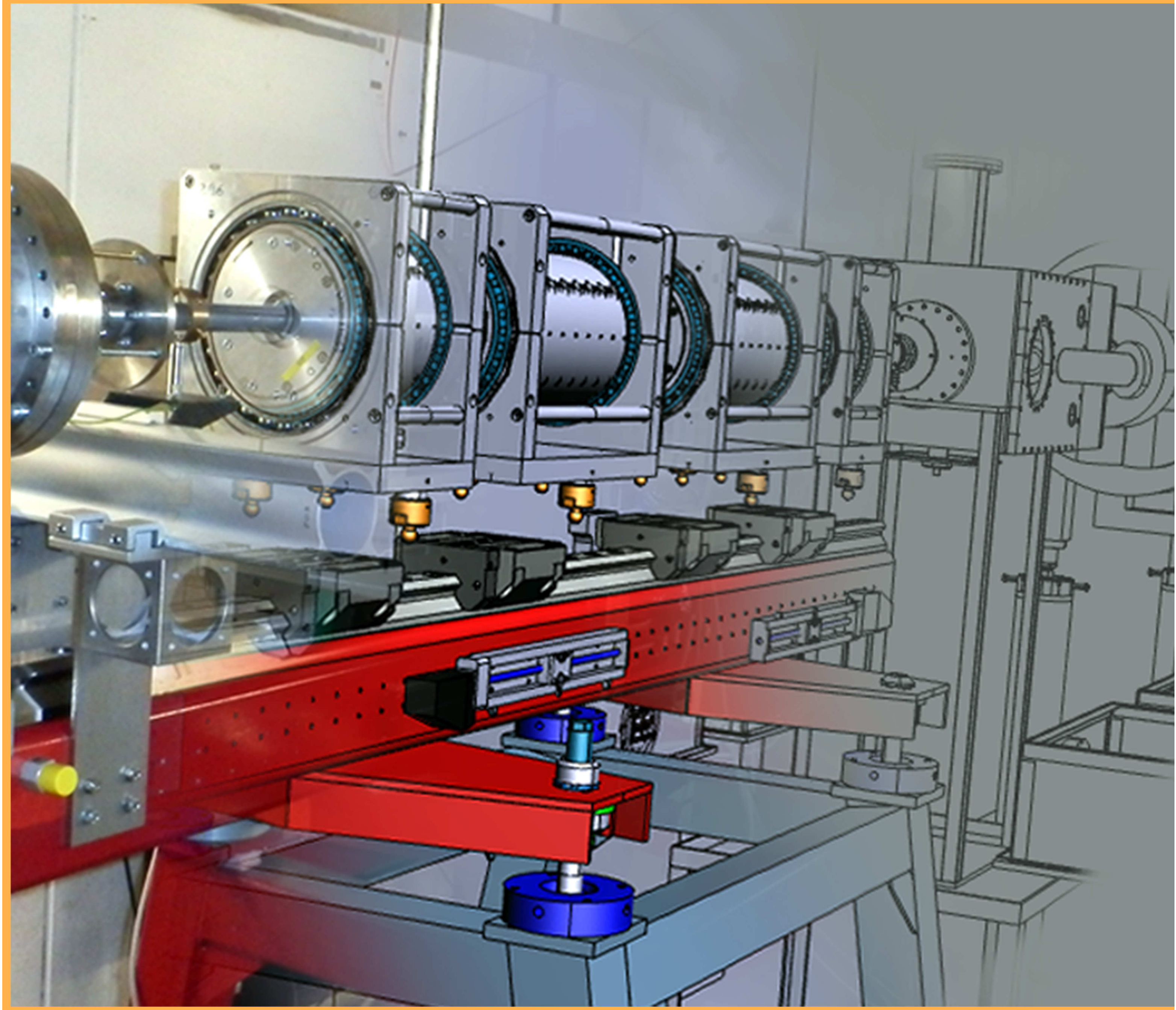

GSI Helmholtzzentrum für Schwerionenforschung GmbH
Member of the Helmholtz Association

From design to implementation: Shown are the quadrupole lenses which are part of the prototype of the proton microscope PRIOR. The target chamber of the HHT experimental area is indicated in the background.

See DOI:10.15120/GR-2015-1-APPA-MML-PP-02 pages 275-276 in this report.

Cover design: Philipp-Michael Lang.

GSI Scientific Report 2014

GSI Report 2015-1
<http://www.gsi.de/library/GSI-Report-2015-1/>
DOI:10.15120/GR-2015-1

Some contributions are already published in other publications of the GSI:

Helmholtz Institute Jena: Annual Report 2014, https://repository.gsi.de/record/180855:
APPA-MML-PP-03, APPA-MML-AP-07, APPA-MML-AP-08, APPA-MML-AP-10, APPA-MML-AP-11, APPA-MML-AP-13, APPA-MML-AP-16, APPA-MML-AP-17, APPA-MML-AP-20, APPA-MML-AP-24, APPA-MML-AP-26, APPA-MML-AP-28, FG-GENERAL-14

Weyrich, K.; Hoffmann, D.: News and reports from High Energy Density GEnerated by Heavy iOn and laser Beams 2013 - 2014 https://repository.gsi.de/record/108765:
APPA-MML-PP-02, APPA-MML-PP-08, FG-GENERAL-44, FG-SIS100-12

Friese, V. ; Sturm, C.: CBM Progress Report 2014, https://repository.gsi.de/record/97909:
MU-NQM-CBM-01, MU-NQM-CBM-02, MU-NQM-CBM-03, MU-NQM-CBM-04, MU-NQM-CBM-06, MU-NQM-CBM-07, MU-NQM-CBM-08, MU-NQM-CBM-09, MU-NQM-CBM-11, MU-NQM-CBM-12, MU-NQM-CBM-13, MU-NQM-CBM-14, MU-NQM-CBM-15, MU-NQM-CBM-16, MU-NQM-CBM-17, MU-NQM-CBM-18, MU-NQM-CBM-19, MU-NQM-CBM-20, MU-NQM-CBM-21, MU-NQM-CBM-22, MU-NQM-CBM-23, MU-NQM-CBM-24, MU-NQM-CBM-25, MU-NQM-CBM-26, MU-NQM-CBM-27, MU-NQM-CBM-28, MU-NQM-CBM-29, MU-NQM-CBM-30, MU-NQM-CBM-31, MU-NQM-CBM-32, MU-NQM-CBM-33, MU-NQM-CBM-35, MU-NQM-CBM-37, MU-NQM-CBM-38, MU-NQM-CBM-40, MU-NQM-CBM-41, MU-NQM-CBM-42, MU-NQM-CBM-44, MU-NQM-CBM-45, MU-NQM-CBM-46, MU-NQM-CBM-47, MU-NQM-CBM-48, MU-NQM-CBM-50, MU-NQM-CBM-53, MU-NQM-CBM-54, MU-NQM-CBM-55, MU-THEORY-20, MU-THEORY-22

ISSN: 0174-0814
and GSI Report 2015-1

Publisher: GSI Helmholtzzentrum für Schwerionenforschung GmbH,
Planckstr. 1, 64291 Darmstadt, Germany, <http://www.gsi.de>
GSI is a member of the Helmholtz association of national research centres <http://www.helmholtz.de>.
E-only-edition: <http://www.gsi.de/library/GSI-Report-2015-1/>
DOI:10.15120/GR-2015-1

Editor: Katrin Große,
Contact: gsilibrary@gsi.de, phone: +496159 712610, fax: +496159 713049.
Publication date: December 2015

For the production of this report templates and scripts of the JACoW collaboration (Joint Accelerator Conferences on Web <http://www.jacow.org>) were used.

Contents

Searching a $\Sigma(1385)N-\Delta(1232)Y$ dibaryon in p+p collisions at 3.5 GeV*

J. Berger-Chen†[1,2], *L. Fabbietti*[1,2], *and the HADES collaboration*
[1]Physik Department E12, Technische Universität München, 85748 Garching, Germany; [2]Excellence Cluster 'Origin and Structure of the Universe' , 85748 Garching, Germany

Introduction

This analysis is motivated by a recent three-body Fadeev calculation of the $\pi\Lambda N-\pi\Sigma N$ coupled channel system with $I=\frac{3}{2}$ and $J^P=2^+$ [1]. In that work a $\pi\Lambda N$ resonance was predicted located around 10-20 MeV/c^2 below the $\pi\Sigma N$ threshold (2267 MeV/c^2). This resonance can be viewed as an s-wave dibaryon $\mathcal{Y}$ with $(Y,I,J^P)=(1,\frac{3}{2},2^+)$ and is equivalent to an $\Sigma(1385)N-\Delta(1232)Y$ quasibound state bound by over 50 MeV. Experimentally, the p+p data measured with the HADES setup at an beam energy of 3.5 GeV are very well suited to search for this state, since the provided energy is well above the $\Sigma(1385)$ production threshold. Furthermore, the double charged dibaryon $\mathcal{Y}^{++}$ can be explicitly identified in p+p interactions through the exclusive reaction $pp\to\mathcal{Y}^{++}K^0\to\Sigma^+pK^0$.

Analysis Procedure

To enhance the contribution of the above reaction in the analyzed data sample, events with the four charged particles proton, π^+, π^+ and a π^- were selected explicitly. Thereby, the proton is supposed to be a primary particle, the π^+ should stem from the Σ^+ decay and the other two pions should originate from a K^0_S meson. That way, only the branching of the Σ^+ into a neutron and a π^+ ($BR\approx 48.31\%$) was considered. As a first attempt, it was tried to reproduce the data with a model, that does not include the explicit formation of an intermediate $\mathcal{Y}^{++}$. A cut on the K^0_S mass in the $\pi^+\pi^-$-invariant mass distribution was applied, which lead to a data sample, that consists only of K^0_S production channels ($pp\to K^0_S+X$) and background. The background, which is mainly related to combinatorics of non-strange reactions, was modeled by means of a sideband analysis with respect to the missing mass distribution to the proton, π^+ and π^- (MM(p,π^+,π^-)). More details on this procedure can be found in [2]. The remaining contributions from channels, that produce a K^0_S in the final state, were simulated by means of an incoherent Monte Carlo cocktail including 14 reactions. The cross sections and kinematics of these reactions were settled in another analysis of the same data set [3]. That means, only the yield of the background in the selected event sample needed to be determined. This was done by fitting the background with fixed K^0_S contributions to the two distributions MM(π^+,π^-) and $cos\Theta^{\pi^+\pi^-}_{cm}$ at once.

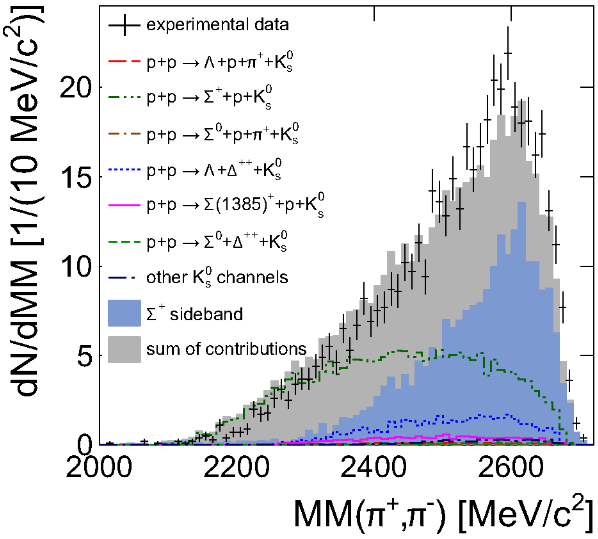

Figure 1: Missing mass spectrum to the π^+ and π^- with a cut on the K^0_S and the Σ^+ mass. The contributions of the K^0_S reactions are according to the findings of [3].

Preliminary Results

The missing mass spectrum MM(π^+,π^-), which includes cuts on the K^0_S and the Σ^+ masses, is depicted in Figure 1. On top of the data (black crosses), the contributions of the background (filled area) and the K^0_S channels (curves) are shown. The sum of all these contributions fits very nicely to the experimental data without any inclusion of a dibaryon channel. This is obvious, since no enhancement is visible at 10-20 MeV/c^2 below the $\pi\Sigma N$ threshold (2267 MeV/c^2), where the $\mathcal{Y}$ resonance is expected. Nevertheless, an upper limit for the $\Sigma(1385)N-\Delta(1232)Y$ dibaryon in this data sample assuming an incoherent cocktail can still be extracted and will be the next step to do.

References

[1] H. Garcilazo *et al.*, "Relativistic three-body calculations of a Y=1, I=3/2, JP=2+ $\pi\Lambda N$–$\pi\Sigma N$ dibaryon", Nucl. Phys. A 897 (2013) 167–178.

[2] J. Berger-Chen *et al.*, "Search for a $\pi\Lambda N-\pi\Sigma N$ dibaryon in p+p@3.5 GeV", arXiv:1410.8004v1 [nucl-ex] (2014).

[3] G. Agakishiev *et al.*, "Associate K^0 production in p+p collisions at 3.5 GeV: The role of $\Delta(1232)^{++}$", Phys. Rev. C 90 (2014) 015202.

---

* Work supported by Excellence Cluster Universe.

† jia-chii.chen@tum.de

DOI:10.15120/GR-2015-1-MU-NQM-HADES-01

K* reconstructed in pp reactions at 3.5 GeV*

D. Mihaylov†[1,2], *L. Fabbietti*[1,2], *K. Lapidus*[1,2], *and the HADES collaboration*
[1]Physik Department E12, TU München, James-Franck-Str. 1, 85748 Garching, Germany; [2]Excellence Cluster "Universe", TU München, Boltzmannstr. 2, 85748 Garching, Germany

The investigation of $K^{*+}(892)$ production in 3.5 GeV $p+p$ reaction is of great interest, due to the lack of experimental data at energies near to the production threshold [1, 2]. In addition, the available $p+Nb$ data will allow us to study the in-medium modifications of the $K^{*+}(892)$ in the future by using the results obtained from the current analysis as a reference. The production of $K^{*+}(892)$ can be easily studied by reconstructing it from its decay into a neutral kaon and a charged pion (Fig. 1). Thus we performed the analysis of the $K^{*+}(892)$ production in $p+p$ collisions at 3.5 GeV.

Figure 1: The short-lived K^{*+} decays at the primary vertex into a K^0_S and a π^+. The K^0_S decays into a pair of charged pions after a short time.

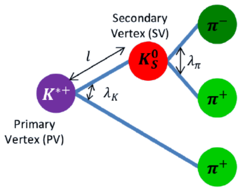

The reconstruction of the $K^{*+}(892)$ can be summarized as follows: (i) Following the scheme shown in Figure 1 and applying appropriate topological cuts, the $K^0_S\pi^+$ pairs are reconstructed; (ii) the invariant mass spectrum of the $K^0_S\pi^+$ pairs is fitted with a modified Breit-Wigner function, taking into account the background, phase space limitations and detector resolution. This allows to extract the yield of the $K^{*+}(892)$. The total yield is well above 1000 K^*s, which gives the opportunity to perform a single differential analysis by dividing the data into five transverse momentum bins; (iii) Assuming uniform phase space distribution, we simulate the two dominant $K^{*+}(892)$ production channels using the PLUTO event generator: $p+p \to p+K^{*+}+\Lambda^0$ and $p+p \to p+K^{*+}+\Sigma^0$. Then the response of the detector is simulated using HGeant. The result is analyzed in the same way as the experimental data. Thus, as the acceptance and efficiency correction factor for the experimental data, we can use the ratio between the number of reconstructed K^*s after HGeant and the number of K^*s generated in PLUTO. Due to the small difference in the correction factor between the two simulated channels we use only the Λ associated production channel for the correction of the data; (iv) by normalizing the K^* yield to the elastic pp scattering cross section observed in this experiment, we can find the differential cross section for each p_T bin. The integration of the spectrum delivers the total K^* production cross section; (v) It is possible to investigate the data for spin-alignment effects. This was performed and no hint for such effects was present within uncertainties.

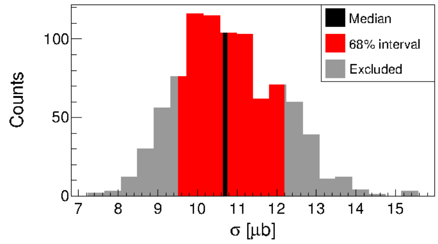

Figure 2: Systematic result for the $K^{*+}(892)$ total production cross section. Any topological cuts that did not produce meaningful result (e.g. the fit of the IM spectrum did not converge) were excluded.

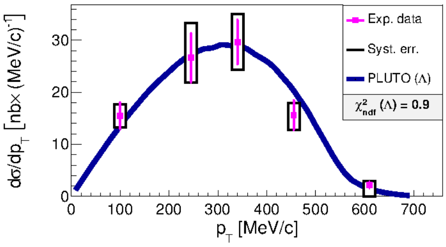

Figure 3: Differential production cross section of the $K^{*+}(892)$ as a function of p_T.

In order to investigate the stability of the reconstruction procedure and to obtain information on its systematic error, this analysis was performed over 1200 different cut combinations. The distribution of the results for the total $K^{*+}(892)$ production cross section resulting from those iterations is shown in Figure 2. The final cross section was obtained by taking the median of this distribution, the systematic error was obtained by taking the 68% central interval, and the statistical error was taken as the average statistical error over all topological cuts. As shown in Figure 3 the obtained distribution of the differential cross section in p_T is in a good agreement with the prediction of pure Λ associated production of the $K^{*+}(892)$. Because of the relatively large error it is difficult to evaluate the yield resulting from the Σ associated production channel.

References

[1] Baldini *et al.*, "Numerical Data and Functional Relationships in Science and Technology", Springer, Volume 12b, 1988.

[2] Bockmann *et al.*, "Inclusive K*+(892) production in pp and π^+p interactions", Nucl. Phys. B 166 (1980) 284.

---

* Work supported by BMBF and the Excellence Cluster "Universe".

† dimitar.mihaylov@mytum.de

DOI:10.15120/GR-2015-1-MU-NQM-HADES-02

Dipion and dielectron production in quasi-free np reactions with HADES *

H. Kuc[1], *P. Salabura*[1], *and B. Ramstein*[†2]
[1]Jagiellonian University, Crakow, Poland; [2]IPNO, Orsay, France

The origin of the yield excess in the inclusive dielectron production in np over the pp collisions measured by HADES [1] still needs to be clarified to provide a global reliable interpretation of dielectron spectra measured in nuclear collisions by HADES. Several attempts to solve this issue by including a contribution from off-shell ρ meson were recently proposed [2,3,4]. Since the main decay of the ρ is the channel with two charged pions, an analysis of this channel provides an important constraint for dielectron spectra [5]. Furthermore, the results on dipion production provide valuable verification of the di-baryon formation, recently reported by the WASA collaboration [6,7], in a complementary phase space region as covered by HADES. We report on results on exclusive dipion and dielectron production in np collisions in the deuterium formation channel.

Signal selection

The quasi-free np reaction was studied using measurements of the dp reaction with a deuterium beam of 2.5 GeV. The quasi-free np reaction was tagged by the proton spectator detection at small angles (0.3-7°) in the Forward Wall with a velocity close to the beam velocity. Since for both $np \rightarrow de^+e^-$ and $np \rightarrow d\pi^+\pi^-$ reactions, the deuteron angular distribution is very forward peaked, very few deuterons reach the HADES detector, which covers polar angles from 18° to 85°, while the detection in the Forward Wall (FW) is more suited. Due to the large statistics in the $np \rightarrow d\pi^+\pi^-$ channel, both cases (deuteron detected in FW or in HADES) were investigated, while for the more rare $np \rightarrow de^+e^-$ channel, only the detection of the deuteron in the FW was investigated. Deuterons are identified in HADES with a very high purity using the correlation between time-of-flight and momentum. For the deuteron identfication in the FW a coplanarity constraint on all particles in the final state was used, in addition to cuts on the time-of-flight to suppress events corresponding to the unbound processes ($np \rightarrow np\pi^+\pi^-$ or $np \rightarrow npe^+e^-$) [5].

Dipion production

After a subtraction in each bin of the background contribution using the coplanarity condition, the experimental distributions of the $pn \rightarrow d\pi^+\pi^-$ have been compared to the predictions of a model provided by M. Bashkanov [6], which includes conventional t-channel processes (double $\Delta(1232)$, $N(1440)$ and $N(1520)$ excitation), as well as the contribution of a dibaryon (d*) with a mass 2.38 GeV and a width $\Gamma \sim 70 MeV$, as suggested by the results of the WASA collaboration in the $pn \rightarrow d\pi^0\pi^0$, $pn \rightarrow d\pi^+\pi^-$ and $pp \rightarrow d\pi^+\pi^0$ reactions [2,3]. The model underestimates the yields measured in the case of the deuteron detected in HADES, which might be due to a contamination of non quasi-free processes. However, when the deuteron is detected in the FW, a reasonable description of the yields and differential distributions is achieved, while the conventional sources alone underestimate the measured yields [5]. A procedure to unfold the neutron momentum distribution and extract the $np \rightarrow np\pi^+\pi^-$ cross section as a function of the center-of-mass energy ($\sqrt{s}$) of the np pair was applied to the experimental data, as well as to simulated events generated either with the model [6] or with a phase-space model. The results are shown in Fig.1. The data have been normalized using quasi-free pp elastic scatter-

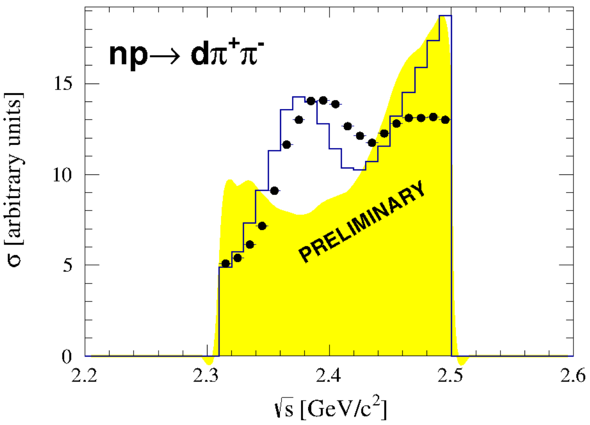

Figure 1: Cross-sections (full symbols) for the quasi-free $pn \rightarrow d\pi^+\pi^-$ reaction deduced from measurements with a deuteron beam at 2.5 GeV, where the two pions are detected in HADES and an additional charged particle is detected in the Forward Wall [5]. The blue histogram shows the result of a simulation taking into account double $\Delta(1232)$, $N(1440)$ and $N(1520)$ excitation, as well as the contribution of a dibaryon with a mass of 2.38 GeV. The data have been normalized using quasi-free pp elastic scattering and are compared to the model predictions on the same absolute scale. The yellow area shows the distribution expected for a phase space simulation of the reaction with an arbitrary normalization.

---

* Work supported by CNRS/IN2P3 (France) and by grant 2013/10/M/ST2/00042 (Poland).

[†] ramstein@ipno.in2p3.fr

DOI:10.15120/GR-2015-1-MU-NQM-HADES-03

ing events and are compared to the model predictions on the same absolute scale, which is displayed here in arbitrary units. The results obtained with the phase space distributions have an arbitrary normalization. A peak is observed in our experimental data. Even though located at a slightly larger $\sqrt{s}$, it is very similar to the one predicted by the model, where it is attributed to the d* contribution. Though systematic effects still need to be investigated, this result seems to confirm the observations of the WASA collaboration.

Dielectron production

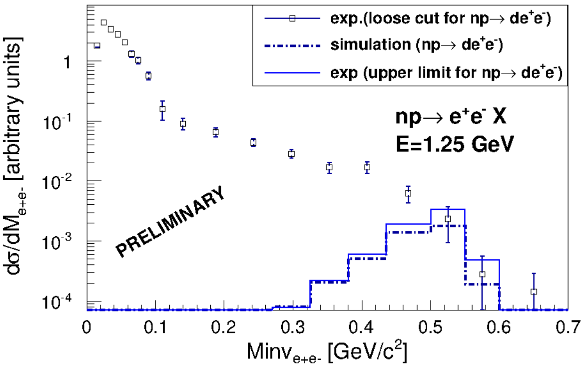

Figure 2: $np \longrightarrow Xe^+e^-$ reaction as a function of the e^+e^- invariant mass [5]. The empty squares and full blue line show experimental results corresponding respectively to a loose cut based on time-of-flights to enhance the contribution of the $np \longrightarrow de^+e^-$ channel and to the upper limit for this reaction. The results of a simulation of the $np \longrightarrow de^+e^-$ process are shown as a dot-dashed blue line. The data have been normalized using quasi-free pp elastic scattering and are compared to the model predictions on the same absolute scale.

In the dielectron channel, no signal for $np \longrightarrow de^+e^-$ reaction is visible. However, the Feldman & Cousins method was applied to extract an upper limit for the differential cross sections of this reaction using constraints from the coplanarity condition. To show the power of this method, this upper limit is displayed in Fig. 2, in comparison to the experimental differential cross sections obtained after appplying only time-of-flight cuts on the FW hits. This upper limit is in agreement with the predictions of [3], where the $np \longrightarrow d\gamma$ differential cross sections are deduced from the known photo disintegration ($np \longrightarrow d\gamma$) cross sections and the extension to virtual photon emission is based on the Vector Dominance Model. However, it is overestimated by 60% by the model [4], which uses an off-shell ρ production due to the $\Delta\Delta$ Final State Interaction.

References

[1] G. Agakichiev et al., Phys. Lett. **B690** (2010) 118.

[2] R. Shyam and U. Mosel Phys. Rev. **C82** (2010) 062201.

[3] B. Martemyanov et al. Phys. Rev. **C84** (2011) 047601

[4] M. Bashkanov and H. Clement Eur. Phys. J. **A50** (2014) 107.

[5] H. Kuc, PhD thesis, Paris-Sud University, Dec. 2014.

[6] P. Alardson et al., Phys. Rev. Lett. **106** (2011) 242302.

[7] P. Alardson et al., Phys. Lett. **721** (2013) 229.

The meaning of signals in pΛ deviation spectra*

E. Epple†[1,2], *L. Fabbietti*[1,2], *and the HADES collaboration*[1]
[1]Excellence Cluster 'Origin and Structure of the Universe' , 85748 Garching, Germany; [2]Physik Department E12, Technische Universität München, 85748 Garching, Germany

Motivation for the analysis

The announcement of a signal of the kaonic nuclear cluster "ppK^-" in p+p reactions (M= 2267 MeV/c^2, Γ= 118 MeV/^{2}) has raised a lot of interest and controversy [1]. The signal appeared in a so-called deviation spectrum (DEV) in IM$_{p\Lambda}$ ($p\Lambda$ invariant mass) from the $pK^+\Lambda$ final state which was produced from a p(2.85 GeV)+p collision system. A DEV spectrum is a division of the measured event distribution by a simulated event distribution. Any signal not included in the simulation which is present in the data will appear in this spectrum as a deviation from unity. Large criticism was raised towards this analysis as the simulations to which the data were compared to contained simple phase space production of the three particles $pK^+\Lambda$. As several experiments have shown that this is not a good assumption for the production dynamics of this final state, the interpretation of the DEV spectrum in Ref. [1] is questionable. The $pK^+\Lambda$ final state is dominated by final-state-interaction between the $p\Lambda$ pair, the cusp-structure at 2.13 GeV in the $p\Lambda$ invariant mass spectrum and the evident presence of N* resonances as a source for the $K^+\Lambda$-pair. This knowledge leads to the assumption that measured data that are divided by phase space simulation will a priory never lead to a DEV spectrum which coincides with unity.

To clarify that point we have repeated the analysis of Ref. [1] on data measured by the HADES detector.

The deviation analysis

The data used for that purpose is a set of events specifically selected to contain mainly the final state of $pK^+\Lambda$ [2, 3]. This final state was obtained from p(3.5 GeV)+p collisions and consists of about 20.000 events. The observable that may contain interesting information whether the kaonic cluster "ppK^-" has left its fingerprints in the data is the invariant mass of $p\Lambda$; these are the decay products of the latter. To cross check the results of Ref. [1], we have also produced phase space simulations of the discussed final state that contain no specific dynamics between the three particles. The simulations were filtered by the HADES acceptance and the event selection procedure. Figure 1 shows the result when the measured data are divided by the phase space simulation (red histogram). As the experimental data can not be described by phase space simulations, as was shown before [3], the spectrum deviates from unity. The very crucial point which we want to stress in this analysis is that further applied cuts do act differently on the data and the simulation, in case the simulations do not describe the data properly. This causes the DEV spectrum to change under varying cut conditions as it is nicely illustrated by the additional histograms in Fig. 1. The long-dashed histogram shows the DEV spectrum under the same cuts as applied for Ref. [1] ($|cos\theta_p|$ < 0.6 and -0.2< $cos\theta_{K^+}$ <0.4). The stricter restriction of the proton angle ($|cos\theta_p|$ < 0.4) leads to the green histogram. While a selection of data under the condition $M_{K^+\Lambda}$ >1810 MeV/c^2 is shown in short dashed. Evidently, structures appear which have nothing to do with an additional physics signal in the data. This questions the interpretation of the structure in Ref. [1]. This result will be the topic of a forthcoming publication.

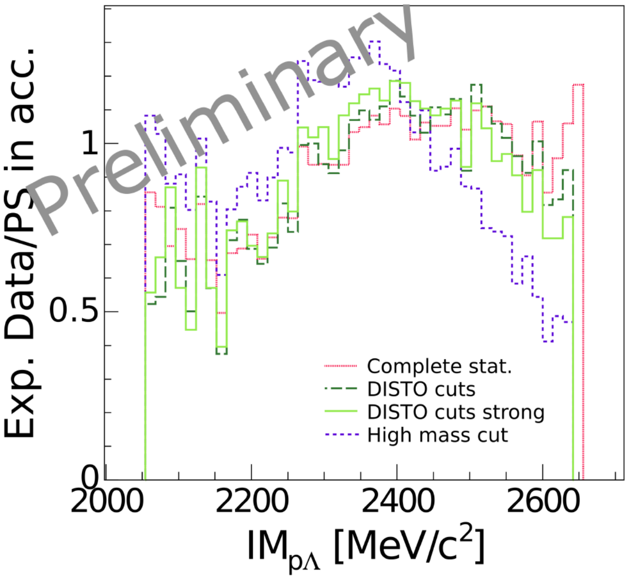

Figure 1: Different deviation spectra, obtained by dividing the reconstructed $pK^+\Lambda$ statistic by phase space simulations in the HADES acceptance.

References

[1] T. Yamazaki *et al.*, Phys. Rev. Lett. **104**, 132502 (2010)

[2] G. Agakishiev *et al.* [HADES Collaboration], Phys. Lett. B **742**, 242 (2015)

[3] L. Fabbietti *et al.* [HADES Collaboration], Nucl. Phys. A **914**, 60 (2013)

---

* Work supported by VH-NG-330 and the DFG cluster of excellence 'Origin and Structure of the Universe'

† eliane.epple@ph.tum.de

DOI:10.15120/GR-2015-1-MU-NQM-HADES-04

Λ production in 3.5 GeV energy p-p reactions at HADES*

R. Lalik[1,2], *E. Epple*[1,2], *and L. Fabbietti*[1,2]

[1]Physik Department E12, Technische Universität München, 85748 Garching, Germany; [2]Excellence Cluster Origin and Structure of the Universe, 85748 Garching, Germany

The understanding of Λ hyperon production in proton-proton reactions is important for a further understanding of strangeness interactions in nuclear matter and it has been studied by HADES at a beam energy of 3.5 GeV. To be able to compare the experimental results with theoretical predictions, resonant and non-resonant contributions to the total production spectrum have been considered, also employing several exclusive Λ-channel analyses from the same reaction. In particular the influence of intermediate resonances like Σ^*, Δ^{++} or N^* to the inclusive Λ production has been considered. Pinning down all contributions will help in tuning transport models (GiBUU and UrQMD) as well will serve in the understanding of the production mechanism of Λ in proton-nucleus reactions. These result will also help to understand future measurements at SIS100 at FAIR.

The Λ baryon is reconstructed in HADES by its charged hadronic decay into a proton and a negative pion. These particles are measured using MDC gas chambers, arranged in four layers of a tracking device immersed in a toroidal magnetic field. Bending of the track in the magnetic field allows to reconstruct the momentum of the particle. This quantity, together with energy deposition of charged particle, are uniquely correlated for each particle species by the Bethe-Bloch equation, allowing for particle identification. Using Invariant Mass technique for combined proton and pion tracks, the mother particle is reconstructed. The primary vertex is reconstructed by intersecting the Λ track with all other tracks leaving the reaction region. The secondary decay vertex of the Λ is associated to the intersection of the proton and pion pairs used in the invariant mass analysis. By applying topological cuts on the secondary and primary vertexes, the misidentification background is reduced and the final yield results in 164 455 candidates with a signal to background ratio of 3.02 in a 3σ mass fit region (fig. 1).

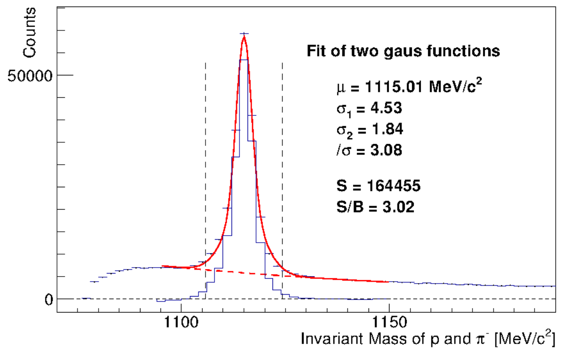

Figure 1: Reconstructed Λ signal yield in pp reaction.

Experimental data have been corrected for the geometrical acceptance and reconstruction efficiency using a simulation model (Pluto) for the production of the contributing channels. The simulation model in this energy range is based on a resonant production model by Tsushima et al. [1,2], where the largest fraction of the kaon production (associated with Λ production) goes through resonant channels (around 90 %, the rest goes via phase-space). Most of the considered channels were measured exclusively at HADES in the same reaction and published by the HADES collaboration [3–6]. A complementary PWA model incorporates results of Partial Wave Analysis by E. Epple [6] for the $pK^+\Lambda$ channel.

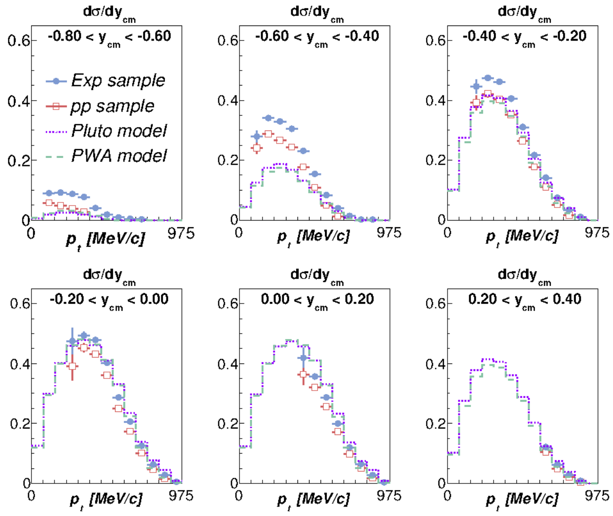

Figure 2: Comparison of experimental data to two models.

Results show good agreement of production yields in mid-rapidity region (fig. 2) but also higher yield of Λs in back-rapidity region. This extra production was partially attributed to hyperon production in Kapton windows of the liquid Hydrogen target and is currently under investigation – further disagreement could imply that the URQMD and GiBUU models need to be further tuned to be able to model the Λ production in p+p collisions at 3.5 GeV.

References

[1] K. Tsushima et al., Phys. Lett. B 390 (1997), p. 29-35

[2] K. Tsushima et al., Phys. Rev. C 59 (1999), p. 369-387

[3] G. Agakishiev et al., Phys. Rev. C 90 (2014), p. 015202

[4] G. Agakishiev et al., arXiv:1410.8188 [nucl-ex]

[5] J. Siebenson, PhD thesis, TUM 2013

[6] E. Epple, PhD thesis, TUM 2014

---

* Work supported by BMBF 05P12WOGHH.

DOI:10.15120/GR-2015-1-MU-NQM-HADES-05

Exploring two-particle correlations in p+Nb reactions*

O. Arnold[1,2], *L. Fabbietti*[1,2], *and the HADES collaboration*[1,2]
[1]Physik Department E12, Technische Universität München, James-Franck-Str. 1, 85748 Garching, Germany;
[2]Excellence Cluster 'Origin and Structure of the Universe', Boltzmannstr. 2, 85748 Garching, Germany

The HADES collaboration measured in 2008 the collision of a proton with a niobium nucleus ($\mathrm{p} + ^{93}\mathrm{Nb}$), where the kinetic energy of the proton was $E_{\text{kin}} = 3.5\ \text{GeV}$. This pA system offers the possibility to study two-particle correlations in an interesting environment, namely in a small system at rather low energies which means low multiplicity. On the one hand side we can compare the results with trends established in heavy-ion collisions at much larger energies to see similarities or find differences and their explanations and on the other hand the measurements are free from correlation-disturbing effects like mini-jets which are produced at LHC energies. The latter point is a good reason to investigate the interaction of particles where the interaction strength is not well established (e.g. between Λ hyperons and protons). It was found in [1] that the $\mathrm{p}\Lambda$ correlation function is sensitive to the size of the particle emission region because the strong interaction between both particles is large enough that they can interact in their final state.
Two-particle correlations are experimentally determined by the ratio:

$$C(k) = \frac{A(k)}{B(k)}. \qquad (1)$$

Here $A(k)$ is the distribution of particles from the same event as a function of the relative momentum in the pair rest frame $k = \frac{1}{2}|\mathbf{p}_a - \mathbf{p}_b|$ and $B(k)$ is the corresponding distribution of pairs from mixed event. This ratio is sensitive to the spatial extension of the particle emitting region for small relative momenta $k < 100\ \mathrm{MeV/c}$. We started in the analysis to establish features of the source e.g. its size and shape. For this purpose we used particles where the interaction is well known: protons and pions. For pions it is also possible to extract a three dimensional source information by measuring the correlations in the longitudinally comoving system (LCMS). In the proton case we can apply the Koonin model with a Gaussian source assumption to the data, which describes the proton-proton correlation function theoretically. We extracted a source size of $2.078 \pm 0.010\ (\text{stat})\ \text{fm}$. For negatively charged pions we extracted a slightly smaller Gaussian source size of $1.797 \pm 0.016\ (\text{stat})\ \text{fm}$. In a next step we compared our measurements to predictions of transport models (UrQMD [2]) and we calculated the correlation function with help of the correlation afterburner CRAB [3]. The result is shown in Figure 1, which displays the comparison of the UrQMD result to the experimental measurement. UrQMD is able to describe the measurements quite well. For this reason we trust UrQMD that it also describes the momentum and configuration space of $\Lambda\mathrm{p}$, which allowed us to determine the source function from UrQMD simulations. We found that for $\Lambda\mathrm{p}$ pairs the source size is 1.24 times smaller compared to the proton-proton case. We will use this information to extract the (spin averaged) scattering length and effective range of the $\Lambda\mathrm{p}$ interaction. With help of CRAB we can also test different two-particle interaction models and constrain their parameter space.

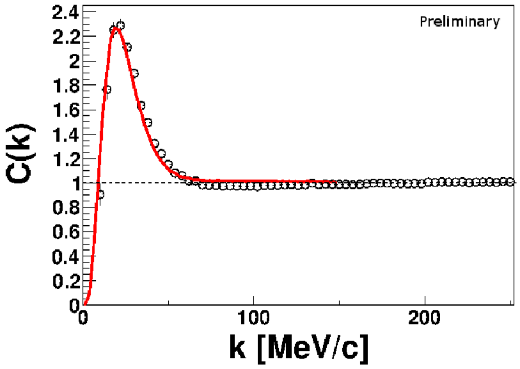

Figure 1: Proton-proton correlation function. The open circles show the experimental correlation function corrected for all inefficiencies. The (red) solid line is the correlation function determined from UrQMD simulations.

To summarize, we measured two-particle correlations in a pA system. We extracted the source size for like-sign pions and for protons. The measurement of the proton source size helped us to pin-down the interaction region of the $\Lambda\mathrm{p}$ pair. With this information we are able to study the interaction between these particles and test different interaction hypothesis with help of the correlation afterburner CRAB.

References

[1] F. Wang, S. Pratt, , "Lambda-Proton Correlations in Relativistic Heavy Ion Collisions", Phys. Rev. Lett. 83, 3138

[2] S. A. Bass *et. al.*, "Microscopic Models for Ultrarelativistic Heavy Ion Collisions", Prog. Part. Nucl. Phys. 41 (1998) 225-370

[3] S. Pratt, "Correlation afterburner CRAB version 3", http://www.pa.msu.edu/~pratts/freecodes/crab/home.html

---

* Work supported by HIC4FAIR

DOI:10.15120/GR-2015-1-MU-NQM-HADES-06

Backtracking algorithm for lepton reconstruction with HADES *

P. Sellheim[1] *for the HADES Collaboration*
[1]Goethe-Universitä Frankfurt, Frankfurt am Main, Germany

Events recorded in Au+Au collisions at a beam energy of 1.23 GeV/u have the highest multiplicities measured with HADES [1]. The track reconstruction and particle identification in the high track density environment are challenging. In case of dileptons: (i) A Ring Imaging Cherenkov detector (RICH) [2] is essential since it is the most important detector component for single lepton identification; (ii) one has to cope with large combinatorial background stemming from γ conversion and π^0 Dalitz decays.

In order to further improve the purity and efficiency of an electron sample, a new backtracking algorithm using information provided by tracking and Time-of-Flight detectors is applied. Furthermore in the special case of close tracks, with opening angles smaller than 4°, rings are overlapping and do not have a perfect ring shape. Thanks to its excellent double hit resolution, by using the expectation of nearby tracks backtracking will be able to resolve such patterns and identify both leptons.

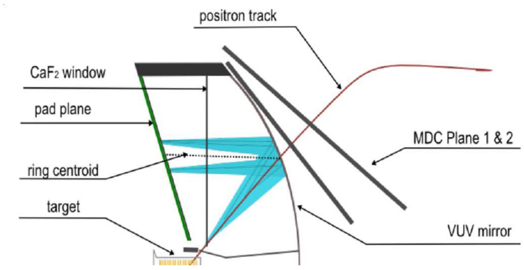

Figure 1: Schematic side view of the RICH detector. A positron track shows usage of angular information to determine a ring center.

In detail, only tracks preselected by velocity information provided by Time-of-Flight detectors and energy loss measured in Multi-wire drift chambers are used as possible lepton candidates. Those candidates are used to predict a possible ring on the RICH pad-plane based on angular track information (see Fig.1). Out of it the centroid position on the RICH photon detection plane is fixed. Using a simulation based ring parametrization, potential areas with a high photon hit probability are predicted.

An example of a ring prediction is shown in Figure 2. Two predicted rings and photon hits measured by the photon detection plane are plotted. The most basic observables are the sum of charge, pads and clusters. Pads where horizontal and vertical neighbors have a lower charge than the pad itself are called maxima and are summed up as well. Additionally a ring quality based on the difference between the actual photon hit and the most probable hit position is calculated. For special cases of overlapping rings, information of shared maxima is also considered. An application of the backtracking algorithm to simulated and real data has shown that the number of pads per ring and maxima per ring are the most powerful to distinguish between leptons and hadrons. Especially maxima are a good measure since they correspond to the number of photons per ring.

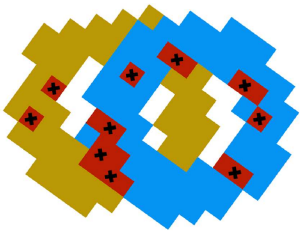

Figure 2: Overlapping rings predicted by ring parametrization. Fired RICH Pads are indicated by dark red boxes and the maximum position of clusters is marked with crosses.

Finally, backtracking was also tested for close pair rejection in simulated data. Above 2° ring predictions are not overlapping anymore. Therefore backtracking information is useful to identify the close partner of a lepton in order to reject close pairs. Figure 3 demonstrates a further rejection of combinatorial background due to a reduction of close pairs. In contrast the signal of ω pairs is not reduced significantly.

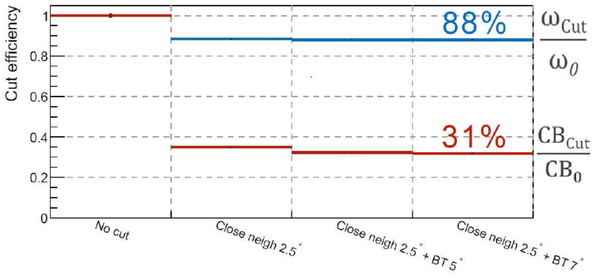

Figure 3: Cut efficiency of close pair cuts. Additionally to a close neighbor cut demonstrated in the second column backtracking information is used in columns 3 and 4 for further close pair rejection.

References

[1] G. Agakishiev and the HADES collaboration , Eur.Phys.J.A 41 (2009) 243-277

[2] K. Zeitelhack and the HADES collaboration, Instr. Meth. A 433 (1999) 201-206

---

* This work has been supported by BMBF (05P12RFGHJ), GSI, Helmholtz Alliance EMMI, HIC for FAIR, HGS-HIRe and H-QM.

DOI:10.15120/GR-2015-1-MU-NQM-HADES-07

Acceptance correction for the dilepton combinatorial background in HADES*

S. Harabasz[1,2] *for the HADES Collaboration*
[1]Technische Universität Darmstadt, Darmstadt, Germany; [2]Jagiellonian University, Kraków, Poland

In 2012 HADES [1] has measured Au+Au collisions at a beam kinetic energy of 1.23 GeV/u. In the data analysis, single e^+/e^- tracks are identified by an appropriate selection cut in a multivariate feature space of RICH ring observables, time-of-flight, PreShower and energy loss signals, provided by corresponding detectors [2].

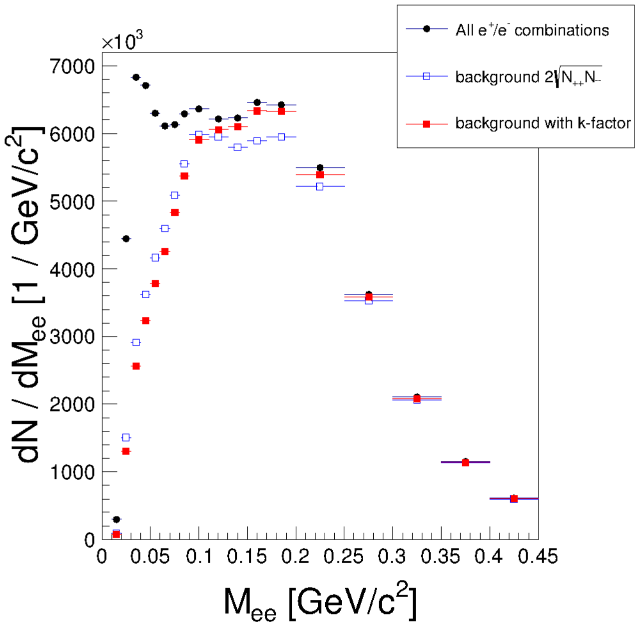

Figure 1: Invariant mass of all e^+/e^- combinations and CB calculated as geometrical average of e^+e^+ and e^-e^- yields and also weighted with the k-factor.

In heavy-ion collisions the only viable method for extracting the signal of correlated e^+/e^- pairs is to combine all e^+ and e^- in the event and then, from final spectra (invariant mass, rapidity, transverse momentum etc.), subtract the contribution due to combinatorial background (CB). The background can be estimated as $N_{+-}^{\mathrm{bgr}} = 2\sqrt{N_{++}N_{--}}k$ with $k = \frac{\kappa_{+-}}{2\sqrt{\kappa_{++}\kappa_{--}}}$, where N's represent yields of like-sign lepton pairs and κ's are acceptances of the detector system for pairs of different signs. Here only the ratios of acceptances are involved, so it is enough to compare yields of uncorrelated pairs of different signs obtained from event mixing [3].

In the current work we intend to prove the necessity of correcting the combinatorial background for the pair acceptance. Single track identification is performed in a way discussed in the Annual Report 2013 [2].

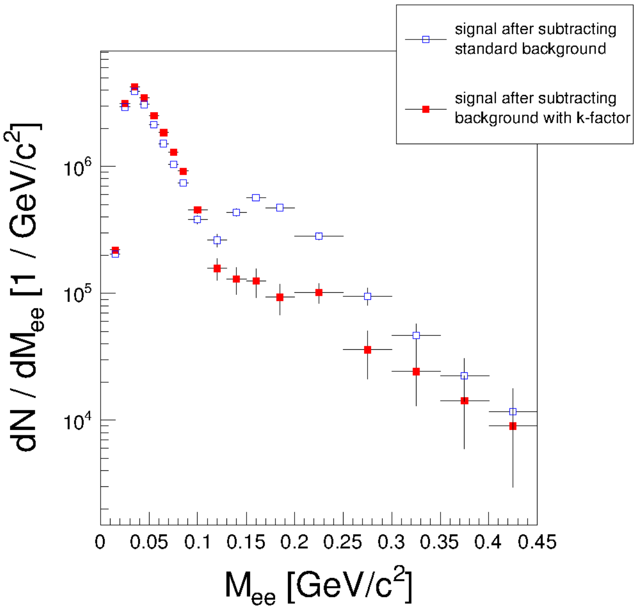

Figure 2: Invariant mass distribution of dilepton signal (not efficiency-corrected) after subtracting combinatorial background calculated in the two ways.

Fig. 1 shows the distribution of invariant mass of all e^+/e^- pair combinations and the combinatorial background calculated with the acceptance asymmetry factor k and without it. Background calculated in a simple way cannot follow the enhancement of the yield between 0.1 and 0.2 GeV/c². This is reflected also by signal spectra obtained after subtracting CB, as shown in Fig. 2, where an unphysical maximum appears at around 0.15 GeV/c².

As systematic study of the multi-differential behavior of the k-factor and its dependence on the way how the event mixing is performed and on the regions of the HADES acceptance is currently on-going.

References

[1] G. Agakishiev et al. (HADES Collaboration), Eur.Phys.J.A41:243-277, 2009

[2] S. Harabasz et al. "Electron identification in Au+Au collisions at 1.23 GeV/u in HADES using multivariate analysis", GSI Scientific Report 2013

[3] M. Köhler, Nucl. Phys. A931 (2014) 665-669

---

* Work supported by VH-NG-823, BMBF (06FY9100I and 06FY7114), HIC for FAIR, EMMI, GSI, HGS-HIRe and H-QM.

DOI:10.15120/GR-2015-1-MU-NQM-HADES-08

π^0 reconstruction via conversion method in Au+Au at 1.23AGeV with HADES*

C. Behnke[1], *J. Stroth*[1,2], *T. Galatyuk*[2,3], *M. Gumberidze*[2,3] *for the HADES Collaboration*[1]
[1]Goethe-Universität, Frankfurt; [2]GSI; [3]TU, Darmstadt

Lepton pairs emerging from decays of virtual photons are one of the most promising probes of dense hadronic matter. Comprehensive information on meson production is thereby mandatory to benchmark and constrain contributions from freeze out. In this context the neutral pion and eta mesons are of particular interest as they contribute largely to the dilepton spectrum via their Dalitz decays $\pi^0/\eta \rightarrow \gamma e^+e^-$. HADES [1] in April/May 2012 measured the collision system Au+Au at the highest achievable beam energies (presently at SIS18), E_{kin} = 1.23 GeV/u. Since HADES has no photon detector yet, the measurement of the photonic decays of the π^0 is only possible via external conversion of photons in detector material. Average conversion probabilities of π^0 decay photons obtained from simulations is on the order of 0,36% (taking into account the Au target, the target holder, the δ-electron shield, the beam pipe and the RICH radiator gas). To study π^0 reconstruction leptons have been identified using the correlation between the velocity (β) and the momentum. Such identified leptons have been joined into opposite sign e^+e^- pairs and further combined into $e^+e^-e^+e^-$ multiplets. In the next step of the analysis, topological selection criteria on opening angle between the leptons in a given pair were used to identify conversion pairs (α_1 <2.5°) and Dalitz pairs (α_1 <7.5°) at the same time (for details see [2,3]). The angle between the two photons is restricted to be in the kinematically possible region $\Theta_{\gamma\gamma}$ 10-50. Fig. 1 shows a preliminary invariant mass spectrum of $e^+e^-e^+e^-$ multiplets. A clear signal peak is visible at the nominal mass position of the π^0 (135 MeV). The mass spectrum is shown together with a background obtained via event mixing. Simulations show that the main background in the 4 lepton invariant mass spectrum originates from uncorrelated photons and virtual photons. After subtraction of the background and fitting the remaining spectrum with a Gaussian peak the extracted count rate is in the order of 8000 signal counts. This allows for a phase space depended analysis. In Fig. 2 the extracted and efficiency corrected yields as a function of transversal mass M_t and rapidity Y are shown. Due to missing acceptance for low momentum leptons (P <50 MeV/c) the spectra only shows the high $p_\perp$ yield of the π^0. This can be fitted with a single slope fit and a mean slope parameter can be extracted.

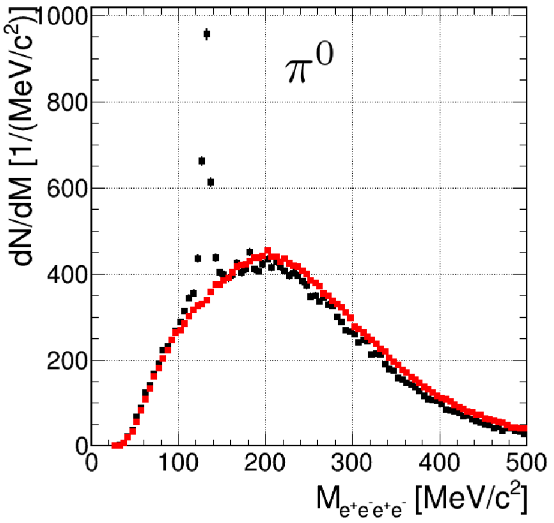

Figure 1: 4 lepton invariant mass spectrum after the topological cuts, together with event mixing.

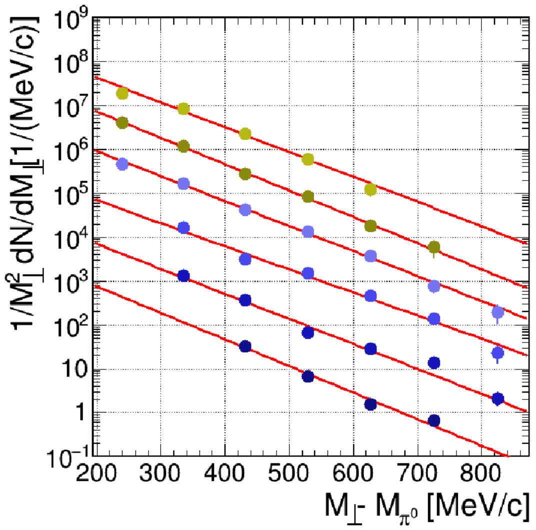

Figure 2: Efficiency corrected transversal mass yields as a function of rapidity (Rapidity: 0.2,0.4,0.6,0.8,1.0,1.2,1.4)

References

[1] G. Agakishiev *et al.*, Eur. Phys. J. A **41** (2009) 243

[2] G. Agakishiev *et al.*, Phys. Rev. C 88, 024904 (2013).

[3] C. Behnke, J.Phys.Conf.Ser. 503 (2014) 012015

---

* Work supported by BMBF (06 FY 9100 I), HIC for FAIR, VH-NG-823,HGS-Hire, H-QM and EMMI

DOI:10.15120/GR-2015-1-MU-NQM-HADES-09

Production of charged pions in the Au+Au at 1.23 AGeV reaction[*]

M. Gumberidze[1], *P. Tlusty*[2] *and H. Schuldes*[3] *for the HADES Collaboration*
[1]Technische Universität Darmstadt, Darmstadt, Germany; [2]Nuclear Physics Institute, Academy of Sciences, 25068 Rez, Czech Republic; [3]Institut fur Kernphysik, Johann Wolfgang Goethe-Universitat, 60438 Frankfurt, Germany

The High Acceptance DiElectron Spectrometer HADES [1] is devoted mainly to study production of dielectron pairs from proton, pion and nucleus induced reactions at 1-2 AGeV. At the same time, the spectrometer provides detection and high quality identification of charged particles with a large solid angle.

In this contribution we focus on the analysis of charged pion production in Au + Au collisions at 1.23 AGeV. The results contribute to the data from systematic studies of pion production in heavy ion collisions with an unprecendented statistics, and serve as an input for the normalization of the dielectron data obtained in the same experiment.

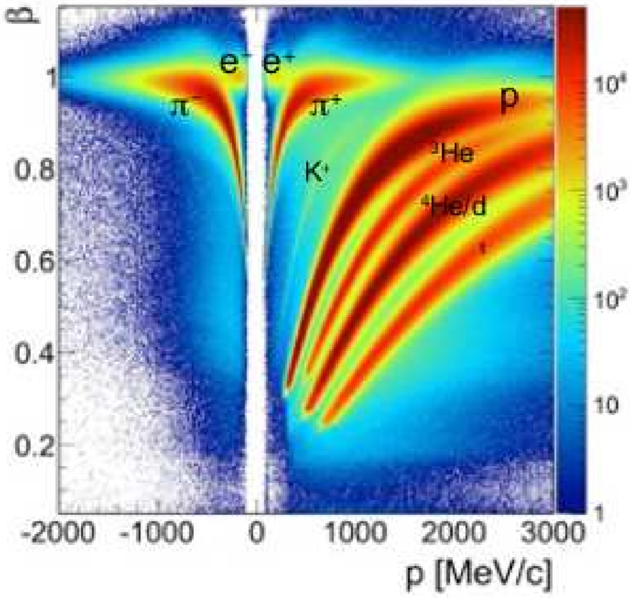

Figure 1: Velocity vs. charge-times-momentum of charged particles in HADES.

In April/May 2012, HADES has measured rare and penetrating probes in Au+Au collisions at 1.23 AGeV. About seven billion collisions have been recorded in with an event rate of 10 kHz.

For the particle identification, the velocity of particles detected in the time-of-flight detectors as a function of momentum was used (Fig. 1). Resulting yields were corrected for efficiency, acceptance and purity of the PID method, as well as for the detector and tracking inefficiencies using Monte Carlo simulations.

Preliminary results on π^- production are presented in Figure 2, showing the measured transverse mass distributions of π^- in different intervals of rapidity. The transverse-mass (m_t) distributions have been fitted for each rapidity bin using the sum of two exponential functions:

$$\frac{1}{m_t^2}\frac{dN(y)}{dm_t} = C_1(y)e^{-\frac{m_t}{T_1(y)}} + C_2(y)e^{-\frac{m_t}{T_2(y)}}$$

with $m_t = (p_t^2 + m^2)^{1/2}$, and p_t as transverse momentum. $C_{1,2}$ are normalizations and $T_{1,2}$ the inverse slope parameters.

Due to the wide acceptance of the present experiment we will be able to do a direct comparison of the HADES data with the results of previous experiments of charged pions done by e.g. FOPI collaboration [2].

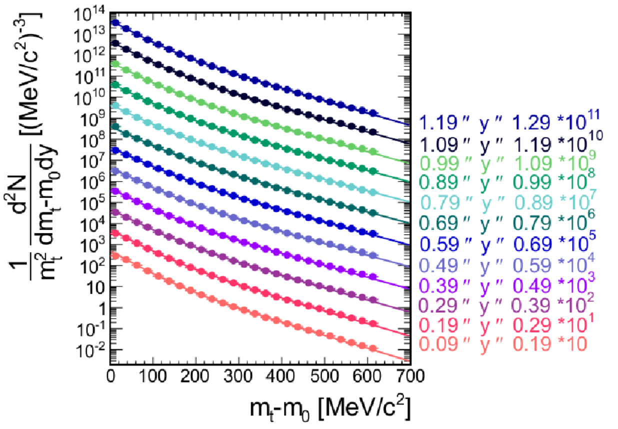

Figure 2: Transverse-mass distributions for negatively charged pions in different slices of rapidity. Full lines show the results of fits to the data (closed points) using the sum of two exponential functions.

Our preliminary results show that the p_t and y integrated negative pions yields are consistent with the FOPI data. More detailed comparisons are ongoing.

References

[1] G. Agakishiev *et al.* [HADES Collaboration], Eur. Phys. J. A 41 (2009) 243.

[2] W. Reisdorf et al. (FOPI Collaboration) Nucl. Phys. A 781 (207) 459-508.

---

[*] Work supported by TU Darmstadt: VH-NG-823, GSI, Helmholtz Alliance HA216/EMMI, SIP JUC Cracow: 2013/10/M/ST2/00042 and NN202198639, HIC for FAIR, NPI Rez: GACR 13-067595 and AS CR M100481202, HGS-HIRe and H-QM.

DOI:10.15120/GR-2015-1-MU-NQM-HADES-10

Revisiting hadron production at SIS energies using new HADES data *

M. Lorenz †[1,2], *T. Scheib*[2], *H. Schuldes*[2], *and the HADES collaboration**
[1]University Utrecht, Netherlands; [2]GU, Frankfurt, Germany

We present preliminary results on the production of hadrons with strangeness content (K^+, K^-, K^0_s, Λ and ϕ) in Au+Au collisions. At the measured center of mass energy of $\sqrt{s}$ = 2.4 GeV all hadrons carrying strangeness are produced below their free nucleon-nucleon threshold. While the K^-/K^+ ratio nicely fits the trend observed at higher energies, we find a strong rise of the ϕ/K^- ratio.

The data taking took place in April/May 2012. The readout was started with a multiplicity trigger, running with an average rate of 8 kHz during the spills. The total data sample corresponds to 7.3x10^9 events. Reconstructed tracks pass a track selection based on several quality parameters delivered by a newly developed high density tracking algorithm. Afterwards, hadrons are identified using the time-of-flight measurement.

In order to minimize systematic errors due to efficiency corrections and extrapolations in rapidity, we build ratios of the corrected yields at mid-rapidity for various hadron species which feature a comparable width in rapidity. The resulting K^-/K^+ ratio can be directly compared to the previously obtained systematics at similar energy, without correcting for the different centrality selections of the various experiments, as both kaons experience a similar A_{part} dependence [1]. The measured ratio K^-/K^+ fits into the trend observed at slightly higher energies and extrapolated down to the beam energy of 1.23 A GeV.

An interesting observable is the ϕ/K^- ratio: It shows a flat trend at high energies, and is experimentally observed to rise towards lower energies [2]. This rise can be reproduced in the framework of the statistical model, if the suppression of strangeness is handled by introducing a strangeness correlation radius R_c within which strangeness has to be exactly conserved [3]. It is important to realize that, as the ϕ conserves strangeness by definition, it is not suppressed by the strangeness correlation parameter in contrast to the other particles containing strange quarks.

We simultaneously fit the π^-/p, K^0_s/Λ, K^-/K^+ and the ϕ/K^- ratio using the freely available statistical model THERMUS [4]. Similar as for our fit to the Ar+KCl data sample [5] we constrain the charge chemical potential μ_Q using the ratio of the baryon and charge numbers of the collision system, conserve the baryon number on average via the chemical potential μ_b and calculate strangeness canonically by introducing the additional sub volume defined by R_c. As we are restricted to ratios we fix the radius of the fireball R arbitrarily to 3 fm. In this way we find the chemical freeze-out at a temperature of $T_{chem} = (47 \pm 5)$ MeV and at a baryochemical potential of $\mu_b = (799 \pm 22)$ MeV. The ratio R_c/R is determined to 0.3 ± 0.2 while the χ^2/d.o.f. of the fit corresponds to 1.2. We note that our freeze-out point fits remarkably well to the result obtained in [6] for a similar system but restricted to fewer identified particles. Also R_c/R agrees within errors with the value obtained in our Ar+KCl fit of 0.5 ± 0.3. Going from the medium-sized Ar+KCl system (measured at 1.76 AGeV) to the heavy Au+Au system the ϕ/K^- ratio rises strongly. This effect is reproduced by statistical model calculations, using the above discussed parameters (especially R_c).

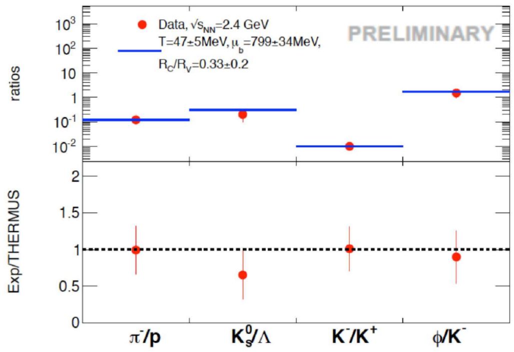

Figure 1: Comparison of hadron yields ratios of model and data, together with values obtained for the free parameters of the statistical model fit, see text for details.

References

[1] A. Forster, F. Uhlig, I. Bottcher, D. Brill, M. Debowski, F. Dohrmann, E. Grosse and P. Koczon *et al.*, Phys. Rev. C **75** 024906 (2007).

[2] A. Mangiarotti *et al.* [FOPI Collaboration], Nucl. Phys. A **714** 89 (2003), G. Agakishiev *et al.* [HADES Collaboration], Phys. Rev. C **80** 025209 (2009).

[3] I. Kraus, J. Cleymans, H. Oeschler, K. Redlich and S. Wheaton, Phys. Rev. C **76**, 064903 (2007).

[4] S. Wheaton and J. Cleymans, Comput. Phys. Commun. **180** 84 (2009).

[5] G. Agakishiev *et al.* [HADES Collaboration], Eur. Phys. J. A **47** 21 (2011).

[6] J. Cleymans, H. Oeschler, K. Redlich and S. Wheaton, Phys. Rev. C **73**, 034905 (2006).

---

* Work supported by GSI, HIC4FAIR, HGShire

† m.lorenz@gsi.de

DOI:10.15120/GR-2015-1-MU-NQM-HADES-11

Investigations concerning the set of MVA input variables*

C. Ungethuem[1] *for the HADES collaboration*
[1]TU Darmstadt, Darmstadt, Germany

To reconstruct a dilepton spectrum measured by HADES in the Au (1.23 GeV) + Au reaction one first has to apply several cuts on the data to identify leptons. Besides the so-called "hard cut" method, the multivariate analysis (MVA) can be used to apply a multidimensional cut, which reaches higher lepton sample purity and a higher efficiency.

Each particle which was detected in HADES is characterised by a set of observables, like the velocity β, the reconstructed momentum, specific energy loss in drift chambers and in Time of Flight detector, electromagnetic shower information and ring properties as provided by the RICH detector. Each observable can help to distinguish between leptons (signal) and hadrons (background). The most powerful one is the ring matching quality, called richQa variable, which is defined as

$$\text{richQa} = \sqrt{(\Delta\phi sin\theta)^2 + \Delta\theta^2} \tag{1}$$

with

$$\Delta\theta = \theta_{Ring} - \theta_{Runge-Kutta}, \tag{2}$$

$$\Delta\phi = \phi_{Ring} - \phi_{Runge-Kutta}, \tag{3}$$

where ϕ_{Ring} is the azimuth angle and θ_{Ring} the polar angle of the reconstructed ring center, combined with the corresponding track angles reconstructed by the Runge-Kutta method. The input samples for training the neural network of the MVA are defined by the richQa value. Signal (leptons) has a richQa $< 0.5°$, whereas the background (hadrons) has a richQa $> 7°$. After training the neural network, which is offered by the TMVA [1], with the signal and background data samples one gets an Multi Layer Perceptron (MLP) classifier as a response, taking values between 0 and 1. After a cut on the MLP and richQa value, around 70 % of all lepton candidates survive with a lepton purity larger than 99 %. The β versus momentum distribution before and after a cut based on the experimental data is shown in Fig. 1. Two different cases were investigated: Training the neural network with or without using θ as an input variable. Looking through the momentum distribution in Fig. 2 (upper panel) one can conclude that there are no differences visible between the two cases. To determine purity in the experimental data the "rotated RICH detector" method is used. One rotates the RICH detector, which consists of six sectors, software wise by 60° and after pursuing the same data analysis one gets only the wrongly matched rings to reconstructed tracks, i.e. the back-ground. Also in the "rotated RICH detector" analysis one can conclude that it makes no difference if θ is included or not as an input variable to MVA. Therefore we kept θ as an input variable for further analysis.

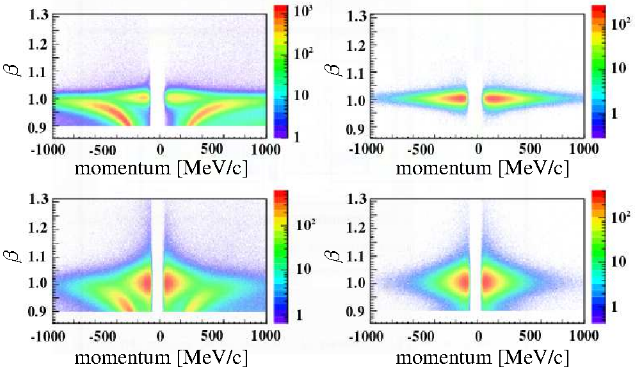

Figure 1: **Left:** Measured β vs momentum distribution without cut. **Right:** Identified leptons after a cut on MLP > 0.6 and richQa < 2.
(Upper panel: RPC detector, Lower panel: TOF detector)

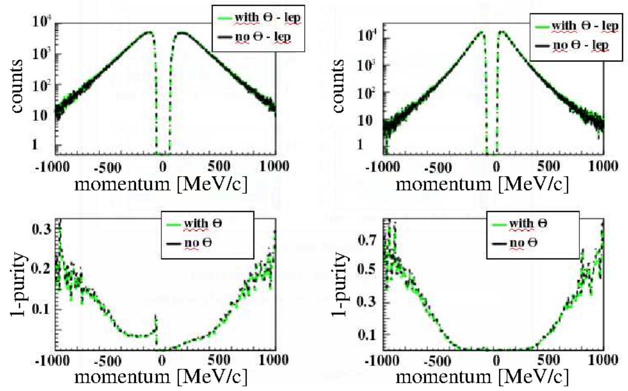

Figure 2: **Upper panel:** Momentum distribution for leptons before and after applied cuts. **Lower panel:** Rotated RICH momentum distribution divided by the "normal" momentum distribution of identified leptons.
(Left: RPC detector, Right: TOF detector)

References

[1] A. Hoecker et al., "TMVA - Toolkit for Multivariate Data Analysis", (2007) arXiv:physics/0703039

---

* Work supported by VH-NG-823, Helmholtz Alliance HA216/EMMI and GSI

DOI:10.15120/GR-2015-1-MU-NQM-HADES-12

Reconstruction of virtual photons with HADES*

S. Harabasz[1,2], *P. Salabura*[2], *T. Galatyuk*[1] *and M. Gumberidze*[1] *for the HADES Collaboration*
[1]Technische Universität Darmstadt, Darmstadt, Germany; [2]Jagiellonian University, Kraków, Poland

Introduction

The HADES [1] explores strongly interacting baryon-rich matter at moderate temperatures using rare and penetrating probes. It operates in the beam-energy range of $1-2A$ GeV where relatively long-lived states of compressed matter are formed. The challenge is to detect them in the laboratory by isolating their unambiguous signals. Among the observables for investigating the microscopic properties of such states of matter, virtual photons are one of the most promising. Baryon-driven medium effects influence significantly the ρ meson in-medium spectral function and are considered [2] to be the key for describing the low-mass dilepton spectra measured at low energies.

Au+Au data analysis

About seven billion Au+Au collisions at $1.23A$ GeV have been recorded in April/May 2012 with the mean data rate during the flat top of the extracted beam of 100 MBytes/s and an event rate of 10 kHz.

Data readout was triggered by a first-level (LVL1) decision requiring charged particle multiplicity MUL ≥ 20 in the Time-of-Flight wall, selecting the 40% most central Au+Au collisions. All events with a positive LVL1 decision were written to tape (in total $4.5 \cdot 10^9$ events). Track reconstruction, electron identification, and electron pair (opposite- and like-sign) reconstruction were performed as described in [3].

Combinatorial background (CB) was obtained from same-event like-sign pairs using the geometric mean $\frac{dN^{CB}_{+-}}{dM} \equiv 2 \times \left(\frac{dN_{++}}{dM} \times \frac{dN_{--}}{dM}\right)^{1/2}$ to account for correlated background from double conversion of π^0 decay photons or conversion of the photon accompanying Dalitz decays, as well as for uncorrelated e^+e^- stemming from multi-pion decays. The final invariant-mass distribution was obtained by subtracting the CB pairs from all same-event opposite-sign pairs.

HADES does not provide data corrected for the geometrical acceptance. Only efficiency effects due to the analysis cuts and the intrinsic detection efficiency are corrected for directly during the data analysis, before comparing final measured spectra to theoretical models. The reconstruction efficiency of single tracks was determined using a track embedding technique.

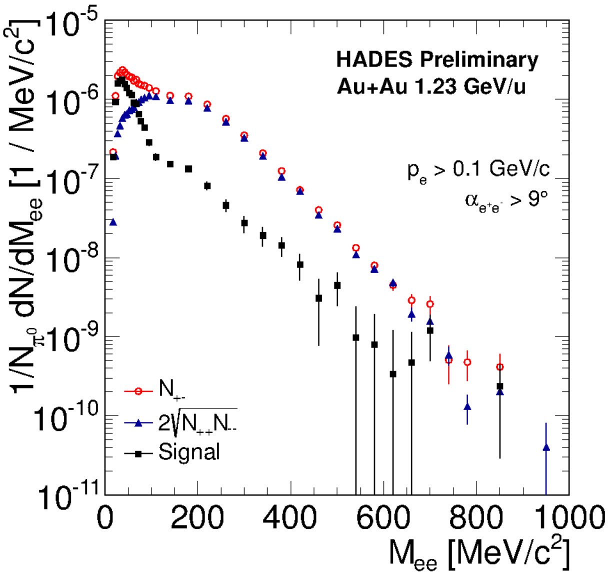

Figure 1: Invariant-mass distribution of all (open red circles), signal (black squares) lepton pairs measured with HADES in the $1.23A$ GeV Au+Au reactions. The background of uncorrelated combinations obtained from geometrical average of same-event like-sign pairs is shown as well (blue triangles).

The resulting invariant-mass spectrum of dielectrons, corrected for detector and reconstruction efficiencies, is shown in Fig. 1. In total, 1.3×10^5 signal pairs, 2×10^4 thereof in the region above 0.15 GeV/c^2 with a signal-to-CB ratio of 0.1, were reconstructed. This statistics is high enough to characterize the dielectron yield beyond the mass distribution and will allow to compare the data to predictions from various model calculations [4, 5, 6].

References

[1] G. Agakishiev *et al.* [HADES Collaboration], Eur. Phys. J. A 41 (2009) 243

[2] R. Rapp, J. Phys. Conf. Ser. 420 (2013) 012017

[3] S. Harabasz *et al.* [HADES Collaboration], J.Phys.Conf.Ser. 503 (2014) 012014

[4] J. Weil *et al.*, J. Phys. Conf. Ser. 426 (2013) 012035

[5] E.L. Bratkovskaya *et al.*, Phys. Rev. C 87 (2013) 6, 064907

[6] S. Endres *et al.*, Acta Phys. Polon. Supp. 7 (2014) 1, 173-182

---

* Work supported by TU Darmstadt: VH-NG-823, GSI, Helmholtz Alliance HA216/EMMI, SIP JUC Cracow: 2013/10/M/ST2/00042 and NN202198639, HIC for FAIR, HGS-HIRe and H-QM.

DOI:10.15120/GR-2015-1-MU-NQM-HADES-13

Cherenkov photon detection with the HADES RICH in Au + Au collisions*

T. Kunz[†1], *J. Friese*[1] , *K. Schmidt-Sommerfeld*[1]
[1]Phys. Dept. E12, TU München, Garching, Germany

In the past years, the HADES experiment has undergone a mayor upgrade of the detector readout and DAQ system [1] to enhance its performance stability and count rate capabilities also for collision systems like Au + Au. Within this enterprise, the GASSIPLEX based frontend electronics of the gaseous MWPC type **R**ing **I**maging **Ch**erenkov detector has been replaced by readout cards utilizing the APV25S1 amplifier chip [2]. The photon detector is operated with CH_4 at normal pressure and equipped with a CsI photo cathode sensitive in the wavelength region 150 nm < λ < 200 nm. Consequently, we have performed a dedicated study of the MWPC response to single photo electrons and updated the detector modelling in the HADES analysis and simulation framework Hydra such as to allow for proper electron and positron identification in the recent Au + Au experimental runs.

In an off-line experiment we have used ^{241}Am α-particle induced xenon excimer emission around $\lambda \sim 170$ nm to illuminate the whole detector plane with a photon areal density $10^{-3}\ \mathrm{cm}^{-2} < \rho < 10^{-1}\mathrm{cm}^{-2}$ per emission event. Events triggered by correlated α-particles were recorded with rates 0.1 kHz < R < 30 kHz for various MWPC anode voltages $2200\ \mathrm{V} < U_{an} < 2500\ \mathrm{V}$. Up to $\sim 10^4$ photo electron induced signals have been recorded for each of the 28272 pads allowing for a systematic study of the detector response to single VUV photons.

The zero bias pulse height distribution for each pad exhibits for nearly all voltages a clear single photo electron signal at higher amplitudes. A sample spectrum is shown in the left panel of Figure 1. Recorded photon signals with noise suppressing 3σ thresholds (Figure 1, right panel) show after noise subtraction for each photon a pad cluster size ranging from 1 to 4 pads with an average multiplicity $\langle M_{pad} \rangle = 1.3$. Simulations with tuned detector model parameters reproduce amplitudes and pad coupling in all aspects reasonably well. The photo electron detection efficiency varies in the range $0.88 < \varepsilon_{se} < 0.94$ across the whole pad plane. With a preliminary calibration of the emitted photon yield per trigger we extract a ~ 20% reduction of the overall photon detection efficiency compared to values determined in experimental runs before.

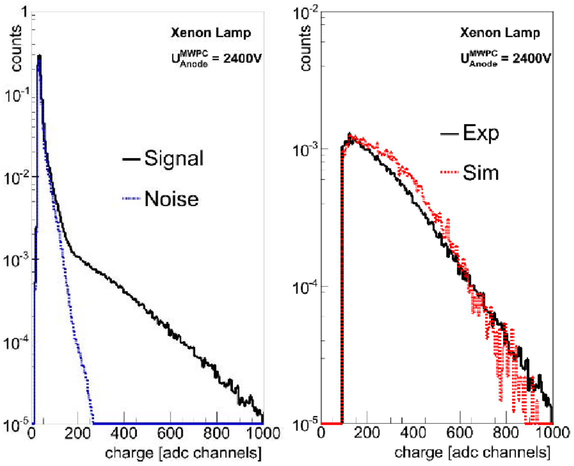

Figure 1: Pulse height spectra with noise contribution (left) and for single photon signals after noise subtraction in comparison to detector simulations (right).

Cherenkov photons radiated by electrons and positrons from reconstructed π^0 – Dalitz e^+e^- pair decays were then used to verify the photon detector response in Au + Au reactions at E = 1.23 AGeV. In spite of the high charged particle multiplicity environment and significant background in the photon detector, Cherenkov rings could be identified and analysed. The observed signal distributions of the ring and pad patterns show reasonably good agreement with the VUV lamp data and the detector model simulations. Figure 2 shows as an example the pad multiplicity per ring (left panel) and the relative cluster type abundances attributed to single and multiple photon hits in the ring (right panel).

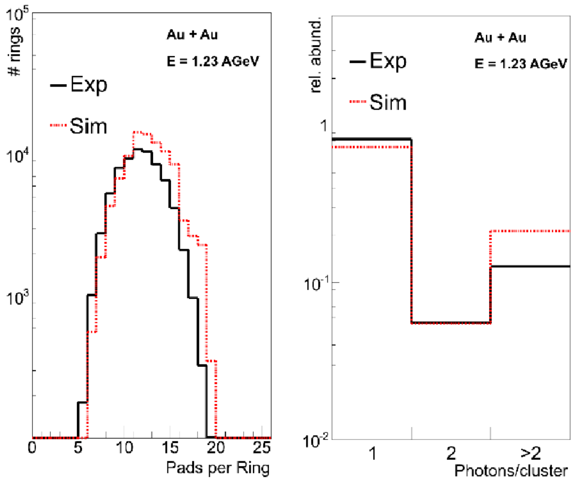

Figure 2: Pad multiplicity and cluster type abundance distributions in identified Cherenkov rings measured and simulated for reconstructed e^+/e^- tracks in Au + Au collisions.

After more than a decade of operation, the MWPC photon detector with the new frontend electronics is still capable to detect Cherenkov rings even in Au + Au collisions, albeit with a somewhat lower overall efficiency.

[1] J. Michel et al., IEEE Trans. Nucl. Sci. 58 (2011)
[2] L.L. Jones et al., CERN/LHCC/99-09 162

---

* Work supported by BMBF 05P12WOGHH, GSI TMLFRG316

[†] Tobias.Kunz@tum.de

DOI:10.15120/GR-2015-1-MU-NQM-HADES-14

Analysis of the microstructure of Cosmic Ray air showers using the HADES RPC ToF wall detectors

J. A. Garzón[*1] *and G. Kornakov*[2] *on behalf of the HADES RPC ToF wall group*
[1]LabCAF, F. Física, Univ. Santiago de Compostela, Spain; [2]Technische Universität Darmstadt, Germany

Abstract

Five days long, in October 2009, during the commissioning of the HADES RPC ToF wall detectors, more than 30 million of events with cosmic ray data were taken with unprecedented accuracy at the Earth's surface. A careful analysis of those data did allow to study the microstructure of cosmic ray air showers and to unveil some evidence of previously unseen features.

The HADES RPC ToF wall commissioning

One of the most important steps in the upgrade of the HADES (High Acceptance DiElectron Spectrometer), aimed at increasing the nuclear masses accessible, was the development of a new time of flight wall based on the modern tRPC (timing Resistive Plate Chamber) technology. The new detector was commissioned using cosmic rays during a couple of months in Fall 2009 close to the HADES cave. During this period, all of the $\sim$ 1.2 m^2 sextants of the detector where operated in couples, one on top of each other, at a distance of roughly 30 cm. A very patient work was done in order to synchronize all read out channels, and getting a data sample offering a track time resolution of $\sim$ 170 ps, a mean position resolution of $\sim$ 5 cm^2, a granularity of $\sim$ $100/m^2$ and a track mean angular resolution of $\sim 4°$.

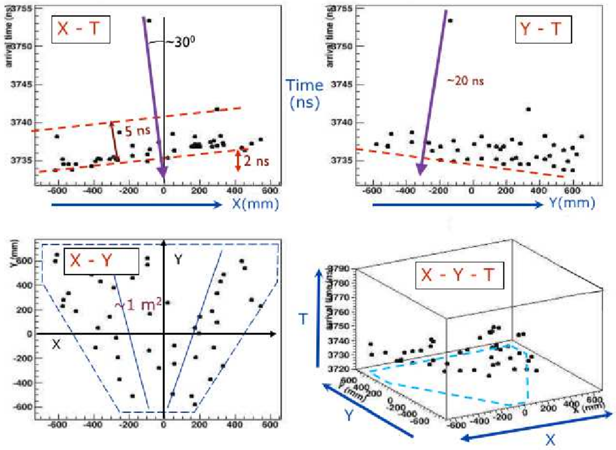

Figure 1: Example of high multiplicity event with all the space-time projections. Most of the particles arrive in a few ns time interval and one isolated particle arrived delayed by $\sim$ 20 ns.

The analysis of the data

Despite having detector cells of different shapes and sizes and a very odd truncated trapezoidal shape[1], we analyzed the data looking for the main features of the showers. Fig. 1 shows the space-time projections of a typical high multiplicity event.

Some of the most important effects we observed are [1]:

- Most of the high multiplicity showers show a sharp front edge allowing a good estimation of the arrival direction of the shower. A more detailed analysis showed that this direction is very well correlated with the arrival direction of the fastest particles.

- Using well known parameterizations it is possible to get an estimation of the energy of the primary cosmic rays for high multiplicity events. Unfortunately, we didn't have any external detector to perform an appropriate "calibration" of our detector.

- Many of the high multiplicity bundles of particles had a very much narrower time width (a few ns) than the typical widths observed using much bigger detectors with worse time resolution or granularity.

- Many of the bundles of particles detected seem to show a lumpy aspect. Perhaps those structures are due to narrow electromagnetic showers induced by the decay of high energy muons in the atmosphere. If this were the case, a more detailed analysis of the data could allow to make an estimation about the electron/muon ratio and, as a consequence, a guess of the mass of the primary cosmic ray.

In order to go deeper in the understanding of the observed effects, and to confirm or reject them, a spin-off detector, TRAGALDABAS [2], has been installed at the Univ. of S. de Compostela, in Spain, for the regular study of cosmic rays. The detector is also based on the RPC technology and make use of both the HADES RPC wall front-end electronics and the HADES TRB DAQ board.

References

[1] D. Belver et al. *Analysis of the space-time microstructure of cosmic ray air showers using the HADES RPC TOF wall.* JINST 7 (2012) P10007

[2] A. Blanco et al. *TRAGALDABAS: a new RPC based detector for the regular study of cosmic rays.* JINST 9 (2014) C09027

---

[*] juanantonio.garzon@usc.es

[1] The detectors were designed in order to offer a regular occupancy in central heavy nucleus-nucleus collisions.

DOI:10.15120/GR-2015-1-MU-NQM-HADES-15

Pion and dielectron production with pion-proton reactions*

HADES Collaboration
[1]www-hades.gsi.de

The combination of the secondary pion beam available at GSI with the universal HADES detector represents a worldwide unique facility to study hadron and dielectron production. The corresponding experimental programme was initiated in summer 2014 by studies of strangeness production off nuclei (see contribution [1]) and dielectron production in π^--p reactions. The main goal of the second experiment was to study inclusive and exclusive (with $\pi^-p\rightarrow e^+e^-n$ final state) dielectron production in the energy region of the second resonance ($\sqrt{s}\sim1.5$ GeV). The studies of exclusive channels allows, for the first time, to measure the Dalitz decay of the $D_{13}(1520)$ resonance $D_{13}(1520)\rightarrow e^+e^-n$. This long awaited result is an important step towards for a complete understanding of the ρ meson coupling to baryons, crucial also for the broadening of the ρ meson spectral function in nuclear matter [2]. Furthermore, these measurements of inclusive and exclusive dielectron production provide an important reference for the already measured p-Nb system [3], where a significant excess of e^+e^- yield below the vector meson pole has been attributed to secondary pion-nucleon interactions [4].

In order to separate the resonant from non-resonant contributions in the dielectron channel, final states with hadrons have to be investigated as well. For this purpose the excitation functions of the one pion and the two-pion production around the pole of the $D_{13}(1520)$ resonance have been simultaneously measured. In particular, new data on exclusive $\pi^-p\rightarrow\pi^+\pi^-n$ channels are of special importance. These data will be analyzed with the partial wave technique to disentangle the different waves that build up coherently the measured final state and will provide an independent measure of the production amplitude of the ρ meson in its main decay channel. Generally, these data are badly needed to understand the mechanism of two pion decays of various resonances in this energy region. The old bubble-chamber experiments, on which is based all our knowledge about charged pion production, provided only about 240 000 events in the energy interval of $\sqrt{s}$ =1.32-1.93 GeV. The situation is a bit better for the $\pi^0\pi^0$ final state which has been accurately measured by the Crystal Ball collaboration from threshold up to $\sqrt{s}$ 1.525 GeV. Since the ρ meson cannot decay into neutral pions, the new HADES data, which improve the data base by at least two orders of magnitude, will provide a stringent constraint on ρ production at these energies. As already mentioned above, the branching ratios of the resonance decays to ρN are known with bad precision. In the PDG, several resonances important for the in-medium spectral function of the ρ meson, like $D_{13}(1520)$, $S_{31}(1620)$ and the $P_{13}(1720)$, have large branching ratios 20-30%, 7-25% and even larger than 70%, respectively. However, much lower values of these branching ratios are found in some recent PWA analyses. For instance, these branching ratios are respectively 10% ±3%, 12%±9% and 10%±13% in the analysis done by the Bonn-Gatchina group [5]. Lower values for the $P_{13}(1720)$ (lower than 6%) and for the $D_{13}(1520)$ (9%) are found respectively by the KSU [6] and Pittsburg-Argonne [7] groups. With the new precise HADES data on charged pions, the situation can be clarified for the $D_{13}(1520)$ and future HADES experiments with pion beams at higher energies will improve the situation for the higher mass resonances as well.

The experiment was conducted with a primary ^{14}N beam, provided by the SIS18 synchrotron, with an intensity close to the space-charge limit of $0.8\text{-}1.0\times10^{11}$ ions/spill. The pions were transported to the HADES target, located 33 m downstream of the production point, by a beam line composed of a lattice of 7 quadrupole and 2 dipole magnets. For pions with a central momentum (p_0) a transmission of about 56% with respect to the entrance solid angle was achieved. The calculated transmission decreases gradually as the π-momenta depart from the central, reaching zero for pion momenta of $p_0\pm6\%$. The transmission can be represented to first order by a Gaussian distribution with a variance of $\delta p/p_0=1.5\%$. The pion intensity distribution at the exit of the pion beam line (last quadrupole) depends on the selected p_0, reaching a maximum of about 10^6 pions/spill at $p_0=1.0$ GeV/c and decreasing to about half of this value at $p\cong0.690$ GeV/c where our measurements were performed. These intensities are the result of the combined effect of the beam size at production target and of the transmission, mostly driven by the dedicated tuning of the different magnets and the respective apertures defined by the vacuum vessels. For a beam of negative pions, the purity is high and the small contamination by electrons and muons has been estimated to be lower than a few %. Together with their low interaction probability this contamination does not constitute a handicap for the experiment. A dedicated tracking system (CERBEROS) [8], composed of two silicon strip-detectors along the pion chicane and a start detector [9]

---

* Work supported by INFN-LNS Catania (Italy); LIP Coimbra (Portugal): PTDC/FIS/113339/2009; SIP JUC Cracow (Poland): 2013/10/M/ST2/00042 and NN202198639; GSI Darmstadt (Germany): Helmholtz Alliance HA216/EMMI; TU Darmstadt (Germany): VH-NG-823, Helmholtz Alliance HA216/EMMI; HZDR, Dresden (Germany): 283286, 05P12CRGHE; Goethe-University, Frankfurt (Germany): Helmholtz Alliance HA216/EMMI, HIC for FAIR (LOEWE), GSI F&E, BMBF 06FY9100I; TU München, Garching (Germany): BMBF 06MT7180; JLU Giessen (Germany): BMBF:05P12RGGHM; University Cyprus, Nicosia (Cyprus): UCY/3411-23100; IPN Orsay, Orsay Cedex (France): CNRS/IN2P3; NPI AS CR, Rez, (Czech Republic): MSMT LG 12007, GACR 13-06759S.

DOI:10.15120/GR-2015-1-MU-NQM-HADES-16

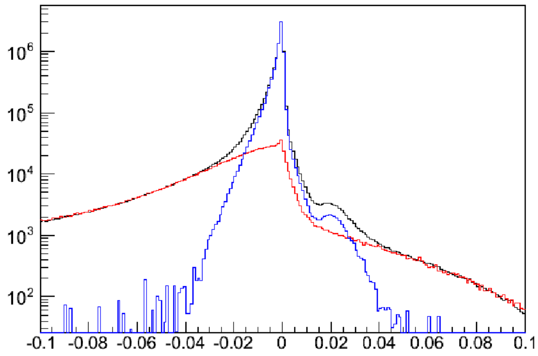

Figure 1: Missing mass squared of the π^--p system obtained after angular conditions to select π-p elastic scattering events. Data obtained at a pion beam momentum p=0.69 GeV/c are shown for the polyethylene (black) and carbon (red) targets. The difference is displayed as a blue curve.

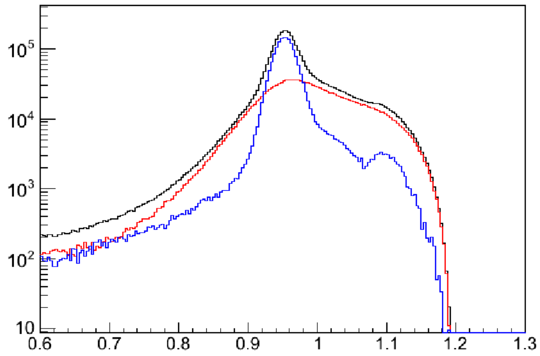

Figure 2: Missing mass of the $\pi^-\pi^+$ system. Data obtained using a pion beam momentum p=0.69 GeV/c are shown for the polyethylene (black) and carbon (red) targets. The difference is displayed as a blue curve.

right in front of the HADES, has been developed and successfully used to measure the momentum of each beam particle. From the measured positions of the hit on the two detectors, the pion momentum is reconstructed with a resolution ranging from 0.1% to 0.3% over the acceptance window. This allows for a precise reconstruction of the total center-of-mass energy in pion-nucleon interactions.

Calculations of the pion beam optics have shown that the beam spot at the HADES target position exceeds the diameter of the target (12 mm) and can cause significant background from beam interactions in the narrow RICH beam tube or target holder. In order to reject this background and to also provide start time information a position sensitive detector was placed 30 cm in front of the target. Two types of targets were used for π^--p experiments: polyethylene of 46 mm thickness (containing 4×10^{23} protons and 2×10^{23} carbon) and pure carbon for the background subtraction.

Produced particles where reconstructed by means of the HADES detectors. Fig. 1 shows distribution of the missing mass squared of the π^--p system obtained for the π-p elastic scattering events, selected by angular correlations between identified pion and proton tracks at p_0=690 MeV/c. The black curve shows distributions obtained with the polyethylene target, while the red curve shows the same distribution but resulting from the carbon target. The latter one is normalized to the same yield on the left side of the prominent peak corresponding to the signal from the elastic scattering (blue line), which has been obtained as a difference between the two measured distributions. As one can see, the quasi-elastic peak obtained from the carbon target is much broader. A small peak at 0.0196 $(\mathrm{GeV/c^2})^2$, corresponding to the inelastic channel with one additional pion produced clearly visible in the subtracted distribution, is not observed. The separation between elastic and quasi-elastic scattering is very useful for the subtraction of background originating from the reactions on carbon inside the polyethylene target for other reaction channels. For example, Fig. 2 shows the missing mass distributions of the two charged pion system measured with the polyethylene (black line) and the carbon (red) targets. The latter one was normalized by scaling the number of collected events from the two targets with the factor deduced from the analysis of the elastic events, described above. As one can see in the subtracted distribution (blue line), the signal from the $\pi^-p\rightarrow\pi^+\pi^-n$ final state is clearly visible as a peak around the nominal neutron mass. The background under the peak from the interactions on carbon is on the level of 25-30% only and can be accounted for by the partial wave analysis using the events from the carbon target. Similar distributions have also been obtained for the other beam momenta of p=0.656, 0.748 and 800 MeV/c.

The dielectron analysis is in progress and preliminary results show almost 600 signal pairs with a mass M>140 MeV/c^2 [10]. The ongoing detailed analysis of the dielectron mass and angular distributions in relation with the two pion data will be crucial for the estimation of off-shell ρ meson production.

References

[1] K. Lapidus et al. (HADES Coll.), “Charged kaon production in pion-nucleus reactions at 1.7 GeV/c”.
[2] R. Rapp, J. Wambach, Adv. Nucl. Phys. A 25 (2000).
[3] G. Agakishiev et al. (HADES Coll.), Phys. Lett. B 715 (2012) 304.
[4] J. Weil et al., Eur. Phys. J. A 48 (2012) 111.
[5] A. Anisovich et al., Eur.Phys.J. A48 (2012) 15.
[6] M. Shrestha and D. Manley, Phys.Rev. C86 (2012) 055203.
[7] T. Vrana, S. Dytman, and T. Lee, Phys.Rept. 328, 181 (2000).
[8] J. Wirth et al. (HADES Coll.) this report.
[9] J. Pietraszko et al. (HADES Coll.), this report.
[10] F. Scozzi et al. (HADES Coll.) this report.

Tracking pions with CERBEROS* at the HADES spectrometer†

J. Wirth[1,2], *L. Fabbietti*[1,2], *R. Lalik*[1,2], *L. Maier*[1], *Alessandro Scordo*[3], *and the HADES collaboration*
[1]Physik Department E12, Technische Universität München, 85746 Garching, Germany; [2]Excellence Cluster "Origin and Structure of the Universe", 85746 Garching, Germany; [3]INFN LNF, Frascati, Italy

In 2014 the HADES collaboration performed two successful experimental campaigns with secondary pion beams. Since the momentum distribution of the produced pion beam is very broad, two fast tracking stations were installed along the pion chicane following the pion production target to reconstruct the momentum of each individual pion (Fig.1). Both stations consist of a double sided silicon strip sensor with a large active area (10×10 cm^2). The sensors are read out with a n-XYTER ASIC chip [1]. Due to its self-triggering architecture and local storage capability, the chip enables tracking and online beam monitoring at high rates. The TRB3 board [2] on which the trigger logic is implemented completes the readout chain and integrates the system into the Hades DAQ. All hits registered by the n-XYTER are buffered inside this board and only events correlated in time with the CTS (Central Trigger System) are send to the Event Builder.

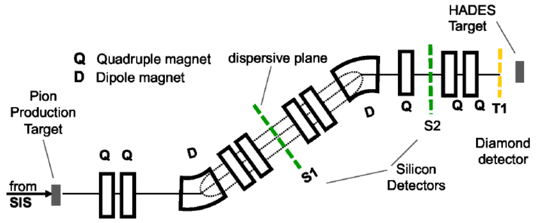

Figure 1: Schematic of the pion beam chicane. The positions of the two tracking stations are indicated in green. The first station is located at the dispersive plane.

The pion momentum is reconstructed relying on the beam optics transport calculation using the four spatial coordinate informations provided by the tracking system. A large momentum spread translates into a large x-position deviation at the dispersive plane where the first detector is located. The requested resolution of $< 0.5\%$ is two orders of magnitude better than the spread in momentum due to the beam line acceptance of about 8% and therefore allows for the exclusive analysis of reaction channels.

Prior to the actual physics production run with the secondary pion beam, the calibration of the reconstructed momentum was performed. The calibration was carried out with a proton beam with six different known momenta with respect to the central beam momentum of 2.68 GeV/c set by the accelerator. Figure 2 presents the seven momenta reconstructed on the basis of the beam optics calculation and the four spatial coordinates. All seven different values can be clearly distinguished and are in good agreement with the reference values. Since not all the momenta focus in the first detector plane the resolution of the various reconstructed momenta differ. But all resolutions are below the envisaged value of 0.5%.

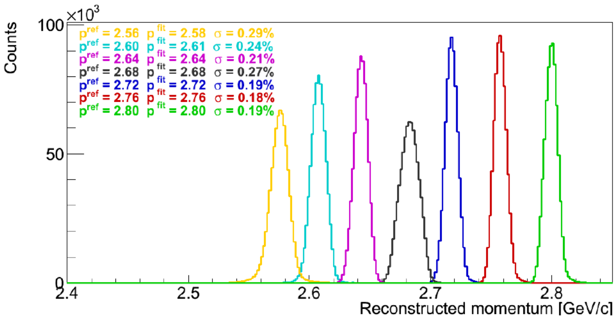

Figure 2: Reconstructed momentum calibration performed with six known momenta with respect to the central beam momentum of 2.68 GeV/c, set by the accelerator.

The momentum distribution of the pion beam is much broader due to its secondary nature and only limited by the beam line acceptance. The reconstructed spectrum of the pion momentum is shown in Fig.3. The maximal transmission occurs at the central beam momentum of 1.7 GeV/c with an asymmetric transmission for different momenta.

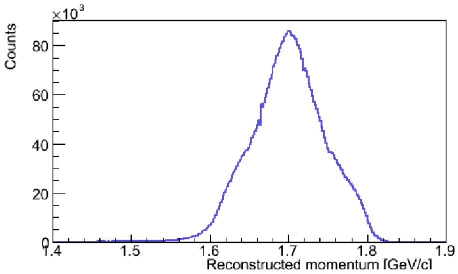

Figure 3: Reconstructed momentum distribution of the secondary pion beam at a central beam momentum of 1.7 GeV/c.

References

[1] A.Brogna et al., *Nucl. Instr. and Meth.*, A 568 (2006) 301.
[2] M. Traxler et al., *J. Instrum.*, 6(12) (2011) C12004.

---

* Central Beam Tracker for Pions
† Supported by VH-Ng-330, TMFABI1012 and BmBf 05P12WOGHH

DOI:10.15120/GR-2015-1-MU-NQM-HADES-17

Optimization of the HADES secondary pion beam spectrometer*

B. Ramstein†[1], *E. Atomssa*[1], *T. Hennino*[1], *L. Hijazi*[1], *W. Koenig*[2], *J. Biernat*[3], *and P. Salabura*[3]
[1]IPNO, Orsay, France; [2]GSI, Darmstadt, Germany; [3]Jagiellonian University, Crakow, Poland

The GSI pion beam

To maximize the pion yield in the momentum range around 1 GeV/c, the secondary pion beam is obtained by the interaction of a fully stripped 2 GeV/nucleon ^{14}N ion beam with an intensity close to the SIS18 space charge limit of 0.8-1.0 10^{11} ions/spill impinging on a 10 cm thick Be target. In these conditions, the pion flux at the HADES target is about 5 10^5 π/spill at 1 GeV/c and decreases by a factor 2 at 0.7 GeV/c and 1.3 GeV/c. The pions are then transported to the HADES target, located 33 m downstream of the production point by a beam line composed of a lattice of 7 quadrupole and 2 dipole magnets, as shown in Fig.1 of [1].

Optimization of the spectrometric pion line

While the pion flux at the entrance of the spectrometric beam line is determined by the primary beam characteristics and the target nature and geometry, the setting of the beam line needs to be adjusted to maximize the transmission and reduce the size of the beam spot on the HADES target. This optimization is particularly important in studies of the production of rare probes, like dielectrons and strange particles and in the use of the HADES liquid hydrogen target with its diameter of 12 mm. In addition, to reject background events and select exclusive channels in the π-nucleon reaction, an event-by-event reconstruction of the pion momentum and positions by means of position measurements in two newly-built in-beam Si-strip detectors [1] has been introduced.

For these studies, a Monte Carlo simulation was carried out. In a first step, a TRANSPORT [2] program code based on a given geometrical configuration of the spectrometric beam line and detectors is used to fit the quadrupole strengths to fulfill general constraints (focus in horizontal and vertical planes at the intermediate and final images, where the detectors will be placed and achromaticity in both vertical and horizontal directions at the HADES target point). In the usual beam optics formalism, a particle with momentum p and horizontal and vertical positions (angles), x (θ) and y (ϕ), respectively in the plane transverse to the optical axis are described by an array of five coordinates, ($x(1)$, $\theta(2)$, $y(3)$, $\phi(4)$, $\delta(6)$). The number in brackets is the index of the corresponding coordinate and $\delta = (p - p_{ref})/p_{ref}$ is the momentum offset with respect to the reference momentum p_{ref} corresponding to particles on the optical axis. The TRANSPORT program allows to calculate the first and second order transport coefficients T_{ij} and T_{ijk} relating the coordinate array at any position in the beam line to the one at the production target. In a second step, these coefficients are used in a MonteCarlo simulation to trace the particles all along the spectrometer within the geometrical acceptance of the magnets, detectors and HADES target. In this way, the transmission and the envelope of the beam is followed step by step. Due to the tilt angle (21.75°) of the two dipoles, horizontal and vertical planes are coupled. In particular, the dispersion terms in the vertical plane associated to the coefficients T_{36}, T_{336} and T_{366} and the coupling terms associated to the coefficients T_{14} , T_{146} and T_{32} cannot be neglected.

The first part of the spectrometric line is fixed, but the positions of the last three quadrupoles (two 1 m long and one 0.4 m long) and of the two detectors have been adjusted to minimize both the global transmission loss and the size of the beam envelope at the HADES target. The global transmission, measured with respect to the entrance of the spectrometer is about 56% for δ=0 and decreases gradually as a function of $|\delta|$, reaching zero for $\delta = \pm 6\%$. Most of the losses are due to the apertures of the magnets, especially the second dipole and the following quadrupoles. In the presence of the LH2 target, with a 12 mm diameter, additional losses of about 35% are expected. In addition, some background is expected from interactions with the inner tube, 48 mm in diameter placed upstream of the target. Due to second order terms, the transmission is larger for positive values of δ. As a result, the δ distribution can be represented to first order by a Gaussian distribution centered at +0.5% and a variance of 1.5%. While a possible shift of the primary beam in the horizontal direction would just shift the momentum distribution, with no significant change of the global transmission, the sensitivity to a vertical shift is much larger. This is due to the large value of the magnification coefficients T_{33} which reaches values as large as -70 at the second detector position. As an example, a shift of 1 mm would induce a decrease of the acceptance by 50%. The vertical alignement of the primary beam has therefore to be adjusted very carefully. In the first experiment performed in 2014 with the pion beam, the transmission pattern was found to be in very good agreement with the calculations [1]. The measured rates allow to confirm a pion flux of 5 $10^5\pi$/spill on target at 1.0 GeV/c.

---

* Work supported by .

† ramstein@ipno.in2p3.fr

DOI:10.15120/GR-2015-1-MU-NQM-HADES-18

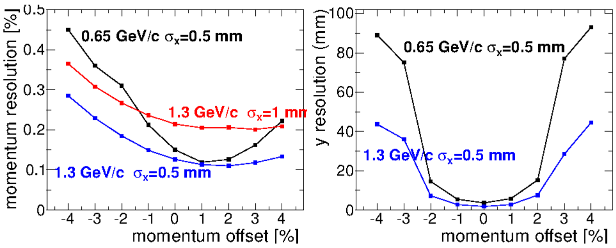

Figure 1: Left: Pion momentum resolution as a function of the momentum offset δ for different values of reference momenta and primary beam transversal sizes. Right: Same for the vertical position resolution at the HADES target.

Pion momentum and position reconstruction

The principle of pion momentum, angle and position reconstruction is based on the relation between the measured positions (X_1, Y_1) and (X_2, Y_2) in two detectors placed in the spectrometric line and the beam particle coordinates at the production target $(x_0, \theta_0, y_0, \phi_0, \delta)$, which can be written using the first and second order transport coefficients, as discussed above. To solve this set of 4 equations with five unknowns, x_0 is set to 0 and the corresponding neglected terms will then contribute to the resolution on the coordinate reconstruction. In addition, terms with negligible contributions are not taken into account, leading to the following relations:

$$\begin{aligned} X_i = & \quad T^i_{12}\theta_0 + T^i_{14}\phi_0 + T^i_{16}\delta \qquad (1) \\ & + T^i_{126}\theta_0\delta + T^i_{146}\phi_0\delta + T^i_{166}\delta^2 \\ Y_i = & \quad T^i_{32}\theta_0 + T^i_{33}y_0 + T^i_{34}\phi_0 + T^i_{36}\delta \qquad (2) \\ & \quad T^i_{336}y_0\delta + T^i_{346}\phi_0\delta + T^i_{366}\delta^2 \end{aligned}$$

where $i = 1, 2$ is the detector index. These equations are solved iteratively, determining in a first step θ_0 and δ by neglecting the coupling to the vertical plane. Fig.1 (left) shows the pion momentum resolution for reference momenta of 0.65 GeV/c (black curve) and 1.3 GeV/c (blue curve) as a function of the momentum offset δ. These results have been obtained in a simulation with realistic beam conditions (x_0 and y_0 distributed following gaussians with variances of 0.05 cm and θ_0 and ϕ_0 uniformly distributed with intervals of half-width respectively 10 and 50 mrad) and taking into account the design geometry of the in-beam Si strip detector [1], with a position resolution of 800 μm and a thickness of 300 μm. For pions travelling along the optical axis, the resolution is about 0.1%. This value grows linearly with the beam spot size, as demonstrated by the red line corresponding to a variance in x_0 of 0.1 cm. The dependence on $|\delta|$ of the resolution is due to the effect of multiple scattering in the first detector, which affects the momentum determination only for trajectories away from the optical axis and decreases with increasing pion momentum. In the range $|\delta| < 3\%$, where the transmission is significant, the resolution stays better than 0.4%, even at the lowest momenta. It has been checked that the impact on the selection of exclusive channels ($\pi^- p \to n e^+ e^-$ or $\pi^- p \to n \pi^+ \pi^-$) of the pion momentum resolution is a factor 3 lower than the impact of the momentum resolution of particles detected in HADES.

By using the reconstructed values θ_0, y_0, ϕ_0 and δ of the pions, an estimate of their positions at the HADES target can be deduced by using the appropriate transport coefficients. The resolution on the position measurements is dominated by the effect of the multiple scattering. Its dependence on the primary beam transverse position is therefore very weak. The resolution on the horizontal position is almost independent on δ, with values of the order of 9.6 mm at 0.65 GeV/c and 4.6 mm at 1.3 GeV/c. The resolution on the vertical position at the target depends both on the reference momentum and on the offset, as displayed in Fig.1 (right).

To check the validity of the beam line description, a proton beam of known momentum (2.7 GeV/c) has been used [1]. Its incident angle and position could be varied up to ±1.4 mm in x_0, ±2.2 mrad in θ_0, ±0.7 mm in y_0 and ±7 mrad in ϕ_0. The spectrometric beam line was used with different settings, corresponding to values of δ for the proton beam ranging from -4.3% to 4.7%. The impact positions on the Si detectors were used to deduce, when possible, experimental values of the transport coefficients. The most important dispersion term T^1_{16} is found only 3% lower than the value calculated with the TRANSPORT code. Taking into account the observed deviations for measured coefficients and potential deviations for unmeasured ones, the resolution stays below 0.3% for a reference momentum of 1.3 GeV/c.

Purity and future perspectives

The purity of the negative pion beam is not an issue. Even if a sizeable fraction of electrons from the π^0 Dalitz decay and of muons from in-flight pion decays might reach the target, a negligible contribution to the measured events is expected due to their low interaction rates. At larger momenta, kaons can be produced, but most of them will decay before reaching the HADES target. In the future, the possibility to use a positive pion beam will be studied. This will require the separation of protons using time-of-flight information and possibly the use of a proton beam at the maximum energy to reduce the relative yield of protons. The use of a primary proton beam can also be preferable to increase the pion flux at momenta above 1.5 GeV/c.

References

[1] J. Wirth et al., "Tracking Pions with CERBEROS at the HADES spectrometer", contribution to this report.

[2] PSI Graphic Transport Framework by U. Rohrer based on a CERNSLAC- FERMILAB version by K.L. Brown et al, 2007. URL `http://aea.web.psi.ch/Urs_Rohrer/MyWeb/trans.htm`.

DOI:10.15120/GR-2015-1-MU-NQM-HADES-18

A diamond start detector array for the HADES pion beam

W.Koenig[1], *J.Pietraszko*[1], *L.Chlad*[3], *A.Rost*[2], *M.Träger*[1] *for the HADES collaboration*
[1]GSI, Darmstadt, Germany; [2] TU Darmstadt, Germany; [3]NPI Rez, Czech Republic

Requirements

The secondary pion beam produced by a high intensity 2AGeV primary N beam from the SIS18 differs significantly from standard beams: the beam spot at the HADES target has a diameter of about $\sigma \approx 1$ cm with large tails mainly due to the wide momentum range of about 6% causing 2nd order deviations along the transport line [1]. The latter cause reactions at the compact beam-pipe in front of the pion target. Thus, the start detector has to fulfil several points:

1) rejecting pions from the beam halo
2) providing monitoring of the beam focus
3) providing a start time of the reaction for particle identification via time-of-flight (≈100 ps)
4) mounted close to the reaction target under strict space and power limitations.
5) high efficiency for minimum ionizing particles
6) position resolution of ≈ 1mm σ for reconstruction of the reaction point on a segmented target

Design

To fulfil the above requirements a compact array of 9 single crystal diamond detectors has been designed with low noise preamplifiers directly attached to the segmented diamonds (see Fig. 1). The diamond size amounts to 4.6*4.6 mm^2, the thickness to 300μm. For better position resolution and to keep readout capacitance low, each diamond is divided into 4 quadrants. The array is build out of two PC boards mounted inside the Hades Rich detector directly behind each other 13 cm upstream of the reaction target. They are supported by three 33 cm long PCB rods which also contain the 36 signal lines as Cu stripes in inner (well shielded) layers. A set of 6 low noise, single stage booster and shaper amplifiers outside the vacuum pipe supplements the analogue setup. All amplifiers are based on the RF transistor BFP720.

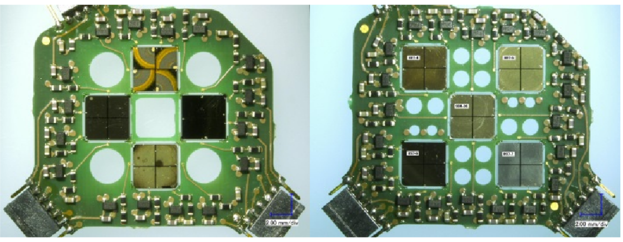

Figure 1: Two PCB boards containing 4/5 segmented diamonds and 16/20 preamplifiers. Both form a 14*14 mm^2 array with 36 pixel.

Results

The two dimensional position distributions of pions dominantly reacting with a target of 12 mm diameter is shown in Fig. 2. The spatial size of a detector channel amounts to 2.3*2.3 mm^2. Due to the distance of 13 cm between target and start detector, the angle of incidence of the pions is needed to obtain a radial hit point on the target. This angle can be obtained from the X,Y position on a tracking stage upstream in the beam-line [2].

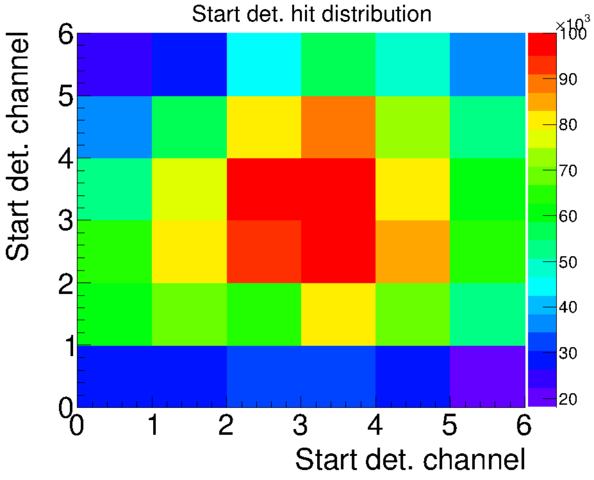

Figure 2: Intensity distribution of the secondary pion beam on the start detector triggered by target reactions.

The time resolution achieved during the beam time in September 2014 was only $\sigma \approx 190$ ps, about a factor 2 above the value expected from tests with single diamonds. It is mainly due to a limitation of the HV to 200V due to charging-up effects of the mounting points at the corners of the diamonds when irradiated with a high flux of charged particles.

Improvements

In order to improve the time resolution the HV limitation due to an exponentially increasing leakage current for some diamonds when irradiated has to be removed. This is currently under investigation. Operation at a HV of 600 V could be achieved for a different mounting procedure of the diamonds in a test setup. This yields a factor ≈ 2.5 faster drift times of electrons and holes resulting in larger signals with shorter rise times. A test with MIPS (2.9 GeV protons) at COSY resulted in a resolution of $\sigma = 90$ ps.

References

[1] B. Ramstein et. al., Optimization of the HADES secondary pion beam spectrometer, this scientific report
[2] J.Wirth et. al., Tracking Pions with CERBEROS at the HADES spectrometer, this scientific report

Acknowledgement: The strong support obtained from the GSI detector and target laboratories is highly appreciated.

DOI:10.15120/GR-2015-1-MU-NQM-HADES-19

Neutron response of the HADES time-of-flight detectors*

R. Holzmann[†][1] *for the HADES collaboration*
[1]GSI, Darmstadt, Germany

In the HADES detector, charged-hadron ID is based mostly on energy-loss, momentum and time-of-flight information [1]. The latter, in particular, is obtained from resistive-plate chambers, the RPC [2], at small polar angles ($15^\circ - 45^\circ$) and from plastic scintillators, the TOF [3], at large angles ($45^\circ - 85^\circ$). Using data gathered in August 2014 with a secondary pion beam [4-6], we have now also investigated the response of these systems to fast neutrons.

In this experiment, aimed mostly at studying baryon resonances in $\pi^- + p$ reactions, a π^- beam of 690 MeV/c impinged on a 46 mm thick polyethylene (CH_2) target. Detecting a coincident $\pi^-\pi^+$ pair in HADES and applying 4-momentum conservation, the missing-mass distribution shown in Fig. 1 is obtained. The exclusive reaction on hydrogen, $\pi^- + p \to \pi^- + \pi^+ + n$, can be selected by cutting on the neutron mass peak and thus tagged neutrons with known 4-momentum can be prepared. The right side of Fig. 1 shows the difference distributions of polar angle and momentum of these tagged neutrons w.r.t. the corresponding values of so-called *neutral hits* observed in the RPC. As neutral hits we consider isolated hits not associated with any of the fully reconstructed and identified charged tracks through HADES and we calculate their momentum from the time of flight by assuming a straight neutron trajectory originating at the event vertex. The remarkably strong correlations between expected and actually measured hits we take as proof that we do indeed observe neutron interactions in the RPC. Similar results (not shown) are also obtained for the plastic scintillator rods.

Comparing the number of actually observed with the number of calculated neutral hits we can determine the neutron detection efficiency as a function of angle and momentum. Figure 2 shows our preliminary result based on 1/4 of the total available statistics. Neutron detection efficiencies are of order $O(10^{-2})$ and both, RPC and TOF, display a strong momentum dependence. Note that our RPC result is consistent with findings from a study done by the R3B collaboration on their prototype RPC modules [7]. The response of plastic scintillator to fast neutrons has been investigated extensively in the past [8] and calculations based on those data are in fair agreement with our result (see Fig. 2).

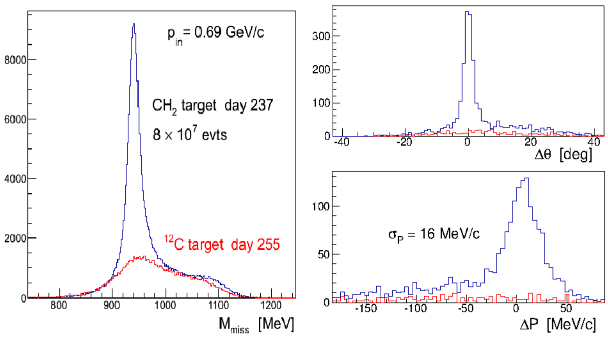

Figure 1: Left: measured missing-mass distribution of $\pi^-\pi^+$ pairs in the $\pi^- + p \to \pi^- + \pi^+ + n$ reaction. Right: angle and momentum differences of observed and expected neutral hits in the HADES RPC. Background from reactions on carbon nuclei (shown in red) has been obtained in a separate measurement done with a ^{12}C target.

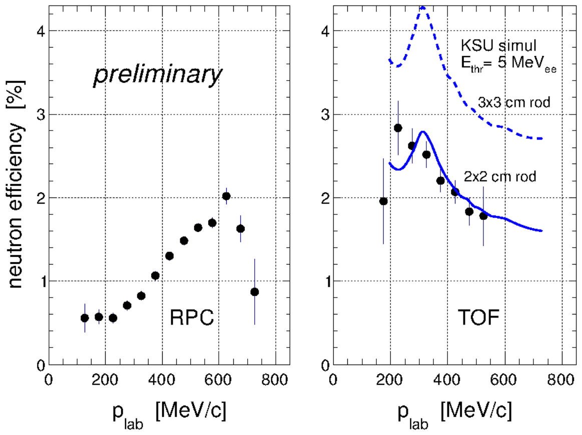

Figure 2: Measured neutron detection efficiency as function of neutron momentum in RPC (left) and TOF (right). The lines are calculations done with the KSU model [8] for 2×2 cm and 3×3 cm plastic scintillator rods, respectively.

References

[1] G. Agakishiev, et al., Eur. Phys. J. A **41** (2009) 243.

[2] A. Blanco, et al., Nucl. Instr. Meth. A **661** (2012) S114.

[3] C. Agodi, et al., Nucl. Instr. Meth A **492** (2002) 14.

[4] J. Diaz, et al., Nucl. Instr. Meth. A **478** (2002) 511.

[5] P. Salabura, et al., contribution to this Scientific Report.

[6] J. Wirth, et al., contribution to this Scientific Report.

[7] M. Röder, et al., Eur. Phys. J. A **50** (2014) 112.

[8] R. A. Cecil, et al., Nucl. Instr. Meth. A **161** (1979) 439.

---

[*] Work supported by EMMI.

[†] r.holzmann@gsi.de

DOI:10.15120/GR-2015-1-MU-NQM-HADES-20

A method for online multichannel inclusive reconstruction of pion induced reactions in HADES *

G. Kornakov[†] [1] *for the HADES Collaboration*
[1]Technische Universität Darmstadt, Germany

During the HADES [1] campaign of pion induced reactions a method to produce the inclusive invariant mass spectra for all possible reaction channels was implemented. This tool is helpful in order to have a quick estimation of the data quality and to guide more detailed analyses later.

The general reconstruction strategy usually starts from a predefined reaction, or channel, of interest which is analysed in detail and filtered out from all events and particle traces. This strategy fits very well during data taking for checking the performance of the apparatus and to confirm or modify expectation values and adjust data taking for accomplishing the main goals of a certain experiment. Here we present a different approach, a method for making a general overview of the measured data. Its main goal is to allow a broader perspective of the collected data for a later more detailed and careful analysis.

As observable for identifying various cases we chose the invariant mass of a group of reconstructed particles, considering from 1 up to N possible particles in the final state. The method is implemented in an iterative way: first all the track candidates are selected and sorted. Then they are labelled as candidates with a certain ID, i.e. protons, electrons, pions and kaons. Then all the electromagnetic components are combined into π^0 and γ in case they meet the kinematical requirements. Those tracks are removed from the general list. Then the same strategy is applied to the hadrons. Once a single list is built, these particles are combined into sets of 2, 3, up to 5 particles. Then, those which fit to a certain abundant short lived particle like Λ, ϕ or ρ are added to the general list and their constituents are subtracted and all the combinations with these particles in the final states are produced once again, independently if those channels are forbidden or their cross section is very low. Finally, for the uncorrelated background calculation two methods are used: random rotation in the azimuthal direction of the particles in the event and by the event mixing technique. Before starting the procedure with a new event, all the lists are stored in buffers for later mixing. The produced histograms at the end are stored in a ROOT file and also printed to a document in order to provide a simpler and sorted presentation.

This method was applied systematically to the data taken by Hades on pion-induced reactions on tungsten, carbon and polyethylene during July of 2014. Clear spectra of broad resonances, both mesonic and baryonic, were clearly seen (Fig. 1) and used as a assessment of quality and analysis possibilities in this data beyond the programmed physics goals.

This method relies on a very high quality data set produced during data taking; that means that all the subsystem calibrations and geometrical alignment must be performed in a very short time and precise way [2].

The general conclusion about this method is that it provides a broad overview of the measured reaction and together with specific analyses helps for further data taking. Also, this method can be applied later to already measured data in order to unveil possible, not yet investigated hidden physics cases.

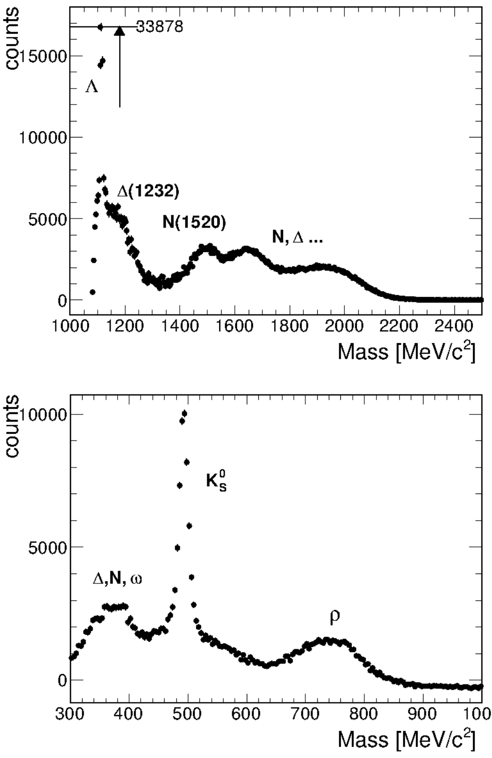

Figure 1: Upper panel: pπ^- inclusive invariant mass, lower panel: $\pi^-\pi^+$ inclusive invariant mass from 1.7 GeV/c π^-+C.

References

[1] P. Salabura, this Scientific Report.

[2] O. Pechenova et al., The alignment strategy of HADES, NIMA Volume 785, 2015

---

* Work supported by VH-NG-823, HA216/EMMI, HIC for FAIR, GSI.

[†] g.kornakov@gsi.de

DOI:10.15120/GR-2015-1-MU-NQM-HADES-21

Importance of the HADES RICH for di-electron analysis in pion induced reactions*

F. Scozzi[1,2] *and the HADES Collaboration*[1]
[1]TU Darmstadt, Germany; [2]IPNO, Orsay, France

In summer 2014 the High Acceptance Di-Electron Spectrometer (HADES) experiment at GSI took data from pion-induced reactions using three targets: tungsten, carbon and polyethylene, at several pion beam momenta. These data permit to investigate hadron and di-electron production. The main objective for di-electron studies is the understanding of the coupling of virtual photons to baryonic resonances by analyzing the process $\pi N \rightarrow e^+e^-N$, a process for which neither experimental data nor reliable theoretical predictions exist. A clear understanding of the elementary reactions is also important for the interpretation of di-electron production in heavy-ion collisions. The main challenge of this type of analysis is to distinguish di-electrons, that are very rare probes, from the hadronic background. The identification of e^+e^- is usually performed in HADES through appropriate cuts on time-of-flight, energy loss, shower signal and RICH observables. Especially the HADES RICH detector is essential to achieve a required purity in the electron selection. On the other side, it reduces the efficiency to detect an electron/positron.

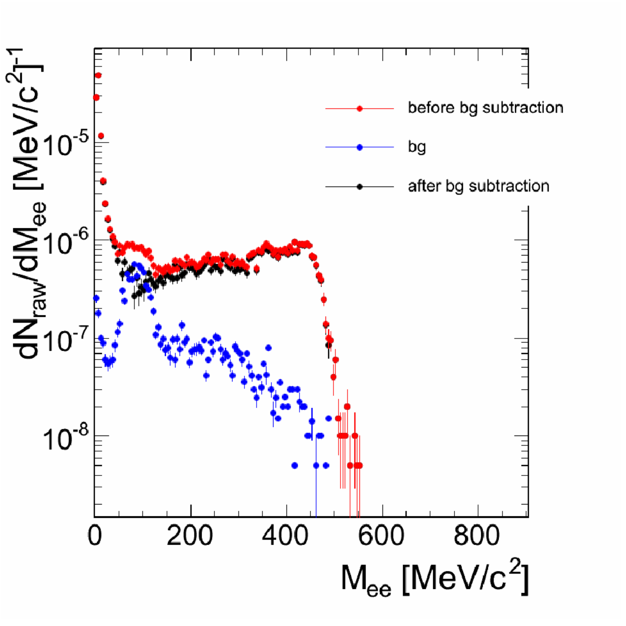

Figure 1: Di-electron invariant mass reconstructed from π^- + polyethylene target reactions at 0.69 $\frac{GeV}{c}$

In order to get a larger statistics, one may hope that the RICH detector is not necessary for electron identification being at low energy and in an environment with low multiplicity. In Fig. 1 the di-electron spectrum from data coming from the interaction of a pion beam witm momentum equal to 0.69 $\frac{GeV}{c}$ with a polyethylene target is shown before and after background subtraction (background is calculated using the geometrical average). In order to understand the slope at 200 $\frac{MeV}{c^2}$ the same identification conditions were applied to data coming from the interaction of pions beam with a momentum equal to 1.7 $\frac{GeV}{c}$ with a tungsten target.

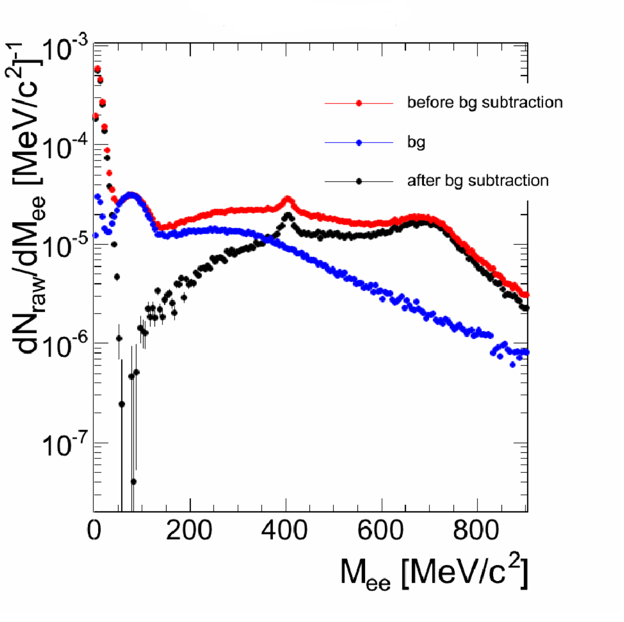

Figure 2: Di-electron invariant mass reconstructed from π^- + tungsten target at 1.7 $\frac{GeV}{c}$

In Fig. 2, at around 400 $\frac{MeV}{c^2}$ it is now possible to observe clearly the peak due to K_{0s}, obtained from misidentified pions (the shift of the peak from the nominal position is due to the fact that the mass of electrons is assigned also to these particles), that also create the structure at higher masses. From this spectrum it is possible to infer that also the structure in the PE spectrum is due to misidentified pions.

---

* Work supported by VH-NG-823, Helmholtz Alliance HA216/EMMI and GSI

DOI:10.15120/GR-2015-1-MU-NQM-HADES-22

Charged kaon production in pion-nucleus reactions at 1.7 GeV/c*

L. Fabbietti[1,2], *K. Lapidus*[†1,2], *A. Scordo*[3], *and the HADES collaboration*

[1]Physik Department E12, Technische Universität München, 85748 Garching, Germany; [2]Excellence Cluster 'Origin and Structure of the Universe' , 85748 Garching, Germany; [3]INFN Laboratori Nazionali di Frascati, 00044 Frascati (Roma), Italy

The production of strangeness in pion-nucleus reactions allows to probe effects of cold nuclear matter, such as the modification of the hadron spectral functions at zero temperature and normal nuclear density. The kaons (K^+, K^0), produced inside the nucleus, are characterized by a relatively large mean free path ($\lambda \approx 5$ fm for $p_K < 900$ MeV/c) and feel a repulsive potential of moderate strength (about +30 MeV [1], cf. discussion in [2]). The case of antikaons (K^-) is much more involved, as these hadron species propagate in an attractive potential that has a sizeable imaginary part, related to the in-medium absorption. Existing data on the in-medium effects in the antikaon production at nuclear targets are very scarce [3].

In summer 2014 the HADES collaboration successfully performed a pilot pion beam run ($p = 1.7$ GeV/c) employing carbon and tungsten targets. For each target more than 100 million of events were collected. Charged kaons can be reconstructed by means of time-of-flight and momentum measurements combined in the mass observable. For ^{12}C and ^{184}W targets, separately, about 100×10^3 K^+'s and 10×10^3 K^-'s were reconstructed (Fig. 1). The rich statistics of the charged kaon sample allows to perform a two-dimensional analysis of the kaon phase space.

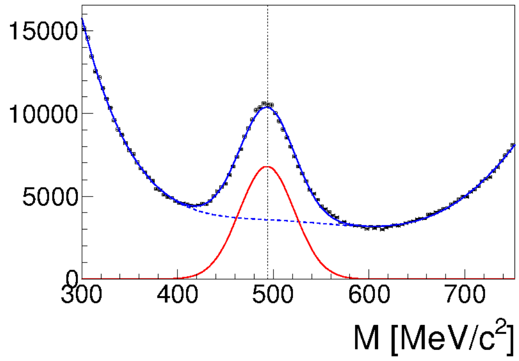

Figure 1: K^+ signal in the mass spectrum of positively charged particles (πC run). The dashed vertical line shows the nominal charged kaon mass. A fit with a gaus (signal) plus a 5th order Chebyshev polynomial (background) is shown.

Figure 2 shows raw doubly-differential (transverse momentum vs. rapidity) yields of K^+'s reconstructed in the pion-carbon run. Thanks to the high statistics of the data sample and the large acceptance of the HADES setup, a major part of the kaon phase space can be accessed. This will allow, after the application of necessary efficiency corrections, to extrapolate the kaon yield to the full solid angle and extract the production cross section. The FOPI collaboration has demonstrated [1], that for the pion beam the total K^0 production cross section scales with the surface of the target nucleus ($\sigma_{tot}^{K^0} \propto A^{2/3}$, where A is the mass number). An analogous behaviour is expected for K^+'s. The new HADES data allows to extract the A-dependence of the production cross section for antikaons as well, which till now has not been done for pion-induced reactions. A deviation of the exponent from the value of 2/3 would indicate: a) an increased absorption of the antikaons (a smaller value of the exponent) or b) a decreased threshold for the antikaon production due to the attractive potential (rise of the exponent).

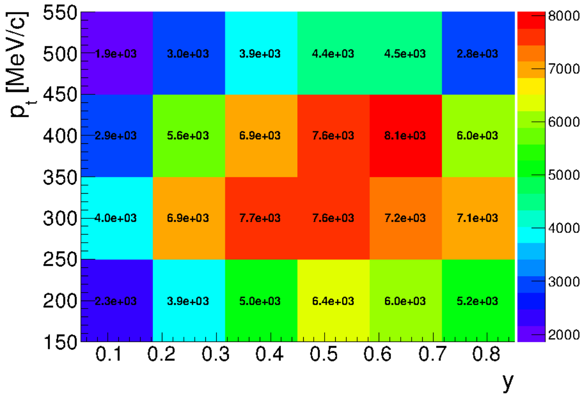

Figure 2: Raw K^+ yields extracted in pion-carbon run. No efficiency corrections have been applied.

References

[1] M. L. Benabderrahmane *et al.* [FOPI Collaboration], "Measurement of the in-medium K^0 inclusive cross section in π^--induced reactions at 1.15 GeV/c," Phys. Rev. Lett. **102**, 182501 (2009).

[2] G. Agakishiev *et al.* [HADES Collaboration], "Medium effects in proton-induced K^0 production at 3.5 GeV," Phys. Rev. C **90**, 054906 (2014).

[3] W. Scheinast *et al.* [KaoS Collaboration], "First observation of in-medium effects on phase space distributions of antikaons measured in proton-nucleus collisions," Phys. Rev. Lett. **96** 072301 (2006).

---

* Work supported by BMBF 05P12WOGHH

[†] kirill.lapidus@ph.tum.de

DOI:10.15120/GR-2015-1-MU-NQM-HADES-23

Response of HADES Electromagnetic calorimeter modules on inclined gamma-beam[*]

O. Svoboda[†,1], *B. Kardan*[2], *G. Korcyl*[3], *W. König*[4], *A. Kugler*[1], *S. Linev*[4], *O. Petukhov*[5], *J. Pietraszko*[4], *P. Ramos*[1], *A. Rost*[6], *P. Tlustý*[1], *and M. Traxler*[4]

[1]Nuclear Physics Institute of ASCR, Rez; [2]Goethe-Universität, Frankfurt; [3]Smoluchowski Institute of Physics, Jagiellonian University of Kraków, Poland; [4]GSI, Darmstadt; [5]Institute for Nuclear Research, Russian Academy of Science, Moscow, Russia; [6]TU Darmstadt, Darmstadt

The electromagnetic calorimeter (ECAL) will soon become a new detector in the HADES spectrometer as a part of the upgrade for experiments with beams from the FAIR facility. The ECAL TDR was approved in 2014 and the production of the ECAL support construction will start in 2015. A module assembly and monitoring system construction is running in parallel. A short ECAL description can be found in [1]. Tests of single ECAL modules using the tagged gamma beam from the MAMI facility at Johannes Gutenberg Universität Mainz were done in the beginning of 2014. A short experiment description and first results on relative energy resolution were presented in [2].

Beside the relative energy resolution, also the response of single detector modules to gamma beams coming close to the module border or under non-zero angles were studied in detail. The response to a non-parallel beam is of high importance as most of the ECAL modules will be under non-zero angle to the incoming particles (see figure 1).

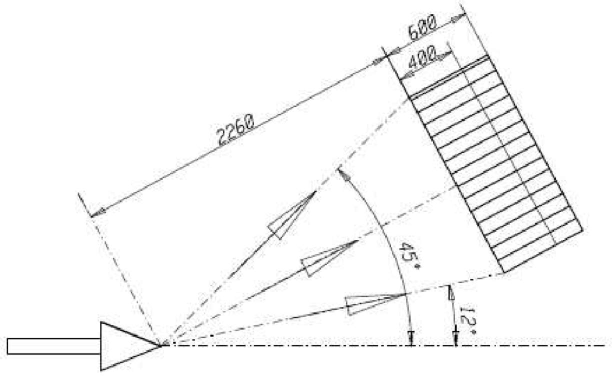

Figure 1: Modules layout in the vertical plane along the beam axis.

Two different inclination angles (6 and 12 degrees) and four hit positions (-2cm, center of module, +2cm, +4cm) were measured and analyzed in detail. As demonstrated on figure 2, the original photon energy can be reconstructed by summing the signal from neighbor modules. This is possible due to a short path length of secondary particles in the non-active volume between the modules.

For parallel beams coming close to the module border, a small part of the total photon energy is lost as the secondary particles are traveling a longer distance in the non-active volume between the modules. This will be eliminated with a calculated correction table.

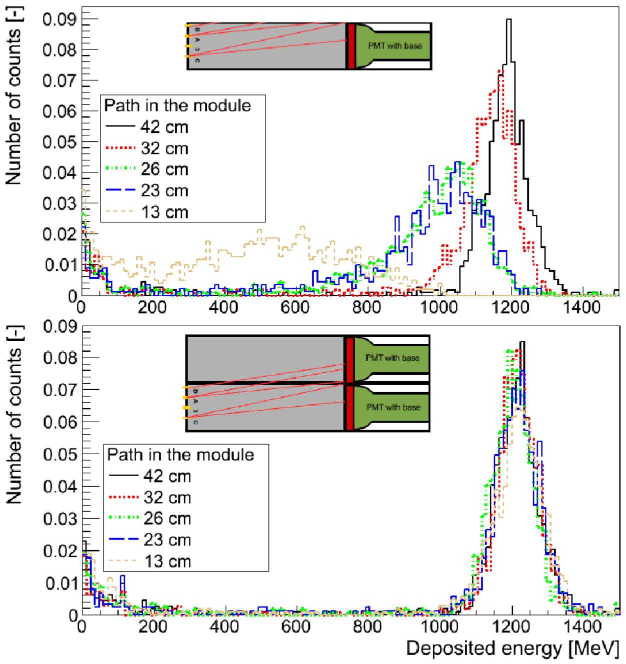

Figure 2: Energy deposited in the primary module (upper histogram) and sum of energies from two neighbouring modules (lower histogram). The energy of primary photons was 1213 MeV, various inclination angles and hit positions resulted in a varying "path length" in the hit modules.

Simulations are being performed to understand these detector features and to tune the analysis code for first measurements with the detector in 2017.

Acknowledgements

Authors are grateful to A. Thomas and other members of the A2 collaboration for their help with this measurement.

References

[1] O. Svoboda et al., "Electromagnetic calorimeter for the HADES@FAIR experiment", 2014 JINST 9 C05002

[2] O. Svoboda et al., "Test of the HADES Electromagnetic Calorimeter modules on gamma beam", GSI Scientific Report 2013 (2014) 12

---

[*] Work supported by GSI, HIC for FAIR, EMMI and Czech MSMT LG 12007, GACR 13-067595 and AS CR M100481202 grants, and by European Community FP7 – Capacities, contract HadronPhysics3 n. 283286.

[†] svoboda@ujf.cas.cz

DOI:10.15120/GR-2015-1-MU-NQM-HADES-24

Optimizing the PaDiWa-AMPS TDC and QDC front-end electronics for the HADES pion beam Hodoscope*

A. Rost†[1], *L. Chlad*[2], *W. Koenig*[3], *and J.Pietraszko*[3] *for the HADES Collaboration*
[1]TU Darmstadt, Darmstadt, Germany; [2]Nuclear Physics Institute of ASCR, Rez, Czech Republic; [3]GSI, Darmstadt, Germany

The HADES pion beam experiment has started to take data in summer 2014. A dedicated tracking system CERBEROS [1] and a Start detector have been used to measure the momentum, the position and precise time of the pions in front of the spectrometer. A Hodoscope was located behind the spectrometer and was used as an additional beam position monitor detector. The Hodoscope [2] is built from 16 plastic scintillator rods with the dimensions of 10x5x100 mm, aligned horizontally. The scintillation signal of the rods is read out on each side by Hamamatsu R3478 photo-multiplier tubes (PMTs) providing to get horizontal position information.

Fast TDC and QDC with online monitoring in real-time were needed to control the direction of the pion beam in the spectrometer. The PaDiWa-AMPS front-end board for the TRBv3 [3] was used to measure the time and the charge information of the PMT signals. The TDC is implemented in an FPGA by the tapped delay method. A high precision charge measurement is achieved by implementing a modified Wilkinson-ADC method, so that actively discharging of the integrated signal results in a fast crossing of the threshold. The width of the pulses, which are proportional to the charge, are measured by the well-established TRBv3 platform. Because it is realized based on the KISS (Keep it Small and Simple) principle, it is possible to modify the front-end electronics with little effort and adapt it to different PMT signal shapes. The first version of the PaDiWa-AMPS front-end electronics was optimized for HADES ECAL PMTs and was already successfully tested under beam conditions [4].

In Fig. 1 (left) a Hodoscope PMT signal is shown. In comparison, HADES ECAL PMT pulse-shapes have an amplitude of about 1 V and a pulse-width of about 50 ns. An adaption to the smaller and shorter Hodoscope signals was needed. By modifying the input attenuation of the PaDiWa-AMPS front-end board and by reducing the integration time by an FPGA design update, a significant improvement in the signal-to-noise ratio and in the rate capability has been achieved. In Fig. 1 (right) the charge measurement of the Hodoscope version is shown.

By subtracting the measured time information of the Start detector t_0 from the Hodoscope t_1 and with the assumption $\sigma^2 \approxeq \sigma^2_{\mathrm{Hodo}} + \sigma^2_{\mathrm{Start}}$ a time measurement precision of the Hodoscope and the Start detector could be estimated. After time-walk corrections and for events with the pion beam aligned in the central part of both detectors a time resolution of $\sigma_{\mathrm{Hodo}} \approxeq \sigma_{\mathrm{Start}} \approxeq \frac{\sigma_{\mathrm{Fit}}}{\sqrt{2}} = 196\,\mathrm{ps}$ could be achieved (see Fig. 2).

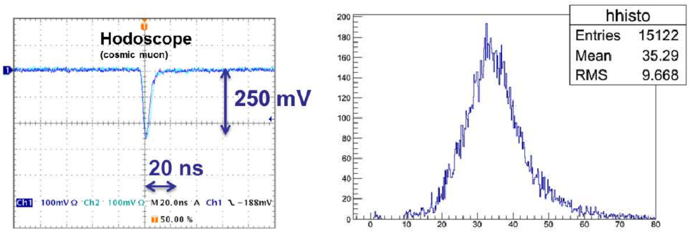

Figure 1: PMT pulse-shape of the Hodoscope (left). The measured charge encoded in the width of the integrated and linearly discharged signal (right).

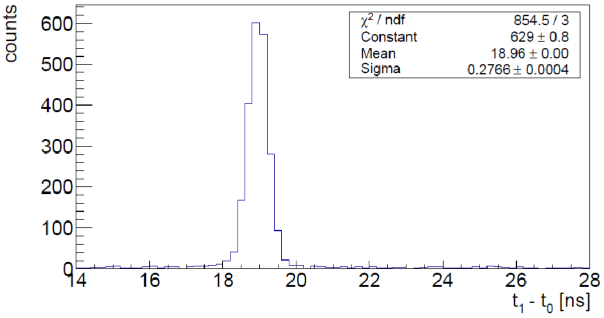

Figure 2: Time difference between Hodoscope and Start detector after time-walk corrections and for events with pion beam aligned in the central part of both detectors.

References

[1] L. Fabbietti et al., “Integration of the Pion-Beam Tracker into the HADES DAQ”, GSI Scientific Report 2013

[2] J. Diaz et al., “Design and commissioning of the GSI pion beam”, Nucl.Instrum.Meth., 2002, Volume 478, Issue 3, p. 511-526

[3] M. Traxler et al., “A Precise Multi-Channel QDC FEE utilizing FPGAs as Discriminators and Delay Elements Based on the TRB3 as TDC and Readout Platform”, GSI Scientific Report 2013

[4] O. Svoboda et al., “Test of the HADES Electromagnetic Calorimeter modules on photon beam”, GSI Scientific Report 2013

---

* Work supported by VH-NG-823, HA216/EMMI, HIC for FAIR, GSI.

† a.rost@gsi.de

DOI:10.15120/GR-2015-1-MU-NQM-HADES-25

DABC as event builder at HADES experiment[*]

J. Adamczewski-Musch[1], *S. Linev*[1]
[1]GSI, Darmstadt, Germany

Introduction

The Data Acquisition Backbone Core (DABC) is a software framework for distributed data acquisition [1]. Due to its plug-in mechanisms it is extendable to various data formats and experiments. For several test set-ups of trb3 frontend readout, a DABC plug-in had already been developed that could receive and combine HADES *trbnet* data packets via UDP connections [2]. These developments have now been completed to cover the full functionality of the previous HADES event building software. This includes interfacing the EPICS based HADES control system, the ORACLE run statistic data base, and the RFIO tape storage of GSI. Initialization procedures of the DABC event builder processes have been fully integrated into the existing HADES DAQ configuration. Moreover, by means of DABC stream server socket the connection to HADES online quality monitoring analysis could be improved. In 2014 DABC was applied for data taking of several beam times at HADES experiment.

DABC integration to HADES

Figure 1 shows the integration of DABC into the HADES data acquisition system [3]. The digitized data from the front-end TRB boards is send via Gbit-Ethernet UDP to event builder processes that have been replaced by DABC. The shared memory interface to the existing EPICS control and run synchronisation system has been implemented fully compatible with the previous event building software *hadaq*, i.e. it is possible to operate the DAQ with “mixed” event builders (DABC and *hadaq*). To achieve such flexibility, the existing HADES DAQ set-up scripts have been extended in a way that each event builder process can be started with the same settings (receiving UDP ports, file output, etc.) either with DABC or *hadaq*. These parameters are passed from the startup script to the DABC process by shell environment variables, which are evaluated in the DABC xml configuration file generic for all event builders. On the other hand, DABC logging and debug output have been attached to the HADES logging facility based on Linux *syslogd*, so most important event builder messages are available here.

HADES data taking “run statistics” (start/stop time, number of events) is exported to ORACLE data base by means of intermediate text files written by the event builders. This data base interface has also been implemented in DABC. HADES event data is written in *hld* file format both to an array of local hard disks, and via Gbit Ethernet sockets to the RFIO tape library of GSI. The *hld* file output plug-in had previously been implemented to DABC [2] and has now been extended by the HADES requirements:

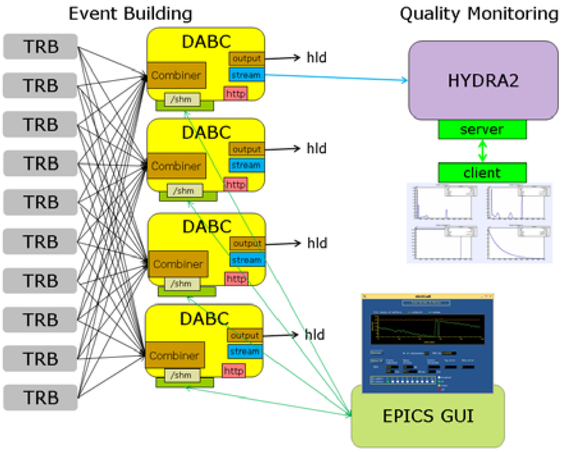

Figure 1: HADES data acquisition and quality monitoring with DABC event builders

- the file names must contain run id and event building node;
- files of all event builders must automatically close and re-open when the run id is changed, which is synchronized via EPICS;
- for load balancing of the local disk arrays, the destination partition for each new file is distributed to the event builders from a demon process via shared memory;
- the event builders may connect to the GSI tape storage by a dedicated RFIO interface library that has been embedded to DABC.

Improved online monitoring

The HADES Quality Analysis (QA) online monitoring needs a sample of event data to analyse and watch the detector states in a quasi live display (Fig.1). Formerly this was provided by temporary “small files” written by one of the 16 event builders and read back by the QA process via an NFS mounted disk. Since DABC can deliver event data to a client via an “MBS stream server” socket, this connection has now been implemented and used by the HYDRA2 QA process. So intermediate files and common disk access are not required anymore, and the *stream server* is available even if no event data is collected to disk. Additionally, several different analysis clients could connect to the DABC event builder and can receive the same event samples simultaneously. Moreover, stability and reconnect time of the QA process have been improved because such client/server socket connection lacks most problems of concurrent producer/consumer file I/O.

---

[*] PSP code: HADES 1.1.2.4

DOI:10.15120/GR-2015-1-MU-NQM-HADES-26

Beamtime experiences

In May 2014 a HADES proton beam time was performed to prepare and align for the subsequent pion beam times. Here for the first time one event builder process (EB5) ran with DABC, all others still with previous *hadaq* software and the old QA file export. In July 2014 the first HADES pion beam time block also applied one DABC event builder. However, here DABC was handling event builder node EB2, uniquely receiving all special calibration events and serving the QA process via *stream server* socket. Finally at the second “production” pion beam time in August/September 2014 [4], DABC was running all event builders. The performance limit without data loss of this system has been measured with a 25 kHz pulsed trigger at 29 frontend systems, feeding usually 3 active event builder processes only with full disk and tape file output. Here each event builder could handle data rates of 38Mbyte/s with a maximum CPU load of 78%. This test goes far beyond the typical observed pion beam event rates of < 2 kHz, so data taking with DABC worked well and was sufficient here.

From such beam time experience several improvements and bug fixes have been added, concerning e.g. EPICS data rate monitoring, debug output of missing data senders, no data buffer loss at long spill pauses, and run statistics export. Additionally, internal performance of DABC framework and plug-ins could be developed further in the scope of HADES application.

Conclusions and outlook

DABC has proved to be suitable for production event building and data taking of HADES sized experiments. Due to its flexibility it was possible to fully support all features of the former *hadaq* event builder software and control environment. Moreover, additional DABC features like event data *stream server*, or http control web server, have opened up further possibilities for online monitoring and control at HADES experiment.

References

[1] J. Adamczewski-Musch, H.G. Essel, N. Kurz, S. Linev, “Dataflow Engine in DAQ Backbone DABC” IEEE TNS Vol.57, No.2, April 2010, pp 614-617

[2] J. Adamczewski-Musch, S. Linev, E. Ovcharenko, C. Ugur, “HADES trbnet data formats for DABC and Go4”, GSI Scientific Report 2012, GSI-SR2012-PHN-SIS18-ACC-41

[3] J. Michel et al., “The upgraded HADES trigger and data acquisition system”, JINST 6 C12056, 2011

[4] HADES pion beam time 2014, this report

DOI:10.15120/GR-2015-1-MU-NQM-HADES-26

Low-purity IIa scCVD diamond material for high-current heavy-ion experiments in HADES/CBM at FAIR *

J. Pietraszko†[1], *L. Chlad*[2,3], *L.M. Donaldson*[4], *W. Koenig*[1], *A. Rost*[5], *and M. Träger*[1] *for the HADES and CBM Collaborations*

[1]GSI, Darmstadt, Germany; [2]Nuclear Physics Institute of the ASCR, Czech Republic; [3]Charles University in Prague, Czech Republic; [4]University of the Witwatersrand, South Africa; [5]TU Darmstadt, Germany

The physics program of the planned HADES and CBM experiments at the FAIR facility requires high current beams, especially the CBM experiment which plans to operate at up to 10^9 ions/s. Thus, a critical requirement of the beam and T0 detectors for these experiments is high rate capability and radiation hardness. The position of the detector in the beam line has to be optimized such that the count rate per channel stays below 10^7 ions/s (readout limitation) and the detector area (cost) remains affordable. The high purity scCVD diamond material, called Electronics Grade (EG) diamond, is perfectly suited for this application [1] but is very expensive with prices in the order of £1500.00 [2] for a single 4.5 mm x 4.5 mm x 0.3 mm plate. In this project we performed a feasibility study of using lower purity scCVD diamond material which is more than factor of 7 cheaper than the EG material. Both types of material belong to the same class of diamond, IIa [3]. The EG type is the highest purity commercially available with nitrogen contamination N_{contam} <5 ppb whereas the low purity IIa diamond, used in this experiment, has N_{contam} <1 ppm. The prototype detector with an active area of 4.5 mm x 4.5 mm and a thickness of 500 μm was metallized with 50 nm Cr layer, covered by a 150 nm gold layer and annealed at 500 °C prior to the experiment. The detector was mounted to PCB with 2 stages of amplification as shown in Fig.1.

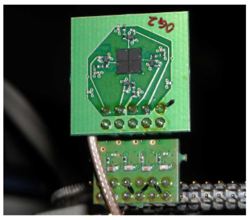

Figure 1: Low purity IIb scCVD diamond mounted on the test PCB.

The experimental setup, shown in Fig.2, was designed such that the 400 MeV/c carbon beam would first pass through the test detector and then though a EG detector. Charged particles crossing the diamond detector produce excess charge carriers which drift following the electrical field and generate signals in the readout electronics. In the lower purity diamond, with chemical impurities (mainly nitrogen), the charge carriers are trapped and can stay in the trap for several hours. This leads to incomplete charge collection [1]. It was expected that at very low rate, at the beginning of the experiment, the low purity material should show large signal amplitude fluctuations but it was thought that if subjected to a sufficiently high beam intensity such that all traps were filled, it could perform like an EG detector. Indeed, during the first 30 minutes of the test experiment the signal amplitudes from low purity diamond were on average about a factor of 10 lower than from the EG reference detector. After about 45 minutes of irradiation at 10^5 C ions/s the signal amplitude saturated at a value comparable to the EG diamond and the low purity plate performed like an EG diamond. Based on the reference detector we estimated the time resolution of both detectors. The time difference spectrum is shown in the Fig.3 and the measured time resolution is $27\,\text{ps}/\sqrt{2} \approx 19\,\text{ps}$.

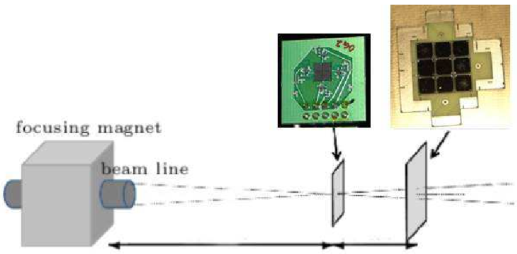

Figure 2: Sketch of the beamline setup.

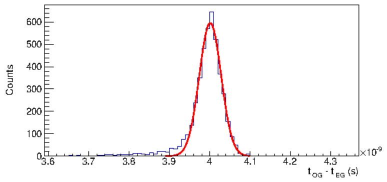

Figure 3: Time difference measured between EG diamond and the low purity diamond. The obtained resolution of the system, is 27ps σ.

References

[1] E. Berdermann et al., Diamond detectors for heavy ion measurements, Proc. XXXVI International Winter Meeting on Nuclear Physics, Suppl. N. 112, Bormio 1998, Italy.

[2] Element Six, EG prices, [online], Available: http://www.e6cvd.com/cvd/page.jsp?pageid=309&prod=46.

[3] Element Six, Classification of Diamond, [online], Available: http://www.e6cvd.com/cvd/page.jsp?page id=353&lang=en.

---

* Work supported by GSI Summer student program and HIC for FAIR

† j.pietraszko@gsi.de

DOI:10.15120/GR-2015-1-MU-NQM-HADES-27

High-resolution tracking based on scCVD diamond detector for straw tube detector tests *

J. Pietraszko[†1], *W. Koenig*[1], *and M. Träger*[1] *for the HADES and CBM Collaborations*
[1]GSI, Darmstadt, Germany

The scCVD diamond material has been extensively employed for single charged particle detection in high-energy experiments. A fast and radiation hard detector such as this is required and is perfectly suited to record the arrival time of the beam particles, especially in high current experiments, to deliver the reaction time T0 of the heavy-ion (HI) collisions. It has also been demonstrated that the scCVD diamond detector can detect not only HI but also minimum ionizing particles (MIPs) [1] with time resolution, σ, better than 100 ps. The excellent timing properties and charge collection efficiency make this type of detector very attractive for high precision detector tests. In this project, we have demonstrated the excellent position resolution capability of the scCVD diamond detector. This detector was used as a reference detector for straw tube performance studies described in [2]. A high purity scCVD detector with an active area of 4.3 mm x 4.3 mm and a thickness of 300μm was metallized with a 50 nm Cr layer, covered by a 150 nm gold layer and annealed at 500^{o}C prior to the experiment. The detector was mounted to a PCB with 2 stages of amplification, as shown in the Fig.1.

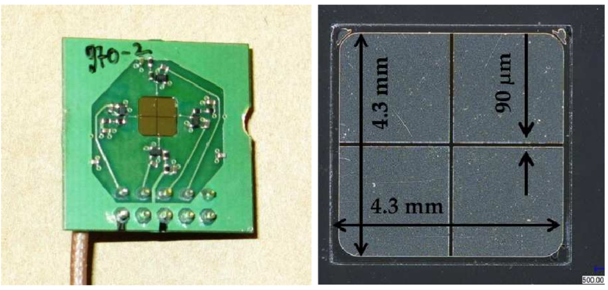

Figure 1: (left) ScCVD diamond mounted on the test PCB, (right) readout electrodes on the scCVD diamond detector.

The concept of high precision position determination is based on charge sharing between two channels when a particle crosses the 90μm gap between the detector electrodes. As shown in Fig.2, the signal height measured by means of this detector is very stable and is equal to about 15 mV. This is an analog signal from 2.95 GeV protons (MIPs) after two stages of amplification. The signal quality reflects the excellent charge collection efficiency of the high purity scCVD diamond material. Owing to this property, the charge sharing method can be used to determine the position of the particle in the 90μm gap by performing a simultaneous measurement of the signal amplitudes.

The concept was tested with a straw tube detector [2].

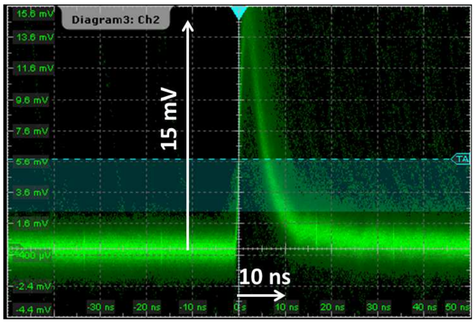

Figure 2: Superposition of about 100 waveforms recorded from the scCVD diamond with a 2.95 GeV proton beam at Cosy Jülich.

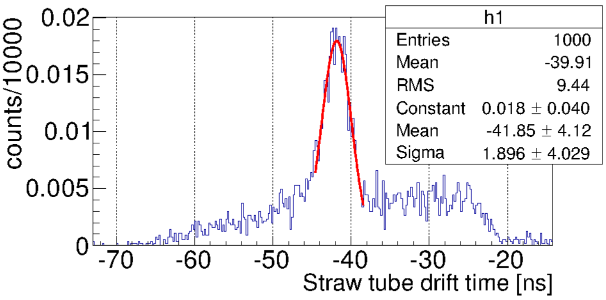

Figure 3: Drift time spectrum from the straw tube measured for one tracker position.

Using diamond position information and precise time measurement the straw tube position resolution has been determined to be about 160μm. This value includes the contribution of the diamond detector. Knowing that this value is very close to the values measured in different experiments we deduced preliminarily that the diamond position resolution has to be better than 50μm. There is also on-going data analysis based on a self-tracking method to determine the position resolution without using the diamond detector. This will allow to determine precisely the position resolution of the diamond tracking detector.

References

[1] J. Pietraszko et al., Diamonds as timing detectors for minimum-ionizing particles, NIM A 618 (2010) 121–123

[2] M. Träger et al., Performance of the straw tube readout based on PADI chip, GSI annual report, 2014.

---

[*] Work supported by HIC for FAIR

[†] j.pietraszko@gsi.de

DOI:10.15120/GR-2015-1-MU-NQM-HADES-28

Feasibility study for a MAPMT readout of the HADES RICH*

K. Schmidt-Sommerfeld[1], *J. Friese*[†1], *T. Kunz*[1],
[1]Phys. Dept. E12, TU München, Garching, Germany

The HADES RICH is equipped with a MWPC type photon detector and a solar blind CsI photon converter. Operational since 1999, the device starts to suffer from ageing effects in gas amplification, quantum efficiency and hence e^+/e^- - identification power. In view of future experiments with π^- beam and HI induced collisions at SIS and FAIR energies [1] we have studied the feasibility of a MWPC replacement by multi anode photo multiplier tubes (MAPMTs). Driving perspective is an enhancement of the e^+/e^- - identification efficiency and count rate capability. Since commercially available MAPMTs offer pixel sizes similar to the pad dimensions of the present detector, geometrical and granularity effects on ring recognition efficiency are expected to be negligible. Hence, the existing radiator-mirror system may stay unchanged.

We have studied basic RICH performance aspects [2] utilizing the properties (QE and geometry) of Hamamatsu H8500C tubes foreseen also in the CBM RICH [3]. The bi-alkali photo cathodes shift the spectral sensitivity of the present detector from the VUV to the 200 nm < λ < 600 nm region and may lead to additional background effects.

In a first step, we have investigated the scintillation light yields of several purified radiator gases [2]. The gas samples were excited with $^{32}S^{8+}$ beams (E = 90 MeV) and ^{241}Am α-particles. The spectral distributions (Figure 1) show very little emission for C_4H_{10} but a pronounced structure around 300 nm for C_4F_{10}. The total light yield in the MAPMT sensitive region has been estimated for these gases to $Y_{C4H10} < 2 \pm 1$ and $Y_{C4F10} \sim 160 \pm 60$ photons per MeV energy deposit. As known for other cases, a few percent admixture of other gases (O_2, etc.) can quench the scintillation light significantly without affecting the Cherenkov yield.

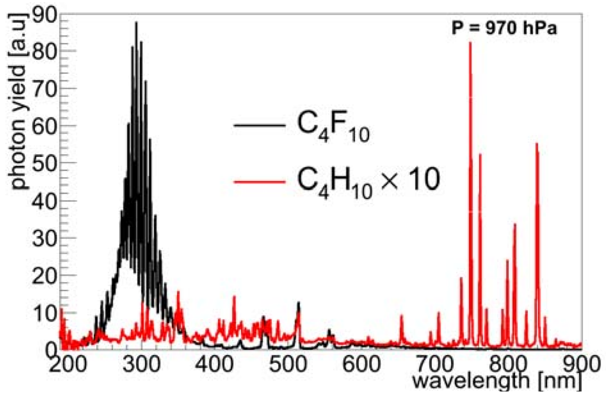

Figure 1: Spectral distributions of scintillation light emitted from purified C_4F_{10} and C_4H_{10} gas samples.

Simulation results for a pure electron sample with homogeneous phase space coverage show a strong increase of recognized rings preferably at lower polar angles and thereby short effective radiator lengths (see Figure 2, left), due to the high MAPMT quantum efficiency. Since scintillation background is negligible for reactions with low track multiplicities, the gain in e^+e^- - pair detection efficiency allows considerable signal enhancement and beam time saving for π-beam experiments. In Au + Au collisions, however, the average energy deposit $\Delta E \sim 130$ MeV/event in the standard radiator gas C_4F_{10} leads to ~ 20.000 scintillation photon hits on the detector plane. Predominantly in the area close to the beam axis they give rise to a substantial amount of fake rings. True Cherenkov rings may, however, still be discriminated to a large extent due to their significantly better ring quality parameters (pattern matrix PM QA, see right panel of Figure 2). Hence, more refined ring finder algorithms and/or selection of different radiator gas mixtures are feasible options easy to realize.

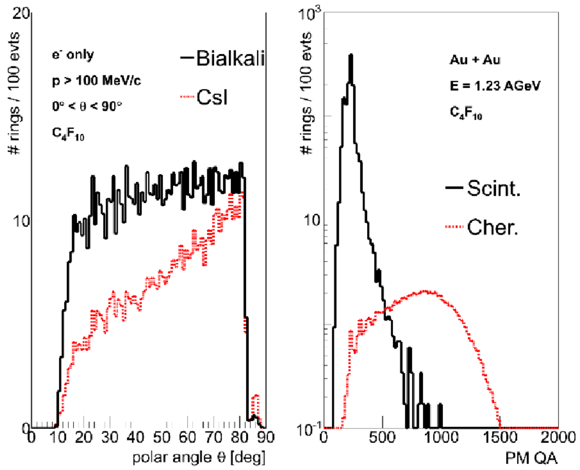

Figure 2: Simulated angular distribution of Cherenkov rings for pure electrons (left) and ring qualities PM of all rings in Au + Au collisions (right) for MAPMT readout.

The MAPMT readout of the HADES RICH has very promising perspectives for the future HADES experimental programme. We have therefore started a joint effort with the CBM RICH collaboration to elaborate on and realize this upgrade scheme within the upcoming two years.

[1] P. Finocchiaro et al., TDR HADES-100, GSI 2013
[2] K. Schmidt-Sommerfeld, Mast. Thes., TUM 2014
[3] C. Höhne et al., TDR CBM-RICH, GSI-2014-00528

---

* Work supported by BMBF 05P12WOGHH, GSI TMLFRG1316
[†] juergen.friese@ph.tum.de

DOI:10.15120/GR-2015-1-MU-NQM-HADES-29

Rebuild of a layer-1 HADES drift chamber, enhancement through a high precision planar fibre-composite milling facility*

J.Weinert[1], *J.Hehner*[1], *C.J.Schmidt*[1], *S.Schwab*[1], *the HADES collaboration, and the FAIR@GSI division*[1]

[1]GSI, Darmstadt, Germany

The 4-layer MDC tracker is an essential element of the HADES detector arrangement [1,2]. Each MDC-layer consists of 6 trapezoidal drift chambers arranged around the symmetry axis of the spectrometer just behind the RICH detector and is optimized for low-mass tracking. The MDC chambers themselves comprise 13 multi wire planes of cathode, anode and sensing wires, oriented in 6 different stereo angles The cell sizes increase with the layer number, the first layer features a cell size of 5 x 5 mm^2.The currently operating MDC modules are assembled as a sandwich of 16 frames, see Fig. 1, where the outer ones carry a Mylar window, whereas the sandwiched ones provide the tension for the wire planes. Due to the large acceptance required by the HADES setup the width of these frames is limited, which places a major challenge on the technical design w.r.t. mechanical stability and gas tightness especially for modules of layer 1. The entire stack is O-ring sealed between the planes to allow for disassembly in case of wire failure. It is the unsatisfactory precision of these seals together with the overall length of sealing line of about 40 m that has caused severe problems or sometimes even complete malfunction of these chambers (layer 1) in the past.

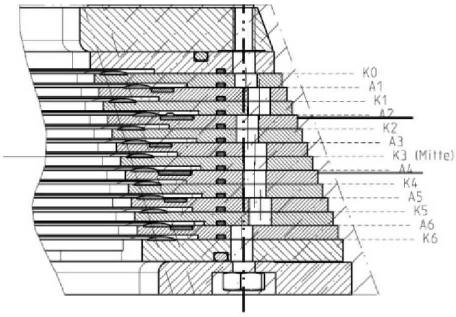

Figure 1: Stack-up of the HADES MDC frames. Alignment and wire tension is provided by means of cotter pins in the middle of the drawing.

Towards a future upgrade of this system and the operation of HADES at FAIR, a prototype MDC is under construction at the detector laboratory. This work addresses these issues through the establishment of CAD-CAM large area precision machining for these frames. The full frame is made of Vetronit EGS-103 sheets and occupies an area of about 1m^2. It is sealed to the next one in the stack by means of a circumferential O-ring of 1.0 mm diameter. For the full stack to assure wire-plane spacing as well as sealing, the material was ground to thickness by the manufacturer. For machining grooves for the O-ring, signal connecting flex cables as well as for in-frame counting gas distribution, high precision milling on an area of about 1 m^2 on both sides of the frame is indispensable. To this end, a precision vacuum table with alignment pins was constructed for the existing CAD-CAM milling station at the detector lab. Smooth finish machining in this fibered material can be achieved through very high spindle speeds and diamond enhanced tools. Preground fibre composite sheets may be vacuum clamped to this table, using an adequate underliner vacuum fleece for homogeneous clamping. Provisions are added so that even a cut out frame may be securely held this way.

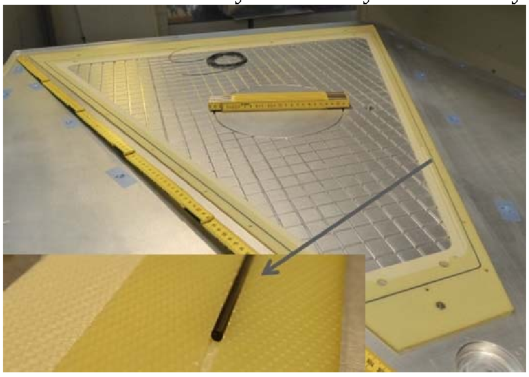

Figure 2: An MDC layer-1 wire frame made of Vetronit EGS-103 composite. The inset depicts a zoom of the O-ring sealing groove to hold the 1 mm diameter seal.

Machining results were evaluated on the first MDC frames. The depth of the O-ring groove proved a precision of less than 20µm, where about half this value may be attributed to the limit of precision for the raw material employed.

Conclusion

The procedures and tools prepared allow for adequate machining of fibre composite sheets into large detector frames. This is an enabling capability for future FAIR gaseous detector construction as well as a possible HADES MDC upgrade.

References

[1] G. Agakishiev et al. The High-Acceptance Dielectron Spectrometer HADES, Eur. Phys. J. A 41, (2009), 243.
[2] C. Müntz et al. Nucl. Instrum. Meth. A 535 (2004), 242.

DOI:10.15120/GR-2015-1-MU-NQM-HADES-30

Preparing the HADES tracking system for high-rate experiments at SIS100

C. Wendisch *[1], *L. Lopes*[2], *T. Hennino*[3], *C. Müntz*[4], *and J. Stroth*[1,4] *for the HADES Collaboration* †
[1]GSI, Darmstadt, Germany; [2]LIP, Coimbra, Portugal; [3]IPN, Orsay, France; [4]Goethe-Universität, Frankfurt, Germany

The future physics program of HADES at FAIR demands high detection standards, also in the operation stability of the tracking system comprising four layers of planar drift chambers. Due to the expected increase in beam energy and intensities at SIS100 compared to SIS18, the particle load on the wire chambers will significantly rise by a factor of 2-3. Thus, the choice of the counting gas becomes crucial with respect to aging of the detector. In this respect isobutane, used so far as quencher gas, is known to be not suitable, because it has the tendency to polymerise, triggering deposits on the wire surfaces causing aging. For this reason a different quenching gas has to be employed. CO_2 is known to not cause any aging effect [1]. It was used in the two inner layers of drift chambers MDC I & II (in front of the magnetic field) successfully demonstrating a stable performance in a gas mixture of Ar/CO_2 in recent beam-times (Au(1.23 AGeV)+Au 2012, π(0.7 GeV/c)+A 2014). This motivated to test also the significantly larger two outer layers MDC III & IV, having twice larger cell sizes and four times the active area compared to MDC I & II, for the option of operating with this counting gas.

Plateau curve measurements.

Hence, systematic tests have been performed, applying different concentrations of the new quenching gas CO_2 in the counting gas Ar/CO_2. The corresponding working point for each gas mixture was determined by measuring the relative number of tracks per triggered cosmic muons as a function of the applied high voltage, depicted in Figure 1. Compared to the gas mixture Ar/isobutane (84% / 16%) with a working point at -1700 V the new mixtures require significantly higher potentials of -1850 V to -2150 V, depending on the concentration of CO_2. Therefore the electrostatic forces between the wires increase, which requires the validation of the high voltage stability, considering the known creeping of the mounted aluminium wires during the time span of more than 10 years since the chamber construction.

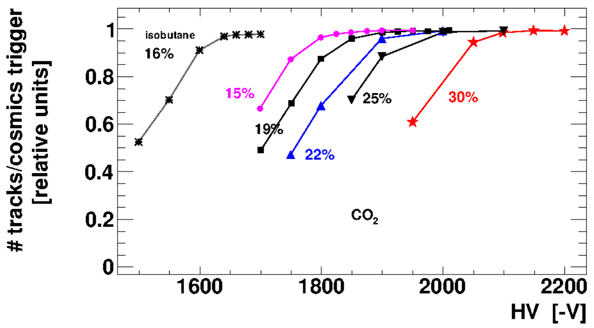

Figure 1: Relative efficiency of MDC IV for cosmic muons (MIPS) as function of high voltage for different argon based counting gas mixtures with isobutane or CO_2, concentrations given in the labels.

High rate stability tests.

Based on the verified stability up to the highest potential of -2200 V of all 12 outer drift chambers, also a stable operation under particle load has to be confirmed. To do so, a powerful x-ray source [2] is utilised to mimic the total number of particles per wire layer of a heavy-ion collision and the resulting occupancy distribution along the chamber (basically the polar angle dependence). As displayed in Figure 2, a reasonable match is achieved, generating the maximal load on the wires close to the beam pipe. A long term test was started providing a spill structure and load similar to reactions of Au+Au at 1.23 AGeV and a beam intensity of 10^7 ions/s corresponding to a detector ionization current of 2.5 μA per wire layer. Within this test the optimal fraction of CO_2 will be determined by finding the balance between risk, stable operation and signal quality.

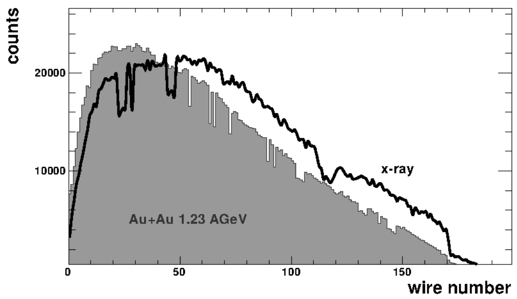

Figure 2: Occupancy of MDC III as a function of the wire number for heavy-ion collisions (Au+Au at 1.23 AGeV, grey) compared to x-ray irradiation (E_γ^{max} = 25 keV, black)

References

[1] W. Blum, W. Riegler and L. Rolandi, "Particle Detection with Drift Chambers", p. 429ff, Springer-Verlag (2008)

[2] "Mini-X X-Ray Tube", AMPTEK INC., 14 DeAngelo Drive, Bedford, MA 01730-2204 U.S.A., http://www.amptek.com

---

* c.wendisch@gsi.de

† Work supported by BMBF, HIC for FAIR and GSI.

DOI:10.15120/GR-2015-1-MU-NQM-HADES-31

DOI:10.15120/GR-2015-1-MU-NQM-HADES-31

Radiation hardness of the PSD APDs for the CBM experiment[*]

V. Kushpil[1], *A. Kugler*[1], *S. Kushpil*[1], *V. Mikhaylov*[†][1,2], *O. Svoboda*[1], *and P. Tlusty*[1]
[1]NPI of ASCR, Řež, Czech Republic; [2]CTU, Prague, Czech Republic

The projectile Spectator Detector (PSD) of the CBM experiment is designed to register forward spectator nucleons and fragments emitted in nucleus-nucleus collisions at very low polar angles. It will be used to determine the collision centrality and the reaction plane orientation.

The PSD is a fully compensating modular lead-scintillator calorimeter. The Avalanche Photo-Diodes (APD) are used to read out the scintillation light via wavelength shifting fibers. An important characteristic of the APD is its radiation hardness to a neutron fluxes of 10^{13} n/cm^2 which corresponds to two months of CBM experiment operation.

Two different APD samples, Ketek PM3375 and Zecotek MAPD-3N, were irradiated at the NPI Řež Cyclotron Facility by quasi-monoenergetic secondary neutron beam with energy of 35 MeV. A sample of Zecotek APD was irradiated with a dose of $3.4 \pm 0.2\ 10^{12}$ n/cm^2, while two samples of Ketek APDs were irradiated with $2.5 \pm 0.2\ 10^{12}$ n/cm^2. Doses were measured with a special PIN diode calibrated with a dose equivalent to 1 MeV neutron [1]. The operation temperature during the tests was kept at $22 \pm 0.5°$ C.

The APD characteristics were measured before and after the irradiation. The Capacitance-Voltage (C-V), Current-Voltage (I-V), and Capacitance-Frequency (C-F) characteristics were studied using dedicated testing setup at NPI Řež [2,3]. After irradiation, the C-V technique showed significant decrease of hysteresis and fast but not complete self-annealing. The I-V curve revealed about 1000 times increase of dark current after irradiation. The C-F study showed significant increase of short-living traps in Silicon. The test results suggest an increase of internal APD noise, especially of the high frequency, which dependents on the amount of short-living traps in the APD volume.

Figures 1 (2) show the results of the Ketek (Zecotek) APD tests with LED and cosmic muons. Both APDs have a maximum signal (noise) amplitude of about $0.3 - 0.4$ V (0.05 V) which corresponds to $20 - 30$ ph.e (3 ph.e). After irradiation both APDs are unable to resolve single photons due to high noise levels. This is not critical for the PSD performance since there are at least 15 ph.e. produced in one PSD module already by a cosmic muon. The signal and noise peaks for irradiated Ketek APD are very close which makes it very difficult to separate signal from noise. On a contrary, signal and noise peaks for Zecotek APDs are well separated from each other, what allows reliable signal from noise separation even after irradiation.

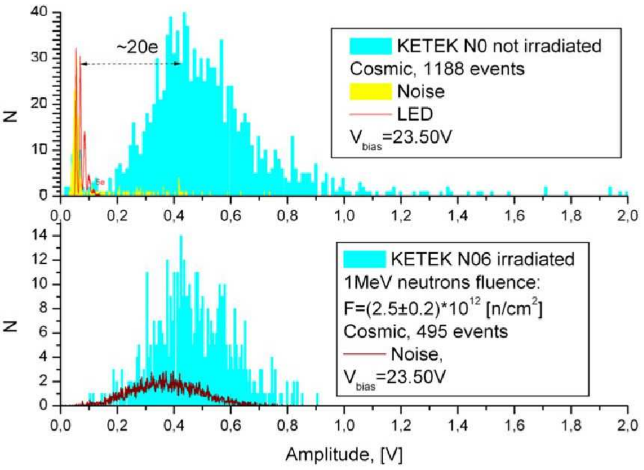

Figure 1: Test results with LED and cosmic muons of Ketek APD before (upper) and after (lower) irradiation.

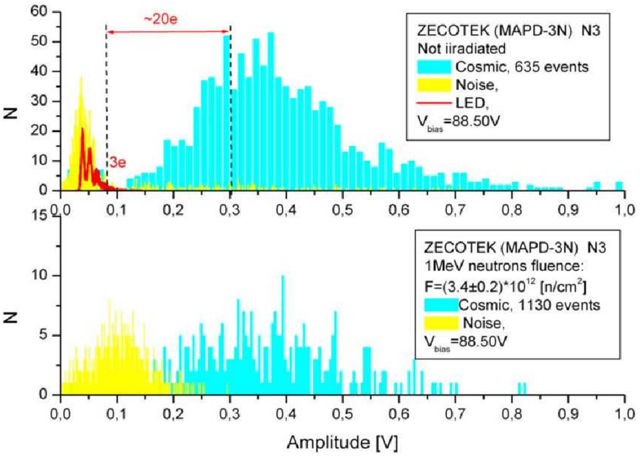

Figure 2: Test results with LED and cosmic muons of Zecotek APD before (upper) and after (lower) irradiation.

References

[1] V. Kushpil, S. Kushpil and Z. Huna, EPJ Web of Conferences 24 (2012) 07008.

[2] V. Kushpil, V. Mikhaylov, S. Kushpil, P. Tlusty, O. Svoboda, A. Kugler, doi:10.1016/j.nima.2014.11.071

[3] V. Kushpil, S. Kushpil, JINST 7 (2012) C01084.

---

[*] Work supported by the European Community FP7 – Capacities, contract HadronPhysics3 n°283286, LG12007 of the MECR and M100481202 of the ASCR grants, by project MSMT LG14004 of Co-operation Program between JINR and NPI in 2013-2014.

[†] mikhaylov@ujf.cas.cz

DOI:10.15120/GR-2015-1-MU-NQM-CBM-01

Test of prototype CBM detector components with proton beams at COSY*

J. Heuser[1], *R. Adak*[2], *T. Balog*[1], *S. Chattopadhyay*[2], *D. Dementyev*[7], *A. Dubey*[2], *D. Emschermann*[1], *J. Eschke*[3], *V. Friese*[1], *P. Ghosh*[4,1], *T. Heinz*[1], *V. Khomyakov*[5], *P. Koczon*[1], *P. Larionov*[4,1], *J. Lehnert*[1], *Ie. Momot*[4,1], *W.F.J. Müller*[1], *W. Niebur*[1], *A. Oancea*[4], *F. Uhlig*[1], *J. Saini*[2], *S. Samanta*[2], *M. Singla*[1], *I. Sorokin*[1,6], *C. Sturm*[1], *C. Stüllein*[4], *D. Varga*[8], *A. Wolf*[1], *and P. Zumbruch*[1]

[1]GSI, Darmstadt, Germany; [2]VECC, Kolkata, India; [3]FAIR, Darmstadt, Germany; [4]Goethe University, Frankfurt, Germany; [5]ITEP, Moscow, Russia; [6]KINR, Kiev, Ukraine; [7]JINR, Dubna, Russia; [8]Wigner RCP, Budapest, Hungary

Teams of the CBM collaboration have performed several in-beam tests of prototype detectors and electronics in 2014. In April at GSI, TOF and TRD detectors were examined in a parasitic ion beam steered onto a target. Prototypes of the TRD, RICH and TOF detectors were under test in a mixed electron-pion beam in November at the CERN-PS. Two campaigns of beamtime took place at COSY, Research Center Jülich, within beam time blocks provided to support FAIR related detector developments. In August, a team spent one week with testing prototype electronics under intense proton irradiation. In December, a week of beam time focused on studies of neutron-irradiated silicon microstrip sensors for the STS detector system, response measurements of a full-size triple-GEM sector for the MUCH detector system, and further studies of radiation effects in FPGA and LDO electronics. We report here on the December test at COSY.

The CBM test bench, 3 m long, is installed in the JESSICA cave into which the proton beam of COSY is extracted. Intensities from minimum 10^4 to maximum 10^9 protons per seconds can serve testing different objects. While detector systems are preferrably tested at lower impinging particle rates, and only for load tests at higher rates, electronics is required to be tested in high beam intensity conditions. The beam can be focused down to about 0.5 cm r.m.s diameter at the objects under test. Beam defocusing to areas of a few cm^2 is possible.

The aim of the beam time campaign was to study the performance of two full-size CBM prototype components, double-sided silicon microstrip sensors for the Silicon Tracking System and a full-size GEM sector for the Muon Chambers, as well as several electronics components for the read-out chains. The double-sided silicon microstrip sensors were produced in two technical versions which were to compare. Prior to the experiment, the sensors had been irradiated at the KIT irradiation facility to 2×10^{14} 1 MeV neutron equivalent fluence matching the integrated "lifetime" exposure expected in CBM running conditions. The detectors were operated in a thermally insulated station at a temperature of -8 °C, achieved with a flow of chilled nitrogen gas. The station was part of a telescope shown in Fig. 1 (top) comprising also two reference stations to define the proton tracks, and one further station with a STS prototype module under test. The full-size prototype GEM sector seen in Fig. 1 (bottom) was produced at CERN from 500 by 471 mm GEM foils in a three-foil stack, segmented into several areas, altogether having 1200 read-out pads with progressively increasing size.

The read-out of both the silicon and the GEM detectors was achieved with n-XYTER based front-end electronics and the DABC data acquisition system. The data collected allowed studying the detector response including charge collection properties.

At the downstream end of the test stand, boards with prototype electronics were placed on the beam. Already during detector operation, tests of FPGA electronics at moderate beam intensities allowed investigating single-event upsets. Dedicated runs at highest intensities were done with analog power regulating electronics (LDO) and memory components, after the conclusion of the detector tests.

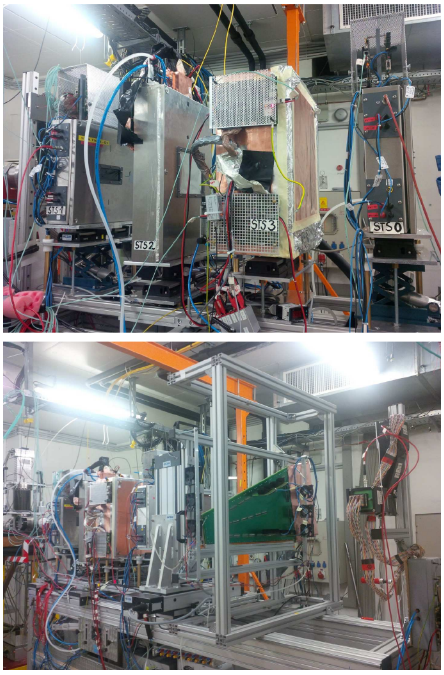

Figure 1: (Top) Telescope with four silicon detector stations. The second to the right operates the irradiated sensors. (Bottom) A full-size prototype GEM sector was installed further downstream comprising a triple-GEM foil stack.

---

* Work supported by EU-FP7 HadronPhysics3, HIC-for-FAIR, H-QM and HGS-HIRe. We acknowledge various support by IKP, FZ Jülich.

DOI:10.15120/GR-2015-1-MU-NQM-CBM-02

Event-by-event extraction of kinetic and chemical freeze-out properties in the CBM experiment*

V. Vovchenko[1,2,3,4], *I. Kisel*[1,2,3], *and D. Anchishkin*[4,5]
[1]Goethe University, Frankfurt, Germany; [2]GSI, Darmstadt, Germany; [3]FIAS, Frankfurt, Germany; [4]Taras Shevchenko University, Kiev, Ukraine; [5]Bogolyubov Institute for Theoretical Physics, Kiev, Ukraine

The future CBM experiment at FAIR is designed to study properties of strongly interacting matter produced in heavy-ion collisions at high baryon densities. It will employ high intensity beams and large acceptance detectors. One important task is to extract the thermal parameters of matter at stages of kinetic and chemical freeze-out from the observed data. The extraction of thermal parameters is implemented as a package within the CBMROOT framework.

The kinetic freeze-out temperature of charged pions is extracted from their measured momentum spectrum. In the simplest scenario the particles are assumed to have a Boltzmann momentum distribution with no collective flow. To test the method, a 1000 Monte Carlo (MC) events with thermally distributed pions ($T = 128$ MeV) were generated and then processed in CBMROOT. Reconstructed STS Tracks, as well as the initial MC Tracks, were used to calculate the average transverse mass of pions $\langle m_T \rangle$, which was then used to estimate the temperature. Due to limited detector acceptance, and due to imperfect reconstruction efficiency, the mean transverse mass of STS tracks differs from the MC one. Therefore, an appropriate correction was performed using the known momentum dependence of acceptance function and reconstruction efficiency. Figure 1 depicts the extracted Boltzmann temperature on the event-by-event level. It is seen that the extracted temperature has a Gaussian-like distribution around the theoretical value of 128 MeV when one uses MC Tracks (blue line) or STS Tracks with proper correction on acceptance (red line). If one neglects this correction on acceptance then one gets essentially different (incorrect) value of temperature (green line). The procedure, developed for this model, can be used as a basis for analysis in the framework of more complex and more realistic models.

The parameters of the chemical freeze-out are extracted by fitting the measured particle ratios in the framework of the Hadron Resonance Gas model. All strange and non-strange hadrons which are listed in the Particle Data Tables are included and the model is implemented in CBMROOT and works similarly to the THERMUS package [1]. The grand canonical ensemble formulation is used and excluded volume corrections are included in the framework of the thermodynamic mean-field approach [2]. The fit can be performed on event-by-event level and also on the inclusive spectra level. Figure 2 shows the extracted temperature and baryonic chemical potential from MC events generated in the thermal model with $T = 100$ MeV and $\mu_B = 550$ MeV. For each parameter extraction a set of 10 events was used, and the fit error estimates were calculated and depicted as well. The extracted values are consistent with the theoretical input.

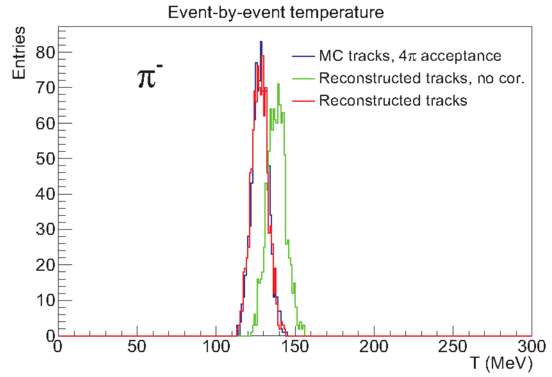

Figure 1: The temperature of pions extracted on event-by-event level using the MC tracks (blue line), STS tracks without acceptance correction (green line), and STS tracks with correction on acceptance (red line).

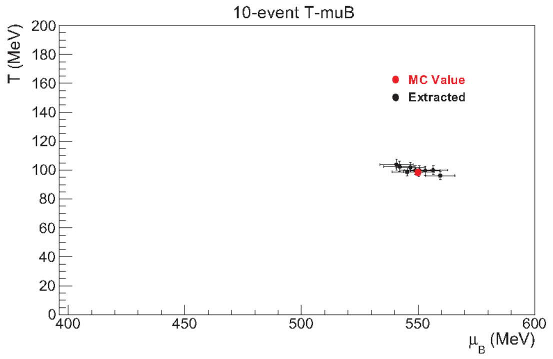

Figure 2: The temperature and the baryonic chemical potential extracted from the 10-event sets in the framework of the Hadron Resonance Gas model. The theoretical MC values is shown by the red dot.

References

[1] S. Wheaton, J. Cleymans, and M. Hauer, "THERMUS — A thermal model package for ROOT", Comput. Phys. Commun. 180 (2009) 84.

[2] D. Anchishkin and V. Vovchenko, "Mean-field approach applied to relativistic heavy-ion collisions", arXiv:1411.1444 [nucl-th]

---

* Work supported by the Hessian LOEWE initiative through the Helmholtz International Center for FAIR (HIC for FAIR)

DOI:10.15120/GR-2015-1-MU-NQM-CBM-03

4-Dimensional cellular automaton track finder for the CBM experiment[*]

V. Akishina[1,2,3] *and I. Kisel*[1,2,4]
[1]Goethe-Universität, Frankfurt am Main, Germany; [2]GSI, Darmstadt, Germany; [3]JINR, Dubna, Russia; [4]FIAS, Frankfurt am Main, Germany

The CBM experiment at FAIR will focus on the measurement of rare probes at interaction rates up to 10 MHz. The beam will provide free stream of particles, so that some events may overlap in time. It requires the full online event reconstruction not only in space, but also in time, so-called 4D (4-dimensional) event building. A time-slice is reconstructed in parallel between cores within a CPU, thus minimising communication between CPUs. This is a task of the First-Level Event Selection (FLES) package.

The FLES reconstruction package consists of several modules: track finding, track fitting, short-lived particles finding, event building and event selection. The Cellular Automaton (CA) track finder is fast and robust and thereby will be used for the online track reconstruction. This method benefits from enumeration suppression by introducing a phase of building short track segments at an early stage before going into the main combinatorial search. The reconstruction efficiency for the primary tracks with momentum higher than 1 GeV/c in case of event-based analysis (see 3D column of Table 1) is 96.1%.

As a special study of the CA track finder stability the algorithm behavior was investigated with respect to the track multiplicity. For the study a super-event, which includes a number of minimum bias events, was reconstructed with no time information taken into account. In a super-event we combine space coordinates of hits from a number of Au+Au minimum bias events at 25A GeV and give it to the CA track finder as an input to reconstruct with a regular procedure. The reconstruction efficiency dependence is stable: the efficiency for all tracks changes by 4% only for the extreme case of 100 minimum bias events in the super-event (see (3+1)D column of table 1), comparing to the case of event-based analysis.

The time information was included to the algorithm. It has resulted in a higher reconstruction efficiency (see 4D column in table 1). In particular the time information drastically decreased ghost and made the reconstruction 3.7 times faster than without the time information ((3+1)D column of Table 1). The speed now is 8.5 ms and comparable with the event-based analysis. The CA track finder was fully parallelised inside the time-slice. The parallel version shows the same efficiency as a sequential one and achieves a speed-up factor of 10.6 while parallelising between 10 Intel Xeon physical cores with a hyper-threading.

The first version of event building based on 4D track finder was implemented. The hits time measurements distribution illustrating the complexity of defining event borders in a time-slice is shown Figure 1 with blue color, the resulting distribution of reconstructed track time – with black. Reconstructed tracks clearly represent event-corresponding groups. The FLES package is ready for the 4D reconstruction of time-slices in CBM.

Efficiency, %	3D	(3+1)D	4D
All tracks	83.8	80.4	83
Primary high-p	96.1	94.3	92.8
Primary low-p	79.8	76.2	83.1
Secondary high-p	76.6	65.1	73.2
Secondary low-p	40.9	34.9	36.8
Clone level	0.4	2.5	1.7
Ghost level	0.1	8.2	0.3
Time/event/core	8.2 ms	31.5 ms	8.5 ms

Table 1: Track reconstruction performance for 3D event-by-event analysis, super-event (3+1)D and time-based 4D reconstruction for 100 mbias Au+Au collisions at 25A GeV.

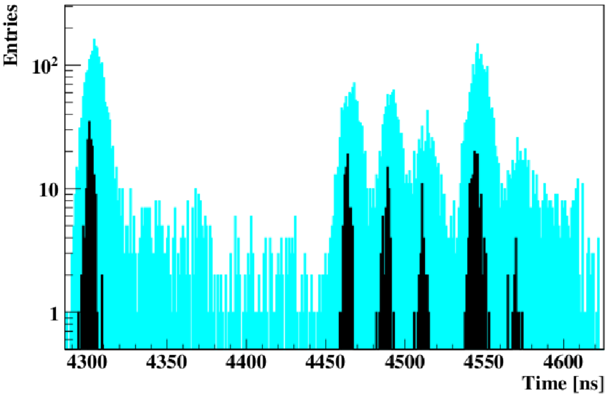

Figure 1: Distribution of time measurement in a part of a time-slice at the interaction rate of 10^7 Hz: hit time measurement (light blue), track time (black).

References

[1] I. Kisel, I. Kulakov, and M. Zyzak, “Standalone First Level Event Selection Package for the CBM Experiment”, IEEE Transactions on Nuclear Science, 60 (2013) 3703

[2] V. Akishina, I. Kisel, “Online 4-Dimensional Reconstruction of Time-Slices in the CBM Experiment”, submitted to IEEE Transactions on Nuclear Science

---

[*] Work supported by HICforFAIR, FIAS and HGS-HIRe for FAIR.

DOI:10.15120/GR-2015-1-MU-NQM-CBM-04

Monitorig system for radiation hardness tests of electronic components for future FAIR experiments.

S. Löchner[1] *and P. Koczoń*[1]
[1]GSI, Darmstadt, Germany

Electronic components installed in the field of reaction products in future experiments at FAIR have to be radiation hard. At present, selected parts undergo exhaustive tests with use of intense minimum ionising particles' beams, mostly 3 GeV protons at Jülich sychrotron facility. A control system based on ARDUINO processor has been developed to monitor the components status in situ .

Monitoring system requirements

For components like DC/DC converters or LDO voltage stabilisers the output voltage level as well as expected transient voltage spikes rate has to be monitored during irradiation. Voltage level monitoring (input and output) requires relatively low readout frequency below 1 Hz and can be implemented on inexpensive ARDUINO-Nano system. It is programmed to control an optocoupler based set of relays to govern applied input voltages (for each of 12 channels separately) and reading an ADC values of output voltages for each channel. System supervises the output voltage level and - if needed - switches off the malfunctioning channels to avoid its influence on other DUTs. Measurement status is logged on a local memory and displayed via implemented web server on connected clients. The control electronics has to be placed far away from the device under test in order to avoid spurious effects due to the irradiation.

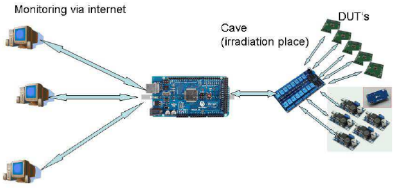

Figure 1: Block diagram of the system testing a set of DC/DC converters controlled by ARDUINO processor.

Hardware realisation

A base plate equipped with two sets of clamps and a PCB-holder has been prepared to accomodate different devices under test (DUTs). They have to be placed in a row such that the irradiating beam punches through all of them. A small scintillator placed on the beam axis behind tested chips and read out by a photomultiplier monitors the beam intensity. Its signals are also registered by ARDUINO system on separate counter and stored with time stamps spill by spill. This information helps to estimate precisely beam intensity integral. One raw of electrical clamps is supplied with input voltage (controlled by ARDUINO via set of relays) for the DUTs. Their outputs are wired via second clamps raw to the multiplexer and ADC on controller board to supervise output voltage levels.

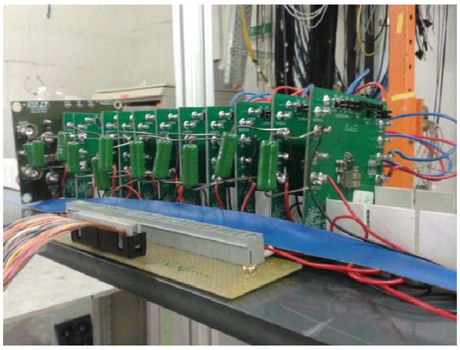

Figure 2: Base plate with PCB card holder and wiring.

ARDUINO control system

The processor itself can be programmed in a C-like programing language with use of different libraries to serve standard functionality (time server, SD-card I/O, internet I/O). Main loop of the program consists of output voltage check channel by channel, input voltage check, counter readout, internet service, timer service. The voltage read out values are compared to the upper and lower threshold values which can be defined for each channel. In case of over- or under voltage in three consecutive readout steps the affected channel is switched off.

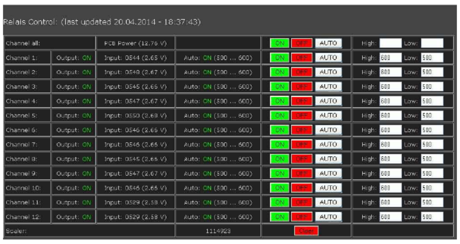

Relais Control: (last updated 20.04.2014 - 18:37:43)

Channel all:		PCB Power (12.76 V)		ON OFF AUTO	High:	Low:
Channel 1:	Output: ON	Input: 0544 (2.65 V)	Auto: ON (500 ... 600)	ON OFF AUTO	High: 600	Low: 500
Channel 2:	Output: ON	Input: 0548 (2.67 V)	Auto: ON (500 ... 600)	ON OFF AUTO	High: 600	Low: 500
Channel 3:	Output: ON	Input: 0545 (2.66 V)	Auto: ON (500 ... 600)	ON OFF AUTO	High: 600	Low: 500
Channel 4:	Output: ON	Input: 0547 (2.67 V)	Auto: ON (500 ... 600)	ON OFF AUTO	High: 600	Low: 500
Channel 5:	Output: ON	Input: 0550 (2.68 V)	Auto: ON (500 ... 600)	ON OFF AUTO	High: 600	Low: 500
Channel 6:	Output: ON	Input: 0546 (2.66 V)	Auto: ON (500 ... 600)	ON OFF AUTO	High: 600	Low: 500
Channel 7:	Output: ON	Input: 0546 (2.66 V)	Auto: ON (500 ... 600)	ON OFF AUTO	High: 600	Low: 500
Channel 8:	Output: ON	Input: 0545 (2.66 V)	Auto: ON (500 ... 600)	ON OFF AUTO	High: 600	Low: 500
Channel 9:	Output: ON	Input: 0547 (2.67 V)	Auto: ON (500 ... 600)	ON OFF AUTO	High: 600	Low: 500
Channel 10:	Output: ON	Input: 0546 (2.66 V)	Auto: ON (500 ... 600)	ON OFF AUTO	High: 600	Low: 500
Channel 11:	Output: ON	Input: 0529 (2.58 V)	Auto: ON (500 ... 600)	ON OFF AUTO	High: 600	Low: 500
Channel 12:	Output: ON	Input: 0529 (2.58 V)	Auto: ON (500 ... 600)	ON OFF AUTO	High: 600	Low: 500
Scaler:			1114923	Clear		

Figure 3: Control output of the monitoring system.

References

[1] http://www.arduino.cc/

DOI:10.15120/GR-2015-1-MU-NQM-CBM-05

Mirror misalignment control system and prototype setup

J. Bendarouach[*1], *C. Höhne*[1], *and T. Mahmoud*[1]
[1]Justus Liebig University, Giessen

An important aspect to guarantee a stable and precise operation of any RICH detector is the alignment of the mirrors. The alignment itself has two aspects: the initial alignment during setup and a misalignment monitoring during operation. For the monitoring, methods have been established based on data or an independent control of the mirror positions. The CLAM method, developed by COMPASS [1] is an example of the latter and is tested for a future realization in the CBM-RICH. This article describes a test setup on a small scale that has been implemented in the RICH prototype and tested in beam during the RICH beamtime at CERN-PS in November 2014.

The principle of the CLAM (Continuous Line Alignment Monitoring) alignment procedure [1] is to monitor over time mirror displacements via photographic images. A grid of retro-reflective material is glued on the inner part of the RICH entrance window.

The grid is made of retro-reflective stripes, forming a regular grid-shaped pattern, and of photogrammetric target dots, glued at each of the stripes crossings and on the mirror frame (Fig. 1 left). A set of four cameras are arranged at the edges of the entrance window and around each camera a set of three LEDs are fixed (Fig. 1 right). The LEDs are switched on to illuminate the grid through the mirrors.

A downscaled version with one camera only has been implemented in the RICH prototype detector and tested at CERN.

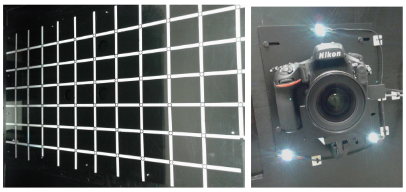

Figure 1: CLAM equipments used in the RICH prototype. Retro-reflective grid, with target dots (left). CLAM camera, surrounded by three LEDs (right).

Figure 2 shows two pictures taken for the aligned mirror system (left picture) and with misalignment by 2 mrad of the lower left mirror (right picture). Figure 3 illustrates ring reconstructions using these two setups. For the misaligned case an extreme example is shown with a B axis of the ellipse fit of 3.6; the average radius is 4.6.

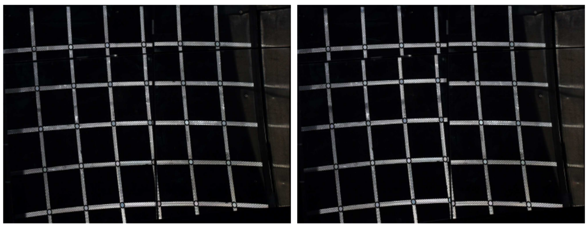

Figure 2: Reflection of the grid on the RICH mirrors. Lines not broken at mirror edges is a sign of alignment (left). If they appear broken this reveals misalignment (right). Here lower left mirror misalignment is 2 mrad.

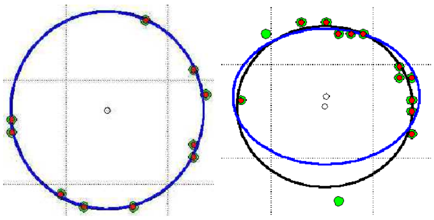

Figure 3: Single event reconstructions for beams going between the two lower mirrors. Ring reconstruction using an aligned setup (left) and a misalignment of 2 mrad (right).

A first qualitative look at mirror displacements can be given, when looking at the continuity of the reflected stripes. Indeed if a mirror is displaced with regard to one of its neighbors, stripes will appear broken at mirror edges (Fig. 2 right). Stripes are then cut into two shifted parts. According to the shift, it is possible to deduce the relative misalignment of mirrors [2].

A quantitative evaluation can also be made with this setup, when considering photogrammetry. From the relative positions of target centers to external marked reference points, the orientation of mirrors can be extracted [3]. This procedure will be implemented in a next step.

Currently the analysis of the beamtime data is ongoing and correction routines for the misalignment are in preparation.

References

[1] S. Costa et al., Nucl. Instr. Meth. Phys. Res. A 553 (2005) 135

[2] M. Sulc et al., Nucl. Instr. Meth. Phys. Res. A 595 (2008) 194

[3] L. Steiger et al., Nucl. Instr. Meth. Phys. Res. A 639 (2011) 219

---

[*] This work was supported by HIC for FAIR, by the GSI F&E-Cooperation with Giessen, and by BMBF grant 05P12RGFCG.

DOI:10.15120/GR-2015-1-MU-NQM-CBM-06

Fast analog signal processor FASP-02 *

V. Cătănescu[1]
[1]NIPNE, Bucharest, Romania

A second version of FASP ASIC dedicated for high counting rate CBM TRD prototypes developed by Bucharest group [1] - [4] was designed and produced. Similar to the first version [5], it is based on AMS 0.35 μm N-well technology. The die size is 4.65 mm x 3.45 mm. Besides the main features of its previous version, new ones are implemented in FASP-02, considering the specific architecture of the fast TRD prototypes mentioned above and the results obtained in the tests carried out in the meantime. The most relevant new features are:

- 16 input channels
- selectable positive or negative polarity of the input signals
- multiplexed analog outputs, i.e. selectable semi-Gaussian or flat top
- channel wise clock synchronized logic time for individual ADC
- channel wise logic time signal generated at the selectable threshold level or at the signal peak detection, accordingly to the user setting
- selectable trigger of neighboring channels relative to the one with the signal over the threshold
- tilted and rectangular pairing of the triangular pads

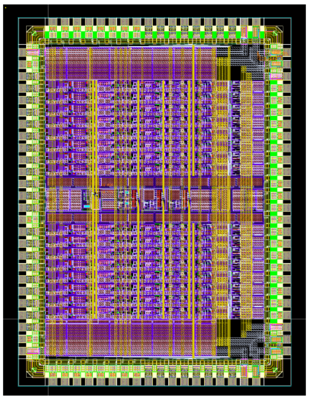

Figure 1: Photo of the FASP-0.2 ASIC

Good response to double pulse, to high pulse rate, fast recovery from positive/negative overload, base line restoration due to pulse rate shift, detector leakage current, temperature and voltage supply variations are also implemented to FASP-0.2 ASIC. Additionally the self trigger capability working with a new channel wise input/output interface enhances the performances of the new FASP-0.2 ASIC.

Table I

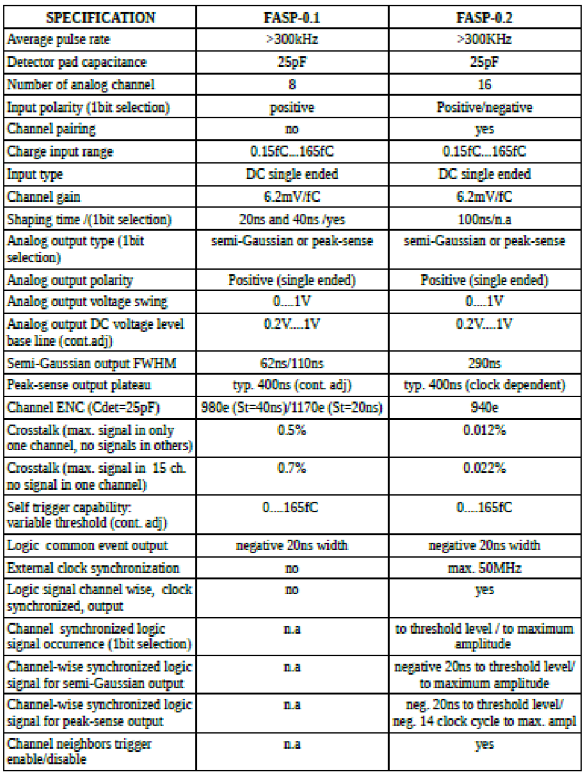

SPECIFICATION	FASP-0.1	FASP-0.2
Average pulse rate	>300kHz	>300KHz
Detector pad capacitance	25pF	25pF
Number of analog channel	8	16
Input polarity (1bit selection)	positive	Positive/negative
Channel pairing	no	yes
Charge input range	0.15fC...165fC	0.15fC...165fC
Input type	DC single ended	DC single ended
Channel gain	6.2mV/fC	6.2mV/fC
Shaping time /(1bit selection)	20ns and 40ns /yes	100ns/n.a
Analog output type (1bit selection)	semi-Gaussian or peak-sense	semi-Gaussian or peak-sense
Analog output polarity	Positive (single ended)	Positive (single ended)
Analog output voltage swing	0....1V	0....1V
Analog output DC voltage level base line (cont.adj)	0.2V....1V	0.2V....1V
Semi-Gaussian output FWHM	62ns/110ns	290ns
Peak-sense output plateau	typ. 400ns (cont. adj)	typ. 400ns (clock dependent)
Channel ENC (Cdet=25pF)	980e (St=40ns)/1170e (St=20ns)	940e
Crosstalk (max. signal in only one channel, no signals in others)	0.5%	0.012%
Crosstalk (max. signal in 15 ch. no signal in one channel)	0.7%	0.022%
Self trigger capability: variable threshold (cont. adj)	0....165fC	0....165fC
Logic common event output	negative 20ns width	negative 20ns width
External clock synchronization	no	max. 50MHz
Logic signal channel wise, clock synchronized, output	no	yes
Channel synchronized logic signal occurrence (1bit selection)	n.a	to threshold level / to maximum amplitude
Channel-wise synchronized logic signal for semi-Gaussian output	n.a	negative 20ns to threshold level/ to maximum amplitude
Channel-wise synchronized logic signal for peak-sense output	n.a	neg. 20ns to threshold level/ neg. 14 clock cycle to max. ampl
Channel neighbors trigger enable/disable	n.a	yes

The shaping time for FASP-0.2 is increased to 100 ns in order to accomplish the requirements of the new TRD prototypes with a drift region of 4 mm. The crosstalk is about ten times lover compared to FASP-0.1. The main specifications for FASP-0.1 and FASP-0.2 can be followed in Table I, where the new features and the modified specifications for FASP-0.2 can be followed.

References

[1] M. Petriş et al., Nucl. Instr. Meth. A,**714**(2013), 17
[2] M. Petriş et al., Nucl. Instr. Meth. A,**732**(2013), 375
[3] M. Târzilă et al., CBM Progress Report (2012) 80
[4] A. Bercuci et al., This Report
[5] V. Cătănescu, CBM 10^{th} Collaboration Meeting Dresden, Sept 25-28, 2007

---

* Work supported by EU-FP7/HP3 Grant No 283286 and Romanian NASR/CAPACITATI-Modul III contract RO-FAIR F02 and NASR/NUCLEU Project PN09370103

DOI:10.15120/GR-2015-1-MU-NQM-CBM-07

Status of CBMnet readout and the prototype ASIC[*]

S. Schatral[1,2], *F. Lemke*[1], *I. Som*[3], *T.K. Bhattacharyya*[3], *and U. Bruening*[1]
[1]University of Heidelberg, Mannheim, Germany; [2]GSI, Darmstadt, Germany; [3]Indian Institute of Technology Kharagpur, Kharagpur, India

Front-end read-out status

The CBMnet protocol is currently present in all stages of the CBM data acquisition (DAQ) network for the TRD and STS readout. Beside the two FEE ASICs using CBMnet links over HDMI cable, the cores are also integrated in the Read-Out Controller (ROC), the FLES Interface Board (FLIB) and further FPGA to FPGA interconnects. For these links Xilinx Gigabit Transceiver over SFPs are used. A typical setup is depicted in 1. To improve the link stability under influence of radiation, a reworked CBMnet Version 3.0 has been developed and implemented, containing a link layer, various physical layer implementations and more network related building blocks to deliver generally required features in CBM network devices. Implementations have been optimized for FPGA and ASIC use. The logic is built in such a way, that a malfunction triggered by a single event effect is detected and the corresponding functional blocks are reset. In this manner, the data acquisition over a long time is possible without any interruption. Larger test beam read-outs with up to three SPADICs per ROC have been tested in laboratory and under beam. The FLIB physical layer implementation has been tested intensively to work reliable under all conditions. The design can handle up to eight links now.

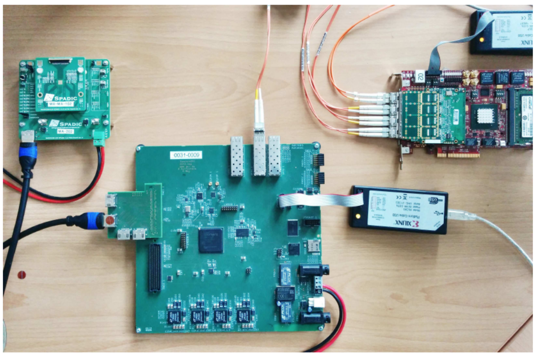

Figure 1: Read-out with FLIB, Syscore3 and SPADIC

Prototyping of a readout aggregation ASIC

A prototype of the readout and aggregation ASIC has been designed together with the Indian Institue of Technology Kharagpur (IITKGP). Therefore, an internship student from IITKGP was visiting the University of Heidelberg for half a year in 2014. This was possible because of successfully raised additional funding from the Heidelberg Center South Asia. This mixed-signal ASIC consists of a full-custom 5Gb/s serializer/deserializer, designed by the IITKGP including design elements such as phase-locked loop, bandgap reference, and clock data recovery, and a digital designed network communication and aggregation part designed by the computer architecture group of the University of Heidelberg.

In addition, there are test structures and an I2C readout integrated to ease bring up and monitoring. A specialty of this test ASIC is the aggregation of links featuring different data rates, running with bundles of 500 Mb/s LVDS [1]. This enables flexible readout setups of mixed detectors respectively readout of various chips. There are 1x, 2x, or 4x LVDS connections available enabling up to 2 Gb/s for a front-end connection. The prototype will be able to run in a mixed configuration, e.g. one 1x, two 2x, and one 4x. A prototype structure diagram depicting the link configuration possibilities is presented in figure 2. As communication protocol for the prototype, a unified link protocol is used including control messages, data messages, and synchronization messages on an identical lane. The design has been successfully simulated, verified, and hardware emulations using Spartan 6 FPGAs. The miniASIC mixed-signal design has been prepared and simulated together with the collaboration partners from the IITKGP. The first chance in 2015 for a submission using the TSMC 65nm LP Europractice process will be taken.

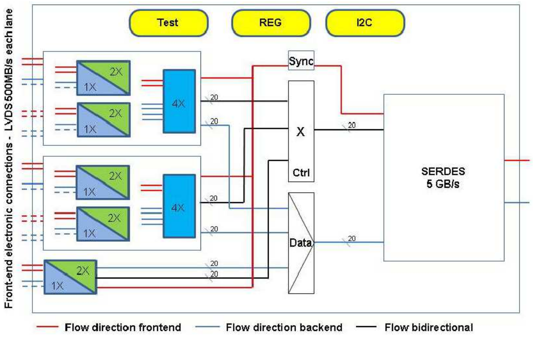

Figure 2: Link connection diagram for HUB ASIC

References

[1] S. Schatral, F. Lemke, U. Bruening, "Design of a deterministic link initialization mechanism for serial LVDS interconnects", Journal, doi:10.1088/1748-0221/9/03/C03022, VOL. 9, No. 03, pages C03022, March 2014.

---

[*] Work supported by GSI, BMBF FAIR-CBM 05P12VHFCE

DOI:10.15120/GR-2015-1-MU-NQM-CBM-08

Towards the Data Processing Boards for CBM experiment*

W. Zabolotny[†] [1], G. Kasprowicz[1], A. Byszuk[1], M. Guminski[1], K. Pozniak[1], and R. Romaniuk[1]
[1]Institute of Electronic Systems, Warsaw University of Technology, Warszawa, Poland

The Data Processing Boards (DPB)[1] are important part of the CBM readout and detector control systems, providing concentration (possibly combined with local preprocessing) of readout data, before they are sent to the First Level Event Selector (FLES). Additionally DPBs should provide fast and slow control for the Front End Electronics (FEE), distribute the reference clock, and time-critical information, like synchronization and flow control messages from the Timing and Flow Control system (TFC).

To allow testing of different possible implementations of listed functionalities, the versatile prototyping Open Hardware platform - AMC FMC Carrier Kintex (AFCK) [2] was created. The first version of AFCK is shown in figure 1.

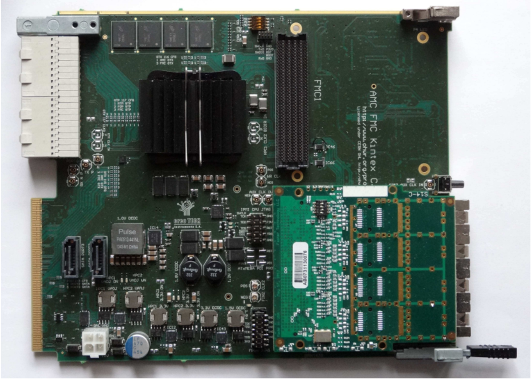

Figure 1: The AFCK board with an FMC card with 4 SFP+ cages connected to the FMC2 connector.

The AFCK board may be used in an MTCA crate or in stand-alone mode. The board is equipped with the XC7K325T FFG900 FPGA, containing 16 high speed GTX transceivers, which can be connected to 2 FMC slots (4 GTXs to each) or to the RTM connector. Another 8 GTXs may be connected to the MTCA backplane ports 0 to 11. This solution allows to test different transceivers mounted on FMC boards, without modifying the AFCK board itself. AFCK is also equipped with flexible clocking system allowing it operate with gigabit links of different speed and also to recover a jitter cleaned clock signal from a high speed receiver. The board is also equipped with 2GB of DDR3 SDRAM which may be used to store the processed data, but also for debugging purposes. Those resources make the AFCK board a suitable platform for development of data concentration and preprocessing algorithms.

First series of AFCK boards was manufactured and functionality tests were performed. High speed communication capabilities were tested with standard IBERT tests provided by Xilinx. Stable 10 Gbps transmission was achieved via GTXs connected to the FMC1 slot, while 5 Gbps transmission was possible via GTXs connected to the FMC2 and RTM (10 Gbps in FMC2 should be achievable in next revision of the board).

A few basic IP core blocks, suitable for use in the prototype DPB firmware were developed or ported and tested. These include the IPbus[3] core allowing to control board via 1 Gbps Ethernet interface and the GBT-FPGA[4] core used to communicate with GBTx ASICs. The Ethernet transmission of readout data at 10 Gbps rate was tested using the FADE IP core and protocol[5]. Stable transmission of 4x10 Gbps data streams was achieved using 4 SFP+ transceivers plugged in FMC board connected to FMC1. Porting of the White Rabbit[6] IP core to the AFCK board is currently in progress.

Results of tests performed with the AFCK board will be used to design the cost optimized version of DPB prototype.

Verification of the STS-XYTER communication protocol developed in collaboration with GSI and AGH [7] was performed in simulations and in hardware, using the KC705 evaluation board. The IPbus accessible controller, allowing to synchronize communication with the model of STS-XYTER (provided by the AGH team) and to control it, was developed and successfully tested. To achieve that, a dedicated environment for hardware-software cosimulation of IPbus connected IP cores was prepared.

Verified blocks used in controller will be used for development of prototype DPB firmware, after porting to the AFCK board.

References

[1] W. Zabolotny and G. Kasprowicz, "Data processing boards design for CBM experiment", November 2014, Proc. SPIE, vol. 9290,pp. 929023-929023-11

[2] http://www.ohwr.org/projects/afck/wiki

[3] https://svnweb.cern.ch/trac/cactus

[4] https://espace.cern.ch/GBT-Project/GBT-FPGA/default.aspx

[5] http://opencores.org/project,fade_ether_protocol

[6] http://www.ohwr.org/projects/white-rabbit/wiki

[7] K. Kasinski and W. Zabolotny and R. Szczygiel, "Interface and protocol development for STS read-out ASIC in the CBM experiment at FAIR", November 2014, Proc. SPIE, vol. 9290, pp. 929028-929028-10

---

* Work partially supported by GSI

† wzab@ise.pw.edu.pl

DOI:10.15120/GR-2015-1-MU-NQM-CBM-09

Performance of the straw tube readout based on PADI chip*

M. Träger[1], *J. Pietraszko*[1], *J. Frühauf*[1], *M. Ciobanu*[2], *C. J. Schmidt*[1] *and the FAIR@GSI division*[1]
[1]GSI, Darmstadt, Germany, [2]ISS Bucharest, Romania

A prototype of the CBM MUCH straw tube detector [1] consisting of six individual straws of 6mm inner diameter and approx. 22cm length was flushed with a gas mixture of Ar/CO_2 (70/30) at ambient pressure. The straw anodes signals where connected to the PADI-6 ASIC [2] inputs via single twisted pair cables, decoupled by HV capacitors of 400pF and protected by PIN diodes in back-to-back orientation

The PADI have been mounted and wire bonded at GSI Detector Laboratory to the FEET-PADI6-HDa PCB [3]. For every PADI-6 with four input channels the discriminator threshold could be adjusted by a dedicated potentiometer to 'just above noise'-level ($Q_{Thr} \approx 2.2fC$).

The experiment has been conducted at the COSY accelerator in Jülich. Protons of 2.95GeV energy at an intensity of $I \approx 5 \cdot 10^3 s^{-1} cm^{-2}$ in a nearly elliptical beam spot ($x \approx 7.6mm, y \approx 15mm$) where hitting two neighbouring straw tubes and the tracking diamond detector in about 20mm distance downstream.

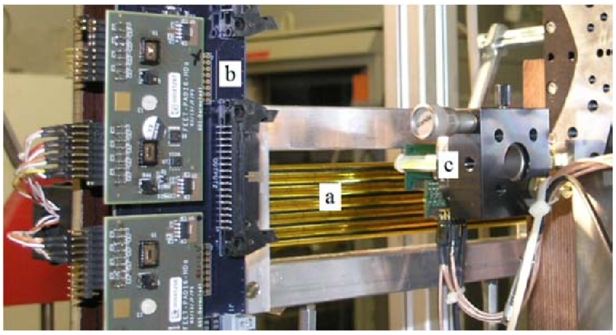

Figure 1: Experiment setup with straw tubes (a), PADI readout (b) and diamond tracking detector (c).

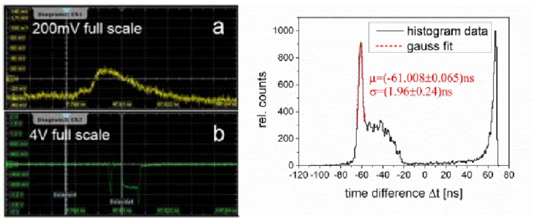

Figure 2: PADI-6 analogue output (a) and corresponding discriminator signal (b), 200ns full scale. (right) Example histogram of proton tracks near the straw wall. Background events show full range of drift times for this straw. Inefficiency hits are at the upper end of the spectrum.

The straw tubes, and as a consequence of this - their anodes, where placed horizontally and aligned in parallel to the $(0.09 \cdot 2.1)mm^2$ gap between two electrodes of the diamond tracker. The trigger for the measurement was set to choose only signals with charge sharing between these electrodes. So only particles, traversing the gap were recognized [4]. Additionally the tracking detector was mounted on a movable stage with micrometre precision to define the particle track distance to the anode wires.

After LVDS-NIM conversion only signals of one straw detector (figure 2) and two signals (D1, D2) from the diamond electrodes where fed into the R&S® RTO1044 (4GHz, 10GS/s) digital oscilloscope. The time difference $\Delta t = t_{trigger} - t_{straw}$ between the trigger ($D1 \cap D2$) and the PADI discriminator output was measured and analysed. Δt corresponds to the electron drift time in the straw and additional signal latencies.

The main drift time peak of the Δt histogram in the range $-60ns \leq \Delta t \leq -20ns$ was fitted with a Gauss function for different track positions over two straw diameters (figure 2). A mean drift time resolution of $\sigma_{\Delta t} = 2.26ns$ was achieved (1.8ns...2.7ns) corresponding to a mean position resolution of $\sigma_{\Delta y} = 157\mu m$ with the measured electron drift velocity (see figure 3). Further analysis is needed for data taken with the self-tracking method for two straws.

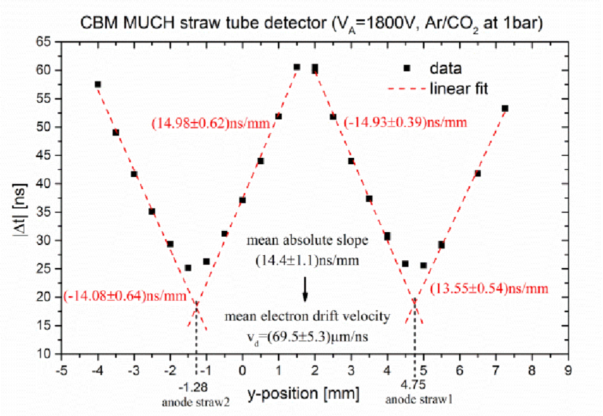

Figure 3: electron drift time dependent on the track position y (error bars are smaller than symbols). The electron drift velocity for the used detector gas was calculated.

References

[1] V. Peshekhonov et al., "Straw tube subsystem of the CBM muon detector", Physics of Particles and Nuclei Letters, March 2012, Volume 9, Issue 2, pp 172-179.

[2] M. Ciobanu et al., "PADI, an ultrafast Preamplifier - Discriminator ASIC for Time of Flight Measurements", Nuclear Science, April 2014, IEEE Transactions ,Volume 61, Issue 2, pp 1015-1023.

[3] J. Frühauf et al., "Hardware Development for CBM ToF", GSI Report 2013-1, 292 p.

[4] J. Pietraszko et al., "High resolution tracking based on scCVD diamond detector for straw tube detector tests", this report.

---

* Work supported by FAIR@GSI PSP code: 1.1.1

DOI:10.15120/GR-2015-1-MU-NQM-CBM-10

CBM First-level Event Selector data management developments*

H. Hartmann[1], *J. de Cuveland*[1], *and V. Lindenstruth*[1]
[1]FIAS Frankfurt Institute for Advanced Studies, Goethe-Universität Frankfurt am Main, Germany

The First-level Event Selector (FLES) is a high performance computing cluster functioning as the central event selection system in the CBM experiment. It combines data from a large number of input links to time intervals and distributes them to the compute nodes, via a high-performance network. Simultaneously, the FLES carries out online analyses and complete event reconstruction on the data. Data rates at this point are expected to exceed 1 TByte/s.

The FLES system will consist on one hand of a scalable supercomputer with custom FPGA-based input interface cards and a fast event-building network and will be constructed largely from standard components. On the other hand special developed software allowing to process the incoming data in real-time builds up the FLES.

A small scale, highly customizable platform, the Micro-FLES cluster was installed at GSI. Eight identical compute nodes provide a total of 192 logic cores and 512 GB memory plus one head node for infrastructural services. This test system enables studies on the development of the FLES such as elaborating performant software for timeslice building.

A *timeslice* is the fundamental data structure managing access to all detector raw data of a given time interval. In addition to existing timeslice building prototype software based on InfiniBand Verbs investigations of a more high-level interface to the network hardware have been performed using MPI. For this purpose a specialized micro benchmark test suite was developed simulating the FLES timeslice building use case. Benchmark results for simultaneous data transfer on the Micro-FLES are displayed in Fig 1. When communication is established only between three nodes, MPI's performance compares to the maximum data rate of point to point communication for Infiniband Verbs (green curve) on the Infiniband-FDR network. However, the data rate decreases by 15% when all eight nodes of the Micro-Fles are participating in an any-to-any communication. Further tests on bigger compute cluster are neccessary to evaluate the achievable data rates for MPI on a big scale and are currently under investigation.

In 2014 the FLES demonstrator system was upgraded signifciantly to the Micro-FLES2. First, the Micro-FLES2 was equipped with the latest Mellanox dual Connect-IB HCAs (mlx5), in addition to the existing Mellanox dual ConnectX-3 cards (mlx4). Overall the new cards are faster than the old as shown in Fig. 2. A data rate of 6 GB/s can be achieved using only one of the four ports, already. Furthermore, the new cards feature a 16x PCIe 3.0 interface and therefore allow to saturize the full bandwith of both ports. An accumulated data rate of 18 GB/s can be achieved utilizing all Infiniband ports. With this first upgrade the Micro-FLES2 can send data from node to node three times as fast as before (e.g., 18 GB/s instead of 6GB/s). The improved performance is essential for the development of timesslice building software.

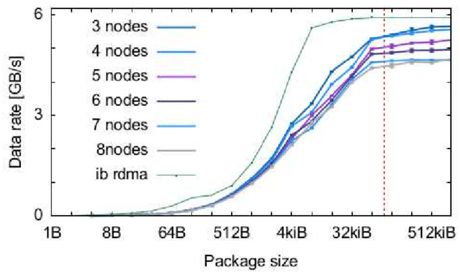

Figure 1: MPI benchmark on the Micro-FLES.

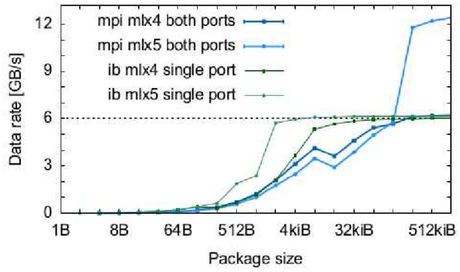

Figure 2: Perfomance tests for the Micro-FLES2.

Secondly, two further Mellanox SX6036 36-port 56Gb/s switches were installed in order to realize different network setups such as a fat tree. This helps investigating routing issues in the development of software when distributing the incoming data. The previous existing switch was connected with full bidirectional bandwidth to both of the new switches making them leaves of a fat tree. All first ports of mlx4 and mlx5 for each node were connected to leaf-switch1 and all second ports to leaf-switch2. Using this setup the network structure and blocking ratio in case of a fat tree can be configured dynamically via the provided internet interface of the switches. The upgraded Micro-FLES2 provides better performance and a greater flexibilty in testing different scenarios allowing to evaluate a greater varity of possibilites for the final system – the FLES.

---

* Work supported by BMBF (05P12RFFCP) and HIC for FAIR

DOI:10.15120/GR-2015-1-MU-NQM-CBM-11

CBM FLES input interface developments*

D. Hutter[1], *J. de Cuveland*[1], *and V. Lindenstruth*[1]
[1]FIAS Frankfurt Institute for Advanced Studies, Goethe-Universität Frankfurt am Main, Germany

The First-level Event Selector (FLES) is the central event selection system in the CBM experiment. Its task is to select data for storage based on online analyses including a complete event reconstruction. To do so, the FLES timeslice building has to combine data from all input links to time intervals and distribute them to the compute nodes. To allow for efficient timeslice building, detector data streams are partitioned into microslices prior to combining them. Microslices are specialized containers covering a constant timeframe of real time, which is the same for all subsystems. This allows data agnostic, subsystem independent timeslice building. This partitioning will be done by the Data Processing Boards (DPB) as they are the last stage of the read-out tree which has to contain subsystem specific components.

The FLES input interface is realized by a custom FPGA PCIe card, the FLES Interface Board (FLIB). Its purpose is to provides the optical interface to the DPBs as well as the interface to the FLES input nodes. The current development is based on the commercial HTG-K7-PCIE board form Hitech Global. It features a Xilinx Kintex-7 FPGA, a 8x PCIe 2.0 interface, up to eight 10 GBit/s links and optionally 8 GB of DDR3 memory.

The FPGA design includes the protocol for receiving microslices, a pre-processing engine preparing microslices for timeslice building and a custom full off-load DMA engine. Once configured the DMA engine is capable of constantly transferring microslices and meta data to the PCs memory without involving the host CPU. The only task the CPU needs to perform is to acknowledge processed data segments occasionally to allow reusing buffer space. A measurement of the DMA performance for one to four 10 Gbit/s microslice streams is given in Fig. 1. For up to three steams, data is transmitted at full input speed. For four streams, the input data rate exceeds the available PCIe bandwidth. The achieved maximum data rate is 3345 MB/s, which matches the absolute maximum PCIe data rate for the given configuration.

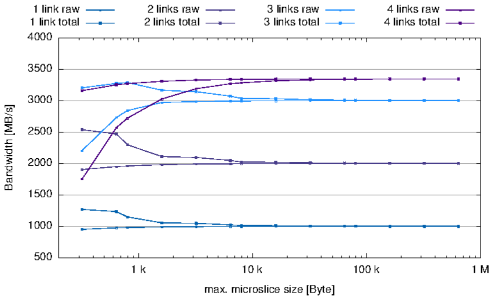

Figure 1: FLIB read-out bandwidth

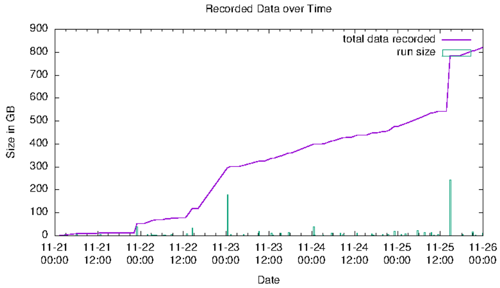

Figure 2: Recorded testbeam data over time

For demonstration and testing the input interface concept in real live applications, the FLIB and flesnet software have been used for read-out in the CERN-PS 2014 testbeam at T9 beamline. In contrast to the final system, current setups lack the DPB layer and do not support the creation of microslices. A specialized FLIB prototype firmware therefore includes a mockup of the DPB design and is capable of directly receiving CBMNet messages as delivered by the CBM front-end electronics. Simplified microslices are generated inside the FLIB and subsequently handled in the same way as foreseen for the final setup. Thus the setup is capable of delivering fully build timeslices to any given consumer. In case of the testbeam, timeslices were written to disk and simultaneously published via a ZMQ socket to CBMroot clients for front-end calibration and online monitoring. In addition the firmware and software includes support for front-end configuration and synchronization over CBMnet which is accessible via a ZMQ interface or from within CBMroot.

During the testbeam a single FLIB in conjunction with the flesnet software was successfully used to read-out up to six detector setups in different configurations. Three different flavors of data sources have been employed, Syscore 2, Syscore 3 and TRB boards. Figure 2 shows an overview over five days of data taking. In total 888 GB of data in 84 runs was written to disk without any major read-out related problems. Online performed data consistency checks and first offline analysis did not reveal any issues with the data.

To support future setups including DPBs the FLES interface module is currently under development. It will provide a 10 GBit/s link transferring microslices to the FLIB enabling full featured microslice creation on the DPBs.

---

* Work supported by BMBF (05P12RFFCP) and HIC for FAIR

DOI:10.15120/GR-2015-1-MU-NQM-CBM-12

Yield studies on a fully integrated sensor for the CBM-MVD*

B. Linnik[1], *D. Doering*[1], *M. Deveaux*[1], *and J. Stroth*[1,2] *for the CBM-MVD collaboration*
[1]Institut für Kernphysik, Goethe University Frankfurt, Germany; [2]GSI Darmstadt, Germany

The CBM-experiment will study the phase diagram of hadronic matter in the region of highest baryon densities by means of rare probes like open charm particles. Reconstructing those particles calls for a vertex detector providing a unique combination of excellent spatial resolution, light material budget and high rate capability. To match those requirements, we intend to use CMOS Monolithic Active Pixel Sensors, which are developed by the PICSEL group of IPHC Strasbourg and evaluated at the IKF Frankfurt within an common R&D project.

A first fully integrated sensor, MIMOSA-28, was developed in the AMS $0.35\ \mu\mathrm{m}$ CMOS process and it is used in the STAR-HFT since 2014. However, this sensor does not match the requirements of CBM regarding radiation tolerance and readout speed. Therefore, the sensor architecture was migrated to a novel $0.18\ \mu\mathrm{m}$ process. This process was found to provide a higher tolerance to ionizing radiation [1]. Moreover, its higher packing density allows for reading two lines in parallel, which accelerates the readout by a factor of two with respect to the elder design.

In 2014, a first fully integrated prototype sensor (FSBB-M0) was realized in the new process [2]. The sensor was realized in two flavors (FSBB-M0a and FSBB-M0b), which differ slightly in the dimensions of some transistors. It features 416×416 pixels of $22 \times 33\ \mu\mathrm{m}^2$ pitch and it is read out within $40\ \mu\mathrm{s}$ via a pair of discriminators at the end of each column. Hereafter, the digital data is zero-suppressed and sent out via two 320 Mbps digital links. The sensitive surface of the FSBB is $13.7 \times 9.2\ \mathrm{mm}^2$. The final sensor of the CBM-MVD will presumably consist of three FSBBs. The FSBB-M0 was tested at the CERN-SPS and provided a detection efficiency for minimum ionizing particles of $\gtrsim 99,5\%$, a noise occupancy of $\lesssim 10^{-5}$ and a spatial resolution of $< 5\ \mu\mathrm{m}$ in both dimensions [3], which matches the requirements of CBM.

To test the robustness of the design and to assess the production costs for the CBM-MVD, we measured the production yield of the FSBB. In accordance with our experience, we assumed that flaws due to production mistakes would turn into a measurable deterioration of the noise of the sensors. A total of 25 (17 FSBB-M0a and 8 FSBB-M0b) sensors was bonded on PCB and operated with a suited readout system. By measuring the transfer functions we revealed the temporal noise (TN) of the individual pixels and the fixed pattern noise (FPN), which is caused by the offset of the dark signal of the pixels.

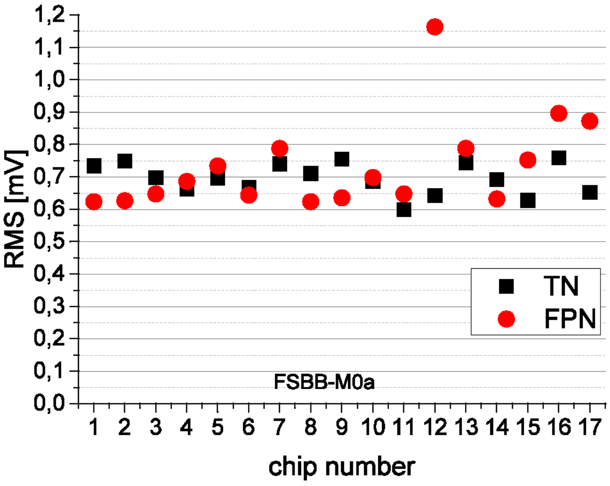

Figure 1: Temporal noise and fixed pattern noise measurement of all 17 FSBB-M0a chips.

The results of the study on the FSBB-M0a are shown in Fig. 1. We found all sensors tested to be operational and they provided a $\mathrm{TN} = (0.70 \pm 0.05)\ \mathrm{mV}$ and $\mathrm{FPN} = (0.73 \pm 0.14)\ \mathrm{mV}$. Only one of the tested sensors showed a higher FPN of $\sim 1.2\ \mathrm{mV}$, which might still be acceptable. Similarly good results were observed with the eight FSBB-M0b tested, which all found being operational (not shown).

We conclude that a first full size sensor meets the requirements of CBM with respect to surface size, data rate and spatial resolution. Moreover, the design mostly meets the specification in terms of readout speed. Measurements demonstrated that the sensor provides a good detection of minimum ionizing particles and the production yield was found to exceed 95%.

References

[1] D. Doering et al. Noise performance and ionizing radiation tolerance of CMOS MAPS using the $0.18\ \mu\mathrm{m}$ CMOS process. *J. of I.*, 9(05):C0551, 2014.

[2] F. Morel et al. MISTRAL & ASTRAL: two CMOS Pixel Sensor architectures suited to the Inner Tracking System of the ALICE experiment. *J. of I.*, 9(01):C01026, 2014.

[3] Marc Winter. Private communication.

---

* This work has been supported by BMBF (05P12RFFC7), HIC for FAIR, HGS-HIRe and GSI.

DOI:10.15120/GR-2015-1-MU-NQM-CBM-13

Non-ionizing radiation hardness of CMOS Monolithic Active Pixel Sensors manufactured in a 0.18μm CMOS process*

D. Doering[1], *M. Deveaux*[1], *B. Linnik*[1], *and J. Stroth*[1,2] *for the CBM-MVD collaboration*
[1]Institut für Kernphysik, Goethe-University Frankfurt, Germany; [2]GSI Darmstadt, Germany

Modern 0.18 μm CMOS processes provide numerous features, which may allow for decisive progresses in the read-out speed and the radiation tolerance of the CMOS Monolithic Active Pixel Sensors (MAPS) to be used in the Micro-Vertex-Detector of CBM. Together with the PICSEL group of IPHC Strasbourg, we aim to exploit those features by migrating the successful architecture of our sensors toward this novel technology. This work reports about our findings on the first prototypes manufactured with the new technology.

A weak point of CMOS sensors is the slow diffusion of signal charge in the undepleted active medium. A sufficient radiation hardness was only achievable with very small pixels, which do not provide the required readout speed. A few years ago, this obstacle was alleviated by the upcoming availability of CMOS processes providing a high-resistivity epitaxial layer of 1 kΩcm. It could be demonstrated that this increases the non-ionizing radiation hardness by more than one order of magnitude. Therefore pixels of this high-resistivity AMS-0.35-process having a pitch of $20 - 30$ μm achieved the design goal of a non-ionizing radiation hardness in the order of 10^{13} $\mathrm{n_{eq}/cm^2}$ [1].

Using this technology, a first vertex detector based on CMOS sensors is taking data in the heavy-ion experiment STAR since 2014.

Achieving the required non-ionizing radiation hardness, the ionizing radiation hardness and read-out speed of sensors in the AMS-0.35-process were not sufficient for the application in modern vertex detectors, e.g. in ALICE and CBM. Therefore, a novel $TOWER - 0.18$ μm process was exploited and found to provide a higher tolerance to ionizing radiation [2]. Moreover, the smaller feature size allows for the integration of a more complex logic into the pixel providing a faster read-out. An additional feature of this process is the use of very high resistivity epitaxial layers up to 6 kΩcm. It was expected, that this would improve the non-ionizing hardness further, which would allow for larger pixels and therefore for a faster sensor readout.

To test this assumption, the prototype sensor MIMOSA-34 was designed, irradiated to 10^{13} $\mathrm{n_{eq}/cm^2}$ and tested hereafter. The sensor provides elongated pixels with a pixel pitch between 22 μm $\times$ 33 μm and 33 μm $\times$ 66 μm. Figure 1 shows the response to photons of an Fe-55-source of the largest pixel. Its charge collection efficiency is reduced by radiation damage from 34% to 25% for the seed pixel and from close to 100% to 62% for the charge of the full cluster. The signal to noise ratio, as measured with a Sr-90-β-source, decreases from 49 to 35. According to our experience with other sensors, this signal to noise ratio is sufficient to provide an excellent detection efficiency.

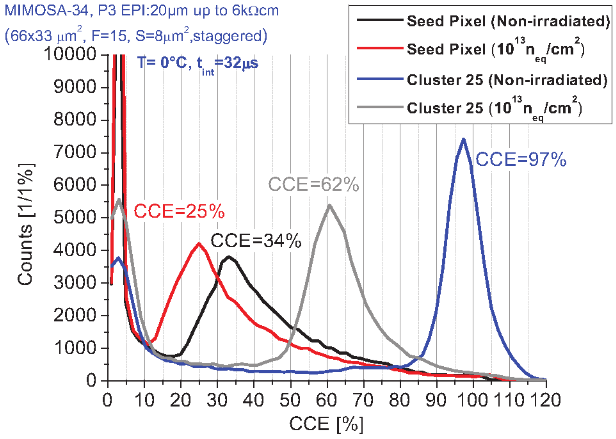

Figure 1: Signal response to photons after a radiation dose of 10^{13} $\mathrm{n_{eq}/cm^2}$.

In conclusion, the novel process is likely to provide a tolerance to 10^{13} $\mathrm{n_{eq}/cm^2}$ as needed for CBM even in combination with a 33 μm $\times$ 66 μm pixel pitch. Consequently, this pitch seems now limited by the need for matching a spatial resolution of 5 μm rather than by the radiation tolerance. The latter allows for increasing the pixel pitch of the vertex detector, which comes with significant advantages in terms of readout speed and reduced power consumption.

References

[1] D. Doering et al., Pitch dependence of the tolerance of CMOS monolithic active pixel sensors to non-ionizing radiation, Nuclear Instruments and Methods A, **730**, 111, 2013.

[2] D. Doering et al., Noise performance and ionizing radiation tolerance of CMOS Monolithic Active Pixel Sensors using the 0.18 μm CMOS process, Journal of Instrumentation, **9**(05) C0551, 2014.

---

* This work has been supported by BMBF (05P12RFFC7), HIC for FAIR and GSI.

DOI:10.15120/GR-2015-1-MU-NQM-CBM-14

Status of the CBM MVD simulation model*

S. Amar-Youcef[1], *M. Deveaux*[1], *E. Krebs*[1], *B. Linnik*[1], *B. Milanovic*[1], *Ph. Sitzmann*[1], *T. Tischler*[1], *and J. Stroth*[1,2]

[1]Goethe-Universität, Frankfurt, Germany; [2]GSI, Darmstadt, Germany

The MVD simulation model is subject to a major revision and considerable progress has been achieved. In the following its motivation and status are discussed.

Motivation

Due to its proximity to the target and its excellent spatial resolution the MVD is the dedicated detector to resolve secondary vertices. In addition, its capability to clean-up background in di-electron spectra is subject of a dedicated study [1]. However, the primal implementation in simulation lacked in a realistic description (with respect to e.g. the material budget or peculiar sensor features) for advanced studies. These studies are needed to develop strategies to achieve best performances, to analyze critical points and to finalize the concept of the MVD and its tools.

The revision of the MVD model, to be incorporated to the CbmRoot simulation framework, aims at a more realistic description of the current understanding of the MVD. Before, in the standard scenario, the MVD was simplified as two homogeneous discs at 5 cm and 10 cm downstream the target, with an outer (inner) radius of 2.5 cm (0.5 cm) and 5 cm (0.5 cm), respectively. As no representation of individual sensors was included, this simplification possesses many limitations. The limitations involves mainly sensor properties beyond the hit response as e.g. the data parallelism of sensors, the rolling-shutter frame read-out, bandwidth limitations, busy circuits, a definition of a fake hit rate, time stamping and the data format.

The new approach [2] addresses these issues and is based on a segmented geometry with four stations (at 5 cm, 10 cm, 15 cm and 20 cm downstream the target) including all relevant features. Its underlying sensor characteristics are borrowed from MIMOSIS. The detailed geometry was elaborated in CAD. The conversion from the respective description into the ROOT geometry format was conducted by a dedicated tool. In this way we are able to respond very quickly to changes in the detector design.

Along with the proper representation of the gradual material budget, there is the possibility to incorporate the missing features mentioned above, as hits are assigned to sensors now. The data parallelism is incorporated by restructuring the data processing through the three process steps called digitizer, clusterfinder and hitfinder. Here, the corresponding data representations called Monte Carlo (MC) hits, digis (firing pixels) and clusters, which serve as input for the respective process step are assigned to the respective sensors. All further properties of the sensors are incorporated within the digitizer. As previously mentioned digis are particularly important, as they describe the response of the sensor to impinging hits mimicked by the digitizer. Apart from the generated pattern of single hits the interference among hits is important to consider. This is implemented in the digitizer by creating the signal amplitudes and distributions of all hits before jointly discriminating to generate the binary charge measurement. Hits from consecutive events might pile-up and/or neighboring hits merge. This is particularly true due the long integration time of one frame of $\sim 30\ \mu s$. The respective output is dependent upon the features included as listed above. These features require a definition of the temporal sequence of the recorded MC hits accordingly. Its considerations are relevant especially for the time-based track reconstruction of CBM. The time-based consideration is a necessary condition to use the reconstruction software with real data, too.

In order to verify the performance in the reconstruction (e.g. tracking) matching of all data states is incorporated. All geometry information are accessible via the 'GeoHandler'-Class. For the tracking a simplified representation of the material budget is provided in the form of a map in dedicated files provided together with the digitizer.

In order to study the impact of misalignment the position of the individual sensors can be modified within simulation.

Status

The new MVD geometry and data processing has been incorporated and uploaded to CbmRoot. All functionality has been re-established and can be used within the event-based reconstruction. Due to constraints on the part of CbmRoot, the time-based reconstruction is not fully available for the time being. Likewise the MVD model does not yet comprise all the details. However, all preparations necessary have been provided. The pile-up of events can be studied via background events. Moreover, further details related to the performance of the sensor (as e.g. aging with the integrated radiation dose, noisy pixels, different pixel geometries) have not yet been treated.

The current representation of the MVD in simulation is the prerequisite to allow for realistic simulations on the performance of the MVD in secondary vertexing and background rejection in di-electorn spectroscopy.

References

[1] Erik Krebs, "Background rejection in the dilepton analysis with the CBM-Micro Vertex Detector", this report

[2] Philipp Sitzmann, "Integration eines sensorbasierten Detektorresponsemodells", Master-thesis 2015

---

* Work supported by BMBF (05P12RFFC7), HIC for FAIR and GSI

DOI:10.15120/GR-2015-1-MU-NQM-CBM-15

PRESTO: PREcursor of the Second sTatiOn of the CBM-MVD*

M. Koziel[1], *T. Tischler*[1], *C. Müntz*[1], *and J. Stroth*[1,2] *for the CBM-MVD collaboration*[1]
[1]Institut für Kernphysik, Goethe-Universität, Frankfurt, Germany; [2]GSI Darmstadt, Germany

This report summarizes the activities undertaken to construct a precursor of a quadrant of the second MVD-station.

The PRESTO (PREcursor of the Second sTatiOn) project of the CBM-MVD addresses the double-sided integration of 15 MIMOSA-26 sensors (dummies and working sensors, 9 of these on the front in a 3×3 and 6 sensors on the back in a 2×3 arrangement) onto a 8×8 cm^2 CVD diamond carrier [1] featuring a thickness of 150 μm. The PRESTO module will employ new flex cables (FPC) [2] providing all signals needed to operate and read out the sensors (10 FPCs in total), see fig. 1.

To assembly this module, new sensor positioning jigs aiming for a sensor positioning precision with respect to the support and the neighboring sensors of below 100 μm were manufactured. To evaluate the integration concept, the RAL-247 adhesive [3] and the new jigs, a dummy PRESTO module has been assembled employing 50 μm thin MIMOSA-26 dummies and a 200 μm thin glass plate which serves as sensor carrier, see fig. 2.

In the process of gluing, the inclusion of air bubbles should be avoided due to the vacuum operation of the MVD and the use of thinned sensors. This triggered a study focusing on optimizing the preparation of the glue, its dispensing and the quality assurance of the results. The number of air bubbles introduced into the glue during its mixing process has been significantly reduced by degassing it in an exicator at about $4 \cdot 10^{-1}$ mbar for about 1 hour. However, this did not prevent the air bubbles to appear after the gluing of the sensors onto the carrier. The introduced air bubbles featured a size of about $100 - 300$ μm diameter. To verify their impact on the 50 μm thin sensor dummies, the cured module has been placed inside a small vacuum chamber which has been evacuated for about 48 hours to a value of $4 \cdot 10^{-1}$ mbar. The visual inspection of the sensor dummies using a high precision microscope did not reveal any mechanical damage. Further studies will be addressed with working sensors to check on-the-fly any possible correlation between sensor performance, pressure and bubble sizes.

The gluing of the dummy sensors onto the glass carrier demonstrated that a glue volume of $3 - 5$ μl (different glue volume used for each row of sensors) is sufficient to dispense a uniform and thin (about $10 - 17$ μm) layer underneath the sensors. The horizontal sensor-to-sensor distances were measured to be below 5 μm. The vertical variation in the distances between the sensor edges were measured to be of about 20 μm. The achieved precision is significantly below the envisioned one. Next steps comprise the establishing of procedures for the integration of the FPCs, the exercise of double-sided bonding and the verification of the vacuum compatibility.

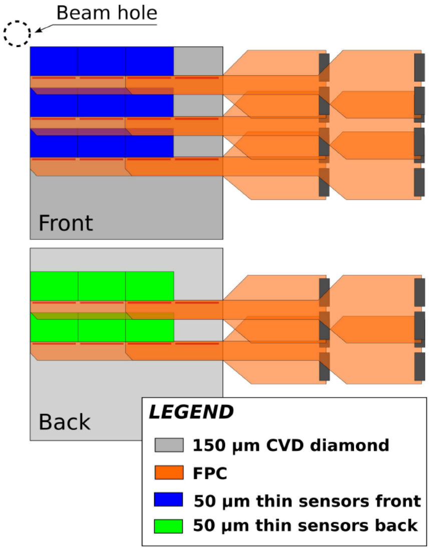

Figure 1: Sketch of the arrangement of the sensors and the FPCs with respect to the support carrier within the PRESTO module.

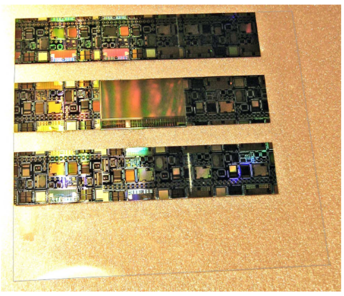

Figure 2: Assembled dummy module of PRESTO.

References

[1] Diamond Materials GmbH, Germany

[2] P. Klaus et al., "Ultra-low material budget Cu flex cable for the CBM-MVD. "GSI annual report 2014.

[3] Private communication, Simon Canfer Rutherford Appleton Laboratory, Composites and Materials Testing Group, UK.

---

* This work has been supported by BMBF (05P12RFFC7), EU-FP7 HadronPhysics3, HGS-HIRe, GSI and HIC for FAIR.

DOI:10.15120/GR-2015-1-MU-NQM-CBM-16

The CBM MVD read-out electronics*

M. Wiebusch[1], *J. Michel*[1], *M. Koziel*[1], *B. Milanovic*[1], *S. Amar-Youcef*[1], *P. Klaus*[1], *J. Stroth*[1,2], *and the CBM-MVD collaboration*

[1]Goethe-Universität Frankfurt; [2]GSI, Darmstadt, Germany

Electronics

The CBM Micro-Vertex-Detector (MVD) front-end electronics serve as an intermediating device between the Monolithic Active Pixel Sensors (MAPS) and the DAQ system (based on the TRB3 system developed by HADES). In the current connection scheme, one TRB3 FPGA board can support up to 16 sensors of type "MIMOSA-26" in parallel. The front-end electronics are necessary to supply the sensors with electrical power and to convert between different digital signal standards. The central element of these custom-built PCBs is the converter board. In addition to remote controlled power supplies, signal switches and drivers, it features an ADC section to monitor the sensor's momentary electrical parameters. The sensors have to be supplied with a sensitive external biasing voltage, the so-called clamping voltage, which gets distributed to all sensor pixels. Several generation and distribution schemes were implemented to investigate which setup results in the best noise performance.

Measurements

The MIMOSA-26 provides a test mode to measure the discriminator transfer function[1] of all pixels. The slope steepness is directly related to the temporal noise of the sensor. The read-out sytem was extended to operate and read out the sensor in this test mode. The recorded data is evaluated by a dedicated ROOT-based analysis software. Noise tests with MIMOSA-26 are ongoing. However, preliminary results concerning the influence of the clamping voltage suggest that it is beneficial to generate this reference voltage as close to the sensor as possible and to use decoupling capacitors, if possible, next to the bonding pads on the flex print cable. These results are in particular important for the development of the next generation of cables[2]. Furthermore, the ADC section on the converter board can be used to perform systematic scans in order to characterize the sensors. As an example of such an automatic scan, Fig. 1 shows the dependence of the sensor's current consumption on the discriminator threshold setting.

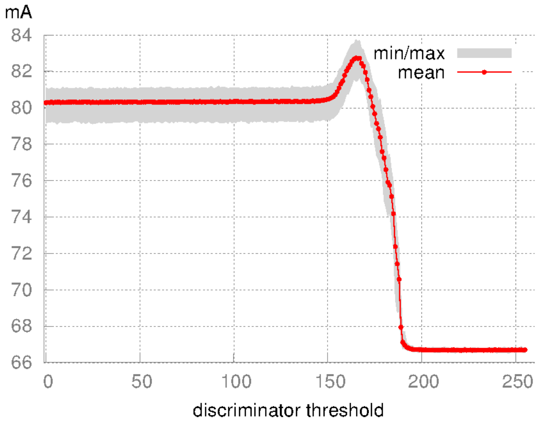

Figure 1: The current consumption (digital VCC) of a MIMOSA-26 sensor as a function of the discriminator threshold. Data acquired with front-end electronics onboard monitoring devices.

Laboratory instrumentation

When characterizing sensors, it is desirable to investigate the temperature dependence of certain sensor parameters. Until recently, such tests were conducted using a large cooling system which circulates coolant through a cooling block to which the sensors under test are attached. The sensors are now operated on a small copper platform which is cooled with a peltier element. A PID controller implemented on a microcontroller senses the temperature of the platform by means of a onewire temperature sensor and regulates the current through the peltier element. The device features a small display and a simple user interface, alternatively it can be remote controlled via a USB connection. The platform can be cooled down to circa $-10°\mathrm{C}$ within few minutes while consuming 50 W. Overall, the set-up was greatly reduced in size, while at the same time improved in usability.

PRESTO

Current activities focus on bulding a prototype[1] of a quadrant of the second station of the MVD. For now, MIMOSA-26 sensors are used in this project though they do not qualify to be used in the final detector. Parts of the front-end electronics are currently redesigned to fit the spacial constraints of the set-up.

References

[1] M. Koziel, T. Tischler et al., PRESTO: PREcursor of the Second sTatiOn of the CBM-MVD, this issue.

[2] P. Klaus et al., Ultra-low material budget Cu-based flexible cable for the CBM-MVD, this issue.

---

* Work supported by BMBF (05P12RFFC7), HIC for FAIR and GSI

[1] The firing probability of a binary pixel as a function of discriminator threshold; usually has the form of a sigmoid function.

DOI:10.15120/GR-2015-1-MU-NQM-CBM-17

The CBM-MVD: Progress in Mechanical Integration *

M. Koziel[1], *T. Tischler*[1], *C. Müntz*[1], *M. Deveaux*[1], *and J. Stroth*[1,2] *for the CBM-MVD collaboration*
[1]Institut für Kernphysik, Goethe-Universität, Frankfurt, Germany; [2]GSI Darmstadt, Germany

This report summarizes the activities undertaken towards the construction of the Micro Vertex Detector (MVD) of the Compressed Baryonic Matter (CBM) experiment.

Quality assurance of 50 μm thin PRESTO sensors: Thinned MIMOSA-26 sensors will be used for assembly the so called PRESTO module. PRESTO addresses the double-sided integration of 15 MIMOSA-26 sensors (dummies and working sensors) onto a 8×8 cm^2 CVD diamond support (see [1] for more details). Sensors will be connected with the R/O system by means of a newly designed ultra-low material budget flex cable employing commercially available processes based on copper traces [2]. Constructing the PRESTO allows to estimate the integration yield providing that the employed sensors are tested prior to assembly. Up to now, 18 MIMOSA-26 AHR sensors thinned to 50 μm were probe tested using the setup described in [3]. The setup allows testing the standard operation modes of the sensor as well as measure the fixed pattern and temporal noise by the means of so called s-curves. 12 sensors were found without a significant number of dead/noisy pixels; they were qualified as fully operational. Four sensors exhibiting some dead rows/columns were marked as faulty. The two remaining sensors were not operational due to a power supply short (one sensor) and problems while powering one out of the four MIMOSA-26 sub-matrices. The estimated yield was then of about 65% which is in agreement with expectations for this type of sensors [4]. The temporal noise was found to be of about 1.6-1.8 mV and the fixed patter noise of about 0.5-1.0 mV. This is by factor of 2-3 higher than the noise specified by a sensor provider. This was nevertheless as expected since the sensor power signals were generated outside the probe card. The addressed probe tests allowed also to establish test procedures required for non-destructive tests of thinned CMOS sensors and can be applied for testing the final MVD sensors.

Development of a custom made glue: An "ideal" adhesive for the integration of the sensors onto their supports should be easy to dispense in a thin and uniform layer—calling for a low viscosity—, radiation hard as well as flexible (to compensate for the thermal expansion mismatches between the sensor and their support material) within the temperature range foreseen for the operation of the MVD sensors. Since there are none "on-shelf" products that meet these requirements, a custom-made, two compound adhesive with a working name RAL-247 was manufactured at the Rutherford Appleton Laboratory (RAL), Composites and Materials Testing Group, UK. The glue features a glass temperature of -45 °C, a viscosity of below 100 mPa·s and a curing time of 48 h at +50 °C. To investigate its radiation hardness, RAL-247 samples were irradiated with X-rays to 100 Mrad and to a proton dose of about 10^{15} n_{eq}/cm^2. The irradiated samples were sent to RAL for further Dynamic Mechanical Analysis tests which unraveled no significant change of properties [5] that confirms the expected radiation hardness at the range of radiation doses expected at the MVD.

Development of the heat sinks for the MVD: The operation of the MVD in vacuum requires a continuous cooling of the sensors to limit radiation induced defects as well as noise. To keep the material budget of the individual MVD station as low as possible, the cooling approach of the MVD employs highly thermal conductive sensor support materials (CVD diamond [6] and encapsulated high performance graphite) in the acceptance of the MVD and actively cooled aluminum-based heat sinks outside of this area. To evaluate the cooling concept and its vacuum compatibility, half-station heat sinks of the first three MVD stations were manufactured at COOLTEK GmbH. The heat sinks incorporate a buried cooling pipe and have thermally been simulated prior their manufacturing using a worst case scenario for the sensor power dissipation plus an additional safety factor of four. These heat sinks are currently being evaluated under laboratory conditions focusing on their vacuum compatibility [7]. The heat dissipation of the MVD sensors is provided by kapton insulated flexible heaters from OMEGA Engineering, INC.

References

[1] M. Koziel et al., "PRESTO: PREcursor of the Second sTatiOn of the CBM-MVD." GSI annual report 2014.

[2] P. Klaus et al., "Ultra-low material budget Cu flex cable for the CBM-MVD. "GSI annual report 2014.

[3] M. Koziel et al., GSI annual report 2013.

[4] L. Greiner et al., CPIX 2014, Bonn, Germany

[5] Private communication, Simon Canfer Rutherford Appleton Laboratory, Composites and Materials Testing Group, UK.

[6] Diamond Materials GmbH, Germany

[7] G. Kretzschmar et al.,"Vacuum compatibility of the CBM-MVD." GSI annual report 2014.

---

* This work has been supported by BMBF (05P12RFFC7), EU-FP7 HadronPhysics3, HGS-HIRe, GSI and HIC for FAIR.

DOI:10.15120/GR-2015-1-MU-NQM-CBM-18

An ultra-low material budget Cu-based flexible cable for the CBM-MVD *

P. Klaus[1], *J. Michel*[1], *M. Wiebusch*[1], *M. Koziel*[1], *T. Tischler*[1], *S. Schreiber*[1], *C. Müntz*[1], *and J. Stroth*[1,2] *for the CBM-MVD collaboration*
[1]Goethe-Universität Frankfurt; [2]GSI, Darmstadt, Germany

The CBM Micro-Vertex Detector (MVD) relies on employing a material budget x/X_0 per detector station of 0.3% (first station) to 0.5% (following stations) to allow for a secondary vertex resolution of better than 70 μm with typical pixel pitches of about 20 μm. To reach this ambitious goal, all components in the acceptance of the detector have to be challenged w.r.t. their impact on the material budget, while at the same time maintaining their cutting-edge performance regarding mechanical and electrical properties as well as radiation hardness. In addtion, the sensor readout has to be robust with low noise occupancy, which puts strong constraints on the electrical properties of the rather long cables connecting the sensors with the front-end electronics (FEE) being outside the acceptance of the detector. Especially in the outer stations, substantial parts of those cables are placed inside the acceptance and hence contribute to multiple scattering. Those cables are flexible printed circuits (FPC) and provide power to the CMOS Pixel Sensors (CPS), allow to control them, and to read out the hits. The previous-generation cable was not specifically optimized for ultra-low material budget, being a copper-based cable with a layer thickness of about 25 μm. It was successfully tested in a beamtime with the CBM-MVD prototype [1].

Reducing the dominant factor of the material budget meant reducing the thickness of the copper layer, see Tab. 1. The cable was redesigned with a readout to the side (see Fig. 1), a smaller feature size (80 μm) and thus a reduced total cable width, and copper traces with a thickness of only 12 μm. The cables were manufactured using a commercial technology offered by ILFA [2].

Table 1: Material budget of the new cable.

Layer	d [μm]	x/X_0	Si-equiv [μm]
Coverlay	26	0.009 %	8.6
Copper	$40\% \cdot 12$	0.033 %	31.3
Polyimide	25	0.009 %	8.2
Sum	63	0.051 %	48.1

Some problems may arise from the ultra-thin layout though: Without an accompanying ground layer, the traces will not have an excellently controlled impedance. In addition, the resistance of the power supply lines becomes substantial. To compensate for this, their width was increased to 360 μm resulting in visible areas of higher material budget in Fig. 1. Dedicated tests with a new sensor test stand will evaluate the effect of the missing shielding and possible impedance mismatch of signal lines as well as the higher resistance of the power supply lines. This test stand comprises a compact, Peltier-based temperature control unit, and a readout chain using a special test mode of the sensor which makes it possible to measure transfer functions. This allows to deduce the temporal and fixed pattern noise of a reference sensor to conduct extensive systematic tests of flex cable generations.

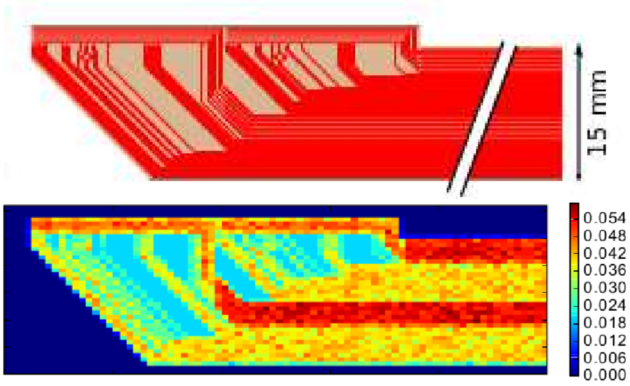

Figure 1: CAD layout of the new ultra-thin FPC showing the bonding zone and the part of the cable situated in the acceptance of the detector (top); an analysis of its material budget in % of x/X_0 (bottom).

Another possible approach to reach an even smaller material budget employs Aluminium instead of Copper for the conductive layer. Aluminium has a smaller conductivity (3.5010^7 S/m vs. $5.96 \cdot 10^7$ S/m) but at the same time a much larger radiation length (88.97 mm vs. 14.36 mm), suggesting an improvement in the material budget by a factor of 3.6. The downside of this non-standard Aluminium-based technology is the lower production reliablity, and thus higher cost and production times.

To summarize, a new ultra-thin design of the FPC for the CBM Micro-Vertex Detector was created and the cables produced. Its suitability will be analyzed including its electrical performance and integration stability. Further technologies to reduce the material budget even more are being evaluated.

References

[1] M. Koziel *et al.*, Nucl. Instrum. Methods **A 732** (2013) 515

[2] ILFA Industrieelektronik und Leiterplattenfertigung aller Art GmbH, Hannover, Germany

---

* Work supported by BMBF (05P12RFFC7), HIC for FAIR and GSI

DOI:10.15120/GR-2015-1-MU-NQM-CBM-19

Multi-strange (anti)baryon enhanced production at FAIR energies

I. Vassiliev[1], *I. Kisel*[1,2,3], *M. Zyzak*[1,2,3], *V. Vovchenko*[1,2,3,4], *and the CBM Collaboration*
[1]GSI, Darmstadt; [2]FIAS, Frankfurt am Main; [3]Goethe-Universität, Frankfurt am Main; [4]Taras Shevchenko University, Kiev, Ukraine

One of the predicted signatures of the phase transition from nuclear matter to a deconfined phase is the enhanced production of multi-strange particles. Additionally the yield of particles carrying strange (anti)quarks is expected to be sensitive to the fireball evolution and formation of the Quark Gluon Plasma (QGP). In order to estimate the effect of QGP creation in the heavy ion collisions we used PHSD 3.0 model [1] — a microscopic off-shell transport approach that consistently describes the full evolution of a relativistic heavy-ion collision from the initial hard scatterings and string formation through the dynamical deconfinement phase transition to the QGP, as well as hadronization, and to the subsequent interactions in the hadronic phase. The yield of Ω^+ hyperon ($\bar{s}\bar{s}\bar{s}$) seems to be very sensitive to the production mechanism at the FAIR energies. The results of our calculations are shown in Fig. 1, where the red points correspond to the partonic phase mechanism and the blue ones — to subsequent interactions in the hadronic phase. Each point is calculated for 5M central Au+Au PHSD (HSD) events. According to the PHSD 3.0 model, most of the Ω^+ particles are produced in the QGP phase.

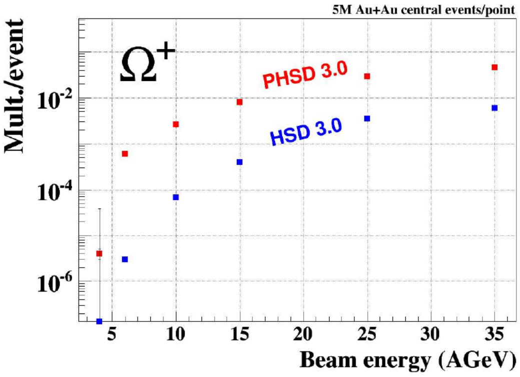

Figure 1: Yields of Ω^+ as a function of the beam energy calculated in the PHSD and HSD models. Each point corresponds to $5 \cdot 10^6$ central Au+Au PHSD (red) or HSD (blue) events.

Multi-strange hyperons will be identified in the CBM experiment by their decays into charged hadrons, which are than detected in the Silicon Tracking System (STS) and the Time-of-Flight (TOF) detector.

To study the performance of multi-strange hyperon reconstruction in the CBM experiment, several sets of $5 \cdot 10^6$ central Au+Au PHSD and HSD events at 4, 6, 10 AGeV for the SIS-100 case and at 15, 25 and 35 AGeV for the SIS-300 energy range have been simulated. The high statistics allows to calculate also the $\Omega^\pm$ reconstruction efficiency directly, avoiding signal embedding into the PHSD events. Together with the wide range of the beam energies, it allows to investigate the systematic behavior of different physics observables, e.g. direct and elliptic flow, excitation function and antihyperon-to-hyperon ratios.

The Ω^+ hyperon decays into $\bar{\Lambda}K^+$ with the branching ratio of 67.8% and $c\tau$ = 2.46 cm. The STS v13d geometry with 8 double-sided segmented strip detectors, cables and support frames was used for the event reconstruction. Particle identification with the realistic "umbrella" shaped TOF v13a geometry for the SIS-100 energies and v13b for the SIS-300 energies were applied. The KF Particle Finder [2] package was used to reconstruct Ω^+. A typical reconstructed invariant-mass spectrum is shown in Fig. 2. The red line indicates the fit the signal and background by a polynomial plus Gaussian function.

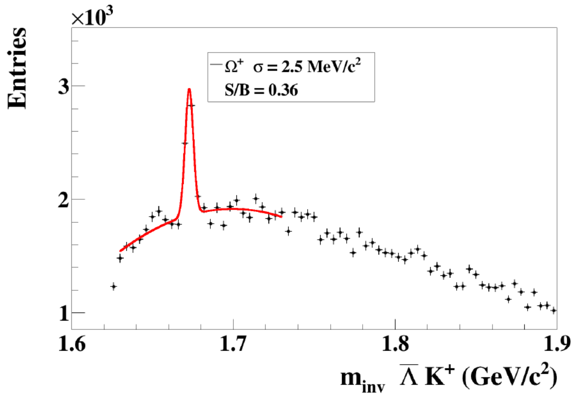

Figure 2: Reconstructed invariant-mass distribution of $\bar{\Lambda}K^+$ pairs in central Au+Au collisions at 25 AGeV, the red line indicates the signal plus background fit by a polynomial plus Gaussian function.

The Ω^+ reconstruction efficiency results in about 6.2% for central PHSD events. A good signal to background ratio of about 0.36 is observed due to the TOF antiproton particle identification procedure and KF Particle $\bar{\Lambda}$ reconstruction.

References

[1] E.L. Bratkovskaya, W. Cassing, V.P. Konchakovski, O. Linnyk, *Parton-Hadron-String Dynamics at Relativistic Collider Energies*, Nucl. Phys. A 856 (2011) 162-182.

[2] I. Kisel, I. Kulakov and M. Zyzak, *Standalone First Level Event Selection Package for the CBM Experiment*, IEEE Transactions on Nuclear Science, vol. 60, No. 5, October 2013, p. 3703.

DOI:10.15120/GR-2015-1-MU-NQM-CBM-20

ϕ meson production in Au+Au collisions and its reconstruction feasibility in the CBM experiment

V. Vovchenko[1,2,3,4], *I. Vassiliev*[1], *I. Kisel*[1,2,3], *and M. Zyzak*[1,2,3]
[1]GSI, Darmstadt, Germany; [2]FIAS, Frankfurt, Germany; [3]Goethe University, Frankfurt, Germany; [4]Taras Shevchenko University, Kiev, Ukraine

The CBM experiment at FAIR is aimed to study properties of QCD diagram at high baryon densities and moderate temperatures. One of the most interesting particles among other rare probes is ϕ meson, which consists of $s\bar{s}$ pair and can decay inside the fireball. In that case it carries a direct information about the production of $s\bar{s}$ pairs. Production of ϕ in heavy-ion collisions have earlier been studied in other experiments, such as HADES [1] and NA49 [2], however, the existing up to now data is rather insufficient in the CBM energy range.

To study the production of ϕ mesons at CBM energies and higher, and feasibility of its reconstruction, a minimum bias Au+Au events were generated in the UrQMD-3.4 model at 4–160 AGeV energies. For each energy 1 million of events was generated (see Fig. 1). Among these events only 10% of the most central were considered. The centrality was determined in accordance with the charged multiplicity in the rapidity window of $|y_{\text{c.m.}}/y_{\text{beam}}| < 0.5$. Additionally, 10^4 central (impact parameter $b = 0$ fm) events generated in PHSD-3.0 model [3] were analyzed as well for comparison.

One should note that ϕ meson has a relatively small lifetime ($c\tau \simeq 45$ fm), and there is a certain probability for it to decay inside the fireball. For this reason ϕ meson is not considered as a stable particle in transport models such as UrQMD and PHSD by default. Therefore, in order to calculate the ϕ multiplicity they are forced to be stable with respect to decays in UrQMD and PHSD by adjusting the corresponding flag.

The precise measurements of ϕ/K^- ratio allows to extract the fraction of K^- coming from ϕ decay [1]. The results of calculations for this quantity within UrQMD and PHSD are depicted in Fig. 1. Additionally, experimental data of HADES and NA49 collaborations is shown by symbols with error bars. We note that NA49 data is for Pb+Pb collisions. The data shows a plateau in energy dependence at higher collision energies. This effect is qualitatively well reproduced in UrQMD and PHSD. At low energies ($p_{\text{lab}} \lesssim 7$ AGeV), however, the data [1] show an increase of the ϕ/K^- ratio. Taking into account that available data in this energy range is rather insufficient, future measurements at CBM may help to clarify the presence of such effect.

In order to study ϕ-mesons reconstrucion feasibility 5 millions of central Au+Au events at 6 AGeV were simulated. K^+ and K^- identified in the TOF detector are combined to pairs by the KF Particle Finder package. The resulting invariant-mass distribution for the K^+K^- pairs is shown in Fig. 2 where the ϕ signal is clearly visible.

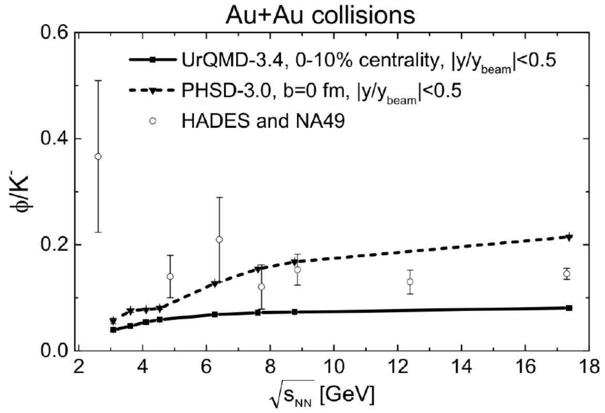

Figure 1: Energy dependence of ϕ/K^- ratio, calculated in UrQMD and PHSD. Experimental data of HADES and NA49 collaborations is depicted symbols with error bars.

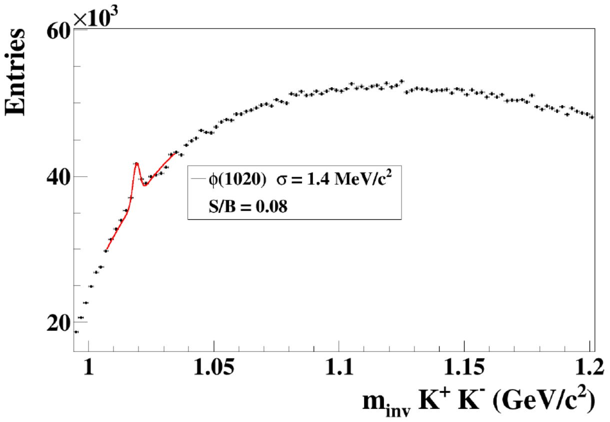

Figure 2: Invariant-mass distribution of K^+K^- pairs for 5 millions of central Au+Au events at 6 AGeV. The shape of combinatorial background is estimated by the mixed-event technique.

References

[1] G. Agakishiev *et al.* [HADES Collaboration], Phys. Rev. C 80 (2009) 025209.

[2] C. Alt *et al.* [NA49 Collaboration], Phys. Rev. C 78 (2008) 044907.

[3] E.L. Bratkovskaya, W. Cassing, V.P. Konchakovski, O. Linnyk, *Parton-Hadron-String Dynamics at Relativistic Collider Energies*, Nucl. Phys. A 856 (2011) 162-182.

DOI:10.15120/GR-2015-1-MU-NQM-CBM-21

π^0 reconstruction through a γ-conversion method with KF Particle Finder in the CBM experiment*

M. Zyzak†[1,2,3], *I. Kisel*[1,2,3], *and I. Vassiliev*[1]

[1]GSI, Darmstadt, Germany; [2]Goethe-Universitaet Frankfurt, Frankfurt am Main, Germany; [3]Frankfurt Institute for Advanced Studies, Frankfurt am Main, Germany

The CBM experiment is being designed to study heavy-ion collisions at extremely high interaction rates and track densities. One of the main observables for CBM are light vector mesons decaying through dilepton channels, that are of the particular importance for the physics program of the experiment. Because of the low branching ratio the key issue for reconstruction of light vector mesons is background suppression. Being a major source of this background, π^0 and γ-conversion have to be carefully studied.

The main decay channel of π^0 is a $\pi^0 \to \gamma\gamma$ channel with a branching ratio of 98.8%. The γ can be reconstructed in the Silicon Tracking System (STS) when it was converted into an electron-positron pair on the material or support structures of the detector: $\gamma \to e^+e^-$. To study this decay π^0 reconstruction through a γ-conversion method was implemented in the KF Particle Finder package for short-lived particle reconstruction.

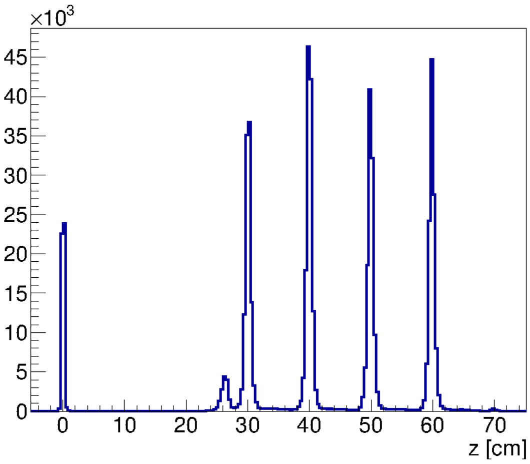

Figure 1: Distribution of γ-particles reconstructed z-position. The obtained histogram represents position of the target, a beam pipe window and four stations of the STS detector.

At the first stage tracks from electrons and positrons registered in STS are selected using particle identification (PID) information from the Ring Image Cherenkov Detector (RICH), Transition Radiation Detector (TRD) and Time of Flight (ToF) detector. Selected tracks are combined into γ-candidates. Based on the Kalman filter mathematics, the KF Particle Finder package allows to achieve high reconstruction quality of the particles. For example, distribution of the reconstructed z-position nicely represents the structure of the detector: the target at 0 cm, the beam pipe window at 26 cm and four stations of the STS detector at 30, 40, 50 and 60 cm (see Fig. 1). Then the γ-candidates within 3σ region around the peak position (0 MeV/c^2) are selected and combined with each other. High quality of the γ-candidates allows reconstruction of π^0 with a width of 1.7 MeV/c^2 and signal to background ratio of 0.77 already for 5 million central AuAu events at 25 AGeV (see Fig. 2).

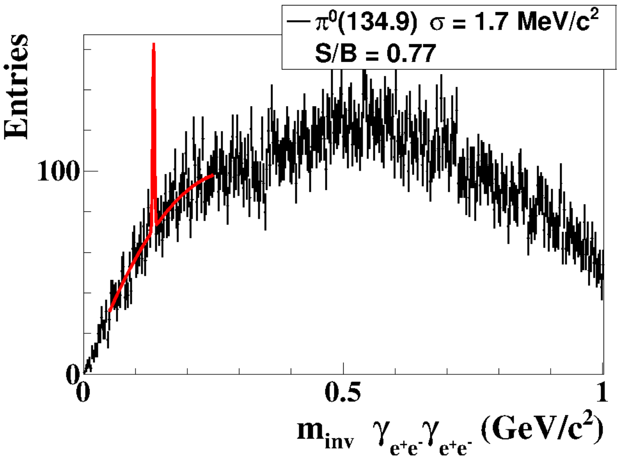

Figure 2: Mass distribution of $\gamma\gamma$ pairs for 5 million central AuAu events at 25 AGeV using PID information form RICH, TRD and ToF detectors. The peak from π^0 is nicely seen with a width of 1.7 MeV/c^2 and a signal to background ratio of 0.77.

Average gamma conversion factor within the STS detector is about 6.5%. This gives a probability of $4 \cdot 10^{-3}$ for both γ-daughters to produce tracks. Taking into account efficiency of the track finding, PID detector and particle construction the overall π^0 reconstruction efficiency is about 10^{-6}. However, the big advantage of the method is high resolution and signal to background ratio.

Summarizing, π^0 reconstruction was implemented in the KF Particle Finder package. High quality of the obtained π^0 particles makes it possible to study the background for dielectron decays of the rare probes.

---

* Work supported by HICforFAIR, FIAS and HGS-HIRe for FAIR.

† m.zyzak@gsi.de

DOI:10.15120/GR-2015-1-MU-NQM-CBM-22

Background rejection in the dilepton analysis with the CBM-Micro Vertex Detector*

E. Krebs[1], *T. Galatyuk*[2,3], *and J. Stroth*[1,3] *for the CBM collaboration*
[1]Goethe-Universität, Frankfurt, Germany; [2]Technische Universität Darmstadt, Germany; [3]GSI Darmstadt, Germany

The light vector mesons ρ, ω and ϕ are excellent probes of the strongly interacting matter under extreme conditions. Their leptonic decay channels of interest as leptons leave the hot and dense fireball without strong interaction and may reveal information on the characteristics of the matter created in the collisions. Single electron or positron tracks from incompletely detected γ-conversions and Dalitz decays of π^0-mesons are the most abundant source contributing to the significant combinatorial background. This study aims at exploring the use of MVD hits topology to reduce this background, despite of the fact that additional background is produced due to the material budget of the MVD.

To do so, electron pairs from meson decays have been simulated from a thermal source for central Au+Au reactions at SIS-100 energies such that the meson spectra are consistent with p_T and rapidity distributions measured by NA49 [1]. The decays of various sources simulated with the Pluto[2] event generator are embedded into the hadronic environment calculated with UrQMD transport model calculations. The magnetic field was set to 100% strength and δ-electrons with energies above 1 MeV have been added equivalent to a 10 kHz interaction rate.

The strategy of background rejection comprises several steps. In order to identify leptons from photon conversions that were produced outside of the target region, each reconstructed track is extrapolated to the primary decay vertex and removed from the analysis depending on its deviation to the vertex. One characteristic for conversion pairs is their small opening angle. A wedge cut is applied taking into account the opening angle of an identified electron to its closest neighbor with particle identification and product of the momenta of the two tracks. As lepton tracks from background sources can predominantly be found at low transverse momenta such tracks are rejected as well [3].

The MVD of the CBM experiment can further contribute to reduce this background by including points from the MVD into the track reconstruction. An improved rejection of pairs originating from the target region could be observed. Previous studies have shown that the MVD stations are also a source for γ conversions which can not be effectively rejected by the vertex extrapolation cut, especially in the first two stations closest to the target. Extrapolating tracks to the first MVD station and requiring that they are in its acceptance helped to better suppress off-vertex tracks from γ-conversions and resulted in an improved signal-to-background ratio for the low mass vector mesons ρ, ω and ϕ as depicted in Tab. 1. The invariant mass spectrum of the full cocktail after all analysis steps is presented in Fig. 1.

Mass Range $\left[\frac{\text{GeV}}{\text{c}^2}\right]$	MVD Stations	S/B	$\text{S}/\sqrt{\text{S}+\text{B}}$
$0-0.15$	0 4	6.56 8.27	31.3 29.4
$0.15-0.6$	0 4	0.10 0.14	3.7 3.7
$0.6-1.2$	0 4	0.15 0.21	4.9 5.4
$\omega \to e^+e^-$	0 4	0.67 0.96	7.4 8.0
$\phi \to e^+e^-$	0 4	0.13 0.19	0.74 0.86

Table 1: Signal-to-background ratios and significance for dilepton decays in different mass regions.

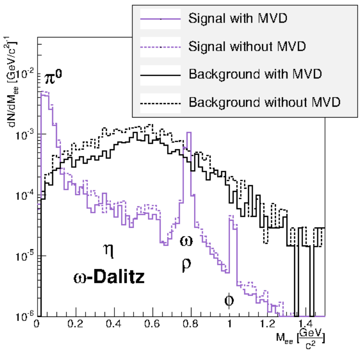

Figure 1: Invariant mass spectrum after all cuts are applied for central AuAu collisions at 8AGeV.

There have been major updates to the CBM software with more realistic digitization and geometries for the CBM detectors, including the MVD [4]. The effects on the dielectron reconstruction are under investigation.

References

[1] C. Alt et al. (NA49 Collaboration), Phys. Rev. C 78, 044907 (2008)

[2] I. Froehlich et al., arXiv:0708.2382

[3] T. Galatyuk, PhD Thesis, Goethe-Universität, Frankfurt am Main, (2009)

[4] S. Amar-Youcef et al., Status of the CBM MVD simulation model, this report

---

* This work has been supported by BMBF (05P12RFFC7), HIC for FAIR, HGS-HIRe, H-QM, and GSI.

DOI:10.15120/GR-2015-1-MU-NQM-CBM-23

Collision centrality determination in the CBM experiment*

S. Seddiki[1], *M. Golubeva*[2], *A. Kugler*[3], *V. Mikhaylov*[3,4], *I. Selyuzhenkov*[1], *and P. Tlusty*[3]
[1]GSI, Darmstadt, Germany; [2]INR RAS, Troitsk, Russia; [3]NPI of ASCR, Řež, Czech Republic; [4]CTU, Prague, Czech Republic

The magnitude of the impact parameter b in a heavy-ion collision is not known experimentally. Estimating b is important for the study by CBM of many physics observables, e.g. the event-by-event fluctuations of conserved quantities at mid-rapidity or collective flow. The multiplicity of produced particles in the overlap zone of the nuclei can be used as an experimental proxy of the b value. All events are sorted in centrality classes, with most central one being the collisions with highest multiplicity ($b \approx 0$) of the produced particles and peripheral one with the lowest multiplicity (when b value is about the sum of the radii of the two nuclei). Since the b value and particle multiplicity are correlated only on average, for a given multiplicity (centrality) class of events only an average $\overline{b}$ value and its spread σ_b can be estimated.

The projectile Spectator Detector (PSD) of the CBM experiment is designed to register forward spectator nucleons and fragments emitted in nucleus-nucleus collisions at very small polar angles. The multiplicity of spectators can also be used as an independent way to determine centrality. In the case of spectator measurements, the most central events correspond to a low spectator multiplicity (small energy deposition in the PSD), while peripheral events result in a large amount of spectators (large energy deposition in the PSD).

The performance of the centrality determination was studied using the DCM-QGSM heavy-ion collision event generator [1]. The PSD was either used as a standalone detector utilizing correlations between the energy deposited in different PSD subevents (segments), or in a combination with the CBM Silicon Tracking System (STS) which measures the multiplicity of produced particles at midrapidity. In the case of the PSD standalone analysis, it was required to have at least 40 GeV of energy in the PSD1 subevent or a total energy in two PSD2 and PSD3 subevents above 15 GeV to exclude very peripheral collisions with only few heavy fragments.

Figure 1 shows the performance of the centrality determination for Au+Au collisions at E_{beam} = 10 AGeV. The PSD is positioned at 8 m from the target. Centrality classes are defined by using various detector subevent combinations. The top panel shows the average impact parameter value $\overline{b}$ (central value) and σ_b (as the error bars) versus the centrality estimate from different subevent correlations. The bottom panel presents the same information in terms of impact parameter resolution $\sigma_b/\overline{b}$ of different centrality estimators. The $\overline{b}$ and σ_b were determined from Gaussian fits of the impact parameter distribution for a given centrality class.

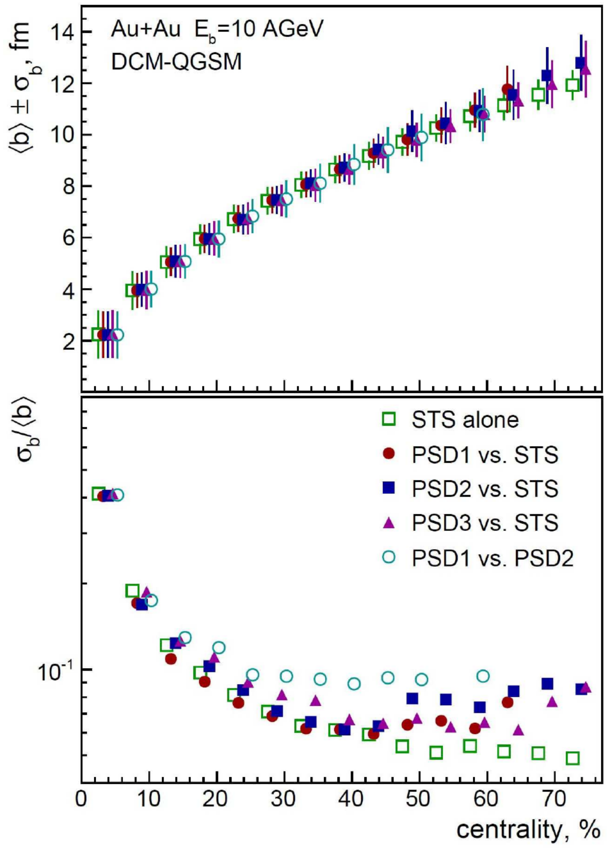

Figure 1: Average $\overline{b}$ and width σ_b of the impact parameter distribution (top); impact parameter resolution ($\sigma_b/\overline{b}$) vs. centrality (bottom).

The results in Fig. 1 demonstrate that the PSD can be used standalone for the centrality determination and, depending on the collision energy, has a comparable impact parameter resolution $\sigma_b/\overline{b}$ to that of the STS. This provides an independent method in the CBM experiment for the centrality determination with detected spectator fragments. When used together with the STS detector, the PSD helps to improve the overall centrality determination in the centrality range of 0-40% and allows for centrality determination in narrow classes with a width of at least 5%.

References

[1] The SHIELD code, www.inr.ru/shield/index.html.

---

* Work supported by the European Community FP7 - Capacities, contract HadronPhysics3 n° 283286.

DOI:10.15120/GR-2015-1-MU-NQM-CBM-24

Anisotropic flow and reaction plane reconstruction with the CBM experiment*

V. Mikhaylov†[1,2], *M. Golubeva*[3], *A. Kugler*[1], *V. Kushpil*[1], *S. Seddiki*[4], *I. Selyuzhenkov*[4], *and P. Tlusty*[1]
[1]NPI of ASCR, Řež, Czech Republic; [2]CTU, Prague, Czech Republic; [3]INR RAS, Troitsk, Russia; [4]GSI, Darmstadt, Germany

The projectile Spectator Detector (PSD) of the CBM experiment is designed to register forward spectator nucleons and fragments emitted in nucleus-nucleus collisions at very low polar angles. It will be used to determine the orientation of the collision reaction plane. The accuracy of the reaction plane determination with the PSD depends on the multiplicity and energy distributions of spectators and the magnitude of their directed flow, v_1.

The PSD performance is studied with simulated Au+Au collisions in the beam energy range 2-30 AGeV, which corresponds to that of future accelerator rings SIS100/SIS300 at FAIR. To identify the most suitable heavy-ion event generator for the performance study, the simulated directed flow with UrQMD [1], DCM-QGSM [2], LA-QGSM [2], and HSD [3] heavy-ion event generators is compared with experimental data from E895 [4] and STAR [5] Collaborations. Figure 1 shows this comparison in terms of the slope of proton directed flow at midrapidity, $F_y(v_1) = dv_1/dy$. Protons are used for the directed flow comparison because they are the most abundant particles in this kinematic region. The magnitude of the directed flow generated with different collision generators varies significantly, while DCM-QGSM seems to be the most consistent model in describing the data over the whole energy range. The possibility of collision fragment generation in the spectator region and the qualitative agreement with the experimental data for directed flow justifies the use of DCM-QGSM for the PSD performance study.

The CBM detector response is simulated with the GEANT4 Monte-Carlo package for three different configurations: (1) ”PSD-accept.” when simulated azimuthal distributions of the particles within geometrical acceptance of the PSD [$0.215° < \theta < 5.0°$ for $E_{beam} = 2 - 8$ AGeV and $0.115° < \theta < 2.7°$ for $E_{beam} = 30$ AGeV] were used without simulating the actual PSD response; (2) ”PSD-geom.,B=0” when PSD response is simulated without CBM magnetic field (this allows to study the bias due to finite PSD segmentation); (3) ”PSD-geom.,B>0” - same as configuration (2) but with magnetic field on.

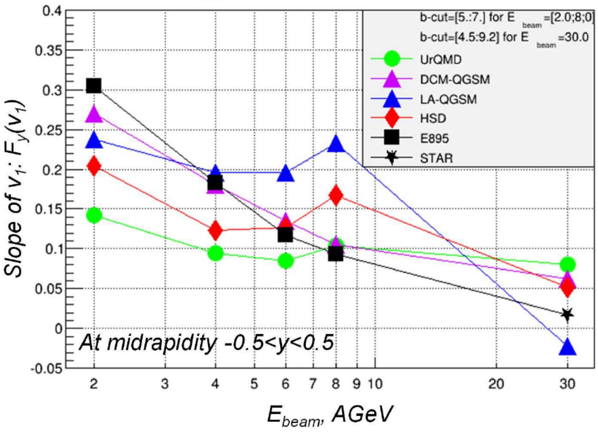

Figure 1: The slope of proton directed flow at midrapidity simulated with different collision generators is compared with E895 [4] and STAR [5] experimental data.

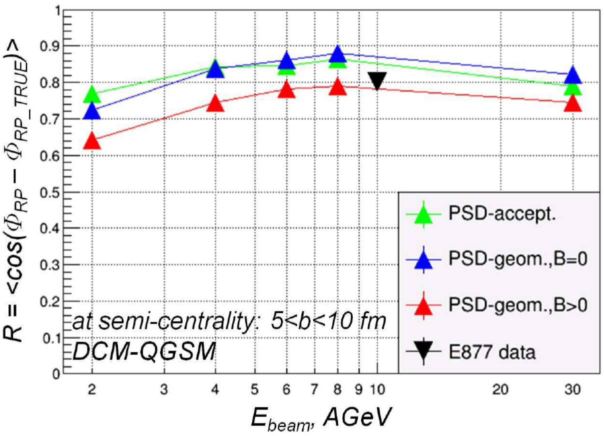

Figure 2: Reaction plane resolution correction factor for v_1. Results are from DCM-QGSM model and E877 [6] data.

Reaction plane resolution, quantified in terms of correction factor used in the directed flow measurement, is shown in Fig. 2. Resolution simulated with the DCM-QGSM generator is similar to that of the E877 experiment [6]. The transverse segmentation of the PSD seems to have a small effect. While the CBM magnetic field introduces a significant bias, the reaction plane resolution is still high even in presence of the magnetic field.

References

[1] The UrQMD model, urqmd.org.

[2] The SHIELD code, www.inr.ru/shield/index.html.

[3] The HSD model, fias.uni-frankfurt.de/ brat/HSD/index1.html

[4] H. Liu et al. (E895), Phys. Rev. Lett. 84 (2000), p. 5488.

[5] L. Adamczyk et al. (STAR), Phys. Rev. Lett. 112 (2014).

[6] 7. J. Barrette, et al. (E877), Phys. Rev. C55 (1997), p. 1420.

---

* Work supported by the European Community FP7 - Capacities, contract HadronPhysics3 n° 283286 and grant LG12007 of the Ministry of Education of the Czech Republic.

† mikhaylov@ujf.cas.cz

DOI:10.15120/GR-2015-1-MU-NQM-CBM-25

The GBT based readout concept for the CBM Silicon Tracking System

J. Lehnert[1], *W. Müller*[2], *and C.J. Schmidt*[1]
[1]GSI, Darmstadt, Germany; [2]FAIR, Darmstadt, Germany

The sensors of the CBM Silicon Tracking System (STS) are read out by frontend boards (FEB) with 8 STS-XYTER ASICs for 128 channels each implementing the analog frontend, analog-to-digital conversion and the readout of buffered hits via multiple serial links. A subsequent stage with data aggregation from several ASIC links and an electrical-to-optical interface is required before transfering the data to the FPGA based data processing boards (DPBs) located in some distance at the detector site where preprocessing and further data transfer occur. The aggregation stage is located in the cooled STS detector box inside the CBM magnet, which implies that the hardware must fulfill conditions in terms of radiation hardness, magnetic field, space contraints and thermal environment.

GBT Devices

A concept was devised for the STS readout to implement the aggregation and optical readout functionality on a separate readout board (ROB) using the GBTX, SCA and Versatile link devices [1] developed at CERN. The devices of the GBT project are mainly designed as interface between on-detector and off-detector electronics for future LHC experiment upgrades in a radiation environment up to tens of Mrad. The GBTX ASIC implements up to 56 SLVS links (E-Links) as electrical frontend interface with link speeds of 80, 160 or 320 Mb/s and a total bidirectional user bandwidth up to 4.48 Gb/s on the high speed serial link. Latencies of data throughput in the GBTX are fully deterministic. The Versatile Link devices are radiation hard optical transceivers and (twin) transmitters in SFP formfactor modules.

The STS Readout Chain

The ROBs for the STS will contain 1 GBTX device as master connected to an optical transceiver (VTRx), 2 GBTX devices connected to an optical twin transmitter (VTTx) and a GBT-SCA (Slow Control Adapter) device for I^2C based control of the 2 GBTX without optical downlink (see Fig.1). The GBTX uplinks will be operated in the widebus mode (without forward error correction) and therefore provide 3x14 frontend links at 320 Mb/s each. Fourty of these links are used to connect to the FEBs. Three types of FEBs will be used with either 1, 2 or 5 readout E-Links per ASIC depending on the local data load, resulting in a maximum of 5, 2.5 or 1 FEBs of the different types connected to a single ROB. With additional spatial contraints from system integration (no connections across quarter stations, no cable crossings) the total number of ROBs for the STS amounts to approx. 1000, with 3000 optical readout links and 1000 control links. For ASIC timing and control, one single E-Link output and one phase adjustable 160 MHz clock are connected from the master GBTX to each FEB; the control responses use any of the readout uplinks. All E-Links between FEBs and ROBs will be AC-coupled in order to allow the connection of a single ROB to multiple FEBs operated at different potentials together with their connected sensors. The ROBs will be located at the sides of the STS detector box outside the detector acceptance. Flexible flat cables of approximately 0.6 m length will connect the stacks of FEBs for a given quarter station of the detector to the corresponding stack of ROBs.

The version 2 of the STS-XYTER ASIC[2] will implement the GBTX E-Link interface with a configurable number of 1 to 5 readout links and a synchronous readout and control protocol that was specifically developed for the STS-XYTER readout via GBTX [3]. A demonstrator board with a single GBTX and Versatile Link components will be available from CERN for initial tests in early 2015 and a CBM ROB prototype with full functionality is currently being prepared. Larger quantities of the devices from the sole production run are expected end of 2015.

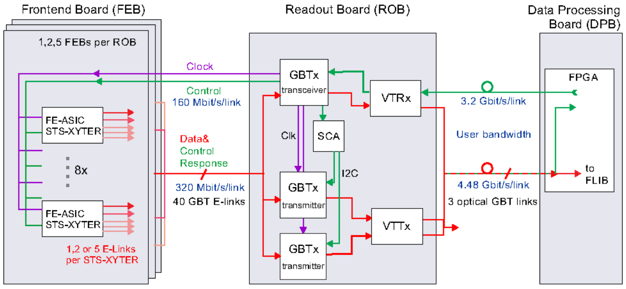

Figure 1: The STS readout chain with the readout board based on GBTX and Versatile Link components.

References

[1] P. Moreira et al., CERN Document Server CERN-2009-006.342

[2] R. Szczygiel et al., CBM Progress Report 2014, Darmstadt 2015

[3] K. Kasinski et al., Proc. SPIE 9290 (2014) 929028

DOI:10.15120/GR-2015-1-MU-NQM-CBM-26

Development of software tools for the prototype readout chains of the CBM Silicon Tracking System

I. Sorokin[1,2], *M. Krieger*[3], *J. Lehnert*[1], *W.F.J. Müller*[1], *E. Ovcharenko*[4,5], *and F. Uhlig*[1]
[1]GSI, Darmstadt, Germany; [2]KINR, Kiev, Ukraine; [3]ZITI, Mannheim, Germany; [4]ITEP, Moscow, Russia;
[5]JINR, Dubna, Russia

Development and characterization of detector prototypes requires powerful, flexible, and reliable software tools, such as data acquisition, slow control and on-line/off-line monitoring systems. The present STS prototype readout chain includes the n-XYTER 1.0 and STS-XYTER 1.0 front-end ASICs, the SysCore versions 2 and 3 (SCV2, SCV3) readout boards, and the FLIB interface board [3]. Whereas the FLIB-based data acquisition system is covered in [4], the present report covers the controls and monitoring tools for the front-end ASICs and readout boards, as well as the USB-based readout system.

Controls

A control server library, which provides a high-level interface to various CBMNet [2] devices, such as the front-end ASICs and the SCV2 and SCV3 readout boards, has been developed. Having in mind its usage for the final experiment, the control server enables sending command sequences to a large numbers of CBMNet slaves in parallel.

Client libraries with device-specific macro commands were also developed. For the systems, based on SCV2s and n-XYTERs, these commands include transactions over the I^2C interface (which is needed for n-XYTER configuration), as well as over the SPI interface (which is used for controlling the ADC). Additionally, the possibilities to switch n-XYTER between the self-triggering and externally-triggered operation modes was provided. A possibility to configure the AUX block of the SCV2 was provided as well. For the systems, based on the STS-XYTER ASIC and SCV3 readout boards, only simple configuration scripts with hard-coded default settings are currently available.

In future it is planned to connect the data acquisition system to the control libraries. This will enable to receive the feedback from the system immediately after changing a setting, and to use this information for taking decisions on further adjustments. Thus, for example automatic trimming of the thresholds will be possible. This will also simplify performing various parameter scans and calibrations.

Both the server and the client libraries are provided together with the dictionaries for the CERN ROOT interpreter. This enables to use the ROOT interpreter as convenient environment for interactive system configuration.

On-line and off-line monitoring

The development of the on-line/off-line monitoring tools is still in progress. Unpackers for the n-XYTER and STS-XYTER raw data were implemented in CbmRoot [5]. For the STS-XYTER, basic checks of the self-consistency of the data is performed. Thus, it is checked whether the epoch numbers within an individual epoch message are consistent, and whether the epoch messages from each data link are coming in the right sequence. For the hit messages the bit parity check is performed. Also the correctness of the detector transport message (DTM) number is checked at the stage of microslice unpacking.

An analysis library, evaluating the hit rates per channel, hit amplitude distributions, total data rate, etc. was implemented. It is a simple, but essential system diagnostic tool.

Particular care was taken to optimize the code for high performance, in order to achieve maximum analysis throughput.

USB-based readout for SCV3 and STS-XYTER 1.0

Along with the FLIB-based data acquisition system, a data acquisition system operating over USB has been developed. This enables external R&D groups to quickly deploy the SCV3-based setups, and operate them without the need of using the FLIB board. Same control and on-line analysis tools can be used with systems, read out over USB. Transporting up to 27 MB/s of data was achieved, and it is limited by the USB bus.

References

[1] A.S. Brogna et al., n-XYTER reference manual, unpublished. http://hipex.phys.pusan.ac.kr/drupal/sites/default/files/nXYTER.pdf

[2] F. Lemke, S. Schatral, U. Bruening, Status of the CBMnet based FEE DAQ readout, GSI Scientific Report 2013 (2014), Darmstadt, p. 86

[3] J. de Cuveland, D. Hutter, V. Lindenstruth, Status of CBM First-level Event Selector Prototype Developments, GSI Scientific Report 2012 (2013), Darmstadt, p. 89

[4] D. Hutter, J. de Cuveland, V. Lindenstruth, CBM FLES input interface developments, this report

[5] M. Al-Turany, D. Bertini, CbmRoot: Simulation and Analysis framework for CBM Experiment, GSI Scientific Report 2006 (2007), Darmstadt, p. 3

DOI:10.15120/GR-2015-1-MU-NQM-CBM-27

Towards the STSXYTERv2, a silicon strip detector readout chip for the STS

K. Kasinski, R. Kleczek, R. Szczygiel, P. Grybos, and P. Otfinowski
AGH University of Science and Technology, Cracow, Poland

STS-XYTER as a 128+2 channel full-size prototype IC dedicated for silicon strip detector readout for the STS was fabricated in 2013 [1]. Fig. 1. presents the test PCB developed at AGH used for functional verification. It provides on-board 5 separate power domains with dedicated low-noise LDO regulators, ERNI connector for sensor attachment, interconnects for test interface, test points and AC-coupled CBMnet interface (HDMI connector). The board is controlled by SysCore V3 (CBMnet) and NI FPGA (test interface) cards.

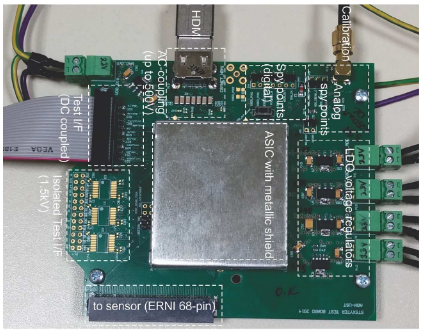

Figure 1: Test PCB for the STSXYTER ASIC.

The architecture details of the chip and test results were presented and published in [2]. Detailed tests using silicon sensors (e.g. CBM05) are currently being prepared. Using the same setup it was possible to further evaluate the chip. Fig. 2. shows the thermal image of the STS-XYTER chip on the test PCB. The thermal resistance was estimated to be approx. 52 °C/W, but it needs to be verified on the final FEB board in the environment similar to the final application as well. The temperature coefficients measured for various biasing points of of the ASIC evaluated for ambient temperatures of 7–85 °C are:

ADC_vdiscr_ref = -0.622 mV/°C,
ADC_ibias_corr = -0.312 mV/°C,
BG_iref = +0.154 mV/°C,
ADC_vref_n = -0.366 mV/°C,
ADC_vref_p = +0.286 mV/°C,
DISCR_bias_t = -0.435 mV/°C.

The STSXYTERv2 which will be an evolution of the STSXYTER prototype ASIC among the small fixes the changes include:

- new concept of the digital back-end (focused on the use of GBTx chip as a data concentrator), reaching hit bandwidths 9.4–47 MHit/s/chip,
- definition of the new communication protocol optimized for the conditions and requirements of the CBM experiment. The preliminary protocol was published [3] and is currently a subject of fine-tuning,
- configurable front-end (gain, bandwidth) for possible support of gas detectors (MUCH),
- new pad layout supporting quality test with pogo-probes and reduced connectivity required for regular operation,
- testability and temperature stability improvements of the in-channel ADC,
- further optimization of the analog front-end towards lower noise and better stability.

The STS-XYTERv2 ASIC is currently being under development. It is expected to be taped-out in Q2 of 2015 via Europractice services.

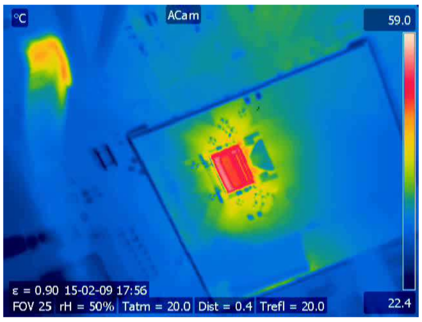

Figure 2: Thermal imaging of the operating ASIC on the test board.

Acknowledgment

We would like to thank the colleagues from GSI and WUT Warsaw for the efforts towards verification and specification of the new requirements.

References

[1] P. Grybos *et al.*, “STS-XYTER - a prototype silicon strip detector readout chip for the STS”, CBM Progress Report 2012, Darmstadt 2013, p. 17.

[2] K. Kasinski *et al.*, “STS-XYTER, a High Count-Rate Self-Triggering Silicon Strip Detector Readout IC for High Resolution Time and Energy Measurements”, IEEE NSS/MIC, 2014.

[3] K. Kasinski, W. Zabolotny, R. Szczygiel, “Interface and protocol development for STS read-out ASIC in the CBM experiment at FAIR”, Proc. SPIE 9290, doi: 10.1117/12.2074883.

DOI:10.15120/GR-2015-1-MU-NQM-CBM-28

Development of a CO_2 cooling prototype for the CBM Silicon Tracking System*

J. Sánchez[1], *J. M. Heuser*[1], *W. Niebur*[1], *C. Sturm*[1], *H. R. Schmidt*[2], *A. Lymanets*[2], *P. Petagna*[3], *B. Verlaat*[3], *and L. Zwalinski*[3]

[1]GSI, Darmstadt, Germany; [2]University of Tübingen, Tübingen, Germany; [3]CERN, Geneva, Switzerland

The CBM Silicon Tracking System is based on silicon sensors with double-sided strip readout. These sensors must be kept at least at -5° C to ensure the required performance. Due to this cooling demand the design and manufacturing of a 1 kW prototype called TRACI-XL, shown in Fig. 1, was chosen as the best option as starting point for specifying the technical features and requirements of the final cooling plant.The main heat sources of the detector are the read-out electronics, which dissipate about 40 kW according to the current specifications and they must be removed completely. This does not mean that the final plant will be 40 times bigger but it will allow to scale the experimental results and to get conclusions about the CO_2 nucleate boiling behavior and to start the engineering development of the cooling plates, fluid distribution and other important aspects.

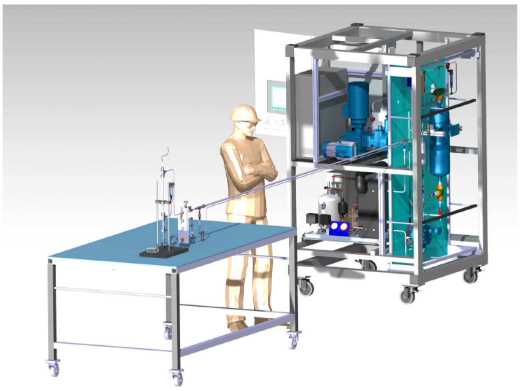

Figure 1: A CATIA model of TRACI-XL.

Preparations for the commissioning phase

In order to ensure a correct performance of the plant an exhaustive protocol has been defined. The commissioning phase comprises the following tests:

- Safety verifications: Electrical safety (Electrical cabling, PLC I/O testing, alarms testing), mechanical safety (Pressure test and leak test).
- Basic functionalities tests: Real conditions analog alarm testing, chiller operation, pump operation, accumulator pressure regulation.
- Advanced performance tests: Automatic procedure testing, stable chiller operation over the full operating range, stable pressure (temperature) regulation in every condition, stable flow control.
- Thermodynamic performance: Test with a 1 kW dummy load in a wide range of temperatures, test with gradual power supply, shock test: sudden disconnection of electronics.

The PLC parameters such as pressures, temperatures, mass flow, alarms, interlocks etc. can be forced to bring the plant to extreme conditions and to check that all the safety and recursive procedures work as expected. In addition a 1 kW dummy heat load which simulates the future connected read out electronics was developed. This experimental heat source is based in a 3/4" pipe with a concentric fire rod providing a power of 1 kW and the respective sensors.

Finalizing the assembly stage

Once the concept design phase finished, the mechanical assembly stage (Fig. 2) takes a great relevance because it is the moment to introduce changes into the design after analyzing the evolution of the prototype and detecting possible defects or improvements. Parts of the mechanical frame were adapted to gain in stability and to reduce noise installing materials for vibration damping. Some other parts were relocated in order to facilitate the accessibility to every component in case they must be replaced, or distributed to ensure sufficient ventilation in the plant.

Figure 2: Vacuum pump set-up with condensing unit.

References

[1] R. W. Lockhart, R. C. Martinelli, Chem. Eng. Progr., Vol. 45 (1949), p. 39-45

---

* Work supported by EU-FP7 CRISP.

DOI:10.15120/GR-2015-1-MU-NQM-CBM-29

Studies of correlated signals in CBM STS Silicon Microstrip Sensors*

V. Pugatch[1], *J. Heuser*[3], *P. Larionov*[1], *M. Pugach*[1,2], *I. Sorokin*[1,3], *and C. Sturm*[3]
[1]KINR, Kiev, Ukraine; [2]Goethe University, Frankfurt, Germany; [3]GSI, Darmstadt, Germany

Physically correlated signals in adjacent strips of a microstrip detector appear due to charge sharing. A significant fraction of tracks is reconstructed from two- and three-strip cluster events where analogue read-out improves the position resolution. Non-physically correlated signals originated by cross-talk, pick-up or common mode fluctuations may also occur in read-out channels. Measurements of charge sharing between adjacent strips of the CBM05 and CBM06 prototype silicon sensors designed for the CBM Silicon Tracking System were performed at KINR [1]. In a two-dimensional (E_i x E_{i+1}) energy distribution of physically correlated events loci from an alpha-particle source were clearly observed in adjacent strips i and (i+1) (Fig. 1).

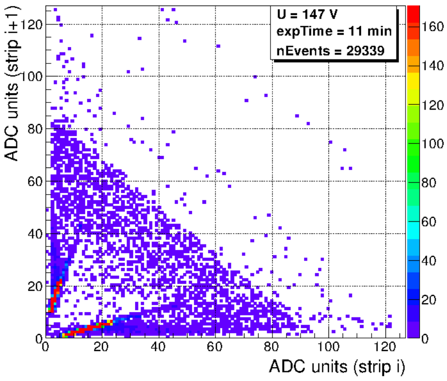

Figure 1: Two-dimensional (E_i x E_{i+1}) energy distribution in adjacent strips i and (i+1) obtained with alpha-particles.

Detailed studies revealed also non-physical correlated events populating loci from the very low amplitudes along the straight lines and reaching the positions of the alpha particle contribution. Among possible explanations we considered a cross-talk with the channels (i-1) and (i+2) located in close vicinity to the ones under the test. Correlated event studies were carried out recently with n-XYTER readout electronics at GSI. Examples of data obtained are shown in Fig. 2.

In the upper panel physically correlated events at the p-side triggered by MIP β-particles from ^{90}Sr are observed along the expected line (most probable value) with a sum of amplitudes around 140 ADC counts. The simulated noise distribution is shown in the middle part of Fig. 2. The events populating the loci alongside the straight lines originating from the (0.0 × 0.0) coordinate are apparently correlated non-physical events (see lower Fig. 2). These signals simultaneously appearing at adjacent strips i and (i+1) are initiated either by the digital part of the n-XYTER chip and/or by external powerful electromagnetic sources. It is worthwhile to notice that such events were also observed at n-XYTER channels not connected to the microstrip detector at all though with a low, yet significant amplitude of up to 40 ADC counts. The results of these studies have to be taken into account in the test measurements with a newly designed STS-XYTER microchip as well as in building the infrastructure for power lines, shielding and grounding of the STS detector. Further studies with the ALIBAVA read-out system [2] are planned to clarify the origin of the non-physical correlated events.

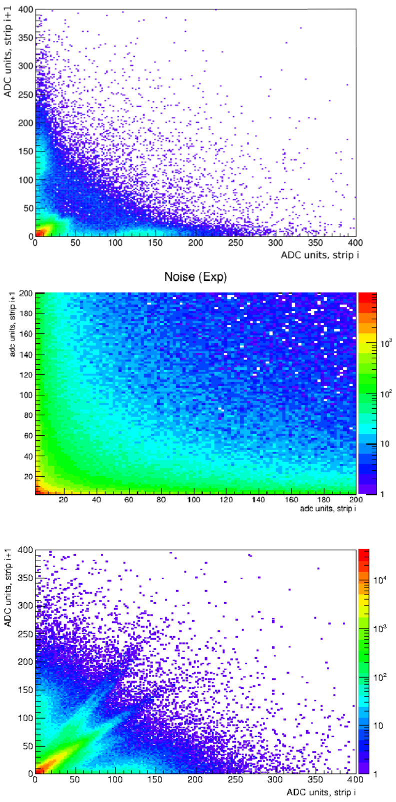

Figure 2: Two-dimensional (E_i x E_{i+1}) amplitude distribution of events in adjacent strips 'i' and '(i+1)' of the CBM05 sensor. Data taken with ^{90}Sr source (upper: p-side; lower: n-side). A simulated noise distribution is shown in the middle panel.

References

[1] I. Panasenko *et. al.*, CBM Progress Report 2014
[2] https://www.alibavasystems.com

---

* Work supported by HIC-for-FAIR, H-QM and HGS-HIRe.

DOI:10.15120/GR-2015-1-MU-NQM-CBM-30

Charge collection in STS silicon microstrip sensors at their surface layer*

I. Panasenko[1], *V. Dobishuk*[1], *J. Heuser*[2], *V. Kyva*[1], *V. Militsiya*[1], *Ie. Momot*[1,3], *V. Pugatch*[1], *and M. Teklishyn*[1]
[1]KINR, Kiev, Ukraine; [2]GSI, Darmstadt, Germany; [3]Goethe University, Frankfurt, Germany

To provide radiation tolerant devices for the CBM experiment (Silicon Tracker Station) prototypes of silicon microstrip sensors have been produced in two technologies. For the short-long stereo-strips connection, either double-metallization lines (“double metal” sensor) or a single-metallization design with an external microcable (“single metal” sensor) have been manufactured. We report here the results of studies performed for those sensors with the Pu (triplet) alpha-source and laser (640 nm wavelength). Both methods provide test of the charge collection at the sensor surface layer where double metallization is laid out. Measurements were carried out exploring discrete electronics and the fast-slow coincidences setup at KINR. This allows studying a charge sharing between adjacent strips of the silicon sensor hit by alphas or laser pulses. The degradation of the cluster finding efficiency in the vicinity to the double-metal connecting lines in heavily irradiated microstrip silicon sensors has been observed [1].

The CBM05H4 ‘double metal’ and ‘single metal’ (HAMAMATSU) sensors were full depleted at 80 V. In a two-dimensional (E_i x E_{i+1}) energy distribution of events in adjacent strips ‘i’ and ‘(i+1)’ three loci for a ^{239}Pu, ^{238}Pu and ^{233}U alpha-particles source are shifted by $\sim$ 20 % to lower energies for the double metallization sensor in comparison with the single metal one. Also the widths of loci are larger. The evaluation shows that this could be explained by the alpha-particles energy loss and straggling in the SiO_2 isolation layer present only in the sensor with a second metallization layer. Biasing voltage scan has demonstrated expected performance for these sensor types, while CBM06C6 (CiS production) have shown appearance of the dead layer ($\sim$ 25 μm) in the interstrip gap at full depletion voltage.

Also measurements with a 640 nm laser beam (7 μm spot) scanned over the sensor area were performed for sensors irradiated at the KINR isochronous cyclotron up to the 2*10^{14} 1 MeV n_{eq}/cm^2. Figure 1 shows two dimensional distribution of amplitude of charges originated in the interstrip gap of the CBM05 non-irradiated sensor illuminated by the scanning laser beam. It demonstrates excellent position resolution achieved: beam spot position is indicated by figures of 15 μm, 18 μm, 21 μm etc. Figure 2 illustrates degradation of the charge collection by 30% in the irradiated sensor (the locus of laser events is shifted to lower amplitudes region). Analysis of data for other sensors is in progress. Tests with the ^{90}Sr β-source will be made soon exploring the ‘ALIBAVA’ microelectronics readout system.

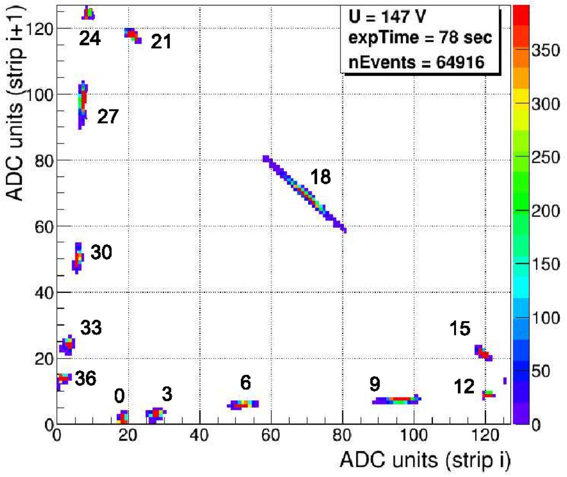

Figure 1: CBM05 – non-irradiated sensor: Laser scan in the interstrip gap.

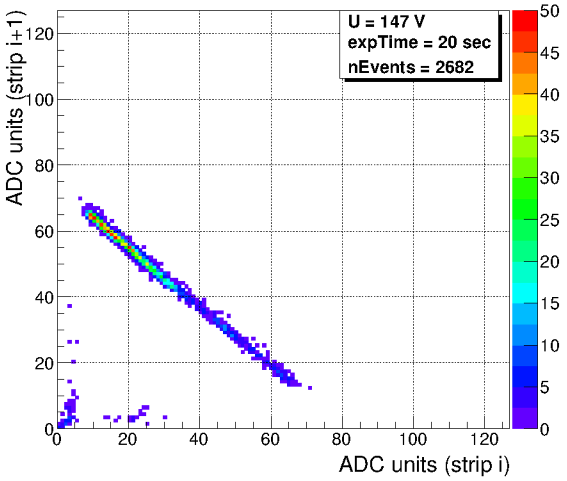

Figure 2: CBM05 – irradiated sensor: Laser scan in the interstrip gap.

References

[1] A. Affolder et al., Radiation damage in the LHCb vertex locator, JINST 8 (2013) P08002, arXiv:1302.5259.

---

* Work supported by HIC-for-FAIR.

DOI:10.15120/GR-2015-1-MU-NQM-CBM-31

Charge sharing in micro-strip sensors: experiment and simulation*

H. Malygina[1,2], *V. Friese*[3], *J. M. Heuser*[3], *A. Senger*[3], *and I. Sorokin*[2,3]
[1]Goethe University, Frankfurt, Germany; [2]KINR, Kiev, Ukraine; [3]GSI, Darmstadt, Germany

In December 2013 [1] and December 2014 [2] a prototype setup of the Silicon Tracking Systerm (STS) for the CBM Experiment was tested in a 2.4 GeV/c proton beam at the COSY synchrotron (Jülich, Germany). In the middle station, which could be rotated around its vertical axis, CBM05 prototype sensors (n-side with 0^0 stereo-angle, p-side with 7.5^0, $285{\pm}15$ μm thick) were under a test aiming at studying charge sharing. The n-XYTER read-out chips were triggered by a hodoscope. The equivalent noise charge of about 8 ADC promoted adapting the threshold of 20 ADC in the cluster finder to cut off the noise.

Charge sharing between two fired strips is described by $\eta = S_R/(S_R + S_L)$ with $S_{R(L)}$ being the signals on the right (left) strip of the cluster [3]. The left panel in Fig. 1 shows the measured distribution of η. Positions and widths of the peaks depend on characteristics of the sensor and the readout electronics (e.g. strip pitch, signal-to-noise ratio, coupling capacitance, threshold, etc.). For inclined tracks the η-distribution is essentially asymmetric. The position of the cluster with respect to the left strip can be calculated as $x_\eta = p\left(\int_0^\eta \frac{dN}{d\eta'}d\eta'\right)\left(\int_0^1 \frac{dN}{d\eta'}d\eta'\right)^{-1} = pf(\eta)$, where p is the strip pitch and $f(\eta)$ is obtained from measurements (see the right panel of Fig. 1).

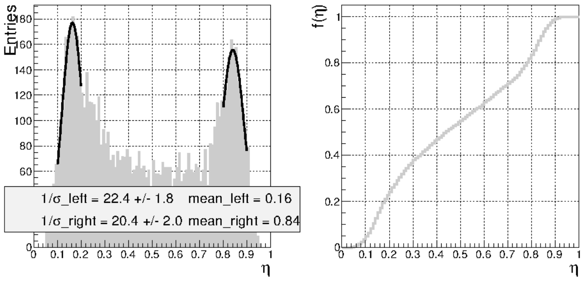

Figure 1: *Left:* η measured for p-side of CBM05 with Gaussians fitting the peaks. *Right:* $f(\eta)$. Perpendicular tracks.

Investigating cluster size distribution at different beam incidence angles is a good tool to verify the simulations of charge sharing in a silicon strip detector (implemented in the advanced model of the digitizer in CbmRoot). Figure 2 presents a typical distribution at one angle. Assuming the n-XYTER calibration [4] to be accurate, we get the reconstructed charge (Fig. 3) smaller than the one modelled. This indicates additional effects. Imposing 20% less charge from the sensor than expected from its thickness alone (on top of the 5% loss due to the trigger signal delay affecting the signal sampling in the ASIC) yields a better agreement. This is still to be explained.

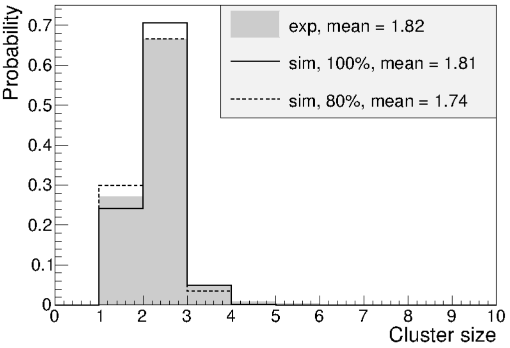

Figure 2: Cluster size distribution for slightly inclined tracks (10^0). Experimental data for n-side (the gray filled histogram), simulations with no (the solid line) and 20% (dashed) additional charge loosing.

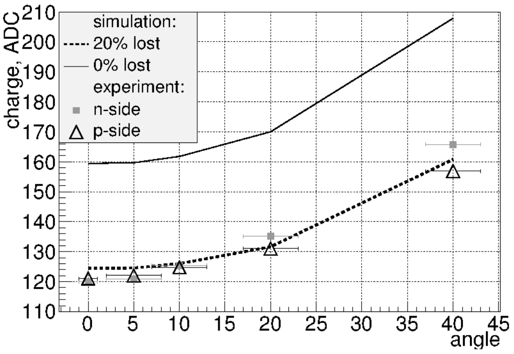

Figure 3: Most probable registered charge in dependence of track angles. The points show the experimental data from beamtime 2013 (the open triangles – p-side, the filled squares – n-side, the uncertainties in the angle measurements are drawn with bars) and the modelled data are represented by the lines (the solid line – no charge losses in the sensor, the dashed – 20% losses).

References

[1] T. Balog et al., CBM Progress Report 2013 (2014) p. 32

[2] J. M. Heuser et al., *Test of prototype CBM detector components with proton beams at COSY*, this report

[3] R. Turchetta, Nucl. Instrum. Methods A335, 44-58 (1993)

[4] I. Sorokin et al., CBM Progress Report 2012 (2013) p. 14

---

* Work supported by HIC-for-FAIR, H-QM and HGS-HIRe.

DOI:10.15120/GR-2015-1-MU-NQM-CBM-32

Data throttling procedures for the STS-XYTER based read-out of the CBM Silicon Tracking System

T. Balog, W.F.J. Müller, J. Lehnert, and C.J. Schmidt
GSI, Darmstadt, Germany

In high interaction rate experiments using a continuous beam such as the Compressed Baryonic Matter experiment CBM at FAIR, beam intensity fluctuations are a critical issue. When such fluctuations occur, they will lead to a sudden increase in occupancy in the detector. For detector systems closest to the target such as the Silicon Tracking System STS, this may result in a local or even global overload situation, where the read-out bandwidth cannot cope with the incoming data load. In consequence, incomplete event information may be transmitted.

In conventional, triggered systems overload situations are handled by common dead time mechanisms which discard the affected fraction of events. In continuous beam experiments with freely streaming readout, however, no such trigger is available and overload would lead to uncontrolled data losses that might yield the collected data overall as none analyzable. Apart from event overlap and local pile-up, the fundamental question may be stated as: "How can one register all the data of most of the events rather than most of the data of all the events." In order to prevent complete clogging of the data chain, a throtteling mechanism is needed, that allows to inhibit acquisition of data from scrambled, not interpretable events in favour of clearing the data path for uncompromized sets of event data, once the overload condition has cleared.

In the STS the STS-XYTER read-out ASIC will be used [1]. This read-out chip is a dedicated custom design for the STS. Each readout channel is equipped with a 5 bit flash ADC. The statistically incoming hits are buffered in a per channel fifo eight levels deep and subsequently read out using a token ring scheme that is set-up to have oldest data read-out first.

Clearly, every single channel may, by pure statistical fluctuations, suffer signal pile-up or even a fifo overflow. This situation will be marked to the adjacent data elements but is not the key issue demanding throtteling. It is rather the situation of a sudden, potentially regularly appearing intensity increase that yields the average data load to be higher than the readout bandwidth. In such a situation, good data in the queue should still be read-out, but data belonging to potentially incomplete events should not cause an uncontrollable system deadtime before new data may be taken upon recovery. Further, the system should resume operation coherently.

To this end various measures have been foreseen in the design of the readout ASIC:

- Pile-up and fifo-overflow are indicated on the data elements of the particular channel.
- Channel fifo overflow conditions are counted on the chip and will realease a response report when beyond some configurable level.
- Fifos may be cleared coherently through a command.

The protocol for communication with the ASIC [2] was designed to ensure fast transfer of both the fill status reports from the ASICs and of the required responses (commands to stop -for emptying fifos- and to restart acquisition or for fast clearing of fifos).

The above provisions in the ASIC will allow to identify a problematic situation, realize throtteling as well as a coherent DAQ restart from a global control point such as the data processing board (DPB) layer through various mechanisms. No further complicated logic is needed nor foreseen in the radiation exposed front-end electronics. All further steps in the evaluation of throttling conditions can be flexibly implemented in the FGPA based DPB layer [3] based on the dedicated throttling information provided by the ASICs and on information gained directly from monitoring the ASIC hit data stream, for example indications on the ASIC fifo fill state from the difference between readout time and creation time of individual hits.

A simulation model was developed using the hardware description language SystemC [4] and some simulative pre-studies have been carried out. The model currently implements a simplified structure of an STS-XYTER ASIC and allows to investigate throttling by variation of parameters like event rate, channel fifo overflow thresholds and timing of global throttling decisions. Additional simulations need to be realized to verify adequate system performance through such throttelling strategies.

References

[1] K. Kasiński et al., "Towards the STS-XYTERv2, a silicon strip detector readout chip for the STS", this report

[2] K. Kasiński et al., "STS-HCTSP, an STS Hit & Control Transfer Synchronous Protocol", this report

[3] W. Zabołotny et al., "Towards the Data Processing Boards for CBM experiment", this report

[4] SystemC website: http://www.systemc.org

DOI:10.15120/GR-2015-1-MU-NQM-CBM-33

A scalable neutron source for detector radiation hardness test*

E. Friske[1] *and H. R. Schmidt*[1,2]
[1]Universität Tübingen, Tübingen, Germany; [2]GSI, Darmstadt, Germany

Silicon detector radiation hardness

During operation of the STS, the silicon strip detectors are expected to be irradiated with large numbers of neutrons, some sectors in excess of 10^{12} $\mathrm{n_{eq}/cm^2/month}$ [1], with an accumulated dose of 10^{14} $\mathrm{n_{eq}/cm^2}$ [3].

To test detector performance and particularly changes in the semiconducting properties due to neutron induced activation, a neutron source with high flux is necessary. Unfortunately, reactors with sufficient neutron flux are heavily occupied. This leads to irradiation campaigns with very short irradiation times (in the order of minutes) in which the desired neutron dose is achieved [2].

To get a more realistic representation of the irradiation process, an exposure of days or weeks with defined annealing phases is more desirable. To fulfill these goals a scalable neutron source with good accessibility is required.

Neutron source

Present source The current neutron source consists of a gas cell filled with deuterium gas under a pressure of a few bar. A 2 MeV deuteron beam from the Rosenau accelerator passes an entrance window of a few microns thickness to induce deuterium fusion. However, even at this thickness the heat load on the entrance window reduced it mechanical stability, limiting both the beam current and the pressure of the gas cell.

Due to the limitations of both the accelerator and the window currently the neutron production is limited to a rate of $\approx 10^{12}\mathrm{n_{eq}/cm^2/week}$. As this rate is about two orders of magnitude below the required total dose, it would take way too long to accumulate with the current setup. To solve these issues, a new gas cell is currently being manufactured, based on [4].

Cryogenic source The new neutron source currently in production consists of a steel endcap for the accelerator beam pipe. Mounted inside the endcap is the actual cell, cooled by liquid nitrogen. In contrast to [4], the gas cell is cooled by a copper finger reaching into a liquid nitrogen dewar. The entrance window is fixed to a thick copper disk sealing off the gas cell. (A technical sketch is shown in Fig. 1.)

This setup has several advantages over the present cell:

The enclosed deuterium gas is more dense by a factor of 4 compared to room temperature, and the lower ambient temperature should increase the durability of the entrance window, allowing higher beam currents.

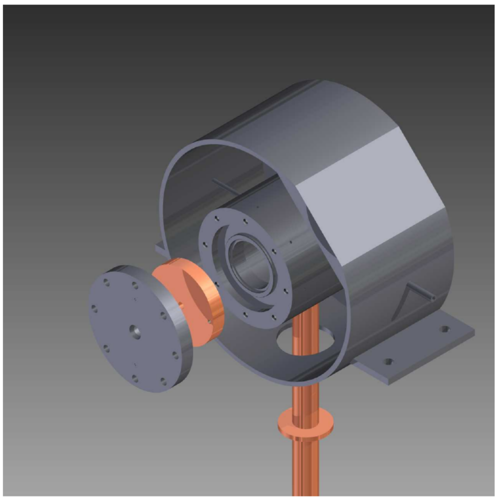

Figure 1: Schematic view of the cryogenic source

Combining these effects, it should be possible to increase both beam current and beam energy (to the accelerator's limit), which both significantly increases the neutron yield. In addition, the detector can be put within a few cm of the gas cell, providing maximum solid angle coverage. These improvements should increase the neutron flux by at least one order of magnitude, but the actual gain has to be determined once the cryogenic source is operational.

Before the new source can be put into operation additional tasks have to be performed, including tests of possible window materials and the cooling system.

References

[1] V. (eds.) Friese and C. C. Sturm. CBM progress report 2013, 04 2013.

[2] Singla, M. [GSI, Darmstadt]. Development of radiation tolerant microstrip sensors for the CBM silicon tracking system, 03 2014.

[3] Sorokin, I. [Frankfurt University]. *Characterization of silicon microstrip sensors, front-end electronics, and prototype tracking detectors for the CBM experiment at FAIR*. PhD thesis, 04 2014.

[4] W. Von Witsch and J. G. Willaschek. High-pressure gas target for the production of intense fast-neutron beams. *Nuclear Instruments and Methods*, 138:13–17, Oct. 1976.

---

* Work supported by GSI(CBM).

DOI:10.15120/GR-2015-1-MU-NQM-CBM-34

Quality assurance of CBM-STS silicon micro-strip sensors using pulsed infra-read laser*

P. Ghosh[1], *J. Eschke*[2], *and J. Heuser*[3]
[1]Goethe University, Frankfurt, Germany; [2]FAIR, Darmstadt, Germany; [3]GSI, Darmstadt, Germany

The Silicon tracking system (STS) of the CBM experiment is aimed to reconstruct the trajectories of the hundreds of charged particles created in heavy-ion collision, and to determine their momenta with a resolution of around $\Delta p/p \approx 1\%$. This precision is prerequisite for high-resolution mass measurements of e.g. rare probes and implies a thin detection system, with high-resolution space-point measurement and capable of interaction rates up to 10 MHz. The STS will comprise 1220 silicon micro-strip sensors from which 896 detector modules will be constructed [1]. Quality assurance of the sensors is an important pre-requisite for the detector module production as the assembly steps are non-reworkable to a good extend. These tests can be either invasive or non-invasive as explained below. From the results entered into a database, one can identify sensors or detector modules with certain characteristics and grade them according to their performance.

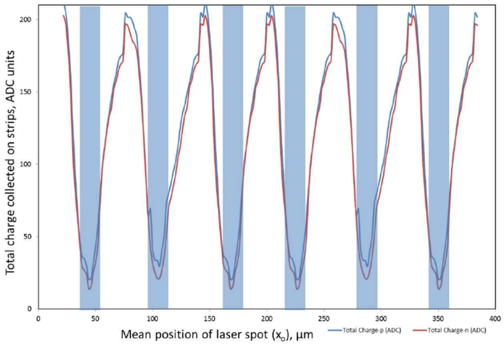

Figure 1: Amplitude response of a few strips from a detector module scanned with a laser spot.

Invasive methods are the characterization with methods that require physical contact of probes to the objects. The important features are: (i) this allows detailed analyses of the device under test (DUT), (ii) this leaves scratches or marks on the surface, (iii) this is limited to sensors, not to detector modules, (iv) this method involves passive electrical measurements using a wafer prober and micro-probing needles [2].

Non-invasive methods are the characterization with methods that do not require physical contact of probes. The important features are: (i) a few significant parameters of the DUT can be investigated, (ii) this leaves no scratches or marks on the surface, (iii) this is not limited to bare sensors but can be applied to detector modules, (iv) this method involves injection of localized charge using a pulsed infra-red laser [3].

The laser test stand (LTS) is developed with the idea to perform key quality assurance tests on silicon detector modules. The significant parameters that can be analysed or investigated using the LTS are: (i) Uniformity of charge collection (or strip integrity) from scanning the strips. An example of such laser scan is shown in Fig. 1. (ii) Operation voltage from the bias scan. An example of charge collection as function of the bias voltage is shown in Fig. 2 (a). (iii) Charge coupling to neighbour and next-neighbour strips from bias scan. An example is shown in Fig. 2 (a). (iv) Ratio of AC-coupling to inter-strip capacitance from amplitude response at specific positions. An example is shown in Fig. 2 (b). (v) Charge sharing function (η) in the inter-strip region can be determined. Figure 3 shows η-function dependence with the position of the laser spot.

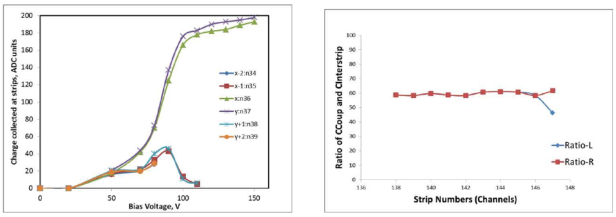

(a) (b)

Figure 2: a) Operating voltage determination and charge sharing between neighbouring and next to neighbouring strips and b) Ratio of coupling to inter-capacitance.

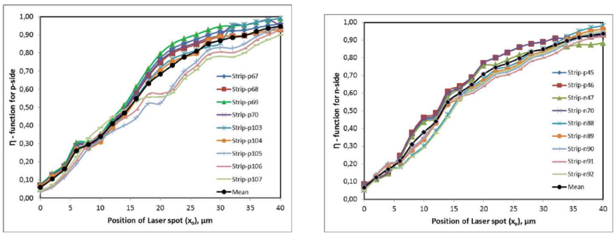

(a) (b)

Figure 3: Charge sharing measurements in the inter-strip region of a silicon detector module: a) p-side and b) n-side.

References

[1] P. Ghosh, J.Phys.: Conf. Ser. 503 012028, 2014

[2] P. Ghosh, PoS (Bormio 2013) 018, 2013

[3] P. Ghosh, CBM Progress Report 2013, Darmstadt 2014, p. 48

---

* Work supported by HIC-for-FAIR, H-QM and HGS-HIRe.

DOI:10.15120/GR-2015-1-MU-NQM-CBM-35

Development of a laser test system for the characterization of prototype silicon micro-strip sensors*

P. Ghosh[1], *J. Eschke*[3], *W. Niebur*[2], *P. Zumbruch*[2], *and J. Heuser*[2]
[1]Goethe University, Frankfurt, Germany; [2]GSI, Darmstadt, Germany; [3]FAIR, Darmstadt, Germany

For the characterization and quality assurance of prototype micro-strip sensors produced for the CBM Silicon Tracking System (STS), a semi-automated infra-red pulsed laser test system has been developed [1]. The amount of energy deposited by the laser light is chosen such, that it is equivalent to charge created by a minimum ionizing particle. The purpose of this investigation is to understand the charge sharing and uniformity of sensor performance in the inter-strip regions. Two prototype sensor, namely CBM02 (double-sided, 256 strips/side, pitch = 50 μm, full read-out) and CBM05 (double-sided, 1024 strips/side, pitch = 58 μm, one-eighth read-out) have been investigated [2]. The strips on the sensors are read-out via self-triggering n-XYTER based front-end electronics.

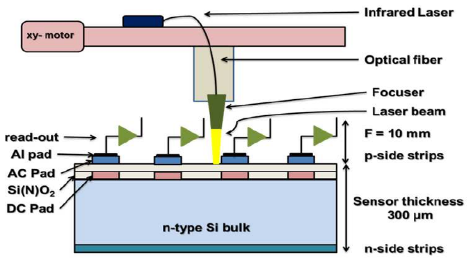

Figure 1: Schematic representation of the laser set-up

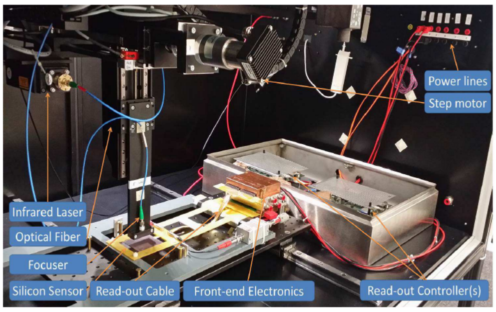

Figure 2: Components of Laser Test Stand.

The automated tests are performed at several positions across the sensor. The laser beam is focused to a spot-size of (σ_{spot}) $\approx$ 12 μm. The duration ($\sim$ 5 ns) and power (few mW) of the laser pulses are selected such that the absorption of the laser light in the 300 μm thick silicon sensors produces about 24 000 electrons, which is similar to the charge created by minimum ionizing particles (MIP). The wavelength of the laser is chosen to be 1060 nm because of the absorption depth being of the order of the thickness of the silicon sensors [3]. Figure 1 shows the measurement set up in a schematic view. Figure 2 shows various components installed in the laser test stand. The laser beam is transmitted through a 6 μm thick optical fibre to a single focusing system, which focuses the light to a spot of about 12 μm diameter. The working distance is about 10 mm [1]. The laser focuser is calibrated to a focused position on the sensor surface as a function of the number of strips fired with a signal just above threshold. At this reading the proper focal distance has been achieved. Figure 3 shows a measurement of the charge sharing function (η) in the inter-strip region. The η function is defined as the ratio of charge collected by either strip divided by the sum of both. The EPICS device control is used to control the step motor. A special program with a user interface has been developed to operate and move with the laser over the active area of the sensor to perform several measurements automatically. The data acquisition software DABC accesses the motor position information from EPICS. The on-line and off-line analysis is performed using the Go4 analysis tool.

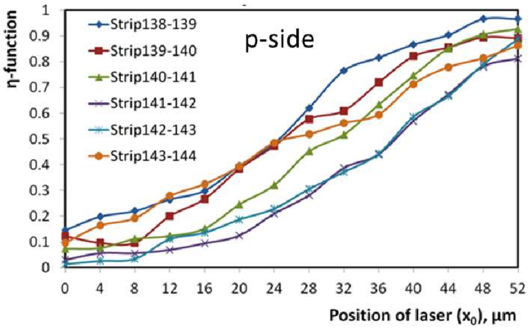

Figure 3: Charge sharing function (η) as a function of the position of the laser spot on one side of the sensor.

References

[1] P. Ghosh, PoS (Bormio 2013) 018, 2013

[2] P. Ghosh, J.Phys.: Conf. Ser. 503 012028, 2014

[3] P. O'Connor *et al.*, Proc. of SPIE Vol. 6276 62761W-1, p. 2

---

* Work supported by HIC-for-FAIR, H-QM and HGS-HIRe.

DOI:10.15120/GR-2015-1-MU-NQM-CBM-36

Tooling for CBM STS module assembly*

D. Soyk†1, *C. Simons*1, *R. Visinka*1, *the CBM collaboration*1, *and the FAIR@GSI RBDL*1
1GSI, Darmstadt, Germany

The CBM STS module assembly needs tooling to simplify and speed up fabrication [1]. For several assembly steps specialized assembly tools are needed.Assembly will comprise the following steps: First, 2 layers of microcables need to be bonded on to the STS-XYTER chip to form a a"chip-cable". Secondly, 8 chip-cables must be bonded to the CBM STS sensors side by side for readout of the full 1024 channels for every sensor side. Additionally, on singlemetal sensors an interstrip connecting cable must be allocated and bonded on one side of the sensor. It serves to interconnect the inclined strips that end on the sensor side to form a continuous strip over the sensor. Therefore a whole set of assembly tools must be developed and - if needed - improved. To start with simplest element, the tool for the first cable layer on the chip was design, produced and tested. This first version was already shown in[1]. In figure 1 the improved version is depicted.It has small bumps to avoid crashes between the bond needle and the tool. This change increases the safety of operations and will be an advantage for the mass production by reducing the machine downtime due to such crashes. The chip and the cable in this design were still held by vacuum and manipulated via a bottom-side mechanics. Secondly, a tool for bonding of the second layer of the micro cable to the chip was designed.Because of the presence of the first layer, already bonded and glued to the chip, the second cable layer needs to be mounted from the top side. The chip is still fixed from the bottom-side, but the jig for micro cable mounting is now above it. This does increase the height of the tool, but this height is not a showstopper, because the operating range of the tab-bond needle is not above the cable but the chip. See figure 2.

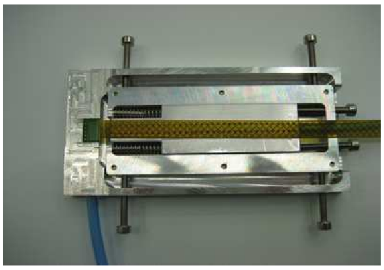

Figure 1: Tool for 1st layer on chip

To assembly the microcables with the chips to the sensor a third tool with a movable bottom-side sensor holder and a top-side mechanics for the microcables was designed (see figure 3). It turned out that a movable sensor holder is not the best way for this assembly step, because the flimsy microcables are destroyed if they're moved too strong. An improvement of this tool is in work. Fortunately it also turned out, that this tool could be used to bond the interstrip connecting cables on the p-side of the sensor (see figure 4).

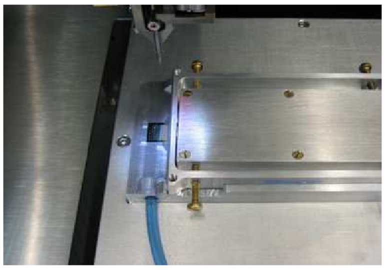

Figure 2: Tool for 2nd layer on chip

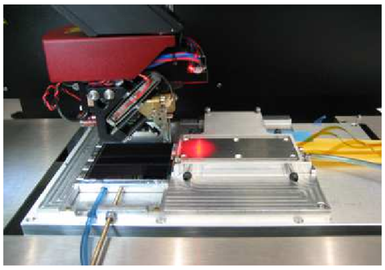

Figure 3: Tool for 1st and 2nd layer on sensor

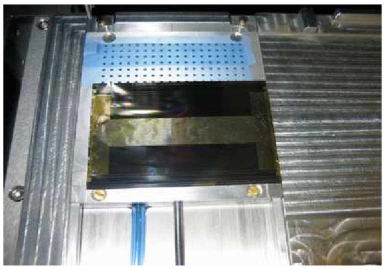

Figure 4: Insterstrip cable on sensor

References

[1] D. Soyk et al., "Development of a tool for CBM STS module assembly", editors: V. Friese and C. Sturm, CBM Progress Report 2013, Darmstadt, ISBN 978-3-9815227-1-6

---

* Work supported by FAIR@GSI PSP code: 1.1.1

† d.soyk@gsi.de

DOI:10.15120/GR-2015-1-MU-NQM-CBM-37

Modification of CBM-STS micro-cable stack-up*

D. Soyk[1], *C.J. Schmidt*[†1], *V. Kleipa*[1], *I. Sorokin*[1], *the CBM collaboration*[1], *and the FAIR@GSI RBDL*[1]

[1]GSI, Darmstadt, Germany

During several years of development of the CBM modules, the STS sensors and the CBM STS-XYTER chips were carefully studied and designed. Despite this careful evolution, the design and study of the connecting part between the sensor and the chip had not been addressed in such intensity. Some studies on the electrical behavior were performed, while all questions of cable stockage were addressed this year. In [1] the cross section of the cable - like it was used for the electrical simulation - is described.

In figure [1] the modified cable stack-up is shown.

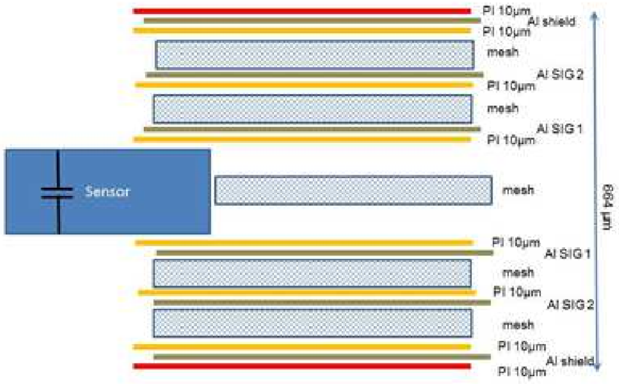

Figure 1: Schematic side view of the micro cable stack up for one CBM module. The red layer on the top and the bottom of the cable is the newly introduced insulation layer. In the middle, at the side of the sensor, the meshed layer to reduce crosstalk between the two sensor sides was newly introduced.

The geometry of the signal strands with a height of 14μm and a width of 46μm is kept, also the pitch between the strands remains 116μm on each signal layer. As substrate for the strands 10μm thick polyimide will be used.

The thickness of the mesh will be kept at 100μm, but a study is beeing done to find a mesh material with a lower mean dielectric constant.

Also a additional layer of meshed material will be inserted between the microcable for the n- and p-side of the sensor. With this layer the crosstalk between the signals of both sensor sides should be minimized.

The shielding layer will be modified. The thickness of the aluminum will be reduced to 14μm (instead of 30μm) and the polyimide will have a thickness of 10μm (instead of 20μm). With these changes the same aluminium polyimide film may be used for the signal layers, as well as for the shielding layers.

Due to the fact that the sensors of different modules of a ladder are on different potentials, it could be an advantage to introduce a additional layer of polyimide insulation on the outside of the shielding. This allows us to keep the shielding potential for each sensor side and for each sensor in a ladder on a defined and independent level, namely the reference level of the pre-amplifier input stage. With these additional two insulating layers of 10μm and the meshed layer in between, the total thickness of the stack is 664μm per module.

The modified stack-up of the micro cable was already presented by C.J. Schmidt at the 24th CBM collaboration meeting in September 2014 [2]. The research for a mesh material with lower dielectric constant is ongoing. This cable stack-up will now be realized for the next module prototype.

References

[1] J. Heuser et al., Technical Design Report for the CBM Silicone Tracking System, GSI Report 2013-4, Darmstadt, ISSN 0171-4546, figure 4.10

[2] C.J. Schmidt, “Status of module development”, 24th CBM Collaboration Meeting

---

* Work supported by FAIR@GSI PSP code: 1.1.1

[†] c.j.schmidt@gsi.de

DOI:10.15120/GR-2015-1-MU-NQM-CBM-38

Fixtures for quality assurance of STS silicon sensors and STS-XYTER ASIC *

C. Simons[1], *C. J. Schmidt*[1], *V. Kleipa*[1], *K.Kasinski*[2], *and the FAIR@GSI RBDL*[1]
[1]GSI, Darmstadt, Germany; [2]AGH University of science and technology, Krakow, Poland

To assure the functionality of the silicon microstrip sensors and the quality of bond contacts of the microcables on the STS-XYTER-chip, fixtures are needed, that preferably allow on one hand for non-destructive handling and measurements as well as easy and fast procedures on the other. Several companies were asked for proposals and aps Solutions GmbH had the most promising one: test sockets with Pogo Pins for contacting. *Pogo Pin* is a registered trademark of a US company (*WinWay Technologies*); they are also called spring loaded contacts. Formed like a cylinder, it contains two peaked, spring-loaded pins that make secure contacts with two electronic circuits. For the Pogo Pins different combinations on tip shapes, structures, materials and plating are available so that the particular application may be optimized.

Test socket for the silicon sensors

The challenge for the different quality measurements of the double-sided sensors is the need for simultaneous biasing contacts from bottom and top side. This problem can be solved with a fixture that consists of a bottom and a top socket. Both sockets include a Pogo Pin to which the bias voltage is applied via a small pcb. The bias pads on the sensor have a comfortable size of 400 μm × 150 μm to facilitate contacting. With the help of a wafer prober equipped with a movable chuck, the strips may then be stepped through for investigation by means of a probe card. The schematical layout of the fixture and its installation on a wafer prober are shown in Figs. 1 and 2.

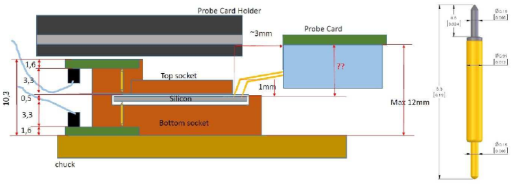

Figure 1: Draft design of the sensor test socket.

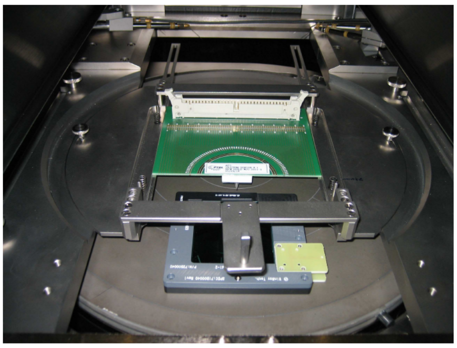

Figure 2: Test socket and probe card on wafer prober.

Test socket for the STS-XYTER-chip

Each traceline of the microcables that connect the silicon microstrip sensor to the STS-XYTER-readout-chips has to be TAB-bonded onto the pads of the sensors on one side and on the chip on the other. These contacts should be checked before applying the protective glob-top because TAB-bonds without contact may be rebonded. The quality check can be put into practice by taking the chip into operation, a minimal set of essential connectivity has been elaborated with the chip designers towards this end. A probe card, that is typically chosen as a good solution for operating a chip without wirebonding, cannot be used for this test because it only works in combination with a wafer prober that assures alignment and positioning. The STS-module (STS-XYTER + microcable + sensor) would need to be placed on the chuck of the prober, inhibitive because of the module size and the fragility of the module. Therefore working with a test socket with Pogo Pins is an appropriate solution. The chip by itself is placed into the socket that will have an opening for the microcable. Several requirements regarding the test pad size, pitch and general arrangement and balance of connections across the chip have to be taken into account. Proposals for the pad layout of the STS-XYTER are under development with consultation of *aps Solutions GmbH*. Continuative tasks for the execution of tests are the development of a modified STS-XYTER board and suitable software.

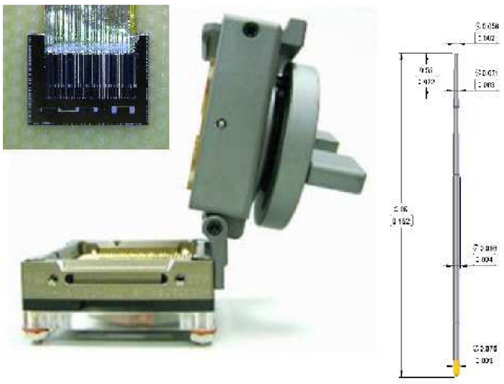

Figure 3: Test socket for ASICs.

---

* Work supported by FAIR@GSI PSP code: 1.1.1

DOI:10.15120/GR-2015-1-MU-NQM-CBM-39

Status of the CBM STS CAD design

Jochen Kunkel[1], *Sergey Belogurov*[2], *Jorge Sánchez Rosado*[1] *for the CBM STS collaboration*
[1]GSI, Darmstadt, Germany; [2]ITEP, Moscow, Russia

A virtual model of the planned CBM STS detector system gets designed in the CATIA CAD software in full detail [1]. It is used to visualize the space dependencies of all sub-systems like mechanics, electronics and cooling. In this report the status of the work on this model is shown.

Repository

Several people of the CBM STS collaboration work with the CAD model. Since they work in different institutes all over the world a platform was needed to enable collaborative work. As control system Subversion was chosen because of the instant availability and the ease of use. GSI hosts a Subversion server on which all CAD files are now located. This Repository not only gives access for everybody involved but also brings file versioning and backup.

Sensor layout

The sensor layout has been improved in the area around the beampipe and in the outer edges at the large stations. To optimise the amount of different parts and lengths of cables the readout electronics have been re-arranged to appropriate positions (see Fig. 1 and Fig. 2). Now only 16 different lengths of carbon ladders are needed.

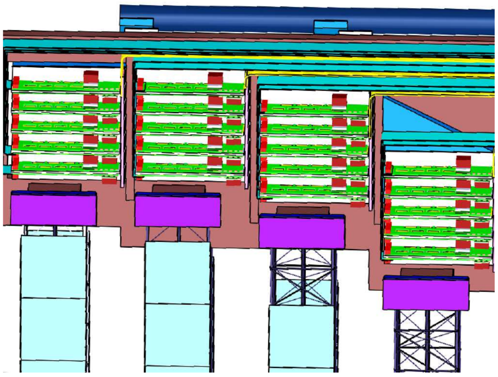

Figure 1: Detailed view of the upper end of ladders. Space between uppermost sensor and electronic not optimised for cables lengths (not shown).

Cooling plates

The detailed construction of the cooling plates has started (see Fig. 3). Different manufacturing methods and their influence to the shape of the plates were considered. Two special joining processes (with and without additional material) for aluminium are tested. At first two different sizes of plates are designed to prove the desired cooling power, pressure stability and the reliability of the production process.

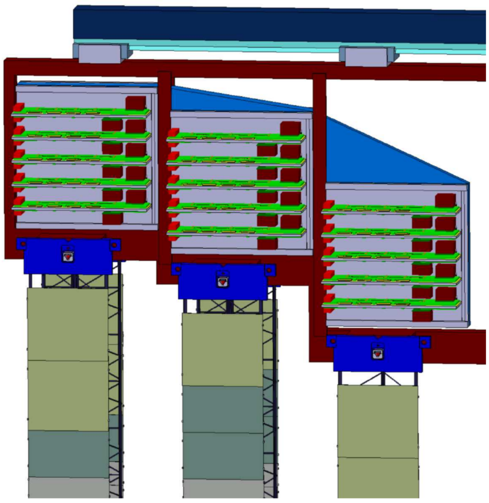

Figure 2: Detailed view with re-arranged electronics. Distances between sensors and electronics shorter and more regular.

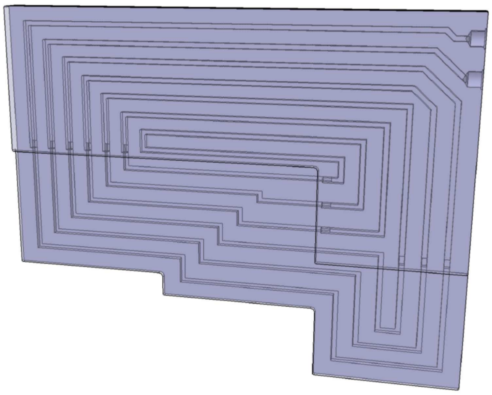

Figure 3: Semi-transparent view of a cooling plate. Length of inside channel is more than 5 m, cross section 4 × 4 mm. Connectors will be at the upper right corner.

References

[1] S. Belogurov, A. Kolosova and J. Kunkel, CBM Progress Report 2013 (2014), p. 46

DOI:10.15120/GR-2015-1-MU-NQM-CBM-40

Neutron irradiated prototype CBM-STS microstrip sensors tested for double metal or cable interconnections of the end strips*

M. Singla[1], *P. Larionov*[2], *I. Momot*[2,3], *T. Balog*[1], *J. Heuser*[1], *I. Sorokin*[1,3], *and C. Sturm*[1]
[1]GSI, Darmstadt, Germany; [2]Goethe University, Frankfurt, Germany; [3]KINR, Kiev, Ukraine

The Silicon Tracking System (STS), the core detector of the CBM experiment, is located in the dipole magnet to provide track reconstruction and momentum determination of charged particles from beam-target interactions. The STS will have double-sided silicon microstrip sensors mounted onto a low-mass carbon fibre support structure. The strips on one side of the double sided silicon microstrip sensors are tilted to have 7.5^0 stereo angle. This allows to reconstruct multiple hits from the same sensor at the expense of a poorer spatial resolution in vertical direction [1]. To have read out only from one sensor side, the end strips from one edge of the sensor were connected to the end strips on the other end as shown in Fig. 1. This interconnection can be provided via double metallization (DM) or by using external interstrip cables (SMwC). However, the central strips were the full strips without any kind of interconnections (region II in Fig. 1).

Test results of these prototype sensors before and after their exposure to neutron equivalent fluences of $2{\times}10^{14}$ $n_{eq}cm^{-2}$, as they are expected for the worst case scenario in the CBM experiment, will be disucssed. The sensors were irradiated at Karlsruhe Institute of Technology (KIT), Germany.

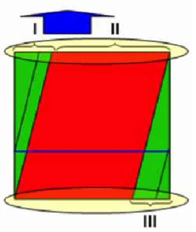

Figure 1: Sensor topology to read out inclined sensor strips.

All the measurements were performed in a refrigrator at temperatures between -5^0 C to -10^0 C to limit the radiation-induced effects on detector current and to prevent thermal runaway [2]. Four sensors were selected for the measurement of variation of leakage current with bias voltage (IV), bulk capacitance versus bias voltage (CV), and for charge collection tests for the central strips (region II in Fig. 1) and for the end strips (with these special interconnection scheme, region I in Fig. 1) with a ^{90}Sr source. In this report only the results from central strips will be discussed. The list of the sensors under test is given in Table 1 along with their sizes, thickness, types of the connections and full depletion voltage before irradiations (extracted from the capacitance-voltage measurements). These sensors were mounted in the printed circuit boards and were wire bonded to read out about 10 strips for each sensor side using self-triggered n-XYTER chip.

Table 1: Specifications for the sensors under tests. The naming convention in the left column encodes the prototype generation (5 or 6), the manufacturer (H = Hamamatsu, C = CiS), the sensor height/strip length in cm (4 or 6), and the wafer number.

name CBM0-	size cm × cm	thickness μm	inter-connection	V_{fd} ±5 V
5H4-W18	6 × 4	327	SMwC	68
5H4-W10	6 × 4	331	DM	75
6C6-W14	6 × 6	293	SMwC	94
5C6-W6	6 × 6	291	DM	98

Charge collection studies were performed with ^{90}Sr for the sensors under test by applying suffieciently high reverse bias. Results are shown in Fig. 2 for all the sensors with either double metal interconnection scheme or single metal with external microcable bonded on its top p-side. As can be seen in Fig. 2, the charge collection efficiency degrades after the irradations. These sensors were also tested in-beam at COSY, Research Center Jülich, in December 2014. Before concluding on the type of the p-strip interconnection scheme, one should also consider the beamtime results about charge collection and detection efficiency of these sensors. This work is still in progress.

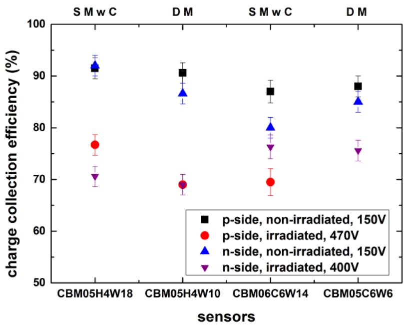

Figure 2: Charge collection results with ^{90}Sr, comparing the sensors before and after irradiation.

References

[1] J. Heuser et al., Technical Design Report for the CBM Silicon Tracking System, GSI Report 2013-4

[2] M. Moll et al., *Nucl. Instrum. Methods. A* 439 (2000), p. 282

---

* Work supported by HIC-for-FAIR, H-QM and HGS-HIRe.

DOI:10.15120/GR-2015-1-MU-NQM-CBM-41

STS-HCTSP, an STS Hit & Control Transfer Synchronous Protocol*

K. Kasinski[1], *W. Zabolotny*[2], *J. Lehnert*[3], *C.J. Schmidt*[3], *W.F.J. Müller*[4], *and R. Szczygiel*[1]

[1]Department of Measurement and Electronics, AGH University of Science and Technology, Cracow, Poland; [2]Institute of Electronic Systems, Warsaw University of Technology, Warszawa, Poland; [3]GSI, Darmstadt, Germany; [4]FAIR, Darmstadt, Germany

The data communication between STS detector readout chip (STSXYTERv2 [1]) and the Data Processing Board DPB [2] via the GBTx data combining ASIC [3] requires a robust and optimized protocol.

The specific requirements and a preliminary protocol was published in [4]. During development of the STSXYTERv2 and DPB systems the protocol was further refined.

The protocol specification includes a detailed description of: frames' structure in both uplink & downlink directions, methodology for time-allocating hits and error correction, link synchronization procedures (enabling low-level reset, bit position alignment and optimal adjustment of data/clock delays) and specification of STSXYTERv2-specific registers.

The protocol is optimized for the data structure of the STS detector read-out ASICs but can be reused also in other systems. It maximizes the hit data throughput in the uplink (from ASIC to DPB) direction and data integrity in downlink (from DPB to ASIC) direction. The protocol is fully synchronous. Both uplink and downlink frames use 8b/10b encoding for DC-balance, and the frames in each direction have constant lengths and are transferred continuously.

Downlink frames support 4 request types: *no_op* (no operation), *WRaddr*, *WRdata*, *RDdata* (used for register access with 14-bit payload). A 4-bit chip address enables both individual chip addressing on FEBs and broadcasting messages. Since full-path delay can reach 1 μs, multiple commands in-flight are supported by using a sequence number. Each register access command should be acknowledged on the uplink. The error correction scheme is the modified selective repeat ARQ, where not-acknowledged requests are retransmitted and register values can be verified by readback. The frames are 60-bit long (after 8b/10b encoding) and last 375 ns. They consist of K28.5 comma character, 4-bit chip address, 4-bit sequence number, 2-bit request type, 14-bit payload (address/data) and 16-bit CRC (0xC86C).

The uplink communication contains mainly hit data but also control responses and special information (e.g. alerts). After all optimizations a throughput of 9.41 MHit/s/link is achieved, which results in a 71% link occupancy for the design target of 250 khit/s/channel in a 5 links/ASIC configuration. The frames have constant length of 30-bits (after 8b/10b encoding), last 92.75 ns and support 5 frame types: dummy hit (equivalent of no_op, used to filling the link when idle and to transfer the timestamp MSB to keep the synchronization), hit (containing: 6-bit channel address, 5-bit ADC value, 10-bit timestamp LSBs, 1-bit error status marker), TS_MSB (used for data compression, transfers triplicated 6-bit timestamp MSBs and 4-bit 0x9 CRC), RDdata_ack (acknowledge message for RDdata command, contains 14-bit register content, 3-bit sequence number LSB and 4-bit 0x9 CRC), Ack (general acknowledge message with 2-bit ack-type: ack, nack, alert, 4-bit sequence number, 1-bit configuration parity, 4-bit status, 6-bit current timestamp, 4-bit 0x9 CRC).

The chip has built-in mechanisms for monitoring the link itself and the in-ASIC data flow. Multiple alert states can be configured and generated. The DPB is informed on the alert status by ack frames or error status markers in hit frames. Further information on alerts and means to manage them are foreseen in the ASIC's address space.

The link synchronization procedure is used for tuning of data/clock delays in GBTx ASIC and also for alignment of frame and bit positions. Even though during regular operation the comma characters are periodically transferred they are not used for on-line synchronization but only for link monitoring. During link synchronization, special, 20-bit characters beyond 8b/10b code (SOS: start of sync, EOS: end of sync) are used together with K.28.1 and K.28.5 characters. SOS and EOS can be easily detected in any state of the link and can be used to remotely reset the chip and communication. SOS triggers the procedure. First, using a SOS character, the clock/downlink data phases are adjusted, then K.28.1 is used to adjust the uplink data phases. The procedure is ended by EOS character. Finally bit and frame alignment is made on the first comma characters received through the links during regular operation.

References

[1] K. Kasinski, et al., "Towards the STS-XYTERv2, a silicon strip detector readout chip for the STS", CBM progress report 2014, Darmstadt 2015.

[2] W. Zabolotny et al., "Towards the Data Processing Boards for CBM experiment", CBM progress report 2014, Darmstadt 2015.

[3] J. Lehnert, et al., "The GBT Based Readout Concept for the CBM Silicon Tracking System", CBM progress report 2014, Darmstadt 2015.

[4] K. Kasinski, W. Zabolotny, R. Szczygiel, "Interface and protocol development for STS read-out ASIC in the CBM experiment at FAIR", Proc. SPIE 9290, Photonics Applications in Astronomy, Communications, Industry and

---

* Work supported by GSI

DOI:10.15120/GR-2015-1-MU-NQM-CBM-42

High-Energy Physics Experiments 2014, 929028, doi: 10.1117/12.2074883.

DOI:10.15120/GR-2015-1-MU-NQM-CBM-42

Long-term stability of the STS prototype sensors irradiated to 2×10^{14} n_{eq}cm^{-2}

P. Larionov[1]
[1]Goethe Universität, Frankfurt, Germany

The Silicon Tracking System (STS) is the core tracking detector of the Compressed Baryonic Matter (CBM) experiment. The STS silicon sensors [1] will be operated during long periods of time continuously. During the operation a high level of radiation damage is expected to impact on the sensors. The exposure of 1×10^{14} 1 MeV neuton equivalent per cm^2 is the harshest scenario for sensors in the innermost areas of the STS stations, close to the beam axis, after several years of running. In this work, the long-term stability of the leakage current of highly irradiated prototype sensors has been investigated.

Prototype sensor	Vendor	Sensor size, cm	Interconnection technology
CBM05H4	Hamamatsu	6.2×4.2	Double-Metal
CBM05H4	Hamamatsu	6.2×4.2	External cable
CBM05C6	CiS	6.2×6.2	Double-Metal
CBM06C6	CiS	6.2×6.2	External cable

Table 1: Prototype sensors used for tests.

To study the impact of irradiation on the properties of the sensors, the latest STS prototype sensors have been irradiated to 2×10^{14} n_{eq} cm^{-2} at KIT, Karlsruhe. The following prototype sensors with two different strip interconnection technologies [1], indicated in Table 1, were used for the tests. All the measurements were performed at -5°C to reproduce the real operating conditions of the CBM experiment. The sensors were placed inside the shielded box with connected N_2 supply to keep the humidity at the lowest possible level.

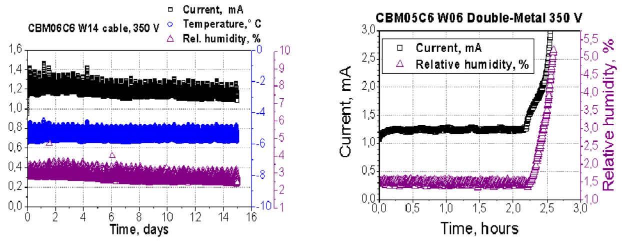

(a) (b)

Figure 1: a) Long-term stability of the leakage current of the CBM06C6 prototype sensor; b) Measurement results of the humidity impact test.

During a single measurement, the leakage current of the sensor at 350 V reverse bias voltage, and the temperature and humidity of the surrounding air were monitored in steps of 30 seconds. Figure 1a indicates the measurement result of the CBM06C6 sensor prototype during 15 days of continuous operation. The temperature of the air fluctuated within 1°C periodically during the measurement because of the cooling device's operating principle, keeping the mean value of - 5.5° C.

$$I(T) \propto T^2 exp(-E_g/2k_BT) \qquad (1)$$

This resulted in a leakage current fluctuation due it's temperature dependance that is shown in Eq. 1. Moreover, it was observed that the leakage current is also sensitive to the humidity variation. The correlation between leakage current and the relative humidity curves are shown in Fig. 1 a, b. This can be explained by the introduction and rearrangement of negative charges in a humid air on the oxide surface which leads to surface depletion and consequent increase in the leakage current, as the surface generation becomes added to the bulk leakage current [2], [3].

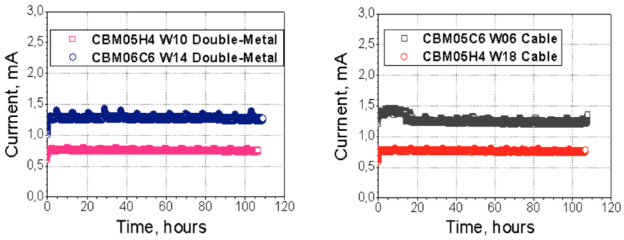

Figure 2: Leakage current stablity: sensors with double-metal (left) and external microcable (right) technologies.

Figure 2 shows the results obtained for all prototype sensors for a 110 hours time period. All the presented data points have been normalized to the values at the reference temperature (-5°C) to exclude the temperature variation impact using Equiation 1. The humidity variation for the selected time period was considered to be negligible. The measurement results show stable behaviour of the leakage current for the sensors with both double-metal and external microcable interconnection technologies.

This work is supported by HGS-HIRe, H-QM, HIC for FAIR.

References

[1] CBM collaboration, Technical Design report for the CBM Silicon Tracking System, GSI Report 2013-4.

[2] M. Laakso, P. Singh, P.F. Shepard, Nucl. Instr. and Meth. A **327** (1993) 517-522.

[3] F.G. Hartjes, Nucl. Instr. and Meth. A **552** (2005) 168-175.

DOI:10.15120/GR-2015-1-MU-NQM-CBM-43

A Front-end electronics test board for the CBM Silicon Tracking System*

V.Kleipa[1], *C. Simons*[1], *D. Soyk*[1], *C.J. Schmidt*[1], *J. Carpenter*[1], *the CBM collaboration*[1], *and the FAIR@GSI RBDL*[1]

[1]GSI, Darmstadt, Germany

The 896 modules of the CBM Silicon Tracking System will be equipped with two front-end electronics boards (FEBs) each, carrying per board eight STS-XYTER ASICs that read out the silicon micro-strip sensors of the modules [1]. The boards will be stacked at the top and bottom layers of the detector, mounted in a shelf structure that is in contact with a cooling plate to remove the power dissipated by the electronics. Due to the spatial contstraints there, the board dimensions are restricted to the limited size, as shown in Fig. 1. At the same time, the board has to provide the infrastructure for achieving the full output band width needed to read out the detector. This translates to realizing up to 5 LVDS pairs per final ASIC, a high-density challenge for the FEB design and prototyping.

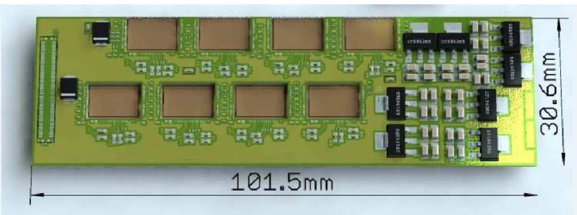

Figure 1: Rendering of the STS front-end electronics board comprising 8 STS-XYTER ASICs arranged in a fixed pattern on two double-rows of 4 ASICs each. Power supply section with LDOs on the right. The small components are decoupling capacitors to common and communication ground.

For assembly test purposes, a PCB was produced onto which 8 STS-XYTERv1 ASICs can be mounted but not having any electrical functionality. Only the top and bottom layers are covered with a gold layer for test bonding of ASICs and cables. During its layout, it turned out that only one of the four readout channels of each ASIC could be routed to the digital I/O connector, limited due to the available space in between the ASICs. This technological problem is the subject of current work.

In order to prepare a test equipment for a complete read-out chain from sensor to GBTx boards, an intermediate FEB board has been designed that is not constrained to the small dimensions. The PCB, called FEB4, hosts only four ASICs. Its layout is shown in Fig. 2. This PCB comprises the required power supply LDOs. All I/O channels of each ASIC are linked to a connector. In addition, the required high-voltage capacitors (rated 250 V) for bias decoupling have been added to the differential LVDS connections. In Fig. 3(a) the board's assembly pads for passive devices are visible. For the devices' case size, the norm *0201[m]* had to be chosen in order to fit them between the ASICs. This board is currently being used for testing of the STS-XYTERv1 chips. One ASIC wire-bonded to the board is shown in Fig. 3(b).

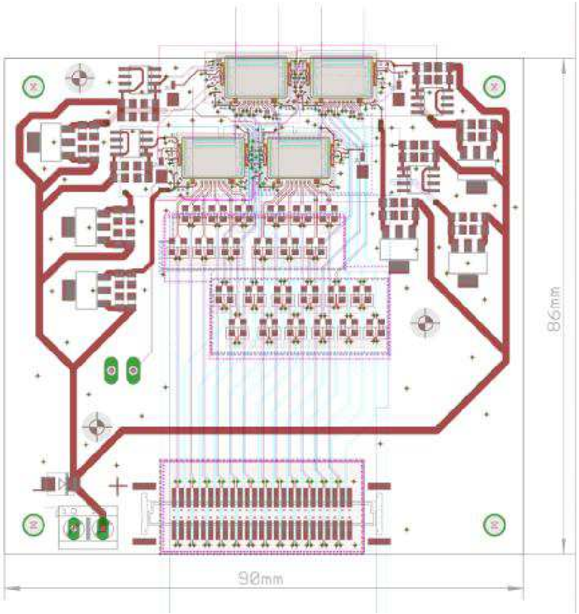

Figure 2: Layout of a front-end board comprising four read-out ASICs and all outgoing LVDS data lines on a somewhat relaxed geometrical footprint (FEB4).

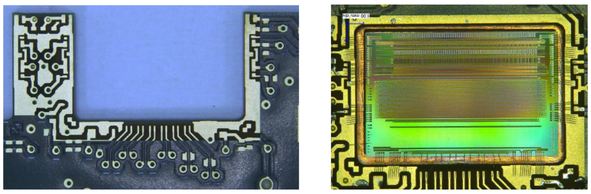

(a) (b)

Figure 3: (a) High-density region in between the openings for the STS-XYTER ASICs on FEB4, filled with the full set of LVDS lines, micro-vias and connecting pads for high-voltage decoupling capacitors. (b) STS-XYTERv1 ASIC installed into FEB4 and wire-bonded to its power supply, control and outgoing data lines.

References

[1] V. Kleipa et al., CBM Progress Report 2013 (2014), p. 36

---

* supported by EU-FP7 HadronPhysics3 and by FAIR@GSI PSP code: 1.1.1

DOI:10.15120/GR-2015-1-MU-NQM-CBM-44

Development of a 124mm long silicon strip sensor for the CBM STS*

D. Soyk[†][1], *C.J. Schmidt*[1], *the CBM collaboration*[1], *and the FAIR@GSI RBDL*[1]
[1]GSI, Darmstadt, Germany

The new segmentation of the CBM STS ladders [1] requires to design and produce a silicon strip sensor with 62mm width and 124mm height. This new long sensor will replace the 2 daisy-chained 62mm sensors.

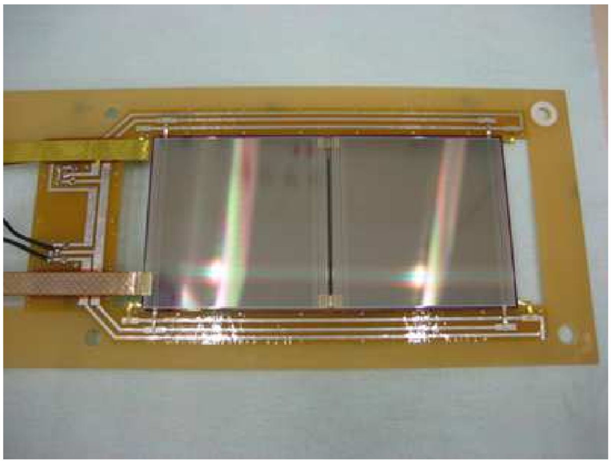

Figure 1: 2 daisy-chained 62mm sensors

In figure [1] a technological prototype, produced by LTU LED Technologies of Ukraine ltd, Kharkov, Ukraine, is shown. Between the 2 sensors 2 short daisy-chain-cables are shown. That serve to connect the strips from one sensor to the next. In the final version, all strips of the sensors must be connected. Therefore a daisy-chain-cable with the full width must be produced and bonded onto the sensors. Every sensor also needs a cross connection on the p-side that links inclined strips ending on one lateral side to a corresponding strip on the other lateral side. It is not jet finally resolved, whether such connection should be realised on an additional metal layer or with a seperate microcable. If the sensor is single-metal, additionally for each sensor a interstrip-connection-cable must be bonded on the p-side of the sensor. Together with the research institute CiS Forschungsinstitut für Mikrosensorik und Photovoltaik GmbH, Jena, Germany the plan was developed to produce a single 124mm x 62mm sensor in double-side and double-metal technology on a 6 inch wafer. If it is possible to solve all technological challenges, the production of a module with 124mm sensorheight would become much simpler. The production and assembly of 2 interstrip cables and the production and assembly of one daisy-chain-cable could be made unnecessary. Also the bonding process of these 3 cables will be avoided. This reduction of fabrication and manufacturing steps will increase reliability and yield. Additionally the replacement of the daisy-chained sensor by one sensor will reduce the assembly effort because the daisy-chained module must be installed on a special frame before it is mounted on the ladder. In figure [2] the layout of the wafer is shown.

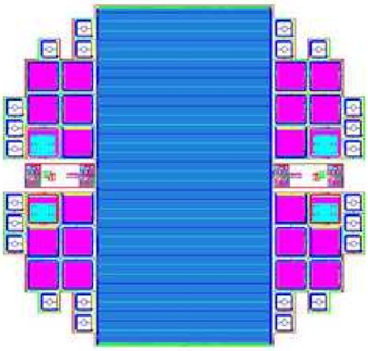

Figure 2: Layout of the 6 inch wafer with the 124mm x 62mm STSsensor in the middle, around the sensor CBM baby sensors and test features.

At the moment the design of the 124mm sensor is finished and the production of masks has already started. The design of the AC- pads will follow the classification of pad layout, described in [2].

References

[1] J. Heuser et al., Technical Design Report for the CBM Silicone Tracking System, GSI Report 2013-4, Darmstadt, ISSN 0171-4546

[2] D. Soyk et al., "Silicon strip sensor layout for the CBM Silicon Tracking System", editors: V. Friese and C. Sturm, CBM Progress Report 2013, Darmstadt, ISBN 978-3-9815227-1-6

---

* Work supported by FAIR@GSI PSP code: 1.1.1

[†] d.soyk@gsi.de

DOI:10.15120/GR-2015-1-MU-NQM-CBM-45

Improvement of ultra-light microcables production at LTU for the CBM Silicon Tracking System

V.M.Borshchov[1], *I.T.Tymchuk*[1], *C.J.Schmidt*[2], *V.G.Kucherenko*[1], *G.I.Nikitskiy*[1], *J.M.Heuser*[2], *M.A.Protsenko*[1], *J.Eschke*[2,3], *R.A.Kushniruk*[1], *L.V.Klimova*[1], *and K.M.Liholitova*[1]

[1]LED Technologies of Ukraine (LTU) Ltd, Kharkov, Ukraine; [2]GSI, Darmstadt, Germany; [3]FAIR, Darmstadt, Germany

Ultra-light micro-cables are the key component for the CBM-STS. They are employed to realize the analogue signal interconnection between detector and readout for the STS at minimized material budget. Taking into account the complexity of micro-cables and their required quantity a few "bottlenecks" in the production line have been identified and improvements were realized on the production line. Additionally the preliminary technological regimes were defined and a test batch of micro-cables (100 pieces) was manufactured within the framework of the STCU partner project P635.

For the detector modules two kinds of interconnection components will be employed [1-2]:

- ultra-light interconnection microcables based on aluminium-polyimide adhesiveless dielectrics (connecting microcables, interstrip cables, daisy-chain cables, shielding layers).
- meshed spacers based on Kapton or polyimide (narrow and wide meshed spacers).

The typical technological process of micro-cable and spacer manufacturing includes the following main technological operations based on photolithography and chemical wet etching processes: chemical cleaning of the substrate, photoresist coating on the substrate, photoresist exposure, photoresist development, aluminium etching (for interconnecting micro-cables), polyimide etching and finally photoresist removal.

Taking into account that large numbers of components in a considerable design variety need to be produced for the CBM STS (about 58 thousand micro-cables and spacers) the available technological equipment and the production line were analyzed with the aim to identify possible production "bottlenecks" which might result in production yield issues or even a suspension of production. The available equipment allows to produce the required components but two "bottlenecks" were identified:

- equipment for photoresist coating needed duplication,
- an exposure unit for photoresist exposing needed to be duplicated.

The following equipment was in consequence supplied by GSI to LTU Ltd within the STCU partner project, both from Bungard Elektronik, Germany:

- a Dip Coater RDC 21-K type,
- a parallel beam exposure unit EXP8000.

The equipment was installed and tuned in the clean room at the cable production site in Kharkov (Fig. 1). Process parameters for the operation of these machines for the different types of components were investigated and preliminary regimes were chosen.

Based on these parameters, a first pilot batch of microcables was produced and delivered to GSI so that the module assembly processes could be elaborated (48 laminated and 52 non-laminated test microcables 11 cm and 21 cm long). Samples of test cables are depicted in Fig. 2. The cable production line at LTU has been strengthened towards the large scale serial production of micro-cables for the CBM-STS. Technological regimes on the newly installed equipment were investigated and a batch of test microcables produced. This is a starting point for further production process optimization towards yield.

Figure 1: Dip coater RDC 21-K (left) and exposure unit EXP8000 (right) installed at LTU.

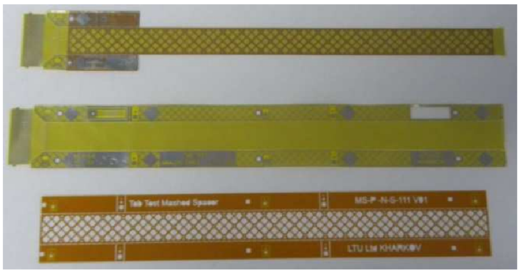

Figure 2: Experimental micro-cables for the development of the TAB-bonding assembly steps at GSI.

References

[1] V.M. Borshchov et al., CBM Progress Report 2013, p. 41

[2] C.J. Schmidt et al., CBM Progress Report 2012, p. 18

DOI:10.15120/GR-2015-1-MU-NQM-CBM-46

Radiation hardness tests on electronic components for CBM/STS low voltage power supply.

S. Löchner[1], *P. Koczoń*[1], *and A.Rost*[1]
[1]GSI, Darmstadt, Germany

Electronic components installed in the field of reaction products in future experiments at FAIR have to be radiation hard. At present, selected parts like DC/DC converters and LDO voltage stabilisers undergo exhaustive tests with use of intense minimum ionising particles' beams, mostly 3 GeV protons at Jülich sychrotron facility.

Testing setup

For components like DC/DC converters or LDO voltage stabilisers the output voltage level as well as expected transient voltage spikes rate due to the Single Event Upsets has to be monitored during irradiation. Voltage level monitoring (input and output) requires relatively low readout frequency below 1 Hz and can be implemented on inexpensive ARDUINO-Nano system [1]. Fast transients have been investigated on 4 trace digital oscilloscope Rhode-Schwarz RTO1044 [2] (triggering threshold has been setup to 15 mV). Measurement results have been recorded in nonvolatile memory and analysed.

Selected ASICs

For the radiation hardness tests several DC/DC converters have been chosen. Selection criteria like circuit efficiency, chip size, low coil inductivity, apropriate output voltage and sufficient output power as well as voltage setting flexibility have been applied. Only one model of the LDO stabilizer produced in rad hard technology has been examined until now. Alltogether 10 test boards with LTC3605 and 3 Boards with LTC3610 (Linear Technology) and 4 boards containing LM2596S (Texas Instruments) have been tested in two beam times. A GaN based ISL75051SRH has been abandoned according to producer information on radiation hardness of only 100 krad. All tested ASICs have been powered on during irradiation runs.

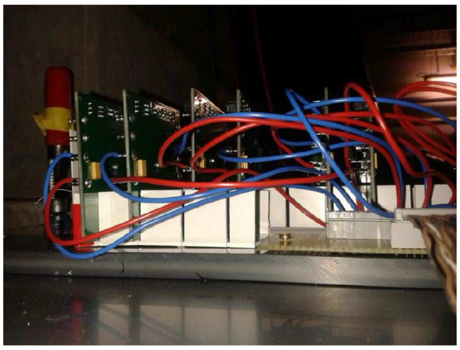

Figure 1: Base plate with PCB card holder and wiring.

Test boards have been placed in a holder which assured their position with respect to the proton beam during the measurement as shown in Fig.1.

Test results

PCBs with tested chips have been placed in a row along the beam axis such that the irradiating beam punched through all of them. A small ionisation chamber placed on the beam axis behind tested chips has been used to monitor the beam intensity. The beam profile has been investigated with Gafchromic dosimetric film [3]. In course of irradiation the film developes a spot corresponding to the shape of the proton beam with optical density corresponding to the integrated beam intensity (Fig.2). The total dose is known from the measurement with the ionisation chamber. Using film densitometry precise beam intensity distribution can be estimated and - consequently - the dose at ASIC chips.

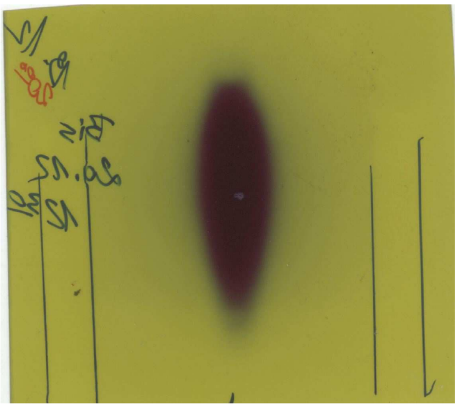

Figure 2: Beam spot on Gafchromic self-developing dosimetric film.

Neither of tested DC/DC converters survived more than $4.3*10^9$ protons. No fast transients have been observed on LDO voltage stabilisers which have absorbed only 10^8 protons (measurement was stopped for technical reasons before planned dose was reached).

References

[1] S. Löchner and P. Koczoń GSI Annual Report 2014

[2] http://www.rohde-schwarz.de/de/Produkte/messtechnik-testsysteme/aerospace-and-defense/messtechnik/oszilloskope-fuer-ad/RTO.html

[3] http://www.ashland.com/products/gafchromic-radiotherapy-films

DOI:10.15120/GR-2015-1-MU-NQM-CBM-47

Low and high voltage powering concept for the CBM Silicon Tracking System

C.J.Schmidt[1] *and P. Koczoń*[1]
[1]GSI, Darmstadt, Germany

Due to the radiation damage of the silicon sensors of CBM-STS detector their performance will deteriorate in course of experimental activity. Gradual increasing of their depletion voltage will improve the efficiency again and prolongate their life time. This procedure will be applied for each one of almost 1000 sensors separately what forces floating low and high voltage power supply architecture.

Requirements for low voltage powering of one silicon sensor.

The silicon Tracking System of CBM will be operated together with Micro Vertex Detector inside the magnetic field of 1 Tesla and rather small volume of about 1 m^3 [1]. To minimise the scattering of the reaction products tracked by the system only silicon sensors, their supporting structure and signal cables will be installed inside of the detector acceptance. The readout and converting electronics and its cooling as well as power converter will be installed on the detector circumference. Altogether almost 40kW of heat has to be removed from STS box to reach working conditions of -5 ^{o}C for silicon sensors. All the cooling system tubing, low and high voltage cabling, data transmission and control links sockets have to be connected on only 1.5 m^2 of surface of the upstream wall of the detector hausing. At least two different voltages are necessary for the STSxyter readout ASIC [3, 4] and additional two for the GBTx [5] and optical converter.

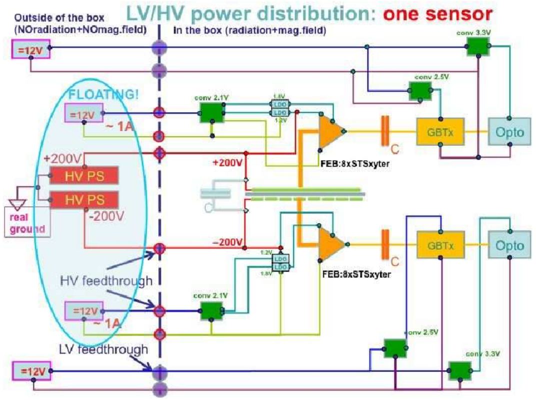

Figure 1: Low and high voltage powering of one silicon sensor..

Each sensor will be operated in a floating manner, e.g. p- and n-side will sense one half of the depletion potential (positive and negative) and the readout ASICs (and its powering) has to be applied "on top" of the sensors' depletion voltage. The last component shaping low voltage should be as close as possible to the front end ASIC in order to minimise amount of the noise irradiated into the system. High depletion voltage (low current) can be generated and controlled from the outside of the STS volume. All used electronic parts inside the STS box should be radiation hard and should stand a magnetic field strength of at least 1T.

Proposed powering for CBM-STS detector

The schematic diagram in Fig.1 shows proposed power distribution system. Both sides of the sensor (central part in Fig.1) are supplied with positive and negative depletion voltage generated outside of the magnetic field (+200V and -200V in this case, red lines in Fig.1) with a common grounding. Sensor's strips are connected to the STS-xyter readout ASIC on the Front Electronic Board FEB with micro-cables (orange elements in Fig.1). ASICs powering of 2.2V and ca 4A (per FEB) will be generated by FEAST DC/DC converter placed on the side part of the cooling plate [2]. It supplies two LDOs converting the input voltage to 1.8V (digital) and 1.2V (analog part) of ASIC. The latter has to be grounded in the sensor vicinity to +200V or -200V respectively. Input power of 12V and about 1A is delivered from outside for each sensor separately. This construction minimises grounding loops and assures separation of strong and weak current flow. A GBTx chip is equipped with many e-links and can communicate with more than one FEB simultaneously so GBTx circuitry has to be galvanically isolated from STSxyter chips. GBTx and optical interface require their own power which will be generated from dedicated 12V lines and additional FEAST converters (uppermost and lowermost parts in Fig.1 in green). STSxyter as well as GBTx power stabilisation will be realised by LDO components placed directly on corresponding PCB boards. Vertical dashed line in Fig.1 depicts the boarder of the high irradiation and magnetic field region (front wall of the STS detector box) and little circles – electrical connectors to the high (in red) and low (in blue) voltage DC generators.

References

[1] CBM STS Technical Design Report, 2012

[2] http://project-dcdc.web.cern.ch/project-dcdc/

[3] http://repository.gsi.de/record/51956/files/PHN-NQM-EXP-22.pdf

[4] Nuclear Science Symposium and Medical Imaging Conference (NSS/MIC), 2013 IEEE

[5] GBTx Project: https://indico.cern.ch/event/113796/session/7/contribution/37/material/slides/0.pdf

DOI:10.15120/GR-2015-1-MU-NQM-CBM-48

MPRC performance evaluation in a heavy ion beam test at GSI*

I. Deppner†[1], *N. Herrmann*[1], *P.-A. Loizeau*[1], *C. Simon*[1], *Y. Söhngen*[1], *M. Ciobanu*[2], *J. Frühauf*[3], *and M. Kis*[3]

[1]Physikalisches Institut Universität Heidelberg, Heidelberg, Germany; [2]ISS, Bucharest, Romania; [3]GSI, Darmstadt, Germany

The CBM Time-of-Flight-wall will be composed of Multi-gap Resistive Plate Chambers (MRPCs) [1]. In order to approach a final MRPC design several counters from different groups were tested in October 2014 in a heavy ion test beam time in the Hades-cave of GSI. A Sm beam of an incident energy of 1.1 AGeV beam energy was used to produce a spray of reaction products by hitting a 5 mm thick lead target. By this a full illumination of the counters has been achieved that is extremely important for determining the counter properties under real usage condition.

Figure 1 depicts the test beam setup that is constitued from two parts. Each part consist of two MRPC counters under test, a reference MRPC and a plastic scintillator in front and behind the counter stack. The scintillators were read on both sides with PMTs. The counters in the upper part of the setup were located close to the beam line in order to get the highest possible particle flux. The counters under test were a narrow strip prototype from Bucharest [2] (called Buc2013) and a PAD-MRPC [3] from Tsinghua University, China. These two counters were mounted in the upper part on a rail in order to exchange their position. The measured flux (estimated from the plastic scintillator) at this position was about 1 kHz/cm^2. In the lower part of the setup the counter under test was a full size prototype from Heidelberg [4] (called HDMRPC-P2) that was exchanged after half of the beam time by a strip counter from Tsinghua University. These two counters have similar dimensions and the same pickup electrode geometry. However, they differ significantly in the design of the HV regions (single stack (P2) vs. double stack (Tsinghua). The measured flux at the location of these counters was about a few hundred Hz/cm^2. Additional timing information was provided by a diamond detector which was installed a few cm in front of the target.

The data acquisition during this in-beam test was based on the TRB3 platform [5] providing trigger and readout handling more than 30 FPGA-TDCs with 32 timing channels each. The TDCs digitize the arrival times of both leading and trailing edges of LVDS signals created by the preamplifier/discriminator ASIC PADI [6] directly connected on the MRPC readout electrodes. The width of these LVDS signals corresponds to the time over discrimination threshold (ToT) of the analog detector signals. The TDC core [7] is implemented on Lattice ECP3 FPGAs, residing both on the TRB3 board and on TDC front-end cards (CBM-TOF-FEE1) hooked up in close vicinity to the MRPCs [8].

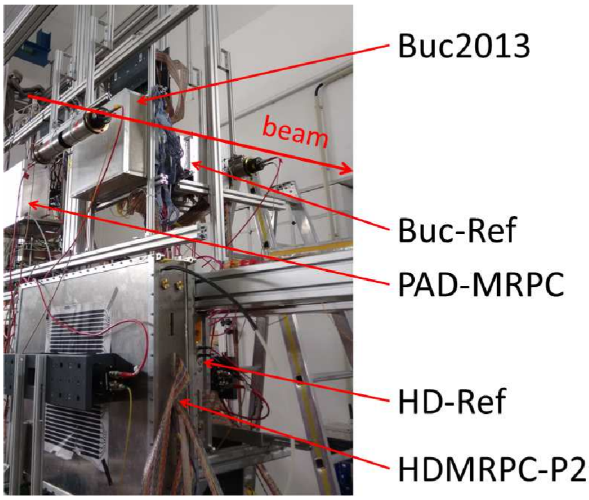

Figure 1: Setup used in the Oktober beam time. For details see text.

The analysis of the data proceeds in the following steps:

1) Data unpacking and TDC nonlinearity calibration: For the nonlinearity calibration 8 hours of data taking is used for a calibration file in order to have a statistical sufficient data sample that ensures sufficient population in every TDC bin.

2) Time and position offset calibration, cluster building and walk correction: A firing strip delivers a time information on both ends of the strip. The mean of the two signals provides the arrival time of the signal of the strip. The difference delivers in combination with the signal velocity the position of the hit along the strip. Neighboring firing strips in the MRPC are grouped together to a cluster if they are correlated in time and space. The correlation window was set to 500 ps in time and about 8 cm in space. The cluster time is calculated by taking the mean of the strip times weighted with the time over threshold information. In an event several cluster can occur on the MRPC surface.

3) Particle velocity spread and hit position correction. Steps 2 and 3 are done iteratively.

4) Data analysis with different cut settings: Cuts are applied on the reference counters in order to provide an as clean as possible event sample.

Here we present the results obtained with the Heidelberg prototype HDMRPC-P2. Figure 2 shows the counter efficiency as function of the applied high voltage (HV) for a PADI6 threshold of 150 mV (red triangles) and for 200 mV (blue squares). The efficiency is calculated by comparing the matched hits between the counter under test and the ref-

---

* Work supported by BMBF 06HD7141I and EU/FP7 HadronPhysics3

† deppner@physi.uni-heidelberg.de

DOI:10.15120/GR-2015-1-MU-NQM-CBM-49

erence MRPC with the matched hits between the diamond start counter and the reference MRPC. At an applied high voltage of ±10.5 kV the effect of the discriminator threshold is visible. A smaller electric field produces smaller signals that can be detected with a lower threshold. This effect disappears with higher HV i.e. with higher electrical field. The outlier at ±12.5 kV needs further investigation. An overall efficiency of larger than 98 % is observed at the nominal working voltage (±11 kV to ±11.5 kV). The statistical errors are to small to be visible in the plot.

The system time resolution obtained between HDMRPC-P2 and HD-ref is presented in Fig. 3. It is calculated by subtracting the time of those clusters from both counters that have the best χ^2 - matching value i.e. those that are best correlated in time and space. The excitation function of the time resolution shows a broad minimum at about ±11.0 kV (corresponding to an electrical field of 125 kV/cm) for both threshold settings. The best system time resolution is about 62 ps. Assuming both MRPCs have the same performance the individual MRPC has a time resolution in the order of 44 ps including the jitter of all electronic components. The increase towards higher voltages can be explained by two facts: 1) with higher voltage more and more streamers are produced and 2) the increasing noise rate disturbs the cluster time. The results at a PADI6 threshold of 150 mV are slightly worse than for 200 mV. The statistical error is about 0.5 ps.

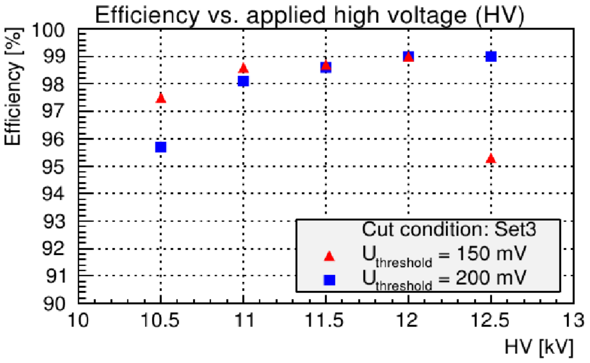

Figure 2: Efficiency as function of the applied high voltage at a PADI6 threshold of 150 mV (red triangles) and 200 mV (blue square).

Figure 4 illustrates the mean cluster size as function of the applied high voltage (HV) for a PADI6 threshold of 150 mV (red triangles) and for 200 mV (blue squares). The data show an almost linear increase with HV for both thresholds reaching a maximum at ±12.0 kV. At ±12.5 kV the mean cluster size drops again and has the same value for both threshold settings. This behavior is still under investigation.

We acknowlegde the contributions of all members of the CBM-TOF group to this report.

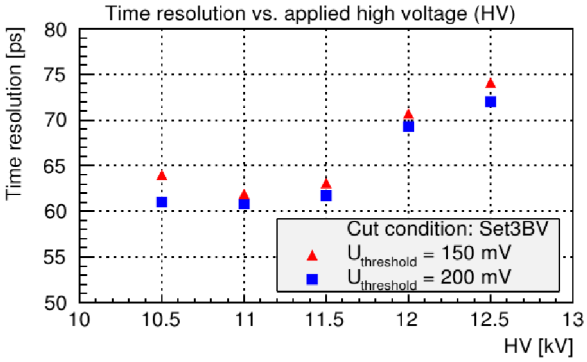

Figure 3: System time resolution as function of the applied high voltage at a PADI6 threshold of 150 mV (red triangles) and 200 mV (blue square).

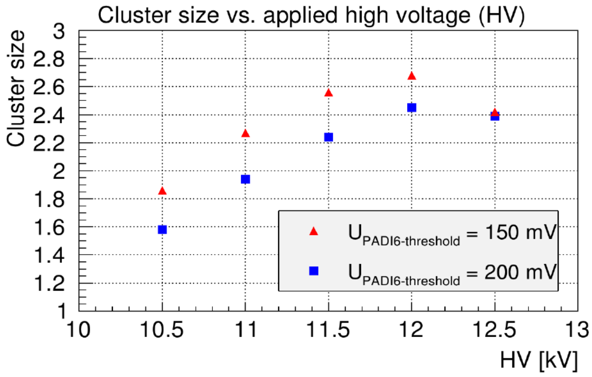

Figure 4: Mean cluster size as function of the applied high voltage at a PADI6 threshold of 150 mV (red triangles) and 200 mV (blue square).

References

[1] I. Deppner et al, Nucl. Instrum. and Methods A, Volume 661, Supplement 1, 2012, Pages S121 - S124

[2] V. Aprodu et al, CBM Progress Report 2013

[3] WeiPing Zhu et al, Science China Technological Sciences, November 2013, Volume 56, Issue 11, pp 2821-2826

[4] I. Deppner, PHD thesis, Heidelberg 2013

[5] A. Neiser et al, Proceedings of Topical Workshop on Electronics for Particle Physics 2013 (TWEPP 2013) Perugia, Italy, 23-27 September 2013, JINST 8 C12043 http://dx.doi.org/10.1088/1748-0221/8/12/C12043

[6] M. Ciobanu et al, PADI, an Ultrafast Preamplifier - Discriminator ASIC for Time-of-Flight Measurements IEEE Transactions on Nuclear Science. 03/2014; DOI: 10.1109/TNS.2014.2305999

[7] C. Ugur, G. Korcyl, J. Michel, M. Penschuk, M. Traxler, Proceedings of 2013 IEEE Nordic-Mediterranean Workshop on Time-to-Digital Converters (NoMe TDC 2013) Perugia, Italy, October 3 2013,,Proc. IEEE NoMe TDC 2013 (2013) http://dx.doi.org/10.1109/NoMeTDC.2013.6658234

[8] C. Ugur, J. Frühauf, J. Hoffmann, N. Kurz, T. Schweitzer, M. Traxler, GSI Scientific Report 2013

DOI:10.15120/GR-2015-1-MU-NQM-CBM-49

Cosmic-ray and in-beam tests of 100 Ohm transmission line MGMSRPC prototype developed for the inner zone of CBM-TOF *

M. Petriş[1], *V. Aprodu*[1], *D. Bartoş*[1], *A. Bercuci*[1], *G. Caragheorgheopol*[1], *F. Constantin*[1], *V. Duţă*[1], *M. Petrovici*[1], *L. Prodan*[1], *A. Radu*[1], *L. Rădulescu*[1], *and V. Simion*[1]

[1]NIPNE, Bucharest, Romania

As a solution for the high granularity required for the most inner zones of the CBM-TOF, a new MGMSRPC prototype (called RPC2013), was designed and built. Constructive details of the tested prototype are presented in [1]. The strip structure of the readout and high voltage electrodes, (4.19 mm strip pitch with 2.16 mm width and 200 mm strip length) was decided based on APLAC simulations. The aim was to obtain a differential readout impedance as close as possible to 100 Ω in order to match the input impedance of the front-end electronics. The prototype is based on low resistivity ($\sim 10^{10}$ Ω·cm) glass plates in order to cope with the high values of the counting rate anticipated for the inner zone of the CBM-TOF wall. High counting rate tests performed with MGMSRPCs using low resistivity glass electrodes were already reported [2, 3].

The response of the new prototype was first tested with cosmic rays and radioactive sources in the detector laboratory of Hadron Physics Department from IFIN-HH. The prototype was operated at 2 x 5.5 kV high voltage with 95%$C_2F_4H_2$ + 5%SF_6 gas mixture. For this measurements the strip signals were processed by fast amplifiers/discriminators NINO chips [4], their differential output being converted by CAEN V1290A TDCs.

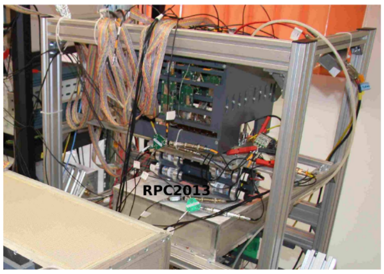

Figure 1: Cosmic ray experimental set-up.

The experimental setup used in the cosmic ray test is presented in Fig. 1. The position along the strips, triggered by the plastic scintillators positioned above the detector across the strips, is presented in the left side of Fig. 2 as a function of strip number. The right part of Fig. 2 shows the correlation between the position along the strip and position along the 10 cm length plastic scintillator, readout at both ends.

The in-beam tests of this prototype were performed in an in-beam test campaign of CBM-TOF Collaboration in October 2014 at GSI Darmstadt and at CERN-PS accelerator in November 2014, in an in-beam test campaign of different subsystems of CBM Collaboration. In the CERN in-beam test the MGMSRPC signals were processed by the same electronic chain as in the cosmic ray test. As reference for time resolution estimation was used a plastic scintilator readout at both ends. Preliminary results show a time resolution of 52 ps using pure $C_2F_4H_2$ and of 61 ps using a gas mixture of 95%$C_2F_4H_2$ + 5%SF_6, after performing walk corrections and subtraction of the contribution of the reference counter. The October 2014 in-beam test was focused on the compatibility with the PADI8 new FEE, aiming to be used in the CBM-TOF wall. The MGMSRPC signals were converted by FPGA TDCs [5]. Data analysis is in progress.

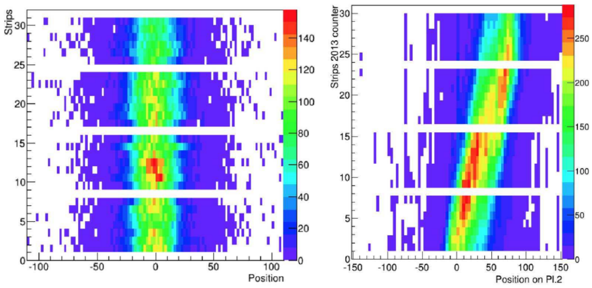

Figure 2: Cosmic-ray test: left side - position along the strip as a function of strip number; right side - correlation between position along the strips and position in the platic scintillator.

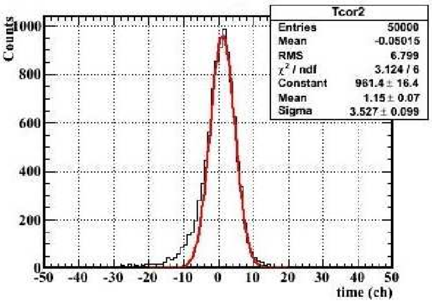

Figure 3: CERN in-beam test time spectrum using a gas mixture of 95%$C_2F_4H_2$ + 5%SF_6.

References

[1] V. Aprodu et al., CBM Progress Report 2013, p.79

[2] M. Petrovici et al., JINST 7 (2012) P11003

[3] A. Bălăceanu et al., CBM Progress Report 2013, p. 78

[4] F. Anghinolfi et al., Nucl.Instr.and Meth. A533(2004)183

[5] J. Frühauf et al. CBM Progress Report 2012, p.71

---

* Work supported by EU-FP7/HP3 Grant No 283286 and Romanian NASR/CAPACITATI-Modul III contract RO-FAIR F02 and NASR/NUCLEU Project PN09370103

DOI:10.15120/GR-2015-1-MU-NQM-CBM-50

Lithographic integration of Aluminum read-Out traces on CVD diamond for the CBM micro vertex detector*

C. Müntz[†1], *N. Bialas*[1], *M. Koziel*[1], *J. Stroth*[1,2], *R. Weirich*[1], *R. Visinka*[2], *A. Meier*[3], *F. Völklein*[3], *and the CBM MVD collaboration*[1]

[1]Goethe-University Frankfurt, IKF; [2]GSI, Darmstadt, Germany; [3]Hochschule RheinMain, IMtech

The Micro Vertex Detector (MVD) [1] of the Compressed Baryonic Matter (CBM) experiment at FAIR aims at a challenging material budget of only a few per mille radiation length for each of the detector stations. This allows for the high-precision secondary vertex reconstruction needed to identify e.g. rare open charm particles emitted in violent heavy ion collisions. The detector will be operated in vacuum and relies on dedicated CMOS monolithic active pixel sensors (MAPS) [2] thinned to 50 μm, mounted on sheets of 200 μm thick poly-crystalline CVD diamond [3], which features a thermal conductivity of about 2000 W/mK, i.e. about four times the one of copper, and a high mechanical stability (Young's modulus of 1050 GPa). A conventional sensor module comprises the carrier for mechanical support and cooling, the sensors, dedicated glue and thin flex cables used to control and read-out the sensor. A standard method to connect the sensor is wedge bonding of 25 μm aluminum wires. This concept was realized for the MVD prototype [1]. A feasibility study is focusing on the option to merge the functionalities of the carrier and the read out, aiming at further improving the material budget and at the same time reducing the steps of integration by sparing the dedicated flex cable.

The technology of choice is photolithography of microscopic traces directly on the CVD diamond carrier for reading out and biasing the sensor. Employing aluminum for the traces with a thickness of up to 3 μm is mandatory for reducing the material thickness and the probability of γ-conversion. However, it triggers questions related to mechanical and electrical properties, such as adhesion and conformity of the traces as well as impedances, respectively. These questions were addressed in a study accomplished by GSI Darmstadt (detector laboratory) and Hochschule RheinMain (IMtech) Rüsselsheim, w.r.t. the lithographic part, and the IKF (characterization). Here, we report on the first step of the project, which focuses on placing dedicated aluminum traces on CVD diamond.

Figure 1 depicts the final demonstrator module. Part of this module, as indicated in the plot, is subject of this report. Different lithographic techniques have been explored, focusing on adhesion reliability, realizing rather thick traces of 3 μm, and getting the known effect of under-etching under control. For example, chemical (wet) etching has been contrasted to the lift-off technique. Figure 2 depicts typical pictures of the samples under evaluation at the IKF.

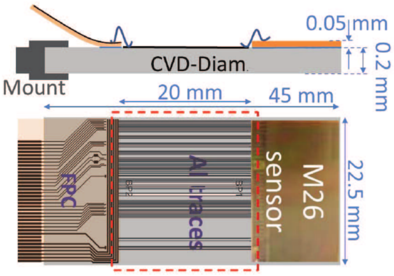

Figure 1: The demonstrator, comprising the sensor ("M26"), the CVD diamond carrier with Al traces and the flex cable to connect to the read out. The broken red line depicts the part of the project reported here.

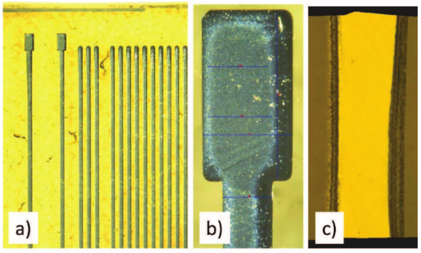

Figure 2: Pictures of Al traces with typical widths of 50 - 100 μm attached to the CVD diamond carrier: a) different geometries, b) zoom of a pad, c) typical under-etching.

The electrical characterization in in progress, focusing on high-precision measurements of resistances and line-to-line capacities in view of operating a dedicated pixel sensor. To do so, the Al traces have been connected by means of wire wedge bonding, so far revealing no problem with the adhesion of the 50-100 μm wide Al traces to CVD diamond surface. This has to be confirmed with pull tests. The electrical characterization will also allow for assessing the conformity of the traces, e.g. with respect to the trace thickness. In a next step, the employed processes will be further optimized, based on the results, also exploring the option of providing up to 5 μm thick Al traces, before preparing the final demonstrator hosting a sensor chip.

References

[1] M. Koziel et al., Nuclear Instruments and Methods in Physics Research A 732 (2013) 515–518C

[2] Picsel group of IPHC Strasbourg, http://www.iphc.cnrs.fr/-PICSEL-.html

[3] Diamond Materials, http://www.diamond-materials.com

---

[*] Work supported by GSI, BMBF (05P12RFFC7) and EU-FP7 HadronPhysics3

[†] c.muentz@physik.uni-frankfurt.de

DOI:10.15120/GR-2015-1-MU-NQM-CBM-51

Free running acquisition system for Transition Radiation Detectors - in beam tests -*

F. Constantin[1], *D. Bartoş*[1], *A. Bercuci*[1], *G. Caraghergheopol*[1], *V. Cătănescu*[1], *M. Petriş*[1], *M. Petcu*[1], *and M. Petrovici*[1]

[1]Horia Hulubei National Institute for Physics and Nuclear Engineering, Romania

The present acquisition system was developed as a test benchmark of a free running concept for high counting rate TRDs [1] based on FASP ASIC [2] and analog converters of the type foreseen to be implemented in a later stage in a hybrid updated version of FASP analog processor. This version can operate 64 TRD readout channels with a sample rate of 2 Msps and 12 bits resolution MAX 11105 ADCs. The system is based on a Spartan 6, SP601 evaluation board and a custom designed board for MAX 11105 analog converters [3,4]. Two such systems were built, each of them processing data from 32 pads. In order to merge the correlated data between several subdetectors, a synchronization signal is used. The main tasks assumed by the system are: data unpacking from the 2 x 32 MAX 11105 and synchronisation management, capture of the MBS_sync signal from a MBS (Multi-Branch System) system [5], packing the data and Ethernet transmission through UDP protocol. The mixed acquisition system, a trigger driven (MBS) and the free running, generates acquisition files which are later paired by a dedicated software. Data for TRD were collected based on the free running system described above while Cerenkov and Lead Glass by information was taken by the MBS system. The correctness of the data synchronisation is proved by the electron and pion pulse height distributions at three different momenta presented in Figures 1, 2 and 3.

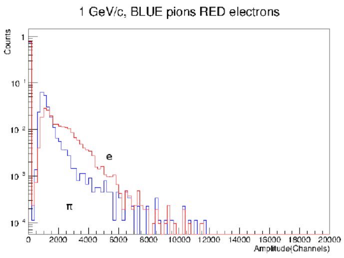

Figure 1: Pulse height distributions for electrons (red) and pions (blue) at 1 GeV/c momentum

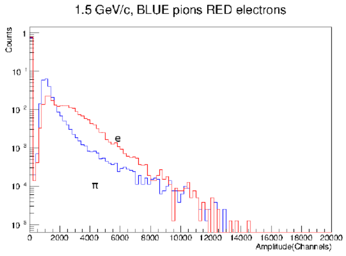

Figure 2: 1.5 GeV/c momentum

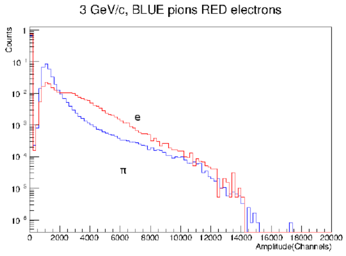

Figure 3: 3 GeV/c momentum

References

[1] M. Petris et all Two dimension position sensitive real size CBM-TRD prototype. PHN-SIS18-ACC-38

[2] V.Catanescu, CBM 10th Colaboration Meeting, Sept. 25-28,2007, Dresden

[3] http://www.xilinx.com/publications/prod_mktg/sp601_product_brief.pdf

[4] http://www.maximintegrated.com/en/datasheet/index.mvp/id/6419

[5] https://www.gsi.de/work/fairgsi/common_systems/csee_electronics/datenverarbeitung/datenerfassung/mbs.htm

---

* Work supported by Romanian NASR/CAPACITATI-Modul III contract F02 and NUCLEU contract PN09370103

DOI:10.15120/GR-2015-1-MU-NQM-CBM-52

Construction and test of a new CBM-TRD prototype in Frankfurt *

M. Tanha, W. Amend, H. Appelshäuser, A. Arend, A. Arend, C. Blume, P. Dillenseger, S. Gläßel, and F. Roether
Institut für Kernphysik, Goethe-Universität Frankfurt, Germany

A new TRD prototype based on a thin Multi Wire Proportional Chamber (MWPC) without a drift region and with carbon frame was designed at the Institute for Nuclear Physics in Frankfurt (IKF) and tested in the test beam at CERN-PS in November 2014. According to this design, two identical real-size prototypes in outer dimensions of $586 \times 580 \times 38.5$ mm^3 were developed with a pitch of 2.5 mm between field and sense wires. Cathode (field) wires made of Cu-Be with a diameter of 80 μm are placed between gold-plated tungsten anode (sense) wires with a diameter of 20 μm. The gas gap region, distance between entrance window and pad-plane, is 3.5+3.5 mm (see Fig. 1). The chamber were build with the same type of pad-plane as used in the prototypes from Münster [1].

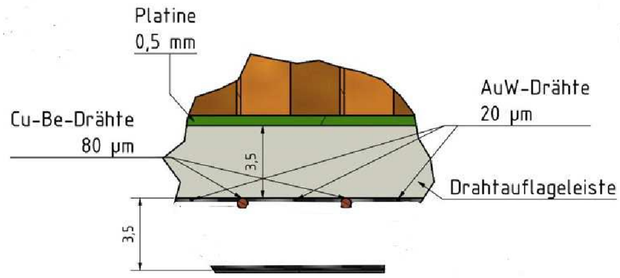

Figure 1: Schematic drawing of alternating wires, their pitch and diameters.

Applying cathode wires with alternating HV (alternating wires) has an improving result as it reduces the effect of a deformation of the cathode plane by about a factor of 6, which distorts the gas gain inside the detector via electric field deformation [2].

The MWPC with thin and symmetric geometry (3.5+3.5 mm) provides fast signal collection and efficient e/π separation, which is desired in the CBM experiment [3]. The carbon frame, instead of an aluminium or vetronit frame, provides optimum mechanical properties, low thermal expansion, high friction resistance and low material budget. Figure 2 shows the technical drawing of the prototype with the aforementioned components.

Figure 3 shows the gas feed-through that is embedded inside the frame in the corners. Thus, it meets the structural conditions of the TRD chambers, which will have to be mounted close to each other in the final setup.

The data from the CERN-PS test beam in November 2014 are currently being analysed. The development of a large size (1.0×1.0 m^2) prototype of the TRD is planned at the IKF.

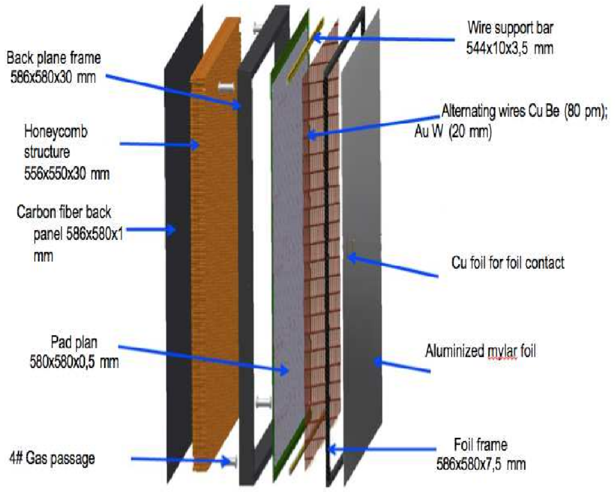

Figure 2: Technical drawing of a TRD prototype with alternating wires and carbon frame.

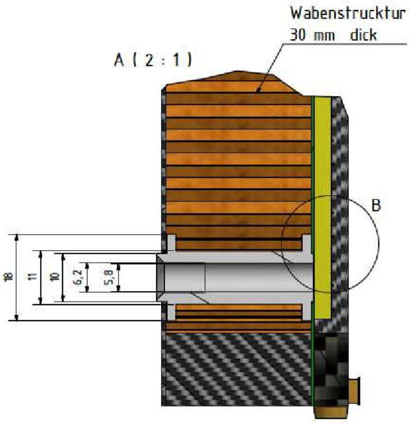

Figure 3: The gas feed-through inside the frame.

References

[1] C. Bergmann et al., "Test of Münster CBM-TRD real-size detector and radiator prototypes at the CERN PS/T9 beam line", CBM Progress Report 2014.

[2] S. Gläßel, CBM Progress Report 2013, p. 70.

[3] E. Hellbär, CBM Progress Report 2012, p. 54.

---

* Work supported by BMBF, HIC4FAIR and HGShire.

DOI:10.15120/GR-2015-1-MU-NQM-CBM-53

Construction and commissioning of a setup to study ageing phenomena in high rate gaseous detectors

A. Abuhoza[1,2], *U. Frankenfeld*[1], *J. Hehner*[1], *C.J. Schmidt*[1], *and H.R. Schmidt*[3]

[1]GSI, Darmstadt, Germany; [2]Goethe-Universität, Frankfurt, Germany; [3]Eberhard-Karls-Universität, Tübingen, Germany

A setup, dedicated to the investigation of ageing properties of gaseous detectors due to materials used for their construction has been constructed and commissioned at the GSI detector laboratory. An outstanding feature of the setup is that tedious and repetive measurements can be conducted fully automated.

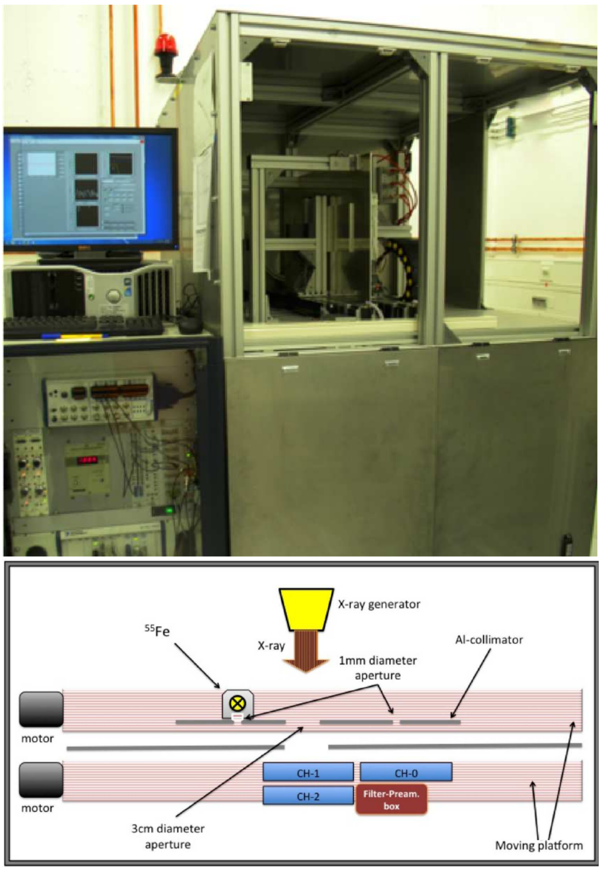

Figure 1: Photograph of the setup mounted in a metallic enclosure and the associated data acquisition system (top). Sketch of the components of the ageing setup (bottom).

The setup consists of three identical Multi Wire Proportional Chambers (MWPCs) mounted onto a moving platform, an X-ray generator to produce ionizing radiation and an ^{55}Fe source for gain diagnostics. A second moving platform holds an aluminium collimator plate which has three different apertures. Two of the chambers are flushed with gas which has passed through outgassing boxes containing the materials under investigation. One of the chambers is operated with clean gas for reference purposes. All gas lines are equipped with individual Mass Flow Controllers.

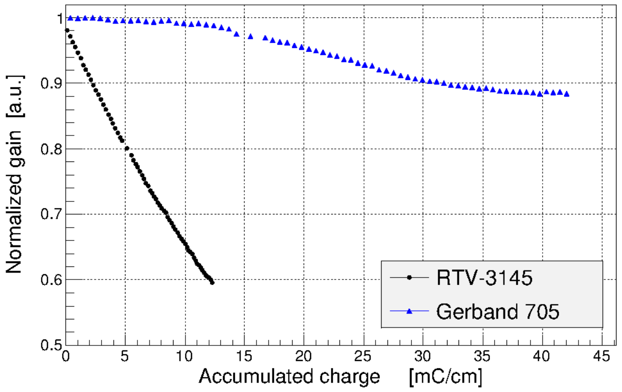

Figure 2: Normalised gain of chamber tested with Gerband 705 (blue) and chamber tested with RTV-3145 (black) as a function of accumulated charge per unit length of the anode wires.

The measurements are carried out with a premixed gas mixture of ArCO$_2$ (80/20). The data acquisition and control system based on LabView is configured to allow fully automated measurements during long term tests. Figure 1 shows a photograph of the setup and a sketch of the components.

Before fabrication of the MWPCs, simulations of their electric field and gain had been done using a combination of a gas simulation program (Magboltz) and a electric field simulation program (Garfield). The accuracy of the gas temperature measurement has been greatly improved which allows a very accurate correction of the gain measurement. Over a period of eight months, cleaning procedures have been developed and all sources of contamination of the equipment have been eliminated. Thereafter, the setup has been operated with very stable behaviour, evidenced by the fact that around 0.5% peak-to-peak residual variation of the normalised gain has been achieved. Thus the setup shows the required high stability to be used for precise ageing studies.

First ageing tests have been carried out with two materials over two weeks: Aluminium tape named Gerband 705 and a adhesive/sealant named RTV-3145. At the end of these two weeks, the ageing rate (R) caused by Gerband 705 was about 0.3%/mC/cm while it was 3%/mC/cm for RTV-3145. The blue and black curves of Fig. 2 illustrate the normalised gain of the MWPC contaminated with Gerband 705 and RTV-3145, respectively, as a function of the accumulated charge per wire length.

DOI:10.15120/GR-2015-1-MU-NQM-CBM-54

Two-dimensional MWPC prototype for CBM TRD*

A. Bercuci[1], *D. Bartoş*[1], *G. Caragheorgheopol*[1], *V. Cătănescu*[1], *F. Constantin*[1], *M. Petriş*[1], *and M. Petrovici*[1]

[1]IFIN-HH, Bucharest, Romania

Introduction

The signal induced on a segmented conductive electrode is used in a large number of MWPC applications for position information. Additionally, the firing anode can be used for orthogonal position information at an increased operational cost. The draw back of such procedure is the poor localization along the wire and the impossibility to operate in conditions of high local occupancies and counting rates. In the current report the performance of an innovative geometry of the read-out electrode is presented. The $2D$ information can be extracted in high fluxes without additional anode read-out channels.

The TRD MWPC for CBM

The TRD developed in Bucharest for the CBM experiment [1] is characterized by a 4 mm drift and a 2×4 mm amplification regions and wire pitches of 1.5 mm for the cathode and 3 mm for the anode wires (see Fig. 1 left). The conductive electrode is segmented in triangular shaped pads of 7.3×27.7 mm^2 and 0.2 mm spacing arranged as in Fig. 1 right with respect to the anode wires.

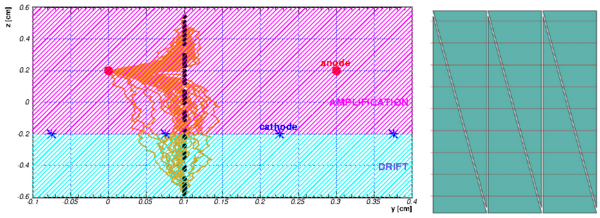

Figure 1: Active volumes (drift, amplification) and elements (anode, cathode wires and the pad plane structure) as well as signal formation in the TRD as simulated in Garfield++ [2].

The Local Anode Identification method

Due to varying cross section of pads with respect to anode wires in our current set-up and localization of the induced signal the Pad Response Function (PRF) varies with the position of firing anode wire along the pads. Thus one can build an Anode Response Function (ARF) for anode identification. In Fig. 2 left the method is tested using an uniform illumination of the TRD detector with a ^{55}Fe source. For each PRF value nine maxima are found corresponding to the anodes covered by a pad-row. Each local maxim is fitted and the mean and sigma parameters of the Gaussian distribution are extracted (see markers on Fig. 2 left and the sin interpolation). A very good separation between each curve is obtained for the whole pad height.

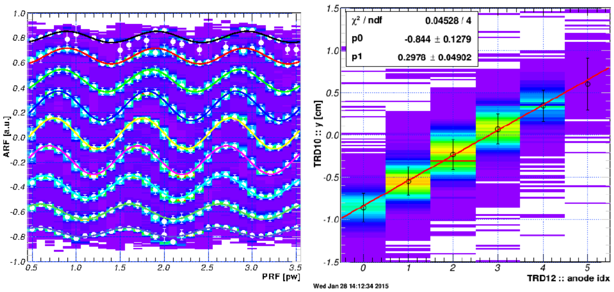

Figure 2: ARF correlations with PRF as measured with TRD prototype for a uniform illumination with ^{55}Fe (left) and with the position measurement by a reference TRD for MIPs (right) respectively. The slope of the fit ($p1$) gives the measured distance beteen anodes in cm.

In November 2014, the TRD prototype operated with Xe/CO_2 $(80/20)$ was tested with MIPs at CERN-PS. To estimate the resolution of the ARF method a reference position sensitive TRD was mounted orthogonal to it. The reference detector was operated in the rectangular shaped pads geometry for good position resolution across pads. The correlation between position measurements in the reference detector and anode identification by ARF is shown in Fig. 2 right. The measured distance of 2.98 ± 0.05 mm between anode wires corresponds to the designed pitch of 3 mm. The measurement across pads is performed for the time being using the parring of triangular pads. A resolution of $\approx$ 500 μm is obtained for ^{55}Fe position scan operated with Ar/CO_2 $(80/20)$ and FASP v0.1 [3] FEE.

Conclusions

It was demonstrated that the usage of a varying PRF along pads can provide good local anode identification. The method opens the possibility of using reduced *effective* pad geometries with implications in position resolution at constant read-out costs and experimental material budgets.

References

[1] M. Tarzila et al., CBM Progress Report (2012) 80.

[2] Garfield++ http://garfieldpp.web.cern.ch/garfieldpp

[3] V. Catanescu, CBM 10^{th} Collaboration Meeting Dresden, Sept 25-28, 2007

---

* Work supported by Romanian ANCSI/CAPACITATI Modul III Contract F02 and NUCLEU Project Contract PN 09370103.

DOI:10.15120/GR-2015-1-MU-NQM-CBM-55

Bit Error Rate Tester

P. Miedzik[1,2] *and P. Koczoń*[1]
[1]GSI, Darmstadt, Germany; [2]Politechnika Warszawska, Warsaw, Poland

For electronic components which transmit digital data the bit error rate is the figure of merit which has to be controlled. Electronics which will be installed in the field of reaction products in future experiments at FAIR has to be radiation hard. At present, selected electronic parts undergo exhaustive tests with use of intense minimum ionising particles' beams, mostly 3 GeV protons at Jülich synchrotron facility. To monitor data transmitting components during irradiation a Bit Error Rate Tester (BERT) has been developed.

BERT requirements

Randomly generated bit patterns are sent to the tested device and compared to the transmitted back bit series. In order to avoid spurious errors due to e.g. bit flips in the source or the receiver of the test data by ionising particles both of them have to be placed far away from the device under test. Moreover, the generated bit patterns have to be representative for the data to be collected in real high energy experiment and transmitted in a form of future data transmission (8bit/10bit and 64b/66b line coding). Transmission lines based on copper wires as well as on glass fibers as different carriers have to be tested with transmission frequency as high as planned for coming experiments. Block diagram of the Bit Error Rate Tester is presented in Fig.1. In the following some details of the construction of the bit pattern tester and its performance is described.

BERT construction

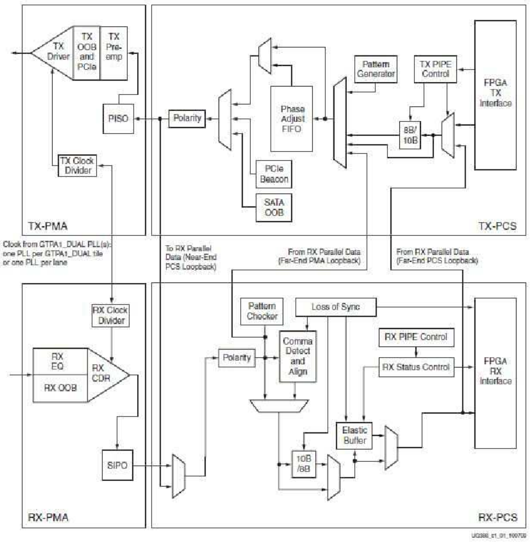

Figure 1: Simplified block diagram of GTP Transceiver

A standard PC as host (powering, programming environment) for the Spartan6 FPGA based card with GTP transceiver is used (Fig.2). Serial input and output of the card is using differential signalling via SFP interface or plane interface for transmission on copper line. Various parameter such as driver swing, TX pre-emphasis or receiver equalization might be adjusted to adapt this device to different standards. A random bit sequence generator implemented in the FPGA delivers patterns $2^7 - 1$ or $2^{31} - 1$ bit long according to polynomials $x^7 + x^6 + 1$ (PRBS7) and $x^{31} + x^{28} + 1$ (PRBS31) [1]. On receiver side incoming bits are stored into history shifting buffer and they are used to compute further expected incoming bits using the same PRBS algorithms.

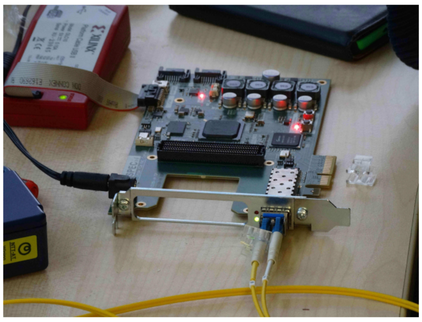

Figure 2: PC card with FPGA and I/Os.

BERT test results

An error-counter is incremented in case of discrepancy between sent and received patterns and monitoring software can display - apart of the test conditions - the error rate corresponding to certain transmission speed. Two lengths of transmission medium have been used (400 and 1000 m lines of glass fiber) for bit patterns generated with PRBS 31-bit with differential output swing of 200 mV and transmission speed of 2.5 Gbps In this particular configuration bit error rate was $1.42 * 10^{-14}$ after almost 8 hours of run. Transmission line has been disturbed mechanically to test proper detection of the transmission errors what resulted immediately in drastically increase of the bit error rate.

References

[1] `http://www.xilinx.com/support/documentation/user_guides/ug386.pdf`

DOI:10.15120/GR-2015-1-MU-NQM-CBM-56

A new approach to detect hyper nuclei in the phase space distributions generated by microscopic transport models *

A. Le Fèvre†[1], *Y. Leifels*[1], *J. Aichelin*[2], *Ch. Hartnack*[2], *E. L. Bratkovskaya*[3], *and V. Kireyev*[4]
[1]GSI, Darmstadt, Germany; [2]SUBATECH-EMN Nantes, France; [3]FIAS, Francfort, Germany; [4]JINR, Dubna, Russia

The process of production of complex fragments in heavy ion collisions is big challenge for transport models in which single particle propagation is the relevant degree of freedom. However, cluster formation affects the single particle spectra and should not be omitted. Identifying clusters within transport codes is all but simple. Quantum effects, the different parts of the nuclear potential, like bulk, asymmetry energy and pairing, acting in a complicated environment at finite temperatures influence the fragment yields. We developed an improved clusterisation algorithm which aims at predicting more realistically cluster yields in the framework of microscopic transport models. This new approach is able to reconstruct fragment [3] and hyper nuclei yields from single particle phase space distributions of various transport codes (QMD as well as BUU type codes).

It has been derived from the Simulated Annealing Clusterisation Algorithm [1]. Unlike commonly used coalescence models based only on the momentum-coordinate space proximity, it relies in addition on maximizing the overall binding energies of clusters. This method has the advantage of identifying fragments much earlier during the collision, typically just after the system ends its overlap ("passing time" t_{pass}). The fragment partitions can then reflect the early dynamical conditions. We cast the binding energy in analogy with the liquid-drop model but with a density dependence, with the following contributions: attractive and repulsive potential between nucleons V_{NN} (Skyrme mean field), a Yukawa surface correction, and optionally the asymmetry potential V_{asy} and other quantum effects. To create hyper nuclei, we consider the strange quark as inert and use $V_{\Lambda N} = \frac{2}{3} V_{NN}$.

Fig. 1 illustrates the crucial role of the phase-space overlap between the Λ's – peaked at mid-rapidity – and clusters – the bigger the closer to the spectators – in creating hyper nuclei. Hence, the yield ratios between ${}^3_\Lambda H$ and ${}^4_\Lambda H$ are very different at mid-rapidity (abs(y_0)<0.5) and in the projectile spectator region (y_0>0.7), resp. 8.2±1.7 and 1.4±0.2. Fig. 2 shows the influence on the hyper nucleus yields of the clusterisation time: like for normal clusters, in the tiny (1-2)t_{pass} time interval, at mid-rapidity they are at the highest and strongly decrease afterwards, whereas they are stabilized in the spectator regions.

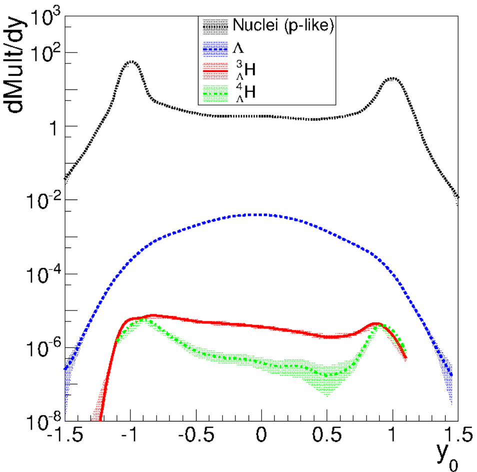

Figure 1: Multiplicity versus rapidity of clusters, Λ's, ${}^3_\Lambda H$ and ${}^4_\Lambda H$ hypernuclei as predicted by our clusterisation algorithm applied at $2t_{pass}$, on events generated by the IQMD transport model [2] for the ^{6}Li+^{12}C collisions at 2 $A.GeV$ incident energy, all impact parameters. The rapidity y_0 is expressed in the NN reference frame, scaled to the projectile rapidity.

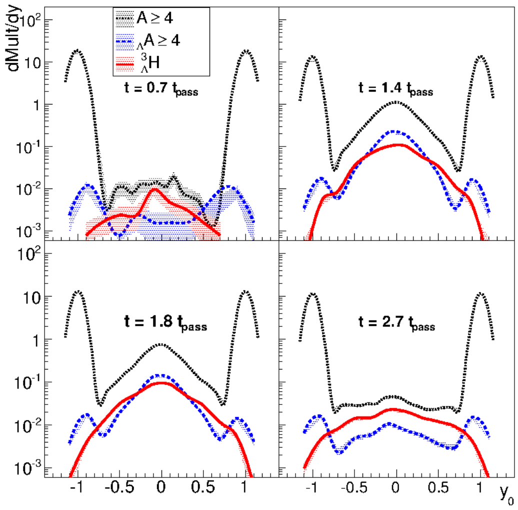

Figure 2: Same as Fig. 1 for heavy ($A \geq 4$) (hyper)clusters and ${}^3_\Lambda H$, at various clusterisation times, applied on pHSD [4] event predictions of the collisions of ^{197}Au +^{197} Au at 11.45 A.GeV incident energy and 6 fm impact parameter.

References

[1] R. K. Puri and J. Aichelin, J. Comput. Phys. **162**, 245 (2000).

[2] Ch. Hartnack et al., Eur. Phys. J. A **1** (1998) 151.

[3] K. Zbiri, A. Le Fèvre, J. Aichelin et al., Phys. Rev. C **75** (2007) 034612, A. Le Fèvre et al., Phys. Rev. C **80** (2009) 044615.

[4] W. Cassing, E.L. Bratkovskaya, Nucl. Phys. A **831** (2009) 2.

---

* Work supported by the GSI/CEA/IN2P3 Exchange Programme.

† A.LeFevre@gsi.de

DOI:10.15120/GR-2015-1-MU-NQM-FOPI-01

Modification of hadron properties at normal nuclear matter density invested in pion-induced reactions with FOPI spectrometer. *

V. Zinyuk[†1], *N. Herrmann*[1,2], *and the FOPI Collaboration*[2]
[1]Physikalisches Institut, Universität Heidelberg, Germany; [2]GSI, Darmstadt, Germany

The behavior of strangeness and anti-strangeness in nuclear matter is a subject of various theoretical and experimental debates. Theoretical models (and experimental evidence) suggest that production and dynamics of strange particles in nuclear medium is connected to fundamental properties of Quantum Chromo Dynamics [1]. In particular - the partial restoration of chiral symmetry in dense matter results in the modifications of particles' properties such as mass, lifetime and consequently a change of production and absorption cross sections are expected.

The ϕ vector meson is a pure $s\bar{s}$ state with a free mass of 1019.5 MeV/c^2. In nuclear medium, already at normal nuclear matter density, the spectral function of ϕ mesons is predicted to change, showing a mass shift of a few MeV/c^2 and a significant broadening [2]. Experimental evidence for the in-medium modification of the ϕN cross section [3, 4] and mass modification [5, 6] have been published, however the findings disagree with theoretical predictions.

The FOPI Collaboration in cooperation with the GEM-TPC Collaboration has recorded about 5.5M collisions for each $\pi^- + {}^{208}Pb$ and $\pi^- + {}^{12}C$ systems in the S339 experiment. The chosen incident beam momentum of p_π = 1.7 GeV/c is slightly above the threshold momentum for the reaction $\pi^- + p \rightarrow \phi + n$ (p_{th} = 1.56 GeV/c). The ϕ mesons are produced with small momenta and have a reasonable probability to decay inside the target. These experimanetal conditions make the observation of possible in-medium modifications at $\rho = \rho_0$ feasible.
The ϕ meson decays preferentially into kaons:

$$\begin{aligned}\phi(1020) &\rightarrow K^+K^- \ (49.2\%) \\ &\rightarrow K^0_L K^0_S \ (34\%)\end{aligned} \tag{1}$$

With the FOPI detector system the charged kaons final state is accessible.

Fig.1 shows the invariant mass distribution of correlated K^+K^- pairs produced in carbon and lead targets. Blue points represent the mass distribution of uncorrelated K^+K^- pairs from different events, and therefore describe the combinatorial background. In both targets a clear excess is visible at the nominal mass of the ϕ meson.
From the evaluation of different selection criteria and background description strategies the ratio of ϕ mesons produced per event in lead to carbon targets is obtained:

$$\frac{N_{Pb}}{N_C} = 0.512 \pm 0.079(stat.) \tag{2}$$

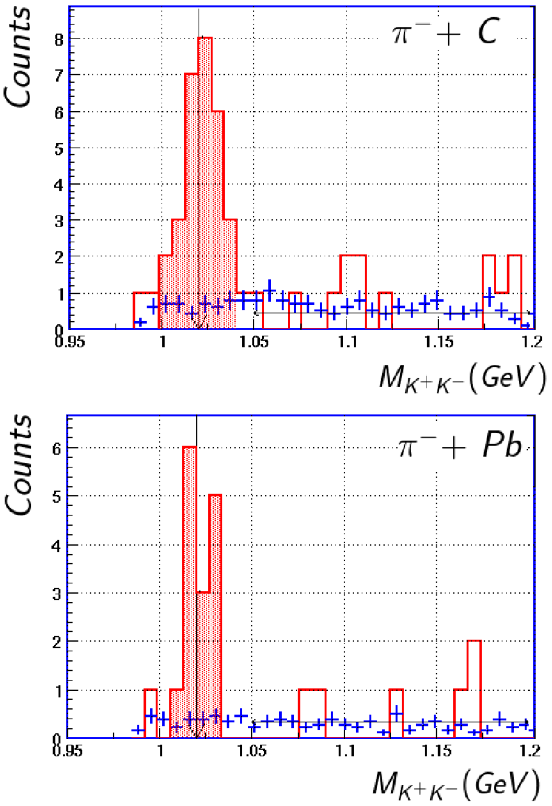

Figure 1: Invariant mass spectrum of correlated K^+K^- pairs(red) and the combinatorial background(blue).

This ratio can be interpreted as an indication for the suppression of ϕ mesons in nuclear matter. However, a detailed understanding of (anti-)strangeness production and exchange in the considered systems is crucial to conclude on the influence from the nuclear medium. The evaluation of other strange and anti-strange particles (i.e. K^+, K^-, K^0, Λ) is in progress.

References

[1] W. Weise, Prog. Theo.Phys.Suppl. **149** (2003) 1.

[2] F. Klingl, T. Waas and W. Weise, Phys.Lett.B **431** (1998) 254.

[3] T. Ishikawa *et al.*, Phys.Lett.B **608** (2005) 215.

[4] P. Mühlich and U. Mosel, Nucl.Phys.A **765** (2006) 188.

[5] R. Muto *et al.*, Phys.Rev.Lett **98** (2007) 042501.

[6] K. Ozawa *et al.*, Nucl.Phys.A **698** (2002) 535c.

---

* Work supported by BMBF 05P12VHFC7.

[†] v.zinyuk@gsi.de

DOI:10.15120/GR-2015-1-MU-NQM-FOPI-02

No track without errors

M. Berger[1,2] *and the GEM-TPC Collaboration*[1,2,3,4,5,6]

[1]Physik Department E12, Technische Universität München, Garching, Germany; [2]Excellence Cluster 'Origin and Structure of the Universe', Garching, Germany; [3]GSI Helmholtzzentrum für Schwerionenforschung GmbH, Darmstadt, Germany; [4]Helmholtz-Institut für Strahlen- und Kernphysik, Bonn, Germany; [5]Universität Heidelberg, Heidelberg, Germany; [6]Stefan Meyer Institut für Subatomare Physik, Wien, Austria

In past experiments, Time Projection Chambers (TPCs) have been equipped with a gating structure to prevent the migration of avalanche ions created during gas amplification – traditionally realized with Multi Wire Proportional Chambers (MWPCs) – in order to maintain drift field homogeneity. This, however, limited the application of TPCs to experiments with trigger rates smaller than $\mathcal{O}(10^3\,\mathrm{Hz})$. To overcome this limitation a TPC with GEM (Gas Electron Multiplier) foils [1] exploiting their intrinsic ion backflow suppression, has been built [2]. This GEM-TPC has a drift length of 728 mm, an inner radius of 50 mm and an outer radius of 155 mm. For the readout a padplane with hexagonal shaped pads with 1.5 mm radius was used.

For tests with cosmic tracks and different heavy ion beams as well as for a physics experiment with a pion beam the GEM-TPC was employed together with the FOPI spectrometer [3].

To reduce the data rate and to introduce the possibility of an early noise suppression, pad hits are collected in entities called clusters which are defined by an amplitude, a position and an uncertainty. This is done by a full 3D local minima search which is independent of the pad shape or pad plane geometry. The clusters are then passed to the pattern recognition algorithm performing track finding employing a conformal mapping method [4]. Finally, a track can be fitted to these clusters. For this the Kalman Filter implementation provided by the GENFIT [5] framework is used.

For track fitting it is mandatory to have a precise knowledge of the uncertainty on the cluster position. The uncertainty of this position is strongly dependent on the track topology. For example, along the track the pad hits are uniformly distributed while perpendicular to the track the pad hit distribution is broadened by diffusion. Therefore the uncertainty has to take the track topology into account.

In order to avoid a completely model dependent uncertainty a new method is implemented using only measured values. In order to incorporate the track topology a prefit has to be performed. After this prefit the new clusters are created by stepping through the track and collecting the pad hits. These pad hits are projected onto a plane perpendicular (see left side of Fig.1) to the track and fitted with a two dimensional Gaussian function. The new cluster position is then calculated by the position of the plane and the position of the mean from the fitted function. The position uncertainty is simply the uncertainty on the mean also given by the fit which is a 2x2 matrix defined in the coordinate system of the plane. To extend the uncertainty into 3D space a new covariance matrix is created using equation 1 where **V** is a 3x3 matrix containing the two eigenvectors of the original matrix and an vector along the track. **S** is a 3x3 diagonal matrix with the corresponding eigenvalues. Figure 1 (right side) shows the resulting uncertainty ellipsoids and the eigenvectors of the final covariance matrix.

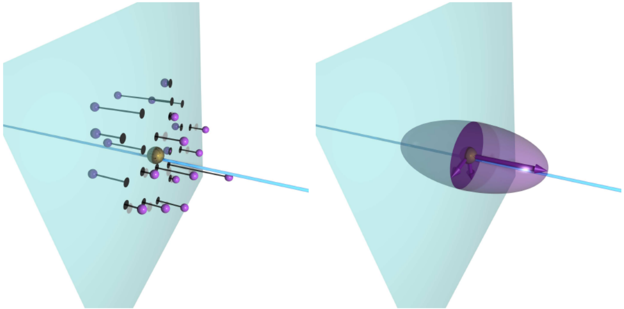

Figure 1: Left panel: Pad hits (purple spheres) projected onto a plane (turquoise) perpendicular to the track (light blue). The projected pad hits are depicted as black disks and the resulting cluster position is shown in gold. Right panel: Final resulting uncertainty of the cluster is shown as transparent purple ellipsoid. The eigenvectors (scaled by the eigenvalue) are shown as purple arrows and the uncertainty ellipse from the fit is shown in dark purple.

$$\mathbf{COV} = \mathbf{VSV}^{-1} \tag{1}$$

This method however may treat several detector intrinsic features not properly, like the different types of measurements of X-, Y- and Z-coordinates. X and Y are measured on a pad plane while the Z coordinate is reconstructed with a drift time measurement. The proper treatment of such features is investigated at the moment.

References

[1] F. Sauli, NIM A, 386 (1997), 531

[2] L. Fabbietti et al., NIM A, 628 (2011), 204-208

[3] K. Hildenbrand, GSI Nachr. 91-02, 6 (1992)

[4] J. Rauch, Journal of Physics: Conference Series 396 (2012) 022042.

[5] C. Höppner et al., NIM A 620 (2010) 518.

DOI:10.15120/GR-2015-1-MU-NQM-FOPI-03

DOI:10.15120/GR-2015-1-MU-NQM-FOPI-03

Measurement of the anti-nucleus $^{4}\overline{\mathrm{He}}$ with the ALICE apparatus at the LHC*

B. Dönigus†[1], *A. Kalweit*[2], *N. Löher*[3,4] *for the ALICE Collaboration*

[1]Institut für Kernphysik, Goethe Universität Frankfurt, Frankfurt, Germany; [2]European Organization for Nuclear Research (CERN), Geneva, Switzerland; [3]ExtreMe Matter Institute EMMI and Research Division, GSI Helmholtzzentrum für Schwerionenforschung, Darmstadt, Germany; [4]Institut für Kernphysik, Technische Universität Darmstadt, Darmstadt, Germany

Heavy-ion collisions at the LHC give the opportunity to measure all known particles in higher abundances than it was possible before, like for example light (anti-)nuclei. These heavy particles are rarely produced, because the production probability decreases with increasing mass. But the energy regime reached at the LHC leads to large production probabilities even for these particles, as described for example by thermal models [1, 2]. So far, data of Pb–Pb collisions at $\sqrt{s_{\mathrm{NN}}} = 2.76\,\mathrm{TeV}$ were taken in the years 2010 and 2011.

Furthermore, the unique particle identification capabilities of the ALICE detector [3] allow for the measurement of rarely produced states created in Pb–Pb collisions.

In fact, ALICE has already observed four anti-alpha candidates [4] in the data set of 2010, whereas the first anti-alphas were detected by the STAR Collaboration at RHIC in Au–Au collisions [5].

Anti-matter studies have the advantage that the anti-particles suffer only from annihilation when detector material is crossed, whereas on the matter side a substantial background is created via knockout from the material.

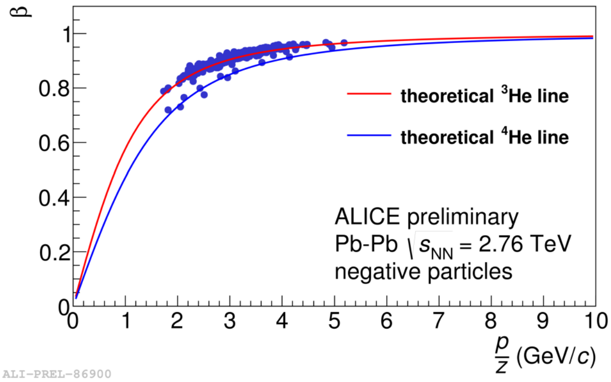

Figure 1: Velocity β measured with the TOF detector as function of the rigidity $R = p/z$ shown for $^{3}\overline{\mathrm{He}}$ (red line) and $^{4}\overline{\mathrm{He}}$ (blue line).

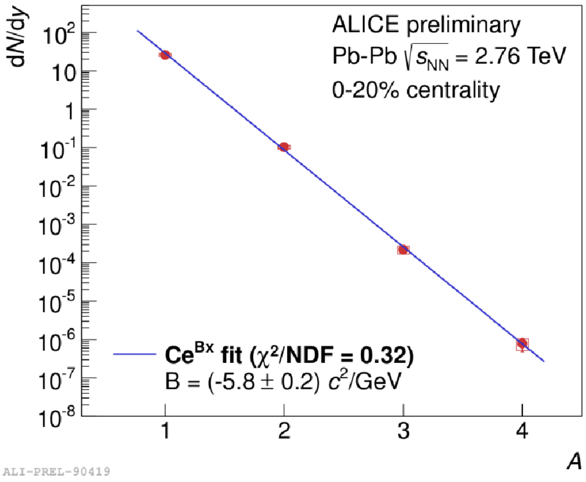

Figure 2: Production yields $\mathrm{d}N/\mathrm{d}y$ for nuclei from protons down to $^{4}\overline{\mathrm{He}}$.

The excellent performance of the Time-Projection Chamber (TPC) [6] and the Time-Of-Flight detector (TOF) [3] allows for the clear identification of all stable particles over a wide range in rigidity $R = p/z$, where p is the track momentum and z is the charge number. Here results for 38 million Pb–Pb collisions at $\sqrt{s_{\mathrm{NN}}} = 2.76\,\mathrm{TeV}$, recorded in the heavy-ion run of November 2011 are presented, where a trigger mix of minimum bias, semi-central and central events was applied. Furthermore an offline trigger selecting all $^{3}\overline{\mathrm{He}}$-nuclei or heavier candidates using the TPC $\mathrm{d}E/\mathrm{d}x$ measurement is used. For a clear identification of the $^{4}\overline{\mathrm{He}}$ the velocity β measurement of the TOF detector is required in addition, as shown in figure 1.

The resulting measured production yield $\mathrm{d}N/\mathrm{d}y$ for $^{4}\overline{\mathrm{He}}$ is plotted in figure 2. In addition the production yields $\mathrm{d}N/\mathrm{d}y$ for protons, deuterons and ^{3}He are shown. An exponential fit is performed (blue line). This leads to a penalty factor of ~ 330 for each additional nucleon, which means for example that $^{4}\overline{\mathrm{He}}$ a factor 330 less produced than ^{3}He.

References

[1] A. Andronic *et al.*, Phys. Lett. B 697 (2011) 203

[2] J. Cleymans *et al.*, Phys. Rev. C 84 (2011) 054916

[3] B. Abelev *et al.* (ALICE Collaboration), Int. J. Mod. Phys. A 29 (2014) 1430044

[4] A. Kalweit for the ALICE Collaboration, J. Phys. G: Nucl. Part. Phys. 38 (2011) 124073

[5] H. Agakishiev *et al.* (STAR Collaboration), Nature 473 (2011) 353

[6] J. Alme *et al.*, Nucl. Instr. Meas. A 622 (2010) 316

---

* Work supported by GSI, BMBF, Helmholtz Alliance HA216/EMMI, H-QM, and HGS-HIRe

† b.doenigus@gsi.de

DOI:10.15120/GR-2015-1-MU-NQM-ALICE-01

Centrality dependence of particle production in p-Pb collisions at ALICE [*]

A. Andronic[1], *J. Gronefeld*[1,2], *M.L. Knichel*[3], *J. Otwinowski*[1,4], *A. Toia*[1,5] *for the ALICE Collaboration*

[1]GSI Darmstadt; [2]Technische Universität Darmstadt; [3]Universität Heidelberg; [4]The Henryk Niewodniczanski Institute of Nuclear Physics, Polish Academy of Sciences, Cracow, Poland ; [5]Universität Frankfurt

With the ALICE detector at the LHC the physics of the Quark-Gluon Plasma is investigated in collisions of lead nuclei. In those collisions the number of participating nucleons - thus the collision centrality - is an important parameter. While in Pb–Pb collisions the connection of geometrical centrality to physical observables as particle multiplicity is direct, in p–Pb collisions this connection is difficult. In Pb–Pb collisions the number of participating nucleons grows with increasing overlap of the nuclei and as a result the produced particle multiplicity increases. To determine the collision centrality, a Glauber-Monte-Carlo simulation is compared to measured multiplicity distributions. This method is used with various detectors eg. the forward V0A, the midrapidity inner tracking system (ITS) or the zero-degree neutron calorimeter ZNA, located 114 m away from the interaction point. Not only the intervals of centrality are calculated, but also the number of binary nucleon-nucleon collisions $N_{\rm coll}$ is estimated.

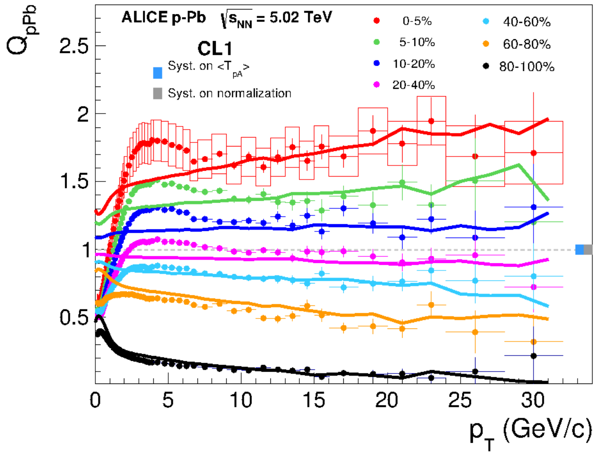

Figure 1: The measured $Q_{\rm pPb}$ for charged primary particles obtained with CL1 in comparison to G-PYTHIA (lines).

One observable of interest is the nuclear modification factor $Q_{\rm pPb}$. It quantifies the effects of the nuclear matter in p–Pb collisions in comparison to pp collisions.

$$Q_{\rm pPb}\,(p_{\rm T}\,;{\rm cent}) = \frac{1}{\langle T_{\rm pPb}^{\rm Glauber}\rangle}\,\frac{dN_{ch}^{pPb}/dp_{\rm T}}{d\sigma_{ch}^{pp}/dp_{\rm T}} \qquad (1)$$

In this formula N_{ch}^{pPb} represents the yield of charged particles in pPb collisions while σ_{ch}^{pp} is the cross section in pp collisions. $T_{\rm pPb}^{\rm Glauber}$ is the nuclear overlap function calculated with Glauber-Monte Carlo ($T_{\rm pPb}^{\rm Glauber} = N_{\rm coll}/\sigma_{\rm NN}^{\rm inel}$). In this notation $Q_{\rm pPb}$ is distinguished from $R_{\rm pPb}$, as the centrality selection can introduce a bias not related to nuclear effects. Hence, $Q_{\rm pPb}$ can be different from unity even in the absence of nuclear effects.

Figure 1 shows the biased $Q_{\rm pPb}$ for centrality intervals obtained using the second layer of the ITS. Additionally calculations with a PYTHIA event generator coupled to p–Pb Glauber-Monte Carlo (G-PHYTHIA) are shown, which reproduce well the bias at high $p_{\rm T}$. In order to minimize the biases from the centrality selection and guarantee a robust determination of $\langle N_{\rm coll}\rangle$ the so called hybrid method was introduced. Hereby the centrality selection relies on the energy deposited in ZNA, while $\langle N_{\rm coll}\rangle$ is calculated using the assumption that the charged particle multiplicity at mid-rapidity is proportional to $N_{\rm part}$. Other assumptions use the proportionality of $N_{\rm coll}$ to the yield of high-$p_{\rm T}$ particles, or to the total charged multiplicity measured with V0A in the Pb-side at forward rapidity. The variations on $N_{\rm coll}$ obtained with the three methods is below 10% and accounts as an uncorrelated systematic uncertainty. Figure 2 shows the $Q_{\rm pPb}$, consistent with unity at high $p_{\rm T}$ for all centrality classes, with some Cronin-enhancement at $p_{\rm T} \sim 3\,GeV/c$ stronger in central collisions.

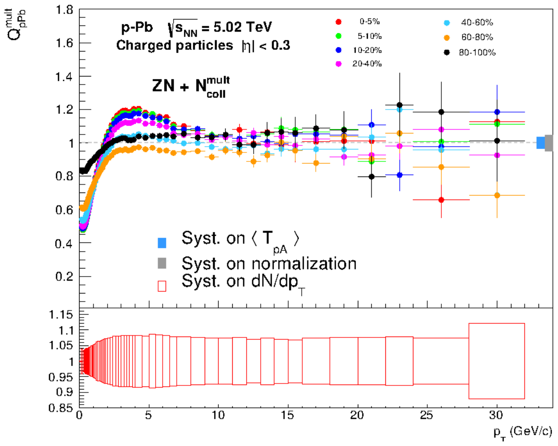

Figure 2: The $Q_{\rm pPb}$ in classes of centrality determined with the hybrid method.

References

[1] ALICE Collaboration, Eur.Phys.J. C74 (2014) 3054, arXiv:1405.2737 [nucl-ex].

[2] ALICE Collaboration arXiv: 1412.6828

---

[*] Work supported by GSI, BMBF, Helmholtz Alliance HA216/EMMI, H-QM, and HGS-HIRe

DOI:10.15120/GR-2015-1-MU-NQM-ALICE-02

Charge dependent correlations with identified hadrons relative to the reaction plane with the ALICE experiment at the LHC*

J. Onderwaater[1]*, and I. Selyuzhenkov*[2] *for the ALICE Collaboration*
[1]TU Darmstadt, Darmstadt, Germany; [2]GSI, Darmstadt, Germany

Conservation of parity in strong interactions is one of the fundamental open questions in QCD. The parity symmetry in QCD can be violated spontaneously via instanton and sphaleron transitions. Inside hot QCD matter created in a heavy-ion collision, these interactions in the presence of the strong magnetic field generated by the colliding ions may lead to a separation of charges [1] along the field. This phenomenon is known as the Chiral Magnetic Effect (CME). Since the magnetic field is aligned perpendicular to the reaction plane, which is spanned by the impact parameter and the beam direction, the separation of charges can be measured with a P-even two-particle correlation relative to the reaction plane [2]:

$$c_{\alpha\beta} = \langle \cos(\varphi_\alpha + \varphi_\beta - 2\Psi_{\mathrm{RP}}) \rangle . \qquad (1)$$

Here α and β denote the charges of the particles with azimuthal angle φ. The reaction plane angle, Ψ_{RP}, can be estimated from the azimuthal distribution of particles created either in the collision overlap region or in the forward (spectator fragments) region. The ALICE experiment has several subdetectors with full azimuthal coverage which together cover a wide pseudorapidity range needed for reconstruction of the reaction plane and the CME study. Figure 1 shows the event plane resolution correction factor for the Time Projection Chamber (TPC), as well as for forward multiplicity detectors (V0-A/C, FMD-A/C and T0-A/C).

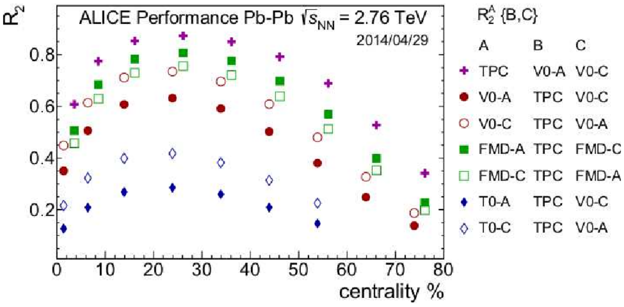

Figure 1: Resolution correction factor R_2 estimated for different ALICE subdetectors with the 3-subevent method [3].

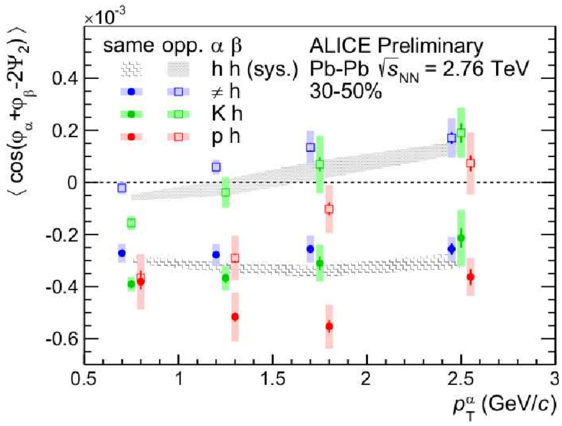

Figure 2: Results for $\langle \cos(\varphi_\alpha(p_{\mathrm{T}}^{\alpha}) + \varphi_\beta - 2\Psi_{\mathrm{RP}}) \rangle$ in the 30-50% centrality range.

The magnitude of the resolution correction factor depends on the particle multiplicity in the detector and the magnitude of the collective flow of those particles. Due to large number of particles produced at midrapidity, the large acceptance TPC has good sensitivity to the orientation of the reaction plane, while for forward detectors with smaller acceptance, such as T0, it is significantly reduced. These independent estimates of the collision symmetry plane in different kinematic ranges provide needed information for a systematic study of the correlation measurements relative to the reaction plane.

The ALICE experiment has previously measured the correlator in Eq. (1) for charged hadrons. While a significant charge dependence was observed, it likely contains contributions from other physics effects which are backgrounds to CME. The strongest background candidate is effects due interplay of Local Charge Conservation (LCC) with the anisotropic flow. The effect of flow on the charge dependent signal can be studied differentially with identified hadrons, for example:

$$c_{\alpha\beta}(p_{\mathrm{T}}^{\alpha}) = \langle \cos(\varphi_\alpha(p_{\mathrm{T}}^{\alpha}) + \varphi_\beta - 2\Psi_{\mathrm{RP}}) \rangle . \qquad (2)$$

In Fig. 2 this correlation is shown for different charge combinations of one identified hadron α (pion, kaon, and proton) and one charged hadron β. Significant dependence of the charge separation as a function of the identified hadron transverse momentum p_{T}^{α} is observed. Detailed model calculations of the contributions from LCC and CME effects are needed to make a quantitative conclusion about possible CME signal in the observed charge correlations.

References

[1] D. Kharzeev Phys. Lett. B633 (2006) 260-264

[2] S. Voloshin Phys. Rev. C70 (2004) 052901

[3] A. Poskanzer and S. Voloshin Phys. Rev. C58 (1998) 1671-1678

---

[*] Supported by GSI, BMBF, H-QM, HGS-HIRe, and Helmholtz Alliance HA216/EMMI

DOI:10.15120/GR-2015-1-MU-NQM-ALICE-03

Development of an online calibration framework for ALICE

S. Weber[1] *for the ALICE Collaboration*
[1]TU Darmstadt, Darmstadt, Germany

The time projection chamber (TPC) is the main tracking and particle identification device of the ALICE detector [1]. Its working principle is the ionization of gas by traversing charged particles, and the acceleration of the freed electrons to readout chambers, where they are multiplied and an electrical signal is produced. Before the produced data can be used for reconstruction, it has to be calibrated to compensate for changes in physical conditions, as the drifting velocity or the gain factor. Currently, calibration of the data is done offline, after storing the raw data to disk. The result of the calibration is then stored in a special database, which can be used later in reconstruction.

For run 3 of data taking, starting after the long shutdown 2 of the LHC, which is foreseen for the year 2018, major upgrades of the TPC and of other parts of the ALICE detector are planned in order to cope with higher luminosities which will be delivered [2]. By replacing the current readout chambers of the TPC witch Gas Electron Multipliers (GEMs), it will be possible to operate in a continuous readout mode [3]. The produced data will increase by a significant factor, which means that a reduction in data volume before storage of about a factor 20 will be necessary. For an efficient data size reduction (e.g. removal of detector hits which cannot be associated to particle tracks), the data has to be calibrated, this means the calibration process has to be moved to the ALICE online data taking chain after the readout of the detector data, i.e. to the ALICE High Level Trigger (HLT) [4].

In order to transfer the calibration procedure to the online environment, a special framework has been developed. On the one hand, functionality to handle the data in the online environment has been implemented. Furthermore, the online environment makes it necessary that calibration procedures are finished in a certain amount of time according to the interaction rate, i.e. within some milliseconds per collision. For this reason, new data structures were developed, which possess a “flat” memory layout, which makes them easier to serialize and stream in memory between different processes, compared to the existing data structures, which have a rather complex memory structure and are hence not suited for use in an online environment.

For backward compatibility and to be able to compare the performance of the two approaches, it was made sure that the same calibration procedures can be run both in the existing offline and the new online environment without code changes. It is foreseen to use the LHC run 2 to test the newly developed framework in terms of its physics performance and use the obtained experience for run 3, when online calibration will be mandatory.

Figure 1 shows the data flow for both the online and the offline calibration. Tests have been conducted on the performance of the conversion of input data from the detectors to the new and the old data format. It could be demonstrated that the new data format needs significantly less time to be produced than the old one. Currently investigations are ongoing on how the performance of the calibration tasks changes when using the new data formats compared to the old ones.

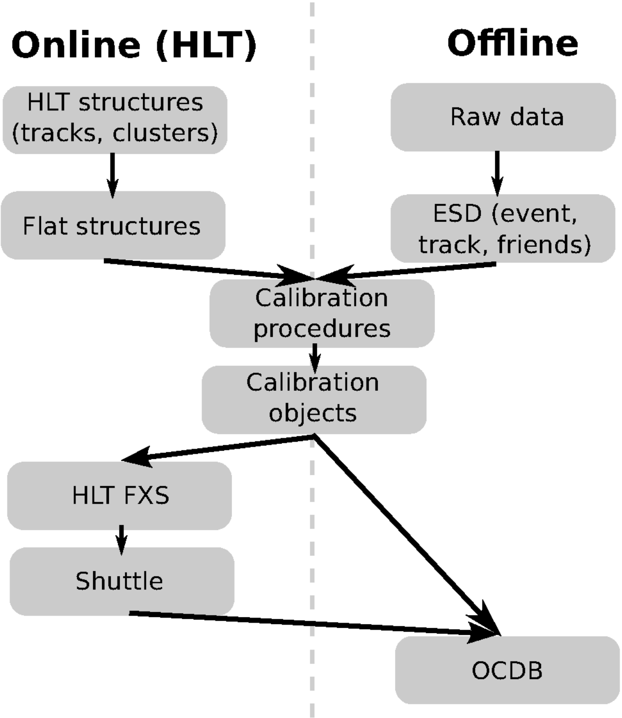

Figure 1: ALICE TPC calibration procedure in online and offline environment.

References

[1] Alme, J. et al., “The ALICE TPC, a large 3-dimensional tracking device with fast readout for ultra-high multiplicity events”, Nucl.Instrum.Meth.A622:316-367,2010

[2] ALICE Collaboration, “Upgrade of the ALICE Experiment: Letter of Intent”, CERN-LHCC-2012-012

[3] ALICE Collaboration, “Upgrade of the ALICE Time Projection Chamber”, CERN-LHCC-2013-020

[4] ALICE Collaboration, “Performance of the ALICE Experiment at the CERN LHC”, Int. J. Mod. Phys. A 29 (2014) 1430044

DOI:10.15120/GR-2015-1-MU-NQM-ALICE-04

Measuring the stability of GEM detectors against electrical discharges *

P. Gasik[†][1,2], *F. Dreher*[1,2], *L. Fabbietti*[1,2], *A. Mathis*[1,2], *R. Muenzer*[1,2], *S. Weber*[1,2], *and the ALICE TPC collaboration*

[1]TU München, Excellence Cluster 'Origin and Structure of the Universe', Boltzmannstr. 2, 85748 Garching, Germany;
[2]TU München, Physik Department E12, James-Franck-Str. 1, 85748 Garching, Germany

The requirements of a new generation of experiments in particle and nuclear physics are driving the development of new gaseous detectors. Novel devices must handle the high luminosities planned at future hadron and electron colliders as well as meet the requirements of large experiments such as the substantial active areas to be covered by their detectors. Among the new innovative detector techniques, the Gas Electron Multiplier (GEM) [1] is foreseen to be widely used in future large-area detectors.

The key parameters for a long-term operation of such detectors in a harsh environment of high- rate experiments are: radiation hardness, ageing resistance and stability against discharges. So far, the only comprehensive discharge studies in the gas electron multiplier were reported in [2] and concern mainly Ar-based gas mixtures. We performed discharge probability studies in single, triple and quadruple GEM structures in Ne- and Ar-based gas mixtures. In this report we present the results obtained with a triple-GEM setup performed in a Ne-CO_2 (90-10) gas mixture with and without additional 5% of nitrogen.

The scheme of the experimental setup used for discharge probability studies is shown in Fig. 1. The detector housing of the setup comprises a $10\times10\,\mathrm{cm}^2$ GEM holder, a drift cathode and a readout anode.

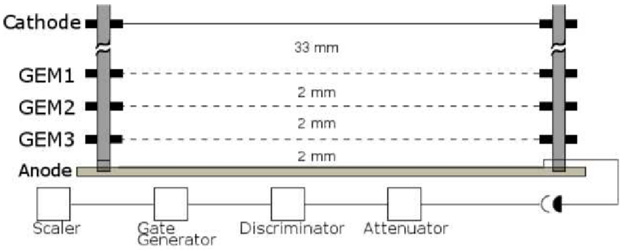

Figure 1: Experimental setup.

High voltage is applied to the GEM stack via a resistor chain which defines potential on each GEM electrode. The detector is operated with the "standard" HV settings that are commonly used with triple GEM structures, scaled in order to vary the total gain. The gain of the setup at given HV settings is determined by the usual method of recording the current at the pad plane and the rate of absorbed X-rays of known energy (an ^{55}Fe is used).

The occurrence of a spark in a GEM foil is detected according to the readout scheme presented in fig. 1. A raw signal induced on the pad plane is attenuated (1-31 dB) and then directed into the discriminator unit which filters out signals induced by alpha particles of $\mathcal{O}(100\,\mathrm{mV})$ and trigger on discharge signals of $\mathcal{O}(10\,\mathrm{V})$. Due to the fact that the raw signals are often modified by the noise (signal oscillations) a gate is created when the discriminator threshold is exceeded which is then counted by a scaler. This way, multi-counting of the same signal can be avoided.

The discharge probability is defined as the ratio of the number of detected discharges over the total number of particles irradiating the detector. For the studies presented in this report, the detector was irradiated with highly ionising, 6.4 MeV α particles emitted with a rate of $\sim$0.5 Hz from an internal, gaseous ^{222}Rn source randomly distributed within the active area of the detector.

Figure 2 shows the results of a gain scan for two different Ne-based gas mixtures. The measurements are performed at high gas gains to acquire a sufficient number of sparks with the low-rate ^{220}Rn source. Clearly, the addition of N_2 to the gas mixture has a noticeable effect on the discharge behaviour. The discharge probability observed in Ne-CO_2-N_2 (90-10-5) is one order of magnitude lower than in Ne-CO_2 (90-10). The addition of nitrogen to the Ne-CO_2 mixture alleviates the instability issue. Nitrogen provides better quenching for neon and allows for higher fields without amplification in transfer and induction gaps.

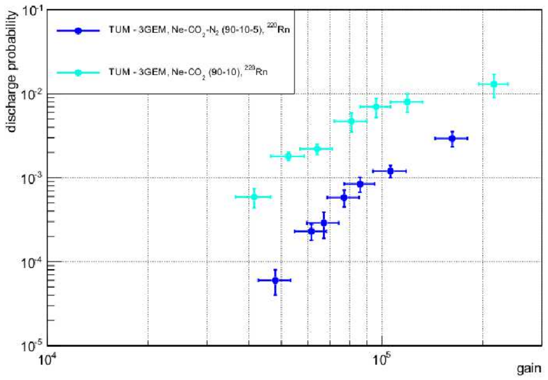

Figure 2: Discharge probability in Ne-based mixtures.

References

[1] F. Sauli, NIM **A386** (1997) 531

[2] S. Bachmann et *al.*, NIM **A479** (2002) 294

[3] C. Altunbas et *al.*, NIM **A490** (2002) 177

---

* Work supported by BMBF 05P12WOGHH and Excellence Cluster 'Universe'

[†] p.gasik@tum.de

Development of a 4-GEM large-size prototype for the ALICE TPC upgrade *

P. Gasik[†1,2], *L. Fabbietti*[1,2], *A. Mathis*[1,2], *R. Muenzer*[1,2], *and the ALICE TPC collaboration*
[1]TU München, Excellence Cluster 'Origin and Structure of the Universe', Boltzmannstr. 2, 85748 Garching, Germany;
[2]TU München, Physik Department E12, James-Franck-Str. 1, 85748 Garching, Germany

ALICE at the LHC at CERN is planning a major upgrade of the central barrel detectors, including the TPC, to cope with an increase of the LHC luminosity after 2018. A full-size prototype of a TPC Inner Read-Out Chamber (IROC) was produced and tested during the test-beam campaign in the fall of 2014. It was equipped with a quadruple Gas Electron Multiplier (GEM [1]) employing GEM foils with a pitch of 140 μm ("Standard" - S) and 280 μm ("Large Pitch" - LP). The subsequent GEM foils in the stack have been installed according to the S-LP-LP-S configuration presented schematically in fig. 1. The design and assembly procedure of the 4-GEM prototype follows closely that of the triple GEM prototype built and tested in 2012 and described in details in [2, 3]. A notable modification with respect to the 2012 setup is that the induction gap (between GEM4 and the pad plane) was reduced from 4 mm to 2 mm. The new 4-GEM IROC employs also a cover electrode, which is used to minimise drift-field distortions at the edges of the GEM stack.

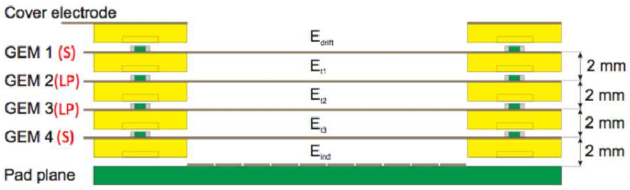

Figure 1: Schematic picture of the 4-GEM IROC

Several HV settings were used with the prototype, including the one defined as 'baseline' for the ALICE GEM readout chambers optimised for the ion backflow and energy resolution [4]. A resistor chain was used to supply the potentials on the subsequent GEM electrodes. The GEM IROC was installed in a test field cage with a drift length of 115 mm and commissioned with radioactive sources. The prototype is operated in Ne-CO_2-N_2 (90-10-5) gas mixture, which is the nominal gas mixture for the upgraded TPC.

Figure 2 shows a gain curve obtained for the prototype using a ^{55}Fe source. The gain is scaled with a common scaling factor (SF) applied to all GEM potentials. The nominal gain of 2000 is obtained for $SF \approx 100\%$. The value of ion backflow corresponding to this setting is 0.63% and the energy resolution of a ^{55}Fe peak $\sigma = 11.3\%$ [4].

The dE/dx resolution of the prototype was evaluated in a test beam campaign at the CERN PS with 1 GeV/c pions and electrons. The relative energy resolution $\sigma\left(\mathrm{d}E/\mathrm{d}x\right)/\langle\mathrm{d}E/\mathrm{d}x\rangle$ obtained for electrons ($\sim 9.1\%$) and pions ($\sim$ 10.4%) is comparable to the resolution of the MWPC IROC [4].

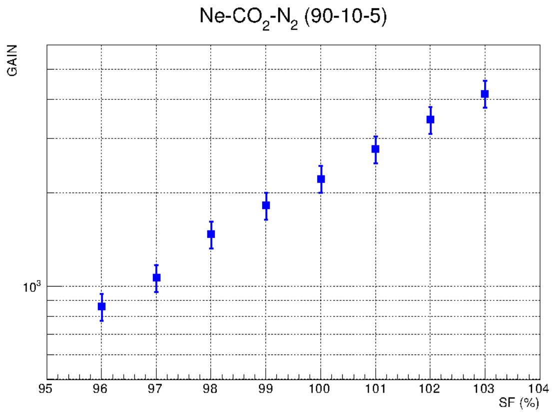

Figure 2: Gain curve obtained in Ne-CO_2-N_2 (90-10-5) for the 4-GEM IROC using scaled 'baseline' HV settings.

Stability of the chamber was evaluated in a test beam at the CERN-SPS. The discharge probability was measured using showers of hadrons produced by a high-intensity secondary pion beam with a momentum of 150 GeV/c impinging on a 30-40 cm thick iron absorber. The average beam intensity was $\sim 6 \times 10^6$ particles per spill, resulting in an average in-spill rate of $\sim$1.2 MHz. The number of particles accumulated during the experiment is $N_{\mathrm{tot}}^{\mathrm{SPS}} = (4.7 \pm 0.2) \times 10^{11}$. The chamber was operated with the 'baseline' settings at the gain of 2000. In total, three discharges were detected in the detector. This translates into a discharge probability of $(6 \pm 4) \times 10^{-12}$ per incoming hadron. This result is of the same order of magnitude as the one obtained by the LHCb Collaboration where the discharge probability of 3-GEM detectors operated with an isobutane-CF_4-based gas mixtures was measured under similar conditions [5].

References

[1] F. Sauli, NIM **A386** (1997) 531

[2] P. Gasik, JINST **9** (2014) C040394

[3] ALICE Collaboration, CERN-LHCC-2013-020 (2013)

[4] ALICE Collaboration, CERN-LHCC-2015-002 (2015)

[5] G. Bencivenni et $al.$, NIM **A494** (2002) 156

---

* Work supported by GSI, BMBF, BMBF 05P12WOGHH, Excellence Cluster 'Universe'

[†] p.gasik@tum.de

DOI:10.15120/GR-2015-1-MU-NQM-ALICE-06

Consolidation and upgrade of the ALICE TPC*

C. Lippmann[1], C. Garabatos[1], T. Morhardt[1], A. Deisting[2], and D. Vranic[2], for the ALICE collaboration

[1] GSI, Darmstadt, Germany; [2] Ruprecht-Karls-Universität Heidelberg, Germany

Preparation for LHC RUN2

In 2014 the long shutdown period of the LHC ended. Several consolidation activities have been carried out to prepare the ALICE TPC for the upcoming data taking period Run2, which will start in mid 2015. During Run2 much higher collision rates as compared to RunI will be produced. The consolidation activities include the replacement of the Ne-CO_2 gas mixture by Ar-CO_2 and the installation and commissioning of a new Gas Chromatograph to provide the precise gas composition for online calibration. Several faulty front-end electronics cards have been replaced during the shutdown. A redundant Ethernet networking system has been deployed in order to overcome occasional failures of certain hardware located in the experimental cavern. Finally, the high voltage network has been improved by further segmentation of HV channels and by the addition of a fast current monitoring system, in order to gain better understanding of detector behaviour due to e.g. sudden beam losses.

An ambitious project aimed at improving the read-out scheme and the stability under radiation has been developed during the shutdown. A new Read-out Control Unit (RCU2) will allow one to at least double the maximum data read-out speed by doubling the number of read-out buses as compared to the current implementation. This in turn will allow for doubling the statistics for Physics analysis.

The new board has been designed based on a state-of-the-art FPGA, which integrates an inherently reliable flash-based FPGA fabric, a 166 MHz processor, and high-performance communication interfaces, all on a single chip. Extensive tests, including radiation hardness, have been performed on engineering samples. The upgrade will be implemented during the technical stops in 2015.

TPC Upgrade with GEMs

The TPC Upgrade [1] for Run3 consists of the replacement of the 72 multi-wire proportional readout chambers by new chambers based on GEM technology, and the replacement of the current front-end electronics by new cards which will allow for trigger-less, continuous readout.

Substantial R&D has been carried out by various groups, including the GSI group at CERN, in order to customise a GEM structure capable to provide excellent tracking and particle identification under the extreme occupancies anticipated in RUN3.

With the found solution, the space-charge density produced by back-drifting ions in the absence of a gating technique is minimised by the arrangement of quadruple GEM stacks with different hole spacings. This configuration has proven to be highly efficient in ion trapping and preserves the particle identification capabilities of the TPC. Moreover, it is robust against the development of discharges.

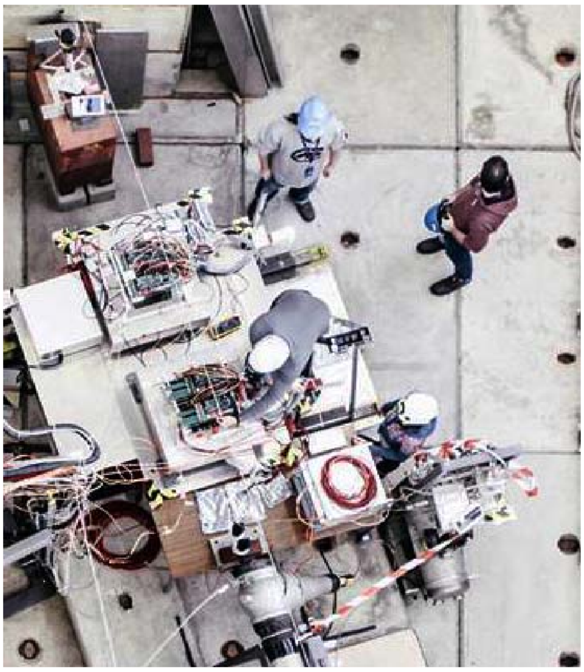

Figure 1: Experimental setup with two full-size prototypes at the CERN Proton Synchrotron.

The GSI group at CERN has coordinated two test beam campaigns at CERN; one at the Proton Synchrotron, where the d*E*/d*x* performance of full-size prototypes has been demonstrated, and one at the Super Proton Synchrotron, where the discharge rate under hadronic showers has been confirmed to stay below tolerable limits.

A collaboration-wide effort to design a completely new read-out system has seen substantial progress during 2014. In particular, the new TPC read-out electronics will feature continuous read-out of all events at data rates up to 1 TByte/s. Fast data links to remote read-out units and online processing and compression are also being developed.

References

[1] ALICE Collaboration, CERN-LHCC-2013-020; ALICE-TDR-016.

---

[*] Work supported by GSI, BMBF, Helmholtz Alliance HA216/EMMI, H-QM, and HGS-HIRe.

DOI:10.15120/GR-2015-1-MU-NQM-ALICE-07

DOI:10.15120/GR-2015-1-MU-NQM-ALICE-07

Slow-control system for the Hydrogen Cluster-Jet Test Facility at GSI *

B. Zwieglinski[1], *A. Chlopik*[1], *A. Gerhardt*[2], *G. Kesik*[1], *J. Lühning*[2], *H. Orth*[2], *and A. Trzcinski*[1]
[1]NCBJ, Warsaw, Poland; [2]GSI, Darmstadt, Germany

The present Hydrogen Cluster-Jet Test Facility at GSI has its origin in FERMILAB as a target in the E760/E835 experiment [1]. After dismounting and installation at GSI in the laboratory specially adapted for working with flammable gases, it is reinstated in its cluster-jet operation capability, serving in the same time as a testing ground for many elements of the future PANDA cluster-jet target [2]. We refer in this note to some results obtained in the course of development of its slow-control system.

The whole target system is foreseen [2] to be driven using National Instruments (NI) hardware and software, in the well-known LabVIEW environment. This can be achieved using essentially three elements: a PC, a programmable logic controller and the software that runs on both. The programmable logic controller to drive the PANDA target system is the NI *CompactRIO*. It combines an industrial real-time controller and reconfigurable field-programmable gate array (FPGA) chassis intended for industrial machine control and monitoring applications.

Soon after reinstallation of the Facility at GSI a cRIO-9074 with a few I/O modules have been installed, thus permitting experimenting with the slow-control of its vacuum and hydrogen-flow subsystems. An ultrapure hydrogen is supplied to the nozzle of the cluster-jet generator through a heated Pd-cell [Resource Systems Inc., mod. RSD-75]. This purifier requires that the Pd-alloy barrier is never heated or cooled in the presence of hydrogen. Therefore, for example, the 'turn-on' procedure evolves through the following operations performed step-wise:

- evacuation of the crude and pure gaslines to assure that no hydrogen is inside the Pd-filter,
- evacuation of the inlet gasline to the nozzle and the nozzle chamber,
- turning-on heating and setting the proper temperature of the Pd-filter,
- setting the proper pressure and flow-rate of the pure H_2 through the nozzle.

After completion of this stage, the system can be operated in a stable mode under the control of cRIO. Turning it off starts with evacuation of the crude and pure gaslines to remove traces of hydrogen from the Pd-filter, next takes place the evacuation of the inlet gasline to the nozzle and the nozzle chamber, afterwards the Pd-filter is purged by venting with nitrogen and its heating can be turned-off. The above listed elementary operations have been merged into two procedures within which they are executed automatically by the c-RIO. A nice GUI has been prepared to watch changing states of the system as it evolves in time on the PC screen .

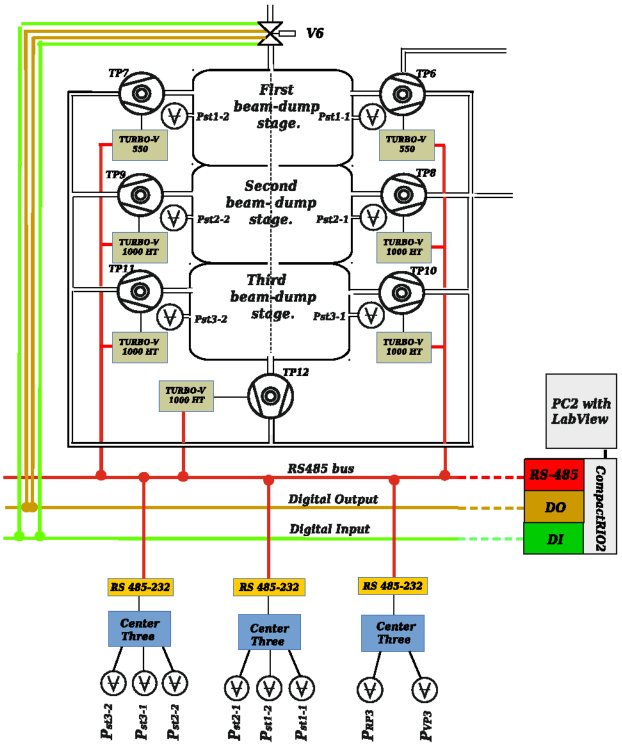

Figure 1: Vacuum devices of the cluster-jet beam dump served by the slow-control system.

An arrival of the cluster-jet beam dump from INFN-Genova marked a new milestone in the Facility's activity. The PANDA cluster-jet beam-dump features three differentially pumped chambers, each chamber pumped with a pair of turbomolecular pumps (TPs) and equipped with a pair of vacuum sensors - one for low- and one for high-vacuum range. An axis of rotation of the seventh TP (TP12 in Fig. 1) is shifted off the cluster-jet axis (marked with the broken line), so that clusters landing on its blades are destroyed immediately into atomic hydrogen and removed outside the beam-dump by the pump. Overall the cluster-jet beam dump plays an important role of minimizing hydrogen reverse load to the HESR beam-pipe with circulating antiprotons.

---

* Work supported by HadronPhysics3 - Transnational Access to GSI: Project SlowContr/Zwiegl.

DOI:10.15120/GR-2015-1-MU-HADRONS-01

A scheme of the beam-dump together with the vacuum devices is presented in Fig. 1. Due to lack of available space the fore-vacuum part has been ommited from Fig. 1. Slow-control is accomplished with the aid of $CompactRIO_2$ [$CompactRIO_1$ is foreseen for the cluster-jet source] using the three indicated C-modules. The lines leading to each of them represent in fact a bunch of conductors joining e.g. a single pin (out of the 32) in the DO-module with a particular wire going to a particular valve. The DI pins receive the status information. A control of TPs (including their turning-on and -off and following in real-time their essential working parameters, such as rotation speed, power consumption and temperature) is accomplished via a serial bus RS-485 permitting to access individually each TP via its controller. Reading of vacuum-pressure sensors involves conversion of their signals into digital form within the Center-Three units with the further making them individually addressable with the aid of RS232↔RS485 converters.

The part displayed in Fig. 1 has already been programmed in LabVIEW and its operation tested in a one-by-one and simultaneous turning-on and -off the seven turbopumps. A project of the rest of the vacuum system has been developed. It will be implemented and tested together with the rest of the future cluster-jet target for PANDA.

References

[1] G. Garzolio et al., Nucl. Instr. and Meth. A519 (2004) 558

[2] Technical Design Report for the P̄ANDA Internal Targets: The Cluster-Jet Target and Developments for the Pellet Target, The P̄ANDA Collaboration: W. Erni et al., http://www-panda.gsi.de/archive/TargetTDR/Targets_TDR.pdf

DOI:10.15120/GR-2015-1-MU-HADRONS-01

New secondary vertex finding procedure for the HypHI project

C.Rappold[*][1,2], *T.R. Saito*[1,3,4], *and V. Bozkurt*[1]

[1]GSI, Darmstadt, Germany; [2]Justus-Liebig-Universität Giessen, Germany; [3]Johannes Gutenberg-Universität, Mainz, Germany; [4]The Helmholtz Institute Mainz, Mainz, Germany

The first experiment of the HypHI collaboration aimed to demonstrate the feasibility of the hypernuclear spectroscopy by means of heavy ion beam induced reactions. Later, a second experiment of the HypHI collaboration was performed using a ^{20}Ne beam at $2A$GeV on a ^{12}C target. In the track reconstruction of the experimental data of this second experiment, the track multiplicity is about 5 to 10 times more that in the first experiment. New criteria for the track and event reconstruction had to be implemented in order to reduce the background contribution. In the event reconstruction, the vertex finding procedure is based on the geometrical closest distance approach between the daughter track candidates. An additional algorithm has been implemented in order to have another criteria on the vertex quality. While, a vertex fitting procedure is the best step to judge the goodness of the vertex reconstruction, the speed of the vertex fitting procedure is relatively slower than any vertex finding step. Thus a first step is set to reduce the number of vertex candidates. For this purpose a more advance vertex finding step was implemented based on the algorithm described in publication [3]. The algorithm principle is the consider position covariance matrix of the track, obtained after the track fitting, to create of tube representation in 3D around the track as a 1σ standard deviation in the 3D space. At a given z-position, an ellipse corresponding to the covariance is calculated. With this tube representation, a probability of being close to the given track can be calculated, denoted as $f(\mathbf{r}) = \exp(-0.5(\mathbf{r} - \mathbf{r_{track}})^T \mathbf{C}^{-1}(\mathbf{r} - \mathbf{r_{track}}))$. Then a vertex position $\mathbf{v}$from where each considered track originate will have to satisfy the criteria that it has to be close to the track tubes. For this, a vertex function :

$$V(\mathbf{v}) = \sum_{i=0}^{n} f_i(\mathbf{v}) - \frac{\sum_{i=0}^{n} f_i^2(\mathbf{v})}{\sum_{i=0}^{n} f_i(\mathbf{v})} \qquad (1)$$

is used to defined a probability to be as close as possible to the all n considered track tubes. By finding the maximum of the probability vertex distribution, the improved vertex position can be determined. Additionally a covariance matrix of the maximization procedure can be inferred and associated to the vertex position. During this maximization of $V(\mathbf{v})$ procedure, if the track set does not have a maximum, the vertex candidate is then rejected since it corresponds of the case where the track tubes are not close enough to define an non-null value for $V(\mathbf{v})$. Figure 1 shows the track tubes for two different tracks and the obtained probability distribution $V(\mathbf{v})$. The calculation are performed in 3D, however for easier representation the projection to XY, XZ and YZ global axis are shown in Figure 1.

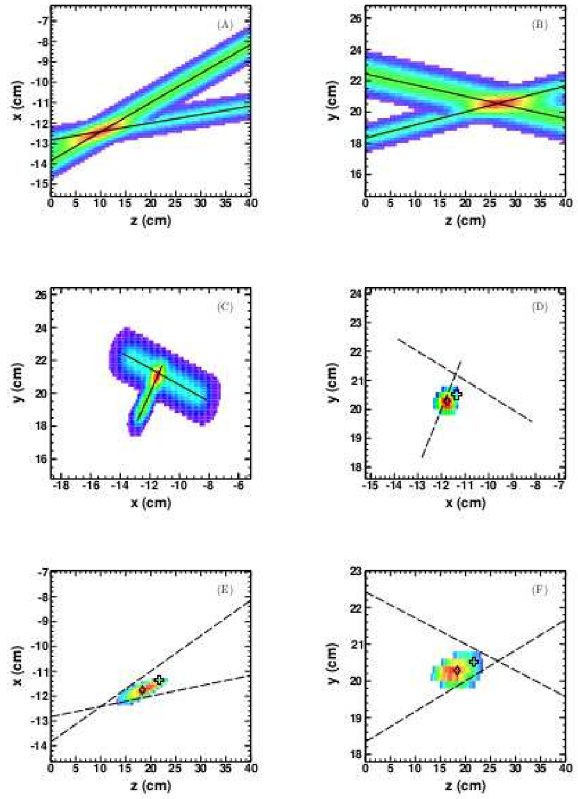

Figure 1: Profiles of the two 3D track tubes are shown in panel (A), (B) and (C), and profile of vertex probability obtained by the algorithm of [3] are shown in panel (D), (E) and (F). In panel (A), (B) and (C), the solid black lines are the tracks and the profiles corresponds to the tubes formed by the 1-σ standard deviation from the position covariance matrix of the associated track. In panels (D), (E) and (F), the dash lines represent the track, the cross marker the seed of the geometrical closest distance approach calculation and diamond marker the position of the highest probability obtained by the algorithm of [3]. In those panels, the profile represents the probability distribution.

References

[1] C. Rappold *et al.*, Nucl. Phys. A **913**, 170 (2013).

[2] C. Rappold *et al.*, Phys. Rev. C **88**, 041001 (2013).

[3] D.Jackson *et al.* Nucl Instr. Meth. A **388**, 247 (1997).

---

[*] c.rappold@gsi.de

DOI:10.15120/GR-2015-1-MU-HADRONS-02

Improved particle identification with probabilistic approach for the HypHI project

C.Rappold[*][1,2] *and T.R. Saito*[1,3,4]

[1]GSI, Darmstadt, Germany; [2]Justus-Liebig-Universität Giessen, Germany; [3]Johannes Gutenberg-Universität, Mainz, Germany; [4]The Helmholtz Institute Mainz, Mainz, Germany

The first experiment of the HypHI collaboration aimed to demonstrate the feasibility of the hypernuclear spectroscopy by means of heavy ion beam induced reactions. The phase 0 experiment was performed with a ^{6}Li beam at $2A$GeV impinged on a stable ^{12}C target material. The main goal of the experiment was to produce, reconstruct and identify decay vertexes of Λ particle and ${}^{3}_{\Lambda}$H, ${}^{4}_{\Lambda}$H [?]. With the finalized data analysis of Phase 0 experiment, the first results show that the experimental method is viable for the study of hypernuclei [1, 2, 3].

Possible improvement on the particle identification is necessary in order to improve the event reconstruction of the Λ and hypernuclear candidates. During the track reconstruction the particle identification has to define which track corresponds which particle or fragment. The idea for improving the identification is to perform a maximum likelihood ratio test for each particle hypothesis. From the track reconstruction, the kinematics of the track is determine and a partial particle identification is associated to the track thanks to the time-of-flight measurement.

For each track, its velocity $\beta_{measured}$ is calculated from the measured time-of-flight and path length, then a probability of being π, K, proton, deuteron, triton for the case of charge $Z = 1$ species is given. Theoretically, we know that $\beta = p/\sqrt{p^2 + m^2}$, where p and m correspond to the momentum and mass of the particle, therefore for a measured momentum $p_{measured}$ and a given mass we can calculate that should be the velocity $\beta_{likelihood}$. The particle identification are usually defined by a side band as explained in [1]. Following the same PID cut than in [1], the probability of being a given particle $P((\beta_{measured}, p_{measured})|id)$ is then defined by a Gaussian probability density function at $\beta_{measured}$. The mean value and standard deviation of the Gaussian function are β_{theory} and $\beta_{theory} \pm \beta_{sideband}$. This probability of identification is given for each particle hypothesis and correspond how close or how far is the measured momentum and measured velocity of the track from each hypothesis. Finally, the maximum likelihood ratio test is performed for the each hypothesis, $P(a) = P((\beta, p)|a)/\sum_{id}(P((\beta, p)|id)$ where a corresponds to the tested species (π, K, proton, deuteron, triton) and id corresponds for all the species. The particle identification is then decided by the highest ratio.

The probability of identification can also use to improve the selectivity of the good track candidates. This new procedure of the particle identification was tested on the experimental data of the phase 0 experiment. Figure 1 shows the mass spectrum of the track reconstruction calculated from the $m = p * \sqrt{1./\beta^2 - 1.}$ with a first p-value cut at $p > 0.05$. The black line represents the mass spectrum from the current situation of the final results published in [1]. The red line shows under the same conditions that the black line with a additional cut on the probability of identification. A clear separation is now possible with this probabilistic particle identification. A huge background suppression of bad track reconstruction can be seen, and all species can be identified directly in the mass spectrum instead of the β-momentum correlation plot.

The clear improvement of the particle identification shown for the phase 0 experiment data will help to the current data analysis of the phase 0.5 experiment of ^{20}Ne+^{12}C.

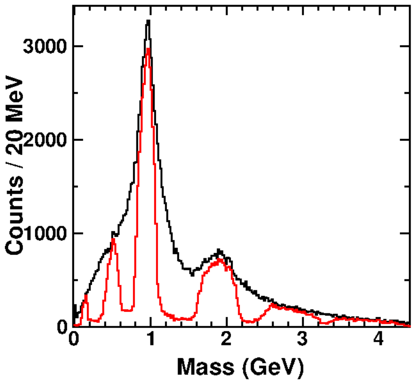

Figure 1: Improved particle identification in the mass spectrum. Initial mass spectrum after the track reconstruction and p-value cut at $pv > 0.05$ is shown in black line. The red line shows the improved mass spectrum of the track reconstruction when the probability of identification is used by setting a minimum probability.

References

[1] C. Rappold *et al.*, Nucl. Phys. A **913**, 170 (2013).

[2] C. Rappold *et al.*, Phys. Lett. B **728**, 543 (2014).

[3] C. Rappold *et al.*, Phys. Rev. C **88**, 041001 (2013).

[4] T.R. Saito et al., Letter Of Intent of HypHI project.

---

[*] c.rappold@gsi.de

DOI:10.15120/GR-2015-1-MU-HADRONS-03

A partial wave analysis for p + p $\rightarrow$ p + K^+ + Λ in the GeV energy scale*

R. Muenzer[1], *E. Epple*[1], *L. Fabbietti*[1], *the HADES and FOPI Collaboration*, *J. Ritman*[2], *E. Roderburg*[2], *F. Hauenstein*[2], *and M. Maggiora*[3]

[1]Physik Department E12, Technische Universität München, Excellence Cluster 'Origin and Structure of the Universe', 85748 Garching, Germany; [2]Forschungszentrum Jülich; [3]University of Turino

The understanding of strangeness production is a key-aspect of the description of the strong interaction between hadrons. The production channel p+p$\rightarrow$ p + K$^+$ + Λ is of major interest, since it rather dominant in the strangeness production in elementary and heavy ion collisions in the GeV energy range. The production of this final state can proceed via several intermediate channels, like for example nucleon resonances. While the existence of such resonance is well known, their properties and influence to the production of strangeness is not quantitatively understood upt ot now. Furthermore, structures like the Σ-N Cusp can occur in the $p + K^+ + \Lambda$, which is interpreted as a direct coupling between the Σ-N channel to Λ-p channel[1]. Also exotic matter like kaonic nuclear clusters can be produced in this reaction resulting in the same final state. This state was predicted by several theory groups but experimental results are very controversial up to now[2, 3, 4].

The description of all the production channels, that can contribute to the p K^+ Λ final state, requires a special analysis framework. For the analysis the Bonn-Gatchina Partial Wave Analysis (PWA) framework is used [5]. This kind of analysis enabled us to extract the strength of different production channels taking into account the different kinematical and quantum mechanical constraints. In this framework the transition amplitude from an initial wave to a final state is parameterized as a function of the energy and phase. The wave functions of different transitions with the same quantum numbers can mix, which leads to interference. Since the amplitudes and phase parameters of these transitions are not known, they have to be fitted by the PWA.

This method has been used to describe the experimental data measured at the HADES [6, 7] and FOPI [8]. In figure 1 the p-Λ invariant mass is plotted. The black cross show the experiential results. The different colored lines correspond to the 5 best solutions, which have been obtained by a systematical analysis using the BG-PWA framework.

In the analysis it was shown that interferences play an important effect in the description of the experimental data. This complicates the search for exotic matter, since the signature can be washed out. On the other hand it was shown, that the extraction of the different N* contribution by performing the PWA of a data sample at one beam energy only is not feasible, since ambiguities show up. Based on these results, an analysis program is ongoing in which further available data sample obtained also by the DISTO and the COSY-TOF collaboration, will be analyzed in a combined approach. In the following table the available exclusive statistics for different beam energies is listed. The goal of the combined analysis is to provide an energy dependend description of the production mechanism. This will allow to pin down the contribution of different production channels in a more precise way.

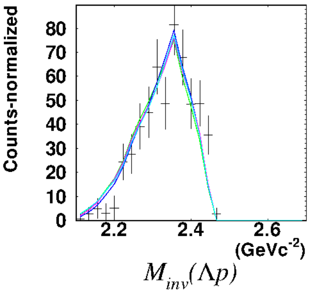

Figure 1: Λp invariant mass of FOPI experimental data (black dots) and PWA solutions (colored lines)

Beam Energy	Experiment	Statistics (k Events)
1.92	COSY-TOF [11]	150
2.15	DISTO [9]	121
2.16	COSY-TOF [10]	43
2.25	COSY-TOF [12]	36
2.40	COSY-TOF [12]	1.6
2.5	DISTO [9]	304
2.85	DISTO [9]	424
3.1	FOPI [8]	0.9
3.5	HADES [6, 7]	21

References

[1] S. El-Samad et. al. Eur. Phys. J. A (2013) 49
[2] T. Yamazaki et al., Phys. Rev. C76, 2007, 045201
[3] M. Agnello, et al. (FINUDA Collaboration), Phys. Rev. Lett. 94,2005,212303
[4] T. Yamazaki et al., Phys. Rev. Lett. 104, 2010 , 132502
[5] A.V. Sarantsev et. al., Eur.Phys.J. A25,2005,441-453
[6] E.Epple, PhD Thesis, TU München, 2014
[7] G. Agakishiev et al., arXiv:1410.8188 [nucl-ex], 2014
[8] R.Münzer, PhD Thesis, TU München, 2014
[9] M.Maggiora, Nucl.Phys. A835 (2010) 43-50
[10] M.Roder *et al.*, Eur. Phy. J.A. 49 (2013) 157
[11] F.Hauenstein, PhD Thesis , Uni. Erlangen (2014)
[12] S. Abd El-Samad et al., Phys. Lett. B 688 (2010), 142-149

---

* Work supported by DFG Projekt FA 898/2-1

DOI:10.15120/GR-2015-1-MU-HADRONS-04

Lifetime of ALD-coated microchannel plate PMTs*

F. Uhlig[1], *A. Britting*[1], *W. Eyrich*[1], *A. Lehmann*[†][1], *and PANDA Cherenkov subgroup*
[1]Physikalisches Institut IV, Universität Erlangen-Nürnberg, Erwin-Rommel-Str. 1, D-91058 Erlangen

Microchannel-plate photomultipliers (MCP-PMTs) are the preferred photon sensors for the PANDA DIRC detectors for hadron identification. They reach a sub 50 ps time resolution and can be used for single photon detection in magnetic fields up to 2 Tesla [1]. MCP-PMTs are available as multi-anode devices with a good gain uniformity and a moderate cross talk among the anodes [2]. The main drawback until recently was a serious aging problem caused by feedback ions from the rest gas hitting and damaging the photo cathode (PC). This results in a fast diminishing quantum efficiency (QE) while the integrated anode charge increases [3].

Approaches such as higher tube vacuum, electron scrubbing of the MCP surfaces, protection films or modified PCs were tested by the manufacturers to increase the lifetime of MCP-PMTs. The breakthough against the aging issue finally came with the application of an atomic layer deposition (ALD) technique: in a sophisticated procedure the MCPs are coated with an ultra-thin layer of usually Al_2O_3 or MgO which significantly reduces the desorption of atoms from the MCP material. In 2011 PHOTONIS was the first manufacturer to supply us with a prototype of an ALD-coated MCP-PMT (9001223) to measure its lifetime.

In Fig. 1 the results of a comparative measurement of several types of MCP-PMTs are shown which is ongoing since 2011. By a simultaneous illumination within an environment similar to PANDA conditions the systematic uncertainties are minimized and a fair comparison of the different tubes is possible. For monitoring purposes the pulse heights are continuously recorded at a highly prescaled rate during the illumination. Spectral and spacial QE scans are performed every few days/weeks or months, respectively. From the plots it is obvious that the lifetime of the recent MCP-PMT models has tremendously increased in comparison to former tubes (open dots at the left side of the figure).

In the ALD-coated PHOTONIS MCP-PMT (9001223) the degradation of the QE starts after 6 C/cm^2. This is seen in Fig. 1 and in the QE chart of the whole PC surface in Fig. 2 (upper right), where the left half shows a significantly reduced QE. No sign of aging is observed yet at 5 C/cm^2 in another MCP-PMT (9001332) with the same specifications [4]. In both tubes the right half of the PC is not illuminated.

In our comparative aging measurement (see Fig. 1) we have meanwhile identified three MCP-PMTs (PHOTONIS XP85112 9001223 and 9001332; Hamamatsu R10754X-07-M16M KT0001) which fulfill the PANDA requirement of an integrated anode charge of >5 C/cm^2 without a significant QE degradation. This is an important result because it implies that after several years of investigations we have finally found photon sensors that survive the high rate environment at the DIRC focal planes for at least 10 years.

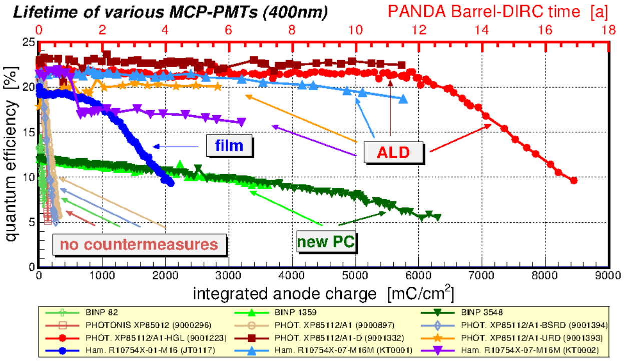

Figure 1: QE at 400 nm for old (open) and recent, lifetime-enhanced (solid dots) MCP-PMTs versus the anode charge.

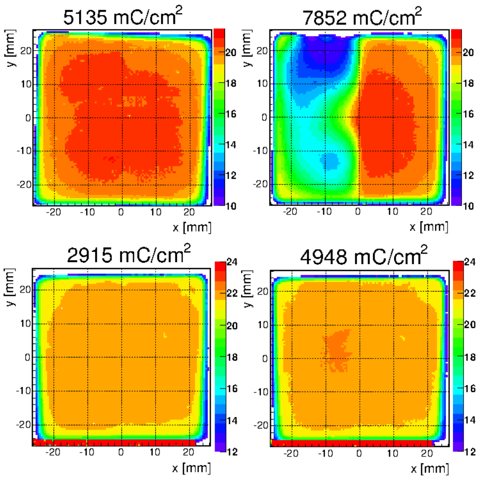

Figure 2: QE at 372 nm as a function of the PC surface for two XP85112 MCP-PMTs: 9001223 [upper row] and 9001332 [lower row]. In both tubes the right half ($x > 0$) of the PC was covered during the whole illumination.

References

[1] A. Lehmann et al., Nucl. Instr. and Meth. A 595 (2008) 173

[2] A. Lehmann et al., Nucl. Instr. and Meth. A 639 (2011) 144

[3] A. Lehmann et al., GSI Scientific Report 2010, p. 106

[4] F. Uhlig et al., doi:10.1016/j.nima.2014.11.046

---

* Work supported by GSI (contracts EREYRI1416 and ERANTO1419) and BMBF

[†] Albert.Lehmann@physik.uni-erlangen.de

DOI:10.15120/GR-2015-1-MU-HADRONS-05

Laser test stand for double-sided silicon microstrip sensors[*]

R. Schnell[†][1], *K.-Th. Brinkmann*[1], *M. Kesselkaul*[1], *B. Wohlfahrt*[1], *and H.-G. Zaunick*[1]

[1]II. Physikalisches Institut, Justus-Liebig-Universität Gießen, Heinrich-Buff-Ring 16, 35392 Gießen, Germany

Introduction

A test stand based on an infrared laser was set up as a tool for tests and verifications of double-sided silicon strip detector modules. It can be used to study prototype assemblies with silicon sensors. Furthermore, it can be used to test front-end chips for timing, pile-up behavior and rate capability. This test stand is planned to be used for quality assurance tests of modules of double-sided silicon microstrip sensors for the $\overline{\text{P}}$ANDA Micro-Vertex-Detector (MVD) [1]. Systematic and reproducible tests can be done in order to verify the full functionality prior the integration in the detector. A laser test stand enables a variety of test options while being more flexible compared to test beam times at accelerator facilities.

Laser Test Stand

The system is build around a laser with a wavelength of 1060 nm. Light of this wavelength has an attenuation length in silicon in the order of 1 mm, therefore electron-hole-pairs are created nearly uniformly inside a sensor with a thickness of several 100 μm. Together with the short pulse length of less than 200 ps (FWHM) it emulates the signal generation of a charged particle crossing a silicon detector. The external triggering of the laser with a jitter better than 40 ps and a minimum time difference of 12.5 ns between triggers allows measurements for time resolution and pile-up behavior. The intensity of the laser can be adjusted, which relates to different energy depositions. A micro-focus optic at the end of the single-mode optical fiber allows a minimum beam diameter of 10 μm. The laser is moved via an x-y-stage with a travel of 100 x 100 mm^2. It features position accuracy and repeatability better than 1 μm. An additional device allows the manual adjustment of the z-axis for focusing the laser on the sensor. The movement of the x-y-stage and the triggering of the laser is software controlled. The readout of the detector modules employs the same VME FPGA-based DAQ system [2] that is used for lab tests with radioactive sources and test beam times. Figure 1 shows a photograph of the test stand studying a double-sided silicon microstrip sensor bonded to APV25 front-end chips [3].

Figure 1: The picture shows the setup. The working area with the laser and the x-y-stage is housed in a light tight box lined with black foil. The rack below comprises laser driver, controller of the x-y-stage and auxiliary components. The readout components can be seen on the right.

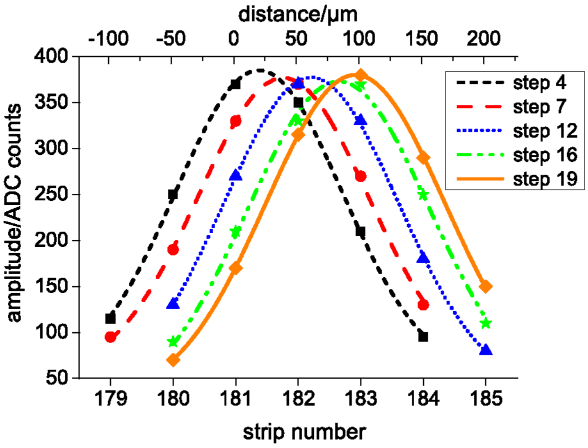

Figure 2: The plots shows the induced charge into different strips of a sensor with 50 μm strip pitch for various positions of the laser. Each curve illustrates the signal distribution in the strips at one position. Several steps with a step size of 5 μm were performed.

References

[1] $\overline{\text{P}}$ANDA Collaboration, arXiv:1207.6581v2 [physics.ins-det], November 2011.

[2] R. Schnell et al., JINST 6 (2011) C01008.

[3] L. Jones, “APV25-S1: User guide version 2.2”, RAL Microelectronics Design Group, (2001).

---

[*] This work was supported by BMBF (grant no. 05P12RGFP6), JCHP-FFE and HIC for FAIR.

[†] Robert.Schnell@exp2.physik.uni-giessen.de

DOI:10.15120/GR-2015-1-MU-HADRONS-06

Weak decays of mesons with charm and meson distribution amplitudes*

A. Schäfer[1] *and V. M. Braun*[1]
[1]Regensburg University, Regensburg, Germany

Exclusive processes and Distribution Amplitudes

The aim of this project is to analyze data which will hopefully be obtained by $\overline{\text{P}}$ANDA with first principle QCD. This chapter aims at explaining what we mean with this statement.

Although QCD is the exact theory of strong interactions and as such subject to intense investigations since decades many of its aspects are still only poorly understood. In fact, the applicability of QCD to any given problem has to be based on exact factorization proofs, Operator Product Expansion analysis (OPE) etc. Whenever it is applied to problems for which these prerequisites are not fulfilled one is only developing a model rather than performing a first principle theory calculation. This fact greatly limits the speed with which the range of phenomena accessible by state of the art QCD can grow. Presently hard exclusive reactions that can be described by Distribution Amplitudes (DAs) are one of the "new territories" in this sense.

For the heavy, potentially exotic mesons which are planned to be produced at FAIR the information one will get are primarily masses and decay characteristics for various channels. This information boils down to just a few numbers which can only characterize some parameters of DAs.

The nice thing about decay reactions for, e.g., XYZ mesons is that the relatively large charm quark mass allows to use perturbative QCD techniques, though it is not large enough to justify a purely leading twist, leading order treatment. We are working on state of the art QCD calculations taking also such corrections into account. The most important theoretical tool to do so are DAs, not to be confused with parton distribution functions (PDFs). Very roughly speaking a PDF is related to the square of a parton wave-function with all other partons as well as any transverse momentum being integrated out. Therefore, leading twist, leading order PDFs can be interpreted as probabilities. In contrast DAs are roughly speaking parton wave functions of only the leading Fock state of a hadron with any transverse momentum being integrated out. Therefore it is a wave function not a probability and not positive definite even at leading order and leading twist.

The hard scale is crucial because the coupling to all higher Fock states is suppressed by additional hard propagators, see Fig.1. To the extend that the K^- DA is known, the decay rate depends only on the D structure. In a completely analogous manner one can extract information on the structure of unknown mesons from their semi-leptonic decay rates into known hadrons and also in principle from their decay rates into pairs of known hadrons.

More formally the difference between the DAs and the more well known PDFs, GPDs, TMDs etc. can be described as follows: The latter parametrize matrix elements of the form (with two, possibly identical, hadrons H and H' with momenta P, P' and spin S, S' and some reaction-specific operator $\mathcal{O}$

$$\langle H'(P',S')|\mathcal{O}|H(P,S)\rangle \tag{1}$$

while DAs parametrize matrix elements of the form

$$\langle 0|\mathcal{O}|H(P,S)\rangle \quad . \tag{2}$$

Obviously, both types of matrix elements test the hadronic wave functions in complementary ways. One has to determine as many of them as possible to pin down the latter better and better. It is a bit of an anomaly that up to now far less theoretical effort was invested into the exploration of DAs than for PDFs, GPDs, etc. which on the other hand means that presently it is relatively easy to make progress. Technically speaking the consistent QCD treatment at the medium large energies which are typical for hadron physics is in both cases very demanding but possible.

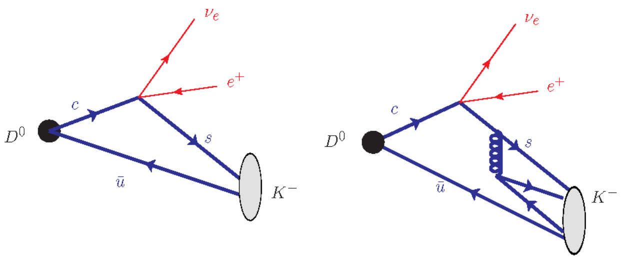

Figure 1: Contributions to the decay matrix element for $D^0 \to K^- e^+ \nu_e$.

Determination of DAs

We perform extensive calculations aiming at the systematic determination of hadron DAs, using perturbative QCD (pQCD), light-cone sum rules (LCSRs) and Lattice QCD (LQCD). To proceed, the DAs are expanded into Gegenbauer polynomials (which are the eigenfunctions of the leading order evolution equations) and the different investigations can then be related by combining all results for the expansion parameters. The resulting parametrisation provides then the input for the determination of decay rates. As

---

* Work supported by GSI F+E RSCHAE1416

DOI:10.15120/GR-2015-1-MU-HADRONS-07

we do not yet have results from the present project, which aims at describing, e.g., the semi-leptonic decay of the D_s into a pion pair, we present in the following as illustration some results from projects funded by other sources.

One of the main issues in this field are the BaBar and BELLE data on another exclusive process, namely the $\gamma^*\gamma\pi$ form factor. The experimental data favor rather strange looking pion DAs, see Fig.2, with enhancements close to the end points. The leading Fock state of a pion consists of just a quark antiquark pair with longitudinal momentum fractions x and $1-x$. Therefore, the pion DA is a function of x and the momentum scale only. The leading deviation from the asymptotic form is parametrized by the parameter a_2. A recent large scale lattice simulation of our group [2] resulted in the value $a_2^{\overline{MS}} = 0.1364(154)(145)$ where the first error is the statistical and the second the systematic error. The different curves in Fig.2 correspond to $a_2 = 0$ (green dots), $A_2 = 0.10$ (solid line) and $a_2 = 0.14$ (dashed line). Obviously we are getting close to the precision at which we will be able to settle this problem. Let us add that the analysis which resulted in the solid line in Fig.2 and which was the technically most advanced one is also compatible with $a_2 = 0.14$, i.e. from the data alone both models are admissible.

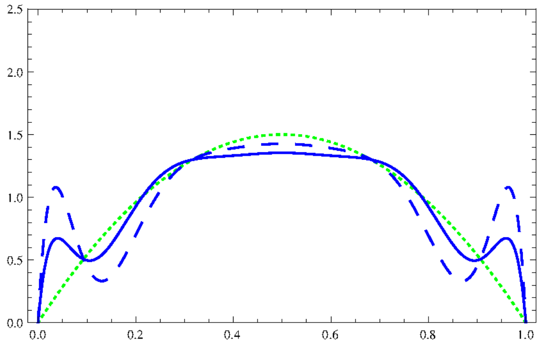

Figure 2: Pion DAs extracted from an analysis of the BaBar (dashed) and combined BaBar and Belle data in comparison to the asymptotic distribution amplitude (green dots).

We perform and performed similar analysis for the ρ, K, η and η' mesons, allowing to analyze information for all exclusive decays of new heavy meson states into these hadrons.

As another example we have calculated in [3] the branching ratios Eq.(3) showing that as soon as the experimental errors get smaller by a factor of two or so one will be able to pin down the purely gluonic contribution of the η, η' wave functions. (The experimental errors must become smaller than the potential gluonic contribution which is parametrized by the gluon Gegenbauer coefficient B_2^g.)

$$\begin{aligned}
\frac{\Gamma\left(D_s^+ \to \eta' e^+ \nu_e\right)}{\Gamma\left(D_s^+ \to \eta e^+ \nu_e\right)} &= 0.37 \pm 0.09\,(B_2^g) \pm 0.04 \\
Exp: &\ \ 0.36 \pm 0.14 \\
\frac{\Gamma\left(D^+ \to \eta' e^+ \nu_e\right)}{\Gamma\left(D^+ \to \eta e^+ \nu_e\right)} &= 0.16 \pm 0.06\,(B_2^g) \pm 0.02 \\
Exp: &\ \ 0.19 \pm 0.09 \\
\frac{\Gamma\left(B \to \eta' e^+ \nu_e\right)}{\Gamma\left(B \to \eta e^+ \nu_e\right)} &= 0.50 \pm 0.29\,(B_2^g) \pm 0.05 \\
Exp: &\ \ 0.67 \pm 0.24 \pm 0.1 \qquad (3)
\end{aligned}$$

Baryon DAs

Let us add that the same types of analysis can be performed for baryons and we do so for the complete SU(3) Octet. Though this is probably less relevant for $\overline{\text{P}}$ANDA we show the result for the DAs of the nucleon and the two lowest negative parity nucleon resonances. In this case the leading Fock state consists of three quarks with $x_1 + x_2 + x_3 = 1$ which explains the triangular shape of the plot.

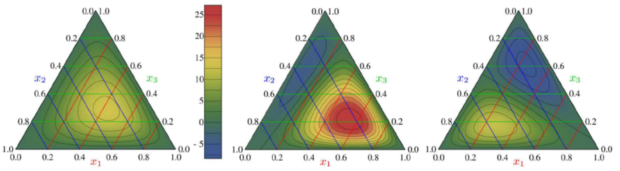

Figure 3: The nucleon, $N^*(1650)$ and $N^*(1535)$ distribution amplitude taken from [4].

Conclusions

We have tried to give a short introduction to the role the analysis of exclusive hadron decays at $\overline{\text{P}}$ANDA could play to pin down the quark gluon structure of known and new hadrons. As far as QCD is concerned all of these calculations touch the limits of what is technically feasible today and will require much more theory work to become more precise. However, what is missing most to put all of this to work is high-precision data from $\overline{\text{P}}$ANDA.

References

[1] S. S. Agaev, V. M. Braun, N. Offen and F. A. Porkert, Phys. Rev. D **86** (2012) 077504 [arXiv:1206.3968].

[2] V. M. Braun *et al.*, arXiv:1503.03656 [hep-lat].

[3] N. Offen, F. A. Porkert and A. Schäfer, Phys. Rev. D **88** (2013) 3, 034023 [arXiv:1307.2797].

[4] V. M. Braun *et al.*, Phys. Rev. D **89** (2014) 9, 094511 [arXiv:1403.4189].

Studies for the PANDA software trigger

F. Nerling[*1,2], *A. Denig*[3], *K. Götzen*[1], *D. Kang*[2], *R. Kliemt*[1], *K. Peters*[1,4], *and the PANDA Collab.*[1]
[1]GSI, Darmstadt, Germany; [2]HIM, Mainz, Germany; [3]Univ. Mainz, Germany; [4]Univ. Frankfurt, Germany

The PANDA experiment is one of the key experiments at the future FAIR facility that provides an anti-proton beam of momenta 1.5–15 GeV/c with excellent energy resolution. Using an hydrogen (proton) and various nuclear targets, PANDA will carry out a broad physics programme comprising topics of hadron spectroscopy, nucleon structure, hadron in nuclei as well as hypernuclear physics.

Given the production cross-sections for the reactions of interest either not being known precisely or being predicted by theory to be rather small (pico- to nanobarn range), the average design luminosity (for the high luminosity mode) is projected to be $L = 2 \cdot 10^{32}\mathrm{cm}^{-2}\mathrm{s}^{-1}$. The high total $\bar{p}p$ cross-section of about 60-100 mb results in an average reaction rate of $\dot{N} = 20\,$MHz, reaching peak values of up to $\dot{N} \approx 40\,$MHz. With an average event size of 10–20 kB, we expect a total raw data rate of roughly 200 GB/s. Assuming a duty cycle of 50 %, the data stream would produce 3000 PB per year to be stored, and thus the data rate has to be reduced by about a factor of 1000 in order to reduce the required storage capacity down to affordable few PB per year. Due to the similarity of the detector signatures of interesting signal and background events, a sophisticated filtering strategy has to be developed that goes far beyond conventional hardware based trigger schemes and that is based on the concept of a trigger-less read-out. This approach of continous sampling and buffering of the data, i.e. without any classical gated trigger signal, allows to pre-analyse the data in order to decide to either reject or keep events and write them to disc. Technically, the challenge is to perform a high-level reconstruction procedure online and provide the information to effectively separate signal from background events already during data taking.

Table 1: List of physics channels presently under study.

Physics topic	Reaction channel	Trigger
Electromagn.	$p\bar{p} \to e^+e^-$	$p\bar{p} \to e^+e^-$
Exotics	$p\bar{p} \to \phi\phi$	$\phi \to K^+K^-$
Charmonium	$p\bar{p} \to \eta_c\pi^+\pi^-$	$\eta_c \to K_SK^-\pi^+$
	$p\bar{p} \to J/\psi\pi^+\pi^-$	$J/\psi \to e^+e^-$
	$p\bar{p} \to J/\psi\pi^+\pi^-$	$J/\psi \to \mu^+\mu^-$
Open charm	$p\bar{p} \to D^0\overline{D^0}$	$D^0 \to K^-\pi^+$
	$p\bar{p} \to D^+D^-$	$D^+ \to K^-\pi^+\pi^+$
	$p\bar{p} \to D_s^+D_s^-$	$D_s^+ \to K^+K^-\pi^+$
Baryons	$p\bar{p} \to \Lambda\bar{\Lambda}$	$\Lambda \to p\pi^-$
	$p\bar{p} \to \Lambda_c\bar{\Lambda}_c$	$\Lambda_c \to pK^-\pi^+$
Background	$p\bar{p}$ generic (DPM)	–

The present studies are restricted to a subset of 10 physics reaction channels (Tab. 1), still covering the main physics topics addressed by PANDA, at 4 different centre-of-mass energies, covering the whole range of about 2–5.5 GeV/c accessible by PANDA. In total a set of ∼150 observables has been explored and those, which allow for an efficient signal to background separation, are applied in addition to the initial cuts on the corresponding invariant masses. The studies were carried out using events generated by a simple toy Monte Carlo and compared to the results obtained from the full detector simulation using `PandaRoot`. As optimisation approach, two strategies have been realised, optimisation for high signal detection efficiencies and for strong background suppression.

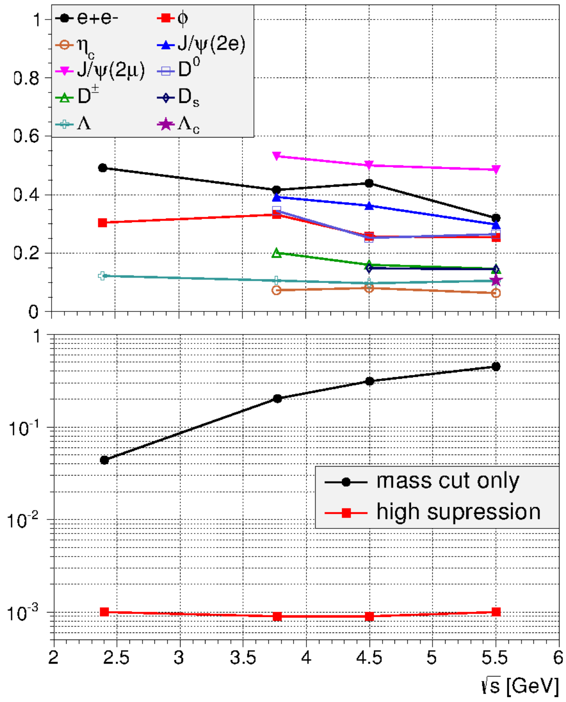

Figure 1: Compilation of present results: Achieved signal detection efficiencies *(top)* when optimising for a 10^3 background reduction factor *(bottom)*.

The present results based on the full detector simulation are summarised for the ansatz of optimisation for background suppression in Fig. 1. The achieved signal efficiencies vary from about 6–50 %, strongly depending on the given physics channel, while the intended background suppression factor is met over the full range of centre-of-mass energies. More realistic results will come soon, and even though more work is needed also on the hardware side, these first preliminary results serve as a proof of principle.

---

[*] F.Nerling@gsi.de

DOI:10.15120/GR-2015-1-MU-HADRONS-08

Search for charmonium-like exotic states with the BESIII experiment

F. Nerling[1,2], *K. Götzen*[1], *R. Kliemt*[1], *K. Peters*[1,3], *and the BES-III collaboration*[1]
[1]GSI, Darmstadt, Germany; [2]HIM, Mainz, Germany; [3]Univ. Frankfurt, Germany

The BESIII experiment [1] at the BEPCII e^+e^- collider in Beijing, China, started data taking in 2009. Large data samples at centre-of-mass energies corresponding to J/ψ, ψ' and $\psi(3770)$ resonances have been recorded. More recently, data were also taken between about 4 GeV and 4.4 GeV, allowing for the study of the so-called XYZ states. Recent discoveries of charged states in the charmonium mass region – ten years after the discovery of the $X(3872)$ by Belle – make this field a very active one that will continue to be very exciting until the nature of these new states will be understood. One highlight is the recent discovery of the $Z_c(3900)^\pm$ state [2] by BESIII, confirmed by Belle; it is manifestly an exotic state.

For understanding the nature, a precise measurement of the lineshapes is needed as it is only possible in a direct formation experiment. The physics analysis of BESIII data offers an excellent opportunity for hadron spectroscopy, in particular for the search for further charmonium-like (exotic) XYZ states. In contrast to the $p\bar{p}$ annihilation experiment PANDA/FAIR, only $J^{PC}=1^{--}$ mesons can be directly produced in formation at BESIII, whereas other J^{PC} states can only be studied in production reactions with additional recoil particles being produced. Before PANDA will help solving the puzzle of the new XYZ states by precise measurements of the lineshapes, there is not only the great chance to complete the observation of entire multiplets and to explore further decay channels with BESIII, but also to bridge the period until PANDA will start data taking. Already analysing similar but complementary real data from BESIII to keep and gain important experience on this newly very active field of research, is a perfect preparation of physics analysis of PANDA data, including the developement of software analysis tools.

The first charged charmonium-like state was discovered by BESIII in the reaction $e^+e^-\to J/\psi\pi^+\pi^-$ at a centre-of-mass energy $\sqrt{s}=4.26\,\mathrm{GeV}$, corresponding to the the $Y(4260)$ resonance. The signal was observed in the $J/\psi\pi^\pm$ invariant mass distributions [2], leading to the direct formation and subsequent decay chain $e^+e^-\to Y(4260)$, with $Y(4260)\to Z_c(3900)^\pm\pi^\mp$, and $Z_c(3900)^\pm\to J/\psi\pi^\mp$. Importantly, the $Z_c(3900)^\pm$ is a charged state while it couples to a $c\bar{c}$ state. It can thus not be a charmonium state; speculations comprise interpretations as a tetraquark state or a hadronic molecule.

Preliminary BESIII results show also a significant and similar structure in the $J/\psi\pi^0$ invariant mass measured in the isospin-partner channel $e^+e^-\to J/\psi\pi^0\pi^0$. Evidence for the neutral partner of the $Z_c(3900)^\pm$ in the CLEO-c data was published [3]. The determination of the spin-parity is needed for the interpretation, especially if the charged and neutral partners have the same, the corresponding isospin triplet would be established. Further decay channels are under investigation. Replacing the J/ψ by an h_c, a clean narrow structure has consistently been observed in the invariant mass of both, $h_c\pi^+$ (Fig. 1, top) and $h_c\pi^0$ (Fig. 1, bottom), whereas the masses obtained from the fits of about 4.02 GeV/c^2 are consistent within uncertainties [4]; this state is referred to the $Z_c(4020)$. Another decay channel of the $Z_c(3900)$ that we started to analyse at GSI is $\eta_c\pi$. Due to the low cross-section distributed over various decay modes, all 16 hadronic final states need to be included in our analysis – first results will come soon.

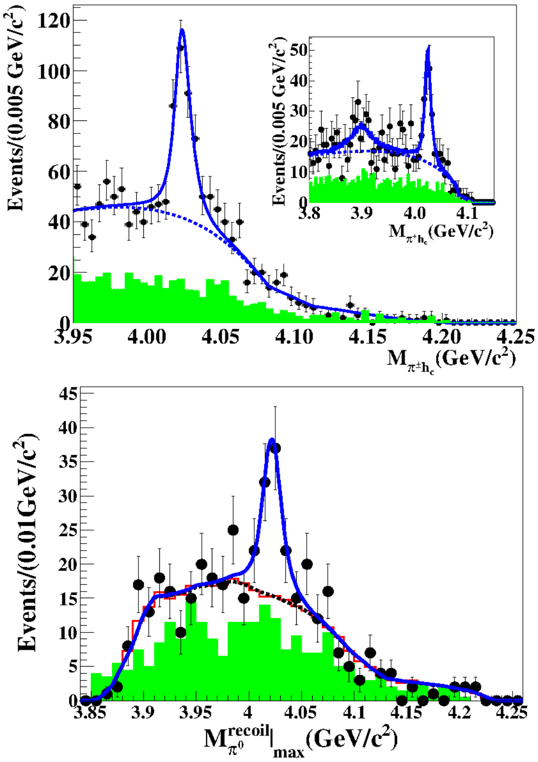

Figure 1: Recent observation of the new charged *(top)* and neutral *(bottom)* narrow state referred to the $Z_c(4020)$ [4].

References

[1] BESIII Collaboration, M. Ablikim *et al.*, Nucl. Instr. Meth. **A614** (2010) 345.

[2] BESIII Collaboration, M. Ablikim *et al.*, Phys. Rev. Lett. **110** (2013) 252001; Belle Collaboration, Z. Liu *et al.*, Phys. Rev. Lett. **110** (2013) 252002.

[3] T.Xiao, *et al.*, Phys. Lett. **B727** (2013) 366; 1304.3036.

[4] BESIII Collaboration, M. Ablikim *et al.*, Phys. Rev. Lett. **111** (2013) 242001; Phys. Rev. Lett. **113** (2014) 212002.

DOI:10.15120/GR-2015-1-MU-HADRONS-09

DIRC-based PID for the EIC central detector*

R. Dzhygadlo[†1], *K. Peters*[1,2], *C. Schwarz*[1], *and J. Schwiening*[1]
[1]GSI, Darmstadt, Germany; [2]Goethe Universität Frankfurt, Germany

The planned Electron-Ion Collider (EIC) is expected to be the next large accelerator facility for high energy and nuclear physics in the USA. This unique, high luminosity polarized collider will address many questions about QCD and strong interaction physics [1]. The central detector of the EIC (see Fig. 1) will have a general purpose character that should offer high performance for a wide range of processes and kinematics.

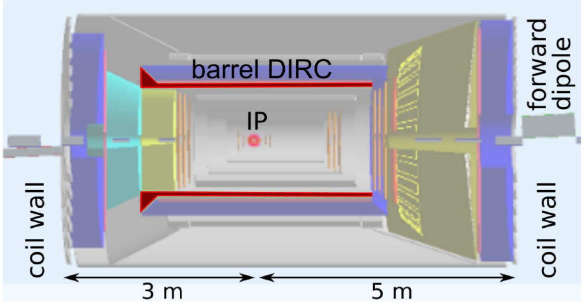

Figure 1: The central detector concepts developed at JLab and BNL. The Barrel DIRC location is highlighted in red.

One of the key requirements for the central detector is to provide radially compact Particle Identification (PID) (e/π, π/K, K/p) over a wide momentum range. It is expected that the PID system will need to include one or more Cherenkov counters to achieve this goal. With a radial size of only a few cm, a DIRC counter (Detector of Internally Reflected Cherenkov light) is potentially a very attractive option. The BABAR DIRC has proven to be robust, easy to operate, and to provide clean separation between pions and kaons for momenta up to about 4 GeV/c. Several new DIRC projects (Belle II, PANDA, LHCb, GlueX) are being prepared around the world. A future EIC DIRC can benefit from many aspects of these R&D efforts, but it also provides its own unique set of challenges and priorities, in particular due to the higher momenta of the produced particles compared to the other DIRC counters, and because of the impact of the DIRC readout volume on the neighboring detector components.

The *DIRC@EIC* R&D Collaboration was formed by groups in the United States and Germany[1] in 2011 with funding from DOE. The goal is to investigate ways to extend the momentum range of clean pion/kaon separation of DIRC counters from 4 GeV/c, the current state of the art, to about 6 GeV/c, required for the EIC detector. Possible design improvements include a complex focusing system, multi-anode sensors with smaller pixels, a time-based reconstruction algorithm, and chromatic dispersion mitigation using fast photon timing.

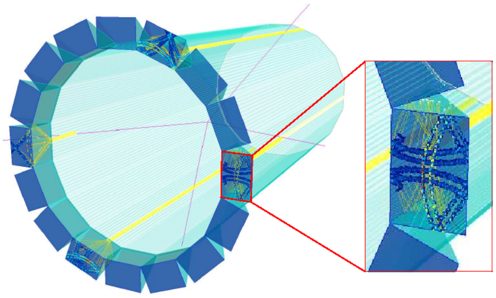

Figure 2: Geant simulation of an EIC DIRC design with narrow bars and compact prisms. The zoom shows the accumulated hit pattern for 4 GeV/c momentum kaons.

Detailed detector simulations, using Geant [2] and standalone ray-tracing software, are used to optimize the design configuration of the DIRC counter in terms of the performance and the best integration with the EIC detector. Fig. 2 shows the Geant simulation for the EIC DIRC in a geometry with narrow bars as radiators and compact fused silica prism as expansion volumes.

Figure 3: Photo of the novel 3-component lens prototype.

The first example of a real-world application of these new design ideas is the prototype of an improved multi-component spherical lens (see Fig. 3) which was built and tested in the Barrel DIRC prototype in the summer of 2014 with a pion beam at GSI. The analysis of the data is still ongoing, first results indicate that the new lens offers a significant improvement over simple two-component lenses. This result is of particular interest to the PANDA Barrel DIRC design, demonstrating the synergies of the two projects.

References

[1] A. Accardi, et al., arXiv:1212.1701 [nucl-ex]

[2] S. Agostinelly, et al., Nucl. Instr. and Meth. Phys. Res. Sect. A 506 (2003) 250; J. Allison, et al., Nuclear Science, IEEE Transactions **53** (2006) 270-278.

---

[*] Work supported by DOE, Generic Detector R&D for an Electron Ion Collider

[†] R.Dzhygadlo@gsi.de

[1] University of South Carolina, GSI Helmholtzzentrum für Schwerionenforschung GmbH, The Catholic University of America, Old Dominion University, Thomas Jefferson National Accelerator Facility.

DOI:10.15120/GR-2015-1-MU-HADRONS-10

PWA study of cusp in p + p → p + K^+ + Λ with Flatté distribution*

S. Lu[1,2], *R. Münzer*[1,2], *E. Epple*[1,2], *L. Fabbietti*[1,2], *J. Ritman*[3], *E. Roderburg*[3], *F. Hauenstein*[3],
M. Maggiora[4], *and Hades and FOPI Collaboration*
[1]Physik Department E12, Technische Universität München; [2]Excellence Cluster "Origin and Structure of the Universe",
85746 Garching, Germany; [3]Forschungszentrum Jülich; [4]University of Turino

In the last years, strangeness production in nucleon-nucleon collisions has attracted interest for a number of reasons. Within a new analysis approach, a combined PWA analysis of the HADES and FOPI data togehter with data sets measured at the DISTO and COSY-TOF experiments will be performed. The description of all the production channels, that can contribute to the p K^+ Λ final state, requires a special analysis framework. For this analysis, the Bonn-Gatchina Partial Wave Analysis (PWA) framework is used [3]. In this framework the transition amplitude from an initial wave to a final state is parameterized as a function of the energy and phase. The wave functions of different transitions with the same quantum numbers can mix, which leads to interference. Since the amplitudes and phase parameters of these transitions are not known, they have to be fitted by the PWA[4].

In addition to the Λp FSI and N^* resonance excitations, a pronounced narrow structure is observed in the Dalitz plot and in its projection on the pΛ-invariant mass. There is, a peak structure appears at the p + p → N + K^+ + Σ threshold and is interpreted as ΣN cusp effect.

The figure shows the spectra of the this pΛ invariant mass, taken at the COSY-TOF spectrometer at a beam energy of 2.28 GeV[1]. A peak structure appeared in this spectra. In this work an incoherent sum of different contributions with description by the full MC simulation was applied.

For a description of the experimental data by using the BG-PWA, the first approach was to use a Breit-Wigner parametrization. The figure 2 shows the spectra of pΛ invariant mass with the experimental data taken at COSY-TOF at center of mass energy of 2.16 GeV together with the PWA results. The two distributions are in good agreement. To improve the description in a more physical way, a Flatté parametrization of the cusp signal is more suited. This also takes into account the coupling strength of Λp and Σp.

For the Λp and Σp cases the Flatte' parametrization has the following mathematical expression[1]:

$$\frac{d\sigma}{dM_{\Lambda p}} \sim \frac{\Gamma_{\Lambda} p}{|m_R{}^2 - m_{\Lambda p}{}^2 - i m_R{}^2(\Gamma_{\Lambda} p + \Gamma_{\Sigma} p)|^2} \qquad (1)$$

$$\Gamma_{\Lambda p} = g_{\Lambda p} * q_{\Lambda p}, \Gamma_{\Sigma p} = g_{\Sigma p} * q_{\Sigma p} \qquad (2)$$

In our work, we are using PWA to simulate the cusp structure and to better understand this peak structure.

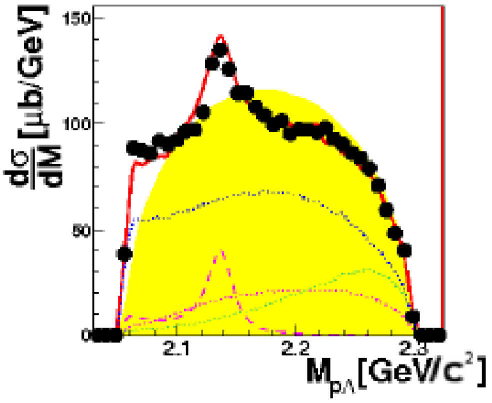

Figure 1: Differential cross-section distributions of the invariant-mass systems of pΛ.The shaded areas indicate phase-space distributions. The dotted lines the contributions of N^* resonances. The dashed line the ΣN cusp effect and the solid line the full MC simulation[1].

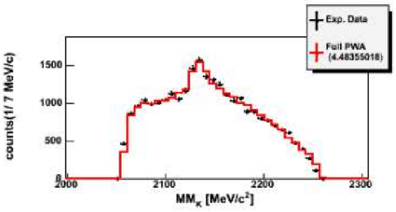

Figure 2: pΛ invariant mass .The black dots are experimental results and red solid curve corresponds to the BG-PWA using Breit-Wigner parametrization.

References

[1] S.Abd El-Samad *et al.*, arXiv nucl-ex (2012) 1206.0426

[2] S. M. Flatté, Phys. Lett. B 63 (1976) 224

[3] A.V. Sarantsev et. al., Eur.Phys.J. A25,2005,441-453

[4] R. Muenzer, GSI report (2015)

[5] Philipp Klose, Bachelor thesis, TUM,(2014)

---

* Work supported by DFG Projekt FA 898/2-1

DOI:10.15120/GR-2015-1-MU-HADRONS-11

Development of the Germanium detector array for $\overline{\rm P}$ANDA*

M. Steinen†[1], *S. Bleser*[1], *M. Martinez Rojo*[1], *J. Pochodzalla*[1,2], *A. Sanchez Lorente*[1], *J. Gerl*[3], *I. Kojouharov*[3], *and J. Kojouharova*[4]

[1]HI Mainz, Mainz, Germany; [2]Institut für Kernphysik, Mainz, Germany; [3]GSI, Darmstadt, Germany; [4]THM Friedberg, Friedberg, Germany

The $\overline{\rm P}$ANDA experiment aims at the high resolution γ-spectroscopy of double Λ hypernuclei. For this purpose a dedicated electro-mechanically cooled Germanium detector array will be placed inside the $\overline{\rm P}$ANDA barrel spectrometer is needed.

The positioning of the detector at backward polar angles does not avoid the irradiation by still a large particle background. Therefore, in order to evaluate the effect of this irradiation a test experiment at COSY in Jülich was performed. A 5 cm thick carbon target was bombarded by a proton beam with a momentum of 2.78 GeV/c and the generated secondaries were used to irradiate an electro-mechanically cooled single crystal detector prototype located at a polar angle of 120°. The particle spectrum in this angular range is comparable to the expected background seen by the germanium array in $\overline{\rm P}$ANDA experiment conditions.

The spectrum of a ^{60}Co source was measured during spill pauses to check the influence of the irradiation on the peak shape. Figure 1 shows the broadening of the line shape due to the increasing radiation load of the crystal.

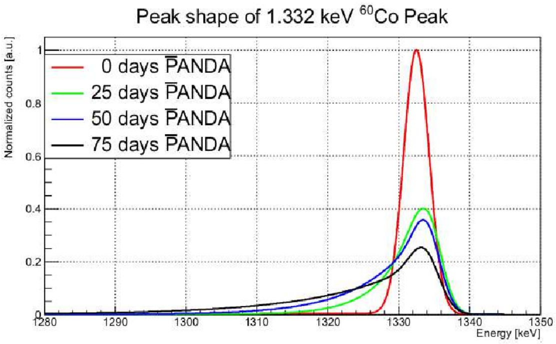

Figure 1: Higher radiation of the germanium detectors results in a broader, non-gaussian peak shape

A detailed analysis of the data shows a non-linear correlation between the calculated risetime and the energy of the signal of γ which depends on the irradiation. This is shown in figure 2 and will allow to correct at least partially the degradation of the peak shape. The analysis of this is ongoing.

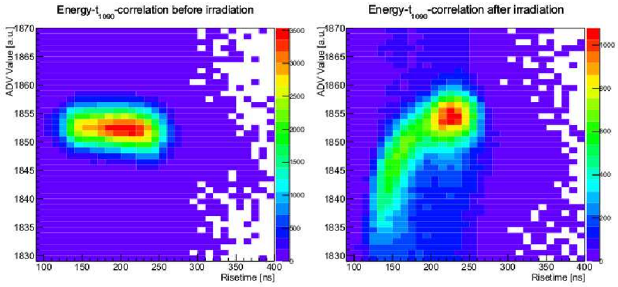

Figure 2: Comparison of the risetime energy correlation before (left) and after (right) the irradiation.

Simultaneously, the development of a triple crystal prototype is pursued (figure 3). The cryostat of this detector will be optimized using the latest thermal simulation results[1]. A new Cooler[2] is tested which might offer more cooling power while being small enough to fit inside the $\overline{\rm P}$ANDA barrel spectrometer.

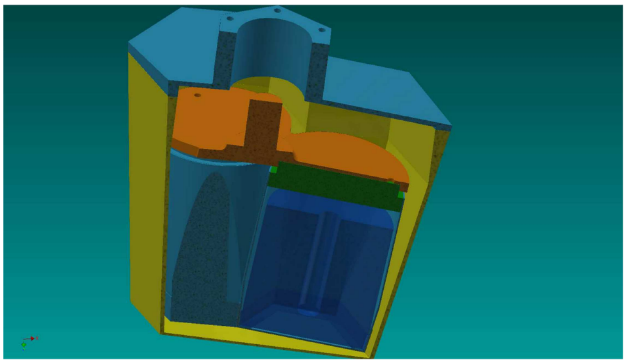

Figure 3: CAD drawing of the triple crystal prototype in development

Additionally the tests in Jülich revealed that an actively resetting preamplifier for the germanium is needed. This will be implemented in future prototypes and the existing prototype will be modified accordingly for further test beams in 2015.

References

[1] J. Kojouharova, "Optimization of electrically cooled complex HPGe Detector" http://www.kph.uni-mainz.de/Dateien/Waermerechnungen_Zwischenbericht2.pdf

[2] SUNPOWER CryoTel CT Datasheet http://sunpowerinc.com/download/cryotel-ct-datasheet-pdf/

---

* Work supported by European Community Research Infrastructure Integrating Activity 'Study of Strongly Interacting Matter' HadronPhysics3 (SPHERE) under the FP7, GSI and HI Mainz.

† steinen@kph.uni-mainz.de

DOI:10.15120/GR-2015-1-MU-HADRONS-12

The primary and secondary target for the hypernuclear experiment at $\overline{\mathrm{P}}$ANDA*

S. Bleser†[1], *F. Iazzi*[2], *M. Martinez Rojo*[1], *J. Pochodzalla*[3], *A. Sanchez Lorente*[1], *and M. Steinen*[1]
[1]Helmholtz-Institut Mainz, Germany; [2]Politecnico di Torino and INFN, Sez. di Torino, Italy; [3]Institut für Kernphysik, Johannes Gutenberg-Universität Mainz, Germany

Gamma spectroscopy of double Λ hypernuclei will be one of the main topics addressed by the $\overline{\mathrm{P}}$ANDA experiment at the FAIR facility at Darmstadt. For this project a dedicated hypernuclear detector setup will be installed. In addition to the general purpose of the $\overline{\mathrm{P}}$ANDA detector it consists of a primary nuclear target for the production of Ξ^-+ $\bar{\Xi}$ pairs, a secondary active target for the formation of hypernuclei and the identification of associated weak decay pions as well as a germanium detector array to perform high precision γ spectroscopy.

The primary reactions $\overline{p}$ on a ^{12}C nucleus were simulated in several runs of GiBUU calculations to get a realistic momentum distribution of the Ξ^-. In the experiment a thin diamond filament will be used to produce those low momentum Ξ^-. For the positioning of the primary filament target in the beam halo a stage with piezo motors for a two-dimensional motion was designed and is currently under construction, fig. 1. The mounting of five linear piezo motors equipped with targets guarantees an easy replacement in the case that a filament breaks. The specifications of the linear motors could be confirmed in experimental tests and their functionality in vacuum and after irradiation during a beam time at COSY in Jülich was validated.

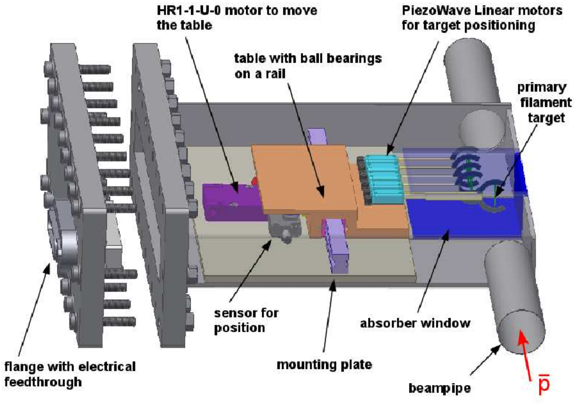

Figure 1: Vacuum chamber with target mechanics.

In order to stop the Ξ^- hyperons and track pions from the decay of the produced double hypernuclei, the secondary target is composed as a compact structure of silicon microstrip detectors and absorber material. In the area of the sensor layers an absorber window is inserted to the target chamber which also serves as first volume to decelerate and stop the Ξ^-, fig. 2. Stability and material tests were carried out for sheets of B_4C and CFC placed to a target chamber frame.

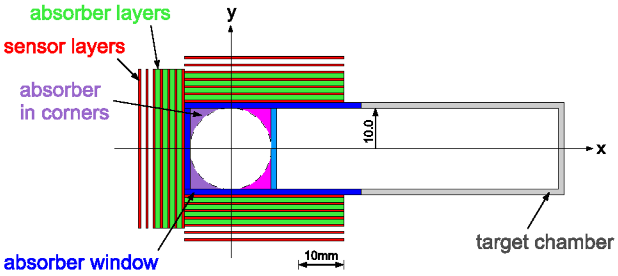

Figure 2: Arrangement of the secondary target layers in the x-y plane which is orthogonal to the beam direction.

In order to optimize the geometry of the secondary target, the stopping probability of Ξ^- hyperons and the reconstruction accuracy of weak decay pions were studied in detailed simulations. The $\Lambda\Lambda$ hypernuclei are created where the Ξ^- are stopped in the absorber volumes, fig. 3 (left). The momenta of the weak decay pions are reconstructed in the sensor layers. As one example the summed pion spectrum from the decay

$$ {}^{11}_{\Lambda\Lambda}B \longrightarrow {}^{11}_{\Lambda} B + \pi_1^- \longrightarrow {}^{11} C + \pi_2^- + \pi_1^- \qquad (1) $$

is shown in fig. 3 (right).

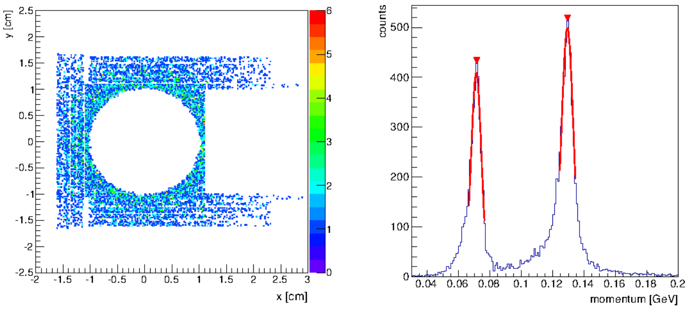

Figure 3: Simulation results of Ξ stopping and π tracking.

The resolution for the higher and lower momentum is 6.7% and 10.7%, rspectively. For a single pion a reconstruction efficiency of 58.6% was achieved.

---

* Work supported by European Community Research Infrastructure Integrating Activity 'Study of Strongly Interacting Matter' HadronPhysics3 (SPHERE) under the FP7, GSI and HI Mainz.

† bleser@kph.uni-mainz.de

DOI:10.15120/GR-2015-1-MU-HADRONS-13

Search for η' mesic nuclei by (p,d) reaction at FRS*

Y. K. Tanaka[1] *and the η-PRiME collaboration*
[1]The University of Tokyo, Tokyo, Japan

We report an inclusive measurement of the ^{12}C(p,d) reaction around the η' emission threshold aiming to search for η' meson-nucleus bound states (η' mesic nuclei) [1]. The large mass of the η' meson is attributed to the $U_A(1)$ anomaly effect, which contributes to the η' mass only with spontaneous and/or explicit breaking of chiral symmetry [2, 3]. In a high density medium, due to partial restoration of chiral symmetry, the η' mass is theoretically expected to be reduced [2]. This leads to an attraction between η' and a nucleus and to the possible existence of η' mesic nuclei [4].

In August 2014, we performed a pilot experiment to inclusively measure the missing-mass spectrum of the ^{12}C(p,d) reaction using a 2.5 GeV proton beam accelerated by SIS 18. The proton beam impinged on a carbon target to produce η' mesic states. The momentum of the ejectile deuteron was analyzed by the FRS to obtain the missing mass of the reaction.

The experimental setup at the FRS is shown in Fig.1. The proton beam with an intensity of about 10^{10}/s was incident on a 4 g/cm^2 thick carbon target. A newly-developed ion optics with a dispersive focal plane at S4 was applied to the FRS so that the momentum of the deuteron can be derived from a measured position at the S4 focal plane. Multi-wire drift chambers (MWDCs) and TPCs were used to measure the particle track, and scintillation counters (SC2H, SC2V, SC41, SC42) were used for time-of-flight (TOF) measurements. Cherenkov counters (mini-HIRAC, HIRAC, TORCH) were installed to tune a DAQ trigger.

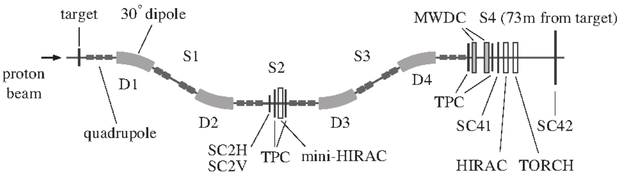

Figure 1: A schematic view of the experimental setup at the FRS.

At the S4 focal plane, protons are observed as background with a rate of about 2×10^5/s, while the rate of the deuterons is about 1×10^3/s. The deuterons are identified by the TOF between S2 and S4, since the velocities of the deuterons ($\beta_d \sim 0.84$) are different from those of the protons ($\beta_p \sim 0.95$). At the trigger level, about 99.5 % of the protons are rejected by a DAQ trigger which requires coincidence of the scintillator signals at S2 and at S4 with a time difference corresponding to the deuterons. The remaining 0.5% is due to two or more than two accidental protons which can trigger the DAQ. In the offline analysis, almost all the multi-proton events are removed by selecting single pulses in the scintillator signals recorded by a waveform digitizer.

For the calibration of the spectrometer, the $d(p,d)p$ elastic scattering was measured using a 1.6 GeV proton beam and a CD$_2$ target. Figure 2 shows the position and the angle measured by the MWDCs overlaid for five scaling factors for the FRS magnetic fields. Ion-optical parameters (focus, dispersion, and higher-order aberrations) are determined by these measurements. Moreover, from the widths of the elastic peaks, the missing-mass resolution in the production measurement is evaluated to be about 2 MeV/c^2 (σ), which is sufficiently smaller than the expected natural width of the η' mesic nuclei.

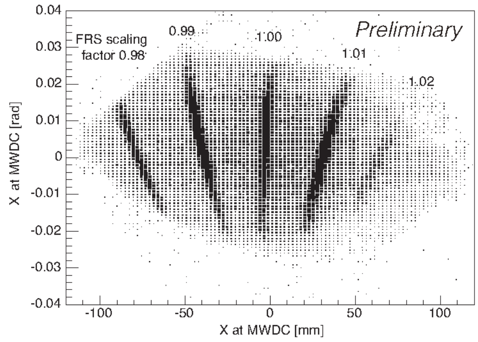

Figure 2: The horizontal position and angle measured by the MWDCs in the calibration. The figure is overlaid for five scaling factors of the FRS magnetic fields.

The measurement of the ^{12}C(p,d) reaction was performed for about 75 hours. The region of the excitation energy from -90 MeV to +40 MeV from the η' production threshold was investigated by scaling the FRS magnetic fields from 0.98 to 1.02. High statistical sensitivity was achieved by accumulating about (5-10)$\times10^6$ deuterons for each FRS setting. The analysis of the missing-mass spectra is presently ongoing.

For FAIR, we plan a semi-exclusive measurement of the (p,dp) reaction by tagging protons emitted in the decay of the η' mesic nuclei. An inclusive measurement of the (p,d) reaction with better statistics is planned as well.

References

[1] K. Itahashi *et al.*, Prog. Theor. Phys. **128**, 601 (2012).
[2] D. Jido *et al.*, Phys. Rev. C **85**, 032201(R) (2012).
[3] S. H. Lee and T. Hatsuda, Phys. Rev. D **54**, 1871 (1996).
[4] H. Nagahiro *et al.*, Phys. Rev. C **87**, 045201 (2013).

---

* The experiment was performed in the framework of the Super-FRS collaboration for FAIR.

DOI:10.15120/GR-2015-1-MU-HADRONS-14

Optical properties of the PANDA barrel DIRC prototype radiator bars*

M. Krebs†[1,2], *G. Kalicy*[1,2,3], *K. Peters*[1,2], *C. Schwarz*[2], *and J. Schwiening*[2]
[1]GSI, Darmstadt, Germany; [2]Goethe-Universität, Frankfurt, Germany; [3]now at Old Dominion University, Norfolk, Virginia, USA

The PANDA experiment at the Facility for Antiproton and Ion Research in Europe (FAIR) at GSI, Darmstadt, will study fundamental questions of hadron physics and QCD. The Barrel DIRC (**D**etection of **I**nternally **R**eflected **C**herenkov light) is a fast Ring Imaging Cherenkov counter, which will provide hadronic particle identification (PID) in the central region of the PANDA target spectrometer. In order to meet the PID requirements, the Barrel DIRC has to provide precise measurements of the Cherenkov angle, which is the crucial quantity for the identification of traversed particles. The Cherenkov photons propagate through the radiators by total internal reflection until they reach the detection plane, which is equipped with optical sensors. The radiators, long rectangular bars made from synthetic fused silica, have to meet very strict optical and mechanical requirements. Properties like squareness and parallelism of the sides, very smooth polished surfaces, and sharp corners are of critical importance to ensure that the Cherenkov photons reach the optical sensors without angular distortions.

A motion-controlled system using lasers with three different wavelengths (an additional UV laser will be added later), shown in Fig. 1, was set up in the new DIRC optics lab to measure important radiator quantities like transmittance and reflectivity.

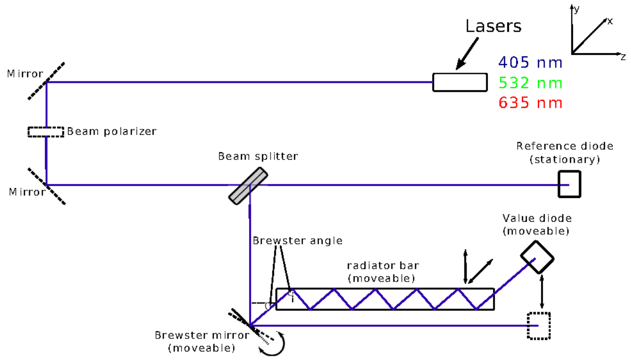

Figure 1: Schematic drawing of the current setup in the DIRC optical lab.

The laser beam enters the radiator at Brewster angle to minimize the reflected intensities of the polarized laser light at the bar ends. Depending on length and orientation of the bar the beam is internally reflected up to 31 times until it exits the bar and hits the (value) photodiode. The second (reference) diode is used to correct for laser intensity fluctuations. The transmission T is given as the double ratio of the intensities recorded by the value and reference diodes with and without the laser passing through the bar. The coefficient of total internal reflection R is calculated as $\mathsf{T} = \mathsf{R}^\mathsf{N} \cdot \exp\left(-\frac{\mathsf{L}}{\Lambda}\right)$, where N is the number of internal reflections, Λ the attenuation length of fused silica at this wavelength (determined in a separate measurement in the same setup), and L the optical pathlength inside the bar. The calculated transmission values are shown as a matrix plot in Fig. 2.

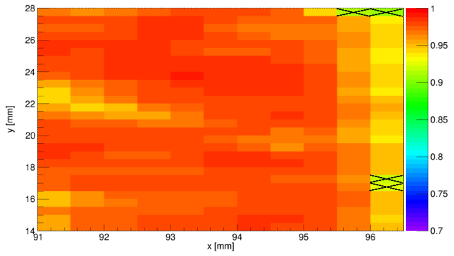

Figure 2: Transmission matrix for a radiator bar made by Schott-Lithotec. The black crosses mark measurements for laser locations that deviate more than 3 σ from the mean transmission value. The values on the X- and Y-axis represent the positions of the linear motors, which move the radiator.

The areas with smaller transmission values are the result of small imperfections of the bar and surface pollution. The beveled edges of this particular bar can lead to a diffusion of the laser beam when it exits the radiator bar near the edge, causing an intensity loss on the photodiode, leading to drop of the calculated transmission. The measured mean transmission value is $T = 0.975 \pm 0.005$.

The setup, based on a smaller system designed for the tests of shorter bars [1, 2], was installed and commissioned in the fall of 2014, including a detailed study of the systematic uncertainties. The system is now ready for the evaluation of a number of prototype radiator bars, made by different manufacturers, to determine if their fabrication processes meet the PANDA Barrel DIRC requirements.

References

[1] R. Hohler, “Prototyp-Radiatoren eines Barrel-DIRC für das PANDA-Experiment”, PhD thesis, Frankfurt, Germany, 2011

[2] G. Kalicy, “Optical Properties of Radiators for the PANDA Barrel DIRC”, N14-156, IEEE, Anaheim, USA, October 2012

---

* Work supported by EU FP7 grant, contract no. 227431, HadronPhysics2, and HGS-HIRe

† m.krebs@gsi.de

DOI:10.15120/GR-2015-1-MU-HADRONS-15

First beamtime results for PANDA EMC barrel prototype Proto 120*

P.Wieczorek[1], *H.Flemming*[1], *and the FAIR@GSI project*[1]
[1]GSI, Darmstadt, Germany

Introduction

In 2014 the PANDA Barrel EMC prototype Proto 120 was tested during a beamtime at MAMI in Mainz. The mechanical design and construction was done by IPN in Orsay. The carbon alveoles and associated tools were produced by the laboratory of IHEP in Russia. The KVI group in Groningen designed and built the differential line driver. GSI delivered the charge sensitive preamplifier ASICs (APFEL ASIC [1]) with rigid flex PCBs and the signal distributor boards which was developed for PANDA. The integration of the components, the cooling setup and the operation of the prototype during the beamtime was done by the II. Physikalisches Institut of the Giessen University. The goal of the beamtime was to identify the system energy resolution with particular focus on the APFEL - ASICs developed at GSI.

Readout Electronics

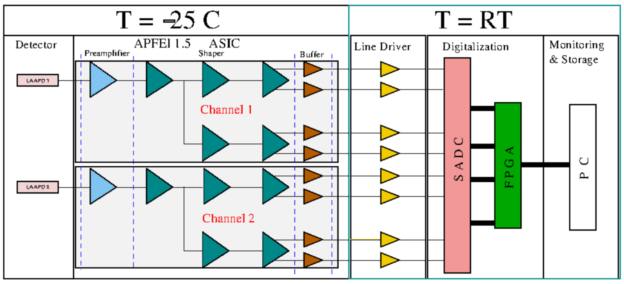

Figure 1: Readout architecture for each crystal of the EMC prototype Proto120.

Figure 1 shows the used readout architecture. Each detector crystal is covered by two large area APDs (LAAPDs) read out by the APFEL 1.5 ASIC. For better resolution the crystals, LAAPDs and the ASICs were cooled down to $T = -25°C$. The differential output signals from the ASIC were buffered with the 100 Ohm line driver and digitized by the sampling ADC (SDAC). The triggered events can be monitored online and are stored for a detailed analysis.

Measured Results

For the first test of the PANDA Barrel Proto 120 only small matrix of 3 × 3 crystals was assembled and measured. After analysis the detailed results were presented at the workshop in Rauischholzhausen by C.Rosenbaum from Giessen University [2].

The focus was to determine the energy resolution as a function of the injected energy. Tagged photons with known energies were used to calibrate each crystal first. Accordingly the beam was injected to the central crystal and the data of the hole matrix was read out with the in figure 1 presented architecture. Unfortunately two crystal readouts were not working. Figure 2 shows a comparison between the latest measurement and the results of the former test setup Proto 60. To take the two missing crystal readout into account the corresponding channels have been masked in the analysis of the Proto 60 data.

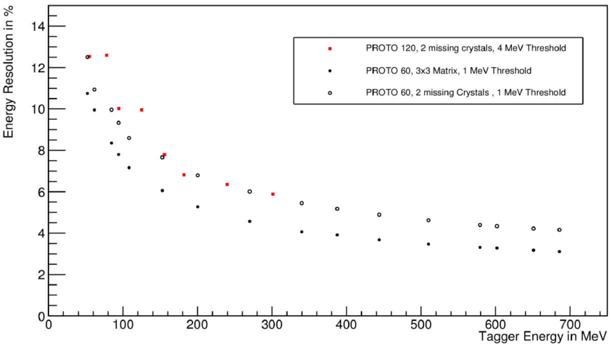

Figure 2: Energy resolution as a function of tagger energies for different PANDA EMC prototypes [2].

The different setups show an equivalent energy resolution. To improve the setup performance of Proto120 a new riged Flex PCB with electrical modification concerning detector biasing and shielding was developed and produced for the next beamtime.

Summary and Outlook

After the successful beamtime 2014 an additional beamtime in spring 2015 is forseen to measure a complete working 3 × 3 and additionaly a 4 × 4 matrix. Afterwards the final decision for the ASIC mass production will be fixed.

References

[1] P. Wieczorek and H. Flemming, "Low Noise Preamplifier ASIC for the PANDA EMC", IEEE Nuclear Science Symposium 2010, Knoxville, USA, NSS-N47-74, Published in NSS/MIC, 2010 IEEE

[2] C. Rosenbaum, "Status on PROTO 120", EMC Workshop Rauischholzhausen, 24 November 2014

---

* Work supported by EU (contract number: RII3-CT-2004-506078) cooperation with FAIR@GSI PSP code:14110.

DOI:10.15120/GR-2015-1-MU-HADRONS-16

Performance of the PANDA barrel DIRC prototype in a pion beam at GSI*

C. Schwarz†[1], *R. Dzhygadlo*[1], *A. Gerhardt*[1], *K. Goetzen*[1], *G. Kalicy*[1,2,3], *M. Krebs*[1,2], *H. Kumawat*[1,4], *D. Lehmann*[1], *M. Patsyuk*[1,2], *K. Peters*[1,2], *G. Schepers*[1], *J. Schwiening*[1], *M. Traxler*[1], and *M. Zühlsdorf*[1,2]

[1]GSI, Darmstadt, Germany; [2]Goethe Universität Frankfurt, Germany; [3]now at Old Dominion University, Norfolk, Virginia, USA; [4]Bhabha Atomic Research Center, Mumbai, India

The PANDA[1] detector at FAIR will measure the decay products of antiproton-proton annihilations in the energy domain of charmed quark production. A Barrel DIRC counter, inspired by the successful BaBar DIRC [2], will perform charged particle identification (PID) in a polar angle range between 22° and 140°. Several test experiments with beams at GSI, CERN, and MAMI-C have been performed to evaluate a series of increasingly complex Barrel DIRC prototypes.

In the summer of 2014 a pion beam at GSI was shared with the HADES experiment during several beam times. Pions with a momentum of 1.7 GeV/c were produced by a primary 2 AGeV N-beam from the heavy ion synchrotron SIS18 and transported to Cave-C with the help of the beam transport calculation MIRKO [3]. A scintillating trigger counter with 5 cm diameter selected about 1000 pions/s.

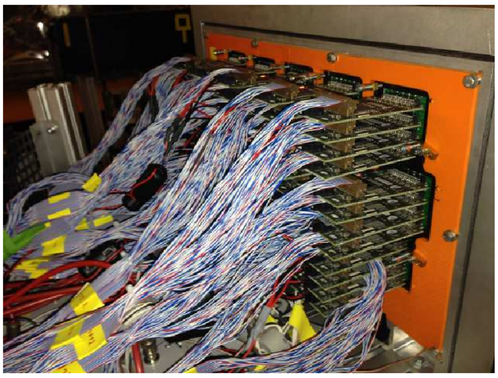

Figure 1: The array of 15 PHOTONIS PLANACON MCP-PMTs and 60 PADIWA3 discriminator boards with the cables towards the TRB3 TDCs.

The beam hits the radiator plate (17 mm × 160 mm × 1250 mm), coupled to a 30 cm-deep expansion prism, both made from synthetic fused silica. The produced Cherenkov cone is reflected within the plate by total internal reflection. Due to high-quality optical surfaces the opening angle of the cone is preserved. The expansion prism converts the directions of the photons at the radiator end into position information on the detection plane, which is equipped with a 3×5 array of XP85012 [4] Microchannel-Plate PMTs (MCP-PMTs). A total of 960 pixels were read out by 60 PADIWA3 discriminator cards, shown in Fig. 1. The photon time of arrival and the time-over-threshold were measured by TDCs on a total of 24 trigger and readout boards (TRB3) [5]. An example for the observed Cherenkov images is shown in Fig. 2. The top three rows show the prediction from simulation, which agrees well with the experimentally observed pattern, shown in the bottom three rows.

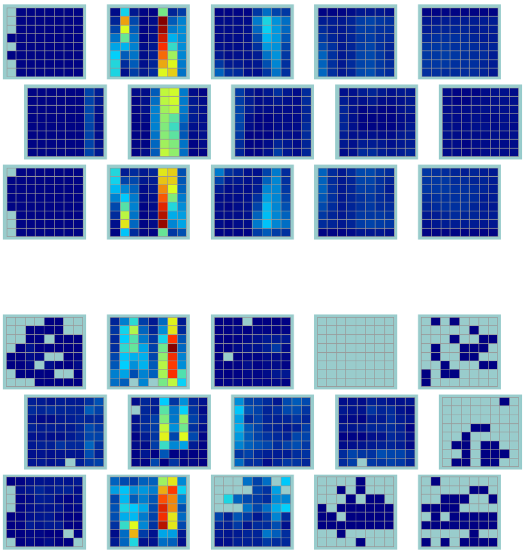

Figure 2: Top: Simulated Cherenkov image measured with 3x5 pixelised MCP-PMTs. Bottom: The measured image. The particle track hits the radiator plate with an angle of 120 degree.

More detailed studies, in particular of the wide radiator plates in combination with focusing optics, and direct measurements of the PID performance, are scheduled for the summer of 2015 during two test beam campaigns at CERN. The results will form the basis for the Technical Design Report, expected to be completed by mid-2016.

References

[1] PANDA Collaboration, Physics Performance Report (arXiv:0903.3905v1), 2009.

[2] I. Adam, et al., Nucl. Instr. and Meth. A 538 (2005) 281.

[3] B. Franczak, MIRKO, Proceedings of the Europhysics Conference on Computing in Accelerator Design and Operation, Berlin (1983).

[4] http://www.photonis.com.

[5] C. Ugur, et al., IEEE Nordic-Mediterranean Workshop on Time to Digital Converters, 2013, DOI: 10.1109/NoMeTDC.2013.6658234.

---

* Work supported by HGS-HIRe, HIC for FAIR, and EU FP7 grant #227431.

† C.Schwarz@gsi.de

DOI:10.15120/GR-2015-1-MU-HADRONS-17

Time-based simulation of the PANDA barrel DIRC*

R. Dzhygadlo†[1], *K. Götzen*[1], *G. Kalicy*[1,2,3], *H. Kumawat*[1,4], *M. Patsyuk*[1,2], *K. Peters*[1,2], *C. Schwarz*[1], *J. Schwiening*[1], *and M. Zühlsdorf*[1,2]

[1]GSI, Darmstadt, Germany; [2]Goethe Universität Frankfurt, Germany; [3]now at Old Dominion University, Norfolk, Virginia, USA; [4]Bhabha Atomic Research Center, Mumbai, India

The PANDA Barrel DIRC detector [1] will be used for hadronic particle identification in the high luminosity PANDA experiment at FAIR. The main task of the Barrel DIRC is to separate charged pions and kaons with better than three standard deviations for polar angles between 22° and 140° and particle momenta between 0.5 and 3.5 GeV/c. In the baseline design the PANDA Barrel DIRC is constructed from 16 radiator modules, each comprising 5 narrow fused silica radiator bars (1.7 cm × 3.2 cm × 240 cm) surrounding the beam line at a radial distance of 47.6 cm.

Realistic event-by-event simulations of different design options of the DIRC detector were performed within the PandaRoot framework [2, 3]. One of the main aspects of the current development is the time-based simulation, which is important in order to represent the real structure of the data output stream from the experiment. The time-based data structure introduces additional challenges to the data processing. One such challenge is related to the possible loss of Cherenkov photons due to the pile-up of events and the dead time of the photon detector. Another is a result of ambiguous assignment of Cherenkov photon signals (hits) to different events. The time-based simulation was implemented for the Barrel DIRC in order to study how these effects influence the performance.

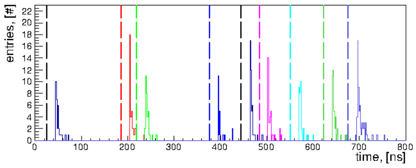

Figure 1: Time spectrum of detected photons after assigning time stamps. Colors represent different events. The vertical lines indicate start times of the events.

After the event is created a time stamp is assigned to each even/hit (see Fig. 1). Then hits are stored in a time-ordered buffer based on time stamp and pixel ID. If the same pixel is hit within the assumed dead time then the hit is discarded. Fig. 2 shows the map of hit loss probability as a function of dead time and event rate. The photon detectors, together with DAQ system, are expected to have a dead time of about 40 ns. At the design event rate of 20 MHz this yields a hit loss probability of about 5%.

Finally, hits are extracted from the time-ordered buffer for each event using the start time of the event and a time window, which is chosen conservatively to be 100 ns, in order collect all hits from the Barrel DIRC. Fig. 3 shows the time window as a shaded area for different events.

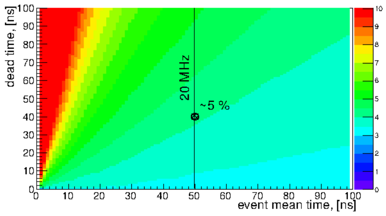

Figure 2: Map of the hit detection inefficiency due to the pile-up of events. The color scale indicates the percentage of lost hits.

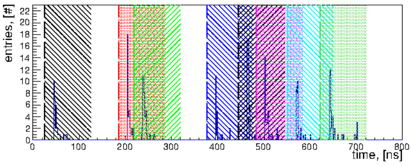

Figure 3: Time spectrum of detected photons after the hit finder. Shaded areas indicate the time window of reconstructed events.

Due to the pile-up, the reconstructed event could obtain hits from neighboring events. However, tracks from consecutive events are very unlikely to hit the same radiator module. Therefore, the corresponding hits are well-separated in pixel space and in reconstructed Cherenkov space and typically successfully associated to the correct events.

According to the DPM event generator simulation [4] 4% of events contain more than one particle hitting a radiator module. In those cases the overlapping hit patterns are successfully separated using the measured photon arrival time. This method leads to the correct association of hits to tracks in 90% of events with multiple particles per DIRC module, demonstrating that the design is rather robust in dealing with the time structure of PANDA events.

References

[1] M. Hoek, et al., Nucl. Instr. and Meth. Phys. Res. Sect. A 766 (2014) 96.

[2] S. Spataro, J. Phys. Conf. Ser. 331 (2011) 032031

[3] R. Dzhygadlo, et al., Nucl. Instr. and Meth. Phys. Res A 766 (2014) 263.

[4] A. Capella, et al., Physics Reports, vol. 236, no. 4-5, pp. 225–329, 1994.

---

* Work supported by HGS-HIRe, HIC for FAIR, and EU FP7 grant #227431.

† R.Dzhygadlo@gsi.de

DOI:10.15120/GR-2015-1-MU-HADRONS-18

Antihyperon potentials in nuclei via exclusive antiproton-nucleus reactions*

Alicia Sanchez Lorente[†1], *Sebastian Bleser*[1], *Marcell Steinen*[1], *and Josef Pochodzalla*[1,2]
[1]HI Mainz, D-55099 Mainz, Germany; [2]Institut für Kernphysik, D-55099 Mainz, Germany

The interaction of individual baryons or antibaryons in nuclei provides a unique opportunity to elucidate strong in-medium effects in baryonic systems. While for neutrons and protons as well as some strange baryons experimental information on their binding in nuclei exists, information on antibaryons in nuclei are rather scarce. Only for the antiproton the nuclear potential could be constrained by experimental studies. The (Schrödinger equivalent) antiproton potential at normal nuclear density turns out to be in the range of $U_{\overline{p}} \simeq -150\text{MeV}$, i.e. a factor of approximately 4 weaker than expected from naive G-parity relations [1]. Gaitanos *et al.* [2] suggested that this discrepancy can be traced back to the missing energy dependence of the proton-nucleus optical potential in conventional relativistic mean-field models. The required energy and momentum dependence could be recovered by extending the relativistic hadrodynamics Lagrangian by non-linear derivative interactions [3, 2, 4] thus also mimicking many-body forces [5]. Considering the important role played e.g. by strange baryons and antibaryons for a quantitative interpretation of high-energy heavy-ion collisions and dense hadronic systems it is clearly mandatory to test these concepts also in the strangeness sector. Of course, the question if and to what extend G-parity is violated by antihyperons in nuclei is also a challenging problem by itself.

Antihyperons annihilate quickly in nuclei and no experimental information on the nuclear potential of antihyperons exists so far. As suggested recently [6], quantitative information on the antihyperon potentials may be obtained via exclusive antihyperon-hyperon pair production close to threshold in antiproton-nucleus interactions by means of the transverse momentum asymmetry α_T which is defined in terms of the transverse momenta of the coincident particles

$$\alpha_T = \frac{p_T(\Lambda) - p_T(\overline{\Lambda})}{p_T(\Lambda) + p_T(\overline{\Lambda})}. \qquad (1)$$

to the depth of the antihyperon potential. However, these schematic simulations ignored rescattering processes and refractive effects at the potential boundary. These effects may erode the two-body character of the $\overline{\Lambda}\Lambda$ production and may thus diminish or even destroy the sensitivity of α_T to the assumed antihyperon potential. In order to go beyond the schematic calculations presented in Refs. [6] and to include simultaneously rescattering, refraction and absorption effects, we performed first realistic calculations of this new observable with a microscopic transport model.

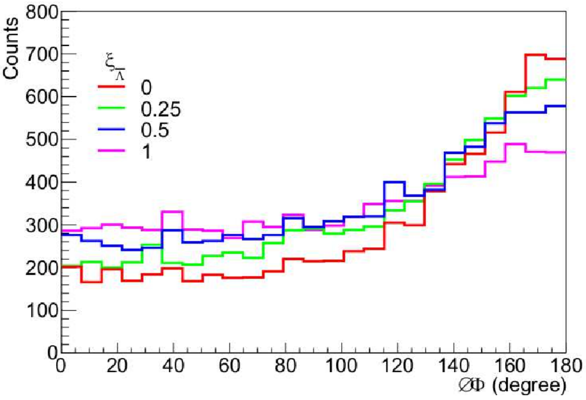

Figure 1: Coplanarity of coincident $\Lambda\overline{\Lambda}$-pairs produced exclusively in 0.85 GeV $\overline{\text{p}}$+^{20}Ne interactions. The different histograms show the GiBUU predictions for different scaling factor $\xi_{\overline{\Lambda}}$ of the $\overline{\Lambda}$-potentials.

We have studied the exclusive reaction $\overline{\text{p}}$+^{20}Ne→ $\overline{\Lambda}\Lambda$ at beam energies of 0.85 GeV and 1 GeVwithin the Giessen Boltzmann-Uehling-Uhlenbeck transport modell (GiBUU, Release 1.5) [7]. These energies correspond to antiproton momenta of 1.522 GeV/c and 1.696 GeV/c, respectively. At 0.85 GeV the excess energy with respect to the elementary reaction $\overline{\text{p}}$ +p→$\overline{\Lambda}\Lambda$ amounts to only 30.6 MeV. Therefore, the $\overline{\Sigma}\Lambda$ and $\Sigma\overline{\Lambda}$ channels are not accessible and also the production of a pion in addition to a $\Lambda\overline{\Lambda}$-pair can be neglected. In order to explore the sensitivity of the transverse momentum asymmetry on the depth of the $\overline{\Lambda}$-potential we have performed a series of calculations where only the antihyperon potentials were modified by a single scaling factor, leaving all other input parameters of the model unchanged. The calculations were performed at the High Power Computing Cluster HIMSTER located at the Helmholtz-Institute Mainz. Each GiBUU-Job comprised 1000 parallel events.

The delicate interplay between the Fermi motion of the struck nucleon, the absorption, rescattering and refraction at the nuclear surface of the produced hyperons and antihyperons is illustrated by the coplanarity of the $\overline{\Lambda}\Lambda$-pairs. Fig. 1 shows the difference between the azimuthal angle of the free $\overline{\Lambda}$ and Λ. Already for zero $\overline{\Lambda}$-potential, the coplanarity is strongly blurred. With increasing potential depth for the $\overline{\Lambda}$, the coplanarity is even less pronounced. The significant deviation from 180^o demonstrates the influence of secondary scattering prior to the emission of the $\overline{\Lambda}$ or Λ or

---

* Work supported by HI Mainz

† lorente@kph.uni-mainz.de

DOI:10.15120/GR-2015-1-MU-HADRONS-19

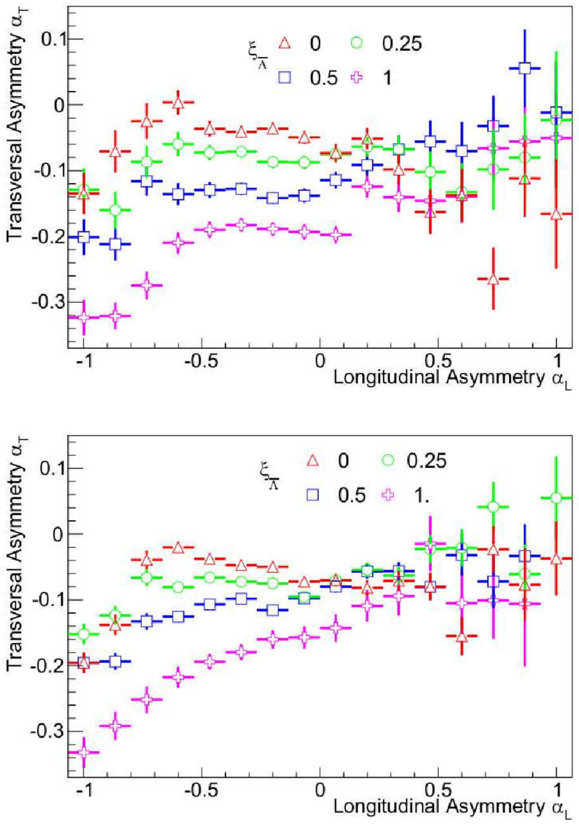

Figure 2: Average transverse momentum asymmetry as a function of the longitudinal momentum asymmetry for $\Lambda\bar{\Lambda}$-pairs produced exclusively in 0.85 GeV (top) and 1 GeV (bottom) $\bar{p}^{20}$Ne interactions. The different symbols show the GiBUU predictions for different scaling factor $\xi_{\bar{\Lambda}}$ of the $\bar{\Lambda}$-potentials.

a deflection at the potential boundary.

In Fig. 2 we show the GiBUU prediction for the transverse asymmetry α_T (Eq. 1) for different scaling factors $\xi_{\bar{\Lambda}}$ of the $\bar{\Lambda}$-potential. As in Ref. [6] we plot the average α_T as a function of the longitudinal momentum asymmetry α_L which is defined for each event as

$$\alpha_L = \frac{p_L(\Lambda) - p_L(\bar{\Lambda})}{p_L(\Lambda) + p_L(\bar{\Lambda})}. \tag{2}$$

For 0.85 GeV (top) as well as 1 GeV (bottom) antiproton energy a remarkable sensitivity of α_T on the $\bar{\Lambda}$-potential is found at negative values of α_L. Despite the concern mentioned before, secondary effects do not wipe out the dependence of α_T on the antihyperon potential. Both, the significant larger sensitivity as compared to the schematic calculation in Ref. [6] as well as the shift of the average α_T towards more negative values are linked to the substantial transverse momentum broadening for the $\bar{\Lambda}$-hyperons by secondary scattering. For positive values of α_L where the antihyperon is emitted backward with respect to the Λ-particle, the statistics in the present simulation is too low to draw quantitative conclusions. But even in this region of α_L a systematic variation of α_T with the antihyperon potential might show up with improved statistics.

The international Facility for Antiproton and Ion Research (FAIR) will provide high intensity antiproton beams with momenta between 1.5 GeV/c and 15 GeV/c. A unique feature of antiproton interactions in the energy range of PANDA is the large production cross section of hyperon-antihyperon pairs [8]. At its full luminosity the production rate of $\bar{Y}Y$-pairs range from a few 100 per second for the $\bar{\Xi}\Xi$-channel, up to a few thousand per second for the $\bar{\Lambda}\Lambda$-channel in the elementary $\bar{p}p$-reaction. Due to the strong absorption of antibaryons in nuclei this production rate will be lowered depending on the size of the target nucleus in antiproton-nucleus collisions. According to the GiBUU calculations presented above, for a typical medium size target nucleus like ^{20}Ne still several hundreds free $\bar{\Lambda}\Lambda$-pairs can be produced per second. For a nuclear target in this mass range and at maximum interaction rate, approximately 10 reconstructed $\bar{\Lambda}\Lambda$-pairs per second are expected [9]. Therefore, already a measurement period of about one hour will provide a statistics exceeding that of the GiBUU simulations shown above. This will be sufficient to reach a precision of about 10% for the scaling factor $\xi_{\bar{\Lambda}}$ of the antilambda potential. These numbers illustrate that even on rather pessimistic assumption about the luminosity and/or the availability of the antiproton beam during the commissioning phase of the PANDA experiment, one can reach unique and relevant information on the behavior of strange antibaryons in nuclei shortly after the delivery of the first antiproton beam at FAIR.

References

[1] A.B. Larionov, I.A: Pshenichnov, I.N. Mishustin, and W. Greiner, Phys. Rev. C **80** (2009) 021601(R).

[2] T. Gaitanos, M. Kaskulov, H. Lenske, Phys. Lett. B **703** (2011) 193.

[3] T. Gaitanos, M. Kaskulov, U. Mosel, Nucl. Phys. A **828** (2009) 9.

[4] T. Gaitanos, M. Kaskulov, Nucl. Phys. A **899** (2013) 133.

[5] R.O. Gomes, V.A. Dexheimer, S. Schramm. C.A.Z. Vasconcellos, arXiv:1411.4875 [astro-ph.SR].

[6] J. Pochodzalla, Phys. Lett. B **669** (2008) 306.

[7] O. Buss *et al.*, Phys. Rep. **512** (2012) 1.

[8] Physics Performance Report for PANDA: Strong Interaction Studies with Antiprotons, arXiv:0903.3905 [hep-ex]

[9] $\bar{\text{P}}$ANDA Collaboration, Technical Progress Report (GSI Darmstadt), pp. 1-383 (2005).

DOI:10.15120/GR-2015-1-MU-HADRONS-19

A non disturbing monitoring system for cluster beams*

S. Grieser[†] [1], *D. Bonaventura*[1], *A.-K. Hergemöller*[1], *B. Hetz*[1], *F. Hordt*[1], *E. Köhler*[1], *A. Täschner*[1,2], *and A. Khoukaz*[1]

[1]Institut für Kernphysik, Westfälische Wilhelms-Universität Münster, Germany; [2]GSI, Darmstadt, Germany

A cluster-jet target is highly eligible for storage ring experiments, e.g. for the future $\overline{\text{P}}$ANDA experiment at FAIR [1]. Such targets achieve high constant beam densities which can be adjusted easily during operation. To analyze the cluster beam thickness in real time during the experiment a new non disturbing method was developed, which might be used for a control system for constant luminosities. The design and construction of this system were attended by tests at the cluster-jet target MCT1S. This target was built up and set successfully into operation at the University of Münster and will be used for measurements on the direct ion acceleration induced by high-energy laser pulses at the University of Düsseldorf [2]. To determine the cluster beam properties the beam was visualized by a diode laser in a distance of $33\,\mathrm{cm}$ behind the Laval nozzle in combination with a CCD camera. With this setup investigations on the beam thickness, position, and size were made. Figure 1 shows such a background corrected image of the cluster beam. The projection on the ordinate corresponds to the distribution of the cluster beam and can be described by [3]:

$$p(x) = I_0 \cdot p_e(x - x_0) + I_U \qquad (1)$$

$$p_e(x) = \int\limits_{-\infty}^{\infty} dy \int\limits_{x-\frac{d}{2}}^{x+\frac{d}{2}} \frac{1}{2}\left(1 - \mathrm{erf}\left(\frac{r-R}{s}\right)\right) dx. \qquad (2)$$

Equation (1) is a multiplication of an intensity I_0 with a radial function and an additive background I_U. The radial distribution can be excellently described by an error function, which is a convolution of a Gaussian distribution and a rectangular function (see Figure 1, a). Therein is $r = \sqrt{x^2 + y^2}$, d complies with the resolution (one pixel), x_0 corresponds to the position of the maximum intensities, R to the radius, and s to the smearing of the cluster beam. Figure 2 shows the measured intensity for different stagnation conditions. For these measurements the temperature and pressure at the nozzle were varied. The measurements were performed in the liquid area of hydrogen to achieve the highest thickness. The intensity, which corresponds directly to the thickness, enhances with decreasing temperature and increasing pressure. Since the described monitoring method represents an elegant possibility to perform precisely an online cluster beam analysis on e.g. position, intensity, thickness, size, and stability without affecting the cluster beam, this method will be optimized for the final $\overline{\text{P}}$ANDA cluster-jet target.

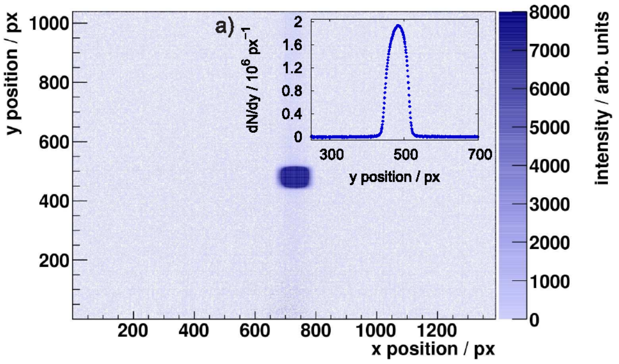

Figure 1: Image of the hydrogen cluster beam at stagnation conditions of 16 bar and 22K (exposure time 15s). The cluster beam direction is from left to right. a) Intensity distribution.

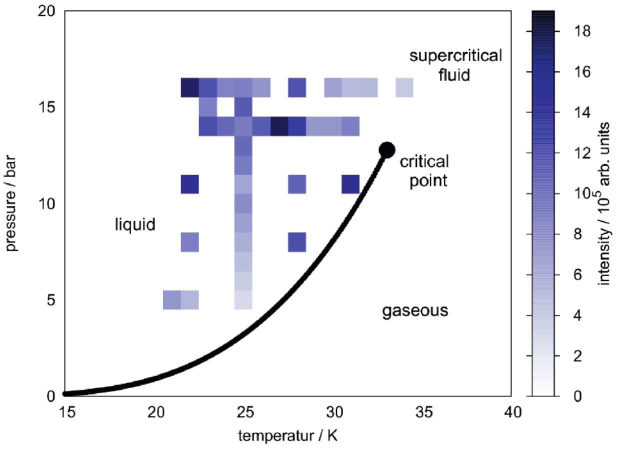

Figure 2: Scattering light intensities for different stagnation conditions. For high pressure and low temperature, the highest intensity and therefore thickness can be achieved.

References

[1] A.-K. Hergemöller, Design and Special Features of the Cluster-Jet Target for $\overline{\text{P}}$ANDA, GSI Scientific Report 2014 (2015).

[2] S. Grieser, The cluster-jet target MCT1S and the analysis of cluster beams, Master Thesis, University of Münster, 2014, Germany.

[3] A.-K. Hergemöller, Preparation of Cluster Beams and the Construction of the final Cluster Source for the $\overline{\text{P}}$ANDA Experiment, Master Thesis, University of Münster, 2013, Germany.

---

[*] Work supported by HGShire, EU(FP7), BMBF, and GSI.

[†] s.grieser@uni-muenster.de

DOI:10.15120/GR-2015-1-MU-HADRONS-20

Design and special features of the cluster-jet target for $\overline{\text{P}}$ANDA*

A.-K. Hergemöller[†1], *D. Bonaventura*[1], *S. Grieser*[1], *B. Hetz*[1], *F. Hordt*[1], *E. Köhler*[1], *A. Täschner*[1,2], *and A. Khoukaz*[1]

[1]Westfälische Wilhelms-Universität, Münster, Germany; [2]GSI, Darmstadt, Germany

The first target to be operated at the $\overline{\text{P}}$ANDA experiment will be a cluster-jet target. A prototype of this cluster-jet target has already been built up in full $\overline{\text{P}}$ANDA geometry at the University of Münster [1] and operates successfully for years. With this device it is routinely possible to achieve hydrogen target thicknesses of more than $2 \times 10^{15}\,\frac{\text{atoms}}{\text{cm}^2}$. The target thickness is stable in time and can easily be adjusted by varying the pressure or temperature of the used gas before entering the nozzle. Based on the experience with performance of the prototype, the final $\overline{\text{P}}$ANDA cluster source was designed and is currently under construction at the University of Münster (Fig. 1). The cluster beam itself is produced by the expansion of pre-cooled gases in a Laval nozzle (for further information concerning the Laval nozzle see [2]). For gas cooling a cold head is used which allows lowest temperatures of about 9 K without gas flow, which is more than sufficient for the target operation. A conical skimmer arranged behind the nozzle extracts the cluster beam from the residual gas and followed by a second orifice, the collimator, which defines the final size and shape of the cluster beam. Moreover, the cluster source includes a nozzle tilting system, allowing for an adjustment of the nozzle system relative to the experimental setup. With this system it is possible to select highly intensive core beams located within the cluster beam leading to highest target thicknesses [3]. To observe these core beams the skimmer chamber includes two camera ports on opposite sites of the chamber. For an optimal extraction and adjustment of the cluster beam towards the interaction point, skimmer and collimator are installed on xy-tables. To provide the required vacuum conditions the skimmer and collimator chambers are pumped via differential pumping systems. Due to the high gas load in the skimmer chamber, a pumping station consisting of two roots pumps combined with two fore pumps with an overall nominal pumping speed (for air) of up to $7800\,\frac{\text{m}^3}{\text{h}}$ is used. This pumping system simultaneously provides the pre-vacuum for the collimator chamber, where two turbo molecular pumps with a pumping speed (for air) of $2000\,\frac{\ell}{\text{s}}$ each are installed. Subsequently to the collimator chamber the transition vacuum chamber provides the connection to the vacuum of the HESR. For this chamber, additional camera ports are included, allowing for an online cluster beam and thickness monitoring without influencing the cluster beam itself. This non disturbing measurement principle is described in [4]. For the test operation of the $\overline{\text{P}}$ANDA target a slow control system is developed. This slow control for instance contains the control of the stepper motor devices for the nozzle tilting system and the adjustment of skimmer and collimator, the operation of the pneumatic valves and the vacuum pumps as well as the hydrogen pressure control. Above that, a monitoring of relevant parameters, e.g. pressures, gas temperature and gas flow at the nozzle, is included. After full implementing and all necessary tests in Münster, the target might be installed at the COSY accelerator for a first test operation in an experimental environment.

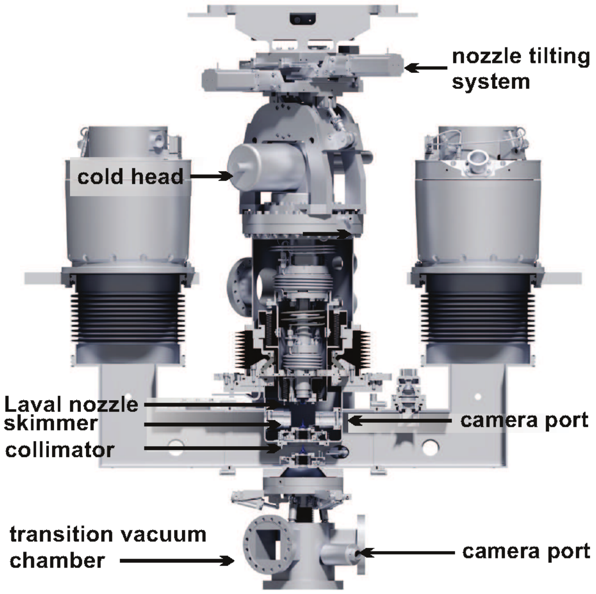

Figure 1: Main components of the cluster source for $\overline{\text{P}}$ANDA.

References

[1] A. Täschner et al., Nucl. Instr. and Meth. A660 (2011) 22-30, doi: 10.1016/j.nima.2011.09.024.

[2] S. Grieser, A new Production Process for Laval nozzles, GSI Scientific Report 2014 (2015).

[3] E. Köhler et al., Design and performance of the future cluster-jet target for PANDA at FAIR, in proceedings of STORI‘11 conference, PoS(STORI11)063.

[4] S. Grieser, A Non Disturbing Monitoring System for Cluster Beams, GSI Scientific Report 2014 (2015).

---

* Work supported by HGShire, EU(FP7), BMBF and GSI.

[†] a.hergemoeller@wwu.de

DOI:10.15120/GR-2015-1-MU-HADRONS-21

A new production process for laval nozzles*

S. Grieser†[1], *D. Bonaventura*[1], *A.-K. Hergemöller*[1], *B. Hetz*[1], *F. Hordt*[1], *E. Köhler*[1], *A. Täschner*[1,2], *and A. Khoukaz*[1]

[1]Institut für Kernphysik, Westfälische Wilhelms-Universität Münster, Germany; [2]GSI, Darmstadt, Germany

A cluster-jet target continuously produces a flux of cryogenic solid clusters by the expansion of pre-cooled gas within a fine Laval nozzle. For the production of clusters the geometry of the nozzle is essential. The short inlet zone converges to the narrowest inner diameter of, e.g., 30 μm of the nozzle and is followed by a long divergent zone with an opening angle of, e.g., 7°. Figure 1 shows the cluster production process with a Laval nozzle. The possibility to produce new fine Laval nozzles ensures the operation of cluster-jet targets, e.g. for the $\overline{\text{P}}$ANDA experiment, and opens the way for future investigations on the cluster production process to optimize the required target performance [1], [2]. A new production line was started where as a first step the model of the counterpart of the long outlet zone, the trumpet, is turned out of acrylic glass. It has a diameter of 30 to 60 μm at the narrowest point (see Figure 2). Through the galvanic deposition of copper the nozzle body is produced, and the copper can be released from the acrylic glass. In the next step chloroform is used to remove possible remainders of the acrylic glass. This technique ensures an accurate and clean extraction of the trumpet. The inlet zone of the nozzle is performed by a 90° cone bore. A laser technique establishes the connection between inlet and outlet zone of the nozzle. Figure 3 shows a cut through a new produced nozzle by wire erosion. A first set of 11 Laval nozzles with inner diameters between 42 μm and 105 μm was successfully produced.

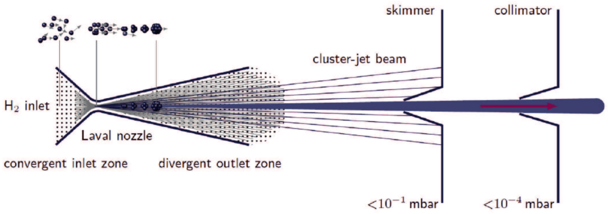

Figure 1: Sketch of the cluster production process [3].

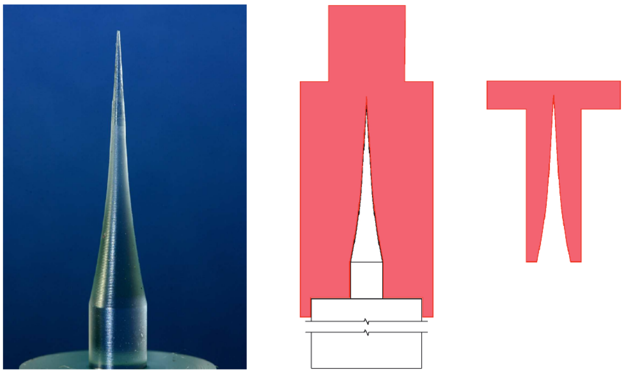

Figure 2: Left: Previously used counterpart of the trumpet. Center: Galvanic deposition of copper (red/dark) on the acrylic glass (white/bright). Right: Final shape of nozzle is turned out.

Figure 3: Cut through a new Laval nozzle.

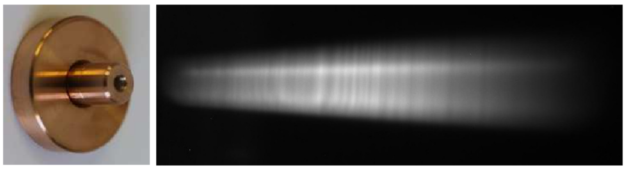

Figure 4: Left: Image of a successfully produced nozzle. Right: First cluster beam performed with a new nozzle. Beam direction is from left to right [4].

Initial measurements with these new nozzles were made at the $\overline{\text{P}}$ANDA cluster-jet target prototype. Figure 4 presents the first cluster-jet beam of a new nozzle with the characteristic high intense core beam structures. For the future more Laval nozzles with different geometries will be produced and additional measurements with these new nozzles at the $\overline{\text{P}}$ANDA cluster-jet target prototype towards higher performance will be realized.

References

[1] A.-K. Hergemöller, Design and Special Features of the Cluster-Jet Target for $\overline{\text{P}}$ANDA, GSI Scientific Report 2014 (2015).

[2] S. Grieser, PhD Thesis, University of Münster, 2015, Germany.

[3] E. Köhler, PhD Thesis, University of Münster, 2015, Germany.

[4] E. Köhler, Laval Nozzle Production for Internal Targets, GSI Scientific Report 2012 (2013).

---

* Work supported by HGShire, EU(FP7), BMBF, and GSI.

† s.grieser@uni-muenster.de

DOI:10.15120/GR-2015-1-MU-HADRONS-22

Model of a cable routing for the $\overline{\text{P}}$ANDA-EMC forward endcap[*]

C. Schnier[†, 1], *M. Albrecht*[1], *M. Fink*[1], *F.-H. Heinsius*[1], *T. Held*[1], *T. Holtmann*[1], *M. Kümmel*[1], *B. Kopf*[1], *S. Leiber*[1], *P. Musiol*[1], *M. Pelizäus*[1], *J. Pychy*[1], *T. Schröder*[1], *C. Sowa*[1], *M. Steinke*[1], *T. Triffterer*[1], *and U. Wiedner*[1]

[1]Ruhr-Universität Bochum, Germany

Introduction

The forward endcap of the $\overline{\text{P}}$ANDA-EMC [1] will contain 768 Vacuum Photo Tetrodes (VPTTs) and 6176 Avalanche Photodiodes (APDs) for the measurement of scintillation light. The forward endcap will be cooled down to −25 °C to increase the scintillation light output. A charge integrated low noise preamplifier is directly attached to each single VPTT and APD.

For supply and readout each VPTT (APD) photodetector preamplifier unit has to be equipped with 6 (8) cables.

The units are connected with 17 cm long cables to printed circuit boards [2], which are mounted on an aluminium backplate. The available electronics space inside the forward endcap is just 33 mm and the only available cable feedthroughs are located at the border of the backplate because of contiguous detectors. This space is needed for the different cables from single units and also for other components like temperature sensors and light fibres. To ensure a suitable way of cable positioning, a cable routing model has been developed.

Cable Routing Model

Short ways between the photo detectors and the readout electronics are provided with the cable routing model of the forward endcap. In addition to this, the cable routing accords with the mounting sequence of the photodetector units from the inner to the outer side avoiding numerous cable crossings.

The foreseen cables fulfill the requirements on electrical properties as well as radiation hardness. Through maximizing the number of grouped cables it is possible to decrease the number of rectangular feed-through holes, which simplifies the insulation procedure. For this, the design of the backplate was used, which provides more space between each unit at the border than in the middle. Overall about 8500 cables and more than 15400 light fibres have to be routed outside the insulated volume.

The cable routing model allows the use of the available space outside the endcap by 36 well positioned feedthrough holes, which are correlated with the location of readout electronics to decrease cable length. The chosen routing of VPTT units allows the full utilization of needed readout electronics with just a minumum of extra cables and cable crossings inside the forward endcap.

Further Development

Due to the fact that the forward endcap will be cooled down to −25 °C, the cable feed-through holes will be insulated [3], which reduces the possible hole size down to a height of 15 mm. The holes in the cable feed-through frame at the border of the backplate have to be vacuum tight to avoid formation of ice. Therefore a method of durable bonding is under investigation.

Figure 1: Routing scheme of the backplate part for one half of the forward endcap.

References

[1] $\overline{\text{P}}$ANDA-Collaboration, EMC Technical Design Report, 2008.

[2] C. Schmidt et al., “On VPTTs and signal cables and connectors”, talk, $\overline{\text{P}}$ANDA XLIX Collaboration Meeting.

[3] S. Leiber et al., “Development of the Insulation for the $\overline{\text{P}}$ANDA-EMC forward endcap”, GSI Scientific Report 2014.

---

[*] Work supported by BMBF and EU

[†] E-mail: cschnier@ep1.ruhr-uni-bochum.de

DOI:10.15120/GR-2015-1-MU-HADRONS-23

Development of the insulation for the $\overline{\text{P}}$ANDA-EMC*

S. Leiber[†1], *M. Albrecht*[1], *M. Fink*[1], *F.-H. Heinsius*[1], *T. Held*[1], *T. Holtmann*[1], *M. Kümmel*[1], *B. Kopf*[1], *P. Musiol*[1], *M. Pelizäus*[1], *J. Pychy*[1], *C. Schnier*[1], *T. Schröder*[1], *C. Sowa*[1], *M. Steinke*[1], *T. Triffterer*[1], *and U. Wiedner*[1]

[1]Ruhr-Universität Bochum, Germany

Introduction

The Electromagnetic Calorimeter (EMC) of the $\overline{\text{P}}$ANDA experiment consists of two endcaps and a barrel part and is placed inside a superconducting solenoid. Lead tungstate ($PbWO_4$) will be used as scintillator material because of its compactness, fast response, sufficient energy resolution over the large range of photon energies and an adequate radiation hardness.

The operation temperature of the $\overline{\text{P}}$ANDA-EMC is set to -25°C to increase the light yield by a factor of ≈ 4 when compared to room temperature at +25°C. The average temperature gradient of the light yield amounts to $\sim$ -3%/K [1].

In order to achieve a stable operation temperature, a thermal insulation under the constraints of a low thermal conductivity, a high mechanical stability, a proper thermal shock resistance in the given temperature range, and high precision in size and thickness is necessary. Further requirements are a minimal contribution to the material budget and a small thickness due to the space limitations inside the solenoid.

The EMC Endcap Prototype

A full-size prototype of a cut-out of the inner section of the EMC forward endcap of the $\overline{\text{P}}$ANDA experiment consisting of 216 lead tungstate crystals has been set up. To fulfill the requirement of a stable operational temperature of -25°C with a small temperature gradient inside the cooled volume, the prototype is cooled by three cooling circuits: the front cooling, the main cooling connected directly to the aluminium backplate, and a dried air cooling system.

Thermal insulation is realised using vacuum insulation panels with a thickness of 30 mm. These vacuum insulation panels consist of a micro porous core and a gas barrier film. They are sealed with a glass fiber wrapping to increase the mechanical shock protection. The thermal conductivity including aging and edge losses of these panels is 0.007 W/(m·K) and 0.020 W/(m·K) if the protection wrapping is damaged and the panels are aired [2].

Tests under realistic conditions during several beamtimes at the SPS accelerator at CERN, at ELSA in Bonn and at MAMI in Mainz, have proven that the chosen vacuum insulation panels fulfill the requirements mentioned above [3].

Further Development

For the $\overline{\text{P}}$ANDA-EMC forward endcap an insulation with a thickness of 20 to 30 mm is foreseen, limited by the available space. For maintenance and repairs, the front and back insulation parts will be attached in a removable manner to the front cooling plates in front of the crystals or to the aluminium back cover of the electronics space, respectively. To feed through all cables from the cooled inside to the outside at room temperature, 36 openings [4] are foreseen, which have to be insulated individually.

The insulation will be split up into several parts of small thickness to achieve a stacked and overlapping arrangement of the panels to avoid thermal bridges at the borders of the panels.

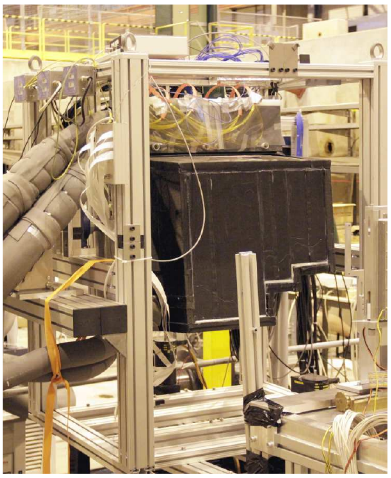

Figure 1: Front view of the prototype with the mounted insulation (black).

References

[1] $\overline{\text{P}}$ANDA Collaboration, EMC Technical Design Report, 2008.

[2] va-Q-tec, Product Data Sheet for va-Q-vip B, http://www.va-q-tec.com, Jan. 29, 2015.

[3] J. Becker, Analyse des Zerfalls $\chi_{cJ} \rightarrow K^+K^-\eta$ bei BES-III und Entwicklung eines Kühlsystems für den Prototypen des PANDA-EMC, Dissertation, Ruhr-Universität Bochum, 2012.

[4] C. Schnier et al., Model of a Cable Routing for the PANDA-EMC Forward Endcap, GSI Scientific Report 2014.

---

[*] Work supported by BMBF and EU

[†] E-mail: stephan@ep1.rub.de

DOI:10.15120/GR-2015-1-MU-HADRONS-24

DOI:10.15120/GR-2015-1-MU-HADRONS-24

Alternative experimental setup for hypernuclear spectroscopy at FRS/SuperFRS

*C.Rappold**[1,2], *T.R. Saito*[1,3,4], *C. Scheidenberger*[1,2], *and H. Geissel*[1,2]
[1]GSI, Darmstadt, Germany; [2]Justus-Liebig-Universität Giessen, Germany; [3]Johannes Gutenberg-Universität, Mainz, Germany; [4]The Helmholtz Institute Mainz, Mainz, Germany

The first experiment of the HypHI collaboration aimed to demonstrate the feasibility of the hypernuclear spectroscopy by means of heavy ion beam induced reactions. The final results show that the experimental method is viable for the study of hypernuclei [1, 2]. For this first experiment a ^{6}Li beam at $2A$GeV on a Carbon target was used.

A new set of experiments at FRS fragment separator is under study [3, 4]. The design study for a first experiment at FRS is on-going, which the experiment would focus on demonstrate this time that a hypernuclear spectroscopy can be performed within the FRS. A new dedicated apparatus for exclusive measurement can be set up within the fragment separator FRS, in contrast to the experimental apparatus devoted to inclusive measurement of the first experiments of the HypHI project. In this report, the alternative design of the experimental apparatus that could be placed into S2 area of FRS will be presented.

The alternative setup would consist of a solenoid magnet in order to analyze the momentum of the π^- meson with an high acceptance while the fragments would enter the second part of the FRS for their momentum measurement. Within the solenoid magnet several stage of detection is under consideration. The size of the simulated solenoid magnet are 70 cm long with a radius of 50 cm, the magnetic field considered in the simulation vary from 0.3 T to 0.7 T. From the inner radius to the outer radius an inner cylindrical hodoscope, a TPC chamber and outer cylindrical hodoscope were considered respectively. Because of the Lorentz boost of the projectile spectator, the daughter particles and fragments of the produced hypernuclei are boost forward and does not stay within the solenoid apparatus. Therefore, a endcap of trackers and time-of-flight walls is considered to increase the detection acceptance of the light particles like the π^- of the mesonic weak decay. Figure 1 shows a 3D view of the S2 area, with it walls in grey box. The conceptual solenoid magnet system is shown with its endcap. It can be seen that the apparatus is quiet contact considering the dimension of the S2 area.

The angular deviation of the fragments through the magnetic field of the solenoid was estimated in order to determine if the optics of the FRS after S2 would not be too much affected. In left panel of Figure 2, the estimated deviation is shown given a mean value of 1.5 degree for magnetic field of 0.3 T. Additionally a first estimation of the momentum resolution of the π^- was also performed. In the right panel of Figure 2, the distribution of the momentum resolution as a function of the π^- momentum is shown. A reasonable momentum resolution could be achieved with such a apparatus, while the geometrical acceptance of the pi^- would much larger that in the case of the double dipole magnets described in [4].

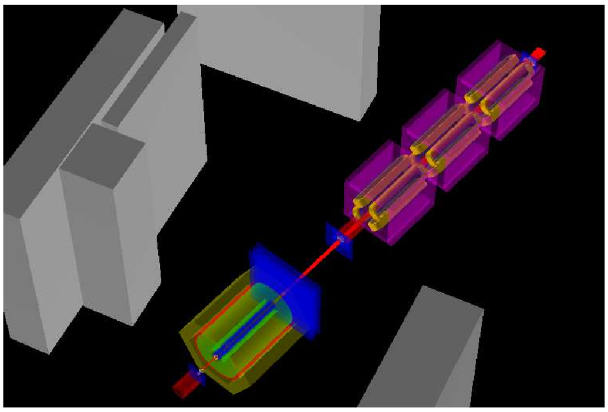

Figure 1: 3D view of the experimental apparatus in the S2 area of the FRS with the solenoid magnet.

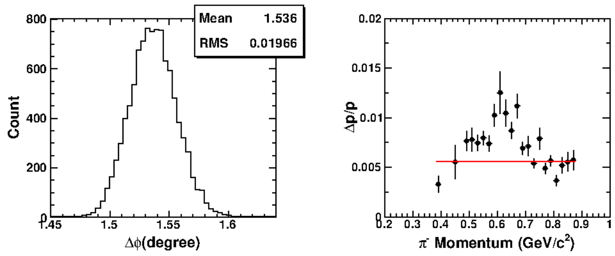

Figure 2: In the left panel, the fragment transversal angle $\Delta\Phi$ after going through the solenoid magnet. In the right panel, the π^- momentum resolution as a function of its momentum.

References

[1] C. Rappold *et al.*, Nucl. Phys. A **913**, 170 (2013).

[2] C. Rappold *et al.*, Phys. Rev. C **88**, 041001 (2013).

[3] C. Rappold *et al.*, GSI Scientific Report 2012 [GSI Report 2013-1] (2013) p. 176.

[4] C. Rappold *et al.*, GSI Scientific Report 2013 [GSI Report 2014-1] (2014) p. 101.

---

* c.rappold@gsi.de

DOI:10.15120/GR-2015-1-MU-NUSTAR-FRS-01

Experimental setup for hypernuclear study at the Super-FRS

C.Rappold[*1,2], *T.R. Saito*[1,3,4], *C. Scheidenberger*[1,2], *and H. Geissel*[1,2]
[1]GSI, Darmstadt, Germany; [2]Justus-Liebig-Universität Giessen, Germany; [3]Johannes Gutenberg-Universität, Mainz, Germany; [4]The Helmholtz Institute Mainz, Mainz, Germany

The first experiment of the HypHI collaboration aimed to demonstrate the feasibility of the hypernuclear spectroscopy by means of heavy ion beam induced reactions. The final results show that the experimental method is viable for the study of hypernuclei [1, 2]. For this first experiment a ^{6}Li beam at $2A$GeV on a Carbon target was used. A second experiment with a ^{20}Ne beam with the similar condition was also performed, preliminary results show that again Λ hyperon and $^3_\Lambda$H were identifiable.

A new set of experiments at FRS fragment separator is under study [3, 4]. The design study for a first experiment at FRS is on-going, which the experiment would focus on demonstrate this time that a hypernuclear spectroscopy can be performed within the FRS. A new dedicated apparatus for exclusive measurement can be set up within the fragment separator FRS, in contrast to the experimental apparatus devoted to inclusive measurement of the first experiments of the HypHI project. In this report, the first design of the experimental apparatus that could be placed into S2 area of FRS will be presented. The aim of the first experiment would the use a ^{6}Li beam on the carbon target in order to produce the $^4_\Lambda$H hypernucleus as a reference species since it has been already identified in the phase 0 experiment. It will be considered as a benchmark to show the feasibility of the hypernuclear spectroscopy within FRS. Secondly, $nn\Lambda$ bound state can be also search again for confirming its existence.

At S2 area, a detection apparatus consisting of a couple of dipole magnets could be install in order to separate the π^- meson of the mesonic weak decay of produced hypernuclei, while the positively charged fragments would enter the second part of FRS for precise determination of their momentum. The second dipole magnet is placed in such a way that it will correct the deflection of the fragments induced by the first dipole magnet in order to allow them to enter on beam axis the second part of the FRS. Detectors that have been already developed for the first experiment of the HypHI project can used in a similar way to track charged particles around the decay volume. Thus, the fiber detectors and drift chamber could be place in the upstream of the first magnets. The π^- mesons are then detected with a set of hodoscope walls and drift chambers in order to complete the information needed for the track reconstruction. Complete design of the detection apparatus is still on-going, which aims to minimize the pion multiscattering within the detection layers to improve as much as possible the momentum resolution of the pions.

The transport optics calculated and simulated by MOCADI, is also used in order to determine the momentum and geometrical acceptance of the fragment within the second part of the FRS. Currently, the simulation code for the Monte Carlo simulation of the apparatus at S2 is coupled with the MOCADI code: at first the full set of events is produced and propagated up to the entrance of the second part of the FRS, then those events are set as input for the MOCADI simulation code. At the end, event per event, and fragment per fragment within the event, the fragment transport through S2 to S4 is performed and registered. The final acceptance is then estimated. Coupling the two code will allow us to determine the trigger rate and hypernuclear yield that could be expected during such experiment. Those estimations are still on-going. The optics of the couple of dipole magnets with the first magnet stage of the second part of the FRS (S2-S4) is also under investigation.

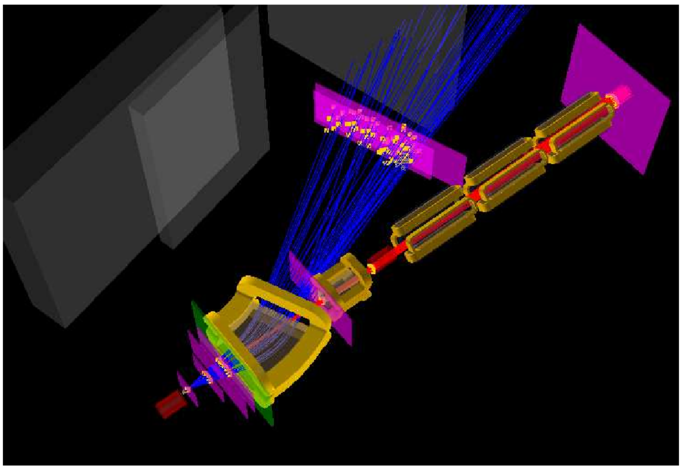

Figure 1: 3D view of the experimental apparatus at S2 area of the FRS. The couple of dipole magnets is shown with the simulated events of deuteron and π^- meson from the $nn\Lambda$ decay.

References

[1] C. Rappold *et al.*, Nucl. Phys. A **913**, 170 (2013).

[2] C. Rappold *et al.*, Phys. Rev. C **88**, 041001 (2013).

[3] C. Rappold *et al.*, GSI Scientific Report 2012 [GSI Report 2013-1] (2013) p. 176.

[4] C. Rappold *et al.*, GSI Scientific Report 2013 [GSI Report 2014-1] (2014) p. 101.

---

[*] c.rappold@gsi.de

DOI:10.15120/GR-2015-1-MU-NUSTAR-FRS-02

Radiation hardness tests of Si detectors for Time of Flight measurements at the Super-FRS*

O. Kiselev[1#], *A. Bezbakh*[2], *N. Egorov*[3], *I. Eremin*[4], *V. Eremin*[4], *N. Fadeeva*[4], *A. Fomichev*[2], *M. Golovkov*[2], *S. Golubkov*[3], *A. Gorshkov*[2], *A. Knyazev*[2], *C. Konkov*[3], *D. Kostyleva*[2], *S. Krupko*[2], *D. Mitina*[4], *I. Mukha*[1], *C. Nociforo*[1], *A. Prochazka*[1], *F. Schirru*[1], *R. Slepnev*[2], *A. Shepelev*[4], *Y. Tuboltsev*[3] *and E. Verbitskaya*[4]
[1]GSI, Darmstadt, Germany; [2]JINR, Dubna, Russia; [3]Research Institute of Material Science and Technology (RIMST), Zelenograd, Russia; [4]Ioffe Institute, St. Petersburg, Russia.

The beam diagnostics of the Super-FRS consists of several stations of different kind at the defined positions along the pre- and main-separator [1]. Besides position and energy-loss, in case of measurements with slow extracted-beams, the Time of Flight (ToF) information is a key aspect for the beam identification. The main design parameters of the ToF detector are the time resolution ≤50 ps (rms), active area up to 380 x 50 mm^2 and the ability to stand the rates of the relativistic ions up to 10^7 per spill over the whole active area.

Few beam tests of Si detector prototypes have been performed. In 2012, several prototypes with different thickness (100, 300 and 600 μm) and small active area (~25 mm^2) have been tested at GSI using ^{197}Au at 750 MeV/u and ^{238}U at 370 MeV/u beams [2]. The detector signals were digitized directly by the fast digital oscilloscope. The time resolution, calculated using a method similar to the one implemented in a leading edge discriminators with amplitude corrections, was found to be ~20 ps (rms, averaged value). The measured energy resolution was close to few percent.

Another experiment with ^{40}Ar beam at 40.5 MeV/u was performed in February 2014 in JINR, Dubna, at the fragment separator ACCULINNA.

Figure 1: Si strip detectors inside the scattering chamber of ACCULINNA separator.

The performance of four silicon detectors, one of those large-area (41 cm^2), with different geometry, under heavy irradiation was investigated (Fig.1). The intensity of the beam was up to 10^9 ions/s and the diameter of the illuminated area varied from 10 to 40 mm. The irradiation was performed in several steps; before the first irradiation and after each irradiation, the performance of the detectors was measured at reduced beam rate. The total fluence reached $2.3\cdot10^{13}$ ions/cm^2, compatible to the one obtained by HADES collaboration with diamond detectors [3]. The changes of the silicon material were monitored using the special small Si detector and the TCT technique [4]. In addition to the fast oscilloscope, fast preamplifiers with discriminators PADI [5] and a VFTX2 FPGA TDC [6] have been used for the signal processing. The detectors were cooled to -20° C in order to prevent heating up due to the irradiation. The results showed that the performance of the detectors did not change much (amplitude decreased in 10%) after the irradiation to 10^{11} ions/cm^2 (equivalent of a year of Super-FRS operation). Thus, the time resolution of the full-size detector even after a year of Super-FRS operation can be down to 30-40 ps.

Another test experiment has been performed at GSI in August 2014 with ^{197}Au beam at 1 GeV/u. One full-size prototype and several small detectors were measured. In addition to the above mentioned readout methods, two types of Flash-ADCs were used – DT5742 (12 bit, 5 Gs/s) and DT5743 (12 bit, 3.2 Gs/s), both are from the company CAEN.

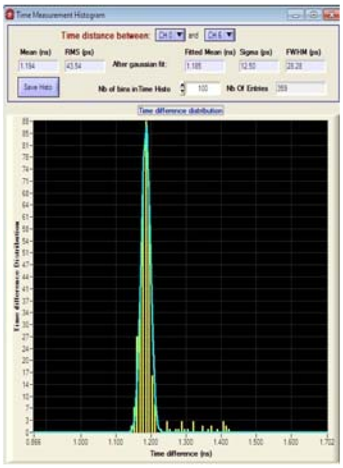

Figure 2: Time-of-flight resolution (measured by the waveform digitizer DT5743) of the small detector and one of the strips of the large Si strip detector.

Using the recorded waveforms, the time resolution between the small detectors and the single strips of the large detector were obtained using the Constant Fraction Discriminator (CFD) method. In order to avoid losses due to

DOI:10.15120/GR-2015-1-MU-NUSTAR-FRS-03

the lower than needed sampling frequency, the data points were interpolated by the 3-points splines. It has been demonstrated that the time resolution using fast digitizers can reach values down to 13 ps rms (Fig.2). Unfortunately, relatively large dead time of the waveform digitizers prevents to use them for the high-rate applications.

Additionally, a set of Si samples was irradiated to get quantitative information on Si detectors degradation rate under heavy ion irradiation. From the physical point of view, degradation of silicon under irradiation is a result of the crystalline lattice damage by impinging radiation. Two groups of the radiation defects are distinguished: extended disordered regions or clusters produced via direct interaction of the high energy particle with the Si atoms, and point defects generated in a separate crystalline cell via ion interaction with the electrons in the crystal.

The electronic properties of clusters cannot not be explained in terms of simple microscopic parameters like activation concentration, activation energy and trapping cross-section well describing the physical properties of point defects. Therefore their effect on the detector parameters is evaluated via changing certain detector characteristic, in particular, the current of reverse biased detector operated at full depletion mode as a most predictable and simple parameter. This current *I* is generated by clusters and point defects and is proportional to the irradiation fluence *F*. The slope of *I-F* characteristic α proportional to *dI/dF* is a specific parameter depending on the ratio between introduction rates of clusters and point defect. Therefore the current-related damage rate α normalized to the unit volume is a unique characteristic for scaling other radiation effects [7] like degradation of the free carriers trapping time, changes of the effective concentration in the detector sensitive region and, finally, for modeling the detector long-term operational scenario [8] for planning the experiments.

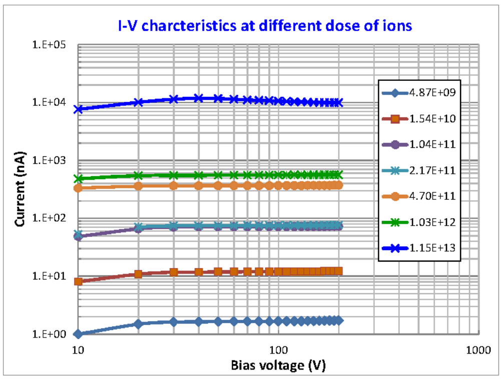

Fig. 3 I-V characteristics of irradiated detectors. The irradiation fluence is in the legend.

The damage rate α was measured for the run of multi-fluence irradiation of 120 Si test detectors. The detector set included pad detectors with a sensitive area 5 x 5 mm^2 and a thickness of 300 μm processed from high resistivity Si (10 kΩcm). The detectors were installed on the plates from Al foil which then were placed in the frames combined together in a solid block for irradiation. The installed detectors had nearly identical I-V characteristics with the reverse current less than 1 nA per detector. The ions passed through 7 detector layers, whose total thickness was less than the range of ^{40}Ar ions in silicon. The fluence was controlled by the time of irradiation, and as soon as the certain fluence was reached the layer was taken out from the irradiation area, while the rest were left for future irradiation. Just after irradiation the detectors were placed in the fridge (T = -20 C°) till their evaluation.

The I-V characteristics of the irradiated detectors measured at room temperature are presented in Fig 3. All of them were measured with the activated guard ring for cleaning-up the bulk generated current from the surface leakage. Up to the fluence $1 \cdot 10^{11}$ ions/cm^2 the characteristics exhibit the current saturation. A linear fit of the saturated current vs F curve (Fig. 4) gives $\alpha = 7.8 \cdot 10^{-17}$ A/cm.

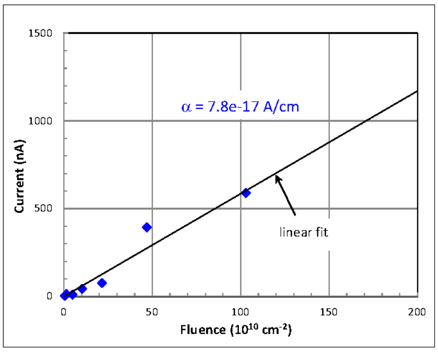

Fig. 4 Measured values of the saturated current vs fluence and their linear fit.

Table 1 Summarizes current-related damage rates for relativistic protons, ^{40}Ar ions and the 1 MeV neutrons as a reference type of irradiation.

Table 1

Radiation	Damage rate, A/cm	Scaling factor
Protons	$2.5 \cdot 10^{-17}$	0.62
^{40}Ar ions	$7.8 \cdot 10^{-17}$	1.95
Neutrons	$4 \cdot 10^{-17}$	1

The analysis of the samples is still going on. Once done, it will be unique data never measured systematically with heavy ions.

References

[1] M. Winkler et al., GSI Annual Report 2010, p. 133.
[2] O. Kiselev et al., GSI Annual Report 2012, p. 172.
[3] J. Pietraszko et al., Nucl. Instr. and Meth. A, 763 (2014) p. 1.
[4] V. Eremin et al., Nucl. Instr. and Meth. A, 372 (1996) p. 388.
[5] M. Ciobanu et al., IEEE Transactions on Nuclear Science, Vol. 61, No. 2 (2014) p. 1015.
[6] J. Frühauf et al., GSI Annual Report 2012, p. 300.

DOI:10.15120/GR-2015-1-MU-NUSTAR-FRS-03

[7] K. Hara et al., Nucl. Instrum. and Meth. A 636 (2011) p. 83.
[8] E. Verbitskaya et al., Nucl. Instr. and Meth. A 754 (2014) p. 63.

DOI:10.15120/GR-2015-1-MU-NUSTAR-FRS-03

Twin GEM-TPC prototype (HGB4) beam test at GSI – a development for the Super-FRS at FAIR

*F. García[*1], R. Turpeinen[1], R. Lauhakangas[1], E. Tuominen[1], J. Heino[1], J. Äystö[1], T. Grahn[2], S. Rinta-Antilla[2], A. Jokinen[2], R. Janik[3], P. Strmen[3], M. Pikna[3], B. Sitar[3], B. Voss[4], J. Kunkel[4], V. Kleipa[4], A. Gromliuk[4], H. Risch[4], I. Kaufeld[4], C. Caesar[4], C. Simon[4], M. kìs[4], A. Prochazka[4], C. Nociforo[4], S. Pietri[4], H. Simon[4], C. J. Schmidt[4], J. Hoffmann[4], I. Rusanov[4], N. Kurz[4], P. Skott[4], S. Minami[4], M. Winkler[4]*

[1]Helsinki Institute of Physics, University of Helsinki, 00014 Helsinki, Finland
[2]University of Jyväskylä, Department of Physics, 40014 Jyväskylä, Finland
[3]FMFI Bratislava, Comenius University, Bratislava, Slovakia
[4]GSI Helmholtzzentrum für Schwerionenforschung, Darmstadt 64291, Germany

INTRODUCTION

The GEM-TPC detector will be part of the standard Super-FRS detection system, as tracker detectors at several focal stations along the separator and its three branches.

GEM-TPC DETECTOR DEVELOPMENT

In order to satisfy the requirements of the Super-FRS a GEM-TPC working group was created. From 2009 different designs were proposed and after two generations of GEM-TPCs [1] were built and tested, one of the main requirements, which was not yet completely tested was a close to 100% tracking efficiency at high rates, therefore the twin configuration was introduced. The main idea behind this new design is to place two GEM-TPCs one close to the other one and flipped in the middle horizontal plane, in such a way that the electric field of the field cages will be in opposite directions. Results from simulations indicate that this configuration can potentially achieve a close to 100% tracking efficiency at up to 1 MHz rate.

BEAM TEST AT GSI

The twin prototype called HGB4, shown in Fig. 1 was fully designed and assembled at the GSI Detector Laboratory in 2014.

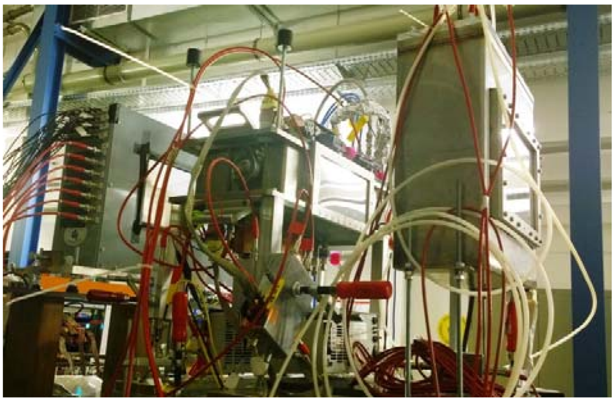

Fig. 1. The HGB4 (midlle) at Cave-C during in beam test.

After a successful commissioning, the chamber was moved to Cave-C for beam tests. This detector was tested by using Ca, Bi and U beams from SIS18 of about 300 MeV/u. This campaign was used to carry out measurements of the Control Sum (c.s.) for different electric fields.

$$c.s. = T_{up} + T_{down} - 2T_{ref}$$

Where: $T_{up} + T_{down}$ is the sum drift times for both field cages and T_{ref} is the reference time from the plastic scintillator. In order to measure the drift time the signal from the bottom of the third GEM was picked up. The c.s. was measured by using a multihit TDC (Caen V1290) for different fields starting from 150 V/cm up to 320 V/cm. We measured the Control Sum for different fields starting from 150 V/cm up to 320 V/cm.

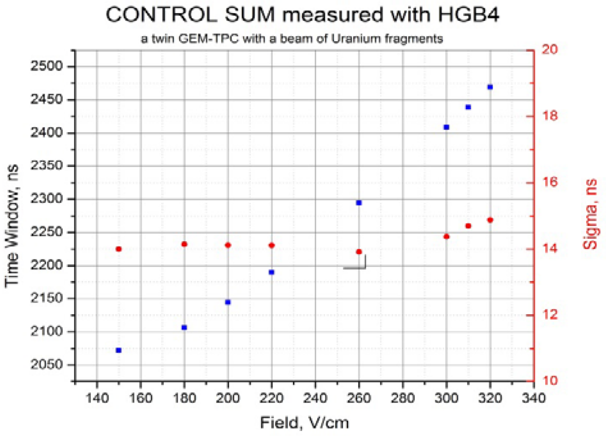

Fig. 2. The HGB4 Control Sum (blue dots) and its sigma (red dots).

From the Fig. 2 one can see that the sigma of the c.s. distribution slightly changes with different fields, indicating the possibility to operate at lower field without degradation, however more test are planned in the future to confirm these results.

REFERENCES

[1] F. Garcia et al., 2011 IEEE Nuclear Science Symposium conference record, ISSN: 1082-3654, pp. 1788-1792.

DOI:10.15120/GR-2015-1-MU-NUSTAR-FRS-04

First beam test of a Cherenkov detector prototype for a TOF measurements at the Super-FRS

N. Kuzminchuk-Feuerstein[*1], *N. Ferber*[1,2], *E. Fiks*[3], *I. Kaufeld*[1], *and B. Voss*[1], *and the Super-FRS collaboration*[1]

[1]GSI, Darmstadt, Germany; [2]RheinMain University of Applied Science, Rüsselsheim, Germany; [3]National Research Tomsk Polytechnic University, Tomsk, Russia

In order to separate and identify fragmentation products with the Super-FRS at FAIR a high resolving power detection system is required for position and Time-of-Flight (TOF) measurements. For the future TOF measurements a Cherenkov detector employing Iodine Naphthalene ($C_{10}H_7I$) with an optical refractive index n=1.705@589 nm is proposed. The liquid is kept in a cuvette with an aluminium frame (170x50 mm). The entrance and exit window of the cuvette is made out of the borosilicate glass BK7 coated with Aluminium (0.15 μm) to act as a mirror for the Cherenkov photons. SF-10 glass plates (10x50x2 mm) are glued to the right and left side of the cuvette with an optical glue. Those glass plates make it possible that reflected photons escape from the cuvette on the sides where they are transported via UV-transmissive PMMA light guides (LG) onto two photomultiplier tubes (PMTs) of Hamamatsu type H2431-50. The layout of the Cherenkov detector is shown in Fig. 1. The proof-of-principal operation of the prototype Cherenkov TOF detector has been tested with a Ni^{59} ion beam at CaveC at GSI. In particular the timing resolution and detection efficiency were measured. In the experiment two plastic scintillator detectors were installed in front and behind the Cherenkov detector and were used as reference detectors for the efficiency measurement. Each of them were equipped with two PMTs on the left and right ends. The observation of the coincidences between signals from two scintillators is used as confirmation that the ion beam passed through the Cherenkov detector. For traversing particles fulfilling the condition of the emission of Cherenkov light and photons are created in the liquid coincidences between PMT1&PMT2 are recorded. The scintillator signals coming from 4 photo-multipliers are first treated with the constant-fraction discriminators and afterwards used to create coincidences in the logic unit (AND). When coincidences between the front and back scintillator signals take place the final AND unit delivers a signal for external triggering of the oscilloscope. Raw waveforms from PMT1& PMT2 and from one PMT of each scintillator are stored with a digital oscilloscope LeCroy. Time stamps of the waveformes were determined with a software CFD method. The timing resolution of the detector is considered as a jitter between time signals detected by PMT1 and PMT2. For more details about the measurements and data analysis see [2]. The measurements were done within several regimes of low/high energies as well as low/high intensities. After passing through all the materials installed in front of the detector the lowest energy of 288 MeV/u used in this test was just enough for the creation of Cherenkov photons. According to the calculation at this energy about 11687 Cherenkov photons were created in a range of wavelengths of 390-650 nm. Poor detection efficiency and timing resolution were measured in this case. Increasing the beam energy to 1.5 GeV/u as well as increasing the particle intensity from 10^3 to $0.6 \cdot 10^6$ ions/spill improve the timing by a factor of 2. Fig. 2 shows the change in the relative efficiency and timing resolution for 1.5 GeV/u at different intensities. After the measurement the liquid transmission spectrum was rechecked with UV spectrometer in order to check for aging effects. No degradation of the light output was observed. To improve the timing resolution further improvements of the cuvette construction and electronics are necessary.

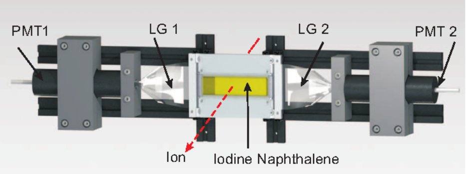

Figure 1: 3D figure of the Cherenkov detector with the main components.

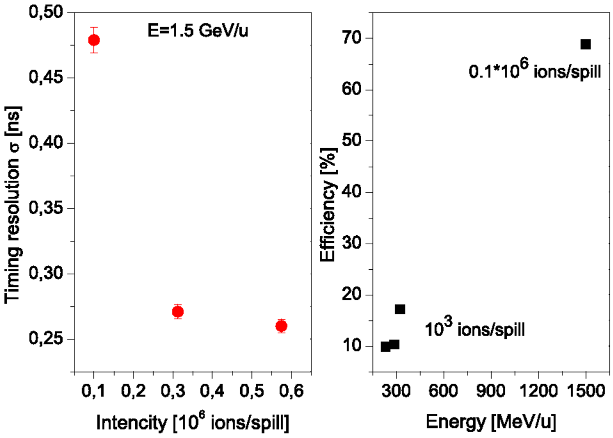

Figure 2: Left: Influence of the intensity on the timing resolution at maximal energy of 1.5 GeV/u. Right: Relative detection efficiency depending on the beam energy.

References

[1] N. Kuzminchuk-Feuerstein et. al.,, GSI Scientific Report 2013 (2014) 103

---

[*] n.kuzminchuk@gsi.de

DOI:10.15120/GR-2015-1-MU-NUSTAR-FRS-05

[2] N. Ferber, Master thesis, RheimMain University of Applied Science, Rüsselsheim, 2014

DOI:10.15120/GR-2015-1-MU-NUSTAR-FRS-05

Development of a large area TEGIC-detector for heavy ions *

S. Maurus †1, *R. Gernhäuser* 1, *M. Winkel*1, *L. Maier*1, *S. Winkler*1, *C. Nociforo*2, *S. Pietri*2, *and J. Hucka*2

1Physik Department E12, Technische Universitat München, Germany; 2GSI Darmstadt, Germany

Upcoming new accelerator facilities with increased intensities for primary and secondary beam experiments are taking established detector systems to their limit of operation and require faster detectors for the beam identification. We have designed a concept for a full-scale Tilted Electrode Gas Ionisation Chamber (TEGIC) with a position sensitive extension and realized and tested it with a full scale detector prototype.

The most common method of element identification of secondary beams produced by fragmentation reactions is by the precise measurement of the energy loss in the active volume of a detector. Due to the high intensities Solid State Detectors (SSDs) are facing radiation damage which can alter their properties or even destruct the devices. Gas detectors however are radiation hard detectors as their active volume gets continuously exchanged and makes them the perfect candidate.

Typically used MUlti Sample Ionisation Chambers (MUSIC) have a limited rate capability due to long drifting paths for the charges produced. To overcome these limitations a new concept was introduced, the Tilted Electrode Gas Ionisation Chamber (TEGIC) [1], consisting of planar electrodes tilted by 60 degree with respect to the beam axis in combination with a fully digital readout for pile up treatment.

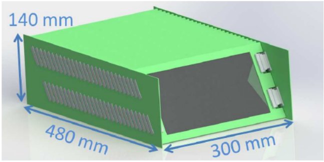

Figure 1: CAD rendered model of the 27 detector electrodes mounted on PCBs inside the detector housing (from [2]).

Figure 1 shows a typically structure for a internal component of the TEGIC-Detector. For the electrodes thin (d = 2 μm) Mylar foils which are coated on both sides with a conductive layer (Aluminum d = 250 nm) and stretched on standard PCB frames. The foils of the position extensions consist also of Mylar foils (d = 5 μm) with chemical etched conductive strips structured in x and y on one side each.

The electrodes are connected alternating to ground or potential to provide a drift field between neighbouring electrodes. Every anode is read out individually and connected to a charge sensitive pre-amplifier MPR-16 (Mesytec) to measure the energy loss for each segment independently.

A test experiment was performed at the FRS using a primary uranium beam at E = 1 AGeV and a Be target (d = 2.5 g/cm^2) to produce a heavy secondary beam cocktail in the mass region around Z = 50. For a systematic study of the energy loss a resolution of $\Delta Z \sim 0.64$ (FWHM) was obtained for ions in this range. A correlation of the identified fragment charges from the standart FRS MUSIC detector and the TEGIC detector is plotted in Figure 2.

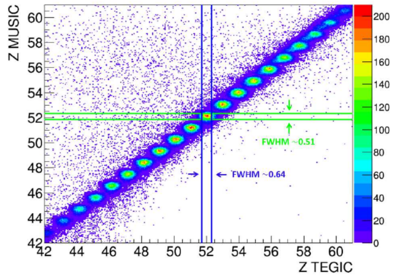

Figure 2: Z MUSIC versus Z TEGIC for ions in the range of Z = 50 with respective resolutions (from [2]).

For the position reconstruction which is presented as a correlation with the standard FRS TPC in Figure 3 a resolution of approximately $\Delta Y = 0.7$ mm for the TEGIC is obtained. Non linearities in the charge distribution over the 12 mm wide strips are still under investigation.

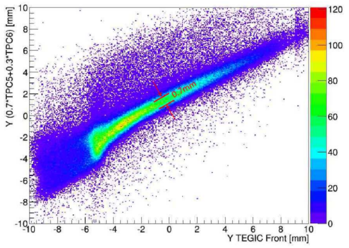

Figure 3: y position TPC versus y position TEGIC with a resolution of $\Delta Y = 0.7$ mm. The non linearities in the charge distribution are still under investigation (from [2]).

References

[1] K. Kimura et al., NIM A 538 (2005), 608-614

[2] S. Maurus, Development of a Large Area TEGIC-Detector for Heavy Ions, MSc thesis, Technische Universitat München (2015)

---

* Supported by BMBF (05P12WOFNF) and GSI (TMLFRG1316)

† steffen.maurus@tum.de

DOI:10.15120/GR-2015-1-MU-NUSTAR-FRS-06

Direct Mass Measurements from Uranium Projectile and Fission Fragments in Ground and Isomeric State *

C. Hornung[1], *S. Ayet*[1,2], *J. Ebert*[1], *T. Dickel*[1,2], *H. Geissel*[1,2], *E. Haettner*[1,2], *I. Miskun*[2], *S. Pietri*[2], *W. R. Plaß*[1,2], *S. Purushothaman*[2], *M. P. Reiter*[1], *A.-K. Rink*[1], *C. Scheidenberger*[1,2], *H. Weick*[2], *P. Dendooven*[3], *M. Diwisch*[1], *F. Greiner*[1], *F. Heiße*[2], *C. Jesch*[1], *N. Kalantar-Nayestanaki*[3], *R. Knöbel*[1,2], *J. Lang*[1], *W. Lippert*[1], *I. Moore*[4], *A. Pikhtelev*[5], *I. Pohjalainen*[4], *A. Prochazka*[2], *M. Ranjan*[3], *M. Takechi*[2], *J. S. Winfield*[2], *X. Xu*[1,2], *and M. I. Yavor*[6]

[1]II. Physikalisches Institut, Justus-Liebig-Universität Gießen, Germany; [2]GSI Helmholtzzentrum für Schwerionenforschung GmbH, Darmstadt, Germany; [3]KVI-CART, University of Groningen, The Netherlands; [4]University of Jyväskylä, Finland; [5]Institute for Energy Problems of Chemical Physics, Russian Academy of Sciences, Chernogolovka, Russia; [6]Institute for Analytical Instrumentation, Russian Academy of Sciences, St. Petersburg, Russia

With the FRS Ion Catcher [1] several projectile and fission fragments were produced in an online experiment in October 2014, separated in-flight, range-bunched, slowed down at the FRS and thermalized in a cryogenic stopping cell (CSC) [2, 3]. A Multiple-Reflection Time-Of-Flight Mass Spectrometer (MR-TOF-MS) [4] served as mass tagger behind the FRS and performed high accuracy mass measurements of several short-lived exotic nuclei produced with low yields.

In the preparation of the online experiment the performance of the MR-TOF-MS was improved. The kinetic energy of the ions in the time-of-flight section of the MR-TOF-MS has been increased to 1300 eV. Mass resolving powers (FWHM) for ^{133}Cs of 120,000, 220,000 and 420,000 of 2.3 ms, 4.6 ms and 18.3 ms total time-of-flight have been obtained, respectively. A novel RF quadrupole-based switchyard was installed and commissioned in the beam line. It provides the opportunity to additionally inject calibrant ions into the RF beam line by merging beams from up to 5 beam lines.

Several projectile fragments produced by bombarding 1000 MeV/u ^{238}U on a ^{9}Be target were measured for the first time directly by MR-TOF-MS with different charge states. Among these $^{213}\mathrm{Rn}^{1+}$ and $^{220}\mathrm{Ra}^{2+}$ with a half-life of only 19.5 ms and 17.9 ms, respectively.

In the region of the chart of the nuclides of the doubly-magic nucleus ^{132}Sn several nuclei have long-lived nuclear isomers. Various fission fragments of Uranium and their long-lived isomers were measured with the MR-TOF-MS with up to 430 turns, corresponding to a time-of-flight of 15.3 ms. The ground state and $19/2^{-}$ isomer of ^{133}I were separated and measured simultaneously at a mass resolving power of 370,000 with the MR-TOF-MS (see figure 1). This allows the determination of the mass of both states directly and therefore the excitation energy of the isomeric state. Furthermore, the abundance ratio between the ground state and the isomer was measured. This will lead to a better understanding of the production mechanism of exotic nuclei at accelerator facilities.

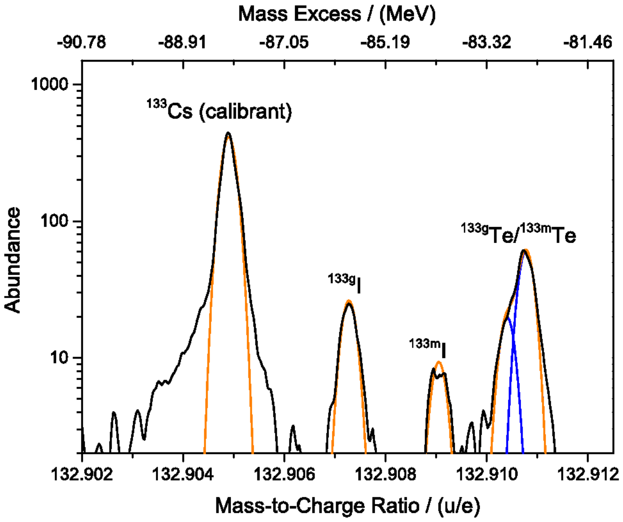

Figure 1: Fission fragment mass spectrum (430 turns) produced by 1000 MeV/u ^{238}U on a ^{9}Be target after a time-of-flight of 15.3 ms in the analyzer of the MR-TOF-MS.

High accuracy mass measurements of the ground state and $25/2^{+}$ isomer of ^{211}Po were performed. In addition, the MR-TOF-MS, equipped with a Bradbury-Nielsen gate (BNG), was used as isomer separator to deliver a pure isomeric beam to a silicon detector was placed. Alpha spectroscopy of the isomer was performed. This work opens up new perspectives for decay experiments with isomers.

References

[1] W.R. Plaß et al., NIM B 317 (2013) 457-462.

[2] M. Ranjan et al., Eur. Phys. Lett. 96 (2011) 52001.

[3] S. Purushothaman et al., Eur. Phys. Lett. 104 (2013) 42001.

[4] T. Dickel et al., NIM A 777 (2015) 172-188.

---

* Work supported within the collaboration agreement between the GSI and KVI-CART, University of Groningen, by the BMBF under contracts no. 05P12RGFN8, by the state of Hesse (LOEWE Center HICforFAIR), by JLU Giessen and GSI under the JLU-GSI strategic Helmholtz partnership agreement, and by EC FP7 - Capacities, contract ENSAR no. 262010

DOI:10.15120/GR-2015-1-MU-NUSTAR-FRS-07

Thermaization and extraction of ^{238}U projectile and fission fragments produced at 1000 MeV/u in the prototype cryogenic stopping cell for the LEB*

M. P. Reiter[1], *A.-K. Rink*[1], *F. Amjad*[2], *S. Ayet*[2], *J. Bergmann*[1], *P. Dendooven*[3], *T. Dickel*[2], *M. Diwisch*[1], *J. Ebert*[1], *A. Estrade*[2], *F. Farinon*[2], *H. Geissel*[1,2], *F. Greiner*[1], *E. Haettner*[2], *F. Heisse*[2], *C. Hornung*[1], *C. Jesch*[1], *N. Kalantar-Nayestanaki*[3], *R. Knoebel*[2], *J. Kurcewicz*[2], *J. Lang*[1], *W. Lippert*[1], *I. Miskun*[2], *I. Moore*[4], *I. Mukha*[2], *C. Nociforo*[2], *M. Petrick*[1], *M. Pfuetzner*[2], *S. Pietri*[2], *W. R. Plaß*[1,2], *I. Pohjalainen*[4], *A. Prochazka*[2], *S. Purushothaman*[2], *M. Ranjan*[3], *S. Rinta-Antila*[4], *C. Scheidenberger*[1,2], *M. Takechi*[2], *Y. Tanaka*[2], *H. Weick*[2], *J. S. Winfield*[2], *X. Xu*[2], *and M. Yavor*[5]

[1]Justus-Liebig-Universität, Giessen, Germany; [2]GSI, Darmstadt, Germany; [3]KVI-CART, University of Groningen, Netherlands; [4]University of Jyväskylä, Finland; [5]Institute for Analytic Instrumentation, St. Petersburg, Russia

At the Low-Energy-Branch (LEB) of the Super-FRS at FAIR, projectile and fission fragments will be produced at relativistic energies, separated in-flight, range-bunched, slowed-down and thermalized in a cryogenic stopping cell filled with ultra-pure helium gas, featuring enhanced cleanliness and high extraction efficiencies. Using an RF carpet with fine electrode spacing enables operation at high stopping gas densities. After extraction from the CSC the ions will be delivered to the high precision low-energy experiments MATS and LaSpec. A prototype CSC [1] for the LEB has been successfully commissioned at the FRS Ion Catcher at GSI [2].

During several experiments [3] in 2011, 2012 and 2014 up to thirteen ^{238}U projectile and six fission fragments have been produced at 1000 MeV/u, stopped, thermalized and extracted from the CSC. For the first time ^{238}U fission fragments produced at 1000 MeV/u were stopped and extracted from the prototype CSC. Total efficiencies of up to 15 % were reached for projectile fragments, about half of this value for fission fragments. Fig. 1 and 2 show the section of the nuclear chart of all nuclides extracted from the CSC and succesfully identified either by α-spectroscopy or mass measurements using a multiple-reflection time-of-flight mass spectrometer [4]. The fragments were extracted without any significant contribution of adducts or molecular contaminants, demonstrating the excellent cleanliness of the CSC. Furthermore no evidence for a element depended extraction was observed. The rate capability of the CSC has been studied in detail, first analysis shows that the CSC perfromes well under higher rates.

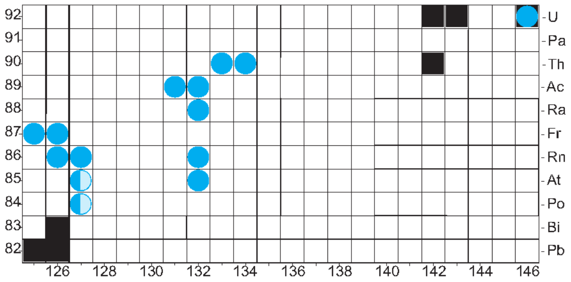

Figure 1: Section of the chart of nuclides showing the projectile fragments produced and measured at the FRS Ion Catcher experiments; half circles indicate the presence of a long lived isomeric state, solid squares indicate stable isotopes.

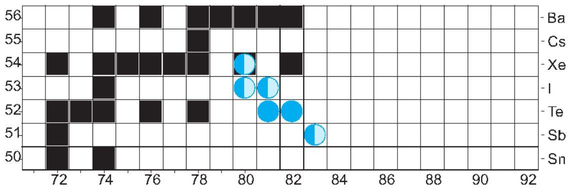

Figure 2: Fission fragments produced and measured at the FRS Ion Catcher experiments; half circles indicate the presence of a long lived isomeric state, solid squares indicate stable isotopes.

The CSC was operated online at areal densities of up to 6.3 mg/cm^2 helium, which is about two times higher than ever reached before for a stopping cell with RF ion repelling structures (RF Carpet). Despite the high areal density the extraction time of ions from the CSC was about 24 ms, enabling the extraction of short-lived fragments, e.g. ^{220}Ra^{2+} with a half-life of only 17.9 ms. For the future LEB stopping cell the areal density will be increased by a factor of about 5, reaching higher stopping and extraction efficeincies, while decreasing the extraction times down to 5 ms. In addition the extraction of ions in higher charge states will be enhanced. Therefore being perfectly suitable for experiments with exotic nuclei at FAIR.

References

[1] M. Ranjan et al., Eur. Phys. Lett. 96 (2011) 52001.

[2] W.R. Plaß et al., NIM B 317 (2013) 457-462.

[3] S. Purushothaman et al., EPL 104 (2013) 42001.

[4] T. Dickel et al., NIM A 777 (2015) 172-188.

---

* Work supported within the collaboration agreement between the GSI and KVI-Cart, University of Groningen, by the BMBF under contracts no. 05P12RGFN8, by the state of Hesse (LOEWE Center HICforFAIR), by the JLU-GSI strategic Helmholtz partnership agreement, and by EC FP7 - Capacities, contract ENSAR no. 262010

DOI:10.15120/GR-2015-1-MU-NUSTAR-FRS-08

An RFQ based beam line and mass filter to improve identification capabilities at the diagnostics unit of the prototype CSC for the LEB *

I.Miskun[2], *M.P.Reiter*[1], *A-K.Rink*[1], *T.Dickel*[1,2], *S.Ayet*[2], *J.Ebert*[1], *H.Geissel*[1,2], *F.Greiner*[1], *E.Haettner*[1,2], *C.Hornung*[1], *W.R.Plaß*[1,2], *S.Purushothaman*[2], *and C.Scheidenberger*[1,2]

[1]Justus-Liebig-Universität, Giessen, Germany; [2]GSI, Darmstadt, Germany

In the vicinity of gas-filled stopping cells vacuum pressures are typically too high for operation of conventional electrostatic beam lines. In this high pressure environment radio frequency quadrupoles (RFQ) can provide an efficent ion transport. Advantages of RFQ beam lines are their high transmission efficiencies of nearly 100%, ability to operate at high pressures, compactness ($\approx$ 1m length) and diverse range of applications, e.g. cooling, bunching, mass separation and beam diagnosis.

Such an RFQ based beam line [1] for the prototype cryogenic stopping cell (CSC) [2] has been commissioned successfully at the FRS Ion Catcher at GSI [3]. Recently, the identification of ions in the diagnostics unit (DU) of the RFQ beam line was done by α spectroscopy, but this way of identification is only suitable for α decayed nuclei. In order to improve the identification capabilities of the DU the extraction RFQ of the CSC was modified to operate as an RF-DC mass filter [4]. Thus it is possible to identify ions by their mass-to-charge ratio directly behind the stopping cell. Fig. 1 shows a mass spectrum of ions produced by a discharge ion source mounted inside the CSC. The mass spectrum shows ions from the electrode material of the discharge source (Fe, Cr etc.) and from a ^{223}Ra recoil ion source. The mass filter can provide mass-to-charge information of ions between 30 u/e and 250 u/e. This mass spectrum has a resolving power of 10, while achieving a transmission of 80 %. Besides mass identification, the extraction RFQ can be used as a mass filter, transmitting a narrow mass window only and reducing the number of transmitted ions down to the required mass region. As seen in Fig. 1, if the mass filter is tuned for transmission of mass 140 u, the main ion current (mass 65 u) is surpressed by four orders of magnitude.

The mass resolution can be increased further, but as shown in Fig. 2 higher resolving powers lead to reduced transmission. Despite the high pressures the mass-filter provides mass selective ion transport with resolving powers of up to 150 at residual gas pressures of $8.4 \cdot 10^{-2}$ mbar. The performance of the mass filter at high residual gas pressures is of special importance, as the buffer gas emerging from the CSC is pumped away in the extraction region and therefore the areal density of the CSC is determing the residual gas pressure in the DU.

The rough mass identification of ions directly behind the CSC allows systematic investigations of the performance of the CSC. Furthermore the transmission of the downstream beam line can be optmized based on the meassured mass-to-charge ratio. In addition the mass filter can surpress unwanted ions and decrease space charge effects and contaminations inside the more sensitive parts of the downstream low energy beam line.

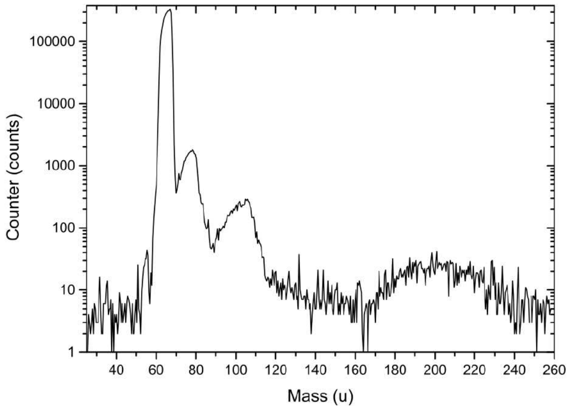

Figure 1: Mass spectrum of ions produced by a discharge ion source inside the CSC measured using the extraction RFQ mass filter

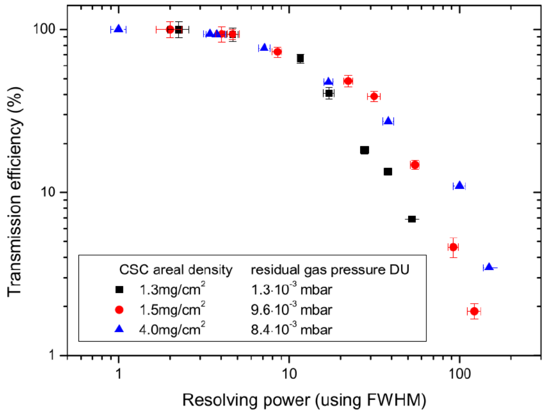

Figure 2: Transmission efficiency vs. mass resolving power of the extraction RFQ mass filter at different residual gas pressures in the DU and the corresponding areal densities inside the CSC.

References

[1] E. Haettner, GSI Scient. Report 2011,Nustar-FRS-25,P167

[2] M. Ranjan et al., Eur. Phys. Lett. 96 (2011) 52001.

[3] W.R. Plaß et al., NIM B 317 (2013) 457-462.

[4] I. Miskun, Diploma thesis, 2015

---

* Work supported by the BMBF under contracts no. 05P12RGFN8, by the state of Hesse (LOEWE Center HICforFAIR), by JLU Giessen and GSI under the JLU-GSI strategic Helmholtz partnership agreement

DOI:10.15120/GR-2015-1-MU-NUSTAR-FRS-09

Upgrade of the GADAST detector by 16 $LaBr_3$ scintillator detectors*

I. Mukha [1], *V. Dunin*[2], *A. Fomichev*[3], *S. Krupko*[3], *A. Bezbakh*[3], *S. Baraeva*[3], *A. Gorshkov*[3],
A. Knyazev[3], *P.G. Sharov*[3], *C. Scheidenberger*[1], *H. Simon*[1], *and R. Slepnev*[3]
[1]Helmholzzentrum GSI, Darmstadt, Germany; [2]Veksler and Baldin Laboratory of High Energy Physics, JINR, Dubna, Russia; [3]Flerov Laboratory of Nuclear Reactions, JINR, Dubna, Russia

The GAmma-ray Detector Around Secondary Target (GADAST) can be used in the middle of the FRS and Super-FRS fragment separators [1], which helps to exploit their unique performance in a separator−high-resolution-spectrometer mode. The main part of the GADAST consisted of 64 large-size scintillating CsI(Tl) crystals is in production at JINR, Dubna. The GADAST demonstrator of 16 such detectors has been successfully tested at FRS GSI in 2012 [2]. In order to upgrade the GADAST at forward angles, we build in addition an array of 16 $LaBr_3$ scintillator crystals (cylinders of 1x4 inches) with improved light readout and electronics being able to work at high counting rates up to 10^6 s^{-1} with the energy resolution of 3 %.

During the upgrade of GADAST, the 64 CsI(Tl) detectors have received a new mechanical structure (4 crystals in one cluster), which allows for various geometries of the GADAST setup depending on experimental task. Each crystal is coupled with a photo multiplier tube (PMT) either of R7600U-300 Hamamatsu (40 units in total) or 9106SB ET (24 units) types. The in-house developed electronics, being operated at +12 V only, provides a high-voltage (HV) bias, strong amplification of the detector signals and their shaping as well as logical signals via a delay line of 0.8 μs. However, the CsI(Tl) detectors work at counting rates $\leq 3*10^4$ s^{-1}, which is not sufficient at forward angles where counting rates are very high.

Figure 1: The components of the $LaBr_3$ detector.

Scintillation $LaBr_3$ crystals are much faster and provide better energy resolution. Thus we have developed a cluster of 16 detectors with $LaBr_3$ crystals. Dimensions of the crystals were chosen of 2.5 cm in diameter (in order to minimize a Doppler broadening of detected γ-rays) and 10 cm in length (to detect γ-rays up to energies of 10-20 MeV). We have chosen a PMT type 9142SB ET with an enforced voltage divider and a plate with combined HV-bias, preamplifier of dinode signals and shaper (similar to those developed for the CsI(Tl) detectors [2]). The components of the disassembled $LaBr_3$ detector are shown in Fig. 1.

Performance of the developed detectors is illustrated in Fig. 2, where the γ-ray spectrum measured from ^{137}Cs source shows the energy resolution of 3.0(1) % (the full width at half maximum (FWHM) of the peak of 662 keV γ-rays measured with a shaping time of 0.5 μs). The obtained energy resolution is even better than the resolution of 3.4 % reported by the St. Gobain manufacturer. The low energy detection threshold of ~50 keV is achieved.

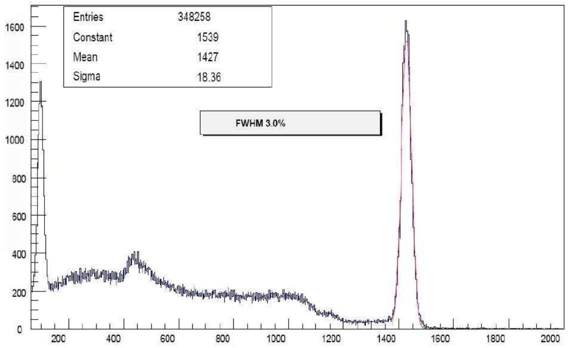

Figure 2: The γ-ray spectrum of a standard ^{137}Cs source measured with the developed $LaBr_3$ detector. The right peak corresponds to 662 keV γ-transitions.

The detector GADAST is ready for experiments since 2014. We plan to use it at the new ACCULINNA-2 (JINR, Dubna) fragment separator [3] and later at the FRS and the Super-FRS fragment separators [4]. Applications of the developed detectors are possible also for the other experiments of the NUSTAR collaboration of FAIR.

References

[1] I. Mukha *et al.*, "Gamma detector around a secondary target (GADAST) at the middle of the fragment separator FRS", LoI 49 to the G-PAC GSI (2010), unpublished.

[2] I. Mukha *et al.*, "First Operation of the GADAST, GAmma-ray Detector Around a Secondary Target in the Middle of FRS: Measurements of inelastic Scattering of ^{17}Ne", GSI Scientific Report 2012, PHW-ENNA-EXP-45, p.175, http://repository.gsi.de/record/52876.

[3] A.S. Fomichev *et al.*, "Long-range plans for research with radioactive ion beams at JINR", JINR Communication E7-2012-73, Dubna, 2012.

[4] "Scientific program of the Super-FRS Collaboration: Report of the collaboration to the FAIR management", GSI Report 2014-4, doi:10.15120/GR-2014-4.

---

* Work supported by the grants BMBF GSI-JINR and Helmholz-Rosatom for FAIR.

DOI:10.15120/GR-2015-1-MU-NUSTAR-FRS-10

Status of ion-optics for the Super-FRS*

J.S. Winfield†[1], H. Geissel[1,2], B. Franczak[1], E. Kazantseva[3], R. Knoebel[1,2], I. Mukha[1], G. Münzenberg[1], C. Nociforo[1], W.R. Plaß[1,2], S. Purushothaman[1], C. Scheidenberger[1,2], H. Weick[1], M. Winkler[1], M. Yavor[4], and the FAIR@GSI division[1]

[1]GSI, Darmstadt, Germany; [2]JLU, Giessen, Germany; [3]TU Darmstadt, Germany; [4]RAS, St. Petersburg, Russia

Introduction

While the basic ion-optics for the Super-FRS were already established some years ago [1], several changes to the magnet layout have necessitated re-optimizations. Three baseline ion-optics files corresponding to the High Energy, Low Energy and Ring branches should be kept up-to-date. Since the main "work-horses" for the Super-FRS ion-optics are GICOSY [2] and MIRKO [3], translations between the respective input files are frequently made. Various improvements to the translation programs have been made over the last few years. Besides which, COSY-Infinity [4] is also used and has to be maintained. Furthermore, the example files for the simulation programs MOCADI [5] and LISE++ [6], which are based on the transfer matrices generated by GICOSY, need updating if the ion-optics change.

Since many users need, in particular, MOCADI and LISE++ simulations to plan beamline equipment (such as detectors, slits, focal-plane chambers) as well as future experiments, it is convenient to make template input files available for download on a website [7].

Lattice changes

One change affecting all of the Super-FRS ion optics has been the revision of the radiation-resistant quadrupoles after the production target. The revised first quadrupole FPF1QT11 has a smaller aperture and is shorter than the original design. FPF1QT12 on the other hand is longer, but has the same pole gap as before. Importantly, both magnets are further from the target in order to make room for the target chamber, flanges, bellows and pillow seals. Monte Carlo simulations show that while the nominal horizontal angular acceptance is reduced from the "standard" 40 mrad to 38 mrad, the effect on the overall transmission to the end of the Super-FRS is reduced by less than 1%. The change in quadrupole fields also has affected the $2^{nd}-$order corrections. With the usual vertical focus condition at FPF2 for 20 Tm beams, the normal-conducting sextupole magnet FPF2KS11 is pushed slightly beyond its limit in order to correct fully the [A,DD] aberration. By moving the y-focus somewhat beyond FPF2, the required field in FPF2KS11 is reduced and 20 Tm beams can be again fully corrected to high order.

Additional space for detectors and a "slow-down" degrader was needed at the FLF2 focal plane (end of the Low Energy Branch). The previous drift space of 2 m was doubled to 4 m. The ion optics for the Energy Buncher was verified with this increased drift space.

The layout of LEB Energy-Buncher/Spectrometer has been revised. It consists of two dipole stages deflecting the beam in opposite directions, forming an S-shape (Fig. 1). There is a cross-over in the ion trajectories between the two dipole stages so that the resolving power adds together. The final adjustment to the lattice has been the addition of three vertical steerers, which are included in the common quadrupole-sextupole cryostats.

The first dipole stage of the LEB Energy Buncher can be operated as a large acceptance spectrometer for HISPEC/DESPEC [8]. Another mode is to use the Main Separator of the Super-FRS as an "Analyser", coupled and dispersion-matched to the LEB, the ion-optics of which is changed to an "Energy-loss Spectrometer". In this way one obtains very high resolving power [9], despite the large emittance of RIBs produced by fragmentation or fission.

Simulations with MOCADI

The possible loss in beam transmission due to the deflection of dipole vacuum chambers under atmospheric pressure was considered. For the super-conducting dipoles, the deflection is negligible ($\leq$ 1 mm). For the radiation-resistant dipoles in the Pre-Separator, the vacuum chambers must be large enough horizontally to accommodate various charge states of the beam, and ANSYS calculations [10] have shown that the transverse deflection of these chambers can be up to 5.7 mm. However, even such a reduction in the vertical acceptance gives $< 1\%$ transmission loss.

Certain experiments proposed within the Super-FRS collaboration [11] require light RIBs, e.g. ^{24}Ne, slowed-down to Coulomb-barrier energies. The energy distribution and transmission of such ions produced by fragmentation and slowed by achromatic or mono-energetic degraders have been calculated with MOCADI. In addition, the feasibility of experiments using such secondary beams to bombard "stack" targets within a gas cell to produce heavy ions of interest to SHE research [12] has been studied.

Magnet field quality calculations

The availability of random numbers and unlimited order calculations have made COSY-Infinify a useful Monte-Carlo tool to study magnet misalignments [13] and the field quality of vertical steerers in the Super-FRS. In the latter case, dummy elements with sextupole (B_6) and de-

---

* Work supported by FAIR@GSI Super-FRS PSP code: 2.4.1

† winfield@gsi.de

DOI:10.15120/GR-2015-1-MU-NUSTAR-FRS-11

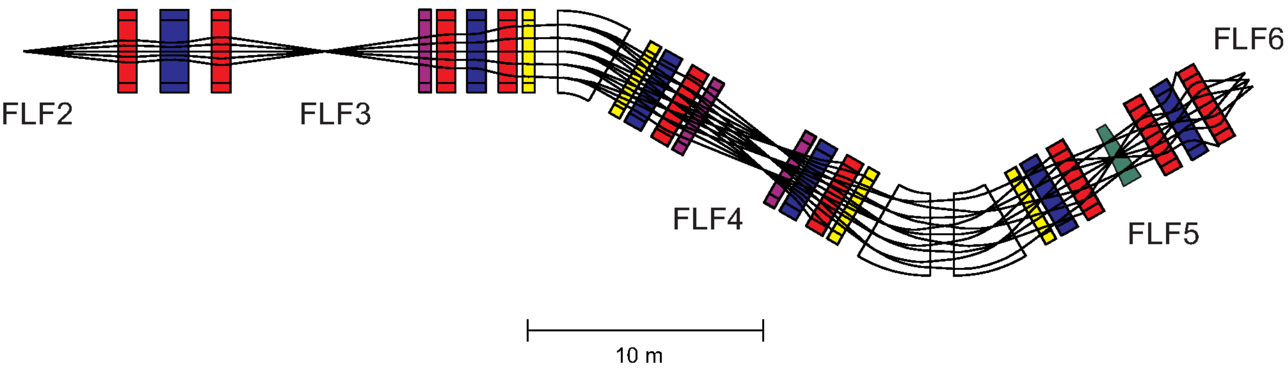

Figure 1: Revised layout of the LEB Energy Buncher, starting from the exit of the Low Energy Branch of the Super-FRS (FLF2). The colour scheme is: x- and y-focusing quadrupoles (red and blue, respectively), sextupoles (yellow), vertical steerers (purple). The mono-energetic degrader is at FLF5 (green wedge). The cryogenic stopping cell would follow after FLF6. The beam trajectories are for an emittance ϵ_x of 255 mm mrad and a momentum spread of $\Delta p/p = \pm 2.5\%$.

capole (B_{10}) random fields were used in place of actual steerer magnets. The strength of the contaminating fields was stepped from zero up to a value where there was a significant loss in resolving power of the fragment separator. For each step, a loop of 50 iterations with different random numbers was used to average out fluctuations in the resolving power (see Fig. 2). The maximum allowable contaminating field is chosen as that resulting in no more than 1% loss in resolving power (red line in Fig. 2). The result, $\Delta B_6/B_2$, where $\Delta B_6 \approx 1.4 \times 10^{-3}$ T and $B_2 = 0.2$ T for 20 Tm beams, showed that the field quality previously specified in the Super-FRS Parameter List of January 2014 could be significantly relaxed.

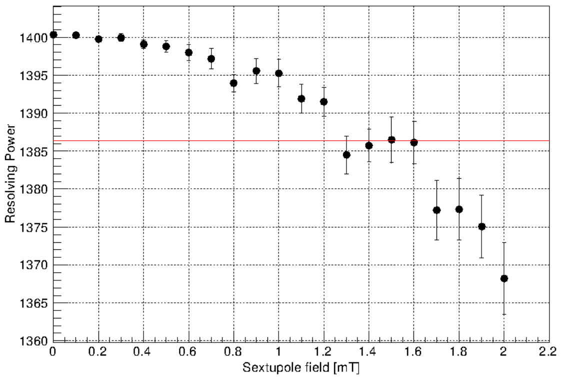

Figure 2: Second-order momentum resolving power at the dispersive focal plane FMF2 against sextupole fields (in millitelsa) in vertical steerer magnets. The error bars are the standard deviation of 50 calculations at each sextupole field strength. The red line represents 99% of the resolving power with no sextupole field.

MIRKO [3] has been extended espcially for the FRS and Super-FRS, and has been used in a somewhat similar way as above, to establish the required field quality of the Energy Buncher dipoles, quadrupoles and sextupoles. With MIRKO, the width of the projected image at the achromatic focus can be used as a quality factor.

References

[1] H. Geissel et al., Nucl. Instr. Meth. B 204 (2003) 71

[2] M. Berz, B. Hartmann, K. Lindemann, A. Magel and H. Weick, Univ. Giessen, 1986-1998 (unpublished)

[3] B. Franczak, “Computing in Accelerator Design and Operation”, Lecture Notes in Physics, vol. 215 (1984) p. 170

[4] K. Makino and M. Berz, Nucl. Instr. Meth. A 558 (2005) 346

[5] N. Iwasa et al., Nucl. Instr. Meth. B 126 (1997) 284

[6] O. Tarasov, D. Bazin, Nucl. Instr. Meth. B 266 (2008) 4657

[7] http://web-docs.gsi.de/∼winfield/

[8] J.S. Winfield et al., “Mass measurement by track reconstruction with the LEB spectrometer”, GSI Scientific Report 2012 (2013) 209

[9] H. Geissel et al., Nucl. Instr. Meth. B 317 (2013) 277

[10] K. Dermati, private communication, GSI 2014.

[11] C. Scheidenberger et al., “Unique separator-spectrometer experiments at the frontiers of nuclear physics: the Super-FRS Scientific program”, INPC-2013, Florence, Italy, EPJ Web of Confs. 66 (2014) 11034

[12] G. Münzenberg et al., “SHE Research on the way to NUSTAR and FAIR”, EXON-2014, Kaliningrad, Russia, 8-13 September 2014 (submitted)

[13] J.S. Winfield et al., “Magnet Alignment and the Super-FRS Resolving Power and Transmission”, GSI Scientific Report 2008 (2009) 88

DOI:10.15120/GR-2015-1-MU-NUSTAR-FRS-11

New results from combined isochronous mass spectrometry experiments with 238 U fission fragments at the FRS-ESR facility [*]

M. Diwisch[1], *R. Knöbel*[1,2], *H. Geissel*[1,2], *Z. Patyk*[3], *W. R. Plaß*[1,2], *C. Scheidenberger*[1,2], *H. Weick*[2], *K. Beckert*[2], *F. Bosch*[2], *D. Boutin*[1,2], *C. Brandau*[1,2], *L. Chen*[1,2], *I. J. Cullen*[4], *C. Dimopoulou*[2], *A. Dolinskii*[2], *B. Fabian*[1], *M. Hausmann*[5], *O. Klepper*[2], *C. Kozhuharov*[2], *J. Kurcewicz*[2], *N. Kuzminchuk*[1], *S. A. Litvinov*[2], *Y. A. Litvinov*[2], *Z. Liu*[4], *M. Mazzocco*[2], *F. Montes*[5], *G. Münzenberg*[2], *A. Musumarra*[7], *S. Nakajima*[8], *C. Nociforo*[2], *F. Nolden*[2], *T. Ohtsubo*[9], *T. Ozawa*[10], *M. Steck*[2], *B. Sun*[11], *T. Suzuki*[8], *P. M. Walker*[4], *N. Winckler*[6], *M. Winkler*[2], *and T. Yamaguchi*[8]

[1]Justus-Liebig Universität Gießen, Gießen, Germany; [2]GSI, Darmstadt, Germany; [3]Soltan Institute for Nuclear Studies, Warsaw, Poland; [4]University of Surrey, Guildford, United Kingdom; [5]Michigan State University, East Lansing, USA; [6]Max Planck Institut für Kernphysik, Heidelberg, Germany; [7]Laboratori Nazionali del Sud, INFN Catania, Italy; [8]Saitama University, Saitama, Japan; [9]Niigata University, Niigata, Japan; [10]University of Tsukuba, Tsukuba, Japan; [11]School of Physics, Peking University, Beijing, China

The established correlation matrix method [1] has been applied to two different isochronous mass spectrometry (IMS) experiments. The analyzed experiments were performed with uranium fission fragments, but differ in the usage of the $B\rho$-tagging method [2].

In IMS experiments the storage ring can only be tuned to be isochronous for one specific mass-to-charge ratio (m/q). Particles with different m/q are only isochronous in a very limited $B\rho$ region. For these other m/q and large $B\rho$ deviations the mass accuracy of the method is reduced. In order to overcome this problem the $B\rho$ tagging technique uses slits at a high dispersive region in the FRS to accept only particles with a relative $B\rho$ deviation of 10^{-4}. This increases the mass accuracy but decreases the transmission efficiency. Besides the experimental differences in both experiments also the analyses of the data have been performed with different restrictions to the accepted data.

In previous analyses of the data in [3] and in [4] [5] additional restrictions were imposed on the measured data by removing events with poor isochronicity which then achieved a high mass accuracy down to a few 100 keV. In the new analysis there are no restrictions to both data sets and also single particles could be analyzed. Taking also single particles into consideration very exotic nuclei could be analyzed in the new method for the first time. In order to be able to achieve a reasonable error for those nuclei, which did not fulfill the conditions in each single experiment in the first place, both data sets have been combined [6].

Combining the two experimental data sets the masses of more than 15 nuclides could be analyzed for the first time (figure 1).

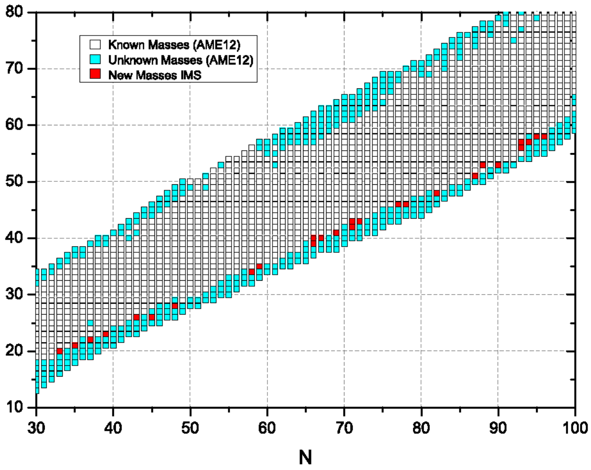

Figure 1: Figure 1: The chart of nuclides indicating nuclides with known in [7] (white), unknown (blue) and newly measured (red) masses.

A special relevance for nuclear astrophysics has the mass of ^{130}Cd because this nuclide is a candidate for an r-process waiting point. The mass of this nuclide has a large impact on network calculations for nuclear astrophysics to explain the solar abundances of elements.

References

[1] T. Radon et al., Phys. Rev. Lett. 78, (1997), p.4701-4704

[2] H. Geissel et al., Hyperfine Interactions 173, (2006), p.55-60

[3] M.Matos, PhD Thesis, JLU Giessen, (2004)

[4] R. Knöbel, PhD Thesis, JLU Giessen, (2008)

[5] B. Sun, Phys. Lett. B 688, (2008), p.294-297

[6] M. Diwisch, PhD Thesis in preparation, JLU Giessen, (2015)

[7] M. Wang, Chin. Phys. C, 36, (2012), p.1603-2014

---

[*] Work supported by the BMBF under contract No.06GI9115I, by the HGF (NAVI) , by Justus-Liebig-University Giessen and GSI under the strategic Helmholtz partnership agreement and by the Hessian Ministry for Science and Art (HMWK) through the LOEWE Center HICforFAIR

DOI:10.15120/GR-2015-1-MU-NUSTAR-FRS-12

Study of the HPGe detector radiation damages by pulse shape analysis

I.Kojouharov[1], *D.Kocheva*[2],*J.Gerl*[1]
[1]GSI, Darmstadt, Germany; [2] Univesity of Sofia, Sofia, Bulgaria

Motivation

Application of the HPGe detectors in accelerator driven gamma-spectroscopy experiments is often carried out in an environment rich of fast neutrons and charged particles. Interacting with the germanium, these particles cause radiation damages which are the limiting factor for the life of the detector and useful data collected.

The radiation damages cause an enhanced trapping probability of the charge carriers. Since the detrapping occurs rather late after the charges are collected, it does not contribute to the pulse height and effectively these charges are treated as a DC current. As a result a strong tailing of the low energy slope of the gamma-line is to be observed. Quantification of this tailing is done by the ratio $\frac{FWTM}{FWHM}$ where FWTM and FWHM are the width of the gamma-line at 1/10th and half maximum of the line. It requires a very good statistics and generally is sensitive only to high degree of damage, thus becoming a not good definition for the deformation of the line. In this study we focused our attention on the correlations between the shape of the pulse from the detector and the degree of radiation damage.

Experimental results

The trapping effects distort the pulse shape at its higher part [1]. The incomplete charge collection leads to ballistic deficit, i.e. the pulse is slightly lower. Therefore, comparing the rise times of the pulse at the beginning (the time the pulse to reach 30% of its height) and at the end (the time to pulse to reach from 80% to 100% of its height) sheds light of the effectiveness of the trapping process.

The degree of the radiation damages has been studied experimentally comparing two almost equal HPGe encapsulated detectors (EB capsules) - one has been irradiated by fast neutrons and the other one is undamaged showing good charge collection. Their properties before irradiation have been rather equal, so that any charge carrier traps due to incomplete purification of the material or crystal growth process are not supposed to distort the results. The measurements have been carried out by ^{60}Co source and the pulse shapes have been directly digitized after the preamplifier [2]. The waveforms are gated with the 1173 and 1332 keV lines.

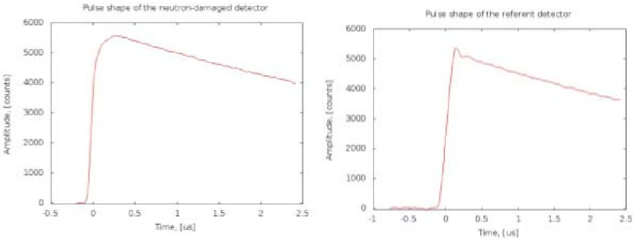

Figure 1: The electron collection dominated pulse shape from a damaged detector (left) and from an undamaged detector (right).

The charge carries, in these case electrons, are collected at the core n-contact of the N-type HPGe crystal by an AC-coupled preamplifier. The outer p-contact of the detector is grounded. The signal shapes from the damaged and undamaged detector are shown on Fig.1 left and right respectively. Depending on the position of the interaction, the electrons collection can dominate generation of the pulse (Fig.1 left) or the holes (Fig.2). This study has been limited to the electron collection dominated pulses.

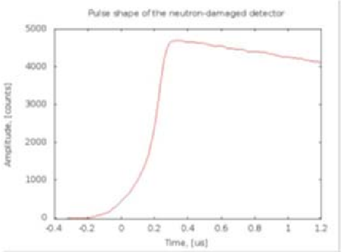

Figure 2: The holes collection dominated pulse from a damaged detector.

The plots of the rise times at the end of the pulse (T80-100) vs. the rise times at the beginning T30 of the pulses for the both detectors are shown on Fig.3, left for the undamaged and right for the damaged ones.

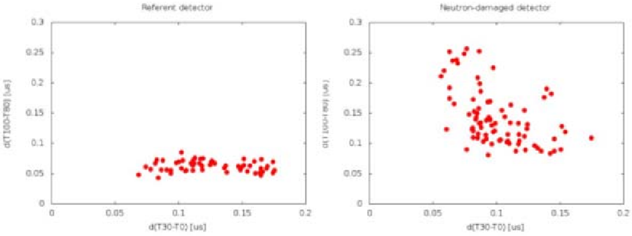

Figure 3: The T80-T100 vs. T30, left is the undamaged detector, right is the damaged one.

The shapes of the pulses coming from the damaged detector clearly differ from those coming from the undamaged ones. Similar effects can be attributed also to the results of the studies [3]. Despite that a comprehensive pulse shape analyse has not been reported, the evolution of the pulses due to the radiation damage suggests a related behaviour.

The statistic of the pulse shapes in this study is not high enough to draw a more detailed conclusion concerning the radiation damage effects. Also a highly damaged crystal has been selected, thus a possible observation thresh-

DOI:10.15120/GR-2015-1-MU-NUSTAR-GS-01

old for the damages degree cannot be stated. Therefore, more comprehensive study of these effects has to be carried out, also with respect of the irradiation evolution.

Acknowledgements

The authors would like to thank to V.Jordanov and the company LABZY, who kindly provided the Multichannel Analyser nano-MCA® used in this study.

References

[1.] G. Knoll, Radiation Detection and Measurements, John Wiley and Sons, 2000.

[2.] http://www.labzy.com/index.html#nanoMCA-SP

[3.] M. Steinen, S. Bleser et al., Development of the Germanium detector array for PANDA, GSI Annual report 2014, in press.

DOI:10.15120/GR-2015-1-MU-NUSTAR-GS-01

Evolution of collectivity in the vicinity on ^{208}Pb: Preliminary results*

M. L. Cortés†[1,2], *T. Alexander*[3], *L. G. Sarmiento*[4], *M. Reese*[1], *D. Rudolph*[4], *Z. Podolyák*[3],
N. Pietralla[1], *J. Gerl*[2], *and the PreSPEC and AGATA Collaborations*
[1]TU Darmstadt, Darmstadt, Germany; [2]GSI, Darmstadt, Germany; [3]University of Surrey, Guildford, United Kingdom;
[4]Lund University, Lund, Sweden

Knowledge on the spectroscopic data of nuclei in the region of ^{208}Pb provides key information to probe parameter sets of nuclear models, both shell-model and mean-field based. It also serves as a basis for the extrapolation of any nuclear model into the area of actinides and super-heavy nuclei. Since ^{208}Pb is the heaviest doubly-magic nucleus known to date, it is also the last firm anchor point for extrapolations. Within the PreSPEC-AGATA campaign at GSI [1], fragmentation of a ^{208}Pb beam at 1GeV/u on a 2.5 g/cm^2 Be target was performed to study Pb, Hg and Pt isotopes. Charge and mass-to-charge ratio of the incoming particles were obtained in an event-by-event basis using the standard FRS detectors [2]. Figure 1 shows the identification plot obtained for the reference isotope ^{206}Pb. The reduced Z resolution observed is due to the creation of charge states during the passage of the heavy ions through the ionization chambers and other material in the S4 area. The solid line, containing 73% of the events, indicates the gate used to select the isotope of interest and to avoid background events. Incoming particles were focused in a 400 mg/cm^2 thick Au target to perform relativistic Coulomb excitation. Particle identification after the target was obtained by combining the measurements of energy loss and total kinetic energy in the LYCCA calorimeter [3] as shown in Figure 2. The solid line indicates the gate used to select Pb ions. γ rays emitted after the reaction were detected using the AGATA [4] array. Gates on particle-γ time, scattering angle and crystal multiplicity were applied to observe the decay of the target nuclei after Coulomb excitation. Figure 3 shows the energy spectrum obtained using an 10 ns time gate, a scattering angle between 2 mrad and 20 mrad and crystal multiplicity lower than 4. The observed peak at 547.5 keV comes from the $7/2^+ \rightarrow 3/2^+$ transition in Au. The total number of counts observed for this transition is 66(31). Changes on gates used, as well as background subtraction will be performed to increase the statistics and to improve the peak-to-total ratio. Doppler correction will be performed to obtain the projectile de-excitation γ peak.

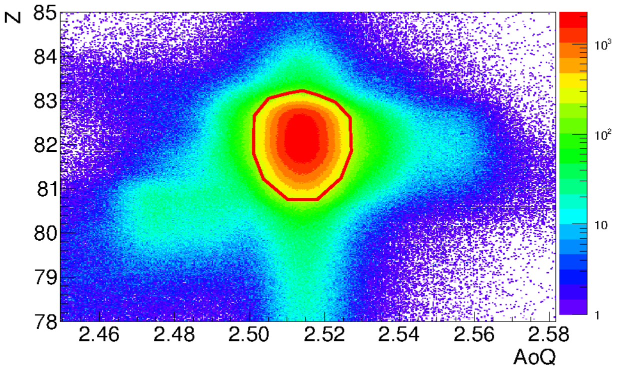

Figure 1: Incoming particle identification: AoQ vs Z as measured in the FRS

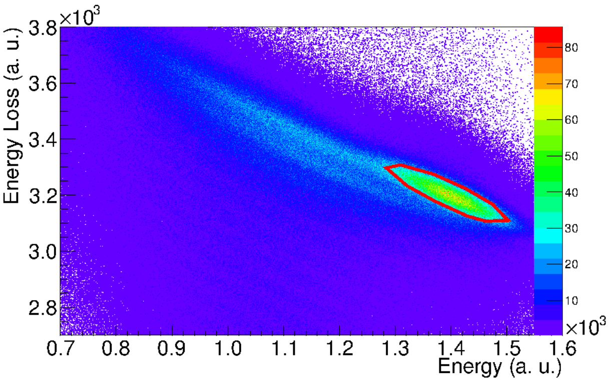

Figure 2: Outgoing particle identification: Total kinetic energy vs. Energy loss in the LYCCA calorimeter

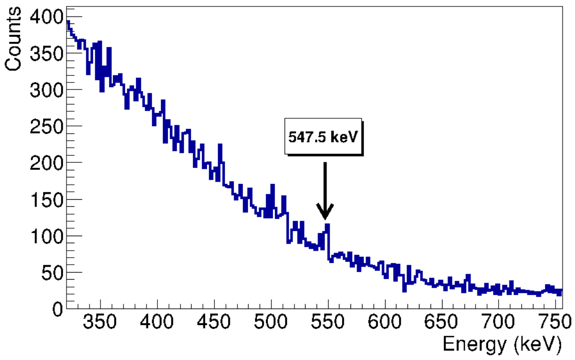

Figure 3: Energy spectrum measured by AGATA showing the 547.5 keV $7/2^+ \rightarrow 3/2^+$ transition in Au.

References

[1] N. Pietralla et al., EPJ Web of Conferences 66 (2014) 02083.
[2] H. Geissel et al., Nucl. Instr. Meth. B 70 (1992) 286.
[3] P. Golubev et al., Nucl. Instr. Meth. A 723 (2013) 55.
[4] S. Akkoyun et al., Nucl. Instr. Meth. A 668 (2012) 26.

---

* Work supported by BMBF NuSTAR.DA - TP 6, FKZ: BMBF 05P12RDFN8 (TP 6), HGS-HIRe

† m.l.cortes@gsi.de

DOI:10.15120/GR-2015-1-MU-NUSTAR-GS-02

Study of the background observed at PreSPEC *

G. Guastalla[1,2], *M. Górska*[1], *J. Gerl*[1], *I. Kojuharov*[1], *N. Pietralla*[2], *S. Pietri*[1], *D. Ralet*[1,2], *and H. J. Wollersheim*[1]
[1]GSI, Darmstadt, Germany; [2]TU Darmstadt, Darmstadt, Germany

Introduction

The PreSPEC setup in combination with the relativistic rare isotope beams provided by the FRagment Separator (FRS) [1] provided unique opportunities for key nuclear structure studies on exotic nuclei. However, the large amount of background radiation co-produced is a great challenge for the data analysis process. Even after a detailed analysis and the application of strict conditions, a large component of the background can remain in the γ-ray energy spectra and often hamper the observation of the transition of interest. A dedicated analysis has been therefore performed in order to better disentangle the components of the background that affects γ-ray energy spectra and understand their nature and origin. Data of a PreSPEC experiment with the EUROBALL cluster array [2] have been used for the analysis reported here.

Analysis

The hits recorded in the cluster array were observed to be grouped in four energy ranges and to form four peaks in the time distribution. One time peak was composed by hits produced by the interaction of the beam in the target area (prompt γ-rays) and their energy values were in the expected range (i.e., for this data, from $\sim$ 0.08 MeV to 6.8 MeV). A time peak preceding the prompt and two time peaks following it, instead, were formed by hits with energy values out of the standard range, which could be associated to a saturation of the front-end electronics. The relation between the time of the hits and the multiplicity of the hits per cluster and per event allowed to observe a peculiarity of the delayed hits: while the hits in the prompt time peak have mainly multiplicity one, the hits in the first delayed time peak have mostly multiplicity six (see Fig. 1).

This information, together with correlations with other observables as energy-loss, beam position at the target and distribution of the hits in the array, gave indications that the cluster array was hit by high-energy particles coming with the beam, which saturated the preamplifiers. Moreover, the deposition of very high energy provoked the alteration of the response of the other crystals in the same cluster and explains the detection of high multiplicity of energy signals. It can be notice that the highest multiplicity value in Fig. 1 is six and not seven, which is the number of crystals in a cluster. This is due to the fact that the seventh hit was always recorded in the time range before the prompt.

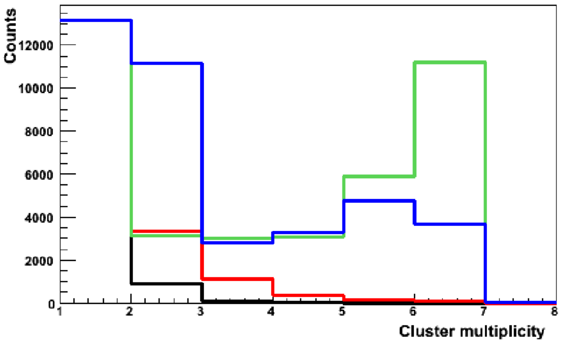

Figure 1: Cluster multiplicity of the hits according to different time ranges , normalized at the values for multiplicity one. No energy condition has been applied. For hits in the prompt time range (red line) and the one before the prompt (black line), the cluster multiplicity is mainly one. Hits in the first delayed peak (green line), in addition to the peak at multiplicity one, a peak at multiplicity six is also present. In the most delayed peaks (blue line), the cluster multiplicity is mainly one and two but higher multiplicities are also present in a considerable amount.

Conclusion and Outlook

In addition to the known background radiation [3, 4], indications of high-energy particles interactions with the γ-ray spectrometer, provoking a loss of the detection efficiency and a worsening of the quality of the data, have been observed. The saturation of a full cluster was calculated to occur in more then 30% of the events. As these events are occurring mainly in the inner ring of the EUROBALL cluster array, which is also the ring with a better detection efficiency for the in-flight emitted γ rays[1], they can substantially reduce the detection efficiency of the array.

A continuation of the analysis using the tracking capabilities of AGATA [5] as well as other dedicated background measurements will further clarify the origin of this radiation and of other background components. However, from the new information obtained from this analysis on the background, several improvements of the setup can be suggested, in view of new challenging experiments in the future with HISPEC/DESPEC at the FAIR facility: implementation of high-energy thresholds for the hits in the γ-ray spectrometer, introduction of fast-reset modules in the

---

* Work supported by the Helmholtz International Center for FAIR (HIC for FAIR) within the LOEWE program by the State of Hesse, the BMBF under grant No. 05P12RDFN8by

DOI:10.15120/GR-2015-1-MU-NUSTAR-GS-03

front-end electronics and addition of a shield between the identification and tracking detectors and the target area.

References

[1] H. Geissel et al., “The GSI projectile fragment separator (FRS): a versatile magnetic system for relativistic heavy ions”, Nucl. Instr. Meth. B70 286s, 1992.

[2] W. Korten and S. Lunardi, “Achievements with the EUROBALL spectrometer”, scientific and technical report, http://web-docs.gsi.de/ wolle/PreSPEC/index.html.

[3] H.J. Wollersheim et al., “Rare Isotopes INvestigation at GSI (RISING) using gamma-ray spectroscopy at relativistic energies ”, Nucl. Instr. Meth. A537, p. 637, 2005.

[4] P. Bednarczyk et al., “In-beam γ-ray angular distribution and lifetime measurements”, Acta Phys. Pol. B, vol. 41, pp.505-510, 2010.

[5] S. Akkoyun et al., “AGATA-Advanced GAmma Tracking Array”, Nucl. Instr. Meth. A668, p. 26-58, 2012.

---

[1] due to the Lorentz boost

DOI:10.15120/GR-2015-1-MU-NUSTAR-GS-03

Investigation of heavy ion-induced charged particle background for γ-ray spectroscopy experiments*

M. Reese †1, *P. Boutachkov* 2, *M. Cappellazzo* 3, *M. L. Cortés* 1, *J. Gerl* 1, *G. Guastalla* 2, *C. Lizarazo* 2, *N. Pietralla* 1, *H. Schaffner* 2, *and the PreSPEC collaboration*

[1]Institut für Kernphysik, Technische Universität Darmstadt, Germany ; [2]GSI Helmholtzzentrum für Schwerionenforschung GmbH, Darmstadt, Germany; [3]Institut für Kernphysik, Universität zu Köln, Germany

A tracking device for light charged particles was built. It was used for quantitative measurements of secondary particles created in ion-matter interaction, that are a source of background in γ-ray spectroscopy measurements with fast heavy ions.

Introduction: In the RISING [1] and PreSPEC [2] campaigns, in-flight γ-ray spectroscopy experiments with exotic beams were performed at the final focal point of the GSI Fragment Separator (FRS) [3]. It was observed [4], that the HPGe detectors were subject to impacts of charged particles that are produced by the interaction of the ion-beam with the detector and target material in the beam-line. For the planning of upcoming HISPEC experiments at the Low Energy Branch of Super-FRS, better understanding of this particular type of background is of great interest.

Experimental setup: In order to measure direction and energy of the particles, a detector with two parallel layers (see Fig. 1) of segmented plastic scintillators was built. Each layer consists of four strips with dimensions of $100 \times 20 \times 5\,\mathrm{mm}^3$, coupled to two PMTs at each end (Hamamatsu R7400 for layer A, and R9880U for layer B). The MBS DAQ was triggered by a signal in the FRS ToF-stop scintillator. Time and amplitude signals from all PMTs were recorded for each event by a multihit-TDC and a QDC, respectively. In both layers, the segmentation allows to locate a hit with 2 cm precision in the vertical direction. A similar resolution is achieved in the horizontal direction by comparison of the left and right PMT signal amplitudes.

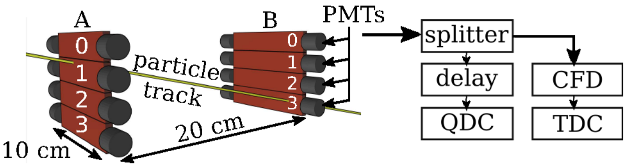

Figure 1: Schematic drawing of the active parts of the tracking detector: two layers (A and B) of four plastic scintillator strips (red bars), coupled to photomultipliers (black cylinders) on both sides. The yellow line indicates a particle trajectory. A block diagram of the electronics of one PMT signal is shown on the right hand side.

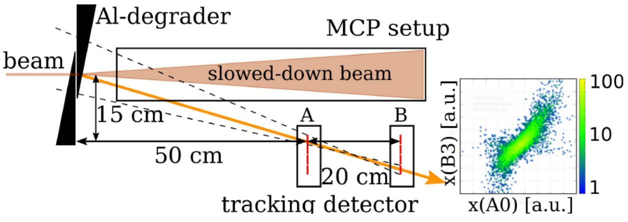

Figure 2: Schematic drawing of the setup, where the beam enters from the left hand side and is slowed down in the Al-degrader. Our tracking detector was mounted below the MCP setup, where it could measure charged particles from nuclear reactions inside the degrader (thick, yellow arrow) and other FRS detectors further upstream. Dashed lines indicate the vertical field of view of the A_0-B_3 detector pair. The 2D-histogram shows the measured correlation of horizontal position in the A_0 and B_3 strips.

An incident ^{132}Xe primary beam with $E_{\mathrm{kin}} = 300\,\mathrm{MeV/u}$ from SIS-18 was transported to the final FRS focal point. There, it passed standard FRS detectors [5] (TPC, MUSIC, scintillator) and a variable Al-degrader (Fig. 2). Coincident events in the A and B layers of the detector were caused by charged particles produced in nuclear reactions of ^{132}Xe with the FRS detectors and the degrader. Data were taken with various degrader settings ranging from 1.9 to $2.1\,\mathrm{g/cm}^2$. Fig. 2 shows coincident events in strip A_0 and B_3 that indicate a high abundance of charged particle radiation from the degrader, that was the thickest single piece of matter in the beam. Coincident events in other pairs of strips A_i-B_j were detected if $i < j$, i.e. corresponding to trajectories that point to the FRS detectors in front of the degrader (not shown in Fig. 2). Practically no coincident events have been detected in pairs of strips where $i >= j$.

Time-of-flight and energy-loss data will be analyzed further to gain information for quantitative prediction of the particle background in γ-ray spectroscopy experiments.

References

[1] H.-J. Wollersheim et al., NIM A 537, (2005) 637.

[2] N. Pietralla et al., EPJ Web of Conferences 66 (2014) 02083.

[3] H. Geissel et al., NIM B 70 , (1992) 286 .

[4] G. Guastalla et al., this report.

[5] www-wnt.gsi.de/frs/technical/FRSsetup/detectors-new.asp

---

* Work supported by BMBF NuSTAR.DA - TP 6, FKZ: BMBF 05P12RDFN8 (TP 6), HGS-HIRe

† reese@ikp.tu-darmstadt.de

DOI:10.15120/GR-2015-1-MU-NUSTAR-GS-04

PRESPEC-AGATA setup: Optimizing the target positions with Bayesian data analysis*

D. Ralet[1,2], *M. Fouesneau*[3], *J. Gerl*[2], *N. Pietralla*[1,2], *S. Pietri*[2], *and the PreSPEC and AGATA collaboration*[1]

[1]Technische Universität Darmstadt, Darmstadt, Germany; [2]GSI Helmoltzzentrum für Schwerionenforschung GmbH, Darmstadt, Germany; [3]Max-Plank-Institut für Astronomie, Heidelberg, Germany

Abstract

The target position in spectroscopy experiments such as PreSPEC-AGATA [1] influences the signal-to-noise ratio. Therefore precise information on the position of the target is needed to find low cross-section γ-ray transitions. The optimal positioning of a target is a non-trivial question. This report establishes a unidimensional model allowing a robust determination of the target even with a low signal-to-noise ratio.

The model is probabilistic and allows us to find N Doppler-corrected γ rays while accounting for atomic background. The model assumes the transitions to generate Gaussian spectral features on top of an exponential decay background. We proceed to the fit of the model with the PreSPEC-AGATA nuclear structure experiment *S428*, while naturally folding in measurement uncertainties. Within the Bayesian analysis framework, we are able to optimize the width of the γ-ray transitions and characterize related uncertainties as a function of the position of the target.

For this particular experiment, we find that the optimal position is shifted by -1 mm along the horizontal axis (x) and -4 mm along the vertical axis (y) with respect to the measured position. We demonstrate the power of our model and analysis method, that is applicable to the calibration of other experiments.

Introduction

In the PreSPEC-AGATA experiments [1], we measure the target position at the beginning of the experiment. This measurement is subject to uncertainties. To refine the position measurement and reduce uncertainties, we use the sensitivity of the AGATA array [2] to Doppler correct the two K-α X-rays of the uranium beam emitted in flight at half the speed of light. Specifically, the Doppler correction requires knowledge of the emission angle of the X-rays. Therefore we need to measure the position of the interacting uranium ion on the target, and the position of the X-rays detected in AGATA. The comparison of the pulse shape inside an AGATA crystal with a data-base provides the interaction position of the X-rays in the detector [2]. In this present work, we neglect variations due to the AGATA detectors and we focus on the target positioning uncertainties only.

Minimization technique

Generation of a mesh of offsets We suppose that the (x, y) position [1] of the target might be shifted with respect to the measured position. In order to consider all realistic target positions, we generate a mesh of offsets in the (x, y) plane. We set the mesh resolution to 1 mm, which corresponds to the resolution achieved to determine the ion position on the target. At each position offset of the mesh, we Doppler correct the X-rays with their re-calculated angle of emissions.

Model the data at each point of the mesh In order to determine precisely the width of the transitions, we need to model our data at each point of the mesh with a model that includes the two X-ray transitions, the background radiations, and the measurement uncertainties. We consider our model $M(\vec{E}, \vec{\Pi})$ as parametric function of $\vec{E}$ a set of energies, and $\vec{\Pi}$ a set of parameters.

Definition of the Likelihood The determination of the parameters of our model that reproduce our data requires the definition of similarity. In a Bayesian approach, we can define this similarity as a Likelihood function $p(Data(\vec{E})|Model(\vec{E}, \vec{\Pi}))$. It quantifies the similarity between our $Data$ and the $Model$ given a set of parameters $\vec{\Pi}$. The law of large numbers allows us to approximate the observed number of counts N_{obs} at given energy E by a Gaussian distribution. Thus, we define our Likelihood function as:

$$p(N_{obs}(\vec{E}) \mid N_{pred}(\vec{E}, \vec{\Pi})) = \frac{1}{\sqrt{2\pi N_{pred}(\vec{E}, \vec{\Pi})}} \exp\left(-\frac{1}{2}\frac{(N_{obs}(\vec{E}) - N_{pred}(\vec{E}, \vec{\Pi}))^2}{N_{pred}(\vec{E}, \vec{\Pi})}\right),$$

where $N_{pred}(\vec{E}, \vec{\Pi})$ is the predicted number of counts by the model at an energy E.

Determination of the model parameter For each parameter of our model, we provide an *a-priori* range of variation, that defines our parameter space. In order to constrain our two X-rays transition, we add a condition on the energy difference between the first and second X-ray transition.

The parameter space needs to be explored in order to find the set of parameters $\vec{\Pi}$ that maximizes the Likelihood

---

* This work was supported by the BMBF under Nos. 05P09RDFN4, 05P12RDFN8, and by the LOEWE center HIC for FAIR.

[1] The (x, y) plane is perpendicular to the beam axis.

DOI:10.15120/GR-2015-1-MU-NUSTAR-GS-05

probability. The exploration needs to converge quickly to the absolute maximum of Likelihood and to avoid local maxima. Therefore, we explore the parameter space with a Monte-Carlo Markov-Chain algorithm called *emcee* [5].

Establishment of the model

The model takes into account the two X-ray transitions of uranium at 94.6 and 98.4 keV.Their energy separation is close to the limit of resolution that can be achieved under Doppler broadening effect [4]. In addition, the beam induces a substantial background and we observed an unknown transition at energy of ~115 keV, that both need to be modelled properly too. The blue curve in Fig. 1 corresponds to the data.

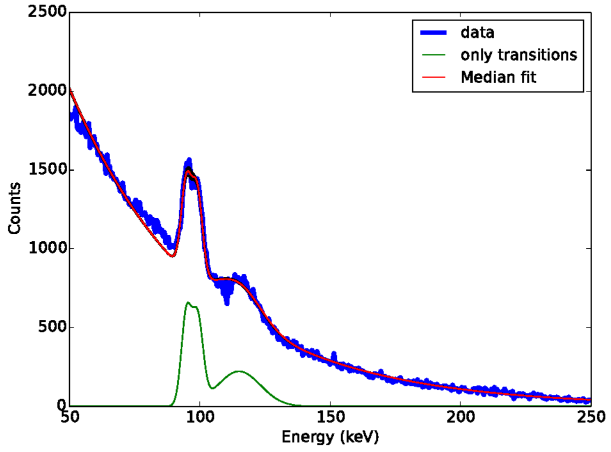

Figure 1: Doppler corrected histogram of the uranium X-ray transitions is plotted in the figure together with the fit. The blue curve is the observed dataset, while the red line indicates our "best-fit" model. The green curve shows only the transition components of our model.

Transitions model We first assume that each of the N transitions generates a Gaussian line in the energy spectrum. Thus, we have three parameters to describe the i-th line: the count amplitude A_i, the mean energy μ_i, and the energy variance σ_i^2. The i-th transition can be described by:

$$g_i(E; A_i, \mu_i, \sigma_i) = \frac{A_i}{\sqrt{2\pi\sigma_i^2}} \exp\left(-\frac{(E-\mu_i)^2}{2\sigma_i^2}\right).$$

Background continuum The background in our case represents a source of noise to find our transitions in the spectra. This noise is mostly induced by the beam. We model this component with a unique exponential decay function:

$$noise(E) = A \cdot \lambda \exp\left(-\lambda E\right),$$

with an amplitude A and the decay parameter λ.

Mixture model Once we have defined the transition features and the noise, we can combine the different components as the sum of all transitions on top of the continuum:

$$M(E; \Pi) = \sum_{i=1}^{n} g_i(E; E_i, \sigma_i, A_i) + noise(E; A, \lambda),$$

where $\vec{\Pi}$ is the vector of all the parameters:
$\vec{\Pi} = \{(E_i, \sigma_i, A_i)\}_{i\in[1..n]} + (A, \lambda)\}$.

Result on the optimum target position

We used a Monte-Carlo Markov-Chain (MCMC) method to optimize our model, and in particular, we used a specific implementation: *emcee* [5]. With this method, we determine at each point of the mesh, the optimum set of parameters $\vec{\Pi}$ and therefore optimum width of the two X-ray transitions. The plot of the width of the transition as a function of the offset in both x and y direction is shown in Fig. 2.

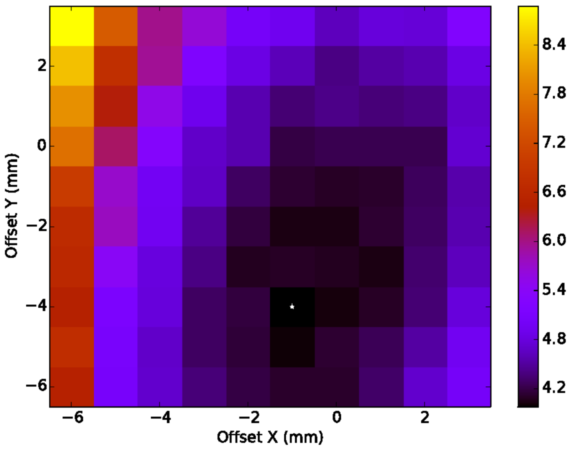

Figure 2: Each (x, y) bins corresponds to an offset applied to the measured target position. We weight each bins by the product of the two X-ray median widths. The white star highlights the minimum obtained in an offset $(x, y) = (-1, -4)$ mm. The X-Ray median widths are indicated by the color bar on the right-hand side.

The product of the transition width is minimum at a position offset of $(x, y) = (-1, -4)\ mm$. The curve in red in Fig. 1 corresponds to our model evaluated for the median value of our set of parameters $\vec{\Pi}$, with the optimum target offset.

Conclusion

The model we describe in this paper, along with the introduction of a Bayesian data analysis techniques allows us to determine the optimum target position for the PreSPEC-AGATA experiment. This newly determined position improves the energy resolution obtained after Doppler correction. Indeed the width of the transition of the 94.6 keV

X-ray transition pass from $\sigma = 1.99^{+10}_{-9}$ keV for the measured target position to $\sigma = 1.92^{+9}_{-8}$ keV after the target shift [2].

The thick target (700 mg/cm^2 beryllium) implies a large velocity spread, and therefore a substantial Doppler broadening. It becomes necessary to include the latter into the model. Moreover, we will consider the angle of emission of the X-rays to further increase the precision and accuracy of the calibration.

References

[1] "On the Road to FAIR: 1st Operation of AGATA in PreSPEC at GSI", N. Pietralla et al., EPJ web of Conferences 66, 2014

[2] "AGATA Advanced GAmma Tracking Array", S. Akoyun et al., NIM A668, 2012

[3] "LYCCA", P. Golubev et al., NIM A723, 55-66, 2013

[4] "Rare ISotope INvestigation at GSI (RISING) using γ ray spectroscopy relativistic energies", H.J. Wollersheim et al., NIMA 537, 2005

[5] "emcee: The MCMC Hammer", D. Foreman-Mackey et al., Publications of the Astronomical Society of the Pacific 125, 2013

---

[2] The error on the width values are given at the percentile of 16, and 84.

DOI:10.15120/GR-2015-1-MU-NUSTAR-GS-05

Low-energy electric and magnetic dipole excitations in ^{52}Cr *

N. Tsoneva[1,2], *M. Bhike*[3], *Krishichayan*[3], *H. Lenske*[1,4], *G. Rusev*[5], *A.P. Tonchev*[6], *and W. Tornow*[3]
[1]Institut für Theoretische Physik, Universität Gießen; [2]INRNE, 1784 Sofia, Bulgaria; [3]Department of Physics, Duke University, Durham, NC 27708 , and, Triangle Universities Nuclear Laboratory, Durham, NC 27708; [4]GSI Darmstadt;
[5]Chemistry Division, Los Alamos National Laboratory, Los Alamos, NM 87545; [6]Physics Division, Livermore Lawrence National Laboratory, Livermore, CA 94550

Electric and magnetic dipole strengths, below and around the neutron-emission threshold of ^{52}Cr (S_n = 12.034 MeV), are studied in the framework of the nuclear energy-density-functional (EDF) theory and an extended version of the Qusiparticle-Phonon Model (QPM) [1, 2]. The QPM results presented here are consistent with our previous analyses of $E1$, $E2$, and $M1$ excitations in various nuclei [1, 2, 3, 4, 5, 6, 7]. The theoretical results are compared with measurements from ^{52}Cr(γ,γ') photon scattering experiments which have been performed using the nearly monoenergetic, 100% linear polarized photon beams produced at the HIγS facility of TUNL [8]. Twenty beam energies have been used to cover the energy range from 5.0 to 9.5 MeV and to uniquely identify and measure the dipole states in ^{52}Cr. Twenty six dipole excitations were identified and their parity quantum values were unambiguously determined from the measured azimuthal intensity asymmetry of nuclear resonance fluorescence transitions. For the analysis of the experiment a sufficiently large QPM model basis, constructed of up to three-phonon (microscopically described) configurations with J^{π} from $1^{\pm}$ to $6^{\pm}$ and excitation energies E_x up to 9.8 MeV is implemented [8]. From EDF mean-field calculations we derive that the ^{52}Cr nucleus exhibits a neutron skin with a thickness of δr = 0.056 fm. As a result, the first QRPA 1^-_1 state with excitation energy E_x = 8.366 MeV, and the second QRPA 1^- state with excitation energy E_x = 9.473 MeV are almost pure neutron two-quasiparticle states, where the major contribution is due to transitions from weakly bound neutron orbitals. Further analysis of transition densities of these states shows features typical for skin nuclei [2, 6]. Thus, the QRPA 1^- excitations below $\sim$ 9.5 MeV in ^{52}Cr could be associated with a genuine Pygmy Dipole Resonance (PDR) mode [1, 2, 9]. The total PDR strength obtained from the QRPA calculations is $\Sigma_{0MeV}^{9.5MeV} B(E1; g.s. \rightarrow 1^-_{PDR})_{QRPA} \uparrow = 13 \times 10^{-3}$ e^{2}fm^2 which exhausts about 0.1% of the Energy-Weighted Sum Rule (EWSR)[10]. As the excitation energy is increased, the isovector contribution to the dipole strength increases, and the state vectors show an increase of the out-of-phase neutron to proton contribution which is generally associated with the Giant Dipole Resonance (GDR) [2, 6].

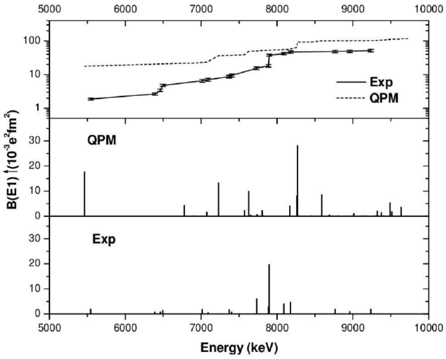

Figure 1: (color online) Distribution of observed $B(E1) \uparrow$ strength for resonantly excited states between 5.1 and 9.5 MeV in ^{52}Cr is compared with values obtained from three-phonon QPM calculations. A comparison of the measured and calculated QPM cumulative $E1$ strength is shown in the upper panel.

Theoretically, it is clear that the QRPA is unable to account for higher multi-particle-multi-hole correlations and interactions resulting from core polarization effects [11]. The later could induce dynamical effects related to redistribution of strength, and strongly affect the gross and fine structure of dipole strength functions. By comparing the QRPA with the multi-phonon QPM calculations, it is seen that the pure two-quasiparticle QRPA strengths in the PDR region is strongly fragmented over many 1^- excited states, once the coupling to multiphonon configurations takes place. Thus, the lowest-lying 1^- state, which is without a QRPA counterpart, is predominantly given by a two-phonon quadrupole-octupole excitation of the $[2^+_1 \otimes 3^-_1]_1$-configuration, which accounts for $\approx 75\%$ of the QPM wave function [8]. The strongest QPM 1^-_{max} state in the energy range below 9.8 MeV is located at E_{QPM}= 8.270 MeV and the corresponding transition probability is $B(E1; g.s. \rightarrow 1^-_{max})_{QPM} \uparrow$ = 28.14 × 10^{-3} e^{2}fm^2. The theoretical results compare well with the experimental findings, which give for this state E_{exp}= 7.897 MeV and $B(E1; g.s. \rightarrow 1^-_{max})_{QPM} \uparrow$= 19.7(10) × 10^{-3} e^{2}fm^2, and also with the results of Pai *et al.* [12]. The QPM calculations indicate that the 1^-_{max} state contains contributions of the low-energy tail of the GDR, which is the reason for the strong $B(E1)$ transition rate.

The comparison between the measurements and the QPM E1 spectral distribution and the cumulative $B(E1)$ strength in ^{52}Cr is presented in Fig. 1. In general, the shape of the QPM cumulative $B(E1)$ strength as well as the 1^- level distribution are found to be in a good agreement with the experimental data. In particular, for the whole measured energy range E_x = 5.1 - 9.5 MeV the

---

* Work supported by the HIC for FAIR, GSI-JLU Giessen collaboration agreement, the U.S. Department of Energy Grant No DE-FG02-97ER41033 and BMBF grant 05P12RGFTE.

DOI:10.15120/GR-2015-1-MU-NUSTAR-GS-06

QPM calculations predict a summed $B(E1)$ strength of $\sum B(E1)_{QPM}\uparrow = 111.4\times 10^{-3}\mathrm{e}^2\mathrm{fm}^2$. In comparison, the experiment finds $\sum B(E1)_{exp}\uparrow = 51.2(16)\times 10^{-3}\mathrm{e}^2\mathrm{fm}^2$, approximately a factor of two less strength.. The observed difference between the measured and calculated total $B(E1)$ values could be related to experimental sensitivity limits and branchings to excited states, which are unaccounted for by the existing dipole data in ^{52}Cr.

The main aim of this work is to perform unambiguous parity assignments of the low-energy dipole states in ^{52}Cr and a precise separation between electric $E1$ and magnetic $M1$ excitations. Experimentally it is achieved in measurements of azimuthal asymmetries of NRF γ-rays using a 100% linearly polarized and quasi-monochromatic photon beam [3, 4, 8]. The $M1$ data are analysed theoretically by three phonon QPM calculations. In the determination of the nuclear magnetic transition moments a quenched effective spin-magnetic factor $g^s_{eff} = 0.8 g^s_{bare}$ is used, where g^s_{bare} denotes the bare spin-magnetic moment. The quenching factor agrees very well with accepted QPM values [11], shell-model calculations and experimental data [13, 14, 15]. A reliable description of the fragmentation pattern of the magnetic dipole response function is important for understanding the spin dynamics of the nucleus. The analysis of the QRPA $M1$ strength of 1^+ excitations with energies up to E_x = 20 MeV indicates that this part of the spectrum is mostly due to transitions of spin-flip type related to the neutron and proton $1f_{7/2}\rightarrow 1f_{5/2}$ two-quasiparticle components, respectively [8]. The detailed studies of the $M1$ response function, performed by three-phonon QPM calculations, show that the coupling of natural parity phonons to multi-phonon 1^+ states induces additional orbital contribution to the $M1$ transitions. Consequently, the observed $M1$ strength at excitation energies between 5 and 10 MeV contains an orbital part of about 11%. In comparison the QRPA calculations provide us a very small amount of orbital M1 strength of about 3.3 % of the total QRPA $B(M1)$ transition probability, up to E_x = 20 MeV [8]. The total QPM $M1$ strength summed over 1^+ states from E_x = 5 to 9.5 MeV can be compared directly with the present data. The results are presented in Fig. 2. The theoretical findings give $\Sigma^{9.5\mathrm{MeV}}_{5\mathrm{MeV}} B(M1)_{\mathrm{QPM}}\uparrow$ = 3.1 μ^2_N. which is in good agreement with the experimental value of $\Sigma^{5.1\mathrm{MeV}}_{9.5\mathrm{MeV}} B(M1)_{exp}\uparrow$ = 2.94(9) μ^2_N [8].

The observation of the spin-flip $M1$ resonance structure around 9.1 MeV in ^{52}Cr has been discussed along with the systematics of dipole excitation transition strength distributions in fp-shell nuclei [8]. Such concentration of $M1$ strength around 9.2 MeV is confirmed in the three-phonon QPM calculations and explained as fragmented spin-flip 1^+ excitations [8].

In conclusion, a common observation is that the QRPA is unable to describe the low-energy $E1$ and $M1$ spectral distributions. However, a detailed explanation could be obtained in multi-phonon model like the three-phonon QPM, which can describe well the observed experimentally fragmentation pattern of the low-energy dipole strength. The good agreement between the calculated and measured total $M1$ strength is a signature that the quenching is handled reliably well in the chosen approximation. A better understanding could be achieved with more comprehensive knowledge of the nature of the intrinsic nuclear moments, meson-exchange currents and branching ratios from excited states, which might be of importance for further improvements. Supported by the U.S. Department of Energy Grant No DE-FG02-97ER41033 and BMBF grant 05P12RGFTE.

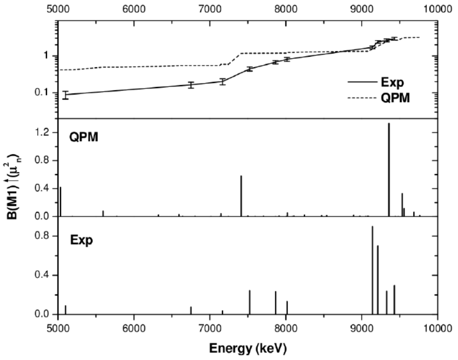

Figure 2: (color online) Distribution of observed $B(M1)\uparrow$ strength in ^{52}Cr in the energy range between 5.1 and 9.5 MeV is compared with the values obtained from three-phonon QPM calculations. A comparison of the measured and calculated QPM cumulative $M1$ strength is shown in the upper panel.

References

[1] N. Tsoneva, H. Lenske, Ch. Stoyanov, Phys. Lett. **B586**, 213 (2004) and refs. therein.

[2] N. Tsoneva, H. Lenske, Phys. Rev. C **77**, 024321 (2008) and refs. therein.

[3] A. Tonchev *et al.*, Phys. Rev. Lett. **104** 072501 (2010).

[4] G. Rusev *et al.*, Phys. Rev. Lett. **110**, 022503 (2013).

[5] N. Tsoneva, H. Lenske, Phys. Lett. **B695** 174 (2011).

[6] R. Schwengner *et al.*, Phys. Rev. C **87**, 024306 (2013).

[7] B. Özel-Tashenov *et al.*, Phys. Rev. C **90**, 024304 (2014).

[8] Krishichayan, M. Bhike, W. Tornow, G. Rusev, A.P. Tonchev, N. Tsoneva, and H. Lenske, Phys. Rev. C submitted.

[9] D. Savran, T. Aumann, and A. Zilges, Prog. Part. Nucl. Phys. **70**, 210 (2013).

[10] B. L. Berman, At. Data Nucl. Data Tables **15**, 319 (1975).

[11] V.G. Soloviev, *Theory of complex nuclei* (Oxford: Pergamon Press, 1976).

[12] H. Pai *et al.*, Phys. Rev. C **88**, 054316 (2013).

[13] P. von Neumann-Cosel *et al.*, Phys. Lett. **B443**, 1 (1998).

[14] K. Langanke, G. Martinez-Pinedo, P. von Neumann-Cosel, A. Richter, Phy. Rev. Lett. **93**, 202501 (2004).

[15] S.E. Koonin, D.J. Dean, K. Langanke, Annu. Rev. Nucl. Part. Sci. 47, 403 (1997).

Shielding and compton suppression capabilities of the EUROBALL BGO back-catchers*

C. Lizarazo[1,2], *G. Li*[1], *H. Schaffner*[1], *I. Kojouharov*[1], *J. Gerl*[1], *N. Pietralla*[2], *and the PreSPEC Collaboration* [1]

[1]GSI, Darmstadt, Germany; [2]Institut fur Kernphysik, Teschnische Universitat Darmstadt, Germany

The current status of the EUROBALL BGO back-catchers that will be used for the DEGAS project have been investigated. Measurements of the energy spectrum of a ^{137}Cs gamma-ray source with a cluster of 7-fold germanium detectors were performed. Compton-suppression on the germanium energy spectrum was done via offline analysis using the simultaneous measurements of time and energy of a back-catcher unit and the Germanium cluster. Geant4 simulations provide a better understanding of these measurements that will help to improve the design of the DEGAS shielding.

Introduction. The DESPEC Germanium Array Spectrometer DEGAS is a key device on the Decay Spectroscopy (DESPEC) experiment that will be conducted in the future FAIR facility. The purpose of DEGAS is the detection of gamma-rays of very exotic nuclei that will be produced by the Super-FRS and stopped in the AIDA implanter. DEGAS has to have a sensitivity good enough in order to detect efficiently the isomeric gamma-rays of these exotic nuclei and discriminate them from the intense background expected from the secondary radiation produced at the Super-FRS beam-line as well as the environmental background radiation [1]. The BGO crystals of the former EUROBALL back-catchers will be re-configured and placed in the front and side faces of DEGAS such that they will shield the Germanium detectors from all the different background sources allowing as well compton suppression on the Germanium energy spectrum. In this work the shielding and compton suppression capabilities of a back-catcher unit have been tested.

Experimental Setup. A back-catcher unit composed of 6 BGO crystals has been placed in the rear side of a RISING cluster of 7-fold germanium detectors. A ^{137}Cs source has been placed at three different positions as it is indicated in Figure 1. On each case, energy and time spectra for each BGO and Ge crystal have been measured. The trigger of the (MBS) DAQ system is generated by the signal of the first crystal fired in the setup, either Germanium or BGO. Event by event, the time of each crystal's signal relative to a common stop time (provided by the trigger) has been measured. The energy information of the Ge and BGO has been processed with the VME modules V785 ADC and V792 QDC, respectively. Since the rising time of the BGO energy signals ($\sim$ 80 ns) are much faster than the typical ones from the Germanium detectors ($\sim$ 400 ns) they have been delayed 300 ns before they are send to the QDC.

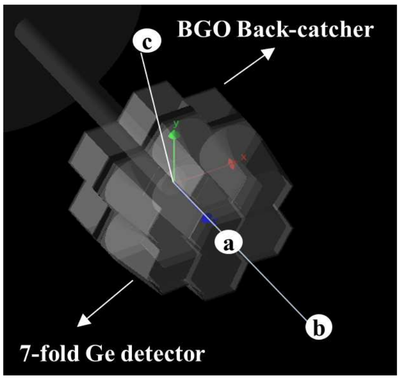

Figure 1: Experimental setup and different source's positions.

Compton suppression performance. When a photon hits a Germanium crystal and is scattered to -at least- one BGO, its total energy cannot be accurately reconstruted by add-backing the energies deposited on the two crystals since the BGO scintillators have very poor intrinsic energy resolution. This event will contribute to the background distribution registered in the germanium energy spectrum and therefore can forbid the observation of peaks with similar energies that correspond to low-probability unknown transitions of nuclei of intereset. Nevertheless, the BGOs can be used to suppress that compton event since the output signals of the Germanium and the particular BGO crystal where the photon has interacted are correlated in time for this event, which means that the time difference between the two signals is constant. When the time difference spectra between an specific pair of detectors is plotted the coincidence events are found at a time position that corresponds to time difference mentioned previously, as it is shown in figure 2.

For the non-central detectors of the 7-fold cluster, compton suppression of the photons scattered

- a. only at the rear BGO crystal,
- b. any BGO crystal,

has been performed. The resulting energy spectra and the comparison with the spectra with no Compton suppression can be seen in Figure 3. P/T ratios of 0.26 and 0.27 were obtained, respectively.

Active shielding capabilities. Figure 4 shows the energy spectra of the events in coincidence between a non-central germanium detector and its rear BGO crystal for the source

---

* Work supported by GSI cooperation with T. U. Darmstadt/ HGS-Hire.

DOI:10.15120/GR-2015-1-MU-NUSTAR-GS-07

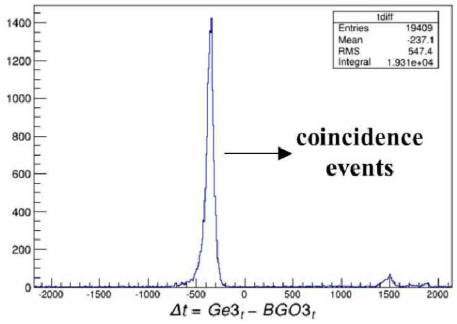

Figure 2: Time difference spectra between a particular combination of BGO-Ge detectors.

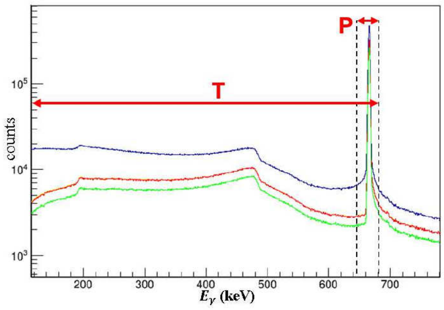

Figure 3: Compton suppression effect on the Germanium energy spectrum testing different anticoincidence conditions.

positions c and b, respectively. When the source was located at the position 'b' the energy deposited in the germanium is in average lower than in BGO. This is explained considering that the photons released from the source first hit the Germanium detector and then are forward scattered to the rear BGO. On the other hand, when the source is located at the non symmetrical position 'c,' the energy registered on the BGO is now in average lower in comparison to the the one registered in the Germanium, which corresponds to the photon forward scattered from the BGO in the direction to the Germanium. These simple observation on the energy distribution of the coincident events allowed to discriminate the different source positions.

References

[1] J. Gerl et. al. "Technical report for the design, construction and commissioning of the DESPEC Germanium Array DEGAS", v12.3, August 2014,

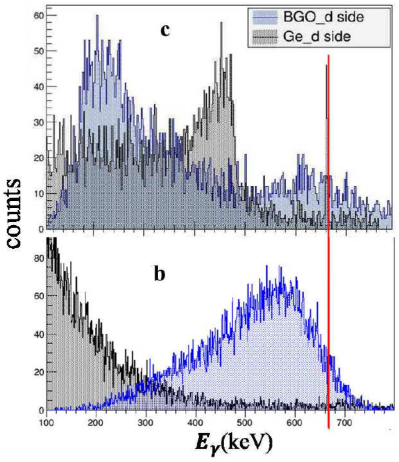

Figure 4: Energy spectra of an specific set of two neighbouring Ge-BGO crystals for events in coincidence when the source placed at positions 'c' and 'b'.

DOI:10.15120/GR-2015-1-MU-NUSTAR-GS-07

Total kinetic energy release in spontaneous fission of ^{255,256,258}Rf[*]

F.P. Heßberger†[1,2], *D. Ackermann*[1], *B. Andel*[3], *S. Antalic*[3], *C. Droese*[2,4], *J. Even*[2], *Z. Kalaninová*[3], *M. Laatiaoui*[2], *J. Piot*[5], *and M. Vostinar*[5]

[1]GSI, Darmstadt, Germany; [2]HIM, Mainz, Germany; [3]Comenius University, Bratislava, Slovakia; [4]Ernst-Moritz-Arndt Universität, Greifswald, Germany; [5]GANIL, Caen, France

Spontaneous fission (sf) is a major radioactive decay mode in the region of transuranium elements. Its study provides valuable information on the stability of heaviest nuclei. Therefore understanding the sf process is decisive for the quest of the upper end of the periodic table.

Main experimental observables are the partial sf half-lives, the hindrance factors for nuclei with odd proton and/or neutron numbers, the total kinetic energy release (<TKE>) as well as the A - and Z - distribution of the sf fragments, and the neutron muliplicities.

The commonly used technique for decay studies of heaviest nuclei, i.e. implantation of the evaporation residues (ER) into a Si detector arrangement ('stop detector') after inflight separation from the projectile beam, is not really suited for measuring <TKE> and/or mass distributions. Firstly, recombination of charge-carriers will occur due to the high ionization density of the sf fragments. Thus, there is no linear dependence between the energy and the registered pulse-height. Specific calibration procedures (see e.g. [1]) have to be applied. Secondly, the implantation depths of the ER is smaller than the range of the sf fragments. Thus, with some probability, one of them will escape the detector, depositing only part of its energy in it. So, the measured energy value will not represent the full energy release in the sf process, and consequently the peak of the energy distribution does not represent the <TKE>. One possibility to solve that problem is to register the escaping fragment in a detector box sourrounding the implantation detector [2]. Yet, it requires a correction of the energy losses of the escaping fragment in the deadlayers of the implantation detecor and the box detector, which introduces some uncertainty.

Alternatively the peak value of the energy distribution recorded in the stop detector can be used as a measure for <TKE>. This procedure requires a reference value and in addition the same mean implantation depths for the nuclei under investigation, as the energy release of the escaping fragment depends on the length of the flight-path through the detector, hence on the implantation depth [2].

As a test case we measured energy distributions for sf products of ^{255,256,258}Rf. The nuclei were produced by the reactions ^{207}Pb(^{50}Ti,2n)^{255}Rf, ^{208}Pb(^{50}Ti,2n)^{256}Rf, and ^{209}Bi(^{50}Ti,1n)^{258}Db $\xrightarrow{EC}$ ^{258}Rf; mean kinetic energies for the ERs from these reactions were equal within ±2.5%, and therefore also, in first order, the implantation depths. The results are compared in fig. 1, where besides the measured mean values (E_{mean}) the widths of the energy distributions are given. For ^{258}Rf a <TKE> value of 197.6±1.1 MeV is reported [3]. Using it as a reference value one obtains <TKE>/E_{mean} = 1.033 and hence <TKE>(^{256}Rf) = 197.0±1.2 MeV, and <TKE>(^{255}Rf) = 198.8±1.0 MeV. This (preliminary) value is comparable for ^{256}Rf with that given in [3] (198.9±4.4 MeV), but more precise; that for ^{255}Rf is somewhat higher than the value <TKE> = 194±2 MeV [4], obtained using the method from [2]. An improvement of the results and also information on the influence of the little energy variations of the ER may be expected from modelling the distributions by, e.g. GEANT simulations.

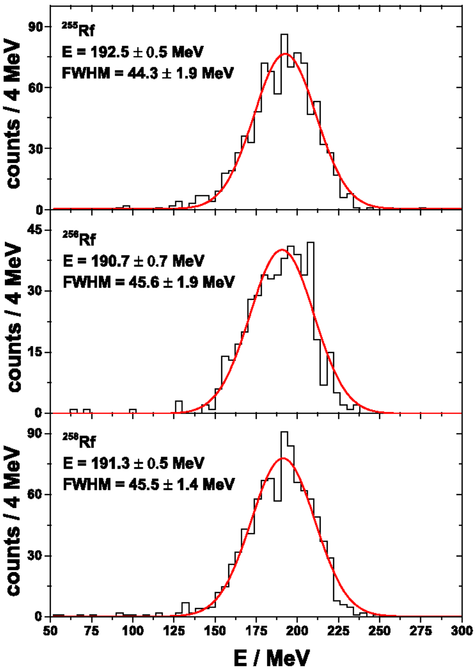

Figure 1: Energy distributions of sf events of ^{255,256,258}Rf measured with the stop detector of SHIP.

References

[1] S.B. Kaufman *et al.*, NIM 115, 47 (1974)

[2] S. Hofmann *et al.*, Eur. Phys. J. A 32, 251 (2007)

[3] J.F. Wild *et al.*, J. of All. and Comp. 213/214, 86 (1994)

[4] S. Antalic *et al.*, subm. to Eur. Phys. J. A (2014)

---

[*] Work supported by GSI(UNILAC)/HI Mainz/European Community FP7 - Capacities, contract ENSAR contract No. 262010/French-German Collaboration agreement INP2 P3-DSM/CEA and GSI/Slovak Grant Agency VEGA, contract No. 1/0576/13

† f.p.hessberger@gsi.de

DOI:10.15120/GR-2015-1-MU-NUSTAR-SHE-P-01

(11^-) isomeric state in ^{194}Po[*]

B. Andel[†][1], *A.N. Andreyev*[2], *S. Antalic*[1], *F.P. Heßberger*[3,4], *D. Ackermann*[3], *S. Hofmann*[3,5], *M. Huyse*[6], *Z. Kalaninová*[‡][1], *B. Kindler*[3], *B. Lommel*[3], *R. Mann*[3], *K. Nishio*[7], *R.D. Page*[8], *B. Sulignano*[3], *and P. Van Duppen*[6]

[1]Comenius University, Bratislava, Slovakia; [2]University of York, York, United Kingdom; [3]GSI, Darmstadt, Germany; [4]HIM, Mainz, Germany; [5]Goethe-Universität Frankfurt, Frankfurt, Germany; [6]KU Leuven, Leuven, Belgium; [7]JAEA, Tokai, Japan; [8]University of Liverpool, Liverpool, United Kingdom

Metastable nuclear excited states - nuclear isomers - are valuable probes for nuclear structure studies. In neutron deficient even-mass polonium isotopes, 11^- isomeric states are systematically present.

The most recent study of excited levels in ^{194}Po was performed at JYFL (Finland) [1]. In decay spectroscopy data, an (11^-) isomer was identified, feeding the 8^+ and 6^+ levels of the ground state band. However, the connection to the ground state band, spin and parity assignment were based only on energy balance and systematic trends in heavier Po isotopes. A ground state band up to the (16^+) and a side band up to the (10) level were established based on in-beam data.

In our experiment, ^{194}Po was produced in the fusion-evaporation reaction ^{56}Fe(^{141}Pr,p2n)^{194}Po at the velocity filter SHIP at GSI, Darmstadt (Germany). Evaporation residues (ERs) were separated from the primary beam and products of other reactions by the SHIP [2] and implanted into a 16-strip position sensitive silicon detector (PSSD). Upstream around the PSSD, six additional silicon strip detectors were placed, forming an opened box (BOX detector) to detect escaping particles. For detection of γ and X rays, germanium clover detector was installed in close geometry to the PSSD.

Our statistics of γ rays from the decay of the isomer was approximately 10 times higher than in the previous study [1], which allowed us to investigate γ - γ coincidences for this isomer for the first time. In order to distinguish γ rays originating in ^{194}Po, we applied correlation search between implantations of ERs and α decays of ^{194}Po within a position window ≤ 0.6 mm and a time window of 1.2 s ($T_{1/2}(^{194}\mathrm{Po}) = 392(4)$ ms [3]). Spectrum of γ rays in coincidence (within ≈ 5 μs) with ERs is shown in fig. 1 c).

In addition to all previously-known transitions, 5 new ones were found (209, 248, 362, 494 and 847 keV). Moreover, we registered also weak transitions from the side band up to the 9^- level, which were reported only from in-beam data so far [1]. Therefore, relevant levels from the side band are populated by an isomeric state, either the (11^-) or another isomer placed above the 9^- level.

For γ - γ coincidence analysis, we required a coincidence of at least two γ rays with ERs. We confirmed the decay scheme of the isomer from [1] except for the transition de-exciting the (11^-) level. We suggest to replace the previously assigned 459 keV transition by the new 248 keV transition.

To determine half-life of the isomer, we employed ER - γ - α(^{194}Po) correlations with time differences between ER - γ within (25 - 200) μs and between γ - α(^{194}Po) up to 1.2 s. We deduced the half-life to be 12.9(5) μs, which is consistent with the previously obtained value of 15(2) μs [1], but more precise.

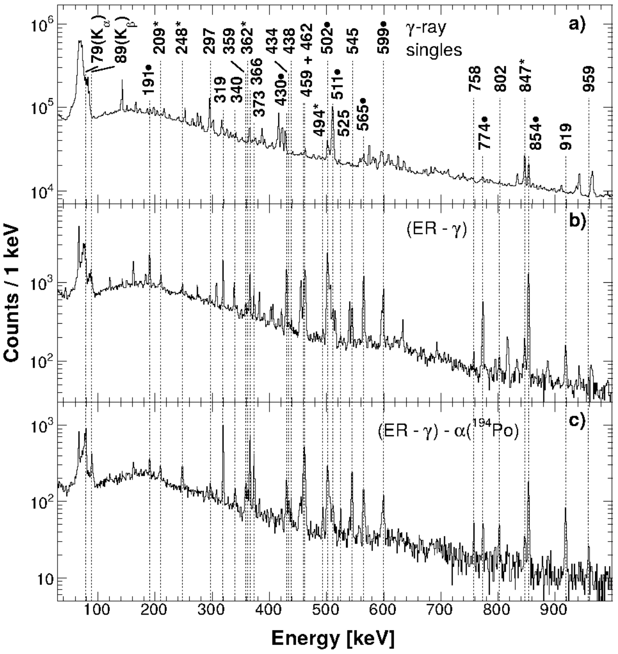

Figure 1: a) all γ rays registered during measurement; b) γ rays in coincidence with ERs; c) γ rays in coincidence with ERs correlated to α decays of ^{194}Po. Energies are in keV, asterisks denote new transitions, full circles denote background lines (mostly from ^{192}Pb).

References

[1] K. Helariutta *et al.*, Eur. Phys. J. A **6**, 289 (1999).

[2] G. Münzenberg *et al.*, Nucl. Instrum. Methods **161**, 65 (1979).

[3] J. Wauters *et al.*, Phys. Rev. C **47**, 1447 (1993).

---

[*] Work supported by GSI(UNILAC), HI Mainz, the Slovak Research and Development Agency (Contract No. APVV-0105-10) and the Slovak Grant Agency VEGA (Contract No. 1/0576/13).

[†] boris.andel@fmph.uniba.sk

[‡] Present address: JINR, Dubna, Russia

DOI:10.15120/GR-2015-1-MU-NUSTAR-SHE-P-02

Alpha decay of ^{227}U and excited levels in ^{223}Th studied at SHIP*

Z. Kalaninova†[1,2], *S. Antalic*[1], *F.P. Heßberger*[3,4], *D. Ackermann*[3], *B. Andel*[1], *B. Kindler*[3], *M. Laatiaoui*[3], *B. Lommel*[3], *and J. Maurer*[3]

[1]Comenius University, Bratislava, Slovakia; [2]JINR, Dubna, Russia; [3]GSI, Darmstadt, Germany; [4]HIM, Mainz, Germany

Alpha decay is a valuable tool to investigate nuclear structure. Analyzing α-γ coincidences, one can localize energy levels in daughter nuclei populated by α decays of parent isotopes. Information of level ordering and placement helps to optimize theoretical nuclear models, which improve our understanding of basic processes in atomic nuclei.

The excited levels in ^{223}Th were studied for the first time in an in-beam measurement in Heidelberg (Germany) already more than 20 years ago [1]. Short time after that, also an out-of-beam study was performed in Louvain-la-Neuve (Belgium), where ^{223}Th was produced by the α decay of ^{227}U [2]. Different levels in ^{223}Th were populated in each of those studies.

We studied the levels in ^{223}Th in an experiment performed at GSI in April 2014. The levels were populated by the α decay of ^{227}U produced in the fusion-evaporation reaction ^{22}Ne + ^{208}Pb. The beam energy was 104 MeV in front of the target. The nuclei of interest were separated from other particles by the velocity filter SHIP and implanted into a focal-plane detector arrangement. A 16-strip position-sensitive silicon detector registered α-decay signals and a germanium clover detector placed close behind the silicon detector registered γ rays.

To avoid admixtures of decays of other isotopes in our analysis, we applied strict conditions on parent, daughter and granddaughter decays. We searched for correlated $\alpha1(^{227}\mathrm{U})$-$\alpha2(^{223}\mathrm{Th})$-$\alpha3(^{219}\mathrm{Ra})$ chains. We accepted position differences of subsequent decays smaller than 0.4 mm and time windows were set to be $90\,\mathrm{ms} < \Delta t(\alpha1\text{-}\alpha2) < 3\,\mathrm{s}$ and $0.5\,\mathrm{ms} < \Delta t(\alpha2\text{-}\alpha3) < 50\,\mathrm{ms}$. During the irradiation time of about two days, we collected in total approximately 50000 nuclei of ^{227}U implanted into the silicon detector.

The detection of $\alpha1$-γ coincidences within a 5-μs time window (see Fig. 1b) allowed us to associate the α decays of ^{227}U with the corresponding levels in ^{223}Th. Based on the analysis of experimental and theoretical conversion coefficients, we assigned tentative characters to observed γ transitions. Consecutively, the improved decay scheme of ^{227}U-^{223}Th was obtained. As an extension to the previous out-of-beam study [2], we identified a new level at 370 keV in ^{223}Th. The weak lines at 396 and 489 keV can also be tentatively assigned to ^{223}Th. In order to verify the suggested decay scheme, we performed Monte-Carlo simulations using the toolkit Geant 4 [3]. Fair agreement was achieved between the simulation and experimental data (see Fig. 1a). More details will be given elsewhere [4].

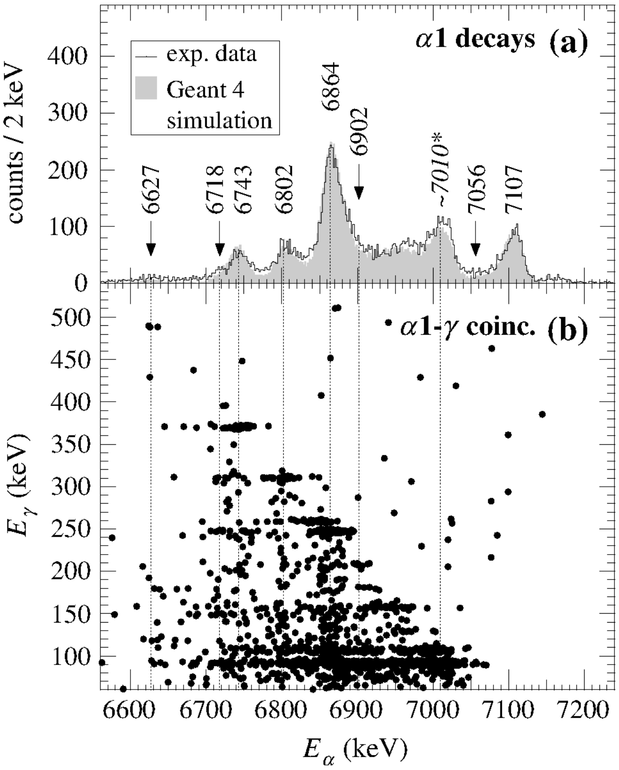

Figure 1: (a) Experimental energy spectrum (black solid line) of $\alpha1$ decays extracted from the $\alpha1$-$\alpha2$-$\alpha3$ correlation search measured in the focal-plane silicon detector. The shaded area represents the Monte-Carlo simulation of the decay of ^{227}U performed by Geant 4 [3]. A peak at ~ 7010 keV marked by an asterisk does not correspond to an α line of ^{227}U, but is created by the summing of α-particle and conversion-electron energies. (b) Spectrum of $\alpha1$-γ coincidences showing γ rays detected within a time window of 5 μs after the $\alpha1$ decays from (a).

References

[1] M. Dahlinger *et al., Nucl. Phys. A* **484**, 337 (1988)

[2] T. Hoare *et al., J. Phys. G: Nucl. Part. Phys.* **17**, 145 (1991)

[3] S. Agostinelli *et al., Nucl. Instr. and Meth. A* **506**, 250 (2003)

[4] Z. Kalaninova *et al., in preparation*

---

* Work supported by the European Community FP7 Capacities, Contract ENSAR No. 262010, the.Slovak Research and Development Agency (Contract No. APVV-0105-10) and the Slovak Grant Agency VEGA (Contract No. 1/0576/13).

† zdenka.kalaninova@gmail.com

DOI:10.15120/GR-2015-1-MU-NUSTAR-SHE-P-03

On the synthesis of neutron-rich isotopes along the N = 126 shell in multinucleon transfer reactions*

O.Beliuskina†[1,2], *S.Heinz*[1,2], *V.Zagrebaev*[3], *V.Comas*[2], *C.Heinz*[1], *S.Hofmann*[2,4], *R.Knöbel*[2], *M.Stahl*[1], *D.Ackermann*[2], *F.P.Heßberger*[2,5], *B.Kindler*[2], *B.Lommel*[2], *J.Maurer*[2], *and R.Mann*[2]

[1]JLU, Gießen, Germany; [2]GSI, Darmstadt, Germany; [3]JINR, Dubna, Russia; [4]IPGU, Frankfurt, Germany; [5]HIM, Mainz, Germany

We studied multinucleon transfer processes in near barrier collisions of heavy nuclei with a goal to investigate possible population of isotopes along the N=126 shell. In particular we investigated deep inelastic transfer (DIT) reactions in the heavy collision system ^{64}Ni+^{207}Pb at 5.0 MeV/u using the velocity filter SHIP and its detection system (see [1]).The isotopic identification was performed via γ-decay spectroscopy in the focal plane of SHIP. All identified isotopes which were directly populated in the reaction are displayed in the chart in fig. 1. As one can see, nuclei were populated in both, neutron-deficient and neutron-rich regions relative to the stability line. From the intensities of the measured γ lines we deduced total production cross-sections for the respective isotopes. As an example the obtained total cross-sections of osmium(Z=76) and platinum(Z=78) isotopes as a function of the nucleon number A are shown in fig. 2 a,b as full circles.

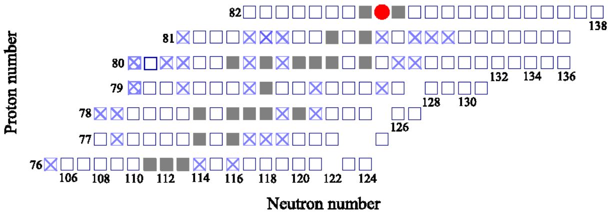

Figure 1: Part of the nuclide chart with the identified isotopes (crosses)

Very similar reactions were studied by another group in ^{64}Ni+^{208}Pb collisions at the beam energy of 350 MeV [2]. The data from [2] for isotopes with osmium and platinum are shown as open circles in fig. 2 a,b. Our measured cross-sections and the ones in [2] differ in most cases within one order of magnitude. In both experiments no new isotopes were discovered or identified, respectively, and as well the N = 126 shell was not reached for nuclei with Z<80.

It is interesting to compare the isotopic distributions and cross-sections reached in DIT reactions with those from fragmentation reactions which is presently the applied technique to produce neutron-rich isotopes in the region below Uranium. The most neutron-rich isotopes for the elements discussed here were so far reached in fragmentation reactions [3, 4].The obtained cross-sections are represented by the asterisks in fig. 2 a,b. The fragmentation and DIT cross-sections are mostly within the same oder of magnitude for the isotopes discussed here and towards the neutron-rich side the DIT cross-sections even tend to exceed the fragmentation cross-sections.

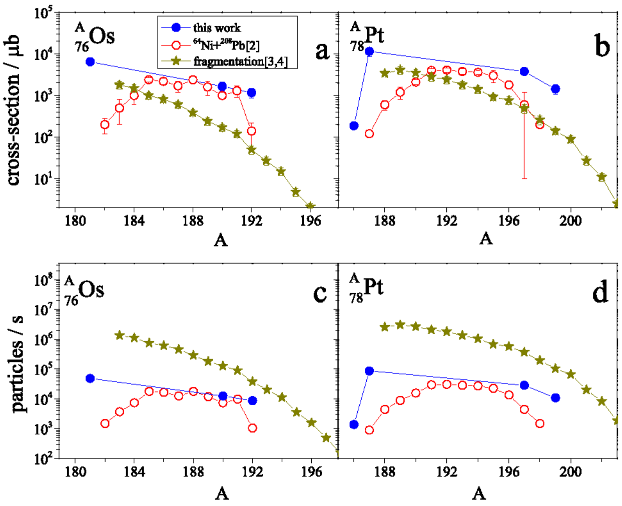

Figure 2: Total production cross-sections (a,b) and count rates (c,d) of DIT and fragmentation reaction products

In the next step we compared the production yields for the observed isotopes which can be expected in DIT and fragmentation reactions (see fig.2 c,d). As one can see, the estimated yields (at the target) for the same isotopes are typically about one or more orders of magnitude higher in fragmentation reactions. This is due to the more favorable experimental conditions in fragmentation reactions concerning the product of beam intensity and target thickness. Therefore, in order to become more profitable than fragmentation reactions, the yields of DIT products have to be increased considerably.

References

[1] O. Beliuskina, et al., Eur. Phys. J. A **50**, 161 (2014)

[2] W. Krolas, at al, Nucl. Phys. A **724**, 289 (2003)

[3] E. Casarejos, et al, Phys. Rev. C**74**, 044612 (2006)

[4] Teresa Kurtukian-Nieto, PhD thesis work, University of Santiage de Compostela, Spain, Januar 2007

---

* Work supported by GSI cooperation with university Giessen/FAIR@GSI PSP code:500457

† o.beliuskina@gsi.de

DOI:10.15120/GR-2015-1-MU-NUSTAR-SHE-P-04

MoDSS – a compact Mobile Decay Spectroscopy Set-up for the investigation of heavy and superheavy nuclei after separation

*D. Ackermann**[1], *F.P. Heßberger*[1,2], *J. Hoffmann*[1], *N. Kurz*[1], *J. Maurer*[1], *A.K. Mistry*[2], *J. Piot*[3], *M. Vostinar*[3], *and P. Wieczorek*[1]

[1]GSI, Darmstadt, Germany; [2]HIM, Mainz, Germany; [3]GANIL, Caen, France

The investigation of the nuclear structure of heavy and superheavy nuclei [1] relies on the performance of advanced comprehensive charged particle and photon detector set-ups, mounted close to the target position for in-beam detection or designed for decay spectroscopy after an ion optical separator, like e.g. the focal plane detector set-up TASISpec [2].

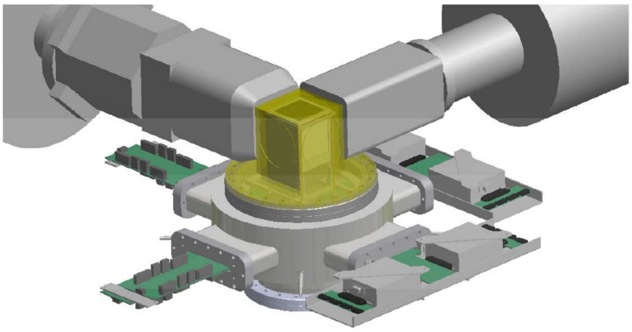

Figure 1: Schematic view of the detector configuration consisting of the aluminum housing of the Si-array surrounded by large volume Ge-detectors (two of five possible are shown here) and the chamber accommodating the two types of complementary electronics.

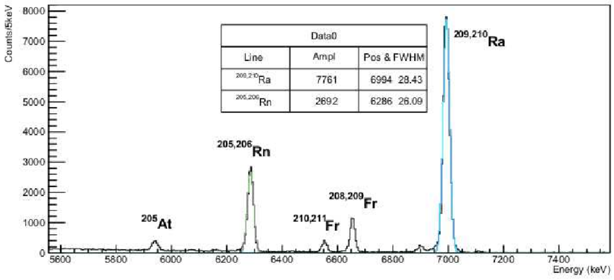

Figure 2: First α spectrum obtained at a test run at the velocity filter of the LISE spectrometer at GANIL using analog signal processing.

troscopy Set-up (MoDSS) for the detection of heavy ion reaction products and its decay radiation and its first test at the LISE setup of GANIL [3], employing the reaction ^{40}Ar+^{174}Yb$\rightarrow^{214}$Ra*. It consists of a combination a 60×60 double sided silicon strip detector (DSSD) with an active area of 60×60 mm^2 of 300 μm thickness, surrounded in its backward hemisphere by four single sided silicon strip detectors (SSSD) of the same dimensions subdivided into 32 strips, forming a cube with one open face upstream for accepting the incoming particles. The array is housed in a compact chamber with thin aluminum windows (1.5 mm) facing the backside of all five detector chips to allow for the detection of γ-rays emitted by the reaction products implanted in the DSSD. In Fig. 1 a schematic view of the set-up is shown together with the chamber, housing the two types of front end electronics employed for complementary signal processing.

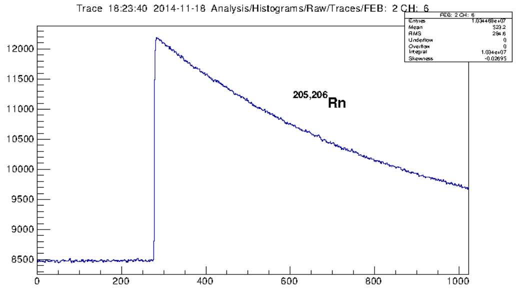

Figure 3: Example trace for an α decay pulse collected during the test run at the LISE velocity filter using the FEBEX [4] based digital MBS electronics.

For the front-end electronics there are two complementary options. An analogue data processing chain consists of a charge sensitive preamplifier (PA) developed by the electronics laboratory of the Nuclear Physics Department of the University of Cologne followed by Mesytec SMT16+ shaper and fed into an analogue data acquisition system (DAQ) on the basis of the GSI multi branch system (MBS). In Fig. 2 an α spectrum is shown, which had been obtained at the velocity filter of the LISE spectrometer at GANIL, Caen, France. At the end of this test run the second DAQ configuration was tested, using a set-up based on the flash ADC module FEBEX3A [4] developed in-house. An example trace taken with this configuration is shown in Fig. 3. As additional option the charge sensitive PA's can be substituted by the APFEL ASIC [5] in combination with the FEBEX DAQ, which provides a fast shaped pulse of 250 ns width and a two output signals for each input with amplification factors of 1 and 16/32 switchable.

References

[1] R.-D. Herzberg, P. Greenlees, Prog. Part. Nucl. Phys. 61, 674 (2008)

[2] L. Andersson et al., Nucl. Instr. and Meth. A 662, 164 (2010)

[3] R. Anne and A.C. Mueller, Nucl. Instr. and Meth. B 70, 276 (1992)

[4] J. Hoffmann et al., GSI Scientific Report 2011, 253 (2012)

[5] P. Wieczorek et al., GSI Scientific Report 2011,251 (2012)

---

* d.ackermann@gsi.de

DOI:10.15120/GR-2015-1-MU-NUSTAR-SHE-P-05

Remarks on the fission barriers of super-heavy nuclei

S. Hofmann[1,2], *S. Heinz*[1], *R. Mann*[1], *J. Maurer*[1], *G. Münzenberg*[1], *S. Antalic*[3], *W. Barth*[1], *H.G. Burkhard*[1], *L. Dahl*[1], *K. Eberhardt*[4], *R. Grzywacz*[5,6], *J.H. Hamilton*[7], *R.A. Henderson*[8], *J.M. Kenneally*[8], *B. Kindler*[1], *I. Kojouharov*[1], *R. Lang*[1], *B. Lommel*[1], *K. Miernik*[5,9], *D. Miller*[6], *K.J. Moody*[8], *K. Morita*[10], *K. Nishio*[11], *A.G. Popeko*[12], *J.B. Roberto*[5], *J. Runke*[4], *K.P. Rykaczewski*[5], *C. Scheidenberger*[1], *D.A. Shaughnessy*[8], *M.A. Stoyer*[8], *P. Thörle-Pospiech*[4], *K. Tinschert*[1], *N. Trautmann*[4], *J. Uusitalo*[13], *and A.V. Yeremin*[12]

[1]GSI, Darmstadt, Germany; [2]Goethe-University, Frankfurt, Germany; [3]Comenius University, Bratislava, Slovakia; [4]Johannes Gutenberg-University, Mainz, Germany; [5]ORNL, Oak Ridge, TN, USA; [6]University of Tennessee, Knoxville, TN, USA; [7]Vanderbilt University, Nashville, TN, USA; [8]LLNL, Livermore, CA, USA; [9]University of Warsaw, Warsaw, Poland; [10]RIKEN, Wako, Saitama, Japan; [11]JAEA, Tokai, Ibaraki, Japan; [12]JINR, Dubna, Russia; [13]University of Jyväskylä, Jyväskylä, Finland

Shell-correction energies determine the stability and the fission barriers of Super-Heavy Nuclei (SHN), the latter being a main factor responsible for their production yield. Although recent experiments performed at FLNR in Dubna (see review articles [1,2]) have confirmed the existence of an island of SHN, the site and strength of highest stability is still uncertain. Predicted Q_α values as shown in Fig. 1a reveal the ambiguity. The macroscopic-micro-scopic (MM) models [3,4] predict a closed proton shell at Z = 114 and thus increasing Q_α values beyond. The chiral mean-field model (CMF) [5] and the semi-empirical model (SE) [6] predict subshells or shells at 120 and 126, respectively, resulting in less steep or even decreasing Q_α values. Experimental data, also shown in Fig. 1a and known up to Z = 116 do not give preference to a specific model. However, decisive information could be obtained from the α-decay properties of elements 118 and 120. The following discussion supports our search experiment for element 120. The study also reveals an important uncertainty related to the prediction of cross-sections of the synthesis of SHN.

Shell-correction energies

Model dependent experimental shell-correction energies can be deduced from measured nuclear masses by subtraction of theoretically determined liquid-drop masses. In our case, however, absolute experimental nuclear masses are not known, but relative values can be determined for nuclei within an α-decay chain using the experimental Q_α values. Normalizing these relative masses to the theoretical ones at the end of the decay chain, which is closer to the region of known masses, where relatively good agreement was established [7], results in a reliable approximation of masses up to the heaviest nuclei of the α-decay chain. In one case, where a relatively long decay chain starting at ^{291}Lv and ending at ^{267}Rf is known, we have performed such an estimate of shell-correction energies. Interestingly, this is the decay chain which would be populated in a 3n channel of the reaction ^{54}Cr + ^{248}Cm.

In Figs. 1b and 1c, we have plotted the so determined shell-correction energies and compare them with theoretical values taken from [3] and [8], respectively. The relative masses of the four lightest nuclei from ^{267}Rf to ^{279}Ds were normalized by a least squares fit to the theoretical masses. In order to distinguish between the so determined masses, shell-correction energies and fission barriers from the theoretical ones, we denote those 'experimental data' in the following.

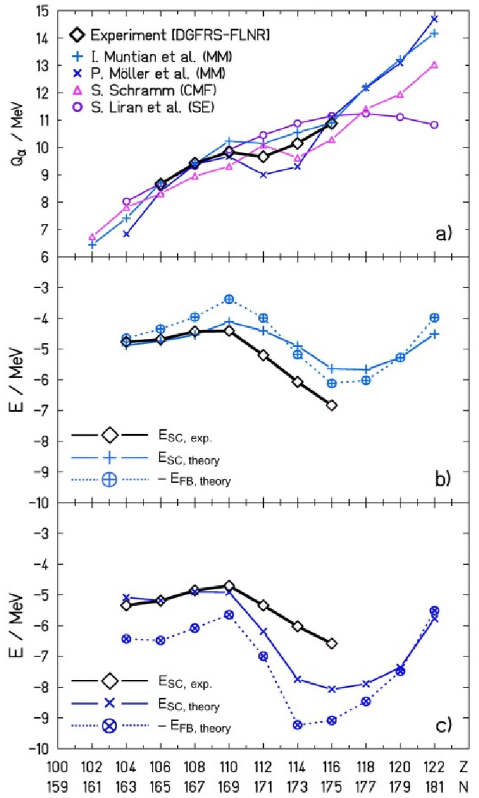

Figure 1: Comparison of experimental and theoretical Q_α values (a) and of experimental and theoretical shell-correction energies taken from [3] in (b) and from [8] in (c) for nuclei of the α-decay chain passing through the isotope ^{291}Lv. Also shown in Figs. 1b and 1c are the negative values (for easier comparison with the shell-correction energies) of the fission barriers connected by dotted lines taken from [9] and [10], respectively.

DOI:10.15120/GR-2015-1-MU-NUSTAR-SHE-P-06

The two curves of theoretical shell-correction energies shown in Figs. 1b and 1c and the experimental ones reveal some common features. A moderate increase occurs from ^{267}Rf to ^{279}Ds followed by a sharp decrease (increasing binding energy), up to ^{291}Lv. This behaviour is well understood in terms of the shell model having a closed proton shell at $Z = 114$ and a low level density above, up to $Z = 126$, which shifts the minimum of the shell-correction energies to $Z = 116 - 118$ (see also Fig. 53 in [4]).

The minimum of shell-correction energies is less pronounced in the calculations of [3] than in [8]. The difference at ^{291}Lv is 2.43 MeV. However, the shapes and also the absolute values of the two model dependent experimental shell-correction energies obtained from fitting the masses to the lowest four theoretical masses are very similar, both having lowest values of –6.8 and –6.6 MeV, respectively, at ^{191}Lv. Especially here we see the importance of the next (^{295}118 and ^{299}120) data points. The Q_α values and deduced shell-correction energies of these two nuclei will provide us with the information of a possible shell or subshell closure at $Z = 120$.

In order to rule out energy shifts due to uncertain Q_α values of odd-A nuclei, we used the measured Q_α values of neighbouring even-even isotopes with decay chains through ^{290}Lv and ^{292}Lv (see Fig. 4 in [11] and Fig. 11 in [12]) for a similar comparison as shown in Fig. 1. In these cases the α decay occurs with high probability between the ground-states resulting in correct Q_α values. Although the chains of these nuclei end by spontaneous fission of copernicium isotopes, the slope of shell-correction energies between copernicium and ^{294}118, respectively, for ^{292}Lv is less than resulting from the calculations [8], but similar as given by the experimental data shown in Fig. 1c for odd isotopes. The trend of shell-correction energies in the case of the odd-A decay chain through ^{293}Lv is similar. This chain is known down to ^{277}Hs. We conclude that the shell-correction energies of nuclei of the elements 114 and 116 and with neutron numbers from 174 to 177 decrease less than predicted by the calculations of [8]. The observation of the same trend in four neighbouring decay chains reveals that less strong shell-correction energies could be adopted for the region of isotopes of elements at and beyond 114 for which strong shell-correction energies are predicted in [8].

The shell-correction energy is the main component which determines the fission barrier of SHN. The mutual dependence becomes obvious in a comparison of the shell-correction energy with the inverse of the height of the fission barrier. On this condition we compare in Figs. 1b and 1c the experimental shell-correction energies with the actually calculated fission barriers given in [9] and [10]. The data in [9] were estimated as the mean value of the neighbouring even-even isotopes. In both cases specialization energy is not considered. Whereas in Fig. 1b [9] the curve of the fission barriers is similar to the one of the shell-correction energies, it is significantly lower in the case of Fig. 1c [10] with maximal differences of 1.35 and 1.49 MeV at ^{267}Rf and ^{287}Fl, respectively. Obviously, the difference is due to pronounced positive shell-correction energies at the saddle point in the latter calculation. Even larger is the difference if compared with the experimental shell-correction energies.

Cross-sections

The height of the fission barrier is primarily responsible for the survival of the compound nucleus (CN) and is, thus, a significant factor contributing to the cross-section of the fusion-evaporation reaction. However, it is not the barrier in the ground-state that is the most important, but the fission barrier height at the excitation energies of the fused system during the evaporation process which is decisive. In the region of SHN, the reduction of fission barriers at excitation energies of several tens of MeV is determined by the damping of shell-correction energies for deformations from zero up to the saddle point, see e.g. [13].

In the case of hot fusion reactions based on actinide targets, the calculated cross-section depends sensitively from the height of the fission barrier. A change by a factor of 200 was obtained for the reaction ^{48}Ca + ^{249}Cf when the fission barrier of ≈5.5 MeV [3] was changed by 1 MeV [14]. Also studied was the influence of the fission barrier on the ER cross-section in [15,16]. The 3n cross-section of the reaction ^{48}Ca + ^{238}U was calculated for fission barriers of 4.5, 5.5 and 6.5 MeV resulting in cross-sections of 0.23, 5.0 and 30 pb, respectively. Considering the uncertainties of fission barriers suggested by a comparison of Figs. 1b and 1c, we have to conclude that calculated cross-sections will differ by one or two orders of magnitude using different model predictions of fission barriers and their dependence on the excitation energy if the entrance channel effects are kept unchanged.

In the case that the relatively high fission barriers shown in Fig. 1c are used in the calculations of cross-sections, then the resulting low CN fission probability is compensated by a strong probability for re-separation of projectile and target nuclei in the entrance channel. The balance becomes especially important for synthesis of nuclei in the region from ^{279}Ds to ^{287}Fl, where the theoretical fission barriers of [10] increase rapidly. If, however, the increase of fission barriers is more moderate as calculated in [9] or suggested by the experimental shell-correction energies, then, the probability for re-separation with increasing Z_1Z_2 has to be more moderate, too. From these arguments follow the conclusions that predicted cross-sections for elements 118 and 120, which use the fission barriers of [10] and which reproduce well the cross-sections of elements 114 and 116, could be higher due to a smaller probability for re-separation in the entrance channel.

References

[1] Yu.Ts. Oganessian, JPG: NPP **34**, R165 (2007).
[2] J.H. Hamilton et al., ARNPS **63**, 383 (2013).
[3] I. Muntian et al., Acta Phys. Pol. B **34**, 2073 (2003).
[4] P. Möller et al., ADND Tables **66**, 131 (1997).

DOI:10.15120/GR-2015-1-MU-NUSTAR-SHE-P-06

[5] S. Schramm, Phys. Rev. C **66**, 064310 (2002).
[6] S. Liran et al., Phys. Rev. C **62**, 047301 (2000).
[7] E. Min. Ramirez et al., Science **337**, 1207 (2012).
[8] P. Möller et al., ADND Tables **59**, 185 (1995).
[9] M. Kowal et al., Phys. Rev. C **82**, 014303 (2010).
[10] P. Möller et al., Phys. Rev. C **79**, 064304 (2009).
[11] S. Hofmann, Russian Chem. Rev. **78**, 1123 (2009).
[12] S. Hofmann, Lect. Notes Phys. **764**, 203 (2009).
[13] J.C. Pei et al., Phys. Rev. Lett. 102, 192501 (2009).
[14] K. Siwek-Wilczyńska et al., IJMP E **19**, 500 (2010).
[15] M.G. Itkis et al., Phys. Rev. C **65**, 044602 (2002).
[16] V.I. Zagrebaev et al., Phys. At. Nucl. **66**, 1033 (2003).

DOI:10.15120/GR-2015-1-MU-NUSTAR-SHE-P-06

RF measurements on the superconducting 217 MHz CH-cavity for the cw demonstrator*

F. Dziuba[†1], *M. Amberg*[1,3], *K. Aulenbacher*[3,4], *W. Barth*[2,3], *M. Basten*[1], *M. Busch*[1], *H. Podlech*[1], *U. Ratzinger*[1], *and S. Mickat*[2,3]

[1]IAP, Frankfurt, Germany; [2]GSI, Darmstadt, Germany; [3]HIM, Mainz, Germany; [1]KPH, Mainz, Germany

The demonstrator project is the first prototype of a new superconducting (sc) continuous wave (cw) linac at GSI for the production of Super Heavy Elements (SHE). The demonstrator consists of a sc CH-cavity embedded by two sc solenoids mounted in a horizontal cryomodule. One milestone of the project is a full perforemance test of the cavity with beam at the GSI High Charge Injector (HLI) which is foreseen in 2016.

Status and RF measurements

The assembly of the 217 MHz CH-cavity up to the helium vessel was finished in 2014 at Research Instruments (RI), Bergisch Gladbach, Germany (see Figure 1). Two surface preparations with BCP (50 and 25 μm) have been performed. The coupler as well as the pick up antenna have been redesigned for the first cold tests at the Institute for Applied Physics (IAP) with low rf power. After mounting the coupler and pick up to the cavity it will be high pressure rinsed and afterwards delivered to the IAP. It is expected that first cold tests of the cavity will be performed in a new vertical cryostat in April 2015. Intermediate rf measurements during the production process of the cavity have been performed at room temperature to determine the final static tuner heights and the lengths of the end caps of the cavity as well to hit the design frequency successively. Regarding a frequency shift of +430 kHz due to thermal shrinkage and pressure sensitivity the design frequency could be reached successfully as shown by Figure 2:

1. cavity without static tuners and temporarily attached end caps with oversize
2. static tuners #1, #4, #6, #7 welded into the cavity
3. left end cap welded to the cavity
4. static tuners #2, #8, #9 welded into the cavity
5. right end cap welded to the cavity
6. 50 μm BCP treatment
7. static tuners #3, #5 welded into the cavity
8. 25 μm BCP treatment

Nevertheless, a third 25 μm BCP preparation is potentially possible without leaving the tuning range of the dynamic tuners. Furthermore, the electric field distribution on the beam axis as well as the external quality factor Q_e of preliminary couplers have been evaluated. All results seem very promising to reach the design gradient of 5 MV/m at 4 K. After successful performence tests the helium vessel will be welded to the cavity.

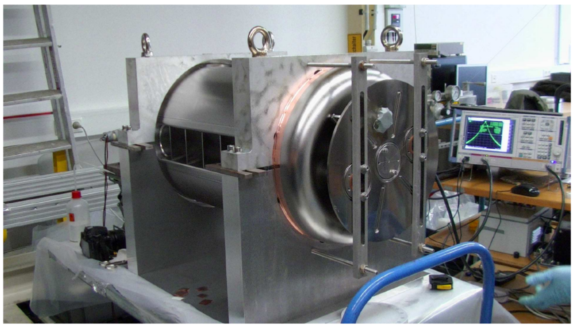

Figure 1: 217 MHz CH-cavity during intermediate rf measurements at RI.

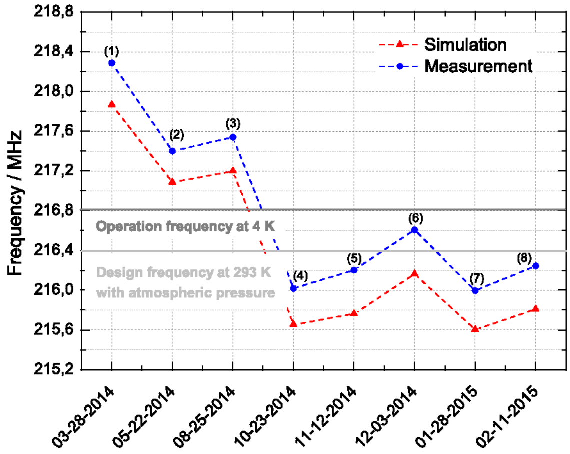

Figure 2: Behavoir of the frequency during the production process of the sc 217 MHz CH-cavity.

References

[1] F. Dziuba et al., FIRST RF MEASUREMENTS OF THE SUPERCONDUCTING 217 MHz CH CAVITY FOR THE CW DEMONSTRATOR AT GSI, In Proc. of LINAC 2014, Geneva, Switzerland (2014)

---

[*] Work supported by HIM, GSI, BMBF Contr. No. 05P12RFRBL, FAIR@GSI PSP code: 6-6-7-05

[†] dziuba@iap.uni-frankfurt.de

DOI:10.15120/GR-2015-1-MU-NUSTAR-SHE-P-07

Remarks on the fission barriers of super-heavy nuclei

S. Hofmann[1,2], S. Heinz[1], R. Mann[1], J. Maurer[1], G. Münzenberg[1], S. Antalic[3], W. Barth[1], H.G. Burkhard[1], L. Dahl[1], K. Eberhardt[4], R. Grzywacz[5,6], J.H. Hamilton[7], R.A. Henderson[8], J.M. Kenneally[8], B. Kindler[1], I. Kojouharov[1], R. Lang[1], B. Lommel[1], K. Miernik[5,9], D. Miller[6], K.J. Moody[8], K. Morita[10], K. Nishio[11], A.G. Popeko[12], J.B. Roberto[5], J. Runke[4], K.P. Rykaczewski[5], C. Scheidenberger[1], D.A. Shaughnessy[8], M.A. Stoyer[8], P. Thörle-Pospiech[4], K. Tinschert[1], N. Trautmann[4], J. Uusitalo[13], and A.V. Yeremin[12]

[1]GSI, Darmstadt, Germany; [2]Goethe-University, Frankfurt, Germany; [3]Comenius University, Bratislava, Slovakia; [4]Johannes Gutenberg-University, Mainz, Germany; [5]ORNL, Oak Ridge, TN, USA; [6]University of Tennessee, Knoxville, TN, USA; [7]Vanderbilt University, Nashville, TN, USA; [8]LLNL, Livermore, CA, USA; [9]University of Warsaw, Warsaw, Poland; [10]RIKEN, Wako, Saitama, Japan; [11]JAEA, Tokai, Ibaraki, Japan; [12]JINR, Dubna, Russia; [13]University of Jyväskylä, Jyväskylä, Finland

Shell-correction energies determine the stability and the fission barriers of Super-Heavy Nuclei (SHN), the latter being a main factor responsible for their production yield. Although recent experiments performed at FLNR in Dubna (see review articles [1,2]) have confirmed the existence of an island of SHN, the site and strength of highest stability is still uncertain. Predicted Q_α values as shown in Fig. 1a reveal the ambiguity. The macroscopic-micro-scopic (MM) models [3,4] predict a closed proton shell at Z = 114 and thus increasing Q_α values beyond. The chiral mean-field model (CMF) [5] and the semi-empirical model (SE) [6] predict subshells or shells at 120 and 126, respectively, resulting in less steep or even decreasing Q_α values. Experimental data, also shown in Fig. 1a and known up to Z = 116 do not give preference to a specific model. However, decisive information could be obtained from the α-decay properties of elements 118 and 120. The following discussion supports our search experiment for element 120. The study also reveals an important uncertainty related to the prediction of cross-sections of the synthesis of SHN.

Shell-correction energies

Model dependent experimental shell-correction energies can be deduced from measured nuclear masses by subtraction of theoretically determined liquid-drop masses. In our case, however, absolute experimental nuclear masses are not known, but relative values can be determined for nuclei within an α-decay chain using the experimental Q_α values. Normalizing these relative masses to the theoretical ones at the end of the decay chain, which is closer to the region of known masses, where relatively good agreement was established [7], results in a reliable approximation of masses up to the heaviest nuclei of the α-decay chain. In one case, where a relatively long decay chain starting at ^{291}Lv and ending at ^{267}Rf is known, we have performed such an estimate of shell-correction energies. Interestingly, this is the decay chain which would be populated in a 3n channel of the reaction ^{54}Cr + ^{248}Cm.

In Figs. 1b and 1c, we have plotted the so determined shell-correction energies and compare them with theoretical values taken from [3] and [8], respectively. The relative masses of the four lightest nuclei from ^{267}Rf to ^{279}Ds were normalized by a least squares fit to the theoretical masses. In order to distinguish between the so determined masses, shell-correction energies and fission barriers from the theoretical ones, we denote those 'experimental data' in the following.

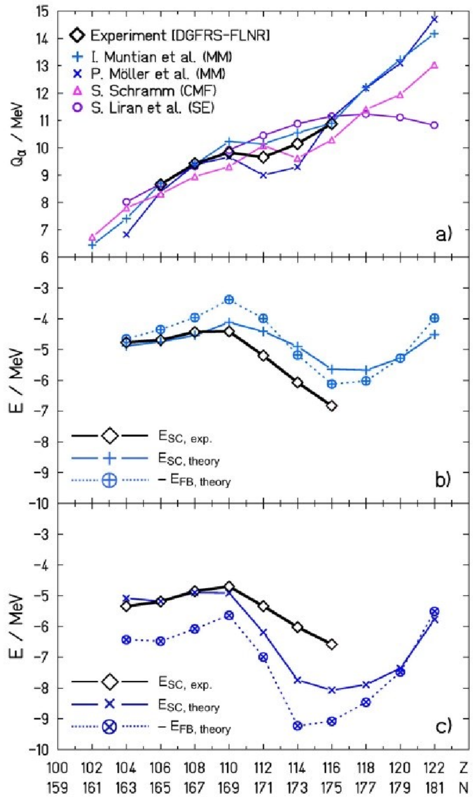

Figure 1: Comparison of experimental and theoretical Q_α values (a) and of experimental and theoretical shell-correction energies taken from [3] in (b) and from [8] in (c) for nuclei of the α-decay chain passing through the isotope ^{291}Lv. Also shown in Figs. 1b and 1c are the negative values (for easier comparison with the shell-correction energies) of the fission barriers connected by dotted lines taken from [9] and [10], respectively.

DOI:10.15120/GR-2015-1-MU-NUSTAR-SHE-P-08

The two curves of theoretical shell-correction energies shown in Figs. 1b and 1c and the experimental ones reveal some common features. A moderate increase occurs from ^{267}Rf to ^{279}Ds followed by a sharp decrease (increasing binding energy), up to ^{291}Lv. This behaviour is well understood in terms of the shell model having a closed proton shell at Z = 114 and a low level density above, up to Z = 126, which shifts the minimum of the shell-correction energies to Z = 116 – 118 (see also Fig. 53 in [4]).

The minimum of shell-correction energies is less pronounced in the calculations of [3] than in [8]. The difference at ^{291}Lv is 2.43 MeV. However, the shapes and also the absolute values of the two model dependent experimental shell-correction energies obtained from fitting the masses to the lowest four theoretical masses are very similar, both having lowest values of –6.8 and –6.6 MeV, respectively, at ^{191}Lv. Especially here we see the importance of the next (^{295}118 and ^{299}120) data points. The Q_α values and deduced shell-correction energies of these two nuclei will provide us with the information of a possible shell or subshell closure at Z = 120.

In order to rule out energy shifts due to uncertain Q_α values of odd-A nuclei, we used the measured Q_α values of neighbouring even-even isotopes with decay chains through ^{290}Lv and ^{292}Lv (see Fig. 4 in [11] and Fig. 11 in [12]) for a similar comparison as shown in Fig. 1. In these cases the α decay occurs with high probability between the ground-states resulting in correct Q_α values. Although the chains of these nuclei end by spontaneous fission of copernicium isotopes, the slope of shell-correction energies between copernicium and ^{294}118, respectively, for ^{292}Lv is less than resulting from the calculations [8], but similar as given by the experimental data shown in Fig. 1c for odd isotopes. The trend of shell-correction energies in the case of the odd-A decay chain through ^{293}Lv is similar. This chain is known down to ^{277}Hs. We conclude that the shell-correction energies of nuclei of the elements 114 and 116 and with neutron numbers from 174 to 177 decrease less than predicted by the calculations of [8]. The observation of the same trend in four neighbouring decay chains reveals that less strong shell-correction energies could be adopted for the region of isotopes of elements at and beyond 114 for which strong shell-correction energies are predicted in [8].

The shell-correction energy is the main component which determines the fission barrier of SHN. The mutual dependence becomes obvious in a comparison of the shell-correction energy with the inverse of the height of the fission barrier. On this condition we compare in Figs. 1b and 1c the experimental shell-correction energies with the actually calculated fission barriers given in [9] and [10]. The data in [9] were estimated as the mean value of the neighbouring even-even isotopes. In both cases specialization energy is not considered. Whereas in Fig. 1b [9] the curve of the fission barriers is similar to the one of the shell-correction energies, it is significantly lower in the case of Fig. 1c [10] with maximal differences of 1.35 and 1.49 MeV at ^{267}Rf and ^{287}Fl, respectively. Obviously, the difference is due to pronounced positive shell-correction energies at the saddle point in the latter calculation. Even larger is the difference if compared with the experimental shell-correction energies.

Cross-sections

The height of the fission barrier is primarily responsible for the survival of the compound nucleus (CN) and is, thus, a significant factor contributing to the cross-section of the fusion-evaporation reaction. However, it is not the barrier in the ground-state that is the most important, but the fission barrier height at the excitation energies of the fused system during the evaporation process which is decisive. In the region of SHN, the reduction of fission barriers at excitation energies of several tens of MeV is determined by the damping of shell-correction energies for deformations from zero up to the saddle point, see e.g. [13].

In the case of hot fusion reactions based on actinide targets, the calculated cross-section depends sensitively from the height of the fission barrier. A change by a factor of 200 was obtained for the reaction ^{48}Ca + ^{249}Cf when the fission barrier of ≈5.5 MeV [3] was changed by 1 MeV [14]. Also studied was the influence of the fission barrier on the ER cross-section in [15,16]. The 3n cross-section of the reaction ^{48}Ca + ^{238}U was calculated for fission barriers of 4.5, 5.5 and 6.5 MeV resulting in cross-sections of 0.23, 5.0 and 30 pb, respectively. Considering the uncertainties of fission barriers suggested by a comparison of Figs. 1b and 1c, we have to conclude that calculated cross-sections will differ by one or two orders of magnitude using different model predictions of fission barriers and their dependence on the excitation energy if the entrance channel effects are kept unchanged.

In the case that the relatively high fission barriers shown in Fig. 1c are used in the calculations of cross-sections, then the resulting low CN fission probability is compensated by a strong probability for re-separation of projectile and target nuclei in the entrance channel. The balance becomes especially important for synthesis of nuclei in the region from ^{279}Ds to ^{287}Fl, where the theoretical fission barriers of [10] increase rapidly. If, however, the increase of fission barriers is more moderate as calculated in [9] or suggested by the experimental shell-correction energies, then, the probability for re-separation with increasing Z_1Z_2 has to be more moderate, too. From these arguments follow the conclusions that predicted cross-sections for elements 118 and 120, which use the fission barriers of [10] and which reproduce well the cross-sections of elements 114 and 116, could be higher due to a smaller probability for re-separation in the entrance channel.

References

[1] Yu.Ts. Oganessian, JPG: NPP **34**, R165 (2007).
[2] J.H. Hamilton et al., ARNPS **63**, 383 (2013).
[3] I. Muntian et al., Acta Phys. Pol. B **34**, 2073 (2003).
[4] P. Möller et al., ADND Tables **66**, 131 (1997).

DOI:10.15120/GR-2015-1-MU-NUSTAR-SHE-P-08

[5] S. Schramm, Phys. Rev. C **66**, 064310 (2002).
[6] S. Liran et al., Phys. Rev. C **62**, 047301 (2000).
[7] E. Min. Ramirez et al., Science **337**, 1207 (2012).
[8] P. Möller et al., ADND Tables **59**, 185 (1995).
[9] M. Kowal et al., Phys. Rev. C **82**, 014303 (2010).
[10] P. Möller et al., Phys. Rev. C **79**, 064304 (2009).
[11] S. Hofmann, Russian Chem. Rev. **78**, 1123 (2009).
[12] S. Hofmann, Lect. Notes Phys. **764**, 203 (2009).
[13] J.C. Pei et al., Phys. Rev. Lett. 102, 192501 (2009).
[14] K. Siwek-Wilczyńska et al., IJMP E **19**, 500 (2010).
[15] M.G. Itkis et al., Phys. Rev. C **65**, 044602 (2002).
[16] V.I. Zagrebaev et al., Phys. At. Nucl. **66**, 1033 (2003).

DOI:10.15120/GR-2015-1-MU-NUSTAR-SHE-P-08

Direct proof of electron capture decay of ^{258}Db*

F.P. Heßberger†[1,2], *D. Ackermann*[1], *B. Andel*[3], *S. Antalic*[3], *C. Droese*[2,4], *J. Even*[2], *Z. Kalaninová*[3], *M. Laatiaoui*[2], *J. Piot*[5], *and M. Vostinar*[5]

[1]GSI, Darmstadt, Germany; [2]HIM, Mainz, Germany; [3]Comenius University, Bratislava, Slovakia; [4]Ernst-Moritz-Arndt Universität, Greifswald, Germany; [5]GANIL, Caen, France

Besides spontaneous fission (sf) and α emission, electron capture (EC) decay is the third essential decay mode of transuranium nuclei, providing valuable information on their nuclear structure. Experimental data are, however, quite scarce in the region of $Z > 100$. The heaviest nucleus for which so far nuclear structure information was obtained is ^{253}Md, produced by EC decay of ^{253}No [1].

Study of EC decay is also of interest from an other point of view: for a couple of odd-odd nuclei sf branches are reported, among them the members terminating the α - decay chains assigned to start from odd-odd nuclei of elements with $Z = 113$, 115 and 117, produced in actinide based 'hot fusion' reactions. Because of the strong hindrance of sf of odd-odd nuclei due to two unpaired nucleons, it can be assumed that the terminating sf activities stem from even-even nuclei produced by EC decay. As the latter is a secure source for emission of K X-rays, the proof of EC decay would go along with an unambiguous Z - identification - which is still missing for all elements $Z > 112$ - of the decaying nucleus and its precursors up to the head of the decay chain. If, further, EC decay populates excited states in the daughter nucleus it also will be a tool for nuclear structure investigations complementary to α emission.

A candidate suited to test the technical feasibility is ^{258}Db, which can be produced in the reaction ^{209}Bi(^{50}Ti,n)^{258}Db with a relatively large cross-section of $\sigma \approx 4$ nb. For that nucleus an EC branch of $\approx 33\%$ was assumed from the ratio of α decays and sf events which were ascribed to sf of ^{258}Rf, the EC-decay daughter of ^{258}Db [2]. A direct proof of this assumption had already been attempted in 1982 at SHIP by measuring delayed coincidences between γ - rays and sf - events; indeed, some candidates for K X-rays were observed as shown in Fig. 1a, but the result was not not regarded as a completely convincing proof [3].

A new experiment was performed in may 2014 at SHIP. In an experimental run of about 200 h irradiation time roughly 1250 sf events were collected. The spectrum of γ - rays (in coincidence with conversion electrons) preceeding an sf event within $\Delta t \leq 39$ ms is shown in Fig. 1b; clearly the $K_{\alpha1,\alpha2}$ and $K_{\beta'1}$ - lines of rutherfordium are visible. From the time distributions (γ-sf) a half-life of 13±11 ms was extracted for the sf activity, which is in-line with the value $14.7^{+1.2}_{-1.0}$ ms [4], reported for ^{258}Rf. The observation of conversion electrons in coincidence with the X-rays further proves the population of at least one excited level in ^{258}Rf, their energy distribution suggest an excitation energy range of $\approx 400 - 500$ keV. Assuming population of the ground-state rotational band this would lead to population of the 8^+ or a higher-spin state.

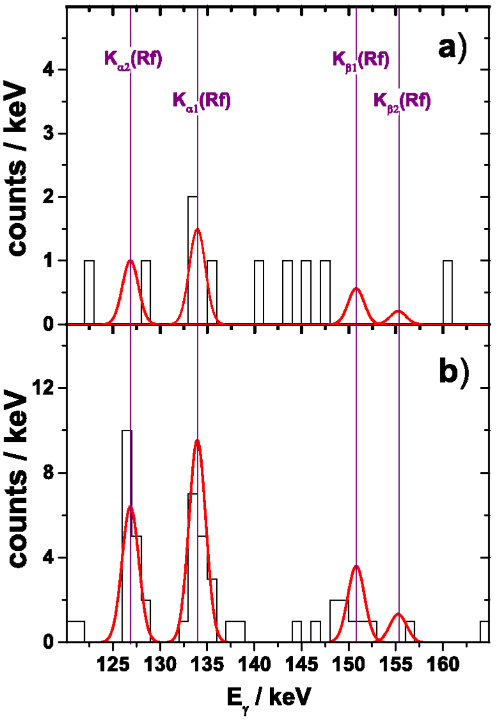

Figure 1: Energy spectra of γ - events observed in delayed coincidence with sf - events a) SHIP experiment in 1982 [3], $\Delta t(\gamma\text{-sf}) \leq 30$ ms, b) SHIP experiment in 2014, $\Delta t(\gamma\text{-sf}) \leq 39$ ms, electron occuring in prompt coincidence with γ - event required; the full red lines represent the expected spectra using the theoretical X-ray energies [5] and a detector resolution of 2 keV(FWHM).

References

[1] S. Antalic et al., Eur. Phys. J. A 47:62 (2011)

[2] F.P. Heßberger et al., Z. Phys. A 322, 557 (1985)

[3] F.P. Heßberger, PHD, TH Darmstadt 1985, GSI Report GSI-85-11

[4] J.M. Gates et al., PRC 77, 034603 (2008)

[5] T.A. Carlson, C.W. Nestor Jr., ADNDT 19, 153 (1977)

---

* Work supported by GSI(UNILAC)/HI Mainz/European Community FP7 - Capacities, contract ENSAR contract No. 262010/French-German Collaboration agreement INP2 P3-DSM/CEA and GSI/Slovak Grant Agency VEGA, contract No. 1/0576/13

† f.p.hessberger@gsi.de

DOI:10.15120/GR-2015-1-MU-NUSTAR-SHE-P-09

Search for atomic transitions in nobelium

P. Chhetri[1], *D. Ackermann*[2,3], *H. Backe*[4], *M. Block*[2,3], *B. Cheal*[5], *J. Even*[6], *R. Ferrer*[7], *F.P. Hessberger*[2,3], *P. Kunz*[6], *M. Laatiaoui*[2], *F. Lautenschlaeger*[1], *W. Lauth*[4], *S. Raeder*[7], *Th. Walther*[1], *and C. Wraith*[5]

[1]TU Darmstadt; [2]HIM, Mainz; [3]GSI, Darmstadt; [4]JGU, Mainz; [5]University of Liverpool, Liverpool; [6]TRIUMF, Vancouver; [7]KU Leuven, Leuven

Relativistic effects influence the valence electron configuration of the heaviest elements having a big impact on their physical and chemical properties. These effects can be described using the modern multi configuration Dirac-Fock (MCDF) and Relativistic Coupled-Cluster [1, 2, 3] calculations. To have a benchmark for theoretical calculations, a comparison between the measured and predicted atomic properties is needed. At present, no spectroscopic data is available for the atomic properties of transfermium elements (Z>100). Thus the study of the atomic structure of these elements is of great interest.

In our experiments we aim to search for the atomic levels of the element nobelium based on the Radiation Detected Resonance Ionization Spectroscopy (RADRIS) [3] technique. ^{254}No can be produced at the UNILAC at GSI with rates of approximately 17/s via the reaction ^{208}Pb(^{48}Ca,2n)^{254}No. The separated fusion-product beam from SHIP is stopped in a buffer gas cell in 90 mbar argon gas of 99.9999% purity and collected on a tantalum filament. After an appropriate collection time, the accumulated ions are then re-evaporated as neutral atoms by a short heating pulse into the buffer gas, during the beam-off period. We then employ a two-step photoionization process to ionize the atoms. In case of resonant ionization, the photoions are transported by suitable electric fields to a particle detector (PIPS detector) where they are identified by their characteristic α-decay.

Laser light for the first excitation-step, from four tunable dye lasers (Lambda Physik, FL series) and an optical parametric oscillator (OPO) (GWU, SFM housing) system, is transported to the experimental setup using UV-fibers. The dye lasers-operated in the UV-range, were pumped by two excimer lasers (Lambda Physik, LPX 210i and EMG104MSC) at 248 nm. The OPO pumped by a frequency-tripled Nd:YAG (Continuum, Precision II) laser, was operated in a frequency mixing mode, delivering light in the range below 400 nm. The 351 nm-light for the second non-resonant step was provided by a high power excimer laser (Lambda Physik, LPX220) and was transported to the experimental setup by high reflectivity UV-mirrors. The wavelengths of the dye lasers and the OPO-system were monitored by wavemeter capable of measuring wavenumbers with a precision of 0.01 cm^{-1}. LabView based software was designed, for experiment control and data acquisition.

Preceding the measurements in nobelium, the cell efficiency was determined using ytterbium, which is the chemical homologue of nobelium. The radionuclide of interest ^{155}Yb was produced by the fusion reaction ^{112}Sn(^{48}Ca,5n)^{155}Yb with a beam intensity of I_p =360 nA$_p$ and a production rate of about 9000/s. A dye laser was set to a wavelength corresponding to the $^1S_0 \rightarrow {}^1P_1$ transition in ytterbium at 25068.5 cm^{-1}. The second non-resonant step was provided by the excimer laser as mentioned before. The resulting alpha spectrum can be seen in Fig.1. A cell efficiency of ϵ^{tot}=1.2% with a selectivity of about 100 has been determined from the data shown in Fig.1. In the second part of the experiment, the search for the $^1P_1$ level in ^{254}No was performed. Theories predict this level to be at about 30300 cm^{-1} [2, 3]. Three dye lasers scanned a range from 28900 cm^{-1} - 30500 cm^{-1} and the OPO-system scanned from 30500 cm^{-1} - 33000 cm^{-1} . A measurement time of 50 s was chosen per step with a step size of 1 cm^{-1}. The data analysis is in progress.

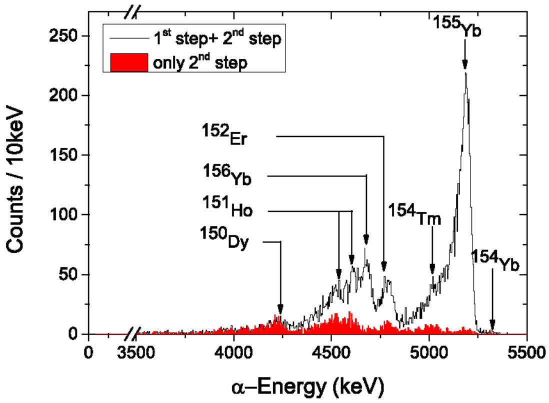

Figure 1: Two step photo-ionization of ^{155}Yb. Alpha spectrum with lasers on (black line) and laser off (red filled area). The measurement was performed at a buffer-gas pressure of 90 mbar, filament temperature of 1175°C, laser excitation energy $\bar{\nu_1}$ = 25068.5 cm^{-1}, $\bar{\nu_2}$ = 28490.03 cm^{-1} with laser pulse energy $E_{\bar{\nu_1}}$=163 μJ and $E_{\bar{\nu_2}}$= 60mJ and laser repetition rate of 100Hz.

Acknowledgements: This work is supported by the BMBF (FAIR NuSTAR 05P12RDFN8) and the Helmholtz-Institut Mainz.

References

[1] S. Fritzsche, Eur. Phys. J. D **33**, 15 (2005)

[2] V. Dzuba et al., Phys. Rev. A **90**, 012504 (20114)

[3] A. Borschevsky et al., Phys. Rev. A **75**, 042514 (2007)

[4] H. Backe et al., Eur. Phys. J. D **45**, 99 (2007)

DOI:10.15120/GR-2015-1-MU-NUSTAR-SHE-P-10

Chemical study of Fl, Cn, their lighter homologs, and Rn at TASCA*

A. Yakushev[1#], L. Lens[2], Ch.E. Düllmann[1,2,3], D. Ackermann[1], M. Asai[4] J. Ballof[2], M. Block[1,3], H. Brand[1], D.M. Cox[5], J. Despotopulos[6], A. Di Nitto[2], K. Eberhardt[2,3], J. Even[3], F. Fan[7], P. Golubev[8], H. Haba[9], W. Hartmann[1], R.-D. Herzberg[5], F.P. Heßberger[1,3], J. Hoffmann[1], A. Hübner[1], E. Jäger[1], J. Khuyagbaatar[1,3], B. Kindler[1], J.V. Kratz[2], J. Krier[1], N. Kurz[1], S. Lahiri[10]; B. Lommel[1], M. Maiti[11], A. Mistry[5], Ch. Mokry[2], K. Moody[6], Y. Nagame[4], J.P Omtvedt[12], Ph. Papadakis[13], Z. Qin[7], D. Rudolph[8], J. Runke[1], I. Rusanov[1], L.G. Sarmiento[8], T, Sato[4], M. Schädel[4], P. Scharrer[3], B. Schausten[1], D. Shaughnessy[6], J. Steiner[1], P. Thörle-Pospiech[2,3], N. Trautmann[2], J. Uusitalo[13], D. Ward[5], M. Wegrzecki[14], N. Wiehl[2,3], V. Yakusheva[3]

[1]GSI, Darmstadt, Germany; [2]University of Mainz, Germany; [3]Helmholtz Institute Mainz, Germany; [4]JAEA Tokai, Japan; [5]University of Liverpool, UK; [6]LLNL Livermore, USA; [7]IMP, Lanzhou, P.R. China; [8]Lund University, Sweden; [9]RIKEN, Wako-shi, Japan; [10]SINP Kolkata, India; [11]IIT Roorkee, India; [12]University of Oslo, Norway; [13]University of Jyväskylä, Finland; [14]ITE, Warsaw, Poland

Chemical studies on superheavy elements (SHE) with closed electron shell configurations, Cn and Fl, address the question of how strong relativistic effects influence chemical properties. This is a challenging task from both physical and chemical points of view due to low production rates and a high background from volatile byproducts disturbing the safe identification of Cn and Fl decay chains. Up to now only a limited number of experiments has been performed, resulting in the identification of only a few decay chains assigned to Cn and Fl isotopes [1-4]. Several attempts on investigation of Fl were performed by a PSI-FLNR collaboration, resulting in the detection of three decay chains from Fl, two chains from ^{288}Fl and one from ^{287}Fl [2,4]. Two Fl atoms, one with the atomic mass number 288 and one with the atomic mass number 289, were observed in an experiment at TASCA [3]. Hence, the determined values of the adsorption enthalpy of Fl on Au are still fairly uncertain due to low statistics.

A new chemistry experiment with Fl was carried out at TASCA in 2014. For the production of ^{288,289}Fl a ^{48}Ca^{+10} beam ($E_{\text{lab}} = 260$ MeV) with an intensity of about $5\cdot10^{12}$ particles/s impinged on ^{244}PuO$_2$ targets. They were electrodeposited on 2.5 µm thick Ti backing foils and had thicknesses of about 800 µg/cm^2 ^{244}Pu. A beam dose of about $2.6\cdot10^{18}$ was accumulated during 10 days of bombardment. TASCA was operated in the High Transmission Mode and its magnetic settings were adjusted to collect the ions with $B\cdot\rho = 2.27$ T·m at the exit of TASCA, where a Recoil Transfer Chamber (RTC; 60x40x20 mm^3) was attached. The RTC inner surface was coated with a Teflon™ layer. Three COMPACT detector arrays (COMPACT^3) were connected to the RTC exit in series. The first array was covered with a SiO$_2$ layer, and the two following ones with Au layers. All layers were 30-50 nm thick. The first two detector arrays were kept at room temperature (+22 °C). A negative temperature gradient from +22 °C to –162°C was applied along the last detector array. A He/Ar gas mixture (He:Ar = 70:30) was circulated in a gas loop and purified with Hydrosorb™ and Oxysorb™ cartridges and a hot titanium getter. The COMPACT arrays were connected to the RTC and to each other with about 20-cm long PTFE capillaries (2 mm inner diameter). In a preparatory experiment, short-lived Pb and Hg isotopes were produced with ^{144}Sm and ^{142}Nd targets, respectively, and ^{219}Rn was produced as a member of the ^{227}Ac decay chain. Prior to measuring their yields and distributions in COMPACT^3, the rates at which Pb and Hg entered the RTC were measured in a 60x40 mm^2 DSSSD mounted in the RTC position. Transport times and yields to COMPACT^3 were optimized with ^{182,183}Hg, due to much higher production rates compared to Pb isotopes. The use of three detector arrays in series allowed separating species with volatility and reactivity ranging from the non-volatile Pb, over the volatile metal Hg, to the noble gas Rn (Figure 1). Pb was adsorbed under diffusion-controlled deposition in the first COMPACT array. Mercury passed the SiO$_2$ array and deposited in the second array, on the gold surface, under diffusion controlled deposition. Radon adsorption started on the last detector array at very low temperature. The data on Cn and Fl are currently under evaluation.

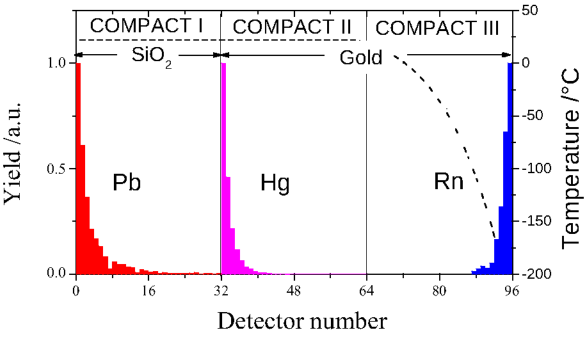

Figure1: Measured Pb, Hg and Rn distributions.

References

[1] R. Eichler et al. Nature **443**, 73-75(2007).
[2] R. Eichler et al. Radiochim. Acta **98**, 133-139(2010).
[3] A. Yakushev et al. Inorg. Chem. **53**, 1624-1629(2014).
[4] D. Wittwer et al. Nucl. Instr. Meth. B **268,** 28-35(2010).

---

* Work supported by the BMBF (project 05P12UMFN6) and the EC FP7 - Capacities ENSAR (No. 262010)

[#] a.yakushev@gsi.de

DOI:10.15120/GR-2015-1-MU-NUSTAR-SHE-C-01

Recoil-α-fission and recoil-α-α-fission chains stemming from element 115

D. Rudolph[1], *U. Forsberg*[1], *Ch.E. Düllmann*[2,3,4], *P. Golubev*[1], *F.P. Heßberger*[2,3], *J. Khuyagbaatar*[2,3], *J.V. Kratz*[4], *L.G. Sarmiento*[1], *A. Yakushev*[2], *D. Ackermann*[2], *L.-L. Andersson*[3], *M. Block*[2], *H. Brand*[2], *D. Cox*[5], *X. Derkx*[3,4], *A. Di Nitto*[4], *K. Eberhardt*[3,4], *J. Even*[3], *C. Fahlander*[1], *J.M. Gates*[6], *J. Gerl*[2], *K.E. Gregorich*[6], *C.J. Gross*[7], *R.-D. Herzberg*[5], *E. Jäger*[2], *B. Kindler*[2], *J. Krier*[2], *I. Kojouharov*[2], *N. Kurz*[2], *B. Lommel*[2], *A. Mistry*[5], *C. Mokry*[3,4], *H. Nitsche*[6], *J.P. Omtvedt*[8], *P. Papadakis*[5], *J. Runke*[2], *K. Rykaczewski*[7], *M. Schädel*[2,9], *H. Schaffner*[2], *B. Schausten*[2], *P. Thörle-Pospiech*[3,4], *T. Torres*[2], *T. Traut*[4], *N. Trautmann*[4], *A. Türler*[10], *A. Ward*[5], *and N. Wiehl*[3,4]

[1]Lund University, Lund, Sweden; [2]GSI Helmholtzzentrum für Schwerionenforschung GmbH, Darmstadt, Germany; [3]Helmholtz Institute Mainz, Mainz, Germany; [4]Johannes Gutenberg-Universität Mainz, Mainz, Germany; [5]University of Liverpool, Liverpool, United Kingdom; [6]Lawrence Berkeley National Laboratory, Berkeley, USA; [7]Oak Ridge National Laboratory, Oak Ridge, USA; [8]University of Oslo, Oslo, Norway; [9]Advanced Science Research Center, Japan Atomic Energy Agency, Tokai, Japan; [10]Paul Scherrer Institute and University of Bern, Villigen, Switzerland

Products of the ^{48}Ca+^{243}Am fusion-evaporation reaction were studied with the TASISpec set-up [1, 2] behind TASCA [3-5]. Thirty correlated α-decay chains originating from different isotopes of E115 were observed [6, 7], produced with an overall production cross section of $\approx$ 10 pb. There are 1+22=23 five-α-long chains linked to the production of ^{287,288}115 [6], in agreement with 2+31=33 chains reported earlier [8]. The combined 22+31=53 chains associated with ^{288}115 yield a statistically solid reference.

Besides these 'long chains', two recoil-α-fission and five recoil-α-α-fission chains are present in the TASISpec data [7]. Interestingly, the interpretation and thus the assignment of these 'short chains' to a certain isotope of E115 turns out to be non-trivial. The issue is discussed with the help of Fig. 1: Panel (a) shows the relevant beginning of the long ^{288}115 reference chain. The average values of the 2+5=7 new short chains in panel (b) are consistent with the numbers in panel (a). This indicates at first sight $\sim$ 5-15% fission or electron-capture branches of ^{284}113 and ^{280}Rg. However, this view is at variance with the *interpretation* of 3+1=4 short chains previously observed at Dubna [8] [panel (c)]. There, one chain, denoted 'D3', is significantly different from all the other E115 chains. However, only including this particular chain in the 3+1=4 averaging procedure generated a seemingly consistent link between E115 and E117 [8, 9] [panel (d)]. Panel (e) provides a refined interpretation of all published E117 data [9, 10]. The rightmost sequence averaged over twelve E117 chains opens for a connection to E115 via 'D3', while the other ten E117 chains would be consistent with (a subset of) other E115 chains [11].

More high-quality spectroscopic data is obviously required. This is necessary to provide the foundation for a relevant nuclear-structure based interpretation of links between decay chains of these two odd-Z elements [7, 11].

The authors thank the ion-source and accelerator staff at GSI. This work is supported by the European Community FP7 – Capacities ENSAR No. 262010, the Royal Physiographic Society in Lund, the Euroball Owners Committee, the Swedish Research Council, the German BMBF, the Office of Nuclear Physics, U.S. Department of Energy, and the UK Science and Technology Facilities Council.

References

[1] L.-L. Andersson *et al.*, Nucl. Instr. Meth. **A622**, 164 (2010).
[2] L.G. Sarmiento *et al.*, Nucl. Instr. Meth. **A667**, 26 (2012).
[3] M. Schädel, Eur. Phys. J. D **45**, 67 (2007).
[4] J.M. Gates *et al.*, Phys. Rev. C **83**, 054618 (2011).
[5] U. Forsberg *et al.*, Acta Phys. Pol. B**43**, 305 (2012).
[6] D. Rudolph *et al.*, Phys. Rev. Lett. **111**, 112502 (2013).
[7] U. Forsberg *et al.*, submitted to Phys. Rev. C.
[8] Yu. Ts. Oganessian *et al.*, Phys. Rev. C **87**, 014302 (2013).
[9] Yu. Ts. Oganessian *et al.*, Phys. Rev. Lett. **104**, 142502 (2010); Phys. Rev. C **87**, 054621 (2013).
[10] J. Khuyagbaatar *et al.*, Phys. Rev. Lett. **112**, 172501 (2014).
[11] D. Rudolph *et al.*, to be published.

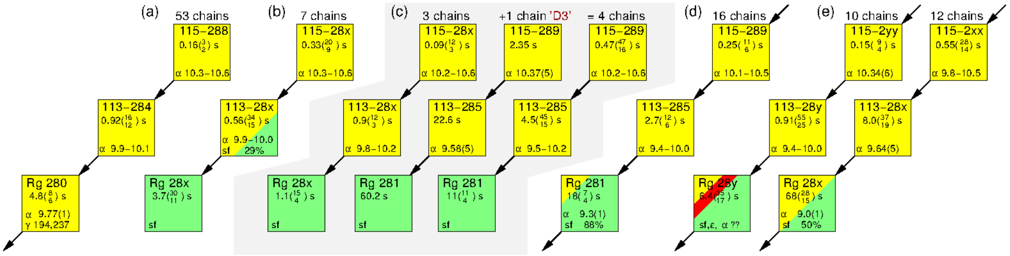

Figure 1: Average values from selections of decay chains of isotopes of E115 to E113 into Rg ($Z = 111$). (a) 53 ^{288}115 reference chains [6, 8]. (b) Seven recoil-α-(α)-fission chains observed with TASISpec [7]. (c) Data from all four recoil-α-α-fission 'Dubna chains' listed in Table III of Ref. [8]. (d) Sixteen chains associated with the decay of ^{293}117, i.e. interpreted to populate the isotope ^{289}115 [9]. (e) Possible re-interpretation [11] of all existing E117 decay data [9, 10].

DOI:10.15120/GR-2015-1-MU-NUSTAR-SHE-C-02

First periodic relativistic calculations of adsorption of the superheavy elements on a quartz surface

V. Pershina
GSI Helmholtzzentrum, Darmstadt, Germany

Gas-phase chromatography experiments provide information about volatility of superheavy elements (SHE) and their homologs as adsorption enthalpies, ΔH_{ads}, on a surface of a chromatography column. Two main types of surfaces are used: gold and quartz. Straightforward theoretical predictions of ΔH_{ads} were made in the past on the basis of cluster calculations for adsorption on metals (e.g., gold [1]), or physisorption models for adsorption on inert surfaces [2]. Periodic codes were until recently not suited for solid state, or adsorption calculations on the SHEs. With further developments of the relativistic quantum theory and computational algorithms, as well as creation of proper basis sets, treatment of those phenomena for $Z \leq 120$ became now possible using the ADF BAND code [3]. Accordingly, we started the 2c-DFT calculations of ΔH_{ads} of Hg, Cn, and Fl on a gold and of Tl and element 113 on a quartz surfaces using this program package. Here, preliminary results for the latter case are presented.

In the presence of oxygen in the chromatography column, element 113 should form 113OH by analogy with TlOH. A quartz surface is very probably fully hydroxylated forming *geminal silanols*, $\equiv Si(OH)_2$, the most stable modification. The M atoms (M = Tl and element 113) may then react with such a surface in the following way

$$\equiv Si(OH)_2 + M\text{-}OH \rightarrow \equiv Si(OH)(OM) + H\text{-}OH, \qquad (1)$$

so that replacement of H of a surface OH group by M can take place. Accordingly, we have optimized a quartz (001) slab cut out of the α-quartz bulk, where the surface O-bonds are saturated with H, i.e., $\equiv Si(OH)_2$. The scalar relativistic (SR) geometry optimization with fully relaxed upper 3 layers of the Si and surrounding O atoms have given the formation energy, E_f, of such a slab as -138.97 kJ/mol. The SR geometry optimization of a slab with Tl or element 113 atoms substituting one H (Fig. 1) have then given E_f of $\equiv Si(OH)(OTl)$ of -137.06 eV and E_f of $\equiv Si(OH)(O113)$ of -137.02 eV. Earlier, we have obtained 4c-DFT D_e(Tl-OH) = 3.68 eV and D_e(113-OH) = 2.42 eV [4]. Taking into account D_e(H-OH) of 4.77 eV, as well as the differences in D_e between H-OH and Tl-OH and between H-OH and 113-OH, the energy balance of reaction (1) was predicted as 1.91 eV for Tl and -0.4 eV kJ/mol for element 113 using the obtained E_f of $\equiv Si(OH)(OM)$ and $\equiv Si(OH)_2$. The single-point SO calculations (i.e., with the SO interaction on top of the SR optimized geometry) have given the reaction (1) energy as 2.32 eV for Tl and -0.47 eV for element 113. These values mean that the reaction will proceed to the right with the formation of the $\equiv Si(OH)(OM)$ complex only for element 113. The Tl-OH bond is obviously too strong in the molecule to be replaced by the $\equiv Si(OH)(O\text{-}Tl)$ one, while the 113-OH one is weak enough, so that the reaction can proceed to the right. Further calculations with the geometry optimization at the SO level and a supercell model treating single adsorbed atoms should be performed to confirm these preliminary conclusions.

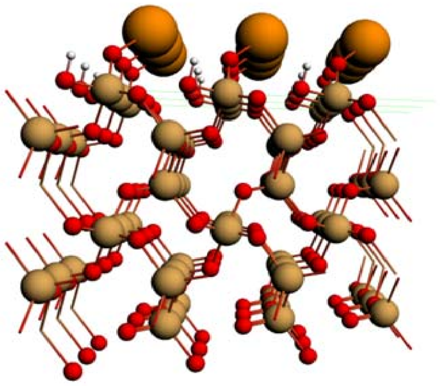

Fig. 1. Atom M (M = Tl and element 113), the largest circles, chemisorbed on the fully hydroxylated quartz surface (side view).

The obtained results are, however, in some contradiction with the measured -ΔH_{ads}(TlOH) of 134 ± 5 kJ/mol on quartz similar to -ΔH_{ads}(TlOH) of 146 ± 3 kJ/mol on gold [5]. Those like values are an indication that the mechanism of adsorption on quartz and gold is obviously the same, caused by long-range interactions. This scenario could be considered in the next study using BAND.

References

[1] V. Pershina, J. Anton, T. Jacob, J. Chem. Phys. **131**, 084713 (2009).

[2] V. Pershina, A. Borschevsky, E. Eliav, U. Kaldor, J. Chem. Phys. **128**, 024707 (2008).

[3] ADF BAND, see http://www.scm.com .

[4] V. Pershina, J. Anton, T. Jacob, Chem. Phys. Lett. **480**, 157 (2009).

[5] A. Serov, *et al.*, Radiochim. Acta **101**, 421 (2013).

DOI:10.15120/GR-2015-1-MU-NUSTAR-SHE-C-03

Synthesis and chemical investigation of Sg(CO)$_6$*

J. Even†[1], A. Yakushev[2], Ch.E. Düllmann[1,2,3], H. Haba[4], M. Asai[5], T.K. Sato[5], H. Brand[2], A. Di Nitto[3], R. Eichler[6,7], F.L. Fan[8], W. Hartmann[2], M. Huang[4], E. Jäger[2], D. Kaji[4], J. Kanaya[4], Y. Kaneya[5], J. Khuyagbaatar[1], B. Kindler[2], J.V. Kratz[3], J. Krier[2], Y. Kudou[4], N. Kurz[2], B. Lommel[2], S. Miyashita[5,9], K. Morimoto[4], K. Morita[4,10], M. Murakami[4,11], Y. Nagame[5], H. Nitsche[12,13], K. Ooe[11], Z. Qin[8], M. Schädel[5], J. Steiner[2], T. Sumita[4], M. Takeyama[4], K. Tanaka[4], A. Toyoshima[5], K. Tsukada[5], A. Türler[6,7], I. Usoltsev[6,7], Y. Wakabayashi[4], Y. Wang[8], N. Wiehl[1,3], and S. Yamaki[4,14]

[1]Helmholtz-Institut Mainz, Mainz, Germany; [2]GSI, Darmstadt, Germany; [3]Johannes Gutenberg-Universität, Mainz, Germany; [4]Nishina Center for Accelerator-Based Science, RIKEN, Wako, Japan; [5]Advanced Science Research Center, JAEA, Tokai, Japan; [6]University of Berne, Switzerland.; [7]PSI, Villigen, Switzerland; [8]Institute of Modern Physics, Lanzhou, Chinese Academy of Sciences, China; [9]Hiroshima University, Japan; [10]Kyushu University, Japan; [11]Niigata University, Japan; [12]University of California, Berkeley, CA, U.S.A.; [13]Lawrence Berkeley National Laboratory, Berkeley, CA, U.S.A; [14]Saitama University, Japan

Gas phase chemical studies of the superheavy elements have been limited to simple inorganic compounds so far [1]. Due to challenging experimental conditions, access to other compound classes was limited. With the combination of physical preseparation and gas-phase chemistry, many limitations could be overcome [2,3]. We succeeded in the synthesis of a carbonyl complex of a superheavy element - seaborgium hexacarbonyl (Sg(CO)$_6$), at the GAs-filled Recoil Ion Separator GARIS [4]. Sg(CO)$_6$ has been predicted to be stable [5] and its adsorption behavior on a SiO$_2$ surface is expected to be very similar to that of W(CO)$_6$ [6]. Thus, we investigated Sg(CO)$_6$ along with W(CO)$_6$. 6-s ^{164}W, and $\approx$ 10-s ^{265}Sg were synthesized in the reactions ^{144}Sm(^{24}Mg,4n)^{164}W and ^{248}Cm(^{22}Ne,5n)^{265}Sg. Evaporation residues (EVRs) were separated from the primary beam and lighter transfer products within GARIS. At the focal plane of GARIS, a recoil transfer chamber (RTC) was installed. The EVRs passed the entrance window of the RTC and were thermalized in a He / CO atmosphere ($\approx$ 600 mbar) in the RTC. The free single ions of W and Sg reacted with CO, forming volatile complexes [7]. The RTC was flushed continuously, transporting volatile compounds through a 10-m long capillary to the Cryo Online Multidetector for Physics and Chemistry of the Transactinides COMPACT [8], a thermochromatography detector array. The chromatography channel is formed by 32 pairs of silicon PIN diodes covered with a SiO$_2$ surface, kept at temperatures between 22°C and -140°C. Volatile compounds adsorb at a certain temperature on the detector surface. The deposition pattern was compared with Monte Carlo Simulations MCS, which allowed determining the adsorption enthalpy $-\Delta H_{ads}$. W and Sg were transported to COMPACT, hence formed volatile compounds with the CO [7]. In total, 15 decay chains assigned to the decay of ^{265}Sg plus three uncorrelated fission event assigned to the decay of ^{261}Rf as a daughter of ^{265}Sg were observed under background-free conditions. The total beam integral was $1.52 \cdot 10^{19}$. Both, the W and the Sg complexes deposited mainly in the last third of the detector (see Fig. 1). The Sg species show the same adsorption behavior as W(CO)$_6$, which supports the assignment to Sg(CO)$_6$ [7]. The experimental distributions and the MCS are shown in Fig. 1.

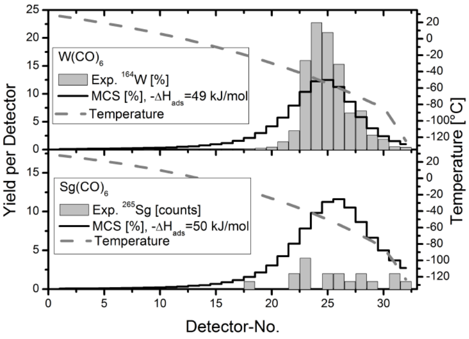

Figure 1: Distribution of ^{164}W and ^{265}Sg in the COMPACT detector array. The bars show the experimental distributions, the solid lines show the results from MCS. (after [7]).

References

[1] A. Türler, V. Pershina, Chem. Rev. 113, 1237 (2013).

[2] Ch.E. Düllmann, Nucl. Instr. Meth. A 551, 528 (2005).

[3] J. Even et al., Inorg. Chem. 51, 6431 (2012).

[4] K. Morita et al., Nucl. Instr. Meth. B 70, 220 (1992).

[5] C.S. Nash, B.E. Bursten, J. Am. Chem. Soc. 121, 10830 (1999).

[6] V. Pershina, J. Anton, J. Chem. Phys. 138, 174301–6 (2013).

[7] J. Even et al., Science 345, 1491 (2014).

[8] A. Yakushev et al., Inorg Chem., 53, 1624 (2014).

---

[*] Work supported by HI Mainz, the German Ministry of Research and Education BMBF contract-No. 06MZ7164,the Reimei Research Program (Japan Atomic Energy Agency), the Swiss National Science Foundation, and the U.S. Department of Energy, Office of Science, Chemical Sciences, Geosciences, & Biosciences (CSGB), Division, Heavy Element Chemistry program. This work was performed at the RI Beam Factory operated by RIKEN Nishina Center and CNS, University of Tokyo. We thank the ion source and accelerator staff for providing intense and stable ion beams.

[†] jeven@triumf.ca, present adress: TRIUMF, Vancouver, Canada

DOI:10.15120/GR-2015-1-MU-NUSTAR-SHE-C-04

Online chemical study of Pb, Hg and Tl on SiO_2 and Au surfaces at TASCA

L. Lens[1], *J. Ballof*[1], *A. Yakushev*[2], *Ch.E. Düllmann*[1,2,3], *H. Brand*[2], *X. Derkx*[1], *A. Di Nitto*[1], *J. Even*[3], *W. Hartmann*[2], *F.P. Heßberger*[2,3] *A. Hübner*[2], *E. Jäger*[2], *J. Khuyagbaatar*[2,3], *B. Kindler*[2], *J.V. Kratz*[1], *J. Krier*[2], *N. Kurz*[2], *B. Lommel*[2], *C. Mokry*[1], *J. Runke*[2], *P. Scharrer*[3], *B. Schausten*[2], *J. Steiner*[2], *P. Thörle-Pospiech*[1,3], *M. Wegrzecki*[4], *N. Wiehl*[1,3], *V. Yakusheva*[3]

[1]Univ. Mainz, Germany; [2]GSI, Darmstadt, Germany; [3]Helmholtz Institut Mainz, Germany; [4]ITE, Warsaw, Poland

Experiments on the interaction of lead (Pb), mercury (Hg), and thallium (Tl) with SiO_2 and Au surfaces were conducted at the gas-filled separator TASCA as preparatory experiments for future studies of the chemistry of element 113 and Fl (flerovium, Z=114).

A first experiment, with Hg focused on the minimization of the transport time for short-lived radionuclides to the gas chromatography setup COMPACT [1]. This is crucial for successful experiments with superheavy elements, due to their low production rates and short half-lives. The complete fusion reaction (188 MeV) ^{40}Ar+^{144}Sm (415 µg/cm^2, ^{144}Sm as SmF_3) was applied to produce Hg, using short (1 s) beam pulses, repeated every 60 s. Hg was separated from unwanted reaction products by the magnetic recoil separator TASCA. In the TASCA focal plane, Hg penetrated a thin Mylar^R window and entered the Recoil Transfer Chamber (RTC) [2], which was connected to the gas transport system and constantly flushed by a He/Ar (70/30) mixture with a flow rate between 0.7-0.85 l/min. A 4 m Teflon capillary (1 mm inner diameter) connected the RTC (volume: 140x40x20 mm^3)) to COMPACT, which was kept at room temperature. The thin capillary led to a reduced pressure in COMPACT, beneficial for getting good energy resolution. The surface of the detector array was covered with a thin gold layer. The carrier gas, purified by Hydrosorb^{TM} and Oxisorb^{TM} cartridges, was circulated in a loop. A mean transport time of 3.6 ± 0.3 s was determined. To reduce this, a Teflon insert inside the RTC (RTC dimensions: 70x40x20 mm^3) was installed and the capillary between RTC and COMPACT was changed to a 20 cm capillary (inner diameter: 1 mm), so the gas flow rate could be increased to 1.7 l/min. Due to these changes, the mean transport time was reduced to 1.5 ± 0.5 s. To avoid losses of reaction products in the RTC, denser carrier gas (e.g., Ar instead of He/Ar) could now be used.

In a second experiment, the adsorption behavior on SiO_2 and Au surfaces of the rather reactive metal Pb was directly compared to that of the less reactive metal Hg, as well as to that of Tl, which is a chemical homolog of element 113. For this, two COMPACT arrays, both kept at room temperature, were connected in series (COMPACT^2). The detectors of the first one were covered with a SiO_2 layer and those of the second one by Au. Previous work showed that Pb should be retained on SiO_2 at temperatures below 600 °C, while Hg can be adsorbed at room temperature on Au, but not on SiO_2 [3-6]. The reactions of 300.8 MeV ^{50}Ti with ^{140}Ce, ^{141}Pr, and ^{142}Nd (400µg/cm^2, present as trifluorides) were used to produce $^{182-184}$Hg, ^{184,185}Tl, and ^{185,186}Pb. Mercury was detected in COMPACT by irradiations of all three targets, produced as a fusion product from different de-excitation channels, or as decay product after α or EC/β^+-decays from Pb or Tl, respectively. Pure Ar was used as carrier gas, which allowed reduction of the RTC depth, but negatively affected the energy resolution. Additionally to Hydrosorb^{TM} and Oxisorb^{TM} cartridges, a hot Ti getter was installed for further reduction of the O_2, H_2O content. As shown in Fig. 1 (upper panel), the separation of Pb and Hg based on their different reactivity towards SiO_2 was achieved.

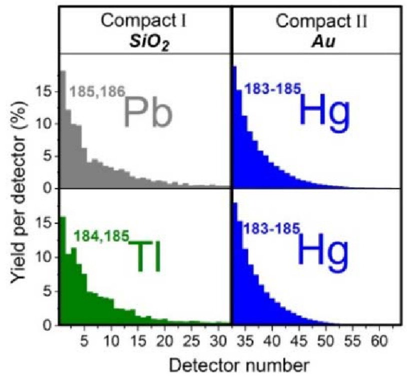

Figure 1: Pb, Tl and Hg distributions in COMPACT^2

Pb was retained under diffusion-controlled deposition in the first COMPACT array, whereas Hg passed this and deposited on the Au surface. The obtained results agree with theoretical predictions [3,7] and helped optimizing the experimental setup for an upcoming Fl experiment. This improved setup allows to directly compare the chemical behavior of Fl, Pb, Hg, Cn and Rn.

For the first time, Tl was investigated in the online regime. Short-lived Tl radioisotopes were pre-separated with TASCA, thermalized in the RTC and carried by Ar gas further to COMPACT, cf. Fig. 1 (lower panel). They adsorbed on the SiO_2 coated detector array, which agrees with offline studies on SiO_2 and Au surfaces [8]. Produced Hg isotopes were detected on the Au surface of the second COMPACT array.

References

[1] J. Dvorak *et al.*, Phys. Rev. Lett. 97, 242501 (2006)
[2] J. Even *et al.*, NIM A 638, 157-164 (2011)
[3] V. Pershina *et. al.,* J. Chem. Phys. 128 024707 (2008)
[4] S. Soverna *et. al.*, Radiochim. Acta 93 (2005) 1
[5] W. Fan, H. Gäggeler, Radiochim Acta 31, 95-97 (1982)
[6] A. Serov, In Proceedings of the 7th International Conference on Nuclear and Radiochemistry (2008)
[7] V. Pershina, Radiochim. Acta 99, 459-476 (2011)
[8] A. Serov *et al.*, Radiochim Acta 101, 421-425 (2013)

DOI:10.15120/GR-2015-1-MU-NUSTAR-SHE-C-05

ALBEGA: A decay spectroscopy setup for chemically separated samples *

A. Di Nitto †1*, A. Yakushev*2*, Ch.E. Düllmann*1,2,3*, J. Khuyagbaatar*2,3*, J. Krier*2*, J. Ballof*1*, J. Bar*7*, T. Budzyński*7*, D.M. Cox*4*, X. Derkx*1,3*, J. Dormand*4*, J.D. Despotopulos*5*, K. Eberhardt*1,3*, J. Even*3*, P. Grabiec*7*, L. Harkness-Brennan*4*, R.D. Herzberg*4*, A. Huebner*2*, E. Jäger*2*, D. Judson*4*, B. Kindler*2*, H. Kłos*7*, J.V. Kratz*1*, J. Kulawik*7*, N. Kurz*2*, L. Lens*1*, B. Lommel*2*, K. Moody*5*, Ch. Mokry*1*, A. Panas*7*, P. Prokaryn*7*, D. Rudolph*6*, J. Runke*2*, I. Rusanov*2*, P. Scharrer*1*, B. Schausten*2*, D. Shaughnessy*5*, D. Szmigiel*7*, A.J. Ward*5*, and M. Wegrzecki*7

1Mainz University, Germany; 2GSI Darmstadt, Germany; 3HIM Mainz, Germany; 4Liverpool University, UK; 5LLNL, Livermore, USA; 6Lund University, Sweden; 7ITE Warsaw, Poland

There are many on-going programmes dedicated to elucidate the nuclear structure of SuperHeavy Elements (SHE atomic number $Z \geq 104$) based on different methods [1]. The SHE are accessed in heavy-ion induced fusion-evaporation reactions, with the nuclear spectroscopy experiments typically performed at in-flight recoil separators.

An alternative approach exploits a chemical isolation system either directly or after separator [2], this was adopted in different experiments [3-5]. A significant improvement of the background conditions was observed applying this method.

A next generation setup for measurements of ALpha-BEta-GAmma decays (ALBEGA) after chemical isolation was recently built. ALBEGA is dedicated to simultaneous measurements of α particles, electrons, photons and fission fragments. Volatile chemical species adsorb on a cooled segmented Si detector. Radiation emitted in the decay is measured with surrounding detectors, cf. Fig.1. The core is a "sandwich" of two segmented Si detectors with a gas channel inside, sensitive to charged particles ("α detector"). A round channel is etched in both wafers, glued together to form a tight channel. At both sides and parallel to the α detector two thicker, segmented Si detectors are mounted (cf. Ref. [6]). The Si detectors are backed by two 3-cm-thick broad energy Ge detectors for X and γ rays. All the detectors were assembled in a packed configuration to maximize the geometrical efficiency.

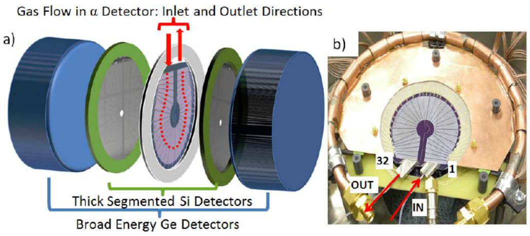

Figure 1: A schematic of ALBEGA, where the arrows indicate the gas flow inside the tight channel (a). A picture of the α detector mounted on the cooling support and connected to the capillaries for gas flushing.

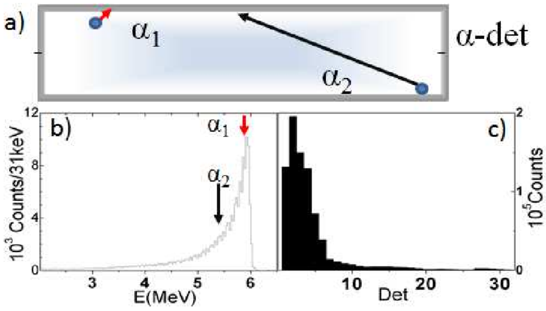

Figure 2: The α particles are emitted isotropically at various angles in the narrow channel (a). Depending on their incident angle, they pass through different effective thicknesses of detector dead layer and gas, thus undergoing energy loss to a different degree, before entering the active detector area. Accordingly, α peaks show characteristic low-energy tailing, e.g. the ^{140}Ce(^{50}Ti, 6-7n) reaction energy spectrum (b). The measured energies corresponding to the two particles α_1 and α_2 are indicated, they have the same initial energy but different path. The distribution pattern observed in the experiment (c) is due to the Hg retention on the inner channel Au coating, and the maximum is observed on the segments at the channel entrance.

The setup was first tested and calibrated with α particles and γ rays produced by decay chains of ^{219}Rn emanated from an ^{227}Ac source. Then the ^{140}Ce(^{50}Ti, 6-7n) reaction was used to produce ^{184,183}Hg, which was preseparated in TASCA [3] and then transported to ALBEGA with rapidly flowing of Ar gas. The energy spectrum and the distribution pattern measured are shown in Fig. 2.

References

[1] M. Leino and F.-P. Hessberger, Ann. Rev. Nucl. Part. Sci. 54, 175 (2004).

[2] Ch.E. Düllmann et al., Nucl. Instrum. Met. A551, 528 (2005).

[3] A. Yakushev et al., Inorg. Chem. 53, 1624-1629 (2014).

[4] J. Dvorak et al., Phys. Rev. Lett. 97, 242501 (2006).

[5] J. Even et al., J. Radioanal. Nucl. Chem. 303, 2457 (2015).

[6] M. Wegrzecki et al., SPIE Proc. 9291 (2014).

---

[*] We thank the ion-source and accelerator staff at GSI. Work supported by BMBF contract-No. 06MZ7164. The development of α-detector was funded by the NCBiR (Poland) under the PBS1/A9/8/2012 Project: SiDET (ID 179409).

[†] a.dinitto@gsi.de

DOI:10.15120/GR-2015-1-MU-NUSTAR-SHE-C-06

Groundstate properties of the unbound $T_z = 5/2$ nucleus ^{15}Ne *

F. Wamers[1,2,3], *J. Marganiec*[2,1,3], *T. Aumann*[2,1], *L. Chulkov*[4,1], *M. Heil*[1], *B. Jonson*[5], *T. Nilsson*[5], *R. Plag*[1], *H. Simon*[1], *and the R^3B Collaboration*

[1]GSI, Darmstadt; [2]Technische Universität, Darmstadt; [3]EMMI @ GSI, Darmstadt; [4]NRC Kurchatov Institute, Moscow; [5]Chalmers Tekniska Högskola, Göteborg

In this report we present our findings on the properties of the recently observed ^{15}Ne [1], with a focus on its groundstate structure and the decay mechanism to ^{13}O.

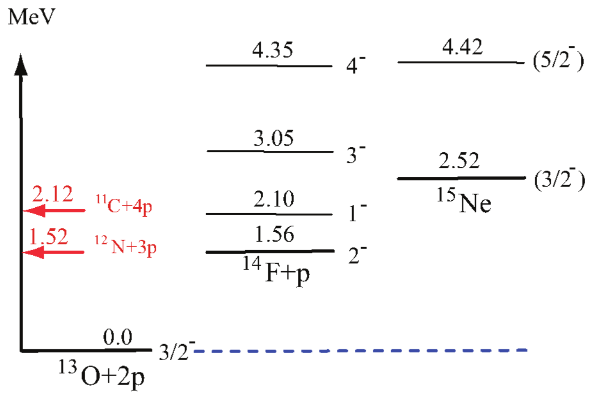

Fig. 1: Level scheme of ^{15}Ne and neighbours along its decay path to ^{13}O [2]. Decay via ^{14}F is energetically possible.

Fig. 1 shows a level scheme of the unbound ^{15}Ne, the also unbound ^{14}F, and the finally bound ^{13}O [2]. In order to cast light on the decay mechanism of the ground state of ^{15}Ne – be it a *diproton*, a *three-body*, or a *sequential* decay via a state in the unbound ^{14}F – we studied its 3-body energy correlations and compared them to those in ^{16}Ne, which is known to decay in a *three-body* way [3, 4, 5].

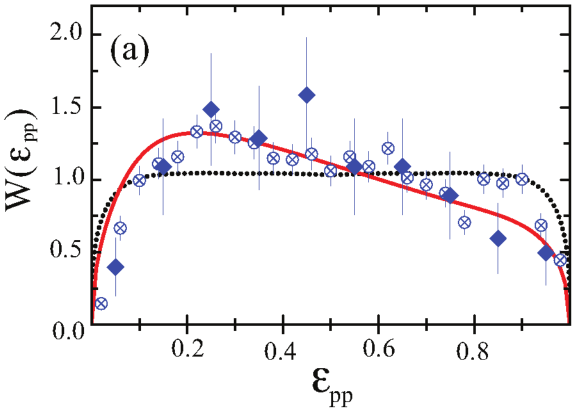

Fig. 2: Fractional relative energy (E_{pp}/E_{fpp}) distributions in the ground states of ^{15,16}Ne [2, 5]. See text for details.

Fig. 2 shows the (E_{pp}/E_{fpp}) fractional relative energy of the ground states of ^{15}Ne (filled diamonds), of ^{16}Ne (open diamonds) and a *three-body* decay calculation for ^{16}Ne [5] (full red line), and a calculation for *sequential* decay of ^{15}Ne via the ^{14}F ground state (black dashed line). The striking similarity to the pattern for ^{16}Ne, combined with the discrepancy to the *sequential*-decay shape, leads us to conclude that, like in ^{16}Ne, also the ^{15}Ne ground state undergoes *three-body* decay.

Furthermore, we used the measured two-proton separation energy of ^{15}Ne of 2.522(66) MeV, translated into an atomic mass excess of 40.215(69) MeV, to deduce the $(1s_{1/2})^2$ occupation probability of its unbound valence-proton pair in the ground state. We followed the approach of Fortune [6] shown in Fig. 3, using a correlation between the $(1s_{1/2})^2$ value for valence-nucleon pairs in $Z = 8, 10$ mirror nuclei and their 2n-2p separation-energy difference in order to predict the ^{15}Ne ground-state energy. Using our measured value of S_{2p} = 2.522(66) MeV, we have turned the relation around to predict an $(1s_{1/2})^2$ content for the ^{15}Ne ground state of 63(5) % (red square in Fig. 3).

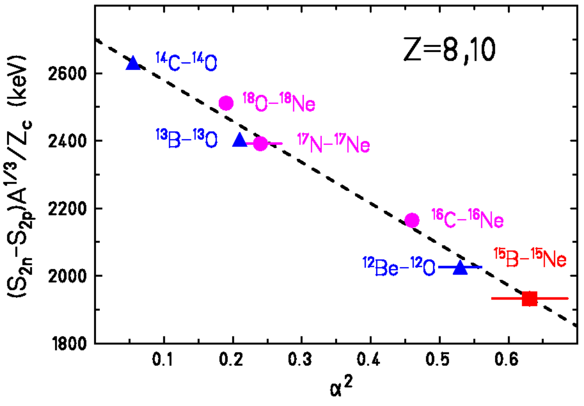

Fig. 3: Relation of ΔS_{2N} to $P((1s_{1/2})^2)$ in $Z = 8, 10$ mirror-nucleus pairs (based on [6]). See text for details.

References

[1] F. Wamers et al., GSI Report 2014-1, 136 p. (2014)
[2] F. Wamers et al., Phys. Rev. Lett. **112**, 132502 (2014)
[3] J. Marganiec et al., Eur. Phys. J. A **51**: 9 (2015)
[4] I. Mukha et al., Phys. Rev. C **77**, 061303 (R) (2008)
[5] L.V. Grigorenko et al., Phys. Rev. Lett. **88**, 042502 (2002)
[6] H.T. Fortune, Phys. Lett. B **718**, 1342 (2013)

---

* Work supported by EMMI, HIC for FAIR, the GSI-TU Darmstadt cooperation, BMBF, and NAVI. (B. J.) is a Helmholtz International Fellow.

DOI:10.15120/GR-2015-1-MU-NUSTAR-NR-01

Spin assignment of the 7.57 MeV state in the unbound nucleus ^{16}Ne*

J. Marganiec[1,2,3], *F. Wamers*[1,2,3], *T. Aumann*[1,3], *L.V. Chulkov*[1,4], *B. Jonson*[5], *T. Nilsson*[5], *H. Simon*[3], *and the R^{3}B collaboration*
[1]TU Darmstadt, Germany; [2]EMMI, GSI Darmstadt, Germany; [3]GSI Darmstadt, Germany; [4]NRC Kurchatov Institute, Moscow, Russia; [5]Chalmers Tekniska Högskola, Göteborg, Sweden

Two-proton decay of the unbound nucleus ^{16}Ne, produced in one-neutron knock-out from a 500 MeV/u ^{17}Ne beam, has been studied at GSI. The beam was directed towards carbon (370 mg/cm^2) or polyethylene (213 mg/cm^2) targets. The reaction products were identified by means of position, energy loss, and Time-of-Flight measurements, using the R^{3}B-LAND setup. Coincidences between ^{14}O and two protons provided the momentum four vectors, which were transformed into the projectile rest-mass frame, where two different sets of non-relativistic Jacobi coordinates (T- and Y-system) were used in the analysis [1].

The internal kinetic energy (the relative energy) E_{fpp} in the three-body system ^{14}O+p+p (see Fig. 1), and the fractional energies in the fragment-proton (ϵ_{fp}) and the proton-proton (ϵ_{pp}) subsystems were reconstructed. The correlation functions normalized to unity, for the fractional-energy distributions $W(\epsilon_{fp})$ and $W(\epsilon_{pp})$ and the angular distributions $W(\cos\theta_{fp})$ and $W(\cos\theta_{pp})$, were constructed and analyzed. The required efficiency and acceptance corrections have been estimated using the Monte Carlo simulations (see Ref. [2] for details).

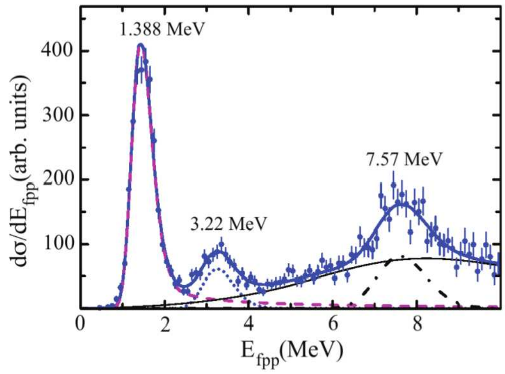

Figure 1: ^{14}O+p+p relative energy spectrum.

Correlations between the decay products from the excited state at the resonance energy 7.57(6) MeV are shown in Fig. 2. The two peaks visible in $W(\epsilon_{fp})$ and $W(\cos\theta_{pp})$ have been associated with transition to the state at $E_{rel} = 2.8$ MeV in ^{15}F. The results of the calculations for the assumed initial spin value $I^\pi = 2^+$ and channel spin $j = 5/2$ are shown in Fig. 2 as dashed lines. The physical background contributions are shown in Fig. 2 as dotted lines. The sum of these two contributions (solid lines) perfectly reproduces the experimental data (see Ref. [2] for details).

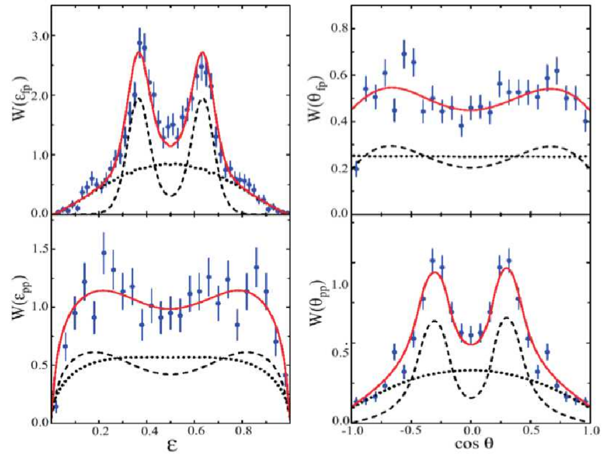

Figure 2: Three-body correlations between the decay products of the $E_{rel} = 7.57$ MeV.

In this case, the initial 2^+ state emits a proton from the $d_{5/2}$ shell feeding the ^{14}O+p in a $d_{5/2}$ shell configuration in ^{15}F. This 2^+ state is unstable and emits two protons. Its width is surprisingly narrow. This suggests that its structure can be more complicated than a ^{14}O+p+p state. This state is also situated above the four proton emission threshold, what indicates a possible many-body structure. And the ^{12}C+4p configuration with four protons in the (sd) shell, could be the cause of such a narrow width of this state [3]. A special case of such a structure could consist of an excited core together with two protons, ^{14}O(2^+)+2p [4]. The theoretical predictions for the position of the second 2^+ state in ^{16}Ne are $E^* = 4.2$ MeV [5] or $E^* = 3.6$ MeV [6], both close to the known position of the second 2^+ state in the mirror nucleus ^{16}C [7]. From this mirror nucleus (the third 2^+ state of ^{16}C is at $E^* = 6.11$ MeV [8]), the investigated state is assumed to be the third 2^+ state in ^{16}Ne.

References

[1] L.V. Grigorenko *et al.*, Phys. Lett. **B 677**, 30 (2009)
[2] J. Marganiec *et al.*, Eur. Phys. J. **A 51**:9 (2015)
[3] H.T. Fortune, R. Sherr, Phys. Rev. **C 87**, 057308 (2013)
[4] I. Mukha *et al.*, Phys. Rev. **C 82**, 054315 (2010)
[5] N.K. Timofeyuk, P. Descouvemont, Phys. Rev. **C 81**, 051301 (2010)
[6] H.T. Fortune, R. Sherr, Phys. Rev. **C 82**, 027310 (2010)
[7] M. Petri *et al.*, Phys. Rev. **C 86**, 044329 (2012)
[8] Y. Satou *et al.*, Phys. Lett. **B 728**, 462 (2014)

---

* Work supported by NAVI, GSI-TU Darmstadt cooperation, HIC for FAIR, EMMI and BMBF. (B.J.) is a Helmholtz International Fellow.

DOI:10.15120/GR-2015-1-MU-NUSTAR-NR-02

Thomas-Ehrman shifts

T. Aumann[1,2], *L.V. Chulkov*[1,3], *B. Jonson*[4], *J. Marganiec*[1,2], *T. Nilsson*[4], *H. Simon*[1], *F. Wamers*[1,2], *and the* R^3B *Collaboration*

[1]Technische Universität, Darmstadt; [2]GSI, Darmstadt; [3]NRC Kurchatov Institute, Moscow; [4]Chalmers Tekniska Högskola, Göteborg

The Thomas-Ehrman shift (TES) is a very important characteristic of the mirror asymmetries related to the structure of nuclei with weakly-bound protons. The TES is especially large when the participating states are unbound against proton emission and when the occupation of the s-shell is large. This is demonstrated in Table 1, where TES for neon isotopes with core+2p structure and their respective mirror nuclei are given. TES is defined as the difference between the excitation energy differences between mirror states with spins I_1 and I_2:

$$\mathrm{TES}(I_1, I_2) = [\mathrm{E}(I_1) - \mathrm{E}(I_2)]_\mathrm{p} - [\mathrm{E}(I_1) - \mathrm{E}(I_2)]_\mathrm{n}. \quad (1)$$

Table 1: Thomas-Ehrman shifts for neon isotopes with core+2p structure and their mirror nuclei. S_{2p} is the two-proton separation energy and $P(s^2)$ the amount of s^2 in the wave function [1, 2]. Uncertainties smaller than 1 keV are not indicated.

Isotope	S_{2p} (MeV)	$P(s^2)$	Mirror	TES (MeV)
^{18}Ne 2^+; 0^+	4.523	19%	^{18}O	-0.095
^{17}Ne $3/2^-$; $1/2^-$	0.973(27)	24%	^{17}N	-0.086(8)
^{16}Ne 2^+; 0^+	-1.388(15)	46%	^{16}C	0.070(46)
^{15}Ne $5/2^-$; $3/2^-$	-2.552(66)	63%	^{15}B	0.573(78)

Attempts to describe the TES for the nuclei ^{17}Ne and ^{16}Ne were made in Refs. [3, 4] within a three-body model, with inert core plus two protons. The conclusion given in Ref. [3] was: *"The computed three-body Thomas-Ehrman shifts are then meaningful although relatively inaccurate"*.

The progress in the spectroscopy of exotic nuclei has given access to isospin multiplets in their ground and excited states. Investigation of isospin symmetry in the isobaric analog states and the properties of the Isobaric Multiplet Mass Equation (IMME) was recently made in Refs. [5, 6]. We have made an IMME analysis using the known masses and excited states of the $A = 16$ quintet. Table 2 gives the result of a least-square fit to the masses of the 0^+ and 2^+ states for $T = 2$ isobaric $A = 16$ multiplet.

Usually the Thomas-Ehrman shift is given as the difference in energies of excited states in mirror nuclei. Here we propose a broader understanding of the TES by analysing the dependence of the positions of excited states on the isospin projection. With the IMME coefficients we may calculate TES for members of the $T = 2$, $A = 16$ multiplet and deduce the energies of the unknown excited 0^+ and 2^+ states in ^{16}F (Fig. 1). We thus predict the 0^+ state at $E^* = 10.087(10)$ MeV and the 2^+ state at $E^* = 11.908(14)$ MeV, which is in good agreement with the estimate made by Fortune [7].

Table 2: Coefficients in the Isobaric Multiplet Mass Equation obtained from a fit to experimental data.

State	a (keV)	b (keV)	c (keV)	$\chi^2_{min}/1$
0^+	17982(3)	-2572(4)	213(2)	3.29
2^+	19771(8)	-2598(10)	220(4)	3.68

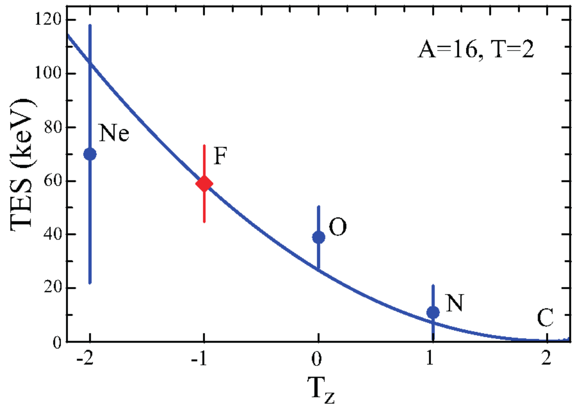

Figure 1: Thomas-Ehrman shift between 2^+ and 0^+ states for members of the isobaric quintet ($A = 16, T = 2$) as a function of the isospin projection.

References

[1] H.T. Fortune, Phys. Lett. B **718**, 1342 (2013).

[2] F. Wamers *et al.*, Phys. Rev. Lett. **112**, 132502 (2014).

[3] E. Garrido *et al.*, Phys. Rev. C **69**, 024002 (2004).

[4] L.V. Grigorenko *et al.*, arXiv:1411.1846[nucl-th], 2014.

[5] M. MacCormik, G. Audi, Nucl. Phys. A **925**, 61 (2014); Erratum Nucl. Phys. A **925**, 296 (2014).

[6] Y.H. Lam *et al.*, At. Nucl. Data Tables **99**, 680 (2013).

[7] H.T. Fortune, Phys. Rev. C **74**, 054310 (2006).

DOI:10.15120/GR-2015-1-MU-NUSTAR-NR-03

Quasi-free scattering from relativistic neutron-deficient carbon isotopes*

M. Holl[1] *and the R*^{3}*B Collaboration*

[1]Institut für Kernphysik, Technische Universität Darmstadt, Germany

The R^{3}B-collaboration conducted an experiment studying quasi-free scattering from light nuclei in a wide A/Z range in August 2010 [1]. Among others, the neutron-deficient carbon isotope ^{11}C was investigated. The study was aimed at determining single-particle properties of nuclei with a focus on a quantitative understanding of absolute spectroscopic factors for which a strong quenching for deeply bound nucleons has been shown in single-nucleon knockout reactions [2].

In this experiment, a ^{40}Ar primary beam was incident on a production target, and the reaction residues of interest were selected and transported to the R^{3}B-LAND setup in Cave C using the fragment separator FRS. The incoming beam was identified using the time-of-flight between two scintillators, one at focus S8 of the FRS and one at the entrance of Cave C, and the energy loss in a PIN diode. The incoming angle of the beam was determined from the position on two silicon strip detectors in front of the target.

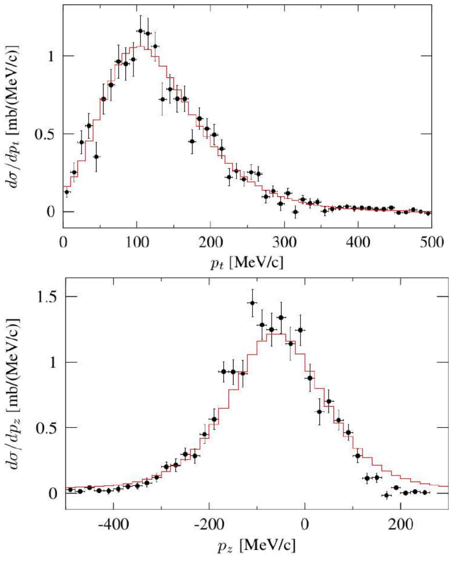

Figure 1: Transversal and longitudinal momentum of ^{10}B fragments measured in coincidence with two protons in the Crystal Ball NaI array. The experimental distributions are compared to results of DWIA calculations [3].

The target area was surrounded by the Crystal Ball NaI-array used for γ and proton detection and a box consisting of four silicon strip detectors. After passing through the ALADIN magnet, the charge, mass, and total momentum of the outgoing fragments were reconstructed using the position and energy information given by two additional silicon strip detectors, two fiber detectors, and a time-of-flight wall.

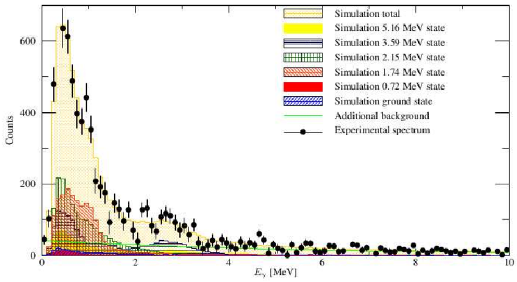

Figure 2: Gamma energy spectrum measured in coincidence with the ^{11}C(p,2p)^{10}B reaction.

Measurements were done using a CH$_2$ target, and background measurements using a carbon target were used to obtain the cross section on hydrogen. The resulting cross section is $\sigma = 17.3(8)$ mb which corresponds to a spectroscopic factor of $C^2S = 2.16(10)$.

In Fig. 1 the transversal and longitudinal momentum distributions of ^{10}B nuclei measured in coincidence with two protons in the Crystal Ball NaI-array are shown. They are compared to results of DWIA calculations [3] which were made under the assumption of a knockout from the $p_{3/2}$-shell and show good agreement.

Figure 2 shows the γ-energy spectrum measured in coincidence with the ^{11}C(p,2p)^{10}B reaction. The population of excited states was determined by fitting simulated responses to single excited states obtained using the R3BRoot framework [4] to the experimental spectrum. It is clear that the overall population of excited states is high ($\approx 50\%$). A strong population of the low-lying excited states is observed, indicating a strong contribution of particle-hole states to the ground state of ^{11}C. This is also in agreement with the observation of large cross sections for the population of low-lying unbound states.

References

[1] T. Aumann et al., 'Direct Reactions of light exotic beams measured in complete kinematics at R3B', GSI Scientific Report 2010, p.166,

[2] A. Gade et al., Phys. Rev. C 77(4) 044306 (2008)

[3] T. Aumann, C. A. Bertulani, and J. Ryckebusch, Phys. Rev. C 88 064610 (2013).

[4] D. Bertini, J. Phys. Conf. Ser., 331 0322036 (2011).

---

* Supported by the State of Hesse (LOEWE Centre HIC for FAIR), and through the GSI-TU Darmstadt cooperation agreement.

DOI:10.15120/GR-2015-1-MU-NUSTAR-NR-04

Multiplicity of light-charged particles investigated with proton-induced fission of ^{208}Pb at different kinetic energies

J.L. Rodríguez-Sánchez[1], *J. Benlliure*[1], *C. Paradela*[1], *H. Álvarez-Pol*[1], *L. Audouin*[2], *Y. Ayyad*[1], *G. Bélier*[3], *G. Boutoux*[3], *E. Casarejos*[4], *A. Chatillon*[3], *D. Cortina-Gil*[1], *T. Gorbinet*[3], *A. Heinz*[5], *A. Kelić-Heil*[6], *N. Kurz*[6], *B. Laurent*[3], *J.-F. Martin*[3], *E. Pellereau*[3], *B. Pietras*[1], *D. Ramos*[1], *C. Rodríguez-Tajes*[7], *D. Rossi*[6], *H. Simon*[6], *J. Taïeb*[3], *J. Vargas*[1], *and B. Voss*[6]

[1]University of Santiago de Compostela, Spain; [2]IPN Orsay, Orsay, France; [3]CEA DAM, Arpajon, France; [4]University of Vigo, Spain; [5]University of Chalmers, Sweden; [6]GSI, Darmstadt, Germany; [7]GANIL, Caen, France

Spallation reactions produce large quantities of light-charged particles (hydrogen and helium isotopes) which are a concern in spallation target design. For instance, the production of tritium is a concern for radioprotection, especially in the case of liquid targets from which it can escape easily. Therefore, a reliable prediction of the light-charged particle yields by high-energy transport codes [1] becomes important for the design of spallation targets. Furthermore, light-charged particle emission has been well established as a sensitive tool in probing the dynamics of heavy-ion-induced nuclear reactions and it could help to investigate some fundamental questions about fission such as the dissipative and transient effects in the last stages of the fission process [2].

In the present work, we report on the first results of a new generation of accurate measurements on multiplicities of light-charged particles in spallation reaction of ^{208}Pb at different relativistic energies: $370A$, $500A$ and $650A$ MeV. The experiment takes advantage of the inverse kinematics technique, in which fission fragments and light particles are emitted in forward direction. Time coincidence with the fission fragments discriminates the particles produced during fission from other reaction channels.

The experiment [3] was performed at the ALADIN-LAND cave at GSI. Measurements were performed with a hydrogen target isolated by two windows consisting of aluminized mylar foils of 35 μm. Fission events were selected in a double multi-sampling ionization chamber (Twin MUSIC) [4]. Between the target and the Twin MUSIC a pipe filled with helium gas was placed to transmit the fission fragments. A Time-of-Flight Wall detector (ToF Wall), based on plastic-scintillator paddles and two photomultipliers (PM) per paddle, was placed in front of the Twin MUSIC to detect the light-charged particles. It consists of two orthogonally-oriented planes with six paddles each ($60\times6\times1$ cm^3), which leave a square hole (12.5×12.5 cm^2) in the middle to transmit the fission fragments. Because the reaction kinematics, while most of the fission fragments go through the Twin MUSIC, a large fraction of the light-charged particles escape the target to reach the ToF Wall. The time and charge of the scintillator signals are registered by using a TDC and a QDC, respectively. The particle multiplicity is provided by the number of fired paddles in each plane and the particle identification is obtained by using the time and the charge signals as shown in the inset of Fig. 1. Detection efficiency was determined from GEANT4 simulations [5] using INCL4.6-ABLA07 [1, 6] for the particle kinematics and the ToF Wall dimensions.

Figure 1 shows the multiplicity for hydrogen-like particles measured at different energies. The multiplicity is strongly correlated with the impact parameter, so that central collisions lead to high multiplicities whereas low multiplicities are related to peripherical reactions that are the major contribution [7]. The average value of the distribution increases with the bombarding energy, as expected because the reactions are more violent.

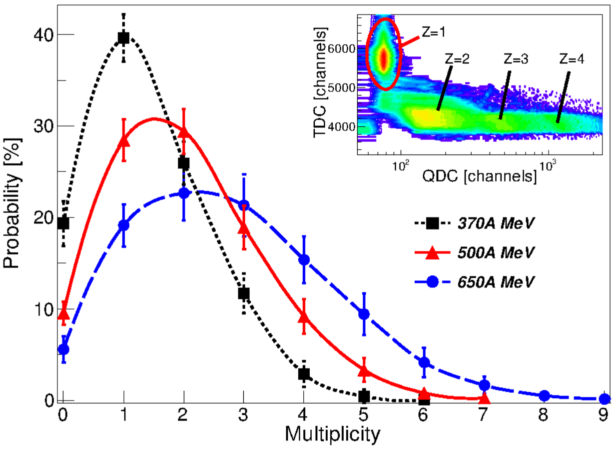

Figure 1: Multiplicity of hydrogen-like particles for ^{208}Pb$+p$ at $370A$ (dotted line), $500A$ (solid line) and $650A$ (dashed line) MeV. The inset shows the identification of particles for evaporation residues. The solid elipse indicates the selection of particles with $Z = 1$, also used for fission.

References

[1] A. Boudard et al., Phys. Rev. C 87, 014606 (2013).

[2] J.P. Lestone, Phys. Rev. Lett. 70, 2245 (1993).

[3] J.L. Rodríguez-Sánchez et al., EPJ 62, 07009 (2013).

[4] J.L. Rodríguez-Sánchez et al., Phys. Rev. C 90, 064606 (2014).

[5] J.L. Rodríguez-Sánchez et al., GSI Sci. Rep. 2013, p. 153.

[6] A. Kelić et al., arXiv:0906.4193v1.

[7] Y. Ayyad et al., Phys. Rev. C 91, 034601 (2015).

DOI:10.15120/GR-2015-1-MU-NUSTAR-NR-05

Status of the analysis of the first EXL experiment at the ESR*

M. von Schmid†1, *J.C. Zamora*1, *S. Bagchi*2, *S. Bönig*1, *M. Csatlós*3, *I. Dillmann*4, *C. Dimopoulou*4, *P. Egelhof*4, *V. Eremin*5, *T. Furuno*6, *H. Geissel*4, *R. Gernhäuser*7, *M.N. Harakeh*2, *A-L. Hartig*1, *S. Ilieva*1, *N. Kalantar-Nayestanaki*2, *O. Kiselev*4, *H. Kollmus*4, *C. Kozhuharov*4, *A. Krasznahorkay*3, *T. Kröll*1, *M. Kuilman*2, *S. Litvinov*4, *Yu.A. Litvinov*4, *M. Mahjour-Shafiei*2,8, *M. Mutterer*4, *D. Nagae*9, *M.A. Najafi*2, *C. Nociforo*4, *F. Nolden*4, *U. Popp*4, *C. Rigollet*2, *S. Roy*2, *C. Scheidenberger*4, *M. Steck*4, *B. Streicher*2,4, *L. Stuhl*3, *M. Thürauf*1, *T. Uesaka*10, *H. Weick*4, *J.S. Winfield*4, *D. Winters*4, *P.J. Woods*11, *T. Yamaguchi*12, *K. Yue*1,4,13, *J. Zenihiro*10 *for the EXL collaboration*‡1

1IKP, TU Darmstadt; 2Univ. of Groningen, KVI-CART, Groningen; 3MTA-Atomki, Debrecen; 4GSI, Darmstadt;
5PTI, St. Petersburg; 6Kyoto University; 7TU München; 8University of Tehran; 9University of Tsukuba;
10RIKEN, Tokio; 11University of Edinburgh; 12Saitama University; 13IMP, Lanzhou

EXL (**EX**otic nuclei studied in **L**ight-ion induced reactions) is a project within NUSTAR at FAIR that aims to investigate nuclear structure at storage rings with direct reactions in inverse kinematics. The investigations are focussed towards very low momentum transfers where, for example, the nuclear matter distribution, giant monopole resonances or Gamow-Teller transitions can be studied [1].

The existing storage ring ESR at GSI, together with its internal gas-jet target, provides a unique opportunity to partially perform this kind of experiments already now. In 2012, we successfully performed an experiment (E105) with stable ^{20}Ne, ^{58}Ni as well as radioactive ^{56}Ni beams interacting with H_2 and ^{4}He targets. The target recoils were measured by a newly developed UHV compatible detector setup based on DSSDs and Si(Li)s (for further details, see [2]).

The main goal was to measure the differential cross section of ^{56}Ni(p,p) at 400 MeV/u in order to deduce the nuclear matter distribution of ^{56}Ni. Figure 1 shows the preliminary differential cross section obtained for this reaction as a function of invariant momentum transfer squared, t. The dashed line corresponds to a fit to the data using Glauber multiple-scattering theory. In this case, the density distribution of the nuclear matter was parametrized with a symmetrized Fermi-function whereby a preliminary RMS point matter radius of 3.5 fm was extracted. This experiment can be considered as the first successfully observed nuclear reaction with stored radioactive beam, ever.

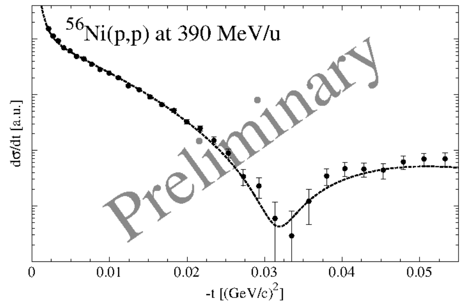

Figure 1: Preliminary differential cross section

Additionally, proof of principle measurements were performed using a ^{58}Ni beam at 100 MeV/u interacting with a ^{4}He target to show the feasibility of investigating giant resonances with EXL [3]. Figure 2 shows the preliminary double-differential cross section for the α inelastic scattering. The dominant contribution is from the **I**so**S**calar **G**iant **M**onopole **R**esonance (ISGMR) excitation. The preliminary results are comparable with previous experiments performed in normal kinematics [3].

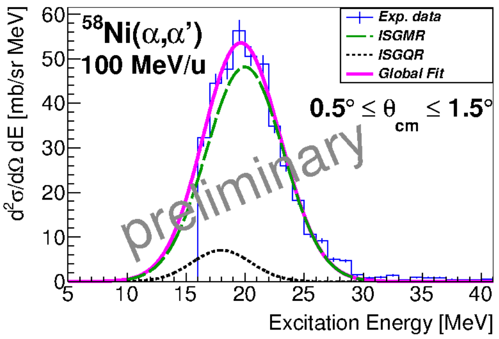

Figure 2: Preliminary double-differential cross section

The experimental campaign has successfully demonstrated the feasibility of the EXL concept and first physics results are on the way. An upgraded detector setup covering larger solid angle is envisaged to be implemented for further reaction experiments at the ESR or the CRYRING at FAIR.

References

[1] H.H. Gutbrod et al. (Eds.), FAIR Baseline Technical Report, ISBN-3-9811298-0-6, Nov. 2006

[2] M. von Schmid et al., EPJ web conf. **66**, 03093 (2014)

[3] J. C. Zamora et al., Physica Scripta (2015), to be published.

---

* This work was supported by German BMBF (06DA9040I and 05P12RDFN8), the European Commission within the Seventh Framework Programme through IA-ENSAR (contract no. RII3-CT-2010-262010), the Hungarian OTKA Foundation No.K106035, the HGF through the Helmholtz-CAS Joint Research Group HCJRG-108, HIC for FAIR, GSI-RUG/KVI collaboration agreement and TU Darmstadt-GSI cooperation contract.

† schmid@ikp.tu-darmstadt.de

‡ http://www.rug.nl/kvi/Research/hnp/Research/EXL/index

DOI:10.15120/GR-2015-1-MU-NUSTAR-NR-06

Test of an R^3B Active Target prototype with a beam of ^{58}Ni

G. Alkhazov[1], D. Balin[1], A. Dobrovolsky[1], P. Egelhof[2], A. Inglessi[1], A. Khanzadeev[1], O. Kiselev[2], G. Korolev[1], B. Löher[2], E. Maev[1], G. Petrov[1], D. Savran[3], J. Silva[3], L. Uvarov[1]
[1]PNPI, Gatchina, Russia; [2]GSI, Darmstadt, Germany; [3]EMMI, GSI, Darmstadt, Germany.

The functionality of a prototype of an Active Target (ACTAR) was tested at the GSI accelerator facility with a beam of ^{58}Ni in April 2014. This detector was designed and constructed for studies of elastic and inelastic scattering of light to heavy nuclei on protons and helium targets. The operating principle and the design of ACTAR are similar to those of the IKAR hydrogen-filled ionization chamber (IC) used at GSI since 1993 in experiments on proton-nucleus scattering in inverse kinematics with beams of light nuclei up to ^{17}C [1, 2, 3].

The main aim of the present test experiment was to prove the possibility of reliable detection of recoiled particles in scattering reactions with a 700 MeV/u ^{58}Ni beam. The ACTAR prototype was constructed with the intention to use it for investigation of inelastic scattering reactions of exotic radioactive nuclei (middle-weight and heavy) on helium. The detector will be later placed inside the CALIFA γ-detector. Another ionization chamber, lager in size, will be built for studying elastic scattering of middle-weight and heavy ions off protons. The anode planes of the ACTAR prototype were designed so that the beam of heavy ions passes across the central anode of 20 mm diameter and possibly the first ring-shaped anode of 40 mm outer diameter. The beam diameter was expected to be smaller than 40 mm. All other anodes around the central anode and the first ring-shaped one were sectioned. The total number of segmented anodes was 66. The signals from all anodes were read out independently by the electronics including preamplifiers, amplifiers and fast 14 bit Flash-ADCs. Along with the information from the ionization chamber, the data from other detectors of the whole set-up were recorded. The beam tracking detectors were placed upstream and downstream of the ACTAR prototype. The IC was surrounded by the γ-detector Crystal Ball (with 162 NaI crystals). The ACTAR chamber was filled with helium-hydrogen (3%) mixture at several gas pressures (2, 5 and 10 bar) for estimation of optimal conditions for registration of recoiled particles with different energy. The energy calibration was performed using a precise pulser and an ^{241}Am α-source. The source was placed on the cathode surface within the chamber. The cathode and the grid of the IC were at –24 kV and –1.2 kV, respectively, provided by new low-noise HV power supplies. The ^{58}Ni beam intensity was ~5 kHz and the total accumulated statistics of elastic scattering events with ^{4}He recoiled particles of 2–15 MeV was about 60000. Figures 1 and 2 show examples of scattering events registered by the ACTAR prototype. The energy resolution in this experiment was estimated to be 20 keV (rms). This value was similar to the one obtained with a pulse generator, demonstrating relatively small influence of the heavy projectiles on the energy resolution of the recoils. One can conclude that reliable registration of recoils in ACTAR with efficiency close to 100% is possible when the energy deposition registered by the anode segments is above 150 keV.

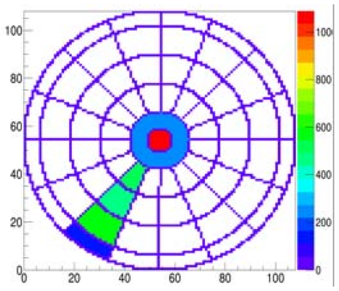

Figure 1: An example of an event registered by the ACTAR prototype. The colour scale represents the energy deposition in keV.

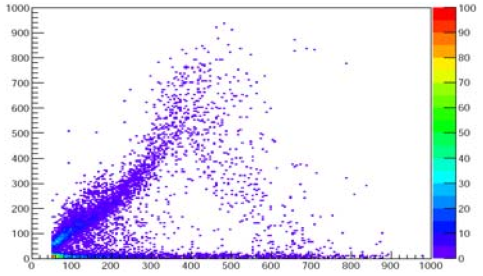

Figure 2: Two-dimensional correlations between the energy depositions of recoil particles registered by neighbouring anode rings along the radius of the ACTAR prototype.

It is also possible to observe pulses from recoils at two central anodes of ACTAR, because fluctuations of the signals produced by the heavy projectiles are relatively small, about 30–40 keV, in agreement with the simulations. This provides a possibility of pile-up rejection and good reconstruction of the total energy deposition of the recoiled particles. The analysis of recoils and γ-rays data is in progress. The experimental data obtained in the test experiment with the ACTAR prototype proved to be of importance for construction of the ionization chambers for the R^3B project. For the first time, the active target of this type was successfully tested with a beam of ions heavier than carbon.

References

[1] G. Alkhazov *et al.*, Phys. Rev. Lett. **78** (1997) 2313.
[2] A.V. Dobrovolsky *et al.*, Nucl. Phys. **A766** (2006) 1.
[3] S. Ilieva *et al.*, Nucl. Phys. **A875** (2012) 8.

DOI:10.15120/GR-2015-1-MU-NUSTAR-NR-07

The DAQ readout library vmelib *

B. Löher[1,2], *A. Charpy*[3], *H. T. Johansson*[3], *H. Simon*[2], *H. T. Törnqvist*[1], *the R³B collaboration , and FAIR@GSI division*
[1]Institut für Kernphysik, Technische Universität Darmstadt, Darmstadt, Germany; [2]GSI, Darmstadt, Germany;
[3]Chalmers Univ. of Technology, Göteborg, Sweden

Introduction

A wide variety of physics experiments depend on the correct initialization and a fast and safe readout of modular electronics connected to data acquisition (DAQ) computers via standardized data buses (e.g. VME, CAMAC, PCIe, or other). A unified and standalone library framework providing the facilities needed to handle the initialization, monitoring and readout tasks in a safe and easy way does not yet exist. Existing libraries are usually either bound to work within a certain DAQ environment, require changes in the code leading to frequent recompilation, are unsafe to use or not meant to be changed by the users at all. In this report we present VMELIB, a library to fill this gap by addressing the points above.

To be a viable option for inclusion in a new project, or even for replacing the specialized readout code in existing applications there are a number of requirements such a library should fulfill: configuration via text files on top of sane defaults; unified API, no dependence on environment; consistency checks (config and data); support standard and fast transfer modes as well as multi-event readout; provide logging and debugging facilities; allow command line diagnostics; unit tests for code quality; emphasis on portability and documentation. The realisation of a few of them in vmelib is discussed below.

Implementation

The lightweight library is written in pure ANSI C, and consists of several components (see Fig. 1): The *config* component reads and parses the configuration. The *crate* component represents crates (i.e. a data bus) and acts as basis for DAQ operation. Each crate contains modules connected to a common data bus. The *module* component represents a generic module. It exposes the common functional elements, such as creation, initialisation, and readout of a physical module, while hiding its specific implementation details. The *util* module contains auxiliary methods for logging, memory allocation and provides the vmelib API that is exported to the environment. The *test* module is a collection of automated offline test cases to ensure correctness of each vmelib component and to prevent regressions.

Configuration is done using text files, which declare a list of crates and their contained modules in a tree-like fashion. A complete configuration file can be very simple, here creating a new Crate object with ID 0 that contains two modules with their respective bus addresses:

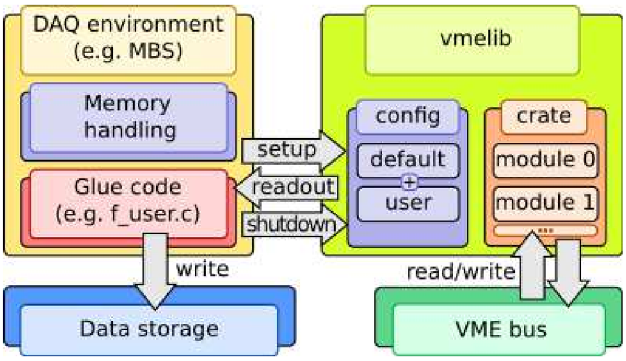

Figure 1: Schematic overview of vmelib (on the right), interacting with a DAQ environment and hardware.

```
CRATE("VME0", 0) {   # Name and crate ID
 multi_event = true  # Use multi-event readout
 GSI_TRIDI(0x02000000) {}  # Type + address
 CAEN_V775(0x00010000) {
   common_start = true
   time_range = 1200 ns
}}
```

Default configurations are part of vmelib and the reason behind crate configurations being concise.

Vmelib provides the functionality to set the configuration and to read data from the modules, leaving data storage and other tasks to the environment. Therefore, the necessary interface to interact with vmelib using a single VME crate consists of only a few function calls:

```
Crate *vmelib_setup(LogCallback, char *cfg_file);
void crate_readout_prepare(Crate *crate);
uint32_t crate_readout(Crate *crate, void **mem);
void vmelib_shutdown(Crate *crate);
```

The complete API consists of a few more functions to allow fine-grained control, where needed.

Use cases

Vmelib has been used in a variety of experimental setups, both for testing and production. The main user is the R³B collaboration, which has used vmelib in experiments together with the MBS data acquisition starting from 2014 at GSI and Riken. The HIγS facility at TUNL has used vmelib successfully for their γ^3 experiments. The flexibility of vmelib allowing for quick changes of module parameters has been particularly appreciated in test setups.

---

* Work is supported by HIC for FAIR, GSI-TU Darmstadt cooperation PSP codes 1.2.2.4, 1.2.5.1.4, and the BMBF project 05P12RDFN8.

DOI:10.15120/GR-2015-1-MU-NUSTAR-NR-08

Status of the R^3B GLAD magnet cryosystem*

Thomas Hackler, Christine Betz, Eugen Momper, David Sanchez-Valdepenas, Claus Schroeder, Cyrill Schweizer, Haik Simon, and the FAIR@GSI division

All GSI, Darmstadt, Germany

The superconducting GLAD (GSI Large acceptance Dipole) magnet will be one of the major components of the R³B experiment to be installed at FAIR at the experimental area. Within the year 2015 we expect the full magnet to arrive at GSI in Cave C for field measurements and first commissioning experiments. To install and run the magnet in Cave C it has to be provided with liquid Helium, and therefore, a new cryogenic system has to be installed at the GSI target hall.

Figure 1: R^3B Glad magnet during the welding of the cryostat at CEA/Saclay

The cold mass of the magnet has a weight of 21 tons and was fully manufactured in 2012.

The superconducting coil was tested successfully in December 2013 at the test facility of the CEA in Saclay in a huge cryostat with a diameter of 5.2 m. With its full current of 3584 Amps it was possible to reach the intended peak field of 6 Tesla.

The GLAD magnet will be provided with Helium at GSI by a used TCF 50 Helium liquefier (year of manufacture 1985) which was used before for cooling cavities at DESY. The cryoplant was moved to Darmstadt in June 2012.

The liquefier was refurbished and upgraded in collaboration with the Linde Kryotechnik Company within the last two years.

The new compressor, the gas management system and the oil removal was first tested successfully at the beginning of 2014. After these tests the bypass system, the oil removal system and the control system were optimized. The cooling water supply of the compressor was improved too to reduce the noise inside the target hall.

To build a completely new automation system for the cryo plant, a PLC control system, based on the UNICOS framework, developed at CERN, was used the first time at GSI.

The complete control and automation system is designed by the industrial controls group and the cryo department in coordination with the R3B experiment, according to specifications from CEA (France) and Linde Kryotechnik. The whole cryo plant is now constructed and documented following the European Pressure Equipment Directive and Machinery Directive as well as associated standards.

In the second half of 2014 preparations for the cooldown of the coldbox have begun. The needed automation functions for the cool down procedure were added to the code of the control system. Prior to installing the turbines in the coldbox, several simulations were done to test and verify the control system part, required for the turbines. The two expansion turbines can be seen as the heart of the coldbox, but they are very expensive as well as fragile while rotating with revolution frequencies up to 4700 1/s.

In December 2014 first cool down tests with built-in turbines started. Before Christmas 2014 the first liquid Helium after over 12 years of downtime was produced by the TCF50 cryoplant.

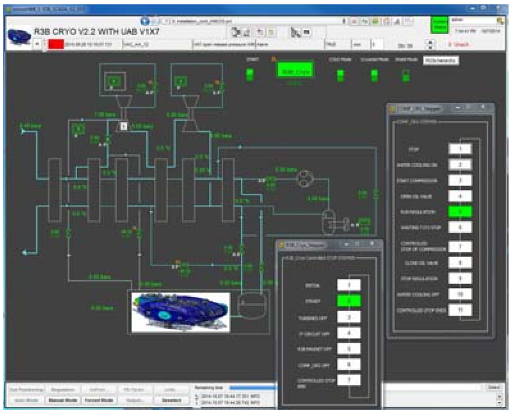

Figure 2: Operator interface of UNICOS for R^3B fridge

Right now, the area between the south entry door of the target hall and Cave C is prepared for the delivery of GLAD, the 60 ton magnet, to be transported by air cushions into its Cave.

Outlook

In 2015 power tests of the coldbox to estimate the maximum cooling power @ 4.5 K and improvements of the control system are planned. Furthermore the isolation vacuum system of the cryostate has to be mounted, its control system hast to be developed and the documentation has to be completed.

---

* Work supported by FAIR@GSI PSP code 1.2.5.1.1.2.

DOI:10.15120/GR-2015-1-MU-NUSTAR-NR-09

The CALIFA endcap

D. Cortina-Gil [*,1], *H. Alvarez-Pol*[1], *T. Aumann*[13], *V. Avdeichikov*[4], *M. Bendel* [†,7], *J. Benlliure*[1], *D. Bertini*[5], *A. Bezbakh*[11], *T. Bloch*[13], *M. Böhmer*[7], *M.J.G. Borge*[2], *J.A. Briz*[2], *P. Cabanelas*[1], *E. Casarejos*[8], *M. Carmona Gallardo*[2], *J. Cederkäll*[4], *L. Chulkov*[12], *M. Dierigl*[7], *D. Di Julio*[4], *G. Fernández Marínez*[13], *E. Fiori*[10], *A. Fomichev*[11], *D. Galaviz*[9], *R. Gernhäuser*[7], *J. Gerl*[5], *P. Golubev*[4], *M. Golovkov*[11], *D. González*[1], *A. Gorshkov*[11], *A.L. Hartig*[13], *A. Heinz*[3], *M. Heil*[5], *B. Heiss*[7], *A. Ignatov*[13], *B. Jakobsson*[4], *H.T. Johansson*[3], *P. Klenze*[7], *D. Köeper*[5], *Th. Kröll*[13], *R. Krücken* [‡,7], *S. Krupko*[11], *F. Kurz*[7], *T. Le Bleis*[7], *B. Löher*[10], *E. Nacher*[2], *T. Nilsson*[3], *A. Perea*[2], *C. Pfeffer*[7], *B. Pietras*[1], *R. Reifarth*[6], *P. Remmels*[7], *H.B. Rhee*[13], *J. Sanchez del Rio*[2], *D. Savran*[10], *H. Scheit*[13], *S. Sidorchuk*[11], *H. Simon*[5], *O. Tengblad*[2], *P. Teubig*[9], *R. Thies*[3], *J.A. Vilán*[8], *M. von Schmid*[13], *M. Winkel* [§,7], *S. Winkler*[7], *F. Wamers*[13], *P. Yañez*[8], *and the R^{3}B collaboration.*

[1]Universidad de Santiago de Compostela; [2]Instituto Estructura de la Materia, CSIC Madrid; [3]Chalmers University of Technology, Göteborg; [4]Lund University; [5]Helmholtzzentrum für Schwerionenforschung, Darmstadt; [6]Goethe University Frankfurt am Main; [7]Technische Universität München; [8]Universidad de Vigo; [9]Centro de Física Nuclear da Universidade de Lisboa; [10]Extreme Matter Institute and Research Division, GSI; [11]Joint Institute for Nuclear Research, Dubna; [12]Nuclear Reseach Center, Kurchatov Institute Moscow; [13]Technische Universität Darmstadt

The R^{3}B experiment (Reactions with Relativistic Radioactive Beams) at FAIR (Facility for Antiproton and Ion Research) is a versatile setup dedicated to the study of reactions induced by high-energy radioactive beams. It will provide kinematically complete measurements with high efficiency, acceptance and resolution, for reactions with relativistic heavy-ion beams up to 1 AGeV, allowing an intense and broad physics program with rare-isotopes.

One of the key detectors in this experiment, CALIFA (CALorimeter for In-Flight detection of γ rays and light charged pArticles), is a complex array of 2560 scintillation crystals, that will surround the R^{3}B target. To cope with the requirements of the R^{3}B program, CALIFA combines the detection of low energy γ rays from single-particle excitations and high-energy γ rays associated with different collective modes. Moreover, CALIFA should be able to detect high energy charged particles emitted from the reaction area.

CALIFA consists of two sections (see Figure 1), a cylindrical 'Barrel' spanning an angular range from 140 to 42 degrees and an 'Endcap' covering the angular range up to 7 degrees. The Barrel is formed by 1952 long CsI(Tl) coupled to APD devices and equipped with a digital readout system. The design of CALIFA Barrel was subject to a Technical Design Report accepted by FAIR management in January 2013 (see [1, 2, 3]) and is presently under construction. CALIFA Endcap has to provide the detection of the most energetic particles in an angular region strongly populated by the light reaction products and gammas (see Figure 1). Table 1 summarises the nominal specifications fixed for CALIFA.

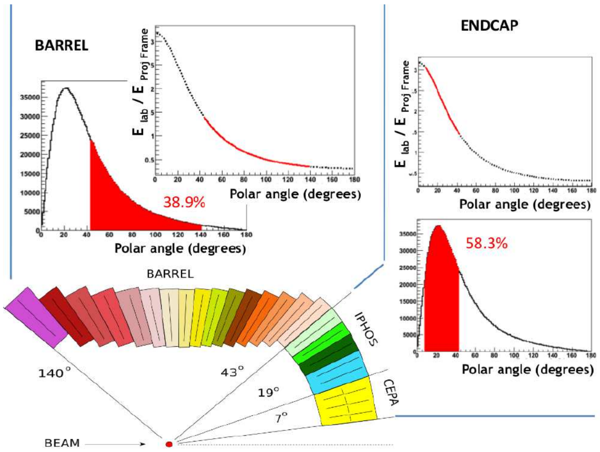

Figure 1: Schematic representation of the CALIFA detector profile. The portion of the angular distribution of emitted γ rays covered by each CALIFA section and the corresponding Doppler shift is highlighted in this figure for a fragment of 700 AMeV.

The CALIFA Endcap

The high-energy of the R^{3}B beams determined the conceptual design of the detector that has to accommodate a large Lorentz boost, particularly in the most forward region. Therefore, one main property of a calorimeter namely the complete kinematic reconstruction of emitted protons must be fulfilled within geometrical constraints, requiring sophisticated detector concepts to be employed.

To provide a feasible solution for the CALIFA Endcap two different detector concepts have been adopted (named the Phoswich and iPhos from now on) (see Figure 2). The Phoswich combines two very high intrinsic resolution scintillators ($La_3Br:Ce$ and $La_3Cl:Ce$) optically coupled and

---

[*] Convener of the CALIFA Working group

[†] PhD thesis, Technische Universität München

[‡] Also affiliated to TRIUMF

[§] PhD thesis, Technische Universität München

DOI:10.15120/GR-2015-1-MU-NUSTAR-NR-10

Intrinsic photopeak efficiency	40 % (at E_γ=15 MeV projectile frame)
γ-ray sum energy resolution $\Delta(E_{sum})$/¡E_{sum}¿	<10 % for 5 γ-rays of 3 MeV
γ-ray Energy resolution	<6 % $\Delta E/E$ for 1 MeV γ-rays
Energy range for protons	Up to 700 MeV in Lab system
Energy resolution, protons stopped	<1 % $\Delta E_p/E_p$ $\frac{\sqrt{(100MeV)}}{\sqrt{E}}$
Energy resolution protons punch though	<7 % ΔE_p/E_p (at E_p=500 MeV)
Full energy peak efficiency for protons	>50 % (for all energies)
Proton-γ-ray separation	for 1 to 30 MeV

Table 1: Nominal specifications of the R^3B calorimeter (at β=0.82).

with a common readout, whereas the iPhos concept is composed by a monolithic CsI(Tl), similar to the most forward crystals of the CALIFA Barrel, that make use of the different decay times present in CsI(Tl) to identify particles. In both cases Pulse Shape Analysis (PSA) techniques are employed to separate punch-through protons from the fully stopped, providing a very good background suppression.

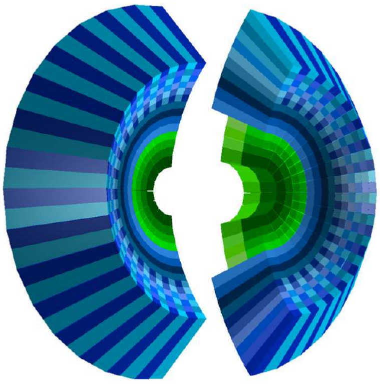

Figure 2: Artistic drawing of the two halves of the CALIFA Endcap. The four inner rings will consist of $LaBr_3/LaCl_3$ phoswich detectors, while the ten outer rings will be provided with the new iPhos detector concept.

The most forward angles up to about 20 deg are covered by Phoswich detectors. In this angular region the lower Doppler dependence on the angle allows for a broader-segmentation. The remaining angular range is covered by iPhos detectors. The granularity of CALIFA has been optimised in a manner to ensure that the final resolution is not dominated by Doppler broadening, but close to the intrinsic resolution of the scintillation material. While aiding energy resolution, an excessively high segmentation would be at the expense of calorimetric properties, consequently the optimum compromise between these factors has been determined. Figure 3 summarises the selected angular aperture for the CALIFA Endcap detectors that would guarantee a γ ray energy resolution between 4-6%, for projectile velocity β=0.82 all over the Endcap angular range.

We will underline the main technical characteristics inherent to this versatile device.

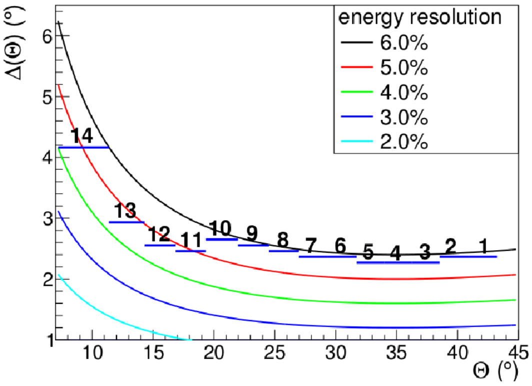

Figure 3: Graphic representation of the polar angular aperture needed as a function of the polar angle for a given projectile velocity (at β=0.82). The coloured lines correspond to different values for the maximum contribution to the energy uncertainty due to Doppler broadening, ranging form 2 to 6 %. Each blue line corresponds to the angular range covered by a crystal ring. Rings 1-10 correspond to the region covered by the iPhos section while rings 11-14 are covered by CEPA.

The Phoswich concept: CEPA

The inner section of the CALIFA Endcap, CEPA will be built as an array of individual phoswich modules (sectors) based on the optical coupling of 7 cm of $LaBr_3$(Ce) with 8 cm of $LaCl_3$(Ce) and readout by metal package PM of Hamamatsu R7600U-200 with E5996 Voltage divider. CEPA is divided into 4 rings divided into 8 sectors. $LaBr_3$(Ce) and $LaCl_3$(Ce) both are very hygroscopic materials that need to be encapsulated. The sectors will be formed by 0.20 mm thick cans of Aluminium. The can holds a 4 mm thick glass exit window, this window divided so that each readout is optically isolated. Each sector will contain 12 crystals; the inner two rings with 2 crystals followed by 2 consecutive rings of 4 crystal in each ring. CEPA comprises 96 double crystals, leading to a total weight of 42 kg and a volume of 9.5 dm^3 .

The Lorentz boost applied to the in-flight emitted γ rays in CEPA can reach a value ≈ 3 (a 10 MeV γ ray

DOI:10.15120/GR-2015-1-MU-NUSTAR-NR-10

could correspond to 30 MeV depending upon the emission angle). At such a high energy, the interaction of γ rays with matter is dominated by pair production. Montecarlo simulations show that, about half of the γ rays of 20 MeV undergo pair production within the first 5 cm of a LaBr$_3$(Ce) crystal, depositing most of their energy in and around the first interaction. Having two layers of different crystals and being able to distinguish between the energy deposited in both, will allow us to implement intelligent add-back algorithms in which, by imposing conditions on one or the other layer (veto or coincidence), one can obtain information about the physical processes and even reconstruct part of the energy lost.

Protons, contrary to γ rays, interact with matter by a continuous deceleration, leaving part of their energy along the track, but they will deposit most of their energy in the final absorption process (Bragg peak). This also favours the use of two layers. Instead of using one very long crystal; it is possible to determine the initial energy by the energy loss in two shorter crystals, and thus avoid the reactions of very high energy protons ($>$200 MeV) where a major part of the energy may be lost due to production of neutral particles (pions or neutrons).
Figure 4 shows an example of proton identification using a CEPA prototype consisting of four 4 cm long LaBr$_3$(Ce)and a 6 cm long LaCl$_3$(Ce) packages. It corresponds to data recorded at the IFJ PAN Kraków cyclotron that can accelerate protons with energies ranging from 70 to 230 MeV. We distinguish in the two-dimensional ΔE-E plot three areas. Protons with energies comprised between 70 - 130 MeV are fully stopped in the first crystal (LaBr$_3$(Ce)) of the phoswich (line A), protons with energies between 130-200 MeV pass through the first crystal but are fully stopped in the second one (LaCl$_3$(Ce)) (line B), whereas the most energetic protons have to be detected by the partial energy deposited in both crystals (line C). The final resolution can be very different as a function of the proton energy and can range from 2 to 7% (for the largest energy in this experiment 230 MeV).

The iPhos concept

The ten outer rings of CALIFA Endcap will consist of monolithic CsI(Tl) crystals using the new iPhos method for the reconstruction of high-energy particles and described in [4]. The crystals are arranged in carbon fibre alveoli filled with four crystals each. The outer 6 rings include two different crystal geometries that are mirror images and follow identical geometrical configuration to Barrel crystals.They provide a smooth gap free transition between Barrel and the most inner 4 rings. Here one alveolus covers 4 crystals in a row to provide the best mechanical stability. The system amounts for 512 crystals of 22 cm long, filling an approximate volume of 90 dm^3 and a weight of 408 kg.

As part of the development of the iPhos concept for the CALIFA Endcap, a beam test at TRIUMF, Vancouver was performed. The TRIUMF H$^-$ cyclotron provides a proton beam with intensities down to 100 particles per second and energies of 355 MeV and 480 MeV. The detector setup consisted of 12 CsI(Tl) crystals with a length of 15 cm and read out by LAAPDs. To modify the incoming beam energies and access a large set of different energies, an active degrader array with 4 cm and 3 cm long CsI(Tl) crystals was used in front of detector. It was shown that the RPID algorithm [5] preserves up to an energy of 480 MeV a nearly constant separation for stopped and punch-through protons, which is N = 13 times larger than the width of the correlation of fast and slow component of the light emission. This favours the use of the iPhos method up to these energy regions.

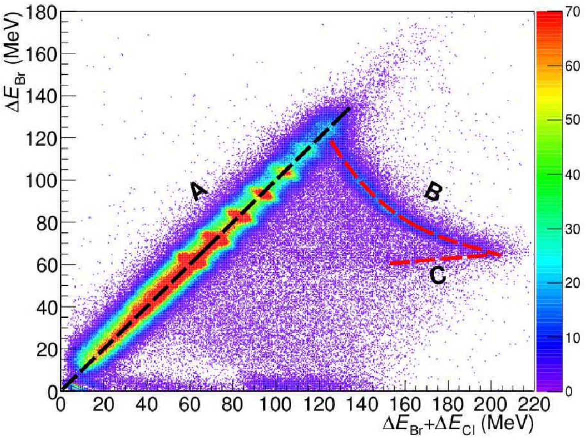

Figure 4: Two-dimensional ΔE-E plot for the runs included in the resolution analysis (protons of 70 - 230 MeV. The 2D histogram has been later projected onto the three lines: A, B and C for the determination of the energy resolution (see text).

Another feature of the iPhos method, also shared by the Phoswich concept, is the discrimination and suppression of nuclear reactions inside the active detector material [4]. In 22 cm long CsI(Tl) crystals used in the CALIFA Endcap, nearly 50 % of protons above 300 MeV cause a non-negligible amount of nuclear reactions and have to be suppressed.

Figure 5 shows a full energy loss spectrum of 500 MeV protons in 250 mm of CsI(Tl). If we assume a (p,2p) experiment at an incoming beam energy of 700 AMeV different cuts can be applied based on the kinematics constraints smeared by the Fermi momentum distribution of the knocked-out proton inside the nucleus. This cut in the RPID parameter space reduces the amount of nuclear reactions dramatically (see Figure 5, red). All events that interact predominantly electromagnetically are located inside the energy loss peak and therefore in good approximation in the energy interval 185 MeV $< E_p <$ 220 MeV. The ratio between all events in the cleaned spectrum to all simulated events defines the efficiency of the detector at 500 MeV. The ratio of events of the cleaned spectrum inside that interval to all events in that spectrum is a measure for the purity of the selection. If not constrained by any kinematics a pure proton cut in the RPID still cleans very efficiently. The characteristic numbers for both cases are shown in table 2.

	Purity	**Efficiency**
(p, 2p)	98,7 %	52,1 %
proton cut	90,5 %	58,1 %

Table 2: Summary of the two characteristic numbers purity and efficiency for (p,2p) reactions and a proton only cut for comparison.

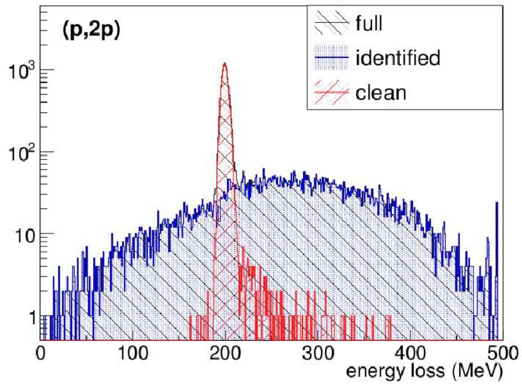

Figure 5: Energy loss spectrum from a GEANT4 simulation for single protons reaching the detector at E_{kin} = 500 MeV (black). Events selected by the minimum bias (p,2p) kinematics cut in the RPID parameter space are shown in red. Events excluded by the iPhos method are shown in blue (from [6]).

The QFS Physics case

The full system has been simulated for a number of realistic physics cases; demonstrating that the detector performance meets the R^3B physics program requirements.

We will use as example the quasi-free reaction (p,2p) induced by a ^{18}O beam at 700 AMeV on a proton target to demonstrate the performance of the CALIFA Endcap. For this kind of experiment CALIFA has the challenging role of detecting the energy of the two protons plus the coincident γ rays from the de-excitation of the recoiling heavy fragments, covering a huge dynamical range. By measuring the energy as well as the momentum direction of both outgoing protons and knowing the incoming beam, the four-momentum vectors in the laboratory frame can be reconstructed.

The simulated excited states for the resulting fragment, ^{17}N, are below the particle separation threshold, so only electromagnetic transitions will occur. In this simulation we allow only the equal population of the ground state and the first two excited states (1373.9 and 1849.6 MeV respectively).

The application of missing mass spectroscopy [8, 9], allows for the reconstruction of the excitation energy independently of the actual measurement of the decay γ rays.

We have made use of the R3BRoot simulation package to evaluate the achievable missing mass resolution ΔM. This quantity depends on the energy resolution of both protons and was evaluated starting from an angular resolution of $\Delta\ \Theta = 1$ mrad. If the energy of one of the protons is measured precisely, the energy resolution of the second is of lesser importance. For example with one proton energy resolution of 1% and the other 7% an invariant mass resolution of ΔM = 2.5MeV can still be achieved.

We show in Figure 6 the spectrum of the reconstructed missing mass of the ground state and the first excited $1/2^+$ state in ^{17}N. The excitation energy peak of the 1850 keV state is clearly shifted. This kind of measurement is a essential part of the R^3B and would contribute to study the role of final state interactions in exotic nuclei.

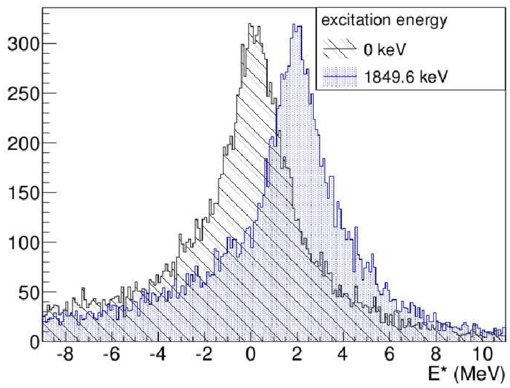

Figure 6: Simulation of the reconstructed excitation energy in ^{18}O(p,2p)17N for the ground state and first excited state at 1849.6 keV.

The detection of γ-rays corresponding to single state is also possible with CALIFA. Figure 7 shows the reconstructed γ ray spectrum after a Doppler correction with respect to the emitting fragment. The final energy resolution achieved with CALIFA nicely allows to separate the full energy peak at 1370 keV and 1850 keV and also the decay branch between these two states at around 480 keV.

Electronics and Trigger Logic

The CALIFA performances could not be achieved without an intelligent and dedicated data acquisition system and trigger logic.

Besides a synchronized trigger mode, in which all channels are read out at the same time in a common deadtime domain, CALIFA will feature a free-running mode, in which channels are self-triggered and record data independently. This trigger mode was successfully tested in a recent experiment performed at GSI in October 2014 in

DOI:10.15120/GR-2015-1-MU-NUSTAR-NR-10

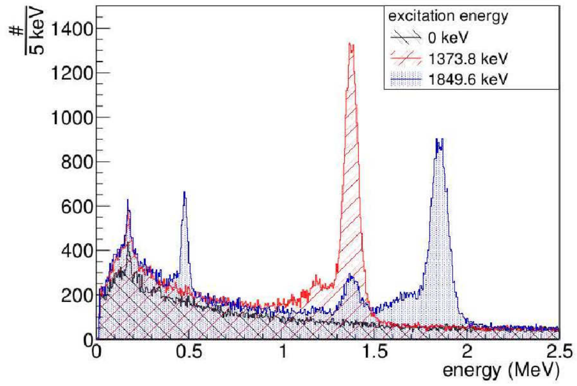

Figure 7: Simulation of the γ-spectrum corresponding to the population of the ground state (black) and the first two excited states of ^{17}N after Doppler reconstruction.

which the R^{3}B event reconstruction was accomplished with the White Rabbit time stamp system which in turn was distributed to the different branches.

In the future, a better event selection at high event rates will be accomplished by complex triggers involving the full information of the calorimeter read out by 200 FEBEX modules. Based on the total energy sum, the event multiplicity or the geometrical distribution of hits, different reaction topologies will be selected. To achieve this, a new concept called the trigger transfer tree protocol (T^{3}P) will combine the trigger data from all 2560 channels in a hierarchical tree structure.

On the channel level, the slope of the detector response is used to get a quick ($\Delta t < 1\,\mu$s) energy estimate to generate crystal triggers. On the cluster level, the energy sum and multiplicity for 16 channels within one FEBEX module is calculated. The cluster level information is sent using a serial protocol over 12 LVDS pairs to a R-FAB (Receiver FEBEX Add-on Board), which is currently under development. The R-FAB combines up to eight of these channels to a single output sent to the next level. The signal will be aggregated in two more tree levels before a global trigger decision is made.

The R-FAB will feature a dedicated FPGA/CPLD hybrid for very fast, "on the fly" calculation. By implementing the trigger modules as FEBEX addon boards, it will furthermore be possible to insert trigger information directly into the MBS data stream for online monitoring.

The development of CALIFA is rather advanced. The CALIFA Barrel is presently under construction. The commissioning of the CALIFA Demonstrator was done in conjunction with other R^{3}B detectors in October 2014. CALIFA Endcap Technical Design Report was endorsed by FAIR for evaluation in November 2014. According to our schedule, the complete CALIFA could be installed and operational in the R^{3}B cave by the end of 2017 ready to accommodate Day 0 experiments.

Acknowledgements

This work has been supported by the following projects MINECO (FPA2012-39404-C02- 01, FPA2012-39404-C02-02, FPA2012-32443, FPA2013-47831-C2-1,FPA2013-47831-C2-1), Xunta de Galicia (GRC2013-11), Swedish research council (VR 2009-3939, VR 2012-4550, VR 2013-4178), GANAS (Eranet), ENSAR (VII PM), HIC for FAIR, BMBF (05P12WOFNF, 05P12WOFNUE, 05P12RDFN8), GSI (TMLFRG1316) and DFG (EXC153).

References

[1] D. Cortina-Gil et al., GSI SCIENTIFIC REPORT 2011 Technical design of the CALIFA/R3B Barrel detector, GSI SCIENTIFIC REPORT 2011

[2] D. Cortina-Gil et al., GSI SCIENTIFIC REPORT 2012 Status of the CALIFA/R3B calorimeter, GSI SCIENTIFIC REPORT 2012

[3] D. Cortina-Gil et al., GSI SCIENTIFIC REPORT 2013 Progress report of the CALIFA/R3B calorimeter, GSI SCIENTIFIC REPORT 2013

[4] M. Bendel. Entwicklung einer neuartigen Nachweismethode für hochenergetische Teilchen im CALIFA-Kalorimeter. *PhD thesis, Technische Universität München* 2014.

[5] M. Bendel et al. RPID - A new digital particle identification algorithm for CsI(Tl) scintillators. *The European Physical Journal A*, 49(69) 2013.

[6] CALIFA collaboration. Technical Report for the Design, Construction and Commissioning of The CALIFA Endcap, 2014.

[7] B. Heiss. Experimental verification of the iPhos energy reconstruction method for the CALIFA calorimeter. *Master thesis, Technische Universität München* 2014.

[8] F. Wamers. Quasi-Free-Scattering and One-Proton-Removal Reactions with the Proton-Dripline Nucleus 17N at Relativistic Beam Energies. *PhD thesis, Technische Universität Darmstadt* 2011.

[9] V. Panin. Fully Exclusive Measurements of Quasi-Free Single-Nucleon Knouckout Reactions in Inverse Kinematics. *PhD thesis, Technische Universität Darmstadt* 2012.

Capability of the Califa Endcap for lifetime measurements of excited nuclear states*

S. Heil[1], *M. Bayram*[1], *M. Petri*[1], *and the R^3B collaboration*[2]
[1]TU Darmstadt, Darmstadt, Germany; [2]GSI, Darmstadt, Germany

Transitional electromagnetic matrix elements offer deep insights into the structure of nuclear wave functions, since the electromagnetic interaction is well known. Providing such key experimental observables is thus very important for refining and testing modern state-of-the-art nuclear structure theories. The most direct, model independent way of determining transitional matrix elements is by measuring the lifetime of excited nuclear states. This type of experiments has been carried out successfully for nuclei at or near the valley of stability, providing a wealth of nuclear structure information. For very exotic nuclei such studies become more challenging, due to the low intensity of the radioactive ion beams. Thus, utilizing a setup with high efficiency and large acceptance, like R^3B, could open a new window of opportunity for this type of measurements.

In this report we investigate the feasibility of performing lifetime measurements of excited nuclear states using the CALIFA Endcap of the R^3B setup [1]. For lifetime measurements using the Doppler effect of a decelerating nucleus, i.e. the Recoil Distance Method, a γ-ray detector with excellent energy resolution is needed. HPGe detectors provide the highest intrinsic energy resolution for γ-ray detection compared to any other detector currently available. However, when dealing with fast beams, other effects dominate the in-beam energy resolution of this detector, resulting in a total energy resolution comparable with other γ-ray detectors, such as $LaBr_3$. The Endcap of CALIFA includes four rings of $LaBr_3$ detectors at the most forward direction (c. f. Fig. 1) and therefore provides a unique opportunity to perform such experiments at the R^3B setup. We have carried out extensive simulations to test the feasibility of lifetime measurements at the R^3B setup using the CALIFA Endcap at a range of beam energies, from 100 MeV/u up to 800 MeV/u, and for different mass regions.

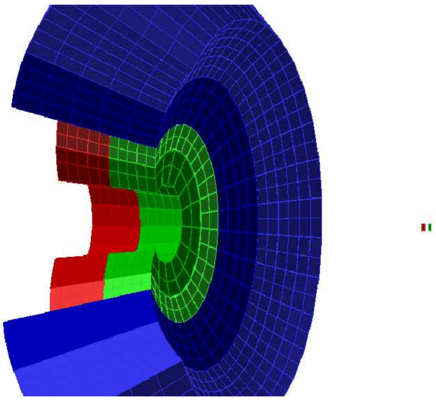

Figure 1: Illustration of the simulated Califa Endcap.

Figure 2 shows the simulated γ-ray spectrum from the innermost $LaBr_3$ detector ring of the CALIFA Endcap when a neutron-rich ^{62}Fe beam at an energy of 97.8 MeV/u gets Coulomb excited in a 300 μm Au foil and further decelerated by a 300 μm Nb foil, with a target degrader separation of 1.2 mm. The first 2^+ state of ^{62}Fe with an excitation energy of 877 keV has a lifetime of 8 ps [2]. The resulting γ-ray spectrum includes the Coulomb excitation contribution of 30% from the degrader [2]. Experimentally this can be disentangled by performing a measurement with a very large target degrader separation. If such a measurement is not possible, e. g. due to beam time constraints, the degrader contribution can be disentangled by cross section considerations. The simulated γ-ray spectra from the $LaBr_3$ detectors of the CALIFA Endcap (c. f. Fig. 2) are very similar to the one obtained with HPGe detectors (c. f. Fig. 1 in [2]) confirming that such experiments are now feasible at the R^3B setup. This expands the R^3B experimental program to a complete new field of experiments. Currently we are developing a compelling experimental program to measure lifetimes of excited states in exotic nuclei using the CALIFA Endcap.

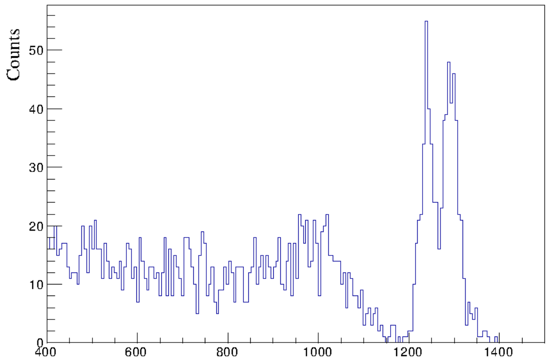

Figure 2: Simulated energy spectrum for the CALIFA Endcap detector ring at 9.9° (LaBr).

References

[1] D. Cortina-Gil et al, "The CALIFA Endcap", GSI Scientific Report 2014

[2] W. Rother, A. Dewald, H. Iwasaki, et al, "Enhanced Quadrupole Collectivity at N=40: The Case of Neutron-Rich Fe Isotopes", Physical Review Letters 106, 022502 (2011)

---

* Work supported by HIC for FAIR

DOI:10.15120/GR-2015-1-MU-NUSTAR-NR-11

NeuLAND - from double-planes to the demonstrator [*]

K. Boretzky[†1], *G.D. Alkhazov*[2], *L. Atar*[3], *T. Aumann*[3,1], *C. Beinrucker*[4], *D. Bemmerer*[5], *D. Bertini*[1], *A. Blanco*[6], *C. Caesar*[3,1], *T.E. Cowan*[5,7], *G. Dentinger*[3], *Z. Elekes*[8], *A. Endres*[4], *P. Fonte*[6], *D. Galaviz*[9], *I. Gašparić*[10], *St. Gohl*[5,7], *V.L. Golovtsov*[2], *T. Heftrich*[4], *M. Heil*[1], *M. Heine*[3], *A. Heinz*[11], *M. Holl*[3], *A. Horvat*[3], *A. Horvath*[12], *H. Johansson*[11], *J. Kahlbow*[3], *A. Kelić-Heil*[1], *R. Kissel*[3], *D. Körper*[1], *D. Kresan*[3], *A.G. Krivshich*[2], *V. Kuznetsov*[2], *S. Lindberg*[11], *L. Lopes*[6], *J. Machado*[9], *J. Mayer*[13], *K. Miki*[3], *L. Netterdon*[13], *T. Nilsson*[11], *E.M. Orischin*[2], *S.G. Pickstone*[13], *R. Plag*[1], *M. Pohl*[4], *R. Reifarth*[4], *T.P. Reinhardt*[7], *S. Reinicke*[5,7], *M. Röder*[5,7], *D. Rossi*[1], *H. Scheit*[3], *F. Schindler*[3], *H. Simon*[1], *M. Sobiella*[5], *K. Sonnabend*[4], *D. Stach*[5], *P. Teubig*[9], *R. Thies*[11], *H. Toernqvist*[3], *L.N. Uvarov*[2], *V.V. Vikhrov*[2], *S.S. Volkov*[2], *A. Wagner*[5], *A.A. Zhdanov*[2], *A. Zilges*[13], *K. Zuber*[7], *the R^{3}B collaboration*, *and the FAIR@GSI division*[1]

[1]GSI, Darmstadt, Germany; [2]PNPI St. Petersburg, Russia; [3]TU Darmstadt, Germany; [4]Univ. Frankfurt, Germany; [5]HZDR, Dresden-Rossendorf, Germany; [6]LIP, Coimbra, Portugal; [7]TU Dresden, Germany; [8]MTA ATOMKI, Debrecen, Hungary; [9]Univ. Lisbon, Portugal; [10]RBI, Zagreb, Croatia; [11]Chalmers Univ. of Technology, Göteborg, Sweden; [12]Eötvös Univ., Budapest, Hungary; [13]Univ. of Cologne, Germany

NeuLAND [1] is one key building block of the R^{3}B experiment which will be commissioned and will perform first physics runs in Cave C at GSI prior to moving to its final destination in the NUSTAR high-energy cave at FAIR. During 2014, the NeuLAND (new Large-Area Neutron Detector) demonstrator has been assembled and tested with fast neutrons from high-energy Coulomb break-up, fragmentation and fission reactions using various isotopes. The demonstrator comprises five so-called double-planes and thus 1/6 of the total NeuLAND detector. Here, we report on the assembly and testing stages of the demonstrator, beam test experiments, and the overall status of the NeuLAND project.

Three GSI test beam times gave the opportunity to investigate the response of NeuLAND to fast neutrons. In the following we report on the different configurations during these experiments and present first, preliminary results.

In a beam time aiming to test various R^{3}B components comprising the active target ACTAR [2] and various beam tracking detectors during April 2014, one NeuLAND double-plane (front-face 250×250 cm^2, 2×5 cm depth) was exposed to fast neutrons originating from (Coulomb) breakup of ^{58}Ni at 500 to 800 AMeV. The 200 NeuLAND photomultipliers (PMTs) were read out using the former LAND electronics TacQuila [3], also for the high-voltage (HV) supply commercial modules, inherited from the former neutron detector LAND, were used. The NeuLAND double-plane was located about 10 m downstream from the target, primary beam and fast beam-like projectile fragments were bent away using the ALADIN magnet and identified by a system of tracking detectors. In order to cope with the large material budget along the beamline, caused by various detectors, tested simultaneously, a very thick Pb target (6 mm) served as a source for neutrons and fast gammas to be detected by NeuLAND. The preliminary results from this test comprise a typical time resolution of $\sigma_t = 100$–150 ps, derived from prompt γ-rays produced at the target, which is compatible with the design goals for NeuLAND. Due to the downstream fragment beam path being in air and the insertion of multiple tracking detectors, a lot of background caused by high-energy protons was detected in the first layer of the NeuLAND double-plane. These findings allowed to cross-check detailed background simulations for future experiments and stimulated a design study for a veto detector for the full size NeuLAND detector.

During summer, the NeuLAND demonstrator support frame at Cave C was sequentially equipped with additional double-planes, see Figure 1. The assembly comprised four double-planes read-out with TacQuila electronics and one double-layer (technically two single layers were built) read out with a prototype of the designated NeuLAND electronics TAMEX [4]. The demonstrator has an active volume of 250×250×50 cm^3 and a weight of more than 4 tons. It comprises 500 individual scintillator bars, 1000 PMTs with their HV supplies and their read-out electronics. The slow control of parameters like thresholds or HV settings was implemented in EPICS and grafical user interfaces (GUIs) were adapted accordingly.

Two GSI beam times were carried out using the NeuLAND demonstrator. At the beginning of October, a beam time with several R^{3}B components was carried out comprising besides NeuLAND also a CALIFA demonstrator, Silicon Tracker ladders and various silicon- and scintillator-based tracking detectors for heavy ions [5]).

---

[*] Work supported by BMBF (05P12RDFN8, 06FY71051, 06KY9136, 06DR134I, NupNET NEDENSAA 05P09CRFN5), by ENSAR, by GSI via the GSI-TU Darmstadt cooperation contract, by GSI F&E (DR-ZUBE and KZILGE1416),by FAIR@GSI PSP code:1.2.5.1.2.5 and by HIC for FAIR

[†] k.boretzky@gsi.de

DOI:10.15120/GR-2015-1-MU-NUSTAR-NR-12

Figure 1: The first NeuLAND double-plane in its frame in Cave C (left), NeuLAND double-plane no. 4 on its way to Cave C (middle,photo: G. Otto) and the demonstrator support frame after insertion of the fourth double-plane (right).

Both fragmentation reactions from the ^{48}Ca beam impinging at 450 to 650 *A*MeV on a carbon target and Coulomb break-up on lead were used to produce fast neutrons for NeuLAND. These data, dominated by one- and two-neutron events are important inputs for the further development of simulation and analysis tools. Figure 2 illustrates a 3D-view of a two-neutron event inside the detector volume.

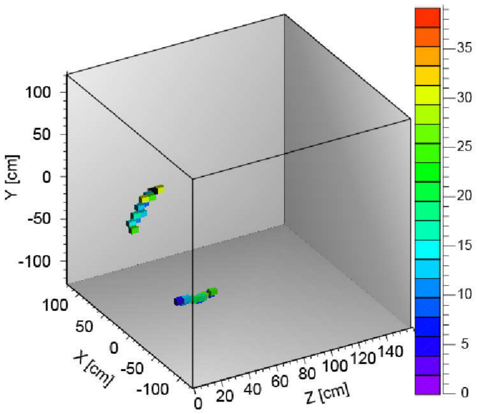

Figure 2: A measured two-neutron event is displayed in the detector volume (depth 40 cm for the TacQuila readout double-planes). The neutrons impinge at the front face (Z=0), a veto condition on the first layer ensures the detection of neutrons and suppresses (background) protons. The colour code represents the energy deposit measured in the corresponding scintillator bars.

Only ten days later the NeuLAND demonstrator joined the SOFIA experiment. Figure3 displays the hit distributions in the 4 double-planes read out with TacQuila electronics. All 400 submodules were functional and well calibrated. Due to the SOFIA fragment trigger, only a minor amount of background is observed at low x-values, originating mostly from secondary particles produced by the projectile fragments on their flight path behind the ALADIN magnet. The analysis of the neutron data will focus on the patterns and multiplicities found as a function of the fission fragment masses measured with SOFIA.

After the successful completion of the GSI beam times, four NeuLAND double-planes and their electronics were crated for the transport to RIKEN, Japan. Logistics challenges due to the oversize of the transport box ($401 \times 344 \times 128\,\mathrm{cm}^3$ and 5.75 tons) were overcome and the detector arrived safely at RIKEN in January 2015. The NeuLAND double-planes have been installed and taken into operation at the SAMURAI setup [6] and will be used in beam times in conjunction with the NEBULA detector [7].

As a next step towards the final detector, the pre-series for the future NeuLAND HV distribution system, an in-kind contribution from PNPI Gatchina, has arrived at GSI and is currently being taken into operation. The pre-series comprises 200 channels in four slim modules with a form-factor allowing the on-board assembly on the NeuLAND double-planes. Within this distribution system, supplied by one HV primary power, each HV channel can be downregulated individually.

The ongoing, stepwise construction and commissioning of the detector is carried out by a collaborative consortium of the University groups of Darmstadt, Frankfurt, Köln, and the GSI RB team. The major part of the construction cost is funded via the BMBF Verbundforschung.

References

[1] NeuLAND webpage, https://www.gsi.de/de/work/fairgsi/rare_isotope_beams/r3b/neuland.htm

[2] G. Alkhazov et al., Test of an R^{3}B Active Target prototype with a beam of ^{58}Ni, contribution to this annual report

[3] K. Koch et al., A New TAC-Based Multichannel Front-End

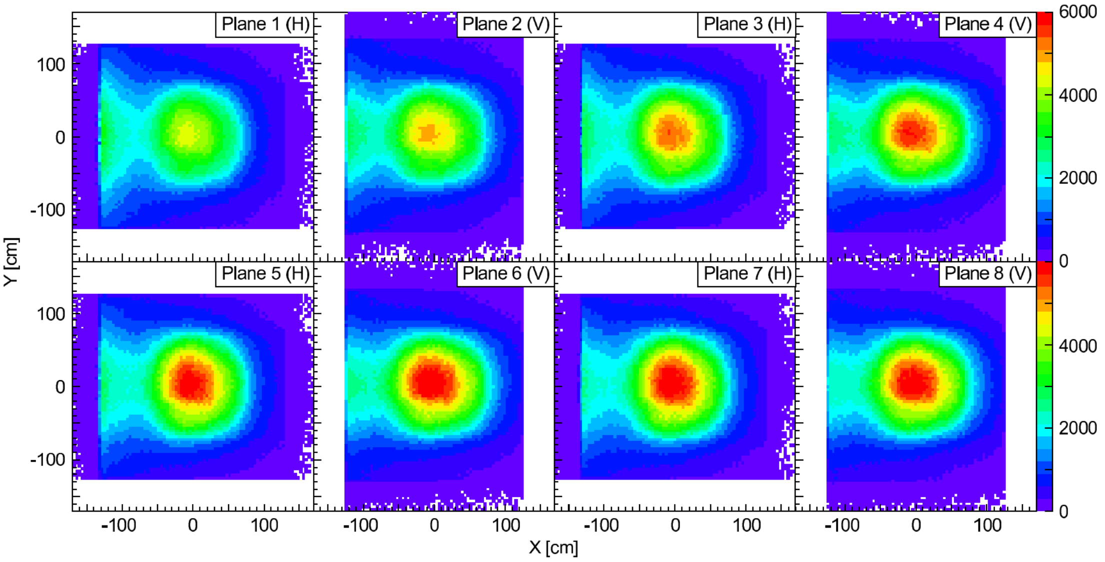

Figure 3: Spatial hit distributions, perpendicular to the beam axis measured in 4 double-planes (8 alternating horizontal and vertical single layers) of the NeuLAND demonstrator, starting with the first horizontal layer in the upper left corner up to the fourth vertical layer in the lower right corner. These spectra were obtained for reactions of ^{238}U beam on a lead target at 700 *A*MeV.

Electronics for TOF Experiments With Very High Time Resolution, IEEE Trans. Nucl. Sci. **52**, 745 (2005)

[4] C. Ugur et al., A Compact Readout System for the R^{3}B High-Resolution Neutron Time-of-Flight Spectrometer (NeuLAND), contribution to this annual report

[5] M. Heil et al., In-beam test of a new TOF wall for the R^{3}B setup, contribution to this annual report

[6] T. Kobayashi et al., SAMURAI spectrometer for RI beam experiments, NIMB **317**, 294 (2013)

[7] Y. Kondo et al., Calibration methods of the neutron detector array NEBULA, RIKEN Accel. Prog. Rep. **45**, 131 (2012)

DOI:10.15120/GR-2015-1-MU-NUSTAR-NR-12

Multi-Neutron detection in R^{3}B at FAIR with alternative detector model

V. Wagner[1], *D. Kresan*[2], *and J. Enders*[1] *for the R^{3}B Collaboration*
[1]TU Darmstadt, Darmstadt, Germany; [2]GSI, Darmstadt, Germany

For the determination of excitation energies in nuclear reactions a high neutron energy resolution and a reliable detection are very important. In the future R^{3}B experiments at FAIR, this will be performed by the New Large Area Neutron Detector (NeuLAND), which is based on a fully-active scintillator concept. NeuLAND consists of 3000 scintillator modules to achieve precise time and position measurements required for the momentum determination via time of flight. Neutrons, emitted from the target, scatter in the scintillator material which leads to the production of charged particles, which deposit energy in a detector module. A dedicated reconstruction algorithm has to find the first interaction of an incident neutron by analysing an event pattern, which will provide necessary measurements for the calculation of the neutron energy [1]. A series of test experiments have been performed at GSI SIS18 with the NeuLAND prototype and the results were compared with the calculations using the R^{3}BRoot framework. An agreement of multiplicity, single paddle energy deposit and total energy deposit distributions has been achieved after introducing a shorter integration time of $\approx$ 20 ns and extending the simulation with an effect of photomultiplier saturation and presence of QDC thresholds. Such an alternative algorithm had to be applied on simulations of the full NeuLAND detector with respect to multi-neutron reconstruction performance. This report shows comparison of described model versus results published in NeuLAND TDR [2].

Simulations

The simulations have been realised using the R^{3}BRoot framework. Secondary particles, created via neutron interaction with the scintillator material, may travel through several modules, thus creating various signals. On its way to the photomultiplier the signal amplitude is reduced because of light attenuation and the finite lifetime of excited states. Those two parameters are given by material constants. The energy loss values from different charged particles are integrated within time window of $\pm$ 20 ns around the first signal, which is significantly lower than was used for the results in [2]. This integration time has to be reconsidered in order to match the read-out set-up of NeuLAND electronics, and can not be used in future simulations as a free parameter. In the next step of the reconstruction, saturation of a photomultiplier is taken into account. The saturation has the form $E' = E \cdot (1 + k \cdot E)^{-1}$ leading to an decreasing output with higher energies. In the final step the energy gets additionally smeared with a Gaussian with 4 % resolution. Due to the modular setup of NeuLAND and the time difference between the two signals in one module, the position of a crossing particle can be determined in both directions. Signals close in space and time are then combined in so-called clusters. Subsequently an algorithm tries to identify secondary hits. Afterwards the number of neutrons is determined from a combined condition on the number of clusters and the total deposited energy in NeuLAND.

Result

Table 1 shows the comparison of results with introduced limited integration time and PMT saturation versus the results from NeuLAND TDR for events with 3 and 4 incident neutrons. There is no significant change in the detection efficiency, but an increase of 3n to 4n misidentification due to declined energy resolution.

		3N	4N
3N	old	55	32
	new	60	34
4N	old	10	57
	new	18	59

Table 1: Comparison of detection efficiency and misidentification of events with 3 and 4 incident neutrons, obtained with the alternative model, versus benchmark results from [2]. The input is ^{132}Sn beam with an energy of 600 AMeV, a relative fragment energy of 500 keV and a distance of 15 m to the target. The columns represent the generated events and the rows the corresponding detected ones.

The decrease of the identification efficiency for one and two-neutron events, as the result of declined total energy resolution, was observed and has to be investigated in details. The work is ongoing in the direction of finding alternative parameters in the model, besides integration time, adjusting which might allow to have an agreement with the prototype experimental data and better full NeuLAND performance in simulation. In addition, the resolution of relative energy reconstruction of one neutron from a reaction with a beam energy of 600 AMeV, a relative energy of 100 keV was studied at a distance of 35 m between NeuLAND and the target. The resulting value is 13 keV, which fulfils the design goal for NeuLAND [2].

References

[1] D. Kresan *et. al*, GSI Scientific Report **2011**, p. 175

[2] R^{3}B Collaboration, Technical Design Report of NeuLAND **2011**

DOI:10.15120/GR-2015-1-MU-NUSTAR-NR-13

A compact readout system for the R3B High-Resolution Neutron Time-of-Flight Spectrometer (NeuLAND)*†

C. Ugur‡[1], *K. Koch*[1], *J. Hoffmann*[1], *M. Heil*[1], *and the FAIR@GSI project*[1]
[1]GSI, Darmstadt, Germany

The R3B High-Resolution Neutron Time-of-Flight Spectrometer consists of up to 30 double planes each containing 100 sub modules of plastic scintillators, which are read out on the far ends by two PMTs. For these 6000 channels a new compact and modular readout system has been developed. The electronics setup is divided into 16 channel amplifier and fast comparator boards. Digitization units using FPGA TDC technology with a timing precision of about 10 ps rms are used. Optional charge measuring boards based on the method of conversion of charge to time-over-threshold and configuration boards to parametrize thresholds, timings, etc. are also available.

The concept of the former readout electronics, TACQUILA, of the LAND experiment is taken as a base for NeuLAND. First, the TAC stage has been replaced by a high-precision TDC in an FPGA implemented on the new timing digitization board, TAMEX, which is designed as a multi-channel front-end electronics card for high precision time and charge measurements. Second, due to the higher data rate and the required enhanced precision, a new charge measuring unit, based on the method of conversion of charge to time-over-threshold, has been developed (QTC).

In addition to service boards, power boards and optical interfaces etc., the main electronics is divided into four parts. The front-end board (LANDFEE) receives the 16 incoming signals from the detector PMTs. These signals are galvanically isolated from the successional circuitry by appropriate transformers. In the next step the signal is divided into two parts: An analog part for charge measurement purposes and the second branch is directed to a fast comparator for timing determination.

The analog signal from LANDFEE is send to the charge measuring board (QTC), where the shaping and integration of the incoming signal takes part. By the method of time-over-threshold, this board delivers a logical signal directly to TAMEX. In parallel, the timing information travels through a connector to TAMEX to determine the timing of the leading and trailing edges of the signal.

An FPGA on TAMEX is used, among other things, as a fast 16 channel TDC. The power and trigger distribution to the cards is done through the backplanes and PCI-express connectors. The data transfer is also done through the backplanes and optical links using the Multi Branch System - MBS.

In order to handle the thresholds, monitor the analog channels, generate a logic OR, build a multiplicity and other things, a dedicated control card, TRIPLEX[2], has been developed as well. With an appropriate branch structure, including the analog signals as well as the digital ones, all planes can be configured and monitored from a central place.

The electronics is tested in the laboratory with a pulser with realistic detector signal shape for the charge and time measurements. The system has charge and time precisions of 0.9% and 16 ps respectively (Figure1).

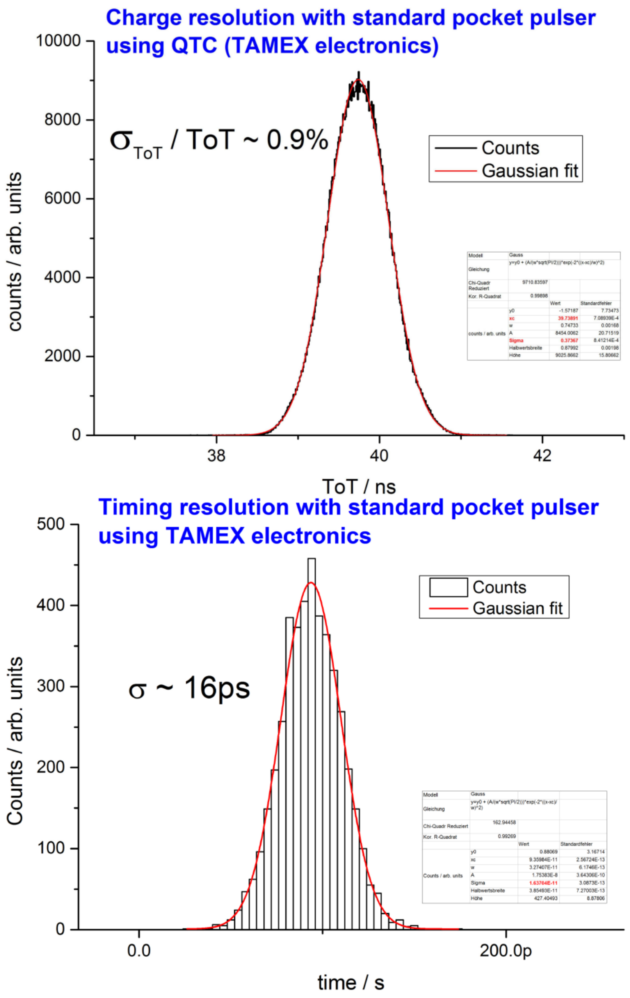

Figure 1: Charge (above) and timing (below) measurements of a pulser with realistic detector signal shape.

---

[*] This report is the summary of the conference report submitted at the "2014 IEEE Nuclear Science Symposium and Medical Imaging Conference" in 08-15 November 2015 in Seattle, WA, USA. The conference report is currently pending.

[†] Work supported by FAIR@GSI PSP 1.2.5.1.2.5.

[‡] c.ugur@gsi.de

DOI:10.15120/GR-2015-1-MU-NUSTAR-NR-14

The system is also tested under heavy ion beam conditions and the first test experiments performed at GSI in October 2014 show that the requirements on charge and time precision are met. The results of these test experiments are discussed by Heil et.al [1] in this GSI Scientific Report.

References

[1] M. Heil et.al, “In-beam tests of a new ToF wall for the R3B setup”, This GSI Scientific Report.

[2] K. Koch et.al, “TRIPLEX, an Upgrade for the TACQUILA System”, GSI Scientific Report 2010, PHN-IS-EE-07.

DOI:10.15120/GR-2015-1-MU-NUSTAR-NR-14

The in-beam tracking detectors of the R^{3}B experiment*

S. Paschalis[1], *G. Alkhasov*[4], *T. Aumann*[1,2], *C. Caesar*[2], *G. Gavrilov*[4], *R. Gernhäuser*[3], *M. Heil*[2], *M. Holl*[1], *J.G. Johansen*[1], *A. Kelić-Heil*[2], *O. Kiselev*[2], *D. Körper*[2], *A. Krivschich*[4], *Y. Litvinov*[2], *D. Maisuzenko*[4], *J. Marganiec*[1], *A. Movsesyan*[1], *M. Petri*[1], *R. Plag*[1], *H. Scheit*[1], *P. Schrock*[1], *H. Simon*[2], *S. Storck*[1], *I. Syndikus*[1], *J. Tscheuschner*[1], *H. Törnqvist*[1], *F. Wamers*[2], *the R*^{3}*B collaboration, and the FAIR@GSI division*

[1]TU Darmstadt, Germany; [2]GSI, Darmstadt, Germany; [3]TU, München, Germany; [4]PNPI Gatchina, Russia

Introduction

The R^{3}B experiment at FAIR is designed to perform kinematically complete measurements of reactions with relativistic radioactive beams with unprecedented efficiency and resolution. This will open up the way to fully exploit the rarest of the isotopes that will be available at the FAIR facility.

The R^{3}B apparatus is located at the high-energy branch behind the Super Fragment Separator (Super-FRS). The fully stripped ions ranging from Helium up to Uranium and moving at energies of about 1 AGeV are first selected and identified by the fragment separator before impinging on the secondary target at the entrance of the R^{3}B setup (see Fig. 1). A large acceptance superconducting dipole magnet (GLAD) is responsible for bending the rigid beams and dedicated detection systems are currently being developed for the efficient and precise detection of all reaction products.

The group of detectors dedicated for the tracking of the incoming beam and the tracking and identification of the beam-like charged particles constitutes an important part of the R^{3}B setup and is the subject of the present report. The Technical Design Report (TDR) for this detection system has been completed and submitted for evaluation in November 2014. In addition, in the last year two in-beam test experiments have been performed and enabled an extensive test of prototype tracking detectors. Here we report first on the choices for the future detectors and then present some results from the in-beam prototype-detector tests.

In-beam tracking detection system

The in-beam tracking detectors are measuring time-of-flight to extract the velocity of the ions, energy loss to obtain their charge, and positions to determine the trajectory of the ions. The timing is performed using plastic-scintillator detectors coupled to photomultiplier tubes. Their shape, size and type vary from few cm to more than one meter, depending on their position along the beam line. Position measurements are realised with a combination of position-sensitive Si detectors and plastic-scintillator fiber detectors. The energy loss is measured by Si and plastic scintillator detectors. Finally, a large area gas detector based on the strawtube detector technology is used for the detection of evaporated protons.

Start detector

In front of and close to the target a small and thin plastic scintillator (LOS) acts as the start timing detector whose time resolution is well below any other detector used in the R^{3}B setup. Its square-shape size of 5×5 cm^2 is optimised for direct coupling with four 2-inch photomultiplier tubes at each side for maximum light collection. The thickness is chosen for each experiment to minimise the material in the beam line while maintaining sufficient light output and excellent time resolution. For example, typical thicknesses for medium-mass nuclei are 200-500 μm allowing for a timing resolution of $\sigma \leq 10$ ps. The timing information is the average of the four photomultiplier signals. The readout of the four photomultiplier signals is performed using the PADI [1] preamplifier board and the VFTX TDC electronics [2].

Si detectors

Thin Si detectors are used along the beam line before and after the target in vacuum. Their purpose is twofold: 1) To obtain with minimum material adequate charge identification and 2) to obtain precise tracking information of the ions that impinge on or emerge from the target. The planned detector types that will be used are position-sensitive Si detectors based on resistive charge division and Si micro-strip detectors. The detectors between the target and the dipole magnet are the largest with a size of 10×10 cm^2 in order to cover most of ±80 mrad acceptance of the dipole magnet. Its thickness of about 100-200 μm is a compromise between minimal angular straggling and sufficient energy loss. Their position resolution requirement is on the order of 100 μm (σ), in both x and y coordinates. The signals from the Si detectors are digitised after the preamplifier stage with the FEBEX readout system [3].

Fiber detectors

Five detection systems based on plastic scintillator fibers are planned to be used for in-beam tracking. Three fiber detectors with an active area of 10×10 cm^2 are planned for position measurements before and after the target, to replace the Si detectors in experiments where the beam

---

* Work supported by BMBF (05P12RDFN8) and (05P12WOFNF), by GSI via the GSI-TU Darmstadt cooperation contract, by HIC for FAIR and by FAIR@GSI PSP code: 1.2.5.1.2.1..

DOI:10.15120/GR-2015-1-MU-NUSTAR-NR-15

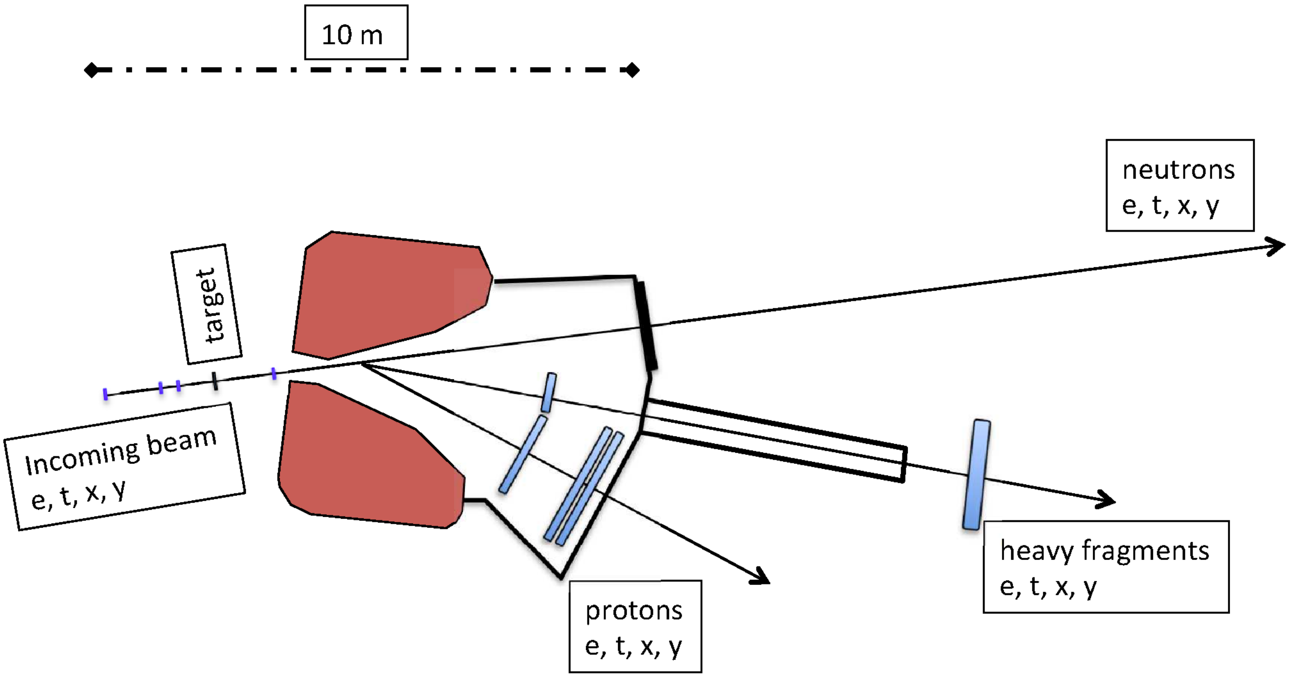

Figure 1: Schematic drawing of the R^{3}B setup showing the position of the in-beam tracking detectors before and after the GLAD dipole magnet.

rate is very high (1 MHz). These detectors will consist of 0.2×0.2 mm^2 square fibers placed in both x and y directions for two-dimensional position measurements. A fiber detector of 40 cm width with a single layer of fibers (x-position only) is used for the very critical first position measurement after the magnet, which serves as the starting point for the determination of the deflection angle. The distance between this detector and the subsequent position measurement is typically several meters, such that the angular measurement is a small fraction of a mrad. However, the angular straggling in the material of this detector is the dominant factor for the angle measurement after the magnet. A much larger fiber detector of 120×80 cm^2 is foreseen at the end of the fragments' flight path. We use two readout schemes. For the small and medium size detectors the fibers are coupled to Multi-Pixel-Photon Counters (MPPCs) whose signals are shaped and digitised with the FEBEX digitiser system. The larger size detector uses Multi-Anode Photomultiplier Tubes (MAPTs) which are read out using the GEMEX boards [4] equipped with n-XYTER readout chips [5].

Time-of-flight wall

The time-of-flight measurement is performed between the LOS detector in front of the target and a large-area-plastic-scintillator wall located at the end of the fragment arm (typically 20 m downstream from the target). At this position the fragments' spatial distribution is very broad and a size of 120×80 cm^2 is required to obtain a satisfactory acceptance. The 120 cm wide wall consists of four layers of vertically placed 2.7 cm wide scintillating paddles (44 paddles / layer). Each paddles is read out by photomultiplier tubes at each end. For the heavier isotopes an outstanding performance of 20 ps (σ) time-of-flight resolution is required. This resolution can be obtained as the average of the time measured by the four layers. The purpose of this wall is, however, twofold as it also acts as a precise nuclear-charge detector for the heavy fragments at the end of their flight path. A charge-to-time converter (QTC) coupled to the PADI preamplifier board and the VFTX TDC electronics will be used for the readout of the signals from the photomultipler tubes.

Straw-tube proton spectrometer

Large area gas detectors of up to 2.6×1 m^2, based on straw-tube technology, are planned in order to measure precisely the trajectory of the evaporated protons. Their position resolution is expected to be about 100-200 μm and they are designed to be vacuum compatible. Four detector stations are planned for obtaining x and y position information at two different locations about 1 m apart in the longitudinal direction. The first detector will be made out of kapton-wall tubes to introduce minimal material budget, and the following stations are made of aluminium-wall tubes.

DOI:10.15120/GR-2015-1-MU-NUSTAR-NR-15

In-beam performance of prototype tracking detectors

Rich data sets have been collected from recent in-beam test experiments (beam ions of ^{58}Ni and ^{48}Ca) where prototypes of the tracking detectors have been used. In this section we report on some of the results.

Si detectors

The Si detectors that have been tested in the two in-beam experiments are listed in Tables 1 and 2 together with some of their characteristics.

Table 1: The types of the Si detector that have been tested in the 1st in-beam experiment (s438) with a ^{58}Ni primary beam. Characteristics of the detectors used are given in the table, R$_p$ stands for the positioning resistance. HM is used for the Hamamatsu S5378 two-dimensional position-sensitive detector type, while X1 is used for the Micron-semiconductor position-sensitive strip detector. The X1 detectors also include both P- and N-type Si.

det name	HM	HM	HM	X1	HM	X1
type	2D	2D	2D	N-1D	2D	P-1D
thick (μm)	300	300	300	300	300	300
size (cm^2)	4.5^2	4.5^2	4.5^2	5.0^2	4.5^2	5.0^2
R$_p$ (kΩ)	2.0	2.0	2.0	1.5	2.0	1.5

Table 2: The types of the Si detector that have been tested in the 2nd in-beam experiment (s438b) ^{48}Ca primary beam. Characteristics of the detectors used are given in the table, R$_p$ stands for the positioning resistance. X1 is used for the Micronsemiconductor position-sensitive strip detector and W1 is a double-sided strip detector (not position sensitive) from the same company. The X1 detectors also include both P- and N-type Si.

det name	X1	X1	W1	X1	X1
type	1D	1D	2D	N-1D	P-1D
thick (μm)	140	140	70	300	300
size (cm^2)	5.0^2	5.0^2	5.0^2	5.0^2	5.0^2
R$_p$ (kΩ)	3.0	1.5	N/A	3.0	1.5

Fig. 2 shows the reconstructed position after selecting interstrip events from two position-sensitive Si strip detectors placed with their strips perpendicular to each other. The reconstructed lines allow for a position calibration of the detectors without the need of an external device and demonstrate their position resolution. The x projection of a y slice of Fig. 2 is shown in Fig. 3 and a position resolution better than 80 μm (σ) is obtained for the central peaks.

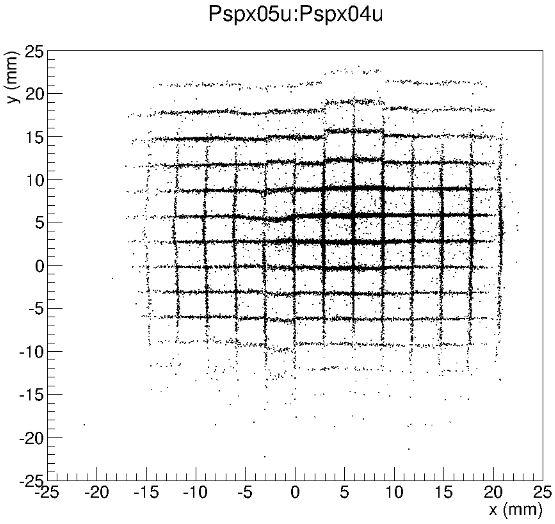

Figure 2: Position reconstructed from two position-sensitive Si strip detectors placed perpendicular to each other (the last two detectors in Table 2). The reconstructed lines in one detector correspond to the interstrip region of the other detector. The interstrip events have been selected by requiring energy signals in neighbouring strips. The detector signals have been gain matched with a linear function, higher order corrections are needed for the detector measuring the y coordinate.

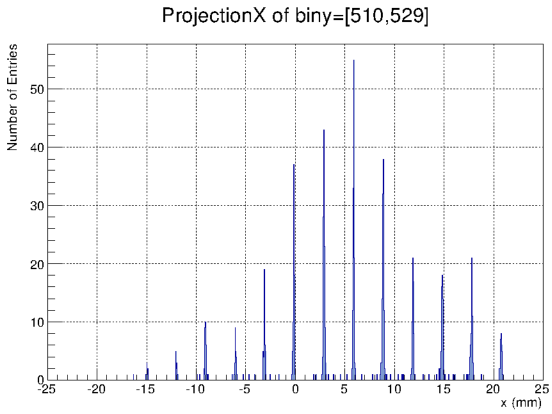

Figure 3: The projection on to the x axis of Fig. 2 for a narrow y slice. The position resolution obtained from a gaussian fit of the most intense central peaks is better than 80 μm (σ).

Fiber detectors

Two fiber detectors made of about 1000 fibres each with a cross section of 200$\times$200 μm^2 and 250$\times$250 μm^2 have been tested during the in-beam test experiments. One of the detectors is bundled in the way suggested in Ref. [6] in order to reduce the number of readout channels. In this detector the fibres are coupled to MPPCs whose signals are shaped and then digitsed by the FEBEX system. The second detector has each of its fibers individually read out by

DOI:10.15120/GR-2015-1-MU-NUSTAR-NR-15

multi-anode photomultiplier tubes. The signals from the PMs are read out using four GEMEX boards which employ two n-XYTER chips each. More details on this second fiber detector can be found in Ref. [7]. A correlation of the positions obtained from the two fiber detectors is shown in Fig. 4 for a dedicated in-beam run in which the field of the dipole magnet preceding the detectors was varied in order to illuminate the full detector size. Besides the strong correlation there is also a substantial number of background events that originate from misidentification of the hit fibers. The analysis for improving this correlation is ongoing.

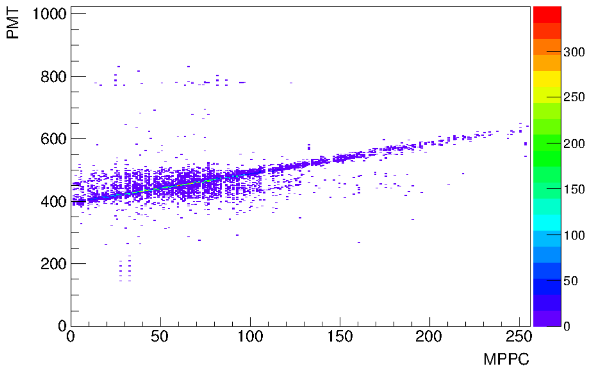

Figure 4: Correlation of x-position measurement, obtained from the two fiber detectors in units of fiber number.

Start detector and time-of-flight wall

A detailed description of the performance of both the start detector (LOS) and the time-of-flight prototype wall from the recent in-beam tests is presented separately in Ref. [8].

References

[1] M. Ciobanu et al, IEE Trans. Nucl. Sci. 61 (2014) 1015

[2] J. Frühauf, J. Hoffmann, E. Bayer and N. Kurz, GSI Scientific Report, 300 (2012)

[3] FEBEX homepage: https://www.gsi.de/work/fairgsi/rare_isotope_beams/electronics/digitalelektronik/digitalelektronik/module/font_end_module/febex.htm

[4] .S. Brogna et al., NIMA 568 (2006) 301

[5] .Vossetal.,GSIScientificreport2011,p.247

[6] S. Paschalis et al. “Heavy-ion tracking detectors for the R3B setup” GSI-SR2013-NUSTAR-KR-10, GSI Report 2014-1

[7] P. Schrock et al., “Development of a Thin Large-Area Fiber Detector for Radioactive-Beam Experiments” GSI-SR2012-PHN-ENNA-EXP-69, GSI Report 2013-1

[8] M. Heil “In-beam tests of a new ToF wall for the R3B setup”, GSI Report 2015

In-beam tests of a new ToF wall for the R^{3}B setup[*]

M. Heil[1], *A. Kelić-Heil*[1], *C. Caesar*[1,2], *J. Frühauf*[1], *M. Gilbert*[3], *J. Glorius*[3], *M. Heine*[2], *J. Hoffmann*[1], *K. Koch*[1], *D. Körper*[1], *N. Kurz*[1], *B. Löher*[2], *R. Plag*[1], *H. Simon*[1], *R. Thies*[4], *C. Ugur*[1], *H. Törnqvist*[1,2], *the R^{3}B collaboration*[1], *and the FAIR@GSI division*[1]

[1]GSI, Darmstadt, Germany; [2]TU Darmstadt, Germany; [3]Goethe Universität, Frankfurt, Germany; [4]Chalmers Tekniska Högskola, Göteborg, Sweden

Introduction

An important part of the R^{3}B setup will be the tracking system which allows the identification of mass and atomic number of the incoming beams as well as of the outgoing beam-like fragments and the emitted protons. Also, precise information on the momentum of the detected particles is required. The main design goals of the tracking system are: Measurement of the nuclear charge and mass with a resolution allowing separation of neighboring nuclei up to the Pb region; Total momentum measurement with a relative resolution of $\Delta P/P<2\text{x}10^{-3}$ (σ); Operation in a high-rate mode (up to 1 MHz) and in a multi-hit mode with large acceptance; Detection efficiency of the combined system should exceed 85%. These goals will be accomplished by using a series of detectors, see [1], placed before and after the large acceptance dipole magnet GLAD. Silicon detectors for energy-loss and position measurement, thin plastic scintillator fiber detectors for position measurements, fast scintillator detectors for timing and energy-loss measurements (ToF wall), and large-area straw-tube gas detectors for evaporated protons flying at forward angles through the spectrometer into the proton arm. Several prototypes of the tracking detectors have been tested during the S438 experiment in 2014 using stable beams of ^{58}Ni and ^{48}Ca at 500 *A*MeV. Especially valuable was also the SOFIA experiment with FRS settings for ^{187}Tl and ^{194}Bi at $\sim$ 700 *A*MeV which could be used in a parasitic manner and allowed us to test the detector properties for heavy nuclei.

In this report the main results of the Time-of-Flight (ToF) wall will be presented. A prototype of the new ToF wall was positioned about 13 m downstream of the target, behind the large-acceptance dipole magnet ALADIN. The ToF wall is based on a fast plastic scintillator material and the active part will cover an area of 120x80 cm^2 in the final stage. It will consist of 4 planes, each containing 44 vertical scintillator paddles with a thickness of 5 mm. The scintillators are read out by photomultipliers on both far ends. The prototype which was used for the tests was equipped with only 6 paddles per plane. In all experiments we have been able not only to measure incoming beams but also their residues created in reactions of incoming particles at different materials situated in front of the detector prototype. Beside the time-of-flight, this detector gives also information on the nuclear charge of the outgoing particles.

In [4] we have reported on LED tests of the ToF wall prototype. Here, we will discuss results obtained with heavy-ion beams in the above-mentioned beam times.

Results

During the beam tests two different read-out systems have been tested: A prototype of a new multichannel electronic card TAMEX [2] combined with the LAND front-end [3] and a general purpose Pre-Amplifier-Discriminator PADI [5] combined with a VFTX module [6]. The PADI system measures the time-over-threshold of the photomultiplier signals whereas the TAMEX electronics utilizes in addition a charge-to-time converter in order to determine the charge of the signal. Both systems have been developed by the GSI EE group.

Furthermore, the influence of different wrapping materials on the light transport in the scintillators were tested.

Time resolution

As discussed in Refs. [4, 7] in order to match the momentum resolution of other parts of the tracking system the relative time-of-flight resolution of the ToF wall should be around $2 \cdot 10^{-4}$ for nuclei in the lead region which translates into a time precision of better than 16 ps (σ) for the ^{197}Bi beam measured here. For lighter nuclei of course the requirements on the ToF resolution are not that strong; e.g. for the ^{58}Ni beam measured in this experiment a ToF resolution of 37 ps is sufficient.

Beam	σ_t **/ ps**	σ_t^{det} **/ ps**
^{48}Ca	52	18
^{58}Ni	41	14
^{194}Bi	22	8

Table 1: Time resolution measured with the ToF wall prototype (PADI electronics) between individual paddles (middle column) and the expected time resolution for the full detector (last column) for different incoming projectiles.

In the present experiments, the intrinsic time resolution of the detector was determined by the measurement of the time difference between two successive scintillator paddles which were hit by the same beam particle. Table 1 contains an overview of the measured time resolution and, based on these values, the expected performance for the full detector with 4 planes. It can be seen that the expected time resolution in all cases is well below the values needed to separate neighboring masses even for nuclei in the lead region.

During the ^{58}Ni beam time the properties of the ToF wall could be monitored for varying beam rates. Time and nuclear-charge resolution have been measured at 5 different rates ranging from 5 kHz to 1 MHz. It could be demon-

---

[*] Work supported by FAIR@GSI PSP code:1.2.5.1.2.1.

DOI:10.15120/GR-2015-1-MU-NUSTAR-NR-16

strated that the excellent performance can be maintained even at very high beam rates up to 1 MHz (see Table 2).

Rate / kHz	σ_t / ps	σ_t^{det} / ps
5	41	14
59	41	14
375	45	16
1000	64	23

Table 2: Time resolution measured with the ToF wall prototype (PADI electronics) between individual paddles (second column) and the expected time resolution for the full detector (last column) for different counting rates in the experiment with ^{58}Ni beam.

Nuclear-charge resolution

In the present experiments, the time-over-threshold measurement of the photomultiplier signals was used to determine the nuclear charge of the ions by energy-loss measurements in the scintillator. In order to separate charge Z from $Z-1$ even for the most challenging heavy beams (e.g. Pb) a nuclear-charge resolution of $\sigma_Z/Z<1\%$ is necessary. Table 3 shows the measured Z-resolution for the test beams and Fig. 1 shows a measured charge spectrum for a ^{194}Bi beam.

Beam	σ_Z	σ_Z/Z / %
^{48}Ca	0.15	0.75
^{58}Ni	0.19	0.68
^{194}Bi	0.34	0.41

Table 3: Nuclear-charge resolution measured with the ToF wall prototype (PADI electronics) for different projectiles.

One can see that even for ^{194}Bi the resolution is good enough to resolve neighboring charges.

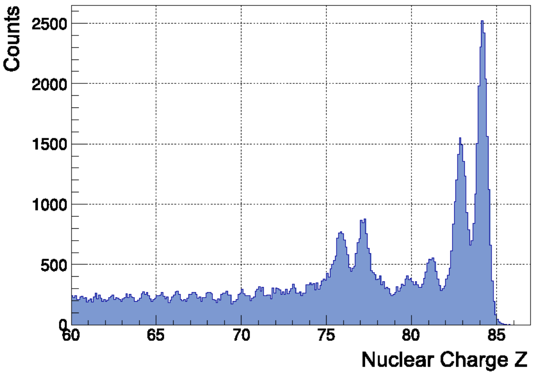

Figure 1: Nuclear-charge spectrum obtained from energy-loss measurements of two scintillator paddles for a FRS setting around ^{194}Bi. The main peak at Z=83 is suppressed by cuts in order to see neighboring charges better.

The performance of the detector was also checked at different beam rates with ^{58}Ni ions and an excellent Z-resolution around 0.2 Z-units (σ) could be achieved for rates up to 1 MHz.

Rate / kHz	σ_Z	σ_Z/Z / %
5	0.19	0.68
59	0.19	0.68
375	0.23	0.82
1000	0.23	0.82

Table 4: Nuclear-charge resolution measured with the ToF wall prototype at different counting rates using ^{58}Ni beam.

Furthermore, we have tested the stability of the nuclear-charge measurements at different rates. In experiments where beam rates can change drastically it is mandatory that the relative shift in the nuclear-charge measurements remains below 1% in order to avoid dependencies of the peak position in the energy spectrum on the counting rate. By choosing a photomultiplier voltage around 400 V, corresponding to signal amplitudes of about 60 mV, we have, during the ^{58}Ni experiment, reached very stable nuclear-charge measurements with relative shifts in Z remaining below 1% also for the highest rates of 1 MHz. This was only possible by using the new electronics read-out developed by the GSI EE group.

Conclusions

We have tested the properties of a prototype of the new ToF wall detector using several beams. We have shown that even in case of nuclei in the lead region we can fulfill the design goals concerning time-of-flight and nuclear-charge resolution even at the highest counting rates of 1 MHz.

References

[1] S. Paschalis et al., "The in-beam tracking detectors of the R3B experiment", Contribution to this report.

[2] C. Ugur et al., "A compact Readout System for the R3B High-Resolution Neutron Time-of-Flight Spectrometer (NeuLAND)", This GSI Scietific Report

[3] C. Caesar et al., "Heading towards FAIR: upgrades on the R3B-CaveC electronics", GSI Scientific Report (2009), p.310.

[4] M. Heil et al., "A new Time-of-flight wall for R3B", GSI Scientific Report 2013, p. 336.

[5] M. Ciobanu et al., IEE Trans. Nucl. Sci. 61 (2014) 1015.

[6] J. Frühauf et al., "VFTX (VME-FPGA-TDC 10ps)", GSI Scientific Report 2012, p. 300

[7] A. Kelić-Heil and M. Heil, "New time-of-flight system for the R3B set-up", GSI Scientific Report 2013, p. 340.

DOI:10.15120/GR-2015-1-MU-NUSTAR-NR-16

FPGA based multi-channel TDC development*

C. Ugur†1*, J. Frühauf*1*, J. Hoffmann*1*, M. Traxler*1*, and the FAIR@GSI project*1
1GSI, Darmstadt, Germany

The FPGA based multi-channel TDC technology has been used by many detector prototypes and experiments in the past years and will continue to be used for further detector tests and data digitisation[1]. The TDC design has been implemented on many electronic boards (TRB3, TAMEX, CBMToF, etc.) and the success of the technology has opened gates for additional implementations (DiRich for CBM), which drives new features and specifications. In this paper two of these new features - double edge measurement in a single channel and new readout scheme for zero data loss - will be discussed.

Pulse width measurements are of special interest in many of the charge measurement (after encoding the pulse charge to a digital pulse width) and Time-Over-Threshold (ToT) measurement applications. In almost all of the FPGA-based TDC applications the pulse width is measured by using two of the channels for leading and trailing edge time measurements separately, which doesn't induce any extra dead time but requires double the number of channels. In the new version of the TDC the leading and trailing edges of a digital pulse is measured by a single TDC channel.

In order to measure both of the edges in a single channel, the trailing edge of the input pulse has to be delayed longer than the dead time of the TDC channel (20 ns). This delay is achieved by stretching the pulse asynchronously in the FPGA by using the routing interconnections between the logic elements. After the successful measurement of the leading edge time, the delayed trailing edge is directed back to the channel in order to measure the trailing edge time. The type of the measured edge is marked in the data with a single bit.

The calculated time difference between the leading and the trailing edges - pulse width - contains a channel offset caused by the delay circuit, which needs to be calculated and subtracted from the result to find the real pulse width value. This value is different for each channel. This offset can be calculated by applying an external pulse to the TDC inputs with a fixed width and subtracting this fixed value from the measured width. As this is generally not possible in experimental setups, a pulse with a fixed width of 50 ns is generated by the internal oscillator of the FPGA and is sent to each channel. The same generated pulse is also used to calibrate the channels. In Figure 1 on the right, the pulse width measurement of a 2 ns pulse on a channel with an offset of $\sim$ 28 ns is shown. On the left the leading edge measurement between two channels in the same TDC is depicted. As seen, the leading edge time and the pulse width can be measured with precisions as low as 9 ps and 12 ps respectively.

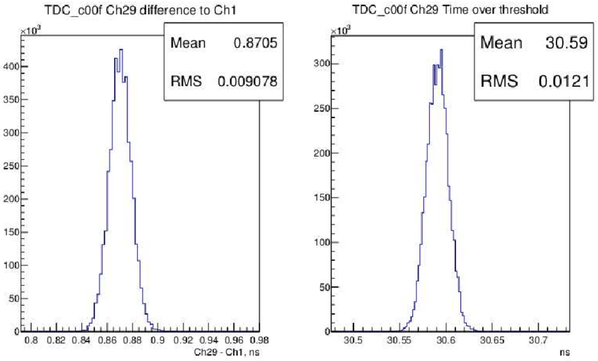

Figure 1: Leading edge (left) and pulse width (right) measurements of a pulse are done with the designed TDC.

The readout algorithm of the old TDC design was suitable only for triggered applications, as some of the hits after the trigger window could be lost during the readout of the data from the channel ring buffers. In order to adapt the TDC to trigger-less applications (such as PANDA) the readout scheme was changed.

In the new TDC a double buffer stage for each TDC channel is introduced. The first stage buffers, which are set as ring buffers, collect data as normal either until the end of the trigger window (in triggered applications) or the readout start signal from the system (in trigger-less applications). At this point the ring buffers are flushed directly to the second stage buffers, which are set as FIFOs. After flushing the first few words, the serialisation of the data from the second stage buffers begins. Any hit signal that might come during this process is saved in the relative ring buffer until the next trigger or readout start signal, hence no data is lost during the readout process.

The TDC development implemented in several electronic boards (TRB3, TAMEX, CBMToF, etc.) has been continued during the past year, introducing new abilities and features for better performance. These enhancements are being successfully tested in the laboratory as well as under beam conditions.

References

[1] C. Ugur et.al, "GSI Scientific Report 2013", p.89.

---

* Work supported by FAIR@GSI PSP codes: 1.4.1.5, 1.1.2.4

† c.ugur@gsi.de

DOI:10.15120/GR-2015-1-MU-NUSTAR-NR-17

MPPC readout of plastic scintillators*

P. Lasko[1], *J. Brzychczyk*[1], *J. Łukasik*[†2], *P. Pawłowski*[2], *C. Schuy*[3], *A. Snoch*[4], *Z. Sosin*[1], *C. Trautmann*[3,5], *W. Trautmann*[3], *M.B. Tsang*[6], *and K.-O. Voss*[3]

[1]Jagiellonian University, Kraków, Poland; [2]IFJ-PAN, Kraków, Poland; [3]GSI, Darmstadt, Germany; [4]University of Wrocław, Poland; [5]Technische Universität Darmstadt, Germany; [6]MSU/NSCL, East Lansing, USA

MPPC, a Multi-Pixel Photon Counter [1], belongs to the family of the silicon photomultipliers similar and competitive in many respects to the standard photomultiplier tubes. The main advantage of these fast light sensors, apart from a small size and relatively low biasing voltage, is their insensitivity to magnetic fields. This was the main reason to test them as light readout devices for prototypes of the Trigger Array designed for the SAMURAI experiments at RIKEN [2]. The Trigger Array has to provide fast (100-150 ns) trigger and veto signals for the SPiRIT TPC chamber placed inside the 0.5 T magnetic field of the SAMURAI magnet. The veto signal has to be generated for heavy (Z>20) fragments passing through the TPC, enabling a quick closure of the gating grid in that case. Thus, the array has to provide in addition a possibility of charge discrimination. A schematic setup of the beam test is presented in Fig. 1.

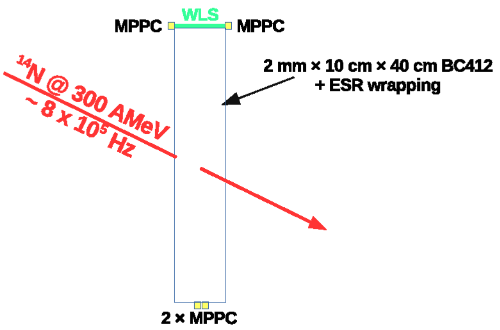

Figure 1: Schematic beam test setup.

During the S333 beam test, the 300 MeV/nucleon nitrogen ions were passing through the 2 mm thick BC412 plastic scintillator wrapped with a highly reflective ESR foil. The signals were read out in two ways: using the two 1×1 mm^2 MPPCs with 10000 pixels attached directly to one side of the scintillator and using the wave length shifting, WLS, fiber (BCF92) read out from both ends by the same type of MPPCs on the other side. The current pulses were amplified with custom designed fast preamplifiers [3] and digitized using the 500 MHz, V1730 digitizer.

Fig. 2 shows a sample wave-form for three nitrogen projectiles coming close in time. On average, the WLS fiber introduces about 2-3 ns delay as compared to the direct readout. The direct readout provides about 1 ns better time resolution (about 15 ns FWHM) and about 0.5 ns faster rise time (about 4.6 ns between 10-90% of the amplitude).

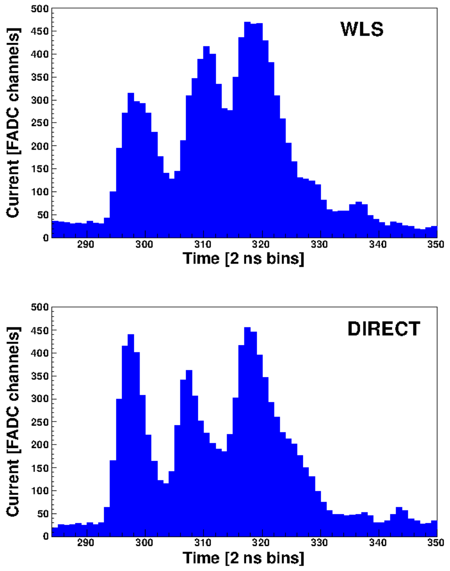

Figure 2: Pulse shapes for three neighboring projectiles readout using the WLS and direct methods with the 500 MHz digitizer.

The WLS readout has been tested because, in the first place, it should assure a better position independence of the amplitude. First tests also showed a slightly better amplitude resolution and a higher light collection, about 40% more as compared to the direct readout. The estimated charge resolution around Z=7 amounts to about 1.6 units of atomic number Z. Since the TPC measurements do not allow for very high beam intensity measurements anyway, a slightly better timing performance of the direct readout was found not to play a decisive role in selecting the final readout method. The final design of the Trigger Array assumes the WLS readout which assures a better position independence of the pulse amplitude, a fast rough charge determination of the passing through ion, and the on-line monitoring of the amplitude deterioration due to the radiation damage of the plastic scintillator. The usage of our custom designed [3] high stability and temperature compensated power supplies for the MPPCs is an additional advantage.

References

[1] http://www.hamamatsu.com

[2] https://groups.nscl.msu.edu/hira/sepweb/pages/home.html

[3] P. Lasko, PHD thesis, Jagiellonian University, in preparation.

---

[*] Work supported by Polish National Science Center (NCN), contract Nos. UMO-2013/10/M/ST2/00624, UMO-2013/09/B/ST2/04064

[†] jerzy.lukasik@ifj.edu.pl

DOI:10.15120/GR-2015-1-MU-NUSTAR-NR-18

DOI:10.15120/GR-2015-1-MU-NUSTAR-NR-18

Relativistic calculations of x-ray emission following a Xe-Bi^{83+} collision *

Y. S. Kozhedub†[1,2], *V. M. Shabaev*[1], *I. I. Tupitsyn*[1], *A. Gumberidze*[3], *S. Hagmann*[3], *G. Plunien*[4], *and Th. Stöhlker*[3,5]

[1]St. Petersburg State University, St. Petersburg, Russia; [2]SSC RF ITEP of NRC "Kurchatov Institute", Moscow, Russia; [3]GSI, Darmstadt, Germany; [4]TU Dresden, Dresden, Germany; [5]Helmholtz-Institut Jena, Jena, Germany

Experimental investigations aimed at the comprehensive study of various processes in low-energy heavy ion-atom collisions are anticipated at GSI and FAIR facilities (Darmstadt, Germany) [1, 2, 3] and require the corresponding theoretical calculations. In a recent experiment [4], the intensities of the post-collisional x-ray emissions have been resolved for collisions of Bi^{83+} ions with Xe target atoms at the projectile energy 70 MeV/u. In the present contribution we study the x-ray emission following the collision theoretically [5].

At this energy the ionization of the target is the dominant process, but the target excitation and the electron capture by the projectile ion are also possible. The excited xenon and bismuth ions decay via Auger processes or radiatively. In any case, the de-excitation processes (Auger or radiative decays) take much more time than the electronic dynamic processes during the collision. Therefore, the collisional and the post-collisional decay dynamics can be viewed as being independent from each other and thus we can treat them separately.

For the collision part, we solve the time-dependent Dirac equation within the semi-classical approximation and an independent electron model using the coupled-channel approach with the atomic-like Dirac-Fock-Sturm orbitals [6, 7]. The many-electron excitation, ionization and charge-transfer probabilities are calculated in terms of single-particle amplitudes employing the formalism of inclusive probabilities [8]. The inner-shell atom/ion processes are comprehensively studied and the corresponding probabilities are presented as functions of the impact parameter. As an example, one can see the probabilities of the Xe q-K-shell-vacancy production in Fig. 1.

The analysis of the post-collisional processes resulting in the x-ray emission is based on the fluorescence yields, the radiation and Auger decay rates, and allows to derive intensities of the x-ray emission. The relative intensities and comparison with the experimental data [4] are presented in Table 1. A reasonable agreement between the theoretical results and the experimental data is observed. The theoretical study demonstrates a very significant role of the relativistic effects, up to 50% for the bismuth x-ray radiation intensities. Thus, investigations of heavy highly charged ion-atom collisions seem very promising for tests of relativistic and QED effects in scattering processes.

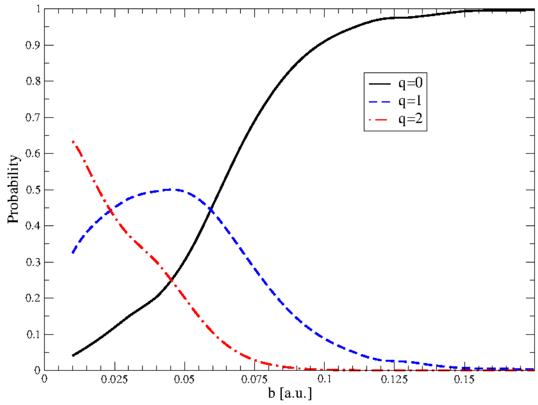

Figure 1: The probabilities of the Xe q-K-shell-vacancy production in the Xe-Bi^{83+} collision as functions of the impact parameter b.

Table 1: Relative intensities of the x-ray radiation for the Xe-Bi^{83+} collision. Both the relativistic (Rel.) and nonrelativistic (Nonrel.) results of the theoretical calculations are presented.

	Theory [5]		Exp. [4]
	Rel.	Nonrel.	
(Xe, L)/(Xe, K)	4.2(6)	4.4	3.6(2)
(Bi, K$_{\alpha_1}$)/(Xe, K)	0.43(14)	0.62	0.59(3)
(Bi, K$_{\alpha_2}$)/(Xe, K)	0.83(30)	0.88	0.69(3)

References

[1] http://www.gsi.de/en/research/fair.htm.

[2] http://www.gsi.de/sparc.

[3] M. Lestinsky *et al.*, *CRYRING@ESR: A Study Group Report* (unpublished).

[4] A. Gumberidze *et al.*, GSI Scientific Report 365 (2011).

[5] Y. S. Kozhedub *et al.*, Phys. Rev. A **90** 042709 (2014).

[6] I. I. Tupitsyn *et al.*, Phys. Rev. A **85**, 032712 (2012).

[7] Y. S. Kozhedub *et al.*, Phys. Scr. **T156** 014053 (2013).

[8] H. J. Lüdde and R. M. Dreizler, J. Phys. B **18**, 107 (1985); P. Kürpick, H. J. Lüdde, Comput. Phys. Commun. **75**, 127 (1993).

---

* Work supported by RFBR (Grants No. 14-02-31418, No. 13-02-00630, No. 12-03-01140-a, and No. 14-02-00241), GSI(ESR), and SPbSU (Grants No. 11.50.1607.2013, No. 11.38.269.2014, and No. 11.38.261.2014). Y.S.K. acknowledges the financial support from the Helmholtz Association and SAEC "Rosatom". The work of A.G. was supported by the Alliance Program of the Helmholtz Association (HA216/EMMI)

† kozhedub@pcqnt1.phys.spbu.ru

DOI:10.15120/GR-2015-1-APPA-MML-AP-01

Spatial characterisation of the internal gas target at the ESR for the FOCAL experiment

T. Gassner[1,2], *H. F. Beyer*[2], *and the FOCAL Collaboration*[1]
[1]GSI, Darmstadt, Germany; [2]Helmholtz-Institute Jena, Germany

The FOCAL experiment involves a highly accurate twin crystal spectrometer, designed to measure the Lamb shift of stored highly charged ions, like hydrogen-like Au^{78+}, with an accuracy down to the few-eV level where higher-order QED contributions become accessible [1]. Since the geometrical configuration of the whole apparatus is of crucial importance, all parameters influencing the final value have to be known as accurately as possible. In this annual report we present our efforts to characterise the internal gas target [2, 3] at the ESR at GSI Darmstadt were in 2012 the FOCAL experiment was conducted.

In the accurate spectroscopy of fast moving ions a recurring task is the transformation of the measured wavelength in the laboratory frame back to the wavelength in the emitter frame. The according relation between the laboratory wavelength λ_{lab} and the emitter wavelength $\lambda_{\mathrm{emitter}}$ is the relativistic Doppler formula

$$\lambda_{\mathrm{lab}} = \lambda_{\mathrm{emitter}}\,\gamma\,(1-\beta\cos(\theta_{\mathrm{lab}})) \qquad (1)$$

with two main unknown: The first unknown is the velocity of the ions hidden in the Lorentz parameters β and γ, the second one is the observation angle θ_{lab} under which the x-ray emission is measured. The velocity can be determined (in case of the ESR) with very high accuracy with the electron-cooler voltage. For determining the observation angle θ_{lab} one has to know the position of (i) the detector and (ii) the position of the emitter. In the FOCAL experiment conducted in 2012 as in many other experiments the position of the x-ray emitter is the volume defined by the intersection of the stored ion beam and the internal gas-jet target of the ESR. Since the detectors where accurately aligned with the help of optical telescopes just before the beam time the remaining unknown is the position and the density distribution of the gas target. Therefore the experiment presented in this report was conducted.

To measure the position, the diameter and the density distribution of the internal gas target of the ESR we decided to use a mechanical gas-scatter approach. At the low particle density of the gas target of only 10^{11} particles/cm^3 encountered other methods considered such as photon scattering or photo absorption/re-emission suffer from prohibitively low event rates. The probe used consisted of an aluminium body on which a Constantan wire of 0.6 mm diameter is tensed. If the gas jet hits the wire the pressure in the target chamber will rise which can easily be detected by standard methods. In order to scan the frame over a suitable position range it was mount on a linear actuator installed under 35° with respect to the ion-beam direction. All anchors for the wire are placed in a way that the wire runs parallel or perpendicular with respect to the ion-beam axis. Therefore it is possible to measure the density profile of the gas target in north-south (longitudinal) and east-west (transversal) direction and to determine a position centroid. In addition to the wire anchors there are also three fiducial marks used by the telescopes located left and right of the ion axis and in-line with the vertical gas-jet, respectively. This alignment is needed to relate our probe and hence the measured gas target position with the reference frame of the ESR.

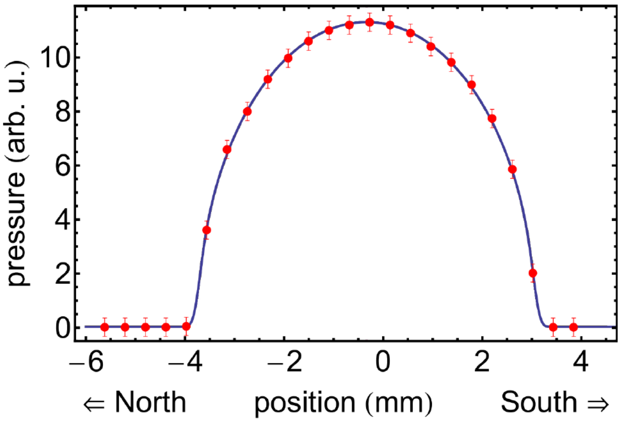

Figure 1: Measured pressure in the target chamber (red dots) as a function of the wire position. The blue curve is the best fit of our model which assumes a round gas-jet, with constant particle density in the center.

Figures 1 shows the measured pressure rise in the target chamber (red dots) and the best fit of our model (blue curve) assuming constant density in the central region of the round gas target. The measurement values are in good agreement with the model enabling us to determine the position and the diameter with an estimated uncertainty of ±0.3 mm dominated by small telescope imperfections leading to a significant reduction of systematic uncertainties.

References

[1] H. F. Beyer *et al.*, Spectrochimica Acta B **64**, 736 (2009)

[2] A. Gruber *et al.*, Nuclear Instruments and Methods in Physics Research A **282**, 87 (1989)

[3] M. Kühnel *et al.*, Nuclear Instruments and Methods in Physics Research A **602**, 311 (2009)

DOI:10.15120/GR-2015-1-APPA-MML-AP-02

Impact parameter sensitive study of inner shell atomic processes at the ESR*

A. Gumberidze[1], *C. Kozhuharov*[1], *R. Zhang*[1], *S. Trotsenko*[1,2], *H. F. Beyer*[1,2], *K.-H. Blumenhagen*[2,3], *C. Brandau*[1,4], *A. Bräuning-Demian*[1], *W. Chen*[1], *O. Forstner*[2,3], *B. Gao*[1], *T. Gassner*[1], *R. Grisenti*[1,5], *S. Hagmann*[1,5], *P.-M. Hillenbrand*[1], *P. Indelicato*[6], *A. Kumar*[7], *M. Lestinsky*[1], *Yu. A. Litvinov*[1], *N. Petridis*[1], *D. Schury*[1,4], *U. Spillmann*[1], *C. Trageser*[1,4], *M. Trassinelli*[8], *X. Tu*[1], *and Th. Stöhlker*[1,2,3]

[1]GSI Darmstadt, Germany; [2]Helmholtz Institute Jena, Germany; [3]Friedrich-Schiller-Universität Jena, Germany; [4]Justus-Liebig-Universität Giessen, Germany; [5]Goethe-Universität-Frankfurt, Germany; [6]ENS, CNRS, UPMC, Paris, France; [7]NPD, Bhabha Atomic Research Centre, Mumbai, India; [8]INSP, CNRS and UMPC, Paris, France

In this contribution, we present a further experiment from our program devoted to impact parameter sensitive studies of inner shell atomic processes for heavy atomic systems [1, 2] at the experimental storage ring (ESR). As compared to the previous measurement [3] whose conclusions were somewhat limited by the relatively poor statistics, in the current experiment we were able to clearly demonstrate the possibility of picking out the characteristic x-rays stemming from the close collisions only.

The experiment was performed with bare and He-like xenon ions (Xe^{54+}, Xe^{52+}) colliding with neutral xenon gas atoms, resulting in a symmetric collision system. This choice of the projectile charge states was made in order to compare the effect of a filled K-shell with the empty one. The final beam energy (for both charge states) was 50 MeV/u. This value of the beam energy was chosen as a compromise between the adiabaticity of the collision and the reasonable beam lifetime/intensity in the ESR after deceleration. Although the energy is not very low, one can still expect significant non-perturbative effects due to the heavy target. In order to obtain information concerning the impact parameter and, in particular to pick out close collisions which are especially important for observing quasi-molecular effects, the scattered projectile ions which had undergone close collisions with the target atoms were detected by a particle detector (plastic scintillator) mounted in a specially constructed movable pocket at $\sim$3.5 m downstream from the target. In the measurement position, the particle detector was covering the projectile scattering angles from $\sim$0.5 - 1.0° which, for the present collision system, corresponds to an impact parameter range of $\sim$35 - 70 fm. In addition to the detector for the scattered projectiles, the x-rays emitted from the interaction zone were observed by an array of detectors mounted at different angles with respect to the ion beam direction. Figure 1 (top part) shows a raw x-ray spectrum for the bare xenon ions recorded by a Ge(i) detector mounted at an observation angle of 35°. Transitions into the K-shell of H-like xenon due to the electron transfer from the target are clearly seen, together with the K-shell radiation of the target atom due to ionization of the corresponding shell. The inset displays the coincidence time spectrum between the x-rays (detected by the detector mounted at 35° observation angle) and the scattered projectiles. In addition, in the bottom part, we display the corresponding coincident x-ray spectrum containing only the x-rays detected in prompt coincidence with the scattered projectiles, i.e. stemming from the close collisions. One can clearly see a dramatic reduction of the projectile Kα radiation in the coincident spectrum. The data analysis is still in progress.

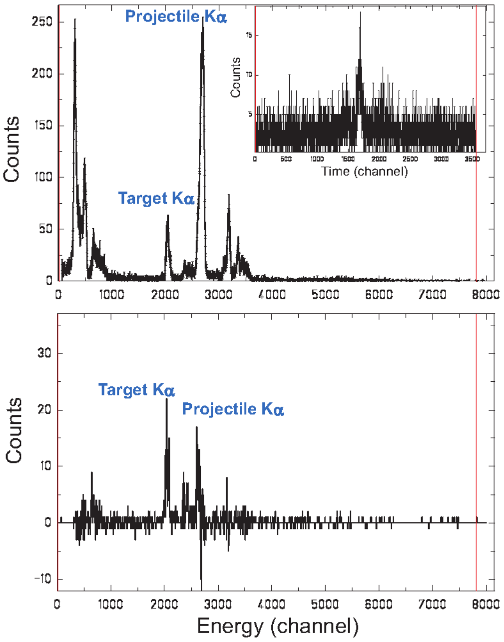

Figure 1: Preliminary results: (top) a singles x-ray spectrum for $Xe^{54+} \rightarrow Xe$ collisions at 50 MeV/u, recorded by the Ge(i) detector at 35° observation angle. (bottom) coincident x-ray spectrum containing only the x-rays detected in prompt coincidence with the scattered projectiles.

References

[1] Dorin-Cezar Ionescu and Thomas Stöhlker Phys. Rev. A 67 (2003) 022705.

[2] F. Bosch, in W. Greiner (ed.) Quantum electrodynamics of strong fields, Plenum Press, New York, 1983, p. 155.

[3] A. Gumberidze et al., GSI Scientific Report 2011, GSI 2012-1, p. 367.

---

* Work supported by Helmholtz Alliance EMMI.

DOI:10.15120/GR-2015-1-APPA-MML-AP-03

The HILITE Penning trap experiment

M. Vogel[1], *S. Ringleb*[4], *W. Quint*[1,2], *G. Paulus*[3], *and Th. Stöhlker*[1,3,4]
[1]GSI, Darmstadt; [2]Ruprecht Karls-Universität Heidelberg; [3]Universität Jena; [4]Helmholtz-Institut Jena

We have built a dedicated Penning trap setup for the preparation of suitable ion targets for irradiation with high-intensity laser light, and the study of subsequent reactions. Of particular interest is the detailed investigation of multiphoton-ionisation of confined particles by highly intense laser light. One important aspect is control over the confined particles' mass, charge, density, localization and optimized overlap with the laser light by Penning trap techniques like the use of trap electrodes as 'electrostatic tweezers' and by application of a 'rotating wall', respectively [1]. Also, the non-destructive detection of reaction products is a central property. The Penning trap setup is designed in a portable fashion, such that it can be attached to existing laser systems easily, see figures 1 and 2.

The interaction of highly intense radiation with matter and the corresponding non-linear effects have been subject of lively research, both theoretical and experimental, especially in the infrared and visible photon energy regimes. Laser systems capable of producing high intensities also at photon energies in the extreme ultra-violet (EUV) and (soft) X-ray regime open access to novel effects like non-linear Compton effects or simultaneous elastic and inelastic photon scattering, and allow multiphoton-ionisation experiments in a new domain. However, experiments have so far not been able to prepare and investigate well-defined particle ensembles and to non-destructively analyse the reaction products with high accuracy, nor were they able to select or prepare products for further studies in a well-defined way.

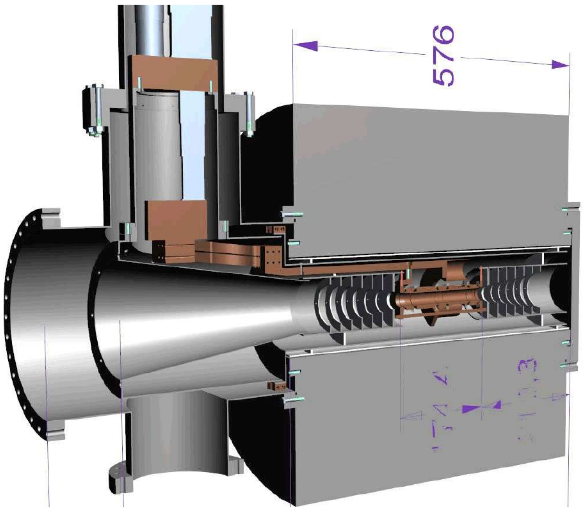

Figure 1: Cut through the HILITE setup in its current state with the Penning trap in the centre of the superconducting magnet.

The particles (atomic or molecular ions) are confined in the Penning trap following in-trap production or capture of externally produced ions. Confined ions can be cooled, compressed, positioned and selected with respect to their mass and charge prior to laser irradiation. The reaction products are analysed by non-destructive methods and hence remain confined for further studies. Such measurements are, for example, able to determine cross sections for multiphoton-ionisation in an energy- and intensity- regime so far not or not sufficiently examined. Additionally, the created electrons may be extracted from the trap and analysed externally. Hence, the reaction energetics may be reconstructed as completely as possible.

Figure 2: Photograph of the HILITE superconducting magnet setup currently located at the HITRAP facility.

We have completed the vacuum system and thermal radiation shielding which hosts the Penning trap inside the magnet bore, and cooled it to cryogenic temperatures using a two-stage cryo-cooler. The magnet has been operated at fields up to 6 T and the vacuum system has successfully been tested to leak rates below the 10^{-10} mbar l/s scale. We will now focus on the operation and detection electronics as well as on connectivity to an external (EBIT) ion source for highly-charged ions.

References

[1] M. Vogel, W. Quint, Th. Stöhlker and G.G. Paulus, Nucl. Inst. Meth. B **285**, 65 (2012).

DOI:10.15120/GR-2015-1-APPA-MML-AP-04

Pulsed beams at TRIGA-LASER and Ca$^+$ isotope shifts[*]

C. Gorges[1], *S. Kaufmann*[1], *T. Beyer*[2], *K. Blaum*[2], *Ch. E. Düllmann*[3,4,5], *Ch. Geppert*[3], *J. Grund*[4], *M. Hammen*[4], *J. Krämer*[1], *Sz. Nagy*[2], *D. Renisch*[3], *R. Sanchez*[5], *and W. Nörtershäuser*[1,3]
[1]IKP, TU Darmstadt, Germany; [2]MPIK, Universität Heidelberg, Germany; [3]Institut für Kernchemie, Universität Mainz, Germany; [4]HIM, Mainz, Germany; [5]GSI Helmholtzzentrum für Schwerionenforschung Darmstadt, Germany

The prototypes of the MATS and LASPEC experiments [1] for FAIR have been established as TRIGA-TRAP and TRIGA-LASER, respectively, at the Institute for Nuclear Chemistry at Mainz University. Together they form the TRIGA-SPEC setup [2] since they have a common beamline that will deliver short-lived isotopes produced inside the research reactor for high-precision Penning-trap mass spectrometry at TRIGA-TRAP and collinear laser spectroscopy at TRIGA-LASER. Here, we report on the progress at the collinear beamline in 2014.

A python based control system called ’TRITON’ has been developed for slow control of the experiment. It is a common frame in which voltages of the ion optics along the beamline, the readings of Faraday cups, pressure gauges, multi-meters, the status of valves along the beamline as well as the laser frequency are monitored and continuously recorded during operation. It allows for beam tuning by changing the ion optical settings and controlling the beam shape analyzing sections equipped with fluorescence screens and faraday cups. Additional devices can be easily added into a database structure, providing a very flexible system for future extensions.

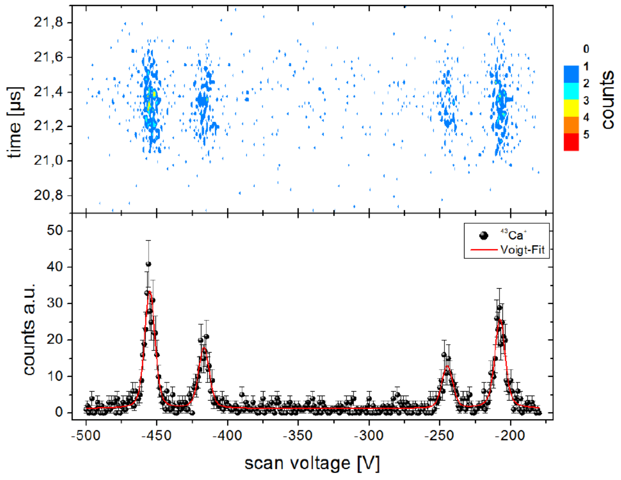

Figure 1: Time resolved spectrum of ^{43}Ca. The upper graph shows the time of flight of individual photons plotted against the scanning voltage. The countrate is color-coded. The lower trace shows the projection of the counts inside the relevant time window and the result of a hyperfine structure fit using Voigt profils.

Real time data acquisition (DAQ) and time-resolved photon detection was realized as a prototype on a field programmable gate array (FPGA). It has been tested using bunched beams produced by the RFQ cooler and buncher in the TRIGA-SPEC beamline. Figure 1 shows a time-resolved spectrum of ^{43}Ca$^+$. A low-intensity beam of this isotope was created from metallic calcium, which was inserted into the online ion source. After mass separation and cooling and bunching in the RFQ, short bunches were released towards the TRIGA-LASER beamline. From the upper chart, representing the photon detection times after release of the bunch from the RFQ, a bunch length of about 600 ns can be extracted. The counts detected between 21.0 and 21.6 μs are projected onto the Doppler-tuning axis in the lower graph and provide the hyperfine spectrum of this isotope. A second FPGA is now implemented into the system to establish all timing signals for the RFQ operation and Doppler tuning as well as the voltage control during a laser scan on the real-time system. this will then be completely embedded in a new phyton-based DAQ system running on a PXI system in which both FPGA’s are implemented.

Additionally, we were able to measure the isotope shifts of ^{42,44,48}Ca with respect to ^{40}Ca in the D2-line of Ca$^+$ and to reduce their uncertainty by about a factor of four. The results can be found in table 1.

Table 1: Isotope shift measurements in the D2-line (1st row) compared with literature [3] (2nd row). The brackets show statistical and systematical errors.

$\delta\nu_{\mathrm{IS}}^{40-42}$ [MHz]	$\delta\nu_{\mathrm{IS}}^{40-44}$ [MHz]	$\delta\nu_{\mathrm{IS}}^{40-48}$ [MHz]
426.4(15)(10)	850.1(10)(20)	1710.6(35)(42)
430.0(180)(40)	842.0(130)(80)	1699.0(190)(160)

The next steps that are taken at TRIGA-LASER are the establishment of the full DAQ system, further specifications of the longitudinal beam emittance of the bunches released from the RFQ, and to establish collinear-anticollinear laser spectroscopy to further improve the accuracy of isotope shift measurements.

References

[1] D. Rodriguez *et al.*, Eur. Phys. J. Spec. Topics **183** 1 (2010).

[2] J. Ketelaer, J. Krämer *et al.*, Nucl. Instrum. Meth. Phys. Res. A **594**, 162 (2008).

[3] A.-M. Martensson-Pendrill *et al.*, Phys. Rev. A **45**, 4675 (1992).

---

[*] Work supported by BMBF under Contract 05P12UMFN8, by the Helmholtz International Center HIC4FAIR, and by PRISMA.

DOI:10.15120/GR-2015-1-APPA-MML-AP-05

Commissioning of a continuous broadband data acquisition for Schottky signals in storage ring experiments at GSI and FAIR*

C. Trageser[1,2], *C. Brandau*[1,2], *C. Kozhuharov*[2], *Yu.A. Litvinov*[2,3], *A. Müller*[1], *F. Nolden*[2], *S. Sanjari*[2], *and Th. Stöhlker*[2,4,5]

[1]Justus-Liebig-Universität, Gießen, Germany; [2]GSI-Helmholtzzentrum für Schwerionenforschung, Darmstadt, Germany; [3]Ruprecht-Karls-Universität, Heidelberg, Germany; [4]Friedrich-Schiller-Universität, Jena, Germany; [5]Helmholtz-Institut, Jena, Germany

During 2013 and 2014 a modular New Time-Capture (NTCAP) data acquisition system for Schottky signals was set-up, tested off-line and finally commissioned with beam at the ESR [1, 2]. The main purpose of this device is to uninterruptedly record the RF-signals of storage ring's Schottky probes with high bandwidth for the typical duration of experimental runs at storage rings (1 - 4 weeks). Presently, the DAQ is optimized with respect to the new Schottky resonator with high quality factor that was installed 2010 at the ESR [3]. The core unit of the NTCAP-DAQ is a vector signal analyzer (VSA, NI PXIe-5663E) that internally shifts the RF signal by a carrier frequency down to frequencies around 0 and decomposes the signal into its in-phase (I) and quadrature (Q) components. With a maximum sample rate of 150 MSamples/s, the VSA is capable to deliver rates up to $7.5 \cdot 10^7$ IQ-Samples/s. The data is recorded as IQ raw-data in the time-domain for further offline processing and analysis. The VSA is supplemented by two latchable fast counter cards (100 kHz readout), a high precision oscillator, a synchronization module that can use network or GPS signals, and second digitizer. The details are described in [2].

The applications of such a versatile DAQ are manifold. The Schottky DAQ can run either stand-alone, or synchronized and seamlessly integrated into other experimental setups: in the latter mode it serves as a "beam-logbook" in support of the main experiment and records essential beam parameters such as the composition of stored species down to a single stored ion, the cooling process, frequency, intensity or stability of the beam. As a main DAQ it can be used for experiments on (time-resolved) Schottky mass spectrometry (SMS) and β-decay studies of highly charged ions, e.g., [4, 5]. It is proposed by our collaboration to also utilize the improved time-resolution that is achieved with the new Schottky resonator [3] for particle detection in atomic and nuclear reaction studies at the internal target or the electron cooler.

Already in the very first tests with a 400 MeV/u C^{6+} beam at the ESR the high performance of the NTCAP-DAQ could be shown. IQ rates of up to $3.5 \cdot 10^7$ IQ-Samples/s corresponding to a data rate of 140MByte/s could be sustained over hours. At the same time the recorded signal showed a high dynamic range, low noise and a low level of spurious distortions [2]. By oversampling of the signal further improve on dynamic range and noise level can be achieved offline using decimation or averaging algorithms before the Fourier transform into the frequency domain. In addition to these initial tests, two main experiments and several smaller measurements at the ESR were supported with our NTCAP-DAQ: in a beamtime on laser spectroscopy of Li-like $^{209}Bi^{80+}$ the DAQ was used to monitor the stability of the ion beam energy during the measurement and thus to help to improve significance and precision of this strong-field QED study. The second major experiment was a two-body β-decay study with single stored ions of $^{142}Pm^{60+}$ aiming at a clarification of the puzzling observation of a modulated non-exponential decay [6]. Figure 1 shows an example of such a decay demonstrating the capability of our DAQ to also work with weak signals on a single particle level.

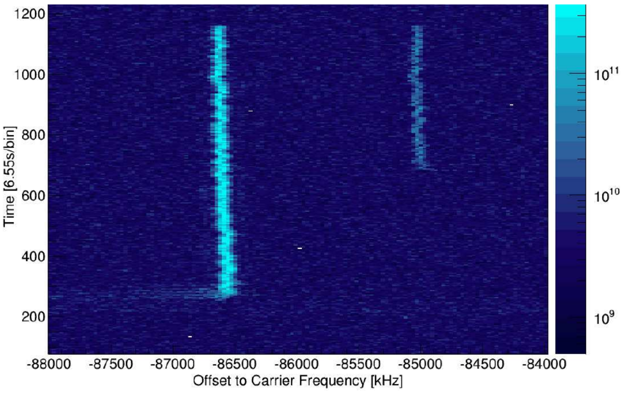

Figure 1: Single EC-decay of $^{142}Pm^{60+}$ (appearance of second trace) recorded with the NTCAP DAQ.

References

[1] C. Brandau et al., GSI Scientific Report 2013, p. 160.

[2] C. Trageser et al., Phys. Scr. T, submitted.

[3] F. Nolden et al., Nucl. Instrum. Meth. A **659** (2011), 69.

[4] Yu.A. Litvinov and F. Bosch, Rep. Prog. Phys. **74** (2011), 016301.

[5] F. Bosch et al., Progr. Part. Nucl. Phys. **73** (2013), 84.

[6] P. Kienle et al., Phys. Lett. B **726** (2013) 638.

---

[*] Work is supported by BMBF (contracts 06GI911I and 06GI7127/05P12R6FAN), by the Helmholtz-CAS Joint Research Group HGJRG-108 and by HIC for FAIR.

DOI:10.15120/GR-2015-1-APPA-MML-AP-06

Dielectronic recombination of rubidium-like tungsten ions

Z. W. Wu[1,2], *Y. Z. Zhang*[2], *Y. B. Fu*[2], *A. Surzhykov*[1], *S. Fritzsche*[1,3], *and C. Z. Dong*[2]
[1]Helmholtz Institute Jena, Germany; [2]Northwest Normal University, Lanzhou, China; [3]University of Jena, Germany

Owing to its high melting point, low sputtering rate and low absorption of tritium, tungsten has been utilized as a plasma-facing material in magnetically confined fusion facilities. Most recently, it was considered as a leading candidate for the divertor and main chamber regions of the International Thermonuclear Experimental Reactor (ITER) tokamak. Inevitably, tungsten ions are expected to be prominent impurities in fusion plasmas. The emitted radiation from excited tungsten leads to substantial plasma cooling that has to be well controlled in order to maintain conditions for nuclear fusion. In addition, dielectronic recombination (DR) is an important atomic process in such plasmas in which an initially free electron is captured by a target ion under simultaneous excitation of one of its bound electrons. This leads to a doubly excited state of the ion that may subsequently stabilize by photon emission. Accurate DR cross sections and rate coefficients are essential for simulating ionization balance of highly charged ions in high-temperature plasmas. Therefore, studies on the DR of tungsten ions have attracted much attention.

In the isolated-resonance approximation, if we assume that the electron velocity obeys the Maxwellian distribution in plasmas, DR rate coefficients can be given by

$$\alpha^{DR}(kT_e) = \left(\frac{2\pi\hbar^2}{m_e kT_e}\right)^{3/2} \frac{g_j}{2g_i} A^a_{ji} B^r_{j,f} \exp\left(-\frac{E_{ij}}{kT_e}\right). \quad (1)$$

Here, kT_e is the electron temperature, E_{ij} the resonance energy, g_i and g_j the statistical weights of initial and intermediate states, respectively. Moreover, $B^r_{j,f}$ denotes the radiative branching ratio and is defined in terms of the Auger decay rate A^a_{ji} and the radiative decay rate A^r_{jf}.

In order to learn importance of different subshell excitations, we perform *ab initio* calculations for DR of Rb-like W^{37+} through the intermediate doubly excited configurations $[Ne](3s^2 3p^6 3d^{10})^{-1} 4s^2 4p^6 4d\, nl\, n' l'$ with $n' \leq 16$ and $l' \leq 9$, and $[Ne]3s^2 3p^6 3d^{10}(4s^2 4p^6 4d)^{-1}\, nl\, n' l'$ with $n' \leq 18$ and $l' \leq 12$, while the contribution from other configurations with larger $n' l'$ is estimated by using the extrapolation procedures [1]. In Figure 1, we display total DR rate coefficients of initially W^{37+} ions together with partial contributions as associated with excitations of the $3s$, $3p$, $3d$, $4s$, $4p$, and $4d$ subshells as functions of the electron temperature. These coefficients are calculated for electron temperatures from 1 eV to 5×10^4 eV. Each partial contribution to total DR rate coefficients is given here by the sum of rate coefficients for the doubly excited configurations $[Ne](3s^2 3p^6 3d^{10} 4s^2 4p^6 4d)^{-1} nln' l'$ with all permitted nl and $n' l'$ combinations. As seen clearly in Figure 1, the excitation of $4p$ subshell dominates total DR rate coefficients in the whole region of electron temperature.

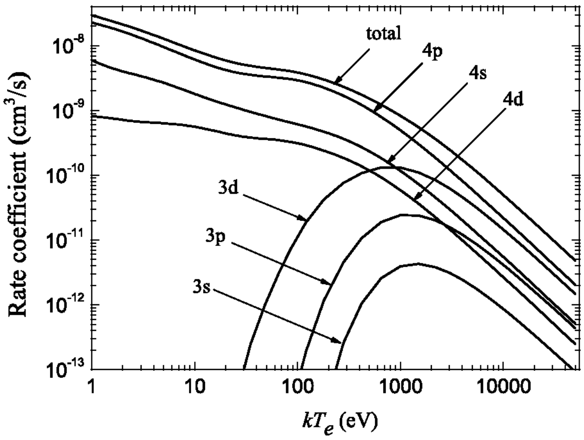

Figure 1: Total DR rate coefficients of initially Rb-like W^{37+} ion and the partial contributions associated with the excitations of $3s$, $3p$, $3d$, $4s$, $4p$ and $4d$ subshells as functions of the electron temperature kT_e. Each partial contribution gives the sum of rate coefficients for all DR channels corresponding to the excitations from nl subshells.

With respect to the excitation of $3l$ subshells, it is found that the DR rate coefficients for the excitation from $3d$ subshell are the largest and that the corresponding DR rate coefficients decrease with the quantum number l. For electron temperatures lower than 100 eV, the excitations of $3l$ subshells are much less significant than the ones of $4l$, and so its contributions to total DR rate coefficients can be neglected. However, as the electron temperature increases, the DR rate coefficients for the excitations of $3l$ subshells start to compete with their counterparts for the $4l$. This behavior arises mainly because of the influence of near-threshold states, since their resonance energies are quite small and since the DR rate coefficients have an $\exp(-E_{ij}/kT_e)$ dependence. Regarding the excitation of $4l$ subshells, the rate coefficients for the $4p$ excitation are the largest, while the contribution from $4s$ and $4d$ subshells cannot be neglected. The largest contributions to the total DR rate coefficients can reach 8% and 21% for the excitations from $4d$ and $4s$ subshells, respectively, even for electron temperatures below 100 eV.

References

[1] Z. W. Wu *et al.*, Eur. Phys. J. D, submitted (2014).

DOI:10.15120/GR-2015-1-APPA-MML-AP-07

Towards a fast calculator for the radiation characteristics of radiative recombination and radiative electron capture

G. Weber[*1,2], *H. Ding*[2,3], *M. O. Herdrich*[2,3], *and A. Surzhykov*[2]
[1]GSI, Darmstadt, Germany; [2]Helmholtz Institut Jena, Germany; [3]IOQ, FSU Jena, Germany

The radiative capture of free electrons (radiative recombination, RR) and bound electrons (radiative electron capture, REC) are among the most important charge changing processes for fast, highly-charged ions passing through matter. In particular for ongoing highly-charged ion studies at the ESR and for future experimental campaigns planned at the CRYRING@ESR and the high-energy storage ring (HESR) of the FAIR facility, precise knowledge of REC characteristics in a broad range of collision energies from about 1 MeV/u up to 5 GeV/u is highly desirable. When low- to medium-Z targets and heavy, highly-charged projectile ions are considered, the to-be-captured electrons can be treated as free particles having a momentum distribution equal to the one of the bound target states. This approximation reduces the REC description to the RR cross section folded with the incident electron momentum distribution. Consequently, both the REC and the RR processes, as well as the photoeffect (the time-reversal of RR), can be treated within the same theoretical framework [1]. While total cross sections can be obtained by an approximate formula with reasonable accuracy, the estimation of angular distributions and polarization properties of the emitted radiation requires a fully relativistic treatment that is numerical expensive. Therefore we recently started the development of a fast calculator (called RECAL) for all relevant characteristics of RR and REC photons. The program is based on a grid of rigorously calculated data points for RR into bare ions, between which interpolation is performed to obtain radiation characteristics for specific collision systems.

For the grid points, differential cross sections and linear polarization values of the RR photons were calculated using parts of the DIRAC toolkit, see [2]. The accuracy of the RR calculation is mainly determined by the accuracy of the continuum wavefunction representing the initial state of the incident electron, which is described by a series expansion in terms of partial waves. A careful choice of the number of partial waves, defined by $\nu = 2\kappa_{\mathrm{max}}$, with κ_{max} being the maximum number for the Dirac angular momentum to be taken into account, is of particular importance. More precisely, a too small choice of κ_{max} may lead to truncation errors, while, on the other hand, a too large value increases significantly computation time (approximately scaling with κ_{max}^3) and eventually leads to an explosion of numerical errors due to the rapid oscillations of the radial part of the continuum wavefunction.

For first test calculations, we generated a RR data base of capture into bare projectiles for atomic numbers Z between 1 and 92 and more than 100 kinetic energies between 2 MeV/u and 1 GeV/u. A comparison of angular differential RR cross sections obtained from the RECAL interpolation algorithm to fully relativistic calculations from [3] is shown in Fig. 1. Here the radiation stemming from the capture of free electrons into the ground state of bare lead ions was studied for several collision energies. An increasing deviation at high collision energies is seen, most probably due to an improper choice of κ_{max} for the underlying RR data base of the RECAL program. Currently, we are working on an optimized data base to provide reliable RR/REC cross section and linear polarization values for arbitrary collisions systems at ion beam energies between 1 MeV/u and 5 GeV/u.

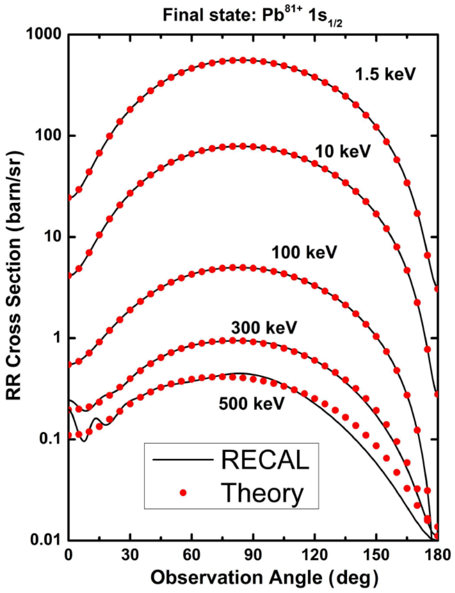

Figure 1: Angular differential RR cross sections for electron capture into the ground state of bare lead ions. Fully relativistic calculations from [3] are compared to RECAL predictions. An increasing deviation at high collision energies is seen due to an improper choice of κ_{max} for the underlying data base of the RECAL calculator.

References

[1] J. Eichler and Th. Stöhlker, Phys. Rep. **439** (2007) 1
[2] A. Surzhykov et al., Comput Phys Commun **165** (2005) 139
[3] A. Ichihara and J. Eichler, At. Data Nucl. Data Table **79** (2001) 187

---

[*] g.weber@gsi.de

DOI:10.15120/GR-2015-1-APPA-MML-AP-08

Lepton spectroscopy at storage rings: from electrons at ESR to positrons at HESR*

P.-M. Hillenbrand[1,2], *S. Hagmann*[1,3], *F. King*[3], *Yu. A. Litvinov*[1], *S. Schippers*[2], *K. E. Stiebing*[3], *and Th. Stöhlker*[1,4,5]

[1]GSI Darmstadt; [2]Universität Giessen; [3]Universität Frankfurt; [4]Universität Jena; [5]Helmholtz-Institut Jena

Electron spectroscopy at ESR

In collisions of heavy highly-charged projectile ions with atomic targets, the energy distribution of the emitted electrons is a characteristic observable for the underlying elementary processes. At the experimental storage ring ESR at GSI, a dedicated magnetic electron spectrometer was built downstream from the gas-jet target, which enabled the measurement of high-energetic electrons emitted in ion-atom collisions within a small cone in the forward direction. Using this electron spectrometer in combination with detectors for emitted x rays and charge-exchanged projectiles, the study of the collision system $U^{88+} + N_2$ @ 90 MeV/u revealed three processes resulting in the emission of electrons with a velocity similar to the projectile velocity, i.e., cusp electrons:

(a) The process of **electron loss to continuum** (ELC) corresponds to the ionization of an electron from the projectile into the projectile continuum during the collision with the target,

$$U^{88+} + N_2 \rightarrow U^{89+} + [N_2]^* + e^-.$$

For the ELC the measured spectrum was compared to first-order perturbation theory using fully-relativistic Dirac wavefunctions [1].

(b) The process of **electron capture to continuum** (ECC) corresponds to the capture of a target electron into the projectile continuum, while the excess energy is carried away by the recoil of the generated target ion:

$$U^{88+} + N_2 \rightarrow U^{88+} + \left[N_2^+\right]^* + e^-.$$

For the ECC the measured spectrum was compared to calculations in the impulse approximation using semi-relativistic Sommerfeld-Maue wavefunctions and to calculations the in continuum-distorted-wave approach [2].

(c) The process of **radiative electron capture to continuum** (RECC) corresponds to the capture of a target electron into the projectile continuum, while the excess energy is carried away by a photon:

$$U^{88+} + N_2 \rightarrow U^{88+} + \left[N_2^+\right]^* + e^- + \gamma.$$

This latter process can be seen as the high-energy endpoint of bremsstrahlung studied in inverse kinematics. For the RECC the measured spectra were compared to calculations in the impulse approximation using semi-relativistic Sommerfeld-Maue wavefunctions, and to calculations using fully-relativistic Dirac wavefunctions [3].

Positron spectroscopy at HESR

Based on the experience gained with the magnet electron spectrometer at the ESR, an experimental concept for positron spectroscopy at the high-energy storage ring HESR at FAIR was developed [4]. The high projectile energy of up to 5 GeV/u accessible at HESR facilitates the study of electron-positron pair production processes through coincidence experiments observing the emitted positron and the singly or doubly charge-exchanged projectile. For the example of collisions U^{92+} + Ar two processes have been contrasted in Ref. [4]:

(a) The process of **bound-free pair production** (BFPP) results in the emission of a positron and a singly charge-exchanged projectile:

$$U^{92+} + \mathrm{Ar} \rightarrow U^{91+} + \mathrm{Ar}^* + e^+.$$

Its theoretical description requires a relativistic two-center approach, since the electron-positron pair is generated in the combined Coulomb field of projectile and target nucleus.

(b) The hitherto unobserved process of **negative-continuum dielectronic recombination** (NCDR) results in the emission of the positron and a doubly charge-exchanged projectile:

$$U^{92+} + \mathrm{Ar} \rightarrow U^{90+} + \left[\mathrm{Ar}^+\right]^* + e^+.$$

Its theoretical description requires a relativistic single-center approach, since the electron-positron pair is generated by the energy released in the recombination of a target electron into a bound state of the projectile ion.

Electron-optical simulations for the design of a positron spectrometer at the HESR derived from the electron spectrometer at the ESR were performed and resulted in the application of BMBF Verbundforschung for developing and building such a positron spectrometer.

References

[1] P.-M. Hillenbrand *et al.*, Electron-loss-to-continuum cusp in U^{88+} + N_2 collisions, Phys. Rev. A **90**, 042713 (2014).

[2] P.-M. Hillenbrand *et al.*, Electron-capture-to-continuum cusp in U^{88+} + N_2 collisions, Phys. Rev. A **91**, 022705 (2015).

[3] P.-M. Hillenbrand *et al.*, Radiative-electron-capture-to-continuum cusp in U^{88+} + N_2 collisions and the high-energy endpoint of electron-nucleus bremsstrahlung, Phys. Rev. A **90**, 022707 (2014).

[4] P.-M. Hillenbrand *et al.*, Experimental concepts of positron spectroscopy at HESR, Phys. Scr., *submitted* (2015).

---

* Work supported Helmholtz-CAS Joint Research Group HCJRG-108 and BMBF Contract No. 05P12RFFAH.

DOI:10.15120/GR-2015-1-APPA-MML-AP-09

Precise polarization studies of radiative electron capture

G. Weber[*][1,2], *H. Ding*[2,3], *H. Bräuning*[1], *R. Hess*[1], *S. Hess*[1], *R. Märtin*[1,2], *U. Spillmann*[1],
S. Trotsenko[1,2], *D. F. A. Winters*[1], *and Th. Stöhlker*[1,2,3]
[1]GSI, Darmstadt, Germany; [2]Helmholtz Institut Jena, Germany; [3]IOQ, FSU Jena, Germany

The capture of electrons into bound states of ions is of significant importance for both experiment and theory in the fields of atomic and plasma physics as well as for astrophysics. The capture process is called radiative if it is accompanied by the emission of a photon that carries away the initial electron's kinetic energy and the binding energy of the final state it is captured into. If the initial electron is considered to be free, the capture process is referred to as radiative recombination (RR), being the time-reversal of the photoelectric effect, whereas the capture of a bound electron is called radiative electron capture (REC) [1].

The REC process is a prominent charge-changing process for fast, highly-charged ions interacting with dedicated target materials or with residual gas being present in the beamlines of accelerators and storage rings. Moreover, when low- to medium-Z targets and heavy, highly-charged projectile ions are considered, the to-be-captured electrons can be treated as free particles having a momentum distribution equal to the one of the bound target states. This so-called impulse approximation reduces the REC description to the RR cross section convoluted with the incident electron momentum distribution. Consequently, both the REC and the RR process as well as the photoeffect can be treated within the same theoretical framework. Moreover, when compared to the photoeffect, the RR/REC process offers several experimental advantages, such as a more uniform emission pattern due to the partial cancelation of retardation and Lorentz transformation for a moving emitter system and the fact that x-rays, in contrast to electrons, can typically leave the target zone unaffected by secondary-collision effects. These facts motivated various REC measurements aiming for a deeper insight into the photoeffect while exploiting the advantageous experimental conditions present for the study of electron capture into fast, highly charged ions.

A first study of the linear polarization of REC photons was published in 2006 [2] where a 4 × 4 pixel Ge(i) detector was used for Compton polarimetry of x-rays emitted in collisions of bare uranium ions with a N_2 target at the experimental storage ring (ESR) of GSI. The experimental findings are presented together with theory values in figure 1a. Having only 16 pixels, the relatively low granularity of the detector resulted in a poor angular resolution of the Compton scattering distribution, which limited the experimental accuracy to an uncertainty between ±5 % and ±10 % with respect to the degree of linear polarization. The much higher granularity of a newly developed Si(Li) polarimeter [3](see figure 1b) enables more precise studies and this instrument was already applied in a series of test measurements also addressing the REC radiation [4,5]. Data analysis is still in progress and we expect an experimental uncertainty for these new polarization studies in the order of ±1 % of the degree of linear polarization. With regard to future experiments at the new FAIR facility it is worth noting that while the existing ESR is limited to typical ion energies not higher than 400 MeV/u for beams of heavy ions, the planned high-energy storage ring (HESR) will reach up to approximately 5 GeV/u for bare uranium. With the extended energy range it will become possible to probe the cross-over effect in the degree of REC photon linear polarization which is predicted to occur at collision energies above 600 MeV/u and for forward emission angles, see the theory data for 800 MeV/u in figure 1a. In terms of the photoeffect this feature indicates that the initially bound electron is no longer preferentially ejected in the direction of the incident photon electric field vector, instead emission along the magnetic field vector is dominant.

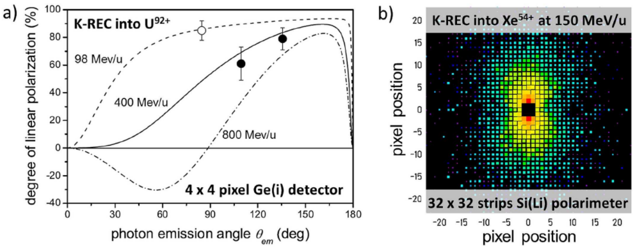

Figure 1: a) Degree of linear polarization of the radiative electron capture (REC) into the K-shell of bare uranium projectiles measured with a 4 × 4 pixel Ge(i) detector applied as a Compton polarimeter [2]. b) Position distribution of Compton scattered K-REC photons inside the Si(Li) polarimeter for the capture into bare xenon ions. Data analysis with respect to the degree of linear polarization is ongoing. The much higher granularity of the new detector is expected to enable significantly more precise measurements compared to the 16 pixel detector.

References

[1] J. Eichler and Th. Stöhlker, Phys. Rep. **439** (2007) 1

[2] S. Tashenov et al., Phys. Rev. Lett. **97** (2006) 223202

[3] G. Weber et al., JINST **5** (2010) C07010

[4] S. Hess et al., J. Phys. Conf. Ser. **163** (2009) 012072

[5] S. Hess et al., J. Phys. Conf. Ser. **194** (2009) 012025

---

[*] g.weber@gsi.de

DOI:10.15120/GR-2015-1-APPA-MML-AP-10

Improved accuracy of in-ring Laser spectroscopy by in-situ electron cooler voltage measurement*

Johannes Ullmann[1,2] *and the LIBELLE collaboration*
[1]Institut für Kernphysik, Technische Universität Darmstadt, Germany; [2]Helmholtz Institute Jena, Jena, Germany

Introduction

Laser spectroscopy experiments of highly charged, heavy ions at the experimental storage ring ESR have been performed for more than twenty years by now [1, 2, 3], aiming at tests of fundamental theories. A conclusive test of bound-state quantum electrodynamics (BS-QED) in strong fields, however, has not been reached so far, because of the large uncertainty arising from the unknown spatial distribution of the nuclear magnetization (Bohr-Weisskopf effect). The method formulated by Shabaev and coworkers [4], defining a specific difference between the hyperfine splittings in hydrogen- and lithium-like ions of the same species removes these uncertainties and provides the possibility to test BS-QED without nuclear uncertainties. Although the attempt in 2011 to measure the hyperfine splitting energies of the ground states in hydrogen- and lithium-like bismuth ions was for the first time successful in detecting both resonances, it yielded a large uncertainty caused by an inaccurate knowledge of the ion velocity [5]. Hence, a second attempt was performed in March 2014 with an improved setup.

Setup

The setup was similar to previous experiment in 2011 and is shown in fig. 1. Ions injected into the ESR were cooled with the electron cooler and confined into two bunches using a radio frequency (RF)-cavity, driven with the second harmonic of the revolution frequency. With a bunched beam, the fluorescence signal-to-background ratio could be improved by 50% compared to coasting beam operation. The bunching frequency was used for tagging the arrival times of single photon counts on the photomultiplier tubes by the data acquisition system with 3.3-ns resolution. This was realized using time-to-digital converters implemented on a VUPROM-device[1]. The fluorescence light detection efficiency was optimized in the two cases using two mirror systems adapted to the specific needs of the respective transition and shown on the right side of 1: For the hydrogen-like ions the detection chamber developed for [2] (upper part) and for the lithium-like species the system developed at the University of Münster [6] were used. The excitation of the hyperfine transition was performed by a dye laser system consisting of a Nd:YAG pump laser and a Sirah COBRA dye-laser that provided pulses with energies of 150 mJ. The target laboratory frame wavelengths of 591 nm and 641 nm were produced by Pyrromethene 597 dye and DCM Special dye, respectively, and the light was delivered to the ESR experimental hall using mirrors with a high-reflectivity coating.

A major improvement of the setup was the in situ measurement of the electron cooler voltage, which is used to determine the ions' velocity for Doppler shift compensation. The data analysis of the previous attempt in 2011 revealed that the calibration of the electron cooler voltage display was insufficient, leading to large uncertainties [7]. To circumvent this, an accurate high-voltage divider was installed. A newly established collaboration with the high-voltage metrology working group of PTB[2] enabled us to use a reference voltage divider featuring a relative accuracy of 10^{-5} [8]. An additional measurement of residual frequencies in the d.c. high voltage using a ripple probe developed at PTB revealed a very clean high voltage signal. Besides the anticipated leap in accuracy, the voltage measurement turned out to be a invaluable diagnostic tool. Energy fluctuations of the ion beam that emerged during beamtime could be identified to originate from a floating drift tube inside the electron cooler, and could be clearly distinguished from fluctuation of the high-voltage power supply that also arose during beamtime. The in-situ measurement allowed us to take all voltage fluctuations into account during the analysis.

First Results

The analysis of the fluorescence data was performed using GO4 and SciPy. A typical resonance for hydrogen-like bismuth recorded in one single scan of the laser wavelength with coasting ion beam is shown in the left part of fig. 2. The resonance wavelength in the laboratory frame was determined by fitting a Gaussian profile to the fluorescence data using the orthogonal distance regression algorithm [10] to take the uncertainty of the laser wavelength determination into account. Although the analysis is still ongoing, first results of the rest-frame wavelength of the ground state hyperfine transition in hydrogen-like bismuth could be obtained [9] demonstrating the advantage of the high-voltage measurements. The analysis of the resonances taken without bunching the ion beam ("coasting beam") resulted in a value roughly 10 times more accurate compared

---

* Work supported by HIC4FAIR, HGS-HIRe, BMBF contract Nos. 05P12PMFAE and 05P12RDFA4.

[1] **V**ME **U**niversal **Pro**cessing **M**odule, an FPGA-based module for VMEbus-systems developed at GSI's experiment electronics department

[2] Physikalisch Technische Bundesanstalt Braunschweig, the German national metrology institute

DOI:10.15120/GR-2015-1-APPA-MML-AP-11

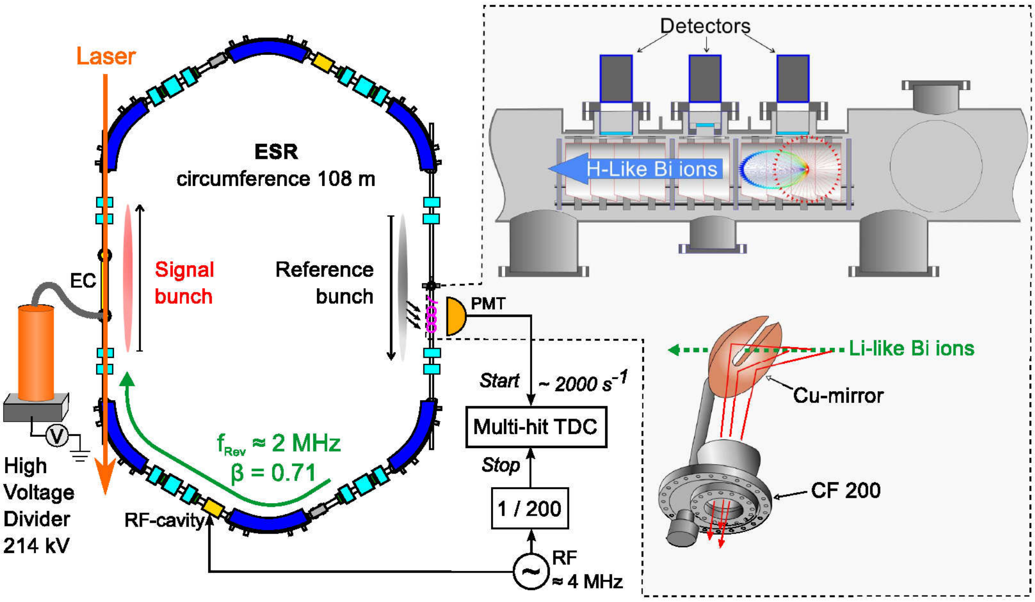

Figure 1: Experimental setup:The voltage of the electron cooler (EC) gun determines the ion velocity in the ESR and is measured with a precise high-voltage divider (HVDC2.1 from PTB). The upper part of the inset shows the detection section used for the hydrogen-like charge state which was reused from [2], the lower part shows the retractable parabolic mirror system [6] for detection of the forward cone-shaped emission characteristic of lithium-like bismuth. All photons detected at one of the two mirror systems are tagged on a VUPROM multi-hit TDC with an absolute time stamp as well as relative to the phase of the revolution frequency.

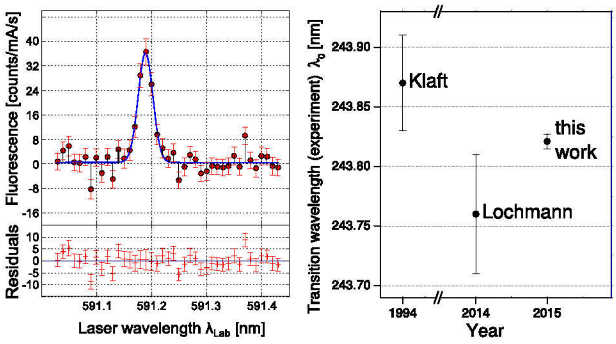

Figure 2: Left: Single resonance signal of hydrogen-like bismuth taken with a coasting ion beam. The fluorescence counts are normalized to ion current and live time of the data acquisition. A fit of a Gaussian profile and the corresponding residuals are also shown. Right: Result of the rest-frame wavelength of the ground state hyperfine transition in hydrogen-like bismuth, compared to previous attempts. The result is compatible with the prior values and its accuracy has been improved by a factor of 10 [9].

to the previous attempts, as shown in the right part of fig. 2.

Conclusion

According to the first results of the LIBELLE 2014 beam time, a QED test using the hyperfine splittings in bismuth ions is in reach now. The accuracy of the obtained hydrogen-like bismuth wavelength is an order of magnitude higher than in all previous attempts and promises a similar leap in accuracy for the lithium-like charge state and, consequently, also for the specific difference. Lifetime measurements for both transitions have been performed as well and are currently under evaluation at the University of Münster. Furthermore, it has been pointed out, that an accurate *in-situ* voltage measurement is vital for laser spectroscopic measurements at the ESR and a valuable diagnostic tool for other experiments using the electron cooler. Hence, a dedicated high voltage divider is currently commissioned and will soon be installed at the electron cooler.

References

[1] I. Klaft et al. *Phys. Rev. Lett.*, **73** (1994), 2425.

[2] P. Seelig et al. *Phys. Rev. Lett.*, **81** (1998), 4824.

[3] Winter. Dissertation, Universität Darmstadt (1999).

[4] V. M. Shabaev et al. *Phys. Rev. Lett.*, **86** (2001), 3959.

[5] M. Lochmann et al. *Phys. Rev. A*, **90** (2014), 030501. PRA.

[6] V. Hannen et al. *J. Instrum.*, **8** (2013), P09018.

[7] M. Lochmann. Ph.D. thesis, Johannes Gutenberg Universität Mainz (2013).

[8] J. Hallstrom et al. *IEEE Trans. Instrum. Meas.*, **63** (2014), 2264.

[9] J. Ullmann et al. *J. Phys. B: At. Mol. Opt. Phys.* (2015). Submitted.

[10] P. T. Boggs et al. *SIAM J. Sci. Comput.*, **8** (1987), 1052.

Capturing highly charged ions in the SpecTrap penning trap*

T. Murböck[1], *G. Birkl*[1], *A. Martin*[1], *K. König*[2], *W. Nörtershäuser*[2], *S. Schmidt*[2], *Z. Andelkovic*[3], *M. Vogel*[3], *V. Hannen*[4], *J. Vollbrecht*[4], *C. Weinheimer*[4], *D. Segal*[5], *and R. Thompson*[5]

[1]IAP, TU Darmstadt; [2]IKP, TU Darmstadt; [3]GSI, Darmstadt; [4]Westfälische Wilhems-Universität, Münster; [5]Imperial College London

The SpecTrap collaboration aims to perform high precision laser spectroscopy of forbidden transitions in highly charged ions (HCIs). Similar experiments performed to date with ions stored in an EBIT or in a storage ring still suffer from Doppler broadening or the difficulties in wavelength conversion between the laboratory frame and the rest frame [1, 2]. Therefore, the SpecTrap experiment employs a cryogenic Penning trap suitable for trapping externally produced ions and sympathetically cooling them with laser cooled Mg^+ ions [3]. Cooling of HCI to the mK-regime will dramatically reduce the Doppler broadening of the fluorescence signal and allow the measurement of the hyperfine splitting of the HCI with an expected relative accuracy of up to 10^{-8} for a stringent test of bound state QED.

In 2014 we have investigated and optimized the transport properties of the low-energy beamline connecting the SpecTrap Penning trap with an electron beam ion source (EBIS). This EBIS is used for production of argon ions with any desired charge state up to bare Ar. The desired charge state can be selected by adjusting the breeding time of argon in the EBIS and the magnetic field of the multi passage spectrometer (MPS). By adjusting the timing of a pulsed drift tube to the time of flight of the desired charge state the ion energy can be reduced for trapping. It has been demonstrated that transport and trapping of any charge state from Ar^{3+} to Ar^{16+} can be selected within a few seconds.

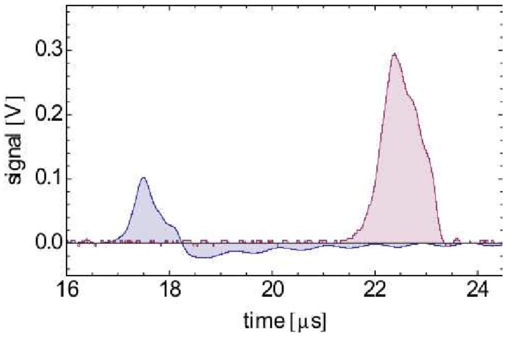

Figure 1: Averaged Ar^{13+} signals at the non-destructive ion detector ($t \approx 17\ \mu s$) and the MCP ($t \approx 23\ \mu s$).

Another method used for ion detection along the beamline is based on low-noise charge amplification in a newly developed detection system. It is formed by a hollow cylinder electrode of the Penning trap and a dedicated cryogenic amplification stage. The detector amplifies the AC voltage signal at the input stage created on the effective input capacitance from ions passing the electrode. Thus the system is used for non-destructive single-pass electronic detection and serves both as a counter and for timing information.

In Fig. 1 an Ar^{13+} ion signal detected with the cryogenic amplifier and with a multi channel plate is shown. The total number of ions of the detected signal amounts to (46000 ± 1000) ions per bunch and is slightly smaller for the multi channel plate measurement due to transport losses. The lowest detectable signal with the detector corresponds to 4000 elementary charges when the detector is operated at room temperature.

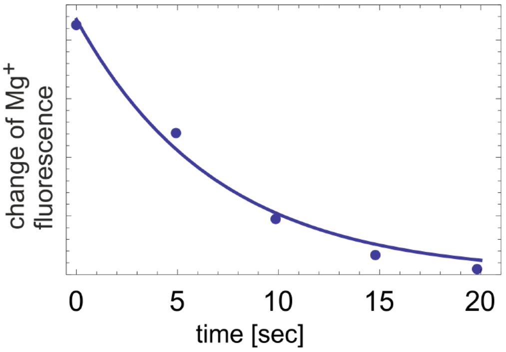

Figure 2: Change of Mg^+ fluorescence intensity after cyclotron excitation of Ar^{3+} as a function of storage time.

For sympathetic cooling the HCI were mixed with a cloud of laser cooled Mg^+ ions. For non-destructive detection the mass dependent cyclotron motion of the HCI was excited with an irradiated radio frequency, while monitoring a change in the Mg^+ fluorescence. The intensity of this change in fluorescence is plotted as a function of storage time in figure 2. Temperature dependent collisions with residual gas limit the HCI storage time, which can be used to estimate the HCI temperature. The exponential decay fitted in Fig. 2 with a time constant of 7 s, is in agreement with the assumption of sympathetically cooled argon ions.

References

[1] Mäckel et al., Phys. Rev. Lett. 107, 143002 (2011)

[2] Lochmann et al., Phys. Rev. A 90, 030501(R) (2014)

[3] Murböck et al., Phys. Scr. T156 (2013)

---

[*] This work has been supported financially by BMBF (05P12RDFA4, 05P12PMFAE), DFG, EPSRC, GSI, HGS-HiRe and HIC for FAIR.

DOI:10.15120/GR-2015-1-APPA-MML-AP-12

Development of ion detectors for the 1–10 MeV/u energy range*

C. Hahn†[1,2], *A. Bräuning-Demian*[3], *A. Gumberidze*[3], *E. Lamour*[4], *J. Rangama*[5], *Th. Stöhlker*[1,2,3], *D. Vernhet*[4], *G. Weber*[1,3], *and the Fit-FISIC collaboration*[2,3,4,5]
[1]Helmholtz Institute Jena, Germany; [2]FSU, Jena, Germany; [3]GSI, Darmstadt, Germany; [4]INSP, Paris, France; [5]CIMAP, Caen, France

Physics case

Within the universe, matter is commonly found in the state of ionized plasma, where collisions between ions occur regularly. The interaction cross sections of the involved charge-exchange processes are largest in the so-called *intermediate regime*, where the electron and relative target–projectile speed are comparable. For a proton colliding with a hydrogen atom, this regime corresponds to an energy of about 10 keV; heavier ions require some 10 MeV. Unfortunately, it is difficult to calculate the relevant cross sections theoretically, as the rigorous electronic treatment of the system amounts to an N-body problem. On the other hand, experimental investigations are hampered by the fact that the probabilities of a variety of interaction mechanisms attain similar magnitudes, which causes "interference effects". Therefore the intermediate collision regime, despite its undeniable importance, is only barely investigated, with experimental data lacking for all but the lightest systems.

The Franco-German *Fit-FISIC* cooperation ("**F**irst steps **t**owards atomic physics of **F**ast **I**on–**S**low **I**on **C**ollisions") constitutes a novel attempt to better understand these ion–ion interactions. Using intense high-quality ion beams that are available at French and German accelerator facilities such as SPIRAL2 and FAIR (currently under construction at Caen and Darmstadt, respectively), collisions of multi-charged ions will be realized under well-controlled conditions [1]. The planned setup is outlined in Figure 1.

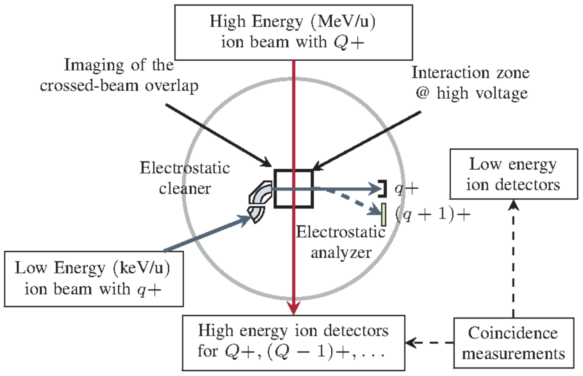

Figure 1: Planned setup for the Fit-FISIC project. Coincidence measurements of the low- and high-energy branches will be used to detect charge-exchange reactions. Figure reproduced from [1]

Ion detector development

As a collaborative effort of both GSI and FSU, a detection system for the high-energy branch of the project is currently being developed. This detector will have to cope with MHz count rates of ions having energies between sub-MeV/u and 15 MeV/u, while remaining windowless so as to not stop impinging ions before they reach the actual sensor material. A movable stage will position the detector relative to the beam of charge-exchanged ions. Since the projected energy and ion range are only scarcely investigated with respect to suitable detector models, extensive research into possible sensor configurations is necessary.

Above all else, radiation hardness is a critical demand: charged particles deposit their energy locally, evident in the so-called *Bragg peak* of the energy loss curve, leading to conventional semiconductor and plastic scintillator detectors being virtually "scorched" by the incident ion flux, which renders them unusable almost immediately.

A favorable material choice for these conditions is artificial diamond, one of the most resilient materials around. CVD diamond also offers a desirably high charge carrier mobility [2], although it is somewhat diminished by grain boundaries present in polycrystalline substrates. Its behavior under prolonged ion bombardment, most notably the long-term signal stability, will be studied in 2015 at tandem accelerators capable of delivering the required ion species and energies.

In parallel, alternative detector models are being considered. Among these, scintillator crystals such as cerium-doped yttrium aluminum perovskite (YAP:Ce) appear particularly promising. The material has been successfully employed to detect ions in earlier experiments, where it exhibited a surprising level of radiation hardness [3]. A test setup to investigate the feasibility of these alternative approaches is currently being assembled at Helmholtz Institute Jena, and will be used for initial measurements in 2015.

References

[1] Fit-FISIC Collaboration, ed., "Project Fit-FISIC: Scientific Document" (2013)

[2] G. Kramberger et al., "Radiation damage in diamond detectors", Vertex 2012 (2012)

[3] M. Tokman et al., "Towards a Determination of QED Effects in Cu-Like Pb Recombination Resonances Near Threshold", Phys. Scripta 2001 (2001) 406

---

* We acknowledge support by the DFG under grant no. STO 346/4-1.

† christoph.hahn@uni-jena.de

DOI:10.15120/GR-2015-1-APPA-MML-AP-13

Bayesian and Akaike information criteria of the EC-decay rate oscillations *

N. Winckler[1] *and the Two-Body Weak Decay collaboration*[1]
[1]GSI, Darmstadt

Introduction

This report is a continuation of the investigations performed in Ref. [1]. In the previous report we pointed out that the Akaike Information Criterion (AIC) and the Bayesian Information Criterion (BIC) could be summarized as follow :

$$\mathrm{IC}_i = -2\log(L(\hat{\theta}_i|\mathrm{data}, M_i)) + A_n K_i \qquad (1)$$

and that, in the frequentist interpretation, the decision making in choosing a model M_1 instead of a model M_0 was equivalent to a likelihood ratio test (LRT) in rejecting the null when:

$$-2\log(L_0/L_1) > A_n(K_1 - K_0), \qquad (2)$$

where the right-hand term of eq. 1 defines the critical points and where $A_n = 2$ for AIC and $A_n = \log N$ for BIC. From these critical points and the likelihood ratio distribution we could evaluate the AIC- and BIC Type I error rate. Because of a lack of statistical consitency in the ω estimator, minimization procedures were not optimal. Therefore, the resulting maximum likelihood estimates of ω and ϕ were in fact local maxima, distributed arround their initialisation values. As a consequence, the interpretation of the previous calculated LRT distribution involves strong underlying prior probabilities in the $\omega - \phi$ space, restricting values to small parameter intervals. We note that, despite these constraints, the previous computed AIC Type I error rate was already very large ($\approx 20\%$).

Another method bypassing local maxima has been used to obtain the LRT distribution [2]. It turned out that the obtained distribution is much more shifted to higher values, which results in a dramatic increase of the AIC- and BIC Type I error rate.

AIC- & BIC Type I error

The distribution found in Ref. [2] is shown in Figure 1 with the AIC- and BIC critical points. The obtained Type I error rates are shown in Table 1. The fact that the distribution is shifted to higher value is a proof in itself that the global maximum likelihoods have been better estimated. This can be better observed when looking at the distributions of the corresponding Maximum Likelihood Estimates (MLE). The MLE distribution of the angular frequency and phase are now flat under the null hypothesis, as expected for unidentifiable parameters.

	EC data (245 MHz res.)	β^+ data (245 MHz res.)	EC data (cap. pick-up)
Sample size N	3616	2912	2989
AIC type I error rate	99.3%	99.3%	99.3%
BIC type I error rate	0.07%	0.11%	0.11%

Table 1: AIC- and BIC Type I error rate for different sample sizes

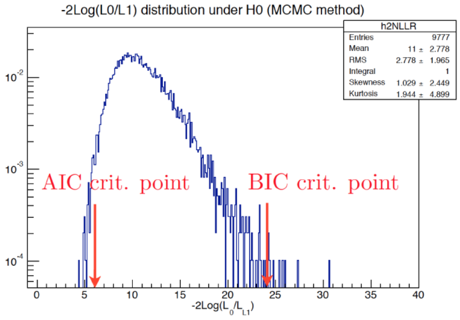

Figure 1: Unbinned maximum likelihood ratio distribution (blue) with the AIC- and BIC critical points (red).

Discussion

It is important to note that, for AIC, these results only depend on the model and on the LRT distribution and do not depend on the data at all. While a probability of 20% to reject the pure exponential decay hypothesis, when it is actually true, can – in this particular problem – cast serious doubts in the reliability of AIC [1], a probability of 99% is obviously not acceptable. Conversely, the BIC has, for the sample size given in table, a much more reasonable Type I error rate of about 0.1%. Accordingly, the BIC is more reliable than AIC in the atempt to reject the null hypothesis of a pure exponential decay. These results have strong consequences in the interpretation of the AIC analysis performed in Ref.[3]. An alternative approach, the computation of the Bayes factor from unbinned likelihood has been performed in Ref. [4].

References

[1] N. Winckler et al., "Further insight into Bayesian and Akaike information criteria of the EC-decay rate oscillations", GSI report (2013)

[2] N. Winckler "Maximum Likelihood Ratio distribution of a modulated exponential decay", GSI report (2014)

[3] P. Kienle et al., "High-resolution measurement of the time-modulated orbital electron capture and of the β^+ decay of hydrogen-like $^{142}\mathrm{Pm}^{60+}$ ions", PLB 726 (2013) 638

[4] N. Winckler et al., "Bayesian Model selection analysis of the EC-decay rate oscillations", GSI report (2014)

---

* This work is part of the EMMI Rapid Reaction Task Force presentation given in Jena, July 2014

DOI:10.15120/GR-2015-1-APPA-MML-AP-14

Relativistic calculations of the isotope shifts in highly charged Li-like ions

N. A. Zubova[1,2], *Y. S. Kozhedub*[1,2], *V. M. Shabaev*[1], *I. I. Tupitsyn*[1], *A.V. Volotka*[1,3], *G. Plunien*[3], *C.Brandau*[4,5,6], *and Th. Stöhlker*[4,7,8]

[1]St. Petersburg State University, Russia; [2]SSC RF ITEP of NRC "Kurchatov Institute", Russia; [3]TU Dresden, Germany; [4]GSI Darmstadt, Germany; [5]ExtreMe Matter Institute EMMI and Research Division GSI Darmstadt, Germany; [6]Justus-Liebig-University Giessen, Germany; [7]Helmholtz-Institut Jena, Germany; [8]Friedrich-Schiller-Universität Jena, Germany

In the past years a great progress was achieved in experimental study of the isotope shifts in highly charged ions. This was done in the dielectronic recombination (DR) experiments at ESR (GSI) [1] as well as applying a high-resolution grating spectrometer at EBIT [2]. The joint analysis of the results obtained in the high-precision theoretical and experimental investigations of isotope shifts in highly charged ions provides determination of nuclear charge radii differences and enables tests of quantum electrodynamics (QED) at strong fields. With the FAIR facilities the isotope shift measurements in heavy ions will be further improved in accuracy and extended to radioactive isotopes with a lifetime longer than about 10 s.

From the theoretical side, to obtain the total value of the isotope shift one needs to evaluate the nuclear size (field shift) and nuclear recoil (mass shift) contributions, including the relativistic and QED effects. Since there exists some discrepancy in the results obtained in Refs. [3] and [4] for heavy ions, we develop an alternative method which merges the perturbative and CI-DFS (configuration-interaction Dirac-Fock-Sturm) calculations [5]. Namely, we calculate the nuclear recoil contributions within the Breit approximation to zeroth and first orders in $1/Z$ and add the related contributions of second and higher orders in $1/Z$, obtained using the CI-DFS method. To derive the nuclear recoil contributions to the binding energies of Li-like ions by perturbation theory, we use the two-time Green's function method [6] with the $(1s)^2$ shell regarded as belonging to a redefined vacuum. The obtained non-QED results are combined with the corresponding QED contributions of the zeroth order in $1/Z$ to get the most accurate theoretical data for the mass shifts in highly charged Li-like ions. In addition, the field shifts are calculated in the framework of the Dirac-Coulomb-Breit Hamiltonian. These calculations, being performed by the CI-DFS method, are compared with the corresponding MCDF (multiconfiguration Dirac-Fock) calculations of Ref. [3]. The QED corrections to the field shifts are also evaluated. In addition, we consider the nuclear deformation and nuclear polarization corrections. As the result, the most precise theoretical values of the isotope shifts for the $2p_{1/2} - 2s$ and $2p_{3/2} - 2s$ transitions in Li-like ions are presented in our paper [5]. The theoretical contributions to the isotope shifts in Li-like thorium and uranium are given in Table 1.

Table 1: Individual contributions to the isotope shifts for the $2p_{1/2} - 2s$ and $2p_{3/2} - 2s$ transitions in Li-like $^{232,230}\mathrm{Th}^{88+}$ and $^{238,234}\mathrm{U}^{89+}$(in meV) with given values of $\delta\langle r^2\rangle$.

	$^{232,230}\mathrm{Th}^{87+}$	
	$^{232,230}\delta\langle r^2\rangle$=0.2050 fm^2	
	$2\mathrm{p}_{1/2} - 2\mathrm{s}$	$2\mathrm{p}_{3/2} - 2\mathrm{s}$
Main contributions		
Field shift	-116.1	-128.7
Mass shift	0.1	0.3
FS plus MS	-116.0	-128.4
QED		
Field shift	0.6	0.9
Mass shift	0.4	0.4
Others		
Nuclear polarization	1.6	1.7
Nuclear deformation	1.5	1.5
Total IS theory	-111.9(22)	-123.9(22)
	$^{238,234}\mathrm{U}^{89+}$	
	$^{238,234}\delta\langle r^2\rangle$=0.334 fm^2	
	$2\mathrm{p}_{1/2} - 2\mathrm{s}$	$2\mathrm{p}_{3/2} - 2\mathrm{s}$
Main contributions		
Field shift	-227.8	-254.5
Mass shift	0.2	0.6
FS plus MS	-227.6	-253.9
QED		
Field shift	1.2	1.8
Mass shift	0.9	0.8
Others		
Nuclear polarization	2.3	2.6
Nuclear deformation	-2.4	-2.7
Total IS theory	-225.6(32)	-251.4(33)

References

[1] C. Brandau *et al.*, Phys. Rev. Lett. **100**, 073201 (2008).

[2] R. Soria Orts *et al.*, Phys. Rev. Lett. **97**, 103002 (2006).

[3] J. Li *et al.*, Phys. Rev. A **86**, 022518 (2012).

[4] Y. S. Kozhedub *et al.*, Phys. Rev. A **81**, 042513 (2010).

[5] N. A. Zubova *et al.*, Phys. Rev. A **90**, 062512 (2014).

[6] V. M. Shabaev, Phys. Rep. **356**, 119 (2002).

DOI:10.15120/GR-2015-1-APPA-MML-AP-15

Proposed determination of small level splittings in highly charged ions

Z. W. Wu[1], *N. M. Kabachnik*[2], *A. Surzhykov*[1], *C. Z. Dong*[3], *and S. Fritzsche*[1,4]
[1]Helmholtz Institute Jena, Germany; [2]European XFEL, Hamburg, Germany; [3]Northwest University Lanzhou, China;
[4]University of Jena, Germany

Highly charged ions (HCI) are known as a unique tool for exploring the interaction of strong electromagnetic fields with matter. In particular the x-ray emission from these ions has been investigated for many years and helped reveal many details about the structure and dynamics of HCI [1]. Moreover, recent studies on the angular distribution and linear polarization of these x-rays provided not only insight into the electron-electron and electron-photon interactions but also showed a rather strong influence of the hyperfine interaction upon the angular x-ray emission of HCI, even if the fine and hyperfine structure of these lines cannot be resolved in detail [2].

Until the present, however, almost all experimental and theoretical investigations on the angular distribution of x-rays have dealt with the photon emission from well-isolated fine-structure levels. In contrast, little attention was paid to cascade emissions that proceed via two (or more) overlapping intermediate resonances. For such cascades, we have therefore explored, by using the density matrix theory, both the photon-photon correlation function as well as the angular distribution of the second photon (if the first photon remains unobserved). General expressions were derived for these distributions, independent of the particular shell structure of the HCI [3]. For the sake of simplicity, let us consider the two-step cascade

$$\begin{aligned} & 1s2p^2 \;\; J_i = 1/2, 3/2 \\ & \longrightarrow \;\; \gamma_1 \, + \left\{ \begin{array}{l} 1s2s2p \;\; J = 1/2 \\ 1s2s2p \;\; J' = 3/2 \end{array} \right\} \\ & \longrightarrow \;\; \gamma_1 \, + \, \gamma_2 \, + \, 1s^2 2s \;\; J_f = 1/2 \end{aligned} \tag{1}$$

of lithium-like ions. These ions have a relatively simple level structure and are known to exhibit a level crossing of the two $1s2s2p$ $J = 1/2, 3/2$ intermediate resonances between $74 \le Z \le 79$. For this decay cascade, indeed, a quite remarkable effect of the level splitting and the alignment of the initial $1s2p^2$ $J_i = 3/2$ resonance is found for the angular distribution of the emitted x-ray photons. For lithium-like W^{71+} ions, for example, Fig. 1 displays the angular distribution of the second-step photon emission for an initially aligned $1s2p^2$ $J_i = 3/2$ resonance with (alignment parameter) $\mathcal{A}_2 = -1.0$ and for four different splittings of the intermediate $J = 1/2$ and $3/2$ levels (all in a.u.).

When compared with the photon emission of isolated levels, the x-ray emission via overlapping resonances is affected also by spin-spin and spin-orbit interactions that give rise to a depolarization (in time) of these intermediate levels. This effect of partially overlapping resonances upon the emission of photons and electrons has been termed *lifetime-induced depolarization* in the literature. If no further details are known about the exact time interval between the subsequent emission processes in some cascade, this depolarization can be characterized by means of so-called depolarization factors that just depend on the energy splitting and the natural width of the intermediate resonances.

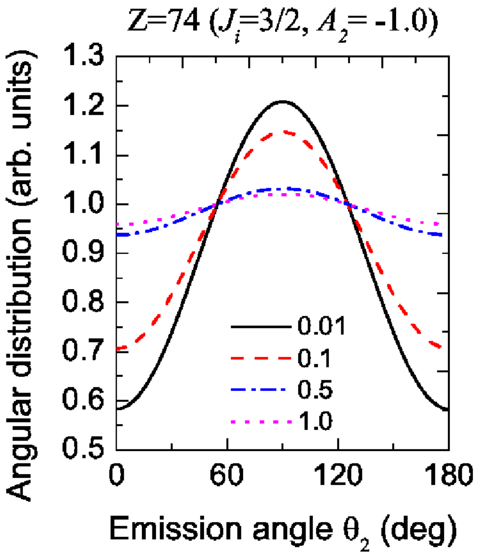

Figure 1: Angular distribution of the second-step photon emission for the cascade (1). See text for further discussions.

Owing to the strong dependence of the photon-photon correlation and angular distribution functions upon the energy splitting of the intermediate levels, we conclude that accurate measurements of the angular x-ray emission may serve also as a tool for determining small level splittings in highly charged ions [3]. Such measurements of the photon angular distributions will be feasible with present-day x-ray detectors and could be carried out at both, heavy-ion storage rings and electron beam ion trap facilities.

References

[1] S. Fritzsche, P. Indelicato and T. Stöhlker, *J. Phys.* **B38**, S707 (2005).

[2] Z. W. Wu, A. Surzhykov and S. Fritzsche, *Phys. Rev.* **A89**, 022513 (2014).

[3] Z. W. Wu *et al.*, *Phys. Rev.* **A90**, 052515 (2014).

DOI:10.15120/GR-2015-1-APPA-MML-AP-16

Narrowband inverse Compton scattering x-ray sources at high laser intensities

D. Seipt[*1,2], *S. G. Rykovanov*[1,2], *A. Surzhykov*[1,2], *and S. Fritzsche*[2,3]
[1]GSI Helmholtzzentrum für Schwerionenforschung, Planckstraße 1, 64291 Darmstadt; [2]Helmholtz-Institut Jena, Fröbelstieg 3, 07743 Jena; [3]Universität Jena, Institut für Theoretische Physik, 07743 Jena

Bright narrowband x- and gamma-ray sources based on the inverse Compton scattering of laser light on high-energy electron beams rely on the Doppler upshift of the laser frequency $\omega' = 4\gamma^2\omega_0$.However, these sources suffer from a limitation of the maximum laser intensity because the longitudinal ponderomotive force in a high-intensity laser pulse will effectively slow-down the electrons, reducing their γ-factor. This gradual slow-down of the electrons as the intensity ramps up leads to a reduced Doppler upshift causing spectral broadening of the generated x- or gamma-rays. Recent results [1, 2, 3] suggest that this ponderomotive broadening could be compensated by suitably chirped laser pulses. This compensation would allow to reduce the bandwidth of the generated x- and gamma-rays and to operate narrowband Compton sources in the high-intensity regime. Here we report on our recent findings on the determination of the optimal frequency modulation and its properties.

Let us assume a high-energy electron with asymptotic four-momentum p (and $\gamma \gg 1$) collides head-on with an intense short laser pulse propagating along the direction $n = (1, 0, 0, -1)$, described by the normalized vector potential $a^\mu = a_0 \varepsilon^\mu g(x^+) \cos \Phi(x^+)$. The laser is assumed to be chirped with a local frequency $\omega(x^+) = \partial\Phi/\partial x^+$, with the light-front time $x^+ = t + z$, and where g denotes the laser's envelope function that changes slowly on the time-scale $1/\omega$. When the electron enters the laser pulse, its momentum has to be supplemented by the pondermotive four-potential

$$p^\mu \to p^\mu + U^\mu\,, \quad U^\mu = \frac{m a_0^2 g^2(x^+)}{4\gamma} n^\mu\,, \tag{1}$$

that describes the longitudinal slow-down.

From the analysis of the scattering amplitude of nonlinear Compton scattering within the framework of strong-field QED in the Furry picture [3] we find the *local* frequency of the ℓ-th harmonic of the scattered x-rays as

$$\omega'_\ell = \frac{4\gamma^2 \ell \omega(x^+)}{1 + \gamma^2\vartheta^2 + \frac{a_0^2 g^2(x^+)}{2} + \chi(x^+)}\,, \tag{2}$$

where $\chi = 2\ell\omega\gamma/m$ denotes the electron recoil, and ϑ is the scattering angle. From Eq. (2) we can determine the optimal laser chirp via the condition $\mathrm{d}\omega'_\ell/\mathrm{d}x^+ = 0$. In other words: The optimal chirping prescription

$$\frac{\omega(x^+)}{\omega_0} = 1 + \frac{1}{1+\gamma^2\vartheta^2} \frac{a_0^2}{2} g^2(x^+) \tag{3}$$

describes how the laser frequency needs to increase during the time of high laser intensity in order to exactly balance the ponderomotive red-shift due to the slow-down of the electrons. Eq. (3) shows that the ponderomotive broadening can be compensated only for just one particular scattering angle ϑ. Moreover, the form of the optimal frequency modulation, Eq. (3), does not depend on the electron recoil during the scattering (no dependence on χ) and it removes the ponderomotive broadening from all higher harmonics in addition to the fundamental line (no dependence on ℓ). A numerical simulation of the compensated nonlinear Compton spectrum taking into account realistic laser focus geometries and electron bunches shows a reduction of the bandwidth from 80% to less than 5%, see Fig. 1.

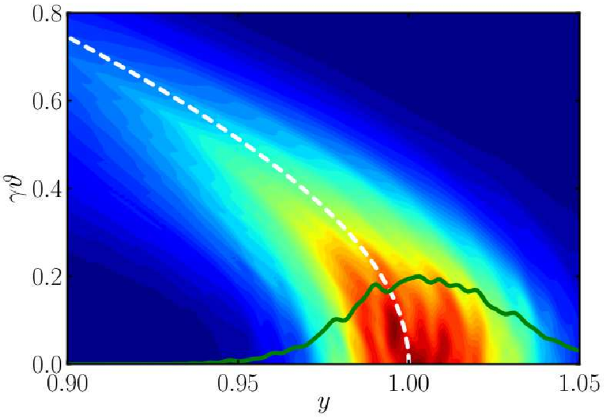

Figure 1: Simulated energy and angular radiation spectrum of a realistic electron beam interacting with a focused laser pulse with peak intensity $a_0 = 2.83$. The solid green line depicts the on-axis line-out of the radiation spectrum ($y = \omega'/4\gamma^2\omega_0$). For simulation parameters cf. Ref. [3].

To summarize, our analysis shows that the compensation of ponderomotive broadening by chirped laser pulses is a promising route towards operating narrowband Compton scattering x- and gamma-ray sources at high laser intensity.

References

[1] I. Ghebregziabher, B. A. Shadwick, and D. Umstadter, Phys. Rev. ST Accel. Beams **16**, 030705 (2013),

[2] B. Terzić, K. Deitrick, A. S. Hofler, and G. A. Krafft, Phys. Rev. Lett. **112**, 074801 (2014).

[3] D. Seipt, S. G. Rykovanov, A. Surzhykov and S. Fritzsche, arXiv:1412.2659.

---

[*] d.seipt@gsi.de

DOI:10.15120/GR-2015-1-APPA-MML-AP-17

Bound electron g-Factor measurements at the HITRAP facility

M. Wiesel[1,2,3], *G. Birkl*[1], *M.S. Ebrahimi*[2,3], *D. von Lindenfels*[2,3], *A. Martin*[1], *W. Quint*[2,3], *and M. Vogel*[1,2]
[1]Institut für Angewandte Physik, TU Darmstadt; [2]GSI, Darmstadt; [3]Ruprecht Karls-Universität Heidelberg

We are currently commissioning ARTEMIS, a Penning trap experiment designed to measure the magnetic moments (g-factors) of highly charged ions. In the theory of bound state quantum electrodynamics (BS-QED) g-factors can be calculated to high accuracies. With the aimed high precision measurement we can test QED at a ppb level and beyond. The method of use is the so-called microwave laser double-resonance spectroscopy, utilizing the fact that for some medium charged ions the fine-structure and for some heavy highly-charged ions the hyperfine-structure splitting is in the optical regime. These ions, such as $^{207}\mathrm{Pb}^{81+}$ and $^{209}\mathrm{Bi}^{82+}$, for example, will be available within the framework of the HITRAP facility ARTEMIS is connected to. For first offline tests, $^{40}\mathrm{Ar}^{13+}$ has been chosen. It has a spinless nucleus, so that the g-factor of the 2p electron can be measured. Due to the high magnetic field of 7 T also first laboratory measurements of higher-order Zeeman effects can be studied.

Figure 1: Photography of the ARTEMIS trap chamber with the electronics, for example ion motion detection circuits, laser inlet and filterboards.

Here we present our progress in the in-trap production of boron-like argon. First, argon gas is injected in the cryogenic adsorption valve that can be heated above the adsorption temperature of argon for ”opening”. The creation of different charge states takes place by electron-impact ionization like the charge-breeding processes used in electron beam ion sources (EBIS). By setting different voltages to the field emission tip, the electron energy is adjusted such that different charge states can be produced. The ions are trapped in a three-fold nested Penning trap ensemble within a ten-electrode mechanically compensated creation trap tower. They are concentrated into one trap. With our superconducting NbTi resonator, the axial motion at 630 kHz is detected non-destructively. By ramping the potential of the trap between 1 V and 250 V, the axial frequencies of the different ion species inside the trap are brought into resonance with the resonator, and thus a spectrum with different M/Q (mass-to-charge ratio) is recorded. With our ultra-high vacuum, storage times (even for the higher charge states like Ar^{16+}) of many hours up to days have been achieved so far.

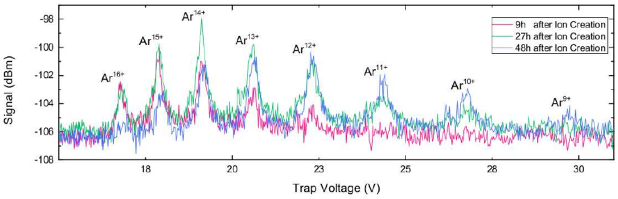

Figure 2: Time evolution and charge exchange of the different argon charge states.Trap voltage is related to the mass-to-charge ratio of the trapped ions.

In a next step, all ion species but Ar^{13+} will be removed from the trap, and the remaining ions will be transported to the precision trap where cyclotron detection and measurements of the electron magnetic moment will take place. The 441 nm laser system has been set up at GSI and is currently being equipped with a secondary tellurium spectroscopy for higher laser stability.

This work has been supported in part by DFG (Grants VO 1707/1-2 and BI 647/4-1), by GSI, HGS-HIRe, and by the IMPRS for Quantum Dynamics Heidelberg.

References

[1] W. Quint, D. Moskovkin, V.M. Shabaev and M. Vogel, Phys. Rev. A **78** (2008) 032517.

[2] D. von Lindenfels, N. Brantjes, G. Birkl, W. Quint, V. Shabaev and M. Vogel, Can. J. Phys. **89**, 79 (2011).

[3] D. von Lindenfels, G. Birkl, D.A. Glazov, A. Martin, G. Plunien, W. Quint, V.M. Shabaev, M.M. Sokolov, M. Vogel, A.V. Volotka, and M. Wiesel, Phys. Rev. A **87** 023412 (2013).

DOI:10.15120/GR-2015-1-APPA-MML-AP-18

Progress of laser cooling of relativistic Li-like C^{3+} ion beams at the CSRe*

W. Q. Wen[1], *H. B. Wang* [1], *Z. K. Huang*[1], *D. C. Zhang*[1], *B. Hai*[1], *X. L. Zhu*[1], *J. Li*[1],
L. J. Mao[1], *R. S. Mao*[1],*J. W. Xia*[1], *J. C. Yang*[1], *Y. J. Yuan*[1], *M. Loeser*[2], *M. Siebold*[2],
U. Schramm[2], *O. Boine-Frankenheim*[3], *L. Eidam*[3], *D. F. A Winters*[3], *G. Birkl*[4],
B. Rein[4], *Th. Walther*[4], *J.F. Zhu*[5], *M. Bussmann*[2] *and X. Ma*[1#]
[1]IMP, China; [2]HZDR, Germany; [3]GSI Germany; [4]TU Darmstadt, Germany; [5]Xidian University, China

Laser cooling is one of the most promising techniques to reach high phase-space densities for relativistic heavy ion beams. Realizing a crystalline ion beam is one of the ultimate goals of laser cooling of heavy ion beams at storage rings [1]. Preparations for laser cooling of relativistic lithium-like C^{3+} are being made at the experimental cooler storage ring (CSRe) in Lanzhou, China [2].

In September 2014 a test experiment was performed with $^{12}C^{3+}$ ion beams at an energy of 122 MeV/u on the CSRe with a pulsed laser system. A schematic view of the experimental setup is shown in figure 1. In the experiment $^{12}C^{3+}$ ions were produced by an Electron Cyclotron Resonance ion source (ECR). In the ECR, a significant fraction of $^{16}O^{4+}$ was produced alongside. Then the ions were accelerated by a Sector Focused Cyclotron (SFC), and injected into the main Cooler Storage Ring (CSRm). After accumulation and acceleration in the CSRm, the ion beams were extracted and injected into the CSRe at the energy of 122 MeV/u (at a velocity of 47% of the speed of light). Since the circumference of the CSRe is 128.8 m, this beam energy lead to the revolution frequency of 1.087 MHz. A pulsed UV laser system from HZDR was employed for this test laser cooling experiment. The closed $2s_{1/2}$—$2p_{1/2}$ optical transition at a wavelength of $\lambda_0 = 155.07$ nm of the Li-like carbon ions was Doppler-shifted to be resonant with the UV-laser at the wavelength $\lambda_{laser} = 257.3$ nm in the experiment ($\lambda_{laser} = \gamma(1+\beta)\lambda_0$).

A Schottky spectrum of an electron-cooled coasting ion beam is shown in figure 2, in which the Schottky signals of $^{12}C^{3+}$ and $^{16}O^{4+}$ ions were separated by electron-cooling. Stable operation of the CSRe was observed over several days, including rf-bunching and diagnostic systems. The injected number of C^{3+} (~5×10^{8}) was sufficient for testing laser cooling. The dynamics of the electron-cooled and RF-bunched ion beams were investigated systematically. However, first results did not yet indicate a strongly interaction of the laser with the ions. The fluorescence from the ions, measured using UV-CPM and UV-PMT detectors, is thereby of great interest since it reflects the interaction between laser and ion beam. Since two ion species were stored simultaneously, there is also the possibility that the laser-cooled $^{12}C^{3+}$ ions sympathetically cool the $^{16}O^{4+}$ ions. Further data analysis is currently in progress.

Laser cooling experiment at the storage ring of the CSRe and ESR are directly relevant for laser cooling and precision laser spectroscopy of highly charged and relativistic heavy ions at the future large facilities such as HIAF in China and FAIR in Germany. At these facilities, laser interaction with highly charged ions (HCIs) will open a new field of atomic physics and nuclear physics [3].

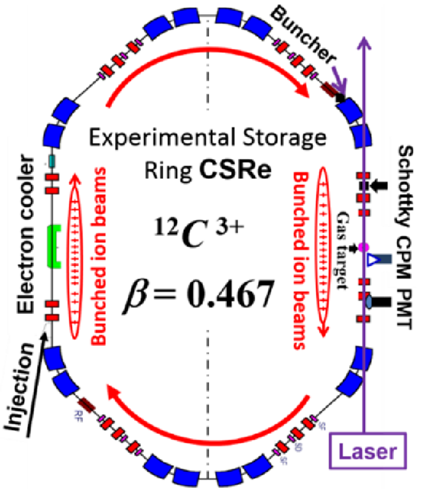

Figure 1: Schematic view of the experimental setup for laser cooling experiments at the CSRe. The locations of the resonant Schottky pick-up, RF-buncher, UV-PMT and the UV-CPM are shown.

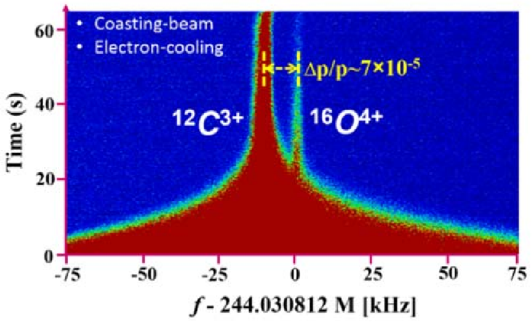

Figure 2: Schottky spectrum of the electron-cooled injected $^{12}C^{3+}$ and $^{16}O^{4+}$ at the CSRe.

References

[1] U. Schramm and D. Habs, Prog. Part. Nucl. Phys. 35 (2004) 583-677.
[2] W.Q. Wen et al., Nucl. Instrum. Meth. A 736 (2014) 75-80
[3] H. Backe, Hyperfine Interact 171 (2007) 93-1

---

* Work supported by NSFC No.11221064, GJHZ1305 and BMBF
# x.ma@impcas.ac.cn

DOI:10.15120/GR-2015-1-APPA-MML-AP-19

Bayesian analysis of the EC-decay rate oscillations - Part I *

N. Winckler[1] *and the Two-Body Weak Decay collaboration*[1]
[1]GSI, Darmstadt

Introduction

In this contribution we perform a Bayesian analysis with the models and data presented in Ref. [1]. We first remind the definitions of the Bayesian quantities computed here, and present the results of parameter estimation analysis. The results of model selection and the conclusion are presented in the part II of this GSI scientific report.

Computation

In the following M_0 denotes the pure exponential decay, and M_1 the modulated exponential decay. This analysis has been performed using the BAT [2] and CUBA [3] C++ packages. All probabilities have been computed from unbinned likelihood, reducing the information loss.

Parameter probabilities

The posterior probability density functions of the parameter(s) of interest θ is given by :

$$P(\theta|\text{data}) = \frac{P(\text{data}|\theta)P(\theta)}{P(\text{data})}, \tag{1}$$

where $P(\theta)$ is the prior probability of θ, $P(\text{data})$ the normalization term, and $P(\text{data}|\theta)$ the marginal likelilihood. The Metropolis algorithm has been used to sample the marginal likelihood distribution. The high resolution of the obtained posterior distributions, as the one shown in figure 1, have been achieved using 10 Markov chains, each with 10 millions iterations. The convergence has been reached after about 140 thousands iterations.

Model probabilities

The posterior probability of a model M_i given the data is given by

$$P(M_i|\text{data}) = \frac{P(\text{data}|M_i)\pi_i}{P(\text{data})}, \tag{2}$$

where π_i is the prior probability of the model M_i, $P(\text{data})$ the normilzation term, and $P(\text{data}|M_i)$ the Bayesian Evidence :

$$P(\text{data}|M_i) = \int_{\overrightarrow{\theta_i}} P(\text{data}|\overrightarrow{\theta_i}, M_i)P(\overrightarrow{\theta_i}|M_i)d\overrightarrow{\theta_i}. \tag{3}$$

Given the models M_0 and M_1, the posterior odds is defined as :

$$\frac{P(M_0|\text{data})}{P(M_1|\text{data})} = B_{01}\frac{\pi_0}{\pi_1} \tag{4}$$

For equal model prior probabilities, the posterior odds reduces to the Bayes factor B_{01}. Both, model probabitlities and Bayes factors have been obtained using the VEGAS Monte Carlo algorithm for the integration of the Bayesian evidence. The obtained relative precisions of the integrals are smaller than 10^{-3}. The results of the computed model probabilities and Bayes factor are presented in the Part II of this report.

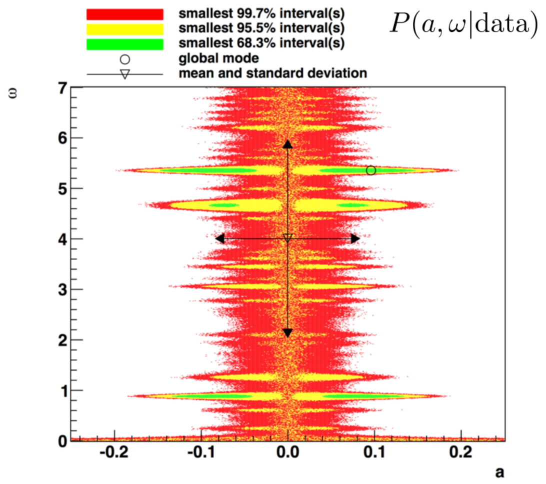

Figure 1: Two-dimensional posterior probability-density for the oscillation frequency ω and the oscillation amplitude a in the 245 MHz resonator EC-data set. The global mode of the posterior $P(a, \omega|\text{data}, M_1)$ is found for $\omega = 5.35$ and $a = 0.09$.

Bayesian parameter estimation

For all parameters, and for all possible combination of parameter pairs, the 1- and 2-dimensional posterior probabilities have been computed using the models M_0 and M_1 and the data presented in Ref. [1]. Different priors have been used. The posteriors computed with uniform prior distributions have shown, as expected, excellent agreements with the unbinned likelihood analysis (see e.g. figure 1 and Ref. [4]).

References

[1] P. Kienle et al., “High-resolution measurement of the time-modulated orbital electron capture and of the β^+ decay of hydrogen-like $^{142}\text{Pm}^{60+}$ ions”, PLB 726 (2013) 638

[2] A. Caldwell, D. Kollar, K. Kroeninger, “BAT - The Bayesian Analysis Toolkit”, Comput. Phys. Commun. 180 (2009)

[3] T. Hanh, “Cuba—a library for multidimensional numerical integration” Comput. Phys. Commun. 168 (2005)

[4] N. Winckler, “Unbinned likelihood Analysis of the EC-decay rate oscillations - Part I and II”, GSI Report 2014 - 2015

---

* This work is part of the EMMI Rapid Reaction Task Force presentation given in Jena, July 2014

DOI:10.15120/GR-2015-1-APPA-MML-AP-20

Progress on Schottky mass spectrometry of ^{152}Sm projectile fragments at ESR *

X. L. Yan[1,2,3,4], *Yu. A. Litvinov*[3,1], *K. Blaum*[4], *F. Bosch*[3], *C. Brandau*[3], *L. Chen*[5], *H. Geissel*[3,5], *R. Knöbel*[3,5], *C. Kozhuharov*[3], *J. Kurcewicz*[3], *S. A. Litvinov*[3,5], *G. Münzenberg*[3], *C. Nociforo*[3], *F. Nolden*[3], *W. R. Plaß*[3,5], *M. S. Sanjari*[3], *C. Scheidenberger*[3,5], *M. Steck*[3], *B. Sun*[7], *X. L. Tu*[1], *H. Weick*[3], *N. Winckler*[3,4], *M. Winkler*[3], *H. S. Xu*[1], *Y. H. Zhang*[1], *and X. H. Zhou*[1]

[1]Institute of Modern Physics, Chinese Academy of Sciences, China; [2]University of Chinese Academy of Sciences, China; [3]GSI Helmholtzzentrum für Schwerionenforschung, Germany; [4]Max Planck Institute for Nuclear Physics, Germany; [5]Justus-Liebig Universität Gießen, Germany; [6]Goethe-Universität, Germany; [7]Beihang University, China

Time-resolved Schottky Mass Spectrometry [1] was employed to the mass measurements of neutron-deficient ^{152}Sm projectile fragments at the FRS-ESR facility. Exotic nuclei were produced by fragmentation reaction of 615 AMeV ^{152}Sm primary beam impinging on a 4.009 g/cm^2 Be-target placed at the entrance of the fragment separator FRS. The fragments were separated in-flight by the FRS and then injected and stored in the storage ring ESR where electron cooling was applied to the stored ions. After cooling, the initial velocity distribution of the stored ions was reduced to typically $\sigma_v/v \approx 1.4 \times 10^{-7}$, thus the ions' revolution frequencies are a direct measure of their mass-to-charge ratios. An example of the measured frequency spectrum is shown in Fig 1.

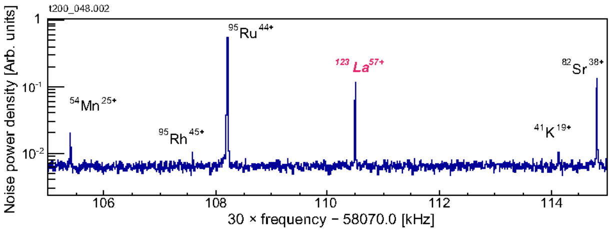

Figure 1: Part of the measured frequency spectrum. The mass of ^{123}La is previously unknown due to AME2012 [2].

The experiment was performed in 2005 [3,4]. The data analysis is now finished and a new mass evaluation method has been developed to reduce the systematic error [5]. Firstly, the input data were carefully prepared, only distinct peaks were taken into account in the mass calibration of the frequency spectra. Then, a local mass calibration was performed in the selected frequency range where the momentum compaction factor α_p of ESR was nearly constant, see Fig. 2. The α_p-values in Fig. 2 were deduced (approximately) from the well-known mass-to-charge ratios of ion-pairs who have neighbouring peaks in the frequency spectra, while the orbital length L was calculated from the ions' velocity, which was defined by the electron-cooler's accelerating voltage, and the ions' revolution frequency:

$$(\alpha_p)_i = \frac{\left[\frac{f_i - f_{i+1}}{f_i}\right]_{exp}}{\left[\frac{(m/q)_{i+1}-(m/q)_i}{(m/q)_i}\right]_{AME}} \quad \text{and} \quad L_i = v_i/f_i. \qquad (1)$$

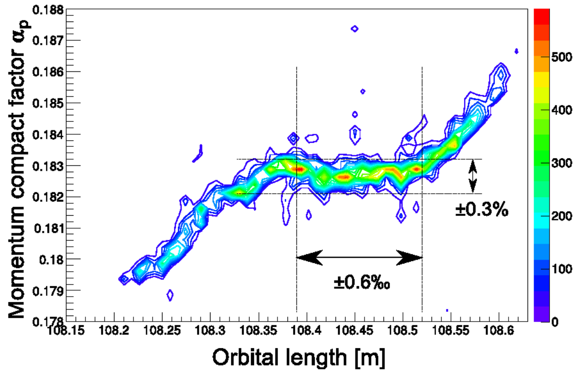

Figure 2: 2-D histogram of the momentum compaction factor deduced in the experiment [6]. The colour code is the count number. Mass calibration of the frequency spectrum has only been done in the selected orbital length range.

After the first step of evaluation, the deviation of the re-calculated mass-to-charge ratios from the tabulated values in AME2012 was found to be a linear function of the ion charge-states for the reference masses [5]. The origin of this systematic deviation is still under discussion. This observation was similar to the finding in ref [7]. After correction of this linear deviation, a typical mass uncertainty of 20 keV has been achieved in our experiment and ten new masses have been determined experimentally for the first time [8]. The mass surface measured in this experiment largely overlapped with our previous measurements [1], and could be used for the consistency check of the data.

References

[1] Yu. A. Litvinov et al., Nucl. Phys. A756(2005) 3.

[2] G. Audi et al., Chin. Phys. C36 (2012) 1603.

[3] Yu. A. Litvinov et al., GSI Scientific Report 2006 (2007) 97.

[4] Yu. A. Litvinov et al., Hyperfine Interact 173 (2006) 55.

[5] X. L. Yan et al., J. Phys. Soc. Conf. Proc. 6 (2015) in press.

[6] X. L. Yan et al., Phys. Scripta (2014) submitted.

[7] L. Chen et al., Nucl. Phys. A882(2012) 71.

[8] X. L. Yan et al., in preparation.

---

* This work is supported by Helmholtz-CAS Joint Research Group HCJRG-108 and the ESR experiment campaign No. E082(2014).

DOI:10.15120/GR-2015-1-APPA-MML-AP-21

Maximum Likelihood Ratio distribution of a modulated exponential decay *

N. Winckler[1] *and the Two-Body Weak Decay collaboration*[1]
[1]GSI, Darmstadt

Introduction

In this contribution we discuss and determine the distribution of the unbinned maximum likelihood ratio test statistic (LRT) with the hypotheses made in Ref. [1]. The study of this distribution is important to correctly assess the statistical significance or to determine the Type I error rate of Akaike or Bayesian information criteria.

Problems

Given the $i.i.d.$ random variable $t \in I$, and the parameter space $\theta = (\lambda, a, \omega, \phi)$ we define the probability density function :

$$f(t, \theta) = N_{\theta,I}(1 + a\cos(\omega t + \phi))\exp(-\lambda t), \qquad (1)$$

where $N_{\theta,I}$ is a normalisation factor depending on θ and the measuring time interval I. We propose to evaluate the LRT distribution, $-2\log(\hat{L_0}/\hat{L_1})$, where $\hat{L_0}$ and $\hat{L_1}$ denote the maximum likelihood of the model $f(t, \theta)$ with $a = 0$ and $a \neq 0$, respectively. There are two connected problems with this hypothesis testing. The first problem is that the hypothesis is a point null hypothesis, which often produce significant results in favour of the alternative hypothesis [2]. The second problem is that, under the null hypothesis, the modulation parameters are *non identifiable parameters*, and in such a case the Wilks's theorem, which says that the asymptotic distribution of the LRT statistic is distributed as χ^2_d, is generally wrong, and the correct asymptotic limit depends very much on the precise problem being investigated [3, 4]. Given the dimension of the identifiable parameter(s) p and the dimension of the non identifiable parameter(s) q, some approaches have shown that an approximation of the asymptotic distribution could be obtain when $p \geq 1$ and $q = 1$ or when $p = 1$ and $q > 1$ [4, 5]. Since in our case we have $p = 2$ and $q = 2$, these approaches cannot be applied. Therefore a Monte Carlo approach has been performed to evaluate this distribution.

Method and Results

In addition to the two problems mentioned above, a third problem arises due to the statistical non-consistency of the maximum likelihood estimate (MLE) of the parameters ω (the first derivative of the likelihood w.r.t. ω is not monotone, and, accordingly, several roots can be found, at least for a finite sample size $N \approx 4000$). Therefore a simple fitting procedure is not reliable and will strongly depends on the initialization of the parameters, the minimization procedure being traped by local maxima.

To evaluate the distribution we first use Monte Carlo toys to simulate the null hypothesis, i.e. a pure exponential decay with the same sample size N as the one in ref. [1]. The maximum likelihood of the two models as well as the corresponding MLE are found by the Metropolis algorithm with an adaptative Breit-Wigner proposal function. This has been achieved using the MCMC engine of the Bayesian Analysis Toolkit [6]. One Markov chain, with a maximum of 10000 iterations, turned out to be more reliable and faster than a maximum likelihood ratio profile. In order to study in addition the pull distributions and bias of each parameters, the (observed) covariance matrix is required. Therefore, the MLEs found by the metropolis algorithm are used to initialize an unbinned maximum likelihood procedure using the roofit package[7].

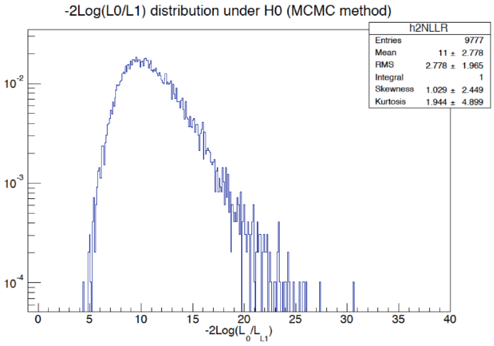

Figure 1: Unbinned maximum likelihood ratio distribution.

Over 10000 iterations of the above procedure about 2% of the MLE were lying on the boundaries. Therefore these MLE have been excluded from the analysis, resulting to a LRT distribution with a sample size of 9777. The resulting distribution is shown in Figure 1 and can be used to test real data with a lower bound $p \geq 1/9777$.

References

[1] P. Kienle et al., Physics Letters B726 (2013)

[2] J. O. Berger and T. Sellke, Journal of the American Statistical Association Vol. 82, No. 397 (1987)

[3] H. Chen and J. Chen, The Canadian Journal of Statistics, Vol. 29, No. 2. (2001)

[4] R. L. Smith, "A Survey of Nonregular Problems", International Statistical Institute congress, 47th session, (1989)

[5] R. G. Davies, Biometrika, 74, (1987)

[6] A. Caldwell, D. Kollar, K. Kroeninger, "BAT - The Bayesian Analysis Toolkit", Comput. Phys. Commun. 180 (2009)

[7] W. Verkerke, "Statistical Software for the LHC" , proceedings of the PHYSTAT LHC Workshop, CERN (2007)

---

* This work is part of the EMMI Rapid Reaction Task Force presentation given in Jena, July 2014

DOI:10.15120/GR-2015-1-APPA-MML-AP-22

Unbinned likelihood Analysis of the EC-decay rate oscillations - Part I *

N. Winckler[1] *and the Two-Body Weak Decay collaboration*[1]
[1]GSI, Darmstadt

Introduction

An unbinned likelihood analysis was performed on the three decay times of stored hydrogen-like ^{142}Pm^{60+} ions data sets presented in [1]. Unlike to usual binned statistics, such as e.g. χ^2 or binned likelihood, the unbinned likelihood statistics is free from information loss and arbitrariness of the binning procedure. This method was applied using two models [1], namely M_0 and M_1, the probability density function of a pure exponential (null hypothesis) and modulated exponential decay (alternative hypothesis), respectively.The computation of the corresponding unbinned likelihood functions L_0 and L_1 was performed using the RooFit C++ package [2].

From this analysis, the following quantities could be obtained : Maximum Likelihood Estimates (MLE), Likelihood Ratio Profile (LRP), Likelihood Ratio Test (LRT), Akaike and Bayesian Information Criteria (AIC and BIC). In this report we present the MLE results. The LRP and LRT analyses, as well as the conclusion, are presented in the part II. The AIC and BIC results are presented in Ref. [3, 4].

Maximum Likelihood Estimates

The results of the unbinned maximum likelihood estimation for different data sets are summarized in Table 1. The Figure 1 shows the fit functions with their 1-σ error bands (dashed line) obtained from the 245 MHz resonator EC-data and rescaled on binned data for presentation. The correlation coefficients are weaks, all having low values ($|C_{\theta_i,\theta_j}| < 0.03$) except for the angular frequency-phase coefficients, which amount to $C_{\omega,\phi} = -0.87$.

	EC data (245 MHz Res.)	β^+ data (245 MHz Res.)	EC data (cap.)
Sample size N	3616	2912	2989
Time interval (s)	[6.0 ; 60.0]	[10.0 ; 60.0]	[6.0 ; 60.0]
$-\log(L_0)$	14340.7	11354.6	11858.2
λ_0	0.013 (1)	0.011 (1)	0.013 (1)
$-\log(L_1)$	14333.3	11351.2	11840.7
λ_1	0.013 (1)	0.011 (1)	0.013 (1)
a_1	0.09 (2)	0.074 (26)	0.15 (2)
ω_1	0.88 (1)	3.09 (27)	0.88 (1)
ϕ_1	2.4 (5)	-2 (1)	1.6 (3)

Table 1: Results of the unbinned maximum likelihood method. The λ parameters denote the total decay rate (i.e. EC and β^+). The a, ω, and ϕ parameters denote the modulation parameters, that is, the amplitude, the angular frequency and the phase, respectively.

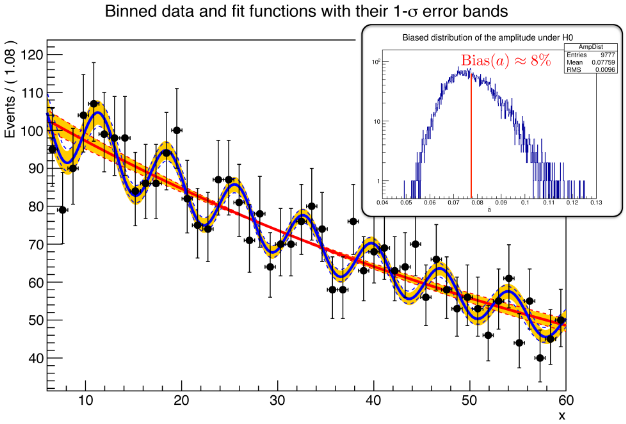

Figure 1: Number of EC decays per 1.08 s of H-like ^{142}Pm^{60+} ions, recorded by the 245 MHz resonator, vs. the time after injection of the ions into the storage ring ESR. Also shown are the fit functions obtained from unbinned Likelihood fits with models: M_0, a pure exponential decay, andM_1, with an additional superposed decay rate oscillation. The data are binned for display only. In this data set, the oscillation amplitude amounts to 9 (2) %. From a Monte Carlo study, we estimate the amplitude due to statistical fluctuations to be 8(1) %, see inset in fig.1.

Bias of the amplitude under H_0

It has been observed that the amplitude estimator is biased under the null hypothesis. The bias amount, e.g. for the sample size of the 245 MHz resonator data, to about $8(1)\%$ (c.f. inset in figure 1), which is compatible with the $9(2)\%$ amplitude found in real data. The bias increases with decreasing sample size, and therefore might contribute to the high significance observed in pick-up data (c.f. part II of this report).

The results of parameter estimations are in good agreement with those obtained with the χ^2-method used in [1]. However, note that, the results in Table 1, have ω constrained in range $[0, 4]$. A likelihood ratio profile showed other maxima depending on the ω or/and data range.

References

[1] P. Kienle et al. PLB 726 (2013) 638

[2] W. Verkerke and D. Kirkby arXiv:physics/0306116

[3] N. Winckler, et al., “Further insight into Bayesian and Akaike information criteria ”, GSI Report 2013 - 2014

[4] N. Winckler, et al., “Bayesian and Akaike information criteria of the EC-decay rate oscillations”, GSI Report 2014 - 2015

---

* This work is part of the EMMI Rapid Reaction Task Force presentation given in Jena, July 2014

DOI:10.15120/GR-2015-1-APPA-MML-AP-23

Study of the two-photon decay in He-like gold

S. Trotsenko[1,2], D.Banas[3], A.Gumberidze[2], C.Kozhuharov[2], R. Zhang[2], A. Ananyeva[2,5], H.Beyer[1,2], K.-H. Blumenhagen[1,7], C. Brandau[2,4], A.Bräuning-Demian[2], W. Chen[2], B. Gao[2], T. Gassner[1,2,7], S.Hagmann[2,5], P.-M. Hillenbrand[2], M. Lestinsky[2], Y. Litvinov[2], N. Petridis[2], S. Schippers[4], D. Schury[2], U.Spillmann[2], C. Trageser[2,4], M. Trassinelli[6], X. Tu[2], D. Winters[2], X. Zhu[2], and Th. Stöhlker[1,2,7]

[1]Helmholtz-Institut Jena, D-07743 Jena, Germany; [2]GSI Helmholtzzentrum für Schwerionenforschung, D-64291 Darmstadt, Germany; [3]University of Kielce, Kielce, Poland; [4]Justus-Liebig-Universität Giessen, Germany, [5]University of Frankfurt, Frankfurt a.M., Germany; [6]INSP, CNRS and UMPC, Paris, France; [7]Friedrich-Schiller-Universität Jena, D-07743 Jena, Germany

Further experiment from our program on studies of the two-photon transitions in heavy highly charged ions [1-3] at the experimental storage ring (ESR) is presented in this contribution.

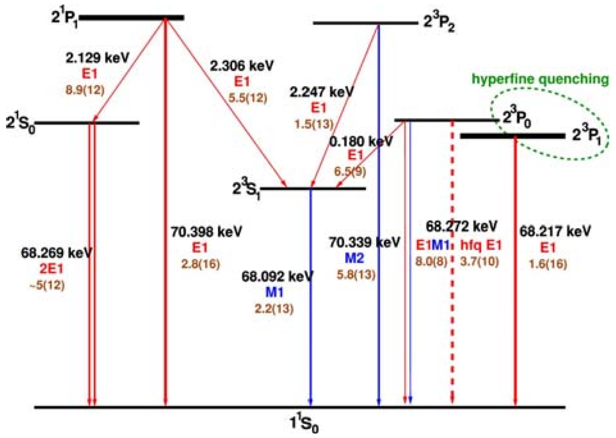

Figure 1: Level scheme of He-like gold with transition energies, decay modes, and transition probabilities indicated. The transition probabilities are in 1/s with numbers in brackets indicating powers of 10 [4].

K-shell ionization of Li-like high-Z projectiles occurring in ion-atom collisions has been found to be a highly selective mechanism for the population of singly excited states (1s2s) in He-like ions [1-3]. They decay to the ground state via M1 (2^3S_1-1^1S_0) and 2E1 (2^1S_0-1^1S_0) transitions (Fig. 1). Most important, this process allows one to measure the undistorted two-photon energy distribution for the 2E1 decay of the [1s2s] ($^1S_0$) state, which is of particular interest for a decisive test of theoretical predictions.

Extending our previous experiments on He-like ions to the measurement of a system with non-zero nuclear spin, we present here first data of the two-photon decay energy distributions in He-like gold (Z=79). The experiment was performed at the storage ring ESR with 300 MeV/u Li-like gold ions (Au^{76+}) colliding with N_2 target. For the details of the experimental setup we refer to [1-3]. In Fig. 2 (bottom) we present a preliminary spectrum measured by a Ge x-ray detector in coincidence with the up-charged Au^{77+} ions. The spectrum is dominated by an intense line at 51.5 keV (lab. frame) corresponding to the M1 de- cay of the [1s2s] $^3S_1$ state and a broad continuum towards lower energies representing the 2E1 decay of the [1s2s] $^1S_0$ level. For comparison, in Fig. 2 (top) we present a total x-ray spectrum (no coincidences). Note, the absence of x-rays lines from the decay of the 2p or higher states (Fig. 2: bottom) ensures that there is no intra/inter-shell excitation simultaneous with the K-shell ionization (compare [1-3]). The data analysis is in progress.

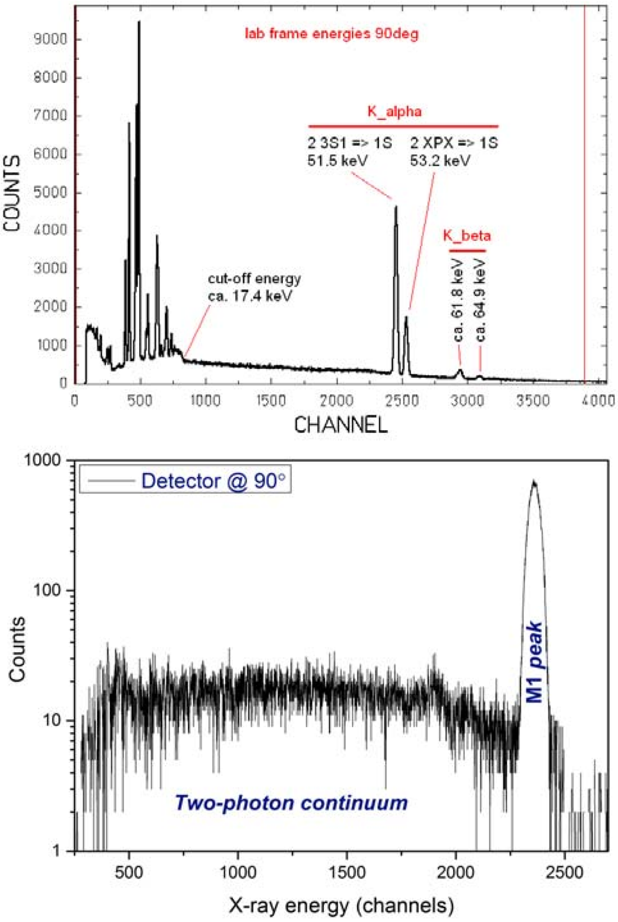

Figure 2: Preliminary projectile x-ray spectra as registered by the Ge-detector without coincidences (top), and with coincidences (bottom) with ionization particle detector.

References

[1] D. Banas et al., PRA 87, 062510 (2013)
[2] S. Trotsenko et al., PRL 104, 033001 (2010)
[3] J. Rzadkiewicz et al., PRA 74, 012511 (2006)
[4] S. Toleikis et al., PRA 69, 022507 (2004)

DOI:10.15120/GR-2015-1-APPA-MML-AP-24

Bayesian analysis of the EC-decay rate oscillations - Part II *

N. Winckler[1] *and the Two-Body Weak Decay collaboration*[1]
[1]GSI, Darmstadt

Bayesian model selection

We present the results of the model probabilities and Bayes factor of the model and data defined in Ref. [1, 2]. The table 1 shows the results obtained for uniform priors and different data sets. In table 1, the uniform prior of ω is defined in $[0, 3]$, which exclude the contribution of the global maximum likelihood at $\omega = 5.35$.

	EC data (245 MHz res.)	β^+ data (245 MHz res.)	EC data (cap. pick-up)
Sample size N	3616	2912	2989
Range (s)	[6,60]	[10,60]	[6,60]
$P(M_0\|\text{data})$	66.3%	84.94%	0.03%
$P(M_1\|\text{data})$	33.7%	15.06%	99.97%
B_{01}	1.97	5.64	0.0003
B_{10}	0.5	0.17	3645.4

Table 1: Model probabilities and Bayes factors results.

Prior sensitivity analysis

In order to study the the prior sensitivities, other prior distributions have been used in the analysis . For example, increasing the range of the uniform prior of the angular frequency to $[0, 7]$ increases the probability of M_1 to about 43%, as larger frequency components in the likelihood function are taken into account.

The use of gaussian priors with mean and width obtained from the 2007 experimental results – i.e. $a = 0.23(4)$, $\omega = 0.88(3)$, $\phi = -1.6(5)$ – have shown, for the model M_1, small probabilities of about 0.3%. This small probability can be explained when considering the likelihood function. The maximum contribution of the likelihood function is found for $a = 0.09(2)$ in the resonator data. The strength of the likelihood is reduced for amplitudes outside the range $a = 0.09 \pm 0.02$. Using a gaussian prior $N_a(0.23, 0.04)$ results in a posterior with small weights in the $a = 0.09 \pm 0.02$ region, reducing the M_1 posterior, and hence the Bayes factor. As a consequence, we note that previous measurements are not supported by the present analysis of the resonantor data, and that this latter does not exhibit a sufficiently strong likelihood at $a = 0.09 \pm 0.02$ to overcome the $N_a(0.23, 0.04)$ subjective prior.

Discussion

According to Jeffreys' scale, the Bayes factor for the 245 MHz resonator β^+- and EC- data have no support for the modulated decay model. This result is independent on the chosen priors. However the EC-data set obtained from the capacitive Schottky pick-up present decisive Bayesian evidence for the modulated decay, which is in complete contradiction with results obtained in resonator data.

As mentioned in Ref. [2], the observable of the pick-up and resonator data are not the same. The pick up data consist of three components, i.e. the decay time, the delay required to electron-cool the ion, and the systematic error in the determination of the observable. The decay time + delay observable has been analyzed as well in the resonator data. The obtained posterior probability is about 33% for the oscillation model, which a priori exlude the delay distribution as being responsible for the difference in the pick-up and resonator data. The main difference remaining between these two data sets are the distribution of the systematic errors in the determination of the observables. These systematic errors are assumed to be small enough to be neglected in the resonator data because of the large signal-to-noise ratio of the ion signatures in the time resolved spectra. This assumption may not be valid for the pick-up time resolved spectra, which present poor signal-to-noise ratio.

Conclusion

We have shown that Bayesian model selection methods do not support the oscillation model in the 245 MHz resonator data but support, nevertheless, oscillation in the pick-up data. This conclusion is corroborated by the results of frequentist hypothesis testing and likelihood analysis [2], by Bayesian information criterion [3] and by an independent Bayesian analysis using the binned likelihood method and the nested sampling algorithms [4]. We note that AIC analysis presents oscillation in the resonator data as well. However, it has been shown [5] that the associated decision making in the AIC framework has a 99% Type I Error rate, discrediting its reliability in our analysis.

Bayesian and frequentist analysis of the decay time + delay in the resonator data have been performed, and do not support the oscillation model. Since the main difference between the significant and non significant data set remains in the systematic error distributions, this result point out to possible uncontrolled systematic effects in the pick-up data.

References

[1] P. Kienle et al., "High-resolution measurement of the time-modulated orbital electron capture and of the β^+ decay of hydrogen-like ^{142}Pm^{60+} ions", PLB 726 (2013) 638

[2] N. Winckler, et al., "Unbinned likelihood Analysis of the EC-decay rate oscillations - Part I & II", GSI Report (2014)

[3] N. Winckler, et al., "Further insight into Bayesian and Akaike information criteria ", GSI Report (2013)

[4] M. Trassinelli, " nested fit", private communication (2014)

[5] N. Winckler, "Bayesian and Akaike information criteria of the EC-decay rate oscillations", GSI Report (2014)

---

* This work is part of the EMMI Rapid Reaction Task Force presentation given in Jena, July 2014

DOI:10.15120/GR-2015-1-APPA-MML-AP-25

Experimental studies on elastic X-ray scattering*

K.-H. Blumenhagen†[1,2,3], *T. Gaßner*[1,2,3], *A. Gumberidze*[3,4], *R. Märtin*[1,3], *N. Schell*[5], *U. Spillmann*[3], *S. Trotsenko*[1,3], *G. Weber*[1,3], *and Th. Stöhlker*[1,2,3]

[1]HI-Jena, Germany; [2]IOQ, University of Jena, Germany; [3]GSI, Darmstadt, Germany; [4]EMMI, Darmstadt, Germany; [5]HZG, Geesthacht, Germany

Photon scattering in the presence of strong electromagnetic fields has been studied in an experiment where hard X-rays (175 keV) were elastically scattered by a high-Z (gold) target. Previous studies already covered a broad range of photon energies and target materials [1, 2]. While in most of those experiments the differential scattering cross section was studied, we performed a combined measurement of the angular distribution and the angle-dependent linear polarization of elastically scattered hard X-rays. As in this energy regime the scattering cross section is relatively small, in particular at backward angles, a high-intensity photon source for monoenergetic hard X-rays was required. Moreover, for our study we wanted to use polarized inicdent X-rays. These requirements made the use of a novel 3rd generation synchrotron radiation source mandatory. On the other hand, we needed an efficient polarization-sensitive detector which could be fulfilled with a large-volume, segmented solid state detector that can act as a Compton polarimeter. The incident 175-keV photon beam was provided by the High Energy Material Science Beamline P07 [3] at the synchrotron radiation source PETRA III at DESY, Hamburg. It was scattered by a thin solid gold target and the scattered radiation was detected by a 2D Si(Li) strip polarimeter [4] and a standard high-purity germanium detector. This setup allowed the parallel measurement of the differential cross section and the polarization. In this report, we present preliminary results for the differential cross section, the analysis of the polarization will follow later. Figure 1 (a) shows the energy spectrum of the germanium detector mounted at a scattering angle $\theta = 30°$. The main features are the Rayleigh peak (elastically scattered photons), the Compton peak (inelastically scattered photons) and the Au Kα and Kβ lines (fluorescence from the target). The differential cross section is obtained by determining the intensity of the Rayleigh peak and normalizing it to (i) the Au-Kα_1 cross section and (ii) the Compton cross section. This procedure allows to cancel effects from the experimental geometry and fluctuations in the incident beam intensity. The main task of the data analysis was the area determination of the Kα_1-, the Compton- and the Rayleigh peak. For the narrow Kα_1- and Rayleigh lines, the sum of an analytical peak shape and a linear background was fitted to the data. For the broad Compton peak, a non-analytical fit curve based on the theoretical Compton profile of gold was created. A Monte Carlo simulation corrected the distribution for photons that were scattered from parts of the target chamber. The spectrum from the simulation - corrected for detector efficiency and resolution was then the fit function. Preliminary results are shown in figure 1 (b).

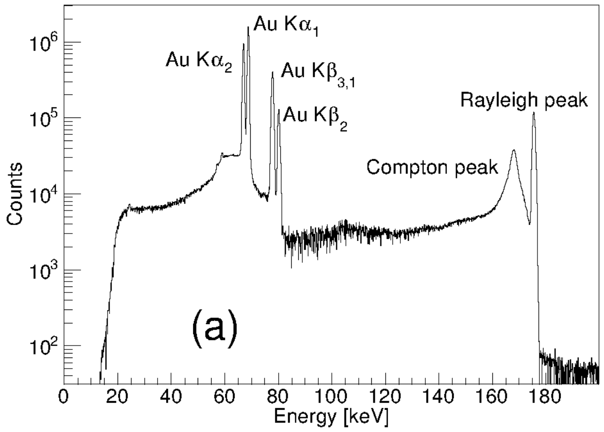

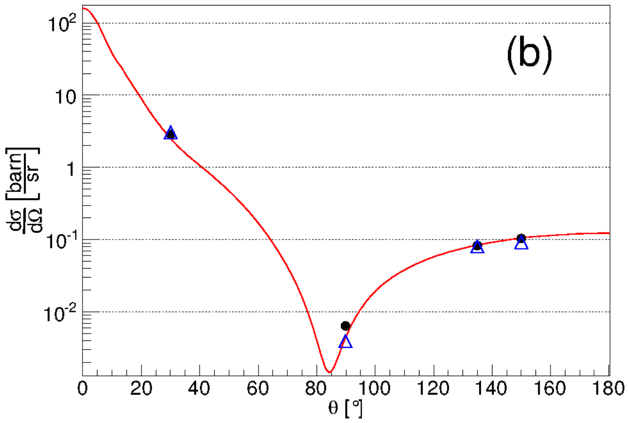

Figure 1: Preliminary results: (a) Energy spectrum of the germanium detector at $\theta = 30°$; (b) Differential cross section: Kα_1 normalization (solid circles), Compton normalization (open triangles), preliminary theory [5] (solid line). Statistical errors are smaller than the point size, systematic errors are not yet included.

References

[1] P. P. Kane et al., Phys. Rep. 140, 75-159 (1986).
[2] D. A. Bradley et al., Radiat. Phys. Chem. 56, 125-150 (1999).
[3] N. Schell et al., Mater. Sci. Forum 772, 57-61 (2014).
[4] D. Protic et al., IEEE Trans. Nucl. Sci. 53, 3181-3185 (2005).
[5] A. Surzhykov et al., submitted to J. Phys. B.

---

* Work supported by HGS-HIRe / Helmholtz Alliance (HA216/EMMI) / DESY and HZG support at beamline P07.

† k.-h.blumenhagen@gsi.de

S-EBIT at HITRAP: Status report

S. Trotsenko[1,2], *W. Chen*[2], *J. Menssen*[1,2,3], *G. Vorobjev*[2], *D. Racano*[2], *A. Gumberidze*[2,4], *C. Kozhuharov*[2], *O. Forstner*[5], *P.-M. Hillenbrand*[2], *F. Herfurth*[2], *R. Schuch*[6], *and Th. Stöhlker*[1,2,4,5]

[1]Helmholtz-Institut Jena, D-07743 Jena, Germany; [2]GSI Helmholtzzentrum für Schwerionenforschung, D-64291 Darmstadt, Germany; [3]Hochschule Rhein Main, University of Applied Sciences, D-65428 Rüsselsheim, Germany; [4]ExtreMe Matter Institute EMMI, D-64291 Darmstadt, Germany; [5]Friedrich-Schiller-Universität Jena, D-07743 Jena, Germany; [6]Department of Physics, Stockholm University, SE-10691 Stockholm, Sweden

The Super-EBIT (S-EBIT) [1] plays an important role for accomplishing the mission of Helmholtz Institute Jena (HI-Jena) towards Facility for Antiproton and Ion Research (FAIR). It considerably expands the opportunities for developing new technologies and procedures for novel experiments with highly charged ions (HCI). In the S-EBIT program of HI-Jena the emphasis is put on X-ray spectroscopy and the interaction of intense laser radiation with HCI, including the respective diagnostics. The project will open up further points of contact, e.g. in the fields of X-ray wavelength standards, astrophysics, and material sciences. The S-EBIT will contribute substantially to the research program at GSI/FAIR as well as to the required R&D activities such as the development of x-ray spectrometers, calorimeter detectors, x-ray optics, and traps for the interaction of intense laser light with highly charged ions. Moreover, the S-EBIT program of Helmholtz Institute Jena is of substantial importance for bridging the gap of the transition time for heavy ion experiments between GSI and FAIR. In particular, as an operating source of highly charged ions during the shutdown period of the GSI accelerator, the S-EBIT will facilitate research and development works indispensable for SPARC experiments at FAIR. Within this decade the new laboratory building at the HI-Jena is expected to be available. This will allow moving the S-EBIT installation from GSI to the HI-Jena where it can be coupled to the available unique laser infrastructure where intense laser pulses with high repetition rate are provided (JETI200, POLARIS). Still, S-EBIT will serve also as an R&D facility for FAIR both in combinations with the intense laser pulses but also as a standalone device.

Currently, the S-EBIT is being installed at the experiment platform of the HITRAP facility [2] at GSI and it will be used not only as a standalone device but also as an ion source for highly charged heavy ions. At the experiment platform, various experimental setups have already been installed and are available for operation such as traps for QED experiments, surface experiments, gas target stations, and recoil ion spectrometers. The HITRAP decelerator is currently getting commissioned and is not yet operational [2] and in particular also first experiments with highly-charged ions in intense laser fields can be anticipated (PHELIX) at the HITRAP location [3].

A brand new transportable frame for the S-EBIT has been manufactured which will allow one to move the source towards experimental installations in order to be able to combine with the already available and planned experiments [2]. Preparations of the new superconducting magnet (4T) have been finalized and it is now being tested for the performance in the new S-EBIT environment. In a superconducting Helmholtz coils configuration of the S-EBIT a special attention has to be paid to efficient cooling of the magnet as it has to perform with the currents of higher than 60 A. In order optimize that the new shielding and cooling parts have being manufactured which are currently undergoing their first cryogenic tests. Also, brand new drift tubes to fit the new 4T-superconducting magnet have been manufactured, which along with the optimized S-EBIT chamber feedthru system will allow a reliable fast ramping of the drift tubes potentials at up to +40 kV. In combination with the -220kV on the e-gun/collector terminal the electron beam energy of 260 keV can potentially be reached. In addition, the work on integrating the S-EBIT control system into the GSI/HITRAP infrastructure is on going.

References

[1] R.Schuch et al., JINST5, C12018 (2010)

[2] Z.Andelkovic et al., GSI Scientific Report 2013 (2014).

[3] M. Vogel, W. Quint, G.G. Paulus and Th. Stöhlker, Nucl. Instr. Meth. B 285, 65 (2012).

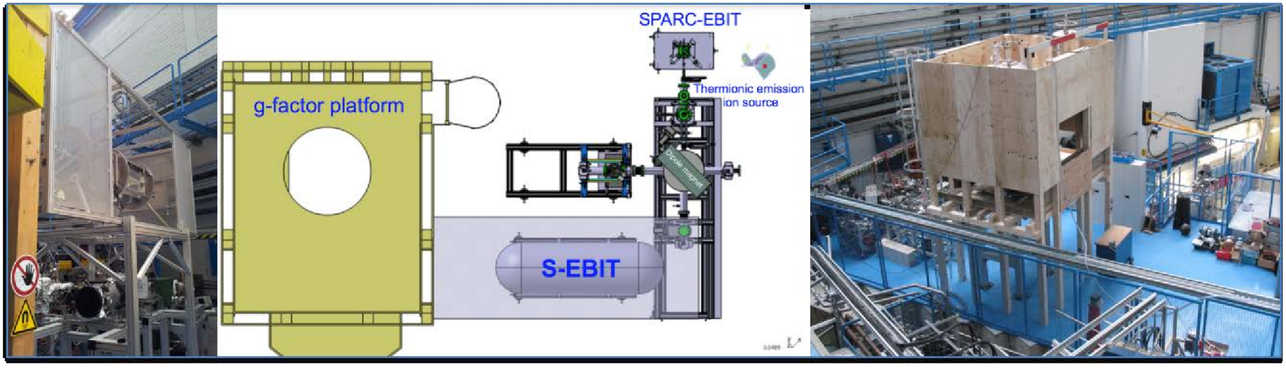

DOI:10.15120/GR-2015-1-APPA-MML-AP-27

Elastic x–ray scattering by neutral atoms: Outer–shell effects *

A. Surzhykov†1, *V. A. Yerokhin*2, *Th. Stöhlker*1,3,4, *and S. Fritzsche*1,3
1Helmholtz Institute Jena, Germany; 2St. Petersburg State Polytechnical University, Russia; 3University of Jena, Germany; 4GSI Helmholtzzentrum, Darmstadt, Germany

With the recent progress in the setup of high brilliance third–generation synchrotron facilities, new opportunities arise to study the elastic scattering of x–rays by heavy atoms. For photon energies below 1 MeV, the main contribution to this elastic processes arises from the interaction of x–rays with bound atomic electrons. This so–called *Rayleigh* scattering attracts considerable attention as a valuable tool for studying the relativistic, many–body and even quantum electrodynamics (QED) effects in many–electron systems. During the last decades, a large number of experiments have been performed to explore the Rayleigh process for a wide range of photon energies and for various targets. In 2012, for example, the elastic scattering of (linearly polarized) hard x–rays by gold atoms has been observed at the PETRA III synchrotron facility in DESY [1]. To better understand the outcome of this experiment, a theoretical investigation of the elastic $\gamma + A \to \gamma + A$ process is required which would account for both the many–body phenomena and the relativistic non–dipole contributions to the electron–photon interaction.

The theoretical analysis of the elastic Rayleigh scattering is usually performed within the framework of the second–order perturbation theory. In this approach, all the properties of the scattered light can be expressed in terms of the transition amplitudes [2, 3]:

$$\mathcal{M}(\omega) = \sum_{\nu} \frac{\left\langle \psi_i \left| \hat{\mathcal{R}} \right| \psi_\nu \right\rangle \left\langle \psi_\nu \left| \hat{\mathcal{R}} \right| \psi_i \right\rangle}{\epsilon_i - \epsilon_\nu \pm \hbar\omega} , \qquad (1)$$

where ψ_i and ϵ_i are the (many–body) wave-function and the energy of the atomic state *before* (as well as *after*) the scattering, $\hbar\omega$ is the photon energy, and $\hat{\mathcal{R}}$ is the electron–photon interaction operator. In Eq. (1), moreover, the summation $\sum_\nu$ runs over the *complete* spectrum of an atom, including not only bound– but also positive and negative energy continuum–states. In order to perform this non–trivial summation over *many–electron* states we employed the independent particle approximation (IPA) in which the photon is scattered by a single (active) electron at a time, while the remaining electrons are kept “frozen” [2, 4].

By making use of Eq. (1) and the independent particle approximation, we have explored the elastic scattering of (completely linearly) polarized x–rays by heavy atoms [4]. In this study, special attention was paid to the question of how various atomic shells contribute to the Rayleigh process. In Fig. 1 we display, for example, the angle–differential Rayleigh cross section for the led target and the incident radiation with energy $\hbar\omega = 145$ keV. In our calculations, we have restricted the summation over the occupied electron shells to the K (red dotted line), KL (maroon dash–dotted line), KLM (green dash–dot–dot line), KLMN (blue dashed line) and the KLMNO shells (black solid line). As seen from the figure, the x–ray scattering by weakly bound outer–shell electrons may dramatically affect the differential cross section. The most pronounced effect can be observed at forward scattering angles, where the cross section is enhanced by more than two orders of magnitude if the interaction of incident radiation with (sub–) valence electrons is taken into account. We argue, therefore, that the angular–resolved measurements of the elastic Rayleigh process, as currently performed at the PETRA III facility, may provide valuable information about electronic shell structure of heavy atoms.

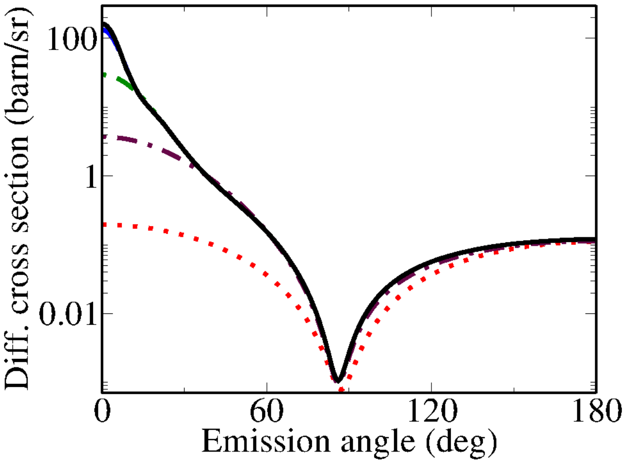

Figure 1: The angle–differential cross section for the elastic scattering of linearly polarized photons with energy $\hbar\omega$ = 145 keV by neutral lead atom. Calculations have been performed within the framework of the independent particle approximation and by taking various atomic shells into account. See text for further details. Data from Ref. [4].

References

[1] K. H. Blumenhagen *et al.*, this Annual Report (2015).

[2] S. C. Roy *et al.*, Rad. Phys. Chem. **56**, 1 (1999).

[3] A. Surzhykov *et al.*, Phys. Rev. A **88**, 062515 (2013).

[4] A. Surzhykov *et al.*, submitted to J. Phys. B.

---

* Work is supported by the BMBF under the project No. 05K13VHA.

† a.surzhykov@gsi.de

DOI:10.15120/GR-2015-1-APPA-MML-AP-28

CsI-Silicon Particle detector for Heavy ions Orbiting in Storage rings (CsISiPHOS)*

M.A. Najafi†[2,3], *I. Dillmann*[1,3,5], *F. Bosch*[1], *T. Faestermann*[2], *B. Gao*[1,6], *R. Gernhäuser*[2], *C. Kozhuharov*[1], *S. A. Litvinov*[1], *Yu. A. Litvinov*[1], *L. Maier*[2], *F. Nolden*[1], *U. Popp*[1], *M. S. Sanjari*[1], *U. Spillmann*[1], *M. Steck*[1], *T. Stöhlker*[1], *and H. Weick*[1]

[1]GSI Helmholtzzentrum für Schwerionenforschung, Darmstadt, Germany; [2]Technische Universität München, München, Germany; [3]Justus-Liebig Universtät Giessen, Giessen, Germany; [4]Goethe Universität Frankfurt, Frankfurt, Germany ; [5]TRIUMF, Vancouver, Canada; [6]Max Planck Institute für Kernphysik, Heidelberg, Germany

The β decay of highly-charged ions at the Experimental Storage Ring (ESR) at GSI Darmstadt has been a rich source of new discoveries about decay properties of atomic nuclei [1,2]. A heavy-ion detector was designed and developed for such decay studies, which is also a prototype of the in-pocket detectors for the future ILIMA programme at the Collector Ring (CR) [3] at FAIR. The detector includes a stack of six silicon pad detectors ($60\times40\times0.5$ mm^3), a double-sided silicon strip detector (DSSD) ($60\times40\times0.3$ mm^3), a tantalum slab as passive absorber ($60\times40\times1$ mm^3), and a CsI scintillation detector ($24\times24\times10$ mm^3). The CsI crystal is coupled to a circular silicon photodiode with a diameter of 35 mm. This configuration serves as a $\Delta E/E$ telescope to be used for detection and identification of each incident ion. The versatile design of the detector allows identification of heavy ions at energies up to 400 MeV per nucleon. Furthermore, the trajectory of the daughter ions and recombined parent ions at the position of the pocket is determined using the DSSD.

In a recent experiment at ESR, the detector was placed in a pocket at an outside position in the northern arc, right behind the dipole. The purpose of this experiment was to measure the β^+ decay rate of H-like ^{142}Pm^{60+} ions into ^{142}Nd^{59+}. To generate the ions of interest, a primary beam of ^{152}Sm was impinged on a beryllium target at the entrance of the Fragment Separator (FRS). The ^{142}Pm^{60+} ions were separated using the FRS and then guided to the ESR. After stochastic and electron cooling, the pocket was inserted to the ring and intercepted the daughter ions. Figure 1 shows the position histogram obtained from the DSSD. In addition to the daughter ions (shown in black), another species is observed that can only be from the mother ions that recombined with an electron in the electron cooler, i.e. ^{142}Pm^{59+} (shown in grey). Figure 2 shows the $\Delta E/E$ histogram, in which ΔE was obtained from the sum of the energy signals of each silicon pad detector and E from the energy signals of the CsI scintillator. With an energy-deposit resolution (FWHM) of 60 MeV at 6.7 GeV, and a total energy resolution of 330 MeV at 56.8 GeV, the detector can identify neighbouring isobars distinctly.

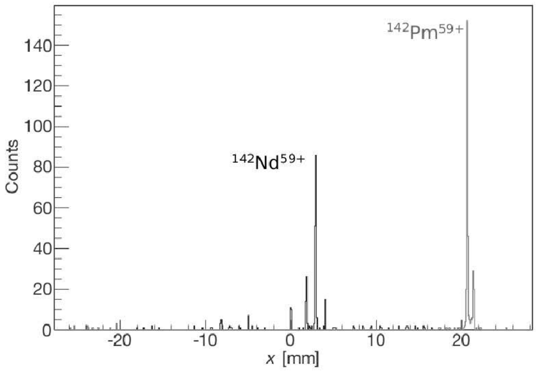

Figure 1: Position of the ions on the DSSD. The grey histogram represents the recombined mother ions, ^{142}Pm^{59+}.

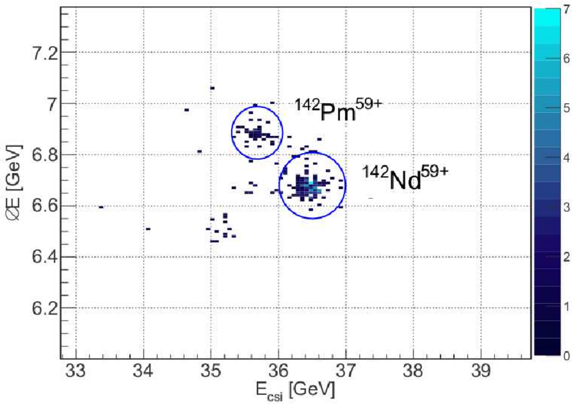

Figure 2: Total energy deposit in silicon pad detectors, ΔE, versus energy in CsI, E_{CsI}.

References

[1] Y. A. Litvinov, F. Bosch, Reports on Progress in Physics 74 (1) (2011) 016301.

[2] F. Bosch, Y. A. Litvinov, T. Stölker, Progress in Particle and Nuclear Physics 73 (0) (2013) 84 – 140.

[3] A. Dolinskii, et. al., Nuclear Instruments and Methods in Physics Research Section B, 266 (19) (2008) 4579 – 4582.

---

* Work supported by the BMBF project 05P12RGFNJ (Multi-purpose pocket detector for in-ring decay spectroscopy), and the Helmholtz association via the Young Investigators Project "LISA: Lifetime Spectroscopy for Astrophysics" (VH NG 627), and the Maier-Leibnitz Laboratory in Munich. Authors are grateful for the essential help of M. Böhmer (TUM), GSI target lab, and GSI accelerator staff.

† m.a.najafi@gsi.de

DOI:10.15120/GR-2015-1-APPA-MML-AP-29

Unbinned likelihood Analysis of the EC-decay rate oscillations - Part II *

N. Winckler[1] *and the Two-Body Weak Decay collaboration*[1]
[1]GSI, Darmstadt

Likelihood Ratio Profile

A likelihood ratio profile w.r.t. the angular frequency ω (c.f. fig. 1) have shown that the global maximum in the range $\omega \in [0, 7]$ in the EC data is found at $\omega = 5.35(1)$. This maximum remains in the complete set of data (sample size of 8663 EC-decays) but is absent in the EC-data obtained with the capacitive pick-up and in the β^+-data of the 245 MHz resonator. The absence of the frequency at 5.35 in the capacitive pick-up data is expected, since the observable of these data correspond to the decay time + the systematic uncertainty + the distribution of the delay required to electron-cool the ion, washing out high frequencies by convolution. We can observe a third maximum at $\omega = 4.68(2)$. The strength of the three observed maxima is sensitive to systematic effects. For example, decreasing the time interval of the data from [6,60] to [10,60] have shown that these frequencies, though remaining, fluctuate in their relative strength, putting them on the same footing.

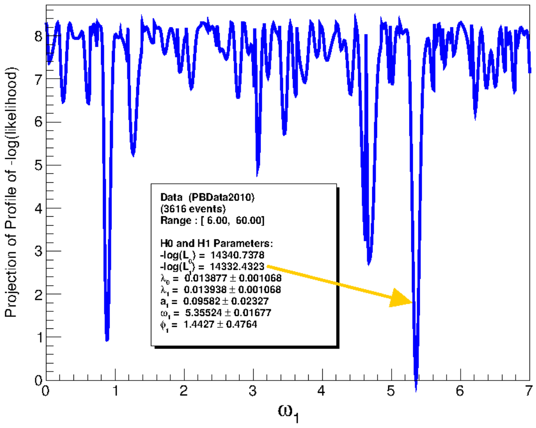

Figure 1: Likelihood ratio profile for the oscillation frequency in the EC-data set. The global maximum is found at 5.35. Two more maxima of smaller strength are obtained with this method at $\omega = 0.88$ and 4.68.

Likelihood ratio test

In order to determine the significance of the modulation, a likelihood ratio test (LRT) was performed. The distribution of the LRT have been obtained by Monte Carlo simulation [1]. The results of the hypothesis tests are shown in table 1.

	EC data (245 MHz Res.)	β^+ data (245 MHz Res.)	EC data (cap.)
Sample size N	3616	2912	2989
Time interval (s)	[6.0 ; 60.0]	[10.0 ; 60.0]	[6.0 ; 60.0]
LRT statistics	14.8	6.8	35
LRT p-value	9.4%	97.5%	$< 0.0102\%$
significance	1.32 sigma	≈ 0	> 3.7 sigma

Table 1: Likelihood ratio test results. Only the capacitive pickup data present significant results.

We note, for the 245 MHz resonator EC-data, that a significance of 1.3 sigma is not sufficient to reject the pure exponential decay. On the other hand the capacitive pick-up data present a significance greater than 3.7 sigma. The boundary in the capacitive pick-up data is due to the sample size of the simulated likelihood ratio distribution. As mentioned above, the obsevable of the pick-up data corresponds to the decay time + a delay (and a systematic error). This observable has been evaluated as well for the 245 MHz resonator data and therefore has been analyzed for comparison. The obtained LRT statistics is 14 which is comparible to the one found for the decay times without delay. This result exclude oscillation in the decay time + delay as well. Note that the significances are obtained from sampled LRT distribution under a clean null hypothesis, i.e. without systematics, which may result in an overestimatation of the significance.

Conclusion

For the resonator data we have shown that an amplitude estimate of 9 (2) % is compatible with a pure exponential decay, that the likelihood $\omega = 0.88$ is not the global maximum, and that the hypothesis test do not reject the pure exponential decay for the EC- and β^+ decay time data. These results are consitent with a pure exponential decay but contradict the pick-up data which present, despite a smaller sample size, a much higher significance for the oscillation model. The analysis of the decay time + delay in the 245 MHz resonator is also consistent with the null hypothesis. Accordingly, the delay distribution cannot explain this difference.

Assuming that the physics signatures are better observed with the 245 MHz resonator data, these results might point out possible sytematic effects that are not under control or artefact in the capacitive pick-up data. A Bayesian analysis coroborate this result [2].

References

[1] N. Winckler, GSI-report “Likelihood ratio distribution” 2014-2015

[2] N. Winckler et al., GSI-report “Bayesian analysis of the EC-decay rate oscillations - Part I and II” 2014-2015

---

* This work is part of the EMMI Rapid Reaction Task Force presentation given in Jena, July 2014

DOI:10.15120/GR-2015-1-APPA-MML-AP-30

Thermal simulations of a C beam stripper for experiments at Spiral2*

N.A. Tahir[1], *V. Kim*[2], *E. Lamour*[3], *I.V. Lomonosov*[2], *A.R. Piriz*[4], *J.P. Rozet*[3], *Th. Stöhlker*[5], *and D. Vernhet*[3]

[1]GSI, Darmstadt, Germany; [2]IPCP, Chernogolovka, Russia; [3]Institut des NanoSciences de Paris,UMR CNRS–Université Pierre et Marie Curie, Paris, France; [4]UCLM, Ciudad Real, Spain; [5]GSI, Darmstadt, Germany; IOQ, Friedrich-Schiller-Universitt, 07743 Jena, Germany; Helmholtz-Institut Jena, 07743 Jena, Germany

We present 3D thermal simulations (excluding hydrodynamics) of a wheel shaped beam stripper made of solid C that has been designed for use in the FISIC (Fast Ion-Slow Ion Collision) experiments at the SPIRAL2 facility. The inner radius, R_1 of the target is 32 cm, the outer radius, R_2 is 35 cm while the beam is perpendicular to the target surface at a radius, R_0 = 33 cm (see Fig. 1). The target is rotated at a rate of 2000 rpm. Several ion species including Ne, Ar and Ni, with the following beam parameters, have been considered. The transverse ion beam intensity distribution in the focal spot is assumed to be Gaussian with σ = 0.5 mm corresponding to the most extreme case. At the exit of the LINAC, the beam comprises of particle bunches, each bunch having a duration of 1 ns while the bunch frequency is 88 MHz that leads to a separation of 10.36 ns between two neighboring bunches.

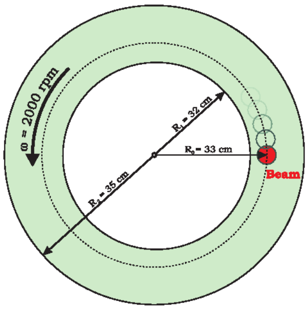

Figure 1: Stripper geometry.

Detailed simulations have been done for the following sets of beam and target parameters.

Case 1: Ne^{7+} with E = 5 MeV/u, I = 10 pμA and N = 6.25x10^{13}/s. Two different target thicknesses, namely, 13 and 100 μg/cm^2, respectively, have been considered.

Case 2: Ar^{13+} (a) with E = 4 MeV/u, I = 10 pμA and N = 6.25x10^{13}/s. Three different target thicknesses including, 4.4, 20 and 320 μg/cm^2, respectively, have been used.

(b) with E = 14 MeV/u, while using four different target thicknesses, namely, 9.5, 32, 105 and 750 μg/cm^2.

Case 3: Ni^{18+} (a) with E = 10 MeV/u, I = 1 pμA and N = 6.25x10^{12}/s. Five different target thicknesses including, 34, 60, 80 190 and 1300 μg/cm^2, respectively, have been considered.

(b) with E = 14 MeV/u, again using five different target thicknesses, namely, 42, 60, 95, 200 and 1450 μg/cm^2, respectively.

These simulations have been performed using a 3D computer code PIC3D [1] which includes ion energy deposition, heat conduction and thermal radiation losses. Two different values of the emissivity, ϵ, namely, 0.2 and 0.8, have been used to check the influence of emissivity on target cooling.

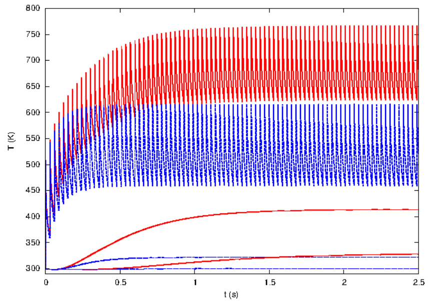

Figure 2: Temperature vs time at R_0 (top curve), R_1 (middle) and R_2 (lowest); red curves (ϵ = 0.2), blue curves (ϵ = 0.8); Ar^{13+}, E = 4 MeV/u, I = 10 pμA and target thickness = 320 μg/cm^2.

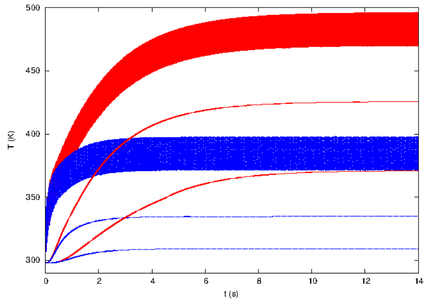

Figure 3: Same parameters as in Fig. 2, but using Ni^{18+}, E = 10 MeV/u, I = 1 pμA and target thickness = 1300 μg/cm^2.

It is seen in Figs. 2 and 3 that the temperature at the center of the focal spot remains safely below the sublimation temperature of C. However, the possibility of material damage due to thermal stresses needs to be addressed. This work is in progress.

References

[1] V.E. Fortov et al., Intnl. J. Impact Eng. 33 (2006) 244.

---

* Work supported by the BMBF

DOI:10.15120/GR-2015-1-APPA-MML-AP-31

Lifetime measurements of the ground state hyperfine transitions in H-like and Li-like bismuth*

Jonas Vollbrecht†[1] *and the LIBELLE collaboration*
[1]Institut für Kernphysik, Westfälische Wilhelms Universität, 48149 Münster, Germany

The goal of the LIBELLE experiment is to determine the energies of the ground state HFS transitions in H-like and Li-like bismuth via laser spectroscopy. If both values are known with sufficient precision, this enables a test of bound state QED in extreme electric and magnetic fields via the calculation of the so-called specific difference of the transitions (see Shabaev et al. [1]). Nuclear structure effects, like the distribution of the magnetic moments, that otherwise mask the QED contribution, are largely canceled out in the specific difference.

Both transitions were successfully measured with the LIBELLE experiment in 2011 [2]. The accuracy was limited, however, by the determination of the ion velocity which is needed for transformation to the rest frame. Besides the investigation of the transition energies the lifetime of the Li-like state was measured as well. With an improved determination of the ion velocity and a high performance data acquisition (DAQ) the beam-time was repeated in March 2014 [3]. The new DAQ was capable to record timestamps for each detected photon which are set in relation to a reference point. For $^{209}\mathrm{Bi}^{82+}$ this reference point is given by the laser shot itself leading to a measurement interval of 30 ms. This is long enough since the lifetime of $^{209}\mathrm{Bi}^{82+}$ is about 400 μs. For $^{209}\mathrm{Bi}^{80+}$ a shutter has been introduced into the laser beam line to extend the decay interval to ~ 1 s, since the expected lifetime is about 80 ms. During measurement cycles the upper HFS state is populated for about 0.5 s, than the shutter is closed and the ions can de-excite for about 1 s.

The ions are compressed into two bunches, one is excited by the laser, the other is treated as reference. The timestamp can be synchronized to the ions revolution period in the ESR to obtain fig. 1 and distinguish between signal and reference peak. For H-like ions the most accurate result is obtained by simply counting all events in the signal peak region as a function of time after laser excitation (see fig. 2, upper plot). For Li-like data a background correction is mandatory, therefore the signal and reference peaks of fig. 1 are fitted via two exponentially modified Gaussians and a constant offset with the difference area as fit parameter. The obtained lifetime curves (fig. 2) can be fitted via an exponential decay model. In case of $^{209}\mathrm{Bi}^{80+}$ the model can be extended taking into account stimulated emission and absorption, to also fit the rising branch of the data during laser excitation. Preliminary lifetimes transformed into the rest frame are given in tab. 1.

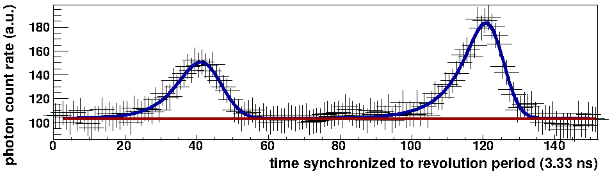

Figure 1: Photon count rate versus photon incident time convoluted with revolution time in 3.33 ns bins.

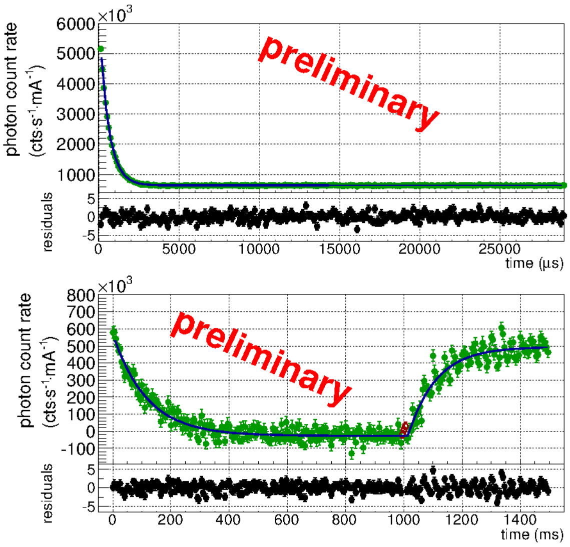

Figure 2: Photon count rate versus decay time for H- and Li-like bismuth together with fit.

Table 1: Preliminary lifetime results transformed in the ions rest frame, compared to other experimental work and theoretical prediction.

	H-like (τ/μs):	Li-like (τ/ms):
this work	(399.15 ± 1.64)	(82.15 ± 2.93)
exp. [4]	(351.0 ± 16.0)	-
exp. [5]	(397.50 ± 1.50)	-
theo. [6],[7]	(399.01 ± 0.19)	(82.0 ± 1.4)

References

[1] V M Shabaev et al, Phys. Rev. Lett., 86 (2001), 3959
[2] M Lochmann et al, Phys. Rev. A 90, (2014), 030501
[3] J Ullmann et al, GSI Scientific Report (2014)
[4] I Klaft, PhD-thesis, Mainz, (1994)
[5] H Winter, PhD-thesis, TU Darmstadt, (1999)
[6] V M Shabaev et al, Can. J. Phys. 76, (1998), 907-910
[7] V M Shabaev et al, Phys. Rev. A 57, (1998), 149-156

---

* This work is supported by BMBF under contract numbers 05P12PMFAE and 05P12RDFA4.

† jonas.vollbrecht@uni-muenster.de

DOI:10.15120/GR-2015-1-APPA-MML-AP-32

Construction and test of a detection system for forward emitted XUV photons*

D. Winzen[†1], *V. Hannen*[1], *H.-W. Ortjohann*[1], *F. Trittmaack*[1], *J. Vollbrecht*[1], *Ch. Weinheimer*[1], *and D. Winters*[2]

[1]WWU Münster, Institut für Kernphysik, Wilhelm-Klemm-Str. 9, 48161 Münster; [2]GSI Helmholtzzentrum für Schwerionenforschung GmbH, Planckstr. 1, 64291 Darmstadt

The Institut für Kernphysik in Münster is currently developing a system for in-vacuum detection of XUV photons in the wavelength range from $<$ 10 nm up to about 250 nm. The system will be installed at the ESR and consists of a movable cathode plate with a central slit that can be positioned around the ion beam axis to collect photons emitted in the forward direction during the de-excitation of stored highly-charged ions. Secondary electrons emitted from the cathode will be guided by a magnetic field and a system of ring electrodes to a multi-channelplate detector (MCP) placed inside the vacuum. A similar detection system for optical photons making use of a movable parabolic copper mirror and a photomultiplier outside the vacuum, has already successfully been applied in the detection of the HFS transition in lithium-like bismuth in the LIBELLE experiment [1, 2]. There it was demonstrated, that the introduction of a suitable optical system at the beam position does not disturb the stored ions apart from a small loss in beam current during the movement of the system.

The electromagnetic design of the detector setup was simulated and optimized using the SIMION 8.1 [3] package (see figure 1) and provided the basis for the actual detector construction. The electric and magnetic field settings from simulation are currently being optimized in test measurements in Münster.

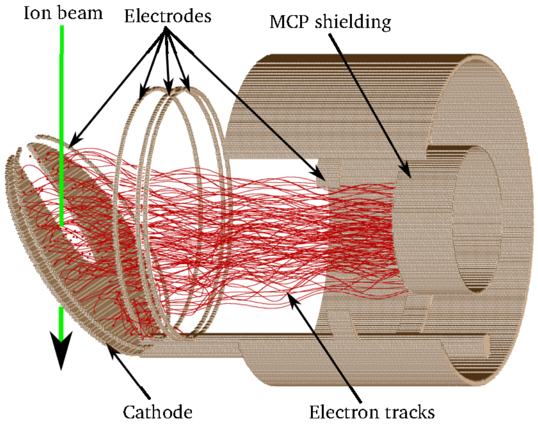

Figure 1: Electrode representation and simulated electron tracks calculated with the SIMION 8.1 package.

Figure 2 displays the setup of the detector system as it is used for these measurements. Five ring electrodes are placed between the cathode plate and the MCP, with the first electrode parallel to the cathode. The CF200 port into which the system can be retracted during injection of ions into the ESR actually acts as an additional sixth electrode on ground potential. Outside the vacuum chamber two solenoid coils are used to create a magnetic field which together with the electrostatic potential guides the electrons to the MCP. For the test measurements an UV-LED with a peak wavelength of 265 nm was installed inside the vacuum as photon source. The measurements aim to find electrode potential and magnetic field settings to maximize the detection probability for secondary electrons. Additionally, further simulations investigate improvements of the electromagnetic design, e.g. by an optimized coil geometry.

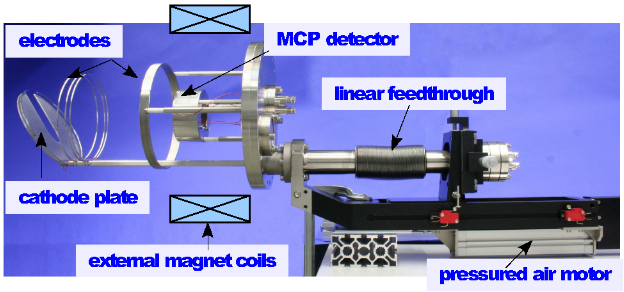

Figure 2: XUV detector system with schematically depicted magnet coils

The new detection system will be used for a measurement of the $^3\mathrm{P}_0$ – $^3\mathrm{P}_1$ splitting in beryllium-like krypton in an anti-collinear laser spectroscopy experiment at the ESR [4]. The meta-stable state $(1s^2 2s2p)$ $^3\mathrm{P}_0$ is populated during the production of the $^{84}\mathrm{Kr}^{32+}$ ions. For the excitation to the $(1s^2 2s2p)$ $^3\mathrm{P}_1$ state, a laser-beam is injected anti-collinear to the ions which are stored at a velocity of $\beta = 0.69$. Due to the Doppler shift, the required wavelength is red-shifted from 118 nm to 276 nm. The photons emitted during de-excitation to the ground state in the forward direction are in turn blue shifted to energies up to 170 eV.

References

[1] M. Lochmann *et al.*, Phys. Rev. A 90, (2014) 030501(R)

[2] V. Hannen *et al.*, Jinst 8 (2013) P09018

[3] SIMION package, Scientific Instrument Services, Inc., http://simion.com

[4] D.F.A. Winters *et al.*, *Laser spectroscopy of the* $(1s^2 2s2p)$ $^3P_0$ – $^3P_1$ *level splitting in Be-like krypton*, GSI Experiment E104

---

* Supported by BMBF under contract number 05P12PMFAE.987

[†] d.winzen@uni-muenster.de

DOI:10.15120/GR-2015-1-APPA-MML-AP-33

Development of a VUV-VIS-spectropolarimeter for target characterisation

Ph. Reiß[*1], *Ph. Schmidt*[*1], *A. Knie*[1], *Ch. Ozga*[1], *and A. Ehresmann*[†1]
[1]Institute of Physics and CINSaT, University of Kassel, Heinrich-Plett-Str. 40, 34132 Kassel, Germany

The interaction of highly charged ions with with atomic or molecular gases and free electrons has been thoroughly studied in the past by means of x-ray and particle spectroscopy. In these experiments, processes like radiative electron capture and dielectronic recombination have been investigated and compared to theory. The calculations, however, have been performed by averaging over all possible channels involving different electronic states of neutral atoms and ions, and then comparing the results with the experiments.

Advantages of Fluorescence Spectrometry

Dispersed fluorescence spectrometry, however, offers the possibility to detect state-specific fluorescence transitions in the projectile or target atoms. In coincidence with x-ray or particle spectrometry, this allows the investigation and testing of different processes during or following the interaction. The technique may also be used in experiments on radiative electron capture, the time-reversed process of photoionization, where an electron is captured from the continuum to a bound state while emitting a photon to be detected, or on dielectronic recombination, when the capture of a free electron leads to the excitation of another electron in the ion. The involved states can be identified by subsequent dipole transitions. Also, time-dependent fluorescence measurements have been shown to pose a monitor for longitudinal beam profiles. In order to evaluate the applicability of the technique, a pilot experiment for fluorescence spectrometry has been carried out at the GSI.

Experimental setup

The experiment has been carried out at the gas target of the ESR storage ring at the GSI, where a jet of neutral Xe atoms crossed a beam of Xe^{52+} and Xe^{54+} ions at 200 MeV/u. For the fluorescence measurements, a Seya-Namioka-type spectrometer has been used as depicted in fig. 1. The dispersive element is an optical grating with a concave radius of 1 m and a line density of 600 l/mm, the opening angle between entrance and exit arm is 70.15°, which is characteristic for this type of spectrometer. The detector is a commercial 1” micro-channel-plate detector from Quantar Technology that uses an S-20 Bialkali photocathode and a resistive anode for position encoding. In this tentative experiment, a view port with a borosilicate viewport was in the path of the fluorescence, restricting the lowest observable wavelength to 200 nm.

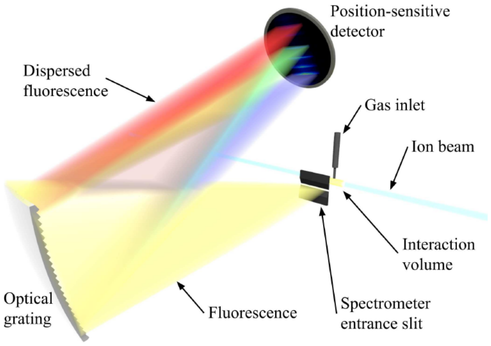

Figure 1: Scheme of the used spectrometer setup. Fluorescence light from the interaction volume passes through the entrance slit of the spectrometer and is dispersed by a spherical reflection grating that projects the dispersed fluorescence onto the surface of a position-sensitive detector. This enables the measurement of a certain fluorescence wavelength range. The width of which depends on the line density of the grating and the size of the detector.

First results

The wavelength range from 200 nm to 650 nm has been scanned and a number of individual fluorescence lines could be measured, most likely stemming from Xe^{2+} and Xe^{3+} ions in the gas target, as shown in fig. 2. A conclusive evaluation is in progress. The experiment showed that the application of fluorescence spectometry at heavy-ion storange rings is feasible. For future experiments, an optimised spectrometer for the use at CRYRING@ESR is planned.

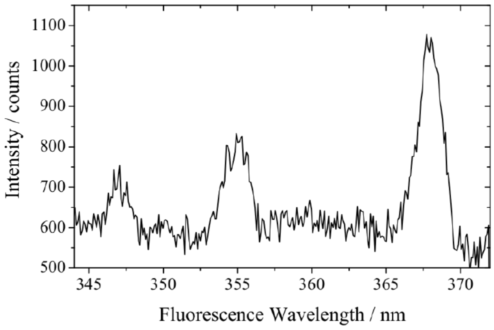

Figure 2: Example for the measured fluorescence spectrum from the Xe gas target, excited by Xe^{54+} ions at 200 MeV/u.

---

[*] Work supported by the HGS-HIRe for FAIR

[†] ehresmann@physik.uni-kassel.de

DOI:10.15120/GR-2015-1-APPA-MML-AP-34

A flexible pulsed ps/ns laser system for ion beam cooling at ESR/SIS100*

T. Beck[1] *and Th. Walther*[1]
[1]Institute of Applied Physics, TU Darmstadt, Germany

Stored relativistic (heavy) ion beams for precise atomic physics experiments are typically cooled by means of electron and/or stochastic cooling, in order to achieve a small relative longitudinal momentum distribution $\Delta p/p = 10^{-4} - 10^{-5}$. Laser cooling was introduced as a third cooling method, because it can provide even colder ion beams. During beamtime at the ESR in 2004, 2006, and 2012, C^{3+} ion beams were stored and successfully laser-cooled [1]. During the latest beam time a cw laser system developed at TU Darmstadt was continuously scanned across the $2S_{1/2} \rightarrow 2P_{1/2}$ transition of $^{12}C^{3+}$ [2]. The kinetic energy of the ions was 122 MeV/u. A relative longitudinal momentum distribution of at least $\Delta p/p = 10^{-6}$ was achieved.

One of the biggest challenges to face with laser cooling is to overcome heating due to intrabeam scattering (IBS). One option to suppress IBS is cooling all ions simultaneously. This technique is known as “white-light cooling” and employs a broad band pulsed laser systems (c.f. figure 1) [3,4].

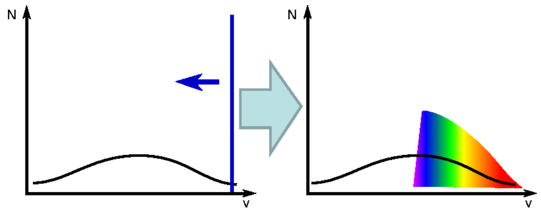

Figure 1: The general idea of white-light-cooling. Instead of tuning a narrowband continuous laser across the resonance cooling the individual velocity classes of the ions, a pulsed laser cools all ions simultaneously. N is the number of ions and v their velocity. Ideally the spectrum of the laser has a sharp edge towards the blue.

Here, we report on the progress of the development of a laser source for white-light cooling. The system will operate at 257 nm with a repetition rate of 1 MHz and a variable pulse length between 80 ps and 50 ns and nearly Fourier limited pulses. (c.f. figure 2). The flexible pulse duration will allow to tailor the output spectrum to match the velocity distribution of the ions.

An external cavity diode laser (ECDL) serves as the master oscillator. Its frequency is mode hop free tunable up to 37 GHz. The power of the ECDL is preamplified up to 9 W using a cw fiber amplifier. New pump laser modules enable very efficient amplification with a slope efficiency of more than 65 %. After amplification, a table top modulator box, consisting of an AOM and two subsequent Mach-Zehnder type EOMs, cuts pulses with a variable length between 80 ps and 50 ns out of the cw laser beam. The box is completely fiber based and easy to integrate into the cw laser setup.

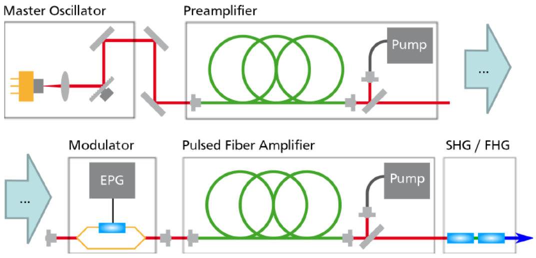

Figure 2: Schematic overview of the pulsed laser system. EPG: electronic pulse generator, SHG: second harmonic generation, FHG: fourth harmonic generation

After the pulses are generated, they serve as a seed for the pulsed fiber amplifier. Currently, it only consists of one amplification stage, but more are to be added in the near future. In the first stage of the pulsed amplifier we reached up to 4.8 mW of average power at 80 ps and 500 mW at 50 ns. The suppression of amplified spontaneous emission was better than 10 dB and with a linewidth of 30 MHz the 50 ns pulses are nearly Fourier transform limited.

In conclusion, we are making good progress towards a new pulsed laser system for cooling relativistic ion beams. Upon completion of the system, tests at the ESR or the CSRe in Lanzhou are possible. In combination with the existing cw laser, smaller momentum spreads and a more stable long time operation are conceivable.

References

[1] D. Winters et al, “Laser cooling of stored relativistic C^{3+} ions at the ESR”, GSI Scientific Report 2013

[2] T. Beck, B. Rein and Th. Walther, “An all solid-state based laser system for laser cooling of relativistic ion beams”, GSI Scientific Report 2013

[3] R. Calabrese, V. Guidi, P. Lenisa, R. Grimm, H.-J. Miesner, E. Mariotti and L. Moi, “White-light laser cooling of ions in a storage ring”, Hyperfine Interactions **99** (1996) 259

[4] S. N. Atutov, R. Calabrese, R. Grimm, V. Guidi, I. Lauer, P. Lenisa, V. Luger, E. Mariotti, L. Moi, A. Peters, U. Schramm and M. Stößel. ”White-light Laser Cooling of a Fast Stored Ion Beam”, Phys. Rev. Lett. **80** (1998) 2129

---

* Work supported by BMBF Grant No. 05P12RDRB2

DOI:10.15120/GR-2015-1-APPA-MML-AP-35

A high resolution measurement of the $1s^2 2s_{1/2} \rightarrow 1s^2 2p_{3/2}$ transition using the coherent resonant excitation of Li-like Uranium ions

A. Ananyeva[1,2], *T. Azuma*[3,4], *A. Braeuning-Demian*[1], *H. Bräuning*[1], *C. Klefner*[1], *S. Menk*[4], *Y. Nakano*[4], *Y. Yamazaki*[4]

[1]GSI, Darmstadt, Germany; [2]Goethe University, Frankfurt am Main, Germany; [3]Tokyo Metropolitan University, Japan; [4]RIKEN Advanced Science Institute, Japan

Introduction

Relativistic projectile ions passing a thin crystal-target experience a coherent periodic perturbation of the frequencies:

$$\nu_{field} = \gamma\, \mathbf{g} \cdot \mathbf{v}_{ion} \qquad (1)$$

where γ is the Lorentz factor, $\mathbf{g}$ is the reciprocal lattice vector of the crystal target and $\mathbf{v}_{ion}$ is the projectile velocity.

If the frequency of the crystal field, being seen by the projectiles, is equal to the frequency ν_{ij} of the transition, from the *i* into *j* state in the ions, Resonant Coherent Excitation (RCE) may occur. In the case of planar channeling conditions the transition energy E_{ij} is given as:

$$E_{ij} = \hbar \gamma v_{ion} \left(\frac{\mathrm{k} \cos\theta}{\mathrm{A}} + \frac{\mathrm{l} \sin\theta}{\mathrm{B}} \right), \qquad (2)$$

where k and l are the crystal Miller indices, θ is the angle between the ions velocity vector v_{ion} and one of the crystal axes, A and B are constants determined by the crystal structure. This relation shows that the excitation energy can be controlled by energy of the projectile and the crystal orientation.

RCE can serve as an efficient tool for the population control of the excited states of the ions in a wide energy range. In earlier studies RCE was demonstrated in middle-heavy highly-charged ion, such as Ar^{17+} or Fe^{25+} [1,2]. Later on, the RCE has been applied for the heaviest stable element, uranium. The $1s^2 2s_{1/2} \rightarrow 1s^2 2p_{3/2}$ transition in U^{89+} was observed by RCE in the field of 10 μm Si crystal, in planar channeling conditions in an earlier experiment [3]. In the present work the experimental conditions were improved in order to measure the transition energy with higher precision [4, 5].

Experiment

A cooled beam of Li-like U ions at 192 MeV/u was supplied by the GSI-ESR facility. The momentum spread of the ion beam $\Delta p/p$ was reduced to 10^{-4} using the electron cooler of the Heavy Ion Storage Ring (ESR). The beam line optics was upgraded to minimize angular divergence. A cooled well-collimated beam of relativistic ions was passing a Si-crystal target placed at (220) planar orientation in the high-precision goniometer.

The RCE was identified from the x-ray emission from the decay of the excited sates of the projectile ions measured as a function of the crystal orientation by rotating the target with a small step using the goniometer. Measurement of the X-ray emission was performed for the same number of the projectiles controlled by the position sensitive particle detector installed behind a charge-state analyser, in the end of the beam line. Four X-ray detectors were mounted around the target under different observation angle, inside the goniometer vacuum chamber. Sum of the four measured X-ray yields as a function of θ angle is presented in figure 1. Number of the detected photons has been normalised to the number of projectile ions.

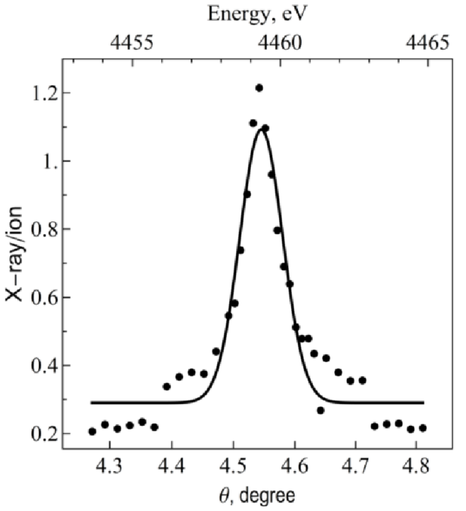

Figure 1: X-ray emission from the decay of the $2p_{3/2}$ excited state of U^{89+} ions passing in 2.5 μm Si crystal at (220) planar channeling conditions.

Maximum of X-ray emission is observed at θ rotation angle around 4.55 degrees. The angular scale has been transformed to electron volts using equation (2). A value of 4459.35±0.72 eV was found for the $1s_{1/2} \rightarrow 2p_{3/2}$ transition. The precision of the method has been improved by order of magnitude, from 10^{-3} to 10^{-4}, by reducing momentum spread and angular divergence of the ion beam.

References

[1] T. Komaki et al., NIM B 146 (1998) 19.
[2] Y. Nakai et al., NIM B 230 (2005) 90.
[3] Y. Nakano et al., Phys. Rev A 87 (2013) 060501(R).
[4] B. Walasek-Höhne et al., “CUPID: NEW SYSTEM FOR SCINTILLATING SCREEN BASED DIAGNOSTICS”, IBIC2014, to be published.
[5] C. Klefner et al. in this Annual Report.

DOI:10.15120/GR-2015-1-APPA-MML-AP-36

DOI:10.15120/GR-2015-1-APPA-MML-AP-36

Radiolysis of carbon-dioxide ice by swift Ti and Xe ions*

C. Mejía[1,2], *M.Bender*[3], *D. Severin*[3], *C. Trautmann*[3,4], *Ph. Boduch*[1], *V. Bordalo*[1,5], *A. Domaracka*[1], *X.Y. Lv*[1], *R. Martinez*[1,6], *H. Rothard*[1,#]

[1]CIMAP-CIRIL-Ganil, Caen, France; [2]PUC, Rio de Janeiro, Brazil; [3]GSI, Darmstadt, Germany; [4]TU Darmstadt, Germany; [5]Observatorio Nacional, Rio de Janeiro, Brazil; [5]Observatorio Nacional, Rio de Janeiro, Brazil; [6]Universidade Federal do Amapá, Brasil

Introduction and Experiment

Ices (H_2O, CO, CO_2, NH_3, ..) are omnipresent in space on comets, the moons of giant planets, dust grains in dense clouds (the birthplaces of stars and planetary systems). They are exposed to cosmic rays, which in turn induce radiolysis, i.e. fragmentation of initial molecules, formation of radicals, and subsequent synthesis of molecules. Even complex pre-biotic molecules such as amino acids can be formed. Due to their high electronic energy loss the heavy ion fraction in cosmic rays yields non-negligible contributions to sputtering and radiolysis, even if protons and alpha particles are more abundant [1].

Heavy-ion beams from large accelerator facilities are useful to simulate the specific effects induced by the heavy ion fraction of cosmic radiation in the laboratory. We complemented the experiments (550 MeV Ti beams) reported in [2] at the UNILAC M-branch, by irradiation with 630 MeV Xe beams. On-line Fourier transform infrared absorption spectroscopy (FTIR) allowed us to follow molecule destruction and synthesis in CO_2 ice deposited at approx. 20 K on a CsI substrate.

Radiolysis and Sputtering of CO_2

As shown in [1,2], cross sections for CO_2 destruction σ_d can be determined from the fluence dependence of molecular column densities (“thickness”). After fragmentation of the initial CO_2 molecules, radicals can combine and form daughter molecules such as CO, CO_3 and O_3. The formation can also be quantified by cross sections σ_f [1]. An important information, needed e.g. for estimating life times of molecules exposed to cosmic rays in space, is the dependence of the cross sections on the amount of deposited energy.

The destruction cross sections and the cross sections for synthesis of CO, CO_3 and O_3 are shown in figure 1 as a function of the electronic energy loss. Data obtained with Ni beams of about 50 MeV [1] and with 0.1 MeV protons [3] are also included. The measurements at GSI were performed with two different charge states both for the Ti and Xe beams, but within experimental uncertainties no related effect was observed. All cross sections are found to be proportional to the electronic stopping power. In contrast, sputtering yields are found to follow a quadratic dependence, in agreement with previous studies [1,3].

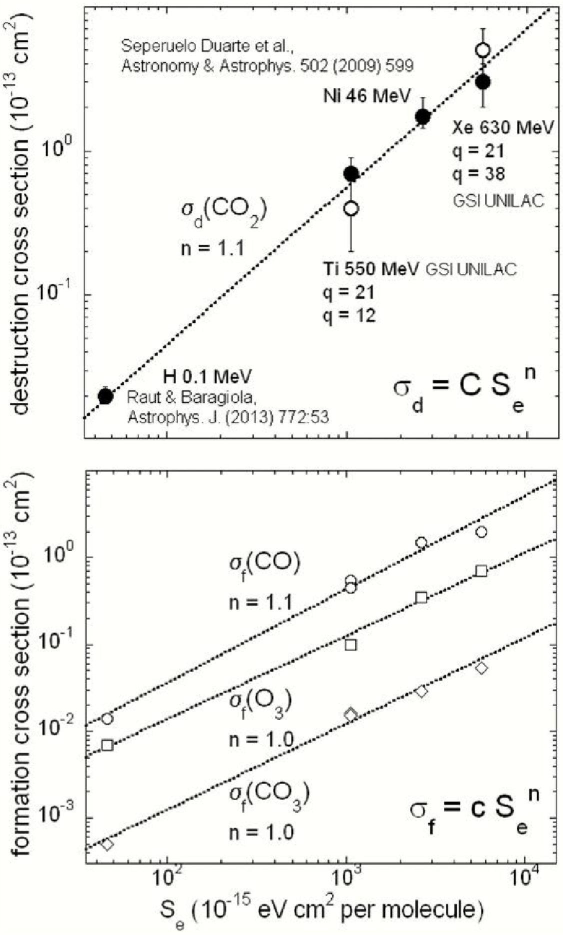

Figure 1: Cross section for destruction of CO_2 (top) and synthesis of CO, CO_3 and O_3 (bottom) as a function of electronic energy loss.

References

[1] E. Seperuelo Duarte, P. Boduch, H. Rothard, T. Been, E. Dartois, L.S.Farenzena, E.F. da Silveira Astronomy & Astrophysics 502 (2009) 599.

[2] M. Bender et al., GSI Scientific Report 2012 SR2012-PNI-INHOUSE-EXP-23 (2013) p. 392

[3] U. Raut and R.A. Baragiola, Astrophysical Journal 53 (2013) 77

---

*Work supported by the European Commision, 7th Framework Program for RTD (2007-2013), Capacities Program (Contract No. 262010, ENSAR), CAPES-COFECUB French-Brazilian exchange program, Conselho Nacional de Desenvolvimento Científico e Tecnológico CNPq, and Chinese Research Council CRC.

#rothard@ganil.fr

DOI:10.15120/GR-2015-1-APPA-MML-MR-01

Ionization efficiency of material sputtered under swift heavy ion bombardment

L. Breuer[1], F. Meinerzhagen[1], M. Bender[2], D. Severin[2], and A. Wucher[1#]

[1]Universität Duisburg-Essen, 47057 Duisburg, Germany
[2]GSI, Darmstadt, Germany

In 2014 a new time-of-flight (TOF) spectrometer was built up at the M-branch of GSI to investigate sputtering phenomena induced by swift heavy ions in the electronic stopping regime. The emphasis of this experiment is put on the ionization efficiency of the sputtered material by comparing the yields of emitted secondary ions and their neutral counterparts.

Experimental setup

A TOF spectrometer is used for the mass selective analysis of sputtered particles (see [1] for construction). Secondary ions emitted from the surface are accelerated to the entrance of the spectrometer by a pulsed electrical extraction field. The ions then travel through a field free drift zone and - depending on their mass/charge ratio-arrive at different flight times at a multichannel plate detector (SIMS). For the detection of sputtered neutral species, the system is equipped with a pulsed VUV laser for post-ionization of atoms and molecules (SNMS) above the surface via single photon ionization at a wavelength of 157 nm (corresponding photon energy:7.9 eV). The setup also includes a 5 keV Ar^+ ion beam directed to the sample area, which allows a comparison to nuclear sputtering and can be used for alignment purposes of the spectrometer.

Common TOF mass spectrometry measurements use short primary ion pulses (≈ 100 ns to several µs) at high (kHz) repetition rates. The UNILAC, however, permits only repetition rates of 1 to 50 Hz at pulse lengths of around 1 ms. In order to accommodate for that difference and make efficient use of beam time, we developed a measurement protocol which enables us to acquire secondary ion and neutral spectra obtained under MeV/u, and keV primary beams as well as without ion bombardment in an interleaved manner throughout a single accelerator pulse cycle. In addition, the keV ion beam can be intermittently switched to dc mode between subsequent accelerator pulses in order to ensure reproducible surface conditions by dynamical sputter-cleaning, which is, for instance, important for the analysis of clean metal surfaces.

First results

With this new setup, secondary ions and neutrals emitted under MeV/u electronic sputtering conditions are analyzed by a TOF spectrometer for the first time. As an example, figure 1 shows spectra of Mo^+ ions and Mo^0 atoms measured for a dynamically sputter-cleaned molybdenum surface under bombardment with 5 keV Ar^+ and 4.8 MeV/u Au^{26+} ions, respectively. From these data, the ionization probability of Mo atoms emitted under electronic sputtering conditions is determined $\alpha_{Mo}^{+} = (4.0 \pm 0.9) \cdot 10^{-5}$ [2].

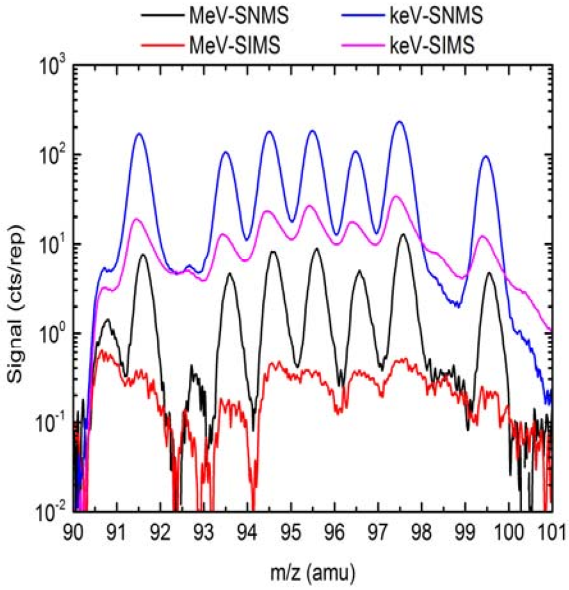

Figure 1: Spectra of Mo^+ ions (SIMS) and Mo^0 atoms (SNMS) measured for a dynamically sputter cleaned molybdenum surface under bombardment with 5 keV Ar^+ and 4.8 MeV/u Au^{26+} ions.

References

[1] Dissertation Michael Wahl, Universität Kaiserslautern, 1995

[2] Dissertation Lars Breuer, Universität Duisburg-Essen, 2015

---

* andreas.wucher@uni-due.de

DOI:10.15120/GR-2015-1-APPA-MML-MR-02

Quantitative outgassing analysis of polymers during heavy ion irradiation

P. Trapp[1], *M. Bender**[2], *D. Severin*[2], *and M. Merkel*[1]
[1]THM, MND, Friedberg (Hessen), Germany; [2]GSI, Darmstadt, Germany

Degradation processes of polymers under heavy ion irradiation have been studied intensively over the past decades [1, 2]. A common approach is measuring outgassing of volatile fragments that are created during irradiation. So far outgassing measurements were conducted in a qualitative way, e.g., as pressure rise observed in a residual gas analyzer (RGA).

The aim of this experiment was to get access to quantitative outgassing. Therefore a calibration of the existing RGA setup concerning pressure measurement and pumping speed was needed. First the pumping speed S for various gas species was determined [3]. With the pressure rise Δp from outgassing fragments and the mean flux of the ion beam $\dot{N}$, one can derive the outgassing yield η (released fragments / incident ion) of volatile fragments:

$$\eta = \frac{\Delta p \cdot S}{\dot{N} \cdot k \cdot T} \qquad (1)$$

We have studied outgassing with respect to the origin of the desorbed gas; whether it is released from the surface or as volatile decomposition fragments out of the bulk of the polymer. For surface cleaning a keV sputter ion source (IQE 11/35 from Specs®) with xenon as sputter-gas was used at a distance of about 50 cm away from the samples.

Polycarbonate (Makrofol®) foils 100 and 30 μm thickness) and polyimide (Kapton®) foils 25 μm thickness) were irradiated at the M3 beamline of the UNILAC [4] at room temperature with xenon, gold and samarium ions of 4.8 MeV/u and a flux of $(1 - 2) \cdot 10^8$ ions/cm^{2}s. The diameter of all samples was 1 cm, and a beamspot of about 8 mm x 8 mm was used for irradiation. Both sides of the polymer were cleaned for 45 min with xenon ions of 500 eV and a flux of 3e13 ions/cm^{2}s. For each sample species, a sample with and without sputter-cleaning was investigated.

The raw RGA data was calibrated with total pressure measurements of the dynamic pressure during irradiation. With the calibrated pressure rise Δp and the ion flux $\dot{N}$ the yield was calculated using equation 1. In figure 1 the outgassing yields for Makrofol® irradiated with gold ions are shown for various gas species. The plots marked with open symbols correspond to sputter-cleaned samples, full symbols to uncleaned foils. The estimated error for the fluence is 5%. Concerning the yield we estimate an error of 10% taking into account uncertainties of the total pressure measurement, pumping speed and flux. We observed that the yield of all sputter-cleaned samples is lower then the uncleaned counterpart; thus the surface condition has a strong effect on the outgassing of the polymer. However in both cases the yields are decreasing with increasing fluence. This could either be due to unsufficient surface cleaning or fluence dependent bulk decomposition induced by material changes. More in-situ investigations are planned. Our measurements clearly show that the surface state contributes to beam induced pressure increase.

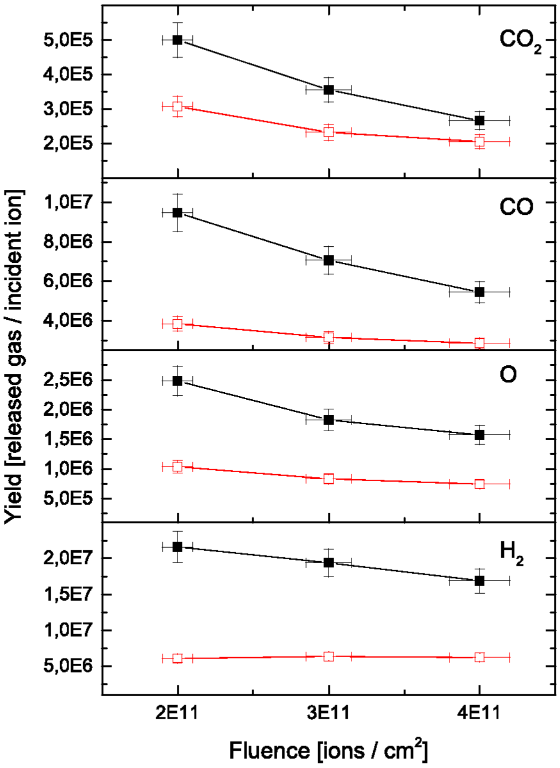

Figure 1: Outgassing-yield η of various gas species for a 100 μm thick Makrofol® foil during irradiation with gold ions. open symbols: sputter-cleaned before irradiation, full symbols: uncleaned. Lines are guides to the eye.

References

[1] T. Steckenreiter et al., Nucl. Inst. Meth. B 131 (1997) 159.
[2] U. H. Hossain et al., Polym. Chem. 5 (2014).
[3] P. Trapp, Internship report, 2014
[4] Baake et al., Rev. Sci. Instrum. 82, 045103 (2011).
[5] R. Kumar et al., NIM B 251, 2006
[6] D. Severin, PhD Thesis, Marburg 2008.

---

* corresponding author: m.bender@gsi.de

DOI:10.15120/GR-2015-1-APPA-MML-MR-03

Ion-induced gas desorption from tungsten targets irradiated with 4.8 MeV/u gold ions

M. Bender[1] and D. Severin[1]*

[1]GSI, Darmstadt, Germany

The release of gas into vacuum, triggered by impinging heavy ions is a critical issue concerning beam losses and was investigated in the past at GSI and CERN [1]. For room temperature targets, the amount of desorbed gas per projectile ion (defined by the desorption yield η) is described by a pure surface process. However, under ion beam exposure, track formation and related thermal spike effects come into play. When a high-energetic ion impacts a target, the material around the ion trajectory is exposed to a short thermal spike, which increases locally the temperature resulting in enhanced thermal desorption. Several experiments with different beams and targets provided desorption yields which are in good quantitative agreement with thermal spike model calculations [2]. Desorption effects are of concern when highest beam intensities are involved, e.g., at the SPIRAL-2 accelerator that will deliver some 10^{14} ions per second on a production target for rare isotopes. Even if the desorption yield is low, the high beam current will lead to enormous gas loads in the range of 10^{-3} mbar l s^{-1}. At the production target special rods are attached which stop the primary beam upon separating the rare isotopes. For thermal reasons the rods have to be made from a high melting material such as tungsten.

The desorption yields of three different tungsten samples were measured at the UNILAC beamline M1. For the irradiation 4.8 MeV/u Au ions with charge states 26+ and 53+ and respective currents of 3e-9 A and 3e-10 A were used. The pulse rate was 2 Hz and the pulse length 1.2 ms. The beam spot had a diameter of 6 mm. The samples stem from the same batch of original rod material. They were brazed onto a Cu block as thermal substrate. The sample thickness was 5 and 3 mm which both is much larger than the projected range of the Au projectiles ($\approx 17\ \mu m$). The base pressure in the irradiation chamber was 1.8 e-8 mbar. During beam exposure, the dynamic vacuum, i.e., the total and partial pressures were recorded. The yields were calculated from the pressure increase inside the vacuum chamber during irradiation.

Figure 1 presents the results of the total desorption yield as a function of the accumulated fluence (top) and the partial pressure evolution for the 3 mm tungsten target irradiated with Au^{26+} ions (bottom). The overall uncertainty is estimated to be around 30% due to the large errors of the pressure and pumping speed measurements. Note that the beam current for the 53+ beam was one order of magnitude less than for the 26+ beam. Hence, within a fixed beamtime, much less fluence is accumulated. For a given sample, the higher charge state leads to higher desorption yields due to the higher energy loss of the 53+ beam [2]. The desorption yield tends to slightly decrease with increasing fluence due to beam scrubbing (cleaning of the surface with the ion beam). However, there are other effects which may increase the desorption yield (see H_2O in Fig. 1, bottom). After the irradiation, the corresponding thick sample contained many macroscopic cracks where gas could be released under beam exposure. The composition of the desorbed gas is predominately H_2, CO and CO_2 (see Fig. 1, bottom) as observed so far for any sample and beam condition. The desorption yields measured for these tungsten samples are surprisingly high compared to earlier measurements using Au or Cu targets [3].

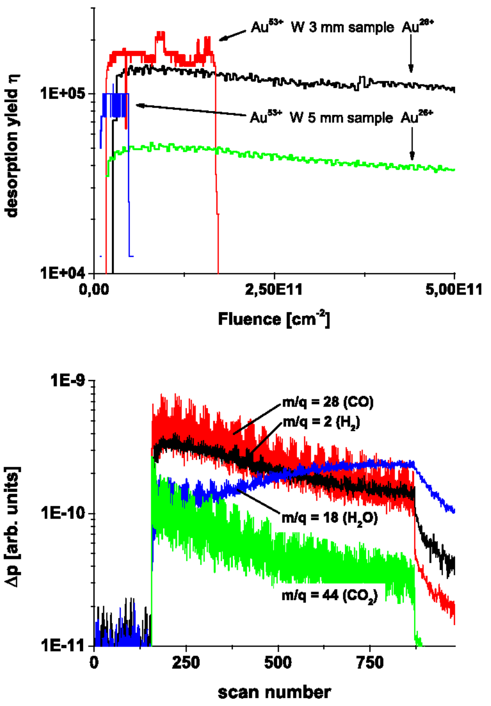

Figure 1: Desorption yield measurement of tungsten samples. Top: yield vs. fluence, bottom: partial pressures of 3 mm tungsten irradiated with Au^{26+}.

References

[1] E. Mahner, et al., PRST-AB **6**, 2003

[2] M. Bender, et al., NIM **B 267**, 2009

[3] M. Bender, et al., NIM **B 256**, 2007

---

* m.bender@gsi.de

DOI:10.15120/GR-2015-1-APPA-MML-MR-04

Redox Response of Actinide Materials to Highly Ionizing Radiation*

Cameron L. Tracy[1#], *Maik Lang*[2], *John M. Pray*[1], *Fuxiang Zhang*[1], *Dmitry Popov*[3], *Changyong Park*[3], *Markus Bender*[4], *Daniel Severin*[4], *Christina Trautmann*[4,5], *Vladimir A. Skuratov*[6], *and Rodney C. Ewing*[7]

[1] University of Michigan, Ann Arbor, MI, USA; [2] University of Tennessee, Knoxville, TN, USA; [3] Carnegie Institute of Washington, Argonne, IL, USA; [4] GSI Helmholtzzentrum, Darmstadt, Germany; [5] Technische Universität Darmstadt, Darmstadt, Germany; [6] Joint Institute for Nuclear Research, Dubna, Russia; [7] Stanford University, Stanford, CA, US

Actinide materials are often exposed to high-energy heavy ion irradiation in the form of fission fragments. These high specific energy particles deposit energy in a material primarily through ionization of electrons along their paths. Subsequent electron relaxation causes atomic displacements, forming a damaged ion track. Actinide dioxides with the fluorite structure are highly radiation tolerant, exhibiting neither phase transformations nor amorphization within tracks. However, the precise nature of their radiation response is not known. It was recently shown that swift heavy ion irradiation reduced the Ce^{4+} in fluorite-structured CeO_2 to Ce^{3+} [1]. This process has important implications for actinide oxides, as their accessible cation electronic configurations vary across the actinide series due to the effects of *f*-electron itinerancy.

To study the radiation response of actinide oxides, powders of ThO_2, UO_3, and the uranium oxide hydration products $UO_2(OH)_2$ (uranyl hydroxide) and $[(UO_2)_8O_2(OH)_{12}](H_2O)_{10}$ (metaschoepite), along with micro- and nanocrystalline CeO_2, were irradiated with 167 MeV Xe and 950 MeV Au ions to fluences of up 1×10^{14} [2]. Irradiation-induced structural modifications were characterized using x-ray diffraction (XRD), while valence changes were tracked using x-ray absorption spectroscopy (XAS).

ThO_2, for which thorium is stable only in a tetravalent state, exhibited unit cell expansion and the accumulation of heterogeneous microstrain under irradiation. These saturated, as a function of fluence, at higher values when the ion energy was increased. This is consistent with the "velocity effect" wherein the radial distance from the ion path within which energy is deposited increases with ion velocity, producing larger tracks, but lower energy densities and less energy available to displace atoms. No valence changes were observed. CeO_2 exhibited the same structural changes, but with a lack of dependence on ion energy, suggesting that they were not caused directly by defect formation but rather by valence reduction. XAS results confirmed the partial reduction of Ce to the trivalent state, with concomitant changes to ionic radii and electrostatic forces driving expansion and microstrain accumulation. No dependence of valence reduction on ion energy was observed, as was also the case for the structural modifications. These results indicate coupling between changes to electronic and atomic structures.

Similar study of CeO_2 nanospheres showed enhanced reduction to Ce^{3+}. To maintain charge neutrality, this reduction requires the segregation of oxygen from ion tracks. The presence of surfaces allows for efficient loss of anions to the environment, promoting radiation-induced reduction of nanocrystalline material. Its unit cell expansion was an order of magnitude larger than that of the microcrystalline material.

Because hexavalent uranium phases are generally based on uranyl coordination polyhedra, radiation-induced valence reduction has a strong effect on their structure. The three such materials tested all transformed under irradiation to fluorite structured UO_{2+x} phases as their U^{6+} was reduced to U^{4+}.

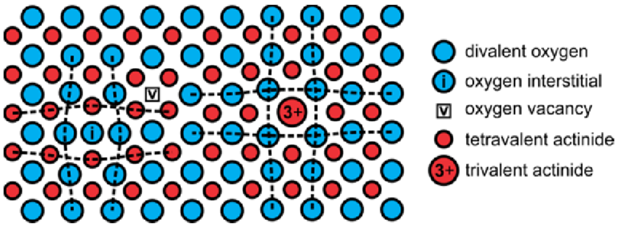

Figure 1: Illustration of the effects of irradiation on fluorite-structured materials. Both Frenkel defects (left) and valence reduction (right) distort the structure.

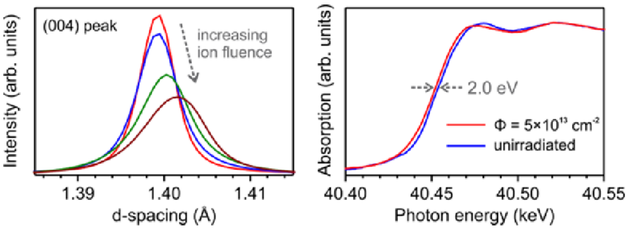

Figure 2: XRD (left) and XAS (right) results for irradiated CeO_2, indicating expansion, microstrain, and reduction.

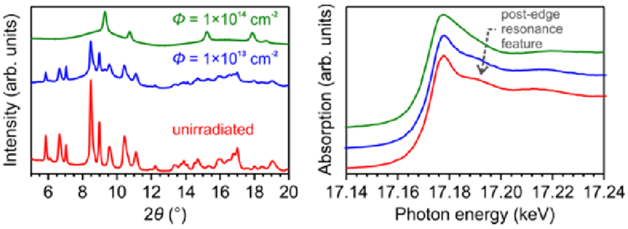

Figure 3: XRD (left) and XAS (right) results for irradiated UO_3, showing production of U^{4+} and a fluorite structure.

References

[1] H. Ohno *et al.*, *Nucl. Instrum. Meth. B* **266** (2008) 3013-3017.

[2] C.L Tracy *et al.*, *Nature Commun.* **6** (2015) 6133.

---

* This work was supported by the Energy Frontier Research Center *Materials Science of Actinides* funded by the U.S. Department of Energy, Office of Science, Office of Basic Energy Sciences (DE-SC0001089).

[#] cltracy@umich.edu

DOI:10.15120/GR-2015-1-APPA-MML-MR-05

In situ defect annealing of swift heavy ion-irradiated CeO_2 and ThO_2*

Raul I. Palomares[1,#], *Cameron L. Tracy*[2], *Fuxiang Zhang*[2], *Changyong Park*[3], *Dmitry Popov*[3], *Christina Trautmann*[4,5], *Rodney C. Ewing*[6], *Maik Lang*[1,]

[1]University of Tennessee, Knoxville, TN, U.S.A.; [2]University of Michigan, Ann Arbor, MI, U.S.A.; [3]Geophysical Laboratory, Carnegie Institution of Washington, Argonne, IL, U.S.A.; [4]GSI Helmholtzzentrum & Technische Universität Darmstadt, Germany; [6]Stanford University, Stanford, CA, U.S.A.

Ceria (CeO_2) and thoria (ThO_2) are isostructural analogues to typical nuclear fuels, such as UO_2. During reactor operation, nuclear fuels are exposed to intense radiation fluxes and temperature gradients. These conditions, in particular fission fragment- and fast neutron-fluxes, generate nanoscale defects and induce adverse effects such as swelling and redox reactions [1]. Such modifications can degrade materials properties relevant to fuel performance.

In this study [2], a hydrothermal diamond anvil cell (HDAC) and synchrotron x-ray diffraction (XRD) configuration was used to investigate the defect annealing kinetics in swift heavy ion-irradiated CeO_2 and ThO_2 at ambient pressure. Swift heavy ions were used to simulate the effect of ionizing fission-fragment irradiation because of the similarity in specific kinetic energies (>1 MeV/nucleon) and energy deposition mechanisms.

Polycrystalline CeO_2 and ThO_2 cold-pressed pellets were irradiated at room temperature at the M2-beamline of the UNILAC of GSI with 945 MeV ^{197}Au ions to a fluence of 2.5×10^{13} ions-cm^{-2}. After irradiation, the samples were transferred into one of two holes that were drilled into a rhenium gasket (Fig. 1) for use with an HDAC. In order to monitor the recovery kinetics of ion-induced defects in CeO_2 and ThO_2, the samples were isochronally annealed for 20 minutes per step in 50-75 K temperature steps from 300-1075 K at beamline 16-BM-D of the Advanced Photon Source, U.S.A.. After each heating step, the samples were quenched to ambient temperature and allowed to equilibrate for 20 minutes. Upon reaching stable temperature, diffraction patterns were recorded.

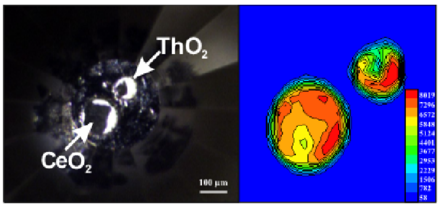

Fig. 1: The HDAC sample chamber as imaged by light microscopy (left) and x-ray absorption (right).

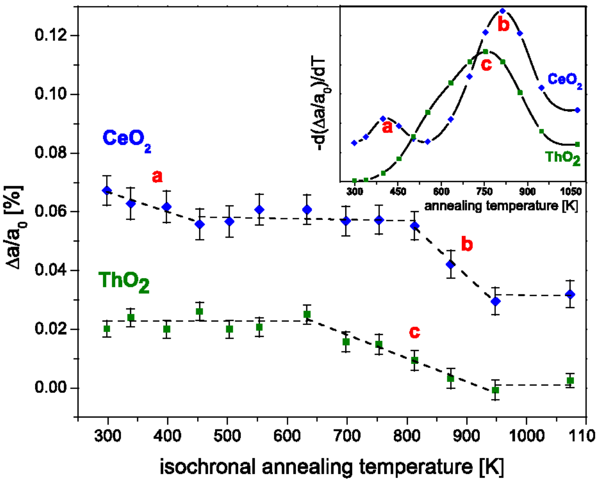

Fig. 1: Fig. 2: The relative change in the unit cell parameter, a, from the unirradiated value, a_0, as a function of isochronal annealing temperature. The inset shows the differential curves of the data.

Irradiation induces unit cell expansion due to the accumulation of isolated point defects which can agglomerate into defect clusters. As a material is heated, these defects are annealed and the unit cell parameter begins to recover. The annealing data indicate that the materials recover at different rates. The differential curves show one defect recovery stage in ThO_2 while there exist two in CeO_2 within the temperature regime investigated (Fig. 2 inset).

Material recovery was attributed [2] to the relaxation of heterogeneous microstrain, and the recombination and annihilation of anion defects (*a* & *c*, Fig. 2). This is followed by cation vacancy migration in CeO_2 (*b*, Fig. 2). The discrepancy in kinetics can be attributed to the redox behavior exhibited by CeO_2 under energetic irradiation [1]. These results suggest that cation electronic configuration plays a significant role in not only the defect production behavior, but also the defect recovery mechanisms of the fluorite-structure oxides.

References

[1] C.L. Tracy *et al.*, *Redox response of actinide materials to highly ionizing radiation.* Nat Commun, 2015. **6**: p. 6133.

[2] R.I. Palomares *et al.*, *In Situ Defect Annealing of Swift Heavy Ion Irradiated CeO_2 and ThO_2*, under review

---

* This work was supported as part of the Materials Science of Actinides, an Energy Frontier Research Center funded by the US DOE Office of Science, Office of Basic Energy Sciences under Award Number DE-SC0001089..

[#] rpalomar@utk.edu

DOI:10.15120/GR-2015-1-APPA-MML-MR-06

Ion-beam induced stresses in polycrystalline α-alumina

S. Klaumünzer[1,2], *M. Bender*[1], *A. Romanenko*[1], *D. Severin*[1,#]
[1]GSI, Darmstadt, Germany; [2]HZ Berlin, Berlin, Germany

When investigating ion-beam induced structural changes of single crystals by in-situ x-ray diffraction, we usually measured only one intense diffraction peak in order to keep a reasonable balance between irradiation time and data collection time. However, this strategy prevents insight into the causes of a large peak shift as it has been observed with the $(11\bar{2}0)$ peak of α-alumina. An alternative approach is to use polycrystalline samples and to measure many diffraction peaks.

Polycrystalline sintered α-alumina (BCE Special Ceramics GmbH, Mannheim, 99.7% purity, density 3.85 g/cm3, average crystallite size ~5 μm) were cut into pieces of 10×10×2.6 mm^3 in size and annealed at 1250°C for 2 h under flowing argon gas in order to remove microcracks and residual strain introduced by the cutting procedure. Subsequently, the pieces were glued with epoxy resin onto copper plates which fit to the sample holder of the x-ray diffraction apparatus in-situ at the UNILAC M2-beamline. The ion beam (^{197}Au, 4.8 MeV/u, ion flux Φ ~2×10^9 ions/cm^2s) was carefully scanned across the samples at normal beam incidence. The specimen temperature during ion bombardment was (25 ± 5)°C. At certain fluences Φ_t the irradiation was interrupted and x-ray diffraction patterns were measured in symmetric Bragg geometry for $24° \leq 2\theta \leq 70°$ using CuK_α-radiation and comprising 8 intense diffraction peaks of α-alumina. The Bragg angles, $2\theta_B$ of the unirradiated sample agreed within < 0.01° with those of a calibration reference sample (α-alumina from NIST, SRM 1976a). No foreign phases could be detected.

Virgin alumina exhibited bright luminescence radiation which decreased rapidly during bombardment. At fluences $>5\times10^{12}$ Au/cm^2 tiny bright spots of luminescence radiation were seen indicating spall-off, which limited the fluence range in which x-ray diffraction yielded reliable results. The $2\theta_B$ position of the 8 diffraction peaks versus fluence is shown in fig. 1. No additional peaks appeared, i.e. the formation of a significant volume fraction of a new (non-equilibrium) alumina phase can be excluded.

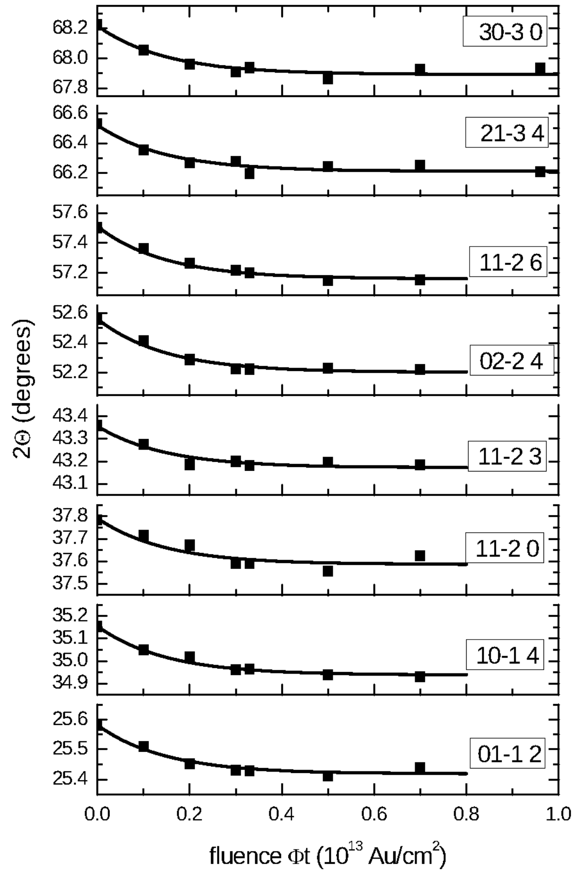

Fig. 1: Variation of the $2\theta_B$ peak position versus ion fluence for eight diffraction peaks of α-alumina. The Miller-Bravais indices are indicated on the right.

Hence, the observed line shifts have to be attributed to in-plane ion-beam induced stresses, which result from an expansion of defective alumina. The lines displayed in fig. 1 are the results of fitting the expression $2\theta_B = 2\theta_{B\infty} + 2\delta\theta_B \exp(-A\Phi_t)$ to the experimental data using a single value $A = 6.8\times10^{-13}$ cm^2 for all reflections. $2\theta_{B\infty}$ denotes an apparent saturation value. The "saturation" elastic strain is given by $\varepsilon_{zz} = -\delta\theta_B/\tan\theta_B$ and is $\varepsilon_{zz} = (5.2 \pm 1)\times10^{-3}$. Neglecting creep, the elastic in-plane stress is $\sigma = -E/(1-\nu)\,\varepsilon_{zz}$. With a Young's modulus E = 416 GPa and a Poisson number $\nu = 0.23$, one obtains $\sigma \approx -2.8$ GPa, which matches with the compressive strength of sintered alumina. Thus, spalling limits and ion-beam induced stresses give rise for the apparent saturation of stress.

[#] d.severin@gsi.de

DOI:10.15120/GR-2015-1-APPA-MML-MR-07

Ion-Beam induced grain rotation in nanocrystalline alumina

S. Klaumünzer[1,2], *M. Bender*[1], *A. Romanenko*[1], *D. Severin*[1,#]
[1]GSI, Darmstadt, Germany; [2]HZ Berlin, Berlin, Germany

Single crystals of α-alumina (orientation [11$\bar{2}$0], 15×10×1 mm^3) were bombarded at room temperature with 4.8 MeV/u Au ions. The transformation of the single crystals into nanocrystals was followed by monitoring the (11$\bar{2}$0)-diffraction peak by CuKα-radiation at the in-situ 3-circle-diffractometer at the UNILAC M2-beamline. The ω-circle (incident x-ray beam) and the θ-circle (diffracted beam) define the diffraction plane. The χ-circle enables a sample tilt relative to the diffraction plane; for $\chi = 0$ the sample normal lies in the diffraction plane and coincides with the ion beam direction. During irradiation χ_i was ±45°. X-ray measurements were done by varying χ and $\omega = \theta$ fixed at the Bragg angle θ_B. The single peak originally located at $\chi = 0$ splits with increasing fluence into two peaks, one located at $\chi_1 = 0$, originating from unmodified material at greater specimen depths, and a second one, located at χ_2, resulting from tilted (11$\bar{2}$0)-lattice planes. The tilt angle $\Omega = -\chi_2$ versus fluence is shown in fig. 1. At a fluence of 1×10^{13} Au/cm^2 χ_i has moved from +45° to −45°. The rotation direction also changed its sign. A symmetric Bragg scan at $\chi = \chi_2$ yields the precise position of θ_B and the peak width of the modified alumina. θ_B decreased by about 0.1°, which is attributed to a volume increase by dislocation production. The width of the modified peak is shown in fig. 2. The change in χ_i is not visible in the behavior of the width.

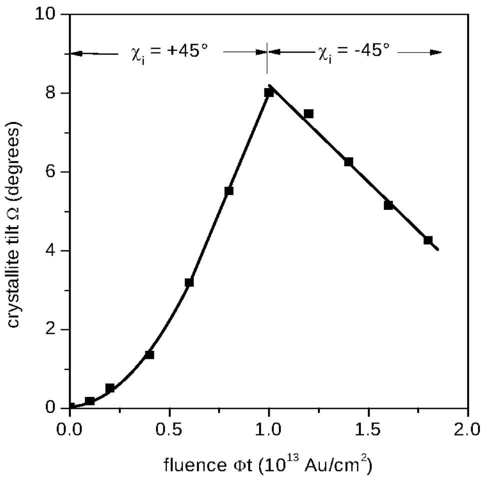

Figure 1: Crystallite tilt Ω versus ion fluence.

Both grain rotation and the square-root dependence of the width (see fig. 2) indicated the action of dislocations. Because the number density of dislocations is of the order of Φt, most of the dislocations are concentrated in newly formed grain boundaries. Thus, at Φt ~10^{12} Au/cm^2 the single crystal is transformed into an aggregate of nanocrystals. The evolution of the grain size is depicted in fig. 3 for two data evaluation strategies.

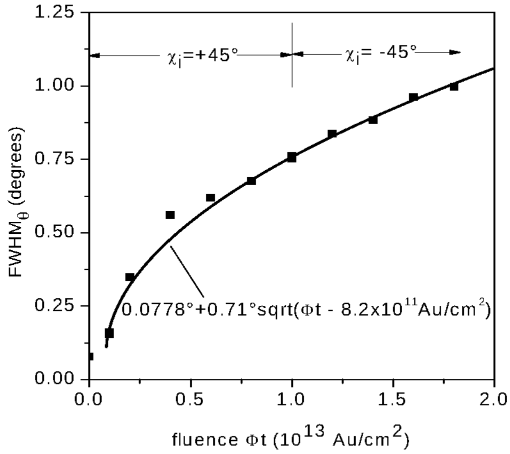

Figure 2: The full width at half maximum FWHMθ of the (11$\bar{2}$0)-Bragg peak of α-alumina as function of ion fluence.

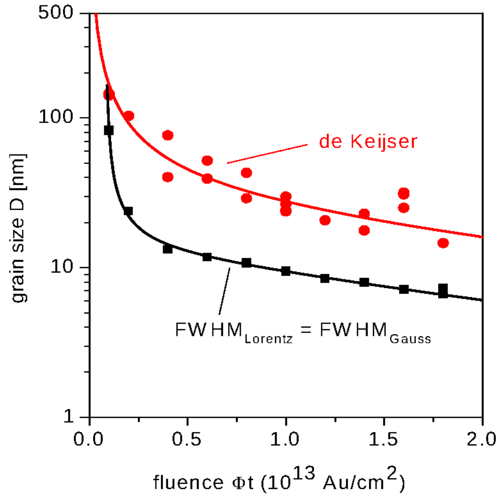

Figure 3: Grain size D versus ion fluence derived from the separation of grain size and strain contributions to FWHMθ. The black curve has been obtained with the usual assumption that the Gaussian and the Lorentzian widths to the Pseudo-Voigt peak widths are equal. The red curve has been obtained by a procedure proposed by de Keijser [1]

[1] de Keijser et al., J. Appl. Cryst. 15(1982) 308-314.

[#] d.severin@gsi.de

DOI:10.15120/GR-2015-1-APPA-MML-MR-08

Luminescence degradation behavior of alumina irradiated with heavy ions of high fluences*

S. Lederer†[1,2], *P. Forck*[1], *E. Gütlich*[1,3], *A. Lieberwirth*[1,2], *and W. Ensinger*[2]
[1]GSI, Darmstadt, Germany; [2]Technische Universität Darmstadt, Germany; [3]Goethe-Universität Frankfurt, Germany

Polycrystalline α-alumina samples (purity: 99.8 %) were irradiated with different fluences at various energies. To compare the degradation behavior of the luminescence, similar ion species were used (^{58}Ni @ 300 MeV/u, at slow and fast extraction mode, measured at GSI and ^{63}Cu @ 0.5 MeV/u, measured at Helmholtz-Zentrum Dresden-Rossendorf). Ion-beam induced luminescence (IBIL) was monitored at wavelengths from 320 to 800 nm.

Scintillation Screens

Scintillating screens are used at accelerator facilities for ion beam diagnostics with very high ion fluxes. However, during irradiation of the material, formation of color centers with one or two trapped electrons occurs [1]. The increasing radiation damage leads to massive degradation of light yield, which is one of the main problems using the screens as an appropriate tool for beam imaging [2]. Due to its radiation hardness, alumina is an interesting material for scintillation applications [3].
Models of scintillator degradation behavior have been developed for many years, whereas many of them are related to the basic approach of Birks and Black [4]. The parameter of technical interest in beam diagnostics is the so called critical half-life fluence Φ_c. Therefore, a modified model according to Miersch et al. [5] is used to determine the dose dependent luminescence behavior and the radiation hardness of the alumina screens.

Results and Discussion

In Figure 1 the relative scintillation yield of alumina as a function of the applied particle fluence is shown. IBIL data are normalized by the initial scintillation yield S_0. The luminescence S decreases for increasing fluence Φ due to enhanced defect creation. To explain the dynamic behavior of the luminescence, the empirical model according to Miersch et al. was used (Eq. 1).

$$\frac{S}{S_0} = \frac{1}{1 + (\frac{\Phi}{\Phi_c})^c} \qquad (1)$$

Within Eq. 1 the factor Φ_c describes the critical half-life fluence, and the exponential value c describes the slope of the scintillation yield's decrease. The model has been used to fit the data in Figure 1, results are summarized in Tab. 1. Half-life fluence Φ_c increases for higher energies, indicating an enhanced radiation hardness. According to SRIM simulations, less defects are created at low electronic stopping powers dE/dx_e, suggesting that the effective quenching of luminescence centers is reduced for higher energies. The exponential value c is also reduced for high energy irradiation due to the less decreasing slope.

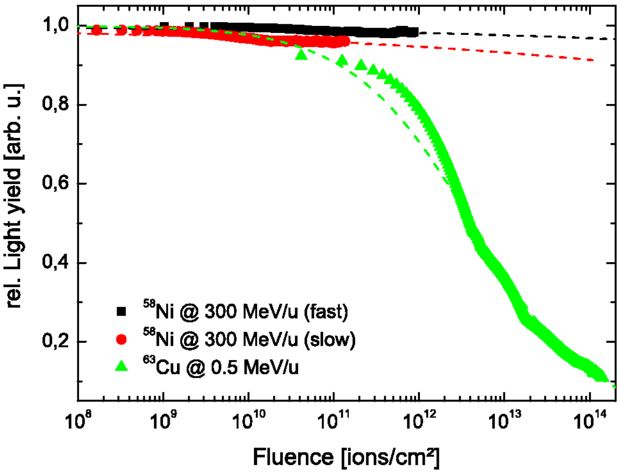

Figure 1: Relative scintillation yield of α-Al_2O_3 versus ion fluence for different ion species at various energies.

Table 1: Derived critical half-life fluences Φ_c and exponential values of c for the alumina samples. The electronic energy loss values are calculated with SRIM-2010 code.

Ion species	Energy [MeV/u]	dE/dx$_e$ [keV/nm]	Φ_c [ions/cm^2]	c [arb. u.]
^{58}Ni (slow)	300	0.9	$1.18 \cdot 10^{26}$	0.13
^{58}Ni (fast)	300	0.9	$9.24 \cdot 10^{22}$	0.11
^{63}Cu	0.5	11.6	$4.17 \cdot 10^{12}$	0.61

The results show, that high energy operation enables a prolonged use of the scintillation screens due to the reduced creation of radiation defects.

References

[1] A. Morono and E.R. Hodgson, J. Nucl. Mater. 249 (1997), 128-132.

[2] E. Gütlich, P. Forck, B. Walasek-Höhne and W. Ensinger, IEEE Trans. Nucl. Sci. 59 (2012), 2354-2359.

[3] N. Khalfaoui, J.P. Stoquert, F. Haas, C. Trautmann, A. Meftah and M. Toulemonde, Nucl. Instrum. Methods B 146 (2012), 247-253.

[4] J.B. Birks and F.A. Black, Proc. Phys. Soc. A 64 (1951), 511.

[5] G. Miersch, D. Habs, J. Kenntner, D. Schwalm and A. Wolf, Nucl. Instrum. Methods A 369 (1996), 277-283.

---

* Work supported by BMBF, grant no. 05P12RDRBJ.
† S.Lederer@gsi.de

DOI:10.15120/GR-2015-1-APPA-MML-MR-09

First Results of in-situ Raman measurements of ion-irradiated calcite*

Sebastian Dedera[1#], Ulrich A. Glasmacher[1], Michael Burchard[1], Markus Bender[2], Daniel Severin[2], Christina Trautmann[2,3]

[1]Institute of Earth Sciences, University of Heidelberg, [2]GSI Darmstadt, [3]Technische Universität Darmstadt

Raman spectroscopy, as a tool to determine specific modifications of minerals exposed to accelerated ions or natural radioactive decay, is widely used in geoscience and materials research. As described in the same scientific report [1], an online and in-situ Raman system was attached at the spectroscopy chamber of the M3-beamline at of the UNILAC.

To test the performance of the Raman systems and display beam-induced changes, calcite ($CaCO_3$) crystals from Chihuahua, Mexico were chosen for the first experiments, because calcite and its fluence-dependent changes in Raman spectra are known from earlier off-line experiments [2,3].

The irradiation of a calcite crystal was performed with 4.8 MeV/u Au ions (2 Hz, pulse length 1.2 ms). After calibration, alignment and focusing of the Raman system, the calcite crystal was exposed to the ion beam in steps from 1×10^9 ions/cm^2 up to a fluence of 1×10^{12} ions/cm^2. After each irradiation step, Raman spectra were recorded with 20 s acquisition time with 3 repetitions.

The Raman spectra of irradiated calcite show four major changes (Fig. 1). With increasing fluence, the bands at 156 and 284 cm^{-1} decrease in intensity, but they are still visible at 1×10^{12} ions/cm^2.

Above 2×10^{10} ions/cm^2, a new band appears at 437 cm^{-1}. Its intensity grows with increasing fluence and reaches a maximum at 5×10^{11} ions/cm^2. Worth mentioning is also that the width of the band at 1087 cm^{-1} gets broader with increasing fluence starting at 5×10^{11} ions/cm^2.

In conclusion, the first results of the new online Raman system at the M3 beamline are very promising. The system operates well and the results for calcite are in quality and quantity agreeable with results known from off-line measurements [2,3]. The setup provides a powerful tool to monitor structural changes of a given material before, during, and after the irradiation with swift heavy ions. A more detailed analysis of the obtained data is in progress.

[1] S. Dedera et al., “Online Raman Measurements on M-Branch”, GSI Science Report 2014

[2] S. Dedera et al., “Online Raman Measurements of Calcite and Malachite During Irradiation with Swift Heavy Ions”, in prep.

[3] S. Pabst et al., Swift heavy ion induced damage in calcite, aragonite and dolomite: a Raman spectroscopic study”, in prep.

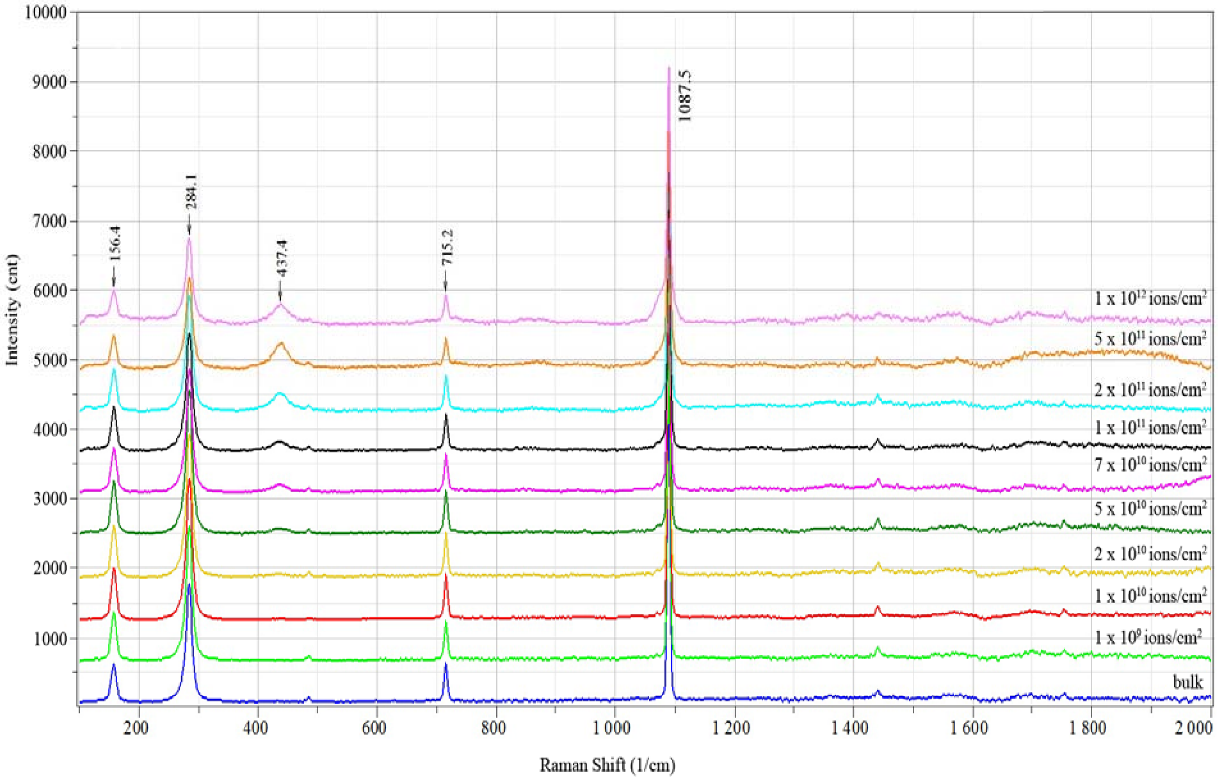

Figure 1: Raman spectra of calcite recorded during irradiation with 4.8 MeV/u Au ions at the new online Raman system of the M3-beamline.

---

* Work supported by BMBF Verbundprojekt 05K10VH1

Sebastian.Dedera@geow.uni-heidelberg.de

DOI:10.15120/GR-2015-1-APPA-MML-MR-10

Online Raman on M-branch: First results *

Sebastian Dedera[1#], *Ulrich A. Glasmacher*[1], *Michael Burchard*[1], *Christina Trautmann*[2,3]

[1]Institute of Earth Sciences, University of Heidelberg, [2]GSI Darmstadt, [3]Technische Universität Darmstadt

Raman spectroscopy, as a tool to determine material change caused by accelerated ions or natural radioactive decay, is widely used in geoscience and material research. Due to many issues in the current workflow with standard equipment, in 2014, an online and in-situ Raman system to irradiate matter with swift heavy ions has been developed. The Raman system is established at the 400 mm spectroscopic chamber of the M3-branch and is fed with accelerated swift heavy ions by the UNILAC. For technical details see the associated report in this volume [1].

To test the system's ability to detect changes in the properties of the irradiated material, calcite has been chosen for first experiments, because calcite reacts very sensitive to ion irradiation and the changes of calcite in Raman spectra are known [2,3]. The calcite crystals from Chihuahua, Mexico were irradiated at the M3 - branch of the UNILAC, GSI with Au^{+26} , 4.8 MeV/u, 2 Hz and an extraction time of 1.2 ms.

After calibration, alignment and focusing of the system, one calcite crystal has been irradiated with Au ions in steps from 1 x 10^{9} ions/cm^{2} until a fluence of 1 x 10^{12} ions/cm^{2}. Raman spectra were taken after each irradiation step with 20 s acquisition time with 3 repetitions.

A first brief analysis of the Raman spectra of calcite show four major changes during irradiation (Fig. 1). The two peaks at 156 and 284 cm^{-1} at the beginning of the spectra are decreasing in intensity with increasing fluence, but they are still visible at 1 x 10^{12} ions/cm^{2}. The next change in the spectra is the peak at 437 cm^{-1}. It arises with increasing fluence and is visible for the first time at 2 x 10^{10} ions/cm^{2}. Its intensity is increasing after this fluence, but it reaches its maximum at 5 x 10^{11} ions/cm^{2}. The last peak to be mentioned is the biggest peak of the spectra at 1087 cm^{-1}. It is getting wider with increasing fluence, starting at 5 x 10^{11} ions/cm^{2}.

In conclusion, the first results of the new online Raman system at M3 are very promising. The system works and the results are in quality and quantity comparable with the results of established methods with all the advantages of o online Raman system with its in situ measurements. After eliminating some minor problems, a powerful tool to measure various materials before, during and after the irradiation with swift heavy ion is at hand. A more detailed analysis of the obtained data is in progress.

[1] S. Dedera et al., "Online Raman Measurements on M-Branch", GSI Science Report 2014

[2] S. Dedera et al., "Online Raman Measurements of Calcite and Malachite during Irradiation with Swift Heavy Ions", in prep.

[3] S. Pabst et al., Swift heavy ion induced damage in calcite, aragonite and dolomite: a Raman spectroscopic study", in prep.

---

* Work supported by BMBF Verbundprojekt 05K10VH1

[#] Sebastian.Dedera@geow.uni-heidelberg.de

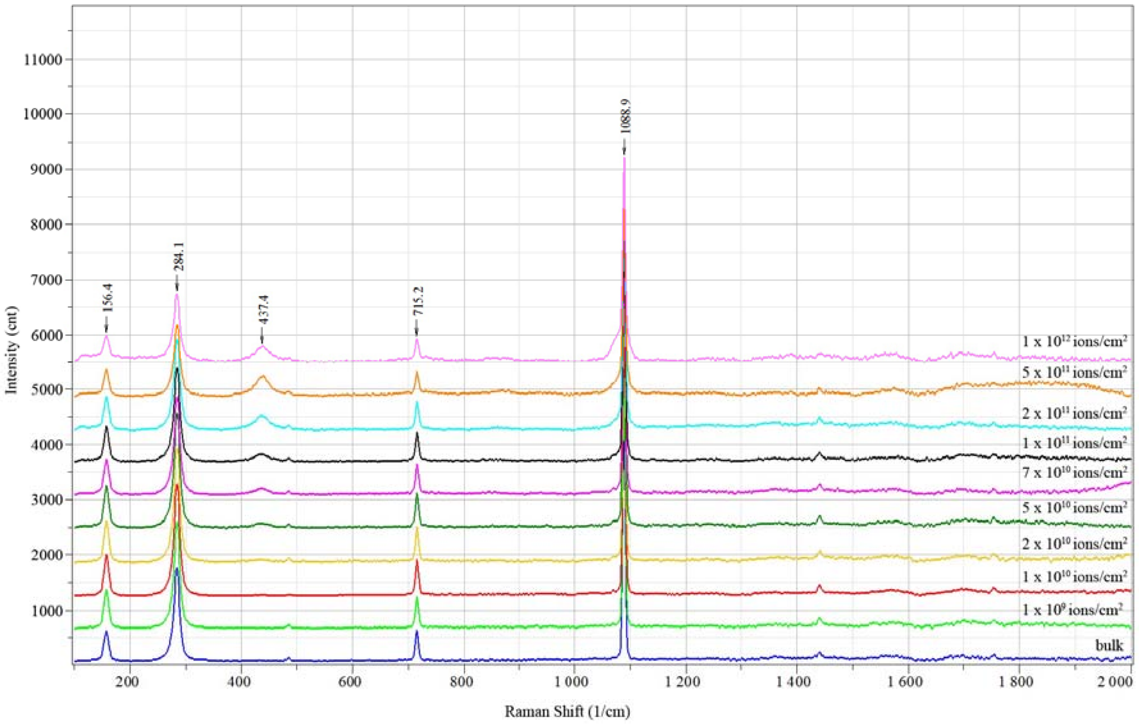

Figure 1: Raman spectra of calcite, taken with the new online Raman system on M3-Branch

DOI:10.15120/GR-2015-1-APPA-MML-MR-11

Raman measurements of heavy ion irradiated water-bearing minerals*

Nicole Schöppner[1#], *Ulrich A. Glasmacher*[1], *Michael Burchard*[1], *Christina Trautmann*[2]
[1]Institute of Earth Sciences, University of Heidelberg, Heidelberg, Germany; [2] Technische Universität Darmstadt and GSI Helmholtzzentrum Darmstadt, Germany

Our research was triggered by the question if crystal water of natural minerals is released during irradiation with swift heavy ions. To answer this question natural microcrystalline malachite ($Cu_2[(OH)_2/CO_3]$) and gypsum ($CaSO_4*2H_2O$) were irradiated at the UNILAC (GSI) with 11.1 MeV/u ^{209}Bi-ions applying fluences between 1×10^6 – 2×10^{12} ions/cm^2. All crystals were analyzed by Raman spectroscopy using the LabRam HR800 UV spectrometer equipped with an OLYMPUS BXFM-ILHS optical microscope, a grating with 1800 grooves per millimeter, a Peltier-cooled CCD detector, and an objective of 50x magnification. For excitation, a blue laser with a wavelength of 473.03 nm was used. The lateral resolution was ~2 µm, the wave number accuracy 0.5 cm^{-1}, and the spectral resolution 1 cm^{-1}.

Malachite and gypsum are both anisotropic crystals, have a monoclinic structure and two optical axes. Malachite has variable crystallographic orientations and growth directions and consequently the intensities of the different malachite bands vary. This variation is demonstrated in Fig. 1 for spectra recorded under different crystallographic directions and cleaving planes.

For irradiated gypsum, significant changes in the Raman spectra appear above a fluence of 1×10^{10} Bi-ions/cm². With increasing fluences the intensity of most Raman bands decreases. This applies especially to the υ_1 stretching mode at 3404 cm^{-1} and the υ_3 stretching mode at 3492 cm^{-1}, which characterize the H_2O bands. The decrease of amplitudes is an indication of irradiation-induced release of water. Although the lattice water is set free, the mineral is not transformed to anhydrite ($CaSO_4$), which is the waterless sulfate. The bands remain at their characteristic gypsum position and do not shift to the anhydrite position.

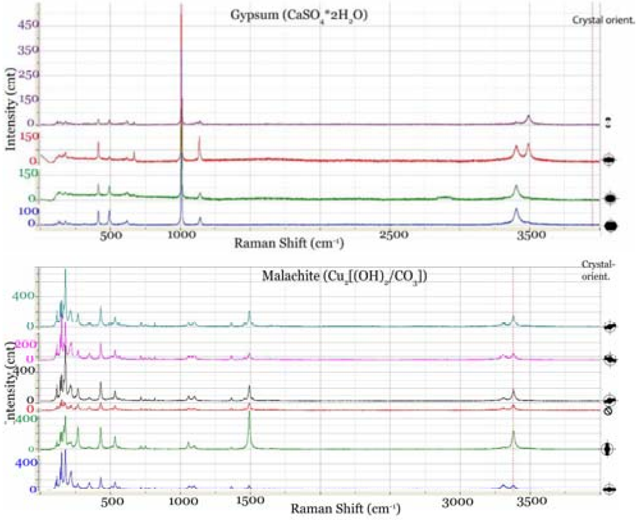

Fig. 1: Raman spectra of gypsum (top) and malachite (bottom) at different crystal orientations.

Also for malachite the amplitude of different Raman bands decrease with increasing fluence. In contrast to the Raman bands of gypsum, the OH stretching vibration modes at 3308 and 3380 cm^{-1} of malachite are equal sensitive than the other bands. Significant changes in the spectra as well as discoloration of the crystal (Fig. 2) also appear above a fluence of 1×10^{10} Bi-ions/cm². The color change from green to black indicates a phase transformation of the irradiated layer showing Raman bands at ~1360 cm^{-1} and ~1580 cm^{-1}, typical for graphite. Under irradiation, the band positions in the malachite spectra slightly change but not systematically.

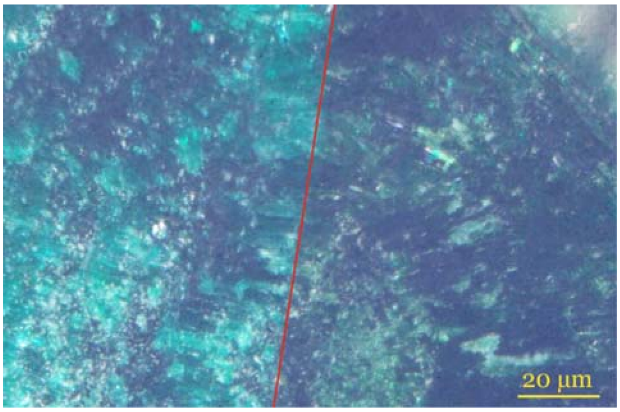

Fig. 2: Malachite sample showing the beginning of discoloration at a fluence of 1×10^{10} Bi-ions/cm² at the right site of the red line. The left side of the crystal is non-irradiated for comparison.

References

[1] S. Dedera, U. A. Glasmacher, M. Burchard , C. Trautmann. "Annealing of Dislocations and Heavy-Ion Induced Tracks in Calcite." In Scientific Report 2011, 2012-1, 689. Darmstadt: GSI, 2012.

[2] S. Dedera, U. A. Glasmacher, M. Burchard and C. Trautmann. "Optimized Etching of Swift Heavy Ion Tracks in Calcite." In Scientific Report 2012, 2013-1, 400 p. Darmstadt: GSI, 2013.

---

*Work supported by HGS-HIRe
#nicole.schoeppner@geow.uni-heidelberg.de

DOI:10.15120/GR-2015-1-APPA-MML-MR-12

Laser flash analysis of irradiated amorphous carbon stripper foils

M. Urban [1], *K. Kupka* [1,2], *M. Tomut* *[2,3], *C. Hubert*[1,2], *A. Romanenko*[1,2], *B. Lommel*[2], *and C. Trautmann*[1,2]

[1]Technische Universität Darmstadt, Germany; [2]GSI, Darmstadt, Germany; [3]NIMP, Bucharest, Romania

For high intensity operation at the planned FAIR accelerator, radiation-hard carbon stripper foils are of interes because they could provide intermediate charge states to SIS and replace both, the gas stripper at 1.4 MeV/u as wel as the foils stripper at 11.4 MeV/u. Fatigue due to cyclic thermo-mechanical stress and additional stresses due to different thermal expansion coefficients of foil and mounting frame have to be understood in order to increase the life time [1, 2]. This report presents a first approach to measure the thermal diffusivity with the laser flash method of pristine and irradiated amorphous carbon (aC) foils. The diffusivity influences the heat transport and the temperature increase during irradiation.

The thermal diffusivity α, which contributes to the thermal conductivity $\lambda(T) = \alpha(T) \cdot c_p(T) \cdot \rho(T)$, can be accessed by laser flash analysis (LFA). The technique measures the temperature evolution of the front side of the specimen after applying a laser pulse (1064 nm, up to 25 J) to the rear side (c_p and ρ are the specific heat and the density). Measurements were evaluated by use of Cowan model [3]. The diffusivity is proportional to the square of the thickness l and the time after 50 % of the maximum temperature is reached at the front side $t_{0.5}$ ($\alpha \sim \frac{l^2}{t_{0.5}}$). This illustrates the importance of sample thickness determination. To measure the foil thickness by means of profilometry the samples were fixed on a silicon wafer and height profiles across the edges of the foils were recorded (Fig. 1). The measurements reveal a great degree of roughness. As second method a thickness gauge was used. This method shows more consistent results (Fig. 2) than the profilometry and were therefore used for further diffusivity measurements.

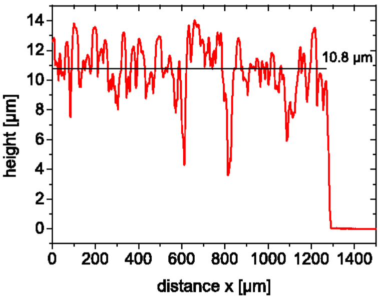

Figure 1: Profilometer scan across the edge of a pristine 709 μg/cm^2 thick aC stripper foil (produced by the GSI target laboratory) glued onto a silicon wafer.

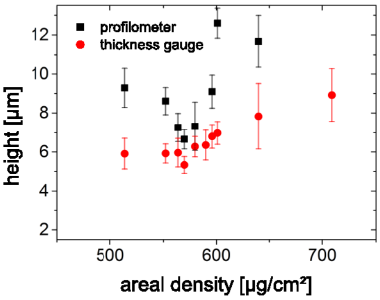

Figure 2: Foil thickness of pristine carbon foils for different deposited areal densities as determined by profilometry and thickness gauge measurements.

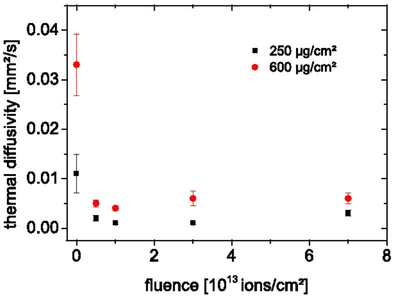

Figure 3: Thermal diffusivity of aC foils versus fluence of 4.8 MeV/u ^{238}U-ions. The 250 μg/cm^2 foils were irradiated behind the 600 μg/cm^2 thick ones.

First laser flash measurements on pristine and uranium irradiated aC foils of 250 μg/cm^2 and 600 μg/cm^2 are presented in Fig.3. Due to the very small value of thermal diffusivity of aC and the strong thickness dependence of α, the measurement values of the thin samples are very low. Nevertheless, for both foils a significant decrease by ion irradiation is observable starting at low accumulated fluences. Further work on the thickness estimation needs to be carried out to improve accuracy of the LFA measurements. More irradiated samples need to be measured by means of LFA technique to verify these results and to understand ion-induced disordering processes leading to diffusivity decrease.

References

[1] M. Tomut et al., GSI Scientific Report,p. 412, (2011)

[2] K. Kupka et al., GSI Scientific Report,p. 409, (2012)

[3] R. Cowan, Journal of Applied Physics, 34, pp.926-927(1963)

---

* M.Tomut@gsi.de

DOI:10.15120/GR-2015-1-APPA-MML-MR-13

Heavy ion induced radiation effects in novel molybdenum-carbide graphite composite materials

M. Tomut[1,2,#], *Y. Xu*[3], *Ph. Bolz*[3], *F. Carra*[4], *E. Quaranta*[4], *P. Hermes*[4], *A. Bertareli*[4], *S. Redaelli*[4], *A.Rossi*[4], *S. Bizzaro*[5], *C. Trautmann*[1,3]
[1]GSI, Darmstadt, Germany; [2] INFIM, Bucharest, Romania; [3]TU Darmstadt, Germany; [4]CERN, Geneva, Switzerland; [5]Brevetti Bizz, Verona, Italy;

Innovative molybdenum-carbide graphite (Mo-Gr) composites were specifically developed for high energy physics applications. These materials are showing a very promising combination of thermal, electrical, and mechanical properties for application in beam protection elements for high-power accelerators. To date very little is known about their structural and dimensional stability and about degradation of functional properties under irradiation. Within the EU, FP7, EuCARD-2 project [1], an intense campaign for testing radiation hardness using different particle beams and energies is taking place at GSI Helmholtzzentrum as well as at Brookhaven National Laboratory (USA) and Kurchatov Institute (Russia).

Mo-Gr composites are processed by Liquid Phase Sintering of molybdenum powder, graphite flakes and pitch-based carbon fibers at temperatures higher than 2000 ºC. First radiation hardness tests of this material with GeV heavy ions (^{238}U, ^{209}Bi, and ^{197}Au) were performed at the UNILAC accelerator at GSI. During irradiation, samples cut in transversal direction, with respect to the orientation of the carbon fibers, start to deform at fluences of 6×10^{12} ions/cm^2 (figure 1, top). Deformation was minimized by pre-annealing the samples at temperatures above 1000 ºC to release internal stresses introduced during Mo-Gr composite processing (figure 1, bottom).

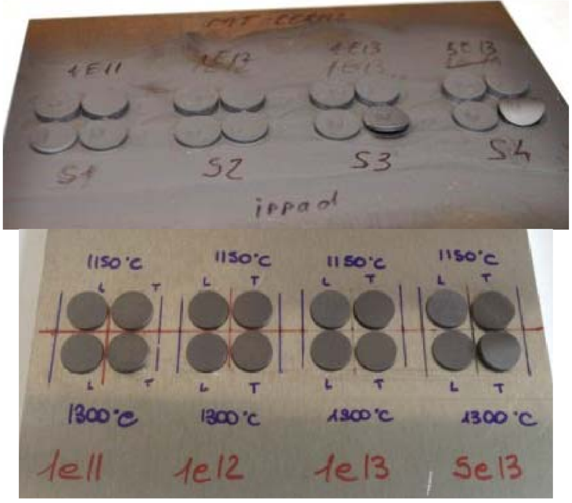

Figure 1: Series of Mo-GR samples cut in two different direction with respect to the orientation of the carbon fibers; (top) non-annealed samples after irradiation with U ions; (bottom) samples annealed at 1150 ºC and 1300 ºC irradiated with Au ions. Both series were exposed to fluences between 1×10^{11} and 3×10^{13} ions/cm^2.

Online infrared (IR) thermography during irradiation was used to monitor ion-induced deformation. Sample deformation causes loss of contact to the sample holder and thus the cooling time of beam-pulse induced temperature spikes increases (figure 3).

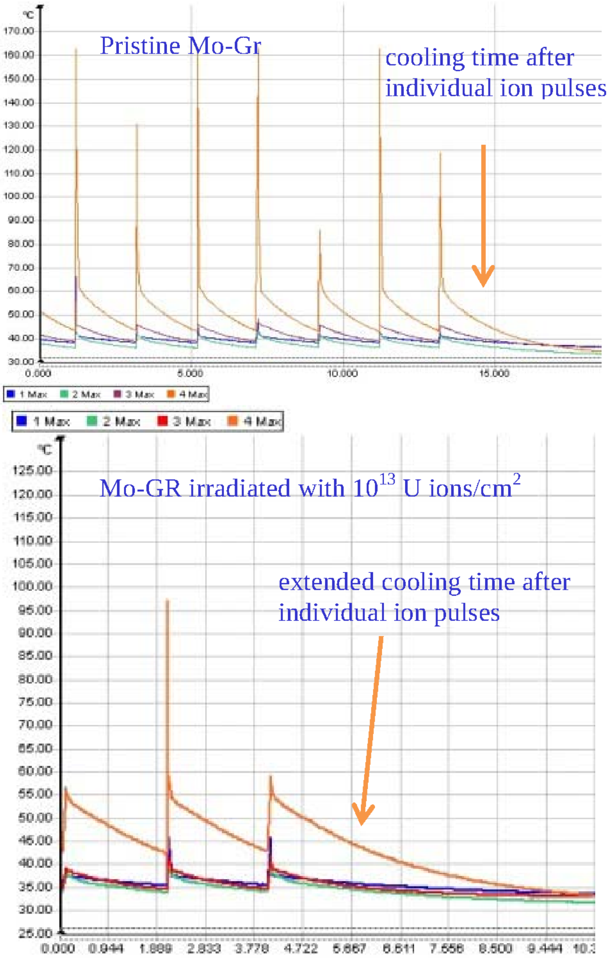

Figure 3: Infrared camera recorded time evolution of sample temperature at the initial state of the irradiation (top) and after exposure to a fluence of about 10^{13} ions/cm^2 (bottom). The irradiation was performed with 1-GeV U ions (frequency 0.6 Hz, 200 µs pulse duration)

Additional activities concentrate on the analysis of ion beam induced modification of the composites by means of Raman Spectroscopy, X-ray diffraction, scanning electron microscopy and nanoindentation.

[1] http://eucard2.web.cern.ch

---

* Work supported by EuCARD2, grant no. 312453

[#] m.tomut@gsi.de

DOI:10.15120/GR-2015-1-APPA-MML-MR-14

Lysozyme recognition with aptamer-modified cylindrical nanopores

M. Ali[1,2,#], *S. Nasir*[1,2], *C. Trautmann*[1,2], *and W. Ensinger*[2]

[1]GSI, Darmstadt, Germany; [2]TU Darmstadt, Germany.

Recently nanofluidic channels/pores have attracted a remarkable attention to miniaturize biosensing devices [1]. The working principle of these nanosized sensors is based on the modulation of ionic transport through the nanopore. The protein pores, *e.g.*, α-hemolysin, have been frequently employed for the sensing of a variety of biomolecules. But the fragile embedding lipid bilayers restrain their suitability for more practical purposes. To date, various routes have been investigated to fabricate synthetic robust analogues of biological ion channels. Amongst the various techniques, ion track technology permits control over the number of pores cm^{-2} (from single to multipore membranes), dimensions and shape of the nanopores. Moreover, the pore surface properties can be tuned on demand *via* exploiting the inherent chemical groups on the pore surface.

Ion current rectification is the main characteristics of pores with asymmetric geometries or pores having non-homogeneous fixed charge distributions on their inner pore surface. Here, we demonstrate that aptamer-protein bioconjugates can provide another useful strategy to incorporate a non-homogeneous fixed charge distribution in cylindrical nanopores leading to ion current rectification.

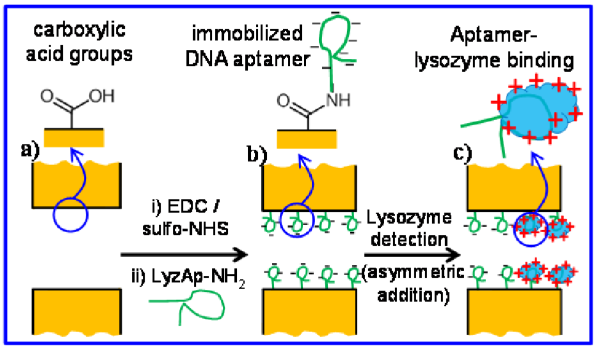

Figure 1: Scheme representing **a)** a cylindrical pore with surface carboxylic acid groups, **b)** the immobilization of DNA aptamer (LyzAp-NH$_2$) via carbodiimide coupling chemistry, and **c)** protein (lysozyme) conjugation.

In this study, single swift heavy ion irradiated polyethylene terephthalate (PET) membranes of 12 µm thickness were used to fabricate single cylindrical nanopores by symmetric track-etching method [2]. The amine-terminated single-stranded DNA aptamer, *i.e.*, 5′-NH_2-$(CH_2)_{12}$-ATC TAC GAA TTC ATC AGG GCT AAA GAG TGC AGA GTT ACT TAG-3′ (LyzAp–NH$_2$) which has the ability to selectively bind with lysozyme (Lyz) protein was selected as model system. The LyzAp–NH$_2$ molecules were covalently immobilized on the pore walls via carbodiimide coupling chemistry (Fig. 1) [3].

After aptamer immobilization, the next step was to study the biomolecular recognition events inside the confined geometries. Figure 2a shows the I–V curves obtained when the modified pore was exposed asymmetrically to lysozyme (pI = 11.35) solutions of various concentrations. Due to its high isoelectric point, Lyz molecules were positively charged in our experimental conditions. Therefore, the binding of Lyz with aptamer chains resulted in the switching of surface charge polarity (Fig. 1c). Because of the opposite polarity of fixed surface charges on either half of the pore, the applied electric potential resulted in an asymmetric flow of ions from the two pore ends. This led to ion current rectification because of high resistance for the flow of ions at positive voltages ($V > 0$) compared to negative ones ($V < 0$).

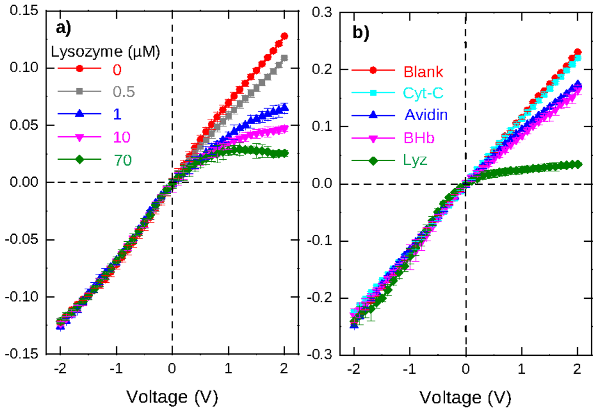

Figure 2: a) I–V curves of aptamer-modified single cylindrical nanopore (d ~20 ± 3 nm) when exposed to different protein concentration, asymmetrically. b) I–V curves of modified single cylindrical pore (d ~ 40 ± 3 nm) upon asymmetrically exposing to an electrolyte solution containing no protein, cytochrome C (180 µM), avidin (5 µM), bovine hemoglobin (5 µM) and lysozyme (70 µM), separately.

Moreover, we have also demonstrated sensor specificity against Cyt-C, avidin and BHb proteins. From the respective $I-V$ curve (Fig. 2b) a slight reduction in positive currents was noticed due to the physical adsorption of large sized protein molecules on the pore opening. But for Cyt-C (almost similar to Lyz in size and polarity) we did not observe any change in $I-V$ curve.

In summary, we have miniaturized a nanofluidic biosensing device based on synthetic nanopores modified with DNA-aptamer molecules. We believe that based on the modulation of nanopore transport properties such nanoporous systems can be further extended for the recognition of a variety of proteins and small organic molecules which exhibit an affinity towards a specific aptameric probe.

References

[1] S. Howorka and Z. Siwy, *Chem. Soc. Rev.* 38 (2009) 2360.
[2] S. Nasir *et al. ACS Appl. Mater. Interfaces* 6 (2014) 12486.
[3] M. Ali *et al. ACS Nano* 4 (2010) 7267.

M.Ali@gsi.de

DOI:10.15120/GR-2015-1-APPA-MML-MR-15

XPS measurements on single Bi_2Te_3 nanowires fabricated by electrodeposition in etched ion-track membranes*

J. Krieg[1,2], *C. Chen*[3], *J. Avila*[3], *C. Trautmann*[1,2], *M.-C. Asensio*[3], *and M.E. Toimil-Molares*[†1]
[1]GSI, Darmstadt, Germany; [2]Technische Universität, Darmstadt, Germany; [3]SOLEIL Synchrotron, Gif-sur-Yvette, France

Bi_2Te_3 belongs to a recently discovered new class of materials, called topological insulators (TI), which form conductive surface states while their bulk material is an ordinary band insulator. These exotic surface states are generated by strong spin-orbit coupling and feature spin-momentum locking of the charge carriers due to time reversal symmetry. For this reason TI materials are of high interest for future electronic applications like dissipationless transport and spintronics [1, 2]. The major challenge to address the surface states is the reduction of the concentration of residual bulk carriers dominating over the signal. Nanowires (NWs) of high surface-to-volume ratio combined with controllable geometric, crystallographic and morphologic properties are excellent model systems to investigate the TI surface states.

Here, we present x-ray photoelectron spectroscopy (XPS) studies with sub-micron resolution on individual 100 nm diameter Bi_2Te_3 NWs. The NWs are synthesized by electrodeposition in etched ion-track templates fabricated by irradiating 30 μm thick polycarbonate foils with GeV heavy ions at the UNILAC accelerator and selective chemical etching of the ion tracks in 6 M NaOH at 50 °C. Subsequently, NWs are electrodeposited within the channels at an applied potential of 0 V vs. SCE at 30 °C. Details on the fabrication and characterization are reported in [3].

After deposition, the NWs were released from the membrane and randomly distributed onto a silicon wafer. Figure 1 displays XPS spectra recorded with an unfocused beam, i.e. from the entire substrate, as prepared (red), after 15 s (blue) and 15 min (black) of Ar plasma cleaning in UHV. The O and C signals indicating contamination of the Bi_2Te_3 surface by i.e. oxidation, polymer residual, etc., decrease with increasing cleaning time. After surface preparation, single NWs were identified in the focused beam mode by scanning the area of interest and detecting only photoelectrons of a certain energy (corresponding to Bi or Te). A representative XPS map is presented in fig. 2 a evidencing the excellent spatial resolution achieved. Single NWs can be distinguished from bundles and analysed in more detail. Figures 2 b and c display two mappings of the single NW marked in fig.2 a (black frame) recorded using Te 55 eV (b) and Bi 68.5 eV (c), respectively. The Te signal is localized on the NW, while Bi signals are detected also at larger distances from the NW surface. Further measurements are required to understand the origin of these signals at 68.5 eV in the NW surroundings.

In conclusion, the first nano-XPS measurements on 100 nm diameter Bi_2Te_3 NWs were successfully performed. A cleaning protocol to obtain highest surface quality was established. Point XPS spectra along the NWs indicate that our NWs are of homogeneous elemental composition.

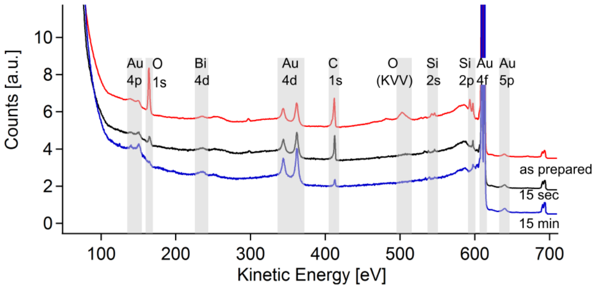

Figure 1: XPS spectra recorded in defocused mode as prepared, after 15 s and after 15 min of Ar plasma cleaning.

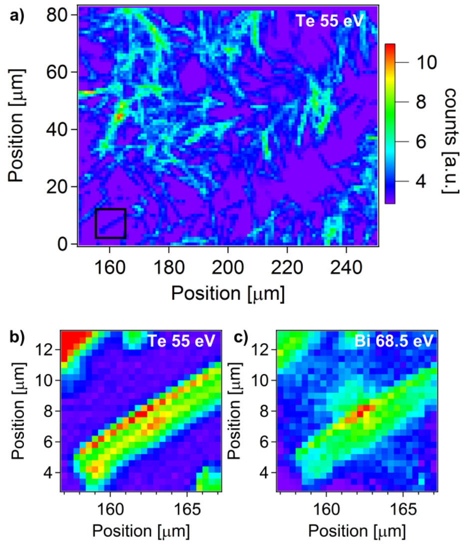

Figure 2: XPS mappings of Bi_2Te_3 NWs: overview (a), single NW recorded by analysing Te (b) and Bi (c) spectra.

References

[1] C. L. Kane, E.J. Mele, Phys. Rev. Lett. 95, 146802 (2005)
[2] M. Konig et al., Science 318, 766 (2007)
[3] O. Picht et al., J. Phys. Chem. C 116, 5367-5375 (2012)

---

* Work supported by DFG (No. SPP 1666) and HGS-HIRe
[†] M.E.ToimilMolares@gsi.de

DOI:10.15120/GR-2015-1-APPA-MML-MR-16

Synthesis of $\mathrm{Au}_x\mathrm{Ag}_{1-x}$ nanowire-networks with controlled composition and defined wire diameter

M. Dyzynski[1,2], *L. Burr*[2,3], *C. Trautmann*[2], *M. E. Toimil-Molares*[2], *and I. Schubert*[2]
[1]Hochschule RheinMain, Rüsselsheim, Germany; [2]GSI, Darmstadt, Germany; [3]Technische Universität Darmstadt, Germany

In this work, three dimensional AuAg-alloy-nanowire-networks with controlled composition and defined wire diameter were fabricated by electrodeposition in ion-track etched polymer templates. These structures are very interesting for applications in sensorics and catalysis since they exhibit a very high surface area and are mechanically stable due to their interconnected nanowires.

For the synthesis of the nanowire-networks, we have irradiated 30 μm-thin polymer foils at the GSI linear accelerator UNILAC with swift heavy ions of initial energy 11.4 MeV/u. Each foil is sequentially irradiated four times under an angle of 45° respective to the polymer surface. The ions damage molecular bonding in the foils and create cylindrical damage tracks. By chemical etching with aqueous 6-M NaOH solution at 50° C these ion tracks are transformed into nanochannels. Under these etching conditions, the etching rate amounts 23 nm/min. By varying the etching time between 2 min and 5 min nanochannels with defined diameter between 60-150 nm were fabricated. After creating a conductive cathode layer by sputtering gold on one side of the foil, nanowires are electrodeposited in the pores. We have deposited AuAg-nanowires using an electrolyte consisting of 50 mmol $\mathrm{KAu(CN)_2}$ and 50 mmol $\mathrm{KAg(CN)_2}$ in a three-electrode set-up. A Ag/AgCl electrode was used as reference electrode and a platinum coil as anode. All deposition potentials are given here vs. Ag/AgCl reference. Wet-chemical dissolution of the polymer leads to free-standing stable nanowire-networks. Fig. 1 shows the SEM image of a network with 100 nm wire diameter.

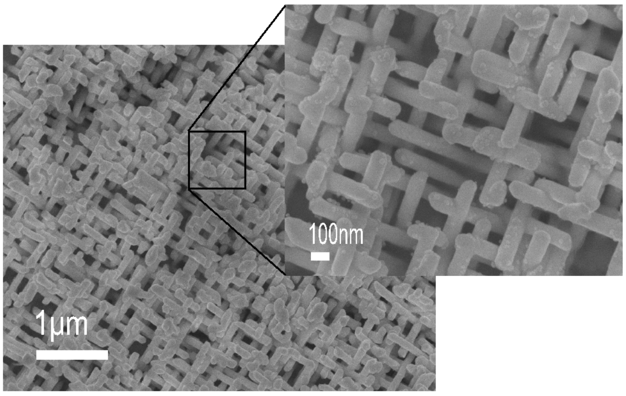

Figure 1: SEM image of a AuAg-nanowire-network with a wire diameter of 100 nm.

The applied voltage during the deposition was varied to create nanowires with controlled Au:Ag concentrations. Fig. 2 shows details of EDX in SEM spectra including the M_α-peak of Au and L_α- and L_β-peak of Ag. All spectra are normalized to the height of the M_α-peak for clarity. Table 1 shows the concentration for networks deposited at voltages between -0.6 and -0.8 V. For the networks at -0.8 V the same Au:Ag concentration in the nanowires is found as present in the electrolyte. In contrast, for arrays consisting of parallel nanowires a Au:Ag concentration of 20:80 was measured at this potential [1]. We attribute this difference in wire composition between parallel nanowire arrays and networks to variations in the diffusion process, due to interconnections among pores and the different effective lengths.

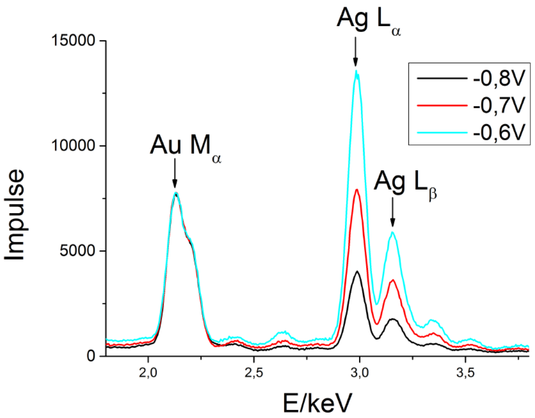

Figure 2: EDX spectra of AuAg-alloy-nanowire-networks deposited at different voltages in the rage between -0.8 and -0.6 V.

Potential/V	Networks Au:Ag[%]	Parallel arrays Au:Ag[%]
-0,8 V	50:50	20:80
-0,7 V	30:70	-
-0,6 V	20:80	-

Table 1: Au:Ag ratio in the nanowires of networks and parallel arrays for different deposition potentials.

References

[1] I. Alber, "Synthesis and Plasmonic Properties of Metallic Nanowires and Nanowire Dimers", PhD thesis, Ruprecht-Karls-Universität Heidelberg, 2012.

DOI:10.15120/GR-2015-1-APPA-MML-MR-17

Metal-organic frameworks shaped into one-dimensional nanostructures via templated electrodeposition*

A. W. Maijenburg[1,#], *L. Movsesyan*[1,2], *C. Trautmann*[1,2], *and M.E. Toimil-Molares*[1,#]
[1]Materials Research, GSI, Darmstadt, Germany; [2]Technische Universität Darmstadt, Darmstadt, Germany

Metal-organic frameworks (MOFs) are a relatively new class of hybrid materials, which consist of metal ions or clusters as the secondary building unit and organic linkers connecting the metallic building units via coordination bonds of moderate strength [1]. Thereby, MOFs combine the robustness and crystallinity of inorganic materials with the flexibility of organic molecules. This opens up the possibility for MOFs to be used in a wide range of applications ranging from gas storage and gas separation to sensors and photocatalysis [1-3].

In this study, MOF nanowires were made via electrodeposition inside etched ion-track membranes in order to precisely control the size, shape and location of the resulting MOF crystals. By controlled oxidation of Cu nanowires in a solution containing 1,3,5-benzenetricarboxylate (BTC) molecules, we synthesised nanowires of the well-known MOF $Cu_3(BTC)_2$, which consists of Cu^{2+} ions as the metallic core linked together by BTC ligands. To the best of our knowledge, this is the first time that templated electrodeposition was used for the synthesis of one-dimensional MOF nanostructures.

Polycarbonate (PC) foils with a thickness of 30 µm were irradiated with Au ions of a total energy of 2 GeV and a fluence of 10^8 ions/cm^2 at the UNILAC linear accelerator of GSI. After irradiation, the ion tracks were transformed to nanoscale pores by chemical etching, which resulted in PC membranes with cylindrical pores with a diameter of ~ 80, 130, 210 and 260 nm. After etching, one side of the PC membranes was coated with ~125 nm of Au using an Edwards S150B sputter coater. Next, the mechanical stability of this Au layer was enhanced by electrodeposition of a thicker Au layer using a commercial gold plating solution (AuSF, METAKEM) at -0.7 V vs. a Au counter electrode in a two electrode setup for 2 h.

Cu nanowires were electrodeposited inside the PC membranes from an aqueous solution containing 1.0 M $CuSO_4$ and 0.2 M H_2SO_4 at a temperature of 60 °C and a potential of -0.1 V vs. a Cu counter electrode for 8 min. The as-deposited Cu nanowires were transferred to $Cu_3(BTC)_2$ using a 50/50 vol% ethanol/water solution containing 5.8 mM BTC and 6.42 M tributylmethylammonium methyl sulfate (MTBS) at a temperature of 55 °C and a potential of 2.5 V vs. a Cu counter electrode for 30 min.

Figure 1 shows XRD patterns of the $Cu_3(BTC)_2$ nanowires with different diameters made in this study. For the thickest nanowires, most of the peaks associated with $Cu_3(BTC)_2$ are visible [2], but as the diameter is decreased, also less reflections are visible in the XRD pattern. The Cu peak is assigned to incomplete conversion of the as-formed Cu nanowires to $Cu_3(BTC)_2$. More interestingly, we also observed a peak associated with Cu_2O, which we relate to be the intermediate product from the conversion of Cu to $Cu_3(BTC)_2$, indicating that the conversion takes place via a two-step oxidation reaction.

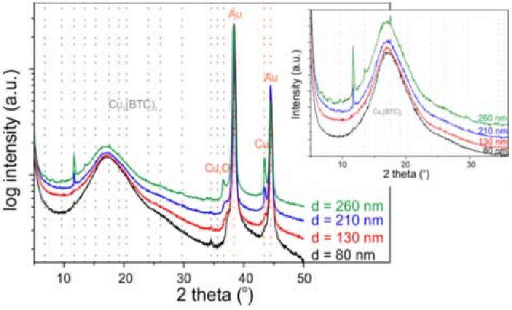

Figure 1: XRD patterns of $Cu_3(BTC)_2$ MOF nanowires with different diameter. The grey dotted lines denote reflections identified to originate from $Cu_3(BTC)_2$ [2]. Inset: Zoom in at a linear scale of the area of interest.

Figure 2 presents selected SEM images of the formed MOF nanowires with a diameter of ~260 nm, which show a smooth surface indicating optimized growth conditions. More interestingly, the nanowires are not completely converted yet and a sharp interface between the bright Cu and the darker $Cu_3(BTC)_2$ segments is observed. This allows us to conclude that the conversion proceeds linearly from the top to the bottom of the nanowire.

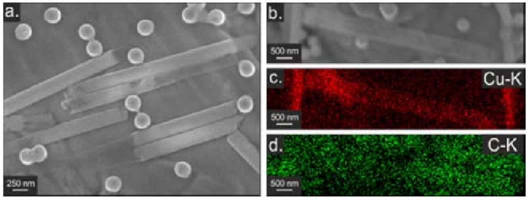

Figure 2: (a,b) SEM images of $Cu_3(BTC)_2$ MOF nanowires with a diameter of 260 nm, and (c,d) EDX maps indicating the distribution of Cu (c) and C (d) in the nanowires shown in (b).

References

[1] M.A. Nasalevich et al., CrystEngComm 16 (2014) 4919.

[2] B. van de Voorde et al., Journal of Materials Chemistry C 1 (2013) 7716.

[3] R. Ameloot et al., Chemistry of Materials 21 (2009) 2580.

---

* Work supported by Humboldt Research Fellowship for postdoctoral researchers.

[#] w.maijenburg@gsi.de, m.e.toimilmolares@gsi.de

DOI:10.15120/GR-2015-1-APPA-MML-MR-18

Properties of DSB: Ce^{3+}, a new inorganic scintillation material

V. Dormenev, K.-T. Brinkmann, R. W. Novotny, H.-G. Zaunick
2^{nd} Physics Institute, Justus-Liebig-Universität, Giessen, Germany.

Self activated scintillation materials like BGO and PWO possess a unique combination of the scintillation and physical properties, including high density fast response and radiation hardness to the electromagnetic part of ionizing radiation. However, heavy materials demonstrate significant damage caused by the hadronic part of the ionizing radiation [1] excluding their consideration in future high-energy experiments at new particle colliders.

Di-Silicate of barium (BaO-$2SiO_2$) doped with cerium (DSB: Ce) is one of the new scintillation materials made from binary stoichiometric compositions and produced like a glass or glass ceramics with a multistep thermal annealing process to obtain the nano-structuring of the material. When doped with Ce^{3+}, the material becomes scintillating. The light yield amounts to approx. 100 photo electrons per MeV deposited energy. Un-doped material has a wide band gap of 4.5 eV and can be used to detect Cherenkov light. The temperature dependence of the scintillation light LY(T) is 0.05 %/°C which is 40 times lower than in $PbWO_4$, for example. Therefore, detectors based on DSB will be tolerant to temperature variation in the range of -20°C to +20°C. Thus, DSB: Ce can be considered to be a perspective material for application in calorimetry.

Several samples have been irradiated at the Radiation Centre (Giessen, Germany) using a ^{60}Co source at a dose rate of 2 Gy/min. Figure 1 presents the transmission spectra of Ce-doped (more than 1% in weight) DSB: Ce, before and after irradiation with γ-quanta.

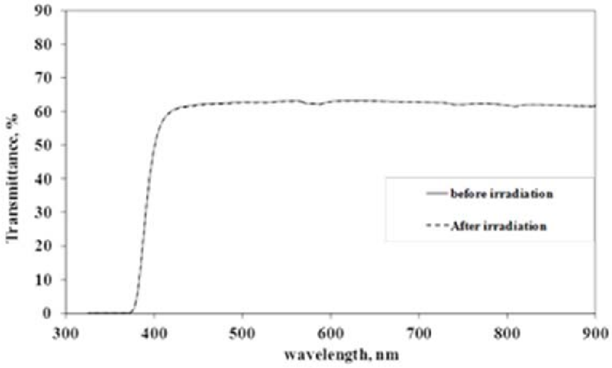

Figure 1: Comparison of optical transmission spectra of DSB: Ce samples before and after irradiation with ^{60}Co with an absorbed dose of 100 Gy measured at room temperature. The thickness of the sample was 4.5 mm.

The effect of stimulated recovery of the radiation damage was observed so far in self-activated scintillation materials, namely $PbWO_4$ [2]. Due to the presence of cerium ions with a high capture cross-section of free carriers was expected that Ce-doped scintillation materials should show a fast recombination of color centers, especially created due to shallow traps.

However, even at a high concentration of Ce^{3+} in the inorganic material our study shows that spontaneous recovery is a relatively slow process. Up to 25% of damaged transmission is recuperated in 6 hours and afterwards induced absorption remains practically stable if the samples kept in the dark. The induced absorption is decreased by a factor of two by annealing at 50°C and completely removed in a short time at 100°C, respectively. Annealing of the majority of the color centers above room temperature and their slow spontaneous recombination at room temperature show that they are due to deep traps which only weakly interact with cerium ions.

Further acceleration of the recombination of these color centers can be achieved by illumination with optical photons. Figure 2 shows the influence of the light illumination on the recovery of the induced absorption coefficient of a heavy doped DSB: Ce sample in comparison with spontaneous recovery at room temperature. This effect is achieved by photons using a LED at a photon flux of $2.9 \cdot 10^{16}$ photons/s exposing the wrapped sample.

However, the time constants for the recovery progressively increase with shifting towards the IR region. Stimulated relaxation provides simultaneous drop of the induced absorption over a wide spectral region. The illumination of the sample with blue light, which causes the ionization of the color centers, provides the fastest recuperation of the radiation induced damage.

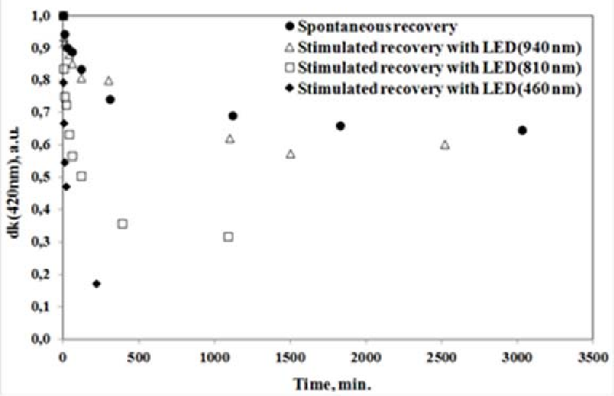

Figure 1: Stimulated recovery with optical photons of different wavelengths of the normalized radiation induced coefficient at 420 nm of a heavy-doped DSB: Ce sample after an absorbed dose of 500 Gy (^{60}Co).

References

[1] E. Auffray, M. Kojik, A. Singovski, Experimental Study of Lead Tungstate Scintillator Proton-Induced Damage and Recovery, IEEE Trans. on Nucl. Sci, 59 (2012) 2219-2223.

[2] A. Borisevich, V. Dormenev, T. Kuske, M. Korjik, S. Lugert, V. Mechinski, O. Missevitch,

DOI:10.15120/GR-2015-1-APPA-MML-MR-19

R.W. Novotny, A. Fedorov, Stimulated recovery of the optical transmission of $PbWO_4$ scintillation crystals for electromagnetic calorimeters after radiation damage, Nucl. Instr. and Meth. in Phys. Res. A 623 (2010) 1082-1085.

DOI:10.15120/GR-2015-1-APPA-MML-MR-19

Operation and improvements of PHELIX

S. Götte[1], *C. Brabetz*[1,2], *W. Cayzac*[1], *U. Eisenbarth*[1], *M. Kreutz*[1], *S. Kunzer*[1], *D. Reemts*[1], *T. Stöhlker*[1,3], *L. Tymura*[1], *F. Wagner*[1,3,4], *B. Zielbauer*[1,3], *and V. Bagnoud*[*1,3]
[1]GSI, Darmstadt, Germany; [2]Johann Wolfgang Goethe University, Frankfurt, Germany; [3]Helmholtz Institute Jena, Germany; [4]Technical University Darmstadt, Germany

The *P*etawatt *H*igh *E*nergy *L*aser for heavy *I*on *E*xperiments (PHELIX) has been operating continuously since 2008. This article reports on the usage of this Helmholtz facility, recent improvements achieved in 2014 and how PHELIX contributed to the scientific program of GSI.

Overview

Figure 1 shows the usage of PHELIX in 2014 in form of a pie-chart. Ten beam times took place, distributed over 88 out of 251 working days (35%, labeled as external beam time). These experiments were prepared typically over a period of about 5 days (additional 23%, marked as experiment preparation). Thus, again more than half of the available time was spent to serve for external experimental usage. This is an increase compared to 2013 but similar to the years before.

The rest of the time, maintenance (27%; this is more than in 2013 where 17% of the time have been used for this purpose) and three development beam times (7%, which is less than in the year before) have been done. The system was shut down for 8% of the year which is the same as in 2013.

During the construction of FAIR, PHELIX is running however with a capacity reduced to 2/3 of its full possibility. This results, for example in a reduced number of beam times in which PHELIX and the UNILAC ion beam are combined. The operation of PHELIX is ongoing, but more and more affected by the set up of FAIR since GSI infrastructure departments are concentrating on their tasks to serve the different building lots at the GSI site as well as upgrading the accelerator to become the injector for the future facility.

Operation of the laser facility

Five of the 2014 beam times were done at Z6, three of them as combined experiments of PHELIX and ions out of the UNILAC. This is less than in the years before, as mentioned above. The other five experiments were made in-house (four at the laserbay, one at the laserlab using the preamplifier only).

The PHELIX data base recorded 2310 laser shots in total. 1353 out of these were registered as experimental shots. The high amount of these is due to the beam time using the preamplifier only which can be used with a repetition rate of one shot each three minutes, while a typical experiment using the main amplifier stage gets typically six shots per day.

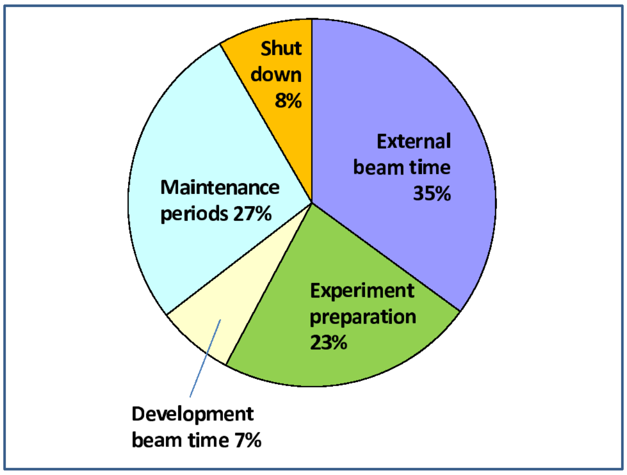

Figure 1: PHELIX usage in 2014

The number of failed experimental shots is less than a percent (in total 11 shots) which is really satisfactory; six of these failures happened due to broken hardware, mainly at the pulsed power system. They could be repaired within hours and did not cause a severe interruption of the experimental campaign. Only four shots were lost due to mistakes made by the laser crew which shows the high expertise of the operators as well as the good support of the PHELIX control system *PCS* to operate the facility. The last failed shot was due to a hardware problem not caused by PHELIX but the accelerator hardware.

The user service has been greatly formalized in the last years. After a positive evaluation, the applicant receives an information about the amount of beam time reserved for his proposal. When the experiment is scheduled and its time slot communicated by the PHELIX group leader, the experimentalist has to prepare a detailed technical design review which has to be presented and discussed at least three months before the beam time is going to happen. Within this review, all technical aspects of the planned experiment down to the screw level have to be addressed as well as the personal and machinery safety. The experimental team (up to six persons) foreseen to enter the laboratory has to be named, the roles and tasks have to be assigned and finally the shot plan has to be presented.

On the day of arrival, the external users get the necessary personal safety equipment, and after the training at the experimental site they can start to set up the experiment.

---

[*] v.bagnoud@gsi.de

DOI:10.15120/GR-2015-1-APPA-MML-PP-01

These formal aspects are normally done within one hour. On the PHELIX side, a link scientist takes care for technical aspects concerning the set up as well as an operator providing the laser in an alignment mode.

During the experiment, PHELIX is operated by a shot director who drives the shot sequence in coordination with the experiment, and an operator setting the laser parameters. The staff for these tasks is changing once per day corresponding to a shift plan prepared before. The activity of the experimentalists is steered by an experimental coordinator out of the external team. This person and the shot director communicate in the morning as well as in advance of each shot what is going to happen.

Internal Improvements

After more than ten years of operation, some of the hardware must be replaced because it is no longer supported and spares become unavailable. It is also the occasion to bring it back to the state of the art. In this view, a new fiber-based nanosecond front-end has been bought and installed at PHELIX. The performance is similar to the existing system [1] but its versatility and the service offered by the Europe based vendor (Photline Technologies) greatly improves the reliability of this subsystem. For similar reasons, a new pump laser (Verdi, manufactured by Coherent Inc.) has been bought for the femtosecond front-end. The operation modes of this subsystem have been extended over the past and reach from a free adjustable pulse contrast level by use of the uOPA system over multi-pulse generation with adjustable delays of picoseconds up to two-beam operation with different pulse durations and tunable energy ratio.

Some devices were replaced because of their lack of long-term reliability. This concerns most notably the high-capacitance Pockels-cell driver of the preamplifier. Furthermore, a new random phase plate was installed and commissioned at the Z6 experimental area to enhance the homogeneity of the laser-focus profile.

Since Microsoft stopped the support of its operating system Windows XP, all the 30 computers of the *PCS* were upgraded or renewed to run Windows 7. Additionally, LabVIEW was changed from LV 2009 to LV 2014, and accordingly the *CS* framework made a huge step from version 3.2 to 3.40.

Contribution to the scientific program

Most of the experiments done at PHELIX are planned and executed in close collaboration with the PHELIX team and the plasma physics department of GSI as mentioned above. A non exhaustive list of such experiments can be found in this report. For instance, the configuration of PHELIX in multi-beam mode allowed the generation and study of magnetic field recombination [2]. An internal beam time was devoted to the generation of Raman-shifted laser pulses for the study of a Raman-amplifier [3]. In addition, using the world-unique laser-ion setup of the Z6 area, two combined laser-ion experiments were performed on the energy loss of ions in plasma in nonlinear interaction conditions, where the ion-stopping theories are still highly incomplete [4].

In 2014, twelve articles have been published basing on experiments and laser developments done at PHELIX [5...16]. Additionally, two doctoral theses dealing with experimental and technical aspects have been finished this year in our group [17, 18]. Furthermore, a technical design report was written concerning a 100 J laser system to be set up in the APPA building at the FAIR site.

Outlook for 2015

By the help of the expert panel PPAC, PHELIX will not run out of experiments to be done in 2015; the first half of the year is scheduled already. A suggestion for a large-scale laser system (the so called Helmholtz Beamline) to be set up in an own laser building at FAIR is in an early project stage and will be continued 2015. Finally, a project is ongoing to upgrade the preamplifier stage of PHELIX in order to increase the repetition rate.

References

[1] https://www.gsi.de/en/start/research/forschungsgebiete_und_experimente/appa_pni_gesundheit/plasma_physicsphelix/phelixnanosekunden_frontend.htm

[2] R. Riquier at al., this report

[3] B. Landgraf et al., this report

[4] W. Cayzac et al., this report

[5] S. Busold et al., Phys. Rev. Spec. Top. Accel. Beams **17**, 031302 (2014)

[6] S. Busold et al., Nuclear Instrum. Methods Phys. Res. A **740**, 94 (2014)

[7] S. Busold et al., Rev. Sci. Instrum. **85**, 113306 (2014)

[8] J. Prokůpec et al., Rev. Sci. Instrum. **85**, 013302 (2014)

[9] H. Y. Zhao et al., J. Phys.: Conf. Ser. **488**, 142004 (2014)

[10] D. Denis-Petit et al., J. Quant. Spectrosc. Radiat. Transfer **148**, 70 (2014)

[11] T. G. White et al., Phys. Rev. Lett. **112**, 145005 (2014)

[12] S. Faik et al., High Energy Dens. Phys. **10**, 47 (2014)

[13] L. Senje et al., Rev. Sci. Instrum. **85**, 113302 (2014)

[14] F. Wagner et al., Opt. Express **22**, 29505 (2014)

[15] F. Wagner et al., Appl. Phys. B **116**, 429 (2014)

[16] K. Li et al., Laser Part. Beams **32**, 631 (2014)

[17] F. Wagner, *Kontrolle des zeitlichen Kontrastes am Lasersystem PHELIX*, doctoral thesis, Fachbereich Physik, Technische Universität Darmstadt, Germany (2014)

[18] C. Brabetz, *Development of specially shaped laser beams for the optimized acceleration of particles*, doctoral thesis, Fachbereich Physik, Johann Wolfgang Goethe - Universität Frankfurt am Main, Germany (2014)

DOI:10.15120/GR-2015-1-APPA-MML-PP-01

Commissioning of the PRIOR prototype*

D. Varentsov[1], *O. Antonov*[2], *A. Bakhmutova*[3], *A. Bogdanov*[3], *C.R. Danly*[4], *S. Efimov*[2], *M. Endres*[5], *A.A. Golubev*[3], *D.H.H. Hoffmann*[5], *A. Kantsyrev*[3], *Ya.E. Krasik*[2], *P.M. Lang*[5], *F.G. Mariam*[4], *N. Markov*[3], *F.E. Merrill*[4], *V.B. Mintsev*[6], *V. Panyushkin*[3], *M. Rodionova*[1,5], *M. Schanz*[5], *L. Shestov*[1,5], *V. Skachkov*[3], *S. Udrea*[5], *K. Weyrich*[1], *C. Wilde*[4], *and A. Zubareva*[6]

[1]GSI, Darmstadt, Germany; [2]Technion, Haifa, Israel; [3]ITEP, Moscow, Russia; [4]LANL, Los Alamos, USA;
[5]TUD, Darmstadt, Germany; [6]IPCP, Chernogolovka, Russia

PRIOR (*Proton Microscope for FAIR*) is one of the three frameworks proposed by the HEDgeHOB collaboration for the future experiments at FAIR. This worldwide unique high-energy proton microscopy (HEPM) facility will be integrated into the HEDgeHOB SIS-100 beam line and employ high-energy ($3 - 10\,\mathrm{GeV}$), high-intensity ($2.5 \cdot 10^{13}$ ppp) proton beams for fascinating multidisciplinary research such as experiments on fundamental properties of materials in extreme dynamic environments generated by external drivers (pulsed power generators, high-energy lasers, gas guns or explosive-driven generators) prominent for materials research and high energy density physics as well as the PaNTERA (*Proton Therapy and Radiography*) experiment, with a great relevance to biophysics and medicine.

Recently, as a result of the international effort of a team of scientists from GSI, LANL, ITEP and TUD a PRIOR prototype has been designed, constructed and commissioned at the HHT area of GSI (Fig. 1 (left)). The PRIOR prototype employs high-gradient NdFeB permanent magnet quadrupole (PMQ) lenses developed by ITEP and provides a magnification of $\approx 4 - 5$ with a field of view of $\approx 15\,\mathrm{mm}$.

Figure 1: The PRIOR prototype PMQ lenses (left) and the pulsed power setup — four high-current generators placed around a small explosion chamber (right) followed by the four PRIOR lenses installed at the HHT area of GSI.

The detector (image collection) system developed by LANL was installed in the newly constructed concrete-shielded detector room $\approx 9\,\mathrm{m}$ downstream the target location. With a pellicle / mirror arrangement, the system employs two cameras simultaneously: a high resolution (4 Mp) CMOS camera (PCO DIMAX HS) used mainly for static experiments and a fast intensified CCD camera (PCO DICAM PRO) for dynamic measurements. $10 \times 10\,\mathrm{cm}$ columnar CsI and plastic BC-400 scintillators were installed for static and for dynamic measurements, respectively.

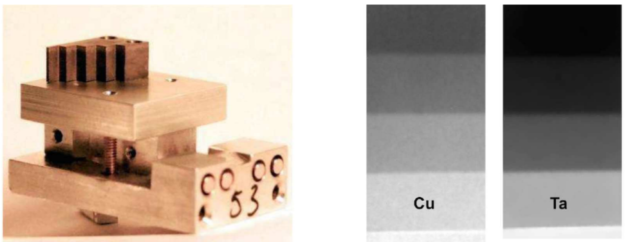

Figure 2: Tantalum step wedge object on a target table (left) and PRIOR proton radiographs (right) of the identical copper and tantalum step wedges (0.56, 2.06, 4.07 and $6.05\,\mathrm{mm}$ step thicknesses).

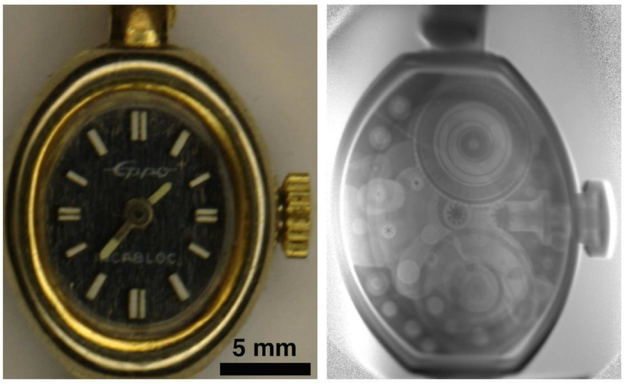

Figure 3: A small women mechanical wrist watch (left) and its proton radiograph (right) obtained with the PRIOR prototype using a 3.6 GeV SIS-18 proton beam at GSI.

In April 2014, an experimental campaign for the commissioning of the PRIOR prototype employing $3.5 - 4.5\,\mathrm{GeV}$, moderate ($10^8 - 10^9$ ppp) intensity proton beams from the SIS-18 synchrotron took place at GSI. In these experiments a large set of small static objects including step wedges (Fig. 2) and sets of wires made of different metals, resolution and matching tuning targets as well as some fancy objects (Figs. 3 and 4) were used in a vacuum target chamber equipped with a 6-axis manipulator. As a result of these experiments, an rms spatial resolution of the prototype of about $30\,\mu\mathrm{m}$ with a remarkable density sensitivity has been demonstrated. It has also been shown that with

---

* Work supported by GIF grant No. 1132-11.14/2011, BMBF grants No. 05K10RD1 and 05P12RDRBK, FRRC contract No. 29-11/13-17 and MES of Russia contract No 14.616.21.0023.

DOI:10.15120/GR-2015-1-APPA-MML-PP-02

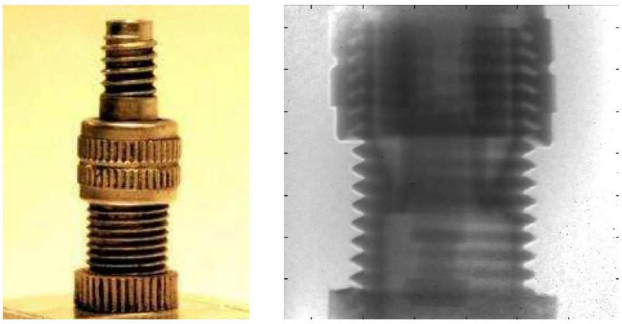

Figure 4: A presta valve from a bicycle inner tube (left) and a PRIOR proton radiograph of its central part (right). One can clearly see the engagement of the threads as well as the valve stem and the details of how this valve is seated.

a sufficient proton beam intensity ($10^{10} - 10^{11}$ ppp) and by using a fast plastic scintillator in the detector system, one can achieve 10 ns or better temporal resolution without significant degradation of the imaging properties.

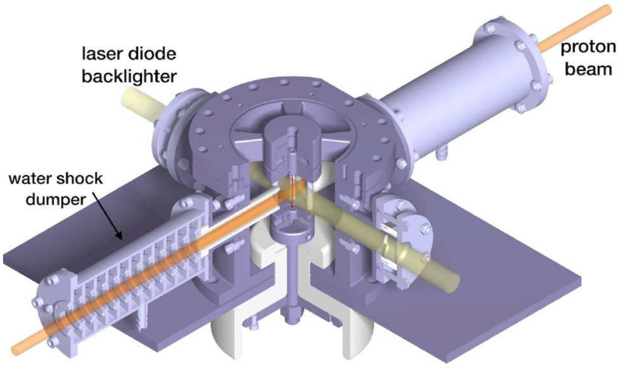

Figure 5: UEWE water filled target chamber. A thin exploding wire (red) in the center of the chamber is illuminated from one side by a proton beam for HEPM measurements, and from the other side — by an optical backlighter for shadowgraphy diagnostics.

For the dynamic commissioning of the PRIOR prototype, a new pulsed power generator had been developed by Technion and GSI (see Fig. 1 (right)). This generator (up to $50\,\mathrm{kV}$, $12.5\,\mathrm{kJ}$ stored energy) was designed to generate warm dense matter states of various metals by underwater electric wire explosions (UEWE) for equation of state studies. A metallic wire ($30 - 50\,\mathrm{mm}$ length, $0.1 - 1\,\mathrm{mm}$ diameter) is placed in the middle of a $\approx 11\,\mathrm{cm}$ diameter explosion chamber (Fig. 5). The wire is quickly heated by a pulsed electric current ($\approx 200\,\mathrm{kA}$, $1.5 - 2\,\mu\mathrm{s}$ rise time) to a dense plasma conditions with about $2 - 3\,\mathrm{eV}$ temperature.

In addition to the HEPM measurements with the PRIOR prototype, an optical shadowgraphy setup consisting of a 450-nm, 4-W fiber-coupled laser diode backlighter, two fast intensified CCD cameras and a streak camera has been installed for target diagnostics. A special effort has been taken to design water shock dumpers in order to minimize the amount of material used to separate the UEWE explosion chamber and the vacuum ($10^{-3}\,\mathrm{mbar}$) PRIOR beam line as well as the water layer thickness in the proton beam direction (see Fig. 5).

In July 2014, a new experimental campaign aiming commissioning of the PRIOR prototype for dynamic experiments took place at GSI. In comparison with the April 2014 run, the proton beam intensity has been increased by more than two orders of magnitude (up to 10^{11} protons per pulse) and a new beam diagnostics for high energy protons (scintillator screens and cameras) has been integrated into the HHT beam line to ensure a good beam alignment and matching.

The dynamic PRIOR experiments have been carried out using the developed UEWE setup. In these experiments, a pulsed current ($\approx 40\,\mathrm{MA/cm^2}$, $5\,\mathrm{GW}$ deposited power) run through a tantalum wire ($0.8\,\mathrm{mm}$ diameter and $40 - 50\,\mathrm{mm}$ length) generating this way warm dense matter states characterized by specific energy deposition level about $10\,\mathrm{kJ/g}$ and $\sim\mathrm{km/s}$ expansion velocities. An example of the proton radiography measurements of an exploding tantalum wire in shown in Fig. 6. In total, about twelve successful dynamic shots with the PRIOR prototype has been made. In these shots, we have varied the power deposited in the $0.8\,\mathrm{mm}$ Ta wires as well as the time moment of the proton radiography imaging. The obtained data is currently being processed and analyzed.

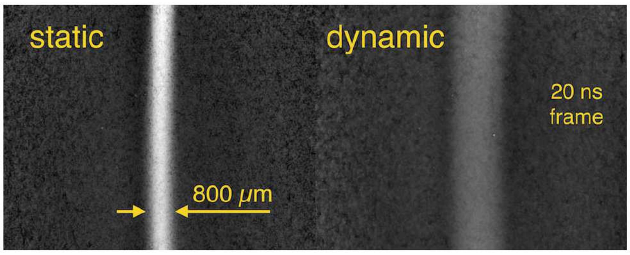

Figure 6: Proton radiographs (20 ns temporal resolution) of a tantalum wire in water before shot (left) and during the explosion (right) driven by the UEWE generator ($\approx 10\,\mathrm{kJ/g}$ specific energy deposition in Ta).

As an unexpected result of the commissioning experiments, we have observed a considerable image degradation caused by the radiation damage of the PMQ lenses (the reduction of the quadrupole strength and increased high-order multipole components) due to large fluences of spallation neutrons which are mainly produced in the tungsten beam collimator located in a close proximity to these permanent magnets. We have also performed special measurements and simulations to study this phenomenon. For the future applications of the PRIOR magnifier at FAIR where much higher proton beam intensities are expected we suggest to either consider using the samarium-cobalt (SmCo) PMQ lenses or, better, to design and employ high-gradient small-aperture radiation-resistant warm electromagnets. The corresponding design study on the final construction of PRIOR for experiments at FAIR has been started.

DOI:10.15120/GR-2015-1-APPA-MML-PP-02

Generation of multimillijoule redshifted beams for stimulated Raman scattering*

B. Landgraf[1,2], *A. Hoffmann*[1], *D. Kartashov*[2], *F. Gärtner*[3,4], *Z. Samsonova*[1,2], *P. Polynkin*[5], *J. Jacoby*[4], *T. Kühl*[1,3], *and C. Spielmann*[1,2]

[1]Helmholtz Institute Jena, Jena, Germany; [2]Institute of Optics and Quantum Electronics, Abbe Center of Photonics, Friedrich-Schiller University Jena, Jena, Germany; [3]GSI, Darmstadt, Germany; [4]Institute for Applied Physics, Plasmaphysics, Goethe-University Frankfurt/Main, Frankfurt/Main, Germany; [5]College of Optical Sciences, The University of Arizona,Tucson, USA

Introduction

Stimulated Raman backscattering (SRBS) is a possible candidate to overcome scaling limitations of state of the art chirped pulse laser amplifiers [1]. SRBS describes a three wave interaction in laser plasmas in which a plasma wave is generated due to the ponderomotive force of a beatwave originating from two counter-propagating and frequency shifted laser pulses. The frequency shift difference defines the optimal plasma frequency. To achieve an efficient energy transfer between the counter-propagating pulses a frequency difference between $5 - 10\%$ ($500 - 1500cm^{-1}$, 50-100 nm for typical CPA systems) is necessary [2].

Redshift with stimulated Raman scattering

The necessary parameters for a seed beam are: i) a well-defined redshift which must be independent of the energy available; ii) a single spatial mode beam and iii) a pulse duration much shorter than the pump pulse. The introduced Group Velocity Mismatch (GVM) it is suitable to partially recompress the pulse and forego further recompression techniques. To support a high total energy output gases are ideally suited for this application. SF_6 provides a 100 nm redshift at 1053 nm ($775cm^{-1}$).

Experimental results

The presented data [3] were collected in the XRay Lab at the PHELIX Laser facility. The laser provides up to 200 J in 500 fs at 1053 nm every 90 minutes. Figure 1 shows the aquired spectra. To generate the seed beam the energy was reduced to 0.1-0.4 J at the axicon every 3 minutes.

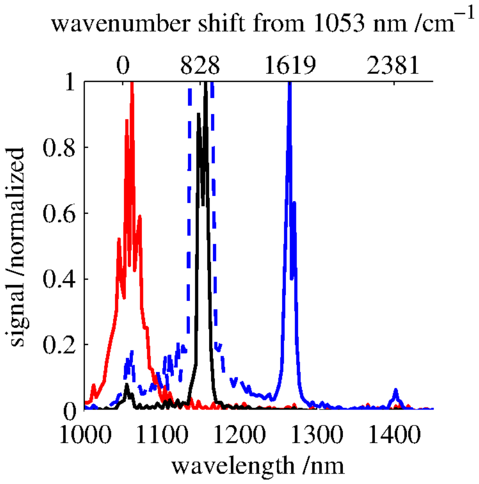

Figure 1: Spectral evolution of Raman shifted pulses using SF_6 with short (black line), long (blue dotted) caustic length, and Ar with significant spectral broadening for fundamental pulses at 1053 nm.

Conclusion

We characterized a simple but reliable method for the generation of redshifted seed beams for SRBS. The results show that with minimal alignment, fitting for few shot systems like PHELIX it is possible to generate customized high quality beams. The redshift is not energy dependent and tunable by the Raman medium and the order of the process used. Results show further a high absolute energy of the seed beam suitable to be used in the nonlinear Raman regime. With these seed source we are now in the favourable situation to complete our SRBS experiment at PHELIX, which will be a major step forward to realize a hight power pulse light source for studying the interaction of intense pulses with heavy ions, or dense plasmas generated with heavy ions, as available at FAIR.

References

[1] V. M. Malkin, G. Shvets, and N. J. Fisch. ”Fast compression of laser beams to highly overcritical powers.” Physical review letters 82.22 (1999): 4448.

[2] R. M. G. M. Trines, et al. ”Simulations of efficient Raman amplification into the multipetawatt regime.” Nature Physics 7.1 (2011): 87-92.

[3] B. Landgraf, et al. ”Generation of multi-millijoule red-shifted pulses for seeding stimulated Raman backscattering amplifiers” Optics Express 23, (2015): 7400–7406.

---

* Work supported by GSI(PHELIX)/HI Jena/HGShire/European Regional Development Fund (EFRE)/state of Thuringia (TMBWK) under Grant No. B 715-08008/TR 18/US Air Force Office of Scientific Research through grants No. FA9550-12-1-0143 and No. FA9550-12-1-0482/US Defense Threat Reduction Agency through grant No. HDTRA 1-14-1-0009

DOI:10.15120/GR-2015-1-APPA-MML-PP-03

Upgrade of GSI's laser-driven ion beamline at Z6*

S. Busold[1,2], *D. Schumacher*[1], *C. Brabetz*[1], *D. Jahn*[3], *F. Kroll*[4], *O. Deppert*[3], *A. Blazevic*[1,2], *V. Bagnoud*[1,2], *and M. Roth*[3]

[1]GSI Helmholtzzentrum für Schwerionenforschung GmbH, Darmstadt, Germany; [2]Helmholtz Institut Jena, Germany; [3]IKP, TU Darmstadt, Germany; [4]Helmholtz-Zentrum Dresden - Rossendorf, Germany

The LIGHT beamline

The German national collaboration "LIGHT" (Laser Ion Generation, Handling and Transport, [1]) has implemented a worldwide unique laser-driven proton beamline at GSI. Compact acceleration up to nearly 30 MeV proton energies is possible from the novel plasma source via the TNSA mechanism, which is driven by the PHELIX 100 TW laser beam. Therefore, at the Z6 experimental area laser intensities of up to 5×10^{19} W/cm^2 are accessible. A pulsed high-field solenoid then provides for the necessary beam collimation and energy selection [2] and typically protons with an energy between 8 and 10 MeV are chosen.

Furthermore, a radiofrequency (rf) cavity is implemented at 2 m distance to the source for phase rotation of the created single bunch, which shows a typical energy spread of around 20% (FWHM around central energy) and high particle numbers of up to 10^9. Energy compression of the bunch below 3% was demonstrated in an experimental run in 2013 [3].

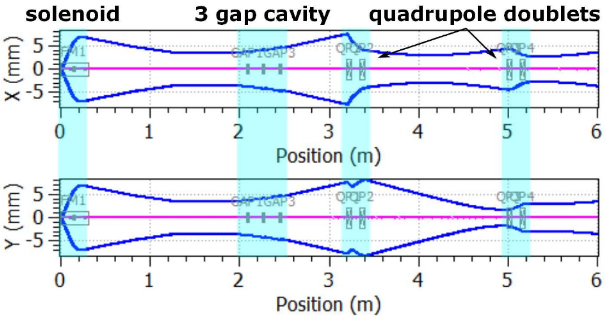

Figure 1: Simulation (code: *TraceWin*) of the 7.8 MeV proton beam size (rms) through the current beamline, from the source up to a new diagnostic chamber at 6 m.

For the 2014 campaign, the beamline has been extended by a diagnostic chamber at 6 m distance to the source, two permanent magnetic quadrupole doublets (50 mm, 25 T/m) for beam transport, see figure 1, and an optional third doublet (80 mm, 85 T/m and 45 mm, 105 T/m) for final focusing of the bunch. The additional space behind the cavity, which is again used at -90 deg synchronous phase but this time at higher rf power to 'over-focus' the bunch in longitudinal phase space, compare figure 2, is necessary as drift space for phase focusing experiments.

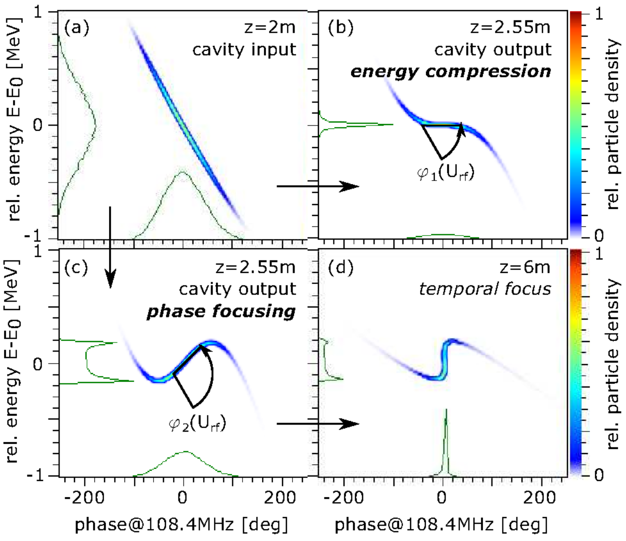

Figure 2: Simulated longitudinal phase space diagrams for the two current operation modes when injecting the laser accelerated proton bunch into the rf cavity at -90 deg synchronous phase: energy compression or temporal compression of the bunch along a drift via phase focusing.

Recent results and outlook

In the 2014 campaign, proton bunches with a central energy of 7.8 MeV were selected from the source and propagated through the beamline, containing typically particle numbers in the range of 2×10^8 to 5×10^8 within FWHM. Their length could be compressed in time to a FWHM bunch length of τ=(462±40) ps.

The transverse beam profile, however, could be reduced in the experiment only to a line focus of 3×18 mm^2 (FWHM). Therefore, the implementation of a second pulsed solenoid at the end of the beamline is planned as a new steep final focusing system to access highest peak intensities. Also the acceleration of not only protons but also carbon, oxygen and flourine will be explored in 2015.

References

[1] S. Busold *et al.*, NIMA **740**, 94-98 (2014)

[2] S. Busold *et al.*, PRSTAB **16**, 101302 (2013)

[3] S. Busold *et al.*, PRSTAB **17**, 031302 (2014)

---

* This work is supported by the Helmholtz Institute Jena.

DOI:10.15120/GR-2015-1-APPA-MML-PP-04

Investigation of high power laser -induced spallation phenomena in target and collimator materials for next generation accelerators*

M. Tomut[1,2,#], *I. Krasiuk*[3], *T. Rienecker*[4], *O. Rosmej*[1],*I. Stuchebryukovr*[5], *A. Schönlein*[1], *K. Khischenko*[3], *R. Belikov*[6]

[1]GSI, Darmstadt, Germany; [2]NIMP, Bucharest, Romania;3Joint Institute for High Temperatures, RAS; [4]Goethe-Universität Frankfurt, Germany;[5]Prokhorov General physics Institute, RAS; [6]Moscow Institute for Physics and Technology, Moscow, Russia

The design of new high power accelerator facilities at FAIR, HiLumi LHC and FCC needs advanced solutions for beam intercepting devices such as production targets, collimators, beam windows, absorbers and dumps. The interaction of high energy, high intensity particle beams with solids induces shock waves, phase and density changes, nano-structuring and spallation. In order to understand the failure mode and to predict component lifetimes, a concerted effort on studying the behavior of traditional and novel material in conditions similar to the operating environment is going on in large collaborations projects such as EuCARD2. Both radiation hardness for high flux beam exposure and dynamic mechanical response during beam impact are investigated for traditional materials like graphite, and for novel composite materials purposely developed for high energy particle beams applications.

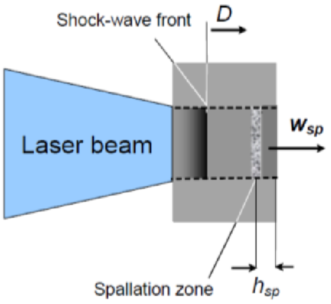

Figure 1: Sketch of the laser – induces spallation experiment on thick targets (D is the shock-wave front velocity and w_{sp} and h_{sp} are, respectively, the velocity and thickness of spallation plate) [1].

Within the experiment P089, investigations of spallation phenomena in different graphite grades, copper-diamond and molybdenum-graphite composites were conducted at the Z6 experimental area, using shock waves induced by the PHELIX laser at GSI. A pulsed laser beam with a wavelength of 530 nm, 1.4 ns pulse duration and energies of 120 J was focused to a spot size of 1.3 mm on the target. Typical beam intensities were about 0.6 ′ 10^{13} W cm–2. For inferring the spall strength s* and strain rate $\dot{\varepsilon}$ we measured the depth of spallation groove h after laser beam impact on the target. The s* and $\dot{\varepsilon}$ values were calculated using a numerical code based on hydrodynamics equations [2]. It was assumed that the ablation pressure pulse on the front target surface has the same shape as the laser pulse. The spallation strength was considered to be the minimum pressure modulus in the spallation plane [1]. Figure 2 shows optical microscope images of ablation crater on the laser facing side of a thick isotropic graphite target and of the rear spallation crater on the same target.

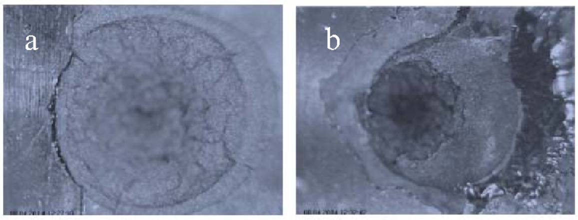

Figure 2: Optical micrographs of (a): ablation spot on the front side and (b): spallation crater on the rear face of a thick graphite target exposed to laser beam.

Raman spectroscopy has been used for first investigations of microstructural transformations induced by the laser shock wave in the sample. As shown in figure 3, the material in the spallation crater shows a higher degree of graphitization than the initial structure, indicating that the material temperature reached values above 2000 ºC. Future detailed Raman spectroscopy mappings of the craters will be performed for investigating the possible formation of high pressure carbon phases like rhombohedral graphite and diamond. Spallation strength values between 1 and 2 GPa were found for isotropic graphite experiencing strain rates between 10^6 and 10^7 s^{-1}.

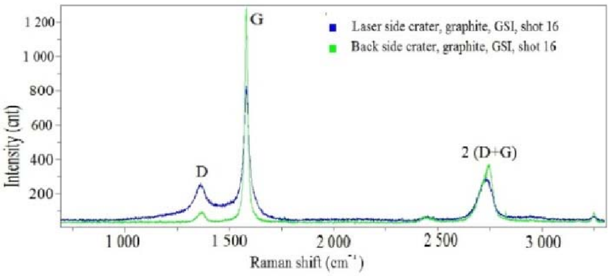

Figure 3: Raman spectra of graphite target after laser beam impact in the ablation crater (blue) and spallation crater (green).

[1] S.A. Abrosimov et al., Quantum Electronics 44 (6) (2014) 530 – 534.

[2] D. Batani, V.I. Vovchenko, G.I. Kanel, et al. Dokl. Ross. Akad. Nauk, 389 (3), 328 (2003).

---

* Work supported by EuCARD2, grant no. 312453

[#] m.tomut@gsi.de

DOI:10.15120/GR-2015-1-APPA-MML-PP-05

Surface parallel electron acceleration using ultra-intense sub-picosecond pulses

J. Y. Mao[1], O. Rosmej[2,3], Y. Ma[4], M. H. Li[4], B. Aurand[2], F. Gaertner[2,3], W. M. Wang[4], J. Urbancic[1], A. Franz[2,3], A. Schoenlein[2,3], B. Zielbauer[2], U. Eisenbarth[2], V. Bagnoud[2], F. Wagner[2,3], K. Li[2], F. Horst[2,3], M. Syha[2,3], H. Ding[5], P. Neumayer[2,3], S. Mattias[1], Y. T. Li[4], M. Aeschlimann[1], L. M. Chen[4], T. Kuehl[2,5,6]

[1]University of Kaiserslautern and Research Center OPTIMAS, Kaiserslautern, Germany, [2]GSI Helmholtzzentrum, Darmstadt, Germany,[3]Goethe University, Frankfurt, Germany, [4]Beijing National Laboratory for Condensed Matter Physics, Institute of Physics, CAS, Beijing 100190, China, [5]Helmholtz Institute Jena, Jena, Germany, [6]Johannes-Gutenberg University, Mainz, Germany

Introduction

In the experiment P090, we investigated the generation of highly collimated target surface electron (TSE) beams with high electron energy and small divergence angle [1,2] from the interaction of a Cu bulk target irradiated by an ultra-intense laser pulse at PHELIX, with the objective to generate high-energy Gamma rays for backlighting of HIHEX targets up to 300 μm Pb.

Experiment

The first experiments in Jan. 2014 were carried out by working at the fundamental wavelength of 1053 nm with a peak power of around 200 TW. The s–polarized laser beam with a duration of $\tau^0 = 500$ fs was focused by an f=1.5m off-axis paraboloidal mirror at a grazing incidence angle onto a Cu bulk target. An additional pre-pulse with adjustable intensity from 0 to 1×10^{-6} was applied 2.8 ns in advance of the main pulse. A schematic picture of the experimental setup is shown in Figure 1. Also, 1% leakage of the main beam was frequency-doubled and applied as a probe beam to monitor the pre-plasma scale and density.

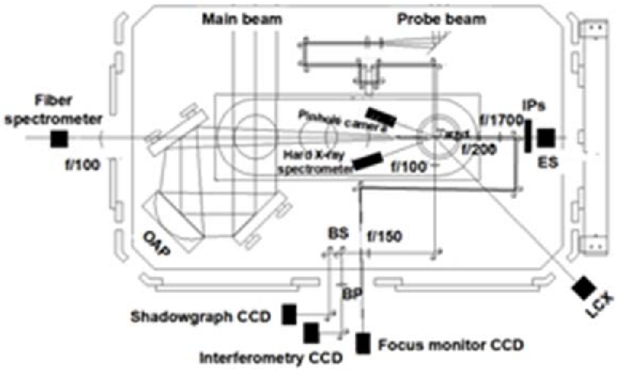

Figure 1: Experiment setup.

We investigated the pre-pulse dependence on the TSE generation. An optimized intensity ratio of the pre-pulse is essential to achieve an effective under-dense pre-plasma. In experiment, the intensity ratio of the pre-pulse was adjustable from $1\times10^{+2}$ to 1×10^{-6} which was 2.8 ns in advance of the main beam, while the consequent pre-plasma density and scale were simultaneously monitored. At the optimized ratio between pre-pulse and main pulse intensities of around 5×10^{-6}, well concentrated and intense TSE electron jets with low divergence were observed at a laser incident angle of 72o, as shown in Figure 2 (a). The divergence of the TSE electron jet was measured to be around 1o (FWHM). By a rough calculation, the energy range of the TSE bunches is around 5 MeV. In the case without pre-pulse, the electron beam becomes divergent and weak, as shown in Figure 2 (b). During the short beam time (5 days), we found that the pre-plasma condition is crucial to generate a high quality TSE Beam.

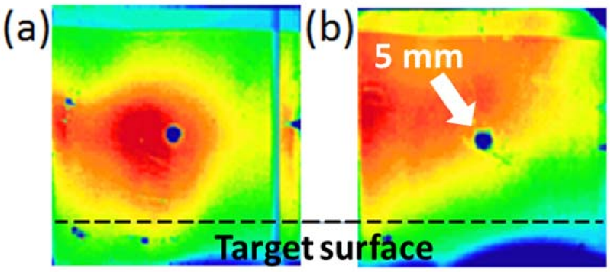

Figure 2: Spatial angular distribution of the TSE beam in the case (a) with the pre-pulse intensity ratio of 5×10^{-6} and (b) without pre-pulse. The hole has a 5 mm diameter. The color-coding shows the relative exposure of an image-plate detector (blue-lowest/red-highest)

Prospects

In the next step, we applied for a longer beam time (10 days) at PHELIX in Jun. 2015, which will provide us another opportunity to continue the experiments above and to deepen our understanding of surface electron acceleration.

References

[1] J. Y. Mao, L. M. Chen, X. L. Ge *et al.*, Phys. Rev. E**85**, 025401 (R) (2012).
[2] J. Y, Mao, L. M. Chen, K. Huang *et al.*, Appl. Phys. Lett., accepted. (2015)

DOI:10.15120/GR-2015-1-APPA-MML-PP-06

X-ray radiography on millimetre-scale high-Z targets for the plasma physics program at FAIR*

P. Neumayer[1,2], *B. Borm*[3], *D. Khaghani*[1,2], *K. Li*[1,2]
[1]EMMI/GSI, Darmstadt, Germany; [2]FIAS, Frankfurt, Germany; [3]Goethe Univ., Frankfurt, Germany.

Heavy ion pulses with unprecedented intensities at the upcoming Facility for Antiproton and Ion Research (FAIR) will offer novel and unique approaches to the generation of dense plasmas, allowing accurate laboratory studies of matter at such extreme conditions. A variety of schemes has been proposed to exploit the opportunities to generate matter at High Energy Density (HED) conditions. In many of these schemes targets undergo a large hydrodynamic evolution, mostly in the so-called warm-dense matter (WDM) regime. For this reason, accurate monitoring of the target density distribution is crucial to verify the target performance. Radiography to measure the target density distribution is considered an indispensable diagnostic technique for future HED experiments at the FAIR facility.

Powerful hard x-ray sources can be realized with high-energy short pulse lasers. When irradiating solid targets with laser intensities $>10^{18}$ W/cm^2 electrons are accelerated to MeV energies, causing emission of energetic bremsstrahlung. Such x-ray sources are being employed at many large HED facilities to enable point-projection radiography with spatial resolution down to 10 µm and temporal resolution of order 10 ps (e.g. [1,2]).

In order to assess the potential of intense-laser-driven hard x-ray radiography as diagnostic for the often large, high-Z targets proposed for FAIR, we have simulated radiographic images for calculations of the target evolution presented by Tahir et al. [3]. X-ray emission spectra are calculated by a Monte-Carlo electron-photon transport code, using a 1-temperature hot electron spectrum with a mean electron energy of 200 keV, corresponding to a focused intensity of about 10^{18} W/cm^2 [4]. We assume a laser pulse energy of 400 J, and conversion of 10 % of the laser energy into this hot electron population, which is typically found in experiments at these conditions [5].

Figure 1 shows simulated radiographic images of the lead target after expansion to conditions near the critical point ($T \approx 5600$ K, $\rho \approx 4$ g/cm^3). As can be seen, an average transmission of approx. 50% at the maximum areal density in the target centre provides a good image contrast. The image noise includes the photon shot noise, absorption statistics, and the energy dependent detection quantum efficiency. A signal-to-noise ratio (SNR) of around 60 suggests that absolute measurement of the areal density with few percent accuracy can be achieved. Also shown in Figure 2 is the signal behind a calibration wedge, consisting of steps with thicknesses from 20 to 600 µm, manufactured from the same material as the target. This provides an absolute calibration allowing to directly relate the image exposure to the areal mass density.

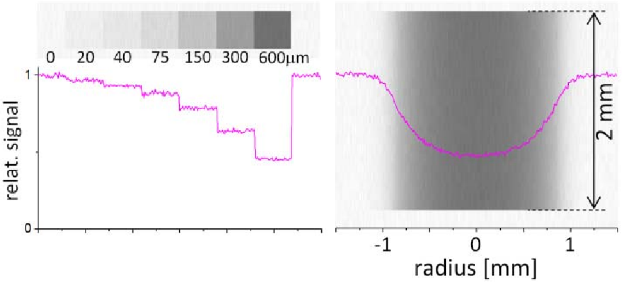

Fig. 1: Simulated radiographs (from [6]) of a Pb calibration step filter (left) and a heavy-ion heated cylindrical Pb-target after expansion for 400 ns.

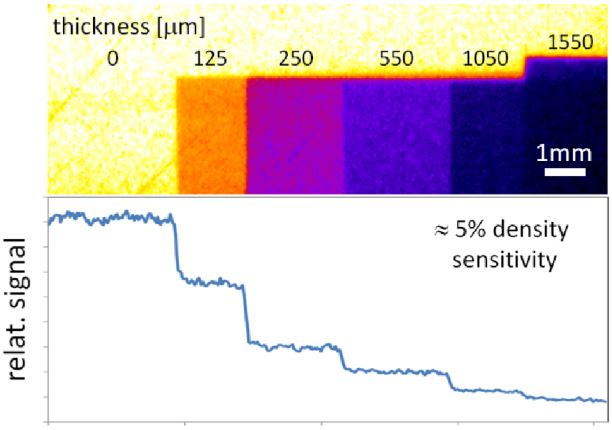

Fig. 2: Radiographic image (top) of a Ta step filter, obtained from a hard x-ray source driven by the PHELIX laser.

A demonstration experiment (P056) was carried out using GSI's high-energy high-intensity laser PHELIX. Laser pulses of 120 J and duration 0.7 ps were focused onto a 5 µm thin Au-foil. Fig. 2 shows a radiographic image of a step filter target made from tantalum sheets of various thicknesses up to 1.5 mm. The SNR in the resulting radiographic image allows for discrimination of areal mass differences of approx. 5 %, in reasonable agreement with our simulations. This demonstrates the viability of intense-laser driven hard x-ray radiography as diagnostic in future dense plasma physics experiments at FAIR [6].

References

[1] P. K. Rambo et al., Appl Opt. 44, 2421 (2005).
[2] J. K. Crane et al., J. Phys.: Conf. Ser. 244, 032003 (2010)
[3] N. A. Tahir et al., Phys. Rev. Lett. 95, 035001 (2005)
[4] F. N. Beg et al., Phys. Plasmas 4, 447 (1997)
[5] P. M. Nilson et al., Phys. Rev. Lett. 105, 235001 (2010)
[6] K. Li et al., Laser and Particle Beams 32, 631 (2014)

---

* This work was supported by the Alliance Program of the Helmholtz Association (HA216/EMMI).

DOI:10.15120/GR-2015-1-APPA-MML-PP-07

Ti-wire isochorically heated by intense short pulse laser*

A. Schoenlein[1], *S. Pikuz*[4], *A. Franz*[1], *J. Jacoby*[1], *O. Rosmej*[1,2], *D. Khaghani*[3], *P. Neumayer*[3], *L. Antonelli*[5], *G. Boutoux*[5], *D. Batani*[5], *J.J. Santos*[5], *and A. Sauterey*[5]

[1]Goethe University, Frankfurt, Germany; [2]GSI, Darmstadt, Germany; [3]EMMI, Darmstadt, Germany; [4]JIHT, Moskau, Russia; [5]University of Bordeaux I, France

For the characterization and the investigation of the behavior of warm dense matter, that will be generated at FAIR, it is necessary, to find diagnostics suitable for these tasks and able to operate under extreme conditions. Already, small samples of WDM, with dimension of a few micrometer, can be generated by using intense short pulse lasers like the PHELIX-facility at GSI.

To generate WDM, high energy densities respectively high pressures ($>1\,Mbar$) are required. During the interaction between an intense short pulse laser and matter, a part of the energy is transferred to electrons. These electrons are accelerated to energies above a few MeV by the ponderomotiv force of the laser field [1, 2].

The experiment was carried out in the laserbay of the PHELIX-laser facility. The experimental setup consisted of Ti-wires with a diameter of $50\,\mu m$ and a length of $2\text{-}3\,mm$. The PHELIX-laser (E_L=$120\,J$, t_p=$500\,fs$, λ=$1064\,nm$) was focused to the tip of the wires with a focal spot size down to $6\,\mu m$, leading to intensities of I_L=$10^{21}\,W/cm^2$ with a ns-contrast up to 10^{-10}. The electrons, accelerated during interaction between laser and wire, penetrate the wire and deposit energy therein, heating the wire up to the plasma state by collisions. Because of their high kinetic energies, the electrones are propagating into the matter with nearly the speed of light. This leads to a heating process that is faster then the expansion of the wire, resulting in an isochoric heating [3].

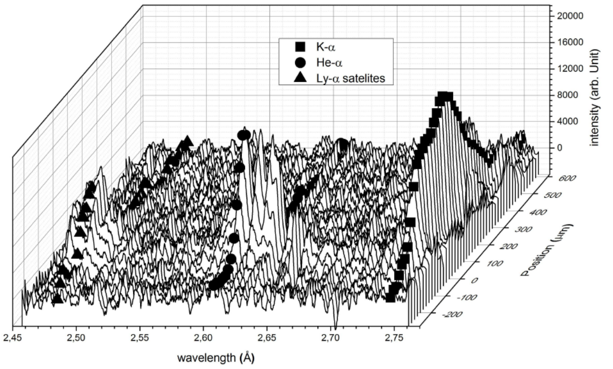

Figure 1: characteristic x-ray spectra along wire axis

While penetrating the wire, the hot electron component ionize the Ti atoms through K-shell ionisation. As a result, characteristic x-rays are emitted. Outer shell electrons are ionised with high efficiency by electrons with bulk temperatures at tens of eV. The energy of inner shell transitions depends on the effective nuclear charge and thus on the charge state of the ions. This leads to a superposition of Kα transitions from Ti^{+1} up to Ti^{+11}. The characteristic x-rays were measured spatially resolved along the wire axis (fig. 1) with a focusing spectrometer with spatial resolution (FSSR), that consists of a spherical bend crystal as dispersive element and x-ray film as detector. With the FSSR spectrometer high spectral ($\lambda/\Delta\lambda$=$3 \cdot 10^3$) and spatial resolution ($50\,\mu m$) can be achieved.

The laser can only penetrate the underdense region of the target. It is mostly absorbed at the critical density of the expanding plasma. At this point, the target is heated to temperatures of a keV, resulting in emission of He-α and Ly-α. The overdense region can only be penetrated by the accelerated particles and is heated to moderate temperatures where a broadened Kα-line is observed (fig.1). The Kα broadening can be calculated by a superposition of emission lines of ionised Ti bulk atoms, weighted by the charge state distribution related to a specific bulk temperature (fig. 2).

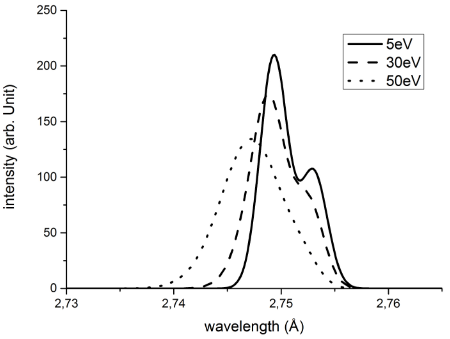

Figure 2: broadening of the Kα-line for different bulk temperatures

It is shown, that WDM can be generated by isochoric heating with hot electrons. Analysis of characteristic x-rays with FSSR provides possibility to distinguish between direct and particle heated areas and allows a spatial resolved temperature diagnostic which helps to investigate the collisional heating process.

References

[1] S. C. Wilks et al., Phys. Rev. Lett **Vol. 69**, Nr. 9, (1992)

[2] A. J. Kemp and L. Divol, Phys. Rev. Lett **109**, 195005 (2012)

[3] Hochhaus et. al., PHYSICS OF PLASMAS **20**, 062703 (2013)

---

* Work supported by HGS-Hire, HIC for FAIR and EMMI

DOI:10.15120/GR-2015-1-APPA-MML-PP-08

Magnetic reconnection in high energy density plasmas *

R. Riquier[1], *R. Smets*[2], *D. Khaghani*[3], *D. P. Higginson*[1], *G. Revet*[1], *and J. Fuchs*[1]
[1]LULI, École Polytechnique, CNRS, CEA, UPMC, 91128 Palaiseau, France; [2]LPP, École Polytechnique, CNRS, UPMC, 91128 Palaiseau, France; [3]GSI, Darmstadt, Germany

Context

Magnetic reconnection is a long standing problem in astrophysics (and more specifically in the Earth magnetosphere), characterized by a β parameter (ratio of kinetic pressure to magnetic pressure) around unity and a large Lundquist number (ratio of Alfven time to resistive time). In HED plasmas, such as those generated by the interaction of an intense laser beam with a solid target, the β parameter is at least about several hundreds, and the Lundquist number is as small as a few hundreds. Despite these large discrepancies, reconnection occurs in HED and astrophysical plasmas in a similar manner, as observed in numerical simulations. Laboratory experiments provide a valuable way to investigate reconnection mechanisms, but experimental studies have been limited in the past, because large and expensive plasma machines (as the MRX machine) were needed. HED laser experiments offer however smaller and affordable setups. [1]

During the irradiation of a solid target by a nanosecond laser pulse, a MegaGauss magnetic field loop is self generated by non-colinear gradients of density and temperature, around the plasma bubble. This magnetic field loop then increases in size with the expanding plasma. Thus in the case of two close-by laser irradiation spots, as illustrated on Fig.1 the magnetic field of each spot will be pushed toward each other. This will lead to compressed anti-parallel field lines and then trigger a reconnection process, converting magnetic energy into kinetic energy.

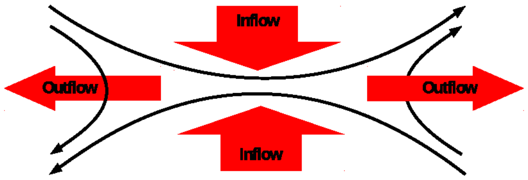

Figure 1: Scheme of the reconnection process.

Setup

We performed an experiment on the PHELIX laser facility in the femtosecond - nanosecond configuration (Exp. P088). The two beams entered the chamber on top of each other. The 50 J, 2 ns pulse at the bottom was separated in two using a 50 % beamsplitter and then focused using $f = 300$ mm lenses on a 23 μm thick Mylar target, driving the plasmas with their fields. The use of random phase plates gave us third order super-gaussians focal spot, with 120 μm Full Width at Half Maximum (FWHM). The 50 J, 500 fs beam was focused on a secondary target (10 μm thick gold) to produce an energy broadband proton beam through the TNSA mechanism. This proton beam probed the main target by the rear and a stack of Radiochromic Films recorded the proton dose modulations due to the deflection of the protons in the magnetic field.

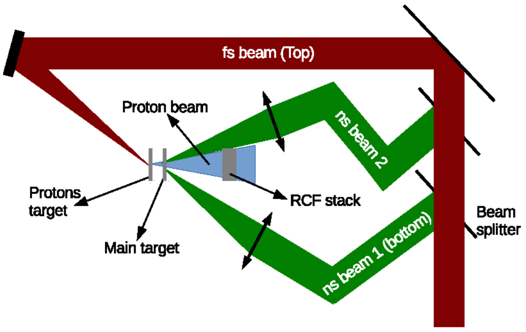

Figure 2: Setup of the experiment.

Preliminary results

In order to look a the dynamic of the system, we changed the delay between the ns and fs laser beams. Fig. 3 shows the results of the proton radiography for different delay (t_0 being the foot of the laser pulse rising slope). These results are presently being analyzed with the help of 3D numerical simulations performed using the code HECKLE [2].

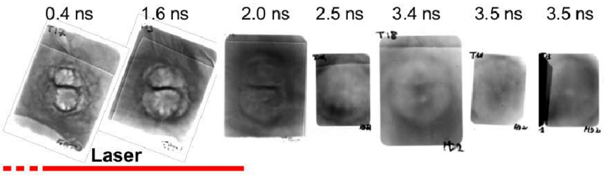

Figure 3: results of the proton radiagraphy.

References

[1] P. M. Nilson et al., PRL 97, 255001 (2006).
[2] R. Smets, N. Aunai, G. Belmont, C. Boniface, and J. Fuchs, Phys. Plasmas 21, 062111 (2014).

---

* support from Laserlab-Europe (EU-FP7 284464)

DOI:10.15120/GR-2015-1-APPA-MML-PP-09

Ion energy loss in plasma beyond the linear interaction regime

W. Cayzac[1], *A. Ortner*[2], *V. Bagnoud*[3,4], *M.M. Basko*[5], *S. Bedacht*[2], *A. Blažević*[3,4], *S. Busold*[3,4], *O. Deppert*[2], *M. Ehret*[2], *S. Faik*[10], *A. Frank*[4], *D.O. Gericke*[6], *L. Hallo*[7], *J. Helfrich*[2], *E. Kjartansson*[2], *A. Knetsch*[8], *D. Kraus*[9], *G. Malka*[1], *K. Pepitone*[7], *T. Rienecker*[10], *G. Schaumann*[2], *D. Schumacher*[3], *An. Tauschwitz*[10], *J. Vorberger*[12], *F. Wagner*[2], *and M. Roth*[2]

[1]Univ. Bordeaux-CEA-CNRS CELIA UMR 5107; [2]Technical University of Darmstadt; [3]GSI; [4]Helmholtz institute Jena; [5]KIAM Moscow; [6]University of Warwick; [7]CEA/CESTA; [8]University of Hamburg & CFEL; [9]University of California; [10]University of Frankfurt; [11]HIC for FAIR; [12]MPI for physics of complex systems

The ion-stopping experiments U281 and U282, as continuations of U274, were performed at the Z6 area of GSI where the UNILAC and PHELIX facilities are available for combined experiments. In this way, two unexplored regimes of heavy ion-plasma interaction, both relevant for Inertial Confinement Fusion (ICF), have been investigated.

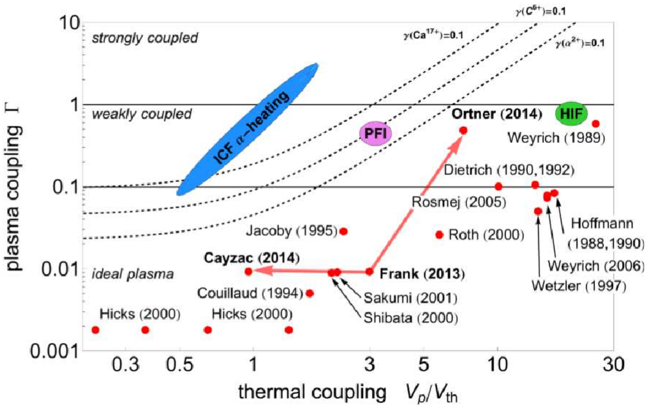

Figure 1: Overview of reported ion energy-loss experiments in plasma as a function of the velocity ratio $\frac{v_p}{v_{th}}$ and the plasma nonideality parameter Γ.

As illustrated in Fig.1, until now most experiments have been performed with projectile velocities much larger than the thermal velocity of the plasma electrons, i.e for $v_p \gg v_{th}$ and in ideal plasmas with the plasma coupling parameter $\Gamma \ll 1$. This so-called linear beam-plasma interaction regime is now well-understood and characterized.

Both described experiments deviate from that linear case. In the first experiment, in the wake of Ref.[1], measurements were performed at the stopping-power maximum in a hot and fully ionized plasma. It corresponds to low-velocity stopping with $v_p \approx v_{th}$. The plasma is ideal but the nonlinearity is important. There, the theoretical stopping-power predictions exhibit large discrepancies and no conclusive experimental data exist. A test of the theories would be highly relevant for alpha-particle stopping in ICF [2].

In the second experiment, following Ref.[3], the energy loss was measured at a higher projectile velocity $v_p \approx 10\, v_{th}$ but in a cold and partially ionized plasma, which is nonideal with $\Gamma \approx 0.5$. This case is highly relevant for heavy-ion fusion (HIF) and proton fast ignition (PFI) in ICF, where the stopping is also incompletely understood.

In the experiment at the stopping maximum, the energy loss of nitrogen ions was measured at a projectile energy of 0.5 MeV/u in a 150–200 eV hot and fully ionized carbon plasma generated with two high-energy laser beams. The experimental setup was optimized in comparison with Ref.[1] by the implementation of an improved random phase plate (RPP) and better-controlled plasma conditions. A preliminary analysis shows energy-loss data significantly below the theoretical predictions, which confirms the results of Ref.[1]. For the interpretation, a more precise calculation of the projectile charge state has been made possible by using cross-section data from non-equilibrium charge-distribution measurements of the beam after 2–40 μg/cm^2 thick carbon foils. Moreover, parametric studies of the plasma simulations pointed out the systematic calculation errors due to the necessary assumption that the plasma is in local thermodynamical equilibrium [2].

In the second experiment, the energy loss and the charge-state distribution of calcium ions at 3.6 MeV/u were measured in a weakly nonideal plasma induced by indirect laser heating [4]. For this purpose, intense laser light was converted in a sub-millimeter sized gold hohlraum into x-ray radiation which then volumetrically heated a carbon foil into a dense plasma state with a temperature of 5–15 eV and an ionization degree of 1.5–3. The data show an increase of the energy loss of 80% compared to the solid state, which is significantly higher than the theoretical predictions. In addition, the mean charge state shows no increase compared to solid carbon within the error bars, as expected from Monte-Carlo simulations [5].

This work has been carried out within the framework of BMBF and HIC4FAIR and of the EUROfusion Consortium and has received funding from the European Unions Horizon 2020 research and innovation program under grant agreement number 633053.

References

[1] W. Cayzac et al., GSI report (2013)

[2] W. Cayzac et al., in preparation

[3] A. Ortner et al., GSI report (2013)

[4] A. Ortner et al., Nucl. Instr. Meth. Phys. Res. B **343**, 123-131 (2015)

[5] A. Ortner et al., accepted for publication in Phys. Rev. E

DOI:10.15120/GR-2015-1-APPA-MML-PP-10

Characterizing the energy distribution and the propagation of laser-accelerated relativistic electrons in mass-limited Ti-wire target

G. Boutoux[5], *A. Schoenlein*[1], *L. Antonelli*[5], *D. Batani*[5], *A. Debayle*[6], *A. Franz*[1], *L. Giuffrida*[5], *J.J. Honrubia*[7], *J.Jacoby*[1], *D. Khagani*[3], *P. Neumayer*[3], *S. Pikuz*[4], *O. Rosmej*[1,2], *J.J. Santos*[5]
[1]Goethe University, Frankfurt, Germany; [2]GSI, Darmstadt, Germany; [3]EMMI, Darmstadt, Germany;
[4]JIHT RAS, Moskau, Russland; [5]CELIA, Université de Bordeaux, Bordeaux, France;
[6]CEA DAM DIF, Bruyères-le-Chatel, France; [7]ETSI Aeronauticos, UPM, Madrid, Spain

Characteristics and transport of relativistic electron beams (REB) generated in high-intensity short-pulse laser plasma interactions are of great interest for relativistic high energy density physics (HED) and applications such as fast electron heating for fast ignition (FI) laser fusion. To investigate warm dense matter (WDM) generated by relativistic laser-accelerated electrons, we studied the interaction of the PHELIX laser with a Ti-wire (experiment number P077). Our experimental setup is illustrated in Fig. 1. Free-standing mass-limited Ti-wires, with a diameter of 50 µm and a length of up to 3 mm, were used as targets. The PHELIX laser beam (E_L=120 J on target, t_P=500 fs, λ=1064 nm) was focused by an off-axis parabola to about 5 µm focal spot on a polished tip of the wire, leading to maximum intensities of I_L=10^{21} W/cm^2 with a ns-contrast up to 10^{-10}. Due to several acceleration mechanisms in the laser field, a flow of relativistic electrons is produced. When electrons propagate in matter, K-shell and Bremsstrahlung emission occurs, making the electrons propagation experimentally traceable. By using a focusing spectrometer with spatial resolution (FSSR) [1], we defined the wire depth where heating by x-rays and thermal electron conductivity can be excluded, and thus, in contrast to existing studies [2], only WDM-generation by hot electrons could be considered. Thereby we were able to measure the hot electrons penetration depth, as well as the warm dense matter (WDM) isochoric-heating deep into the target. In addition, a “Bremsstrahlung cannon” acted as a hard x-ray dosimeter [3] and was used to infer the internal hot electron energy distribution. At high-intensity and high-contrast conditions, we measured a hot electron tail of 2 MeV energies, in good agreement with our “Particle-in-cell” (PIC) simulations (PICLS [4]). By analyzing both broadening and shifting of characteristic K-shell lines in the FSSR, the WDM temperature T_e values along the wire were inferred, see Fig. 2. The maximum T_e achieved by isochoric heating was ~50 eV. On the other hand, the Kα intensity profile along the wire gives rather direct information on the relativistic electron propagation. It was surprisingly found to decrease exponentially up to ~1 mm deep, though a stopping range of 3 mm was expected in cold Ti. To further understand the physics at play, we performed hybrid PIC simulations [5] for the REB transport using a T=2 MeV exponential electron distribution as input. We used a simplified model for the possible reflexing of electrons inside the wire. Indeed, electrons spread in and out of the target dissipating their energy and creating an electric potential at the target surface. This potential is a barrier ϕ that electrons must overcome to escape from the wire. As illustrated in Fig. 2, the best results for reproduction of the T_e values (as well as the Kα profile, not shown here) along the wire were found by estimating <ϕ>~2 MeV. The electron flow description near the surface is a very challenging topic and our model should still be improved. Concerning electron stopping mechanisms in the WDM, the calculated resistive contributions are found to be three times higher than collisional effects. That is why the stopping power was found to be higher than in cold Ti where only collisional effects play a significant role. To conclude, our hybrid PIC simulations clearly demonstrate that both, electron confinement in the wire and competition between resistive and collisional stopping powers in the WDM are the key points to describe the REB transport in a mass-limited target.

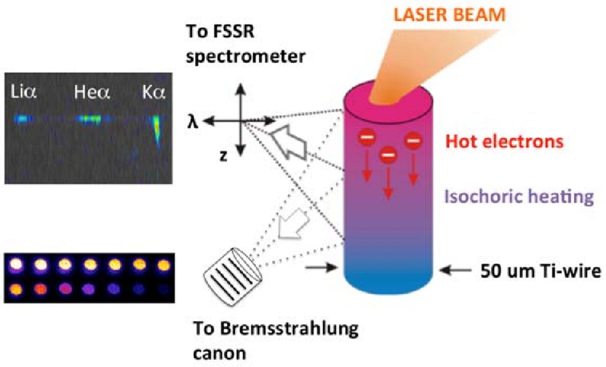

Figure 1: Schematics of our experimental set-up

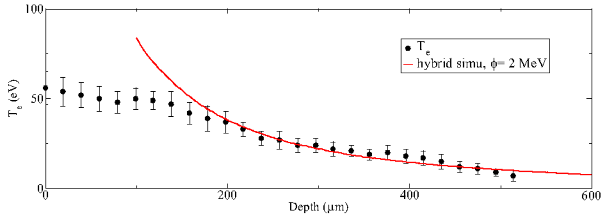

Figure 2: Temperature T_e profile vs. depth in the wire as measured for I=7.10^{20} W.cm^{-2} and 10^{-10} contrast shot. Hybrid PIC simulation with ϕ=2 MeV is also given.

References

[1] see A. Schoenlein et al., in this GSI-report.
[2] U. Zastrau et al., Phys Rev. E 81, 026406 (2010)
[3] C.D. Chen et al., Rev. Sci. Instr. 79, 10E305 (2008)
[4] Y. Sentoku et al., J. Comput. Phys. 227,6846 (2008)
[5] J.J. Honrubia et al., Phys. Plasma 12, 052708 (2005)

DOI:10.15120/GR-2015-1-APPA-MML-PP-11

Study of the effect of the lattice structure on the transport of MA fast electron currents at the PHELIX laser facility*

N.M.H Butler[1], *R.J. Dance*[1], *D.A Maclellan*[1], *R.J. Gray*[1], *D.R. Rusby*[1,2], *G.G Scott*[1,2], *B. Zielbauer*[3], *V. Bagnoud*[3], *D. Neely*[2], *and P. McKenna*[1]
[1]Department of Physics, SUPA, University of Strathclyde, Glasgow, G4 0NG, UK; [2]Central Laser Facility, STFC Rutherford Appleton Laboratory, Oxfordshire, OX11 0QX, UK; [3] GSI Helmholtzzentrum für Schwerionenforschung GmbH, 64291 Darmstadt, Germany

The electrical resistivity of a material in solid state is dependent on the electron mean free path, and thus the lattice structure of the material [1]. Due to the short duration of the laser-generated fast electron bunch (ps), compared to the lattice melt time (tens of ps), the same is true for a solid irradiated by an intense laser pulse. Here, the effects of the electrical resistivity on fast electron transport in solid targets for the cases of diamond and vitreous carbon are considered. Whilst the Z of each is the same, both materials possess significantly different resistivity-temperature profiles in the transient WDM temperature regime (1-100eV), as shown by Maclellan et al. 2013 [2].

For materials where the electrical resistivity is high, the growth rate of resistive magnetic fields within the target is greater, as described by equation (1) :

$$\frac{\partial \vec{B}}{\partial t} = \eta \nabla \times \vec{j}_f + \nabla \eta \times \vec{j}_f \qquad (1)$$

The growth of resistive magnetic fields acts to pinch the fast electron beam, contributing to perturbations in the beam profile by creating localised regions of pinching fields around variations in electron density in the beam [3]. Thus, the beam becomes filamented [4]. This results in a sheath field that is non uniform, and the resulting protons accelerated by the TNSA mechanism also exhibit a highly structured profile, from which the dynamics of the fast electron propagation in the target can be inferred [5, 6]. For materials where the electrical resistivity is lower, the growth rate of instabilities is reduced and, as such, similar structure is not induced in the beam.

In our recent experiment at the PHELIX laser facility, we studied the effects of material lattice structure of carbon allotropes on the resulting electron transport at high laser intensities. We further investigated the effects of laser parameters such as pulse duration and delivered energy on the observed proton spatial profile. The PHELIX laser delivered 200 J of energy to the front surface of the solid targets in approximately 500fs (full width at half maximum, FWHM) duration pulses, resulting in peak intensities of $1 \times 10^{21} W/cm^2$. The spatial intensity profile of the proton beam accelerated from the rear surface was measured by a stack of radiochromic film (RCF) placed 5cm from the target rear surface. Example results from this investigation are shown in figure 1.

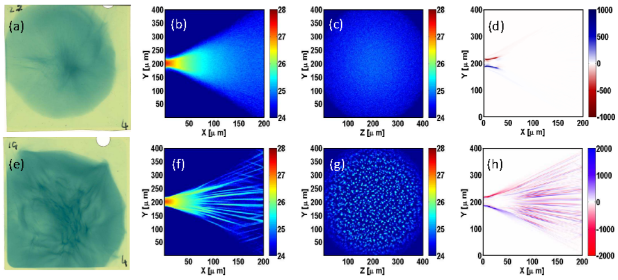

Figure 1: Experimental and simulation results for (top row) diamond and (bottom row) vitreous carbon showing: from L to R, proton spatial dose distributions, $\log_{10}$ fast electron density maps (m^{-3}), in the [X-Y] mid-plane, $\log_{10}$ fast electron density maps (m^{-3}), in the [Y-Z] rear-surface plane, and [X-Y] mid-plane maps of the magnetic flux density (B_z component in Tesla)

The results indicate that when an ordered material is considered, the onset of resistive instabilities inside the target is reduced and fewer instabilities are seeded in the fast electron beam, with a relatively smooth rear surface electron beam profile. In the opposite case of a disordered lattice, structure was seen, implying that growth of instabilities is enhanced with increased resistivity in the transient WDM temperature regime, and that these are a key influence on the onset of resistive instabilities in fast electron beam transport within the target. The RCF images of the proton beam show the obtained experimental results which qualitatively agree with the simulation results. Additional investigations are currently ongoing in order to further characterise the influence of low-temperature resistivity on the propagation of fast electrons.

References

[1] P. McKenna et al, Phys. Rev. Lett 106, 185004 (2011)
[2] D.A. Maclellan et al, Phys. Rev. Lett 111, 095001 (2013)
[3] D.A. Maclellan et al, Phys. Rev. Lett 113, 185001 (2014)
[4] L. Gremillet, G. Bonnaud, and F. Amiranoff, Phys. Plasmas 9, 941 (2002)
[5] S.C. Wilks et al, Phys. Plasmas 8, 542-549 (2001)
[6] D.A. Maclellan et al, Laser Part. Beams 31, 475 (2013)

---

[*] Work supported by EPSRC (Grants No. EP/J003832/1, No. EP/L001357/1, and No. EP/K022415/1), LASERLAB-EUROPE (Grant No. 284464). We acknowledge the support and contribution of the staff at the PHELIX laser facility.

DOI:10.15120/GR-2015-1-APPA-MML-PP-12

New laser energy deposition algorithm for the RALEF-2D code*

S. Faik[1], *An. Tauschwitz*[1], *J. A. Maruhn*[1], *and M. M. Basko*[2]
[1]Goethe University, Frankfurt am Main, Germany; [2]KIAM, Moscow, Russia

Correct modeling of the laser beam evolution and power deposition on unstructured grids is a computationally and numerically challenging task. The first goal for a new algorithm for the radiation-hydrodynamics code RALEF-2D [1] is the calculation of the refracted laser light distribution with minimal numerical diffusion. Therefore a long characteristics approach is applied. The incoming laser beam intensity is spatially discretized into single rays being traced through the computational grid. On the basis of the eikonal equation in geometrical optics [2] the equation of motion of a ray [3] in the undercritical regime, $n_e \ll n_c$, becomes $d^2\vec{x}/dt^2 = -(c^2/2)(\vec{\nabla} n_e/n_c)$. Continuous transitions of the ray trajectories up to the first spatial derivative between the numerical cells are guaranteed by the division of the original two-dimensional quadrilateral grid into triangles. Within each triangle the free electron density $n_e(\vec{x})$ then is uniquely defined piecewise linear by the vertex-centered values n_e and the gradients $\vec{\nabla} n_e$. Inside each triangle a ray with incoming power P_0 deposits the power $P_{dep} = P_0\,(1 - e^{-\kappa})$ given the optical depth $\kappa = \Delta s\ \mathrm{Im}\,(\sigma)$. Here Δs is the length of the ray segment, $\Delta s = \int_0^{\Delta t} c\ \sqrt{1 - n_e\left[\vec{x}\,(t)\right]/n_c}\ dt$, Δt the corresponding transition time, and σ the complex refractive index (per unit length) of the associated quadrilateral cell calculated by Kramers' inverse bremsstrahlung formula.

Figure 1 shows the mesh setup and two simulated ray trajectories for a quadratic density trough test case [3]. With the density profile $n_e(y) = (2n_c/l_y^2)(y^2 - l_y y + l_y^2/2)$, the mesh heigth $l_y = 100$ mm, the temperature dependence $T(y) \propto (n_e(y)/n_c)^{2/3}$, and a fixed Coloumb logarithm and ionization, analytical solutions for the cosine-shaped trajectories and their optical depth exist. The dimensionless trajectory error ϵ_T at the mesh exit point and the relative error ϵ_P in the summed-up deposited powers as functions of the number of quadrilateral cells in the y-direction N_y for a quarter cosine-wavelength are shown in Figure 2.

The second goal for the new algorithm is the calculation of the deposited and reflected powers and the angular distribution of the reflected laser light close to and above the critical free electron density ($n_e \gtrsim n_c$), e.g. at the surface of a solid metal. Therefore the raytracing algorithm is augmented by an one-dimensional wave optics solver for the wave propagation and energy deposition in a stratified medium [2]. A geometrical optics ray can split up into an "overcritical" wave optics ray propagating perpendicular to the critical surface and a reflected geometrical optics ray. Further test simulations will be conducted soon.

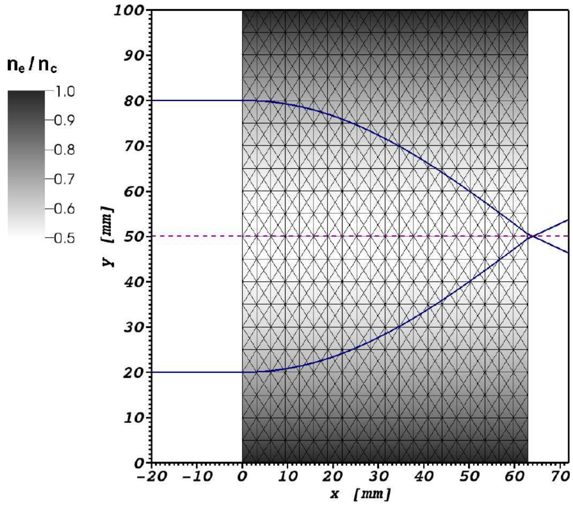

Figure 1: Mesh setup and two simulated ray trajectories for a quadratic density trough test case [3] with mesh heigth $l_y = 100$ mm. Trajectory entry points: $y_a = 20, 80$ mm; analytical trajectory exit point: $y_e^{an} = 50$ mm.

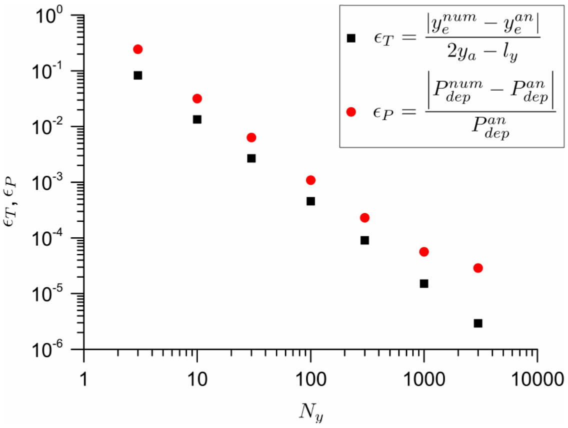

Figure 2: Dimensionless trajectory error ϵ_T at the mesh exit point and relative error ϵ_P in the summed-up deposited powers as functions of the number of quadrilateral cells in the y-direction N_y for a quarter cosine-wavelength.

References

[1] M. M. Basko et al., GSI Report 2010-1 410.

[2] M. Born, E. Wolf, "Principles of Optics", 7th Ed., 2005.

[3] T. B. Kaiser, Phys. Rev. E 61 (2000) 895.

---

* Work supported by BMBF (Project 05P12RFFTR), HIC for FAIR

DOI:10.15120/GR-2015-1-APPA-MML-PP-13

Hydrodynamic simulations of ion-beam heated foils for opacity measurements at FAIR*

M. Schmidt[1], *S. Faik*[1], *An. Tauschwitz*[1], *and J. A. Maruhn*[1]
[1]ITP, Goethe-Universität, Frankfurt am Main

Opacity measurements in ion-beam heated warm dense matter (WDM) will provide a valuable benchmark for the diverging theoretical models and clarify the influence of strong plasma coupling on the absorption coefficient in this regime. Intense ion beams shooting on a thin high-Z foil can be used to create a nearly isothermal sample of WDM, which is needed for frequency-dependent opacity measurements [1]. For this application the influence of a metastable (MS-) compared to an equilibrium equation of state (EQ-EOS) on dynamics of matter passing through the liquid-vapor two-phase region was analyzed.

The simulations were done with the RALEF-2D code [2] using Bismuth as the target material. For generating the MS- and EQ-EOS the FEOS code [3] was used with soft-sphere parameters $\mathrm{m} = 0.8$ and $\mathrm{n} = 3.35$. Following the considerations of Ref. [1] the thickness of the foil was chosen to be $0.3\,\mu\mathrm{m}$ assuming specific energy depositions $\varepsilon_{dep} = 6$, 8 and 10 kJ/g within a 100 ns pulse as expected for the "day one" experiments at FAIR. The simulations were performed in 1D with 100 Lagrangian cells, where in Fig. 1 cell 4 refers to one at the border and cell 50 to one in the middle of the foil. Comparing MS- and EQ-EOS phase trajectories for $\varepsilon_{dep} = 10$ kJ/g on the specific volume-pressure $(v - p)$ plane in Fig. 1 a different behaviour in the two-phase region is visible. Nevertheless after leaving the two-phase region the phase trajectories of the MS case approach the corresponding EQ case trajectories and are nearly identical at $t \geq 52\,\mathrm{ns}$. The simulations show that in case of $\varepsilon_{dep} = 10$ kJ/g after $t = 52\,\mathrm{ns}$ and in case of $\varepsilon_{dep} = 8$ kJ/g after $t = 60\,\mathrm{ns}$ the center of the foil is heated to a temperature $T = 1\,\mathrm{eV}$. This results in a plasma coupling parameter of $\Gamma \approx 1.1$ corresponding to a mean ion charge of $Z \approx 0.9$. In the case of $\varepsilon_{dep} = 6$ kJ/g the temperature of 0.9 eV is reached after the 100 ns pulse. The density and temperature profiles for the $\varepsilon_{dep} = 10$ kJ/g beam after 52 ns can be seen in Fig. 2. As it was expected from Ref. [4] where isothermal expansion of an ideal gas is treated analytically, the density profile is Gaussian-like. The simulation of the metastable branch of the EOS through the unstable spinodal region, as can be seen in Fig. 1, is technically feasible, due to the fact that the region where $c_s^2 \leq 0$ (gray shaded) is not being crossed by the phase trajectory of any cell of the MS calculation for energy depositions higher than 2 kJ/g. Hence, a special treatment of the liquid-vapor two-phase region as proposed in [3] is nonessential in the considered cases for the correct prediction of plasma parameters at $T \approx 1$ eV.

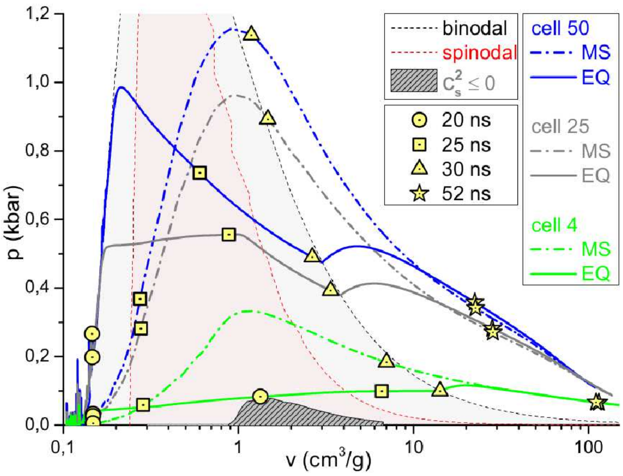

Figure 1: Phase trajectories in the $(v - p)$ plane for $\varepsilon_{dep} = 10$ kJ/g of three selected Langrangian cells with EQ- and MS-EOS.

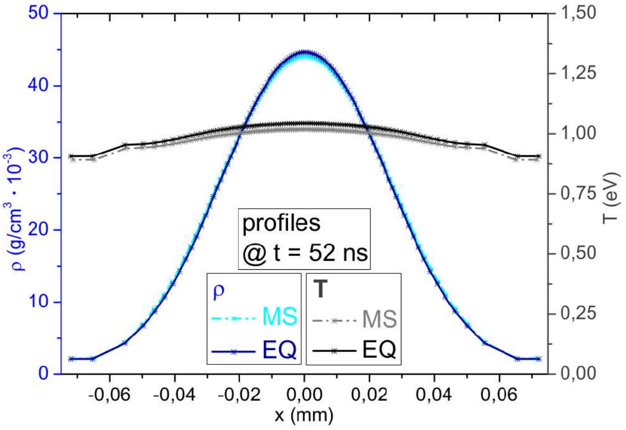

Figure 2: Density ρ and temperature T profiles for $\varepsilon_{dep} = 10$ kJ/g at $t = 52$ ns for EQ and MS branch.

References

[1] An. Tauschwitz et al., Appl Phys B **95** (2009) p. 13.

[2] M.M. Basko et al., GSI Report 2010-1, p. 410.

[3] S. Faik et al., High Energy Density Physics **8** (2012) p. 349.

[4] R.A. London et al., Phys of Fluids **29** (1986) p. 3813

---

* Work supported by BMBF (Project 05P12RFFTR)

DOI:10.15120/GR-2015-1-APPA-MML-PP-14

Simulations of the full impact of the 40 TeV FCC proton beam with solid copper cylindrical target and the problem of hydrodynamic tunneling*

N.A. Tahir[1], *F. Burkart*[2], *R. Schmidt*[2], *A. Shutov*[3], *D. Wollmann*[2], *and A.R. Piriz*[4]
[1]GSI, Darmstadt, Germany; [2]CERN, Geneva, Switzerland; [3]IPCP, Chernogolovka, Russia; [4]UCLM, Ciudad Real, Spain

After the great and unprecedented success of the LHC, CERN is now discussing the possibility of building a new, much more powerful accelerator named the Future Circular Collider (FCC). Table 1 gives the parameters of these two giant machines. To estimate the damage caused by an uncontrolled release of the beam energy, extensive simulations of the full impact of one FCC beam on a solid Cu cylinder with radius 2 cm and length 5 m, are being carried out. The beam is incident perpendicular to the cylinder face, along the axis. These simulations are being done applying the energy deposition code FLUKA and the 2D hydrodynamic code BIG2, iteratively, using an iteration step of 25 ns. In Fig. 1, is presented the energy deposition distribution in the Cu target calculated by FLUKA using solid density. It is seen that the maximum energy deposition per proton is about 920 GeV/g which means that one FCC bunch will deposit 9.2 kJ/g specific energy in the target. This data is used as input to a 2D hydrodynamic code BIG2, to simulate the thermodynamic and the hydrodynamic response of the target. The BIG2 calculations are stopped at t = 25 ns, and the modified density distribution provided by the BIG2 code is used in the FLUKA code for the next iteration. So far we have advanced the calculations up to 250 ns which corresponds to the delivery of 10 FCC bunches.

Table 1: Comparison of LHC and FCC beam parameters

Parameters	**LHC**	**FCC**
Proton Energy	7 TeV	40 TeV
Bunch Intensity	1.15x10^{11}	10^{11}
Number of Bunches Per Beam	2808	8424
Bunch Length	0.5 ns	0.5 ns
Bunch Separation	25 ns	25 ns
Energy Per Beam	362 MJ	5390 MJ
Accelerator Tunnel Circumference	28 km	80 km

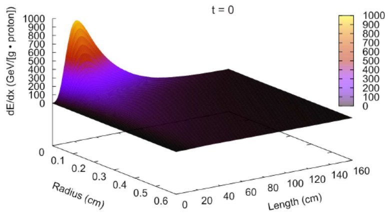

Figure 1: Energy deposition distribution in solid Cu target calculated by FLUKA.

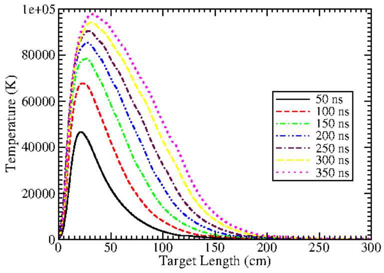

Figure 2: Temperature along target axis at different times.

In Fig. 2 we plot temperature along the target axis at different times during the irradiation. It is seen that at t = 250 ns, which is the time when 10 bunches have been delivered, the maximum temperature is around 90000 K. The extension of the heated zone with time along the longitudinal direction due to the hydrodynamic tunneling is also clearly visible. The corresponding density profiles are plotted in Fig. 3 that show substantial density depletion along the target axis due to the hydrodynamic effects. It is predicted that the FCC protons and their hadronic shower can penetrate up to 100 m in solid copper due to the hydrodynamic tunneling. However a precise answer to this problem can only be provided when this work is completed.

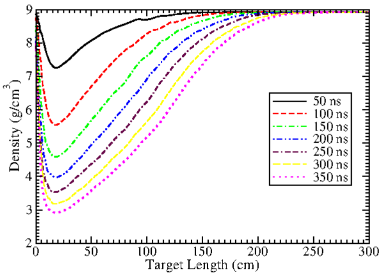

Figure 3: Density along target axis at different times.

---

* Work supported by the BMBF and EuCARD2

DOI:10.15120/GR-2015-1-APPA-MML-PP-15

Beam transmission for inductively coupled plasma stripper*

G. Xu[1,2,3], *J. Jacoby*[1], *Y. Zhao*[2], *G. Xiao*[2], *G. Loisch*[1], *T. Rienecker*[1], *A. Fedjuschenko*[1], *K. Cistakov*[1], *A. Blazevic*[4], *K. Weyrich*[4], *O. Rosmej*[4], *R. Cheng*[2], *J. Ren*[2,3], *A. Schönlein*[1], *J. Wiechula*[1], *T. Manegold*[1], *A. Kutschireiter*[1], *S. Zähter*[1], *R. Maeder*[1], *O. Haas*[5], *and M. Iberler*[1]

[1]Goethe University of Frankfurt, Frankfurt am Main, Germany; [2]IMP, Lanzhou, China; [3]UCAS, Beijing, China; [4]GSI, Darmstadt, Germany; [5]TU-Darmstadt, Darmstadt, Germany

Introduction

Currently for all over the world, the beam stripping methods for accelerators are mainly gas stripping and foil stripping devices. The former's stripping ability does not reach sufficiently high charge states while the latter has the difficulty with long lifetime. However, the plasma stripping method can solve both problems very well. As a consequence, this novel stripper is proposed for the project FAIR (Facility for Antiproton and Ion Research).

Initially, our plasma stripper was realized as the theta pinch which is inductively pulsed device [1, 2, 3, 4, 5]. Differing from the z-pinch, it has no problem with the electrodes erosion which reduces the device lifetime. This theta pinch installed with a differential pumping system was integrated into the accelerator for the beam-plasma interaction experiment on Oct. 2012. The results show a poor beam transmission [6]. To overcome this issue, the theta-pinch device was modified. Meanwhile, another kind of inductively pulsed device named ”screw pinch” is developed as an alternative. In this paper, we will describe the beam transmission for this ”screw-pinch” device.

Experiment

The ”screw pinch” additional owns a z-direction current besides the theta direction which is described well in [4, 5]. This design results in a complicated magnetic field. Hard plastic supports fix coils to reduce their movement during discharge. The differential pumping system also has been improved.

A pulsed beam of Au^{26+} with the energy of 3.6 MeV/u was available for our experiment at Z6, GSI. Considering the discharge time of our ”screw pinch”, a beam pulse duration of about 1 ms is applied to cover the cold gas and discharge states. As a benchmark for beam transmission, the detected beam signal after the cold gas with the same initial pressure is applied. Here, we both use pure hydrogen of 40 Pa for the cold gas case and discharge case. The total capacitance is 25 μF while the operation voltage for discharging is 18 kV.

Results

The beam transmissions both for cold gas and discharge conditions are shown in Fig. 1. The black line below gives the benchmark beam signal. The above red line presents the values for the subsequent shot when the target has the discharge condition which starts at about 402 μs as shown on the oscilloscope. Different from the distinct discrete signal in [6], the beam signal represented by the red lines does not show this enormous discontinuity, big gaps in signals, after discharge. As the signal height after discharge are comparable to the benchmark one, the beam transmission for the ”screw pinch” as a plasma stripper is pretty good.

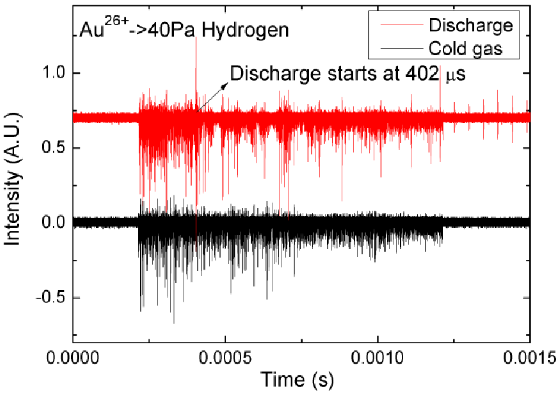

Figure 1: Comparison of beam signals with the cold gas and discharge conditions

References

[1] C. Teske and J. Jacoby, Plasma Science, IEEE Transactions on **36**, 1930 (2008).

[2] C. Teske, J. Jacoby, F. Senzel, and W. Schweizer, Physics of Plasmas (1994-present) **17**, 043501 (2010).

[3] C. Teske, Y. Liu, S. Blaes, and J. Jacoby, Physics of Plasmas **19**, 033505 (2012).

[4] G. Loisch *et al.*, in *Pulsed Power Conference (PPC), 2013 19th IEEE*, pp. 1–7, 2013.

[5] G. Loisch *et al.*, Plasma Science, IEEE Transactions on **42**, 1163 (2014).

[6] G. Xu, J. Jacoby and etc, GSI SCIENTIFIC REPORT 2012, PNI-IONS-EXP-37.

---

* This work is supported by the BMBF Contract No. 05P12RFRB8; The authors of Ge Xu, Andreas Fedjuschenko and Andreas Schönlein get the scholarships from HGS-HIRe for FAIR.

DOI:10.15120/GR-2015-1-APPA-MML-PP-16

Online monitoring of the Bragg peak during pig irradiation*

C. Schuy[1], *M. Rovituso*[1], *C. Graeff*[1], *and M. Durante*[1]
[1]GSI, Darmstadt, Germany

Overview and Experiment

With the increasing number of medical accelerator facilities available there is a growing interest to broaden the field of applications to non-cancer diseases and radiosurgery[1]. Atrial fibrillation is the most common form of cardiac arrhythmia and results in unorganized atrial activity which leads to an abnormal rhythm of the heart. The strain of catheter ablation as a standard treatment to the human body is quite severe due to long anesthetization and therefore radiosurgery is a promising treatment modality[2]. Recently first experiments where performed in pigs with doses ranging from 25 to 55 Gy[3]. The irradiation was observed online with a 6 plane CMOS-based particle tracker[4] monitoring prompt particle emission from the target volume[5] to verify the treatment.

Six MIMOSA-28 silicon pixel sensor where placed approximately 51 cm away from the target volume under an angle of bigger than 90 degree. Prompt particle tracks resulting from the nuclear fragmentation inside the irradiated tissue where recorded in order to verify the planned dose deposition. The tracking system worked stable during the complete measurement campaign and a total of seven pig-irradiation were monitored. A picture of the experimental setup is presented in fig.1. Sensor alignment was performed with primary carbon in a dedicated run in Cave A.

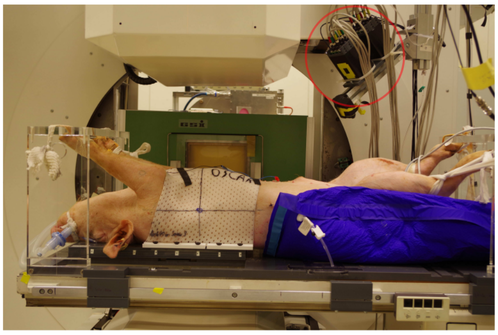

Figure 1: Picture of the experimental conditions in Cave M during irradiation. The tracker (red circle) was approximately 51 cm away from the target volume.

Status

The need for a special run in Cave A due to specific intensity requirements for the alignment of the used sensors poses a problem during data analysis. While removing and rebuilding the tracker in Cave A the relative position of some sensors changed slightly in respect to the holder (approximately 100 - 150 microns) which resulted in a non-optimal alignment of the tracker and lower than expected statistics of reconstructed charged particle tracks. Preliminary reconstructed data is presented in fig.2. The observed time structure of both monitoring systems is in good agreement, but the total number of reconstructed tracks at the moment is low. Currently different alignment procedures are tested to increase the tracking efficiency.

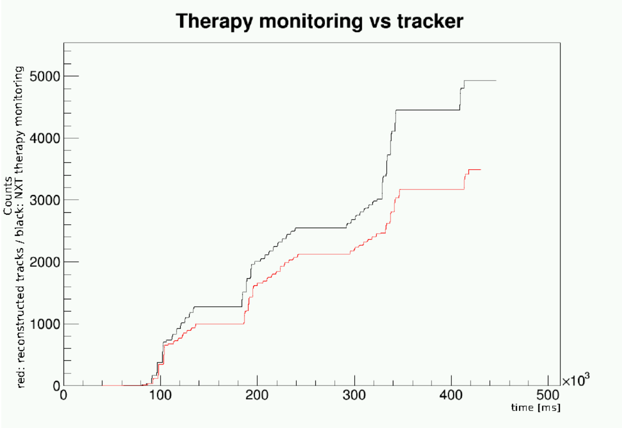

Figure 2: Comparison of the reconstructed tracks vs. time and the change of beam position (NXT) as monitored by the therapy control system.

References

[1] C. Bert, R. Engenhart-Cabillic and M. Durante, “Particle therapy for noncancer diseases”, Med. Phys. 39, 1716 (2012).

[2] A. Constantinescu, “Planning studies for non-invasive treatment of atrial fibrillation with scanned ion beams”, Phd-Thesis (2014).

[3] H. Immo Lehmann, C. Graeff, A. Constantinescu, et al., “Arrhythmia ablation using scanned carbon ion pencil beams in a porcine model: First outcomes from ^{12}C catheter-free ablation”, Abstract for Heart Rhythm Society (2015).

[4] M. Rovituso, C. La Tessa, C. Schuy and M.Durante, “Online Bragg peak monitoring for radiotherapy with ions using pixel sensors”, GSI SCIENTIFIC REPORT (2013).

[5] L. Piersanti, F. Bellini, F. Bini, et al., “Measurement of charged particle yields fromm PMMA irradiated by 220 MeV/u ^{12}C beam”, Phys. Med. Biol. 59 (2014).

---

[*] Work supported by GSI(SIS)

DOI:10.15120/GR-2015-1-APPA-HEALTH-01

Influence of ionizing radiation on early human brain development*

B. Müller[1], *S. Ritter*[2] *and S. Kadereit* [1,#]

[1] University of Applied Sciences Albstadt-Sigmaringen, Sigmaringen, Germany; [2] GSI, Darmstadt, Germany.

The development of the nervous system is extremely susceptible to perturbations. Only slight changes in the tightly orchestrated follow-up of developmental events can lead to dramatic malformations such as spina bifida, mental retardation, reduced IQ, impairment in hearing, autism, stuttering, attention deficits, deficits in affect, aggressiveness, depression and other neurologic diseases. Neurodevelopmental toxicants such as alcohol, mercury and lead have now been well established [1]. Less well established is the impact of low dose environmental pollutants. However, increasing evidence points to a direct correlation of low dose exposure during early development and impairment of neural development, and possibly neurodegenerative diseases [1, 2].

Animal models only insufficiently model human neurodevelopment. Outcome of developmental neurotoxicity (DNT) such as reduced IQ or stuttering are challenging to model in animal models. Embryonic stem cells (ESCs) have been shown to faithfully recapitulate neural development in vitro [3], and are as such ideal to model toxicity to the developing human nervous system.

We have developed a neurodevelopmental model based on human embryonic stem cells (hESCs) in which hESCs are differentiated in a 3-dimensional (3-D) neurosphere model (Fig 1).

This model has been characterized in depth. It recapitulates crucial stages of central nervous system development, and we could demonstrate DNT of methylmercury and of low dose, chronic exposure to chemically inert nanoparticles [4].

This system has now been transferred to the University of Applied Sciences of Albstadt-Sigmaringen and is used within a BMBF-funded project* to investigate the impact of sparsely ionizing X-rays and densely ionizing carbon ions on early human brain development. In parallel, we have established human induced pluripotent stem cells (hiPSCs) and are differentiating the cells in our neurodevelopmental system to assess whether we can detect differences in differentiation capabilities.

Preliminary data obtained for hESCs irradiated with carbon ions (25mm spread-out Bragg peak, LET=75 keV/µm) at GSI indicate that ionizing radiation has a detrimental impact on the ability of neuroepithelial cells to form neurospheres. Neurospheres were smaller and less abundant, indicating toxicity (Table 1). Gene expression was also changed for crucial neurodevelopmental markers.

Future experiments will focus on sparsely ionizing X-rays. Therefore, neural progenitor cells will be exposed to both acute and continues low-dose radiation. Changes in Gene expression will be assessed and electrical activity of neuronal cells will be measured. These experiments will allow elucidating the effects of ionizing radiation on early neural development in more detail and point towards possible impact of exposure during early human development.

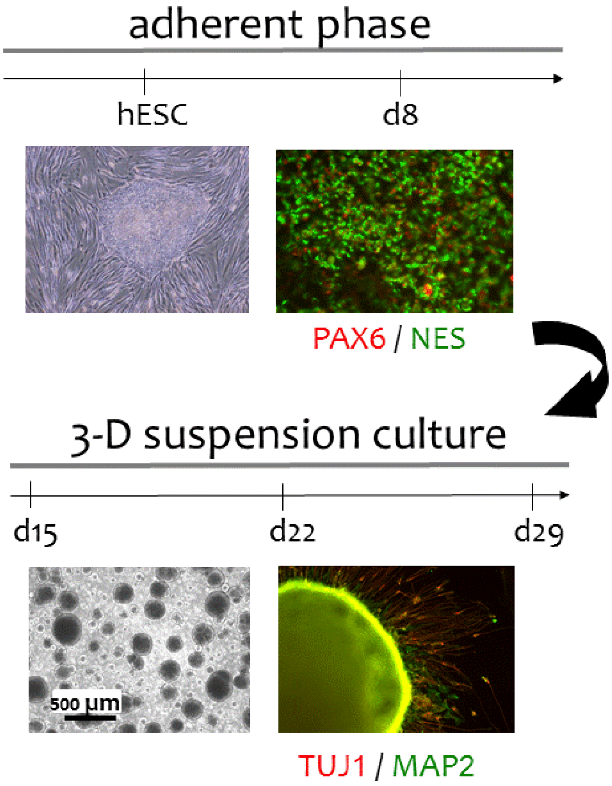

Figure 1: Neurodevelopmental model from hESCs. hESCs (first panel) were differentiated for 11 days in adherence to an almost pure population of PAX6$^+$ central nervous system precursor cells (second panel). On day 11 cells were transferred to suspension cultures where the cells form neurospheres (third panel) and differentiate further to mature neurons (right panel).

Dose	Mean diameter	Standard deviation	Range
0 Gray (n = 17)	413,9 nm	139,7 nm	181-642 nm
1 Gray (n = 23)	282,6 nm	96,8 nm	114-536 nm

Table 1: Reduced neurosphere size after irradiation with 1 Gy carbon ions.

References

[1] Grandjean and Landrigan, Lancet 368:2167 (2006)
[2] Barlow et al., Reprod Toxicol 23:457 (2008)
[3] Barberi et al. Nat Biotechnol 21:1200 (2003)
[4] Hoelting et al. Arch Toxicol 87:721 (2013)

---

* Work supported by BMBF grant 02NUK 025B
# kadereit@hs-albsig.de

DOI:10.15120/GR-2015-1-APPA-HEALTH-02

Catheter-free arrhythmia ablation using scanned carbon ion beams in a porcine model

C. Graeff[1]; H. I. Lehmann[2]; A. Constantinescu[1]; P. Simoniello[1]; P. Lugenbiel[3]; M. Prall[1]; D. Richter[1]; M. Takami[2]; A. Eichhorn[1]; N. Erbeldinger[1]; C. Fournier[1]; R. Kaderka[1]; S. Helmbrecht[4], F. Fiedler[4]; J. Debus[3]; D. Thomas[3]; C. Bert[1]; M. Durante[1] and D. L. Packer[2],

[1]GSI, Darmstadt, Germany; [2]Mayo Clinic/St. Marys Hospital, Rochester, MN, USA; [3]University of Heidelberg, Germany; [4]Helmholtz-Zentrum Dresden-Rossendorf, Germany

Introduction

Cardiac arrhythmias are a wide-spread disease associated with reduced quality of life, increased risks of stroke and sudden cardiac death. Catheter ablation and isolation of arrhythmogenic structures in the heart is the current standard treatment, but is invasive, complex, and shows varying effectiveness especially for progressive disease.

The most common form is atrial fibrillation (AF), a too fast and ineffective contraction of the atria. AF often originates from the pulmonary veins (PV) and can be cured by isolating the veins. For persistent AF, the ablation of the AV node can be a last resort to prevent the AF from affecting the ventricles.

The irregular scars caused by an infarct can lead to ventricular tachycardia (VT), which can cause sudden cardiac death. Homogenizing the scars can cure VT, but is difficult in the left ventricle, where the thick muscle tissue cannot be penetrated completely with catheter ablation.

In this study, scanned carbon ions were investigated as a non-invasive alternative to induce the required electrically isolating fibrosis in the myocardium.

Material and Methods

Eighteen pigs were randomized to irradiation of AV node (AVN), LA-PV junction (PVI), freewall LV, and sham-AVN. Prior to treatment, mapping of cardiac electrophysiology (EP), fiducial marker, and pacemaker implantation were performed at the University of Heidelberg. Cardiac 4DCT images were acquired both with and without contrast agent at HIT Heidelberg. Target and organs-at-risk (OAR) were contoured on the contrast enhanced CT, also used for deformable image registration. The resulting vector maps were transferred to the native 4DCT for treatment planning with GSI's TRiP4D.

PVI and LV were targeted using 40 Gy. AVN was targeted with 25, 40, and 55 Gy. For AVN and PVI, field-specific ITVs were calculated from the 4DCT after adding 5 mm isotropic margins. For LV, only range margins of 2 mm and 2% were used. Up to 15 rescans were applied to counter interplay.

Pigs were anesthetized, respirated, and positioned in a custom-built fixation. Both imaging and treatment were carried out under enforced breath-hold at end-exhale. All animals were irradiated using two opposing fields at GSI Cave M, monitored by online PET. In-room time was in the order of 1.5 to 3h, with most time used for positioning with orthogonal X-rays.

Animals were followed for up to 6 months with extensive analyses ongoing. Skin biopsies were taken before irradiation and in the final follow-up. Skin reaction was closely monitored for up to 12 weeks. Blood samples were collected before and after 4, 8, 12 and 24. The final follow-up included detailed electrophysiological mapping and macroscopic pathological examination.

Cardiac tissue obtained from the targeted area, and areas in the entrance channel of the beam, and out of the beam field, were fixed in 4% formaldehyde and processed for histological analysis or fixed on dry-ice for protein extraction. Control samples of the heart which were not irradiated were also taken.

Results

Analysis of PET images showed accurate targeting. 4D-dose reconstruction showed successful motion mitigation.

After 3 and 6 months, electrophysiological changes and scar formation were observed in the LV target regions. After 4 months, complete AV-block was detected in 40 and 55 Gy animals on surface ECG, persisting until study end in the 55 Gy animal. Lesion formation for PV isolation was almost completely achieved in one animal, leaving only a small gap detectable in EP mapping.

First histological analysis revealed fibrotic changes, i.e. the presence of fibroblasts instead of cardiomyocytes and proteins of the extracellular matrix in tissue 3 months after treatment. The sham control showed a well-organized structure of cardiomyocytes.

A total of 3 animals died from pacemaker infection, 2 further showed signs of infection during the follow-up, with one of those animals from the sham group No irradiation-induced side effects in organs at risk such as skin, oesophagus, aorta or trachea were observed.

Discussion

In conclusion, this study showed the feasibility of non-invasive arrhythmia ablation using scanned carbon ion beams. The ongoing evaluation of tissue samples, in the target and non-target area, will reveal the late effects and radiobiological mechanisms: cell death, inflammation, changed signal transmission, vascular damage, and fibrosis. Together with more detailed electrophysiological analysis this data will form an important foundation for future studies and eventual clinical application.

DOI:10.15120/GR-2015-1-APPA-HEALTH-03

Modelling dose distributions in cell nuclei after irradiation with ultrasoft X-rays

T. Buch[1,2], *E. Scifoni*[1], *M. Durante*[1,2], *M. Scholz*[1], *and T. Friedrich*[1]
[1]GSI, Darmstadt, Germany; [2]FKP, TU Darmstadt, Germany.

The Local Effect Model (LEM) is a mechanistic model to describe cell survival after ion irradiation. Its basic concept is that the biological effect mainly depends on the spatial dose distribution within a cell nucleus, hereby inducing double-strand breaks (DSB) within DNA substructures called chromatin loops.

By means of experimental data, it is known that ultrasoft X-rays (0.1 – 5 keV) show a higher biological effectiveness than high-energy photons. Similar to high-LET irradiation, this is attributed to a rather inhomogeneous dose distribution due to a considerably smaller range of secondary electrons and the higher significance of attenuation of the photons itself, which results in an increasing yield of DSB.

As an extension of LEM for ultrasoft X-rays, this increasing yield can be obtained if the dose distribution of ultrasoft X-rays is known. Employing the track structure simulation program *TRAX*, which is based on the Monte Carlo method, the dose distribution of ultrasoft X-rays can be examined.

Methods

The Monte Carlo based program *TRAX* was developed at GSI to simulate track structures and dose depositions of ion irradiation [1]. Interaction probabilities of various ions with different targets are hereby used for a step-by-step simulation. Since ultrasoft X-rays mainly deposit dose via photoelectric effect [2, 3], the simulation was done using electrons as projectile and water as the cellular target.

In a first attempt, the emission of the photoelectrons is assumed to be isotropic and simulations are done for energies between 200 eV and 4.5 keV, with the emphasis on lower energies up to 1.5 keV. To obtain sufficiently precise results, each simulation involved 10^4 runs. The data obtained by *TRAX* include the doses for different radii around the emission point of the photoelectron, therefore displaying a spherically symmetric dose distribution D(r).

For the analysis of the dose distribution there are two key quantities that need to be examined - the maximum range of the secondary electrons and the center dose at $r = 0$. Maximum ranges for different energies were obtained by simply taking the last data point on which the dose is not equal to zero. Center doses however were obtained by fitting a power line to data points of lower radii and taking the ordinate for $r = 0.1$ nm, since this represents the minimal radial data given out by *TRAX*.

Results and Discussion

The radial dose distributions show similar shapes for all energies. The energy dependence of the maximum range and the center dose are visualized in Fig. 1 and Fig. 2 respectively. It can be seen, that an increasing energy results in an overall more widespread dose distribution, since the increasing range of dose depositions is accompanied by lower dose depositions in the center.

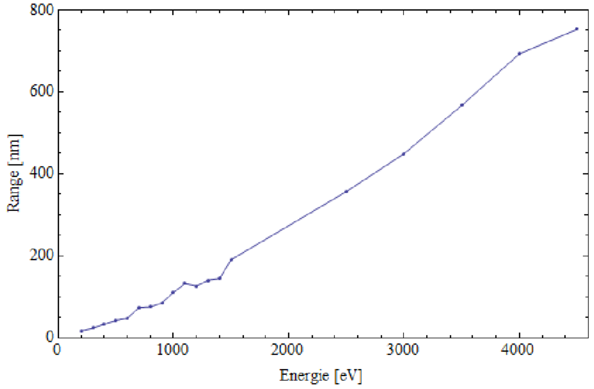

Figure 1: Maximum range over energy

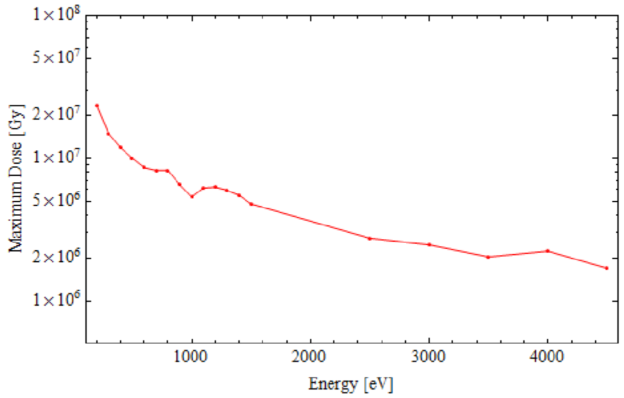

Figure 2: Center dose over energy

As a next step, and hereby presenting a first attempt on the basis of an amorphous track structure, an enhancement factor can be computed that describes the increasing yield of DSB for these distribution patterns due to clustering of single strand breaks on the DNA. Because of the overall broader dose distribution of higher energy photo electrons, it is expected to receive a decreasing enhancement, and therefore a decreasing biological effectiveness with increasing energy. Comparison with experimental data [2] promises to give an instructive insight into the importance of the inhomogeneity for the biological effectiveness of ultrasoft X-rays. Furthermore, since the track ends of ion irradiation also contain low energy photoelectrons, the results may additionally provide further insight into dose depositions induced by ion irradiation.

References

[1] Wälzlein C *et al.*, Phys. Med. Biol. **59** 1441 (2014)
[2] De Lara CM *et al.*, Radiat. Res. **155**, 440 (2001)
[3] Friedrich T *et al.*, Radiat. Res. **181**, 485 (2014)

DOI:10.15120/GR-2015-1-APPA-HEALTH-04

Detection of chromatin decondensation induced by charged particle irradiation using Fluorescence Lifetime Imaging Microscopy*

E. Abdollahi[1], *N. Özgün-Korkusuz*[1], *M. Durante*[1, 2], *G. Taucher-Scholz*[1, 2] *and B. Jakob*[1]

[1]GSI, Darmstadt, Germany; [2]Technical Universität Darmstadt, Darmstadt, Germany

Introduction

Advances in a variety of photonic imaging techniques and development of fluorescent proteins make Fluorescence Lifetime Imaging Microscopy (FLIM) a promising technique for quantitative biophysical measurements. The lifetime of excited electronic states are largely independent of the dye concentration and can provide insight into the local environment as well as dynamics of biological processes. Using widefield microscopy, we showed that ion irradiation induced a local decondensation of heterochromatin at the sites of ion hits in murine chromocenters, which is accompanied by a relocation of the induced double-strand breaks (DSB) to an adjacent euchromatin [1]. Here, to establish a chromatin compaction sensitive probe, we measured the lifetime of DNA binding dyes in ion irradiated and subsequently fixed mouse cells.

Materials and Methods

NIH-3T3 cells were cultured, irradiated and fixed as described in [2]. Irradiation was done using uranium ion (4.7 MeV/u, LET ≈ 15000 keV/µm). For immunofluorescence staining XRCC1 mouse monoclonal and Alexa Fluor 514 anti-mouse antibodies were used. A microscope (Olympus IX71; lens: 60x 1.2 NA water) coupled to a DCS-120 confocal scanner, picosecond diode lasers (405 nm, 445nm, 515 nm) and hybrid detectors (HPM-100-50) (all bh GmbH) were used to produce confocal FLIM images.

Results

The principle aim of the present study was to establish a FLIM setup by which radiation-induced chromatin decondensation in murine cells can be monitored. Up to now, attempts quantifying hetero-chromatic decondensation have been based solely on intensity information [1, 2]. The new FLIM approach considered intensity independent changes in the decay velocity of the excited states due to chromatin density dependent quenching in addition. To test our system, we irradiated NIH-3T3 cells with uranium ions and fixed them by 2% formaldehyde. The site of ion traversals within the chromocenter was determined by the aggregation of the damage marker XRCC1 (Figure 1, panel C). Different DNA dyes were screened. A promising probe is Hoechst 34580 as it shows a reduction of fluorescence intensity corresponding with an increase in lifetime at sites of heterochromatic ion traversal (Figure 1). The profile is calculated by radial angle integration on hit chromocenter indicated by blue crossed lines in Figure 1 panel A and B.

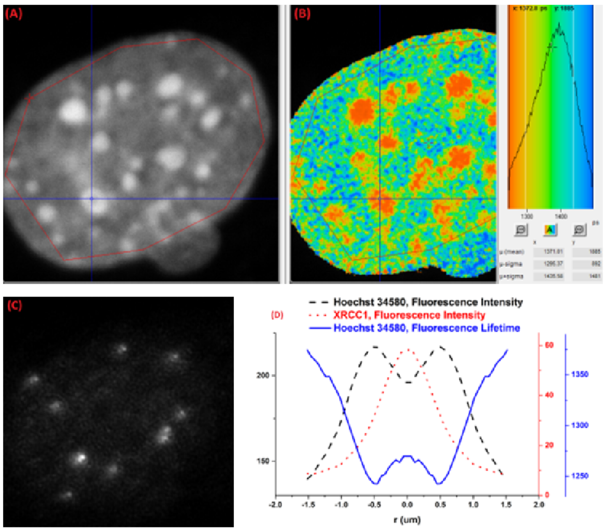

Figure 1: Confocal FLIM image of irradiated and fixed NIH-3T3 cells stained with 1 µM Hoechst 34580. Intensity and lifetime distribution of Hoechst 34580 images depict in panel (A) and (B). Panel (C) Alexa 514 bound to XRCC1 as indicator of ion hits. Panel (D) intensity and lifetime profiles representing depleted DNA staining (dash: intensity and solid: lifetime) at the damage site marked by XRCC1 (dot).

Conclusions

The results of this study indicate that the established FLIM setup is capable of monitoring radiation-induced chromatin decondensation in fixed murine cells. Since the DNA dye Hoechst 34580 reveals clear lifetime discrimination between condensed and non-condensed areas, it will be further characterized in order to use it for the measurement of real time kinetics of radiation-induced chromatin decondensation in living cells during irradiation at the beamline.

References

[1] B. Jakob et al., NAR, 39, (2011) 6489.
[2] I. Müller et al., Mutat Res. 756, (2013) 30.

---

* Work supported by DFG GRK 1657 & BMBF 02NUK037A

DOI:10.15120/GR-2015-1-APPA-HEALTH-05

Detection of radiation induced DNA damage using quantum dot coupled antibodies*

S. Tonnemacher[1,2], *G. Becker*[1], *M. Durante*[1,3], *G. Taucher-Scholz*[1,3] *and B. Jakob*[1]

[1]GSI, Darmstadt, Germany; [2]Goethe-Universität, Frankfurt, Germany; [3]TU Darmstadt, Darmstadt, Germany

Introduction

Resolution in light microscopy is generally limited by diffraction, even if new approaches start circumventing this barrier by either narrowing the excitation point spread function or the localization of single chromophores. Traditionally, electron microscopy covered the realm of higher resolution, but at the cost of more sophisticated preparation of biological samples. Especially difficult is the observation of structures in the interior of the cell nuclei, which need either mechanical sectioning, thus sacrificing the 3D context as in transmission electron microscopy (TEM) [1], or rupturing for scanning electron microscopy (SEM), which is able to provide images of the 3D topology of the sample. However for the detection of epitopes by immunocytochemistry, standard preparation conditions present a hurdle for the delivery of bulky antibody (AB) conjugates. In this study, we established fixation and permeabilisation conditions to deliver quantum dot coupled antibodies to DNA double strand breaks induced by charged particle irradiation under a low angle [2]. These AB-bound quantum dots have a similar size (around 10 to 20 nm) as gold beads, the standard detection method of antigenic structures in SEM.

Materials and Methods

NIH-3T3 cells were cultured and irradiated as described [2]. Irradiation was done using uranium ions (4.7 MeV/u, LET ≈ 15000 keV/µm). Cells were extracted and fixed using Streck tissue fixative as described [3]. Additional permeabilisation using methanol was added after fixation. For immunocytochemical staining γ-H2AX (Millipore) monocolonal-AB was used. Samples were stained sequentially with two different secondary ABs carrying either an organic chromophore (Alexa 488, green) or qdots 625 (red). Fluorescence microscopy was done at a Leica SPE confocal utilizing a 63x 1.3 NA oil lens.

Results

The principle aim of this study was to establish fixation and permeabilisation conditions allowing the delivery of large (10-20 nm) sized probes to internal structures of cells after irradiation, which is a prerequisite for their detection by immunogold-labelling in SEM. Using common formaldehyde based fixation resulted in an exclusion of quantum dots from the interior of cell nuclei in combination with unspecific binding at the outer surface (not shown). Applying prefixation extraction steps in combination with diazolidinyl urea/2-bromo-2-nitropropane-1,3-diol based fixation and Tritonx-100 permeabilisation led to an uptake and binding of quantum dot-labelled antibodies to the targeted structure. The penetration and binding could be further improved using post-fixation permeabilisation by MeOH (Fig. 1 right). Specific labelling could be demonstrated by double-staining with conventional Alexa 488 labelled ABs (Fig.1 left). The bright stripes in the nuclei represent γ-H2AX at DNA DSBs induced by the traversing ions.

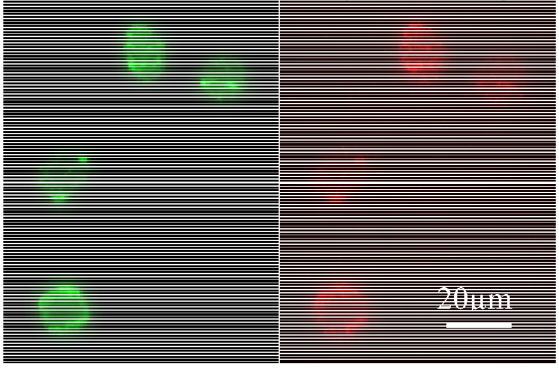

Figure 1: Fluorescence image of NIH-3T3 cell nuclei irradiated with low energy uranium ions. Stripes indicate DNA double strand breaks along the ion trajectories. Left (green) panel shows the organic chromophore Alexa 488 bound to γ-H2AX. Right panel (red) shows the AB-coupled qdots binding to the same primary AB thus indicating an adequate delivery of larger probes to the internal damage sites.

Conclusions

An improved fixation method was established allowing the specific labelling of radiation-induced changes inside the cell nucleus using relatively large probes otherwise excluded. In the next step, this method will be applied to secondary antibodies coupled to 10 nm gold beads at the SEM.

Reference

[1] Y. Lorat et al., DNA Rep., (2015) epub.
[2] B. Jakob et al., Rad. Res., 159; (2003) 676.

---

* Work supported by BMBF 02NUK037A

DOI:10.15120/GR-2015-1-APPA-HEALTH-06

Prediction of asynchronous cell survival with the cell cycle extended GLOBLE model

P. Günther[1], *A. Hufnagl*[1], *T. Friedrich*[1], *L. Herr*[1], *M. Durante*[1,2], *and M. Scholz*[1]
[1]GSI, Darmstadt, Germany; [2]TU Darmstadt, Germany

The Giant LOop Binary LEsion (GLOBLE) model developed at GSI predicts the survival of cells after photon irradiation. This prediction is based on the spatial distribution of Double Strand Breaks (DSBs) in the cell nucleus. An extension of the GLOBLE model was developed in order to predict radiosensitivities of cells, depending on their cell cycle phase. Model predictions are in agreement with measurements from synchronized cell experiments. A next step is to transfer these findings by applying the model to data measured with asynchronous cells. In this context a method to predict the cell cycle specific radiosensitivities from asynchronous cells is investigated. Since the cell cycle plays an important role for photon irradiation, but a less significant one for heavy ion irradiation it is desirable to understand the reasons and implications for therapy.

Methods

One general notion regarding the severity of DNA lesions is that clustered lesions are more harmful to cells than isolated ones. In the GLOBLE model [1] the induction of DSBs on Mbp-chromatin loops after photon irradiation is simulated. One DSB within a loop is defined as an isolated DSB (iDSB), two or more are defined as clustered DSB (cDSB). For photon irradiation the number of iDSBs (n_i) and cDSBs (n_c) is depending on the dose and can be calculated from Poisson statistics. Different lethalities can be assigned to these lesions, ϵ_i for iDSBs and ϵ_c for cDSBs. The cell survival probability S is then given by

$$S = \exp\left[-(n_i \cdot \epsilon_i + n_c \cdot \epsilon_c)\right] .$$

In a recently published work [2] we introduced the option to further distinguish in the GLOBLE model between different repair pathways for the iDSBs. During the G1-phase only the error-prone Non Homologous End Joining (NHEJ) can be used, while in the S-phase the error free Homologous Recombination (HR) gets gradually available. The number of iDSBs which can be repaired with NHEJ (HR) is $n_{i,1}$ ($n_{i,2}$), and their lethality is $\epsilon_{i,1}$ ($\epsilon_{i,2}$). The cDSBs are expected to be equally severe for both pathways. Their lethality ϵ_c does not change. The survival is now given by

$$S = \exp[-(n_{i,1} \cdot \epsilon_{i,1} + n_{i,2} \cdot \epsilon_{i,2} + n_c \cdot \epsilon_c)] .$$

The number of lesions in the different DSB classes can be calculated for all cell cycle phases, and thus their survival probability [2]. To calculate the survival of asynchronous cells the survival rates for all cell cycle phases have to be added and weighted with their proportion. Under the assumption that HR, if available, is error free, this method can also be used in reverse to predict cell cycle phase specific survival from the dose response of asynchronous cell populations. Hence typically measured cell survival curves of asynchronous populations can be exploited to characterize cell cycle dependent dose response.

Results and Conclusion

Predicted survival curves for different cell cycle phases with experimentally inspired lethality parameters are illustrated in fig. 1. They demonstrate a broad variation of radio response within the cell cycle. We checked that the formalism predicts experimental data sufficiently well [2]. The hypothesis above that HR is error free could also be supported.

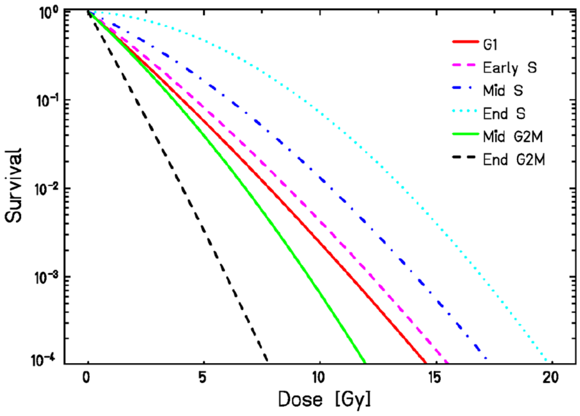

Figure 1: Prediction for cell survival after photon irradiation for cells synchronized in different cell cycle phases.

The prediction of cell cycle specific survival from asynchronous cell populations resulted in similar curves as shown in fig. 1. A first comparison of the model to experimental data is promising.

Our goal for the future is to transfer these findings to ion irradiation, in order to quantify the role of the cell cycle for heavy ion therapy. The presented work is the first step to the cell cycle phase resolved prediction of the relative biological effectiveness for heavy ion irradiation.

References

[1] Friedrich T et al., *Radiat. Res.* 2012 Sept; 178(5): 385-394

[2] Hufnagl A et al., *DNA Repair* 2015 March; 27(1): 28-39

DOI:10.15120/GR-2015-1-APPA-HEALTH-07

Optimization of the chromatid paint FISH assay for the detection of radiation-induced inversions *

N. Paz[1], *E. Nasonova*[1,2], *M. Durante*[1], *and S. Ritter*[1]
[1]GSI, Darmstadt, Germany; [2]JINR, Dubna, Russia.

Inversions are intra-chromosomal events originating from two miss-rejoined breaks, where the resulting chromosome segment is reversed and re-inserted into the chromosome. Since insertions are stable aberrations, i.e. are transmissible to further cell generations, they are an ideal tool for retrospective biodosimetry. Moreover, based on the differences in the track structure of low and high LET radiation it has been proposed that insertions may represent a biomarker of high LET exposure [1].

So far, the available data base is small, mainly attributable to the fact that the detection rate of inversions by routine cytogenetic techniques is low. Recently, a new molecular cytogenetic assay named chromatid paint FISH has been developed enabling the detection of small insertions [2] through the use of fluorescence-labeled directional probes specific to unique sequences along each chromatid. Inversions are microscopically visible as a double-color switch of the hybridization signal from one chromatid to the other as depicted in Figure 1.

For chromatid painting, cells are cultured in medium supplemented with the nucleotide analogues BrdU and BrdC until the first mitosis, and chromosome spreads are prepared. The newly synthesized (BrdU/BrdC substituted) strands are degraded by UV exposure and exonuclease III treatment. Slides are hybridized with Cy3-labeled directional probes resulting in single chromatid painting. Chromosomes are counterstained with DAPI and analyzed under a fluorescence microscope. A Cy3-labeled chromatid appears red, while the other (counter-stained) chromatid appears blue (see figure 1).

We performed chromatid paint FISH assay in peripheral blood lymphocytes, a frequently used cell system to study radiation effects and to estimate risks associated with an exposure. Chromatid painting probe for chromosome 3 was obtained from Kromatid Inc. (Fort Collins, Colorado 80521, USA). Lymphocytes were cultured for 48h in medium supplemented with 5µM BrdU and 1 µM BrdC. Then, chromosome spreads were prepared and the chromatid FISH assay was performed following the manufacturer instructions. Z-stack image acquisition and processing was done with the ISIS software (MetaSystems GmbH, D-68804 Altlussheim, Germany). In parallel, a control slide provided by the manufacturer (i.e. fibroblasts cultured in medium with BrdU and BrdC) was hybridized. Comparison of the samples showed a strong FISH signal intensity along fibroblasts' chromosomes, but weak signal intensity along lymphocytes' chromosomes. Since signal quality will largely depend on the completeness of the denaturation process of the target DNA, we optimized the denaturation temperature for lymphocytes. Samples were denatured for 3 minutes in a temperature range from 68 to 73°C. Optimal signal intensity was achieved by incubation at 70°C. The volume of the probe necessary for hybridization was adjusted to 10µl and spreads were mounted with an 18x18mm cover glass. Notably, hybridization of fresh frozen slides resulted in better FISH signals than air-dried aged slides.

In a first experiment, the background frequency of inversions in chromosome 3 of lymphocytes was determined. Inversions are characterized by a double color switch between sister chromatids, while a single color switch is considered as a false inversion and excluded from the analysis. In total, 86 chromosomes were scored and 2 inversions were observed, i.e. yielding a frequency of 0.02 ± 0.02 in agreement with data reported by Ray et al. [2]. Currently, the frequencies of inversions in lymphocytes after X-ray and after alpha-particles exposure are analysed.

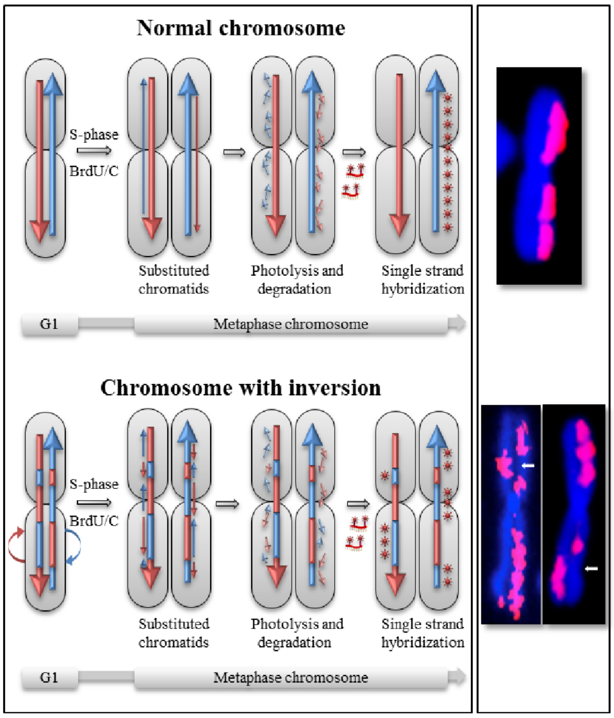

Figure 1: Chromatid paint FISH assay (adapted from Ray et al. [2])

References

[1] M. Hada et al., *Radiat. Res.* (2007) 168: 98-105.
[2] F. A. Ray et al., *Radiat Environ Biophys* (2014) 53:255-263.

---

* Work supported by BMBF, grant 02NUK017A

DOI:10.15120/GR-2015-1-APPA-HEALTH-08

Insights in the molecular basis of a reduced lymphocyte adhesion to irradiated and stimulated primary endothelial cells *

N. Erbeldinger[1], *S. Meyer*[2], *J. Zimmermann*[1], *T. Dettmering*[1], *B. Bertulat*[2], *M. Durante*[1,2], *F. Rödel*[3], *M.C. Cardoso*[2], *and C. Fournier*[1]

[1]GSI, Darmstadt, Germany; [2]Technische Universität Darmstadt, Darmstadt, Germany; [3]Universitätsklinikum Frankfurt, Germany

We reported previously a radiation induced lowered adhesion of immune cells on hybrid endothelial cells (EA.hy.926) as a model of the inner layer of the blood vessel walls [1], which is one possible modification of inflammatory processes in the treatment of chronic inflammatory diseases [2]. Recently, we could further show a relationship between metabolic ROS accumulation and modification of adhesion at low doses in the EA.hy.926 endothelial cell line [3]. We now measured the adhesion of immune cells to primary endothelial cells and assessed NFκB nuclear translocation as a putative molecular basis implicated in the lowered adhesion.

X-ray irradiation (250 kV, 16 mA) of primary endothelial cells (HMVEC) and adhesion assay to TNF-α treated HMVEC was performed with isolated peripheral blood lymphocytes (PBL) according to [1]. TNF-α induced NFκB signalling was analysed in parallel by quantification of the nuclear p65 translocation. Figure 1 shows that the adhesion of non-irradiated PBLs to HMVEC is enhanced by inflammatory TNF-α treatment, whereas the adhesion is reduced in the low dose range (0.1−0.5 Gy) 24h after X-ray exposure. In the presence of TNF-α, non-irradiated EC show nuclear translocation of p65 (not shown), but irradiation did not modify this (Figure 2).

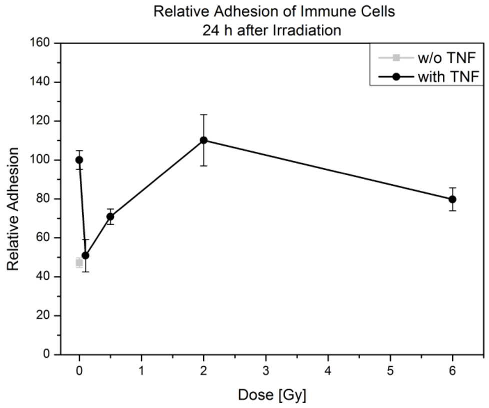

Figure 1: X-ray induced reduced adhesion of PBL to stimulated HMVEC under static conditions normalized to non-irradiated HMVEC. The response for non-stimulated HMVEC is shown as a comparison.

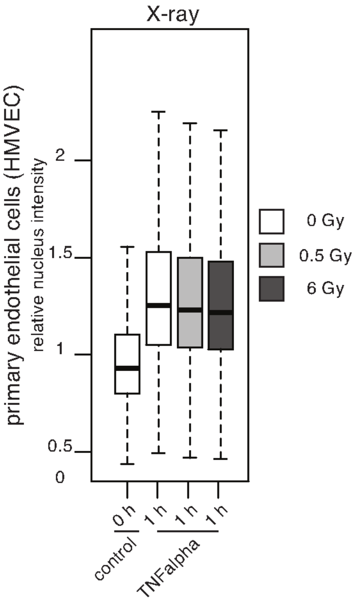

Figure 2: Activation of NFκB signalling via nuclear translocation of p65 in TNF-α stimulated HMVEC 1h after X-ray exposure, normalized to stimulated and non-irradiated HMVEC.

These results confirm that low dose X-ray exposure of primary EC reduces the adhesion of PBL to EC, but rather based on ROS accumulation than on modification of NFκB nuclear translocation.

References

[1] Erbeldinger et al., GSI annual report, 2013

[2] Rödel et al. (2007), IJRB83(6): 357-366.

[3] Large et al. Radiat Oncol (2014), 9:80

---

* Financed by by BMBF (GREWIS, 02NUK017A, 02NUK017F, 02NUK017D), DFG (GRK 1657), FOI Bad Gastein.

DOI:10.15120/GR-2015-1-APPA-HEALTH-09

Developments for the TRAX simulation code

M. Krämer[1], *E. Scifoni*[1], *C. Wälzlein*[1], *and M. Durante*[1,2]
[1]GSI, Darmstadt, Germany; [2]TU Darmstadt, Germany

Developments

The TRAX single interaction Monte Carlo (MC) simulation code has substantially been enhanced in the past years [1]. External cross sections, including Auger effect, for a large variety of materials are available, and have been used e.g. in nanoparticle simulations [2].

These developments were streamlined and incorporated into the code's main branch [3]. In addition, cross section handling was overhauled in order to treat target materials as atoms, molecules (compounds) or mixtures, depending on the interaction type. For example, for electronic interactions a water molecule is seen as a molecule, whereas for nuclear interactions it is a mixture.

Applications

A possible application of the new features is the prediction of microscopic dose deposition in solid state dosimeters, e.g. TLDs. These devices are made of LiF, which might be treated as mixture of Li and F. The single interaction cross sections of the constituents for a variety of ionization, excitation and elastic processes were collected [1]. As a first goal, classical radial dose distributions are generated, which are usually required for LEM type microscopic models [4].

Results

Figure 1 shows a comparison with a conventional (condensed random walk) MC calculation [1], [5]. Substantial differences occur in the inner part (<5nm) of the ion track. These might be due to different (low-energy) cross sections being used, as well as due to a different energy cutoff: 50eV vs 2eV used in TRAX. Figure 2 shows a comparison with the analytical formulae used by [4] to calculate TL dosimeter efficiencies. Here, the agreement appears to be better except for the innermost part. It remains to be investigated, whether the higher core dose will lead to a better agreement of measured and calculated TL efficiencies.

References

[1] C.Wälzlein, PhD Thesis, TU Darmstadt 2013

[2] C.Wälzlein at al., Phys. Med. Biol., 59(2014) 1441-1458

[3] http://bio.gsi.de/DOCS/trax.html

[4] D.Boscolo, this report

[5] Y.S.Horowitz et al., Nucl. Instrum. Methods B 184, (2001) 85-112

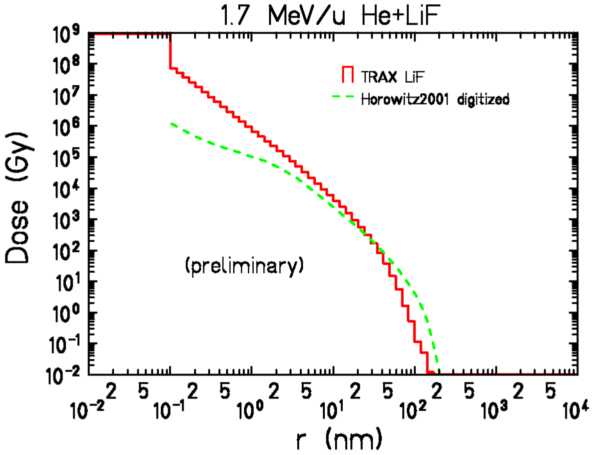

Figure 1: Radial dose profiles for helium ions. Dashed: Reproduced from [5], solid: TRAX calculation.

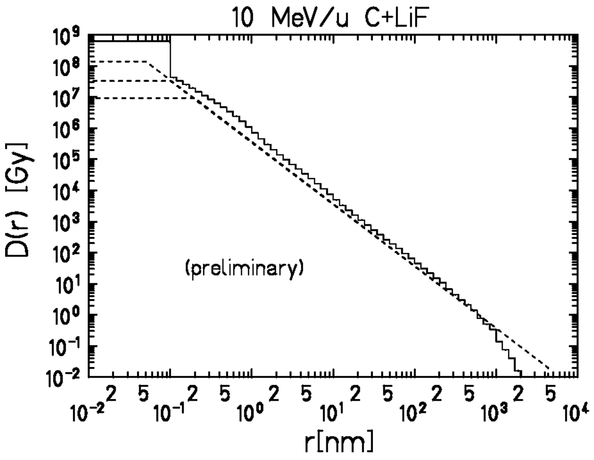

Figure 2: Radial dose profiles for carbon ions. Dashed: analytical formula from [4], solid: TRAX calculation.

DOI:10.15120/GR-2015-1-APPA-HEALTH-10

Helium ion beam modelling

M. Krämer[1], *E. Scifoni*[1], *F. Schmitz*[1], *and M. Durante*[1,2]
[1]GSI, Darmstadt, Germany; [2]TU Darmstadt, Germany

Cross Sections

Soft tissue is mainly water, so cross sections for the collisions ^{4}He+p and ^{4}He+O are required in order to perform transport calculations for radiotherapy [1]. Dedicated experiments to obtain data over the whole energy range are time consuming, thus we rely on nuclear reaction models. We investigated the semiempirical models of Tripathi [2] and Sihver [3], Figure 1. The gross properties are similar, however, we currently prefer the Tripathi model, giving better agreement with experimental data.

Transport Calculation

One of the most important observables is the attenuation of the primary beam, which is usually easier to measure than pure cross sections. Figure 2 shows the result of our deterministic transport calculation compared with experimental results obtained at HIT [4]. At maximum penetration depth, about 50% of the beam is lost due to nuclear reactions.

Radiobiology

Although ^{4}He ions are considered low-LET radiation, their RBE, in particular in the stopping region, is all but negligible. In Figure 3 we show the relevant quantities for a model system (CHO, α/β=8.6Gy, LEM IV) for a typical target depth and a target dose of ≈ 3Gy(RBE). RBE rises steeply towards the distal edge and thus cannot be neglected in treatment planning.

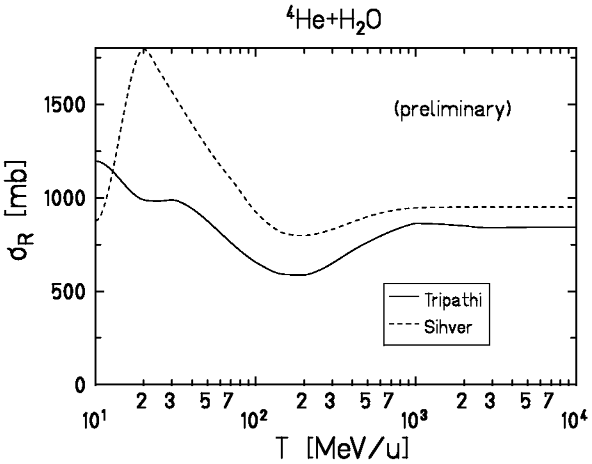

Figure 1: Nuclear reaction cross sections.

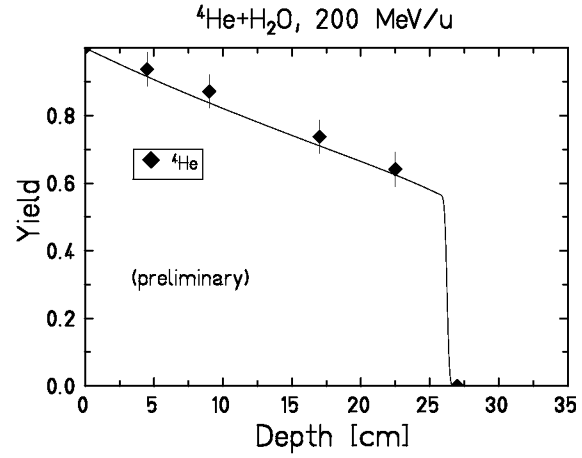

Figure 2: Primary beam attenuation.

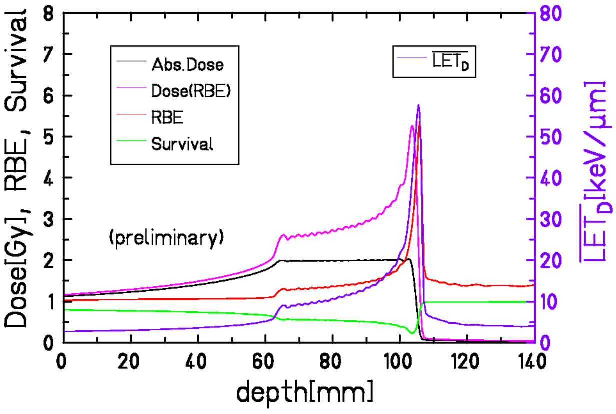

Figure 3: Depth profiles, including dose-mean LET.

References

[1] M. Kraemer, E. Scifoni, C. Waelzlein, M. Durante, “Ion beams in radiotherapy - from tracks to treatment planning” J. Phys.: Conf. Ser., 373 (012017) (2012)

[2] Tripathi et al., “Accurate universal parameterization of absorption cross sections III–light systems” Nuclear Instruments and Methods in Physics Research Section B, 155/4, p.349-356 (1999)

[3] L. Sihver and D. Mancusi, Radiation Measurements, “Present status and validation of HIBRAC” 44/1, p.38-46 (2009)

[4] M. Rovituso et al., “Fragmentation of 120 and 200 MeV/u 4He in water”, this report

DOI:10.15120/GR-2015-1-APPA-HEALTH-11

Fragmentation of 120 and 200 MeV/u ^{4}He in water

M. Rovituso *[1], *C. Schuy*[1], *R. Pleskac*[1], *D. Izraeli*[2], *E. Piasetzky*[2], *M. Krämer*[1], *and M. Durante*[1]
[1]GSI, Darmstadt, Germany; [2]Tel Aviv University, Israel

At present there is a growing interest for cancer therapy using fast Helium ions for the treatment of specific types of tumors. In the late 1960s Lawrence Berkley Laboratory (LBL) introduced radiation therapy with helium ions in patients with metastatic carcinoma [1] . By December 2012 more than 2000 patients with different cancer types have been treated [2].

The therapeutic benefits of using helium beams are lower projectile fragmentation compared to heavier ions like carbon, a sharper lateral beam profile and higher RBE compared to protons. Therefore helium seems to be a good candidate for tumor therapy, particularly suitable for the treatment of pediatric patients.

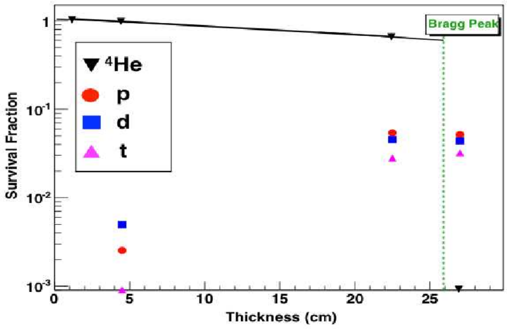

Figure 1: Measured attenuation and fragment buildup of 200 MeV/u ^{4}He in water (preliminary results).

In the present work the attenuation of the primary beam and buildup of fragments were measured as well as their angular and kinetic energy distribution. The measurements were performed in the QS cave of HIT, Heidelberg, with 120 and 200 MeV/u ^{4}He beams impinging on a water target.

The experimental setup was composed of two plastic scintillators of 1 and 9 mm thickness (respectively named START and VETO) and a 14 cm long barium fluoride scintillator (BaF_2). The START detector monitors and counts the incident primary ions, whereas VETO and BaF_2 are used as a ΔE - E telescope for particle identification after the target. Kinetic energy spectra are obtained by using the inverse Time-Of-Flight (TOF) technique [3] between START and BaF_2.

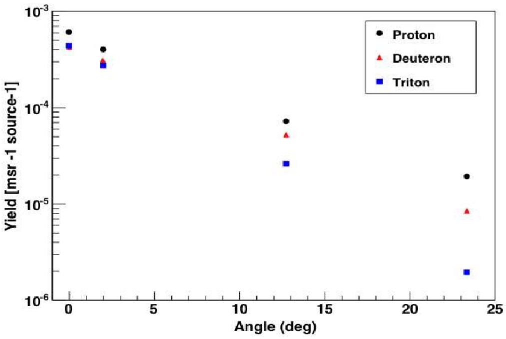

Figure 2: Angular distribution of protons, deuterons and tritons from 120 MeV/u ^{4}He impinging 4.5 cm of water (preliminary results).

The absorption of primary helium ions as a function of water depth was studied by comparing the amount of incident ions impinging on the water target to the number of outgoing helium ions after the target. The survaving fraction versus the thickness of the water target is presented in Fig. 1. While the number of helium ions is decreasing with increasing target thickness due to nuclear fragmentation processes, the number of fragments is increasing (buildup of protons, deuterons and tritons). The fraction of primary ions reaching the Bragg peak position is approximately 65%. An example of the measured angular distributions of hydrogen isotopes is presented in Fig. 2. The produced fragments are forward peaked and show a broad distribution which reaches angles of more than 25 degrees. The proton yield is higher than the one of deuterons and tritons, especially at larger angles. This can be attributed to the isotropic distribution caused by evaporation following the nuclear reaction.

Acknowledgments

I would like to thanks Dr. Thomas Haberer who offers all the needed beam time and to the "accelerator's guys" for their great job. A special thanks to Dr. Stephan Brons for his support, availability and kindness. A big thanks to Dr. Dieter Schardt, his collaboration is always precious for us.

References

[1] J. R. Castro et al., "Clinical results in heavy particle radiotherapy", Annual Report 1980, Lawrence Berkley Laboratory

[2] M. Jermann, "Particle therapy statistics in 2013", Int. J. Part. Ther. 2014, 1, 40-43

[3] K. Gunzert-Marx, "Nachweis leichter Fragmente aus Schwerionenreaktionen mit einem BaF_2-Teleskop-Detektor", PhD Thesis, TU of Darmstadt, 2004.

---

* Work supported by HGS-HIRe.

DOI:10.15120/GR-2015-1-APPA-HEALTH-12

Simulation of double strand break yield after high LET irradiation*

T. Friedrich[1], *M. Durante*[1,2], *and M. Scholz*[1]
[1]GSI, Darmstadt, Germany; [2]Institut für Festkörperphysik, TU Darmstadt, Darmstadt, Germany

Introduction

Double strand breaks (DSB) of the DNA are considered as key lesions of radiation damage. For radiation induced DSB, two coincident single strand breaks (SSB) on opposite DNA strands are needed. These SSB pairs are typically induced by single electrons, as the yield is constant over a large dose range. For very high doses $\gg 100$ Gy the relative contribution of DSB formed by two-electron processes gets more important, and thus the DSB yield increases. Evidence for such SSB clustering interaction was gained in plasmid experiments, where it was found that the SSB need to be closer than some 10 bp. In the inner part of ion tracks, also very high local doses occur, where consequently also an enhanced DSB yield is expected. We developed a Monte Carlo (MC) algorithm and an analytic formulation for the dose dependent DSB yield for photon radiation. The enhancement mechanism of DSB by means of SSB clustering is part of the Local Effect Model (LEM), which considers the spatial distribution of DSB to predict the RBE for charged particle irradiation [1].

Materials and Methods

We used as numerical constants for the yield computation $\alpha_{\mathrm{DSB}} = 30/\mathrm{Gy}$ and $\alpha_{\mathrm{SSB}} = 1250/\mathrm{Gy}$ per cell as DSB and SSB yield after photon irradiation at low doses, respectively. A genomic length $L_{\mathrm{Gen}} = 5.4 \times 10^9$ bp was used. The MC algorithm assumes that SSB are randomly distributed along the genome according to Possonian statistics. SSB pairs leading to DSB are counted. The key idea of the analytic expression is that the probability to find a gap of size s between successive SSB is given by $\rho e^{-\rho s}$, where ρ^{-1} is the average distance between two SSB in bp.

Results

The MC algorithm predicts the expected DSB yield enhancement after photon radiation at very high doses. The analytic computation is a very good approximation of the MC results and can thus be used for quick evaluation within RBE models. In analogy to the linear-quadratic parameters, an $\alpha_{\mathrm{DSB}}/\beta_{\mathrm{DSB}}$ of about 8300 Gy was found, indicating the dose scale where the yield enhancement becomes important. Weighting the local yields over the radial dose distributions in track structures allows to determine the ion-energy specific DSB yield enhancements as shown in Fig. 1 for two values of the maximum distance between two interacting SSB, t, in bp.

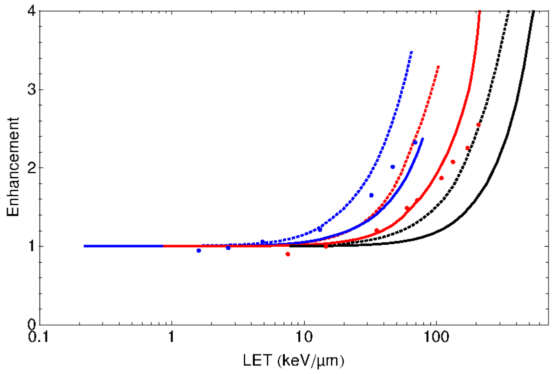

Figure 1: DSB enhancement factor η vs LET for protons (blue), helium (red) and carbon (black) as dotted and solid lines for t = 25 bp and t = 10 bp, respectively, in comparison with model data of the PARTRAC code (data points).

Discussion and Outlook

The DSB enhancement mechanism is expected to be of importance for ion beam tumor therapy. In the regions of high LET a DSB amplification of 1-4 is expected. For low energetic carbon ions as found in therapeutic extended Bragg peaks the local doses in the center of the ion tracks is about 10^5 Gy according to the track structure model of LEM. Consequently most DSB are formed by independent electrons and the DSB density is enhanced, leading to more complex damage. As both the number of DSB and their spatial correlation are important factors for RBE, the SSB clustered DSB formation is an relevant process for the effectiveness of high LET radiation. Concerning its quantification other models such as PARTRAC [2] predict different DSB yields, mostly due to assumed values of t as demonstrated in Fig 1. Here further model comparison as well as experimental investigation of DSB yields for mammalian cells is be needed, and details of the algorithms used [3] within the LEM are subject of current discussion.

References

[1] T. Friedrich *et al.*, Int. J. Radiat. Biol. **88**, 103-107 (2012).
[2] A. Campa *et al.*, Int. J. Radiat. Biol. **81**, 841-854 (2005).
[3] T. Friedrich *et al.*, submitted to Radiat. Prot. Dosim. (2013).

---

* Supported by BMBF within project 02NUK031D.

DOI:10.15120/GR-2015-1-APPA-HEALTH-13

Differentiation of mouse embryonic stem cells into extra-embryonic endoderm stem cells

G.Ciliberti[1-3], S. Ritter[1], M. Durante[1,3], I. Schroeder[1,#]
[1]GSI, Darmstadt, Germany, [2]University Federico II of Naples, Italy, [3]Technische Universität Darmstadt, Germany

The embryonic response to ionizing radiations is poorly characterized. Although teratology was frequently observed after in utero exposure, little is known about the mechanisms involved. At early embryogenesis, a significant contribution to the morphogenetic program is given by the primitive endoderm (PrE) and its derivatives, visceral and parietal endoderm (VE, PE). These extra-embryonic membranes originate within the post-implantation blastocyst and were shown to directly interact with the epiblast, driving the formation of main ventral structures such as head and heart [1]. Stem cells representing the extra-embryonic endoderm (XEN) lineages can be generated *in vitro*, preserving the morphological and functional identity of the *in vivo* counterparts. As observed in recent studies, these cells retain the expression of the typical endoderm markers [2] and still maintain their morphogenetic role [3].
The *in vitro* XEN derivation would represent a simplified tool to assess the early morphogenetic events offering, therefore, the opportunity to investigate the physiologic response to ionizing radiation.

Here, extra-embryonic endoderm stem cells were generated from mouse embryonic stem cells (mESCs) in an attempt to establish a stable population. Pluripotent D3 mESCs were cultured for a prolonged time in XEN medium, and activin A and retinoic acid were employed to induce the endoderm specification according to Niakan et al. [4]. The samples were treated until the XEN morphology was detected in culture. Quantitative PCR analyses were executed to verify XEN differentiation. The expression profile of differentiated cells was evaluated after 30 days of culture and the production of pluripotency (Sox 2, Oct 4) and endoderm (Sox 7, Sox 17, Gata 6) markers was quantified and compared to the ones detected in the undifferentiated samples.
As shown in Figure 1, the pluripotent mESCs retain a higher expression of the transcription factors Sox 2 and Oct 4 and a significantly lower production of the endoderm factors can be detected at this stage.

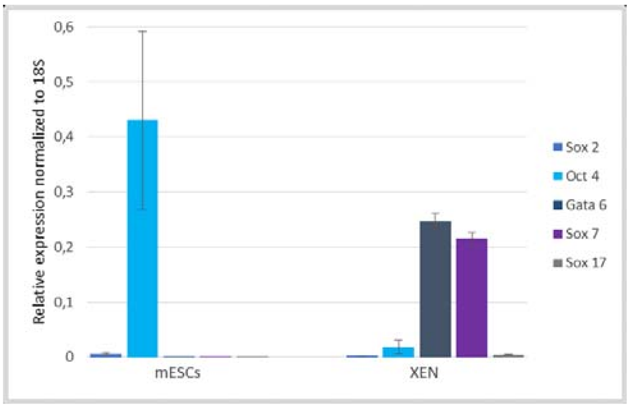

Fig.1 Gene expression profile of mESCs and in vitro derived XEN cells. An increased expression of the endodermic markers Gata 6, Sox 7 and Sox 17 can be detected in the treated cells after 30 days in XEN medium. The quantitative amount of Oct 4 and Sox 2 transcripts significantly decreases during the differentiation.

In the treated cells, however, the expression of Sox 7, Sox 17 and Gata 6 is increased, as expected for XEN lines. As already observed in previous studies, a basal production of the pluripotency markers is preserved in the XEN population, confirming their stem cells identity (fig.1, [4]). Although XEN differentiation was successful, the obtained cell population was still highly heterogeneous, which caused a delayed appearance of XEN colonies impeding the establishment of stable cell lines.
Further improvements are needed to guarantee the selection of the desired cell type and its maintenance and propagation.

References

1. M. Madabhushi and E. Lacy ”Anterior Visceral Endoderm Directs Ventral Morphogenesis and Placement of Head and Heart via BMP2 Expression”. Dev. Cell 21 (2011), 907.
2. L.T. Cho et al., “Conversion from mouse embryonic to extra-embryonic endoderm stem cells reveals distinct differentiation capacities of pluripotent stem cells state”. Dev 139 (2012), 2866.
3. K. Brown et al., “eXtraembryonic ENdoderm (XEN) Stem Cells Produce Factors that Activate Heart Formation”. PlosOne 5 (2010), e13446.
4. K.K. Niakan et al., “Derivation of extraembryonic endoderm stem cells (XEN) from mouse embryos and embryonic stem cells”. Nat Prot 8 (2013), 1028.

[#] i.schroeder@gsi.de

DOI:10.15120/GR-2015-1-APPA-HEALTH-14

Human neurospheres on microelectrode arrays: a model to investigate ionizing radiation effects on neuronal network communication*

M. Mayer[1], *B. Müller*[2], *S. Kadereit*[2], *S. Ritter*[3], *C. Thielemann*[1]

[1]University of Applied Sciences, BioMEMS lab, Aschaffenburg, Germany; [2]University Albstadt-Sigmaringen, Lifescience division, Sigmaringen, Germany; [3]GSI Helmholtz Centre for Heavy Ion Research, Biophysics division, Darmstadt, Germany

Motivation

Ionizing radiation is known to induce numerous effects in cells including cell cycle delay, DNA damage, altered gene expression and cell death. Although there are serious impacts on the organisms, the effects on prenatal development are largely unknown. Data regarding potential biological effects on the prenatal development after in utero radiation exposure predominantly stem from atomic bomb survivors and from animal studies. These results indicate that the developing central nervous system is particularly sensitive to ionizing radiation and that exposure can lead to prenatal death, growth retardation, organ malformation or mental retardation [1]. Yet, there is hardly any information on the effects of ionizing radiation on neuronal network communication, the most vital function of neurons.

To fill this gap we developed a protocol that enables electrical characterization of three-dimensional neurospheres (NS) derived from human embryonic stem cells using microelectrode arrays (MEA). This method allows assessing the electrical activity of neuronal tissue in a non-invasive way. Network functionality typically develops in three phases. First, electrical activity can be detected as random single spikes. In a second phase train-like spiking activity evolves, that further develops into burst-like activity. These bursts represent the mature signalling activity of the network [2].

The measurement of electrical activity of neurospheres on MEAs represents a new and promising tool to investigate the effects of ionizing radiation on the neuronal network communication during early brain development.

Material and Methods

Experiments were performed with human embryonic stem cell derived neurospheres [3].

Human embryonic stem cells (hESCs, WA09 line) were obtained from WiCell (Madison, WI, USA) and cultured according to standard protocol [4]. Differentiation was performed in adherent culture to PAX6$^+$ neural progenitor cells. These early central nervous system precursor cells were replated into suspension to develop to round aggregates, socalled neurospheres [3].

The electrical signals of the neurospheres were recorded by microelectrode arrays. Prior to experiments, MEAs were coated with Polyethyleneimine (PEI) and Laminin. After two weeks in culture, neurospheres were harvested and plated on the centre of the coated MEA chips where they attached and neurons migrated out onto the microelectrodes. Thereafter, the electrical signals were recorded for about one week after plating.

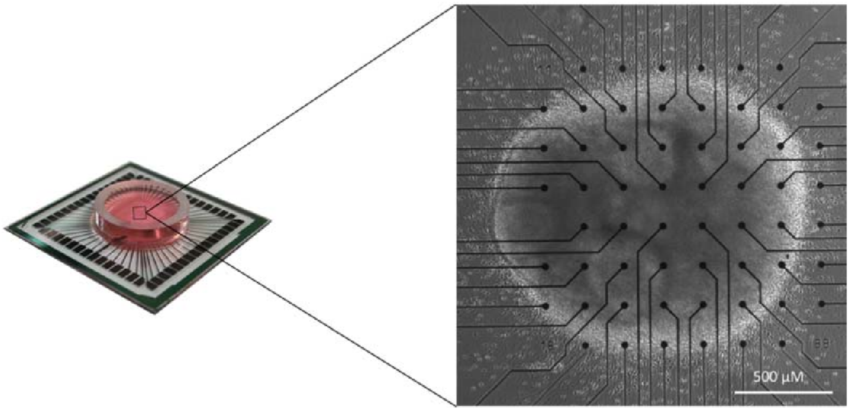

Figure 1: Human embryonic stem cell derived neurospheres on a MEA chip, cultured for two weeks in suspension, prior to plating.

---

* Funding for this project was provided by the Federal Ministry of Education and Research (02NUK025C).

DOI:10.15120/GR-2015-1-APPA-HEALTH-15

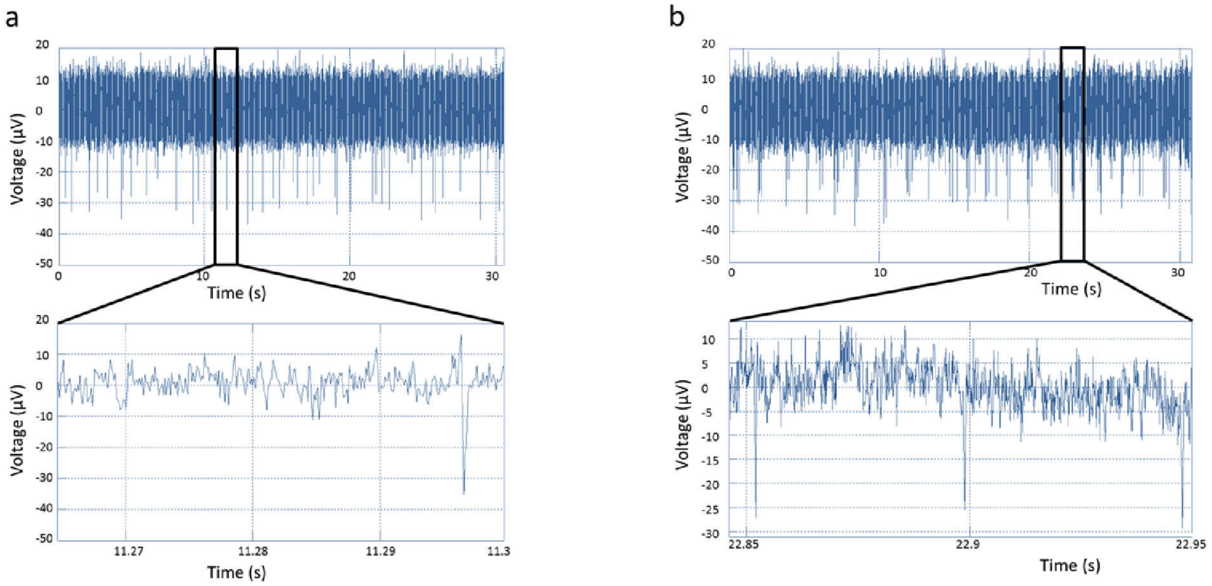

Figure 2: Development of neuronal activity of neurospheres on MEA Chips. (a) One day after the neurospheres are plated on the centre of the MEA chip the first signals are detected. They are random single spikes. (b) After two days of cultivation the cells started to express train-like spiking activity.

Results

PAX6 positive neural progenitor cells re-aggregated to neuronal networks in a 3D neurosphere system. The neurospheres reached sizes up to 600 µm just one day after precursor cells were replated into suspension. After two weeks in culture their size ranges from 600 µm to about 1500 µm. At this stage, neurospheres were plated onto the centre of the MEA chips where they attached to the coated surface and covered the whole electrode array as can be seen in Figure 1.

The first electrical signals could be recorded just one day after the neurospheres were placed on the MEA Chip. At this time electrical activity could be detected as random single spikes (Fig. 2a). After two days the cells started to express train-like spiking activity as can be seen in Figure 2b. These spike-trains consisted usually of three spikes and shows interspike intervals of about 50 ms. The signal amplitude remained constant and ranged between -30 and -40 µV.

However, in this first experiment spikes-trains have not developed into burst-like activity which is defined as at least four spikes with a maximum idle time between those spikes of 100 ms.

Conclusion

Our preliminary results show, that human embryonic stem cell-derived neurospheres represent a promising tool to investigate neuronal network communication in a three dimensional cell culture system.

The model used in this experiment provides many advantages. The differentiation from human embryonic stem cells towards neuronal precursor cells in neurospheres mimics early human brain development [3]. We have shown here that it is possible to detect electrical activity on MEAs and it may be feasible to treat the cells in different stages of differentiation, for example with ionizing radiation, and to analyse electrical activity on MEA chips to determine whether the treatment influenced the neuronal network communication. Another important advantage of this model is that neurospheres can be cultured over a period of several weeks enabling chronic exposure studies.

The fact that no bursts were detected could be related to the short culture and maturation period on the MEA chip of just one week. It is planned to extend this period. In addition, neurospheres in various stages could be plated on the MEA chips to evaluate optimal maturation for electrophysiological studies.

References

[1] McCollough, C.H. et al., “Radiation Exposure and Pregnancy: When Should We Be Concerned?”, RadioGraphics 2007, 27: 909-918

[2] Heikkilä, T.J. et al., “Human embryonic stem cell-derived neuronal cells form spontaneously active neuronal networks in vitro”, Exp Neurol. 2009, 218: 109-116

[3] Hoelting, L. et al., “A 3-dimensional human embryonic stem cell (hESC)-derived model to detect developmental neurotoxicity of nanoparticles”, Arch Toxicol. 2013, 87 (4): 721 - 733

[4] Thomson, J.A. et al., “Embryonic stem cell lines derived from human blastocysts”, Science 1998, 282 (5391): 1145-1147

DOI:10.15120/GR-2015-1-APPA-HEALTH-15

Microenvironment adapted treatment planning for ion beams*

E. Scifoni[1,#], *W, Tinganelli*[1], *, M.Durante*[1,2] *, W. Kraft-Weyrather*[1], *A. Maier*[1], *O. Sokol*[1]*and M.Krämer*[1]

[1]GSI, Darmstadt, Germany; [2]TUD, Darmstadt, Germany.

Internally heterogeneous tumors are strongly correlating with poor prognosis. One of the principal source of biological intra-tumour heterogeneity is the local microenvironment, e.g. the condition of oxygenation verified in different tumor regions, or the concentration of a given radiosensitizer presenting a differential uptake within the malignant tissue.

With particle therapy is now possible to exploit the ion beams radiobiological advantages for targeting the most resistant cells, and through the flexibility of active beam scanning, creating specific adaptive treatment plans [1-4].

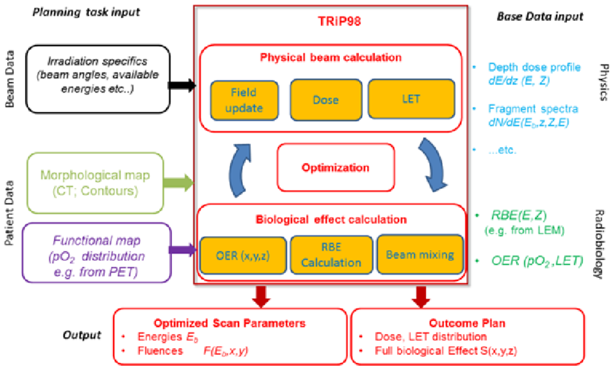

Figure 1: Present structure of TRiP98 code, including the adaptive implementation, which allows processing functional information of the tumor, beside morphology.

Exploiting different ion beams

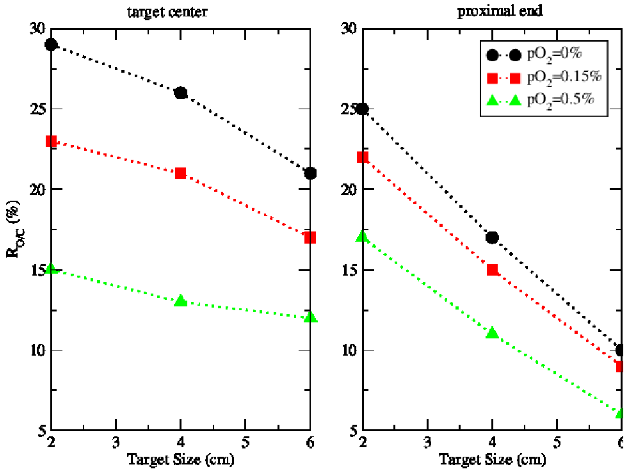

Figure 2: Relative reduction ($R_{O/C}$) of the oxygen enhancement ratio in an hypoxic target by using an oxygen beam with respect to carbon, for different position within the target, size and different level of hypoxia (pO_2).

In this connection, beside the possibilities of plans with carbon ions, which are the established particles in use in the modern facilities, higher LET ions like oxygen-16, offer the opportunity of targeting even more efficiently the regions of increased resistance, e.g. in the case of hypoxia. An example is shown in figure 2. The combination of different ion peculiarities [3] is even more promising.

Experimental verification

The adaptive treatments plans have been verified in several irradiations performed at GSI and NIRS (Japan).

To this aim, specific bio-phantoms composed by cell holders at different conditions were prepared (Figure 2).

The results have been recently submitted [4], showing a remarkable agreement.

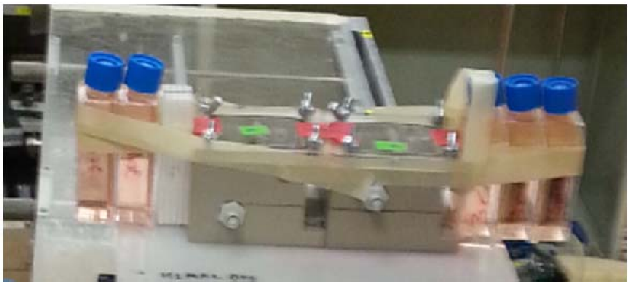

Figure 3: Example of experimental device used for verification of microenvironment adapted treatment planning: biological phantom composed by normoxic cells (tissue culture flasks) and cells at different oxygenation conditions (hypoxic chambers).

References

[1] E. Scifoni, W. Tinganelli, W. K. Weyrather, M. Durante, A. Maier and M. Krämer, “Including oxygen enhancement ratio in ion beam treatment planning: model implementation and experimental verification”, Phys. Med. Biol. 58, 3871-3895 (2013).

[2] M. Krämer, E. Scifoni, F. Schmitz, O. Sokol and M. Durante, “Overview of recent advances in treatment planning for ion beam radiotherapy”. Eur. Phys. J. D 68, 306 (2014).

[3] E. Scifoni, Radiation biophysical aspects of charged particles: from the nanoscale to therapy”, Mod. Phys. Lett. A (2015), in print.

[4] W. Tinganelli, M. Durante, R. Hirayama, M. Krämer, A. Maier, Y. Furusawa, W. Kraft-Weyrather, and E. Scifoni, “Kill-painting of hypoxic tumors with charged particle therapy”, Sci. Transl. Med., submitted (2015)

---

* Work supported by POF III.

#e.scifoni@gsi.de

DOI:10.15120/GR-2015-1-APPA-HEALTH-16

Radon solubility in different types of tissue*

A. Maier[1], *P. van Beek*[1,2], *M. Durante*[1,2], *C. Fournier*[1], *J. Hellmund*[1], *G. Kraft*[1]
[1]GSI, Darmstadt, Germany; [2]TU Darmstadt, Germany.

Introduction

Low doses of ionizing radiation are used for therapy of inflammatory diseases like rheumatoid arthritis. Clinical studies show an increased mobility and less pain of such patients after therapy especially with radon [1]. But the molecular mechanism and the genetic risk of this therapy are not known in detail.

To investigate the effects of radon and its daughter nuclei we studied the radon uptake and the chemical path in different tissues and in mice.

Measurement Setup

For these studies we constructed a Radon exposure chamber that enables to expose samples at various conditions including those of the radon galleries. All parameters like temperature, humidity and radon concentration are permanently monitored and controlled.

To measure the radon kinetics in different types of tissue we exposed tissue samples in the radon chamber and measured the γ-spectrum of the radon decay products in the exposed samples with a HPGe-detector. In our measurements it was possible to distinguish the short living decay products Pb-214 and Bi-214. We recorded the spectra at different time points after exposure and compared the results from different types of tissue like fat or muscle but also activated coal.

Results

In an activated coal sample the decay kinetics are governed by the long life time of the radon (3,8 days) because it is bound via Van-der-Waals force as shown in fig. 1.

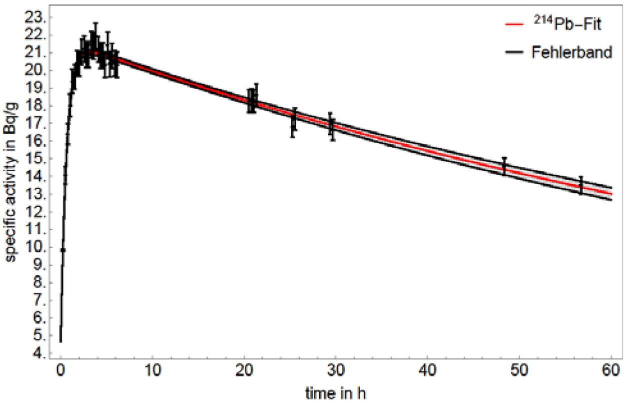

Fig. 1: Measured γ-activity of Pb-214 over 57 hours in an activated coal sample

But in the biological samples the primary radon diffuses out of the samples and the spectra follow the kinetics of the decay of the daughter products. Therefore in the data analysis their radioactive decay has to be combined with a diffusion term for the primary radon.

In fig. 2 a typical measurement with a biological sample is given. The time between two measuring points was 900 s. After two to four hours the measurements were stopped, since the activity reached detection limit.

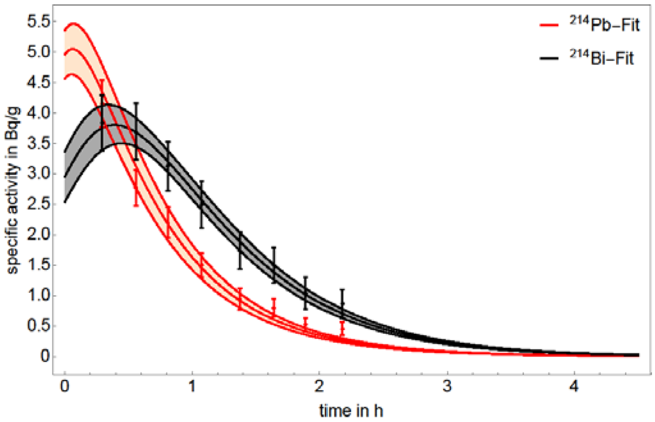

Fig. 2: Measured γ-activity of Pb-214 and Bi-214 over four hours in a tendon sample

With the results from the activities of Pb-214 and Bi-214 we could calculate the initial amount of radon in our sample directly at the beginning of our measurement.

Discussion

In our first measurements we exposed different types of tissue like muscle, fat or tendon. We developed an analysis model and optimized the γ-spectroscopy for the low activities in our samples.

In the future we want to repeat these experiments for better statistics and measure additional types like bone or cartilage. For this we ordered a new detector which we will commission in the following month.

References

[1] A. Falkenbach, J. Kovacs, A. Franke, K. Jörgens, K. Ammer, Radon therapy for the treatment of rheumatic diseases-review and meta-analysis of controlled clinical trials, Rheumatology International, 25(3):205-210, 2005

[2] P. van Beek, Berechnung der Ausbeuten von Radon und seinen Zerfallsprodukten in biologischem Gewebe, Bachelorthesis TU Darmstadt, 2014

---

* Work is supported by BMBF project funding reference number 02NUK017A

DOI:10.15120/GR-2015-1-APPA-HEALTH-17

Biodosimetry of alpha-particle-induced DNA double-strand breaks in murine bones and soft tissues

M. Steinlage[1], *J. Mirsch*[1], *R. Schäfer*[1], *C. Fournier*[2] *and M. Löbrich*[1]
[1]Darmstadt University of Technology, Germany; [2]GSI, Darmstadt, Germany (GREWIS)

Ionizing radiation causes a variety of DNA damages, of which the DNA double-strand break (DSB) stands out as the most hazardous type. The human body is exposed to different types of ionizing radiation on a daily basis. The most relevant source of natural radiation, comprising approximately 40 percent of a person's annual background radiation, is radon gas [1]. Radon (Rn-222) is a radioactive noble gas, which emits three biologically relevant α-particles during its decay chain. Despite its radioactive properties, radon gas is used for its therapeutic effects in radon therapy caves in Bad Gastein and Bad Kreuznach [2].

As part of the GREWIS project, this study is aimed at the biodosimetric measurement of inhaled radon gas in murine tissues. This project is focused on the detection of α-particle-induced DSB tracks in different murine tissues to elucidate the diffusion patterns of radon gas *in vivo* as well as potential organ-specific accumulations.

In the past year, three independent *in vivo* radon experiments, using a total of 18 wild type C57BL/6 mice (female, adults) were performed. A radon exposure chamber was used to expose the mice to a specific radon concentration (40 kBq/m^3 or 440 kBq/m^3) for the duration of one hour. DSBs were visualized in paraffin-embedded tissue sections using highly sensitive immunofluorescence staining for 53BP1 and γH2AX [3]. Analysis of tissue sections of two radon-exposed mice revealed that 15 minutes after the end of the exposure period (440kBq/m^3), excess 53BP1 and γH2AX foci can be detected in bone (Fig.1A), lung (Fig.1B), heart, kidney, and liver tissues.

As radon therapy is predominantly used for the therapy of chronic inflammatory diseases of the musculoskeletal system, a preferential accumulation of radon decay products in bone tissue was investigated. The current results do not support this hypothesis. Only a slight increase of DSBs, comparable to the level in heart or kidney tissue, was detected in bone samples. Similar levels of DSBs in heart, liver, bone, and kidney tissues support a model in which radon can diffuse freely throughout the body.

Lung tissue sections, on the other hand, showed significantly elevated levels of 53BP1 foci after radon exposure. The accumulation of DSBs in the lung is likely caused by the additional dose that is deposited in this organ due to inhaled radon progeny. As radon decays in the air, radon progeny, with an affinity to adhere to aerosol particles, are formed. These complexes subsequently enter the body through the respiratory tract and accumulate in the bronchioles where radon decay products decay further, hence inducing additional DNA damage. The lung is therefore exposed not only to inhaled radon, but also to radioactive radon decay products.

Future efforts will focus on the comparison of results from radon-exposed mice with foci numbers from mice irradiated with a defined dose of X-rays in order to calculate the dose deposited in specific organs after radon exposure.

A) Bone tissue

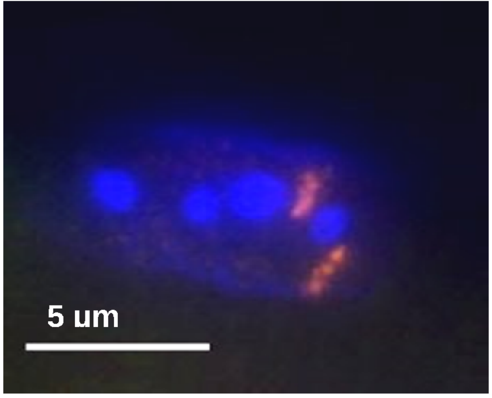

B) Lung tissue

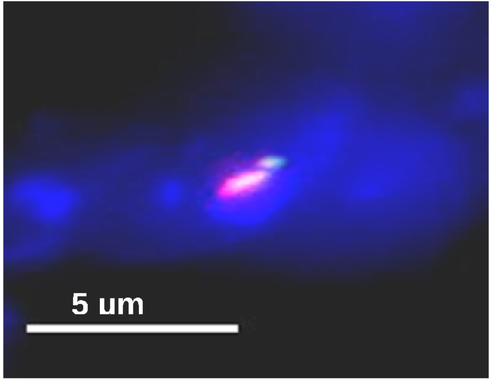

Fig.1: Visualization of DSBs: Tissue samples from mice exposed to 440 kBq/m^3 for one hour. Animals were sacrificed 15 minutes after the end of the exposure period. (A) Co-localizing γH2AX and 53BP1 foci in murine bone tissue. (B) Co-localizing γH2AX and 53BP1 foci in murine lung tissue.

References

[1] Bundesamt für Strahlenschutz
[2] K. Becker. Int. J. Low Radiation Vol. 1 (2004) 334-356
[3] C. Rübe. Clin Cancer Res (2008) 14:6546-6555

Funded by German federal ministry of research and education (BMBF/ 02NUK017E).

DOI:10.15120/GR-2015-1-APPA-HEALTH-18

A non-linear regulation of the antioxidative system in endothelial cells contributes to the anti- inflammatory effect of low dose X-irradiation*

M. Large[1], *S. Hehlgans*[1], *C. Fournier*[2], *C. Rödel*[1], *and F. Rödel*[1]
[1]Goethe-University Frankfurt am Main, Germany; [2]GSI, Darmstadt, Germany

Introduction

Since ionizing radiation exerts its cytotoxic activity in large parts by the generation of reactive oxygen species (ROS), antioxidant systems to maintain cellular redox balances are relevant for radiation response. Moreover, ROS are involved in immunological defense mechanisms and have a physiological role in cellular signaling [1]. A major mechanism in the regulation of oxidative stress/damage homeostasis is activation of the transcription factor nuclear factor E2-related factor 2 (Nrf2), which tightly controls the expression of genes encoding antioxidant proteins [2]. We have recently reported on a diminished activity of the enzyme superoxide dismutase (SOD) and a discontinuous induction of ROS in EA.hy926 endothelial cells (ECs) most pronounced at 24 h after a 0.5 Gy exposure [3]. Based on these findings, analyses were expanded to Nrf2 as a common regulatory element in the antioxidative defense and on functional properties of ROS in the anti-adhesive effects of low dose X-irradiation [4].

Material and Methods

EA.hy926 ECs were either stimulated in a proinflammatory manner by tumor necrosis factor-α (TNF-α; 20 ng/ml) 4 h before or at 20 h after irradiation with X-ray doses ranging from 0.3 to 1 Gy. Expression and DNA binding activity of Nrf2 were analyzed by flow cytometry and colorimetric assays. The impact of ROS on peripheral blood mononuclear cell (PBMC) adhesion was assayed in the presence of the scavenger N-acetyl cysteine (NAC).

Results and Conclusion

As depicted in Figure 1, a non-linear dose response relationship was evident with a relative minimum of protein detection at 0.5 Gy (Fig. 1A) in line with a reduction in Nrf2 DNA-binding activity as quantitated by colorimetric assays (Fig. 1B). Next, to investigate whether low dose X-irradiation modulated induction of ROS is associated with altered functional properties of EA.hy926 ECs, leukocyte adhesion was quantitated in the presence of the ROS scavenger NAC. As shown in figure 1C, PBMC/EA.hy926 EC adhesion was suppressed by more than 50 % after a single dose irradiation with 0.5 Gy in control treated ECs. On the contrary, ROS scavenging by NAC resulted a pronounced increase of adhesion events and thus a partial, but significant ($p < 0.05$) diminution of the anti-adhesive effect of low dose exposure.

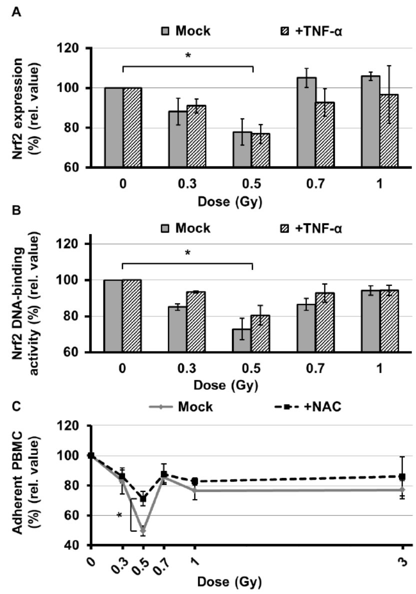

Figure 1: Relative Nrf2 protein detection (A) and colorimetric Nrf2 DNA-binding activity (B) as measured at 24 h after irradiation with single doses as indicated. Data represent mean ± s.e.m from at least three independent experiments. $* \ p < 0.05$ versus non irradiated ECs. (C) Adhesion of PBMC to NAC (10 mM) treated and stimulated (TNF-α: 20 ng/ml) EA.hy.926 EC subsequent to low-dose irradiation. Mock treated cells served as a control. Data are given as mean relative values (± s.e.m) from three independent experiments. $* \ p < 0.05$ versus mock treated controls.

In conclusion, these findings implicate a non-linear expression and activity of a major compound of the antioxidative system that may contribute to a differential regulation of ROS production and via modulation of the adhesion process to the anti-inflammatory effects of low dose radiation therapy.

References

[1] C. Nathan, Nat Rev Immunol 2013; 13:349-361
[2] T. Nguyen, J Biol Chem 2009; 284:13291-13295
[3] F. Rödel, Curr Med Chem 2014; 19:1741-1750
[4] M. Large, Radiat Oncol 2014; 9:80

---

* This research was supported by grants of BMBF (GREWIS, 02NUK017F) and EU (DoReMi, FP7-249689).

DOI:10.15120/GR-2015-1-APPA-HEALTH-19

Comparative studies on the effect of x-ray and heavy ion irradiation on ROS signalling and K^+ channel activation in A549 cells*

B. Roth[1,#], *C. Gibhardt*[1,#], *B. Jakob*[2], *C. Fournier*[2], *and G. Thiel*[1]

[1]Membrane Biophysics, Technische Universität Darmstadt; [2]GSI, Darmstadt, Germany; [#]*equal contribution*

Introduction

Previously, we found that irradiation of the epithelial lung cancer cells A549 with photons resulted in a rapid activation of K^+ channels and a concomitant hyperpolarization of these cells [1]. The signaling cascade, includes a rapid generation of H_2O_2 immediately after irradiation. The latter triggers an increase in the concentration of cytosolic Ca^{2+} and the consequent activation of the human intermediate potassium channel hIK [1]. This channel regulates via hyperpolarization of the plasma membrane important functions such as the cell-cycle transition and cell migration [2]. Here we test whether an irradiation of cells with heavy ions triggers the same signal cascade with an eventual activation of hIK channels.

Material and Methods

Membrane currents and changes in H_2O_2 concentration in cells were monitored as described previously [1,2].

Results

The data in Fig. 1 show the fluorescence of A549 cells, which were either exposed to 10 Gy of X-ray (a) or to 10 Gy of carbon ions (b). As a consequence of photon irradiation all the cells revealed a robust increase in the fluorescence ratio $F_{488/405}$ of the H_2O_2 sensor. This confirms that irradiation with x-ray causes a rapid rise in the concentration of H_2O_2 in cells. When cells were irradiated with C-ions, we found only a small fraction of cells (5%) which responded with an increase in the fluorescence ratio (Fig. 1bi). The majority of cells exhibited no effect (Fig. 1bii). The results of these experiments suggest that 10 Gy x-ray irradiation triggers a large increase in ROS production in cells while an administration of the same doses of carbon ions has no effect.

The results of these experiments predict an x-ray induced activation of the hIK channel while an exposure to heavy ions should not. Indeed our experimental data show that the hIK currents in A549 cells are unaffected by irradiation with heavy ions. In the equivalent experiments with x-rays we found that an irradiation with 1 Gy was already increasing this current by a factor of > 2 [1].

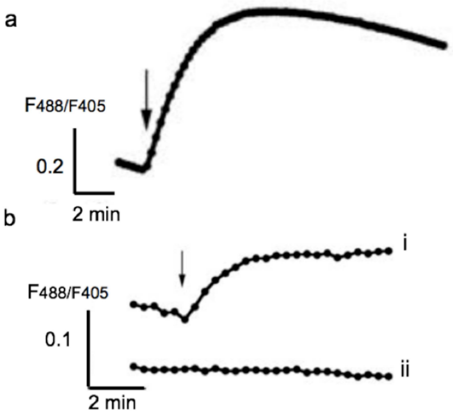

Figure 1: Fluorescence ratio of H_2O_2 reporter HyPer after irradiation of individual cells with 10 Gy X-ray (a) or with 10 Gy C-ions (b). In the latter case only 5% of the cells tested showed a response (trace i) while the majority remained unaffected (trace ii). Cells were irradiated at time indicated by arrow.

Conclusion

The present data show that x-ray irradiation and heavy ion treatment cause different effects in A549 cells. The most significant difference is that heavy ion irradiation has a reduced efficiency in triggering ROS production including the long lasting species H_2O_2. This lack of H_2O_2 production prevents the onset of a signal transduction cascade, which otherwise activates K^+ channels in irradiated cells. As a working hypothesis we assume that the low energy of the heavy ions from the UNILAC presumably generates radicals very close to the ion-track, which may recombine very fast. This could explain the lack of H_2O_2 production after heavy ion irradiation. The heterogenous distribution of radicals, which occurs after x-ray irradiation, may in contrast foster more long lasting ROS species.

References

[1] B. Roth et al. "Low-dose photon irradiation alters cell differentiation via activation of hIK channels", Pflügers Arch.- Eur. J. Physiol. 2014 (in press).

[2] C. Gibhardt et al. "X-ray irradiation activates K+ channels via ROS signaling", JGP 2015 (submitted)

---

* Funded by BMBF 02NUK017B, DFG GRK1657 and HGS-HIRe.

DOI:10.15120/GR-2015-1-APPA-HEALTH-20

Electrophysiological response of mouse embryonic stem cell-derived cardiomyocytes after X-ray and C-ion exposure*

A. Helm[1], *S. Frank*[1,2], *J. Frieß*[2,3], *C. Thielemann*[3], *M. Durante*[1,2] *and S. Ritter*[1,#]
[1]GSI, Darmstadt, Germany; [2]Technische Universität Darmstadt, Germany; [3]University of Applied Sciences Aschaffenburg, Germany

An increased risk for late-occurring ischemic heart diseases is a known consequence of a high dose radiation exposure to the heart [1]. Yet, there is growing evidence coming from epidemiological data for an increased risk at low doses [2]. To address the question whether the electrophysiology of the heart is affected by ionizing radiation, we used mouse embryonic stem cell (mESC)-derived cardiomyocytes as a model system. Cells were cultured on a microelectrode arrays (MEA) enabling electrophysiological measurements [3] and the effects of X-rays and C-ions were examined.

Briefly, commercially available purified mESC-derived cardiomyocytes (Cor.At, Axiogenesis) that build up spontaneously beating networks were used for experiments. Cor.At cells were seeded on the fibronectin-coated MEAs according to the manufacturer's protocol. Radiation exposure was performed two days after seeding applying either C-ions (SOBP, twelve energies ranging from 107-147 MeV/u, mean LET = 75 keV/µm at target position) accelerated at the SIS18 (GSI) or 250 kV X-rays. The doses used for both radiation qualities were 0.5 and 2 Gy. Measurements were conducted up to six days following exposure. Data were subsequently analyzed with the MATLAB-based software *DrCell* developed at University of Applied Sciences Aschaffenburg [4]. Electrophysiological endpoints such as number of active electrodes, beat rate, the QT-interval-like section or the conduction velocity were determined.

Generally, inter-experimental variations were large. Therefore the data sets were not pooled. In figures 1 and 2 data on the number of active electrodes and the beat rate measured two days after exposure to 2 Gy X-rays or C-ions are exemplarily shown. As depicted in figure 1, in each experiment the number of active electrodes was not significantly changed in the irradiated samples compared to the control. The inter-experimental difference in the number of active electrodes between both data sets was pronounced (mean values of 46 and 19 active electrodes for the X-ray and the C-ion experiment, respectively). As shown in figure 2, also the beat rate was not affected by exposure to X-rays or C-ions when compared to the respective controls. Notably, inter-experimental variations of the beat-rate were lower than those observed for the number of active electrodes (about 40 vs. 60 beats/min). Similarly, the QT-interval-like section of the cardiomyocytes' signal and their conduction velocities were not altered after exposure (data not shown).

Altogether our data show that electrophysiological parameters of cardiomyoctes were not affected at two days after exposure to X-rays or C-ions. Currently, measurements performed at later time-points are analyzed to screen for putative effects occurring at later stages.

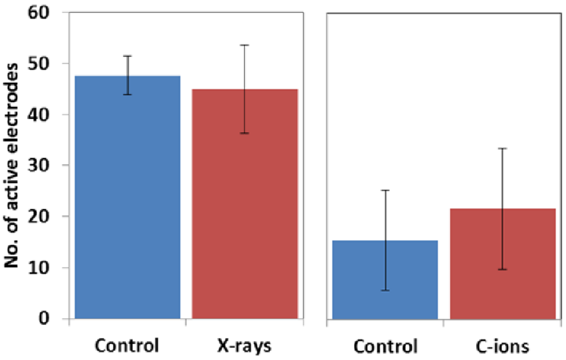

Fig. 1: Number of active electrodes. Measurements were performed two days after exposure to 2 Gy of X-rays or C-ions, respectively (mean values ± SD of a total n ≥ 8).

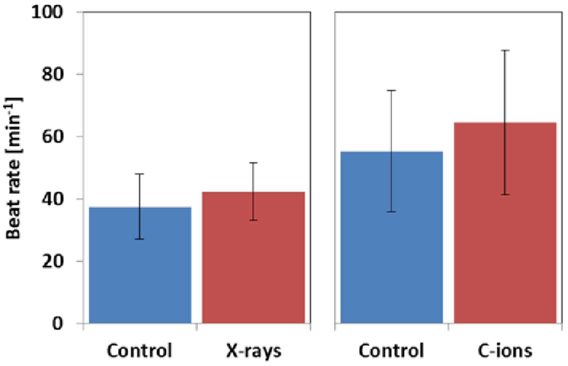

Fig. 2: Beat rate. Measurements were performed two days after exposure to 2 Gy of X-rays or C-ions, respectively (mean values ± SD of a total n ≥ 8).

References

[1] Darby et al., N Engl J Med, 2013, 368(2)
[2] Little et al., Environ Health Perspect, 2012, 120(11)
[3] Helm et al., GSI Scientific Report 2013, 211
[4] Nick et al., SPIJ, 2013, 7(2)

---

* Funded by the Euratom 7th Framework Programme under grant agreement n° 295823.

#s.ritter@gsi.de

DOI:10.15120/GR-2015-1-APPA-HEALTH-21

Modeling time effects in the incidence of deterministic effects of radiation

L. Herr[*1,2], *T. Friedrich*[1,2], *M. Durante*[1,2], *and M. Scholz*[1]
[1]GSI, Darmstadt, Germany; [2]TU Darmstadt, Germany

The Giant LOop Binary LEsion (GLOBLE) model is applicable to model time effects in the cellular response to photon radiation. Since the incidence probability for deterministic effects after irradiation, e.g. pneumonitis or the bone marrow syndrome, is thought to be closely linked to cell death, it was tested whether one can qualitatively reproduce time effects in this incidence probability with the GLOBLE model. It was found that with a decrease of the dose rate during exposure, the GLOBLE model describes very well the clinically observed increase of the dose where 50% of the patients are expected to suffer from a disease.

Methods

The GLOBLE model

The setup of the GLOBLE model is presented in detail in [1]. Briefly, the cellular response to photon radiation is predicted based on two classes of DNA double strand breaks. Isolated DSB (iDSB) reflect single DSB in DNA giant loops and are extpected to be quickly repaired by a cell (half-life time HLT_i) with low lethality (ϵ_i). Clustered DSB (cDSB) represent two or more DSB in a loop and go in hand with a long half-life time (HLT_c) and a high lethality (ϵ_c). Since the total number of DSB is assumed to be constant for a given dose, initially induced DSB are temporarily separated when the dose is protracted over a longer time. Consequently, single DSB in a giant loop might be repaired by a cell before a next DSB occurs in the same loop and the fraction of harmful cDSB decreases. The extent of the inherent reduction of the effectiveness of radiation depends crucially on the rates of DSB induction and repair and can be calculated with the GLOBLE model.

Deterministic effects of radiation

Clinically, it has been observed that the dose D_{50} at which 50% of the exposed patients start to show symptoms attributed to deterministic radiation effects depends linearly on the inverse of the applied dose rate $\dot{D}$ [2]:

$$D_{50}(\dot{D}) = \theta_\infty + \frac{\theta_1}{\dot{D}} \qquad (1)$$

For pneumonitis and the bone marrow syndrome it has been found that D_{50} after acute exposure is θ_∞ = 10 Gy and θ_∞ = 3 Gy, respectively. The extent of the dose rate effect is represented by θ_1 = 30 Gy^2/h and θ_1 = 0.07 Gy^2/h, respectively. The solid lines in figure 1 represent the graphs corrsponding to this empirical approach.

In order to describe time effects in the incidence of deterministic effects with the GLOBLE, pneumonitis and bone marrow syndrome specific parameters found in literature were converted to ϵ_i = 0.00333, ϵ_c = 0.229 and ϵ_i = 0.00333, ϵ_c = 0.09, respectively. In agreement with experimental observations about DSB repair, HLT_i was set to 0.5 h and HLT_c to 5 h.

Results

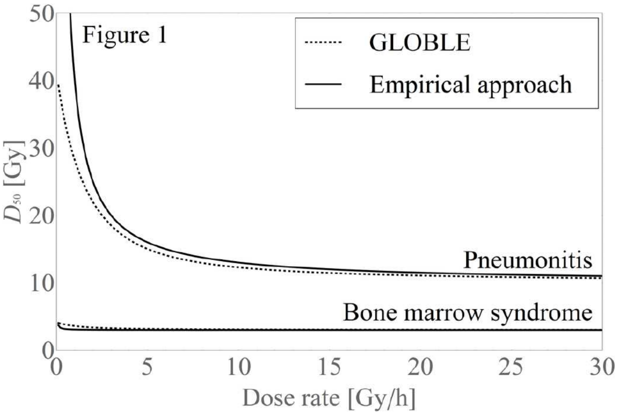

The dashed graphs in figure 1 represent the GLOBLE predictions for time effects in the incidence of deterministic effects after radiation exposure. Obviously, there is a very good agreement with empirical observations (solid lines) down to dose rates of $\dot{D} \approx 3$ Gy/h. A large increase of D_{50} with decreasing $\dot{D}$ is expected for pneumonitis whereas the increase in D_{50} is small for the bone marrow syndrome. Deviations between the empirical formulation (1) and the GLOBLE model at lower dose rates are due to the empirical prediction of infinite D_{50} for $\dot{D} \rightarrow 0$. Since finite D_{50} at low $\dot{D}$ are more plausible, the GLOBLE might provide an advantage in the assessment of the incidence probability of deterministic radiation effects at low dose rates. The general good perfomance of the GLOBLE model demonstrated here supports its potential to be clinically applied.

References

[1] Herr L, Friedrich T, Durante M, Scholz M; PLoS ONE 2014; 1(9).

[2] Edwards AA, Lloyd DC; J Radiol Prot 1998; 18(3).

---

[*] l.herr@gsi.de, supported by Studienstiftung des deutschen Volkes and HGS-Hire.

DOI:10.15120/GR-2015-1-APPA-HEALTH-22

Radiations as source of treatment for Rheumatoid Arthritis: X-rays reverse the effect of TNF-alpha in mouse micromass cultures *in vitro* *

V. Manakov[1], *G. Thangaraj*[1], *C. Fournier*[2], *and P.G. Layer*[1]
[1]Technische Universität Darmstadt, Germany; [2]GSI, Darmstadt, Germany

Introduction

Rheumatoid Arthritis (RA) is an autoimmune disorder which is associated with excess pain due to the accumulation of synovial fluid in the joints and severe cartilage destruction. It has been a huge challenge to find a treatment for this disease. Radon, an inert gas is believed to suppress the severity of the disorder. The mechanism underlying the suppression of pain after Radon exposure is not yet clear. Cholinergic anti-inflammatory pathway (CAIP) is believed to be one of the pathways involved in the suppression of inflammation, though its mechanism of action is yet to be proven. In the present study, we used ionizing radiations (X-rays) as a source of treatment. The results using in vitro cultures showed that treatment with TNF-alpha hindered cartilage and bone formation but X-rays reversed the effects of TNF-alpha. A rise in cholinesterase activity was seen after X-ray treatment, suggesting a possible the involvement of cholinergic system during treatment.

Material and Methods

11/11.5 day-old embryos from pregnant C57BLC wild type mice were collected. Mesenchymal cells were isolated from limb buds, plated as high density micro-mass cultures and incubated for 2 weeks at 37°C. The cultures were then treated with 5 or 10ng/ml human TNF-alpha to mimic a diseased condition in vitro. The cultures were exposed to 0.5, 1 and 2Gy X-rays and were fixed after 3, 5 and 7 days. Alcian blue staining marks cartilage development, while alkaline phosphatase stainings indicates differentiation of osteoblasts. Cholinesterase enzyme activity was visualized by Karnovsky-Roots staining.

Results

TNF-alpha affects mineralization in vivo. hTNF over expressing mice showed reduced Alp activity in vivo compared to wildtype mouse. Transgenic mice were treated with single dose of 0.5Gy X-rays in order to see if X-rays can effectively be used for treatment but at this dosage, no clear effects were noticed.

X-rays reverse the actions of TNF-alpha in vitro. Cultures that were exposed to 5ng/ml TNF-alpha showed severe destruction in cartilage differentiation and also mineralization. 2Gy X-rays reduced the effect of TNF-alpha to a larger extent supporting nodule formation and increased enzymatic activity for alkaline phosphatase suggesting that X-rays reverse the action of TNF but these effects were not observed at 0.5Gy in vitro.

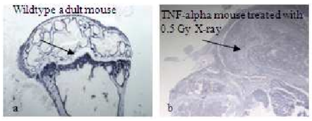

Figure 1: Alp activity in wildtype (a) and 0.5Gy x-ray treated hTNF-alpha over expressing mouse (b). Note Alp activity is severely disturbed in transgenic mouse even after X-ray treatment (arrow) in vivo.

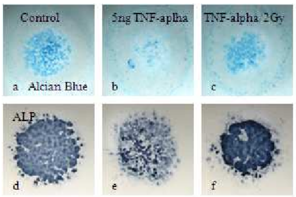

Figure 2: Note that TNF-alpha strongly disturbs cartilage formation (b, while a is control) but X-rays reversed the effects (c). A similar effect is observed in alkaline phosphatase activity as well (d-f).

X-rays increase cholinesterase activity suggesting a role of the cholinergic system during treatment. We provided a direct evidence of the involvement of cholinergic system during cartilage differentiation in our previous report. 5ng TNF-alpha suppressed acetylcholinesterase activity but nterestingly 2Gy X-rays rescued the activity.

Figure 3: Karnovsky and Roots staining for AChE activity revealed that 5ng TNF-alpha down regulated the activity (b, arrow; a, control) while 2Gy X-rays restored it (c, arrow).

Conclusion

– TNF-alpha disrupts cartilage and bone formation in vitro

– X-rays can reverse the effects of TNF-alpha

– A cholinergic mechanism might me involved during treatment

---

* Project is funded by BMBF (GREWIS, 02NUK017A).

DOI:10.15120/GR-2015-1-APPA-HEALTH-23

Biological characterization of a glioblastoma radioresistant subpopulation cells

W.Tinganelli[1], A.Helm[1], W. Kraft-Weyrather[1], B. Wezorke[1], M. Durante[1,2], C. Hartel[1], S. Ritter[1].
[1]GSI, Darmstadt, Germany; [2]Technische Universität Darmstadt

Abstract

Most of the cancers seem to be initiated by stem-like cells. They are characterized by a strong resistance to radiation and chemotherapy and they have a specific molecular signature. Besides this *in vitro* characteristic when injected in immune-deficient mice those cells are able to grow and to form a tumor. These stem-like cells are now known as cancer stem cells (CSCs or also tumor initiating cells TIC). Hypoxia, the lack of oxygen that often occurs in tumor seems to be the perfect niche for those cancer stem cells. In our work we present preliminary results concerning irradiation of TIC in oxic and hypoxic (1% oxygen) conditions with X-ray and carbon ions up to 20 Gy.

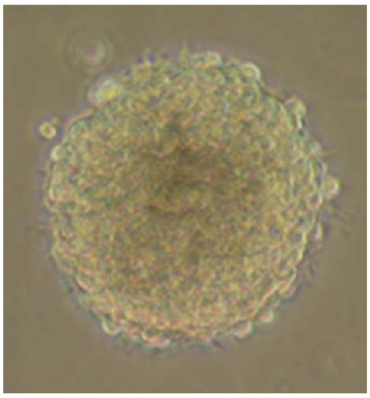

Figure 1: Tumor initiating cells growing as spheroid.

Material and Methods

Cell line: #10-IR cells were established by Dr. E. Kim [1]. **Carbon ion exposure:** energy range 114-160 MeV/u. Mean LET 70 keV/µm. **X-ray exposure:** carried out with an Isovolt DS1 X-ray machine (Seifert) operated at 250 kV and 16 mA with 7 mm beryllium, 1 mm aluminum and 1 mm copper filtering and a dose rate of 3 Gy/min. **Neurosphere formation assay:** Cells were irradiated as single cells and then seeded in 25 cm^2-tissue culture flask. After two weeks the formed spheres bigger than 50 µm were counted as survivors. **3D Spheroid Culture Cell Invasion Assay (Amsbio):** Two weeks after exposure, 50 µl of cell sphere solution were seeded into a microtiter plate with 50 µl of invasion matrix. Pictures were taken seven days after seeding. **Cancer Stem Cells RT² Profiler™ PCR Array (Qiagen):** Performed following the manufacturer‘s protocol; expression of 27 genes (triplicates) involved in pathways related to cancer stem cells were investigated. **ELISA analysis (Life technologies):** Performed following the manufacturer‘s protocol.

Results

Survival curve of irradiated cells revealed a subpopulation of radioresistant cells. This subpopulation (around 20% in oxia and 50% in hypoxia) is resistant up to 20 Gy of X-ray (Fig 2) and carbon ion irradiation (data not shown).

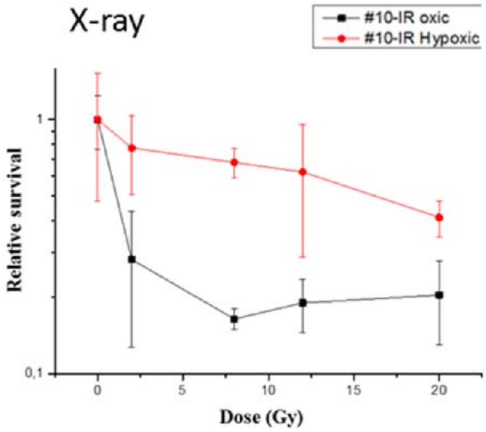

Figure 2: #10-IR cells irradiated with X-ray up to 20 Gy in oxic and hypoxic conditions.

Vascular endothelial growing factor is a cytokine that stimulates vasculogenesis and angiogenesis. Few studies claim that glioblastoma radioresistance may be enhanced by VEGF release [2] and recent studies have demonstrated that VEGF is responsible for the cells’ increase in stemness [3].

Results show that #10-IR cells after irradiation and/or hypoxia increased their VEGF release. The increase was 8 times after carbon ion irradiation (8 Gy) and more than 6 times after 8 Gy of photon irradiation (Fig 3).

Hypoxia seems to be a strong enhancer of the VEGF production. At 8 Gy of carbon ion irradiation, the amount of cytokine release is over 40 times higher compared to the oxic control (data not shown).

DOI:10.15120/GR-2015-1-APPA-HEALTH-24

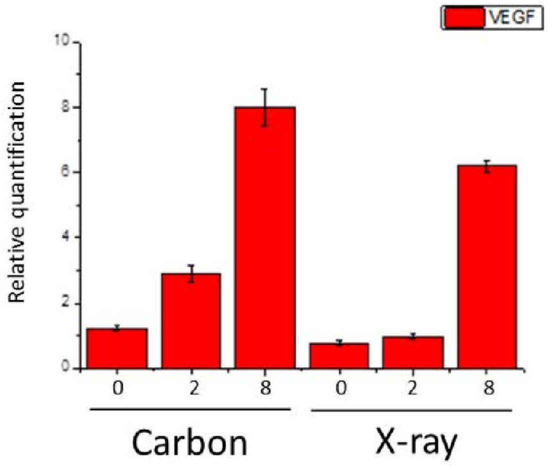

Figure 3: #10-IR Relative quantification of VEGF after exposure to carbon ions and X-ray.

Further investigations were performed to identify the molecular and phenotypical signature of the cells' subpopulation.

First, the invasion capacity was studied two weeks after irradiation (Fig 4). Pictures of the spheres were taken for the sham-irradiated control (panel A) and spheres derived from the progeny of cells exposed to 8 Gy of carbon (B) or X-ray (C). Analysis was performed measuring the outer area of the spheres as well as the inner sphere part (i.e. not migrated) of at least 20 spheres per dose. The two values were then set in relation to estimate the sphere's invasion capacity (data not shown).

The control was found to be highly invasive (panel A), whereas radiation exposure lead to a reduction in the invasiveness. Carbon ions were found to be more effective with respect to the invasiveness reduction at iso-doses of 8 Gy (panel B and panel C).

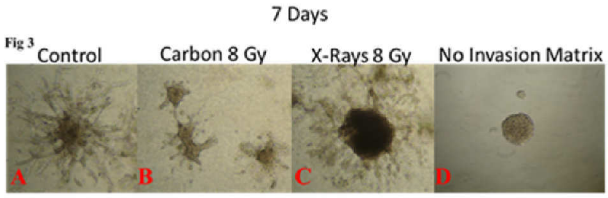

Figure 4: Invasion assay. Panel show sham-irradiated controls (A) and spheres derived from cells exposed to 8 Gy of carbon ions (B) or X-ray (C). Panel D displays a negative control where no matrix gel was added.

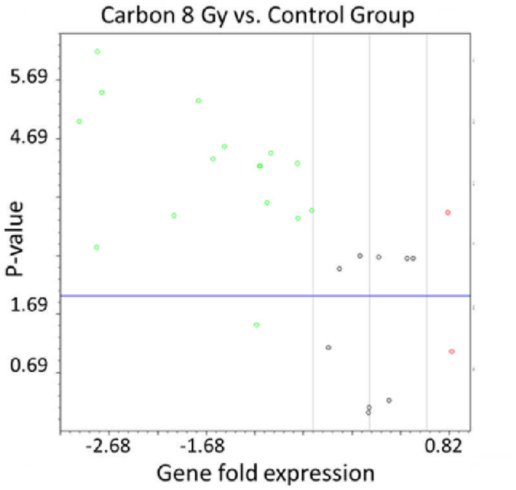

Figure 5: Fold-change results using ΔΔC(t) calculations. The x-fold expression of genes is plotted versus the p-value (green dots: down-regulated genes, red dots: up-regulated, black dots: fold-change is not significantly changed as compared to the control.

Most of the genes involved in the cancer stem cell pathways were down-regulated after exposure to 8 Gy carbon ion.

Conclusion

A radioresistant subpopulation of cells was found in the glioblastoma cell line used in this study. VEGF is well known to stimulate angiogenesis and is discussed to be responsible for an increased stemness and radioresistance of cells. In this work a correlation between radiation under hypoxic conditions and higher VEGF release was found. The increase of dose or the lack of oxygen is directly correlated with the increase in VEGF release. Tridimensional gel assay was used to investigate the invasiveness of this resistant subculture. Particle radiation was found to be more effective than photon radiation to reduce the *in vitro* invasiveness. Moreover, our results suggest that particle radiation affects the expression of genes related to cancer stem cell pathways. Additional experiments are currently performed to confirm these results and to further characterize the subpopulation.

References

[1] Barrantes-Freer A et al. Human glioma-initiating cells show a distinct immature phenotype resembling but not identical to NG2 glia. J Neuropathol Exp Neurol. 72(4) 307-24. 2013.

[2] Hovinga KE et al. Radiation-enhanced vascular endothelial growth factor (VEGF) secretion in glioblastoma multiforme cell lines--a clue to radioresistance? J Neurooncol. 74(2): 99-103. 2005.

[3] Sarah Seton-Rogers. Cancer stem cells: VEGF promotes stemness Nature Rev. Cancer 11(12) 831. 2011.

DOI:10.15120/GR-2015-1-APPA-HEALTH-24

Retrospective analysis of treatment plans robustness in image-guided carbon ion treatment of skull-base tumours.

G. Fattori[1], M. Riboldi[1], E. Scifoni[2], M. Krämer[2], M. Durante[2,3],R. Orecchia[4,5] and G. Baroni[1,4]
[1]Politecnico di Milano, Milano, Italy; [2]GSI, Darmstadt, Germany; [3]Technische Universität, Darmstadt, Germany;
[4]CNAO foundation, Pavia, Italy; [5]IEO, Milano, Italy;

Clinical procedures for patient positioning are designed to minimize systematic errors in the treatment geometry. However, despite the use of advanced technologies, anatomical variations and practical issues limit the accuracy of daily setup. In addition, the estimation of stopping power for different tissues from CT data has intrinsic uncertainties.

In order to quantify the degradation of dose distribution due to such residual uncertainties, we have retrospectively tested the robustness of intensity modulated carbon ion plans for the treatment of clivus chordoma.

Materials and Methods

Ten patients treated at the Centro Nazionale di Adroterapia Oncologica (IT) were selected for this study. The treatment consisted of 16 fractions, 4.4 Gy (RBE) each. In our study we considered the enlarged PTV applied in the first 10 fractions before boosting the treatment to a smaller volume. The PTV was obtained by applying 2 mm expansion from the CTV. The brainstem was included as organ at risk, with a maximum 30% of the fraction dose.

We derived the setup errors from the clinical practice at the institution [1] featuring six degrees of freedom couch and 2D-3D image registration software. We have identified the ±1.0 mm and ±1.0° ranges to cover the 95% of observed residual setup errors. Orthogonal sampling was applied on the error space, thus defining 64 trials to explore the effects of setup errors in a statistically equivalent dataset. Accordingly, the patients' planning CTs were rigidly transformed and considered for dose recalculation.

Treatment planning was based on TRiP98 and LEM-I ($\alpha/\beta = 2$) using 6 mm beam FWHM with 2 mm by 3 mm raster grid in lateral and depth dimensions.

We have evaluated DVH bands at 95% ($D95_{CTV}$) and 105% ($D105_{CTV}$) dose for CTV and 5% ($D05_{OAR}$) for the brainstem. In addition, inhomogeneity (IC) and conformity (CI) indexes were calculated for the CTV.

Setup error cases resulting in larger variation on the target DVH were considered for the analysis of stopping power uncertainties. Only the worst-case scenario reported by Rietzel et al. [2] for head&neck tissues was considered, thus applying ±2.6% deviations from nominal values.

Results

On 7 patients out of 10, the $D95_{CTV}$ error was always below 10% in presence of setup errors. Instead, larger discrepancies were observed in combination with range uncertainties, whereas their effect on the organ at risk is related to the specific patient anatomy (Figure 1).

The CI_{CTV} exhibited reduced sensitivity to setup errors with respect to the IC_{CTV}. Conversely, range uncertainties affected significantly the CI_{CTV}, but minor variations were reported for IC_{CTV}. Higher values for IC_{CTV} in nominal conditions were reported to be prone to large deviation when uncertainties occur. Finally, a strong correlation ($\rho = 0.91$) was found between the nominal treatment plan IC_{CTV} and its score in presence of setup errors.

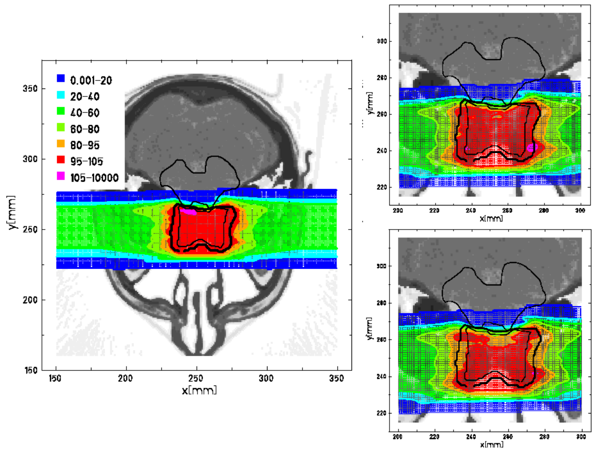

Figure 1: axial dose cut in nominal geometry (left panel), in presence of setup errors (top-right panel) and combination of setup and HU-WE uncertainties (bottom-right panel).

Conclusions and outlook

We have recalculated the patient dose in presence of setup and range errors to test the treatment plan robustness. Even though conformity is generally preserved, the combination of setup and range errors has an impact on the treatment quality. On this basis, we have further investigated the role of fractionation to mitigate the patient dose degradation [3].

References

[1] Desplanques M et al. A comparative study between the imaging system and the optical tracking system in proton therapy at CNAO. J Radiat Res 2013;54:i129–35.
[2] Rietzel E et al. Range accuracy in carbon ion treatment planning based on CT-calibration with real tissue samples. Radiat Oncol 2007;2:14.
[3] Fattori G et al. Dosimetric effects of residual uncertainties in carbon ion treatment of head chordoma. Radiother Oncol 2014; 133 (1):66-71.

DOI:10.15120/GR-2015-1-APPA-HEALTH-25

Radiation response related to inflammation and differentiation in human skin*

J. Wiedemann[1,2], *P. Simoniello*[1], *E. Thönnes*[1], *A. Benzer*[1], *M.Durante*[1,2], *M. Kovacs*[4], *M. Podda*[4], *and C. Fournier*[1,3]

[1]GSI, Darmstadt, Germany; [2]TU Darmstadt, Germany; [3]Hochschule Darmstadt, Germany; [4]Department of Dermatology, Darmstadt Hospital

Introduction

The balance between apoptosis, proliferation and differentiation is important for the homeostasis of healthy skin [1]. In psoriatic skin this balance is disturbed and shifted in the direction of proliferation [2].The symptoms of psoriasis can be alleviated by irradiation with low intensities of UV-light [3] or low doses of ionizing irradiation, such as alpha-particels emitted from a radon source [4]. These effects of UV exposure in skin are quite well understood [3], whereas alterations in skin induced by low doses of ionizing irradiation which explain the clinical effectiveness of radon treatments remain to be elucidated.

We investigated if irradiation with low and clinically used fractionated doses shifts the disturbed balance of apoptosis, proliferation and differentiation back to a normal level by enhancing apoptosis and/or reducing proliferation.

Material and Methods

Human full-thickness skin equivalents (EFT400; MatTek; Ashland) were irradiated using low versus high and single versus fractionated X-ray doses. Samples were fixed 3 days after irradiation and processed for immunohistchemistry. Proliferation was assessed microscopically and Ki67$^+$ cells per field of view were counted. To analyse the status of differentiation sections were stained with Hematoxylin and Eosin.

Results and Discussion

Histological analysis (H&E staining) shows that after low dose X-ray irradiation the basal cells loose their palisadic shape and become more rounded up. This effect is more pronounced after a single dose of 0,5 Gy compared to a fractionated irradiation with 3x 0,17 Gy. The cobblestoned morphology can be related to proliferation of the basal cells which can be a sign of a faster or impaired differentiation process. An enhanced proliferation in the basal layer after a low dose of irradiation could be confirmed by quantification of Ki67 (Figure 2) but was not observed for high X-ray doses like 10 Gy (data not shown). Interestingly, also for a fractionation of 0,5 Gy in 3 doses of 0,17 Gy this effect didn't occure pointing to that a single treshold dose has to be delivered to trigger proliferation .

In addition to the observed changes in morphology of the basal cells which have an impact on tissue organisation and the enhanced proliferation for a low X-ray dose we could show in previous studies that there is no enhancement of cell death (apoptosis and necrosis) after low dose of irradiation. This argues against a irradiation induced shift to enhanced apoptosis and reduces proliferation after low doses. These effects has to be further investigated in a model system which mimics the inflammatory state of psoriatic skin.

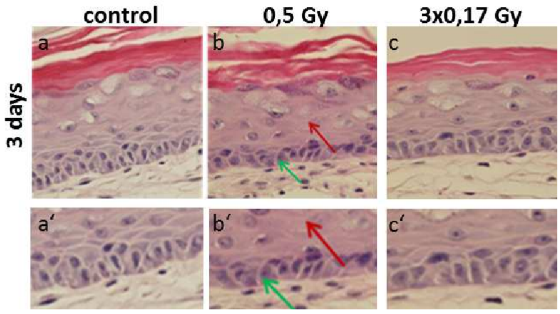

Figure 1: H&E staining of sections from skin equivalents. Changes in the shape of the basal cells (green) and the stratification (red) are indicated with arrows. Pictures a' to c' show a magnification of the basal cells

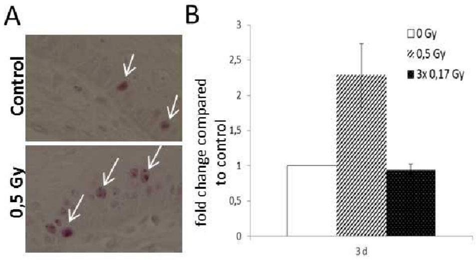

Figure 2: (A) Ki67 staining of skin equivalents. Proliferating cells are labeled in pink and indicated with an arrow. (B) Statistical analysis of Ki67 staining

References

[1] P. Kolarsick et al.,J Dermatol Nurses Assoc, Volume 3, 2011

[2] M. Lowes et al., NATURE Vol 445—22 February 2007, doi:10.1038/nature05663

[3] K. Stein., J Dermatolog Treat.. 2008; 19: 141–145

[4] P. Deetje et al., Verlag Dr. Kovac, 2005

---

* Work supported by GREWIS No. 02NUK017A; DFG (GRK 1657) and HGS-HIRe.

DOI:10.15120/GR-2015-1-APPA-HEALTH-26

NF-κB-dependent DNA damage-signaling differentially regulates DNA double-strand break repair mechanisms in immature and mature human hematopoietic cells

Daniela Kraft[1],, Melanie Rall[2],*, Meta Volcic[2],*, Eric Metzler[1], Aljona Groo[1], Andreea Stahl[2], Daniela Salles[2], Gisela Taucher-Scholz[1], Halvard Bönig[3], Claudia Fournier[1,#], Lisa Wiesmüller[2,#]*
[1] GSI Helmholtz Center for Heavy Ion Research, [2] Department of Obstetrics and Gynecology, Ulm University, [3]Institute for Transfusion Medicine and Immunohaematology, German Red Cross Blood Center, Frankfurt,
*, # these authors contributed equally to this work

Introduction

Hematopoietic stem and progenitor cells (HSPC) are the presumed target for leukemic transformation, which can be induced by ionizing radiation due to failed repair of DNA double-strand breaks (DSBs) and generation of chromosomal rearrangements. As little is known about the repair of radiation-induced DSBs and its accuracy in HSPC, we explored the activity, quality, and molecular components of DSB repair in human HSPC as compared with mature peripheral blood lymphocytes (PBL).

Materials and Methods

The enrichment of HSPCs from CD34+ cell population and PBL from the peripheral blood of healthy donors as well as cultivation were performed as described [1,2]. The usage of different pathways of DSB repair was measured using a plasmid based EGFP-reporter system [3]. To measure repair following inhibition of NF-κB signaling additionally IκBα-SR expression plasmid was added to the DNA mixture. In the NF-κB reporter assay a reporter plasmid for NF-κB-dependent GFP production was included. The statistical significance of differences was determined using nonparametric Mann-Whitney test for unpaired samples (**P*<0.05, ***P*<0.01, ****P*<0.001) with the software GraphPad Prism 5.01. Columns show mean values; bars, SEM.

Results

The measurements of the reconstitution of EGF wildtype gene of the reporter plasmid revealed that HSPC were severely compromised in the usage of Non-homologous end joining (NHEJ) and HR+SSA (Fig. 1), but not in microhomology mediated end joinig (not shown). This result indicates a differential repair pathway usage between HSPC and PBL, although formation and removal of γH2AX foci (not shown) and induction and rejoining of chromosomal breaks [4] is similar for both cell types. Functional screening analysis revealed that DNA repair kinases (ATM/ATR/DNA-PK), p53 signaling and chromatin remodeling do not play a major role in the pathway usage. However, overexpression of the NF-kB inhibiting protein IkBα reduces HR pathway usage in PBL significantly, but not in HSPC (Fig. 2a), pointing to NF-kB signaling as the molecular component underlying the observed differences in pathway usage. This is consistent with the higher transcriptional activity of NF-kB for PBL compared to HSPC observed in a NF-kB reporter assay (Fig. 2b). The low NF-kB activity in HSPC is also related to a concomitant accumulation of 53BP1 foci after irradiation [5] that in turn limits the expression of DSB repair genes and bears a risk for inaccurate repair.

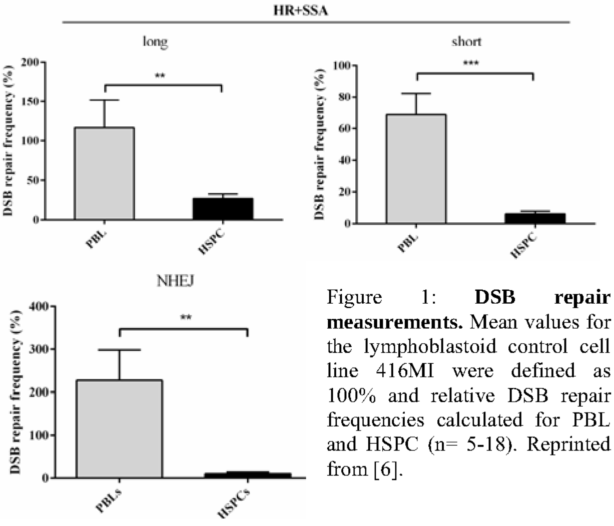

Figure 1: **DSB repair measurements.** Mean values for the lymphoblastoid control cell line 416MI were defined as 100% and relative DSB repair frequencies calculated for PBL and HSPC (n= 5-18). Reprinted from [6].

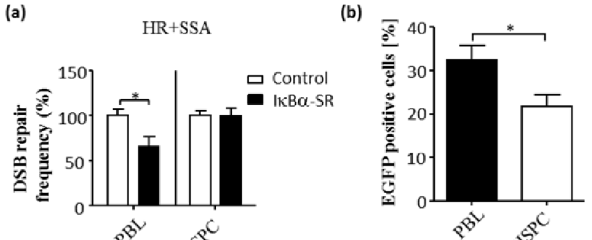

Figure 2: **(a) DSB repair measurements following inhibition of NF-κB signaling.** Mean values for samples nucleofected with control plasmid were set to 100% for each cell type and each experimental day (n=6-12). (b) **NF-κB reporter assay** (n=6). Reprinted from [6].

References

[1] Becker D., IJRB, 2009
[2] Bauer L.et al., GSI report 2011
[3] Akyüz et al., Mol Cell Biol, 2002
[4] Bauer L. et al., GSI report 2011
[5] Becker D. et al., GSI report 2012
[6] Kraft D. et al, Leukemia 2015

Supported by ESA/DLR (A0-10-IBER-2), partially BMWi (50WB1225); DFG, PA3 in Research Training Group 1789 (CEMMA), GRK1657 to A.G.

DOI:10.15120/GR-2015-1-APPA-HEALTH-27

The influence of ionizing radiation on differentiation and function of osteoclasts*

L. Deloch[1#], A. Groo[2#], N. Hoengl[2], B. Frey[1], D. Kraft[2], M. Durante[2,3], U.S. Gaipl[1#], C. Fournier[2#]
[1]Strahlenklinik, UK Erlangen, [2]GSI, Darmstadt, Germany; [3]Technische Universität Darmstadt

Introduction

Rheumatoid Arthritis (RA) is a chronic inflammatory autoimmune disease that has a prevalence of about 1% and is more frequent in women than in men. It is usually accompanied by a symmetric Polyarthritis (PA) with synovial infiltration and invasion of inflammatory immune cells [1]. This often leads to local and systemic cartilage and bone destruction by osteoclasts (OC) as well as inhibition of bone formation by osteoblasts [2]. While there are effective treatments for RA and other degenerative musculoskeletal diseases there are patients that do not respond to these therapies or have to abort treatments due to health related problems. In this case a treatment with low dose-radiotherapy (LD-RT) can be helpful to modulate the immune system and thus lead to an anti-inflammatory effect [3]. However the underlying mechanisms are only fragmentarily understood.
This is why we have examined the effects of LD-RT on osteoclast progenitor cells from healthy donors and on the differentiation of osteoclasts derived from the bone marrow of h*TNF-α* tg mice, an accredited inflammatory mouse model for RA [4].

Material and Methods

Bone marrow from the long bones of 5-6 week old h*TNF-α* tg mice was isolated and stimulated with media containing 10ng M-CSF and 50ng RANK-L. 24h after seeding cells were treated with various doses of X-rays. TRAP-Stain (Sigma) positive cells with at least 3 nuclei were counted as OCs. Decalcified paw sections from locally irradiated animals were analysed using the Osteomeasure™ software (Osteometrics). Human OCs were generated from buffycoats of healthy donors (blood donor service Frankfurt/Main). Differentiation of human OCs from monocytes was initiated by adding RANKL (45 ng/ml) and M-CSF (25 ng/ml). The resorbing activity of OCs was detected on bovine bone slices via toluidin blue staining. Irradiation was performed with X-rays (1Gy/min).

Results

The numbers of differentiated h*TNF-α* tg bone marrow-derived OCs were significantly reduced after administration of X-ray doses of 0.05 – 2.0 Gy (Fig.1A).

Investigation of decalcified, paraffin embedded paw sections revealed a reduction in OCs/mm² in irradiated paws of h*TNF-α* tg mice in comparison to non-irradiated control animals (Fig. 1B). As a functional analysis, the resorptive activity of human OCs after irradiation was determined by calculating the area of resorption pits (Fig.1C). OCs resorbed significantly less bone after exposure to both, low and high dose of X-rays.

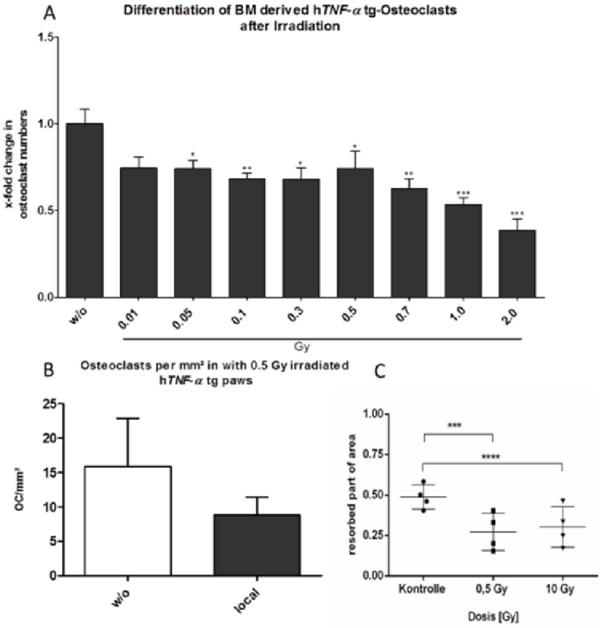

Figure 1: A) Murine bone marrow-derived OCs after treatment with various doses of X-rays. The x-fold change in relation to non-irradiated control cells is displayed. *p<0.05; **p<0.01; ***p<0.001 B) OCs/mm² in TRAP stained paw sections of locally irradiated hTNF-α tg mice as well as control animals (w/o). C) Resorbing activity of human OCs quantified by resorption pits via toluidin blue staining (N=2, n=4).

Conclusion

We suggest a useful supportive role of LD-RT for patients suffering from RA and other degenerative musculoskeletal and inflammatory diseases as X-rays have a considerably decelerating effect on osteoclast differentiation and impair their function. This was not only observed *in vitro/ex vivo,* but also *in vivo* in mice with established PA. This provides an indication that, especially in a pre-existing inflammatory state, X-rays are capable of attenuating the bone-destruction by OCs.

References

[1] Feldmann, M., F.M. Brennan, and R.N. Maini, Rheumatoid arthritis. Cell, 1996. 85(3): p. 307-10.
[2] Schett, G. and J.P. David, The multiple faces of autoimmune-mediated bone loss. Nat Rev Endocrinol, 2010. 6(12): p. 698-706.
[3] Arenas, M., et al., Anti-inflammatory effects of low-dose radiotherapy. Indications, dose, and radiobiological mechanisms involved. Strahlenther Onkol, 2012. 188(11): p. 975-81.
[4] Keffer, J., et al., Transgenic mice expressing human tumour necrosis factor: a predictive genetic model of arthritis. Embo j, 1991. 10(13)

---

* Work supported by BMBF, Grant 02NUK017A and 02NUK017G
# Contributed equally

DOI:10.15120/GR-2015-1-APPA-HEALTH-28

Differentiation of osteoblasts and adipocytes following irradiation*

A.Groo[1,#], *K.Shreder*[1,#], *T.Huhn*[1], *D.Kraft*[1], *H.Bönig*[3], *M.Durante*[1,2], *C.Fournier*[1]
[1]Helmholtzzentrum für Schwerionenforschung GSI, [2]Technische Universität Darmstadt,[3]Institut für Transfusionsmedizin und Immunhämatologie Frankfurt am Main
# these authors contributed equally to this work

Introduction

Chronic inflammatory diseases such as Rheumatoid Arthritis (RA) or Ankylosing Spondylitis are associated with dysregulation of the balance between remodelling and degradation of bones. Chronic inflammatory disorders are treated with anti-inflammatory drugs, but also with ionizing radiation, where joints are locally irradiated with low doses of photons or the patients are exposed in galleries or baths to the α-emitter radon (1). Despite the clinical success, the cellular and molecular mechanisms are largely unknown. As inflammatory processes are closely linked to the regulation of bone metabolism (2) and the differentiation of mesenchymal stem cells (MSC) into osteogenic or adipogenic progenitor cells is linked to bone formation or the production of fat cells (3), we hypothesize that radiation exposure could shift the balance from adipocytes to bone forming osteoblasts (OBs) and thereby counteract the inflammatory processes and bone resorption.

Materials and Methods

OBs were generated from bone marrow aspirates of healthy donors (blood donor service Frankfurt/Main). Differentiation of OBs was initiated by adding β-glycerophosphat and ascorbic acid. Protein expression was analysed by qRT-PCR. Adipocytes were differentiated from commercially available pre-adipocytes (Lonza) by addition of defined adipogenic cocktail, including insulin and 3-isobutyl-1-methylxanthine. Mature adipocytes were identified by Oil Red O staining. Irradiation was performed with X-rays (1Gy/min).

Results

Protein release in osteoblasts following irradiation

The measurement of protein release in OBs following X-ray exposure (Fig.1) has shown that low and moderate dose of ionizing radiation leads to increased protein release of osteocalcin (OCN) (Fig.1), which contributes to bone matrix formation. This results are in line with our previous results (4),where we observed up to 3x fold increased calcium deposition of OBs following exposure to low and moderate doses of X-rays, indicating an accelerated differentiation. However the release of osteoprotegerin (OPG), an inhibitor of osteoclastogenesis, was not affected by irradiation. This indicates that radiation influences rather bone formation than the maturation of osteoclasts via OPG release from irradiated OBs.

Differentiation of Adipocytes

The ongoing experiments include the analysis of gene and protein expression, related to the differentiation of adipocytes and release of pro-inflammatory factors in mature adipocytes after irradiation. The first results do not show significant changes in the differentiation capacity of preadipocytes, assessed by the lipid accumulation (Fig.2). Taken together radiation exposure has an influence on the differentiation progress of osteoblast precursor cells, but not adipocytes precursor cells.

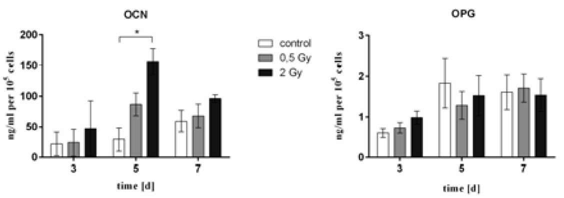

Fig. 1: Protein release in irradiated OBs with X-rays (0.5;2 Gy) after 3, 5 and 7 days. Mean, SEM (N=3). *P<0.05

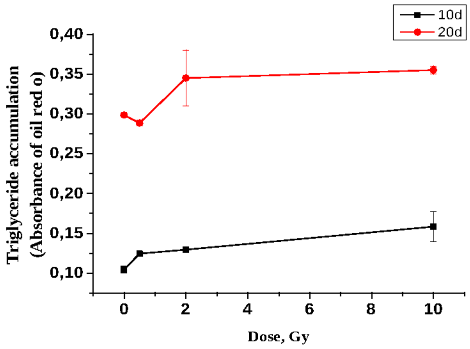

Fig. 2: Effect of X-ray irradiation on adipocyte differentiation. Quantification of stained lipid content in mature adipocytes using Oil Red O extraction and photometric measurement at 540 nm 10/20 days after irradiation. Mean, SEM (N=2)

References

1) BE.Erickson et al, J Altern Complement Med. 2007Apr;13(3):375-79
2) N.Udagawa et al, Arthritis Res. 2002 (4): 281-289
3) I.Takada et al, Nature 2009 Jul 7
4) A.Groo et al, GSI annual reports 2012

---

*Work supported by BMBF (02NUK017A Grewis) and DFG(GRK1657)

DOI:10.15120/GR-2015-1-APPA-HEALTH-29

Complex DNA double strand breaks induced by heavy ions require resection for their repair*

N. B. Averbeck[1], O. Ringel[1], M. Herrlitz[1], T. Syzonenko[1], B. Jakob[1], G. Becker[1], M. Durante[1,2], and G. Taucher-Scholz[1,2]

[1]GSI Helmholtzzentrum für Schwerionenforschung, Darmstadt, Germany; [2]TUD, Darmstadt, Germany

DNA double strand breaks (DSBs) represent harmful lesions, which can jeopardize genomic stability and even can be lethal. Therefore, different repair pathways exist to remove them. The pathway choice is influenced by the complexity of the lesions, which are increasingly difficult to repair with increasing complexity.

Inducing DSBs of a wide range of complexity by irradiating mammalian cells with X-rays or accelerated ions of different velocity and mass, we found that with increasing complexity DSBs become increasingly resected in all cycle stage [1]. To find out whether the observed resection of complex DSBs is relevant for their repair, we measured DSB repair kinetics of ion- and X-ray induced DSBs in cells that were impaired for resection by depletion of the resection factor CtIP (Fig. 1).

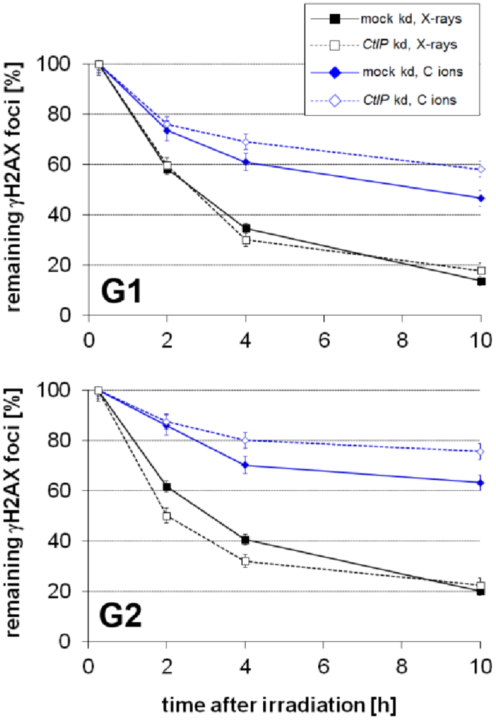

Figure 1[#]: Repair of complex DSBs is resection dependent. Human, immortalized fibroblasts were depleted or mock depleted for CtIP and irradiated with 1.3 Gy X-rays or carbon-ions (LET 170 keV/μm). Aphidicolin treatment prevented G1-cells from moving on to G2 and allowed to discriminate S-phase cells. DSB-repair kinetics were measured by the γH2AX (DSB marker)-foci assay [2] in G2- (CENP-F positive) and G1-cells (CENP-F negative).

We clearly see impaired DSB repair upon C-irradiation, which is due to the increased lesion complexity and was described earlier. CtIP depletion impairs repair of C-ion induced complex DSBs in G2- and G1-cells, but not of X-ray induced DSBs of lesser complexity. Thus, abolished resection does not allow repair of complex DSBs to switch to resection independent pathways suggesting that the pathway choice of these lesions is forced towards resection-dependent repair. Taken together, resection plays an important role within the repair of complex DSBs.

Resection of simple DSBs is cell cycle regulated via 53BP1/RIF1 and BRCA1/CtIP, where the former prevent resection and are replaced by the latter to allow resection in G2-cells [3]. As complex DSBs are resected even in G1-cells we started to analyze how the above factors are involved in the resection regulation of complex DSBs. Therefore, in a first step we studied whether RIF1 is recruited to ion-induced DSBs. We clearly see that RIF1 is recruited to Xe-induced DSBs in G1- and S/G2-cells (Fig. 2); data analyses revealed that almost all G1- and half of S/G2-phase cells are RIF1 positive. Future studies will reveal how resection of ion-induced DSBs is regulated.

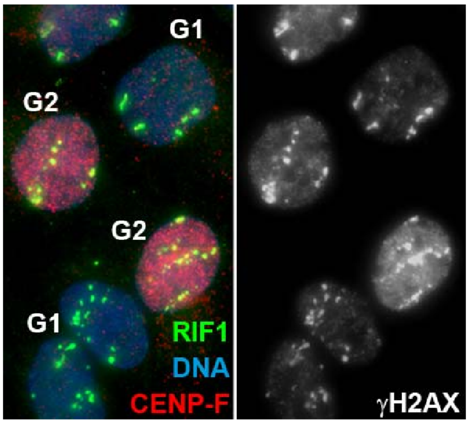

Figure 2: RIF1 is recruited to ion-induced DSBs in G1 and G2-cells. Human osteosarcoma cells were irradiated with Xe-ions in a low angle (9,000 keV/μm; 11.4 MeV/u; 3 x 10^6 p/cm^2) and fixed 1 h after irradiation. CENP-F (red): cell cycle marker, γ-H2AX (white): DSB marker.

References

[1] N. Averbeck *et al.*, “DNA end resection is needed for the repair of complex lesions in G1-phase human cells”, Cell Cycle (2014) 13(16): p. 2509-16.
[2] M. Löbrich *et al.*, “γH2AX foci analysis for monitoring DNA double-strand break repair”, Cell Cycle (2010) 9(4): p.662-9.
[3] J. Lukas and C. Lukas, “Shielding broken DNA for a quick fix”, Science (2013) 339: p. 652 -3.

---

* This work is part of HGS-HIRe and was partially funded by BMBF grant 02NUK001A.

modified version of fig. 3A in [1]; reprinted by permission of Taylor & Francis LLC (http://www.tandfonline.com)

DOI:10.15120/GR-2015-1-APPA-HEALTH-30

PT-PET imaging during arrhythmia ablation in porcine hearts using carbon ion beams

Stephan Helmbrecht[1], *Anna Constantinescu*[2], *Marco Durante*[2], *Wolfgang Enghardt*[3,4], *Anna Eichhorn*[2], *Christian Graeff*[2], *Immo Lehmann*[5], *Patrick Lugenbiel*[6], *Douglas Packer*[5], *Matthias Prall*[2], *Dierk Thomas*[6], *and Fine Fiedler*[1]

[1]Helmholtz-Zentrum Dresden-Rossendorf, Institute of Radiation Physics, Dresden, Germany; [2]GSI, Darmstadt, Germany; [3]Helmholtz-Zentrum Dresden-Rossendorf, Institute of Radiation Oncology, Dresden, Germany; [4]Oncoray, National Center for Radiation Research in Oncology, Faculty of Medicine and University Hospital Carl Gustav Carus, Technische Universität Dresden, Helmholtz-Zentrum Dresden-Rossendorf; [5]Mayo Clinic/St. Marys Hospital, Rochester, MN, USA; [6]University of Heidelberg, Heidelberg, Germany

Introduction

Scanned carbon ion beams were used for arrhythmia ablation in a porcine heart model [1]. The PET system [2] installed at GSI's medical cave M was used for treatment inspection by measurement of the activity distribution that is created as a side product during irradiation. This was the first application of the Particle Therapy-PET technique to monitor carbon ion irradiations of target volumes in the heart.

Materials and Methods

The target volumes were AV-node (AVN), LA-PV junction (PVI), and freewall LV. The doses applied were 25, 40 and 55 Gy in the AVN cases and 40 Gy in the other cases, respectively. Each animal was irradiated with two fields in one single fraction. The PET measurement was performed during the spill pauses and after the irradiation of the first field in each case. The end of the measurement was 10 to 39 min after the end of the irradiation. During the measurements the animals were kept under apnoea to avoid blurring of the activity due to breathing motion. Therefore, a conventional 3D image reconstruction and analysis regime was applied.

Results

PET imaging could be performed successfully in all investigated cases. Examples for the different target volumes are shown in the figures 1, 2 and 3. The activity distributions were obtained from the coincidences captured during the spill pauses of the irradiation. The colorwash image representations are overlaying the contrast agent enhanced X-ray CT images. The activity distribution was nicely related to the target volumes. Severe influences due to biological washout in the extremely well perfused target region was observed as expected. This holds especially true for the PVI cases.

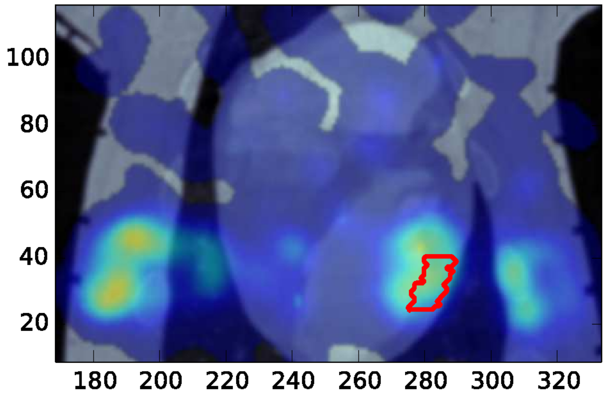

Figure 1: Activity distribution in an freewall LV case overlaying the contrast agent enhanced CT. The beam impings from the left side of the image plane. The target volume is delineated with red color.

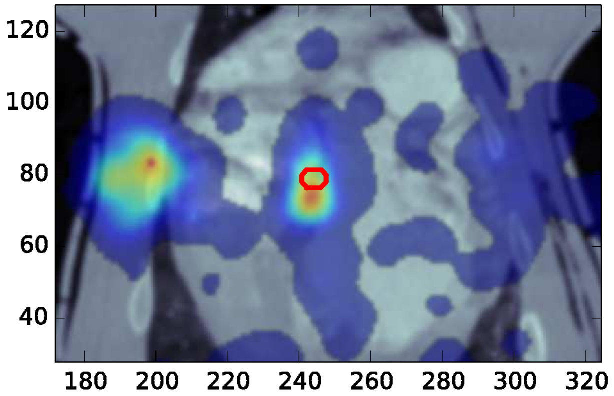

Figure 2: Frontal view of the activity distribution in an AVN case overlaying the contrast enhanced CT. The beam impinges from the left side of the image. The target volume is delineated with red color.

Conclusion

The application of carbon ion beams for treatment of volumes in the heart can be monitored by means of PET. The extreme perfusion conditions require a setup which allows

DOI:10.15120/GR-2015-1-APPA-HEALTH-31

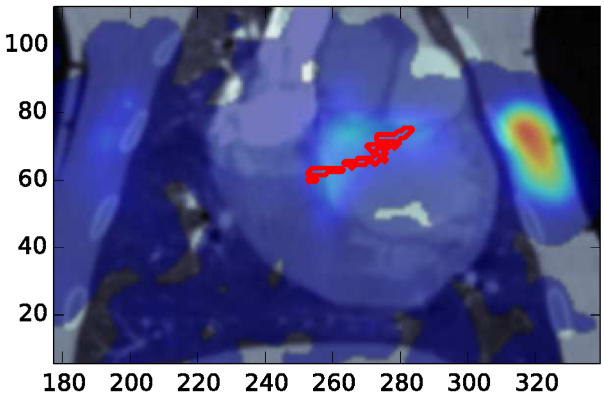

Figure 3: Frontal view of the activity distribution in a LA-PV junction case overlaying the contrast enhanced CT. The beam impinges from the right side of the image. The target volume is delineated with red color.

for a measurement during or immediately after the irradiation. Furthermore, a modeling of the washout is crucial to perform a meaningful prediction of the activity distribution.

References

[1] C. Graeff, H. I. Lehmann, A. Constantinescu, P. Simoniello, P. Lugenbiel, M. Prall, D. Richter, M. Takami, A. Eichhorn, N. Erbeldinge, C. Fournier, R. Kaderka, S. Helmbrecht, F. Fiedler, J. Debus, D. Thomas, C. Bert, M. Durante, D. L. Packer, GSI Scientific Report 2014 (2015), ?

[2] W. Enghardt, P. Crespo, F. Fiedler, R. Hinz, K. Parodi, J. Pawelke, F. Pönisch, "Charged hadron tumour therapy monitoring by means of PET" Nucl. Instr. Meth. A, 2004, 525, 284–288

DOI:10.15120/GR-2015-1-APPA-HEALTH-31

Reproducible immobilization for porcine heart irradiations

M. Prall[1], *H. I. Lehmann*[2], *A. Constantinescu*[1], *P. Simoniello*[1], *P. Lugenbiel*[3], *D. Richter*[1], *M. Takami*[2], *A. Eichhorn*[1], *N. Erbeldinger*[1], *C. Fournier*[1], *R. Kaderka*[1], *K. Anderle*[1], *S. Helmbrecht*[4], *F. Fiedler*[4], *J. Debus*[3], *D. Thomas*[3], *C. Bert*[1], *M. Durante*[1], *C. Graeff*[1], *and D. L. Packer*[2]

[1]GSI Darmstadt (Germany); [2]Heart Rhythm Services, Mayo Clinic (USA); [3]University of Heidelberg, Germany;
[4]Helmholtz-Zentrum Dresden-Rossendorf, Germany

Hadron therapy has already proven to be successful in cancer therapy, and might be a non-invasive alternative for the ablation of cardiac arrhythmias in humans.

In order to experimentally investigate this treatment modality, scanned carbon beams from the GSI accelerator were used to irradiate various targets in beating hearts of healthy pigs. Dose ranging from 25 Gy to 55 Gy was applied during breath-hold in the 100 % expiratory phase under anesthesia. The alignment and breathing phase during irradiation had to reproduce the situation of the treatment planning CT (TPCT) with an accuracy of a few millimeters. A pig immobilization device (PID) allowing reproducibility of shape and position was designed (cf. Figure 1).

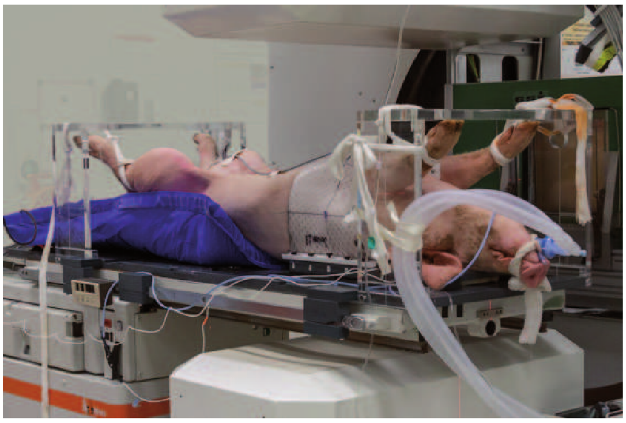

Figure 1: A pig in irradiation position in Cave M at GSI.

Both, TPCT scans and irradiations were performed during breath-hold in the 100 % expiratory phase. Animals were kept in deep anesthesia in order to completely suppress spontaneous lung motion. A computer-controlled ventilator was used (Evita XL by Dräger Medical). With this device, animals were ventilated with intermittent positive pressure ventilation with 14 breathing cycles per minute, 350 ml tidal volume, a positive end-expiratory pressure of 0 mbar and an oxygen concentration of 20 %. A LabVIEW interface running on a personal computer was implemented for remote control, data logging and communication with the beam application and monitoring system at GSI.

TPCTs where acquired at Heidelberg Ion-Beam Therapy Center (HIT) and irradiation was applied at GSI Darmstadt a few days later. This situation was experimentally simulated to estimate the degree of reproducibility: The immobilization and TPCT scan of a test animal was repeated at HIT with about one week delay. For the analysis, one of the two TPCTs first was shifted such that the PIDs were coincident in both scans. A displacement vector field relating the two scans was derived using deformable registration with the Plastimatch module of the medical image analysis software 'Slicer' (B-spline deformable registration, regularization=0.1, grid size=20). Displacement vectors with an absolute magnitude (AM) of more than 5 mm can only be observed in the beating heart. In the remaining volume, the AM is below 5 mm. Throughout the backbone and large parts of the sternum, AM is below 3 mm. AM up to 4 mm can be observed in the lateral chest walls.

Shortly before irradiation, X-ray images were taken both in dorsoventral and lateral direction at Cave M. They were acquired under breath-hold, exactly as during irradiation. Exposure time was about one second. Therefore the target itself, the beating heart, is smeared out and nearby structures had to be used to verify reproducibility of breath-hold. Pairwise comparison of the positions of selected anatomical structures (vertebrae, sternum, diaphragm) was employed. Images were preprocessed using affine and rigid registration. The plugin Landmark Correspondences of the medical image analysis software 'ImageJ' was used. Reproducibility of breath-hold is in the order of 1 mm or below for all anatomical sites considered.

Based on the available data we estimate that the PID combined with a breath-hold, controlled by a clinical ventilator, allows to reproduce the geometrical situation of the TPCTs with an accuracy of better than about 5 mm for the anatomy surrounding the heart (backbone, sternum, chest walls). In irradiations, heart-beat motion was mitigated using the rescanning technique (cf. these proceedings). We currently investigate additional perturbations due to geometrical and temporal variability of the heart motion.

Irradiated animals were dissected after a follow-up period of about six months. The desired target regions exhibit fibrotic tissue, suggesting that immobilization and motion mitigation were sufficient. Analysis is ongoing and numerous technical and biological factors (cf. these proceedings), still under investigation, will influence the final result.

Acknowledgements

The Helmholtz Association funded this work through the Helmholtz-Portfolio Topic "Technology and Medicine". We thank Harry Leidel from the GSI workshop and Elko Schubert for supporting us with the development of the pig immobilization device.

DOI:10.15120/GR-2015-1-APPA-HEALTH-32

Radon diffusion through tissue*

J. Baasner[1,2], *A. Maier*[1], *D. Schardt*[1], *J. Breckow*[2], *M. Durante*[1], *C. Fournier*[1], *G. Kraft*[1]
[1]GSI, Darmstadt, Germany; [2]THM, Gießen, Germany.

For a better understanding of the molecular mechanism of its anti-inflammatory effects we want to investigate the radon diffusion through tissue. In parallel work we measured the primary radon uptake via γ-spectroscopy of the short living radon daughter nuclei Pb-214 and Bi-214 [1]. However, in such experiments the diffusion of radon through tissue cannot be measured directly. Here we report preliminary results on the radon diffusion using alpha spectroscopy.

Experimental Setup

In the diffusion chamber (fig. 1) biological samples like muscle, fat or cartilage can be inserted and exposed to radon at different concentrations when placed inside the larger radon chamber [2]. The diffusion chamber consists of an upper and a lower part which can be screwed together and holds the various samples in between. In the lower section a silicon-detector is used to detect alpha-particles from Rn-222 (half-life 3.8 d) and its decay daughters Po-218 (3.05 min.) and Po-214 (164 µs).
Radon gas can reach the small volume above the detector only by diffusion through the sample.

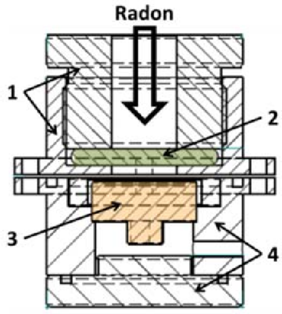

Fig. 1: Measurement setup, 1: upper part, 2: sample, 3: detector, 4: lower part

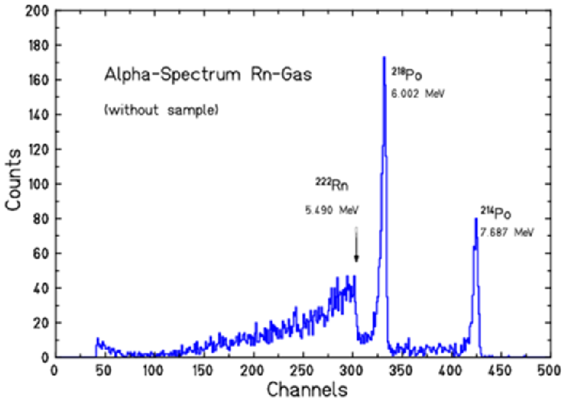

Fig. 2: Alpha spectrum recorded without sample. Acquisition time 2 hours

As a reference we measured spectra of Rn-222 and its daughter nuclei without sample (fig.2). An Am-241 alpha source placed in front of the detector was used for energy calibration. The spectrum shows a broad distribution for alpha particles emitted in Rn-222 decays (range in air 3.9 cm) in the gas volume above the detector, while the decays of the daughter products Po-214 and Po-218 seem to take place mainly at the detector surface (narrow peaks).

Results

In the measurements carried out so far different tissues were exposed with different Rn concentrations over 120 minutes and the corresponding alpha spectra were recorded in intervals of 10 minutes. In fig. 3 we show first results from cartilage tissue with a thickness of 2.5mm. The amount of Radon-222 obtained by integration of the alpha spectrum up to 5.49 MeV is plotted versus time. As expected, the curve for the higher radon concentration during exposure gives higher values than the lower radon-concentration. But the time until reaching saturation is for both samples nearly the same.

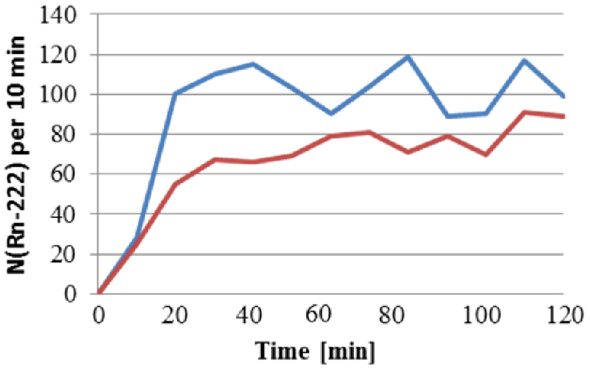

Fig. 3: Integrated amount of Radon-222 in cartilage with different radon concentration: upper curve: 394 ± 6 kBq/m^3, lower curve: 218 ± 5 kBq/m^3

Conclusion

In this work we developed a new method to measure the radon diffusion though various materials via alpha spectroscopy. In first measurements we demonstrated the feasibility of this method and obtained first results. In the future we plan systematic measurements with improved statistics and studies of different types of tissue with different thicknesses. Using this novel technique one can obtain quantitative results necessary to optimize our model for the radon diffusion in different tissues and the distribution of radon in the human body.

[1] A. Maier, P. van Beek, M. Durante, C. Fournier, J. Hellmund, G. Kraft, Radon solubility in different types of tissue, GSI Scientific report 2014

[2] C. Fournier, G. Kraft, A. Maier, Untersuchungen zum genetischen Risiko und zur entzündungshemmenden Wirkung von Radon, StrahlenschutzPRAXIS, 1/2014

---

* Work is supported by BMBF project funding reference number 02NUK017A

DOI:10.15120/GR-2015-1-APPA-HEALTH-33

Comparison of RBE-weighted doses for different ion types in various tissue type combinations

R. Grün[1,2,3], *T. Friedrich*[1], *M. Krämer*[1], *K. Zink*[2,3], *M. Durante*[1,4], *R. Engenhart-Cabillic*[3], *and M. Scholz*[1]

[1]GSI, Darmstadt, Germany; [2]Institute of Medical Physics and Radiation Protection, TH-Mittelhessen, Gießen, Germany; [3]Medical Faculty of Philipps-University Marburg, Germany; [4]TU Darmstadt, Germany

Introduction: The advantage of particle therapy is the inverse depth profile of the ions compared to conventional X-ray irradiation with a higher dose to the tumor region as compared to the surrounding normal tissue. For particle therapy the application of different ion types offer different physical and biological advantages. The purpose of this study is to assess the advantages of ions interesting for particle therapy, i.e. carbon (^{12}C), helium (^{4}He) and protons (^{1}H) for the particular treatment cases of radioresistant tumors and radiosensitive normal tissue, commonly parametrized by the ratio of the parameters α and β from the linear-quadratic (LQ) model with $\alpha/\beta = 2\,\mathrm{Gy}$ in the tumor region (T) and 10 Gy in the normal tissue (N), and vice versa.

Methods: A treatment planning analysis based on idealized target geometries was performed using the treatment planning software TRiP98 [1]. For the prediction of the relative biological effectiveness (RBE) that is required for biological optimization in treatment planning the Local Effect Model (LEM IV) was used [2]. To compare the three ion types the peak-to-entrance ratio (PER) was determined for the physical dose ($\mathrm{PER_{PHYS}}$), the RBE ($\mathrm{PER_{RBE}}$) and the RBE-weighted dose ($\mathrm{PER_{BIO}}$) resulting for different dose-levels, field configurations and tissue types. The peak position value, i.e. dose or RBE, is determined in the center of a 50 mm spread out Bragg peak (SOBP) and the entrance channel (EC) position value at 20 mm proximal from the SOBP.

Results: Figure 1 shows that the advantages of the ions, expressed by a high $\mathrm{PER_{BIO}}$, depend on the physical and biological properties and the interplay of both [3]. In the case of protons the consideration of a variable RBE instead of the clinically applied generic RBE of 1.1 indicates an increased $\mathrm{PER_{BIO}}$ due to an increased $\mathrm{PER_{RBE}}$ for the analyzed configuration. The blue line at a $\mathrm{PER_{RBE}}$ of 1.0 in fig.1 refers to a generic RBE of 1.1 for protons and marks the typical range of the $\mathrm{PER_{PHYS}}$ due to the depth modulation method [4]. Carbon ions show the largest variation of the $\mathrm{PER_{RBE}}$ with tissue type and dose and a benefit for radioresistant tumor types due to their higher LET. Helium ions show an intermediate $\mathrm{PER_{PHYS}}$ and $\mathrm{PER_{RBE}}$ for the α/β-ratio combination of 2_T,10_N. In contrast, for the α/β-ratio combination of 10_T,2_N the three ion types show similar $\mathrm{PER_{BIO}}$, thus indicating no ion type and dose dependence for this tissue type combination.

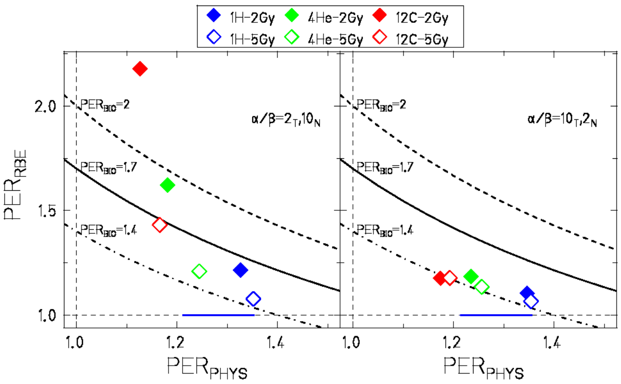

Figure 1: $\mathrm{PER_{RBE}}$ versus $\mathrm{PER_{PHYS}}$ in the case of a 1-field irradiation for protons (blue), helium (green) and carbon (red) at two different optimized RBE-weighted doses of 2 Gy (RBE) (closed symbols) and 5 Gy (RBE) (open symbols), respectively. Left: α/β-ratio combination of 2_T,10_N. Right: α/β-ratio combination of 10_T,2_N. Lines of a constant $\mathrm{PER_{BIO}}$ are added to guide the eye.

Conclusion: The study demonstrated that there is no unique choice concerning the optimal ion for radiotherapy. The expected therapeutic advantage strongly depends on biological as well as physical factors in combination with the treatment field configuration. Protons show a favourable physical depth dose profile compared to helium and carbon ions and are superior especially for radiosensitive tumors. Carbon ions are characterized by a high $\mathrm{PER_{RBE}}$ which is particularly pronounced at lower doses and for radioresistant tumors and are most beneficial in a single field treatment. Helium ions gain from both, the $\mathrm{PER_{PHYS}}$ and $\mathrm{PER_{RBE}}$ and favour of an intermediate $\mathrm{PER_{BIO}}$. Further, for the tissue type combinations with an α/β-ratio of 10_T,2_N the ion type and dose dependence for the case of a 1-field irradiation is negligible since the $\mathrm{PER_{RBE}}$ of helium and carbon ions is dumped and eventually similar to that of protons which seems rather independent on the tissue type combination.

References:

[1] M. Krämer and M. Scholz, Phys Med Biol, (2000) **45**:3319.

[2] T. Elsässer et al., Int J Radiat Onc Biol Phys (2010) **78**:1177.

[3] R. Grün et al., Med Phys, (2015) **42**:1037.

[4] B. Arjomandy et al., Phys Med Biol (2009) **54**:295.

DOI:10.15120/GR-2015-1-APPA-HEALTH-34

Cytokine release and adhesion of immune cells to cardiac endothelial cells [*]

N. Erbeldinger[1,5], *M. Liebig*[1,5], *T. Dettmering*[1], *D. Lowe*[2], *B. Baselet*[3], *R. Benotmane*[3], *S. Tapio*[4], *K. Raj*[2], *M. Durante*[1,5], *and C. Fournier*[1]

[1]GSI, Darmstadt, Germany; [2]Public Health England, Oxford, UK; [3]SCK-CEN, Belgium;
[4]HelmholtzZentrumMünchen, Germany; [5]TU Darmstadt, Darmstadt, Germany

Introduction

The cardiovascular system is nowadays well established as an organ of risk for accidental and therapeutic irradiation. Exposure of the cardiovascular system even with low doses (up to 2 Gy) can lead to an increased risk for the development of cardiovascular diseases (CVD) [1,2]. The underlying mechanism of developing CVD is putatively based on changed cytokine release of vascular cells (endothelial cells and smooth muscle cells), although their interactive pattern is still not understood [3]. In order to investigate the effect of low dosed X-irradiation on the first steps of CVD, we measured cytokine release and adhesion of immune cells after irradiation of cardiac endothelial cells, mimicking the inner layer of an *in vivo* blood vessel. Following we discuss the release of transforming growth factor $\beta 1$ (TGF-$\beta 1$), a cytokine which can have both profibrotic and anti-inflammatory effects, and its relevance on the adhesion of peripheral lymphocytes (PBL) to an endothelial monolayer.

Material and Methods

Human coronary artery endothelial cells (HCAEC) were immortalized by *est2* expression. For analysis of cytokine release, cells were cultured for 3 days prior irradiation. After irradiation with 0.05, 0.1, 0.5 and 2 Gy X-rays, medium supernatants were collected after 4 h, 24 h, 1 week and 2 weeks and frozen at −80°C. Medium was replaced after irradiation/24 h before each time point. TGF-$\beta 1$ concentrations were quantified using ELISA (eBioscience). For functional adhesion assays, FITC-tagged PBL were purified from donor blood and incubated with an EC monolayer 4 h/24 h after irradiation. The adhered PBL were microscopically quantified. Data were analyzed using a custom pipeline written in the R language.

Results and Discussion

In Figure 1A the release of TGF-$\beta 1$ after irradiation of an EC monolayer is shown 4 h after irradiation. In comparison to the unirradiated control, there is a trend towards an increased release after low doses (0.05 to 0.5 Gy), but no change after high doses (2 Gy). In comparison to those results, Figure 1B illustrates the relative adhesion of PBL to an EC monolayer. After irradiation with low doses (0.05 − 0.1 Gy), there is no change in adhesion of PBL detectable, whereas for high doses (0.5 − 2 Gy) increased adhesion takes place.

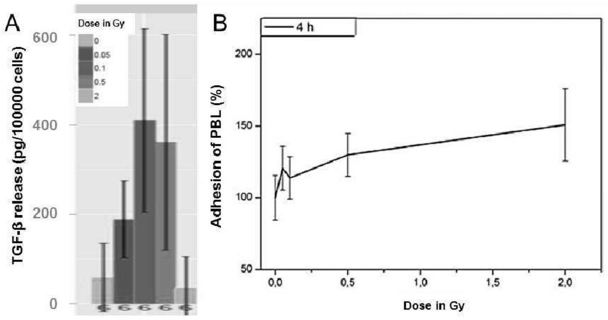

Figure 1: TGF-$\beta 1$ release and adhesion of PBL 4 h after irradiation of an EC monolayer. N=2, n=6.

Cytokine release is well described to mediate attraction of immune cells to damaged tissue, i.e. after irradiation [4]. TGF-$\beta 1$ has pleiotropic properties, since it is a known anti-inflammatory and profibrotic cytokine. The presented results 4 h after irradiation show correlation between no changes in relative adhesion of immune cells and increased TGF-$\beta 1$ release for low doses (0.05 − 0.1 Gy). After irradiation with the highest dose X-ray (2 Gy), no changes in TGF-$\beta 1$ release can be detected in parallel to an increased relative adhesion. This implies dependence between adhesion of immune cells and TGF-$\beta 1$ release, but cannot explain the increased TGF-$\beta 1$ release and in parallel increased adhesion after 0.5 Gy. This points toward an influence of TGF-$\beta 1$ on the adhesion of immune cells, but shows no exclusive interference between both mechanisms. This is in good agreement of the current dogma, that stimulation of the immune system is a complex process, orchestrated by multiple cytokines and other factors.

References

[1] Boerma and Hauer-Jensen. Cardiol Res Pract. 2010 Oct 4;2011. pii: 858262.

[2] Adams et al. Semin Radiat Oncol. 2003 Jul; 13(3):34656.

[3] Schultz-Hector et al. Int J Radiat Oncol Biol Phys 2007 Jan 1; 67(1):108.

[4] Libby et al. Nature. 2011 May 19;473(7347):317-25. doi: 10.1038/nature10146.

---

[*] The research leading to these results has received funding from the Euratom Seventh Framework Programme under grant agreement no. 295823 ("PROCARDIO").

DOI:10.15120/GR-2015-1-APPA-HEALTH-35

Validity analysis of the single ion approach for TLD efficiency calculations *

D.Boscolo[1], *E.Scifoni*[1], *M.Durante*[1], *V.Rosso*[2], *and M.Krämer*[1]
[1]GSI, Darmstadt, Germany; [2]Pisa University, Pisa, Italy

The, recently developed, single ion approach represents a basically analytical method to calculate the relative effectiveness of thermoluminescent detectors [1]. This approach computes the detector response starting from the response of a single ion of the beam. The dose contributions coming from the neighboring tracks are assumed to sum up linearly. This condition is not always satisfied and restricts the validity range of the model especially for high fluences.

In order to test this limitation relative effectiveness calculations have been performed at fixed energy for different fluence values, Figure 1. As expected, for relatively low fluences (below 10^8 cm^{-2}), the effectiveness does not change and the single ion approximation is valid. However, increasing the fluence, supra-linear and saturation effects in the inter-track region start to be significant and affect the relative effectiveness calculation.

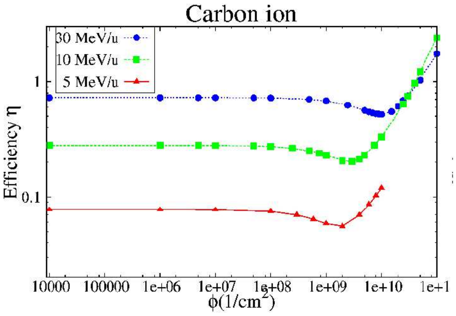

Figure 1: Relative effectiveness calculation with the single ion approach varying the fluence, for carbon ions of different energies.

Moreover, the single ion approach requires the knowledge of the radial dose distribution $D(r)$ and a parametrization of the low-LET dose-response curve for the dosimeter, $TL(D)$ [1]. In the original version of the method we adopted the sub-model implemented in ECLaT[2] and, afterwards, a robustness analysis against changes in these input models has been performed.

In Figure 2 the impact on the effectiveness calculations of two different sets of parameters for the low-LET dose-response curve is shown. The first set (dashed red line) reproduces with a good accuracy the linear region while slightly under-estimates the supra-linearity; this leads to larger values for the relative effectiveness with respect to the second set (solid blue line) which, instead, better reproduces the supra-linearity region in the dose-response curve.

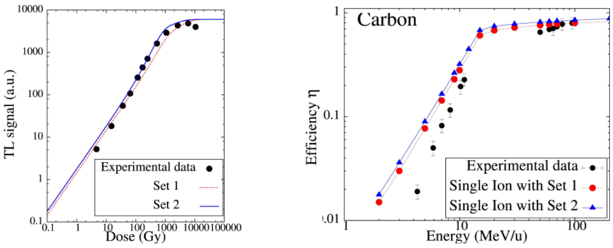

Figure 2: On the left: two possible parametrizations for the low-LET dose-response curve. On the right:relative effectiveness curves calculated with the two different parametrizations

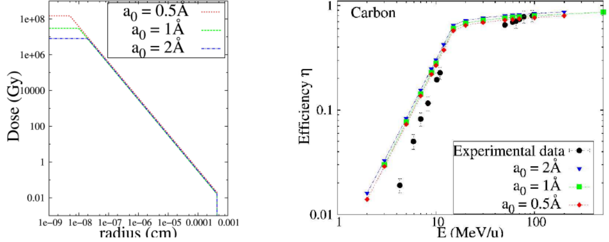

Figure 3: On the left: radial dose distributions for 10 MeV/u carbon ion calculated for different values of the core size a_0. On the right: the impact of the core size a_0 on effectiveness calculation for TLD-700.

Regarding the radial dose distribution the robustness of the method against changes in the core size, a_0, has been tested. On the left panel of Figure 3 the radial dose distribution around the ion for different values of a_0 is shown while, on the right one, effectiveness calculations for different radial dose distribution are compared. For the smaller core, $a_0 = 0.5$ Å, the efficiency values are lower. This observation is consistent with the fact that decreasing the core size the dose in the inner region of the radial dose distribution increases and, thus, the saturation effect is more pronounced.

We can therefore conclude that, although the single ion approach is still at the first stage of development and the single ion approximation limits its validity, it is robust against changes in the input sub-models and the approximation is verified for a wide range of flueces (up to $10^8\mathrm{cm}^{-2}$), including the fluence range used for clinical applications.

References

[1] D.Boscolo *et al.*, "TLD Efficiency calculation for heavy ions: a new approach", GSI Scientific Report 2013 (2014).

[2] O. B. Geiß , *et al.*, "Efficiency of thermoluminescence detectors to heavy charged particles". NIM B, 142:592–598, 1998.

---

* Work supported by University of Pisa Erasmus Placement scholarship.

DOI:10.15120/GR-2015-1-APPA-HEALTH-36

Combined effects of ionizing radiation and cardio-active drugs on human iPSC-derived cardiomyocytes*

J. L. Frieß[1], *A. Heselich*[2], *S. Ritter*[2], *P. G. Layer*[3] *and C. Thielemann*[1]
[1]University of Applied Sciences Aschaffenburg, biomems lab, Germany;
[2]GSI, Biophysics, Darmstadt, Germany;
[3]TU Darmstadt, Developmental Biology and Neurogenetics, Darmstadt, Germany

Motivation

There are multiple cardio-active pharmaceuticals available on the market, extracting various electrophysiological effects upon the human heart. These effects are well known and well characterized [1]. However, there is virtually no information on the combined effects of applied heart pharmaceuticals in conjunction with ionizing radiation. A deeper insight in these effects, however, is of great interest for occupationally exposed groups, heart patients receiving radiation treatments, as well as astronauts. Therefore we examined the influence of X-rays on drug-treated human induced pluripotent stem cell (hiPSC)-derived cardiomyocyte cultures. As a test substance isoproterenol, an analogon of the stress hormone adrenaline, was applied. The applied X-ray dose was 2 Gy. Electrophysiological parameters of the cultures were measured using microelectrode array (MEA) technology for 7 days after radiation exposure. Our results show an increase in the beat rate enhancing property of isoproterenol one day after irradiation. Direct radiation effects on the drug itself could be excluded. This poses many questions on the combined effects of ionizing radiation and stress response.

Materials&Methods

Human induced pluripotent stem cell (hiPSC) –derived cardiomyocytes (Cellular Dynamics, Madison, WI, USA) were cultured on microelectrode array chips (Multichannel Systems, Reutlingen, Germany) for 5 days prior to the experiment (Figure 1). Electrophysiological properties of the cell cultures were measured before and after exposure. Cardiac signals could be recorded for 7 days after treatment and were analyzed in terms of beat rate, conduction velocity, field action potential duration and general spike shape, using the MATLAB-based software DrCell [2]. X-irradiation was performed with 250 kV at 16 mA at a dose rate of 2 Gy/min. First only culture medium supplemented with 500 nM isoproterenol was irradiated with 2 and 7 Gy of X-ray and subsequently applied to the cardiomyocytes. Effects of the irradiated chemical on the cells were monitored for one day. Then cultures were treated with 500 nM of isoproterenol and subsequently irradiated with 2 Gy X-rays. Electrophysiology was then monitored for another 7 days.

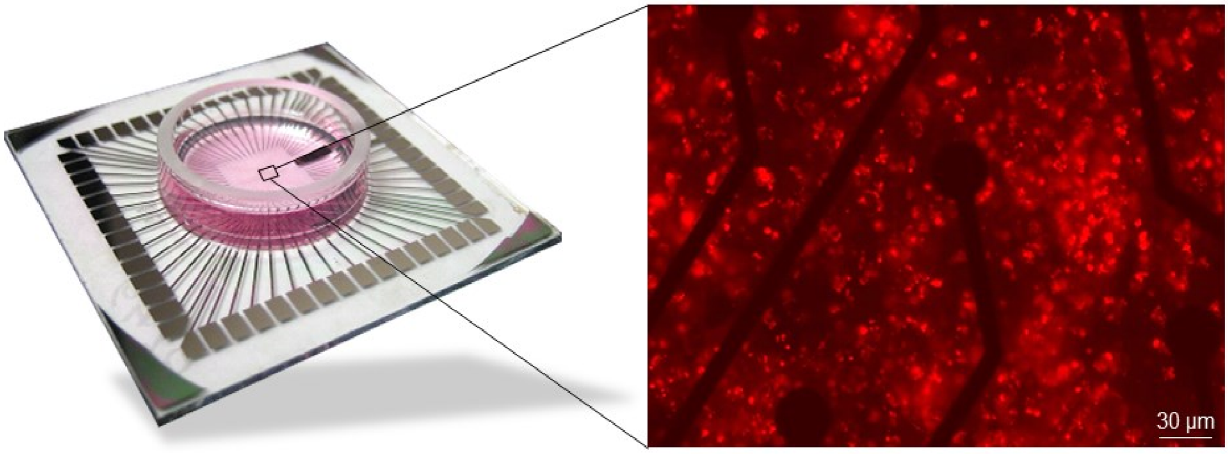

Figure 1: Human induced pluripotent stem cell-derived cardiomyocytes cultured on a microelectrode array at a 100× magnification. Myosin heavy chains are genetically marked with red fluorescent protein. Microelectrodes have a diameter of 30 µm.

DOI:10.15120/GR-2015-1-APPA-HEALTH-37

Results

In a study performed by Guo et al., it was shown that isoproterenol, has a beat rate enhancing effect on hiPSC-derived cardiomyocytes [3]. To examine if ionizing radiation alters the effectiveness of isoproterenol, culture medium containing 500 nM isoproterenol was irradiated with 2 and 7 Gy, respectively. These irradiated media were administered to the cultures and electrophysiology was monitored for 1 day. The experiments showed that irradiation with up to 7 Gy X-rays had only minor effects on the beat rate enhancing property of the pharmaceutical, 1 day after application (Figure 2).

After exclusion of possible radiation-induced effects on the chemical, cardiomyocyte cultures were first treated with isoproterenol and subsequently irradiated with 2 Gy X-rays. The cultures were measured daily for seven days after exposure. One day after treatment, the beat rate of samples exposed to 2 Gy X-ray and 500 nM isoproterenol increases above all other samples (Figure 3).

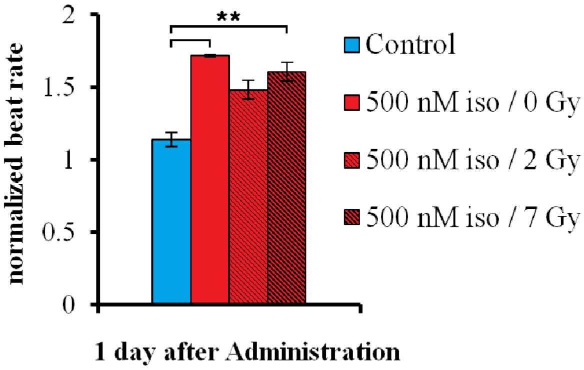

Figure 2: The beat rate enhancing property of isoproterenol is only marginally affected by X-irradiation, 1 day after administration. Data represent medians normalized to the controls before treatment. Error bars represent standard error. $N_{\text{controls}} = 6$; $N_{\text{isoproterenol}}$ 0; 2; 7 Gy = 3 (statistics were performed by two-tailed unpaired t-test, CI = 95%, **$P < 0.01$).

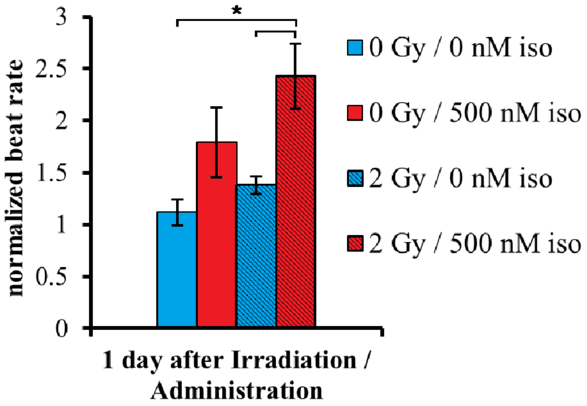

Figure 3: X-irradiation further enhances the beat rate of cardiomyocytes treated with 500 nM isoproterenol, one day after irradiation. Data represent medians normalized to the controls before treatment. Error bars represent standard error. N = 5 (statistics were performed by two-tailed unpaired t-test, CI = 95%, *$P < 0.05$).

Summary

Our data indicate that the exposure to ionizing radiation of cardiomyocytes pre-treated with isoproterenol may further increase the enhanced beat rate of cardiomyocytes. This effect possibly harbours yet unknown threats to people occupationally exposed to ionizing radiation and are either taking heart pharmaceuticals or are exposed to stress, as isoproterenol chemically resembles the stress hormone adrenaline.

References

[1] M. Reppel, P. Igelmund, U. Egert, F. Juchelka, J. Hescheler, I. Drobinskaya, Effect of cardioactive drugs on action potential generation and propagation in embryonic stem cell-derived cardiomyocytes, Cellular Physiology and Biochemistry, 19 (2007) 213-224.

[2] C. Nick, M. Goldhammer, R. Bestel, F. Steger, A. Daus, C. Thielemann, DrCell – A Software Tool for the Analysis of Cell Signals recorded with Extracellular Microelectrodes, Signal Processing: An International Journal (SPIJ), (2013) 96-109.

[3] L. Guo, R.M. Abrams, J.E. Babiarz, J.D. Cohen, S. Kameoka, M.J. Sanders, E. Chiao, K.L. Kolaja, Estimating the risk of drug-induced proarrhythmia using human induced pluripotent stem cell-derived cardiomyocytes, Toxicological sciences : an official journal of the Society of Toxicology, 123 (2011) 281-289.

---

* This work is supported by the DLR and ESA in the frame of the ESA IBER-10 program. Grant #: 50WB1226 And in parts by the German federal ministry of education and research (BMBF). Grant#: 02NUK037A.

DOI:10.15120/GR-2015-1-APPA-HEALTH-37

Expression of housekeeping markers in pluripotent or differentiating mouse embryonic stem cells (ESC) in response to ionising radiation (IR)*

O. Arrizabalaga[1], A. Helm[1], P. Hessel[1], M. Durante[1,2] and S. Ritter[1,#]
[1]GSI, Darmstadt, Germany; [2]Technische Universität Darmstadt, Germany.

ESC are pluripotent cells that have the ability to self-renew indefinitely and, due to their pluripotency, can also give rise to all cell types of the three germ layers. Pluripotent cells and differentiating cells show a completely different protein expression pattern. Housekeeping markers are used for normalization when quantifying protein or RNA expression in cells. They are proteins whose expression does not vary during different stages of the cell; for example during the cell cycle, under hypoxia conditions, or in the case of pluripotent cells, during their differentiation process. Housekeeping markers are used as loading controls for normalizing the quantity of the protein or RNA.

Since exposure to IR affects the expression of genes, including housekeeping ones and the extent of this effect also depends on the cell line, it is important to assess the stability of the genes in each system [1]. Moreover, the use of the geometric mean of more than one housekeeping marker is recommended to reduce variability [2].

In the present study we analysed three housekeeping markers: 18S rRNA, GAPDH and EEF2 in differentiating embryoid bodies (EB), as described previously [3]. EBs were formed from pluripotent mouse D3 ESC which had been irradiated with 0 Gy, 3 Gy X-ray (250 kV, 16 mA) or 3 Gy C-ions (25 mm SOBP, 106-147 MeV/u) [4]. Samples were collected at different time points during the differentiation process. RNA was purified and reverse transcribed according to the manufacturer's instructions (MasterPure RNA purification kit, Epicentre; and High Capacity RNA-to-cDNA kit, Applied Biosystems). 18sRNA, GAPDH and EEF2 RNA expression was analysed using QuantiTect Primer Assays (Qiagen) with Fast SYBR Green master mix (Life Technologies) to amplify the cDNA on a StepOnePlus Real-Time PCR system (Life Technologies).

The expression pattern of the three markers is shown in **Fig. 1**. NormFinder software, a model-based aproach to estimate expression variations of normalization/ housekeeping markers was used. Favourable low variabilities are represented by low stability values (M) [5]. When the data was compared throughout the differentiation period independently of the radiation quality, 18S rRNA was the most stable marker (M=0,233). When radiation quality was analysed independently of the differentiation time, GAPDH yielded the most stable marker (M=0,478). The best stability value was obtained by the combination of 18S rRNA and GAPDH (M=0,221). Hence, the geometric mean of 18S rRNA and GAPDH will be used in subsequent studies to quantify the gene expression of mESC during differentiation after exposure to IR.

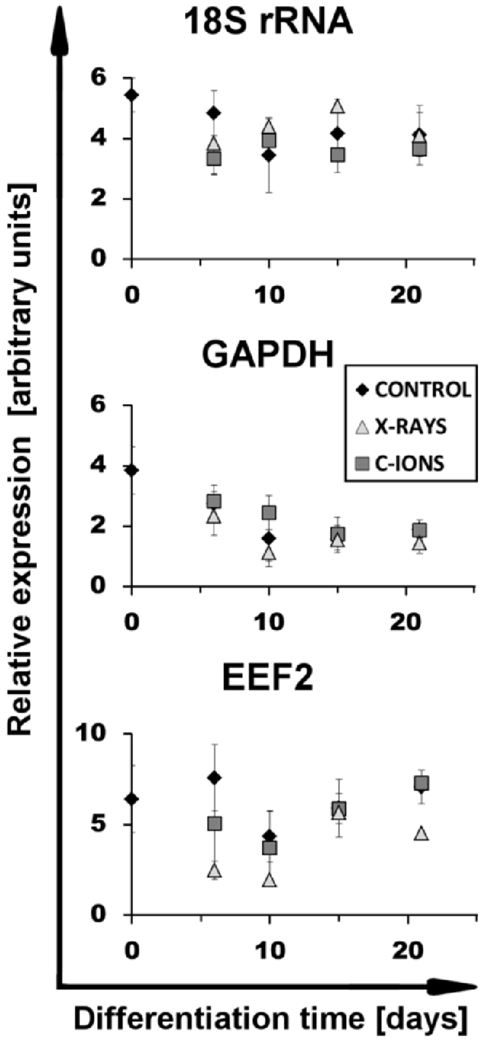

Figure 1: Expression of housekeeping markers during differentiation. 18S rRNA, GAPDH and EEF2 marker expression was quantified in differentiating EBs derived from irradiated pluripotent mouse D3-ESC. Exposure was done with X-rays (triangles) or C-ions (squares), controls were sham irradiated (diamonds).

References

[1] M. Banda et al., Mutat Res (2008), 649: p126-134.
[2] J. Vandesompele et al., Genome Biol. (2002) 3(7): research0034.1-research0034.11.
[3] A. Helm et al., GSI Scientific Report 2010, 455.
[4] A. Helm et al., GSI Scientific Report 2011, 497.
[5] C.L. Andersen et al. Cancer Research (2004) 64: p5245-5250.

---

* The work was supported by BMBF grant 02NUK025A and Euratom 7th Framework Programme under grant agreement number 295823
[#]s.ritter@gsi.de

DOI:10.15120/GR-2015-1-APPA-HEALTH-38

Cardiac differentiation of human embryonic stem cells as a measure for radiation risk in early embryogenesis*

I. Schroeder[1], *S. Luft*[1], *F. Braun*[2], *P. Hessel*[1], *M. Scholz*[1], *M. Durante*[1,3], *and S. Ritter*[#1]
[1]GSI, Darmstadt, [2]Hochschule Darmstadt, [3]Technische Universität Darmstadt, Germany

The early embryo is particularly vulnerable to ionizing radiation responding to exposure with prenatal death, organ malformation or other detrimental ramifications [1]. Thus, a thorough assessment of the radiation risk is mandatory in situations of inevitable or unintended exposure of the conceptus *in utero*. However, our current understanding of radiation induced effects is predominantly based on animal studies or radiation accidents [2] hampering an in-depth evaluation of the underlying mechanisms. Human embryonic stem (hES) cells, derived from the inner cell mass of the blastocyst during embryogenesis, present a valuable tool to examine radiation effects on the early embryo as they can differentiate into all cells of the body mimicking human development *in vitro* [3]. Of special interest is the impact of diagnostic or therapeutic irradiation on the formation of the heart as one of the earliest organogenic processes taking place from week 2-7 in humans (for concise review see [4]). We established a hES cell-based cardiac differentiation protocol, which modulates the Wnt-signaling pathway that is crucial for *in vivo* cardiogenesis [5]. In an insulin-free culture it leads to the stepwise generation of mesoderm (by inducing Wnt via CHIR99021), cardiac mesoderm (by inhibiting Wnt via IWP2), cardiovascular progenitors and beating cardiomyocytes recapitulating all stages of the developing heart within 15 days (Figure 1). Using quantitative PCR, specific markers could be detected at every differentiation stage. In contrast to hES cells and spontaneously differentiating cells, in hES cells subjected to directed differentiation according to Lian et al. [5] the appearance of early cardiomyocytes (d8-d15) was marked by beating clusters and the expression of early cardiomyocyte markers such as alpha myosin heavy chain (aMHC, Figure 2). Further culture led to the synchronization of cardiomyocyte clusters with increased beating rates and an elevated expression of genes specific for mature cardiomyocytes. Successful cardiac development was also evidenced post-transcriptionally by increased levels of cardiac microRNAs. Currently, techniques to determine the beat-rate and other electrophysiological parameters in cardiomyocytes derived from non-irradiated or irradiated hES cells are established. Preliminary data suggest that the cardiac differentiation of hES cells surviving the exposure to 1 Gy X-rays is accelerated leading to premature expression of cardiac markers when compared to unexposed cells. Such acceleration may render the cells unsusceptible to subsequent positional and temporal patterning explaining radiation induced effects such as the above mentioned organ malformations or prenatal death. Currently, the underlying mechanisms are studied in more detail.

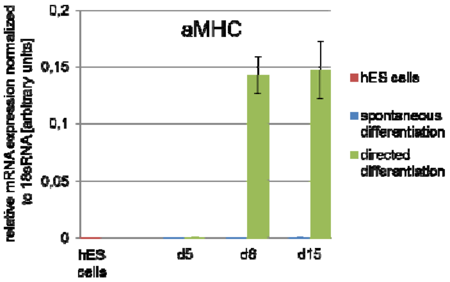

Figure 2. aMHC mRNA expression in cells subjected to spontaneous or directed differentiation according to Lian et al., d: days.

References

[1] C.H. McCollough et al., Radiographics 27 (2007) 909.
[2] ICRP Publication 90, Ann. ICRP 33 (2003).
[3] T. Vazin and W.J. Freed, Restor Neurol Neurosci 28 (2010) 589.
[4] S.M. Evans et al., Circ Res 107 (2010) 1428.
[5] X. Lian et al., Nat Protoc 8 (2013) 162.

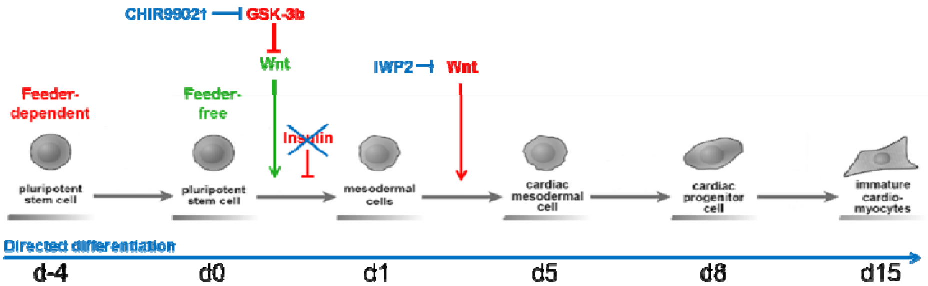

Figure 1. Differentiation scheme according to Lian et al. Differentiation promoting factors are depicted in blue and green, inhibiting factors are shown in red, d: day.

---

* Work supported by BMBF (02NUK025A).
[#] s.ritter@gsi.de

DOI:10.15120/GR-2015-1-APPA-HEALTH-39

Pharmacological augmentation of heavy ion cancer therapy *

Norman Reppingen[1], *Claudia Fournier*[1,3], *and Marco Durante*[1,2]
[1]TU Darmstadt; [2]GSI Helmholtzzentrum für Schwerionenforschung, TU Darmstadt; [3]FH Darmstadt

Heavy Ion Therapy led to unique treatment options in certain types of cancer, extending to more challenging disease entities. However, effects which abrogate treatment success can be active in the patient. For example, tumors generally induce inflammation and a hypoxic environment. This leads to cells which are resistant against direct effects of X-rays and results in a very limited access by the immune system. Which is disadvantageous, as the immune system was shown to contribute significantly to radiotherapy success. Therefore, we devised a pharmacological system which is addressing the resistance against direct effects of radiation and to relieve tumor induced immune suppression. The method was shown to improve the tumor phenotype and to enhance the sensitivity to X-ray- and particle irradiation, yielding more killed cells, expressing more immune activating ligands.

Description of the field

Radiotherapy, Pharmacology and Immune Therapy evolved in different fields of science, following more physical, chemical and biological lines of thinking, respectively. However, it has turned out that the immune system is heavily influencing direct and indirect effects of radiation. Therefore, we recently argued to transform the way radiation is interacting with the immune system of the patient and the tumor pharmacologically.[1]

Description of the project

Exploiting the recent knowledge about exposure pathways and molecular hallmarks of the immunogenicity of radiation and drugs, we first combined two pharmacological entities with radiation. Chloroquine is an established anti malarial drug even in preventive use, CDDO-Me is an anti inflammatory synthetic triterpenoid which is in clinical studies. To further improve the immunological and direct radiation effects, a combined c-Met / VEGFR2 Inhibitor (TKI) was added to the combination, which is already approved for medullary thyroid cancer.

Results

The combination of Chloroquine and CDDO-Me led to increased surface translocation of the immune relevant molecules CD95, MHC-I, Rae-1, Calreticulin and TRAIL. Adding the TKI further enhanced the pro-apoptotic properties of the combined treatment in CT26.WT tumor cells. As apoptotic cells were shown to express more immune relevant molecules on the surface, increased apoptotic cell death is thought to be beneficial for the induction of tumor immune responses. This effect of enhanced tumor cell killing was even more pronounced using carbon ions.

Outlook

Despite this treatment has so far only been tested in vitro by us, a solid and significantly increasing amount of clinical and preclinical evidence points to the beneficial effects of the pharmacological components used for supporting immune therapies. Therefore, it could be envisaged that in a combined treatment, there is significant translational potential for use in carbon ion therapy and other radiation based therapy forms as well.

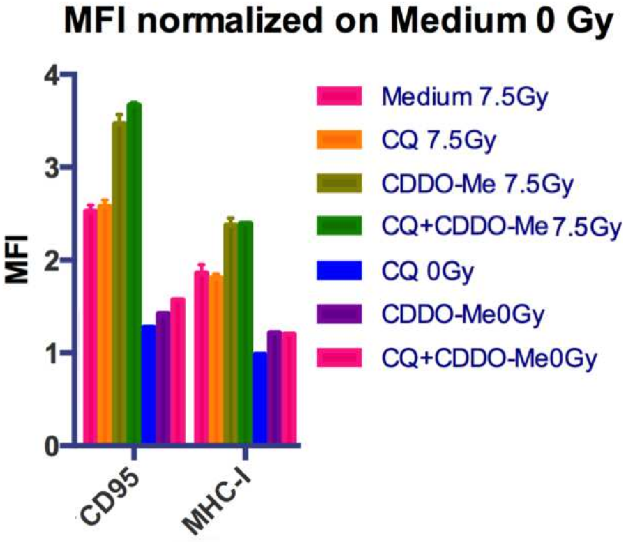

Figure 1: Increased surface translocation of CD95 and MHC-I after irradiation under the influence of Chloroquine, CDDO-Me and the combination thereof. Note: The drug effects became pronounced only in irradiated cells while there was only little change in non-irradiated cells.

References

[1] M. Durante, N. Reppingen and K. Held, “Immunologically augmented cancer treatment using modern radiotherapy ”, Trends in Molecular Medicine, September 2013, Vol. 19, No. 9, 565-582, http://dx.doi.org/10.1016/j.molmed.2013.05.007

---

* Work supported by GSI(UNILAC)/HGShire

DOI:10.15120/GR-2015-1-APPA-HEALTH-40

Experimental and modeling analysis of γH2AX dose response curves in the framework of the GLOBLE model*

F. Tommasino[1,], *T. Friedrich*[1], *B. Jakob*[1], *B. Meyer*[2], *M. Durante*[1,3], *and M. Scholz*[1]
[1]GSI, Darmstadt, Germany; [2]Dep. of Radiation Oncology, Washington University School of Medicine, St. Louis, MO, USA; [3]Institut für Festkörperphysik, Technische Universität, Darmstadt, Germany

Among the spectrum of DNA lesions induced by ionizing radiation, the Double Strand Breaks (DSB) are generally recognized as the type of DNA damage more directly related to cell killing. Nowadays, the γH2AX assay represents one of the methods of choice for the study of DSB induction and processing [1]. The method is based on the phosphorylation of histone H2AX in presence of a DSB. Importantly, the phosphorylation extends over a large chromatin region in the order of the Mbp, reaching its maximum in about 30-60 min after irradiation, and then slowly decaying as the damage is processed [2]. The phoshorylated molecules can be tagged with a fluorescent antibody, giving rise to the so-called *γH2AX foci*, which can then be observed and/or analyzed with different techniques. Consequently, γH2AX foci are considered as a marker for DSB presence.

The Giant LOop Binary LEsion (GLOBLE) model is a radiobiological model developed in order to predict biological effects resulting from photon irradiation [3]. The cell nucleus where the genome is stored is identified with the critical target. The assumption is made, that the higher-order chromatin organization can be described by means of Giant Loop structures, each one involving about 2 Mbp of genome [4]. The simulated nucleus is thus divided into cubic domains of about 500 nm edge length resembling the DNA organization into loop structures. For a given dose, DSB are distributed among nuclear domains, assuming that the level of DSB clustering at the micrometre scale defines the severity of the induced damage.

Our aim here is to compare GLOBLE predictions in terms of DSB induction patterns with measurements of integral γH2AX fluorescence obtained with flow cytometry. This is based on the hypothesis, supported by the literature, that a direct relation exists among γH2AX foci and chromatin domains as defined in the model [1,5]. Specifically, we make the hypothesis that in presence of at least one DSB the whole loop is phosphorylated, and that the presence of additional DSB does not lead to increased fluorescence. After defining as *hit domain* a domain where at least one DSB is induced, we can compare the measured signal with predicted numbers of hit domains.

Fig. 1 shows a typical example of model predictions. The curves are calculated combining the standard domain size of 2 Mbp, or an enlarged one of 8 Mbp, with a DSB induction yield of 30 DSB per Gy and cell nucleus. At high doses the tendency to saturation is observed, reflecting that the majority of available domains are hit. Intuitively, the domain size will influence the dose at which saturation is reached. It thus emerges that this analysis could give indirect indications concerning the actual dimension of chromatin loops.

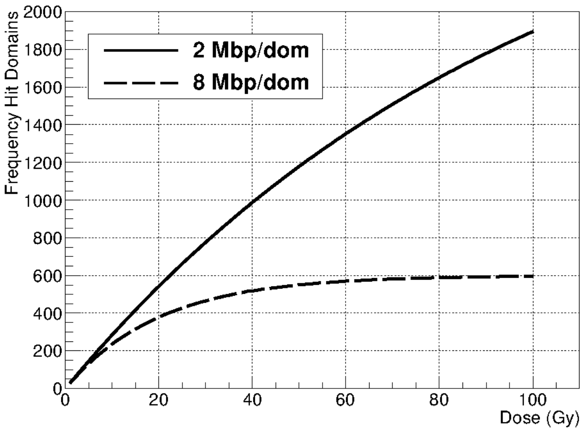

Figure 1: simulated dose response curves calculated assuming a standard DSB induction yield of 30 DSB/Gy and a domain size of 2 Mbp and of 8 Mbp.

Experiments will involve the use of mammalian cell lines, which will be irradiated in an extended dose range. The comparison will allow testing the validity of basic modeling assumptions. The influence of the values assigned to different model parameters (e.g. DSB induction rate, domain size) will be investigated. Importantly, this will be relevant also for the model extension to heavy ion irradiation, which is currently under development in our group. At the same time, the systematic study of γH2AX phosphorylation over a large dose range in different cell lines could contribute to a better understanding of the relation existing between DSB and γH2AX foci, as well as of the phosphorylation process itself.

References

[1] Rogakou et al., J Biol Chem, 273 (1998), pp. 5858-68.
[2] Kinner et al., Nucleic Acid Res, 36 (2008), pp. 5678-94.
[3] Friedrich et al., Radiat Res, 178 (2012), pp. 385-94.
[4] Yokota et al., J. Cell Biol., 130 (1995) pp. 1239-49.
[5] Iacovoni et al, EMBO J, 29 (2010), pp. 1446-57.

---

* This work was supported by a DFG-funded Graduiertenkolleg (GRK 1657). The work is part of HGS-HIRe.

DOI:10.15120/GR-2015-1-APPA-HEALTH-41

DOI:10.15120/GR-2015-1-APPA-HEALTH-41

Neutron star equations of state with optical potential constraint*

S. Antić[1,2] *and S. Typel*[1]
[1]GSI, Darmstadt, Germany; [2]TU, Darmstadt, Germany

Many properties of nuclei and nuclear matter can be well described with modern phenomenological energy density functionals (EDF). A particular strong constraint represents the observation of two pulsars of approx. two solar masses [1]. It requires a sufficiently stiff equation of state (EoS) at densities well above the nuclear saturation density. Since nucleons of large momenta interact with the medium under these conditions, the momentum dependence of the effective interaction is probed. Experimental information on this dependence is given by the optical potential U_{opt} that can be extracted from elastic proton scattering on nuclei in Dirac phenomenology [2].

Standard covariant EDF predict a much too strong energy dependence of U_{opt}. Thus, extensions with derivative nucleon-meson couplings have been developed that respect the optical potential constraint. A linear energy dependence of the nucleon self-energies in early models [3] was recently extended to more general functional forms [4]. In the present work, the latter approach with nonlinear derivative (NLD) couplings was combined with a density dependence (DD) in order to obtain a very flexible EDF. This DD-NLD model provides the equation of state at high densites for all neutron-proton asymmetries. The model can be applied to the description of cold charge-neutral matter in β equilibirum by adding the contributions of electrons. The mass-radius relation of neutron stars is finally obtained by solving the Tolman-Oppenheimer-Volkoff equations [5] with this stellar matter EoS.

In figure 1 the mass-radius relation of neutron stars is depicted for five models. The first (D1) is a conventional covariant EDF parametrization with density-dependent couplings close to a model that successfully describes properties of finite nuclei [6]. It reproduces well-determined nuclear matter parameters at saturation and gives a maximum neutron-star mass well above the observed masses. However, it does not fulfill the optical potential constraint. The other two models, with identical nuclear matter parameters to model D1, are parametrizations of the full DD-NLD model that predict an energy dependence of the optical potential. In model D2, the nucleon self-energies show a Lorentzian form of the energy dependence and in model D3 an exponential dependence is used. The parameter Λ regulated the strength of the energy dependence. Here, representative values are chosen that give optical potentials consistent with Dirac phenomenology at high nucleon energies, for details see reference [7]. The resulting EoS of these parametrizations are considerably softer than that of model D1 and, consequently, much lower maxium neutron star masses are predicted barely reaching masses of ordinary neutron stars.

In the future, the DD-NLD model will be applied to the description of finite nuclei. It remains to be seen whether successful parametrizations for nuclear structure calculations can consistently satisfy the optical potential and maximum mass constraints.

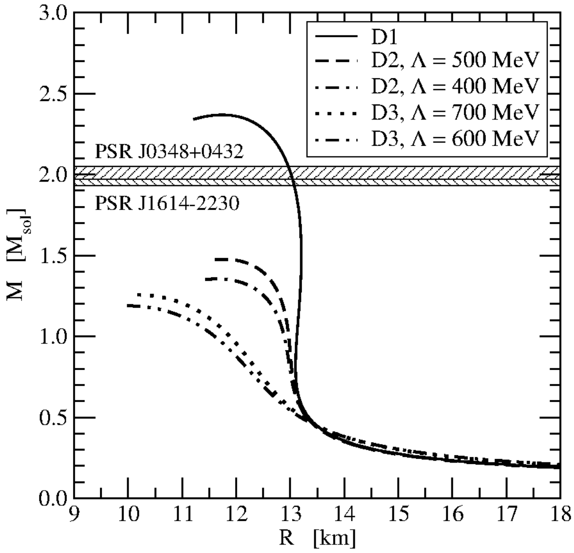

Figure 1: Mass-radius relation of neutron stars for different versions of the DD-NLD model. The shaded bands represent astrophysical mass measurements of two pulsars [1].

References

[1] P. Demorest et al., Nature 467 (2010) 1081; J. Antoniadis et al., Science 340 (2013) 6131. P. Demorest et al., Nature 467 (2010) 1081.

[2] S. Hama et al., Phys. Rev. C 41 (1990) 2737; E.D. Cooper et al., Phys. Rev. C 47 (1993) 297.

[3] S. Typel et al., Phys. Rev. C 67 (2003) 034002; Phys. Rev. C 71 (2005) 064301.

[4] T. Gaitanos et al., Nucl. Phys. A 828 (2009) 9; Nucl. Phys. A 878 (2012) 49; Nucl. Phys. A 899 (2013) 133.

[5] R.C. Tolman, Phys. Rev. 55 (1939) 364; J.R. Oppenheimer and G.M. Volkoff, Phys. Rev. 55 (1939) 374.

[6] S. Typel et al., Phys. Rev. C 81 (2010) 015803.

[7] S. Antic and S. Typel, arXiv:1501.07393[nucl-th].

---

* Work supported by the Helmholtz Association through the Nuclear Astrophysics Virtual Institute (VH-VI-417) and by the Helmholtz Graduate School for Hadron and Ion Research (HGS-HIRe).

DOI:10.15120/GR-2015-1-MU-THEORY-01

Hyperon interaction in nuclear matter and neutron stars*

M. Dhar†2, *H. Lenske*1,2, *and J. Wilhelm*2
1GSI, Darmstadt, Germany; 2Institute for Theoretical Physics, JLU Giessen, Germany

The upcoming hypernuclear experiments planned for FAIR have renewed the interest in hypernuclear physics in general. A key part of all theoretical studies is the knowledge of hyperon interactions in free space and in nuclear matter. Their knowledge also plays a crucial role for solving the so-called *hyperonization puzzle* [1] in a heavy neutron star as PSR J1614-2230 [2]. Concerning hyperon interactions, we reconsider the flavor octet approach, but with special focus on in-medium interactions. A meson exchange model based on SU(3) symmetry is used for determining the free space interaction. The interaction is then used to solve the Bethe-Salpeter (BS) scattering equation to find physical observables. Medium effect has been incorporated into the free space equation by multiplying a two particle Pauli projector operator (Q_P) with the two particle Green function (G_F) resulting in the Bethe-Goldstone equation

$$\hat{T}(q',q) = \hat{V}(q',q) + \int \hat{V}(q',k)G_F(k,q)Q_P\hat{T}(k,q)d^3k \tag{1}$$

where $\hat{T}(q',q)$ is the full-scattering amplitude and $\hat{V}(q',q)$ contains all the irreducible two-particle Feynman diagrams. The density dependence of interaction has been clearly seen in the variation of the in-medium low energy parameters as a direct consequence of the medium effect (Figure 1).

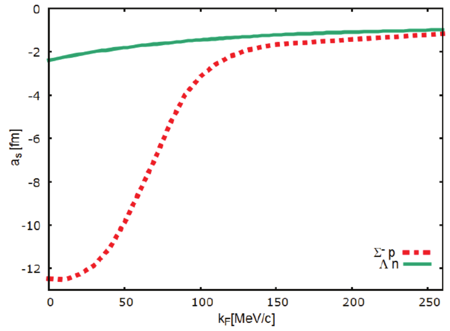

Figure 1: Λn (solid) and $\Sigma^- p$ (dashed) scattering length a_s with the variation of nucleon Fermi momentum $k_{FN}(\rho)$. It is clear from the plots that the scattering lengths attend a steady value as ρ approaches ρ_{sat}.

With increasing density, the Pauli-exclusion principle, are leading to a substantial reduction already at low and moderate densities. Thus, repulsive interactions are effectively increasing with density already on the level of ladder-diagrams. These results indicate the necessity for studying in more detail vector repulsion of hyperon interactions in high density matter as encountered in neutron stars. For a first case study, we use relativistic mean-field theory supplemented by an additional density dependence in the vector meson-hyperon vertices chosen as

$$g_{VY}(\rho) = g_{VY}\left(1 + \alpha_\rho\left(\frac{\rho}{\rho_{sat}}\right)^\beta\right) \tag{2}$$

where α_ρ is negligibly small at $\rho \leqslant \rho_{sat}$ and $\alpha_\rho = \alpha =$ constant above ρ_{sat}. At present, the density dependence is modelled phenomenologically. As constraints, we impose on the one hand the condition that the low-density $(\rho < 2\rho_{sat})$ behaviour of hyperon interactions should not be altered and on the other hand, a neutron star mass above two solar masses should be obtained.

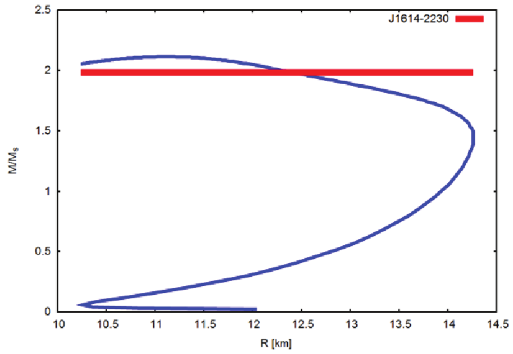

Figure 2: Neutron star mass-radius relation. The mass of J1614-2230 [2] is indicated by a horizontal bar.

Typical results of our calculations for the mass-radius relation are displayed in Figure 2. Already a moderate increase of the vector repulsion, $\alpha = 0.135$ and $\beta = 2$,results in a maximum mass above two solar masses. We find an interesting composition of the neutron star : the neutron star develops a hyperon shell at densities around $3\rho_{sat}$ which at higher density vanishes again.

References

[1] I. Bednarek, P. Haensel, J.L. Zdunik, M. Bejger, and R. Manka, Astronomy and Astrophysics 543 (2912), p. 157

[2] Demorest P.B., Pennucci T., Ransom S.M., Roberts M.S.E.,and Hessels J.W.T., 2010, Nature, 467, p. 1081

---

[*] Work supported by GSI with JLU Giessen cooperation contract, HIC4FAIR, BMBF and DFG.

[†] Madhumita.Dhar@physik.uni-giessen.de

DOI:10.15120/GR-2015-1-MU-THEORY-02

Impact of nuclear reactions on the fate of intermediate-mass stars*

H. Möller[1] *and G. Martínez-Pinedo*[1,2]
[1]TU Darmstadt, Darmstadt, Germany; [2]GSI, Darmstadt, Germany

The evolution of intermediate-mass stars (8 - 12 $M_{\odot}$) represents one of the most challenging subjects in nuclear astrophysics (see e.g. [1,2]). Their final fate is still uncertain and strongly model dependent. They can become white dwarfs, undergo electron-capture or core-collapse supernovae or even proceed towards explosive oxygen-burning and a subsequent thermonuclear explosion. An accurate description of the involved nuclear reactions is crucial for the determination of the pre-supernova structure of these stars. We argue that due to the possible development of an oxygen-deflagration, a hydrodynamic description coupled to a nuclear reaction network has to be used. For selected nuclear species, we include a set of updated reaction rates, for which we discuss their role for the evolution of the stellar core, at the example of SAGB-star models from [2].

In this report, we want to point out the recent advances that we made in understanding the key nuclear reactions that are relevant for the proper modeling of the late stages of these stars. Compared to massive stars, nuclear reactions will operate at much higher densities (10^9 compared to 10^6 g cm^{-3}), where electron-capture (EC) reactions can already operate and influence the evolution of the star. As pointed out in [2], the O-Ne-core of such stars may first undergo a phase of URCA-cooling due to EC on odd-A nuclei and then a phase of rapid energy release due to double-EC on even-A nuclei, rising the temperature in the stellar core.

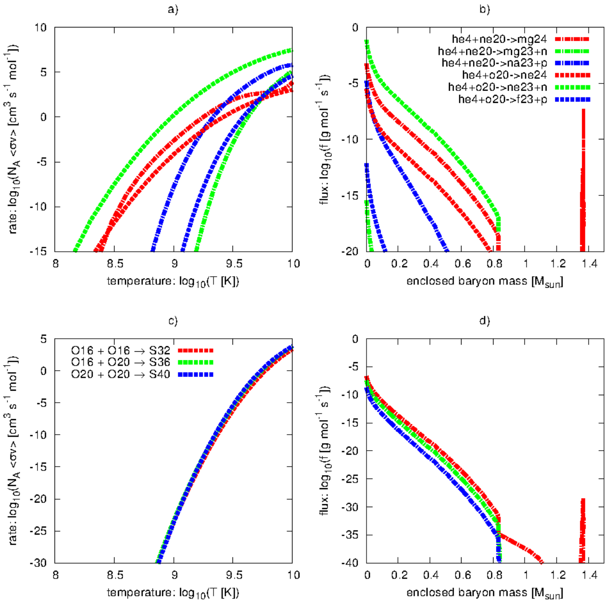

Figure 1: Rates and fluxes for the Ne- and O-burning phase

Prior to the Ne-burning phase, ^{24}Mg is converted into ^{24}Ne and later ^{20}Ne into ^{20}O by EC. Hence, the center of the core consists mainly of ^{16}O and ^{20}Ne but also up to 4% of ^{20}O. This opens new reaction channels that have so far not been considered. They modify the Ne-burning that now proceeds by the reactions $^{20}\mathrm{Ne}\,(\gamma,\alpha)\,^{16}\mathrm{O}$, followed by $^{20}\mathrm{O}\,(\alpha,\gamma)\,^{24}\mathrm{Ne}$. The JINA reaclib rates [3] are displayed in panel a) of Figure 1. Here, we compare the rates of the different reaction channels for the α-capture on ^{20}Ne and ^{20}O. The reaction $^{20}\mathrm{O}\,(\alpha,n)\,^{23}\mathrm{Ne}$ is dominating and we argue that the α-capture on ^{20}O is a competitive process that should be considered in future calculations. This can be seen even better in panel b) where we look at the reaction fluxes for conditions of stellar models from [2] prior to Ne-burning. For a binary rate, the flux is defined as: $f_{\mathrm{AB}\to\mathrm{X}} = \rho N_{\mathrm{A}}\,\langle\sigma v\rangle_{\mathrm{AB}\to\mathrm{X}}\,Y_{\mathrm{A}}Y_{\mathrm{B}}$, with density ρ, projectile abundances Y_{A} and Y_{B} and reaction rate $N_{\mathrm{A}}\,\langle\sigma v\rangle_{\mathrm{AB}\to\mathrm{X}}$.

Once the core reaches temperatures $\gtrsim$ 1.7 GK, the fusion reactions of neutron-rich oxygen isotopes, $^{16,20}\mathrm{O} + {}^{20}\mathrm{O} \to {}^{36,40}\mathrm{S}^*$ may become important (besides $^{16}\mathrm{O} + {}^{16}\mathrm{O} \to {}^{32}\mathrm{S}^*$). Due to the lack of experimental data, we rely on a model by [4] for the calculation of the astrophysical S-factors and calculate the reaction rate, taking into account the different branching ratios. In panels c) and d) of Figure 1, it can be seen that the reaction rates are actually very comparable. In panel d) are shown again the reaction fluxes for the same conditions as in panel b). We find that the contribution of the $^{16}\mathrm{O} + {}^{20}\mathrm{O}$-channel reaches up to 15% of the $^{16}\mathrm{O} + {}^{16}\mathrm{O}$-channel, while the $^{20}\mathrm{O} + {}^{20}\mathrm{O}$-channel is much less important. Considering the uncertainties present in all of these reactions, it is important to perform a careful evaluation of the corresponding S-factors as they can substantially affect oxygen burning in intermediate-mass stars. In addition to that, the fusion involving ^{20}O has Q-values of $\sim$ 30 MeV. This does not only increase the rate of energy release during the fusion phase of oxygen by up 30%, but it also allows for exotic decay channels including the emission of up to 5 neutrons. See [5] for more details.

References

[1] K. Nomoto, ApJ **322** (1987), 206–214.

[2] S. Jones, *et al.*, ApJ **772** (2013), 150.

[3] R. H. Cyburt, *et al.*, ApJS **189** (2010), 240–252.

[4] D. G. Yakovlev, *et al.*, Phys. Rev. C **82** (2010), 044609.

[5] H. Möller, *et al.*, PoS(NIC XIII)125 (2014).

---

* supported by SFB 634, HIC for FAIR, HGS-HIRe and NAVI

DOI:10.15120/GR-2015-1-MU-THEORY-03

Reactions for determination of $\bar{\nu}_e$-spectra from core-collapse supernovae*

A. Lohs[1,2], *G. Martínez-Pinedo*[1,2], *and T. Fischer*[3]
[1]GSI, Darmstadt, Germany; [2]TU Darmstadt, Darmstadt, Germany; [3]U Wroclaw, Wroclaw, Poland

Core-collapse supernovae (CCSN) release a huge amount of gravitational binding energy, mainly in the form of neutrinos of all flavours. The large neutrino flux serves as a signal but also determines the evolution of the supernova explosion mechanism in the first place. Hence, the process of neutrino decoupling from the hot and dense matter of a young protoneutron star (PNS) is of particular interest. For electron antineutrinos $\bar{\nu}_e$ current CCSN-simulations neglect both neutron decay and muon decay. It was argued that these reactions are suppressed compared to e.g. absorption on protons or scattering on nucleons and electrons. However, for absorption of $\bar{\nu}_e$ on protons, the neutrino has to overcome the energy difference between protons and neutrons. Consequently this reaction is suppressed for low neutrino energies. While the PNS cools, the region of neutrino decoupling reaches large densities where strong interaction potentials add up on the energy difference, thereby increasing the threshold for $\bar{\nu}_e$-absorption. Also, low energy neutrinos are the ones that decouple at the highest densities where the threshold is the largest. In contrast, (inverse) neutron decay does not face this problem. The additional incoming electron can supply the energy so that low energetic $\bar{\nu}_e$ can undergo the reaction, too. Furthermore, the inverse muon decay is another interesting opacity source that will be most relevant for $\bar{\nu}_e$ with low energies. Using thermodynamical and chemical conditions from a 1D hydrodynamical supernova simulation with full Boltzmann neutrino transport [1], reactions rates for (inverse) neutron decay and muon decay were derived and calculated

$$\bar{\nu}_e + e^- + p \rightarrow n \qquad \bar{\nu}_e + e^- + \nu_\mu \rightarrow \mu^-$$

Inverse neutron decay is calculated in analogy to neutrino absoprtion [2, 3], including the effect of weak magnetism [4] and considering the full relativistic kinematics for all particles. Strong interactions are treated in the mean field approximation. Inverse muon decay is derived similar to neutrino scattering on electrons [5].

It is found that both reactions are indeed relevant for low energy $\bar{\nu}_e$ with $E < 10\,\mathrm{MeV}$. For these energies, muon decay is among the most important reactions during the first second post bounce. Due to a strong temperature dependence it is suppressed at later times. In contrast, neutron decay is important after the first second post-bounce. Then the decoupling region has moved to densities above $10^{13}\,\mathrm{g/cm^3}$ where strong interaction becomes important. For both reactions the impact manifests in an outward shift of the decoupling region for lower neutrino energies. Thus it is recommended to include them in future dynamic CCSN simulations. In that sense the inverse neutron decay could already be implemented in a simplifying approximation into a new simulation. Figure 1 shows the evolution of the average energy of emitted $\bar{\nu}_e$. In the scenario with neutron decay (dashed line) the average energy is reduced compared to the standard case (solid line) without neutron decay. It is expected that this will lead e.g. to an increased electron fraction in the neutrino driven wind. Intuitively one could expect for muon decay to have a similar effect and further decrease the average energy at earlier times, yet only a dynamic simulation can answer this question relaibly. Also, muon decay couples the spectra of $\bar{\nu}_e$ and ν_μ to each other. The effect of this, while highly interesting, is almost impossible to asses without a full simulation.

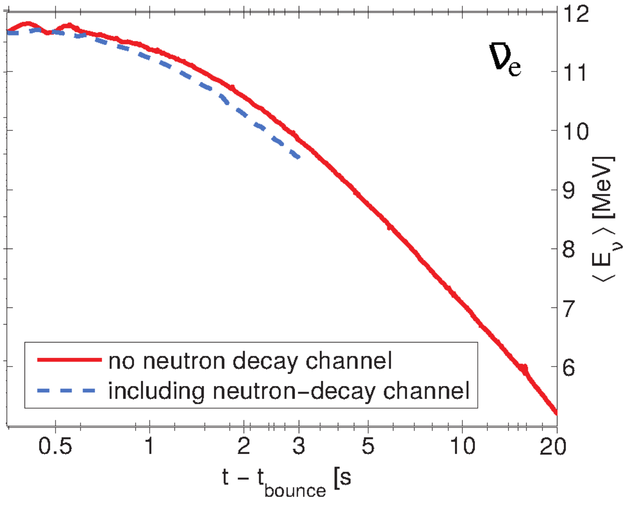

Figure 1: Evolution of average $\bar{\nu}_e$ energy

References

[1] T. Fischer, *et al.*, Astronomy and Astrophysics, **517** (2010), A80

[2] S. Reddy, M. Prakash, and J.M. Lattimer, Phys. Rev. D **58**, 013009 (1998)

[3] A.W. Steiner, M. Prakash, and J.M. Lattimer, Phys. Lett. B **509**, (2001), 10

[4] C.J. Horowitz and G. Li, Phys. Rev. D **61**, 063002 (2000)

[5] A. Mezzacappa, S.W. Bruenn, Astrophysical Journal, **410**, (1993), 740

---

* Work supported by GSI, HGS-Hire.

DOI:10.15120/GR-2015-1-MU-THEORY-04

Neutrino Nucleosynthesis of radioactive nuclei in supernovae[*]

A. Sieverding[†,1], *L. Huther*[1], *G. Martínez-Pinedo*[1,2], *and K. Langanke*[2,1]
[1]Institut für Kernphysik (Theoriezentrum), Technische Universität Darmstadt, Schlossgartenstraße 2, 64289 Darmstadt, Germany; [2]Gesellschaft für Schwerionenforschung Darmstadt, Planckstr. 1, D-64259 Darmstadt, Germany

Core-Collapse-Supernova explosions are the final stage of stellar nucleosynthesis and are crucial for the determination of the chemical composition of material that is ejected and enriches the interstellar medium, forming the basis for the next generation of stars. A major part of this nucleosynthesis happens as the shock front launched from the remnant of the stellar core passes through the layers of the star, increasing temperature and density and triggering nuclear processes. At the same time these layers are irradiated by neutrinos of all flavors, that are emitted as the remnant of the stellar core cools. We have performed nucleosynthesis calculations for a set of models of core-collapse supernovae including an extensive set of neutrino-nucleus interactions. Compared to previous studies of ν-nucleosynthesis, we use neutrino spectra corresponding to reduced average energies in agreement with modern core-collapse simulations [1]. For simplicity we assume, that each type $x \in \{e, \mu, \tau\}$ of neutrino follows a Fermi-Dirac distribution characterized by a corresponding temperatures T_{ν_x} with zero chemical potential. We assume $T_{\nu_e} = 2.8$ MeV, $T_{\bar{\nu}_e} = T_{\nu_{\mu,\tau}} = 4.0$ MeV

The main candidates for neutrino nucleosynthesis are ^{7}Li, ^{11}B, ^{19}F, ^{138}La and ^{180}Ta [2], all of which are observed in the solar system, but are not produced in sufficient amount by supernova simulations without including neutrino interactions. Neutrino nucleosynthesis can push the production factors of those nuclei close to the solar system values, as shown in table 1. Furthermore, reference [3] has discussed the ν-process in supernovae as a production site for the radioactive isotopes ^{92}Nb and ^{98}Tc. Our calculations confirm that charged-current neutrino interactions increase the yield of ^{92}Nb and ^{98}Tc significantly.

Observations of γ-rays allow direct access to the production of radioactive nuclei. Among the most interesting γ-ray sources that indicate active nucleosynthesis are ^{22}Na, ^{26}Al, ^{44}Ti and ^{60}Fe. Neutrinos contribute to the production of ^{26}Al during the explosive phase by two different mechanisms. First, neutrino-induced spallation reactions on the most abundant nuclei int the O/Ne shell, ^{20}Ne,^{24}Mg and ^{16}O increase the number of free protons, which enhances the reaction ^{25}Mg(p,γ), which is the main production channel also without neutrinos. Additionally, the charged-current reaction ^{26}Mg(ν_e,e$^-$) gives significant contributions. Both mechanisms contribute to a similar extent to the production and both occur in the O/Ne layer. In total we find an increase of the ^{26}Al yield by factors between 1.4 and 2.0.

Table 1: Production factors relative to solar abundances from reference [4], normalized to ^{16}O production. Shown are the results from our calculations without neutrinos, with the low energy neutrino spectra we now consider more realistic as stated above. Also shown are the results for the "high" energy neutrino spectra ($T_{\nu_e} = T_{\bar{\nu}_e} = 4.0$ MeV, $T_{\nu_{\mu,\tau}} = 6.0$ MeV) for comparison with [2].

Nucleus	no ν	Low energies	High energies
15 M$_\odot$ star			
^{7}Li	0.001	0.28	2.54
^{11}B	0.007	1.43	6.13
^{15}N	0.67	0.68	0.79
^{19}F	1.02	1.14	1.31
^{138}La	0.07	0.67	1.18
^{180}Ta	0.07	1.14	1.81
25 M$_\odot$ star			
^{7}Li	0.0005	0.11	0.55
^{11}B	0.003	0.80	2.61
^{15}N	0.08	0.10	0.13
^{19}F	0.06	0.24	0.43
^{138}La	0.03	0.63	1.14
^{180}Ta	0.14	1.80	2.81

Similarly, the production of ^{22}Na is increased on average by a factor of 3.1 , mainly due to increased proton captures on ^{22}Ne and ^{23}Na(ν_e,e$^-$ p)^{22}Na. Further contributions are provided by the neutral current neutron evaporation on ^{23}Na and the charged-current reaction ^{22}Ne(ν_e,e$^-$)^{22}Na. We find that the balance of the different production channels and the total enhancement depends

The effect of neutrino interactions on the yields of ^{44}Ti and ^{60}Fe have been found to be at most 2% in the case of ^{44}Ti and even less for ^{60}Fe.

References

[1] T. Fischer, G. Martínez-Pinedo, M. Hempel, M. Liebendörfer, *Neutrino spectra evolution during proto-neutron star deleptonization*, Phys. Rev. D **85** 083003.

[2] A. Heger, E. Kolbe, W. Haxton, K. Langanke, G. Martínez-Pinedo, S. E. Woosley, *Neutrino nucleosynthesis*, Phys. Lett. B **606** 258.

[3] M.-K. Cheoun, *et al.*, *Neutrino induced reactions for ν-process nucleosynthesis of ^{92}Nb and ^{98}Tc*, prc **85** (6) 065807.

[4] K. Lodders, *Solar System Abundances and Condensation Temperatures of the Elements*, Astrophys. J. **591** 1220.

---

[*] Work supported by NAVI, HIC4FAIR

[†] a.sieverding@gsi.de

DOI:10.15120/GR-2015-1-MU-THEORY-05

Neutrino oscillations in core-collapse supernovae*

Meng-Ru Wu†[1,2], *Yong-Zhong Qian*[2], *Gabriel Martínez-Pinedo*[1,3], *Tobias Fischer*[4], *and Lutz Huther*[1]
[1]TU Darmstadt, Germany; [2]University of Minnesota, USA; [3]GSI, Darmstadt, Germany; [4]University of Wrocław, Poland

Neutrinos play essential roles in determining the dynamics and nucleosynthesis of core-collapse supernova explosion since they carry away nearly all the gravitational binding energy released during the collapse. On the other hand, the detection of future Galactic supernova neutrinos could be exploited to explore the physics of core-collapse supernovae and properties of neutrinos. How neutrino oscillations among all three flavors of neutrinos and antineutrinos occur in supernova environment and how will oscillations affect different aspects mentioned above needs to be carefully examined.

We performed a comprehensive calculation of neutrino oscillations in supernovae, including the collective oscillations [1] that may happen due to the presence of large neutrino fluxes above the proto-neutron star and the Mikheyev-Smirnov-Wolfenstein (MSW) flavor transformation [2, 3]. In this study, we employed the neutrino emission characteristics and electron number density profiles calculated self-consistently in an 18 $M_\odot$ supernova model [4] and took into account the time evolution of these quantities over the neutrino emission timescale of $\sim$ 10 seconds. We then examined the effect of neutrino oscillations on different nucleosynthesis processes and on the neutrino signals. [5]

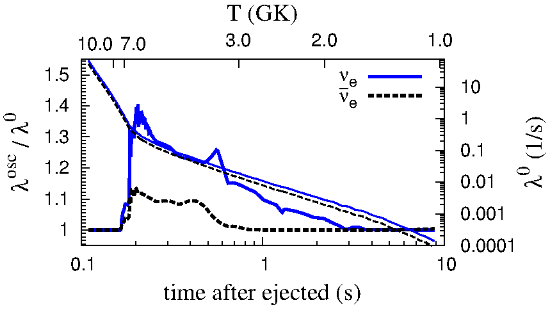

Figure 1: ν_e and $\bar{\nu}_e$ absorption rates $\lambda_{\rm osc}$, including oscillations and λ_0, without oscillations as a function of time.

Fig. 1 shows how collective neutrino oscillations change the ν_e ($\bar{\nu}_e$) absorption rates, λ, on neutrons (protons) for an example mass element ejected by neutrino-heating (the so-called ν-driven wind). Although the ν_e and $\bar{\nu}_e$ absorption rates are enhanced by $\sim 25\%$ and $\sim 10\%$ due to the flavor oscillations of $\nu_e \leftrightarrow \nu_{\mu,\tau}$ and $\bar{\nu}_e \leftrightarrow \bar{\nu}_{\mu,\tau}$ for some period of time, the enhancement occurs after the ^{4}He formation at the temperature $T \sim 7$ GK and before $T \gtrsim 3$ GK when νp process [6] operates such that the overall impact of oscillations on the ν-driven wind nucleosynthesis is negligible.

For the production of the rare isotopes ^{138}La and ^{180}Ta in the O/Ne shell of the star through ν_e absorption on ^{138}Ba and ^{180}Hf, the rates can be enhanced by up to $\sim 80\%$ and $\sim 60\%$ for those two interactions by collective neutrino oscillations and can potentially increase the production of ^{138}La and ^{180}Ta by $\sim 10\%$ when integrating over the neutrino emission time. Note that the above results assume the inverted neutrino mass hierarchy (IH) since in our model collective neutrino oscillations are suppressed in the normal neutrino mass hierarchy (NH).

For the neutrino-induced nucleosynthesis in the He shell, where the mass density $\rho \lesssim 10^3$ g/cm^3, the MSW flavor transformation has to be taken into account. In this supernova model, since the supernova shock only arrives the MSW resonance region at $\sim$ 5 s post bounce, the MSW flavor transformation can be treated adiabatically before that. We found that for the part of He shell located between $5.5 \times 10^4 \lesssim 4 \times 10^5$ km, the reaction $\nu_e + {}^4\mathrm{He} \rightarrow {}^3\mathrm{He} + p + e^-$ is enhanced by a factor of ~ 32 for the NH while $\bar{\nu}_e + {}^4\mathrm{He} \rightarrow {}^3\mathrm{H} + n + e^+$ is enhanced by ~ 17 for the IH, mainly due to the MSW transformation. This may affect the total production of light elements such as ^{7}Li and ^{11}B in supernovae.

Lastly, we looked at the effect of neutrino oscillations on the Galactic neutrino signals for different detection channels of neutrino flavors, e.g. the Super-Kamiokande detector for mainly $\bar{\nu}_e$ and a hypothetical liquid argon detector for mainly ν_e detection. We found that the time-integrated neutrino energy spectra detected during the first 0.5 s of the neutrino emission may be used to infer the neutrino mass hierarchy, when combined with the total detected event rates as a function of time.

References

[1] H. Duan, G.M. Fuller, and Y.-Z. Qian, "Collective Neutrino Oscillations", Ann.Rev.Nucl.Part.Sci, 60, 569 (2010)

[2] L. Wolfenstein, Phys.Rev. D17, 2369 (1978)

[3] S.P. Mikheyev and A.Y. Smirnov, Yadernaya Fizika 42, 1441 (1985)

[4] T. Fischer, S.C. Whitehouse, A. Mezzacappa, et. al., Astron.Astrophys. 517, A80 (2010)

[5] M.-R. Wu, Y.-Z. Qian, G. Martínez-Pinedo, et. al., Phys.Rev. D91, 065016 (2015)

[6] C. Fröhlich, G. Martínez-Pinedo, M. Liebendorfer, et. al., Phys.Rev.Lett 96, 142502 (2006)

---

* Work supported by the Alexander von Humboldt Foundation, US DOE, DFG through SFB 634, HIC for FAIR, and NAVI

† mwu@theorie.ikp.physik.tu-darmstadt.de

DOI:10.15120/GR-2015-1-MU-THEORY-06

Neutrino-driven winds from binary neutron star mergers[*]

A. Perego[1,2] *and A. Arcones*[1,2]
[1]Institut für Kernphysik (Theoriezentrum), Technische Universität Darmstadt, Darmstadt, Germany;
[2]GSI-Helmholtzzentrum für Schwerionenforschung, Darmstadt, Germany

The merger of two neutron stars in a binary system is one of the most powerful events in the Universe. Within a few tens of milliseconds, an extremely hot, hypermassive neutron star (possibly, gravitationally unstable), surrounded by a thick accretion disc, has formed. Besides being a promising progenitor for short gamma-ray-bursts, the expected neutron-rich ejecta can produce a robust r-process. The synthesised neutron-rich nuclei can power an electromagnetic transients, known as kilonova (or macronova) and potentially observed in 2013 [1].

In the post-merger phase, a large fraction of the gravitational energy released during the coalescence process is radiated away by neutrinos, with peak luminosities in excess of $10^{53}\,\mathrm{erg/s}$. The energy deposition caused by the absorption of neutrinos inside the disc, mainly via the processes:

$$n + \nu_e \rightarrow p + e^- \qquad p + \bar{\nu}_e \rightarrow n + e^+ ,$$

drives a wind on a time scale:

$$t_{\rm wind} \sim \frac{e_{\rm grav}}{\dot{e}_{\nu,\rm heat}} \approx 0.07\,\mathrm{s} ,$$

for typical remnant conditions.

We performed detailed, three-dimensional radiation hydrodynamical simulations of the neutrino-driven wind that emerges from the remnant of a neutron star binary merger [2]. We used the Newtonian, Eulerian code FISH [3], augmented by a detailed neutrino leakage scheme that accounts for the heating due to neutrino absorption in optically thin conditions. We evolve the remnant for 100 ms under the influence of neutrino cooling and heating. The initial conditions of our simulation are taken from high resolution SPH simulations of the merger of two neutron stars [4].

We find that a strong baryonic wind is blown out along the original binary rotation axis within a few tens of milliseconds after the merger. After 100 ms, the outer part of the disc has reached an almost stationary state, characterized by smooth gradients in all the relevant quantities. The physical properties of the wind vary significantly between different regions. Due to stronger neutrino irradiation, the polar regions show substantially larger electron fractions ($Y_e \sim 0.3$ - 0.4) than those at lower latitudes ($Y_e \sim 0.2$ - 0.3). Because of the radiation absorption, the entropy inside the wind first increases, then stays constant during the adiabatic expansion ($s \sim 15$ - 20 $k_{\rm B}/\mathrm{baryon}$).

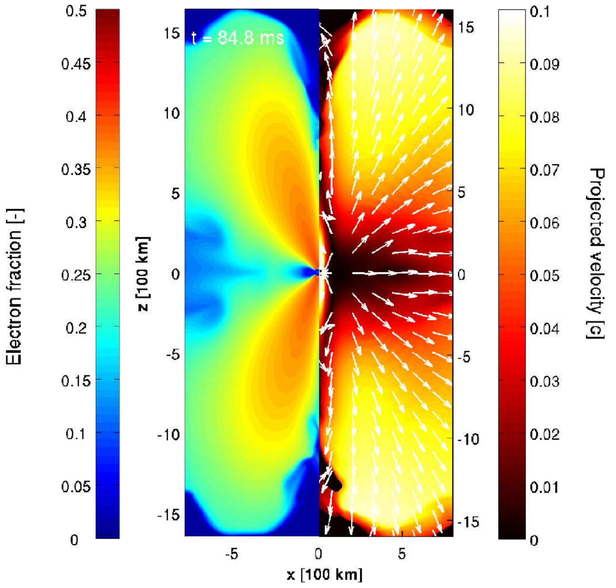

Figure 1: Vertical slices of the 3D domain (y = 0 plane) 85 ms after the beginning of the simulation. We represent the electron fraction (left) and the fluid velocity (right).

Around 100 ms after the merger, $2.1\times10^{-3}\mathrm{M}_\odot$ of matter in the wind is unbound. The polar ejecta produce interesting weak r-process contributions, from A $\sim$ 80 to about 130, while the more neutron-rich, lower-latitude parts produce in addition also elements up to the third r-process peak near A $\sim$ 195. We also calculated the properties of electromagnetic transients that are powered by the radioactivity in the wind. The polar regions produce a transients whose bolometric luminosity peaks around 0.3 days in the UV band. The lower-latitude regions are significantly less bright and peak after $\sim$ 2 days in UV/optical band, due to their much larger content in very heavy elements and the consequently larger matter opacities.

We conclude that the inclusion of the wind contributions in the merger nucleosynthesis and in the light curve prediction is crucial for detailed theoretical predictions, to be compared with present and future observations.

References

[1] N.-R. Tanvir et al., Nature, 2013, 500, p. 547

[2] A. Perego et al., MNRAS, 2014, 443, p. 3134

[3] R. Käppeli et al., ApJS, 2011, 195, p. 20

[4] D. J. Price, S. Rosswog, Science, 2006, 312, p. 719

---

[*] Work supported by Helmholtz-University Investigator grant No. VH-NG-825

DOI:10.15120/GR-2015-1-MU-THEORY-07

Nucleosynthesis of elements between Sr and Ag in neutron- and proton-rich neutrino-driven winds

J. Bliss[1] *and A. Arcones*[1,2]
[1]Institut für Kernphysik, Technische Universität Darmstadt, Darmstadt, Germany; [2]GSI Helmholtzzentrum für Schwerionenforschung GmbH, Darmstadt, Germany

Neutrino-driven winds that follow core collapse supernovae were thought to be the site where half of the heavy elements are produced by the r-process. Although recent hydrodynamic simulations show that the conditions in the wind are not neutron-rich enough for the r-process (see e.g. [7]), lighter heavy elements like Sr, Y and Zr can be produced [1, 8, 4]. However, it is still not clear whether the conditions in the wind are slighly neutron-rich or proton-rich. In Ref. [1], we have studied the formation of lighter heavy elements in slighly neutron-rich ($Y_e < 0.5$) and proton-rich ($Y_e > 0.5$) winds. We have systematically explored the impact of the wind parameters (see e.g. [9, 6]): entropy, expansion time scale and electron fraction Y_e. The wind parameters have been varied within typical conditions values found in wind simulations [2, 3].

An overview of the dependency of the Sr abundances on the wind parameters is shown in Fig. 1. Similar features and trends are obtained for other lighter heavy elements (see [1]).

In neutron-rich winds (upper panel) the abundances of Sr oscillate and exhibit several minima and maxima when the wind parameters are varied. In proton-rich winds (lower panel) we find two main differences. First, the abundances vary smoothly when varying the wind parameters. Depending on the wind parameters the heaviest element that can be produced changes. The overall abundance pattern remains similar for Sr, Y, Zr and Ag. Thus, if neutrino-driven winds are responsible for the observed abundances in very old stars, neutron-rich conditions would not provide the robustness observed in the abundance pattern. Second, most of the ejected matter consists of protons and alpha particles in proton-rich winds, while the amount of heavy nuclei is small ($Y_{\text{seed}} \lesssim 10^{-4}$). In neutron-rich winds alpha particles also dominate the composition but heavy nuclei are more abundant ($Y_{\text{seed}} > 10^{-3}$) than in proton-rich conditions. Hence, if every wind stays neutron-rich for several seconds there would be an overproduction around A=90 [5, 10]. Therefore, not every wind can be only neutron-rich.

Combining nucleosynthesis studies, like the one here, with new and future experimental data and observations, it will give rise to new insights about the supernova neutrinos and explosions.

This work was funded by the Helmholtz-University Young Investigator grant No. VH-NG-825.

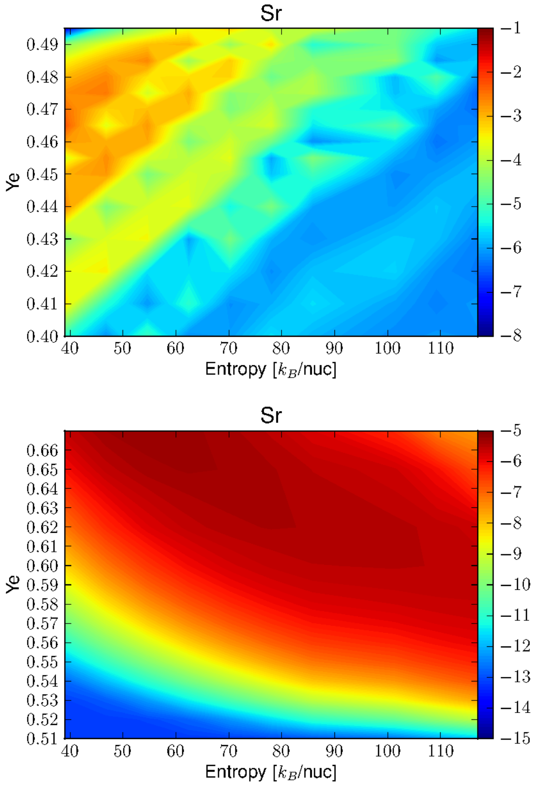

Figure 1: Color contours show the abundance in log scale of Sr for different entropies and Y_e in neutron-rich (upper panel) and proton-rich (lower panel) winds.

References

[1] A. Arcones and J. Bliss, *J. Phys. G*, 41:044005, 2014.
[2] A. Arcones and H.-T. Janka. *A&A*, 526:A160, 2011.
[3] A. Arcones, H.-T. Janka, and L. Scheck. *A&A*, 467:1227–1248, 2007.
[4] A. Arcones and F. Montes. *ApJ*, 731:5, 2011.
[5] R. D. Hoffman, S. E. Woosley, G. M. Fuller, and B. S. Meyer. *ApJ*, 460:478–488, 1996.
[6] R. D. Hoffman, S. E. Woosley, and Y.-Z. Qian. *ApJ*, 482:951–962, 1997.
[7] L. Hüdepohl, B. Müller, H.-T. Janka, A. Marek, and G. G. Raffelt. *Phys. Rev. Lett.*, 104(25):251101, 2010.
[8] Y.-Z. Qian and G. J. Wasserburg. *Phys. Rep.*, 442:237–268, 2007.
[9] Y.-Z. Qian and S. E. Woosley. *ApJ*, 471:331–351, 1996.
[10] S. E. Woosley and R. D. Hoffman. *ApJ*, 395:202–239, 1992.

DOI:10.15120/GR-2015-1-MU-THEORY-08

How many r-processes exist?*

A. Arcones[1,2], *C. J. Hansen*[3,4], *and F. Montes*[5,6]
[1]Institut für Kernphysik, Technische Universität Darmstadt, Germany; [2]GSI Helmholtzzentrum für Schwerionenforschung GmbH, Germany; [3]Landessternwarte, ZAH, Heidelberg University, Germany; [4]Dark Cosmology Centre, The Niels Bohr Institute, Copenhagen, Denmark; [5]Joint Institute for Nuclear Astrophysics, Michigan State University, USA; [6]National Superconducting Cyclotron Laboratory, Michigan State University, USA

Abundances of low-metallicity stars offer a unique opportunity to understand the contribution and conditions of the different processes that synthesize heavy elements. Many old, metal-poor stars show a robust abundance pattern for elements heavier than Ba, and a less robust pattern between Sr and Ag. In our recent paper [1], we show that two nucleosynthesis processes are sufficient to explain the stellar abundances at low metallicity, and we carry out a site independent approach to separate the contribution from these two processes or components to the total observationally derived abundances. Our approach provides a method to determine the contribution of each process to the production of elements such as Sr, Zr, Ba, and Eu. Moreover, we use the deduced abundance pattern of one of the nucleosynthesis components to constrain the astrophysical conditions of neutrino-driven winds from core-collapse supernovae.

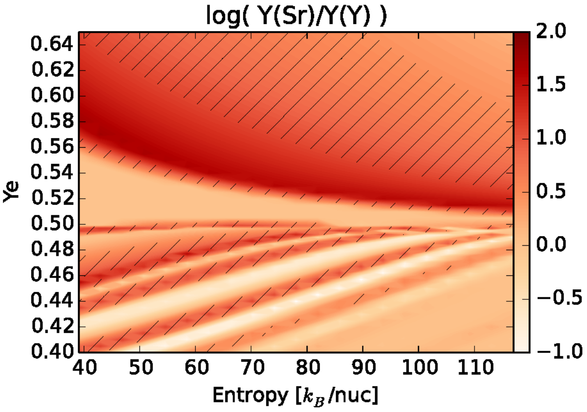

Figure 1: Ratios of abundances for Sr and Y. In the hatched regions the ratios agree with observations, taking into account uncertainties and errors.

Neutrino-driven winds occur after a successful core- collapse supernova explosion, when neutrinos deposit their energy in the outer layers of the neutron stars, and this layer gets ejected (see [2] for a recent review). Although neutrino-driven winds were thought to be the site for the r-process [3], recent hydrodynamic simulations have shown that the required extreme conditions are not reached. It is still possible that the winds have the conditions necessary to produce the lighter heavy elements from Sr to Ag [4]. We have explored which astrophysical conditions are capable of reproducing the observed abundances from Sr to Ag. In order to account for the uncertainty in the wind parameters (entropy, expansion time scale, and electron fraction), we systematically varied them within their expected uncertainty.

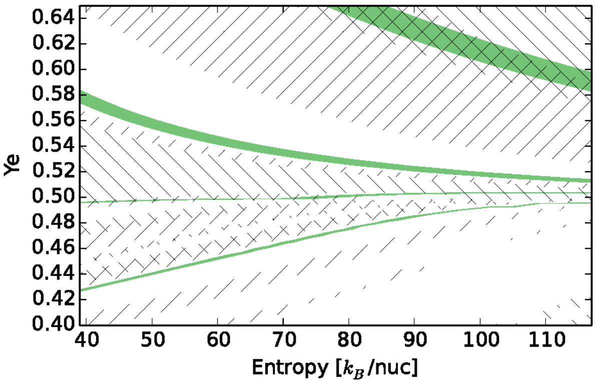

Figure 2: This figure shows the wind parameter space and the regions where the ratios Sr/Y (//), Sr/Zr (\\), and Sr/Ag (green) agree with observations. The three ratios overlap mainly for proton-rich conditions.

Our result are presented in Figs. 1–2. Proton-rich conditions ($Y_e > 0.5$) favor the production of Sr, Y, Zr, and Ag following the observed ratios. If only the observation of Sr, Y, and Zr need to be reproduced, then there are also possible parameter combinations in neutron-rich conditions. Further investigations of the wind and the nuclear reactions involved combined with observations will give rise to new insights on the origin of lighter heavy elements.

References

[1] C.J. Hansen, F. Montes & A. Arcones, *Astrophys. J.* **797**, 123 (2014).

[2] A. Arcones & F.-K. Thielemann, *J. Phys. G* **40**, 013201 (2013).

[3] S.E. Woosley et al., *Astrophys. J.* **433**, 229 (1994).

[4] A. Arcones & F. Montes, *Astrophys. J.* **731**, 5 (2011).

---

* Work supported by Helmholtz-Nachwuchsgruppe VH-NG-825.

DOI:10.15120/GR-2015-1-MU-THEORY-09

Gogny-HFB convergence analysis and Beyond-Mean-Field correlations*

A. Arzhanov†[1,2], *T.R. Rodríguez*[3], *and G. Martínez-Pinedo*[1,2]
[1]Institut für Kernphysik, TU Darmstadt, Germany; [2]GSI, Darmstadt, Germany; [3]Dpto. de Física Teórica, UAM, Spain

Introduction

r-Process stellar nucleosynthesis requires accurate predictions of nuclear properties for nuclei far beyond reach of current experimental facilities. Regardless of the potential astrophysical site, the final elemental abundances are very sensitive to the employed global nuclear mass table [1]. Mean-field approaches based on Hartree-Fock-Bogolyubov (HFB) formalism are as microscopic as possible for global calculations, and thus are expected to be more reliable predicting unknown nuclei. However, in order to further increase predictive power of HFB-based models particular attention must be paid to the following three main issues of the currently used HFB-models.

I. Convergence

Ideally, computed observables should be independent of chosen harmonic oscillator (HO) basis, i.e. *converged.* However, due to basis truncation, and asymptotic behavior of HO–functions, calculations for heavy and/or neutron-rich systems are generally *not fully converged.*

A better treatment of convergence in our global survey [2] of 2180 even-even nuclear masses up to the drip lines based on Gogny-D1S HFB approach noticeably improved agreement with experimental data: *(a)* when compared with the previously published database [3] our results are better converged by $\sim$1.5 MeV; *(b)* the root-mean-square (rms) deviation from the 594 experimental masses in AME12 compilation [4] is reduced from 4.6 MeV to 3.5 MeV with the most sizeable improvement in-between the shell closures; *(c)* numerical noise due to lack of convergence is removed, resulting in smoother two-neutron separation energies for every isotopic chain.

Evident lack of convergence prompted us to perform systematic studies of two recently proposed energy correction schemes: empirical MVS–A [5] and theoretically justified L_{eff}–extrapolation [6]. Unfortunately none of them provide reliable and consistent results for r-process nuclei [7].

II. Beyond-Mean-Field (BMF) Correlations

A significant improvement in precision of HFB models is expected after including the BMF corrections, such as *(i)* particle number, and *(ii)* angular momentum projections, as well as *(iii)* configuration mixing. Because of high computational cost, all pioneer global BMF–surveys using generator coordinate method (GCM) were carried out assuming the so called Gaussian overlap approximation (GOA). We performed global calculation with the mentioned D1S and an improved Gogny-D1M parametrization using the exact implementations of GCM methods assuming axial symmetry. Our results [8] show: *(a)* BMF–effects amount to 5–6 MeV of correlation energy; *(b)* as in all published mass–tables, the BMF–corrections decrease the scatter in the computed masses, especially for light nuclei; *(c)* the neutron and proton shell gaps at N and Z =20, 28 are also slightly reduced, but we do not see the reported previously [3, 9] shell quenching for the remaining shell gaps.

III. Odd-Even Effects

Description of odd-mass isotopes within the same HFB approach requires time-reversal symmetry breaking, which makes computation task an order of magnitude more expensive. In order to make global calculation for all isotopes feasible, we had to employ perturbative nucleon addition method, which inevitably leads to uncertainties, such as *(i)* gradually increasing overestimation of neutron separation energies in vicinity of N-shell closure, and *(ii)* largely exaggerated shell gap. Further investigations of this approximation, as well as possibilities of other methods are the topics of our current research.

References

[1] Arcones A and Martínez-Pinedo G, *PRC83*, 045809 (2011).
[2] Arzhanov A, Rodríguez TR, and Martínez-Pinedo G, *PoS(NIC XIII)*, 066 (2014).
[3] Hilaire S and Girod M, *EPJA33*, 237 (2007), *and* Delaroche J-P et al., *PRC81*, 014303 (2010).
[4] Wang M et al., *CPC36*, 1603 (2012).
[5] Maris P, Vary JP, and Shirokov AM, *PRC79*, 014308 (2009).
[6] Furnstahl RJ et al., *JPG42*, 034032 (2015).
[7] Arzhanov A, Rodríguez TR, and Martínez-Pinedo G, *in preparation* (2015).
[8] Rodríguez TR, Arzhanov A, and Martínez-Pinedo G, *arXiv*:1407.7699 (2014).
[9] Bender M, Bertsch GF, Heenen P-H, *PRC78*, 054312 (2008).

---

* **AA** is supported by the Helmholtz Association through Nuclear Astrophysics Virtual Institute (NAVI), VH-VI-417. **TRR** was supported from the BMBF-Verbundsforschungsprojekt number 06DA7047I. **GMP** acknowledges support by the Deutsche Forschungsgemeinschaft through contract SFB 634 and the LOEWE program launched by the state of Hesse. The calculations were performed on the CPU supercomputer cluster LOEWE-CSC of Goethe University Frankfurt, and PROMETHEUS cluster of the computing facility at GSI Helmholtz Centre for Heavy Ion Research (GSI).

† a.arzhanov@gsi.de

DOI:10.15120/GR-2015-1-MU-THEORY-10

Microscopic description of the ^{12}C continuum

T. Neff[1] *and H. Feldmeier*[1,2]
[1]GSI, Darmstadt, Germany; [2]FIAS, Frankfurt, Germany

The structure of ^{12}C above the three-α threshold poses a challenge for nuclear theory. The ground state band can be well described in the no-core shell model using a harmonic oscillator single-particle basis. However, many of the states in the continuum have a well developed cluster structure, and these states are completely missing in the no-core shell model. Microscopic cluster models have been able to reproduce many properties of these continuum states. On the other hand, the cluster model is an idealization. Experimentally Gamow-Teller as well as $M1$ and $E1$ transitions into continuum states can be observed. Within a cluster model such transitions are forbidden, indicating that for a full picture both shell and cluster structure have to be included in a theoretical description.

Fermionic molecular dynamics (FMD) is a microscopic many-body approach that uses Slater determinants built from Gaussian wave-packets as intrinsic basis states [1]. It contains both harmonic oscillator shell model states and Brink-type cluster configurations as limiting cases and is therefore well suited to study the structure of ^{12}C. Previous FMD calculations [2] treated states in the continuum in a bound-state approximation. This might be justified for the very narrow Hoyle state but is certainly very unreliable for the broad resonances observed higher up in energy.

To address these questions we extended our approach with a proper treatment of the continuum. We first performed a study within the microscopic α-cluster model with full antisymmetrization and a phenomenological two-body interaction [3]. In the internal region the Hilbert space is here built from three-α configurations on a triangular grid. In the external region ^{8}Be-^{4}He configurations are added. Recently we also added the continuum to the full FMD calculation. Here basis states in the internal region have been obtained using variation after projection on angular momentum and parity. For each spin we first vary the parameters of the many-body state to obtain the lowest possible energy. A second basis state is then obtained by minimizing the energy of the second state with respect to its parameters keeping the first state fixed. We further increase the model space by using the radius of the intrinsic states as generator coordinates. The ^{8}Be clusters are obtained by diagonalization in a basis of FMD states and of α-α configurations, treating them as pseudostates. We include two 0+, two 2+ and a 4+ state for ^{8}Be. The microscopic R-matrix method is used to match the microscopic wave functions in the internal region to the asymptotic behavior described by point-like ^{8}Be- and α-clusters. For bound states the asymptotics is given by Whittaker functions, for resonances we match to purely outgoing Coulomb wavefunctions. The energies then become complex, with the real part giving the resonance position and the imaginary part the resonance width. We can also obtain scattering states with real energies by matching to linear combinations of incoming and outgoing Coulomb wave functions which provides the full scattering matrix.

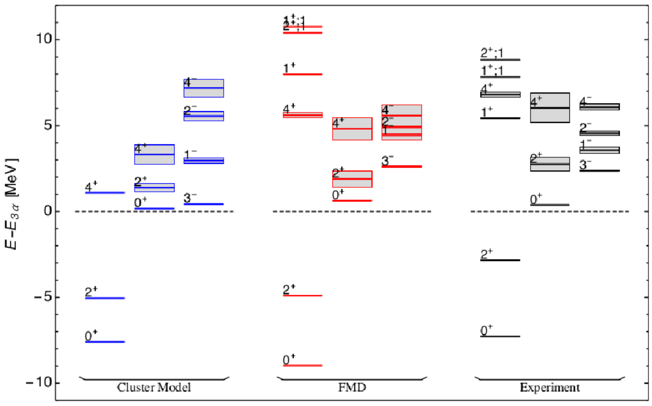

Figure 1: ^{12}C energy spectra obtained within a microscopic cluster model, fermionic molecular dynamics (FMD) compared with experiment. Energies are given with respect to the 3-α threshold. Resonance widths are indicated by gray bars.

In Fig. 1 we show the spectra containing bound states and resonances obtained with the microscopic cluster model and with FMD. The cluster model can not describe spin-flip states like the 1^+ states or the 2^+ (T=1) state. The FMD calculations show in general a good agreement with experimental observations. For example we obtain the 4^+ from the ground state band, the 4^+ state of the Hoyle state band and the 4^- at roughly the same energy, in good agreement with experiment. Future studies will focus on transitions into the continuum. Apart from the monopole strength investigated in [2], recent experiments studied transitions into the second 2^+ state and the 1^- state. Also Gamow-Teller transitions from ^{12}B and ^{12}N and electromagnetic transitions from the 2^+ (T=1) state into the ^{12}C continuum have been measured carefully.

References

[1] T. Neff, H. Feldmeier, Eur. Phys. J Spec. Top. **156**, 69 (2008).

[2] M. Chernykh *et al.*, Phys. Rev. Lett. **98**, 032501 (2007).

[3] T. Neff, H. Feldmeier, J. Phys.: Conf. Ser. **569**, 012062 (2014).

DOI:10.15120/GR-2015-1-MU-THEORY-11

Fission barriers of r-process nuclei using the BCPM energy density functional[*]

S. .A. Giuliani[†][1], *G. Martínez-Pinedo*[1], *and L. M. Robledo*[2]

[1]Institut für Kernphysik (Theoriezentrum), Technische Universität Darmstadt, Schlossgartenstraße 2, 64289 Darmstadt, Germany; [2]Departamento de Física Teórica, Universidad Autónoma de Madrid, E-28049 Madrid, Spain.

The nuclear fission process plays a crucial role during the r-process nucleosynthesis in neutron star mergers (see e.g. [1] for a recent review). In this specific astrophysical site the fission process determines how matter is recycled during the neutron irradiation and the production of superheavy nuclei. The theoretical description of the nuclear fission process is nowadays one of the most challenging and fascinating problems in nuclear physics. In the last years several studies based on the Energy Density Functional (EDF) theory were devoted to this topic. However, despite of the great efforts made to reduce its theoretical uncertainties, the fission process is still far from been satisfactorily described [2].

Here we want to report on the fission properties of the Barcelona-Catania-Paris-Madrid (BCPM) EDF [3, 4]. The fission properties of 330 even-even nuclei in the superheavy region ($92 \leq Z \leq 120$ and $160 \leq N \leq 202$) were computed following the standard Hartree-Fock-Bogoliubov (HFB) theory based in the Self-Consistent Mean-Field Approach. The spontaneous fission lifetimes t_{sf} were computed using the semiclassical approach given by the Wentzel-Kramers-Brillouin (WKB) formalism. Within this formalism, the fission probability can be written in terms of the action integral computed along the fission path. The collective inertias were calculated using the Gaussian Overloap approximation to the Generator Coordinate Method (GOA-GCM). The fission path is obtained by minimization of the HFB energy (static approximation) and constraining the quadrupole moment operator assuming axial symmetry.

Using these prescriptions the BCPM functional predicts an enhanced stability against the spontaneous fission process around the neutron magic number $N = 184$ for the lightest nuclei ($Z \leq 100$). In this region the fission barriers can increase up to 12 MeV leading to long-live nuclei [5]. This general enhancement of the fission barriers is consistent with the predictions obtained in other studies computed using the Thomas-Fermi semiclassical model [6], the microscopic-macroscopic model of Ref.[7] and the HFB14 parametrization of the Skyrme interaction [8].

The competition between the neutron capture process and the neutron-induced fission is driven by the difference between the fission barrier height B_f and the neutron separation energy S_n [9]. In Fig.1 the $R_{BS} = B_f - 0.5 \times S_{2n}$ value is depicted in the (N, Z) plane. As rough estimation is usually considered that nuclei with a $R_{BS} \leq 2$ MeV would fission immediately after capturing a neutron. As a consequence of this estimation, we can conclude that after the magic shell $N = 184$ the production of heavier nuclei is inhibited by the neutron-induced fission. This results agree with the predictions made in Ref.[10] using a combination of the TF barriers and FRDM masses.

For a complete nucleosynthesis modeling, fission yields computations are required. A work in this direction is already in progress.

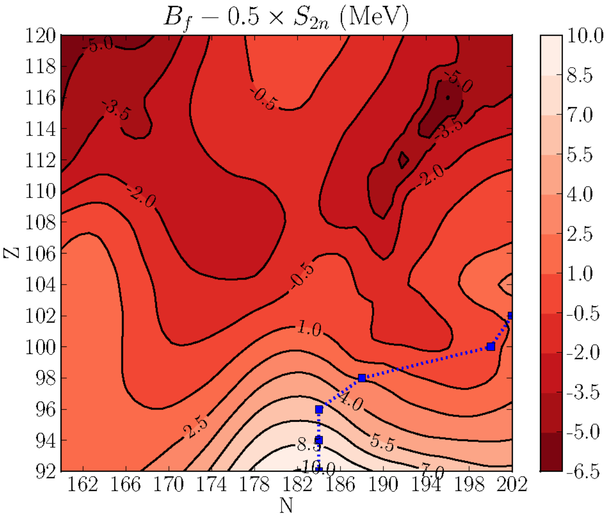

Figure 1: Contour plot of the quantity $R_{BS} \equiv B_f - 0.5 \times S_{2n}$ in MeV computed with the BCPM interaction. Squares represent the heaviest isotope for each nuclei with $Z \leq 102$ and $S_{2n} \geq 4.0$ MeV.

References

[1] S. Goriely, Eur. Phys. J. **A51**, 22 (2015).
[2] S. A. Giuliani et al., Phys. Rev. **C90**, 054311 (2014).
[3] M. Baldo et al., Phys. Rev. **C87**, 064305 (2013).
[4] S. A. Giuliani et al., Phys. Rev. **C88**, 054325 (2013).
[5] S. A. Giuliani et al., PoS (NIC XIII) **095**, (2015).
[6] A. Mamdouh et al., Nucl. Phys. **A679**, 337 (2001).
[7] W. D. Myers et al., Nucl. Phys. **A601**, 141 (1996).
[8] S. Goriely et al., Phys. Rev. **C75**, 064312 (2007).
[9] I. V Panov et al., Astron. Astrophys. **513**, A61 (2010).
[10] I. Petermann et al., Eur. Phys. J. **A48**, 122 (2012).

---

[*] The work of SAG and GMP was supported by the Helmholtz Association through the Nuclear Astrophysics Virtual Institute (VH–VI–417) and the BMBF–Verbundforschungsprojekt number 06DA7047I. The work of LMR was supported by the Spanish MICINN Grants No. FPA2012–4694 and No. FIS2012–34479 and by the Consolider–Ingenio 2010 MULTIDARK CSD2009-00064.

[†] giuliani@theorie.ikp.physik.tu-darmstadt.de

DOI:10.15120/GR-2015-1-MU-THEORY-12

Thermalization of hadrons via Hagedorn states

M. Beitel, K. Gallmeister, and C. Greiner
Institut für Theoretische Physik, Goethe–Universität Frankfurt

Hagedorn states are part of the Statistical Bootstrap model (SBM) [1] having remarkable features. They are very massive hadron-like resonances which are allowed to have any quantum numbers as long as they are compatible with their mass. Hence Hagedorn states can carry charges like baryon number, strangeness or electric charge exceeding those of known hadrons. To obtain the whole zoo of Hagedorn states we solve, in contrast to Ref. [2] where a non-covariant version was examined, a covariant bootstrap equation numerically by ensuring energy–momentum conservation and the conservation of the baryon number B, strangeness S, and electric charge Q. As basis for this bootstrap we use the mass distributions of the known hadronic resonances, as implemented in the transport code UrQMD. The solution provides Hagedorn spectra for different quantum number combinations as function of Hagedorn state's mass. The spectra for charge neutral, meson–like, $(B = S = Q = 0)$ Hagedorn states for two different Hagedorn state radii are shown in Fig. 1. The sum of the hadronic spectral functions with the same quantum numbers is presented to emphasize that our Hagedorn spectra not only exhibit the exponential behaviour for very large Hagedorn state masses but also reproduce the low-mass part. Using these spectra one can formulate the decay widths Γ of Hagedorn states needed in cascading simulations. The decay width of charge neutral Hagedorn states is presented in Fig. 2. As an important feature, all decay widths tend to a constant value greater zero in the infinite mass limit denoting that all Hagedorn states must be unstable.

Now having the decay widths we proceed to examine a decay of a massive Hagedorn state in a cascade until stable hadrons are left only. Apart from the calculated hadronic multiplicities we also looked at the energy distribution of those final particles. We found that all particles exhibit the same temperature, obtained from the Boltzmann distribution's slope as can be seen in Fig. 3. Another remarkable feature is that this (thermodynamic) temperature exactly equals the Hagedorn temperature you obtain from the slopes of the Hagedorn spectra shown in Fig. 1. A detailed discussion about these findings can be found in [3].

References

[1] R. Hagedorn, Nuovo Cim. Suppl. **3**, 147 (1965).

[2] C. J. Hamer and S. C. Frautschi, Phys. Rev. D **4**, 2125 (1971) [Erratum-ibid. D **5**, 1235 (1972)].

[3] M. Beitel, K. Gallmeister and C. Greiner, Phys. Rev. C **90**, 045203 (2014) [arXiv:1402.1458 [hep-ph]].

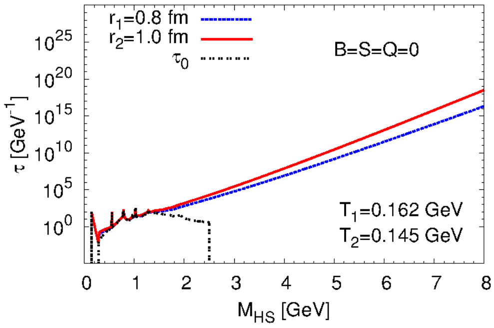

Figure 1: Meson-like $(B, S, Q = 0)$ Hagedorn spectra.

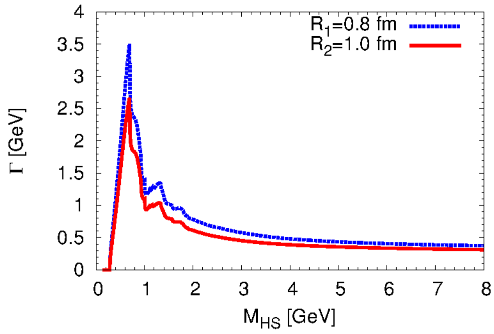

Figure 2: Decay widths of Hagedorn states as in Fig. 1.

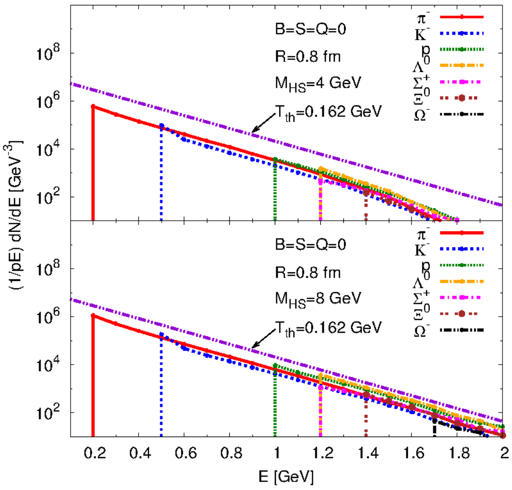

Figure 3: Energy distribution of final hadrons stemming from an initial charge neutral $(B, S, Q = 0)$ Hagedorn state with $r = 0.8\,\mathrm{fm}$ for two initial masses $M_{\mathrm{HS}} = 4\,\mathrm{GeV}$ (up) and $M_{\mathrm{HS}} = 8\,\mathrm{GeV}$ (down)

DOI:10.15120/GR-2015-1-MU-THEORY-13

Spectral functions from the Functional Renormalization Group*

R.-A. Tripolt†[1], *L. von Smekal*[1,2], *and J. Wambach*[1,3]
[1]TU Darmstadt, Germany; [2]JLU Giessen, Germany; [3]GSI, Germany

We present a method to obtain spectral functions at finite temperature and chemical potential from the Functional Renormalization Group (FRG) approach. Our non-perturbative method is thermodynamically consistent, symmetry preserving and based on an analytic continuation from imaginary to real time on the level of the flow equations for two-point functions. In order to demonstrate the feasibility of our method, we apply it to the quark-meson model and present results for the pion and sigma spectral function at finite temperature and density.

The calculation of real-time quantities like spectral functions or transport coefficients for strongly interacting matter is difficult and often hampered by the analytic continuation problem. This problem arises for example in lattice QCD, where discrete numerical data has to be used to reconstruct real-time correlation functions. Within our new approach for the Functional Renormalization Group (FRG), the analytic continuation can be performed on the level of the flow equations, without the need for any numerical reconstruction technique.

In particular, the flow equations for the retarded 2-point functions are obtained from their Euclidean counterparts via the following two-step procedure. First, the periodicity of the bosonic and fermionic occupation numbers with respect to the discrete Euclidean energy $p_0 = 2n\pi T$ is used, i.e.

$$n_{B,F}(E + ip_0) \to n_{B,F}(E).$$

As a second step, the Euclidean energy p_0 is replaced by a continuous real frequency ω as follows,

$$\Gamma^{(2),R}(\omega, \vec{p}) = -\lim_{\epsilon\to 0} \Gamma^{(2),E}(p_0 = -i(\omega + i\epsilon), \vec{p}).$$

The spectral functions are then given by the imaginary part of the retarded propagator, which is given by the inverse of the retarded two-point function $\Gamma^{(2),R}(\omega, \vec{p})$.

In Fig. 1 we show the pion spectral function at $T = 100$ MeV and vanishing chemical potential. Due to thermal processes, the pion is unstable at this temperature, as represented by a peak with finite width, that is Lorentz-boosted to higher energies as the spatial momentum increases. Decay channels at higher energies and additional processes at space-like 4-momenta give rise to non-zero values of the spectral function away from the pion peak.

In Fig. 2 we show the sigma spectral function for different spatial momenta near the critical endpoint. We observe that the sigma meson is stable and exhibits an almost vanishing mass near this second order phase transition, as expected.With increasing spatial momenta, the sigma peak is Lorentz-boosted to higher energies and space-like processes modify the spectral function at $\omega < |\vec{p}|$.

As an outlook, we note that our approach also allows to calculate transport coefficients like the shear viscosity via Green-Kubo formulas. Moreover, the calculation of quark spectral functions and the inclusion of vector and axial-vector mesons represent interesting extensions.

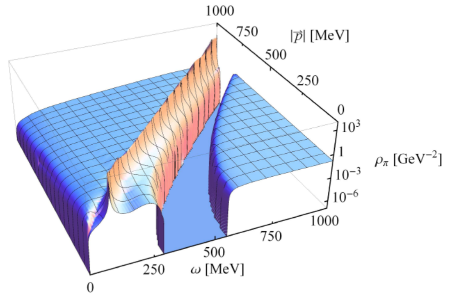

Figure 1: The pion spectral function ρ_π is shown vs. energy ω and spatial momentum $\vec{p}$ at $T = 100$ MeV and $\mu = 0$.

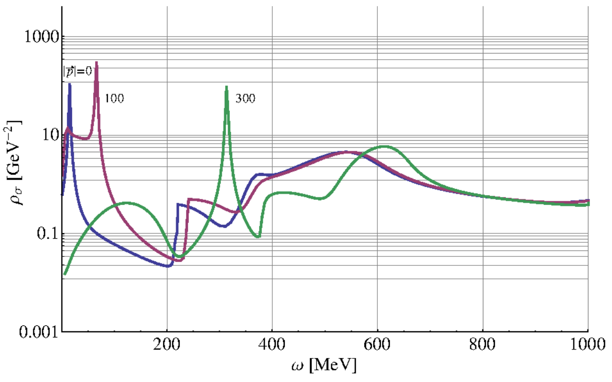

Figure 2: The sigma spectral function is shown vs. energy ω at $T = 10$ MeV and $\mu = 292.97$ MeV for different spatial momenta $\vec{p}$, as indicated by inset labels.

References

[1] R.-A. Tripolt, L. von Smekal, and J. Wambach, Phys. Rev. D 90, 074031 (2014).

[2] R.-A. Tripolt, N. Strodthoff, L. von Smekal, and J. Wambach, Phys. Rev. D 89, 034010 (2014).

---

* Work supported by HIC4FAIR. R.-A. T was supported by GSI through the cooperative agreement with TU Darmstadt.

† tripolt@theorie.ikp.physik.tu-darmstadt.de

DOI:10.15120/GR-2015-1-MU-THEORY-14

The $O(4)$ criticality in the net-baryon number probability distribution*

K. Morita†1, *B. Friman*2, *and K. Redlich*3

1Yukawa Institute for Theoretical Physics, Kyoto University, Japan; 2GSI, Darmstadt, Germany; 3Institute of Theoretical Physics, University of Wrocław

Relativistic heavy-ion collisions provide a unique opportunity to explore possible phase transitions in Quantum Chromodynamics (QCD) at finite temperature and baryon density. Current lattice QCD simulations show, that at vanishing and small density the transition is of the crossover type. However, near the transition temperature the higher order fluctuations of conserved charges reflect the underlying second order chiral phase transition, expected in QCD in the chiral limit.

Fluctuations of the net-proton number, as a proxy for the net-baryon number, have been recently measured by the STAR collaboration in Au+Au collisions at RHIC for a wide range of beam energies [1]. The fluctuation measurements yield event-by-event multiplicity distributions.

Assuming that the event-by-event fluctuations are governed by the grand canonical (GC) ensemble, the probability distribution of the net-baryon number reads

$$P(T,V,N,\mu) = \frac{Z(T,V,N)e^{\mu N/T}}{\mathcal{Z}(T,V,\mu)}, \qquad (1)$$

where $Z(T,V,\mu)$ is the canonical and $\mathcal{Z}(T,V,\mu)$ the GC partition function.

While higher order fluctuations are often characterized by the behavior of cumulants of the probability distribution (1), we directly compute $P(N)$ and discuss its properties near the chiral crossover [2].

In the chiral limit, the critical behavior of QCD at finite temperature is expected to belong to the $O(4)$ universality class, as conjectured by Pisarski and Wilczek and recently supported by lattice QCD simulations. The sixth order cumulant of the net baryon number exhibits a change of sign at the crossover transition. This is a remnant of the $O(4)$ criticality, since in the chiral limit the sixth and the higher order cumulants diverge.

In the following, we utilize the chiral quark-meson (QM) model as an effective approach to describe the $O(4)$ chiral phase transition and employ the functional renormalization group method to account for critical fluctuations in $P(N)$. We introduce the Skellam distribution $P^S(N)$ as a reference for a non-critical behavior. Since criticality in the $O(4)$ transition lies in the higher order fluctuations, except in the vicinity of the $Z(2)$ critical point, we employ a Skellam distribution $P^S(N)$ with the same second cumulant as the $P(N)$ obtained in the model calculation, and compare the two by examining their ratio.

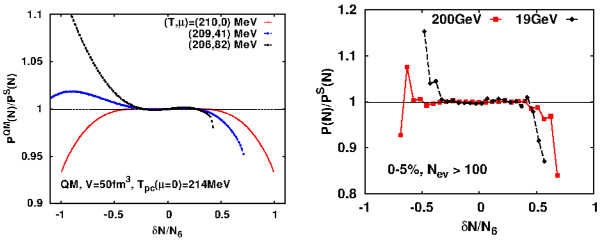

Figure 1: Ratio of probability distribution to the reference Skellam distribution. Left: model calculation. Right: experimental data.

Figure 1-left displays the ratio of these probability distributions as a function of the net baryon number δN normalized by a constant factor N_6 [2], at vanishing and at finite chemical potentials along an approximate freeze-out line. There are some interesting features of this ratio. At $\mu = 0$, $P(N)$ exhibits a narrower tail than $P^S(N)$ at large δN. This property is directly connected with the negative values of the sixth order cumulant, which is a consequence of $O(4)$ criticality.

Moreover, there is asymmetry in the ratio at $\mu > 0$. We note that at $\delta N > 0$ the narrowing of the tail begins at smaller δN than at $\mu = 0$, reflecting a stronger influence of criticality at non-zero net baryon density. This is consistent with the fact that at $\mu \neq 0$ already the third cumulant exhibits critical behavior.

The same ratio can be constructed for the experimental data. In Fig. 1-right, we show the ratio of the *efficiency uncorrected* data to the corresponding Skellam distribution for the most central bin in Au+Au collisions at $\sqrt{s_{NN}} = 200$ GeV and at $\sqrt{s_{NN}} = 19$ GeV. Clearly, the overall behavior is consistent with that expected near the $O(4)$ pseudocritical line. However, before drawing firm conclusions on the presence of critical fluctuations in data, the influence of efficiency corrections and of non-critical effects on $P(N)$ must be carefully examined.

References

[1] L. Adamczyk et al., Phys. Rev. Lett. **112**, 032302 (2014).

[2] K. Morita, B. Friman and K. Redlich, Phys. Lett. **B741**, 178 (2015).

---

* Work supported by HIC for FAIR, EMMI, the YIPQS at Kyoto University, the Grant-in-Aid for Scientific Research from JSPS No.24540271, the Grant-in-Aid for Scientific Research on Innovative Areas from MEXT No.24105008 and the Polish Science Foundation (NCN), under Maestro grant DEC-2013/10/A/ST2/00106.

† kmorita@yukawa.kyoto-u.ac.jp

DOI:10.15120/GR-2015-1-MU-THEORY-15

Fluctuations of the Polyakov loop in the heavy quark regime.*

Pok Man Lo†[1,2], *Bengt Friman*[2], *and Krzysztof Redlich*[1]
[1]University of Wroclaw, Wrocław, Poland; [2]GSI, Darmstadt, Germany

The first-order deconfinement phase transition in SU(3) pure gauge theory is directly connected to the global Z(3) center symmetry and its spontaneous breaking. The transition is eventually washed out by the explicit symmetry breaking induced by dynamical quarks. The strength of the breaking increases as the quark mass decreases. It is thus expected that the transition remains discontinuous in the heavy-quark region and becomes a continuous crossover at some critical value of quark mass. This defines the critical end point (CEP) of the deconfinement phase transition.

Details of the phase structure of the deconfinement transition are revealed by examining the fluctuations of the Polyakov loop. Lattice results on these quantities exist for both pure gauge theory [1] and (2+1)-flavor QCD [2, 3]. However, the theoretical understanding of these quantities remains incomplete. It is therefore important to explore the properties of the Polyakov loop susceptibilities for different number of flavors, as functions of the quark mass in the heavy-quark region, thus bridging the gap between pure gauge theory and QCD.

In SU(3) gauge theory, the Polyakov loop is a complex-valued operator. One can therefore define the fluctuations of the order parameter along the longitudinal (real) and transverse (imaginary) directions. In the figures we show the temperature dependence of the susceptibilities computed within an effective model [4].

While both susceptibilities change with the value of quark mass, only the longitudinal one shows an enhancement near the CEP [4]. The transverse susceptibility decreases monotonically with decreasing quark mass. Thus, for a given N_f, the CEP can be located by finding the global maximum of χ_{L}. For different N_f, the following values of the critical quark masses are obtained:

$$m_{\mathrm{CEP}} = 1.10,\ 1.35,\ 1.48\,\mathrm{GeV}, \quad \text{for}\ N_f = 1, 2, 3. \qquad (1)$$

This trend, increasing m_{CEP} with N_f, is consistent with lattice results. Moreover, the critical mass is found to be increasing with quark chemical potential μ. Consequently, the first-order region of the deconfinement phase transition shrinks with increasing density. Conversely, within the model the critical temperature of the CEP is almost independent of μ.

We conclude that the CEP can be uniquely identified by a singularity of the longitudinal Polyakov loop susceptibility. In the critical region, the longitudinal fluctuation is enhanced. The transverse susceptibility, on the other hand, remains finite at the CEP.

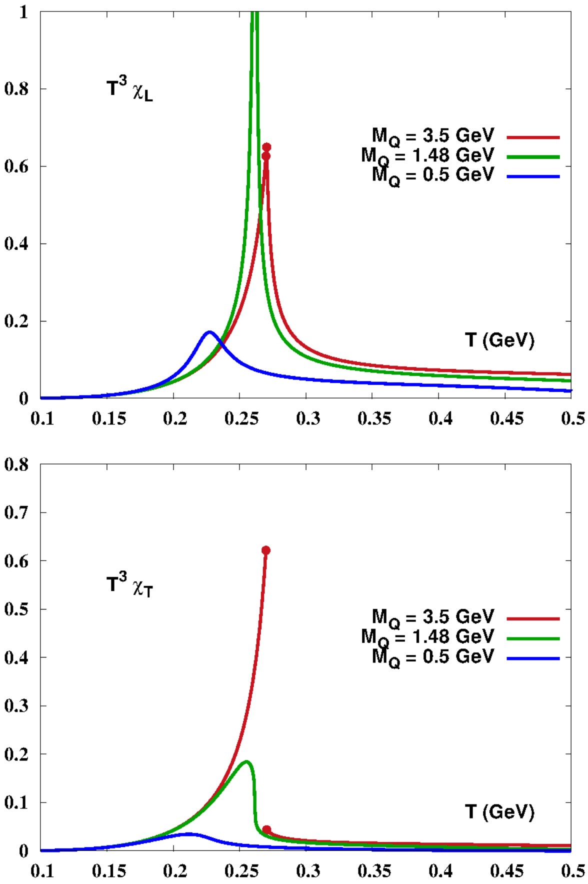

Figure 1: The temperature dependence of the longitudinal χ_{L} and transverse χ_{T} Polyakov loop susceptibilities for $N_f = 3$ and quark masses, $m = 0.5, 1.48,$ and 3.5 GeV.

References

[1] P. M. Lo, B. Friman, O. Kaczmarek, K. Redlich, and C. Sasaki, Phys. Rev. D **88** (2013) 014506.

[2] P. M. Lo, B. Friman, O. Kaczmarek, K. Redlich, and C. Sasaki, Phys. Rev. D **88** (2013) 074502

[3] A. Bazavov *et al.*, Phys. Rev. D **85** (2012) 054503.

[4] P. M. Lo, B. Friman, and K. Redlich, Phys. Rev. D **90**, 074035 (2014).

---

* Work supported in part by FIAS, EMMI, and the Polish Science Foundation, under Maestro grant 2013/10/A/ST2/00106.

† pmlo@gsi.de

DOI:10.15120/GR-2015-1-MU-THEORY-16

A novel Monte-Carlo approach to particle-field dynamics

C. Wesp[1], *H. van Hees*[1,2], *A. Meistrenko*[1], *and C. Greiner*[1]
[1]Institute for Theoretical Physics, Goethe University Frankfurt; [2]Frankfurt Institute of Advanced Studies (FIAS)

Motivated by the problem to identify possible observables suitable for the exploration of the phase diagram of strongly interaction matter in heavy-ion collisions, we have developed a novel algorithm to address the non-equilibrium kinetics of phase transitions of the bulk medium created in such reactions. As known from lattice-QCD calculations at low net-baryon densities and high temperatures, the deconfinement-confinement as well as the chiral phase transition is a smooth cross-over transition. At higher net-baryon numbers (finite baryon chemical potential) one expects a 1^{st}-order transition line with a tri-critical 2^{nd}-order endpoint. In heavy-ion collisions, however the produced medium is a rapidly expanding fireball consisting of strongly interacting matter. Thus the question arises, whether possible signatures of equilibrium phase transitions, including critical fluctuations of conserved charge-like quantum numbers and critical slowing-down close to a 2^{nd}-order endpoint can be expected and, which are the pertinent signatures for such structures in the phase diagram.

The key idea of our novel Monte-Carlo simulation method [1] is to use transition rates of such creation and annihilation processes, $q\bar{q} \leftrightarrow \sigma$ given by the Feynman rules of a quark-meson linear-σ model. The quarks and antiquarks are described as test particles of a classical molecular-dynamics simulation, while the σ field is treated on the classical mean-field level. Monte-Carlo techniques are used to simulate the pair creation and annihilation processes according to these transition-probability rates on a space-time grid.

For a particle annihilation, the corresponding energy and momentum are then transferred to the corresponding mean σ-field as local disturbances in terms of Gaussian wave "packlets". To take into account the inverse process of pair creation as demanded by the principle of detailed balance, the mean field is mapped locally to a momentum distribution with a local temperature, allowing for the "particlelization" of the field. In this way in another Monte-Carlo step a σ-particle with some definite energy and momentum can be chosen according to this local equilibrium distribution, and the decay-probability rate to a $q\bar{q}$ pair can be used to add the corresponding quark and anti-quark to the test-particle ensemble. Note that in addition the relevant net-quark number conservation is fulfilled in the sense of a microcanonical description.

Besides other simple test cases like a simple harmonic oscillator or a 1+1-dimensional Klein-Gordon field coupled to a fluctuating heat bath, we have demonstrated that with such a description the particles reach thermal equilibrium, and the mean field develops the corresponding equilibrium spectrum, preventing the ultraviolet catastrophe due to an effective cutoff due to the finite spatial extent of the interactions with the particles (cf. Fig. 1).

Applications to descriptions of the chiral phase transition in heavy ion collisions are current work of progress.

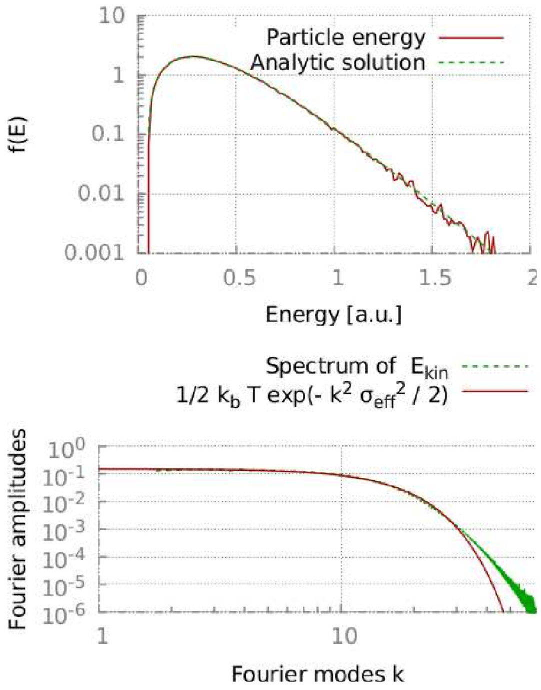

Figure 1: Upper panel: The quark-energy distribution from the kinetic Monte-Carlo simulation after a stationary state has been reached compared to the expected equilibrium-Boltzmann distribution $\propto \exp(-E/T)$. Lower panel: The Fourier spectrum of the mean field in comparison to the classical equipartition theorem, modified by an effective ultra-violet cutoff due to the finite extent of the interaction volume between particle creation and annihilation processes.

References

[1] C. Wesp, H. van Hees, A. Meistrenko, and C. Greiner (2014), `arXiv: 1411.7979 [hep-ph]`.

DOI:10.15120/GR-2015-1-MU-THEORY-17

Systematic investigation of Cooper-Frye negative contributions *

Dmytro Oliinychenko †[1,3], *Pasi Huovinen*[2], *and Hannah Petersen*[1,2]

[1]Frankfurt Institute for Advanced Studies; [2]Institut für Theoretische Physik, Goethe Universität Frankfurt;
[3]Bogolyubov Institute for Theoretical Physics, Kiev, Ukraine

Many models of heavy ion collisions employ relativistic hydrodynamics to describe the system evolution at high densities. The Cooper-Frye formula [1] is applied in most of these models to turn the hydrodynamical fields into particles. However, the number of particles obtained from the Cooper-Frye formula is not always positive-definite. Physically negative contributions of the Cooper-Frye formula are particles that stream backwards into the hydrodynamical region.

We have investigated negative Cooper-Frye contributions and backscattering using a coarse-grained molecular dynamics approach. Au+Au collisions at $E_{\rm lab} = 5$–$160A$ GeV energies have been simulated using UrQMD [2], and a hypersurface Σ of constant Landau rest frame energy density has been constructed. On this surface we have calculated two quantities: The ratio of Cooper-Frye negative to positive contributions (r_{eq}), which assumes local thermal equilibrium, and the ratio of UrQMD particles crossing Σ inward to crossing Σ outward (r_{neq}), which does not assume equilibrium.

We found that at all collision energies $r_{eq} \gg r_{neq}$ [3]. We explain this by a deviation of pions in UrQMD simulation from equilibrium. A non-monotonous dependency of r_{eq} and r_{neq} on collision energy was found with a maximum at 10-20A GeV, maximal r_{eq} being around 13% (Fig. 1 a). The size of the negative contributions is a result of an interplay of several factors: the temperature on the hypersurface, the relative velocities between flow and surface, and the relative amounts of volume and surface emission.

Both r_{eq} and r_{neq} are smaller for hadron sorts with higher mass (Fig. 1 b) and decrease for peripheral events (Fig. 1 c).

References

[1] F. Cooper, G. Frye, Phys. Rev. D 10, 186, 1974

[2] S. A. Bass, M. Belkacem et al., Prog. Part. Nucl. Phys. **41**, 225 (1998); M. Bleicher, E. Zabrodin, et al., J. Phys. G: Nucl. Part. Phys. **25**, 1859 (1999).

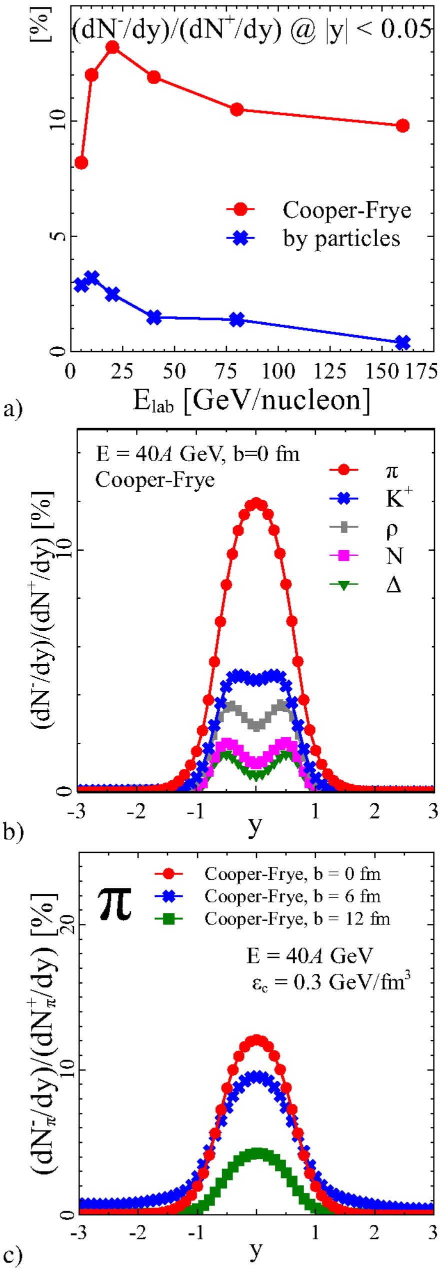

Figure 1: a) r_{eq} and r_{neq} for pions at midrapidity versus collision energy; b) r_{eq} rapidity distribution for different hadron species; c) r_{eq} for pions versus collision centrality

[3] D. Oliinychenko, P. Huovinen and H. Petersen, arXiv:1411.3912 [nucl-th].

---

* This work was supported by the Helmholtz International Center for the Facility for Antiproton and Ion Research (HIC for FAIR) within the framework of the Landes-Offensive zur Entwicklung Wissenschaftlich-Oekonomischer Exzellenz (LOEWE) program launched by the State of Hesse. DO and HP acknowledge funding of a Helmholtz Young Investigator Group VH-NG-822 from the Helmholtz Association and GSI, and PH by BMBF under contract no. 06FY9092. Computational resources have been provided by the Center for Scientific Computing (CSC) at the Goethe University of Frankfurt.

† oliiny@fias.uni-frankfurt.de

DOI:10.15120/GR-2015-1-MU-THEORY-18

K^* dynamics in a nuclear medium[*]

Andrej Ilner[†][1,2], *Daniel Cabrera*[‡][1,2], *and Elena Bratkovskaya*[§][1,2]

[1]Frankfurt Institute for Advanced Studies, Ruth-Moufang-Straße 1, 60438 Frankfurt am Main, Germany; [2]Institut für theoretische Physik, Johann Wolfgang Goethe-Universität, Max-von-Laue-Straße 1, 60438 Frankfurt am Main, Germany

The K^* and the $\bar{K}^*$ are vector mesons that are composed of a light and a strange quark, i.e. the K^* is composed of a u and a $\bar{s}$ quark and the $\bar{K}^*$ is composed of a u and a s quark. We study the in-medium properties of these mesons in a dense and hot nuclear medium. The in-medium properties are based on chirally motivated models and these in-medium effects are parametrised as density or temperature dependent effective masses and widths. For broad in-medium particles we adopt the relativistic Breit-Wigner prescription, i.e. the spectral function

$$A_i(M,\rho_N) = \frac{\frac{2}{\pi}\cdot C_1\cdot M^2\cdot \Gamma_i^*(M,\rho_N)}{\left(M^2 - M_i^{*2}(\rho_N)\right)^2 + \left(M\Gamma_i^*(M,\rho_N)\right)^2}, \quad (1)$$

where C_1 stands for a normalisation constant, which is determined as the spectral function must fulfil the sum rule $\int_0^\infty A_i(M,\rho_N)dM = 1$, and $i = K/\bar{K}, K^*/\bar{K}^*$.

The in-medium effects are based on the complex self-energy obtained by solving the strange meson (off-shell) dispersion relation $E^2 - |\vec{p}^2| - M_i^2 - \Pi_i = 0$, i.e. the width of the spectral function is related to the imaginary part of the self-energy as

$$\mathrm{Im}\,\Pi_i(M,\rho_N) = -\Gamma_i^*(M,\rho_N)\cdot M \quad (2)$$

and the mass shift is related to the real part of the self-energy as

$$\mathrm{Re}\,\Pi_i(M_i^*,\rho_N) = M_i^2 - (M_i^*)^2 \quad (3)$$

(with M_i being the nominal mass in vacuum, i.e. $M_{K^*} = 0.892$ GeV). A vacuum width of $\Gamma_V^0 = 42$ MeV has been used throughout all of our calculations for the vector mesons.

We distinguish two scenarios for energies where the medium is dense and is filled with baryonic particles (FAIR; $\mu_B \neq 0, T \approx 0$) and when the medium is hot and filled with pionic particles (RHIC, LHC; $\mu_B \approx 0, T \neq 0$). The behaviour of strange vector mesons is different for these two media. Additionally the behaviour of a strange particle is different from the behaviour of a strange anti-particle in a dense nuclear medium, whereas it is the same in a hot nuclear medium (we are dealing with an isotopically symmetric pionic medium).

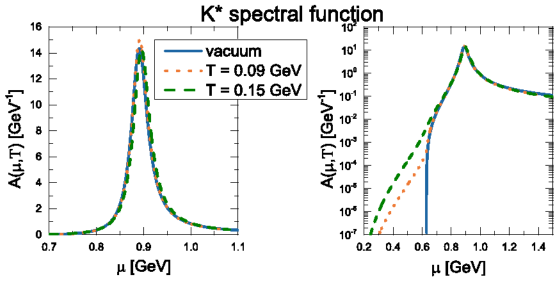

Figure 1: The K^* spectral function is shown as a function of the invariant K^* mass μ for different temperatures T. The blue solid line is for the vacuum case, the orange dotted line is for a temperature of $T = 0.09$ GeV and the green dashed line is for a temperature of $T = 0.15$ GeV. The same results are shown on a linear (left plot) and on a logarithmic (right plot) scale.

In figure 1 one can see spectral function for the K^* (and consequently the $\bar{K}^*$) in a hot, pionic medium. The effects of the medium are negligible, there is only a small mass shift and a very small broadening. However, when looking at the logarithmic plot one can see that the K^* gains some enhancement in the low mass region at temperatures $T > 0$.

For the K^* in a dense nuclear medium the width of the K^* decreases with increasing density since the kaon becomes slightly heavier as a result of the repulsive KN interaction. However, this is compensated by the repulsive self-energy from the K^*N interaction. The resulting K^* self-energy in a $t\rho$ approximation leads to a mildly repulsive K^* mass shift of about 5% (30 MeV) at a density of $\rho_N = \rho_0$. The change in the shape of the spectral function is negligible.

The major effects for the $\bar{K}^*$ in a dense nuclear medium come mainly from both the $\bar{K}\pi$ decay channel and from the highly inelastic $\bar{K}^*N$ interaction, leading to decay widths as large as 200 MeV at normal nuclear matter density $\rho_N = \rho_0$.

References

[1] Andrej Ilner, Daniel Cabrera, Pornrad Srisawad, Elena Bratkovskaya, *Properties of strange vector mesons in dense and hot matter*, Nucl. Phys. A 927 (2014) 249-265

---

[*] Work supported by the Helmholtz International Center for FAIR within the framework of the LOEWE program. A.I. acknowledges support by GSI, HGS-HIRe for FAIR and H-QM. D.C. acknowledges support by BMBF (Germany) under project no. 05P12RFFCQ.

[†] ilner@fias.uni-frankfurt.de

[‡] cabrera@fias.uni-frankfurt.de

[§] Elena.Bratkovskaya@th.physik.uni-frankfurt.de

DOI:10.15120/GR-2015-1-MU-THEORY-19

Strange meson-baryon interaction in hot and dense nuclear matter: from hadronic models to transport simulations*

D. Cabrera†[1,2], *A. Ilner*[1,2], *L. Tolós*[1,3], *J. Aichelin*[4], *E. Bratkovskaya*[1,2], *and W. Cassing*[5]
[1]FIAS, Frankfurt, Germany; [2]ITP, Frankfurt, Germany; [3]ICE (IEEC/CSIC), Bellaterra, Spain; [4]Subatech, Nantes, France; [5]ITP, Giessen, Germany

Introduction

We study the dynamics of strange pseudoscalar and vector mesons in hot and dense nuclear matter within a self-consistent coupled-channel approach based on the meson-baryon chiral Lagrangian. Our results set up the starting point for implementations in microscopic transport approaches of heavy-ion collisions, particularly at the conditions to be met in the future experiments at GSI/FAIR and NICA@Dubna. Such developments are in progress, exploiting the successful collaboration between the transport groups of Nantes and FIAS-Frankfurt.

$\bar{K}N$ interaction in hot and dense matter

In the $\bar{K}N$ sector we focus on the calculation of in-medium (off-shell) transition rates for the most relevant binary reactions involved in strangeness production close to threshold energies (e.g. $\bar{K}N \to \pi\Sigma$), with special attention to the role of sub-threshold hyperon resonances ($\Lambda(1405)$, $\Lambda(1115)$, $\Sigma(1195)$ and $\Sigma^*(1385)$), isospin effects (e.g. $\bar{K}p$ vs $\bar{K}n$, cf. Fig. 1) and the angular dependence of the scattering amplitudes and cross sections (s and p waves are accounted for). Together with the spectral function and the nuclear optical potential of strange mesons and hyperons, our results permit a systematic accounting of medium effects in the $S = -1$ sector regarding the production, propagation and rescattering of light strange hadrons.

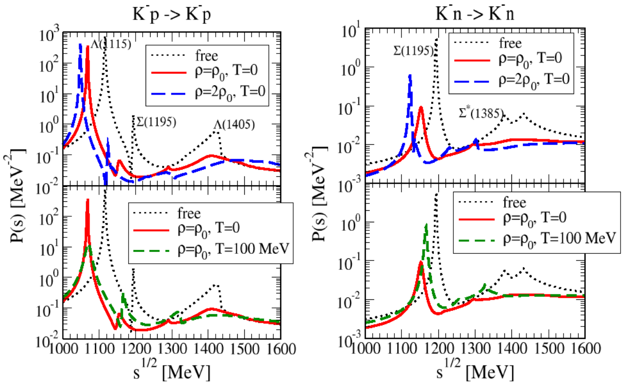

Figure 1: In-medium transition probability $\mathcal{P}$ for the elastic K^-p (left) and K^-n (right) reactions. The peaks associated to the $\Lambda(1115)$, $\Sigma(1195)$ and $\Lambda(1405)$ resonances are clearly visible in the vacuum case.

Strange vector mesons: K^*, $\bar{K}^*$ and ϕ

We have also pursued recent theoretical developments regarding the dynamics of strange vector mesons (K^*, $\bar{K}^*$ and ϕ) in the nuclear medium, in connection with experimental activity from heavy-ion collisions and nuclear production reactions. Our work focuses on the extension to finite temperatures of previous chiral hadronic models for the vector meson selfenergy in dense matter (cf. Fig. 2), where the key mechanisms for medium modification are: (i) the excitation of strange baryon resonances in quasielastic scattering (e.g. $\bar{K}^*N \to \bar{K}^*N$), which translates into resonance-hole modes that mix with the vector-meson quasiparticle peak; and (ii) the decay into hadronic modes (e.g. $\bar{K}^* \to \bar{K}\pi$), where the daughter particles are also dressed and low-energy modes are Bose-enhanced.

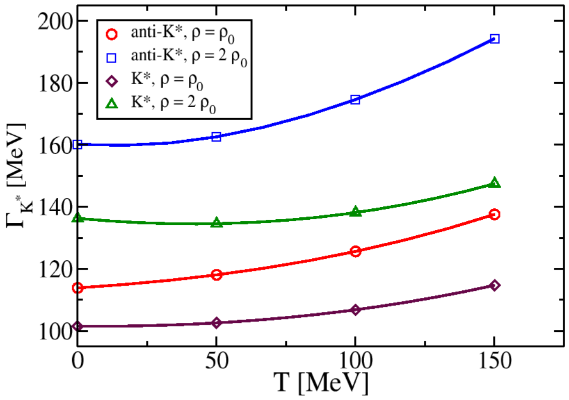

Figure 2: Temperature evolution of the $\bar{K}^*(K^*)$ width – or selfenergy – due to $\bar{K}(K)\pi$ in-medium decays.

References

[1] D. Cabrera, L. Tolos, J. Aichelin and E. Bratkovskaya, "Antistrange meson-baryon interaction in hot and dense nuclear matter", Phys. Rev. C **90** (2014) 5, 055207.

[2] A. Ilner, D. Cabrera, P. Srisawad and E. Bratkovskaya, "Properties of strange vector mesons in dense and hot matter", Nucl. Phys. A **927** (2014) 249.

[3] L. Tolos, D. Cabrera, C. Garcia-Recio, R. Molina, J. Nieves, E. Oset, A. Ramos and O. Romanets *et al.*, "Heavy Mesons in Nuclear Matter and Nuclei", J. Phys. Conf. Ser. **562** (2014) 1, 012010.

[4] D. Cabrera, L. M. Abreu, E. Bratkovskaya, A. Ilner, F. J. Llanes-Estrada, A. Ramos, L. Tolos and J. M. Torres-Rincon, "Strange and heavy mesons in hadronic matter", J. Phys. Conf. Ser. **503** (2014) 012017.

---

* Work supported by the HIC for FAIR framework of LOEWE, GSI, HGS-HIRe and H-QM, and by BMBF project no. 05P12RFFCQ.

† cabrera@fias.uni-frankfurt.de

DOI:10.15120/GR-2015-1-MU-THEORY-20

Formation of hypermatter and hypernuclei within transport models in relativistic ion collisions

A.S. Botvina[1,2], *J. Steinheimer*[1], *E. Bratkovskaya*[1], *M. Bleicher*[1], *and J. Pochodzalla*[*3,4]
[1]Frankfurt Institute for Advanced Studies, Germany; [2]Institute for Nuclear Research RAS, Moscow, Russia; [3]HI Mainz, D-55099 Mainz, Germany; [4]Institut für Kernphysik, D-55099 Mainz, Germany

The investigation of hypernuclei is a rapidly progressing field of nuclear physics, since they provide complementary methods to improve traditional nuclear studies and open new horizons for studying particle physics and nuclear astrophysics. Relativistic ion collisions allow the production of exotic light hypernuclei, heavy hypernuclei, hypernuclear matter at subnuclear densities, and new experimental methods can be implemented beyond the traditional hypernuclear experiments with hadrons.

We use the Ultra-relativistic Quantum Molecular Dynamics (UrQMD) and Hadron-String Dynamics (HSD) models for description of the strangeness production. The interaction of hyperons with nucleons leads to their capture and to the formation of hyper-matter. We describe this process within a generalized coalescence model (CB). The coalescence of baryons is consistent with the hyperon capture in a potential well of large nuclear residues, and the coalescence parameter are expected to be of the same order as for normal fragments. Thus, this procedure gives a possibility to treat the formation of light hypernuclei on the same footing. As an example, Fig. 1 shows the rapidity distributions of light hypernuclei for a coalescence parameter $v_c = 0.22c$ [1]. The light $^3_\Lambda$H nuclei are essentially formed over all rapidities. On the other hand, larger hyperfragments are mostly produced within the spectator region.

With increasing energy the fraction of nuclei around residues increases, since more particles are produced in this region as a result of secondary interactions. Whereas particles originating from midrapidity have higher energy and they are more separated in the phase space. Therefore, despite of an increase of the number of such particles, the total number of clusters may not increase with beam energy. In Figure 2 we show the yields of all hyper-fragments, and also the yields of residues of projectiles and targets with captured hyperons, in relativistic carbon on carbon collisions. Indeed, the production of hypernuclei in such collisions is universal above the threshold ($\sim$1.6 A GeV). The saturation of the yields of hypernuclei means that this kind of reactions can be studied at the accelerators of moderate relativistic energies, e.g., at GSI/FAIR.

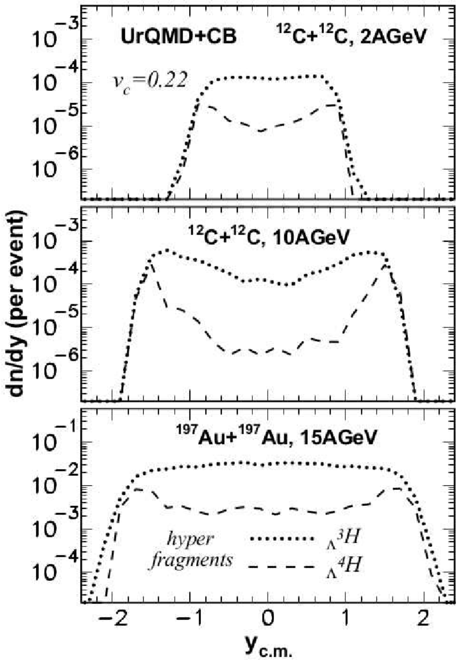

Figure 1: Rapidity distributions of produced $^3_\Lambda$H (dotted lines) and $^4_\Lambda$H (dashed lines) hyper-fragments. The UrQMD and CB calculations are with the coalescent parameter $v_c = 0.22c$ [1].

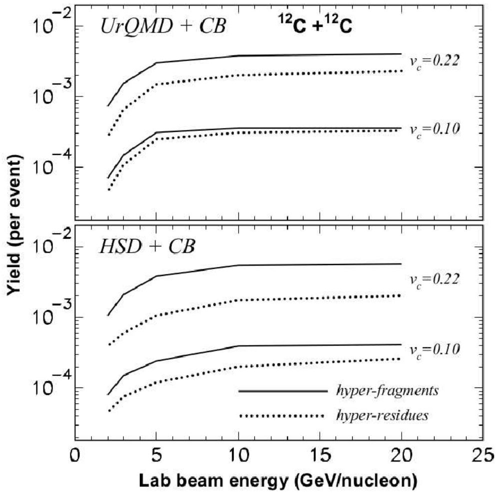

Figure 2: Yields of all produced hyper-fragments (solid lines) and hyper-residues (dotted lines) versus the beam energy in carbon on carbon collisions for realistic coalescence parameters.

References

[1] A.S. Botvina, J. Steinheimer, E. Bratkovskaya, M. Bleicher, J. Pochodzalla, Phys. Lett. B742 , p.7-14 (2015).

---

* pochodza@kph.uni-mainz.de

DOI:10.15120/GR-2015-1-MU-THEORY-21

Creation and annihilation of antimatter at FAIR energies*

P. Moreau[1], *J. Aichelin*[2], *and E. Bratkovskaya*[1]

[1]Frankfurt Institute for Advanced Studies, Johann Wolfgang Goethe Universität, Ruth-Moufang-Strasse 1, 60438 Frankfurt am Main, Germany; [2]Subatech, UMR 6457, IN2P3/CNRS, Université de Nantes, Ecole des Mines de Nantes, 4 rue Alfred Kastler, 44307 Nantes cedex 3, France

The 'Big Bang' scenario implies that in the first microseconds of the universe the entire state has emerged from a partonic system of quarks, antiquarks and gluons – a quark-gluon plasma (QGP) – to color neutral hadronic matter consisting of interacting hadronic states (and resonances) in which the partonic degrees of freedom are confined. Nowadays this early phase can be reproduced in relativistic heavy ion collisions. They show indeed that such a QGP can exists and that it interacts more strongly than hadronic matter. Consequently the concept of a weakly interacting system described by perturbative QCD (pQCD) has to be questioned.

The dynamics of partons, hadrons and strings in relativistic nucleus-nucleus collisions can be analyzed within the Parton-Hadron-String Dynamics approach [1, 2]. In this transport approach the partonic dynamics is based on Kadanoff-Baym equations for Green functions with self-energies from the Dynamical QuasiParticle Model (DQPM) which describes QCD properties in terms of 're-summed' single-particle Green functions [3]. The lattice QCD results, of which the parameters of DQPM are fitted on, lead to a critical temperature $T_c \approx 160$ MeV which corresponds to a critical energy density of $\epsilon_c \approx 0.5\ \mathrm{GeV.fm}^{-3}$.

The aim of this project is with the help of the PHSD to study the creation and annihilation of anti-matter at the FAIR facility in the future CBM and PANDA experiments. Since anti-matter (or antiparticles) doesn't exist in our world it has to be created first by strong interactions before its dynamics can be studied in different hadronic or partonic environments. These experiments aim at the exploration of the QCD phase diagram, especially to find out the order of the phase transition between hadrons and partons at high baryonic densities. In addition we will study the optical potential of different hadrons and the in-medium properties of hadrons in the strange and the charm sector. To verify that our approach is adequate for this study we start out with the calculation of the measured spectra of particles and anti-particles at RHIC energies. We have found a good agreement with the PHENIX data for single particle spectra in Au+Au (figure 1) and p+p (figure 2) collisions at mid-rapidity. One can see that the production of particles and anti-particles in pp collisions is very similar while in Au+Au collisions we observe the effects of anti-baryon absorption at low p_T as well as rescattering on the partonic and hadronic levels.

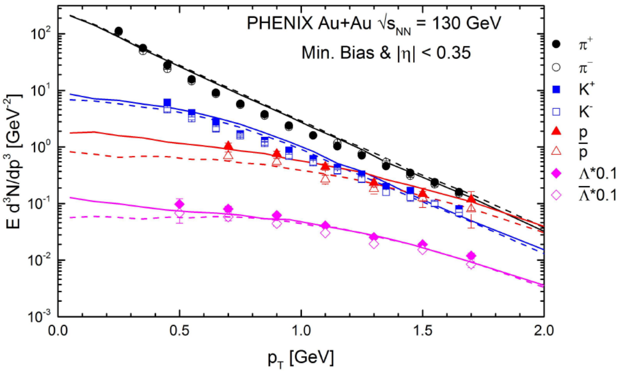

Figure 1: Invariant p_T spectra in Au+Au collisions at $\sqrt{s_{NN}} = 130$ GeV for π^+, π^-, K^+, K^-, p, $\bar{p}$, Λ and $\bar{\Lambda}$ obtained with PHSD, in comparison with the experimental data from the PHENIX collaboration [4, 5].

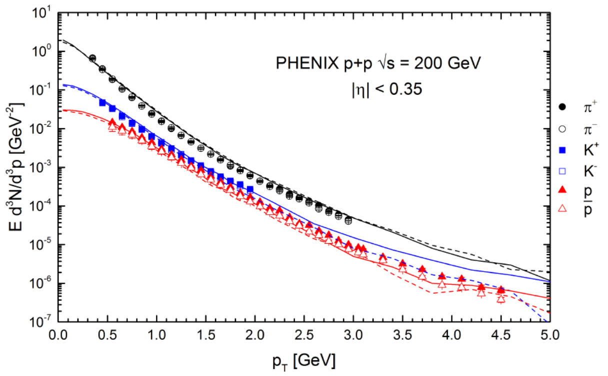

Figure 2: Invariant p_T spectra in p+p collisions at $\sqrt{s} = 200$ GeV for π^+, π^-, K^+, K^-, p and $\bar{p}$ obtained with PHSD in comparison with the experimental data from the PHENIX collaboration [6].

References

[1] W. Cassing and E. L. Bratkovskaya, Nucl. Phys. A **831**, 215 (2009).

[2] E. L. Bratkovskaya, W. Cassing, V. P. Konchakovski and O. Linnyk, Nucl. Phys. A **856**, 162 (2011).

[3] W. Cassing, Eur. Phys. J. ST **168**, 3 (2009).

[4] K. Adcox *et al.* [PHENIX Collaboration], Phys. Rev. C **69**, 024904 (2004).

[5] K. Adcox *et al.* [PHENIX Collaboration], Phys. Rev. Lett. **89**, 092302 (2002).

[6] A. Adare *et al.* [PHENIX Collaboration], Phys. Rev. C **83**, 064903 (2011).

---

* Work supported by HIC4FAIR/HGS-HIRe.

DOI:10.15120/GR-2015-1-MU-THEORY-22

Charm production in the Parton-Hadron-String-Dynamics (PHSD) model *

Taesoo Song[1], *Elena Bratkovskaya*[1], *Hamza Berrehrah*[1], *and Wolfgang Cassing*[2]
[1]Frankfurt Institute for Advanced Studies and Institute for Theoretical Physics, Johann Wolfgang Goethe Universität, Frankfurt am Main, Germany; [2]Institut für Theoretische Physik, Universität Gieβen, Gieβen, Germany

Heavy flavor is one of the important probes to investigate the properties of the hot dense nuclear matter created in relativistic heavy-ion collisions.

Since charm quark production requires high energy-momentum transfer, the number of produced charm quark pairs in relativistic heavy-ion collisions is proportional to the number of binary nucleon-nucleon collisions. Whether two nucleons collide or not in heavy-ion collisions is decided by the nucleon-nucleon inelastic cross section in geometrical method. From the binary collisions, we choose events which produce a charm quark pair by using Monte Carlo method, based on the cross section for charm quark-pair production. Furthermore, we employ Pythia event generator to generate the energy-momentum of charm quark pairs as shown in figure 1.

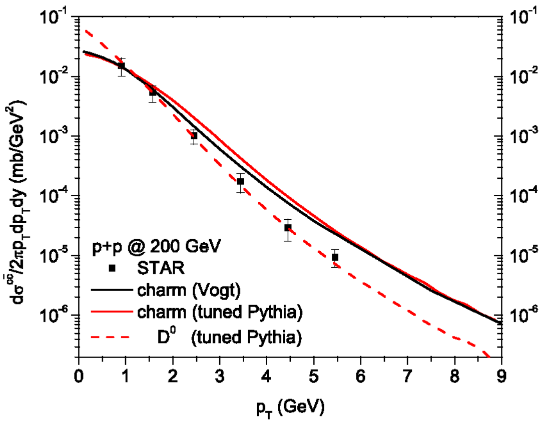

Figure 1: p_T spectra of charm quarks and D mesons from the tuned Pythia simulations compared with FONLL results by Vogt and that of D mesons from the STAR Collaboration.

The produced charm quarks interact with partons in the quark-gluon plasma. We use the cross sections for the scattering of a heavy quark on the off-shell quarks and gluons (of the QGP) whose masses and widths are given by the Dynamical Quasi-Particle Model (DQPM) which reproduces the lattice QCD equation-of-state [1]. Once the local energy density is lower than a critical value (≈ 0.5 GeV/fm^3), the charm quark is hadronzied into a D meson either through fragmentation or through coalescence. The former process is favored by high-p_T charm quarks and the latter one by low-p_T charm quarks. We assume that the probability for coalescence is suppressed in Gaussian form, if the p_T of charm quark is larger than charm quark mass. Hadronized D mesons interact with other hadrons by using the scattering cross sections calculated in a chiral effective lagrangian model where the parameters are fitted to D meson and charmed baryon resonances.

Finally the nuclear modification factor, R_{AA}, is calculated as the number of D mesons produced in heavy-ion collisions divided by that in p+p collisions times the number of binary collisions in heavy-ion collisions as shown in figure 2 for different centralities.

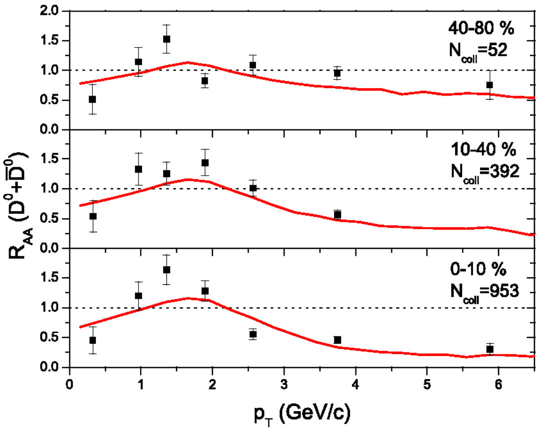

Figure 2: R_{AA} of D mesons from the PHSD simulations in comparison with the experimental data from the STAR Collaboration for Au+Au collisions at $\sqrt{s_{NN}}$ =200 GeV.

References

[1] H. Berrehrah, E. Bratkovskaya, W. Cassing, P. B. Gossiaux, J. Aichelin, and M. Bleicher, Phys. Rev. *C 89* (2014) 054901

[2] T. Song, E. Bratkovskaya, H. Berrehrah, W. Cassing, in preparation

---

* Work supported by HIC4FAIR/DFG.

DOI:10.15120/GR-2015-1-MU-THEORY-23

Heavy-quark dynamics in a hot and dense medium*

H. Berrehrah[1], *E. Bratkovskaya*[1], *W. Cassing*[2], *P.B Gossiaux*[3], *and J. Aichelin*[3]
[1]Frankfurt Institute for Advanced Studies; [2]Institut für Theoretische Physik, Giessen; [3]Subatech, Nantes, France

Introduction

We study the dynamics of on- and off-shell heavy quarks Q in the quark-gluon plasma (QGP) as produced in relativistic nucleus-nucleus collisions. The interactions of heavy quarks with the partonic environment at finite temperature T and finite quark chemical potential μ_q are investigated in terms of transport coefficients within the dynamical quasiparticle model (DQPM) designed to reproduce the lattice-QCD (lQCD) results (including the partonic equation of state) in thermodynamic equilibrium. The collisional scattering cross sections σ^Q_{elas} are evaluated for perturbative partons (massless on-shell particles) and for dynamical quasi-particles (massive on or off-shell particles) using the leading order Born diagrams [2, 3].

Charm spatial diffusion coefficient

Based on σ^Q_{elas} in a finite T and μ_q medium [1, 2, 3, 4], the on- and off-shell heavy quark dynamical collisional energy loss and transport coefficients are computed [1, 3, 4]. As an example, the charm spatial diffusion coefficient D_s is shown in Fig. 1 at finite T (top) and finite T and μ_q (bottom) where our non-perturbative DpQCD model (Dressed pQCD using DQPM pole masses for the partons) is confronted with nuclear many-body calculations below and close to the critical temperature T_c from Ref.[5].

The hadronic and partonic D_s join smoothly and show a pronounced minimum close to T_c at $\mu_q = 0$ as well as at finite μ_q . Close to and above T_c its absolute value matches the lQCD calculations for $\mu_q = 0$. The smooth transition of the heavy-quark transport coefficients from the hadronic to the partonic medium corresponds to a crossover transition in line with lattice calculations, and differs substantially from perturbative-QCD calculations (Moore & Teaney) which show a large discontinuity at T_c. This indicates that in the vicinity of T_c dynamically dressed massive partons should be the effective degrees of freedom in the quark-gluon plasma.

The heavy quark scattering cross sections and transport properties [1, 2, 3, 4] form the basis of a consistent study of the heavy quark dynamics in heavy-ion collisions at FAIR, SPS, RHIC and LHC energies where the partonic processes are implemented into the Parton-Hadron-String-Dynamics (PHSD) transport approach.

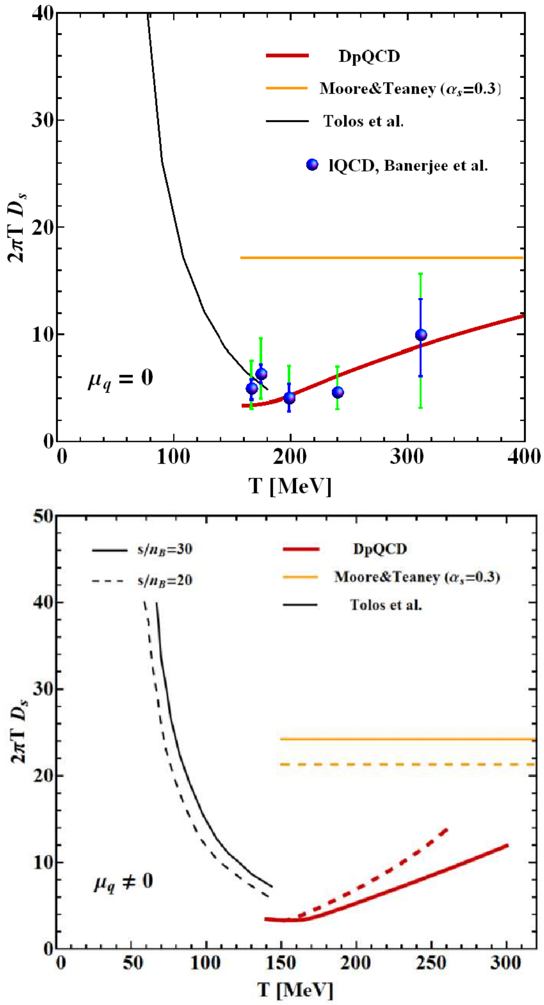

Figure 1: Spatial diffusion coefficient for heavy quarks, D_s, as a function of T for $\mu_q = 0$ (top) and $\mu_q \neq 0$ (bottom). The hadronic diffusion coefficient is taken from [5]. For partonic environment the result from the DpQCD model is compared to pQCD [6], and lattice calculations from Ref. [7].

References

[1] H. Berrehrah, *et al.*, Phys. Rev. C 90 (2014) 051901.

[2] H. Berrehrah, *et al.*, Phys. Rev. C 89 (2014) 054901

[3] H. Berrehrah, *et al.*, Phys.Rev. C90 (2014) 064906

[4] H. Berrehrah, *et al.*, arXiv:1412.1017 [hep-ph]

[5] L. Tolos and J.M. Torres-Rincon, Phys. Rev. D 88, 074019 (2013).

[6] G.D. Moore and D. Teaney, Phys. Rev. C 71, 064904 (2005).

[7] D. Banerjee *et al.*, Phys. Rev. D 85, 014510 (2012).

---

* Work supported by DFG and "HIC for FAIR" framework of the "LOEWE" program. The computational resources have been provided by the LOEWE-CSC.

DOI:10.15120/GR-2015-1-MU-THEORY-24

Directed flow as a phase transition signal in relativistic heavy ion collisions *

J. Steinheimer[1,2], *J. Auvinen*[†,1], *H. Petersen*[1,2,3], *M. Bleicher*[1,2], *and H. Stöcker*[1,2,3]
[1]Frankfurt Institute for Advanced Studies, Frankfurt, Germany; [2]Institut für Theoretische Physik, Goethe Universität Frankfurt, Frankfurt, Germany; [3]GSI Helmholtzzentrum für Schwerionenforschung GmbH, Darmstadt, Germany

Recent STAR data [1] from the RHIC beam energy scan show that the slope of the net-proton directed flow v_1 near midrapidity $y = 0$ changes sign twice within the collision energy range $\sqrt{s_{NN}} = 7.7$ - 39 GeV, which has been predicted by the earlier fluid calculations to be a signal of a first-order phase transition between hadronic matter and quark-gluon plasma. We study this phenomenon utilizing a hybrid model where the non-equilibrium phases at the beginning and in the end of a heavy-ion collision are described by the UrQMD transport model, while the intermediate hot and dense stage is modeled with (3+1)-D ideal hydrodynamics. In [2] we examine the sensitivity of the directed flow v_1 to the order of the phase transition by comparing simulations with a first-order phase transition "Bag model" equation of state (EoS) to calculations with a chiral model EoS, which has a cross-over phase transition.

First, to emulate the earlier fluid calculations, we initialize the cold matter of two colliding nuclei as two distributions of energy and baryon density. The UrQMD model is still utilized for the final hadron gas phase. Figures 1a and 1b show the difference in dv_1/dy between the two equations of state for Au+Au collisions at impact parameter b = 8 fm. While the predicted minimum in dv_1/dy with a first-order phase transition is observed when using isochronous hypersurface for the transition from hydrodynamics to transport (Fig. 1a), the difference between the two equations of state is considerably smaller when using iso-energy density condition for fluid to particle transition (Fig. 1b).

Figure 1c shows the energy dependence of the proton and antiproton v_1 slope at midrapidity, obtained from the full hybrid simulation with the initial non-equilibrium transport phase. The directed flow was calculated using events with impact parameter $b = 4.6 - 9.4$ fm, which approximates the $(10 - 40)\%$ centrality range of the STAR data. The two EoS are completely indistinguishable in the hybrid simulations, questioning the usability of v_1 as a signal of the first-order phase transition. However, the hybrid model results also deviate notably from experimental data, which makes further studies on the topic necessary.

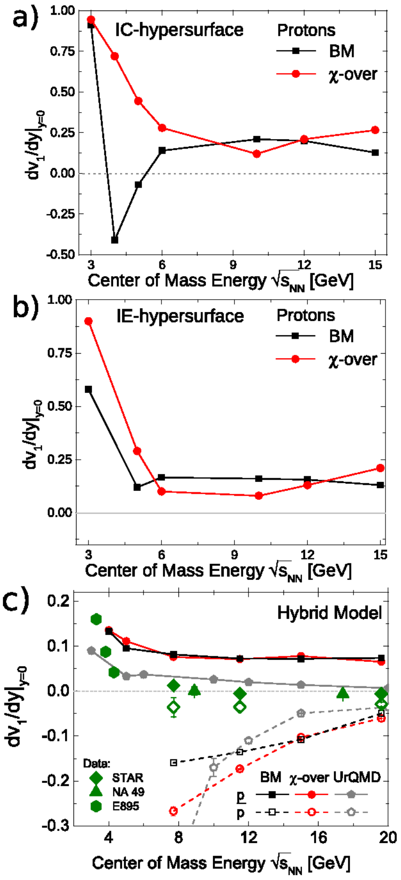

Figure 1: a) and b) Slope of proton v_1 at midrapidity $|y| < 0.5$, calculated for an equation of state with first-order phase transition (black) and cross-over phase transition (red) for isochronous fluid-to-particles transition hypersurface (a) and iso-energy density hypersurface (b) for Au+Au collisions at impact parameter b = 8 fm. c) v_1 slope at midrapidity for protons (solid symbols) and anti-protons (open symbols) for impact parameter range $b = 4.6 - 9.4$ fm, extracted from the hybrid model calculations with a first order (black) and crossover EoS (red). Results are compared with the UrQMD model calculations (grey) and experimental data from STAR, NA49 and E895 collaborations (green). Originally published in [2].

References

[1] L. Adamczyk et al. [STAR Collaboration], "Beam-Energy Dependence of the Directed Flow of Protons, Antiprotons, and Pions in Au+Au Collisions", Phys. Rev. Lett. 112 (2014) 162301

[2] J. Steinheimer, J. Auvinen, H. Petersen, M. Bleicher, H. Stöcker, "Examination of directed flow as a signal for a phase transition in relativistic nuclear collisions", Phys. Rev. C 89 (2014) 054913

---

[*] Work supported by HIC for FAIR and Helmholtz-Nachwuchsgruppe VH-NG-822. Computational resources have been provided by the Center for Scientific Computing (CSC) at Goethe Universität Frankfurt.

[†] auvinen@fias.uni-frankfurt.de

DOI:10.15120/GR-2015-1-MU-THEORY-25

Path-length dependence of jet-energy loss*

B. Betz†[1] *and M. Gyulassy*[2]
[1]Institute for Theoretical Physics, Johann Wolfgang Goethe-University, 60438 Frankfurt am Main, Germany;
[2]Department of Physics, Columbia University, New York, 10027, USA

Jet-quenching observables are considered to be significant probes of the medium evolution during a heavy-ion collision. We performed a systematic study on the jet-energy loss [1] based on a generic energy loss model [1, 2] that can interpolate between a pQCD-based and an AdS/CFT-inspired jet-energy loss prescription. The results were compared to the measured nuclear modification factor R_{AA} and the high-p_T elliptic flow [3] to study the jet-medium coupling κ and the impact of the jet path-length dependence.

The generic energy-loss model

The generic energy-loss model [1, 2] parametrizes the energy loss via

$$\frac{dE}{dx} = \frac{dE}{d\tau}(\vec{x}_0, \phi, \tau) = -\kappa(T) E^a(\tau)\, \tau^z\, T^{c=2+z-a}\, \zeta_q \, .$$

Here, the jet-energy dependence, the path-length dependence, the temperature dependence, and the jet-energy loss fluctuations are characterized by the exponents (a, z, c, q). The jet-energy loss fluctuations are distributed via $f_q(\zeta_q) = \frac{(1+q)}{(q+2)^{1+q}}(q + 2 - \zeta_q)^q$, allowing for an easy interpolation between non-fluctuating ($q = -1$, $\zeta_{-1} = 1$) and fluctuating ($\zeta_q < 1$ for $q > -1$) distributions.

The jets are distributed according to a transverse initial profile specified by the QGP expansion of VISH2+1 [4].

Results

Below we consider an exponentially falling ansatz for the jet-medium coupling, $\kappa(T) = \kappa_1 e^{-b(T-T_1)}$, assuming that the coupling is zero below a certain temperature T_1, representing the freeze-out, where the coupling peaks at a value of κ_1 and falls off for larger temperatures to a value of $1/e$ at a temperature T_e.

Fig. 1 shows the result for the nuclear modification factor and the high-p_T elliptic flow both at RHIC and at LHC energies with and without additional jet-energy loss fluctuations. Given the space-time uncertainties of the hydrodynamic evolution (for details see Ref. [1]), such a temperature-dependent jet-medium coupling represents a decent fit to the measured data.

Conclusions

Performing a systematic study on the jet-energy loss [1] we found (see Table 2 of Ref. [1]) that a pQCD-like energy loss with a temperature running coupling appears to be favored (see Fig. 1). Besides that, a realistic QGP expansion is essential to account for the dependence of the data on transverse momentum p_T, azimuth ϕ, impact parameter b, and collision energy $\sqrt{s}$.

References

[1] B. Betz and M. Gyulassy, JHEP **1408**, 090 (2014) [Erratum-ibid. **1410**, 043 (2014)].

[2] B. Betz and M. Gyulassy, Phys. Rev. C **86**, 024903 (2012).

[3] A. Adare *et al.*, Phys. Rev. C **87**, 034911 (2013); B. Abelev *et al.*, Phys. Lett. B **720**, 52 (2013) and Phys. Lett. B **719**, 18 (2013); S. Chatrchyan *et al.*, Eur. Phys. J. C **72**, 1945 (2012) and Phys. Rev. Lett. **110**, 042301 (2013); G. Aad *et al.*, Phys. Rev. C **86**, 014907 (2012) and Phys. Lett. B **707**, 330 (2012).

[4] H. Song and U. W. Heinz, Phys. Rev. C **77**, 064901 (2008); Z. Qiu, C. Shen and U. Heinz, Phys. Lett. B **707**, 151 (2012).

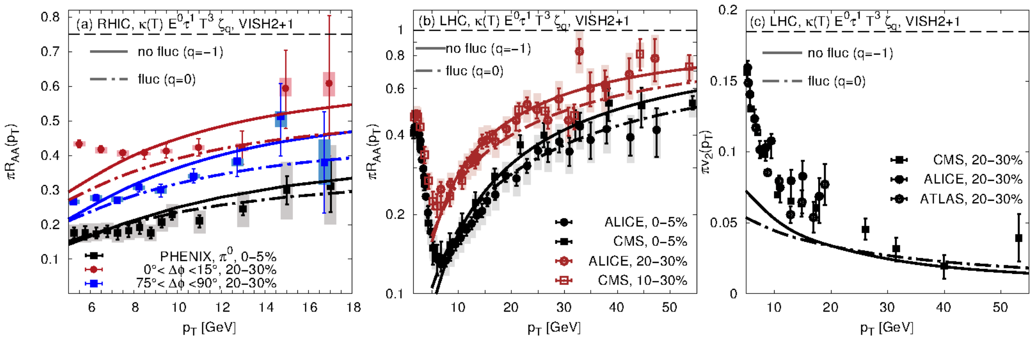

Figure 1: Azimuthal jet tomography at RHIC and LHC for a pQCD-like ansatz (see text for details) [1].

---

* Work supported by HIC for FAIR and DOE.

† betz@th.physik.uni-frankfurt.de

DOI:10.15120/GR-2015-1-MU-THEORY-26

Dileptons in heavy-ion collisions in a coarse-grained transport approach

S. Endres[1,2], *H. van Hees*[1,2], *J. Weil*[1,2], *and M. Bleicher*[1,2]
[1]Institute for Theoretical Physics, Goethe University Frankfurt; [2]Frankfurt Institute of Advanced Studies (FIAS)

Lepton-antilepton pairs (dileptons) and photons provide valuable observables for the properties of strongly interacting hot and dense matter, created in heavy-ion collisions. Due to their penetrating nature they leave the hot and dense fireball nearly unaffected from final-state interactions, enabling insight into the spectral properties of the electromagnetic current-correlation function with relations to the (chiral) phase structure of strongly interacting matter.

In this work, for the description of the bulk-medium evolution the UrQMD transport simulation has been used. A fundamental challenge is the implementation of reliable dilepton and photon production rates from a hot and dense partonic (Quark Gluon Plasma, QGP) and hadronic (Hadron Resonance Gas, HRG) medium. Here, one relies on the application of equilibrium quantum-many body theory to describe the in-medium electromagnetic current-correlation function. In [1] we have followed the strategy to use a coarse-graining approach to make the detailed equilibrium dilepton-production rates of [2], based on hadronic many-body theory, as well as an extrapolation of recent lattice results on the dilepton-production rates to finite momenta [3] applicable within a detailed transport description of bulk-medium dynamics: UrQMD has been run several times for a given heavy-ion collision to provide an ensemble, which samples the bulk-medium evolution on a space-time grid, providing average values for the local energy-momentum and baryon-number density ("coarse graining"). Using a lattice-QCD inspired equation of state, extrapolated to finite baryon-chemical potential, describing the cross-over phase transition from a deconfined QGP to a hot and dense HRG phase of the evolving fireball, local temperatures and chemical potentials (baryon- and pion-chemical potential to take chemical off-equilibrium after chemical freeze-out into account) have been fitted in the local Eckart frame, where the net-baryon-number flow vanishes. In the early phases the fit to an anisotropic hydrodynamical flow pattern has been used.

In Fig. 1 this calculation is compared to the high-precision invariant-mass excess spectrum measured by the NA60 collaboration in $158A$GeV In-In collisions at the CERN SPS. The excellent description of the data demonstrates the feasibility of the coarse-graining method to implement detailed equilibrium many-body calculations of the dilepton rates into realistic bulk-evolution transport descriptions. This shows that the medium modifications of the light vector mesons leading to substantial spectral broadening with small mass shifts describe the low-mass enhancement below the ρ-peak region around $M \simeq 170$ MeV. In the intermediate-mass region, $M \gtrsim 1$ GeV, multi-pion processes and $q\bar{q}$ processes become the prevalent production mechanism. The slope of the mass spectrum in this region directly reflects the space-time weighted average of an invariant temperature (without impact of Doppler blue-shift effects due to radial flow), which is clearly above the critical temperature, $T_{M-\mathrm{slope}} \simeq 205$-$230$ GeV.

Applications of this method to dilepton (and photon) production in heavy-ion collisions over a larger range of collision energies (RHIC beam-energy scan, GSI HADES, and future CBM experiment at FAIR) are in preparation.

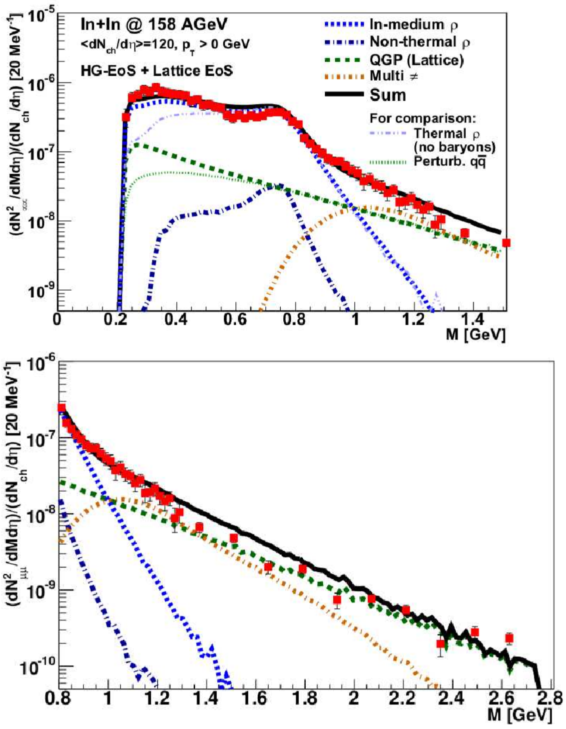

Figure 1: The dimuon invariant-mass spectrum in $158A$GeV In-In collisions at the CERN SPS, compared to the data from the NA60 collaboration [4].

References

[1] S. Endres, H. van Hees, J. Weil, and M. Bleicher (2014), `arXiv: 1412.2554 [nucl-th]`.

[2] R. Rapp and J. Wambach, Eur. Phys. J. A **6**, 415 (1999).

[3] R. Rapp, Adv. High Energy Phys. **2013**, 148253 (2013).

[4] R. Arnaldi et al. (NA60 Collaboration), Eur. Phys. J. C **61**, 711 (2009).

DOI:10.15120/GR-2015-1-MU-THEORY-27

A puzzle in the direct photon production [*]

O. Linnyk[†1], *W. Cassing*[1], *and E. Bratkovskaya*[2]
[1]Justus Liebig University of Giessen, Germany; [2]FIAS; Goethe University Frankfurt am Main, Germany

Recent measurements of direct photon spectra and their v_2 in Au+Au collisions at $\sqrt{s_{NN}} = 200$ GeV by the PHENIX Collaboration [1] stimulated a new wave of interest for real photons, since the thermal QGP photons were expected to dominate the spectra. But the experimental observation that the elliptic flow $v_2(p_T)$ of direct photons is comparable to that of the pions was in contrast to the theoretical expectations. The photons produced in the QGP are not expected to show a considerable flow, because they are dominated by the emission in the initial phase before the elliptic flow fully develops. None of the theoretical models could describe simultaneously the photon spectra and v_2, which is known as the "direct photon puzzle".

Our results for the direct photon p_T-spectra and v_2 [2] are shown in comparison to the PHENIX data in the Figure below. We model the evolution of heavy-ion collisions by using the microscopic non-equilibrium transport approach Parton-Hadron-String Dynamics (PHSD), which describes the initial hard scatterings, string formation, creation of the strongly-interacting quark-gluon plasma as well as dynamical hadronization and the subsequent interactions in the expanding hadronic phase. The photons from QGP give up to 50% of the direct photon yield below 2 GeV/c, but a sizable contribution stems from hadronic sources such as meson-meson (mm) and meson-Baryon (mB) bremsstrahlung. The contribution from binary mm and VN reactions is minor compared to the partonic and bremsstrahlung channels. The hadron bremsstrahlung photons carry large v_2 of the order of the pion v_2, which leads to the direct photon v_2 in agreement with the data within the systematical uncertainties. The PHENIX Collaboration found also that the midrapidity 'thermal' photon yield scales with the number of participants as $dN/dy \sim N_{part}^{\alpha}$ with $\alpha = 1.48 \pm 0.08$. Our predictions gave $\alpha = 1.5$ dues to the dominance of the mm and mB contribution, while the QGP channels scale with $\alpha = 1.7$. Thus, according to the present PHSD results the mm and mB bremsstrahlung turn out to be an important source of direct photons, which contributes towards the resolution of the puzzle.

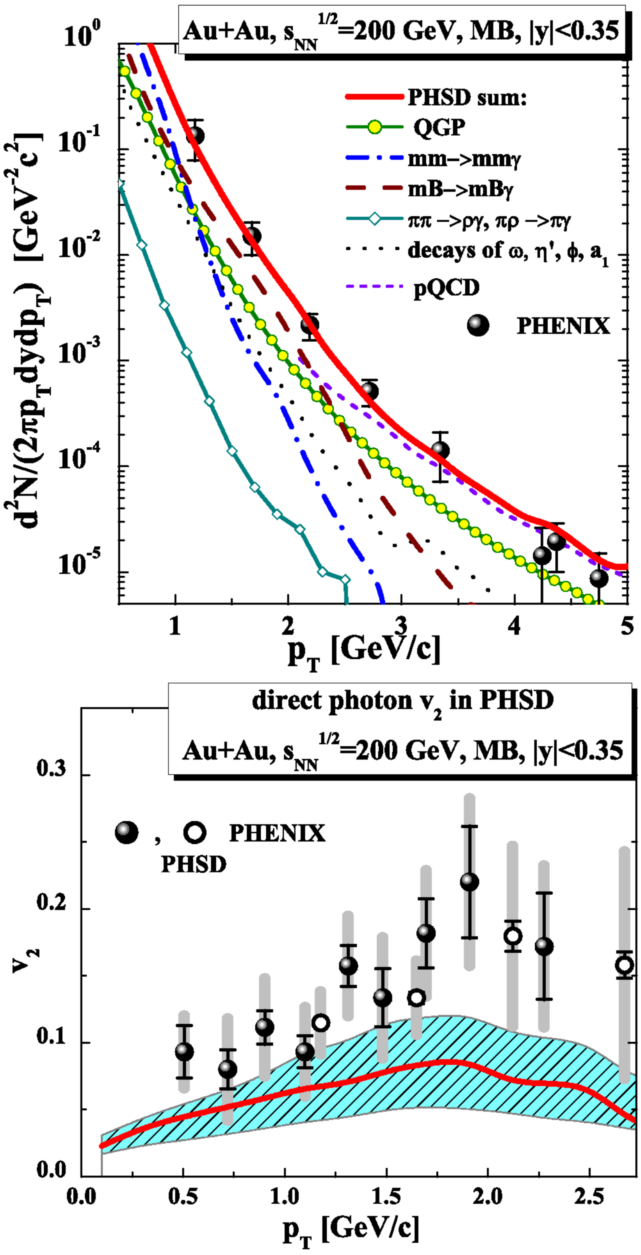

Figure 1: The spectra (up) and elliptic flow (down) for the direct photons produced in Au+Au collisions at $\sqrt{s_{NN}} = 200$ GeV. Our results within the PHSD approach [2] are given by the red solid lines. The PHENIX data (symbols) are from [1].

References

[1] PHENIX Collaboration, A. Adare et al, Phys. Rev. Lett. 104 (2010) 132301; A. Adare et al, Phys. Rev. Lett. 109 (2012) 122302; A. Adare et al, arXiv:1405.3940/nucl-ex.

[2] O. Linnyk et al, Phys. Rev. C88 (2013) 034904; O. Linnyk et al, Phys. Rev. C89 (2014) 034908; O. Linnyk et al, to be published in Phys. Rev. C (2015)

---

[*] Work supported in part by HIC4FAIR

[†] olena.linnyk@theo.physik.uni-giessen.de

DOI:10.15120/GR-2015-1-MU-THEORY-28

Collective excitations and particle production: from static nuclei to reactions at $\overline{\mathrm{P}}$ANDA*

T. Gaitanos[1], *Ch. Moustakidis*[1], *N. Paar*[2], *D. Vretenar*[2], *G.A. Lalazissis*[1], *and H. Lenske*[3]
[1]Dept. of Theoretical Physics, Aristotle University of Thessaloniki, Greece; [2]Physics Dept., Faculty of Science, University of Zagreb, Croatia; [3]Inst. für Theor. Physik, Universität Giessen & GSI Darmstadt, Germany

Collective excitations (CE) play a crucial role in modern nuclear and hadron physics and astrophysics. They are of great relevance for a deeper understanding of the still less known density behaviour of the isovector sector of the Equation of State (EoS) for highly asymmetric matter. Indeed, various modes of CE in finite nuclei are closely correlated to the structure of the neutron star crust, whereas high-energy CE of hadron matter produced in reactions induced by heavy-ions and hadron beams provide more information for highly compressed matter and its composition. The latter is relevant for the inner structure of a neutron star at supra-normal densities far beyond saturation. Our present studies are motivated by the new FAIR project and, in particular, they are directly connected with the forthcoming $\overline{\mathrm{P}}$ANDAexperiments [1].

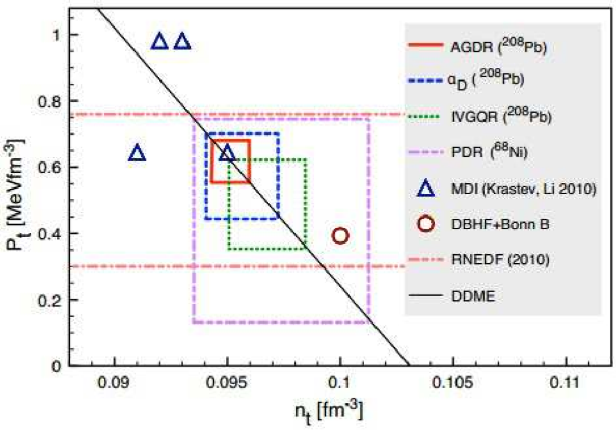

Figure 1: The liquid-to-solid transition pressure P_t for neutron-rich matter versus the transition density n_t. The various rectangles (AGDR, IVGQR, α_D, PDR) correspond to experimental constraints. The MDI, DBHF+Bonn B and the self-consistent RNEDF calculations are shown for comparison [2].

The theoretical study of CE in static finite nuclei is performed within relativistic density functional methods allowing to determine the nature of liquid-to-solid phase for neutron-rich matter. This is shown in Fig. 1, where the transition pressure versus the transition density is shown for various theoretical models: the present approach (DDME, solid line) in comparison with experimental constraints (triangle regions) and other microscopic models. This type of analyses leads to stringent constraints on the low-density thermodynamic state, relevant for the corresponding low-density region in the crust of neutron stars.

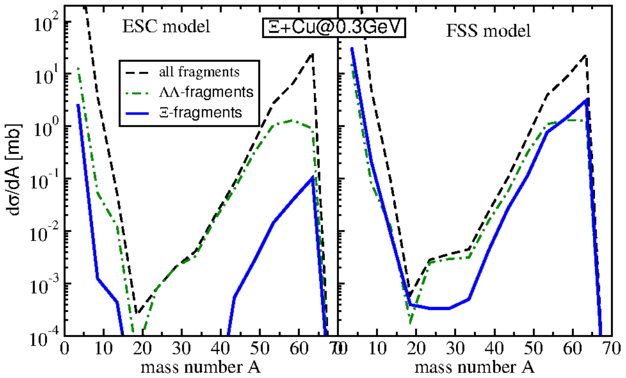

Figure 2: Production cross sections for single fragments (dashed), $\Lambda\Lambda$- (dott-dashed) and Ξ-hypernuclei (solid) versus the mass number for Ξ-induced reactions and two interaction models as indicated [3].

Furthermore, we investigate the dynamics of heavy-ion collisions and antiproton-induced reactions within the relativistic transport theory in the realization of the Giessen-BUU transport model [4]. Collective dynamics excites cold nuclear matter to phases of high compression, with the particular production of long-lived baryons (and mesons). Of importance are here particles with strangeness degree of freedom S, such as the $(\Lambda, \Sigma)(S=-1)$, $\Xi(S=-2)$ and $\Omega(S=-3)$ hyperons. Indeed, the production of multi-strangeness bound systems at conditions beyond ground state is possible. This is shown in Fig. 2 in terms of the production cross sections of single fragments, $\Lambda\Lambda$- and also Ξ-clusters versus the mass number. Here we have used reactions induced by secondary Ξ-beams as they will be available at $\overline{\mathrm{P}}$ANDA. Of particular interest is the very strong dependence of these observables (left and right panels) on the interaction model. Hence, data of this type will serve to constrain YN and YY in-medium interactions under the dynamical conditions of high-energy heavy-ion reactions. We emphasize the relevance of our theoretical results for the future activities at FAIR.

References

[1] A. Esser, et al., Nucl. Phys. A 914 (2013) 519.

[2] N. Paar, *et al.*, Phys.Rev. C90 (2014) 1, 011304

[3] T. Gaitanos, H. Lenske, Phys. Lett. B737 (2014) 256.

[4] O. Buss, *et al.*, Phys. Rep. 512 (2012) 1.

---

* Work supported by BMBF, DFG, HIC for FAIR, and GSI-JLU Giessen collaboration agreement

DOI:10.15120/GR-2015-1-MU-THEORY-29

DOI:10.15120/GR-2015-1-MU-THEORY-29

Evolution and use cases of FairMQ

A. Rybalchenko[1], *M. Al-Turany*[1], *and N. Winckler*[1]
[1]GSI, Darmstadt, Germany

The FairRoot framework [1] is a framework for simulation, reconstruction and data analysis of particle experiments. In the past, FairRoot has been extended with FairMQ, that enables reconstruction and analysis of free streaming data [2] [3]. FairMQ allows to use and extend components called devices to execute user tasks in a multiprocess, multithreaded and/or network environment, connecting them together efficiently.

General Developments

To make FairMQ devices more flexible, a concept of a command channel has been introduced, that allows the devices to change their internal state and configuration in response to external events. The concept has been successfully tested during the PANDA test beam [**?**].

To improve static configuration of FairMQ processes, a flexible system for command line options has been added. Utilizing boost::program_options library, the new options parameters provide support for default, optional and repeated parameters and also enable reading of parameters from external files.

For the dynamic deployment, FairMQ has added a number of features to allow more flexible configuration, such as automatic port finding from a given port range or more granular state transitions to allow access to configured properties. Making use of these features is the Dynamic Deployment System that is currently in development at GSI, which allows to dynamically distribute a user defined set of tasks over a number of nodes using any resource management system [**?**].

In addition to the original binary data transport format, a serialization using either Google Protocol Buffers, Root TMessage or Boost Serialization have been introduced, together with implementation examples. Furthermore, a generic device implementation based on Policy-based Design has been introduced to decouple device functionality from transport format [4].

FairMQ Devices for ALICE experiment

After the Long Shutdown 2, the upgraded ALICE detector will produce over 1 TB of data per second, which is to be distributed from about 250 First Level Processors (FLPs) to O(1000) Event Processing Nodes (EPNs), where each EPN collects sub-timeframes from every FLPs to build a full timeframe as is shown in Fig. 1. In the Alice O^2 software prototype two FairMQ devices have been implemented for transport and distribution of the data from FLPs to EPNs. Both FLP and EPN devices make use of "zero-copy" and multipart messages of ZeroMQ to ensure maximum performance and efficient packaging. The system has been shown to scale to a large number of nodes. Additionally, an algorithm has been implemented on the FLP devices to optimize the usage of the network and to minimize contention when several FLPs are sending to the same EPN. The results of the algorithm can be seen in a histogram in Fig. 2, which shows time intervals between receiving of data from the the same FLP on a given EPN. The application of the algorithm results in a balanced network usage and predictable traffic pattern.

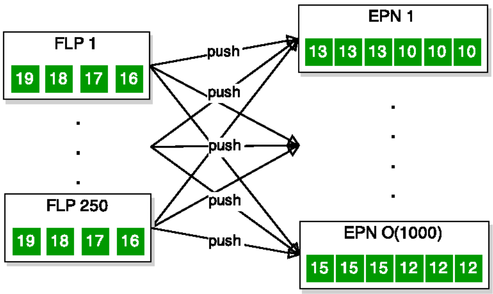

Figure 1: Alice O2 example topology

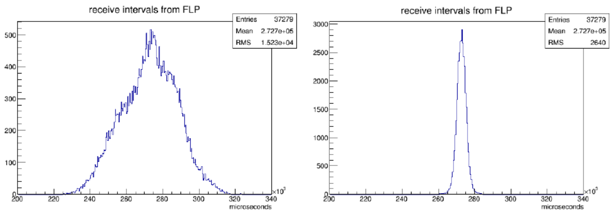

Figure 2: left: without traffic shaping, right: with traffic shaping

References

[1] FairRoot: http://fairroot.gsi.de.

[2] A. Rybalchenko, M. Al-Turany: GSI Scientific Report: Streaming data processing with FairMQ (2014)

[3] M. Al-Turany, D. Klein, A. Manafov, A. Rybalchenko, F. Uhlig: Extending the FairRoot framework to allow for simulation and reconstruction of free streaming data. accepted for publication by, Journal of Physics: Conference Series (2013).

[4] N. Winckler et al.: Generic and modular design for FairMQ devices (2015)

DOI:10.15120/GR-2015-1-INFRASTRUCTURE-IT-01

Generic and modular design for FairMQ devices

N. Winckler[1], *M. Al-Turany*[1], *D. Bertini*[1], *R. Karabowicz*[1], *D. Kresan*[1], *A. Lebedev*[1], *A. Manafov*[1], *A. Rybalchenko*[1], *and F. Uhlig*[1]
[1]GSI, Darmstadt, Germany

Introduction

The ability to combine application-specific functionality with independently developed library modules from a variety of sources is a key benefit of long term software projects maintenance and further development. Two main paradigms are available in C++ for achieving such a goal, that is, Object Oriented Programming (OOP) and Generic Programming (GP).

In OOP, libraries usually enforce that the types must be derived from a common abstract base class of the library, providing implementations for a collection of virtual functions. The strength of this paradigm is the dynamic polymorphism where types supplied to a module can vary at runtime. However, module composition is limited since independently produced modules generally do not agree on common abstract interfaces from which supplied types must inherit. On the other hand, the GP paradigm offers mechanisms for producing modules with clean separation, open for extension and without imposing the need to intrusively inherit from a particular abstract base class. However, in the current C++ standard (C++11), GP paradigm only allows static polymorphism, which limits the applications where dynamic polymorphism is required. This limitation will nevertheless disapear with the introduction of C++Concept [1, 2] in the next C++ standard.

Generic FairMQ devices

Policy based class design

In this contribution, we present a policy based design [3] – a design pattern steming from the GP paradigm – for the FairMQ devices [4, 5]. The pattern usually consists of a child class template, called a host class, which inherit from its template parameters, called policy classes. An important aspect is that, the relationship between base and derived class are inverted w.r.t. usual OOP, that is, the base class (host) is the abstract (implicit) interface while the parent classes (policies) supply an implementation set of specific behaviours, which will be inherited by the host class at compile time. The policies are usually split into orthogonal behaviours, and, for a given policy, there can be an unlimited number of implementations. Moreover the host class can be library independent. This design pattern is particularly adapted to the devices of the FairMQ library, since the latter aims to support the process distribution of various experimental group, each depending on different libraries or data types.

Figure 1 shows the class diagram of three generic devices, namely a sampler, a processor and a filesink. Each device inherit from the FairMQDevice abstract class, and from an input policy, an output policy, and eventually a task policy. The FairMQDevice class handle the communication layer. Depending on the device, the input policies can be a file reader, or a deserialization policy and the output policy can be a serialization or a storage policy.

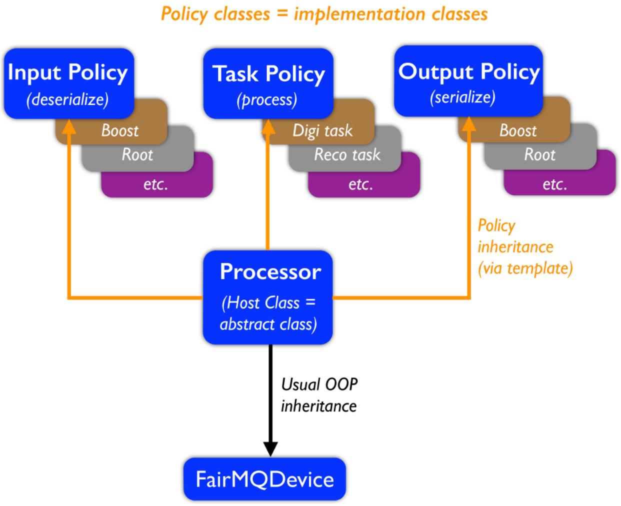

Figure 1: Class diagram of a generic processor.

FairRoot Tutorial 7

An application example of these generic devices can be found in FairRoot/examples/Tutorial7, where different policies are used.

References

[1] B. Stroustrup, et al. “Runtime Concepts for the C++ Standard Template Library”, Proceedings of the 23rd ACM symposium on applied computing (SAC), (2008)

[2] M. Marcus, et al. “Runtime Polymorphic Generic Programming — Mixing Objects and Concepts in ConceptC++”, Multiparadigm Programming 2007: Proceedings of the MPOOL Workshop at ECOOP’07, (2007)

[3] A. Alexandrescu “Modern C++ Design: Generic Programming and Design Patterns Applied” Addison-Wesley Longman Publishing Co., Inc., Boston, MA, USA (2001)

[4] A. Rybalchenko, and M. Al-Turany “Streaming data processing with FairMQ”, GSI Scientific Report (2013)

DOI:10.15120/GR-2015-1-INFRASTRUCTURE-IT-02

[5] M. Al-Turany et al. “ALFA: A new Framework for ALICE and FAIR experiments”, GSI Scientific Report (2013)

DOI:10.15120/GR-2015-1-INFRASTRUCTURE-IT-02

FairMQ application example in CbmRoot

N. Winckler[1], *M. Al-Turany*[1], *D. Bertini*[1], *R. Karabowicz*[1], *D. Kresan*[1], *A. Lebedev*[1], *A. Manafov*[1], *A. Rybalchenko*[1], *and F. Uhlig*[1]

[1]GSI, Darmstadt, Germany

Introduction

The FairMQ package is an asynchronous messaging layer in FairRoot framework aiming to support online/offline data analysis with high data rates[1, 2, 3]. It allows to distribute processes on different nodes (from a laptop to an entire homogenous or heterogenous system with many thousands of cores) and provides the communication layer between these processes.

In this contribution, we present a simple FairMQ application example in the context of the CbmRoot framework[4].

Device topology

The components encapsulating the tasks are called devices and derive from the common base class FairMQDevice. The devices are arranged into topologies, which describe the data flow between the different deployed processes. In this example, the used device topology is shown in figure1 and consists of the following devices:

- Two data sources (called Sampler) sending microslices
- One Merger merging microslices into timeslices
- One FileSink receiving and storing data to file

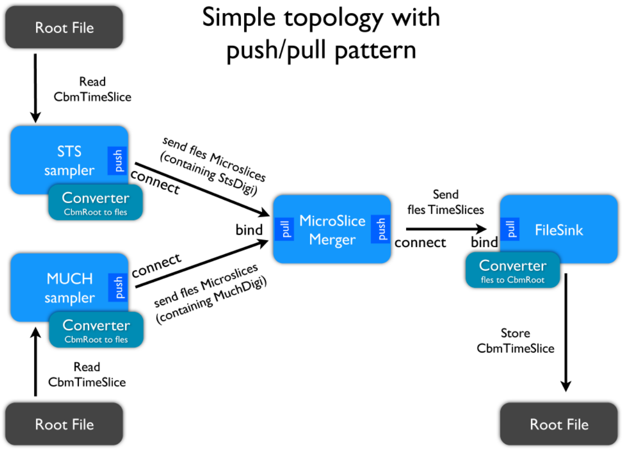

Figure 1: Simple topology involving four processes (2 samplers, 1 merger, 1 FileSink) with the push-pull messaging pattern.

Sampler, Merger and FileSink

The sampler device is used as data source, i.e. it reads data from a file and send them to another device. In this example, the two samplers read from root file the *CbmRoot timeslices*, convert the data into STS or MUCH FLES *microslices*, and then streamed them to the Merger device.

The merger device collect, synchronize and merge the FLES *microslices* streamed by the two samplers into FLES *timeslices*. Once merged, the *timeslices* are streamed to the FileSink device.

The FileSink device collect the data send by the Merger, convert them into CbmRoot data format and store the result into root file.

Summary and outlook

A simple FairMQ application example is available in the CbmRoot simulation framework. Other process nodes (e.g. track finder or track reconstruction task) as well as other messaging pattern (e.g. request/reply, pub/sub) can be easily added to the device topology. A Dynamic Deployment System (DDS) under development will ease the topology generation and deployments[5].

References

[1] D. Klein, “Flexible data transport for the online analysis in a particle physics experiment”, Bachelor Thesis, TU darmstadt (2013)

[2] A. Rybalchenko, and M. Al-Turany “Streaming data processing with FairMQ”, GSI Scientific Report 2013-2014

[3] M. Al-Turany et al. “ALFA: A new Framework for ALICE and FAIR experiments”, GSI Scientific Report 2013-2014

[4] CbmRoot collaboration

[5] A. Manafov, et al. “DDS : A Dynamic Deployment Sytem”, GSI report 2014-2015

DOI:10.15120/GR-2015-1-INFRASTRUCTURE-IT-03

DDS: The Dynamic Deployment System

A. Manafov[1] *and A. Lebedev*[1]
[1]GSI, Darmstadt, Germany

The Dynamic Deployment System (DDS) [1] is a toolset that automates and dramatically simplifies the process of deployment of user defined processes with their dependencies on any resource management system using a given topology.

DDS is a successor of PoD [2]. Unlike PoD, which automates PROOF [3] deployment, DDS will handle any kind of user processes with complex dependencies between processes. The system is designed and being implemented within the new ALFA framework [4].

Concept

A key point of this design is the so called "topology language". DDS is a user oriented system, i.e. definition of topologies is simple and powerful at the same time. The basic building block of the system is a task. Namely, a task is a user defined executable or a shell script, which will be deployed and executed by DDS on a Resource Management System. To describe dependencies between tasks in a topology we use properties. A property is represented as a key-value pair, where a value is any string. DDS implements an efficient engine for properties synchronization. We call it a key-value propagation feature.

Tasks can be grouped into DDS collections and DDS groups. The difference between collections and groups is that collections are a signal to DDS topology parser that tasks of given collections will be executed on the same physical machine. This is useful if tasks have lots of communication or they want to access the same shared memory. A set of tasks and task collections can be also grouped into task groups.

DDS utilizes a plug-in system in order to use different job submission front-ends. The first and the main plug-in of the system is an SSH plug-in, which can be used to dynamically turn a bunch of machines to user worker nodes. The SSH plug-in is a perfect tool for a Cloud based solutions.

Status

During 2014 the core and main modules of the DDS have been developed and the first stable prototype has been released.

The prototype has been tested on Alice HLT cluster using 40 computing nodes with 32 processes per node. DDS's SSH plugin has been used to successfully distribute and manage 1281 AliceO2 user tasks (1 sampler, 640 FLP and 640 EPN [5]). Throughout the test, one DDS commander server has propagated more than 1.5M key-value properties in less than 30 s. Which is a great performance considering early stage of the product development.

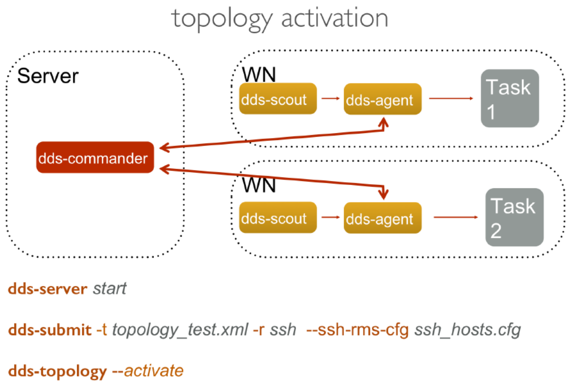

```
dds-server start
dds-submit -t topology_test.xml -r ssh  --ssh-rms-cfg ssh_hosts.cfg
dds-topology --activate
```

Figure 1: Illustration of the DDS topology activation.

Development

DDS is being actively developed using modern development tools, C++11, and Boost libraries [6]. As the continuous integration framework we use BuildBot [7]. The web site and DDS's users manual are based on DocBook [8]. We developed and maintain a unique Git workflow to simplify and secure the development [9].

References

[1] Dynamic Deployment System (DDS), http://dds.gsi.de.

[2] A. Manafov et al, "PROOF on Demand", IT-07, GSI Scientific Report 2012.

[3] TheParallelROOTFacility(PROOF), http://root.cern.ch/drupal/content/proof

[4] M. Al-Turany et al., Status of the FairRoot framework, this report.

[5] A. Rybalchenko et al., Evolution and use cases of FairMQ, this report.

[6] BOOST C++ Libraries, http://www.boost.org.

[7] Buildbot. The Continuous Integration Framework, http://www.buildbot.net.

[8] DocBook, http://www.docbook.org.

[9] Git Workflow, https://github.com/AnarManafov/GitWorkflow.

DOI:10.15120/GR-2015-1-INFRASTRUCTURE-IT-04

Redesign of the FairRootManager

R. Karabowicz[1], *M. Al-Turany*[1], *D. Kresan*[1], *and F. Uhlig*[1]
[1]GSI, Darmstadt, Germany

Introduction

FairRoot is a data simulation and reconstruction framework developed in the Experiment Software group and used by various experiments for the physics analysis. It has originally been designed both to read the input data and to store the output data from/in the root files. The recent requirements of several experiments made it necessary to develop alternative ways of accessing input data, like the MBS systems or LMD files.

In the meantime, it became imperative to unify and standarize the different approaches.

Source

In the original design, the central data manager, the *FairRootManager*, reads the data from the input ROOT trees stored in (multiple) files. The redesigned *FairRootManager* accesses the data inputs via specific implementations of the *FairSource*. The generic *FairSource* class provides abstract functions to access input data. The concrete derived classes include:

- *FairMbsSource* - for reading data from the MBS event server;
- *FairLmdSource* - for reading data from the LMD files;
- *FairFileSource* - for reading data from the root files, it is possible to add many files (creaing chains of input data) or to add friend files (in case if the event data is spread between different files);
- *FairMixedSource* - for mixing of input data from the background file with signal files. Each added signal requires providing of a value of mixing ratio, which determines the occurence of signal events in respect to the background events.

The reorganization allows now easy creation of another, more experiment-specific, implementations of the *FairSource*, should such be needed.

Manager

With the introduced changes, the *FairRootManager* complexity has been greatly reduced and the source file size scaled down by about 55%. The functions that were responsible for reading the input tree structure or comparing integrity of the trees if more input files were provided, were moved to the *FairFileSource* and *FairMixedSource*.

```
FairRunAna* fra = new FairRunAna();
fra->SetBackgroundFile(‘‘file_bg.root’’);
fra->SetSignalFile(‘‘file_sg.root’’);
fra->AddTask(TTask* task);
fra->Init();
fra->Run(ev_start,ev_end);
```

Figure 1: Standard way of adding input files.

```
FairRunAna* fra = new FairRunAna();
FairSource* source = FairMixedSource(‘‘file_bg.root’’);
source->SetSignalFile(‘‘file_sg.root’’);
fra->SetSource(source);
fra->AddTask(TTask* task);
fra->Init();
fra->Run(ev_start,ev_end);
```

Figure 2: Adding FairSource after introduced modifications.

User macros

With the introduced changes the analysis macros, that steer the reconstruction, will slowly undergo a reorganization process. Previously, when only root files were recognized as the input source, the user was setting file names in the *FairRunAna*, as presented in Figure 1. Currently, one has to create an instance of a wanted source and set its properties, compare Figure 2. Such a source is then given to the *FairRunAna*, which passes it to the instance of the *FairRootManager*.

It has to be mentioned that to preserve the compatibility, the previous scenario is still supported, although with a warning message given to the user about code obsolence.

Summary

The goal of the introduced changes is to unify the reconstruction running scenario with different sources of input and to increase the framework modularity.

It has been achieved by introducing an abstract layer (*FairSource*) between the input source and the data manager.

The *FairRunAna* works with different kinds of sources. The experimantal software developers may now easily implement experiment-specific sources.

DOI:10.15120/GR-2015-1-INFRASTRUCTURE-IT-05

FairDB status

Denis Bertini[1]
[1]Scientific Computing ,GSI, Darmstadt, Germany

Introduction

The FairDB Virtual Database [1] provides the user with a well-defined and uniform API for database manipulation extending the FairRoot framework [2][3] initialization scheme to any SQL-Databases systems. This report describes recent developpments of the FairDB core functionality.

Error handling

Errors coming from the virtual database itself are treated using standard C++ exceptions and are automatically logged by the central logger manager class `FairDbExceptionLog`.
All virtual database internal errors or information messages are timestamped and shows the relevant classname , function name and line in the source code where precisely the error occurred. Figure 1 shows an logging output for internally generated SQL statements.

Logging

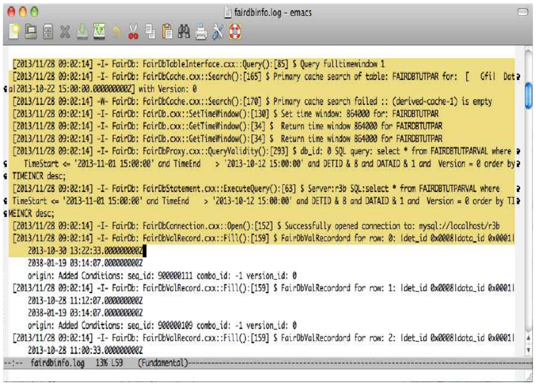

```
[2013/11/28 09:02:14] -I- FairDb: FairDbTableInterface.cxx::Query():[85] $ Query fulltimewindow 1
[2013/11/28 09:02:14] -I- FairDb: FairDbCache.cxx::Search():[165] $ Primary cache search of table: FAIRDBTUTPAR for:  [   Gfil  Dat
al2013-10-22 15:00:00.0000000000Z] with Version: 0
[2013/11/28 09:02:14] -W- FairDb: FairDbCache.cxx::Search():[170] $ Primary cache search failed :: (derived-cache-1) is empty
[2013/11/28 09:02:14] -I- FairDb: FairDb.cxx::SetTimeWindow():[130] $ Set time window: 864000 for: FAIRDBTUTPAR
[2013/11/28 09:02:14] -I- FairDb: FairDb.cxx::GetTimeWindow():[34] $  Return time window 864000 for FAIRDBTUTPAR
[2013/11/28 09:02:14] -I- FairDb: FairDb.cxx::GetTimeWindow():[34] $  Return time window 864000 for FAIRDBTUTPAR
[2013/11/28 09:02:14] -I- FairDb: FairDbProxy.cxx::QueryValidity():[293] $ db_id: 0 SQL query: select * from FAIRDBTUTPARVAL where
   TimeStart <= '2013-11-01 15:00:00' and TimeEnd    > '2013-10-12 15:00:00' and DETID & 8 and DATAID & 1 and  Version = 0 order by
 TIMEINCR desc;
[2013/11/28 09:02:14] -I- FairDb: FairDbStatement.cxx::ExecuteQuery():[63] $ Server:r3b SQL:select * from FAIRDBTUTPARVAL where
 TimeStart <= '2013-11-01 15:00:00' and TimeEnd    > '2013-10-12 15:00:00' and DETID & 8 and DATAID & 1 and  Version = 0 order by TI
MEINCR desc;
[2013/11/28 09:02:14] -I- FairDb: FairDbConnection.cxx::Open():[152] $ Successfully opened connection to: mysql://localhost/r3b
[2013/11/28 09:02:14] -I- FairDb: FairDbValRecord.cxx::Fill():[159] $ FairDbValRecordord for row: 0: |det_id 0x0008|data_id 0x0001|
    2013-10-30 13:22:33.0000000000Z
    2038-01-19 03:14:07.0000000000Z
    origin: Added Conditions: seq_id: 900000111 combo_id: -1 version_id: 0
[2013/11/28 09:02:14] -I- FairDb: FairDbValRecord.cxx::Fill():[159] $ FairDbValRecordord for row: 1: |det_id 0x0008|data_id 0x0001|
    2013-10-28 11:12:07.0000000000Z
    2038-01-19 03:14:07.0000000000Z
    origin: Added Conditions: seq_id: 900000109 combo_id: -1 version_id: 0
[2013/11/28 09:02:14] -I- FairDb: FairDbValRecord.cxx::Fill():[159] $ FairDbValRecordord for row: 2: |det_id 0x0008|data_id 0x0001|
    2013-10-28 11:00:33.0000000000Z
--:--  fairdbinfo.log   13% L59   (Fundamental)------------------------------------------------------------
```

Figure 1: Logging for SQL Statements

Rollback

FairDB implements a dedicated rollback operation which, when applied, let the database ignore all changes that occured after the defined rollback date. In fact the database backs out the changes of the wrong transaction and restores the data consistency that existed when the unit of work was initiated.
In figure 2 the state of the database is first moved from a starting point of consistency (A) to another point of consistency (B) at the end of the transaction. If during the transactional process a failure occurs or if the ending point of consistency is questionable (for example because of wrong data input) it is useful to apply a rollback which can be seen as the exact reverse transaction.

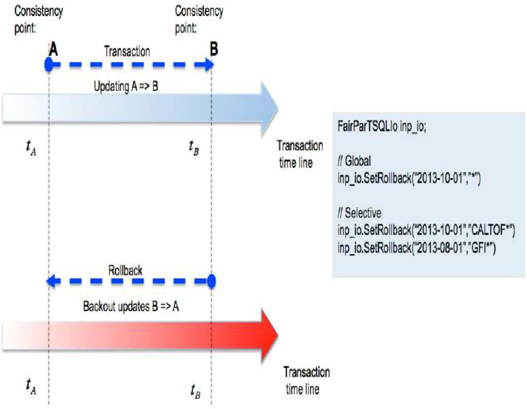

```
FairParTSQLIo inp_io;

// Global
inp_io.SetRollback("2013-10-01","*")

// Selective
inp_io.SetRollback("2013-10-01","CALTOF*")
inp_io.SetRollback("2013-08-01","GFI*")
```

Figure 2: Rollback Mechanism

The R3B condition database

The R3B collaboration is currently implementing its condition database based on FairDB. The database should store together detector hardware components, slow control and analysis parameters in one repository. A complete parameter implementation for the CALIFA as well as the time calibration parameter of the NeuLand detector are available in the R3BROOT framework.

ROOT 6 compliance

The FairDB Virtual Database has been sucessfully ported to the new ROOT version 6. Modifications for the dedicated CINT constructs has been moved to the new Cling standard in a backwards compatible way so that FairDB can run on any ROOT versions.

References

[1] FairRoot Virtual Database (User Manual).

[2] The FAIR simulation and analysis framework 2008 J. Phys.: Conf. Ser. 119 032011

[3] R. Brun, F. Rademakers, P. Canal, I.Antcheva , D. Buskulic, O. Couet, A. and M. Gheata *ROOT User Guide* CERN, Geneva 2005.

DOI:10.15120/GR-2015-1-INFRASTRUCTURE-IT-06

FairDB dynamical SQL processing interface

Denis Bertini[1]

[1]Scientific Computing ,GSI, Darmstadt, Germany

Introduction

The FairRoot Virtual Database FairDB [1] uses internally the services of the ROOT classes `TSQLServer` and `TSQLStatement` to send and execute SQL commands with any of the supported database engine i.e MySQL, Oracle, PostGreSQL and SQLite.
Unfortunately the ROOT framework does only provide low-level drivers to the different SQL database engine. In order to properly interface the different SQL servers, FairDB adds additionnal layer on top of the ROOT framework for multiple database connection handling and SQL automatic translation.

Database multiple connection

FairDB is designed to give the user the possibility to connect to and access data from more that one database. At initialization time, a pool of opened connections to different database engines is created using URL based syntax supported by the `TSQLServer` class.
The user can simply grap one when a transaction needs to be executed and then hand it back eliminating much of the overhead for the creation of connections.
If one connection fails, the next database in the list is used until the complete set of data can be retieved. This gives the user the flexibility to create its own database from a subset of the official one and to put it ahead in the list.

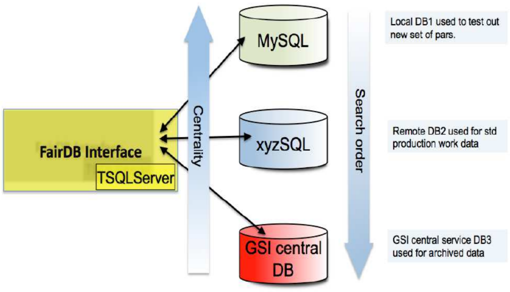

Figure 1: Database connection pool

SQL automatic translation

Since FairDB supports different database engine, it uses a special pre-processing of a given SQL statement in order to translate the statement if needed (Fig [2]). If a SQL translation is needed, a fast parsing is processed and a new adapted SQL statement is dynamically created with all translated tokens. The special SQL parsing and translation is done by the main SQL statement service class `FairDbSQlStatement`.

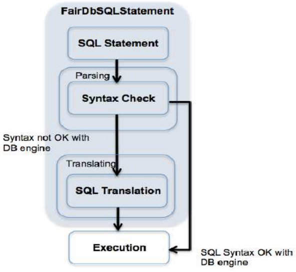

Figure 2: `FairDbSQLStatement` SQL automatic translation mechanism

New ROOT PostGreSQL driver

Required by FairDB, the ROOT low level driver `TPgSQLServer` has been recently corrected and partially rewritten using the `libPq` interface to allow for dynamical table information query. The patch has been accepted and is part of the new ROOT release 5-34-15 [2]. The new driver together with the automatic translation give the user the possibility to store and retrieve parameter with PostGreSQL database centrally supported by the GSI Core-IT team (Fig [3]).

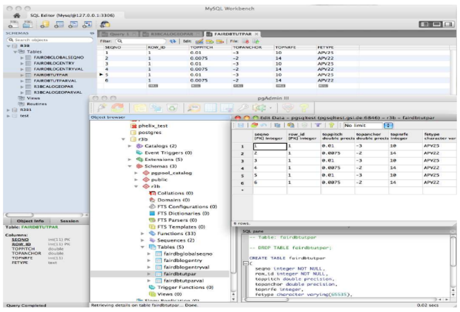

Figure 3: Same Parameter Table created with automatic SQL translation for MySQL and for PostGreSQL

References

[1] FairRoot Virtual Database (User Manual).

[2] R. Brun, F. Rademakers, P. Canal, I.Antcheva, D. Buskulic, O. Couet, A. and M. Gheata *ROOT User Guide* CERN, Geneva 2005.

Parameter handling using multi-part messages

Denis Bertini[1]
[1]Scientific Computing ,GSI, Darmstadt, Germany

Introduction

The FairDbMQ library provides a solution to adapt any parameter initialisation scheme to Message Queue distributed FairMQ tasks [1].

Design

FairDbMQ implements a simple Actor Model for concurrency using ZeroMQ [2] to cope with a large number of distributed tasks requesting asynchroneously parameter initialisation from a RDMS or file system based store. The challenge is then to be able to control the number of processes connecting the database or reading the file.
To solve this problem FairDbMQ separates the *frontend request client* from the *backend reply worker* adding a non-blocking worker queueing daemon in between acting as a proxy (Figure [1]).

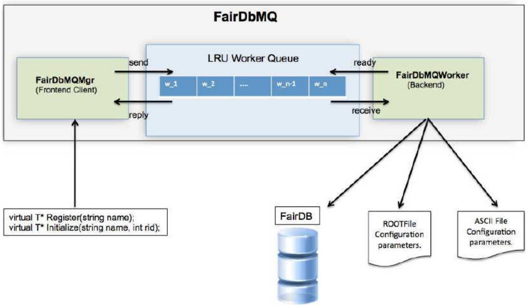

Figure 1: FairDbMQ components

Routing and protocol

The Worker Queue Daemon is continuously listening for connections from the *frontend sockets* and the *backend sockets* via event polling. It also uses ROUTER sockets to perform messages routing, the clients using REQ synchronous socket to connect.
When a initialisation request is sent, the socket identifier is kept as a frame content within the multi part message giving the possibility for the proxy to know to which client it should send back the processed reply (Figure [2]).

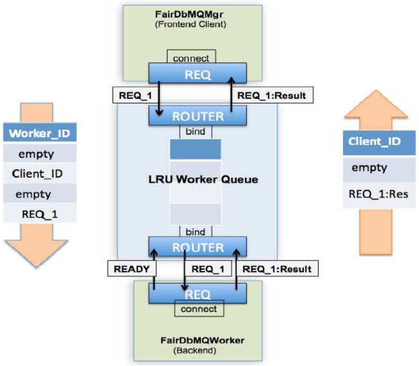

Figure 2: Routing is implemented by a dedicated Protocol using Mutli-part Messages.

Scalability and load balancing

The previous single cluster architecture can be scaled to more than one cluster by swapping a REP client socket with a DEALER socket. The Reply-Request mechanism goes then full asynchronous and request clients as well as worker can talk to more than one proxy (Figure [3]).
Of course, other implementations of a multiple clusters compatible with FairDbMQ design exists like for example connecting 2 proxies together using a ROUTER to ROUTER combination.

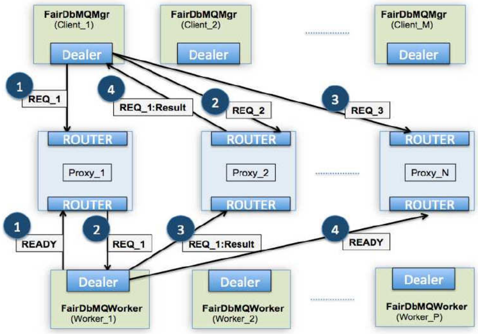

Figure 3: Multiple Cluster Design

Conclusion

The FairDbMQ library implements a custom queueing system to provide a scalable and fault-tolerant request-reply architecture for FairMQ tasks parameter initialisation.

References

[1] The FAIR simulation and analysis framework 2008 J. Phys.: Conf. Ser. 119 032011
[2] ZeroMQ, Martin Sustrik, The architecture of open source application volume 2.

DOI:10.15120/GR-2015-1-INFRASTRUCTURE-IT-08

Implementation of the R3B condition database using FairDB

Denis Bertini[1], *Hector Alvarez Pol*[2], *and Yago Gonzalez*[2]
[1]Scientific Computing ,GSI, Darmstadt, Germany; [2]University de Santiago de Compostella, Spain

Introduction

The R3B condition database should store the parameters required for the description of the R3B detector components and provide the access to the validated data.
The implementation of the R3B Condition Database is based on the FairDB Virtual Database [1].

Califa barrel database

Three databases are needed to describe the Califa Barrel Detector.

- **R3BRoot [2] Runtime DB:** manage basic parameters (geometry, gain, calibration, ...) needed for the Califa data analysis
- **Slow Control DB:** contains devices control and detector status parameters (voltages, temperatures, ...)
- **Laboratory DB:** storing parameters measured in the laboratory characterizing the detector hardware. Many instances of the same database should be synchronized between the differents labs.

Geometry database

The Califa geometry versions are originaly stored in ROOT binary files. A semi-automatic procedure has been implemented to convert the ROOT geometry objects contained in `TGeoManager` into a relational data model (Figure [1]).

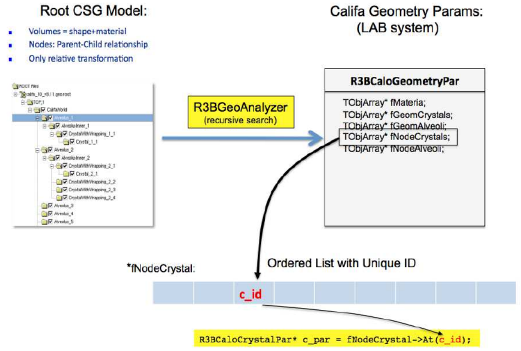

```
TObjArray* fMateria;
TObjArray* fGeomCrystals;
TObjArray* fGeomAlveoli;
TObjArray* fNodeCrystals;
TObjArray* fNodeAlveoli;
```

```
R3BCaloCrystalPar* c_par = fNodeCrystal->At(c_id);
```

Figure 1: ROOT geometry objects to relational model conversion

Lmd file indexing

For each LMD file written by the R3B DAQ system, a complete *run* information could be stored automatically in the database to be used later on for the data analysis initialisation. The figure [2] shows the scheme for storing the *run* information.
The figure [3] shows how the run info is then stored as a dedicated run info table in the R3B database.

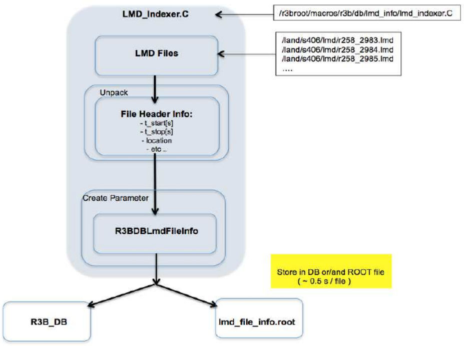

Figure 2: ROOT geometry objects to relational model conversion

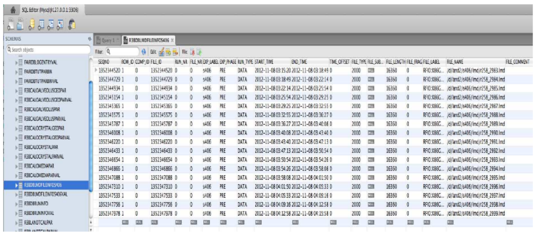

Figure 3: ROOT geometry objects to relational model conversion

Conclusion

The R3B Condition database is implemented based on FairDB. Parameter classes as well as automatic conversion procedures are available in R3BROOT to store relevant information from the DAQ, the Califa and NeuLand Detectors.

References

[1] FairRoot Virtual Database (User Manual).

[2] R3BRoot, simulation and analysis framwork for the R3B experiment at FAIR Denis Bertini 2011 J. Phys.: Conf. Ser. 331 032036

DOI:10.15120/GR-2015-1-INFRASTRUCTURE-IT-09

NeuLAND test-beam data analysis with R3BRoot framework

D. Kresan[1], *M. Al-Turany*[1,2], *F. Uhlig*[1], *the R3B collaboration*[1], *and the FairRoot@GSI group*[1]
[1]GSI, Darmstadt, Germany; [2]CERN, Geneva, Switzerland

NeuLAND prototype

New Large Area Neutron Detector (NeuLAND) is a fully-active modular scintillator, which will be used in the future R3B experiment at FAIR for measurement of neutrons, stemming from the primary nuclear reaction in the target. In order to achieve good resolution of physics observables (such as the relative energy of neutrons and heavy fragment), one needs precise determination of neutrons momentum. On the detector level, this requires precise time and position measurement. A series of experiments was performed at GSI SIS18 by placing the full-size NeuLAND prototype in operation for the purpose of performance tests. In this report, we present the stages of reconstruction algorithms, developed within the R3BRoot framework, which allow to analyse the data from S438 experiment. We will focus on the detector channel mapping, time and position calibration and the velocity spectra of reconstructed hits.

Data analysis

The analysis of S438 experiment was performed by using the R3BRoot framework in the offline mode. Each reconstruction step was implemented as a task, derived from FairTask class. The parameters as the output of calibration tasks were stored in the local database using the functionality provided by FairRoot [1]. Functionality of the remote-event client, also presented in [2], was successfully tested directly during the run, and resulted in multiple corrections and improvements of the software.

Data unpacking and mapping

Experimental data come from the DAQ server (or local file) in the MBS format. Each sub-detector has a dedicated hexadecimal encoder, which stores the data in ROOT objects, supported by R3BRoot. Raw level hits with the values of hardware channels are mapped to the hits with real detector ID by applying cabling scheme.

Time calibration

Each detector module (scintillator bar) was calibrated separately. The distribution of time channels over the whole run data was converted into a time in nanoseconds, assuming that the width of such distribution corresponds to a full clock cycle and that the value of a channel growth linear.

Position calibration

Experimental run with cosmic particles was used for the position calibration of a module. First, the time difference between left and right photomultiplier was used to calculate the position along the bar. The distribution of coordinates per paddle was centered at zero and scaled to match with the length of the paddle (2.5 m). The same data set was used to synchronize time from the neighboring bars.
At this stage we have detector hits containing bar ID number, time and position along the bar.

Results

Figure 1 shows the hit velocity distribution. By applying a narrow cut around the beam velocity, one can effectively suppress low-energy gamma background in the energy deposit spectra.

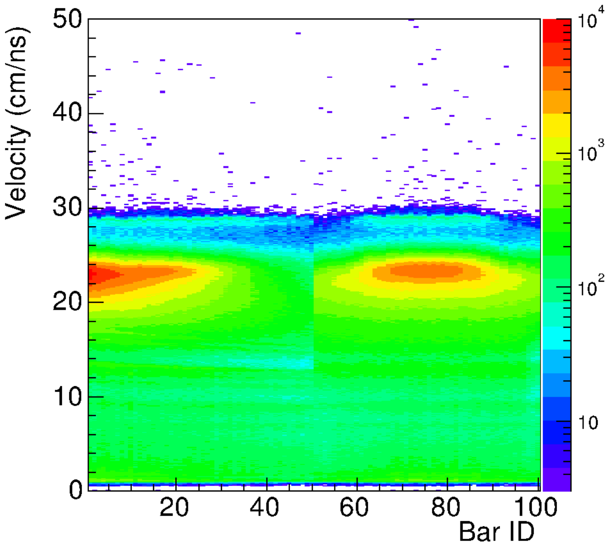

Figure 1: Distribution of the reconstructed velocity versus the detector number. First 50 bars - horizontal, second - vertical orientation. Contribution from gammas around 29 cm/ns is clearly separated from the neutron peak, which is located close to the beam velocity.

References

[1] M. Al-Turany et al., "Status of the FairRoot framework", GSI Scientific Report 2013 (2014) 281

[2] D. Kresan and F. Uhlig, "Remote Event Client Implemen-

DOI:10.15120/GR-2015-1-INFRASTRUCTURE-IT-10

tation in FairRoot Framework”, GSI Scientific Report 2013 (2014) 287

DOI:10.15120/GR-2015-1-INFRASTRUCTURE-IT-10

Parallel minimization via Geneva, ScaLAPACK and MPI on the GSI cluster

J. Knedlik[1], *M.F.M. Lutz*[1], *and K. Schwarz*[1]
[1]GSI, Darmstadt, Germany

The theory group in collaboration with the scientific computing group at GSI is preparing a general framework to predict and analyze hadronic final-state interactions. This is of crucial importance for a successful interpretation of data to be taken by the PANDA collaboration at FAIR. In 2012's Annual Report [1], we discussed our motivation in depth and presented our choices of software for the underlying needs of our framework.

In this report, we want to explore the framework's near final form and the workflow we are using for code developement.

We use Mathematica as the primary physic based developement environment, to ensure easy mathematical correctness and consistency by using Mathematica's internal checks. MathCode C++ is then able to compile Mathematica's code into native C++ code. We further extended this code with our own functions and classes, to enable the usage of ScaLAPACK's scalable solving of linear systems in Mathematica.

The desired use case requires to minimize a function with respect to a specific parameter set. The problem we needed to solve, was to create that function by MathCode C++, which needs ScaLAPACK's cluster wide scale.

Geneva is a C++ library for clustered problem solving by using evolutionary algorithms. In Geneva, in order to minimize our function, a broker sends singular genotypes to clients (in our usecase: varying parameters of our function) to let the clients evaluate their phenotype's fitness (in our usecase: the chisquare of that set of parameters). After many iterations over a well-sized population a good quality minimum will be reached. In combination, we can let Geneva spawn n cluster jobs (Geneva Clients), with m nodes (ScaLAPACK worker nodes) using ScaLAPACK's distributed solving for the analysis of our function with one specific parameter set. We can then iterate over evolutionary generations of these parameter sets, in order to find the parameter set that realizes the global minimum of our function.

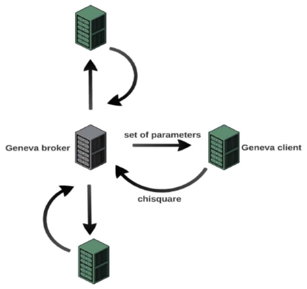

Figure 1: This figure shows the use case. Geneva's broker sends different sets of parameters to every Geneva client. The clients evaluate the functions' chisquare with that specific set of parameters and return them to the broker. The broker in return generates a new population of parameter sets with its evolutionary algorithm in order to find the minimum of our function.

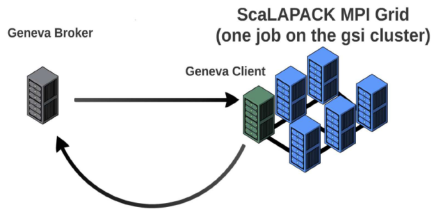

Figure 2: This figure shows how we integrated ScaLAPACK in Genevas workflow. A cluster job builds an MPI grid with all nodes. One node starts the Geneva client daemon and handles the communication of the parameter set to all mpi nodes. All other nodes wait in an application specific workloop. The Geneva client daemon can then utilize the computing power of the other nodes per mpi by using the functions of the mpi workloop(like ScaLAPACK).

In conclusion we have built a developement environment meeting the 2 requirements of both :

- easy usage by utilizing Mathematica and MathCode C++ including mathematical consistency checking
- solving and minimizing the developed Mathematica function on a cluster scale

So far, some problems have already been solved by utilizing Geneva on a singular machine with 64 cores. ScaLAPACK has been successfuly used to solve linear systems of an order of 200K on the GSI Prometheus cluster.

The important task, that is ongoing and well on its way right now, is to merge both of these aspects to show, that the combination of those two fully meet the requirements of our initial use case.

References

[1] J. Knedlik, M. Lutz, K. Schwarz GSI Report 2013-1, **504**, (2013).

DOI:10.15120/GR-2015-1-INFRASTRUCTURE-IT-11

Improved operation for the ALICE Tier2 Centre at GSI

K. Schwarz, A. Kukushev[1]
[1]GSI, Darmstadt, Germany

This article describes the improvements implemented in 2014 to increase the reliability and performance of the ALICE Tier2 Computing Centre at GSI.

ALICE tier2 centre at GSI and ALICE Grid in Germany

The ALICE tier2 centre and the National Analysis Facility at GSI provide a computing infrastructure for ALICE Grid and for the local usage of the German ALICE groups.

The storage resources pledged to the global ALICE community (550 TB) are provided via a Grid Storage Element which consists of an xrootd [1] daemon running on top of the Lustre file system.

In this contribution an enabling technology is described which gives the possibility to include local HPC resources into a distributed computing environment for ALICE and FAIR. A prototype has been implemented which will be operated in production mode for the ALICE tier2 centre at GSI. The work done in this context is also an important contribution to the Data Life Cycle Lab "Structure of Matter/FAIR" within the portfolio project "Large Scale Data Management and Analysis (LSDMA)" [2].

The new storage infrastructure as described in this article can also be used by Grid jobs in the firewall protected environment of the GSI HPC cluster.

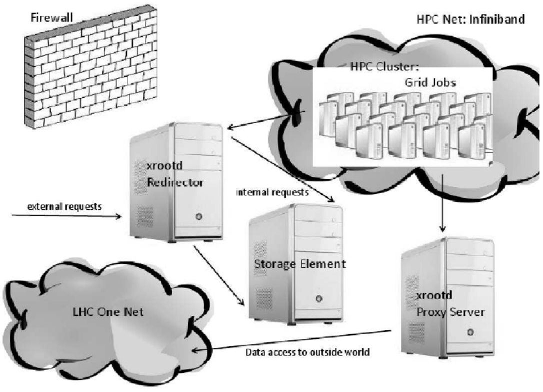

Figure 1: GSI storage setup

The main elements are the xrootd redirector as well as the xrootd forward proxy server. The redirector is using the split directive of xrootd and redirects external clients to the external interface of the GSI storage element and internal clients to the internal interface which is directly connected to the local Infiniband Cluster. The xrootd forward proxy server provides the possibility to Grid jobs running inside the protected HPC environment to read input data from external data sources using the proxy interface. Writing to external storage elements is possible via the same technique. The setup is shown in fig. 1.

Throughout the year GSI participates in centrally managed ALICE Grid productions and data analysis activities, but also analysis jobs of individual users are running on the ALICE tier2 centre. The overall job share of successfully computed jobs in 2014 contributed by the German Grid sites, the GSI tier2 centre and Forschungszentrum Karlsruhe (ALICE tier1 centre) has been 10% of all ALICE Grid jobs worldwide. This corresponds well with the pledged CPU resources for 2014: 7000 HEP-SPEC06 for GSI tier2 (4% of the global T2 requirements) and 30000 HEP-SPEC06 for FZK (27% of the global T1 requirements)

High Level Service Monitoring for the GSI ALICE Tier2 centre

Within a Bachelor Thesis supervised in cooperation with Hochschule Darmstadt a High Level Service Monitoring Tool for the GSI ALICE Tier2 centre has been developed. After identifying the Key Performance Indicators which are relevant for characterizing the smooth operation of the ALICE Tier2 centre a High Level Service Monitoring tool has been implemented in JavaScript using Node.js, the Node.js framework Express.js and Jade for HTML templates. Depending on the functionality red, green, or yellow lights show the current status of the ALICE Tier2 Centre and help in providing a reliable service. A screenshot can be seen in fig. 2

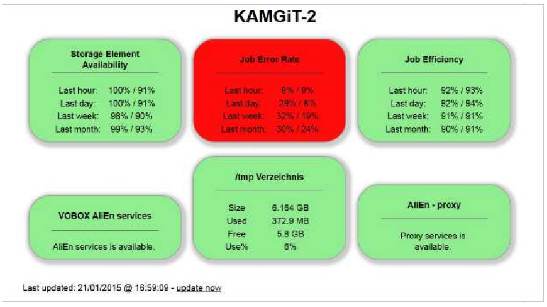

KAMGiT-2

Storage Element Availability
Last hour: 100% / 91%
Last day: 100% / 91%
Last week: 98% / 90%
Last month: 99% / 93%

Job Error Rate
Last hour: 8% / 8%
Last day: 28% / 8%
Last week: 32% / 19%
Last month: 30% / 24%

Job Efficiency
Last hour: 92% / 93%
Last day: 92% / 94%
Last week: 91% / 91%
Last month: 90% / 91%

/tmp Verzeichnis
Size 6.164 GB
Used 372.9 MB
Free 5.8 GB
Use% 6%

VOBOX AliEn services
AliEn services is available.

AliEn - proxy
Proxy services is available.

Last updated: 21/01/2015 @ 16:59:09 - update now

Figure 2: **K**PI **A**LICE **M**onitoring **G**SI **T**ier2

References

[1] http://xrootd.org/

[2] http://www.helmholtz-lsdma.de/

DOI:10.15120/GR-2015-1-INFRASTRUCTURE-IT-12

GSI-HPC Cluster

W. Schön[1], *C. Huhn*[1], *V. Penso*[1], *T. Roth*[1], *J. Trautmann*[1], *the HPC department*[1], *and the IT-Security division*[1]

[1]GSI, Darmstadt, Germany

Abstract:The GSI HPC cluster is mainly used by international collaborations to analyse experimental data (GSI/LHC). The cluster is being extended to be prepare for the needs of FAIR. New concepts to improve cluster scalbility are developed and deployed in new clusters.

Introduction

The FAIR project needs more powerfull computing in terms of FLOPs, I/O rates and online storage capacities. For efficient use of a cluster it is crucial to identify and eliminate bottlenecks. With increasing complexitivity of such a cluster, monitoring, anomaly detection and management are also crucial. In addition, IT security becomes an more and more demanding problem - especially taking into account the international usage of the cluster and the existence of broad bandwidth connections to remote sites.

Compute Power

In an environment typical for GSI, LHC or FAIR experiments, the pure compute power is the most easy problem to solve. Due to the independence of the physics events, parallelization can be done easily by analyzing events simultaneously on a number of cores. No communication between the cores is necessary. The simplest solution is to increase the number of cores in the cluster to enhance the number crunching power. However, more indirect limitations will occur: I/O per node, management of a huge number of cores and nodes, power density, cooling can become critical.

I/O Capacity and Meta Data Perfomance

I/O is the crucial factor in analysing data of large experiments (e.g. CBM or PANDA). If the I/O capacity is not sufficient, the jobs will be I/O bound (jobs will wait for I/O instead of analysing data). Typical simulation jobs or theory calculations are much less I/O demanding. The I/O problem is solved employing parallel cluster file systems at GSI (Lustre [1]). These clusters aggregate the capacity of single RAID groups to a filesystem with a global view to the whole data space. The clusters are designed, built and operated by the HPC department. GSI participates in the development and testing of the Lustre (and is a founding member of the EOFS [2]). In the past three years, the production cluster with about 125 file servers and a 7 Petabyte capacity has provided a fast and reliable storage for all of GSI's working groups. The next generation cluster running the current stable Lustre version an providing 7.7 PB capacity has been set up recently. It will employ two important new features: the data object are now stored on disk using the ZFS [4] file system, which provides protection against data corruption, continuous integrity checking and automatic repair. And the metadata can now be distributed across several servers, improving on one of the general bottleneck of Lustre, metadata performance. In particular, heavy load on the meta data server can severely limit the overall cluster performance. Especially massively parallel concurrent access of jobs to one and the same file can cause problems, slowing down the entire cluster and thus the HPC farm. User code is often making very inefficient use of Lustre, e.g. by writing and reading huge numbers of small files instead of writing one large file. Excessive meta data usage can also be point to bad user code (e.g. nested infinite loops querying meta data). It is therefore necessary to monitor and detect anomal meta data operations to protect the whole system.

Managing the GSI Cluster

The GSI clusters are now being managed by the Chef configuration management tool [5] with great success. Meanwhile, old NFS services and servers have been phased out. Remaining physics data that was not moved to the Lustre clusters has been pooled up in few modern file servers, while distribution of scientific software has been entirely moved to CernVM-FS [6]. The goal to improve stability [3] by avoiding common shared resources for user code and system code apart from Lustre was attained, as was the goal to improve scalability by distributing the data in many instances.

To scale out to the planned size of FAIR T0-Computing, a new open source job scheduler for the GSI batchfarm is being tested [7].

References

[1] Schoen et. al. I/O Optimised Cluster for Data analysis, GSI scientific report 2010

[2] www.eofs.org

[3] Huhn et. al. Comparison ...., GSI scientific report 2011

[4] Open ZFS, http://open-zfs.org/

[5] www.chef.io

[6] cernvm.cern.ch

[7] http://slurm.schedmd.com

DOI:10.15120/GR-2015-1-INFRASTRUCTURE-IT-13

The L-CSC cluster at GSI for lattice QCD - The most power efficient supercomputer in the world in 2014*

D. Rohr[1,2], *G. Nescovic*[1,3], *and V. Lindenstruth*[1,2,3]

[1]Frankfurt Institute for Advanced Studies, Germany; [2]Goethe University Frankfurt, Germany; [3]GSI, Darmstadt, Germany

The L-CSC (Lattice Computer for Scientific Computing) is a new compute cluster installed at GSI dedicated to calculations in the field of Quantum Chromo Dynamics (QCD). QCD is the physical theory describing the strong force, one of the four fundamental interactions in physics. In general, QCD is a non linear, non perturbative theory and the only approach to study it from first principles is Lattice QCD (LQCD). Here, space time is discretized on a four-dimensional lattice, allowing numerical evaluation of the theory. LQCD has extreme demands for memory bandwidth in order to produce results in a reasonable time frame.

In recent years, compute capabilities of supercomputers have increased significantly, but power consumption increased as well. Today, electricity costs for supercomputers are in the same order of magnitude as acquisition costs. Hence, there are strong financial and environmental aspects that advise to build supercomputers with better power efficiency.

Due to the demands of LQCD, the development laid particular focus on memory bandwidth and on power efficiency. Modern GPUs, which can work as a coprocessor in today's compute clusters, offer both: high memory bandwidth and great power efficiency. Accordingly, the chosen architecture uses four GPUs per compute node for L-CSC. This puts high emphasis on GPU computations, while the CPU is merely used for data movement. L-CSC consists of 160 compute nodes equipped either with four FirePro S10000 or four FirePro S9150 GPUs. The reason for the two GPUs models is that the S10000 is better for a higher aggregate compute throughput of small and medium lattices. The S9150 achieves a shorter processing time for individual lattices and can manage larger lattices than S10000. This makes L-CSC applicable for Lattice QCD quite flexibly.

The L-QCD application for L-CSC uses OpenCL and is hence vendor-independent. It was already used with great success on the LOEWE-CSC and Sanam clusters. The $\not{D}$ kernel, which is the computational hotspot of the application, uses the available theoretical peak global memory bandwidth to about 75 %. Since Lattice-QCD is memory bound, there is little room for improvements. This result translates to a compute performance of about 135 GFLOPS on a single S9150 GPU. With four such GPUs, an L-CSC node is more than 10 times faster than a LOEWE-CSC node, which achieves only around 50 GFLOPS. On top of that, with 16 GB of global memory per S9150, L-CSC is no longer subject to lattice size restrictions, which was the case with LOEWE-CSC and Sanam.

In order to demonstrate the power efficiency of L-CSC, the HPL-GPU implementation of the Linpack benchmark, was tuned for the particular hardware. The optimized version attempts to distribute the workload between CPU and GPU such, that it is executed most efficiently - and not necessarily as fast as possible. The cluster thus operates slightly slower, but significantly more efficient [1]. This approach was already quite successful for the Sanam cluster. In addition to the software, the processor parameters such as voltage and frequency have been tuned to operate at the optimal working point with respect to efficiency. HPL-GPU was already employed on the LOEWE-CSC and SANAM clusters and achieved the 8th and the 2nd place in the Green500 lists of the most power efficient supercomputers in the world in 2010 and 2012. With the new power efficient quad-GPU architecture, and with the new HPL-GPU features aimed at improving power efficiency, L-CSC achieved the top spot of the Green500 list in November 2014 with 5293 GFLOPS/W.

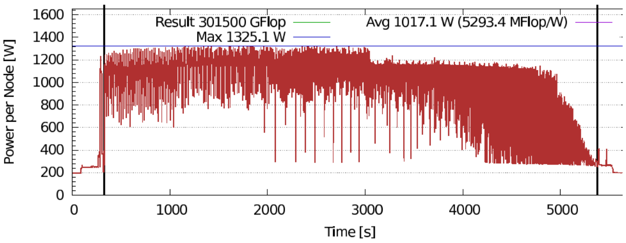

Figure 1: Power measurement of L-CSC during the Linpack run submitted to the Green500 list. The run utilized 56 nodes, the curve shows the average power per node. The final result submitted to the list is 302 TFLOPS with an efficiency of 5293.4 GFLOPS/W. This placed L-CSC 1st in the Green500 list of November 2014.

References

[1] D. Rohr, S. Kalcher, M. Bach, et al., "An Energy-Efficient Multi-GPU Supercomputer", Proceedings of the 16th IEEE International Conference on High Performance Computing and Communications, HPCC 2014, Paris, France. IEEE, 2014

---

* Work supported by GSI, FIAS, HICforFAIR

DOI:10.15120/GR-2015-1-INFRASTRUCTURE-IT-14

DOI:10.15120/GR-2015-1-INFRASTRUCTURE-IT-14

FLUKA studies of the Radiation Environment for Plasma Physics Experiments

S. Damjanovic[1] *and A. Tauschwitz*[1]
[1]GSI, Darmstadt, Germany

The future plasma physics program at FAIR foresees a general-purpose target chamber for a variety of experiments. FLUKA simulations have been performed to assess the radiation level, prompt and residual, due to the interaction of an intense ion beam with a target. The aim was manifold: to optimize the position of the electronic equipment within and near the chamber in order to minimize the risk of component failures due to radiation damage, to estimate the residual dose rates in the vicinity of the chamber, and to determine the cooling times for interventions in order to minimize the exposure of personnel. Furthermore, the induced radioactivity and the complete inventory of radionuclides in each of the components, including the airborne activity, were studied for different safety scenarios.

To obtain realistic radiation fields, the complete geometry of the target chamber, of the beam line with the dump, and of the APPA cave with the surrounding concrete shielding had to be modelled in detail (Fig.1.)

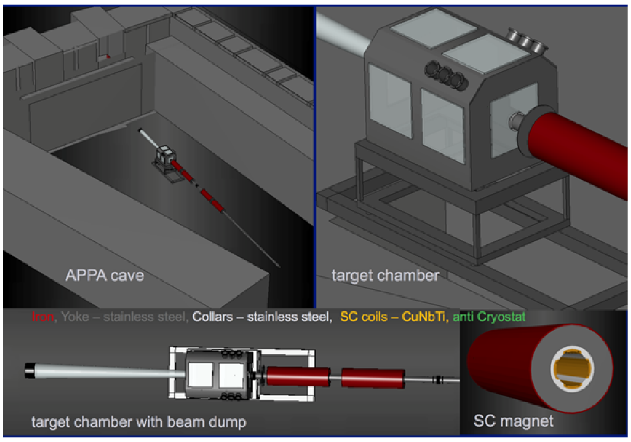

Figure 1: FLUKA geometry of the APPA cave with the beam line, the target chamber and the dump.

The results are based on a focussed uranium beam of maximum intensity (5×10^{11} particles per pulse) at 1 GeV/u, while for the target both extreme situations were considered: a thick lead target which stops the ion beam completely (length 27 mm), and a 100 μm thin aluminium foil with the ion beam mostly deposited in the carbon beam dump. The simulation assume four experimental campaigns per year with 1 shot per 10 minutes for 10 days, and with 80 days between the runs, implying altogether 5760 shots per year.

The study of the energy deposition within the Pb target showed that, although the target is much longer than the range of the primary ions, a high fraction of about 11% of the ion beam energy, i.e. 12 MJ for 5760 shots, is not deposited in the target, but escapes in the form of secondaries which create the radiation field in the cave.

To assess the risk to electronic equipment, three different physics quantities (physical dose, 1MeV-equivalent neutron- and hadron fluence) responsible for the radiation damage were evaluated. The dose was found to exceed 1Gy per experimental shot for equipment in the immediate vicinity of the target (at 10cm distance) and still had a high value of 10 mGy per shot for equipment outside the chamber. A detailed composition of the background radiation in terms of energy spectra of different contributions was determined and will be used to estimate the background for each detector system once the precise location, type and response to different particles is known.

The target material and the chamber with all installations contained will be activated to a level that prohibits immediate access during or directly after an experiment. The target will be evaporated by the ion beam and a new target is used for each shot. The peaked residual dose rate in the chamber (Fig.2) is correct if the activated material can be confined to a small volume around the target position. In this case the dose rate outside of the chamber is determined to 70% by the activated target material and to 30% by the activation of the chamber. In the other extreme case of complete distribution of the activated target over the chamber walls the dose rate outside of the chamber is dominated by the chamber activation.

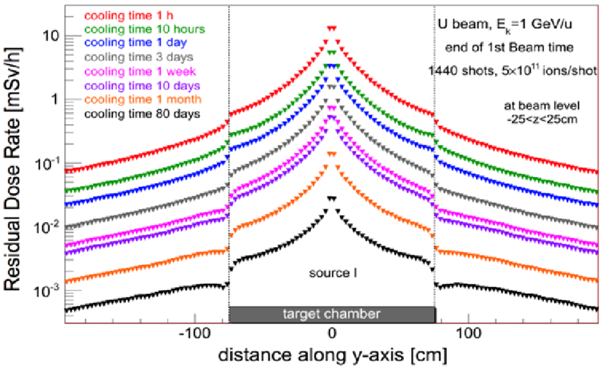

Figure 2: Time dependence of the residual dose rates along a line perpendicular to the beam axis.

The residual dose rates for cooling times between 1h and 80 days were almost the same after the end of the 1st and 4th beam time period (not shown). The original layout of the chamber was using a steel frame with aluminium flanges. It was found that replacing the steel by an aluminium frame results in the same residual dose after few hours but leads to a drop of the activity after few days that is ten times faster than in the original design.

Waste disposal planning and safety issues connected with fire scenarios were also studied, assessing the induced radioactivity and complete inventory of radionuclide for each of the components.

DOI:10.15120/GR-2015-1-MU-SAFETY-01

ANDREA, a compact neutron dosimeter

A. Sokolov[1], *G. Fehrenbacher*[1], *E.Kozlova*[1], *and T.Radon*[1]
[1]GSI, Darmstadt, Germany

Accelerator facilities are widely used for research and medical treatments, still they are sources of radiation potentially harmful for the surrounding environment and people. For the radiation survey the dose rates inside the accelerator tunnels as well as outside the shielding must be monitored. The highest contribution to the dose rate especially in case of high energy and heavy ion acceleration comes from neutron radiation, meaning that the neutron dose detection should be of highest priority. At GSI the approved technique for this purpose implies the GSI ball [1], appropriate for the ambient dose equivalent measurements for neutrons from 10 meV up to 100 GeV energies. Nevertheless this passive dosimeter is quite heavy and large with a diameter of D=31cm. In order to decrease the dimensions, weight and production costs, as well as to improve the characteristics of the dosimeter this work was done.

The main principle of the dosimeter to provide the readout values close to the ambient dose equivalent [2] is to use the moderating outer layer, typically – Polyethylene (PE) or Polypropylene (PP) for lower neutron energies and to use a lead layer in order to improve the response of the detector for higher energies, at which the spallation in form of neutrons ejection takes place. Next to the lead layer there is an additional small moderating layer (PP/PE) with a TLD-card, TLD=ThermoLuminescence Dosimeter.

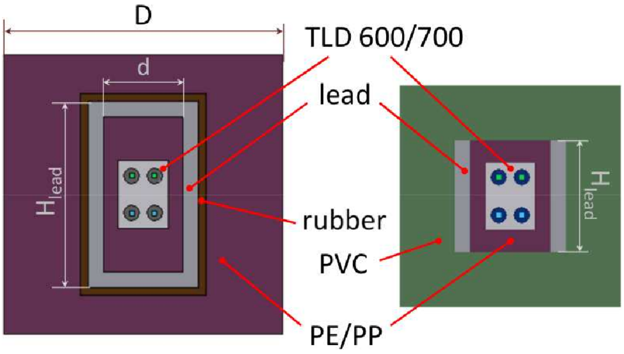

Figure 1: Dosimeter of type 3 (left) and type 5 (right).

Numerous simulations were performed using the FLUKA code [3] in order to obtain a simple and compact design of the dosimeter. First of all the dosimeter was chosen in a form of a cylinder (Fig.1, left), which still had the height of 31cm, but the diameter is only 20 cm. The smaller diameter for this type 1 dosimeter, is possible due to the introduction of an additional rubber layer with a small amount of boron, 5 % of the total mass. One can find the read-out signal in Fig.2, where it is seen that the response function of the dosimeter is close to the desired fluence-to-dose values H*(10) presented in [2]. To improve the response in the higher energy region, especially around 10 MeV, the outer dimensions were kept, while the inner cylinder was increased in diameter providing better moderation in the region of interest. The result is the type 2 detector, see Fig.2. Decreasing the outer diameter significantly influences the response in the low energy region, leading to an overestimation of the dose. This can still be managed changing the concentration of boron in the rubber layer. For the type 3 detector, with a diameter of 16 cm the boron portion was increased to 10 %. The improved response function can be seen in Fig.2.

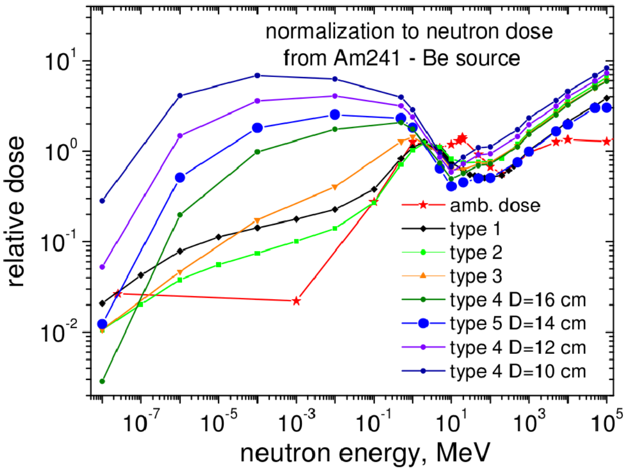

Figure 2: Ambient dose and comparison of response functions for different types of dosimeter.

Still the presence of the rubber layer makes the design more complicated and construction costs higher. To get rid of the rubber another material was chosen for the outer layer - Polyvinylchloride (PVC), which is a cheap and almost non-flammable plastic. In Fig.2 one can see the response functions for the dosimeter of type 4 with different outer PVC diameters from 16 cm down to 10 cm. Usage of the PVC as a moderating material together with a bigger diameter of the inner cylinder provides a possibility to reduce the height of the lead cylinder and get rid of its bottom and top caps, making the design simpler (Fig.1, right), the dosimeter is distinctly lighter and the over-response in the high energy region smaller (Fig.2, type 5). So finally in comparison to the GSI ball the weight is reduced from 19 kg to 4.5 kg and the size from 31 cm to 14 cm, both dosimeters can be seen in Fig.3. The compact design reduces the

DOI:10.15120/GR-2015-1-MU-SAFETY-02

Figure 3: Neutron Dosimeters: ANDREA, type 5 (left) and GSI ball (right).

overall absorption and increases the total signal. Still a slight under-response in the vicinity of 10 MeV and over-response in the low energy region remain and are the issues for further improvements. The name of this type 5 dosimeter is ANDREA=A Neutron DosemeteR for Efficient Area monitoring.

References

[1] G. Fehrenbacher et al, Radiation Protection Dosimetry (2007), Vol. 125, No. 1–4, pp. 209–212 Advance Access publication 16 September 2007.

[2] M. Pelliccioni, Radiation Protection Dosimetry Vol. 88, No. 4, pp. 279–297 (2000) Nuclear Technology Publishing.

[3] A. Fasso et al, "FLUKA: a multi-particle transport code", CERN-2005-10 (2005), INFN/TC_05/11, SLAC-R-773.

DOI:10.15120/GR-2015-1-MU-SAFETY-02

Radiation damage to materials for FAIR

A. Belousov[1], *G. Fehrenbacher*[1], *R. Lang*[1], *T. Radon*[1]
[1]GSI, Darmstadt, Germany

Introduction

The accelerators of FAIR will allow to operate with 10-100 times higher intensities and up to 10 times higher energies than the present GSI accelerators. The prompt radiation will increase respectively. Thus it is very important to make estimations of dose rates in different areas of the facility and accordingly to select building materials considering their radiation hardness.

Dose estimation

Monte Carlo FLUKA [1,2] calculations of dose rates were performed for every FAIR building considering different experiment scenarios. The highest dose rate corresponding to the "worst case" scenario was selected for each area. Knowing the material radiation hardness and the dose rate in the area, we can predict its lifetime and reliability.

Assessment of radiation damage

Figure 1 shows damage versus accumulated dose for different types of materials. Expected accumulated doses after 20 years of FAIR operation are approximately from 10 Gy to 10^9 Gy for different areas. The most sensitive materials to radiation are semiconductors. It is usually not recommended to put semiconductors in the vicinity of high radiation sources. Different polymers have moderate radiation resistance which varies over 5 orders of magnitude. Dose rates in some areas of FAIR will be sufficient to severely damage polymers in relatively short periods of time. Ceramics and especially metals have relatively high radiation resistance.

Most of the radiation hardness data present in the work was taken from CERN test results [3]. They contain descriptions of radiation damage effects to various materials and resulting scales showing how much radiation in Gy each material can withstand keeping its functionality. The scale of 3 conditions was normally used: mild damage, moderate damage and severe damage. Most of the materials were tested in one of the two usual ways: counting the number of 360° bends before break and measurements of the elongation at break. In some cases quantitative mechanical tests and visual tests were performed as well.

Dependence of radiation damage on dose rate

Radiation damage to organic materials may depend not only on the overall dose but also on the irradiation dose rate. The amount of oxygen available by diffusion into the sample, in relation to the number of radiation-produced chemically reactive radicals, or chain scission sites, may strongly influence the amount of permanent damage to the material. Irradiations over longer periods are more problematic than short period exposures with the same dose values in some cases. Dose rate effects are dependent on the chemical structure of the material and sample shape. The amount of oxygen available is a function of the sample thickness, its permeability for gases and the amount of stabilizers added to the polymer control the oxidation damage.

CERN radiation hardness tests were usually performed at high dose rates ranging from 10^4 to10^6 Gy/hour. Dose rates in FAIR will not exceed 10 Gy/hour. This huge difference makes dose rate effect very important in polymer lifetime estimation. Many polymers age about 10 times faster at low dose rates. Based on experimental studies [4] dose rate effects were taken into account for most of the polymer materials of interest.

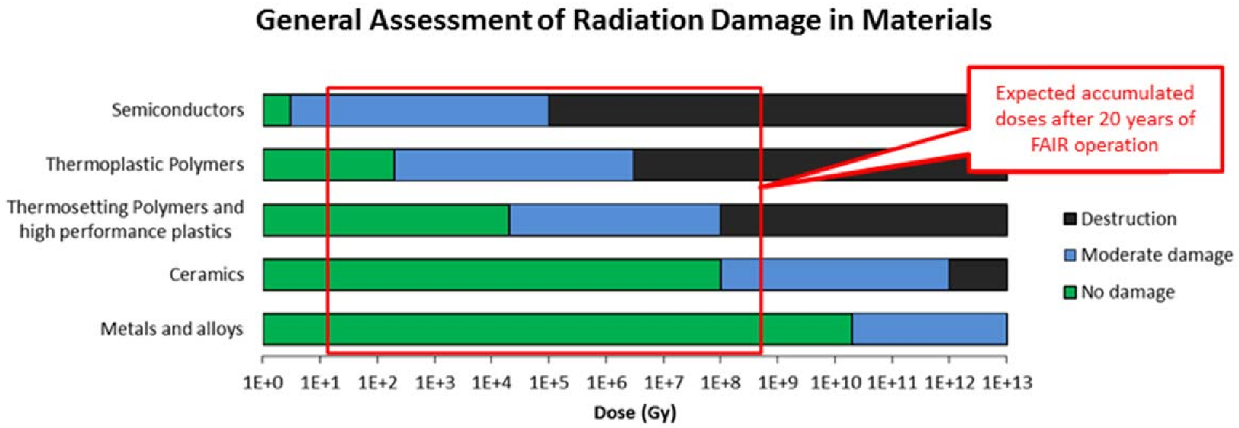

Figure 1: Radiation effects to materials and expected doses occuring in FAIR.

DOI:10.15120/GR-2015-1-MU-SAFETY-03

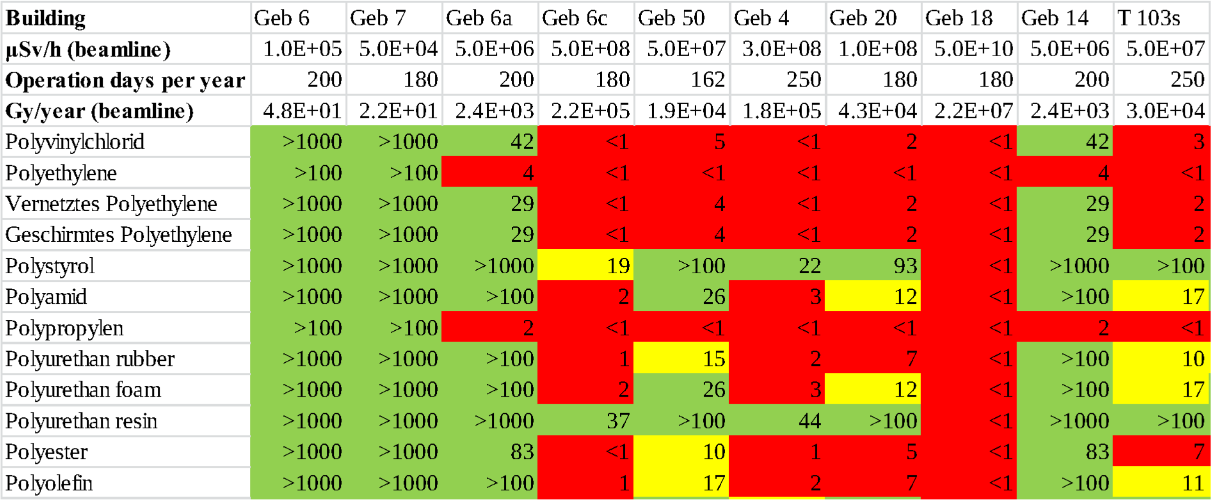

Building	Geb 6	Geb 7	Geb 6a	Geb 6c	Geb 50	Geb 4	Geb 20	Geb 18	Geb 14	T 103s
µSv/h (beamline)	1.0E+05	5.0E+04	5.0E+06	5.0E+08	5.0E+07	3.0E+08	1.0E+08	5.0E+10	5.0E+06	5.0E+07
Operation days per year	200	180	200	180	162	250	180	180	200	250
Gy/year (beamline)	4.8E+01	2.2E+01	2.4E+03	2.2E+05	1.9E+04	1.8E+05	4.3E+04	2.2E+07	2.4E+03	3.0E+04
Polyvinylchlorid	>1000	>1000	42	<1	5	<1	2	<1	42	3
Polyethylene	>100	>100	4	<1	<1	<1	<1	<1	4	<1
Vernetztes Polyethylene	>1000	>1000	29	<1	4	<1	2	<1	29	2
Geschirmtes Polyethylene	>1000	>1000	29	<1	4	<1	2	<1	29	2
Polystyrol	>1000	>1000	>1000	19	>100	22	93	<1	>1000	>100
Polyamid	>1000	>1000	>100	2	26	3	12	<1	>100	17
Polypropylen	>100	>100	2	<1	<1	<1	<1	<1	2	<1
Polyurethan rubber	>1000	>1000	>100	1	15	2	7	<1	>100	10
Polyurethan foam	>1000	>1000	>100	2	26	3	12	<1	>100	17
Polyurethan resin	>1000	>1000	>1000	37	>100	44	>100	<1	>1000	>100
Polyester	>1000	>1000	83	<1	10	1	5	<1	83	7
Polyolefin	>1000	>1000	>100	1	17	2	7	<1	>100	11

Figure 2: Part of the table showing final results of the work. Table cells show material lifetime in years for each FAIR building. Green cells with lifetime above 20 years mean safe to use, yellow cells with lifetime between 10 and 20 years – questionable, red cells with lifetime below 10 years – not recommended to use.

Results

Lifetimes of materials that are going to be used in FAIR construction were estimated considering specific radiation conditions in the accelerator environment. Results were based on CERN radiation test data. Moreover dose rate effect corrections were applied. Instructions and suggestions were given on whether or not a material is reliable to use in certain location. Results were given for about 50 materials and 20 FAIR buildings, 2 locations per building: hottest spot near beam line and near inner wall. Figure 2 shows a part of the table, where the lifetime in years is shown for several materials and locations. It is not recommended to use materials with less than 20 years lifetime, because replacement of damaged components may be complicated due to high activity values.

References

[1] T.T. Böhlen, F. Cerutti, M.P.W. Chin, A. Fassò, A. Ferrari, P.G. Ortega, A. Mairani, P.R. Sala, G. Smirnov and V. Vlachoudis, “The FLUKA Code: Developments and Challenges for High Energy and Medical Applications”, Nuclear Data Sheets 120, 2014, 211-214

[2] A. Ferrari, P.R. Sala, A. Fasso, and J. Ranft, "FLUKA: a multi-particle transport code”, CERN-2005-10, 2005, INFN/TC_05/11, SLAC-R-773

[3] P. Beynel, P. Maier and H. Schönbacher, “Compilation of radiation damage test data, Part III: Materials used around high-energy accelerators”, 1982, CERN 82–10

[4] Hans Wilski, “The Radiation Induced Degradation of Polymers”, Radiat. Phys. Chem. Vol. 29, No. 1, 1987, p 1

DOI:10.15120/GR-2015-1-MU-SAFETY-03

Shielding upgrade for the section S05 – S06 of the SIS18 beam tunnel

F. Stuman, E. Kozlova, R. Lang, T. Radon and G. Fehrenbacher
GSI, Darmstadt, Germany

Introduction

Due to the activation of soil and ground water below and sideward of the section S05 – S06 of the SIS18 beam tunnel, measurements regarding radiation protection and limitation of soil activation have been reviewed to take necessary steps towards an additional shielding in the project of "Link Existing Facility" (GAF). Fig. 1 shows an overview of the current scheme.

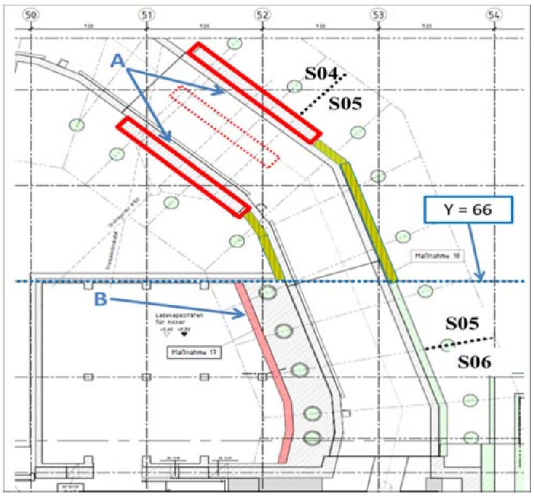

Fig. 1: S05 – S06 and its recommended additional shielding shaded in yellow. Existing shielding of the ESS is shown in red squares (point A) and, the dashed red square represents the assumed beam loss. The red shaded curve of 0.5m width (point B) illustrates the extra shielded east wall of the Kickerraum.

The dominant loss point is located at the Electrostatic Septum (ESS). In this region, where the beam loss rate is expected to be rather high, the existing tunnel is already shielded by 1.5m concrete (2.35 g/cm^3, Fig. 1, red squares at the point A) in all directions. The wall on the east side of the so called "Kickerraum" is planned to be further expanded by 50cm of hematite concrete (4.6 g/cm^3, Fig. 1 point B). The most critical part remains the region, where the additional ESS shielding ends – tangentially into the ground in the 0° direction of the beam – up to the transition of the S06, which, in turn, does not have an additional shielding.

Simulation

A simulation with the FLUKA [1] Monte Carlo code has been performed to estimate the activation levels due to beam losses. For the simulation, beams of protons (*p*, 4 GeV, 3% loss rate, $5 \cdot 10^{12}$ *p*/s) and Uranium ions (^{238}U, 1 GeV/u, 30% loss rate, $5 \cdot 10^{10}$ *U*/s) were used as input parameters for the calculation.

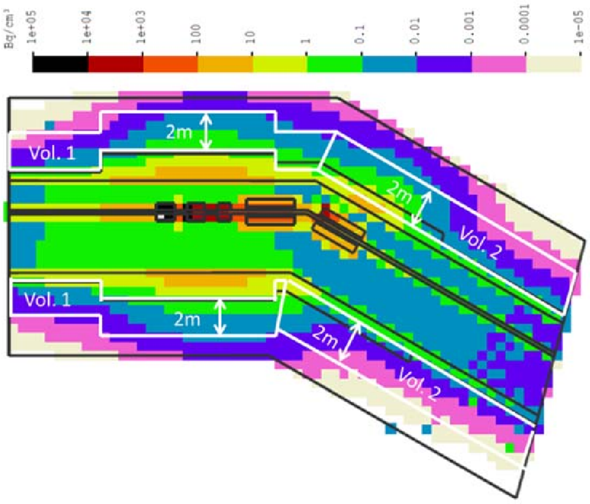

Fig. 2: Level of the activity concentration in units of Bq/cm^3 calculated for an Uranium beam of 1 GeV/u and a loss rate of 30 % at the ESS of SIS18 beam tunnel.

Both scenarios were performed with an irradiation time of 4 years given by the time, in which the ground water flows – east to west – surveyed by evaluators as part of the construction license [2] for FAIR and, a cool down time of 10 years, in which the ground water is being transported. In order to find out the activity concentration of the soil, two defined volumes (Vol. 1 and Vol. 2, Fig. 2) of 1100m^3 and 813m^3, 2m wide on each side of the tunnel, were chosen respectively.

Results

An increased activation hotspot in the 0° direction of the beam, starting from the ESS directly into the soil on the outer part of the tunnel curvature, is clearly visible (Fig. 2). A comparison of these results with those calculated and documented in the FAIR application [3] shows that the activity concentration is an order of magnitude smaller than $7 \cdot 10^5$ Bq/m^3 – the overall concentration of the soil around SIS18 mentioned in [3]. The local hotspot in Vol. 2 in front of the ESS (Fig. 2) is by a factor of 3 smaller than $7 \cdot 10^5$ Bq/m^3. Comparing these results with threshold values of the German Radiation Protection Ordinance for unrestricted release, between 5% (whole S05 volume) and 40% (local hotspot) of the values allowed would be exploited.

DOI:10.15120/GR-2015-1-MU-SAFETY-04

Conclusion

The results of the FLUKA simulations for beams of *p* and ^{238}U have shown that there is no need to strengthen the shielding of the whole region between S05 and S06. Although, due to strong radiation fields in the 0° direction and the activation of the ground environment, an extra and locally based reinforcement is required. A concrete wall of approx. 9m length and 0.5m thickness on the outer side up to at least Y-axis 66 (Fig. 1) and, a concrete wall of 0.5m thickness up to the Kickerraum on the inside part of the tunnel is recommended as an additional shielding (Fig. 1, drawn and shaded in yellow within S05).

References

[1] T.T. Böhlen, F. Cerutti, M.P.W. Chin, A. Fassò, A. Ferrari, P.G. Ortega, A. Mairani, P.R. Sala, G. Smirnov and V. Vlachoudis, “The FLUKA Code: Developments and Challenges for High Energy and Medical Applications”, Nuclear Data Sheets 120, 2014, 211-214

[2] Antrag A – FAIR Gesamtantrag, Antrag auf Errichtung von FAIR gemäß §11 Abs. 1 Nr. 4 StrSchV

[3] Antrag A – Tektur 1, Anlage 23 (Antrag auf Errichtung von FAIR gemäß §11 Abs. 1 Nr. 4 StrSchV)

DOI:10.15120/GR-2015-1-MU-SAFETY-04

Radiation protection update for the FAIR APPA building

R. Lang, A. Belousov, G. Fehrenbacher, T. Radon
GSI, Darmstadt, Germany

In 2011 the FAIR [1] application for construction approval was submitted to the radiation protection (RP) authorities based on -at that time- actual construction plans. In May 2014 the 11th and final part of the application was approved. However, since 2011 these plans underwent a series of changes due to ascertainment of additional needs by e.g. the scientific users, fire protection authorities or just the increasing grade of detail in the evolving FAIR project. These changes have to be reported to the RP authorities as an update of the 2011 application, because they might affect -to some grade- the radiation protection layout. This update-process requires a close monitoring and counseling of the necessary planning steps by the resident radiation protection at GSI, which is mandated to supervise all FAIR RP concerns.

In a first step, the needs of all involved parties are acquired by the RP coordination team involving the architectural layout, requirements of the scientific user and of course the existing RP layout. The new layout is then tested by Monte Carlo calculations deploying FLUKA [2,3] following the basic principle that the new layout has to perform equally or better concerning RP needs. This maxim is laid out to achieve a smooth approval procedure of the updated construction application. These updates range from minor adjustment of shielding walls or niches therein to an entire new wall layout of a whole building like the APPA building "G50". The original layout of the APPA cave is based on a double concrete wall design, where in-between the walls soil layers were used to improve the shielding effect (see Fig.1).

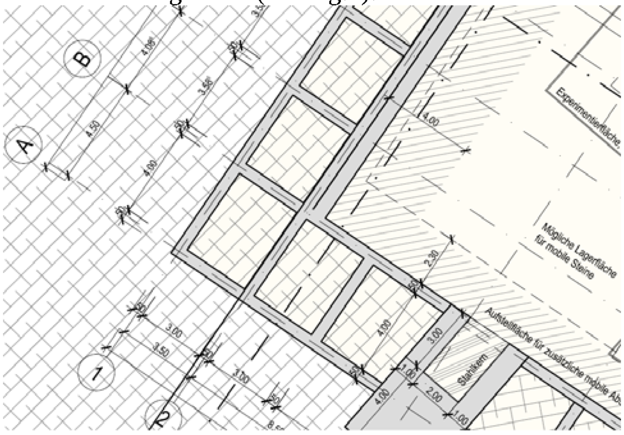

Figure 1: 2011 layout of south-east part of the building G50 with enclosed soil packs on the outside wall.

This rather complicated comb-structure was replaced by a construction with only one concrete layer for the walls, whereby the thickness of the wall was adjusted to fit both requirements: the shielding effect and the limitation of radioactive activation of the soil outside the cave. The effectiveness of the new layout was verified by means of FLUKA shielding calculations [1, 2] simulating a maximum possible beam loss with the U-238 beam with 2GeV/u and 1E10 ions/sec with beam interactions in a target (50%) and the remaining beam depositions in a dump (see Fig. 2). The radiation fields are substantially and sufficiently lowered within the concrete walls. Further adaptions are introduced for the roof shielding in the cave and for the access maze of the cave.

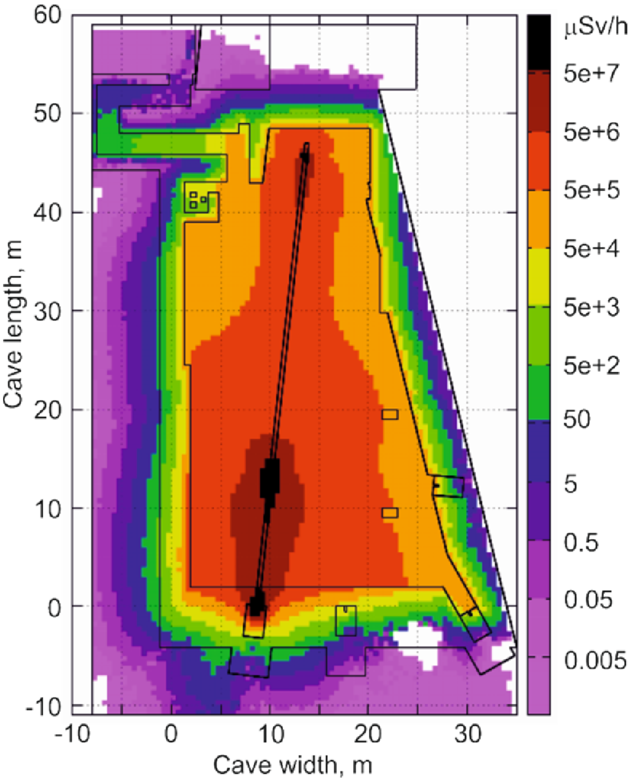

Figure 2: FLUKA calculation of new layout with solid-concrete walls. Dose levels in the surrounding soil (left and bottom) and at the end of the labyrinth (on the top left) are sufficiently low.

References

[1] FAIR Baseline Technical Report, Editors H. H. Gutbrod (Editor in Chief), I. Augustin, H. Eickhoff, K.-D. Groß, W. F. Henning, D. Krämer, G. Walter, September 2006

[2] T.T. Böhlen, F. Cerutti, M.P.W. Chin, A. Fassò, A. Ferrari, P.G. Ortega, A. Mairani, P.R. Sala, G. Smirnov and V. Vlachoudis, "The FLUKA Code: Developments and Challenges for High Energy and Medical Applications", Nuclear Data Sheets 120, 2014, 211-214

[3] A. Ferrari, P.R. Sala, A. Fasso`, and J. Ranft, "FLUKA: a multi-particle transport code", CERN-2005-10, 2005, INFN/TC_05/11, SLAC-R-773

DOI:10.15120/GR-2015-1-MU-SAFETY-05

Radiation protection for SIS 100 – Shielding in the extraction area

I.Conrad, G. Fehrenbacher, R. Lang, A. Sokolov

GSI, Darmstadt, Germany

One of the central buildings of the FAIR-facility [1] is the tunnel for the SIS100 synchrotron. The basic layout and the shielding requirements of the tunnel have been submitted to the radiation protection authorities (HMUELV, now HMUKLV) in 2011 [2] together with the construction permit proposal for other FAIR-buildings. One of the three major concerns for the radiation protection of FAIR is the release of radioactivity through washout of the soil surrounding the beam tunnel by groundwater, the other two are direct radiation and release via airborne activation.

Due to proceeding physical and technical development a series of revisions in geometry took place. To achieve an almost perfect combination of the radiation protection requirements and the needs of the experiments all conditions have to be managed carefully. The new layout is checked with the Monte-Carlo simulation program FLUKA [3] to comply with the regulations of the German Radiation Protection Ordinance (Strahlenschutzverordnung).

The shielding of the maintenance tunnel adjacent to the SIS100 tunnel is designed for the maximum possible beam loss parameters, i.e. a ^{238}U beam at loss rate of 3E10 particles/s and energy of 2.7 GeV/u, occurring in the extraction section of the SIS100. Here during the slow extraction procedure beam losses up to 10% of the primary intensity are expected between two quadrupoles in front of the Lambertson septum [4]. The calculations with the mentioned parameters showed high radiation levels in the soil shielding, therefore the groundwater could be activated. The former geometry (2011) of the extraction section had 2 m concrete walls plus 1 m mobile concrete and 2 m for the basement and ceiling (see Fig. 1).

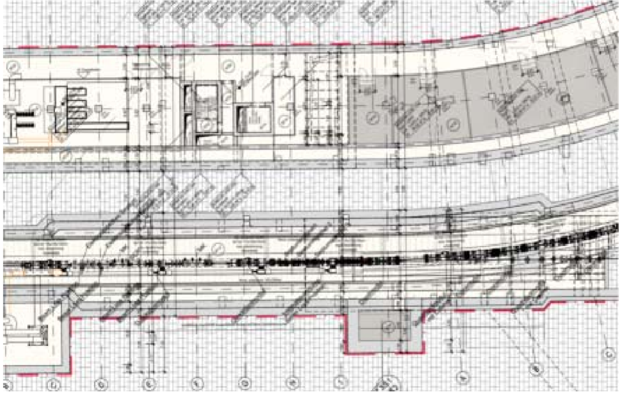

Figure 1: Layout (2011) of extraction section of SIS100 tunnel with beam tunnel (below) and maintenance tunnel (above).

After all calculations it was decided to increase the ceiling and the basement shielding up to 2.5 m (see Fig. 2), which will reduce the groundwater activity much below the allowed limits. For the wall on the outer side of the SIS100 ring a concrete thickness of 2.5 m is found to be sufficient, which will save the construction costs and the wall facing inward the ring tunnel is kept the same (see Fig. 3).

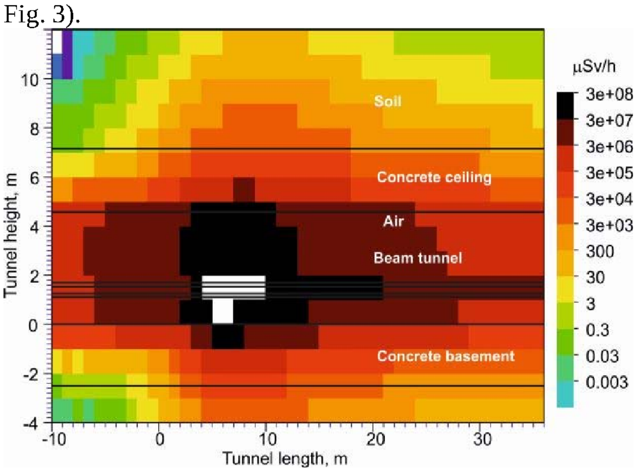

Figure 2: Calculations of the equivalent dose rate in the extraction part of the SIS100 tunnel (Side view). The shielding thickness of basement and ceiling is 2.5 m of concrete.

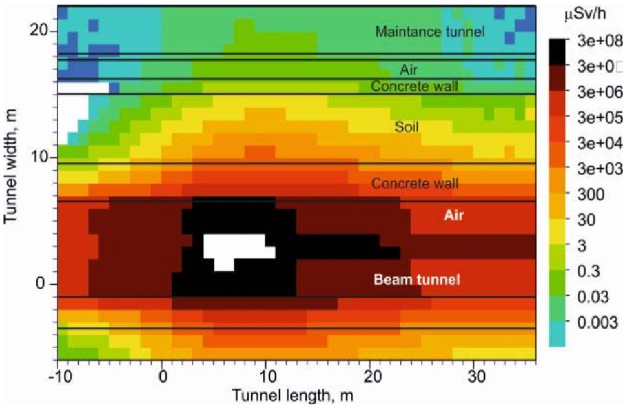

Figure 3: Equivalent dose rate in the extraction part of the SIS100 beam and maintenance tunnel nearby the loss point which is situated in between 2 quadrupoles (Top view).

References

[1] FAIR Baseline Technical Report, Editors H. H. Gutbrod (Editor in Chief), I. Augustin, H. Eickhoff, K.-D. Groß, W. F. Henning, D. Krämer, G. Walter, September 2006.

[2] Antrag für die Errichtungsgenehmigung von FAIR SIS100, 2011.

[3] FLUKA: a multi-particle transport code, A. Fassò, A. Ferrari, J. Ranft, P. R. Sala; CERN-2005-10 (2005), INFN/TC 05/11, SLAC-R-773.

[4] Beam Loss in SIS18/100/300/HEBT Status 10.02.2012 - Version 10.0, P. Spiller et al.

DOI:10.15120/GR-2015-1-MU-SAFETY-06

Dose Measurements at SIS18 and connected experimental halls TR, EX, TH

T. Radon[1], K. Beverung[1], R. Fleissner[1], P. Freml[1], P. Kewes[1], C. Pöppe[1], and J. Sauer[1]

[1]GSI, Darmstadt, Germany

High Current N-Beamtime at SIS

Similar to the situation in 2011 the beam time in 2014 was dominated by high current 1.9 GeV/u N-beams which were accelerated at SIS18 during the second beam time block. The beam was extracted with 6E+10 particles per second at maximum and guided to the pion production target. Due to distinct beam losses in SIS18 and grave losses in the connected high current beam transfer line at that time consequently pronounced activations of the beam line components occurred. Besides the expected activation of the extraction area in the millisievert-per-hour regime a further salient hot spot evolved at the first quadrupole after the electromagnetic septum. A residual dose rate of 1.5 mSv/h was measured at the end of the beam time block, 6 weeks after the end of the high current N-beam time. This residual dose rate was four times higher than previously ever measured at this position. Noticeable activations of several hundreds of microsieverts-per-hour at a couple of positions of the high current transfer beam line especially in the TH2 and TH3 areas showed up still weeks after the end of the runs. The maximum of the residual dose rates was found at the dipole TH3MU1 and the connected diagnosis chamber. Still in January 2015 60 µSv/h have been measured at that position.

The integrated doses during the high current N-beam time which lasted for about 40 days including several interruptions comprised more than 90% of the total annular dose at certain stationary survey measurement points in the halls TR and especially EX, see Fig. 1.

In the course of the N-beam time an explicit activation of air has been detected for the first time at GSI. Peak activity concentrations of more than 1E3 Bq/m^3 for Ar-41 outside controlled areas were measured for some hours. For a later FAIR operation this beam time has been a realistic test case. Planned measures based on Monte Carlo calculations for the future sealing of radiation protection areas of accelerators and experimental areas with subsequent cooling lines to vent stacks could thus be validated.

Prior to another measurement campaign in 2017 or later of such high-current beam-times for the production of pions several precautions minimizing prompt dose-rate, air activation and activation of beam components have to be undertaken. Local shielding of the top of the dipole magnet TH3MU1 and a tracking target with at least 1m of concrete-equivalent including concrete sidewalls of certain strength are appropriate measures as well as enlarging the (vertical) aperture i.e. the beam tube at few components. Finally the top shielding of the pion production target itself would need another layer (0.8m) of concrete slabs.

References

[1] T. Radon, et al. GSI-Report 2011-1 (2011) p. 352.

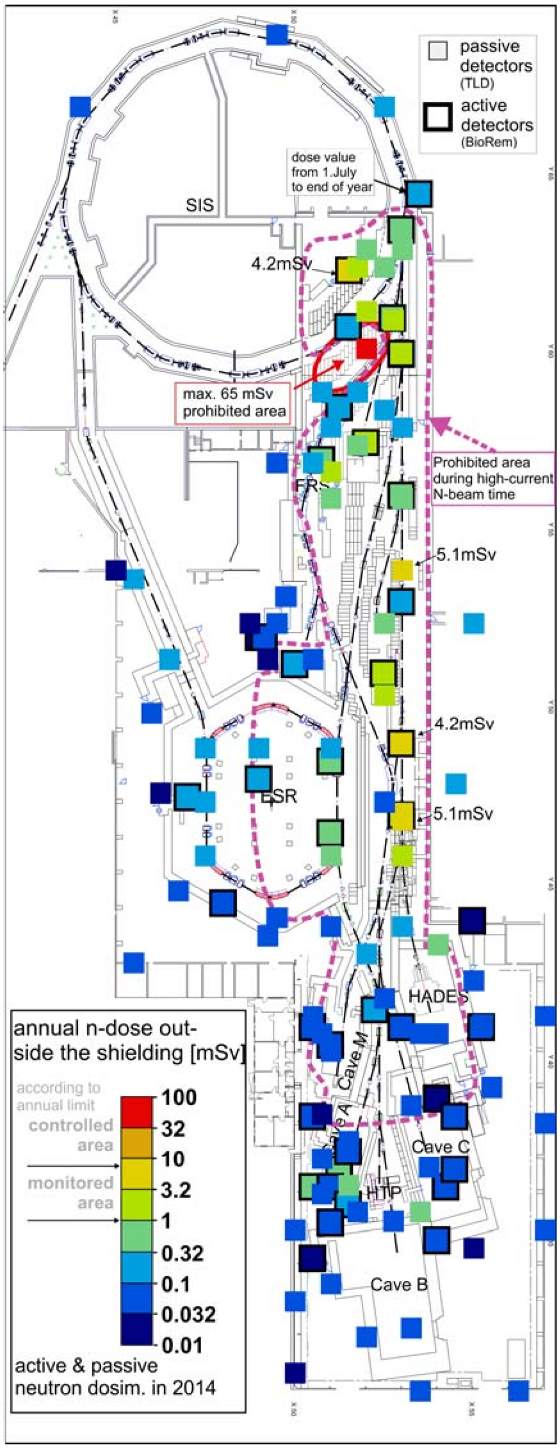

Figure 1: Map of the experimental areas connected to SIS18. Measurement positions of controlled areas are shown with doses recorded by active dosimeters (larger squares with frame) and passive detector (smaller squares).

DOI:10.15120/GR-2015-1-MU-SAFETY-07

Ion source operation at GSI

R. Hollinger, K. Tinschert*, A. Adonin*, D. Agahi, R. Berezov, M. Brühl, B. Gutermuth, F. Heymach, V. Ivanova, R. Lang, J. Mäder, F. Maimone, K. Ochs, P. T. Patchakui, J. Roßbach, P. Schäffer, S. Schäffer, C. Vierheller, A. Wesp, S. Zulauf*

GSI, Darmstadt, Germany

High Current Ion Sources

In 2014 ion sources from Terminal North (MUCIS, CHORDIS and VARIS) and Terminal South (PIG ion sources) were supplying the GSI accelerator with various types of ions. The following Table 1 gives an overview of the ion species, which were delivered for physics and accelerator development experiments. A good representative value for delivered intensity to the linear accelerator UNILAC is the analysed current in the transfer section *UH1* in front of the RFQ.

Table 1: Ion beams generated with high current ion sources in 2014. Filament driven volume type ion sources: MUCIS and CHORDIS; Vacuum arc ion sources: VARIS; Penning type ion sources PIG

Ion species	Duration (days)	Ion source	Beam for experiment	Analyzed intensity (emA)
$^{3}H_3^+$	8	CHORDIS	SIS	0.9
$^{6}D_3^+$	7	CHORDIS	UNI	2.4
$^{15}CH_3^+$	33	CHORDIS	UNI/SIS/ESR	3
$^{28}N_2^+$	52	CHORDIS	SIS/ESR	5
$^{20}Ne^+$	5	PIG	UNI/SIS/ESR	0.1
$^{56}Fe^{3+}$	3	PIG	UNI	0.15
$^{58}Ni^{2+}$	32	VARIS	SIS	5.8
$^{86}Kr^{2+}$	16	MUCIS	SIS	9.5
$^{132}Xe^{3+}$	19	PIG	UNI/ESR	0.05
$^{152}Sm^{3+}$	15	PIG	UNI/SIS/ESR	0.03
$^{197}Au^{4+}$	11	PIG	UNI/SIS/ESR	0.3
$^{197}Au^{8+}$	45	PIG	UNI	0.07
$^{209}Bi^{4+}$	16	PIG	UNI/SIS/ESR	0.07
$^{238}U^{4+}$	53	VARIS	UNI/SIS/ESR	15

From Table 1 it can be deducted that the most requested ion beams in 2014 were gold, uranium and nitrogen. It is also shown that most of the time both terminals were operated at the same time with mostly different ion species.

One of the main highlights of 2014 was the development of CH_3^+ molecular ion beam operation from MUCIS ion source for production of intense proton beam behind the gas stripper [1,2]. This approach allowed reaching up to 25% of the FAIR design proton beam intensity with the existing UNILAC [2].

Another notable highlight is an upgrade of MUCIS new (design 2010) ion source for better performance with heavy gases (Kr, Xe). Stronger Nd-Fe-B permanent magnets (1.4 T instead of 1 T) have been used for generation of multi-cusp field in the plasma chamber. The geometry of filament holder was improved. External magnetic coil was installed around the plasma chamber to focus the plasma bunch and to increase the emission current density in the extraction region. Due to these improvements new record intensities in front of the RFQ of 9.5 mA for Kr^{2+} and of 6.5 mA for Xe^{3+} ion beams have been established. That beats the previous intensity record more than 30% for Kr-case and more than 150% for Xe-case.

Notable performance improvement of VARIS source for $^{238}U^{4+}$ beam was successfully demonstrated in Oct.-Nov. 2014 [3]. Implementation of a new multi aperture (7-holes, ø4 mm) extraction system in the ion source allowed to reduce the horizontal beam emittance (measured in UH1) by 15%, while the vertical beam emittance remained comparable (less than 2% difference) with standard extraction system. Also the source performance with various duty cycles: 1 Hz, 2 Hz and 3 Hz have been tested, showing the principle possibility of high duty cycle operation with existing uranium ion sources.

To fulfil the requirements of future FAIR-experimental programs the tests with Fe^{2+} (required by BIOMAT) and Ag^{2+} (required by CBM) ion beams from high current VARIS ion source have been performed. As the result, stable operation with new intensity records in front of the RFQ of 9 mA and 12 mA for Fe^{2+} and Ag^{2+}, respectively, has been achieved.

Renewing and development of the PIG sources is in process. Two sources are successfully putted into the operation after the complete renewing. For further investigations and development of PIG sources the construction of the new test bench is in process. The investigations will be focused on compactification of the source as well as increasing the beam current and the life time. For these purpose the compact PIG source will be tested on the new test bench.

High Charge State Injector HLI

For the operation of the GSI accelerator the CAPRICE ECR ion source (ECRIS) at the High Charge State Injector (HLI) delivered the ion species listed in Table 1 for various physics experiments in the regular beam time schedule as well as for dedicated ion beam development.

---

* Corresponding authors

DOI:10.15120/GR-2015-1-FG-UNILAC-01

Table 1: Ion beam operation of the HLI-ECRIS in 2014; additional time for tests and beam development in brackets.

Ion species	Auxiliary gas	Duration (days)	Analyzed intensity (eμA)
$^{12}C^{2+}$	O_2	24	100
$^{12}C^{5+}$	He	13(17)	50
$^{14}N^{3+}$	He	16	210
$^{22}Ne^{4+}$	He	8	250
$^{40}Ar^{8+}$	He	23	200
$^{48}Ca^{10+}$	He	26(7)	120(170)
$^{50}Ti^{8+}$	He	21	70

After the long shut down period in 2013 an $^{40}Ar^{8+}$ ion beam was used for machine commissioning at the HLI.

Two beam time periods in 2014 dedicated to biophysics experiments at the SIS under therapy conditions and to biophysics experiments at the UNILAC were provided with $^{12}C^{2+}$ ion beams.

Due to a special constellation of parallel ion beam operation with protons from the high current injector and C ion beam from the ECRIS for experiments of biophysics and material research at the UNILAC $^{12}C^{2+}$ could not be accelerated in the Alvarez section of the UNILAC. The charge state had to be increased to $^{12}C^{5+}$. Such a hydrogen-like C ion beam had not been operated with the ECRIS before. Therefore extensive investigations were necessary for optimization of the operating conditions of the ECRIS before the dedicated beam time. As the ECRIS test facility was not available due to upgrade activities an ion beam development period was performed at the HLI during a gap of the beam time [4].

Upon a request from an experiment at the PHELIX LASER facility a $^{14}N^{3+}$ ion beam had to be established for the first time and could be delivered from the ECRIS in a very stable mode.

The major part of the beam time in 2014 was dedicated to various experiments on Super Heavy Element (SHE) research at SHIP, TASCA and SHIPTRAP, respectively. After the dedicated development of a $^{50}Ti^{8+}$ ion beam from highly enriched isotope material during the past years this beam was delivered to experiments for the first time. Figure 1 shows a mass/charge spectrum taken during this run. An average material consumption of 3.6 mg/h was determined for the whole run.

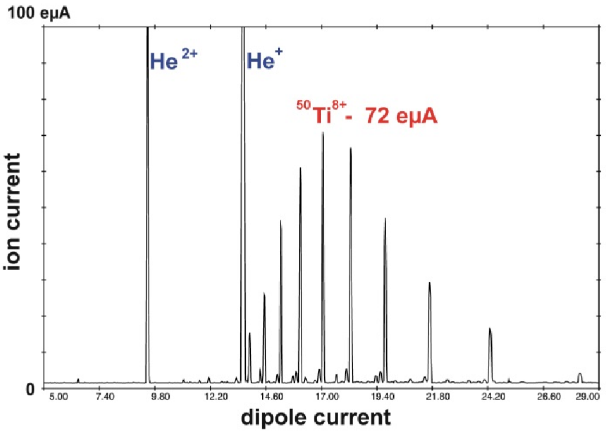

Figure 1: Mass/charge spectrum of ^{50}Ti.

Finally in 2014 a long run with $^{48}Ca^{10+}$ was dedicated to experiments of the Super Heavy Element (SHE) program at TASCA and at SHIPTRAP. This run was characterized by very stable long time behaviour of the ion beam at high intensity with the typical low average material consumption of less than 200 μg/h. For a thermal load test of the target during the final stage of the experiment the intensity of the analyzed $^{48}Ca^{10+}$ in beam could be increased to 170 eμA, a value as high as it could never be obtained before.

During the long shut down period in 2013/14 a major upgrade of the ECRIS facility at the HLI had been performed including the implementation of new TWTA-based microwave transmitters and a new high precision gas injection system for the working gas and for the auxiliary gas, respectively. All components of the new equipment could prove its reliable long term operation.

References

[1] A. Adonin, R. Hollinger, this report.
[2] M. Heilmann et al., this report.
[3] W. Barth et al., U^{28+}-intensity record applying a H_2-gas stripper cell at GSI-UNILAC, to be published.
[4] K. Tinschert et al., Development and Upgrade of the ECRIS Facility, this report.

DOI:10.15120/GR-2015-1-FG-UNILAC-01

UNILAC status report

P. Gerhard[1], *W. Barth*[1], *L. Groening*[1], *M. Maier*[1], *S. Mickat*[1], *U. Scheeler*[1], *H. Vormann*[1], *and C. Xiao*[1]
[1]GSI, Darmstadt, Germany

Operation

After 13 months of shutdown, the UNILAC commissioning began in early January with the start up of all devices and systems. The first beam accelerated to full UNILAC energy (^{40}Ar^{10+} from the PIG) was recorded on 29 January 2014. On 9 February the first beam (^{40}Ar^{8+}) was available in the transfer channel and was subsequently delivered for the commissioning of the synchrotron. The busy, but — having the long shutdown in mind — quite successful commissioning ended on 13 February 2014. Still, operation was affected by numerous and frequent interruptions and breakdowns, though. The major drawback was, that some rf cavities needed additional conditioning in order to accelerate ^{238}U^{28+}, which was requested for the SIS18 commissioning already. ^{238}U^{29+} with less intensity had to be chosen several times throughout the year.

The UNILAC was in operation for nearly 250 days, restricted to two ion species in parallel in order to compensate for the tight beam time schedule in 2014. Delivering high current beams of ^{14}N (CHORDIS), ^{58}Ni (VARIS), ^{1}H and ^{86}Kr (both MUCIS) to the synchrotron for physics experiments and machine development dominated the operation. At UNILAC energies material sciences, biology and SHE experiments (TASCA, SHIPTRAP) were the main recipients for ^{197}Au, ^{209}Bi (both PIG), ^{48}Ca and ^{50}Ti (both ECR). ^{238}U (MeVVA), ^{124}Xe (MUCIS) and ^{132}Xe (PIG) were accelerated for physics experiments and machine development both at the UNILAC and SIS18. Shorter beam times with ^{56}Fe and ^{153}Sm (both PIG) have been conducted mainly for physics experiments, while ^{2}H$_3^+$ (MUCIS) was accelerated for EMTEX (see below), and ^{20}Ne (PIG) for HITRAP. The HLI also provided four weeks of ^{12}C, mainly for therapy development, and ^{22}Ne for TASCA.

For the first time a high current proton beam was accelerated for the synchrotron by cracking ^{15}CH$_3^+$ (CHORDIS) in the gas stripper, thereby delivering 2 mA ($7 \cdot 10^{11}/100\mu$s) of protons with very good beam quality [1, 2].

Shutdown Activities

Due to the short shutdown periods in 2014, no major activities had been carried out. The second buncher cavity in the Alvarez section (BB6) could not be operated at high power levels due to a blocked cooling channel of the spiral. After several rinsing attempts it was finally removed from the beamline, repaired in the workshop during the second beamtime period, and placed back in November. Additionally, two inner tank triplets of the first HSI-IH tank had ground fault. They were operated by means of a work around, one of them will be repaired during the shutdown 2014/15. One drift tube in the Alvarez I tank has a vacuum leak, it will be replaced this year.

Machine Experiments

In May and October successful tests were carried out by the source department to reach higher proton beam intensities by accelerating molecules like ^{15}CH$_3^+$ and C$_2$H$_6^+$ from the MUCIS and crack them in the gas stripper [3]. Increasing the intensity, especially for heavy ions, by using a pulsed gas jet with different gases and thereby increasing the stripping efficiency, also was the topic of very successful machine experiments in February and November conducted in close collaboration with TASCA [4, 5]. Three accelerator beamtimes were dedicated to the emittance transfer experiment EMTEX [6, 7]. During several machine experiments new rf working points for all HSI accelerator cavities were identified using ^{181}Ta^{4+}, and rf breakdowns of the superlens were investigated. Experimental data for advanced DYNAMION simulations of the matching of high current beams to the HSI-RFQ were gathered, and multi charge operation of the poststripper section was studied [8]. In autumn, the amplitude calibration of the bunchers US4BB3 and BB4 was investigated and emittance measurements along the whole UNILAC, especially behind the poststripper section, were conducted [8], besides experiments of the beam diagnostics department related to the longitudinal beam structure. In total, 179 shifts were staffed by the linac department, including assistance for three successful HITRAP beamtimes [9].

References

[1] W. Barth et al., LINAC'14, Geneva, TUPP056

[2] M. Heilmann et al. (this report)

[3] A. Adonin et al. (this report)

[4] W. Barth et al. (this report)

[5] P. Scharrer et al. (this report)

[6] M. Maier et al. (this report)

[7] L. Groening et al., http://dx.doi.org/10.1103/PhysRevLett.113.264802

[8] H. Vormann (ed.), Accelerator Experiments Beamblock 1 & 2 2014, https://www.gsi.de/work/fairgsi/linac_operations/↩ linac/publications/accelerator_experiments/2014.htm

[9] F. Herfurth et al. (this report)

DOI:10.15120/GR-2015-1-FG-UNILAC-02

Development and upgrade of the ECRIS facility

K. Tinschert, R. Lang, J. Mäder, F. Maimone, P. T. Patchakui
GSI, Darmstadt, Germany

Upgrade of the ECR injector setup

A new version of the 1.2 T CAPRICE ECRIS (ECR Ion Source) was assembled and installed at the ECR injector setup (EIS). This version is equipped with a new hexapole construction with improved permanent magnet materials providing increased remanence. Table 1 shows a comparison of the specifications of the magnet materials.

The original 1.2 T hexapoles were assembled in 1999 from 6 cuboids for each pole, which were procured as magnetized single magnet pieces. At present improved technology facilitates the fabrication as one single piece with subsequent magnetization by the manufacturer [1]. As in the original version trapezoidal magnets are filling the space between the pole pieces to provide a closed magnetic flux. The new hexapoles were obtained from the manufacturer as complete items. The improved manufacturing technique should provide a good homogeneity of the magnetic flux density along the pole faces.

Table 1: Comparison of the magnet specifications.

	1,2 T new version		1,2 T original type	
	Pole	Trapezoid	Pole	Trapezoid
Material VACODYM®	745HR	655HR	362HR	383HR
Remanence typ. [T]	1,44	1,28	1,33	1,28
Coercivity [kA/m]	1115	990	1010	980
Temperature max. [°C]	70	150	120	150

In order to check the magnetic field distribution a field mapping was performed by the ENMA (NC Magnets & Alignment) department of GSI. For comparison one of the original hexapoles was included in this series of measurements. Due to the optimized design the magnetic flux density of the new hexapoles could be increased by about 3% with respect to the original design. As the new magnet materials for the poles tolerate lower limits of the operating temperature the cooling technique had to be improved by optimizing the conditions of the cooling water flow.

Ion beam development

Due to special operating conditions of the Alvarez LINAC a $^{12}C^{5+}$ ion beam was requested from the ECRIS. For the generation of hydrogen like C ions all L-shell electrons plus one further K-shell electron have to be ionized in the plasma by successive electron impact ionization. This requires high power operation modes of the ECRIS. In order to optimize for best C^{5+} performance various combinations have been explored. Besides the standard configuration for $^{12}C^{2+}$ ion beam with CO_2 as working gas and O_2 as auxiliary gas, respectively, CH_4 was investigated as alternative working gas, while H_2 or He were used as auxiliary gases. For both working gases the operation at the required high level of microwave power and high magnetic mirror field exhibited strong plasma instabilities inside the quartz gas injection tube at the location of the first electron cyclotron resonance. Therefore the normally used quartz tube was replaced by a pure copper tube of the same dimensions, which led to much better plasma stability. H_2 and He as auxiliary gas turned out to give better performance than O_2. With respect to the fixed frequency operation with the klystron amplifier slightly higher intensity could be obtained by careful frequency tuning of the travelling wave tube amplifier. Formerly CH_4 had been used without additional auxiliary gas for the production of a $^{12}C^{3+}$ beam; however, the absence of auxiliary gas did not facilitate a successful optimization of C^{5+} in the present experiments. Finally the combination of CO_2 with He as auxiliary gas turned out to be the best choice in order to provide stable long term conditions at an intensity level of 60 eμA analyzed C^{5+} beam.

Radiation protection survey

For an improved survey of the X-ray emission from the ECRIS as well as for related studies dedicated X-ray monitors (energy range: 6 keV to 15 MeV) were procured which can be operated continuously under long term conditions with remote data storing for offline analysis.

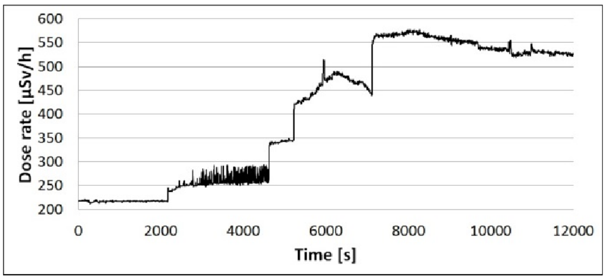

Figure 1: Recorded dose rate during optimization

For a first test one probe was placed next to the extraction of the ECRIS, where a high X-ray level is expected. Figure 1 shows the recorded dose rate during an optimization process of $^{48}Ca^{10+}$ operation in high power mode. The steps in the course of the dose rate are clearly correlated with a stepwise increase of the microwave power from 250 W to 450 W. Phases with plasma instabilities are also identified like around 4000 s in the diagram.

References

[1] VACUUMSCHMELZE GmbH & Co. KG, Grüner Weg 37, D-63450 Hanau, Germany; http://www.vacuumschmelze.de/

DOI:10.15120/GR-2015-1-FG-UNILAC-03

Ion source development of H-rich molecular beam operation for production of high-intensity proton beams at the UNILAC

A. Adonin and R. Hollinger

GSI, Darmstadt, Germany.

The operation of UNILAC high current injector with light ions (M/Q < 8) is strongly limited due to high transmission losses in the LEBT and RFQ. Another limitation is the low extraction voltage applied at the ion source due to the fixed specific ion energy of 2.2 keV/u at the RFQ entrance. These factors make the HSI operation with proton beams extremely inefficient. However the situation can be dramatically improved by production of singly charged heavy (up to M = 50 a.m.u.) molecular ion beams with a high content of hydrogen atoms. These molecular ions can be accelerated in the HSI with much lower transmission losses and when converted into a proton beam at the gas stripper [1].

For the experimental investigations the first two elements from alkane group: methane (CH_4) and ethane (C_2H_6) have been considered because they are non-toxic and could be used in the ion sources under the same safety requirements as a hydrogen gas. The first experiments have been performed with methane gas using high current MUCIS ion source. The mass spectrum of extracted beam is shown on Figure 1. It contains several different molecule species (including higher order alkane chain). However by tuning the operation parameters of the ion source it was possible to optimize the spectrum and get the maximum output of CH_3^+ ions.

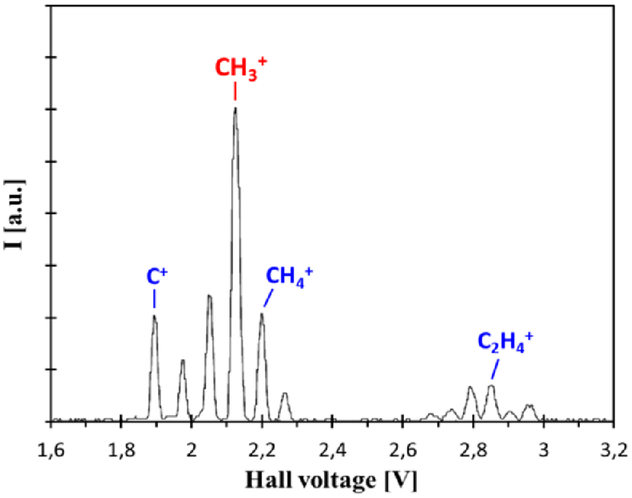

Figure 1: Mass-spectrum of methane gas optimized for CH_3^+ production

The operation was performed with duty cycle of 2 Hz and the pulse length from the ion source of 1 ms. The maximum beam currents achieved in the tests were 11 mA for unanalysed beam and 4 mA for CH_3^+ ions.

Tests with ethane gas have been performed with the same ion source and under the same conditions as with methane. The mass spectrum is more complex than for methane (Fig.2). The production maximum was achieved for $C_2H_4^+$ ions and maximum beam current in front of the RFQ was 2 mA.

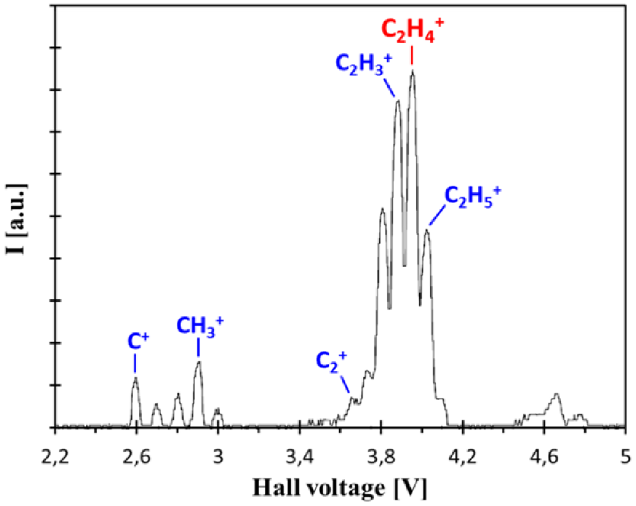

Figure 2: Mass-spectrum of ethane gas optimized for $C_2H_4^+$ production

A notable disadvantage in operation with CH_4 and C_2H_6 gases is strong and relatively fast contamination of the plasma chamber and the extraction system of the ion source with carbon. The carbon ions embedded in the heating filaments make them more fragile and reduce their durability and lifetime. Carbon deposits on the extraction electrodes causes sparking and breakdowns in the extraction system. Thus the operation with alkanes requires a full service of the ion source with cleaning of the plasma chamber once a week. While hydrogen operation requires only a filament service every 7-10 days.

The HSI operation with molecular CH_3^+ ion beam results in proton intensity up to 3 mA behind the gas stripper that is more than 1 order of magnitude higher (at transferline to SIS) than the intensity achieved with hydrogen operation. For further performance improvement of the ion source the optimization of the extraction system for singly-charged molecular beam production and reduction of carbon contamination effect are foreseen. Besides using of more heavy H-rich gases (such as propane, butane, trimethylamine, etc.) could provide better transmission and even higher yield of protons behind the gas stripper for future proton operation.

References

[1] W. Barth et al., LINAC-2014 proceedings.

DOI:10.15120/GR-2015-1-FG-UNILAC-04

Status of the Compact LEBT Project

H. Vormann, A. Adonin, H. Al Omari, W. Barth, L. Dahl, P. Gerhard, L. Groening, R. Hollinger, M. Maier, S. Mickat, A. Orzhekhovskaya, C. Xiao, and S. Yaramyshev

GSI, Darmstadt, Germany

The particle dynamics design of the new high current uranium low energy beam line for FAIR is fixed. Simulations based on uranium beam measurements at the North Terminal 2013 have shown that a straight beam line with quadrupoles as focusing elements allows for best beam quality and transmission [1-3]. The beam line components of this Compact LEBT, to be integrated into the existing High Current Injector (HSI) complex, are now under construction.

Design of the LEBT

Uranium beam measurements at the existing high current ion source North Terminal confirmed the performance of the ion source: From about 50 mA total beam current, 25 mA U^{4+} is provided within an emittance of 280 mm mrad (assumed RFQ acceptance) (Fig. 1).

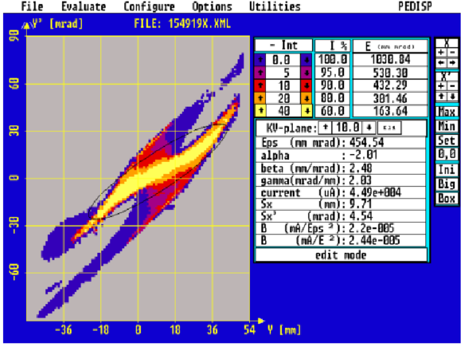

– Int	I %	E (mm mrad)
0.0	100.0	1030.84
5	95.0	530.30
10	90.0	432.29
20	80.0	301.46
40	60.0	163.64

KV-plane: 10.0
Eps (mm mrad): 454.54
alpha : -2.01
beta (mm/mrad): 2.40
gamma(mrad/mm): 2.03
current (uA): 4.49e+004
Sx (mm): 9.71
Sx' (mrad): 4.54
B (mA/Eps ²): 2.2e-005
B (mA/E ²): 2.44e-005
edit mode

Figure 1: Uranium emittance behind ion source (49 mA tot. beam curr., 32 mA U^{4+}, 15 mA within 280 mm mrad).

Based on these measurements beam dynamics simulations have been performed [2, 3]. Considering a minimum distance of at least 4 meters from the new uranium terminal to the switching magnet (restricted space because of existing branches), two focusing elements must be used in this part of the LEBT. A quadrupole quartet (QQ) and a quadrupole triplet (QT) turned out to be the best solution. With this LEBT a focus 1.5 meter behind the QQ can be achieved, allowing for partly scraping off the undesired U^{3+} partition of the uranium beam with a collimator (see Fig. 2) [3].

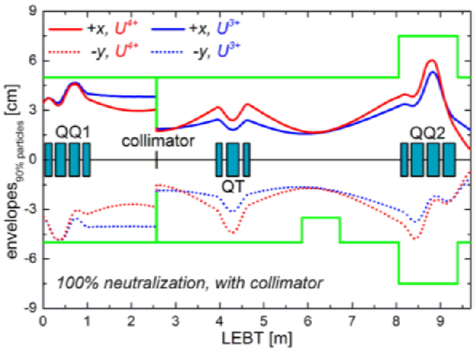

Figure 2: Beam envelopes $U^{3+/4+}$, with collimator.

U^{3+} ions are scraped off in the collimator or will be lost in the following LEBT and RFQ at low energy. Simulations show that more than 15 emA U^{4+} can be transported through the new LEBT [3].

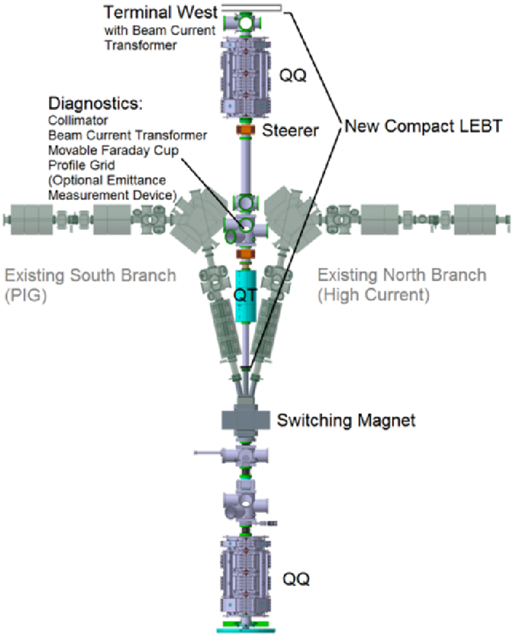

Figure 3: Planned modified HSI-LEBT (Courtesy V. Gettmann).

Besides a beam current transformer with large aperture (115 mm diameter) behind the ion source, a second beam current transformer is foreseen behind the first quadrupole quartet and the collimator, together with a profile grid (width 94 mm) and a movable Faraday cup (diameter 80 mm) as beam diagnostics.

For the commissioning phase, an emittance measurement device is also desirable. To avoid problems from space restrictions, this could be a device measuring only one plane (e.g. only vertically), as the beam shape from the ion source is symmetric.

Status of Components

The tendering for the power supply for the new quadrupole quartet has now started.

Civil construction and stress analysis is starting, magnet design work is going on, and the definition of beam diagnostics components is almost done.

References

[1] L. Dahl, proc. LINAC 2006
[2] S. Yaramyshev et al., proc. IPAC 2014
[3] C. Xiao et al., this report.

DOI:10.15120/GR-2015-1-FG-UNILAC-05

Beam dynamics layout of the compact LEBT*

C. Xiao†[1], L. Groening[1], H. Vormann[1], S. Mickat[1], M. Maier[1], W. Barth[1], S. Yaramyshev[1], and O.K. Kester[1,2]
[1]GSI, Darmstadt, Germany; [2]IAP, Frankfurt am Main, Germany

The present high current VARIS ion source [1] delivers about 50 mA of uranium beam and about 8 mA of U^{4+} was measured behind the HSI. In order to increase the beam intensity downstream the HSI, a dedicated straight LEBT for uranium is proposed as a part of the upgrade and further development of the high current heavy ion linac UNILAC for the Facility for Antiproton and Ion Research (FAIR).

A symmetric beam is required at the entrance to the RFQ. The beam Twiss parameters are determined to be α_f=0.6, β_f=13.6 cm/rad and the transverse acceptance of the RFQ is calculated as A_f=280 π mm mrad. 15.4 mA U^{4+} are inside the RFQ-acceptance already at the source. Beam dynamics design has been performed with the TRACE-3D code [2]. It is optimized to maximize the primary component inside the RFQ acceptance and to minimize the secondary component and transport almost all U^{4+} ions which are in the acceptance form source to RFQ. Beam dynamics simulations have been performed using the multi-particle tracking TRACK code [3]. A macro-particle distribution is generated at the entrance of the new LEBT from the measured phase space distribution directly behind the ion source post acceleration gap. Fig. 1 illustrates final particle distributions at the exit of the LEBT.

Simulations show that 60% (10.5 mA) of the undesirable U^{3+} beam is removed by the aperture and collimator and the remaining U^{3+} beam will be lost in the RFQ. About 50% (15.4 mA) of the U^{4+} beam is transported from the source to the RFQ (for the U^{4+} particles within the RFQ-acceptance, 100% transmission is achieved from the ion source to the RFQ) when the space-charge effects are fully compensated. When the space-charge effects are included (for example 95% compensated), 81% (14.2 mA) of the undesirable U^{3+} beam is removed by the aperture and collimator, and about 44% (14.2 mA) of the desired U^{4+} beam is delivered to the RFQ (for the U^{4+} particles within the RFQ-acceptance, 93% transmission is achieved). The FAIR requirements still impose improvement to 25 mA within the RFQ-acceptance. To this end further developments of the source performance are planned.

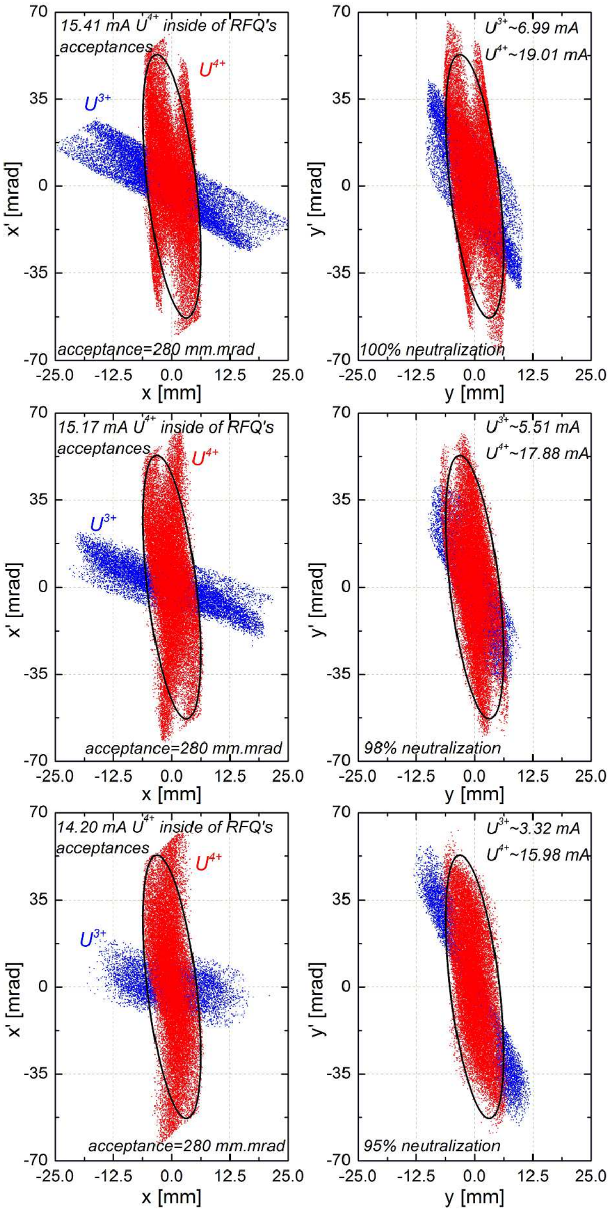

Figure 1: Particle distributions at the exit of the LEBT. Space-charge compensation factor is 100%, 98%, and 95%, respectively. Blue dots indicate the U^{3+} particles, red dots indicate the U^{4+} particles and black ellipses indicate the acceptance of the RFQ.

References

[1] R. Hollinger et al. ReV. Sci. Instrum. **75**, 1595 (2004).

[2] K.R. Crandall et al. LA-UR-97-886 (1997).

[3] P.N. Ostroumov et al. http://www.phy.anl.gov/atlas/TRACK/.

---

* PSP code: 7.1.2.1.

† c.xiao@gsi.de

DOI:10.15120/GR-2015-1-FG-UNILAC-06

Development of a MEBT Design to replace current UNILAC Superlens*

H. Hähnel†1, *U. Ratzinger*1, *R. Tiede*1, *and S. Mickat*2
1IAP, Goethe University, Frankfurt, Germany; 2GSI, Darmstadt, Germany

As part of the UNILAC upgrade, a new MEBT section is proposed [1]. It will provide improved matching to the IH-DTL and therefore a significant reduction in emittance growth and lossless transmission at 20.75 mA U^{4+}. This way the FAIR requirement of 18 mA U^{4+} behind the IH-DTL can easily be reached with the new MEBT. The design comprises of two quadrupole triplet lenses and a two-gap buncher cavity (see Figure 1), providing more flexibility than the existing “Superlens” MEBT [2]. This layout allows to reuse the existing XY-steerer, the vacuum valve and the diagnostics box. It also provides some spare room for additional/redesigned components.

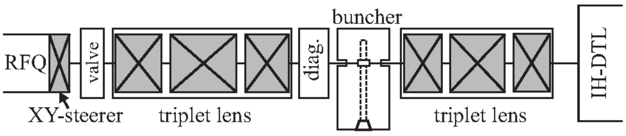

Figure 1: Layout of the proposed MEBT section.

The overall length of the new MEBT is 1.82 m which is 0.4 m longer than the existing MEBT section. The posibility of providing the extra length by moving the IH-DTL is currently being investigated.

At 20.75 mA the simulated losses in the Superlens using the RFQ output distribution after the 2008 upgrade amount to 12 % [1][3]. Losses are caused by insufficient transversal focusing and the limiting aperture of the Superlens.

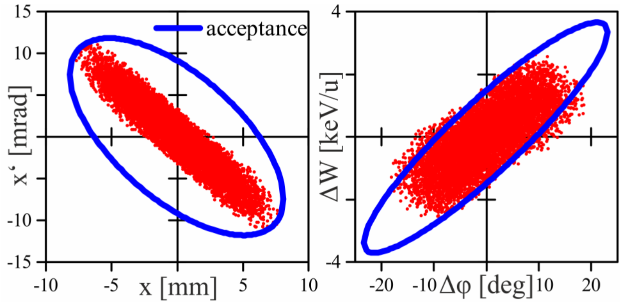

Figure 2: Output distribution of new MEBT with IH-DTL acceptance as reported in [4].

The new MEBT ensures transversal and longitudinal focusing matched to the IH-DTL input acceptance (Figure 2). By using two quadrupole triplet lenses, the design provides some flexibility to compensate changes in the input distribution. The gap voltage of the buncher cavity can also be adjusted if necessary to change longitudinal focusing.

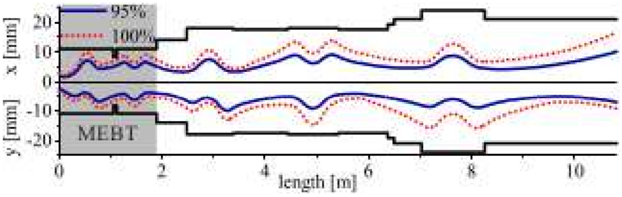

Figure 3: Envelopes of new MEBT and IH1 at 20.75 mA.

Table 1: Prestripper output parameter comparison.

	SL MEBT	**New MEBT**
Total length	1.4 m	1.82 m
Design current	16.5 mA	20.75 mA
Design A/q	65	59.5 (U^{4+})
MEBT-out	for 20.75 mA U^{4+}	
Transmission	87.94 %	100 %
ϵ_{rms} [mm mrad]	x:0.108 y:0.09	x:0.072 y:0.073
ϵ_{rms} [$\frac{keV}{u}$ ns]	0.389	0.358
IH-out		
Transmission	85.7 %	100 %
ϵ_{rms} [mm mrad]	x:0.162 y:0.158	x:0.117 y:0.138
ϵ_{rms} [$\frac{keV}{u}$ ns]	1.279	0.517

A comparison of output parameters of the prestripper section is made in Table 1 showing a reduction of rms emittance growth of 27.8 %, 12.7 % for x-x’,y-y’ and 59.6 % for the longitudinal plane behind the IH-DTL. Simulations with currents from 10 to 20.75 mA U^{4+} show lossless transmission for the MEBT+IH and even low losses at 35 mA U^{4+}. Upgrading the MEBT section would significantly improve the overall UNILAC efficiency and provide flexibility for high current operation which is required for FAIR.

References

[1] H. Hähnel, U. Ratzinger, R. Tiede, MOPP062, Proc. LINAC2014

[2] U. Ratzinger, R. Tiede, MOP31, Proc. LINAC96

[3] All simulations were performed with LORASR.

[4] R. Tiede, “HSI IH-DTL Acceptance Studies”, Talk at IAP-GSI UNILAC-Upgrade meeting, Frankfurt, January 16th, 2014

---

* Work supported by BMBF 05P12RFRB9

† haehnel@iap.uni-frankfurt.de

DOI:10.15120/GR-2015-1-FG-UNILAC-07

Application of the Savitzky-Golay-Filter to analyze the energy-loss of a heavy ion beam in an X-ray-heated CHO-foam

R. Maeder[2] ; T. Rienecker[2]; S. Hagmann[1] ; L. Borisenko[3] ; M. Schächinger[2]; A. Schönlein[2]; S. Zaehter[2]; O. Rosmej[1,2], J. Jacoby[2]

[1]GSI, Darmstadt, Germany; [2]University Frankfurt am Main, Germany; [3] Moscow State University, Russia

Measurements of the ion beam energy loss in low density CHO-foams in solid and plasma states have been carried out at the Z6-experimental area using a combination of the UNILAC ion beam and PHELIX laser pulses.

The Savitzky-Golay-Filter was applied to increase the accuracy of the measured data.

The Ti $^{+12}$ ions, accelerated up to 4.77MeV/u energy, pass the low density 1 mm thick CHO foam layer a Triacetate-Cellulose with the chemical structure $C_{12}H_{16}O_8$. The energy loss in cold foam layer was measured by means of a time-of-flight method. Interaction of a 100-180J PHELIX nanosecond laser pulse with a gold-layered hohlraum, placed above the foam target, gave rise to soft X-ray emission with close to Planckian spectral distribution. Supersonic X-ray waves heat the foam and transfer it from a solid into a hydrodynamically stable plasma layer with homogeneous distributions of density, temperature and ionization degree.

The energy loss in the cold and converted to plasma target was registered by means of the diamond stop-detector, placed 12,126m far away from the interaction region, and evaluated using the data-analysis program Origin9. [1]

The received data is influenced by a low signal-to-noise-ratio, which disturbs the data-sets and reduces the data accuracy. In order to remove these errors and improve the accuracy of the measured data, the Savitzky-Golay-Filter-Method (SGF-Method) was applied.

The Savitzky-Golay-Filter is a digital filter, used to smooth digital data-sets, thus increasing their signal-to-noise ratio without distortion of the data. It is based on the standard method of least squares. Therefore a convolution process, combining the method of least squares with a k-degree polynomial, is used. This process fits every data-point x_i of the data-set I, in an area of k successive adjacent data points. Thus a sum of 2k+1 data points is included in the process. [2]

$$f(x_i) = \sum_{j=-k}^{k} c_n x_{i+j}$$

Variation of the filter-coefficient c_n provides the smoothed data points $f(x_i)$. The efficiency of the smoothing process can be seen in the following graphic, presented in fig.1.

The smoothed data-sets are evaluated and the energy-loss ΔE_i of Ti-Ions in solid- and plasma-foams is recorded.

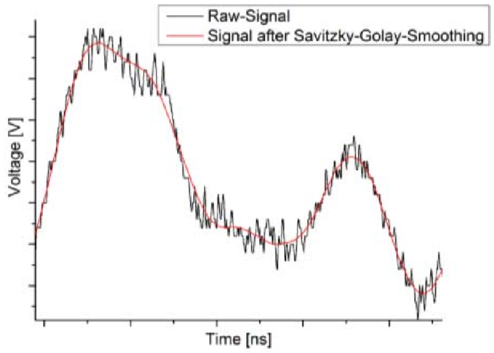

Figure 1: Raw and smoothed data-signals.

The average energy-loss in TAC-foams with 2mg/cc density is compared to theoretical expectation-values and results of former experiments: [3]

	ΔE_S [MeV/mm]	ΔE_P [MeV/mm]
Smoothed data	5,94 ± 1,19	9,01 ± 1,80
Theoretical values	5,61	7,48
Former data	5,56 ± 1,11	9,30 ± 1,19

The application of the Savitzky-Golay-Filter-Method was successful and delivered reliable results. Through increase of the signal-to-noise-ratio, the amount of data, which can be used for analysis, is raised. Additionally the boundaries of the SGF-Method could be established for a signal-to-noise ratio of the magnitude 1.

References

[1] T. Rienecker, R. Maeder, O. Rosmej, et al., “Measurements of the Heavy Ion Stopping in X-ray heated low-density nanostructured targets.” GSI-Report 2013.

[2] D.S.Gilliam, “Mathematical systems theory in biology, communications, computation and finance.” Springer (2003), p.301.

[3] R. Maeder, “Messung des Energieverlustes von Titan-Ionen in CHO-Schaum im Fest- und Plasmazustand” Bsc.-Thesis, Goethe-University, Frankfurt a.M. (2013).

DOI:10.15120/GR-2015-1-FG-UNILAC-08

Performance of a modified 1.4 MeV/u gas stripper for $^{238}U^{4+}$

Paul Scharrer[1], Egon Jäger[2], Winfried Barth[1,2], Mario Bevcic[2], Christoph E. Düllmann[1,2,3], Lars Groening[2], Klaus-Peter Horn[2], Khuyagbaatar Jadambaa [1], Jörg Krier[2], Alexander Yakushev[2]
[1]HIM, Mainz, Germany; [2]GSI, Darmstadt, Germany; [3]Johannes Gutenberg-Universität, Mainz, Germany

The GSI UNILAC will serve as an injector system for the FAIR facility. Therefore it has to meet high demands in terms of beam brilliance. A key projectile for FAIR will be ^{238}U [1]. In current routine operation U^{4+}-ions from a MEVVA ion source are accelerated to 1.4 MeV/u by the High Current Injector (HSI). Inside the adjacent gas stripper, the charge state of the ions is increased to raise the efficiency of further acceleration. Behind the stripper, a system of dipole magnets allows the selection of ions with the desired charge state (U^{28+}) [2].

To increase the beam intensity after the gas stripper, an upgrade program has started to increase the stripping efficiency into the desired charge state. The current gas stripper is based on a supersonic N_2-jet, created through a laval nozzle at 0.4 MPa back-pressure. The continuous gas flow limits the usable gas pressure due to the high gas load for the differential pumping system. This also prevents the optimal use of other promising stripper gases, as a saturated charge distribution cannot be reached [3].

To overcome this limit, a modified gas stripper setup was developed [4]. The flange with the laval nozzle on top of the main stripper chamber was replaced by a new flange, featuring a pulsed gas valve designed for a back-pressure of up to 12 MPa and an opening time down to a few microseconds. The new flange is shown in Fig. 1. To prevent the gas from instantaneous removal, an extension was added to the flange with a T-fitting at the end to match the beam line. This creates a high-pressure interaction zone for the stripping process. The valve is located in the extension, facing down towards the beam line. The pulsed gas injection is triggered by a timing signal of the central accelerator control unit. The valve is opened only when a beam pulse passes the stripper and closed immediately afterwards, decreasing the gas load for the pumping system and lowering the gas consumption by a factor of up to 200.

During two measurement campaigns in 2014 the new stripper setup was tested with a U^{4+}-beam (1 Hz, 100 μs pulse length). An opening time of 0.5 ms was used for the pulsed gas valve. The opening time was chosen based on pressure measurements near the gas inlet as well as beam current measurements behind the stripper. Besides N_2, which allowed comparing the setup to the current gas-jet stripper, the charge spectra were measured for various other gases (H_2, He, O_2, Ne, Ar and CO_2).

For all used gases except H_2, a saturation of the charge state distribution was observed with an increase of the back-pressure. The beam emittance and the energy loss were measured using the determined settings for a saturated charge state distribution. Additionally, the stripping efficiency was measured for every populated charge state. A saturation of the charge state distribution with H_2 could not be observed due to the pressure limitations of the pulsed gas valve. Therefore, one can assume that the average charge state will rise, if the pressure is increased further.

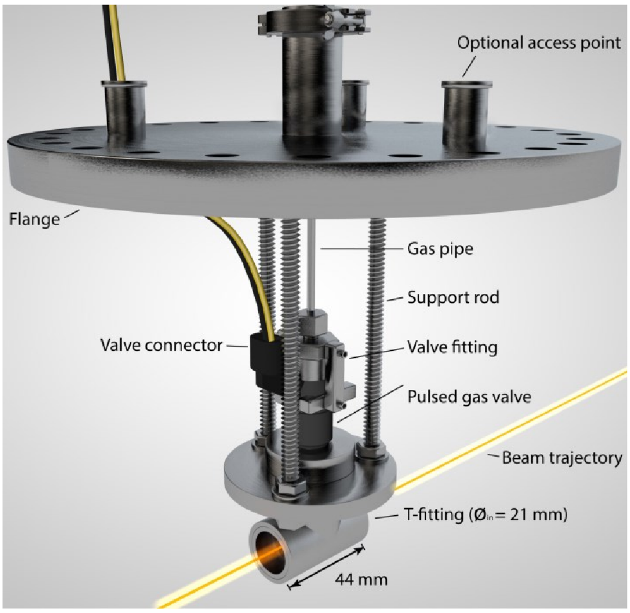

Figure 1: Model of the new stripper flange

Using H_2 with the pulsed gas cell, it was possible to set a new record for the U^{28+} beam intensity behind the gas stripper at the GSI UNILAC [5].

The pulsed gas injection enables various possibilities for the use at the GSI UNILAC, including the simultaneous use of different stripper gases for particular ion beams. Preparing for routine operation, the pulsed gas cell has to be tested and optimized for all to be used types of ion beams.

References

[1] FAIR Baseline Technical Report, Vol. 2, (2006) GSI Darmstadt, p. 355
[2] Barth W. et al., Proceedings of LINAC2000, 21th-25th August 2000, Monterey, California, USA.
[3] Schlitt B. et al., Proceedings of IPAC2013, 13th-17th May 2013, Shanghai, China.
[4] Jäger E. et al., GSI Scientific Report 2013, p. 304.
[5] Barth W. et al., contribution to this GSI Scientific Report.

DOI:10.15120/GR-2015-1-FG-UNILAC-09

High current proton beam operation at GSI UNILAC

M. Heilmann[1], W. Barth[1,2], A. Adonin[1], P. Gerhard[1], R. Hollinger[1],
W. Vinzenz[1], H. Vormann[1], S. Yaramyshev[1]
[1]GSI, Darmstadt, Germany; [2]HIM, Mainz, Germany;

A significant part of the experimental program at FAIR is dedicated to pbar physics requiring a high number of cooled pbars per hour [1]. The primary proton beam has to be provided by a 70 MeV proton linac followed by two synchrotrons. The new FAIR proton linac [2] will deliver a 35 mA beam of 36 µs pulse duration. The recent GSI heavy ion linac (UNILAC) is able to deliver world record uranium beam [3] intensities for injection into the synchrotrons, but it was not dedicated to high intensity proton beam operation relevant for FAIR. In an advanced machine investigation program it could be shown, that the UNILAC is able to provide for sufficient CH_3-beam intensities, cracked (and stripped) in a supersonic nitrogen gas jet into protons and carbon ions [4]. This advanced operational approach results in up to 2 mA of proton intensity at a maximum beam energy of 20 MeV, 100 µs pulse duration and a sufficient rep. rate to fill the SIS18 (max. 2.7 Hz). It could be shown, that the UNILAC is able to serve as a proton FAIR injector for the first time, while the performance is limited to 17% of the FAIR requirements.

MACHINE DEVELOPMENT

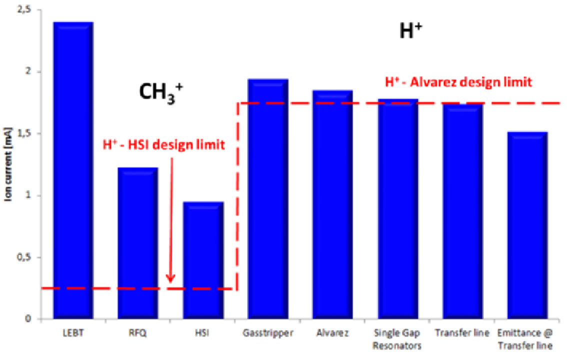

Figure 1: Measured beam current along UNILAC and transfer line to the SIS18; the proton design limit (to fill the SIS18 up to the space charge limit) was reached in the post stripper section.

The MUCIS source [5] was operated with methane (CH_4) gas while a high-current CH_3^+-beam (2.3 emA) is delivered to the HSI. Due to the huge emittance in the LEBT only 50% of the CH_3-beam could be accepted by the HSI-RFQ, minor additional particle losses in the matching section to the HSI-IH-DTL limits the overall HSI-transmission to 40%. Anyway, due to the increased HSI design limitations for the CH_3^+-beam, the improved beam transmission compared to a pure proton beam is evident. Furthermore a triple particle output (for protons) from each CH_3^+ molecule behind the stripping section allows for proton beam operation at the design limit of the poststripper linac (Fig. 1). Strong efforts were launched to push the high current proton beam transmission through the entire poststripper and transfer line to a value of up to 80%.

20 MeV proton beam

The single-gap resonators (SGR) provide intermediate energies between 3.6 and 13.0 MeV/u for all ion species. During the high current experiment protons were pre-accelerated in the UNILAC to a beam energy of 11.4 MeV/u. Inside the following eight single gap resonators, each providing for an energy increase of more than 1 MV, a final energy of 20 MeV could be reached (Fig. 2). This final energy corresponds to 28.5% of the required beam energy of the FAIR p-linac. Besides optimizing the high current proton beam performance for the ongoing GSI experiment program, the UNILAC is able to serve as a high performance proton injector for FAIR-commissioning and for first pbar experiments as a redundant option for the FAIR proton linac injector.

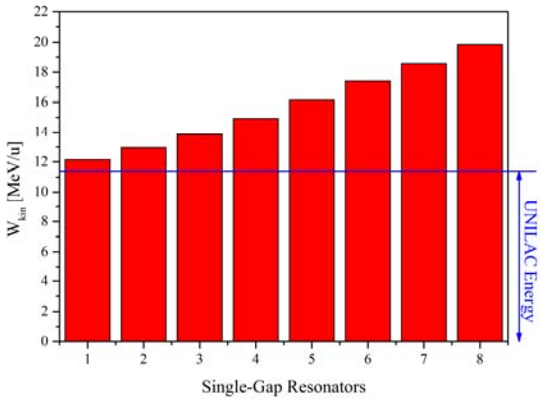

Figure 2: UNILAC operation with eight SGR for maximum proton beam energy of 20 MeV

References

[1] O. Kester, et al., Status of FAIR Accelerator Facility, Proc. of IPAC, Dresden, Germany, p. 2084. (2014)

[2] R. Brodhage et al., First Coupled CH Power Cavity for the FAIR Proton Injector, Proceedings of IPAC, Dresden, Germany, p. 3232 (2014)

[3] W. Barth, et al., GSI Scientific Report 2014

[4] W. Barth, et al., High Current Proton Beam Operation at GSI UNILAC, Proceedings of LINAC, Geneva, Switzerland (2014)

[5] R. Keller, Multi charged Ion Production with MUCIS, GSI Scientific. Rep. 1987, p. 385. (1987)

DOI:10.15120/GR-2015-1-FG-UNILAC-10

Simulation of charge state distributions in stripper applications*

O. S. Haas†1,2 *and O. Boine-Frankenheim*1
1TEMF TU-Darmstadt, Darmstadt, Germany; 2GSI, Darmstadt, Germany

Abstract

The presented work focuses on theoretical studies of the interaction of an heavy ion beam with possible future charge stripping media. The main interest in the presented studies is the final charge state distribution of the ion beam in the context of charge stripping. Different models for solving the corresponding rate equations were devoloped, taking into account ionization, recombination and energy loss processes. In this report one example case relevant for GSI is presented.

Results

The model used for calculations in this section are mainly based on Ref. [1]. The presented example case relevant for GSI is uranium with 1.4 MeV/u and a desired charge state of $q_0 = 28$. The rates for low atomic densities $n < 10^{23}\,\mathrm{m}^{-3}$ in different media are given in Fig. 1. All gas media do not achieve the desired equilibrium charge state, while in case of a hydrogen plasma the equilibrium charge state is actually higher than the desired charge state. Increasing the atomic density to larger than $10^{23}\,\mathrm{m}^{-3}$ leads to the onset of the density effect (see Ref. [1]), increasing the equilibrium charge state.

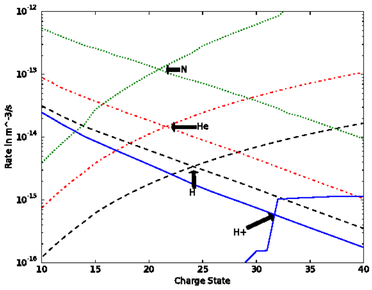

Figure 1: Rates of uranium with 1.4 MeV/u in different gases and a plasma without density effect. Rising and falling curves are the sum of recombination and ionization rates respectively.

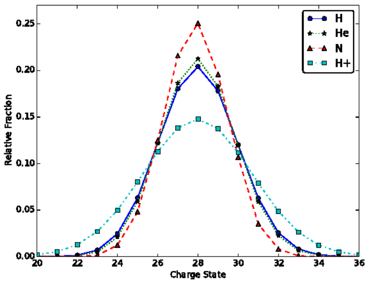

Figure 2: Widths of the charge state distribution for different media. Required atomic density of the gases are $4.65 \cdot 10^{26}\,\mathrm{m}^{-3}$, $1.6 \cdot 10^{27}\,\mathrm{m}^{-3}$ and $3.7 \cdot 10^{27}\,\mathrm{m}^{-3}$ for hydrogen, helium and nitrogen respectively. The density of the hydrogen plasma was assumed to be $10^{23}\,\mathrm{m}^{-3}$ for both electrons and protons.

To compare the charge state distribution widths of the different media the density was increased such that the charge state $q_0 = 28$ is achieved, as depicted in Fig. 2. For the hydrogen plasma the charge state distribution is not in equilibrium, as the desired charge state is smaller than the equilibrium one. This explains the larger charge state distribution width of the plasma stripping medium. In experiments a much broader charge state distribution for nitrogen gas is observed. This however can not easilybe explained by the current model. The charge state distribution width can be approximated as

$$\sigma^2 = \left(\frac{\alpha'_{\mathrm{ion}}(q_0)}{\alpha_{\mathrm{ion}}(q_0)} - \frac{\alpha'_{\mathrm{rec}}(q_0)}{\alpha_{\mathrm{rec}}(q_0)} \right)^{-1} . \tag{1}$$

This implies that either the shape or value of the rates has to be significantly different for nitrogen, or further effects broaden the distribution specifically for heavier gases. The influence of the mean energy loss in the charge stripping process is of minor importance for typical projectile and target paramters.

Outlook

Future studies intend to improve the calculation methods of the necessary cross section, and include detailed models for the gas and plasma conditions (e.g. inhomogenities, multiple electron capture or loss, and ionization degree of the target). Furthermore comparisons are planned with charge state distributions achieved in the different plasma pinch and gas stripper experiments at GSI.

References

[1] T. Peter, J. Meyer-ter-Vehn, "Energy loss of heavy ions in dense plasma. II. Nonequilibrium charge states and stopping powers", Phys. Rev. A 43, 1991, p. 2015

---

* Work supported by HGShire.

† ohaas@gsi.de

DOI:10.15120/GR-2015-1-FG-UNILAC-11

Status of the HE-Linac project at GSI

S. Mickat[1], *M. Droba*[2], *X. Du*[1], *L. Groening*[1], *H. Hähnel*[2], *A. Orzhekovskaya*[1],
U. Ratzinger[2], *A. Seibel*[2], *R. Tiede*[2], *H. Vormann*[1], *C. Xiao*[1]

[1]GSI, Darmstadt, Germany; [2]IAP, Goethe University Frankfurt, Germany

UNILAC Upgrade

The High-Energy (HE) Linac project is defined by the substitution of the existing post-stripper (Alvarez) section of the UNILAC. The substition of the existing Alvarez section is one of the major steps towards an adequate FAIR injector linac. Nevertheless the whole accelerator chain has to be taken into account. Starting from the ion sources to the SIS18 transfer channel every section is re-investigated for improvements in beam quality and intensity. Workpackages are defined together with the Institute of Applied Physics (IAP) at Frankfurt University [1]:

- 3rd ion source terminal and Compact-LEBT [2]
- HSI RFQ
- alternative MEBT design
  for an improved beam matching to the HSI IH [3]
- pulsed gas stripper [4] and Emtex [5]

Alvarez DTL and IH DTL

Concerning the post-stripper section itself, two concepts are discussed: On the one hand the substitution of the existing Alvarez structure by six IH cavities [6], on the other hand the substitution by redesigned and new Alvarez tanks. Regarding the design comprising six IH cavities efforts were made to develop a recipe for finding an optimum parameter setting in daily operation. Such a recipe was not found per se, but the design was optimized, which results in an improvement of transmission through the post-stripper section from 88% to 92%. The beam brilliance behind the post-stripper increased by a factor of 1.5 simultaneously [7]. The transmission is limited by the assumed longitudinal beam particle input distribution. It was set to 20 keV/u·ns for comparison reasons. Activities at GSI focus on the substitution of the post-stripper by an Alvarez section. Nevertheless within the IAP-GSI-collaboration the substitution of the post-stripper by six IH-tanks is followed. At the end of the designing phase both concepts are planned to be presented to an external review committee for receiving a qualified recommendation. Both concepts are compatible to the modernisation of the 108 MHz RF systems of the UNILAC post stripper section [8].

Designing phase

Concerning the Alvarez DTL option investigations about optimizing the rf design have started aiming at improvement of the accelerating field properties and increase of the shunt impedance. First results are promising. Optimising the driftube geometry, especially smoothening the drifttube's cap, lower the surface peak fields. The shunt impedance could be increased by 10 percent. Another task is initiated through discussions with the colleagues, who designed the LINAC4 at CERN. At LINAC4 post-couplers are applied to reduce field instabilities. The function of post-couplers are covered by the two stem suspension of the drifttubes, which is applied at GSI. The angle between the stems as well as the stem configuration of group of drifttubes is playing a key role [9]. All this rf design studies will be complemented by measurements. For that purpose an aluminium rf model (scale 1:3) is ordered. In a start version a ten gap model is planned. It is designed for testing different drifttube shapes and confirming the calculated predictions w.r.t. the stem configuration [10]. Focusing on the optimization of the rf-properties the installation space of the quadrupole, which is usually integrated in the drifttube, is an important issue. Theoretical studies and corresponding measurements at the GSI UNILAC provide evidence of space charge driven resonant emittance coupling in high current operation [11]. The operation at these resonances, which leads to an emittance growth, could be avoided by setting an adequate transverse phase advance. An adequate phase advance can be set if the quadrupoles for the new design are specified to reach 20% higher gradients than the existing. First studies for high gradients quadrupoles, which fit into the smaller installation space of the new drifttube geometry, are done [12].

References

[1] S. Mickat et al., "The status of the HE-Linac project at GSI", GSI Scientific Report 2013

[2] H. Vormann et al., The status of the Compact LEBT project", this report

[3] H Hähnel et al., "Development of a MEBT Design to replace current UNILAC Superlens", this report

[4] P. Scharrer et al., "Performance of a modified 1.4 MeV/u gas stripper for $^{238}U^{4+}$ ", this report

[5] M. Maier et al., "Results of the experiments on emittance transfer EMTEX", this report

[6] G. Clemente et al., Proceedings IPAC2011, WEPS032, San Sebastián, Spain

[7] A. Orzhekovskaya et al., "Optimization of the KONUS beam dynamics for the HE-Linac", this report

[8] B. Schlitt et al., "Modernisation of the 108 MHz RF systems of the UNILAC post stripper section", this report

[9] X. Du et al., "Activities on the HE-Linac DTL cavity rf-design", this report

[10] A. Seibel et al., "Status of the cold model for the HE-Linac cavities", this report.

[11] L. Groening et al., , Phys. Rev. Lett.103, 224801 (2009)

[12] D. Daehn, internal note (2014)

DOI:10.15120/GR-2015-1-FG-UNILAC-12

Development of a KONUS based High Energy Linac for the UNILAC*

H. Hähnel[†1], *U. Ratzinger*[1], *R. Tiede*[1], *and S. Mickat*[2]
[1]IAP, Goethe University, Frankfurt, Germany; [2]GSI, Darmstadt, Germany

To meet the requirements of 15 mA U^{28+} at 11.4 AMeV for injection into the SIS18, the GSI UNILAC has to be upgraded. The Alvarez linac in the poststripper U^{28+} section of the UNILAC is nearing 40 years of operation and therefore has to be replaced to ensure reliable and efficient operation for FAIR. We propose an IH-DTL linac as replacement for the current GSI UNILAC Alvarez. The new design is based on the KONUS beam dynamics concept and delivers high beam quality well within FAIR requirements. It will drastically reduce the fabrication costs and will leave about 30 m within the UNILAC (Fig. 1) for later linac energy upgrades by e.g. 325 MHz CH-DTL cavities as in [1].

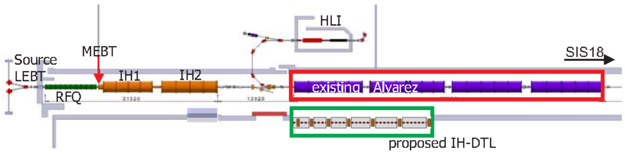

Figure 1: Sketch of the UNILAC accelerator (adapted [2]).

The proposed linac consists of six 108 MHz IH-tanks and seven quadrupole triplet lenses (Fig. 2). It is designed to accelerate 15 mA U^{28+} from 1.4 MeV/u to 11.4 MeV/u. The beam dynamics simulation includes realistic estimations of necessary drift lengths for tank walls, lens housing and phase probes for all lenses. The drift tube aperture is 25 mm and the lens aperture 40 mm with a maximum pole tip field of 1.05 T for the highest gradient of 50.1 T/m. The maximum on axis field is 11 MV/m.

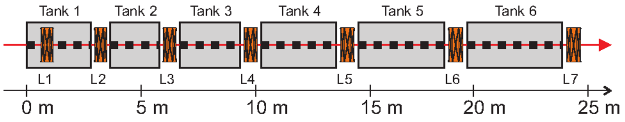

Figure 2: Sketch of the proposed IH-DTL.

Beam Dynamics (preliminary)

Beam dynamics simulations (LORASR) for the proposed high energy linac already show very promising results. The used input emittances are a pessimistic estimation based on the prestripper output emittances using the MEBT upgrade as proposed by the authors in [3]. The transversal input emittances are 0.8 mm mrad (90 %) and the longitudinal input emittance is 6.3 keV/u ns (90 %). A matching section with buncher will be necessary in front of the proposed design.

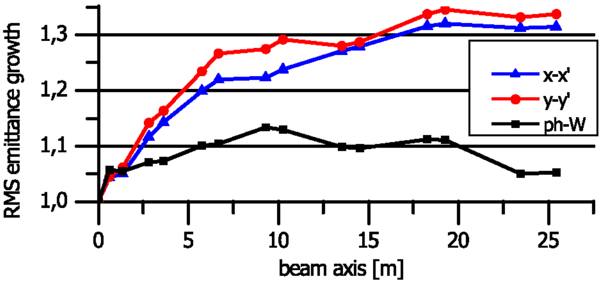

Figure 3: RMS emittance growth of the proposed high energy linac section.

The rms emittance growth along the proposed linac is shown in Fig. 3, indicating only 5.3 % in the longitudinal plane and about 30 % in the transversal planes. Further improvement in the transversal planes is expected to be achieved by adjusting the focusing scheme (Fig. 4).

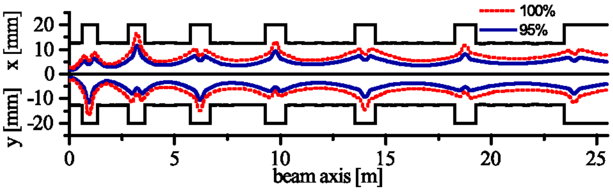

Figure 4: Transversal beam envelopes of the proposed high energy linac section.

In conclusion the proposed concept provides a modern alternative to the Alvarez concept. With a higher RF efficiency and lower production cost it can provide good beam quality. Further optimizations regarding beam quality as well as first CST model studies are currently ongoing at IAP. Final judgment on beam quality relies on the availability of beam dynamics simulations for the proposed new Alvarez.

References

[1] A. Almomani, U. Ratzinger, THPME010, Proc. IPAC2014

[2] S. Mickat et al., MOPP060, Proc. LINAC2014

[3] H. Hähnel, U. Ratzinger, R. Tiede, MOPP062, Proc. LINAC2014

---

* Work supported by BMBF 05P12RFRB9

[†] haehnel@iap.uni-frankfurt.de

DOI:10.15120/GR-2015-1-FG-UNILAC-13

Optimization of the KONUS beam dynamics for the HE-Linac

A. Orzhekhovskaya[1], *G. Clemente*[1], *L. Groening*[1], *S. Mickat*[1], *and B. Schlitt*[1]
[1]GSI, Darmstadt, Germany

Introduction

A new high energy heavy-ion injector (HE-Linac) for the FAIR project was proposed as replacement for the existing post-stripper linac at the GSI UNILAC [1]. Six 108 MHz IH-type drift-tube linac cavities within a total length of about 17 m accelerate the ions (up to U28+) from 1.4 MeV/u up to 11.4 MeV/u (Fig.1). The previous beam dynamics of the entire HE-Linac is based on the KONUS concept [2], with an external magnetic quadrupole triplet lens behind each cavity. Particle tracking was performed with the LORASR code, developed at the IAP, Frankfurt [3]. The optimization of the particle tracking through the HE-Linac [4] with respect to the emittance growth reduction is investigated.

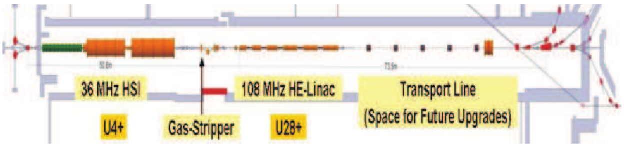

Figure 1: The scheme of the HE-Linac concept.

The Improved Design of HE-Linac

As the first step the influence of the input Twiss parameters on the emittance growth was investigated separately for each of the six cavities. The transverse emittances before the IH1 are 14 mm·mrad and 21 mm·mrad. The assumed longitudinal distribution was generated using the results of measurements for the HIPPI project [5]. The beam current is 20 mA.

The optimum $\alpha_{x,y}$(n) at the beginning of n-th cavity are found in the interval [2.0, 4.0]. The correspondent $\beta_{x,y}$(n) (in mm/mrad) depends on $\alpha_{x,y}$(n) by following rules:

$\beta(1)=0.5\alpha(1)$, $\beta(2)=0.7\alpha(2)$, $\beta(3)=0.9\alpha(3)$,
$\beta(4)=1.3\alpha(4)$, $\beta(5)=1.6\alpha(5)$, $\beta(6)=1.9\alpha(6)$.

These values can be changed by 20%. Then the additional emittance growth is less than 1% for each IH-cavity. For the beam current of 15mA the emittance growth is by 1-2% lower for each tank than for the current of 20mA.

The improved design of the HE-Linac (Fig.2) aims at defined Twiss parameters before each cavity, keeping the KONUS beam dynamics. The triplet gradients and the position of triplets are varied for this matching. The total length of the HE-Linac is increased by 1.4 m. The larger distance between the cavities allows integration of diagnostics devices.

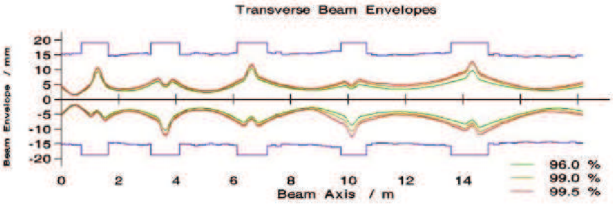

Figure 2: The transverse envelopes through the HE-Linac for the improved design.

The improved design increases transmission from 88% to 92%. By artificial decrease of the longitudinal input emittance from 20 keV/u·ns to 15 keV/u·ns the transmission can be increased up to 100% . The transversal emittance growth along the line is about 35% (instead of 50%). The beam brilliance behind the HE-Linac is about 1.5 times higher for the improved design.

Periodic Solution

The solution is called periodic, if α_x, α_y are the same at the beginning of each period (entrance to the IH-tank) and β_x, β_y change correspondently to the energy growth: $(\beta(n)/\beta(n-1))^2 = \beta\gamma(n)/\beta\gamma(n-1)$. Any α from the interval [2.0, 4.0] satisfy the conditions for the smallest emittance growth in each period and can be fixed for the periodic solution. The energy growth is known from the cavities design. Taking into account, that β defined above can be changed by 20% without significant emittance growth, the periodic solution, corresponding to the energy changes and being inside this 20% corridor, is found as:

$\beta(1)=0.57\alpha(1)$, $\beta(2)=0.72\alpha(2)$, $\beta(3)=0.93\alpha(3)$,
$\beta(4)=1.15\alpha(4)$, $\beta(5)=1.35\alpha(5)$, $\beta(6)=1.53\alpha(6)$.

References

[1] W. Barth, The injector systems for the FAIR project, in: Proc. LINAC08, Victoria, Canada, 2008. p. 31.

[2] R. Tiede et al., KONUS beam dynamics designs using H mode cavities, in: Proc. Hadron Beams 2008, Nashville, USA, 2008, p. 223.

[3] R. Tiede et al., LORASR code development, in: Proc. EPAC2006, Edinburgh, Scotland, 2006, p. 2194.

[4] B. Schlitt et al., Status of the High-Energy Linac Project at GSI, GSI Scientific report 2012, Darmstadt, Germany, p.270

[5] L. Groening et al., Benchmarking of measurement and simulation of transverse rms-emittance growth, PRST-AB 11 (2008), 094201

DOI:10.15120/GR-2015-1-FG-UNILAC-14

Status of the cold model for the HE-Linac cavities

A. Seibel, X. Du, L. Groening, O. Kester, S. Mickat
GSI, Darmstadt, Germany

Design of a ten gap model

In order to meet the challenges of the FAIR project requiring highest beam intensities an upgrade of the existing Universal Linear Accelerator (UNILAC) is planned. The 108.408 MHz post-stripper section is recommended to be replaced after almost 40 years in operation. All activities are focused on substitution of this UNILAC section by an improved Alvarez DTL [1]. Simulations are done to improve the rf-properties. The geometry of the drift tubes is to be changed to improve the ratio of shunt impedance to maximum surface field [2]. This geometry allows a more homogeneous surface current distribution as well.

A test bench for low power rf measurements with a 10 gap aluminum model (scale 1:3) is under construction (Fig. 1). The frequency scales correspondingly to three times 108.408 MHz (= 325.224 MHz). In the simulations the frequency is 324.694 MHz. It is chosen a bit lower than the reference frequency to have some freedom to reach the right frequency after the fabrication and shift it up with tuners. There could be some small unexpected errors in fabrication which influence the frequency. If the frequency is too high it is hard to tune it to lower frequency.

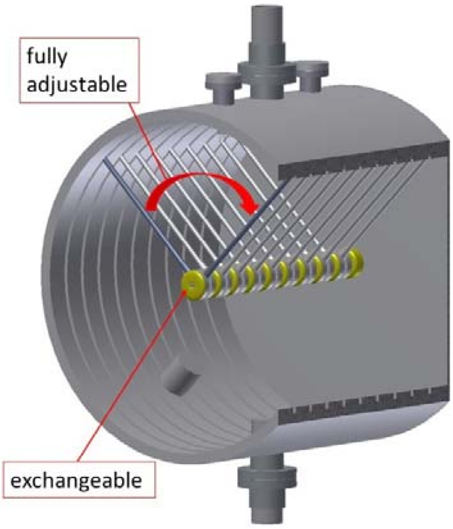

Figure 1: Design of the ten gap Alvarez model for a test bench for low power rf measurements.

The ten gap model with nine full and two half drift tubes at the tank cabs allows to vary the angle between the stems. The stem configuration of each drift tube has an influence on the field stability. In addition the drift tube cabs are dismountable to compare different drift tube geometries as mentioned above.

The goal is to optimize the rf-design geometry with respect to the field distribution stability. The calculated electric field profile along the beam axis shows a flatness better than 3 % (Fig. 2).

With the bead pull method the electrical field distribution will be confirmed as well as the field stability with respect to parasitic modes.

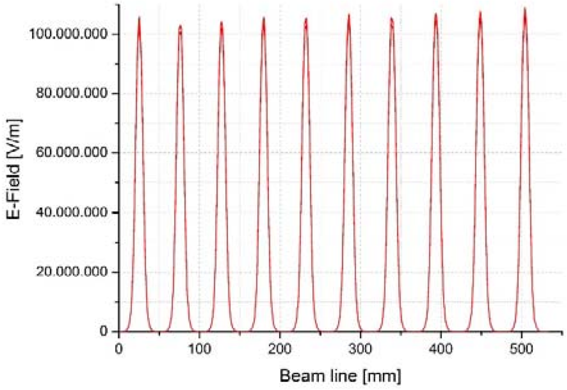

Figure 2: The calculated accelerating electrical field is very flat a βλ-type structure.

Tuning

To match the operation frequency tuners are needed. Three different positions for the tuners along the tank are investigated. The inductively coupling tuners are cylindrical with a diameter of 60 mm. The frequency deviation is 0.4 MHz per Tuner per 100 mm plug-in depth (Fig. 3). The field distribution is independent of the tuner position for all three tuners. The frequency shift of each tuner is the same.

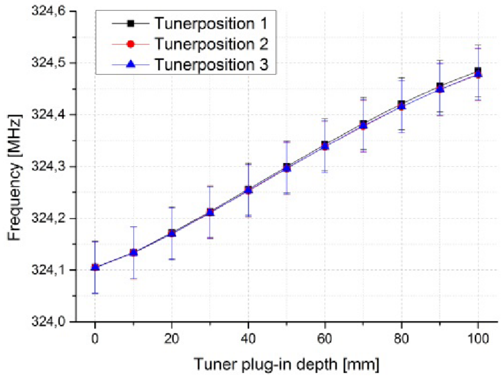

Figure 3: Simulated frequency deviation for the three possible tuner positions to test different fix and dynamic tuners.

Outlook

The fabrication of the 10 gap model is already started. The delivery of the model is expected in summer 2015. Tests are planned at the p-linac test bench.

References

[1] S. Mickat et al., internal report 2014
[2] X. Du et al. (this report)

DOI:10.15120/GR-2015-1-FG-UNILAC-15

Activities on the HE-Linac DTL cavity RF-design

X. Du[1], *L. Groening*[1], *S. Mickat*[1], *A. Seibel*[1,2], *A. Orzhekhovskaya*[1]
[1]GSI, Darmstadt, Germany; [2]Goethe-University, Frankfurt, Germany

Abstract

The new 108 MHz Drift Tube Linac (DTL) of the UNILAC upgrade program at GSI is in the stage of designing and RF simulations. The DTL accelerates heavy ions with a maximum A/q of 8.5 from 1.4 MeV/u to 11.4 MeV/u. The planned accelerator consists of 5 tanks [1]. Several new features have been studied in the design for better performance regarding the peak surface field (E_{surf}), the shunt impedance (ZTT), and the electric field distribution.

Tube optimization

The optimizations started from existing Alvarez cavities at the UNILAC of GSI, with tank1 that has 3.6 MeV/u as output energy. The new tube shape, which is generated by smooth spline function, is used to replace the traditional shape that is based on blend and chamfer as shown in figure 1. With this new tube shape, the surface field is uniformly distributed on the surface of the drift tube keeping the shunt impedance constant, while the maximum E_{surf} is reduced by about 20%. The tube shape is the same for all cells in one cavity.

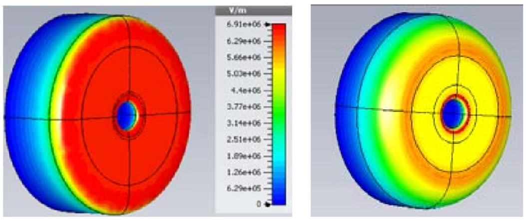

(a) (b)

Figure 1: The surface field distribution on new tube shape (a) and on the original tube shape (b).

Beta profile design

The tube sequence design is based on an optimized 3D tube model, predefined input energy, and maximum E_{surf}. The effective voltage is calculated from a single cell 3D model simulation, which provides the information of power loss, the transient time factor (TTF), maximum allowed E_{surf}, and the shunt impedance. The cell length is defined by the output energy of the former cell. The gap length is defined by the limit of maximum E_{surf} and the operational local frequency. The Visual Basic code in CST-MWS is used to perform continuous cell by cell design. Several different versions for DTL tank1 with different maximum E_{surf} and ZTT are weighted with respect to other considerations such as length of the tunnel and ability of RF power. We prefer a constant average electric field (E_0) with 1.0 Kilpatrick limit for maximum E_{surf}.

Field flatness

The designed electric field distribution may be disturbed in the real cavity due to perturbation, which is caused by mechanical errors. This effect may be decreased by post couplers. The simulation shows that by rotating specific stems in the cavity as shown in figure 2, the TM modes which are close to the operational mode, will be pushed away, and the sensitivity of field flatness to the local frequency uncertainty could be reduced significantly. The improvement is shown in figure 3.

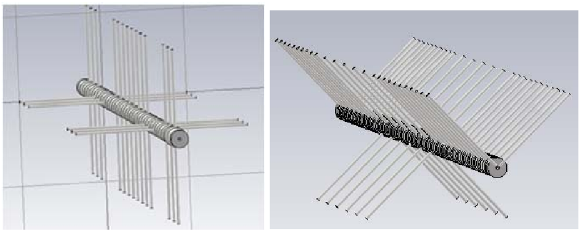

Figure 2: Stem arrangement for better field stability.

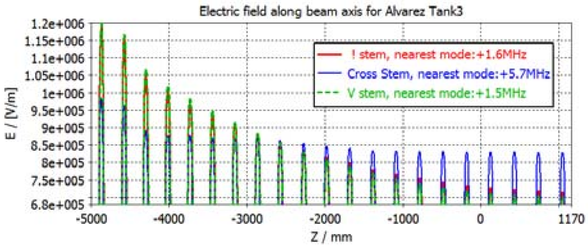

Figure 3: Electric field distribution with perturbation at the first cell of cavity.

The RF design of Alvarez cavities for UNILAC upgrade is in process, magnet design for Tank 1 has started, and the beta profile of other tanks will be designed with the same principle as tank1. A corresponding aluminium 1:3 Alvarez RF model is ordered for mechanical studies and RF measurement [2].

References

[1] S. Mickat et al., this report.
[2] A. Seibel et al., this report.

DOI:10.15120/GR-2015-1-FG-UNILAC-16

Bunch tomography for longitudinal diagnostics at FAIR

O. Chorniy, H.Bräuning, P.Miedzik, A.Reiter
GSI, Darmstadt, Germany

The longitudinal diagnostics is an important tool to observe the beam behaviour under various RF gymnastic processes in FAIR rings. After installation of a dedicated FESA based data acquisition (DAQ) system for bunch measurements [1] the software and hardware parts were expanded providing the ability to perform the on-line bunch tomography. Presently, the system is under further developments which includes fine tuning of the GUI, debugging of the FESA class and final assembling of the electronics.

On-line bunch tomography

Tomographic reconstruction of longitudinal phase space is a reliable instrument in bunched beam diagnostic [2]. At GSI, the first simple on-line tool was realized [1] using Mathematica software and the tomography code. Measurements in the SIS18 were done using the sum signal of a single BPM. The Lecroy oscilloscope was used as DAQ. It was required to preview signal in a form of a waterfall plot and to choose different important parameters for tomography. For this purposes a test GUI in Mathematica was written. The tomographic reconstruction itself was done using a FORTRAN based code written at CERN [2].

After installation of the broadband FCT, the aim was to implement the tomography tool into the new FCT DAQ described below. First tests were performed in a "quasi on-line" regime which means the signal source was signal generator, the timing source was in-house developed timing simulator. A snapshot of the GUI is shown in Figure 1.

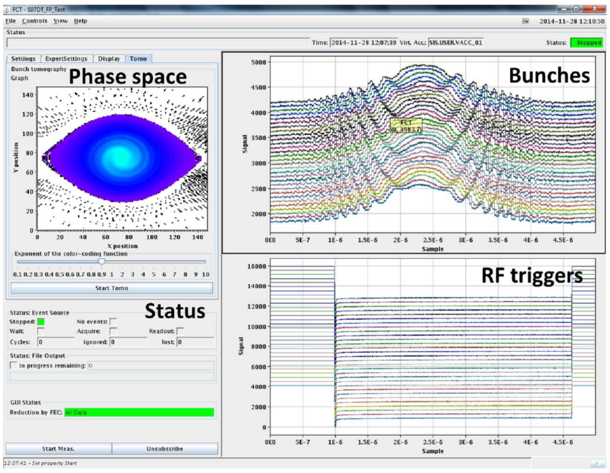

2014-11-28 12:10:50
Time: 2014-11-28 12:07:39 Virt. Acc: SIS.USER.VACC_01 Status: Stopped
Status: Event Source
Stopped: ☑ No events: ☐
Wait: ☐ Acquire: ☐ Readout: ☐
Cycles: 0 ignored: 0 lost: 0
Status: File Output
☐ in progress remaining: 0
GUI Status
Reduction by FEC: All Data
12:07:41 - Set property Start

Figure 1: GUI with reconstructed phase space.

Temporarily, the tomography code resides on the PC where the GUI runs. It is planned to use a dedicated PC with a multi-core CPU in order to accelerate the reconstruction process. A more advanced option is to consider a GPU based tomography, while a speedup of 10-100 times can be achieved in comparison to a CPU. In addition, this option will require the development of a new tomography code.

DAQ system for bunch diagnostics

In parallel to the feasibility study of tomography the online system for the diagnostics using FCT was developed. This system consists of the FAIR specified VME based DAQ with FESA framework based software and Java GUI. The system was successfully tested in 2012 [3].

The length of the synchrotron cycle can ranges up to several seconds. At high sampling rates it will lead to a large amount of raw data. Data reduction can be achieved by triggering the DAQ system on a rate divider output to which the RF master oscillator is connected.

Previously the data reduction was realized using NIM modules. A new FPGA based single board electronics card covering multiple-event functionality including the timing receiver was designed, tested and will be assembled. The board is shown in Fig.2.

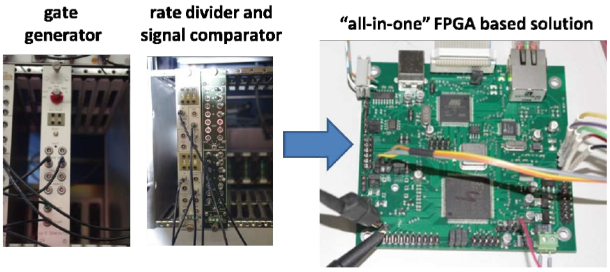

Figure 2: FPGA based single board electronics (right) for multiple-events triggering to replace NIM based solution (left).

References

[1] O. Chorniy, H. Bräuning, T. Hoffmann, H. Reeg, A. Reiter, "A FESA DAQ for Fast Current Transformer in SIS 18", IBIC2013, Oxford, September 2013

[2] S. Hancock, P. Knaus, M. Lindroos, Tomographic measurements of longitudinal phase space density, EPAC98.

[3] O. Chorniy, H. Bräuning, T. Hoffmann, H. Reeg, A. Reiter, M. Witthaus, "New Data Acquisition for Beam Transformers in SIS18 and Transfer Lines", GSI Scientific Report 2013

DOI:10.15120/GR-2015-1-FG-UNILAC-17

Modernisation of the 108 MHz RF systems of the UNILAC post stripper section

B. Schlitt, G. Eichler, S. Hermann, M. Hörr, A. Schnase, G. Schreiber, W. Vinzenz
GSI, Darmstadt, Germany

For the FAIR facility, all ion beams heavier than protons will be provided by the existing UNILAC for injection into the SIS18 synchrotron. Since the UNILAC is in operation successfully since about 40 years, an extensive modernisation of the post stripper RF systems and a replacement of the Alvarez DTL are planned to assure reliable operation for FAIR as well as the required beam quality [1,2]. To match the FAIR conditions, the UNILAC will be converted into a short-pulse accelerator, the RF beam pulse length and duty cycle being reduced from up to 6 ms / 30 % to ≤ 2 ms / ≤ 2 %. Long duty cycle beams will not be provided anymore.

Modernisation of the existing RF systems

Substantial modernisations of the existing post stripper RF systems are planned:

- The old control components of the existing 1.7 MW high power amplifier (HPA) stages equipped with RS 2074HF tubes to feed the five Alvarez tanks will be substituted by state-of-the-art PLCs. Modern fast measurement and interlock systems and commercial control grid power supplies will replace the old equipment.
- 120 – 150 kW solid state driver amplifiers will replace the existing tube drivers. A call for tenders for a prototype was started recently.
- The original relay based control of the 1 MVA anode power supplies for the HPAs will be substituted by modern PLC systems.
- Substitution of the resonance tuning circuits and of the LLRF systems by new developments.

Extensive preparations and developments of these tasks as well as the procurement of various components were performed in 2014. A stepwise realisation of major measures is planned during longer shutdown periods of the GSI accelerators during 2015 to 2017.

New 1.8 MW cavity amplifier prototype

On a long-term schedule, a replacement of the existing high power amplifiers is considered. The development and manufacturing of a 1.8 MW cavity amplifier prototype was ordered to Thales Electron Devices, based on a Thales TH 558SC tetrode, which is widely used worldwide for broadcast transmitters as well as for scientific applications. Thus, there is no known risk concerning the long-term availability of this tube for the coming decades. The design of the cavity amplifier was almost finished by Thales in 2014 (Fig. 1). Manufacturing, RF tests, and delivery of the amplifier are scheduled for 2015. A test bench will be prepared at the UNILAC RF gallery allowing operation of the new amplifier either on a water dummy load or on one of the Alvarez cavities.

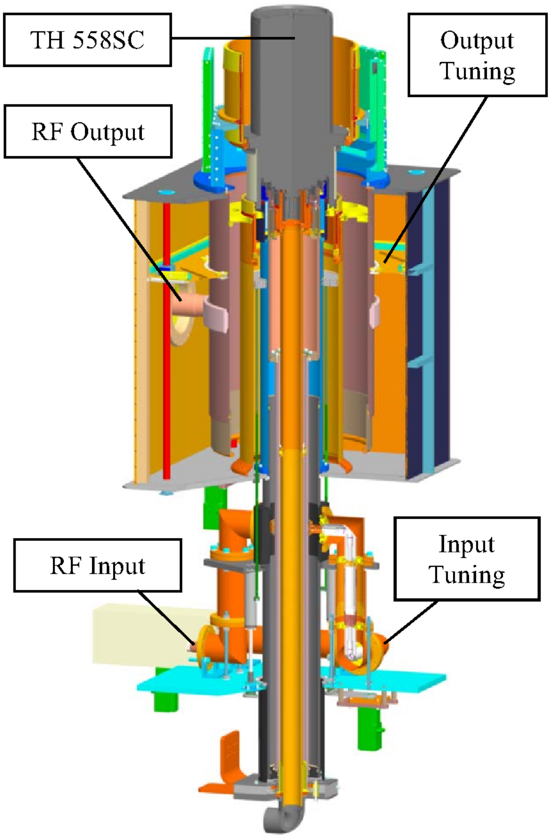

Figure 1: Sketch of the 1.8 MW high power amplifier cavity prototype designed by Thales (by courtesy of Thales Electron Devices, Thonon, France).

D-LLRF system tests

A digital low-level RF (d-LLRF) system designed by industry for 216 MHz linac RF systems for particle therapy facilities [3] was adapted by the supplier to an operating frequency of 108 MHz and was integrated into an existing 160 kW amplifier at GSI [1]. It was tested for RF amplitude and phase control of a single-gap resonator at the UNILAC including ion beam tests using 1.3 mA $^{181}\text{Ta}^{24+}$ beams. Stable operation was achieved within a limited amplitude range and beam loading could be partly compensated by the digital control unit [1]. Further improvements and tests of the system are planned.

References

[1] B. Schlitt, M. Hoerr, A. Schnase, G. Schreiber, and W. Vinzenz, RF system development for the new 108 MHz heavy ion high-energy linac at GSI, LINAC2014, Geneva, Switzerland, TUPP058 (2014).
[2] S. Mickat et al., this report.
[3] Ampegon AG, Turgi, Switzerland.

DOI:10.15120/GR-2015-1-FG-UNILAC-18

Results of the experiments on emittance transfer EMTEX

M. Maier, S. Appel, Y. El Hayek, P. Gerhard, L. Groening, S. Mickat, A. Seibel, H. Vormann, M. Vossberg, C. Xiao

GSI, Darmstadt, Germany

Introduction

EMTEX is an experimental setup to proof the principle of transverse emittance partitioning on an ion beam. According to simulations it is possible to transfer emittance by changing only the magnetic field of a solenoid with a charge state changing stripper inside. The change of charge state in the solenoid changes the set of eigen-emittances and the skew quadrupoles serve to remove inter-plane correlations. The field strength of the solenoid determines the amount of transfer between the eigen-emittances. A detailed description of the concept and the beam line itself is given in [1].

Experimental setup

Besides some matching quadrupoles, the setup shown in Figure 1 consists of a stripping foil inside a magnetic solenoid field to couple the transverse planes and for the emittance transfer. Behind the solenoid a skew quadrupole triplet rotated by 45° is used to remove the coupling.

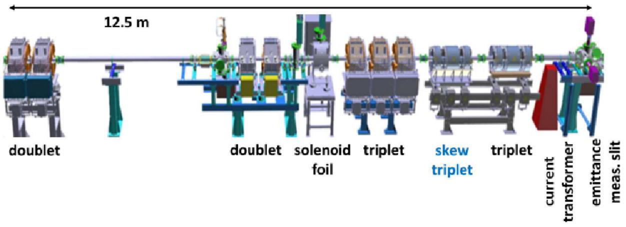

Figure 1: Beam line of EMTEX (Emittance Transfer Experiment) in the transfer channel of GSI.

Results

For the experiment a low intensity beam of $^{14}N^{3+}$ at 11.4 MeV/u was fully stripped to $^{14}N^{7+}$ in a 200µg C-foil placed at the centre of the solenoid. For each solenoid setting full transmission was preserved and the emittances were measured for both planes.

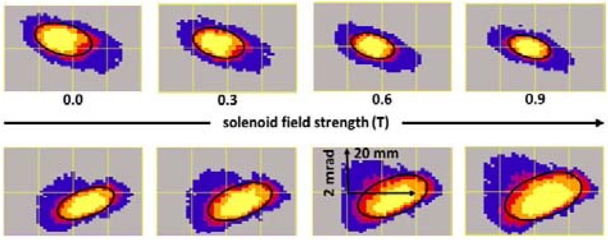

Figure 2: Vertical (upper) and horizontal (lower) phase space distribution measured behind EMTEX for varied solenoid field strength. The black ellipses represent the 4*rms emittances.

Figure 2 shows the measured emittances behind EMTEX for different solenoid field strengths. All other magnet settings were kept constant and the Twiss parameters remained constant. Yet for these solenoid field settings the emittance partitioning changes and, as shown in Figure 3, matches the simulation results [2] very well. For this reason the multi turn injection efficiency into SIS18 has been investigated using this technique [3]. As expected, the reduced horizontal emittance directly translates into increased multi turn injection efficiency shown in Figure 4.

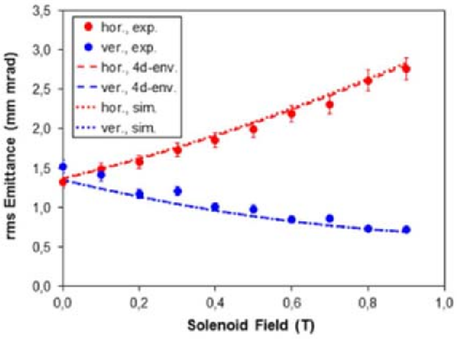

Figure 3: Measured transverse emittances behind EMTEX for different solenoid field strength compared to the simulations.

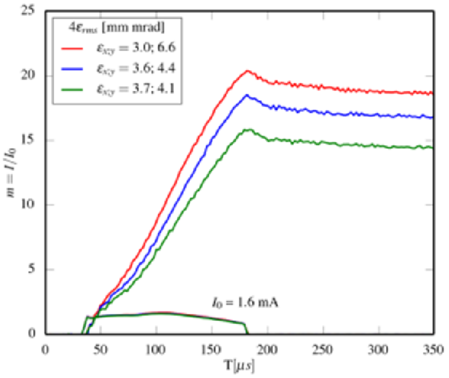

Figure 4: Improved multi turn injection efficiency using EMTEX.

Outlook

To quantify the possible gain factor of this technique the limits should be investigated. This could be achieved by increasing the macro pulse length and thus the injection time above the regularly used 150µs.

References

[1] C. Xiao, et al. PRSTAB **16**, 044201 (2013).
[2] L. Groening et al., PRL **113**, 264802 (2014).
[3] S. Appel, GSI Report 2013-03 (2013).

---

*Work supported by: BMBF-Projekt 05E12CD1
*m.maier@gsi.de

DOI:10.15120/GR-2015-1-FG-UNILAC-19

Status of the High Gradient CH – Cavity*

Ali Almomani[#] and Ulrich Ratzinger
IAP – Goethe Universität, Frankfurt am Main, Germany

This pulsed linac activity aims on compact designs and on a considerable increase of the voltage gain per meter. A high gradient CH – cavity operated at 325 MHz was developed at IAP – Frankfurt. The mean effective accelerating field for this cavity is expected well above 10 MV/m at β = 0.164. This cavity is developed within a funded project. The results might influence the rebuilt and a later energy upgrade of the UNILAC – Alvarez section. Another motivation is the development of an efficient pulsed ion accelerator for significantly higher energies like 60 AMeV. The new GSI 3 MW Thales klystron test stand will be used for the cavity RF power tests. Detailed studies on two different types of copper plating will be performed with this cavity. The first measurement results for this cavity will be presented.

Introduction

Conventional DTL's are seriously limited in maximum field gain by thick walled drift tubes for housing focusing elements. This geometry causes extended parallel surfaces around the gaps loaded by high electric fields. The multipacting probabilities as well as the stored field energies are rather high at these cavities resulting in a reduced field gain. Additionally, maximum achievable electric fields are reduced by the presence of magnetic fields [1].

This paper is focusing on the development of CH – cavities with a high field gradient. One main goal of this work is to prepare for a possible later energy upgrade of GSI – Unilac, which will in future serve as heavy ion injector for the FAIR project.

CH – Cavity Design

At IAP – Frankfurt, a 7 gap CH – cavity (Figure 1) operated at 325 MHz with constant β=0.164 has been developed and expected to have a field gradient of about 13.3 MV/m [2-4]. This cavity was built in NTG GmbH and was delivered to IAP in December 2014. The main parameters of this cavity are given in table 1.

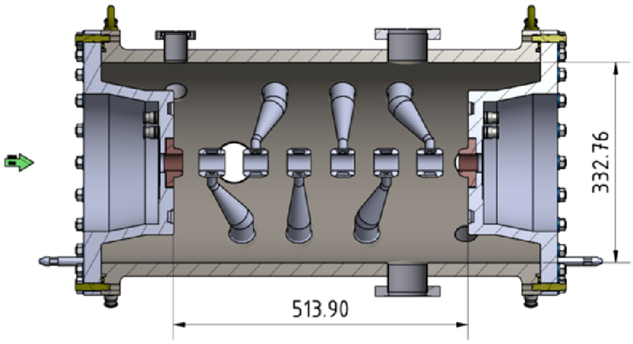

Figure 1: A 3D schematic view of the CH – cavity.

The geometry was optimized for modest surface peak fields – reaching up to 97 MV/m at very small spots on the drift tube edges.

The CH–cavity was built from stainless steel (Figure 2) and will be galvanically copper plated on its inner surface. This will be a challenge for such geometry. The cavity cylinder will contain no screwed connections and the end flanges are sealed by metal joints. Only the end half tubes are from massive copper.

Special care will be taken for the galvanic copper plating of the cavity. Two processes with different bath ingredients will be tested against each other at high rf power levels. Currently, the cavity was sent to Galvano-T for a first copper plating and is expected to be resent by end of March 2015.

Table 1: Main Parameters of the High Field CH – Cavity	
Number of Gaps	7
Frequency (MHz)	325.2
Voltage Gain (MV)	6
Eff. Accel. Length (mm)	513.9
Eff. Accel. Field (MV/m)	13.3
Power Loss (MW)	1.76
Eff. Shunt Impedance (MΩ/m)	52.15
Q_0 – value	12500
Drift Tube Aperture (mm)	27

Figure 2: The 325 MHz high-field cavity before the copper plating.

Conclusion

CH- type cavities may allow for a significant cost and size reduction of future ion linacs in the energy range up to about 100 AMeV.

Detailed investigations on the two different types of copper plating can be performed on this cavity and by using the GSI high power 325 MHz test stand driven by a 3 MW klystron.

References

[1] D. Stratakis et al., NIM A 620, 147–154 (2010).
[2] A. Almomani et al., PRST– AB **15**, 051302 (2012).
[3] A. Almomani et al., IPAC 14, THPWO012 (2014).
[4] A. Almomani et al., LINAC 14, THPB006 (2014).

---

* Work supported by BMBF, contract No. 05P12RFRB9.
[#] a.almomani@iap.uni-frankfurt.de

DOI:10.15120/GR-2015-1-FG-UNILAC-20

4 K and 2 K measurements on the 325 MHz CH-cavity *

M. Busch[†1], *F. Dziuba*[1], *H. Podlech*[1], *U. Ratzinger*[1], *W. Barth*[2,3], *and M. Amberg*[1,3]
[1]Institut für Angewandte Physik, Goethe Universität, Frankfurt; [2]GSI, Darmstadt; [3]HIM, Mainz

At the Institute for Applied Physics (IAP), Frankfurt University, a superconducting 325 MHz CH-Cavity has been designed and built. The 7-cell cavity features a geometrical β of 0.16, corresponding to a beam energy of 11.4 AMeV. The design gradient is 5 MV/m. Main novel features of this resonator are a compact design, low peak fields, easy surface processing and power coupling. Furthermore a new tuning system based on bellow tuners inside the resonator will control the frequency during operation [1]. After the final preparation steps rf measurements at 4 K and 2 K have been performed at the cryo-lab of the Institute for Applied Physics with promising results.

Setup at IAP Cryo-Lab

In April the 325 MHz CH-Cavity returned to IAP after final BCP and HPR at Research Instruments. Then the fully equipped cavity with 40 TLD and four thermal probes has been lowered down the 3 m deep vertical cryostat for power tests (s. Figure 1). After initial pressure issues due to a potential virtual leakage a final pressure of $8 \cdot 10^{-10}$mbar could be achieved. Multipacting conditioning proceeded smoothly.

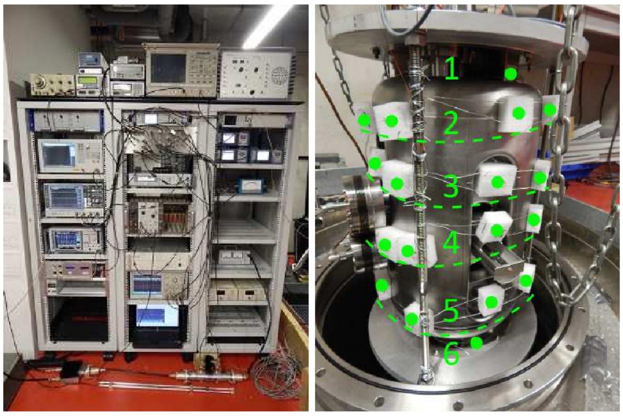

Figure 1: Measurement setup at the cryo-lab. *Left*: Fully equipped racks. *Right*: Array of the TLD on the cavity surface.

Results

The evaluation of the TLD showed only weak radiation events due to field emission after 10 hours of cumulated heavy operation. A small field emitting site is suspected at the bottom of the cavity tank (s. Figure 2). Further surface processing should decrease emission activity continuously. The measured Q vs E curve showed a maximum achievable gradient of 8.5 MV/m at 4 K. After cooling down to 2 K the max field level reached up to 14.1 MV/m limited by thermal quench due to a possible local defect (s. Figure 3) [2].

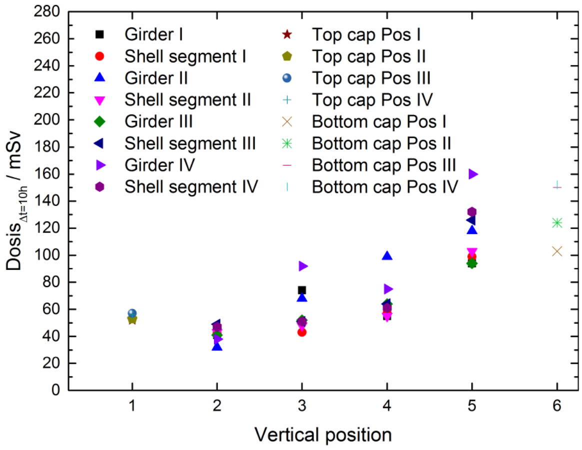

Figure 2: Evaluation of the TLD dosis for the 40 modules.

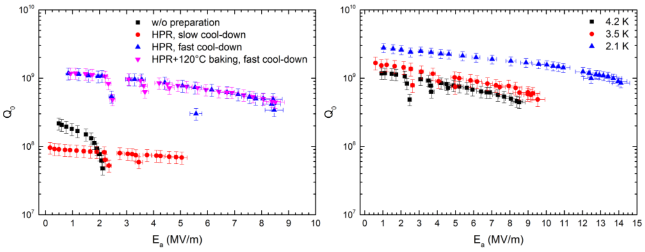

Figure 3: *Left*: Q vs E curve for 4 K measurements and different processed surface qualities. *Right*: Measurements performed at 2 K.

References

[1] M. Amberg, K. Aulenbacher, W.A. Barth, S. Mickat, M. Busch, F.D. Dziuba, H. Podlech, U. Ratzinger, "Structural Mechanical Analysis of Superconducting CH-Cavities", SRF 2011, Chicago, USA.

[2] M. Busch, F. Dziuba, H. Podlech, U. Ratzinger, M.Amberg, "Cold Power Tests of the sc 325 MHz CH Cavity", LINAC 2014, Geneva, Switzerland.

---

* Work supported by GSI, BMBF Contr. No. 06FY7102

† busch@iap.uni-frankfurt.de

DOI:10.15120/GR-2015-1-FG-UNILAC-21

Accelerator operation report

S.Reimann[1], *P.Schütt*[1]
[1]GSI, Darmstadt, Germany

This report describes the operation statistics of the GSI accelerator facility of the year 2014. The information is based on the data of the GSI electronic operation logbook OLOG [1] which allows a detailed evaluation of operation statistics especially for the time-sharing operation mode of the accelerators.

General Overview

After a long (14 months) shutdown period, which already began in 2012, the re-commissioning started in January. From January till November, two major beam time blocks were scheduled, which resulted in an operating time in the same order of magnitude as in 2012. In total, the SIS has been operated for 5832 hours and the UNILAC for 6432 hours (1032 hours are included for the commissioning of the accelerators after shutdown).

The intermediary shutdown period lasted from May 19th till June 24th. Because of performance issues and the obvious misalignment of the ring, the SIS shutdown was brought forward to May 2nd. The break was used to completely realign the SIS. In addition an aperture limiting piece of aluminium foil could be localized and removed from the vacuum chamber.

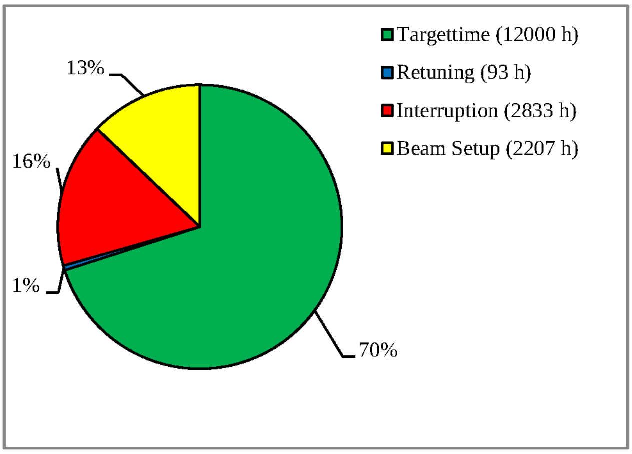

Figure 1: Distribution of overall beam time for all experiments

Figure 1 shows the overall beam time of the whole facility. In total 12000 hours of beam-on-target-time were successfully delivered to the different experiments, which is 70% of total beam time (76% in 2012).

The percentage of interruption time increased by 14%, you find the absolute numbers for 2012 and 2014 in Table 1. Similarly the percentage of the time needed for beam setup increased by 30%. Main reason for this gain was the complicated beam time schedule and the higher percentage of accelerator experiments (22%). At the UNILAC 1575 hours of beam time have been used for accelerator experiments, at the SIS there were 1798 hours and at the ESR 390 hours for accelerator experiments, which is in total an increase by a factor of 6 compared to 2012. At the UNILAC it is even a factor of 8.

Table 1: Overall beam time of the accelerator facility

	2014	2012
Integral target time for all experiments	**12000 h**	12105 h
Beam Setup	**2207 h**	1656 h
Time for retuning	**93 h**	102 h
Time of interruption	**2833 h**	2323 h
Total beam time	**17133 h**	16220 h

Operation for Experiments

Figure 2 gives an overview of target time for different experimental areas. The fraction of the beam branches of the UNILAC are marked in blue, the ESR in green and the different experimental caves behind the SIS are displayed as orange slices. Details corresponding to the different experimental programs are given in [2].

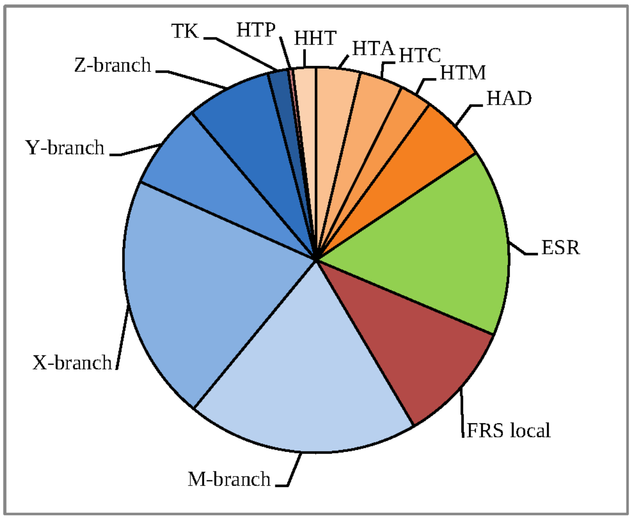

Figure 2: Distribution of target time to the different experimental areas

UNILAC Experiments

Details of the beam time for UNILAC experiments are shown in Table 2. Over the year 23 different experiments have been performed at the UNILAC. In total 6782 hours of target time have been achieved. The main user was the Material Science (2097 hours). The fraction of target time remained almost constant compared to 2012 but an increase of time for accelerator setup was observed.

DOI:10.15120/GR-2015-1-FG-GENERAL-01

Table 2: Beam delivery to UNILAC experiments

	Time	Ratio
Target time for experiments	6782 h	75,2%
Time for retuning	48 h	0,5%
Accelerator setup	1008 h	11,2%
Ion source service	407 h	4,5%
Unscheduled down time	774 h	8,6%
Total beam time	**9018 h**	**100%**

SIS/ESR Experiments

The SIS delivered beams to 19 fixed target experiments and to 7 experiments at the ESR. In total 5219 hours of target time have been achieved. The fraction of target time decreased by more than 10% compared to 2012, which was mainly caused by the increased unscheduled downtime. A more detailed overview is given in Table 3.

Table 3: Beam delivery to SIS/ESR experiments

	Time	Ratio
Target time for experiments	5219 h	64,3%
Time for retuning	45 h	0,6%
Accelerator setup	1199 h	14,8%
Ion source service	114 h	1,4%
Unscheduled down time	1538 h	19,0%
Total beam time	**8115 h**	**100%**

In 2014 the target time for the ESR (direct beam and beam via FRS) increased to 2106 hours. For about 1359 hours the beam was delivered to the local experiments of the FRS. 747 hours of beam time were scheduled for HAD, another main user at the SIS.

Accelerator Operation

Table 4 shows more detailed all unscheduled down time events. In comparison to 2012 the downtime increased by 47%. In addition to the previously described SIS problems, which are excluded from these statistics, a water leak of the newly installed MA-cavity stopped the SIS operation for several days.

The total downtime of power supplies and controls were increased by more than a factor of two, compared to 2012. The main reason for control problems was the high maintenance requirement for old hardware and legacy software during the beam time. The time spent for operation failures increased slightly, which was to be expected in the face of the complex operating mode (switching experiments several times per day) and the special settings for the accelerator experiments.

Table 4: Statistics of all unscheduled down time events

	Down time	No. of events
Power supplies	580 h	412
Vacuum and structures	438 h	119
Beam diagnostics	31 h	19
Operation	38 h	38
Safety-/ Interlock system	38 h	36
Ion Sources	143 h	53
RF system	328 h	434
Controls	164 h	70
Infrastructure	40 h	16
Others / ambiguous	186 h	89
Total of unscheduled down time	**1986 h**	**1286**

During 2014, 19 different isotopes have been accelerated. Figure 3 shows the operation time for each isotope. Besides nitrogen, the heavy elements beyond samarium were dominating the ion source statistics.

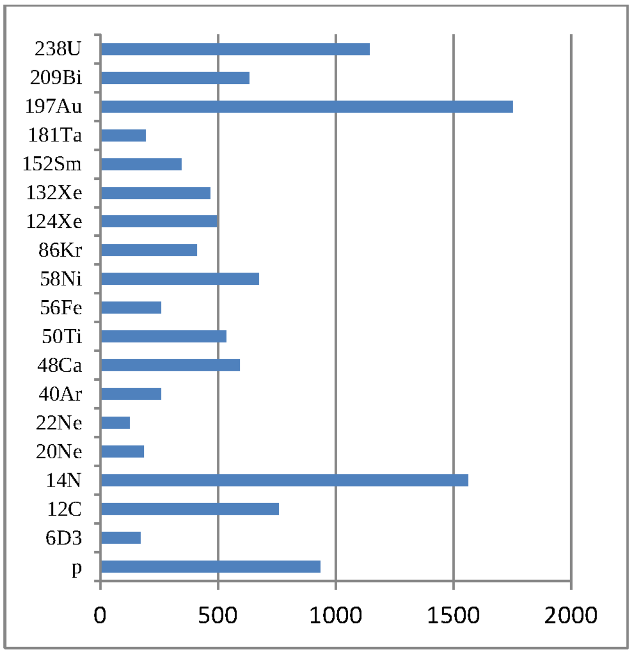

Figure 3: Total beam time for different ion species

References

[1] P.Schuett, the GSI Operation Logbook OLog, WAO2010 (http://wao10.komac.re.kr/PDF/O-17.pdf)
[2] Report of beam time coordinator, this report

DOI:10.15120/GR-2015-1-FG-GENERAL-01

Status of the cw-LINAC demonstrator project

V.Gettmann[2], *W.Barth*[1, 2], *S.Mickat*[1, 2], *M.Amberg*[1], *H.Podlech*[3],
U.Ratzinger[3], *F.Dziuba*[3], *and K. Aulenbacher*[1, 4]
[1]GSI, Darmstadt, Germany; [2]HIM, Institute Mainz, Germany; [3]IAP, Frankfurt, Germany; [4]IKP, Mainz, Germany.

Cryostat and cavity

The Demonstrator is the first section of the proposed cw-LINAC [1]. The fabrication of the Demonstrator is still in progress. The complete system is expected to be at GSI in 2015.

Meanwhile the inner structure of the cavity is fabricated (Fig. 1). The operation frequency was checked at Research Instruments (RI) site during the whole fabrication process dependent on mechanical stress from vacuum, and from cooling down. Frequency shifts are not allowed and has to be compensated by an adequate setting of the static tuners length [2]. Also the change in volume after three times buffered chemical polishing (BCP) has to be taken into account during the tuning process. The chemical treatments etch in total 75 µm of the cavity's surface. After the chemical treatments the cavity is high pressure rinsed and sealed under cleanroom conditions for shipment to the IAP. Here RF performance tests in a cold environment are planned. After successful tests the cavity is sent back to RI for the final step in fabrication. The helium jacked out of titanium as well as the suspending blocks will be welded to the cavity.

Figure 1: The inner structure of the CH-cavity.

The cryostat itself is ready for assembling at Cryogenic Ltd. Site. Most of the parts are on site (Fig.2). The delay in delivery is mainly caused by finding an adequate provider for the µ-metal shield. According to an updated schedule the overall system including the two solenoids and dummy is expected to be completed until May 2015.

Setup at GSI-HLI

The test environment at GSI-HLI is prepared almost. Recently the control room is arranged for the 5kW-RF-Amplifier for the CH-cavity and the 12kW-RF-Amplifier for the cw Buncher. The additional cw buncher cavity is under development an expected in June 2015. Only the RF-piping is outstanding. The liquid helium supply is rearranged and detailed. The 3000 litre tank will be located near the x-ray radiation protection shelter of the demonstrator, and connected via flexible pipe to the cryostat. The exhaust helium gas will be heated, counted via gas meter, and as planned collected in a 25³m recovery balloon.

Figure 2: The cryostat and the two sc solenoids are ready for assembling at Cryogenic Ltd, London.

References

[1] V. Gettmann et al. STATUS OF THE SC CW-LINAC DEMONSTRATOR INSTALLATION, Proceedings annual report 2013, GSI, Darmstadt, Germany.

[2] F. Dziuba et al. A Superconducting 217 MHz CH Cavity for the CW Demonstrator at GSI, Proceedings of SRF 2013 Paris, France.

DOI:10.15120/GR-2015-1-FG-GENERAL-02

Status of the superconducting 217 MHz CH-cavity*

M. Basten[#,1], *M. Amberg*[1,3], *K. Aulenbacher*[3,4], *W. Barth*[2,3], *M. Busch*[1], *F. Dziuba*[1], *M. Heilmann*[2], *D. Mäder*[1], *S. Mickat*[2,3], *H. Podlech*[1]

[1]Frankfurt Universtiy, 60438 Frankfurt, Germany; [2]GSI Helmholtzzentrum, 64291 Darmstadt, Germany; [3]Helmholtz-Institut Mainz (HIM), 55099 Mainz, Germany; [4]KPH Mainz University, 55128 Mainz, Germany

Presently the demonstrator for the sc cw-LINAC at GSI is under construction and its successful beam operation will be the first milestone realizing the new sc cw-LINAC at GSI [1]. The construction of an advanced demonstrator will be the second milestone towards the sc cw-LINAC at GSI. The presently design of the sc cw-LINAC consists of the demonstrator as first cavity and 4 to 5 additional cryomodules with 2 CH-cavities per cryomodule [2,3]. The design of the advanced demonstrator will be used for all cavities in the sc cw-LINAC after the demonstrator. The cavity is designed and optimized for high power applications, consisting of 8 accelerating cells. The design gradient is 5 MV/m. Its frequency is the second harmonic of the High Charge Injector (HLI) at GSI, Darmstadt. Table 1 shows the main parameters of the sc 217 MHz CH-cavity. In Figure 1 the layout of the sc 217 MHz CH-cavity is depicted.

Cavity Design

The design of the cavity is based on 8 equidistant gaps without girders and with stiffening brackets at the front and end cap to reduce pressure sensitivity. The new design avoids girders because they lead to high fabrication costs and extended fabrication duration. Additionally the girders reduce the mechanical stability of the cavity caused by a break of the cylindrical symmetry. The design of the advanced demonstrator without girders is cylindrically symmetrical which leads to significantly higher stability. Additionally the stiffening brackets at both ends of the cavity increase the mechanical stability of the cavity so that the pressure sensitivity is below 5 Hz/mbar.

Parameter	Unit	
β		0.069
Frequency	MHz	215.5
Accelerating cells		8
Length (βλ-definition)	mm	381.6
Cavity diameter	mm	412
Cell length	mm	47.7
Aperture diameter	mm	30
Static tuner		3
Dynamic bellow tuner		2
Wall thickness	mm	3-4
Accelerating gradient	MV/m	5
E_p/E_a		5.2
B_p/E_a	mT/(MV/m)	8.5
G	Ω	51
R_a/Q_0		1045

Table 1: Specifications of the 217 MHz CH-cavity

Figure 1: Layout of the sc 217 MHz CH-cavity.

Status

The basic design of the 217 MHz CH-cavity was finished in 2014. Several simulations with CST-Microwave-Studio have been performed to determine parameters as the optimum drift tube length, optimum stem width and cavity diameter [4]. The missing girders in the 217 MHz-cavity require a new design for the dynamic and static tuners. Because of that many simulations concerning the layout and performance of the bellow tuners have been performed to find the optimum geometry. The call for tender started in december 2014 and will end on february 2015. So the communication with the company will start in february 2015 and will be followed by the production start.

References

[1] F. Dziuba, M. Amberg, K. Aulenbacher, W. Barth, M. Busch, H. Podlech, U. Ratzinger, S. Mickat, Superconducting CH Cavities for Heavy Ion Acceleration, in Proc. of IPAC'13, Shanghai, China, p. 3794-3796 (2013)

[2] W. Barth, K. Aulenbacher, F. Dziuba, M. Amberg, V. Gettmann, S. Mickat, H. Podlech, U. Ratzinger, Further R&D for a New Superconducting cw Heavy Ion Linac@GSI, in Proc. of IPAC'14, Dresden, Germany, p. 3211-3213 (2014)

[3] H. Podlech, Proposal for a Superconducting 217 MHz CH-Cavity, institute report: IAP-ACCC-01122013 (2013)

[4] CST Microwave Studio, http://www.cst.com

---

* Work supported by HIM, GSI

[#]Basten@iap.uni-frankfurt.de

DOI:10.15120/GR-2015-1-FG-GENERAL-03

Performance demonstration of the non-intercepting Bunch Shape Monitor at UNILAC *

B. Zwicker[1,2], *C. Dorn*[1], *P. Forck*[1,2], *O. Kester*[1,2], *and T. Sieber*[1]
[1]GSI, Darmstadt, Germany; [2]IAP, Frankfurt, Germany

A non-invasive Bunch Shape Monitor (BSM) is foreseen to determine the longitudinal bunch structure with a phase resolution of 1.0°, with respect to the 325 MHz acceleration frequency of the FAIR p-LINAC [1]. It is intended to ensure proper longitudinal matching of the accelerating structures. The presented device is based on the creation of secondary electrons by the ion beam passing a section of high local nitrogen pressure. The secondary electrons are accelerated by an external driving potential towards a time-resolved imaging system [2].

Beam-based Measurements

The non-invasive Bunch Shape Monitor (BSM) has been tested at the UNILAC with several ion beams at 11.4 MeV/u and beam currents in the range from 0.08 to 1 mA. Extensive parameter studies have been executed in 2014. Various parts of the hardware were modified in 2013 and the improved functionality of the device has been clearly demonstrated [3]. For the applied beam settings the BSM is able to obtain profiles down to 250 ps rms with a resolution of 34 ps [4]. As expected, non-Gaussian profiles have been obtained.

By using a single gap resonator (SGR) as a rebuncher longitudinal profile changes have been investigated. This matching is confirmed with a phase probe, while the applied power to the SGR is varied. For the beam tests the ER10 has been used, which implies a distance of 55 m to the location of the BSM (TK5 DK1). The focal length of the ER10 has been varied over several tens of meters to ensure the transmission of the focal point through the location of BSM.

In dependence of the focal length the obtained profile rms widths are depicted in Figure 1. The applied voltage has been varied from 0.53 MV to a feasible maximum of 1.0 MV. The focal length f depends on the applied electric gap voltage U_0 to $U_0 \propto 1 / f$. The BSM is able to detect differences even with a small step size of 0.012 MV. For a value of 0.87 MV the minimum is obtained. From linear beam optics a parabolic dependence of the square of the rms width is expected. For better visualization the rms width is depicted, which should match the square root of this parabola fit. Besides width variation, the bunch shape itself changes and reveals a rather complex composition. This is a hint, as expected, of a distorted phase space distribution of the beam due to the IH-structure's KONUS dynamics. It is foreseen to determine an approximated longitudinal emittance with this measurement by using the parabolic fit parameters for σ^2 over 1/f.

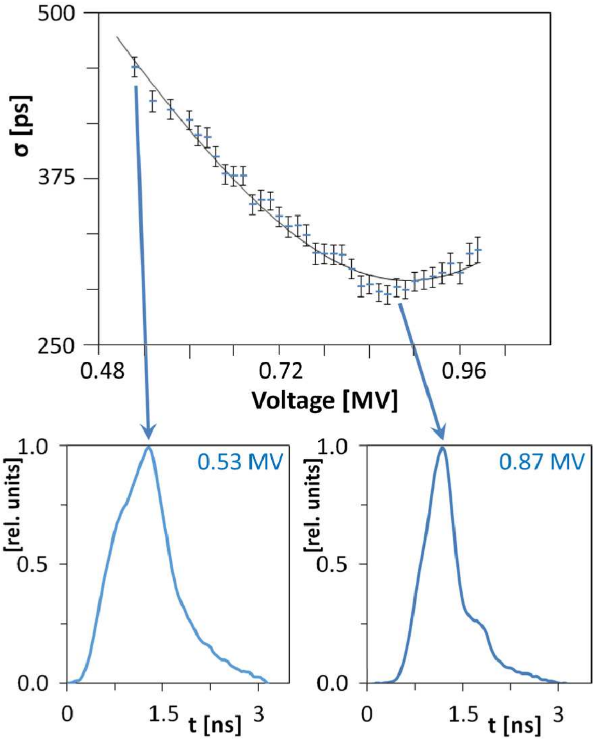

Figure 1: Longitudinal profile widths (rms width of a single Gaussian fit) in dependence of the focal length of single gap resonator ER10. Below are two bunch shapes depicted for different focal length. A non-Gaussian shape is visible. Setting: U^{28+} at 11.4 MeV / u, I = 0.5 mA , τ = 95 μs, p = $5 \cdot 10^{-6}$ mbar, P = 25 W, 16 averages.

References

[1] L. Groening et al., LINAC'12, Tel-Aviv, THPB034, p. 927

[2] P. Forck et al., DIPAC'05, Lyon, p. 48

[3] B. Zwicker et al., IBIC'13, Oxford, MOPC36

[4] B. Zwicker et al., IBIC'14, Monterey, TUDP07

---

* Supported by EU-Project CRISP, WP3 T1 Non-intercepting Bunch Shape Monitors

DOI:10.15120/GR-2015-1-FG-GENERAL-04

Uranium high current development at UNILAC

Winfried Barth[1,2]*, Aleksey Adonin*[2]*, Christoph E. Düllmann*[1,2,3]*, Peter Gerhard*[2]*, Manuel Heilmann*[2]*, Ralph Hollinger*[2]*,*
Egon Jäger[2]*, Jadambaa Khuyagbaatar*[1,2]*, Joerg Krier*[2]*, Paul Scharrer*[1]*, H. Vormann*[2]*, Alexander Yakushev*[2]*,*
Stepan Yaramyshev[2]

[1] Helmholtz Institute Mainz, Germany
[2] GSI Helmholtzzentrum für Schwerionenforschung, Darmstadt, Germany
[3] Johannes Gutenberg-Universität Mainz, Mainz, Germany

Previously a peak record had been achieved in 2007 (Fig.1), while 30% of the FAIR- U^{28+} beam current was accomplished at the end of the transfer line. Caused by a strong High Current Injector (HSI) performance degradation, up to October 2014 the available beam current dropped down to 13% of the design value only. After re-optimization of the complete front end system the HSI is again able to deliver a high uranium beam current. In a short run applying the new fast pulsed high density H_2-gas cell more than a factor of three higher U^{28+} beam current is now available at 1.4 MeV/u. The stripper performance could be optimized applying significantly higher target densities. The new U^{28+} intensity record exceeds the latest peak record by 56% (Fig. 1).

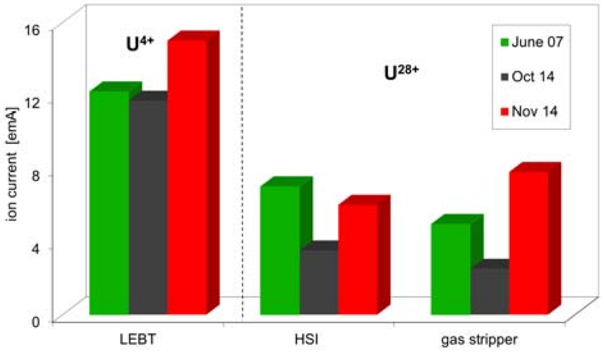

Fig. 1: Achievement of a new uranium beam (28+) intensity record at GSI-HSI and gas stripper section. The former U^{28+}-peak value (2007) was exceeded by 56%.

A new fast pulsed high density gas cell [1] was successfully commissioned with uranium beam from the GSI HSI. Besides, the entire Injector system was optimized for high beam intensity operation. A 25% higher U^{4+} beam current extracted by a newly developed multi aperture beam extraction system (VARIS ion source [2,3]) were used to optimize the Low Energy Beam Transport system and matching line to the RFQ. A beam current of 15.3 emA (Fig. 2) was available for injection into the RFQ. In particular the most sensitive Medium Energy Beam Transport section was optimized for high current high transmission beam transport applying a slightly different set of rf-parameters. With this the HSI was allowed for stable and reliable high current uranium operation. A careful matching of the high power (0.5 MW pulse power) U^{4+} beam to the gas stripper cell was accomplished resulting in a U^{28+} beam current of 7.7 emA (Fig. 2) after stripping and charge separation at 1.4 MeV/u.

Fig. 2: Beam transformer measurement after careful optimization of a VARIS-uranium beam.

The world intensity record for U^{28+} pulse operation could be reached after less than three days of beam time, including 15 hours beam time spent for commissioning of the H_2-gas cell-stripper. More than 50% of U^{28+}- FAIR intensity requirements (and 65% of beam brilliance) was achieved at 1.4 MeV/u. Increased beam currents for all heavy ions are expected - stripper tests are envisaged using Pb-, Au-, Ta-, Xe-, Kr-, CH_3-beams. An upgrade of the HSI [4-6] is potentially sufficient to meet the FAIR performance at the GSI-UNILAC. Further optimization of stripper performance should be started in an advanced machine experiment program. Beam acceleration up to 11.4 MeV/u and transport to SIS18 is the next step to confirm high intensity operation in the SIS18.

References

[1] Scharrer P., et al., Performance of a modified 1.4 MeV/u gas stripper for $^{238}U^{4+}$, GSI scientific report 2014.

[2] Hollinger R., et al., Status of Vacuum Arc Ion Source Development for Injection of High Current Uranium Ion Beams into the GSI Accelerator Facility, Nucl. Instrum. Meth., B 239 (2005) 227.

[3] Hollinger R., et al., Development of a Vacuum Arc Ion Source For Injection of High Current Uranium Ion Beam into the UNILAC at GSI, Rev. Sci. Instrum., Volume II, 2004.

[4] Kolomiets A., et al., Upgrade of the UNILAC High Current Injector RFQ, LINAC08, Victoria, BC, Canada, p. 136-138 (2008).

[5] Vormann H., et al., Straight injection of an intense uranium beam into the GSI high current RFQ, IPAC2014, Dresden, Germany, p. 3217-3219 (2014)

[6] Yaramyshev S. et.al., Advanced Beam Matching to a High Current RFQ, LINAC2014, Geneva, Suisse, to be published (2014).

DOI:10.15120/GR-2015-1-FG-GENERAL-05

Radiation-hard camera tests near the SIS18 extraction

B. Walasek-Höhne[1], *H. Bräuning*[1], *C. Dorn*[1], *R. Fischer*[1], *P. Forck*[1], *H. Graf*[1], *F. Hagenbuck*[1], *K. Höhne*[2], *T. Radon*[1], *U. Scheeler*[3], *C. Schmidt*[1], *M. Schwickert*[1], *K. Steiner*[1], *and J. Wohlers*[1]
[1]GSI, Darmstadt, Germany; [2]FAIR, Darmstadt, Germany; [3]MIT, Marburg, Germany

For imaging applications in the high radiation environment of heavy ion synchrotrons radiation-hard cameras are required. One possible candidate for such cameras at FAIR is the CCIR MegaRAD3 from Thermo Fischer Scientific. First measurements with this camera, which has been installed at the SIS18 extraction point, have been performed.

Technological advances in solid state camera design provide a wider choice of equipment for beam instrumentation. However, our previous experience with CCD based cameras has shown that their performance degrades during operation due to the background radiation (γ, neutrons, etc.) produced by the heavy ion beam (see Figure 1 left). Any semiconductor device operating in a radiation field suffers from degradation due to radiation damages. Energetic particles incident on the semiconductor bulk lose their energy due to ionizing and non-ionising processes as they travel through a given material. The ionising processes involve electron-hole pair production and subsequent energy deposition (dose) effects. The non-ionizing processes result in displacement damage effects, i.e. defects in the semiconductor lattice like vacancies and interstitials [1].

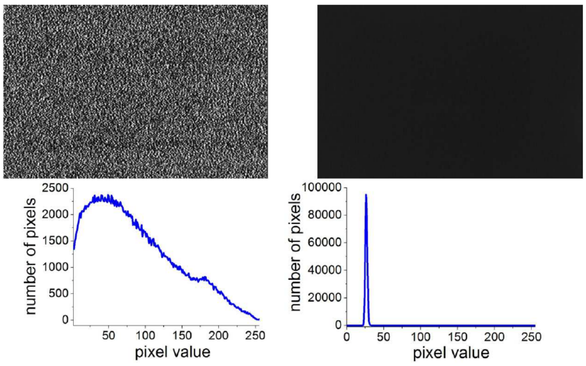

Figure 1: Dark images of the standard CCD camera Sony XC-ES30 (upper left) and the new radiation-hardened solid-state CID camera MegaRad3 (upper right) after a few weeks of irradiation with the corresponding histograms of pixel brightness below (bottom right, bottom left, respectively).

At the GSI SIS18 extraction point a great variety of particles with energy of up to few GeV/u is generated. At this location, where a high radiation level is observed, the CCIR MegaRad3 (8726DX7) radiation-hard solid-state CID (Charge Injection Device)-based camera was installed. According to the manufacturer [2] this device is tolerant to gammas, neutrons, high energy electrons and proton radiation to at least 3 MRad. Only in tests up to 14 MRad a noticeable degradation in the image quality has been reported by the manufacturer.

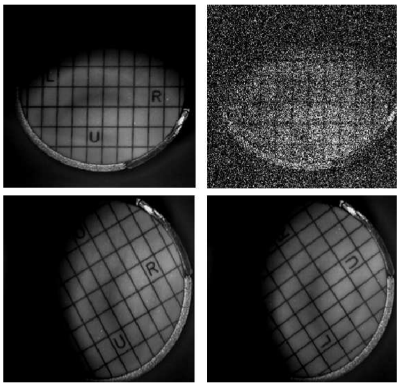

Figure 2: Original pictures of scintillating screen target with progressive level of accumulated dose. Upper left: standard CCD camera before test, upper right: standard CCD camera after few weeks of beam operation. Lower left: Rad-hard camera before test, lower right: standard Rad-hard camera after 8 months beam operation at SIS18.

In our tests, the camera has been placed near the SIS18 extraction. The camera is continuously running since November 2013. The accumulated dose impinging on the camera has been monitored by thermoluminescent dosimeters placed next to the camera. During this test, we found the image quality to be nearly the same after fifteen months of exposure to neutron (accumulated dose: 130 Sv) and γ (accumulated dose: 82 Sv) radiation. As shown in Figure 1 and Figure 2, no significant change in camera performance like loss of contrast and resolution was observed. A standard CCD camera at the same position was out of order due to irradiation within two weeks of operation.

Our first test with this radiation-hard solid-state CID-based camera is very promising. This device exhibits a significant improvement for operation in a radiative area environment as compared to the CCD and CMOS-based cameras. The performed tests show that the camera is not sensitive to radiation damage on the level observed at GSI. This makes this camera suitable for use in precise and reliable profile monitors of high energy heavy ion beams in the vicinity of beam extraction points, targets or beam dumps as well as other higher radiation environments expected at FAIR.

References

[1] S. Hutchins et al., “Radiation tests on solid state cameras for instrumentation” DIPAC 2005 `http://www.JACoW.org/`

[2] S. Bhaskaran, “Research and development efforts at CIDTEC cameras and imagers” 3rd DITANET School 2011 `http://indico.cern.ch/event/112220/contributions/`

DOI:10.15120/GR-2015-1-FG-GENERAL-06

Light output of inorganic scintillating screens induced by fast and slow extracted beams from SIS18*

A. Lieberwirth[1,2,#], *P.Forck*[2,3], *S. Lederer*[1], *W. Ensinger*[1]
[1]TU Darmstadt, Germany, [2]GSI, Darmstadt, Germany; [3]Goethe-Universität Frankfurt, Germany

Scintillating Screens are favoured devices to visualize the transverse beam profile during alignment and are foreseen for the HEBT at FAIR. For high energy ion beams extracted from SIS18 tests on the reproducibility of the scintillation process for different materials were performed to enable a proper choice for FAIR. Moreover, emission spectra were investigated as reported in [1].

Radiation hardness tests were carried out as well. The results concerning ceramic targets in comparison to measurements at UNILAC are summarized in [2].

Experimental Conditions

The investigations were performed with beams of protons, Nitrogen, Nickel, Xenon and Uranium as extracted from SIS18 with 300 MeV/u beam energy and intensities between 10^6 and 10^{10} particles per pulse. At the target location HTP seven different scintillating screens were irradiated in air (P43, P46, YAG:Ce, Chromium-doped and pure Aluminium Oxide). The measurements were performed in slow (300-400 ms) and fast extraction (1 µs) mode to analyze supposed saturation effects.

The scintillation light was recorded by a monochrome camera equipped with a remote-controlled iris and an optical grey filter (transmission ~5 %) to increase the measurement range.

Images with beam induced scintillation profile as well as background images were analyzed by a dedicated Python script to calculate light output (in particular sum of luminescent area) and beam profile characteristics as given by statistical moments. Moreover, a relative light yield was calculated as the light output per ion normalized to the deposited energy. This factor is used to compare the light emission from the targets with respect to the irradiation by different ion species.

Results

For all investigated ions, linearity between the light output with respect to the number of particles per pulse was observed for fast as well as for slow extraction, see Figure 1 exemplary for P43. Statistical moments were analysed in order to investigate changes of the beam reproduction during irradiation. Also the projected beam sizes were found to be independent from the amount of irradiating particles per pulse for each material, apart from variations by operative re-alignment.

The light yields of P43 phosphor for various projectiles relative to the protons light yield are shown in Table 1. A decrease as function of atomic number is clearly observable and the results show a different reaction on the impact of slow and fast extracted beam on the P43 screen. Generally, the light yield varies only by a factor 3 between light and heavy ions. The analysis for other targets is ongoing.

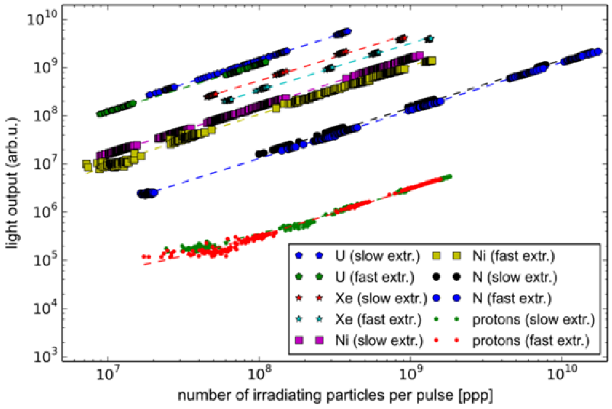

Figure 1: Light output of P43 phosphor screen induced by different ions. All projectiles were accelerated to 300 MeV/u and extracted in fast (1 µs) and slow mode (300-400 ms).

Table 1: Relative light yield of P43 phosphor screen for different projectiles. Proton induced light yield serves as reference. The beam energy at the target is given in brackets. In general ions were fully stripped at the target.

Projectile	Relative Light Yield (slow extr.)	Relative Light Yield (fast extr.)
p	1.00 (299 MeV/u)	1.00 (299 MeV/u)
N	0.97 (297 MeV/u)	0.85 (299 MeV/u)
Ni	0.66 (289 MeV/u)	0.44 (297 MeV/u)
Xe	0.56 (281 MeV/u)	0.34 (294 MeV/u)

Acknowledgements

The authors want to thank the GSI operation team for great support during beam time.

References

[1] A. Lieberwirth, et al., “Luminescence Spectra of Inorganic Scintillating Screens induced by Fast and Slow extracted Beams from SIS18”, GSI Scientific Report 2014.

[2] S. Lederer, et al., “Luminescence degradation behaviour of alumina irradiated with heavy ions of high fluences” GSI Scientific Report 2014.

---

[*] Work supported by BMBF, contract No. 05P12RDBJ.

[#] a.lieberwirth@gsi.de

DOI:10.15120/GR-2015-1-FG-GENERAL-07

Lumineschence spectra of inorganic scintillating screens induced by fast and slow extracted beams from SIS18*

A. Lieberwirth[1,2,#], *P.Forck*[2,3], *S. Lederer*[1], *W. Ensinger*[1]
[1]TU Darmstadt, Germany, [2]GSI, Darmstadt, Germany; [3]Goethe-Universität Frankfurt, Germany

The scintillation process of inorganic material is a subject of high interest for material science. To answer questions of material damage processes the analysis of emission spectra is a common tool to compare possible influence of different ionizing particles.

Results on the spectral emission of inorganic scintillators induced by high energy impact of heavy ions were obtained. The emission spectra show no significant variation within the investigated ranges of ion species and beam intensities.

Setup

At the high-energy experimental test bench HTP investigations on the luminescence spectra of inorganic scintillators were performed in the frame of machine experiments preparing for FAIR project. Altogether seven inorganic scintillating screens (P43, P46, YAG:Ce, Chromium-doped and pure Aluminium Oxide) were mounted behind a beam exit window in air and irradiated with different projectiles from proton to Uranium. All projectiles, i.e. protons, nitrogen, nickel, xenon and uranium ions, were extracted from SIS18 with a beam energy of 300 MeV/u and intensities between 10^6 and 10^{10} particles per pulse (ppp). The measurements were performed in slow (300-400 ms) and fast extraction (1 µs) mode to analyze supposed saturation effects.

Beam-induced scintillation of the target material was explored using an optical spectrometer setup (Horiba CP140-202 and appropriate lens) and recorded by a monochrome CCD camera (15.2 mm diagonal chip size). Simultaneously, the complete scintillation light output was measured with a different camera system, see [1].

Experimental Results

The analysis shows no significant variation in the structure of the emission spectra. Examples of YAG:Ce and P43 phosphor emission spectra are presented in Figure 1.

Despite the fact that the emission intensity increases with increasing number of irradiating particles per pulse, no change in the emission spectra could be observed over the complete irradiation period. Moreover, the light emission of the investigated target seems to be independent of ion species. Within the total irradiation of up to $5 \cdot 10^{13}$ accumulated particles of all investigated projectiles, the formation of defects within the material does not seem to be dominant in this high energy region (see also [2]). These findings are comparable to studies on the light emission induced by other projectiles, like X-ray [3] or photons [4].

Acknowledgements

The authors want to thank the GSI operation team for great support during beam time.

References

[1] A. Lieberwirth et. al., “Light Output of Inorganic Scintillating Screens induced by Fast and Slow extracted Beams from SIS18” GSI Scientific Report 2014.

[2] S. Lederer et. al., “High-temperature scintillation of alumina under 32 MeV $^{63}Cu^{5+}$ heavy-ion irradiation” submitted to NIM-B (2015).

[3] E. I. Gorokhova et al., "Luminescence and scintillation properties of Gd_2O_2S: Tb Ce ceramics." IEEE Transactions on Nuclear Science 52.6 (2005): 3129-3132.

[4] Yanagida, Takayuki, et al., "Evaluation of properties of YAG:Ce ceramic scintillators.", IEEE Transactions on Nuclear Science 52.5 (2005): 1836-1841.

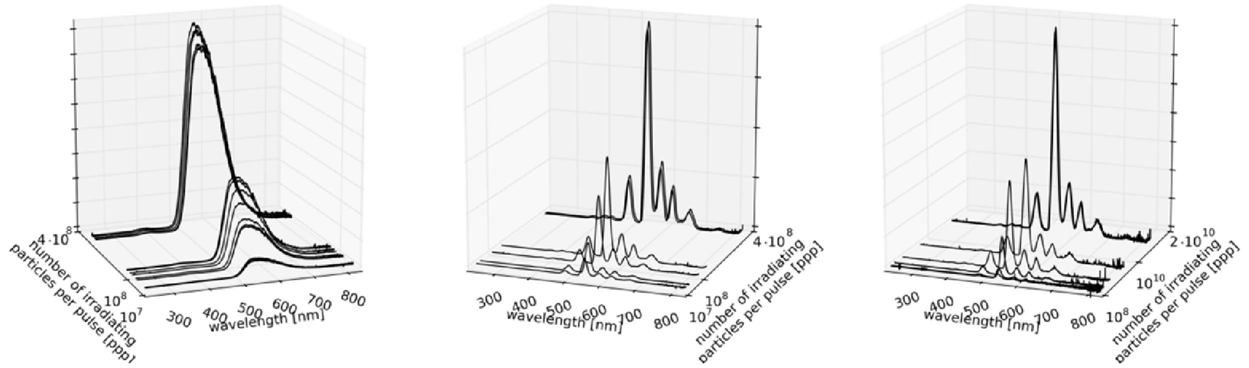

Figure 1: Emission spectra of single crystal YAG:Ce (left) and P43 phosphor (right) screens during irradiation with slow extracted Uranium beam (271 MeV/u, 300 ms extraction) at 10^7 up to $4 \cdot 10^8$ ppp. For comparison P43 spectra during slowly extracted Nitrogen beam (297 MeV/u, 400 ms extraction, 10^7 till $2 \cdot 10^{10}$ ppp) is shown on right side.

---

* Work supported by BMBF, contract No. 05P12RDBJ.

[#] a.lieberwirth@gsi.de

DOI:10.15120/GR-2015-1-FG-GENERAL-08

ESR operation and development

C. Dimopoulou, M. Kelnhofer, C.M. Kleffner, S. Litvinov, F. Nolden,
C. Peschke, N. Petridis, U. Popp, J. Roßbach, S. Sanjari, M. Steck, D. Winters
GSI, Darmstadt, Germany

The ESR storage ring operation extended in 2014 over a rather long total period of 21 weeks due to the fact that many experiments as well as machine and detector development were scheduled before the complete shutdown foreseen for the years 2015 and 2016. A variety of physics experiments were performed using the different operational modes of the ESR.

An experiment to perform precision laser spectroscopy of the hyperfine transition in the hydrogen-like bismuth ion aimed at an improved accuracy in the measurement of the beam energy by monitoring the accelerating voltage of the electrons applied for electron cooling of the stored beam. A high precision high voltage divider provided by Physikalisch-Technische Bundesanstalt (PTB) was installed. It was found that the output voltage of the power supply showed significant variations with time. By continuous measurement of the voltage with the divider the variations of the high voltage could be tracked and corrected in the offline analysis. Despite the problem of the power supply, an improved determination of the beam energy was achieved and a correspondingly improved value of the energy of the hyperfine transition could be measured by laser spectroscopy. After the experiment the supplier of the high voltage generator found a problem with resistors recently installed in the power supply. After replacement of the resistors the usual stable operation was reestablished.

Experiments at the internal target benefitted from recent improvements of the target performance. A target density of 1×10^{13} cm^{-2} is now routinely available with hydrogen gas. In another experiment xenon gas was used with good reliability, however, with a reduced density of some 10^{11} cm^{-2} due to the high beam loss rate of the stored highly charged Xe-ions at the energy of 50 MeV/u.

For various experiments the beam was decelerated in the ESR. For a scheduled experiment with the internal target with hydrogen gas a ^{124}Xe^{54+} beam was decelerated from 230 to 7 MeV/u. So far, this is the lowest energy of an experiment using a stored beam in the ESR and the lifetime of the cooled beam of highly charged ions at the low energy in the residual gas was about 20 s. Due to the target operation and the presence of special detectors in the vacuum, the lifetime decreased to 5 s. Systematic measurements with the stored bare xenon beam at various energies in the range 30 to 7 MeV/u showed a decrease of the lifetime in the residual gas very close to the expected E_{kin}^2–dependence on the kinetic energy E_{kin}. The feasibility of such an experiment using a particle detector installed inside the vacuum chamber of the dipole magnet after the internal target could be demonstrated with the presently achievable vacuum conditions. Unfortunately the experiment had to be cancelled after serious damage to several components caused by a thunderstorm.

In two one week periods with decelerated beam, a beam of bare nitrogen was decelerated to 4 MeV/u for HITRAP commissioning and extracted with the fast kicker extraction. In order to have a short cycle time the nitrogen beam was injected at the low energy of 30 MeV/u which reduced the time for cooling and deceleration of the ion beam to 4 MeV/u to about 30 s.

In the future the ESR has to deliver decelerated ions to the CRYRING which is presently being installed in the target hall south of the ESR. There is no dedicated kicker for fast extraction of a beam from the ESR towards the target hall. However, it was found that with a special closed orbit distortion of the stored beam the existing injection kicker can be used to extract the beam to CRYRING [1]. The implementation of the special orbit distortion and the kick extraction towards CRYRING was investigated first with a stored beam at a rigidity of $B\rho$=3.2 Tm. Subsequently, the rigidity of the stored beam was reduced iteratively to $B\rho$=0.58 Tm, with a ^{14}N^{7+} beam decelerated to 4 MeV/u. This corresponds to the design values for the transfer of beam from ESR to CRYRING. The extraction was successful and the beam could even be transported about 20 m along the transport line. Further beam transport tests suffered from a lack of available test time. It was also found that with the special orbit distortion the beam can be extracted from the same orbit either to HITRAP (northern extraction channel) or CRYRING (southern extraction channel) simply by tuning the angle of the extraction kick. That would even allow a fast change of the destination of the stored decelerated beam by changing the kick strength pulse to pulse. The major disadvantage of this extraction mode with closed orbit distortion is the fact that the large angle of the closed orbit, which has to be applied in the cooling section does not allow electron cooling in the last phase of beam manipulation before extraction.

In October 2014 beam for a channeling experiment in HTA was provided with charge change extracted Li-like U^{89+} ions at 190 MeV/u. This beam was used to recommission the extraction beamline towards the target hall with the help of the new CUPID diagnostics system [2]. An additional vertical steerer and upgraded scintillating screens in the beamline and the experimental cave now allow for a much more precise adjustment of the beam parameters of the extracted ions.

The requirements of minimal transverse divergence of the cooled extracted beam could be fulfilled by widening it to a parallel beam in the target area, that has further been trimmed with slits to a 5×5 mm quadratic beam spot as shown in fig 1.

DOI:10.15120/GR-2015-1-FG-GENERAL-09

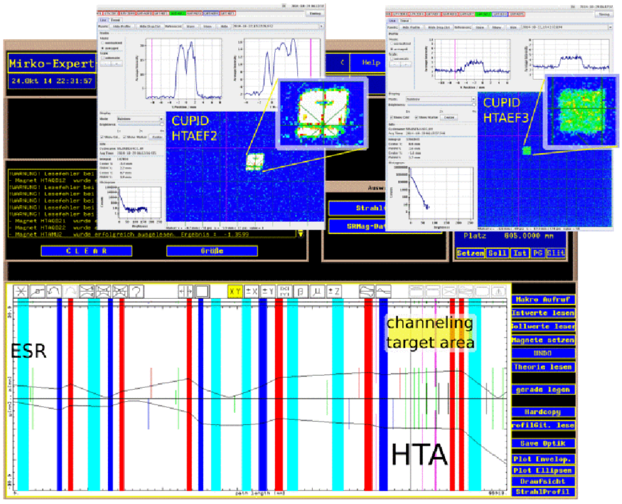

Figure 1: MIRKO envelope of the extracted beam as well as CUPID images of the quadratic beam shape measured with two different scintillating screens in a distance of 2 m installed in the experimental area.

Both transverse emittances could be determined to be smaller than 0.5 π mm mrad (FWHM) with a corresponding divergence of around ±100 μrad in the target area.

The longest experimental period was devoted to a repetition of the measurement of bound-state beta decay of ^{142}Pm^{60+} with better statistics. In previous measurements the reliable operation of the injection kicker was doubted. Missing injection kicks were suspected to compromise the determination of the time of decay of the nucleus. During the new measurement all three modules of the injection kicker were monitored individually. Only 1 failure of the injection kicker was found within 10000 injections during the experiment, proving an excellent reliability of the system. The whole experiment including stochastic precooling and final electron cooling of very few secondary ions stored in one injection showed very reliable operation of the ESR and its technical systems.

Over the year various machine experiments were performed. Studies of the isochronous mode were continued aiming at an increased acceptance for isochronous mass measurements and the improvement of the ion optical model. A measurement of the ring dispersion in the isochronous mode and the comparison with lattice calculations is reported in a separate contribution [3].

In another machine development experiment a proton beam was used to test the ability of the ESR cooling systems to prepare a cooled beam of particles with low charge. This was a study in preparation of the potential future use of the ESR in a chain of decelerators for antiprotons at FAIR. It could be demonstrated that both cooling systems, electron cooling and stochastic cooling, can be used. Stochastic cooling with notch filter and time-of-flight (ToF) cooling was performed. The damping time for some 10^8 protons with an initial rms momentum spread of 4×10^{-4} was about 15 s with ToF –cooling and about 8 s with notch filter cooling. With notch filter cooling even for 1×10^9 protons the damping time was as low as 15 s. For electron cooling the damping time for protons at the edge of the initial momentum distribution was 600 s, which is expectedly much longer than for stochastic cooling. The damping time decreased in the course of the cooling process (Fig.2). On the other hand, the final momentum spread with electron cooling was $2\text{-}3\times10^{-5}$ compared to $1\text{-}2\times10^{-4}$ with stochastic cooling.

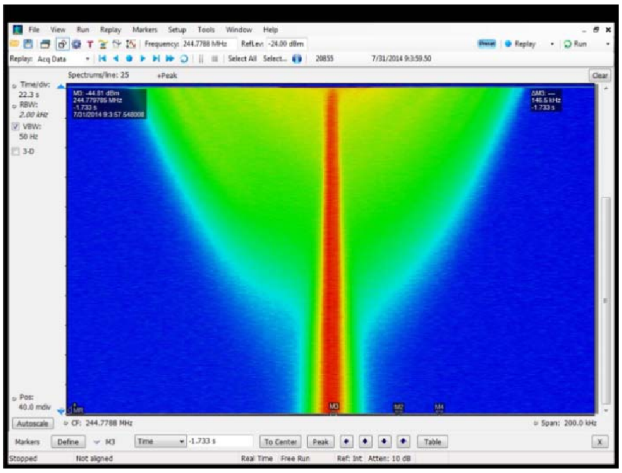

Figure 2: Longitudinal cooling of a proton beam at 400 MeV/u with an electron current of 0.25 A. The total time for the reduction of the momentum spread from 4×10^{-4} to 3×10^{-5} was 7 minutes.

A new controls program for the stochastic cooling system has been developed and is now available for operation of the system. It is a graphical interface which allows control of all components which are needed for operation and tuning of the stochastic cooling system. The new control software is compatible with FAIR standards and will be integrated into the future ESR controls concept.

For an improved understanding of the resonant structure which is used in the ESR for Schottky diagnostics a series of measurements with beam were performed. The main goal was the determination of the sensitivity of the cavity and the dependence of the sensitivity on the beam velocity, which is reflected in the transit time factor of the cavity. Measurements with proton beam at energies between 100 and 400 MeV and more systematic measurements with a ^{58}Ni^{26+} beam in the energy range 14 to 376 MeV/u (velocity range β = 0.17 - 0.71) were performed. For a beam velocity below β= 0.17 the Schottky signal vanished due to transit time factor effects.

References

[1] S. Litvinov et al., this annual report.
[2] B. Walasek-Höhne, et al., "CUPID: New System for Scintillating Screen based Diagnostics", GSI scientific report 2013, p. 307.
[3] O. Kovalenko et al., this annual report.

DOI:10.15120/GR-2015-1-FG-GENERAL-09

Optical beam diagnostics at ESR and beyond*

G. Birkl[†][1], *M. Bussmann*[2], *Z.K. Huang*[3], *X. Ma*[3], *T. Murböck*[1], *H.B. Wang*[3], *W.Q. Wen*[3], *and*
D. Winters[4]
[1]Technische Universität Darmstadt, Germany; [2]Helmholtz-Zentrum Dresden-Rossendorf, Germany; [3]Institute of Modern Physics-CAS, Lanzhou, China; [4]GSI Helmholtzzentrum, Darmstadt, Germany

Laser cooling, applied as a stand-alone cooling technique, or in combination with electron cooling, has high potential to generate relativistic ion beams with high phase-space densities. Even the generation of crystalline ion beams might be accessible. A neccessary prerequisite to reach this goal is the implementation of powerful diagnostics for the characterization of the resulting ion beam parameters. Schottky pick-up techniques [1] will lead a long way in this direction, but might be running short for the highest phase-space densities targeted. Optical diagnostics, making use of the collection of scattered optical photons during resonant excitation of relativistic ions, will open a second window for characterizing the ion beam with improved momentum resolution.

Therefore, we have developed two different detector systems for the UV-range (λ $\sim$150 nm): one system uses a photomultiplier tube (PMT) and is mounted in air (on a CaF_2 viewport), the other system is based on a photochanneltron electron multiplier (PEM) and is mounted *in vacuo* (10^{-11} mbar). Figure 1 shows two PEM systems with shielding (cage + mesh), mounted on linear translators with bellows.

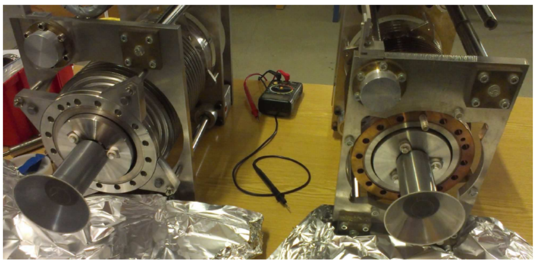

Figure 1: Two moveable PEM detector systems, used for optical diagnostics at the ESR (GSI, Darmstadt). [Now further tested at the CSRe (IMP-CAS, Lanzhou, China).]

During the laser cooling beamtime at the ESR (GSI) in August 2012, these detector systems have been used to detect the fluorescence from laser-cooled carbon ions [2]. At a kinetic energy of 122 MeV/u, or a Lorentz factor $\gamma = 0.47$, the $2s \rightarrow 2p$ cooling transition in $^{12}C^{3+}$ ($\lambda_0 = 155$ nm) is reached by using anti-collinear laser light at a wavelength $\lambda_L = 257$ nm [3]. Figure 2 shows the detected fluorescence signal as a function of time, while the cw-laser system was repetitively scanned over the cooling transition. Therefore, the cw-laser was detuned from the 'red side' (*i.e.* below the transition frequency) to just over the resonance, and back again. During each scan, which took about 30 s, a strong increase in the detected number of fluorescence photons could be recorded at the resonance condition. Strong fluorescence peaks could only be observed when electron cooling was applied in parallel. The overall exponential intensity drop of the signal is due to the limited lifetime of the stored ion beam, caused by charge-changing collisions with the residual gas.

In summer 2013, the detector systems have been shipped to the Institute of Modern Physics (IMP) in Lanzhou, China, for further development and tests at the CSRe. During the experimental run in September 2014, laser cooling of stored, relativistic $^{12}C^{3+}$ ions (@122 MeV/u) was attempted for the first time at the CSRe [4, 5]. Further development of fluorescence diagnostics, especially in the XUV-regime, is required for future laser cooling studies at the HESR ($\gamma \sim 6$) and the SIS100 ($\gamma \sim 12$).

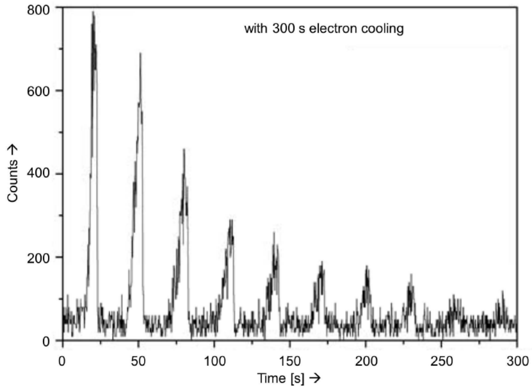

Figure 2: Fluorescence signal ($2p \rightarrow 2s$ transition) from relativistic $^{12}C^{3+}$ ions at the ESR. When the scanning cw-laser is in resonance with the Doppler-shifted cooling transition of the ions, a strong increase in the signal is observed.

References

[1] F. Nolden *et al.*, Nucl. Instr. Meth. Phys. Res. A **659**, 69 (2011).

[2] D. Winters *et al.*, JACOW, COOL 2013 conf. proc., THAM1HA04 166 (2013).

[3] T. Beck *et al.*, GSI Scientific Report (2012).

[4] W.Q. Wen *et al.*, GSI Scientific Report (2014).

[5] M. Löser *et al.*, GSI Scientific Report (2014).

---

* This work has been supported financially through BMBF contract 05P12RDFA3.

[†] gerhard.birkl@physik.tu-darmstadt.de

DOI:10.15120/GR-2015-1-FG-GENERAL-10

Performance of the ESR kicker magnet during E082 *

J. Piotrowski[†1,3], *X. Chen*[1,2], *Yu.A. Litvinov*[1,2], *M.S. Sanjari*[1], *and the Two-Body-Weak-Decays collaboration*

[1]GSI, Darmstadt, Germany; [2]University of Heidelberg, Germany; [3]AGH University of Science and Technology, Kraków, Poland

In October 2014 the second run of experiment E082 *"Single-Ion Spectroscopy of Two-Body β-Decays"*[1] took place. After a shortage of time during the 2012 beamtime, this time 12 days were allocated to performing high precision lifetime measurements of $^{142}\mathrm{Pm}$. The measurements were performed by injecting ions and observing them until they decayed. The data was analyzed online and offline, and the parameter of interest was the exact timing of each decay. In order to get reliable data, one has to assure that injected ions are removed from the *ESR* between injections.

In the first experiment we used the injection kick, considering it powerful enough, to also remove the ions from the ESR stored from a preceding injection. However it was noticed that the *kicker magnet*, that is used to perform injections, had several documented failures and possibly more that went unnoticed. This time the experiment was improved in two ways: there was a dedicated extraction kick at the end of each cycle, and all kicker magnet pulses were monitored and saved using a digital oscilloscope.

The dedicated extraction kick enabled a visual confirmation in the *time resolved Schottky spectra* that all ions had been extracted. Thanks to the monitoring of kicks, it was possible to determine exactly what the failure rate of the kicker magnet is during controlled and repeatable operation for over 10000 accelerator cycles, and get quanititative numbers describing its performance.

Setup

The accelerator was operated using a 70 second cycle. Each cycle began with an injection kick which marked the beginning of data-taking (data acquisition systems were triggered on injection). Injected ions were observed over a 60 second window. After this time an extraction kick was performed, which was followed by a 10 second safety period to finish data acquisition and saving.

The kicker magnet is powered by three power modules. Each module supplies a voltage of up to 80 kV to the magnet and a single module typically suffices to perform a successful extraction of the beam. For the experiment all three modules were used during both extraction and injection phases. The length of the injection kick was set to 500 nanoseconds, and the extraction kicks lasted 1500 nanoseconds. The assumption was that at a revolution frequency of 2 MHz, an extraction pulse lasting 3 full revolutions of the ions would be more than enough to remove all of them with absolute certainty.

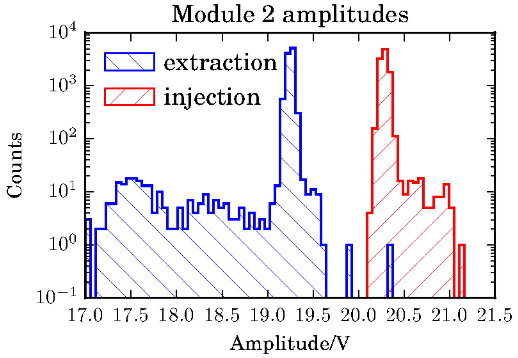

Figure 1: Logarithmic amplitude histogram for module 2. The curves show the extraction (left) and injection (right) amplitudes.

Results

Each power module has a monitoring unit through which a lower-voltage form of the pulse can be observed. We acquired 10359 injection and extraction kicks. We observed that modules 1 and 3 performed reliably throughout the entire experiment. Both delivered a signal with an amplitude of 20 V for injection and 19 V for extraction kicks, both of which are the required values for the monitoring signal. The FWHM of the kicks was around 300 mV. We noticed a single case were the kick was missed by all modules, however as this was a single incident we nonetheless consider the performance to have been extremely stable.

The behaviour of module 2 differed from that of the other modules. A histogram of the amplitudes for module 2 is presented in figure 1. For extraction kicks we counted 242 cases where kicks were weaker than the average amplitude by as much as 2 V. The curves for injections and extractions are visibly different for this one module.

Summary

For the first time in the operation of the *ESR*, the performance of the kicker magnet, crucial to the success of every experiment, has thoroughly been investigated. It was found that 2 out of 3 modules powering the magnet performed without failures in over 10000 accelerator cycles. For module number 2 it was found that the failure rate lies at 0.02%. A value of this magnitude was also confirmed by the Primary Beams High Voltage Pulsed Power group.

Acknowledgments We thank the GSI technical and accelerator groups for invaluable help during the preparation and conduction of the experiment.

References

[1] P. Kienle et al., Phys. Lett. B, 726, 638-645 (2013)

---

* Work supported by Helmholtz-CAS Joint Research Group HGJRG-108, FP7 Marie Curie ITN "oPAC", HGF ARD Program

† j.piotrowski@gsi.de

DOI:10.15120/GR-2015-1-FG-GENERAL-11

Deceleration of ions in the HITRAP facility

Z. Andelkovic[1], *S. Fedotova*[1], *F. Herfurth*[1], *N. Kotovskiy*[1], *B. Maaß*[2], *D. Neidherr*[1], *J. Steinmann*[3], *G. Vorobyev*[1], *and the HITRAP collaboration*[1]

[1]GSI Darmstadt; [2]Technische Universität Darmstadt; [3]Hochschule Darmstadt

The major challenge for experiments with low-energy highly charged ions (HCI) remains their preparation in sufficient quantities. As the only facility of its kind in the world, HITRAP aims to take advantage of the high intensities of HCI production by in-flight stripping of electrons in an accelerator facility for low-energy experiments. By reducing the energy in several steps from production at 400 down to 4 MeV/u and finally to sub-eV in a trap, a bunch of some 10^5 cold HCI can be forwarded with a chosen transport energy to different experiments.

The first stage of the linear decelerator, an interdigital H-type structure (IH), decelerates ions from 4 to 0.5 MeV/u and was successfully commissioned several years ago with deceleration efficiencies close to the theoretical maximum [1]. The commissioning of the second deceleration stage, the radio-frequency quadrupole (RFQ), has proven to be more challenging because of the very large parameter space combined with a relatively low acceptance of the device. An attempt to improve on this brought a new design of the electrodes [2] and offline tests at MPIK in Heidelberg [3]. The modified RFQ was reinstalled at GSI and commissioned during three beamtimes in 2014. Figure 1 shows the signal of the HCI decelerated from 500 to 6 keV by the RFQ, obtained after systematic scans and optimization of the system parameters during the first two beamtimes. The ions leaving the RFQ were sent through a magnetic field of a permanent magnet with integrated slits. As a result, the ions with smaller energy get a larger deflection angle (the left peak in Fig. 1) and can be distinguished from the non-decelerated ions. The last HITRAP beamtime of the year was used for systematic tests of deceleration, as well as to transport the decelerated ions through the low energy beamline towards the cooling trap.

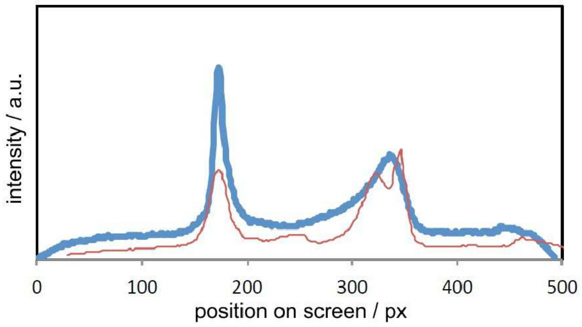

Figure 1: The ion beam from the RFQ after the energy analyser. The thin, red line is the reference signal from the offline tests and the thick, blue line is the online signal from July 2014. The low energy part, i.e. the decelerated ions' signal is the peak to the left. The peak to the right is the undecelerated part of the beam.

The synchrotron cooling of trapped electrons for electron cooling was investigated for the last deceleration stage of HITRAP, the cooling trap. Electrons emitted from a GaAs surface after irradiation with UV light were guided to the trap and stored for extended amounts of time. The cooling effect by synchrotron radiation in the strong magnetic field of the trap was experimentally verified [4]. Further improvements include improvements of the vacuum, the optimization of the ion and electron capture process as well as their mixing and cooling. Detailed simulations of the trapping and the cooling process in the cooling trap have been conducted to that end and show promising results [5].

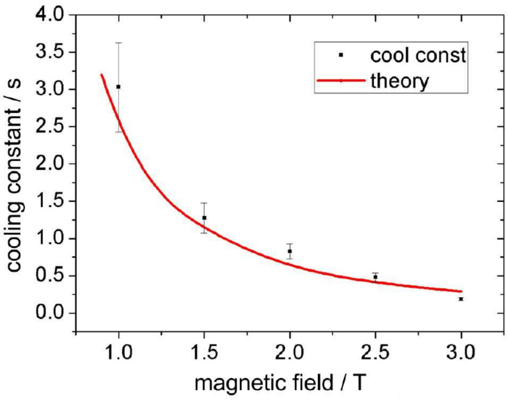

Figure 2: Synchrotron cooling of electrons in the cooling trap. The measured cooling constant of the trapped electrons reduces with the increasing magnetic field. The full, red line shows the value expected from theory.

References

[1] F. Herfurth, et al.: *HITRAP - Heavy, Highly-Charged Ions at Rest - A Status Report*, GSI Scientific Reports 2011

[2] S. Yaramyshev, et al.: *A new Design of the RFQ-Decelerator for HITRAP*, GSI Scientific Reports 2012

[3] M. Maier, at al.: *Offline commissioning of the old and new HITRAP RFQ*, GSI Scientific Reports 2012

[4] B. Maaß: Geladene Teilchen in der Kühlfalle, Master's thesis, TU Darmstadt, 2014

[5] J. Steinmann, PhD Thesis, University Erlangen-Nürnberg, to be submitted, 2015

DOI:10.15120/GR-2015-1-FG-GENERAL-12

The bunch monitoring system of the HITRAP decelerator

A. Reiter, F. Herfurth, W. Kaufmann, C. Krüger, M. Steck
GSI, Darmstadt, Germany

The HITRAP decelerator receives a 3 μs bunch of cooled, highly-charged ions from the experimental storage ring (ESR) and consists of two rebunchers, BB1 and BB2, followed by a drift-tube linac (IH-DTL) and a radio-frequency quadrupole (RFQ). The monitoring system is based on capacitive ring pickups and works for currents above 0.5 μA [1]. In 2014 new purpose-built main amplifiers were installed and extensive tests marked the end of the system development.

Monitoring of Bunched Primary Beam

Rebuncher BB1 generates a longitudinal particle focus at the IH-DTL entrance which decelerates the 4 MeV/u primary beam to ~500 keV/u. Two pickups monitor the mean bunch energy of each extraction by a time-of-flight (TOF) measurement in front of the IH-DTL [2]. A resolution of σ_E=0.7 keV/u was achieved when the energy was changed during a phase scan of rebuncher BB2 [3]. During regular operation BB2 is switched off because it fails to improve the deceleration efficiency. Due to its simplicity, the TOF measurement has been established as reference and the ESR electron cooler voltage is adjusted to a target energy of 4024 keV/u. The TOF energy is 15 keV/u higher than the more accurate ESR energies based on Schottky (4008±3) keV/u or electron cooler voltage (4013±4) keV/u. Despite the small offset, relative changes are correctly detected.

Monitoring of IH-DTL and Buncher BB3

The ideal secondary IH-DTL beam is characterised by a small bunched fraction of accelerated primary ions and the larger, decelerated 500 keV/u design component. A pickup (DP6) monitors amplitude, i.e. deceleration efficiency, and the relative energy of bunches behind rebuncher BB3, which matches the beam to the RFQ acceptance. Fig. 1A presents bunch signals for three BB3 phases. BB3 affects only the decelerated ions, but its field is too weak to influence the remaining primary beam. Using the zero-crossing point of the decelerated bunch signal as reference, a variation in arrival time at the pickup can be converted to an energy shift. Results are shown for a full phase scan in Fig. 1B (dots) together with the data of the Energy Analyzer EA (triangles), a calibrated dipole spectrometer with position-sensitive optical MCP readout [4]. Both data sets are in excellent agreement and follow the expected sine function. The data have not been corrected for occasional glitches in the trigger which produce spurious offsets, most evident at 30° or 50°.

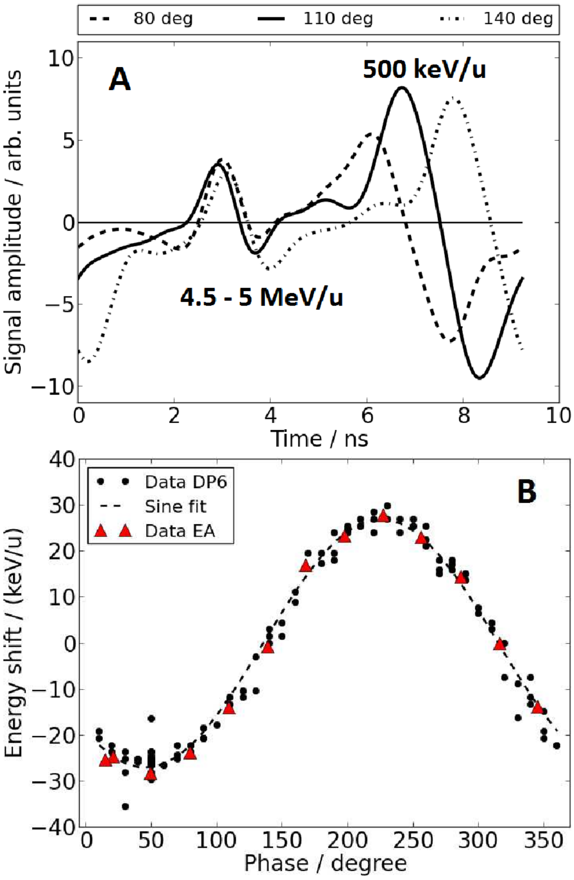

Figure 1: Signals of pickup DP6 for three BB3 phase settings (A). Energy shifts observed by pickup DP6 and Energy Analyzer EA during BB3 phase scan (B).

The HITRAP bunch monitoring system has been completed. Recent tests confirm previous findings and underline the systems' practical potential. The online monitoring system is now part of the standard beam instrumentation.

References

[1] A. Reiter, W. Kaufmann, C. Kleffner, “Novel Analysis for Linac Phase Probes“, GSI Scientific Report 2010

[2] A. Reiter et al., MOPD35, DIPAC 2011, Hamburg, Germany

[3] A. Reiter et al., “Improved Monitoring of the HITRAP Double-Drift Buncher“, GSI Scientific Report 2011

[4] F. Herfurth et al., THB05, HIAT 2012, Chicago, IL, USA

DOI:10.15120/GR-2015-1-FG-GENERAL-13

The status of the CRYRING@ESR project*

F. Herfurth[†1], *M. Lestinsky*[1], *Z. Andelkovic*[1], *R. Bär*[1], *A. Bräuning-Demian*[1], *S. Litvinov*[1], *O. Dolinskii*[1], *W. Enders*[1], *M. Engström*[1], *S. Fedotova*[1], *B. Franzke*[1], *W. Geithner*[1], *O. Gorda*[1], *A. Källberg*[2], *N. Kotovskiy*[1], *A. Reiter*[1], *A. Simonsson*[2], *T. Sieber*[1], *J. Sjöholm*[2], *M. Steck*[1], *Th. Stöhlker*[1], *and G. Vorobjev*[1]

[1]GSI, Darmstadt, Germany; [2]MSL, Stockholm University, Stockholm, Sweden

The low energy storage ring LSR [1] shall provide highly charged ions and antiprotons at low energy for two collaborations at FAIR, SPARC and FLAIR. Those collaborations intend to perform precision experiments pursuing atomic and nuclear physics questions [3]. The LSR is a Swedish in-kind contribution to the FAIR facility in Darmstadt.

The LSR is the swedisch low energy storage ring CRYRING modernized and adapted to the additional needs for injection and ejection of antiprotons and highly charged ions at about 10 MeV/nucleon. CRYRING has been operated at the Manne Siegbahn Laboratory in Stockholm until 2010, was dismantled in 2012 and transported to GSI in the first months of 2013. At GSI it will be installed behind the ESR, as proposed and described in detail in 2012 by a swedish-german working group [2]. This proposal has been accepted end of 2012 by the relevant committees.

CRYRING can decelerate, cool and store heavy, highly charged ions and anti protons injected at about 10 MeV/nucleon down to a few 100 keV/nucleon. It provides a high performance electron cooler and a straight section for flexible experiment installations as for instance a gas jet target. It is equipped with it's own injector and ion source, to allow for standalone commissioning.

In 2014 the design and installation of infrastructure into the newly constructed Cave B included media supplies like cooling water or compressed air, power cabling, magnet cabling, water cooled cabling, signal cabling. The cable routing and cable tray planning and installation has almost been completed. For electrical supply a new low voltage distribution has been conceived and purchased. The integration into the GSI safety systems is ongoing and well advanced. For this the lock and gate system has been reinstalled to ensure controlled access to the cave.

One prerequisite for the physics part of the CRYRING@ESR project, the transport and injection of heavy, highly charged ions from the ESR, has been advanced. The beam line has been modified and setup in large parts. Furthermore, part of the beam time was used to test the extraction and transport of ESR beam. It has been shown successfully that even close to the lower limit of ESR operation, at 4 MeV/u beam energy, it was possible to extract ions towards CRYRING in Cave B and to transport it beyond the first three dipoles.

Figure 1: Photograph of the situation in the CRYRING cave end of 2014. In the foreground the local injector has been setup and is being aligned. In the background visible is the ring structure with its dipoles and the magnetic sections with quadrupole and sextupole magnets.

The local injector has been mechanically put in place. First pumping down tests of the RFQ were conducted successfully. The required pressure has been reached, showing that the RFQ is ready to be operated after all the refurbishing to update for instance it's cooling circuit.

Setting up of the first components of the ring has begun, i.e. all ring dipoles were installed and the GSI technical divisions are completing inspection and preparation of the subsystems installed in the straight sections.

The Electron cooler has been worked at to repair transport damages and to check primarily the vacuum conditions. A testing stand for cryogenic tests is under preparation.

References

[1] H. Danared, et al. (2011) "LSR - Low-energy Storage Ring, Technical design report", Manne-Siegbahn Laboratory, Stockholm University, version 1.3.

[2] M. Lestinsky, et al. (2012) "CRYRING@ESR: A study group report", Project study, GSI, Darmstadt,

[3] M. Lestinsky, et al. (2014), "CRYRING@ESR: Present Status and Future Research", Proceedings of the STORI 2014, 9th International Conference on Nuclear Physics at Storage Rings, Sankt Goar, Germany.

---

* Work supported by GSI/HI Jena/FAIR@GSI PSP code:1.3.4.2./The SPARC collaboration/Uni Krakov/KVI Groningen

† F.Herfurth@gsi.de

DOI:10.15120/GR-2015-1-FG-GENERAL-14

A novel scheme for fast extraction of low energy beams from the ESR to the CRYRING

S. Litvinov[1], *C. Kleffner*[1], *F. Nolden*[1], *M. Steck*[1], *and D. Winters*[1]
[1]GSI, Darmstadt, Germany

The CRYRING@ESR facility [1] will provide the unique possibility for studying properties of low energy cooled heavy beams in the field of atomic and nuclear research within the FAIR project [2]. Heavy ion beams will be stored, cooled and decelerated to the energy of about 4 MeV/u in the ESR and then delivered to the CRYRING. Presently, there is no special kicker magnet which could be used for the fast extraction towards the CRYRING. However, a special distorted closed orbit has been suggested, applying it to the stored beam one can perform the fast extraction with the existing injection kicker magnet.

Calculation

The beam from SIS18 is usually injected into the ESR on the orbit of $\Delta p/p \approx +1\%$, and then stored and cooled (solid black curve in Fig. 1). In order to keep the beam parallel to the electron beam in the cooler section, 4 horizontal correctors in 2 neighboring main dipole magnets are used. The ESR is equipped with one injection and two extraction septum magnets. The horizontal width of the beam pipe around the septums is 104 mm and in addition, there is the narrow knife of 17 mm width of each septum (see Fig. 1). The injection kicker magnet is placed after the first dipole downstream. The beam goes after the kick either to the northern extraction septum (towards the HITRAP) or to the wall (dotted black curve in Fig. 1). In order to extract the beam to the CRYRING, it is necessary to change the trajectory of the kicked beam, such that it avoids the knives of the septa but reaches the southern extraction septum. This orbit distortion has been performed with a special bumped closed orbit, which has been calculated using 8 horizontal correctors in 4 main dipoles (dashed black curve in Fig. 1). Applying the kick on the distorted orbit the beam can freely be extracted to the CRYRING (dotted-dashed red curve in Fig. 1).

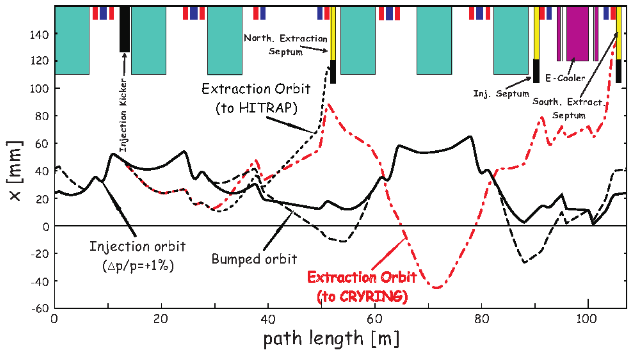

Figure 1: Calculated beam trajectories for one turn in the ESR. The injected stored orbit of $\Delta p/p = +1\%$ is indicated by the solid black curve. Its kicked orbit (extraction to HITRAP) is shown by the black dotted curve. The distorted bumped orbit is marked by the dashed black curve and its kicked orbit (extraction to CRYRING) is shown by the dotted-dashed red curve.

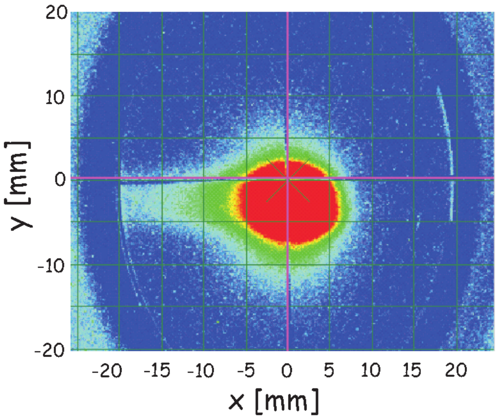

Figure 2: The extracted 100 MeV/u $^{58}\mathrm{Ni}^{26+}$ beam directly after the extraction septum.

Experiment

In August 2014, the calculations could be proven by experiments at the ESR. Firstly, the proposed extraction scheme was verified with 100-400 MeV/u proton and $^{58}\mathrm{Ni}^{26+}$ beams. The extracted beam was measured directly after the septum using a fluorescent screen (see Fig. 2). Later, a $^{14}\mathrm{N}^{7+}$ beam at 30 MeV/u was injected, stored and stepwise decelerated iteratively to the final energy of 4 MeV/u ($B\rho = 0.58$ Tm), the lowest possible magnetic rigidity from the ESR to the CRYRING. At each energy, the beam was successfully extracted, changing only the kick angle of the injection kicker by several tenths of a milliradian. The distortion orbit was unchanged. Despite the lack of experimental time, it could be managed to transport the extracted 4 MeV/u ion beam over a length of 20 m towards the CRYRING for the first time.

References

[1] CRYRING@ESR, A study group report
https://www.gsi.de/fileadmin/SPARC/documents/Cryring/ReportCryring_40ESR.PDF

[2] http://www.fair-center.eu/

DOI:10.15120/GR-2015-1-FG-GENERAL-15

Beam instrumentation for the RFQ injector at CRYRING

A. Reiter, C. Andre, H. Bräuning, C. Dorn, F. Herfurth, O. Gorda, T. Hoffmann, W. Kaufmann,
H. Reeg, T. Sieber, G. Vorobjev, B. Walasek-Höhne, M. Witthaus
GSI, Darmstadt, Germany

In 2015 the CRYRING storage ring will resume operation after its installation in Cave B [1]. Commissioning begins with the compact injector, consisting of ion source branch and radio-frequency quadupole (RFQ) linac. It will provide beams of light charged particles for commissioning of the experimental storage ring.
The beam instrumentation of the injector consists of Faraday cups, scintillating screens, and capacitive pickups. All detector systems are compliant to the new FAIR standards and provide a front-end software architecture (FESA) interface to the accelerator control system. CRYRING will be the first machine to be equipped with the new White-Rabbit timing system.

Ion Source and Dipole Spectrometer

Beams of light, singly-charged ions of 10 keV/u, mainly D^+, will be extracted from a MINIS source. Directly behind the ion source and behind the 90° spectrometer dipole, intensity and distribution of the DC beam can be measured with a Faraday cup (FC) or a scintillating screen (SCR). The compact diagnostics chamber with a single motor drive for both detectors was originally designed by KVI Groningen for the HITRAP facility . The driver unit and the controller are a joint FAIR development of GSI and Slovenian in-kind contributor Cosylab.
Expected beam currents along the injector range from $100\,\mu$A after the source to $1\ \mu$A after the RFQ linac. For the multi-turn injection into CRYRING, the chopper behind the ion source cuts out a $25 - 100\,\mu$s macropulse from the DC beam. Each FC is equipped with a low-noise amplifier, suited for DC and AC operation, with switchable gains of $10^2 - 10^8$ V/A. The output is sampled by a 100 MSa/s ADC with 16 bit resolution in a VME system. Its embedded controller runs the "CryCup" acquisition software.
The SCRs are composed of 25 mm diameter multi-channel plates and P43 scintillators. Beam images are recorded with triggered 10 bit digital CMOS cameras. They are controlled by an industrial PC which hosts the "CUPID " acquisition software. The application takes care of all data handling (image rotation, region cuts, profile calculation) and acts as server to the control system clients [3].
A special camera system with 75 mm fixed-focus lens and optical x4 extender is mounted on the external 0° port of the dipole chamber and looks approx. 3 m upstream into the ion source. During operation it monitors the plasma around the filament, after ion source service or exchange the fixed camera is used to check the re-alignment. The system resolution was measured to be about 20 pixel/mm.

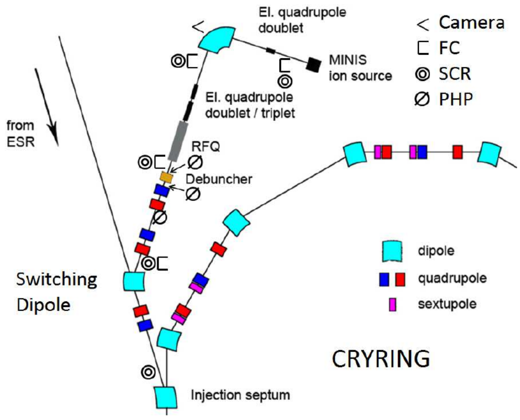

Figure 1: Schematic of RFQ injection for CRYRING; detector positions are indicated with symbols described in the legend. The distance between RFQ and injection is ∼10 m.

RFQ linac and debuncher

The 108.4 MHz RFQ linac accelerates ions of q/A>0.36 from 10 to 300 keV/u. The following debuncher reduces the momentum spread $\Delta p/p$ to $\sim\ 1\%$ and increases the injection efficiency. The new bunch monitoring system analyses pairs of signals selected from 3 pickups (PHP) or RFQ and debuncher tank. The derived information may be the beam energy via time-of-flight, phase relations between beam and rf tank power or the verification of the debuncher operation. Signals are amplified, in the case of PHPs, and routed via a remote-controlled switching matrix to a digital 5 GSa/s oscilloscope. A FESA application integrates amplifiers, switching matrix and data readout. The analysis procedure is identical to the one employed at the HITRAP decelerator and achieves a resolution of ∼10 ps [2].

As in the source branch two FC/SCR pairs, one at the RFQ exit and one after the two quadrupole doublets, measure intensity and distribution of the 300 keV/u beam. In the bakeable area after the switching dipole, a robust, heat-resistant Cromox screen is mounted close to the injection septum on a pneumatic drive. The detectors are part of the readout systems described in the previous section.

References

[1] M. Lestinsky et al., "CRYRING@ESR: A study group report", June 2012

[2] A. Reiter et al., MOPD35, DIPAC 2011, Hamburg, Germany

[3] B. Walasek-Höhne et al., TUPD062, IBIC 2014, Stanford, USA

DOI:10.15120/GR-2015-1-FG-GENERAL-16

Beam test with the Cryogenic Current Comparator*

F. Kurian[1#, 2, 3], *R. Geithner*[3], *P. Huelsmann*[2], *P. Kowina*[1], *R.Neubert*[4], *H. Reeg*[1], *M. Schwickert*[1], *R. Singh*[1], *T. Sieber*[1] *and T. Stoehlker*[1, 3]
[1]GSI, Darmstadt, Germany; [2]Goethe University Frankfurt, Germany; [3] Helmholtz Institute, Jena, Germany;
[4] Friedrich-Schiller-University, Jena, Germany

Cryogenic Current Comparator (CCC) units are foreseen to be installed at various locations of the FAIR facility, for the online measurement of ion beam current down to nA range. In this contribution, successful test measurements of ion beam current using the upgraded CCC at GSI are reported. The CCC data show excellent match of the measured spill structure with the SEM measurements.

For the development of the improved version, the existing CCC system at GSI was refurbished as a prototype for FAIR, to test new sensor components [1]. Based on the studies done on different sensor combinations by R. Geithner *et al.* [2], a new dc-SQUID and new control electronics were selected and installed in the refurbished system. After successful test measurements in lab environment, the CCC was installed in the beam diagnostic test bench HTP at the extraction line of the GSI synchrotron. The signals measured by the CCC were amplified and read out at the equipment room located about 70 m from the beam line.

A built-in single-turn wire loop was used to calibrate the CCC output voltage to equivalent current. Response to known dc currents from a precision source (Keithley 261) in the range of 2 nA to 5 µA was measured. From this, a current sensitivity of 71.5 nA/ϕ_0 was calculated, which is equivalent to 74.2 nA/V output to the oscilloscope.

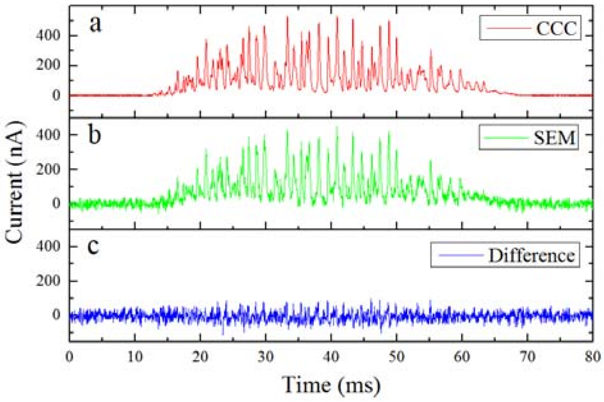

Figure 1: Comparison of the beam current signal measured by (a) CCC, (b) SEM, and the difference between the two signals (c). See text for details.

Slowly extracted Ni^{26+} ion beams at 600MeV/u in the intensity range from 2.8×10^8 particles per spill to 5×10^9 particles per spill were used to test the CCC response to the beam signal. A set of beam signals with the extraction time in the range of 64 ms to 5 seconds at different beam intensities was measured by the CCC. With an anti-aliasing filter (10 kHz cut-off frequency) at the output, the CCC measured the beam current down to 2 nA with a resolution of 1.2 nA rms. To compare the current measured by the CCC with a conventional technique, a Secondary Electron Monitor (SEM) - installed about 1 m downstream the CCC's installation point - was used in parallel. The secondary electron current produced by the SEM was amplified by a trans-impedance amplifier (Femto DHPCA-100).

Figure 1 shows a typical spill structure of an ion beam (about 4×10^9 particles) extracted over 64 ms measured by CCC (a) and SEM (b). The SEM signal was normalized to the CCC signal (normalized to total charge) for comparison. The difference between the spill structures measured by CCC and SEM as plotted in Figure 1 (c) shows excellent agreement. The spikes in the extracted beam, originating from the power converters of the magnets for the resonant extraction, are visible in the CCC measurement as shown in Figure 1. These ripples correspond to 50 Hz and its harmonics in the frequency spectra as expected [3].

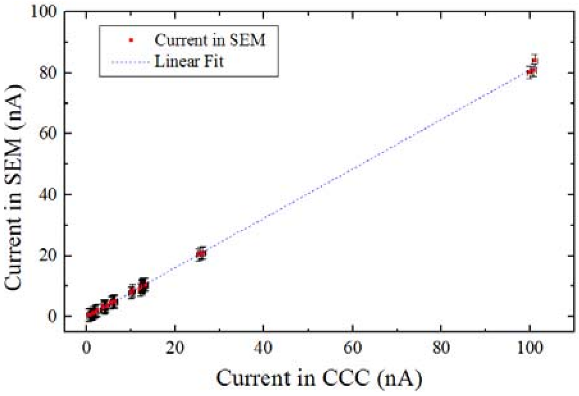

Figure 2: Comparison of the current measurement using CCC and SEM within a bandwidth of 200 Hz.

In Figure 2 the current signals as measured with the CCC are plotted vs. SEM data in the range of 2 nA-105 nA. Whereas the relation is precisely linear (standard error: 0.7%) as expected, the 19% deviation of the measured average current is subject of ongoing examinations.

References

[1] F. Kurian *et al.* "Measurements with the upgraded cryogenic current comparator", IBIC 2013.

[2] R. Geithner *et al.* A Cryogenic Current Comparator for FAIR with Improved Resolution, IBIC 2013.

[3] M. Kirk *et al.* "SIS-18 rf knock-out optimisation studies", IPAC2013, Shanghai, China.

---

* Work supported by Helmholtz Institute, Jena.

[#]f.kurian@gsi.de

DOI:10.15120/GR-2015-1-FG-GENERAL-17

Pressure and temperature dependence of Cryogenic Current Comparator measurements

F. Kurian[1, 2, 3], *P. Huelsmann*[1, 2], *P. Kowina*[1], *H. Reeg*[1], *M. Schwickert*[1], *T. Sieber*[1], *R. Singh*[1] *and T. Stoehlker*[1, 3]

[1] GSI, Darmstadt, Germany, [2] Goethe University, Frankfurt, Germany, [3] Helmholtz Institute, Jena, Germany

One of the key features of the Cryogenic Current Comparator (CCC) is its ability to measure extremely small magnetic fields associated with the beam current [1]. However, in a typical accelerator environment, a number of unavoidable noise sources limit its current sensitivity. Main sources of noise are mechanical vibrations, magnetic stray fields including Earth's magnetic field, electromagnetic interferences and temperature fluctuations.

A low T_C dc SQUID (Superconducting Quantum Interference Device) is used in the CCC as magnetic flux detector. It is operated at 4.2 K which is favourable due to low thermal noise. However, as already observed in former measurements [2], the CCC readout is affected by a drift that is correlated with the pressure inside the CCC cryostat (i.e. pressure of the liquid Helium (LHe) vapours above the LHe surface).

The influence of pressure and hence temperature fluctuations were studied for the refurbished CCC system, installed in the beam diagnostics test bench at HTP [1]. A differential pressure sensor connected to an oscilloscope was used to measure the pressure inside the CCC cryostat. The resolution of this measurement was 0.13 mbar with a signal to noise ratio of 2. The absolute calibration of the sensor is 4.86 mV/mbar and was made by means of a mechanical manometer. A needle valve installed at the cryostat exhaust was used to control the pressure of the boiling LHe. The temperature of the superconducting magnetic shield which includes the ring core and pick up coil, was measured by a silicon-diode temperature sensor (Lakeshore, DT-670B) with an accuracy of 1 mK. The temperature of the SQUID was not monitored directly which is a drawback, as mentioned below.

The CCC was operated in its most sensitive range with a current sensitivity of 118.2 nA/Φ_0 and a current resolution of 6 nA, where Φ_0 is the magnetic flux quantum ($\Phi_0 = h/(2e) = 2.068\times10^{-15}$ Wb). The CCC was calibrated with a known dc current applied to a built-in current loop.

Figure 1 shows the variation of the offset in the CCC measurement and temperature changes with respect to the pressure variation inside the LHe cryostat. The needle valve at the exhaust of the cryostat is closed for about 50 seconds to create an overpressure of 15.3 mbar inside the cryostat by LHe boil-off. This causes a temperature rise of 36.0 mK on the superconducting magnetic shield. The pressure increase of 15.3 mbar result in an instantaneous drift on the CCC output corresponding to an equivalent current of 1.107 µA which is 70% of the full CCC range. The delay of 5 sec in the temperature readout with respect to pressure and CCC readout is due to the bulky magnetic shield that needs more time to reach the same temperature as the SQUID.

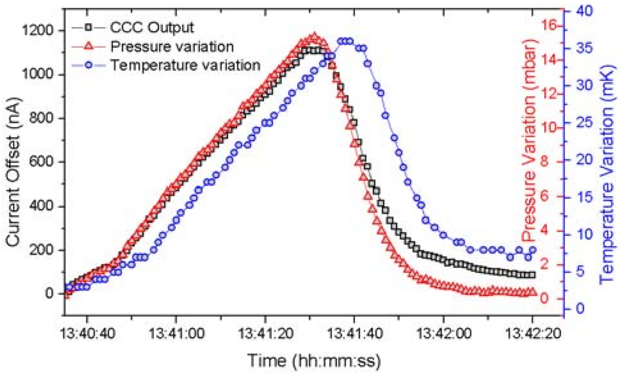

Figure 1: Current offset (black squares) as the result of pressure increase (red triangles) in the LHe cryostat and corresponding temperature variation (blue circles).

The offset of the CCC readout has a linear pressure dependency of 73.7 nA/mbar (0.62 Φ_0/mbar). The corresponding temperature dependence of the CCC offset is 33.5 nA/mK (0.28 Φ_0/mK).

The strong and non-linear temperature dependence of the SQUID drift in presence of an external magnetic field was already observed in other experiments [3], however, only at temperatures lower than 600 mK and explained as an effect of surface defect spins [3 and Refs. therein]. On the contrary, present measurements show by factor of ten stronger and nearly linear drift dependency but at LHe temperature. This may be rather addressed to thermal motion of magnetic flux and/or temperature-dependent critical currents [4].

Since the pressure of the LHe vapour is perfectly correlated with the CCC readout there are two extremely important issues for any future CCC design:

- The pressure of the CCC exhaust must be stabilized (e.g. by means of a pressure regulator) with a precision of better than 1 mbar.
- By simultaneous measurement of the vapour pressure one can calculate and compensate this drift.

References

[1] F. Kurian, et al. *IBIC 2013,* Oxford, UK.
[2] V. Vodel and R. Neubert, private communication.
[3] S. Sendelbach et al., Phys. Rev. Lett. 100, 227006 (2008).
[4] J. Clarke, et al. J. Low Temp. Phys. 25, 99 (1976).

---

* Work supported by Helmholtz Institute, Jena.

#f.kurian@gsi.de

DOI:10.15120/GR-2015-1-FG-GENERAL-19

Closed orbit correction in CRYRING

O. Gorda, A. Bräuning-Demian, A. Dolinskii, F. Herfurth, C.-M. Kleffner, M. Lestinsky, G. Vorobjev
GSI, Darmstadt, Germany

To avoid acceptance limitations in the CRYRING [1], the close orbit (CO) distortions should not be larger than a few mm. During the multi-turn injection from the local ion source the intensity of the stored beam strongly depends on the ring acceptance and therefore it is important to control the CO. For slow extraction, large CO distortions can change the position and the orientation of the phase space separatrix limiting the extraction efficiency. In this report we describe the CO correction system and discuss the magnet alignment requirements based on ion-optical calculations.

In the present CRYRING layout seven horizontal and seven vertical beam position monitors installed in the sections YR02, YR06, YR07, YR08, YR10, YR11 and YR12 (see Fig. 1) will be used for CO measurements.

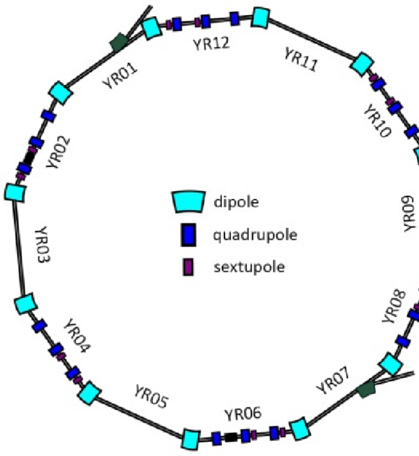

Figure 1: The CRYRING layout.

The CO correction will be provided by six pairs of horizontal and vertical correction magnets. Five pairs are installed in the magnetic sections YR02, YR04, YR08, YR10 and YR12 as described in [2]. In order to leave space for the extraction kicker magnet one horizontal corrector will be installed in section YR06, and a vertical corrector will be moved to section YR07. Additionally, all main dipole magnets have back-leg windings which can be used for corrections of the horizontal CO. According to calculations, a magnet alignment accuracy of 0.1 mm for displacement and 0.3 mrad for roll angle would result in a maximum peak-to-peak CO deviation of a few mm along the ring [3]. In this case, taking into account that the beam position monitors have an absolute measurement uncertainty of 1 mm it is not possible to further reduce the CO deviation. On the other hand, the required alignment accuracy can be slightly relaxed if the available correction magnets are used. Fig. 2 illustrates the calculated distribution of the peak-to-peak CO deviation for magnet displacement and roll accuracy of 0.3 mm and 0.3 mrad, respectively.

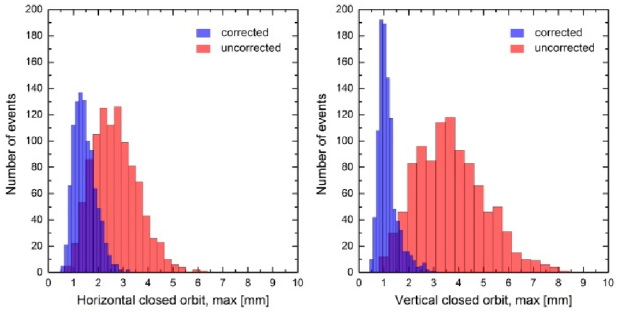

Figure 2: Calculated peak-to-peak deviation of the horizontal (left) and vertical (right) closed orbit.

For these MAD-X calculations 1000 random seeds of alignment errors have been used. The horizontal and vertical CO can be corrected to a RMS value of about 1.5 mm. Kick angles of at most 1.5 mrad, corresponding to a field strength of 0.01 T for a rigidity of 1.44 Tm, are required for correction. This is well within the maximum possible field strength of 0.03 T specified for the correction magnets. As an example, in Fig. 3 calculated CO before and after the correction is shown for several random sets of alignment errors.

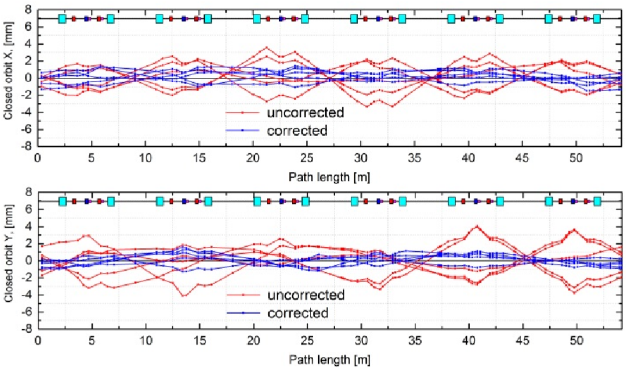

Figure 3: Calculated horizontal (upper) and vertical (lower) closed orbit.

References

[1] Lestinsky M et.al. CRYRING@ESR: A study group report, GSI, 2012.

[2] Danared H et.al. LSR Low-energy Storage Ring, Technical Design Report, MSL, 2011.

[3] Carle P et. al. Magnet alignment and survey in CRYRING, NIM A, v. 366, p.31, 1995

DOI:10.15120/GR-2015-1-FG-GENERAL-20

Status of the proton injector for FAIR

R. Berezov[1], *N. Chauvin*[2], *J. Fils*[1], *R. Hollinger*[1], *V. Ivanova*[1], *C. Ullmann*[3]
[1]GSI, Darmstadt, Germany; [2]CEA, Saclay, France; [3]IAP, Frankfurt am Main, Germany

The FAIR proton LINAC, the synchrotrons for heavy ions SIS18 and SIS100 have to provide the primary proton beam for the production of antiprotons [1]. The injector for the proton LINAC has to deliver 100 mA proton beam with an energy of 95 keV and an emittance of 0.3π mm mrad (normalized, rms) at the entrance of the RFQ.

The injector for the p-linac consists of the microwave ion source with "five electrode" extraction system and a low energy beam transport (LEBT) for matching the beam to the RFQ. The Microwave ion source developed and made in CEA/Saclay, will be able to run in pulsed mode by pulsing the RF generator. The ion source operates with a microwave frequency equal to 2.45 GHz based on ECR plasma production with two coils each with 87.5 mT magnetic field [2]. The five electrodes extraction system consists of a plasma electrode (plasma chamber potential), a puller electrode (50 kV), screening electrode (5 kV) and two ground electrodes [3].

The LEBT composes two short solenoids with two H/V integrated magnetic steerers and a diagnostic chamber, which is shown in the Figure 1. The diagnostic chamber is equipped with an iris, as beam diaphragm for transverse beam limitation, an Alison scanner for emittance measurement, a secondary emission grid (SEM) for direct determination of position and angle distribution, a Wien filter for detection of different ion species as a check of beam composition and a beam stopper. It is also planned to install a 4-grid analyser temporally to measure the space charge compensation during the commissioning of the proton injector.

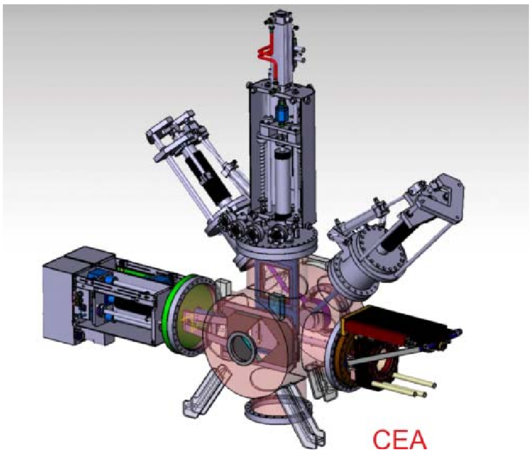

Figure 1. Diagnostic chamber with iris, Alison scanner, Wien filter, SEM grid and beam stopper.

For measuring ion beam intensity two current transformer (ACCT) will be installed behind the pentode extraction system and at the end of the LEBT beam line. The electrostatic chopper will be mounted between the LEBT and the RFQ to cut the beam pulse current to 36 μs. The total length of the compact LEBT is 2.3 m. The length reduced to minimize expected emittance growth along the beam line.

The assembly of the test bench for the commissioning at CEA/Saclay is rather finished. On Figure 2 the 3D model of the test bench is presented. The ion source is located on the platform with a potential of 100 kV inside the Faraday cage. The LEBT is installed outside of the Faraday cage and has ground potential.

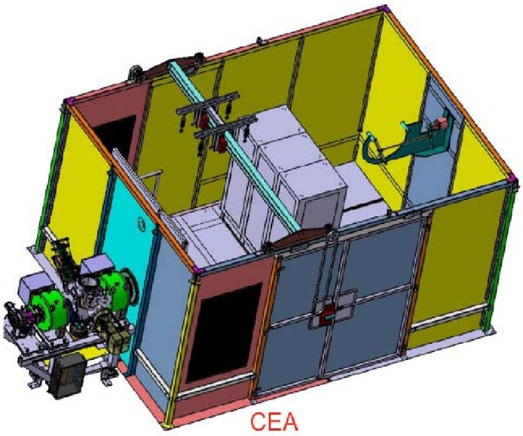

Figure 2: 3D model of the test bench for the commissioning at CEA/Saclay.

The first primary emittance measurement with the Alison scanner directly behind the extraction system is planned in Q2 (2015). After completing the LEBT installation with mini control system and power supplies, planned to start the commissioning in Q4 of 2015. For emittance measurement the mobile slit-grid emittance unit (from GSI) will be installed at the position of the entrance of the RFQ. It is also planned to perform measurements of beam current, stability of the source, space charge compensation and determination of the beam fraction.

References

[1] R. Hollinger, W. Barth et al., "High current proton beam investigations at the SILHI-LEBT at CEA/Saclay", Linac06 (2006) 232.

[2] C. Ullmann, R. Berezov et. al., "The proton injector for the accelerator facility of antiproton and ion research (FAIR)", Rev. Sci. Instrum. 85, 02A952 (2014).

[3] C. Ullmann, R. Berezov et.al., "Status and computer simulations for the front end of the proton injector for FAIR", proceedings of IPAC2014, Dresden, Germany.

DOI:10.15120/GR-2015-1-FG-GENERAL-21

RFQ beam dynamics design for the FAIR Proton Linac*

C. Zhang[#]*, W. Vinzenz*
GSI, Darmstadt, Germany

The FAIR (Facility for Antiproton and Ion Research) Proton-Linac (P-LINAC) will be started with a 325.224 MHz, 3 MeV Radio-Frequency Quadrupole (RFQ) accelerator. To ensure that a beam intensity of $\geq$35 mA can be injected into the downstream synchrotrons, the design beam intensity of this Proton-RFQ (P-RFQ) has been chosen as 70 mA. Based on the so-called NFSP (New Four-Section Procedure) method, two new beam dynamics designs with varying and constant transverse focusing strength, respectively, have been worked out to meet the latest design requirements using a compact structure.

Background

The old reference design (D2009) realized by using the NFSP method [1] and published in 2009 [2] was optimized for 45 mA and can provide good beam performance e.g. $\geq$95% transmission efficiency for up to 100 mA input beams. This 3.2 m long RFQ is very compact at 95 keV such a relatively high input energy $W_{\text{in, RFQ}}$ (when considering the $W_{\text{in, RFQ}}$ values adopted by other comparable machines e.g. CERN LINAC4, J-PARC RFQ-III, and SNS), as the length of the adiabatic bunching section is proportional to β^3 [3].

The recently updated design requirements for the P-RFQ have two main changes: 1) the design beam intensity I_{in} has been fixed as 70 mA for more safety; 2) the allowed maximum surface electric field $E_{\text{s, max}}$ is lowered to 33 MV/m, corresponding to a Kilpatrick Factor (KF) of 1.87 (formerly $KF\leq2.0$).

An important goal of the new design study is to minimize the output longitudinal emittance for making the matching to the downstream DTL easier and avoiding beam losses in the high-energy range.

Design Method & Results

Due to the success with the old reference design, the NFSP method is still adopted for both new designs. Different than the traditional LANL method, this method is characterized by a soft and symmetric pre-bunching, a fast main bunching, and then a fine bunching with a mixture of bunching and acceleration in the longitudinal plane as well as a varying focusing strength in the transverse plane which is adapted to the changing space-charge situation along the bunching process.

Besides a new NFSP design (D2014a), to meet the possible demands for the 4-vane RFQ version, another new design (D2014b) with a constant mid-cell aperture r_0 has been also developed using a so-called modified NFSP (mNFSP) method [4]: it has a NFSP-style longitudinal bunching but with a constant transverse focusing strength throughout the main RFQ.

For both of the new designs [5], the RFQ structure is even 10 cm shorter than that designed in 2009. As a result of the lowered $E_{\text{s, max}}$, the beam transmission efficiencies T are now slightly lower, but still $\geq$90%. However, in both cases, the difference in T for transported and accelerated particles is only 0.1%, which means most particles are well bunched and accelerated (see Figure 1). Meanwhile, from D2009 to D2014b and D2014a, the longitudinal output emittance was significantly reduced by 86% (all particles) / 20% (accelerated particles) and 91% (all particles) / 18% (accelerated particles), respectively.

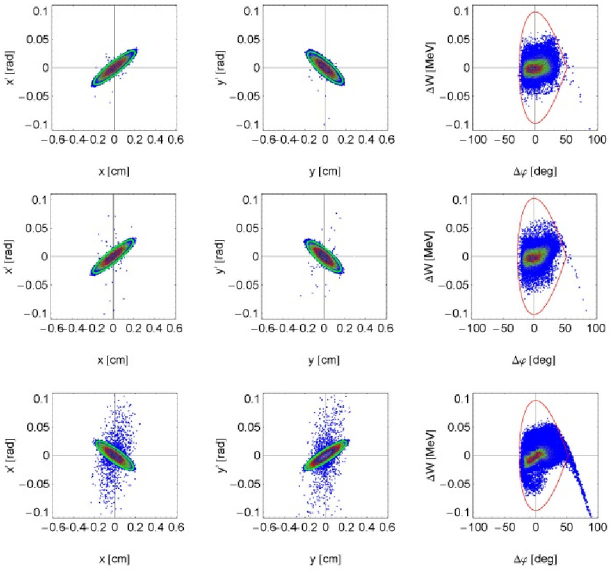

Figure 1: Output Phase Spaces (top: D2014a; middle: D2014b; bottom: D2009).

References

[1] C. Zhang et al., Phys. Rev. ST Accel. Beams 7, 100101 (2004).

[2] C. Zhang, A. Schempp, Nucl. Instrum. Methods Phys. Res., Sect., A, 609 (2009) p. 95-101.

[3] T.P. Wangler, *RF Linear Accelerators*, (Wiley-VCH Verlag GmbH & Co. KG, 2008).

[4] C. Zhang, “RFQ Beam Dynamics Design for Large Science Facilities and Accelerator Driven Systems”, HB’12, Beijing, China, September 2012, p. 419, http://www.JACoW.org

[5] C. Zhang, “Beam Dynamics for the FAIR Proton-Linac RFQ”, IPAC’14, Dresden, Germany, June 2014, p. 3226, http://www.JACoW.org

---

[#] c.zhang@gsi.de

DOI:10.15120/GR-2015-1-FG-GENERAL-22

Copper-plating of prototype cavities for the Proton Linac Accelerator

K. Dermati[1], *J. Boensch*[1], *N. Boensch*[1], *R. Brodhage*[1], *T. Dettinger*[1], *R. Erlenbach*[1], *R. Fuchs*[1], *E. Kammer*[1], *E. Merz*[1], *M. Müller*[1], *N. Norcia* [1], *R. Reiter*[1], *M. Romig*[1], *T. Schiemann*[1], *T. Schneidler*[1], *S. Teich*[1], *D. Volz*[1], *W. Vinzenz*[1]

[1]GSI, Darmstadt, Germany

Introduction

The FAIR anti-proton research program required a dedicated 70 MeV proton injector. The main acceleration of protons in the Proton-Linac will be provided by normal conducting, Crossed-bar, H-mode (CH) cavities according to the requirements and specifications of the accelerator physicists [1], [2]. For a high power RF test at GSI two prototype CH cavities are copper plated in the Galvanic of GSI. The requirement to be achieved was a constant, shiny (mirror finish) copper layer with a thickness of 50 μm all over the inner surface of the stainless steel CH cavities.

There have been two goals to be achieved during the electroplating work. First an exact, high quality copper layer and second the identification and optimisation of the procedure for the copper plating of all the CH cavities of the Drift Tube Linac Structure.

Electroplating / Copper Plating

To comply with the requirements a couple of dummies were produced and copper plated before processing the prototype cavities.

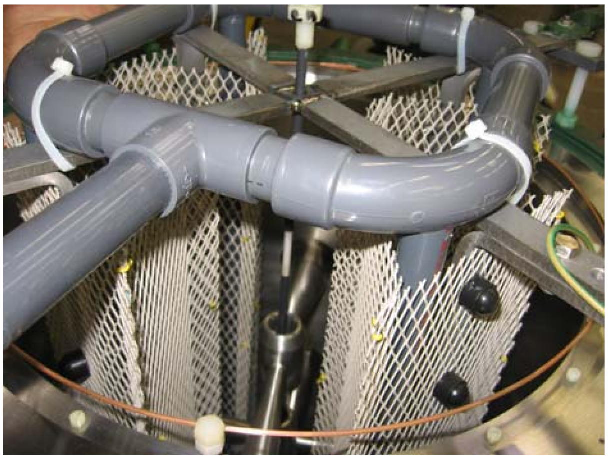

Figure 1: A CH-Cavity prepared for the Electroplating.

Electroplating started after suitable preparation including coating, forming and mounted the expanded metal anode gates. Various parameters should be considered and steered during all process: Shape of the anodes, distance to the surface of the cylindrical wall and stems, deflector plates, amperage, consistence of the baths, agitation during the plating, flow of the electrolyte and action time of each step of the plating.

After a cleaning and strong activation of the surface of the cavities a 15 μm nickel-strike base layer was given. Copper is an active metal and it is difficult directly plating iron-based surfaces. For this reason, such surfaces are first given a nickel-strike base coat, to which the copper can adhere.

The nickel strike bath is based on hydrochloric acid. Its deposition rate was 4,5 A/dm^2. A pulsed current process of 2 minutes current tact and 30 seconds current off was performed to avoid the forming of hydrogen bubbles, “pitting” on the surface. Electrolyte was transferred over the inner surface of the cavity during the current less tact.

The copper bath is based on sulphuric acid with additives which are responsible for the brightness and levelling of the deposited layer. The deposition rate was 3 A/dm^2. According to this ratio and the total inner surface the cavities stayed about two hours in the bath. A final polishing is necessary to get the shiny surface, Figure 2.

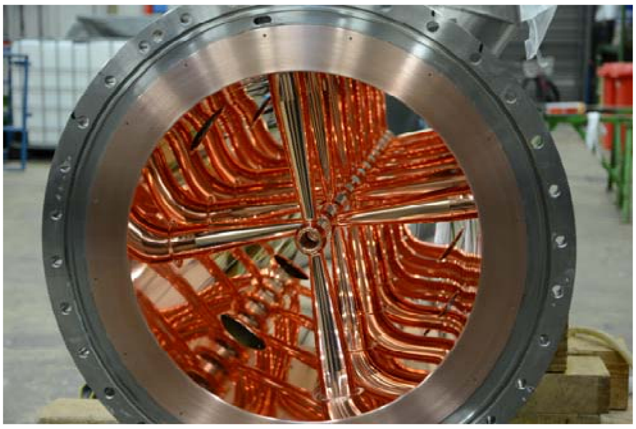

Figure 2: Shiny Copper plated prototype CH-Cavity.

Result

The copper plating of the two prototype CH cavities was commissioned with the expected performance. The required quantity and quality of the copper layer was achieved. The developed procedure and the gained experience might be used for the upcoming accelerator CH structure.

References

[1] Technical Report ”Proton Linac”, https://edms.cern.ch/document/994418/1.

[2] Status of the 70 MeV FAIR Proton Injector, Proceedings of IPAC2013, Shanghai, China, THPWO008.

DOI:10.15120/GR-2015-1-FG-GENERAL-23

Progress of the klystron and cavity test stand for the FAIR proton linac

A. Schnase[1], *E. Plechov*[1], *J. Salvatore*[1], *G. Schreiber*[1], *W. Vinzenz*[1], *C. Joly*[2], *J. Lesrel*[2]
[1]GSI, Darmstadt, Germany; [2]IPN Orsay, CNRS-IN2P3 Université Paris Sud, France

In collaboration between the FAIR project, GSI, and CNRS, the IPNO lab provided the high power RF components at 325.224 MHz for the cavity and klystron test stand [1] in the experimental hall LBH. For initial operation of the 3 MW Thales TH2181 klystron, a high voltage modulator from CERN Linac 4 was received as a loan. The 45 kW amplifiers for the 3 buncher structures of the FAIR proton Linac were carefully checked at the test stand, and prepared for cavity test operation.

Klystron test preparation

The company that originally wanted to provide the high voltage modulator for the klystron faced technical problems and finally abandoned this project. Fortunately the operating voltage and current of the klystrons for the CERN Linac 4 are quite similar to the TH 2181 klystrons foreseen for the FAIR Proton Linac. The Linac 4 repetition rate of 2 Hz is lower, than the 5 Hz rate foreseen for the Proton Linac. The pulse length for the proton Linac is shorter, which provides enough margins for operating the borrowed Linac 4 high voltage modulator. Effort was put into modifying and upgrading the existing infrastructure.

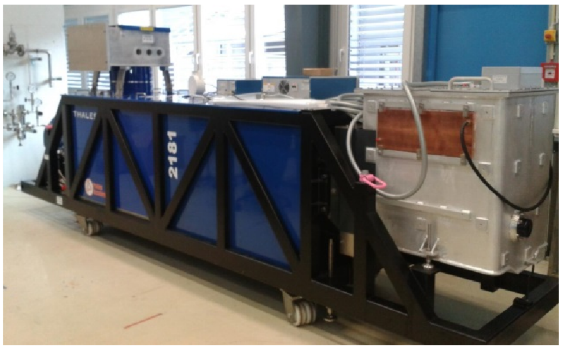

Figure 1: TH2181 Klystron in LBH test area.

The 3 phase electric supply connection was modified to provide sufficient margin for operating high voltage modulator and pulsed transistor amplifiers. At the former setup the auxiliaries were foreseen to be embedded into the modulator. Here we provided an additional rack containing the klystron filament power supply, the 3 solenoid power supplies and the two ion pump power supplies. The company who delivered the circulator for the klystron managed to adapt the cooling temperature range from 30+/-1°C to available 25°C. This allowed simplifying the cooling water distribution, which now can handle testing of klystron and transistor amplifiers.

The heater oil tank was prepared for the CERN modulator, and the filament power supply was tested with the goal to establish the power up and shutdown procedures. In operation of the solenoid power supplies in constant current mode, it was confirmed that they work as expected. The solenoids reach thermal steady state in two hours. The ion pump power supplies and the arc detection require fast acting interlocks. Accordingly the measurement & interlock rack was modified to process the additional signals. Careful checking of the interlock functionality and the signals processed by a PLC will ensure protection of the klystron according to the manufacturer specifications. The fastest response is handled by blanking the low level RF signal within microseconds.

First operation with the klystron will be without applying RF for commissioning and to understand the interaction with the modulator. As next steps, RF power will be send to a dummy load, and then the circulator will be included and measured by calibrated directional couplers. Finally we prepare to exercise the prototype CH cavity in the shielded area.

Transistor amplifier test

In autumn 2014 three 45 kW transistor amplifiers for the 3 (re-)bunchers of the Proton Linac were delivered. The alignment of the amplifiers and the RF output was improved for easier installation and the firmware was adjusted to the expected pulsed operation mode.

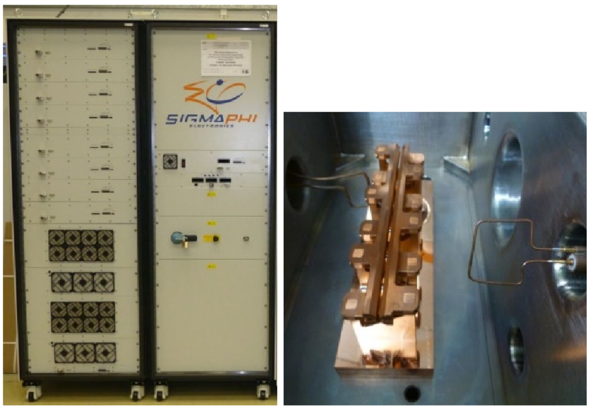

Figure 2: Amplifier (left) and RFQ test cavity structure.

Initial tests were conducted with a 50 Ohm power load at the amplifier output. The required 45 kW pulsed power was confirmed. From University of Frankfurt we received a compact 325 MHz test cavity structure and we prepare a site acceptance test of these amplifiers under pulsed conditions driving a resonant load.

References

[1] J. Lesrel, et. al. “RF Power Systems for the FAIR Proton Linac”, LINAC2014, Geneva, Sept. 2014, MOPP078

DOI:10.15120/GR-2015-1-FG-GENERAL-24

Space charge investigation for low energy ion beams with a 4-grid analyzer

C. Ullmann[1,2], *A. Adonin*[1], *R. Berezov*[1], *R. Hollinger*[1], *V. Ivanova*[1], *and O. Kester*[1,2]
[1]GSI, Darmstadt, Germany; [2]Goethe Universität, Frankfurt

4-grid Analyzer

The 4-grid Analyzer, or Retarding Potential Analyzer (RPA) is dedicated to space charge compensation measurements of ion beams by analyzing the energy distribution of secondary ions accelerated by the beam potential. The RPA consists of four grids, as shown in Figure 1. Grid one is on ground potential to shield the ion beam. Grid two repels electrons coming from the beam tube. The voltage on grid 3 is retarding and can be varied from negative to positive electric potential to filter secondary ions produced during interaction between primary ions and residual gas in the beam. The fourth grid repels electrons produced in the Faraday cup at the end of the RPA. For capturing the signal a current to voltage transformer (I-U transformer) with a high signal acceptance is used.

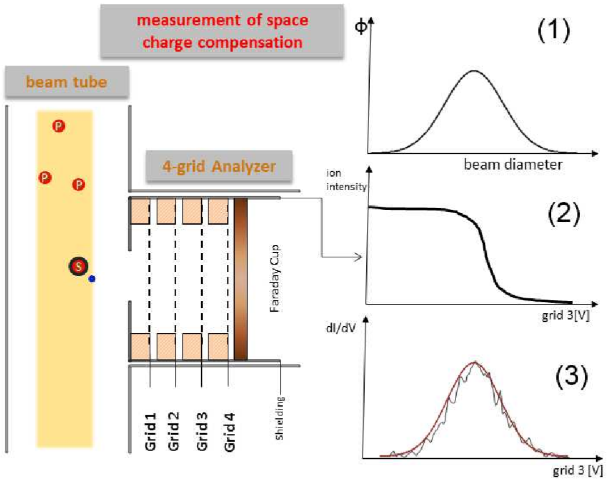

Figure 1: Schematic view of the 4- grid analyzer, data acquisition and analysis.

Secondary ions fully pass the third grid up to a certain potential which leads to a decrease of the Faraday cup signal. (1) shows an example for the ion beam potential as a function of the ion beam diameter. (2) shows the signal captured by the Faraday cup and (3) the estimated ion beam potential received from the measurement by derivation of signal (2). The uncompensated beam potential $\Delta\Phi_{uncomp}$ is calculated using

$$\Delta\Phi_{uncomp} = \frac{I}{4\pi \cdot \epsilon_0 \cdot v_{ion}} \tag{1}$$

Experimental Results

Measurements are performed at the high current test bench and at the high current test injector under variable conditions. First measurements are performed with a high current ion source (MUCIS), single hole extraction system with He and Ar gas. An example for the results is shown in Figure 2.

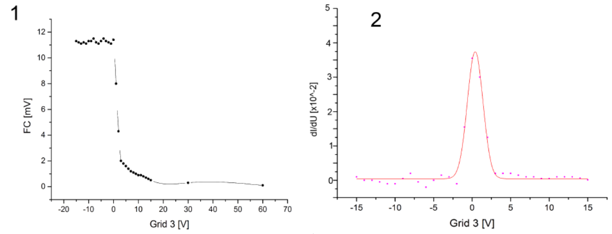

Figure 2: (1) Measurement at high current test bench $U_{Extr} = 20kV$,$I_{FC} = 7mA$; (2) Results via derivation

Above a voltage of $\Delta\Phi_{uncomp} = 122V$. This results in a space charge compensation of the ion beam of apparently 98%.

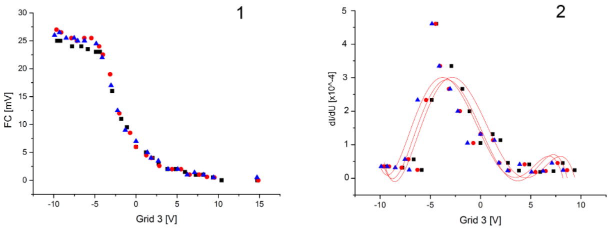

Figure 3: (1)Measurements at HOSTI test injector; $U_{Extr} = 110kV$,$I_{FC} = 10mA$ (2) Results via derivation

At HOSTI the RPA is installed behind a superconducting solenoid to analyze focused ion beams. Potentially inside the solenoid the beam compensation can partly be destroid. In Figure 3 space charge compensation varies round 97% based on $\Delta\Phi_{uncomp} = 23.7V$.

Outlook

It is planned to check on the time dependency of space charge compensation in a pulsed ion beam at HOSTI test bench. Various ion source types with different extraction systems for high current injection will be used to compare light and heavy ion operation as well as metal operation.

DOI:10.15120/GR-2015-1-FG-GENERAL-25

Advanced CST simulations for the FAIR p-LINAC BPMs

M. Almalki[1], *P. Forck*[1], *W. Kaufmann*[1], *T. Sieber*[1], *P. Kowina*[1], *C. Krüger*[1], *O. Kester*[1], *and C. Simon*[2]
[1]GSI, Darmstadt, Germany; [2]CEA-Saclay/DSM/Irfu, Gif-sur Yvette, France

At the planned Proton LINAC of the FAIR facility, fourfold button Beam Position Monitors (BPM) will be installed at 14 locations along the 30 m long FAIR p-LINAC [1,2]. Depending on the location, the BPM design has to be optimized, taking into account an energy range from 3 MeV to 70 MeV, limited insertion length at 30 mm or 50 mm beam pipe aperture. Detailed simulations of the button parameters with the finite element code CST [3] have been executed including pickup capacitance, impedance matching characteristic in time and frequency-domain. Additionally, the signal shape modification with respect to beam parameters, namely beam velocity and bunch length, has been investigated.

Capacitance and Electrical Properties

The pickup capacitance and the electrical properties for different geometries were investigated. The model consists of an inner conductor connected to a button electrode shown in Figure.1.

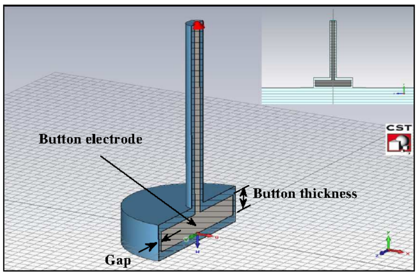

Figure 1: 3D model of the button pickup.

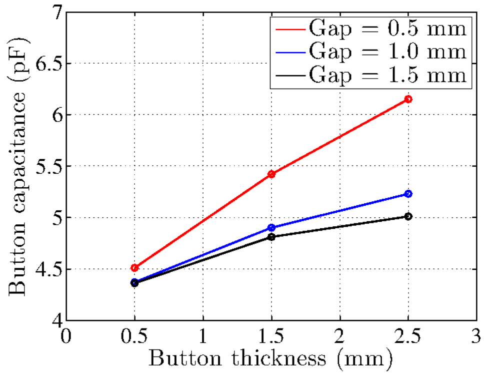

Figure 2: Pickup capacitance as a function of the button thickness calculated by CST Electrostatic Studio solver.

The button geometry has been modified by varying the button thickness and the gap between the button and the housing. The pickup capacitance for different button geometries is shown in Figure.2. A button thickness and gap size of 1 mm each results in a low capacitance, equivalent to high signal, and fits to the commercially available mechanical realization. The influence of further mechanical parameters on signal shape are discussed in [4] using CST Microwave Studio solver.

Bunch Length Investigations

CST Particle Studio was used to characterize the pickup signal width σ_s as a function of Gaussian bunch width σ_b at different beam velocities; β = 0.08, 0.27 and 0.37. The span of simulated bunch width starts from σ_b = 30 up to 960 ps.

The results show a linear relationship between the pickup signal and the bunch width down to a certain limit ($\sigma_b \approx$ 80 ps) shown in Figure.3. Below this limit there is no change in the output signal width as the bunch width decreases further. Those limits (for each β value) are used to estimate the pickup signal and the required analogue band width for signal processing.

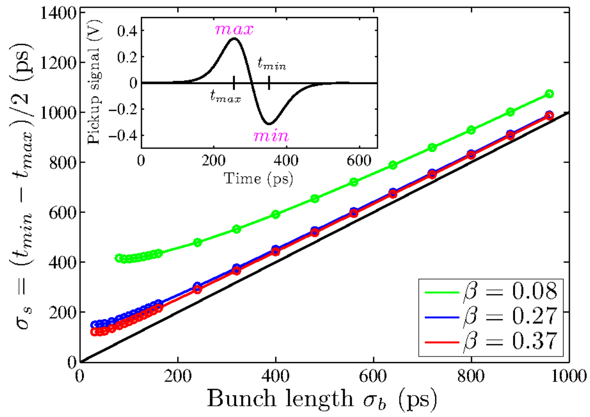

Figure 3: Relationship between bunch width σ_b and pickup signal width σ_s (σ_s calculated from the time difference between min and max values of the pickup signal).

References

[1] L. Groening et al., ”Status of the FAIR 70 MeV Proton LINAC”, LINAC’12, Tel-Aviv, p. 927 (2012).

[2] P. Forck et al., ”Design of the BPM System for the FAIR Proton-LINAC”, GSI scientific report 2010.

[3] https://www.cst.com/.

[4] M. Almalki, PhD Thesis, IAP University of Frankfurt, in preparation.

DOI:10.15120/GR-2015-1-FG-GENERAL-26

High power RF coupler for the FAIR p-LINAC cavities

F. Maimone, W. Vinzenz

GSI, Darmstadt, Germany

HISTORY

Since some decades most of the UNILAC cavities are equipped with the same type of RF couplers. Studies in the 80th have shown that a cylindrical ceramic as vacuum seal is nearly ideal. Compared to ceramic disks the real surface area hit by X-rays is much smaller. From fabrication issues much more manufacturing steps, including metallization of both tube ends, have to be passed.

A general composition is shown in [Fig. 1].

For applications at different power levels and different mechanical environments the design has just to be scaled.

APPLICATIONS

Beside the operation at the UNILAC at 36, 108 and 216 MHz the same kind of loop is used at CERN Linac3 (Lead Linac) at 101 MHz, at the therapy Linacs in Heidelberg (HIT) and Padova (CNAO) at 216 MHz [Fig. 1] and at BNL Upton NY at 100 MHz. The coupler is not built for a dedicated kind of cavity. A range of applications goes from RFQ, IH, Alvarez, Spirals to CH cavities covering a power range from 10th of kW up to 2 MW pulse (at 25% duty factor). Therefore a big number of flange-oriented types with respect to the dimensions of the used RF power lines as well are available.

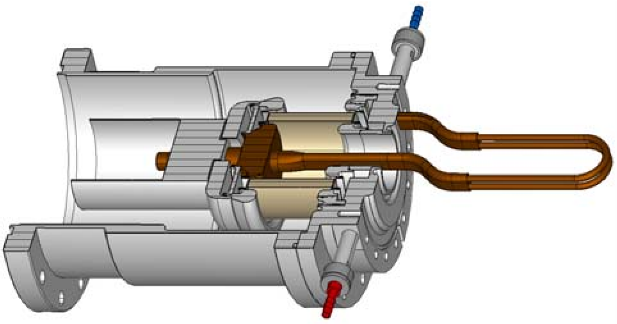

Figure 1: General composition of the GSI RF couplers

HIGH POWER RF COUPLER

The pLINAC providing up to 70 MeV proton beam for the FAIR facility is under construction. The normal conducting DTL of the pLINAC is composed by three Coupled Cross-bar H-mode (CCH) cavities, providing the acceleration up to the energy of 36 MeV, followed by three Cross-bar H-mode (CH) cavities. [1] In order to provide the input power to the CH-cavities a RF inductive coupler has been studied and developed.

The RF power coupler, consisting of a water cooled inductive loop, has to handle up to 3 MW pulsed power at 325 MHz. A dedicated study of the coupling factor and the electromagnetic field for different penetration length of the coupler inside the coupling cell – the intertank unit connecting two neighboured cavities long 2β and hosting the triplet lens - and for different angles with respect to the beam axis has been carried out.

According to the results of the simulations an optimized design of the inductive loop was produced and a prototype of the coupler has been manufactured at the GSI workshop [Fig. 2].

The coupler is vacuum leak tested and low level RF measurements in the build-in condition at the CCH prototype cavity are planned to be performed in March 2015 at the RF test bench.

Figure 2: Prototype of the RF coupler fot the CH-cavities of the pLINAC

References

[1] Technical Report "Proton Linac", https://edms.cern.ch/document/994418/1.

[2] F. Maimone, G. Clemente, W. Vinzenz, Proc. of LINAC2014, Geneva, 2014

DOI:10.15120/GR-2015-1-FG-GENERAL-27

System Simulation of Bunch-to-Bucket Transfer Between Synchrotrons*

T. Ferrand†[1] *and J. Bai*[2]
[1]TEMF, Technische Universität, Darmstadt, Germany; [2]IAP, Goethe Universität, Frankfurt am Main, Germany

Introduction

A model of the low-level RF (LLRF) synchronization topology at SIS18 and SIS100 under Ptolemy II [1] is currently under development. This model enables to simulate the behavior of the synchronization signals during the synchronization procedure at the transfer flattop within the framework of a deterministic bunch-to-bucket transfer. The Java-based heterogeneous structure of the Ptolemy II software offers an intuitive parallelization procedure by splitting the different sub-models in concurrent threads.

Simulation of the LLRF system

The simulated LLRF system is composed of two independent and non-synchronized entities. The first entity is based on the phase advance measurement between a radiofrequency (RF) signal and a reference (REF) signal. The REF signal is derived from the periodically shared BuTiS synchronization signal $T_0 = 10\ \mu$s:

$$f_{REF} = \frac{N}{T_0} \qquad \text{with} \quad N = floor(f_{RF}T_0) \qquad (1)$$

The REF signal is generated by a DDS. A periodic reset of the DDS phase value consistent with the synchronization signal ensures that the phase advance relation between the REF signal and the synchronization signal remains constant. This REF signal can thus be duplicated to provide a fix phase measurement reference.

The phase advance measurement between the RF and the REF signal relies on a frequency transposition and a direct IQ demodulation [2]. This method benefits from a high phase measurement accuracy and a maximum error value of 0.6^o at 5.4 MHz and delivers its phase measurement asynchronously every 3.22 μs, i.e. the delay between the most recent phase advance measurement and the next slope of the synchronization signal is not constant.

The second simulated entity corresponds to an additional DDS module, which duplicates an RF signal in real time. This DDS may receive the same frequency value command as the DDS, which generates the original RF signal such, that duplicated and original RF signals have the same frequency but their phase advance relationship remains free. The measured phase advance from the first entity is used to determine the phase offset with respect to a certain time event such as a trigger derived from the synchronization signal. The duplicated DDS resets at this trigger with the calculated offset, which enables the duplicated RF signal to synchronize with the original RF signal.

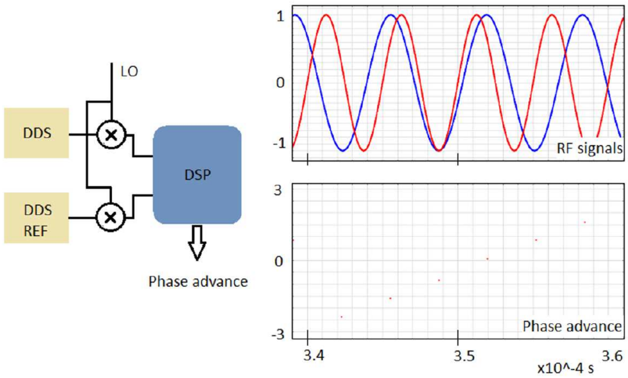

Fig 1, left: representation of the phase measurement entity.
above right: RF signals of 157 and 200 kHz.
below right: relative phase advance measurement.

A conventional synchronization loop may be used to synchronize a DDS RF signal with the locally emulated signal. In the framework of the bunch-to-bucket transfer synchronization between SIS18 and SIS100, a symmetrical implementation of this system may enable duplicating the synchronization RF signals locally, if they are required. The synchronization of such emulated systems needs a data transfer between the two supply rooms only once per acceleration cycle.

Outlook

The implementation of a hardware synchronization system on the basis of this simulation is currently under study and is expected to be implemented in the coming months. This demonstration system may enable to evaluate the reliability and the robustness of the simulation model. A simulation-based optimization for the local resynchronization procedure is foreseen.

References

[1] Claudius Ptolemaeus, editor, “System Design, Modeling, and Simulation using Ptolemy II”, Ptolemy.org, 2014, URL: http://ptolemy.org/books/Systems

[2] H. Klingbeil, “A Fast DSP-Based Phase-Detector for Closed-Loop RF Control in Synchrotrons” IEEE Transactions on Instrumentation and Measurement, Vol. 54, No. 3, June 2005

---

* Work supported by GSI, cooperation with TU Darmstadt.

DOI:10.15120/GR-2015-1-FG-GENERAL-28

Progress in damping of longitudinal beam oscillations during acceleration[*]

D. Lens[†][1], *U. Hartel*[1], *H. Klingbeil*[1,2], *B. Zipfel*[1], *K. Groß*[2], *J. Adamy*[3], *B. Reichardt*[3], *M. Kumm*[4], *K. Möller*[4], *and P. Zipf*[4]
[1]GSI; [2]TU Darmstadt, TEMF; [3]TU Darmstadt, RMR; [4]University of Kassel, Digital Technology Group

Introduction

In the FAIR synchrotrons, coherent longitudinal oscillations of the bunched beam will have to be damped by dedicated feedback systems. While the damping for coasting beam energy has been successfully verified in SIS18 by several experiments (cf. e.g. [1]), the damping of these modes during the acceleration process poses additional challenges. The main technological issues are discussed and a progress status is given. For details on the longitudinal feedback system for FAIR with bunch-by-bunch feedback, we refer to [2].

Status of Main Projects

Group-DDS Phase Calibration

For the low-level RF (LLRF) system, it is essential that reference signals are provided with a phase stability better than 1°, cf. [3]. Such reference signals are generated by DDS modules, which show a frequency-dependent behavior during the acceleration ramp that must be compensated to reach the high accuracy requirements. A compensation strategy using calibration electronics has been employed and verified in beam experiments [3]. In addition, a software tool has been developed which enables a semi-automatic calibration, drastically reducing the effort to perform a calibration of a DDS crate.

Feedback Tuning During Acceleration

A finite impulse response (FIR) filter is used for the damping of longitudinal modes. For this filter, a tuning rule based on the synchrotron frequency was already experimentally verified in the past. In a recent beam experiment [4], the successful damping of coherent quadrupole oscillations during acceleration has now been demonstrated, cf. Fig. 1. The results are currently being used to verify the tuning strategy during acceleration.

FPGA Implementation of Tunable Filter

A dynamically reconfigurable FIR filter has been implemented on an FPGA [5] and will be integrated into the existing framework of the DSP system [1] used for longitudinal feedback. The next step will then include the implementation of the tuning rule for the adaption of the filter coefficients.

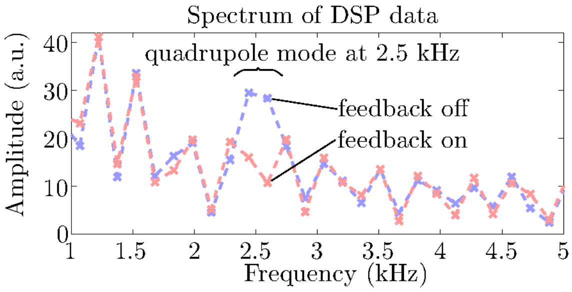

Figure 1: Damping of longitudinal coherent quadrupole modes in SIS18 during acceleration, Sep. 7, 2014.

Optimized Filter Design

The filter implementation [5] in principle allows for more complex filters with a larger number of coefficients than currently used. In a cooperation project with TU Darmstadt (RMR), the potential of these longer filters is currently analyzed. Measurements with beam showed as a proof of principle that the damping of the closed loop may be increased. However, careful investigations are still necessary to study possible implications concerning noise and robustness.

Future Work

The phase response compensation of DDS modules will be automated further to enable periodic calibrations of the reference DDS crate to compensate long-term drifts.

Concerning the damping of longitudinal modes, further steps will be taken towards standard operation as described in [4].

References

[1] H. Klingbeil et al., "A digital beam-phase control system for heavy-ion synchrotrons", IEEE Trans. Nucl. Sci. 54(6)2604:2610 (2007)

[2] K. Groß et al., "Verification of the Longitudinal Feedback Topology in SIS18", these proceedings

[3] B. Zipfel et al., "Generation of RF frequency and phase references on the FAIR site", Proc. IPAC2014, THPRO102 (2014)

[4] D. Lens, "Beam experiment: damping of longitudinal quadrupole oscillations during acceleration in SIS18", GSI memo (2014)

[5] K. Möller et al., "Dynamically reconfigurable FIR filter architectures with fast reconfiguration", Proc. ReCoSoC (2013)

---

[*] Work supported by GSI.

[†] d.e.m.lens@gsi.de

DOI:10.15120/GR-2015-1-FG-GENERAL-29

FAIR HEBT System - status report

F. Hagenbuck, L. Bozyk, A. Krämer, B. Merk, C. Mühle, S. Ratschow, B.R. Schlei, P. Spiller, B. Walasek-Höhne, H. Welker, and C. Will
GSI, Darmstadt, Germany

Modifications in the HEBT System Layout

Based on a decision of the project lead FAIR@GSI and FAIR the direct connection from SIS18 to the Collector Ring (CR) via the last part of the Ring Branch of the Super-FRS was included into the planning of the modularized start version.

The concept for the positioning of safety beam plugs in the HEBT system was further worked out in coordination with the radiation protection department. For the beam plugs in four beam line sections detailed FLUKA studies were performed for accidental beam deposition to determine the expected radiation level in neighbouring areas and to optimize length and material of the beam plugs [1].

Pressure profile calculations of the vacuum system were started to determine number, type and location of pumps.

Status of procurement

In July 2014 the CR-like HEBT magnets (2 dipole, 5 quadrupole magnets) were assigned by FAIR Council resolution to the Budker Institute (BINP, Novosibirsk, Russia) whereas the bulk of the HEBT magnets was already assigned in 2011/2012 to the Efremov Institute (NIIEFA, St. Petersburg, Russia; batch1-3). All related vacuum chambers will be built by BINP. The production of the first pre-series dipole magnet (type dip1s_0) of batch1 (51 dipole magnets and vacuum chambers) started in 2014, the coils are produced (see Fig. 1), the laminations punched and the magnet is expected to be finished in May 2015. The vacuum chamber is expected to be ready in June 2015. The preliminary design review for the second pre-series dipole magnet (type dip13_0) was successfully concluded, currently the manufacturing drawings for the final design review are in preparation. The detailed specifications of batch 2 (17 dipole, 102 quadrupole, 80 steering magnets and vacuum chambers) were released in August 2014. The contracts are still under negotiation with NIIEFA and BINP. The detailed specifications of batch3 (5 dipole, 71 quadrupole, 12 steering magnets and vacuum chambers) are supposed to be available in spring 2015.

Figure 1: Set of coils for pre-series dipole magnet dip1s_0

In May 2014 a first contract between FAIR, the indian shareholder Bose Institute (Kolkata) and the provider ECIL (Electronics Corporation of India Limited) comprising 78 quadrupole power converters was signed. This contract covers all quadrupole power converters needed for the standard quadrupoles (quad2) in the 18 Tm and 13 Tm beamlines of module 0-3. In the meanwhile the conceptual design review for two quadrupole power converter types was successfully concluded (Nov 2014, Jan 2015). With respect to a second contract the detailed specifications of the power converter types for the 18 Tm steering magnets and for further quadrupole magnets were recently given into the EDMS release process.

All technical documents for the HEBT beam diagnostic standard vacuum chambers were handed over to the indian shareholder Bose Institute in 2014. In the tendering process the indian partner was supported in the evaluation of possible providers by GSI experts from the vacuum and quality assurance department. A decision will be taken by an indian selection committee in the beginning of April 2015. A contract with the slovenian in-kind partner was signed in November 2014, comprising HEBT BPM pre-amplifiers, Data Acquisition (for BPM, Beam-Loss Monitor System and Beam Current Transformer) and Pressurized Air Drives and Control. Furthermore several beam instrumentation developments for applications in the FAIR HEBT system were conducted successfully in 2014 as for example a new system for scintillating screen based diagnostics [2].

Building plannning

The review of the 5th preliminary building shell plan of G0704A and G0702A took place. However 3D collision checks could be done only with the 3D model of the buildings whereas the 3D model of the technical building equipment was not available. Additionally the 4th preliminary building shell plan of H0705A was checked informally.

References

[1] S. Damjanovic et al., “FLUKA Simulations of the FAIR HEBT System: Optimization of the Safety Beam Plugs (Diffusors)”, GSI Scient. Report 2014

[2] B. Walasek-Höhne et al., “CUPID: New System for Scintillating Screens based Diagnostics”, GSI Scient. Report 2014

DOI:10.15120/GR-2015-1-FG-GENERAL-30

FLUKA Simulations of the FAIR HEBT System: Optimization of the Safety Beam Plugs (Diffusors)

S. Damjanovic[1], *F. Hagenbuck*[1], *B. Merk*[1], *T. Radon*[1],
[1]GSI, Darmstadt, Germany

The complex High Energy Beam Transport (HEBT) system of FAIR allows for parallel user operation with different beams. To ensure safe operation the installation of safety beam plugs ('diffusors') is foreseen. These are mobile blocks to be used in case of an emergency situation to intercept an unwanted beam and thereby reduce the radiation level in the neighbouring areas accessible by personnel during normal operation. This provides redundancy to interlock magnets. FLUKA studies have been performed for accidental scenarios with such diffusors (named 'Dnn'), individually for D20, D23, D22 and D14, assessing the resulting radiation level and optimizing the diffusor lengths and material.

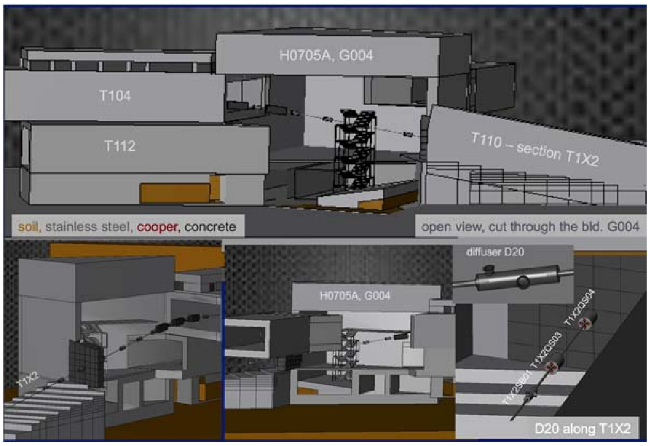

Figure 1: FLUKA geometry of bld. G004 with the diffusor D20 along the sloped beam line T1X2.

To obtain realistic radiation fields, precise modelling of the geometry of the HEBT system over extended regions was required. This includes the complex building G004 with the sloped beam line T1X2 from SIS100 along the tunnel T110 (extraction region) and the complete tunnels T104, T112 (Fig.1), and the tunnel T113 with the beam lines TAP1, TSN1, TAP2, TXL3, TPP1, TPP2 (Fig.2 left). The right part of Fig.2 indicates the two modelled regions with the two shaded areas (upper for Fig.1).

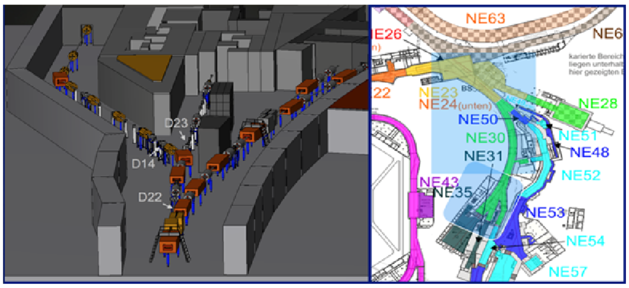

Figure 2: FLUKA geometry of the last section of the tunnel T113 with the diffusors D23, D22 and D14 (left).

The results of the effective dose distribution from a SIS100 proton beam with an intensity of 2.5×10^{13}p at E_k=29 GeV hitting the diffusors D20 and D23 (made of iron) are shown in Figs.3 and 4, resp. It is found that for an accidental scenario with D20 a diffusor length of 20 cm would be optimal. This would lead to effective doses <1μSv at the surface level of bld. G017 (areas NE25 and NE26), allowing for 10 shots per year, and <<1mSv in the areas of NE30 and NE50, allowing for open access to these areas. The length of the diffusors D23, D22 and D14 placed in the last section of the tunnel T113 was optimized to keep the access to the areas NE31, NE35 (antiproton target area and experimental caves) and NE53.

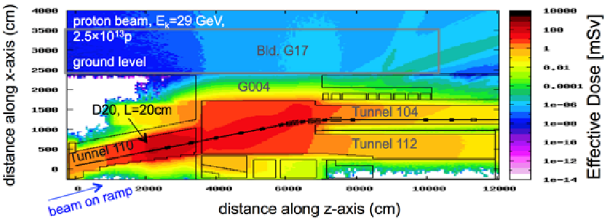

Figure 3: Effective dose for one beam pulse hitting the diffusor D20 placed along the sloped beam line T1X2.

For accidental scenarios with the diffusor D23 where a beam meant to be transported to the APPA cave accidentally was directed to the pbar target area, a minimum length of 40 cm iron would be required to keep the access to all neighbouring areas, while 20 cm would be sufficient for D22 and D14. The replacement of 40cm iron by 20cm tantalum would assure the same length for all diffusors. In the future, two more diffusors, D12 and D13 (intercepting the SIS18 beam) will have to be studied before concluding on the final specification of the material and dimensions of the diffusors and their chambers.

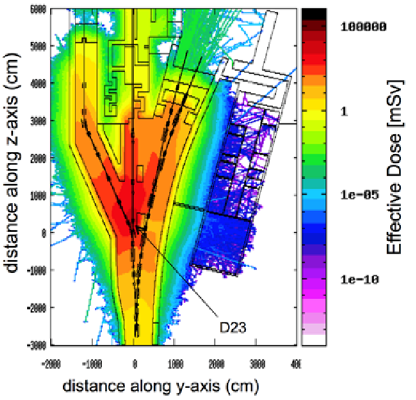

Figure 4: Effective dose for accidental scenario with D23.

DOI:10.15120/GR-2015-1-FG-GENERAL-31

Pilot study of beam position and profile monitoring for the pBar target

A. Reiter, H. Bräuning, J. Frühauf, H. Graf, S. Löchner, M. Witthaus
GSI, Darmstadt, Germany

At secondary target installations like the FAIR antiproton target, monitoring of the beam-target-overlap is a crucial task for the beam instrumentation. For antiproton production an intense 29 GeV proton beam pulse is extracted within 50 ns from the SIS100 synchrotron. The primary beam is focussed after a 3 m drift section in air on a 3 mm Nickel target rod. Because the target station is surrounded by a 1 m iron shielding, the spot size must be derived from detectors in the short drift section. To this purpose the performance of two detectors operating in air has been studied with 300 MeV/u Nickel beams and fast extraction.

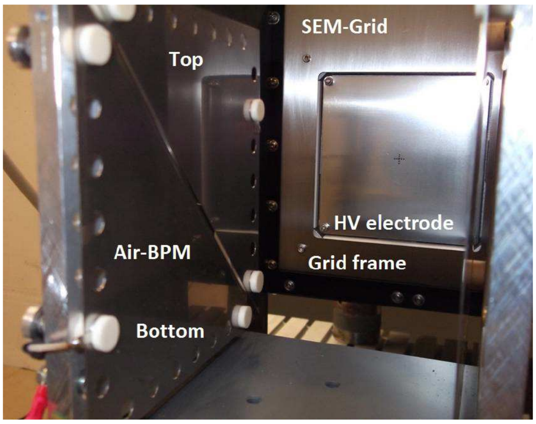

Figure 1: Air-BPM (front) with two electrodes (Bottom and Top) shown on the left; SEM-Grid (at back) with HV electrodes that cover the arrays of Tungsten wires.

Experiment Setup and Results

Two radiation-hard detectors were installed at the end of the HTP beam line next to the dump (see Figure 1):

- ”Air-BPM”: This detector consists of two diagonally-cut 135 mm electrodes, separated by a ground guard, and was placed 50 mm from the beam axis. A vertical motor drive typically moved the device in 1 mm steps.
- SEM-Grid: This detector is an existing GSI design mounted on an external pneumatic drive 20 cm in front of the beam dump. No high voltage was applied.

Both detectors were connected via pulse-stretchers to charge-to-frequency converter POLAND units [1] and read out via FESA, the new FAIR standard for acquisition systems. For each spill offset-corrected data were stored for further analysis. The Air-BPM signals were fed to the POLAND units via 80 m long coaxial cables to emulate the situation in the target hall where 150 m are required.

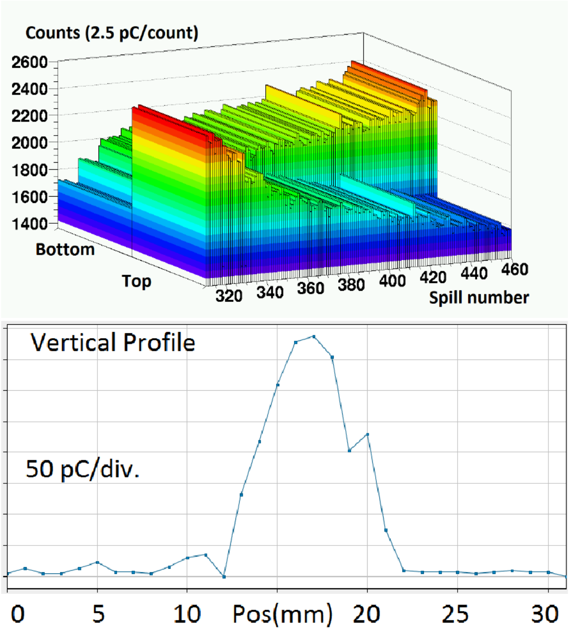

Figure 2: Scan of Air-BPM for 1x10^9 Ni ions (A) and vertical SEM-Grid profile for 2.5x10^9 Ni ions (B).

In Figure 2 detector signals of Air-BPM (A) and SEM-Grid (B) are presented. The Air-BPM was scanned through the beam in 1 mm steps. For each of the 15 positions ten spills were analysed and the normalised ratio ’difference-over-sum’ Δ/Σ calculated. The measured gradient of Δ/Σ=(1.42$\pm$0.02)%/mm is in good agreement with the theoretical value based on the electrode geometry.
The vertical profile shows a smooth distribution with a kink at 19 mm, which might be due to imperfections in the offset subtraction. The full profile width of 10 mm fairly agrees with the data of Cromox screen and SEM-Grid in the upstream diagnostic chamber. The calculated charge integral is only 20% lower than the prediction of Sternglas [2]. Similar ratios have been observed in ref. [3] and by the authors for other data sets of SEM-Grids installed in vacuum. However, the present data are yet too sparce to conclude that the secondary electron yield does not suffer significantly from operation in air. Further data need to back up the present encouraging results.

References

[1] S. Löchner et al., GSI Scientific Report 2013, Darmstadt.

[2] E. J. Sternglas, Phys. Rev. 108 (1957) 1.

[3] C. Nociforo et al., ”Profile Monitors for the Super-FRS”, This Scientific Report.

DOI:10.15120/GR-2015-1-FG-GENERAL-32

Transport concept for highly activated antiproton production targets

M. Helmecke[1], *G. Fehrenbacher*[1], *V. Gostishchev*[1], *R. Hettinger*[1], *K. Knie*[1], *R. Lang*[1], *J. Fitting*[2]
[1]GSI, Darmstadt, Germany; [2]Kraftanlagen Heidelberg GmbH, Heidelberg, Germany.

The antiprotons of the FAIR facility will be produced by a 29 GeV proton beam hitting a nickel target. Then they are focused by a circular magnetic field (magnetic horn) and transferred to the collector ring (CR) [1]. The target and the magnetic horn will become highly activated (up to 10^{11} Bq) during the antiproton production. Dedicated shielding calculations have been performed so far [2].

The target and the magnetic horn have to be exchanged regularly. Their activation leads to several technical challenges: To dismount the target or the magnetic horn these components have to be transported into a hot cell in the building of the Super Fragment Separator (SFRS). It is absolutely mandatory, that during handling and transport target and magnetic horn are surrounded by a sufficient shielding at all times [3]. Additionally, due to the radiation level the access to the target hall is limited (controlled area) and remote handling components have to be used. A target handling concept has been developed that fulfills all of these conditions (see [4]). A study together with Kraftanlagen Heidelberg has been carried out concerning legal aspects of this concept and to develop functional specifications of the necessary handling components in order to obtain the operation permit.

The handling in the pbar building is schematically shown in figure 1: In the first step the target and the magnetic horn are pulled out of the target station by a half-automated transport container via a dedicated rail system (pos. 1). To fix the components a fast coupling system is used. (The target and the magnetic horn are transported separately.) After the transport container is closed it is positioned under a shaft (pos. 2). A shielding flask above the shaft is equipped with a carrying frame that pulls the component through the shaft (pos. 3). Finally the shielding flask is closed (pos. 4) from below and lifted up by a transport trolley to bring it to the SFRS building.

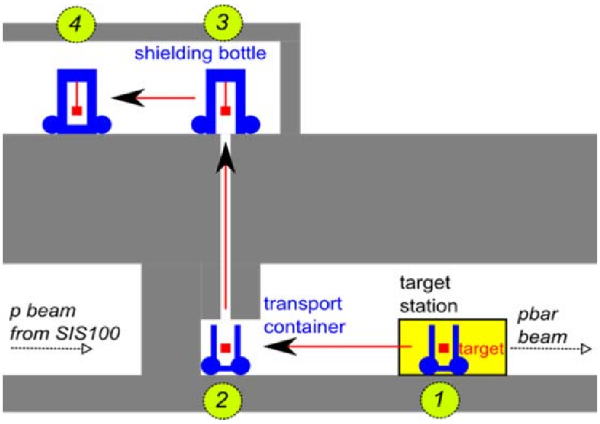

Figure 1: Schematic drawing of the target handling in the pbar building.

Inside of the shielding flask the target or the magnetic horn is fixed vertically, the highest radiation level is at the bottom, the lowest at the top. Figure 2 shows a cut of the flask with the magnetic horn fixed inside at the carrying frame. The wall thickness of the flask is designed in a way that the maximum dose rate at the outer surface is below 100µSv/h. The total weight of the flask is about 24 t.

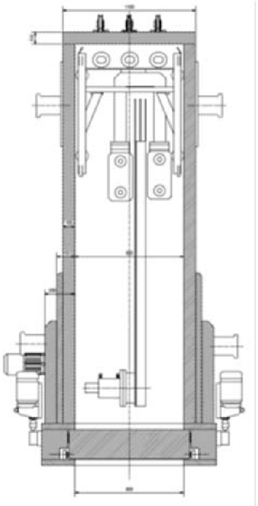

Figure 2: Cut of the shielding flask with magnetic horn and its stripline fixed inside.

Finally inside of the SFRS building the content of the shielding flask is transferred into the hot cell: First a traverse is fixed at the shielding flask that it can be moved by the crane of the building. This crane meets high safety standards, which are already predefined. With this traverse the flask is lowered about 6 m down next to the roof of the hot cell. Then for the final connection with the hot cell an adapter is placed also providing an interlock signal for the shutters of the hot cell and the shielding flask. When both shutters are open the carrying frame of the flask lowers down the component into the hot cell where it is dismounted by a technician of the SFRS group. Then the flask is closed again and is brought back to a parking position in the pbar building. The new target is then brought inside by using the same carrying frame of the shielding flask.

References

[1] Dolinski et al., Nuc. Instr. Meth. A 629 (2011) 16-24.
[2] GSI Scientific report (2011) PNI-ACC-14 483.
[3] 7. Teilerrichtungsgenehmigung, Hessisches Ministerium für Umwelt, Energie, Landwirtschaft und Verbraucherschutz, Wiesbaden (2013).
[4] Technical Design Report on the Antiproton Target and Separator, pbar working group, GSI, Darmstadt (2014).

DOI:10.15120/GR-2015-1-FG-GENERAL-33

Activation of the aluminium target by 200 MeV/u uranium beam *

P. Katrik[1,2,#], *D. Hoffmann*[1,2], *E. Mustafin*[2], *and I. Strasik*[2]
[1]TU Darmstadt, Darmstadt, Germany; [2]GSI, Darmstadt, Germany

Introduction

The paper presents new results of experimental study of the residual activity induced by high-energy heavy ions in common accelerator constructing materials. This study is a part of a broader research activity for validation of Monte Carlo codes and data libraries. There are several publications reporting the activation of different targets by various heavy ions with energies from 500 MeV/u up to 1 GeV/u [1-4].

Experiment and Simulation

The experimental target was designed in the stacked-foil geometry of 70 pieces. The foils were aluminium discs with the thickness of t = 0.1 mm and diameter d = 10 cm. The target was irradiated by 200 MeV/u $^{238}U^{(+73)}$ beam. The total number of projectiles accumulated on the target was 2.8×10^{12} ions. Gamma-ray spectra of each foil were measured individually or in groups of 5 foils together. Two series of measurements were performed: ~6-20 days and ~130-180 days after the end of irradiation. The experimental data were compared with the Monte Carlo simulations by FLUKA 2011.2c.0 code [5]. The residual activities were recalculated to the end of irradiation.

Results and Discussion

Out of all nuclides observed in the spectra we present here only the results for ^{7}Be, ^{22}Na and ^{237}U.

The distribution of ^{237}U (see Table 1) in depth could be used for finding the range of primary ^{238}U ions, because the masses of these nuclei are almost equal [4]. The FLUKA code predicted presence of ^{237}U in only two foils (Nr. 34 and Nr. 35), but we measured activity of this nuclide in the foil Nr. 36 as well. The simulation expects shorter range and about 40% lower production of ^{237}U.

Table 1: Total activity produced by ^{237}U in Al target

Foil Nr.	Depth [mm]	Activity of ^{237}U produced in target [Bq/mm/ion]	
		Simulation	Experiment
34	3.35	$1.262\times10^{-8} \pm 1\times10^{-10}$	$1.546\times10^{-9} \pm 2\times10^{-11}$
35	3.45	$2.710\times10^{-8} \pm 1\times10^{-10}$	$6.276\times10^{-8} \pm 7\times10^{-11}$
36	3.55	0	$3.461\times10^{-9} \pm 2\times10^{-11}$
SUM of Activity:		$\mathbf{3.973\times10^{-8} \pm 2\times10^{-10}}$	$\mathbf{6.776\times10^{-8} \pm 8\times10^{-11}}$

The depth profiles of ^{7}Be and ^{22}Na are presented in Figure 1 and Figure 2, respectively. The simulation is in agreement with the 1st and 2nd set of measurement only in the first foils of the target. In the depth of about 1.25 mm (the vertical line 150 MeV/u) differences between simulation and experimental data become evident. The disparities between the 1st and 2nd set of measurement in the range area are caused due to decaying of short-living isotope which was influencing the 1st set of measurement. In the range area the simulation should be compared with the 2nd set of measurement. One may observe an overestimation of the residual activity in the simulation data.

We observed the discrepancy (of the production of the nuclides in the target) between simulation and experimental data starting from the energy of the primary particles slowed down to 150 MeV/u and/or lower. The biggest difference in the case of ^{7}Be is in the depth corresponding to the primary particle energy of 125 MeV/u (see Figure 1). That is exactly the energy of the change between two Nucleus-Nucleus interaction models in FLUKA code (from Relativistic Quantum Molecular Dynamics for higher energies to Boltzmann Master Equation for lower energies) [5].

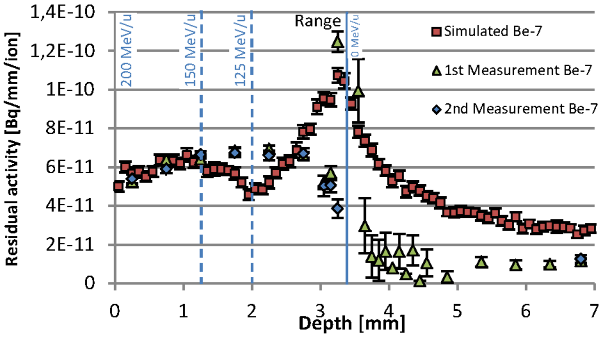

Figure 1: Depth profile of the residual activity of ^{7}Be.

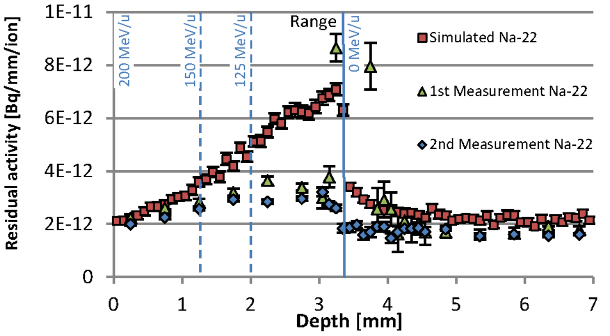

Figure 2: Depth profile of the residual activity of ^{22}Na.

References

[1] I. Strasik at al., Nucl. Instrum. Methods Phys. Res. Sect. B 266 (2008), pp. 3443-3452.

[2] I. Strasik at al., Nucl. Instrum. Methods Phys. Res. Sect. B 268 (2010), pp. 573-580.

[3] V. Chetvertkova at al., Nucl. Instrum. Methods Phys. Res. Sect. B 269 (2011), pp. 1336-1340.

[4] V. Chetvertkova at al., “Activation of Aluminium by Uranium”, HB2010, Morschach, Switzerland, 2010, p. 250-253.

[5] A. Ferrari at al., Reports No. CERN-2005-10, INFT/TC_05/11, and SLAC-R-773.

---

* Work supported by HGS-HIRe.

#p.katrik@gsi.de

DOI:10.15120/GR-2015-1-FG-GENERAL-34

Developments of the Palmer pickup tank for stochastic cooling in the CR

D. J. Barker[1], *R. Böhm*[1], *L. Thorndahl*[2], *and C. Dimopoulou*[1]
[1]GSI, Darmstadt, Germany; [2]CERN, Geneva, Switzerland

Introduction

This report details the design and construction progress made on the Palmer pickup tank for the stochastic cooling system of the collector ring (CR) during 2014 at GSI. The CR is designed for the stochastic cooling of antiprotons and RIBs. For details of the complete stochastic cooling system including particle beam parameters see [1]. For the stochastic pre-cooling of RIBs, we use the Palmer method in combination with pickups of large acceptance to cool injected hot ion beams with large momentum spread. For this purpose Faltin type pickups have been designed and published previously [2]. The Faltin rail is a travelling wave pickup in the form of a rectangular coaxial structure with slots in the top which couple to the beam.

Drawing and Construction

Drawing work on the full tank began and finished 2014 as shown in figure 1, although work on the Faltin rails itself continues. To test the pickup designs prototypes were made. During 2014 drawing work on three different prototypes was completed. Construction and procurement of the prototypes was finished in December. The prototypes are shown in figure 2. The robustness of the assembly method was tested. Microwave measurements made on the prototypes which showed good agreement with simulations and are shown in figure 3.

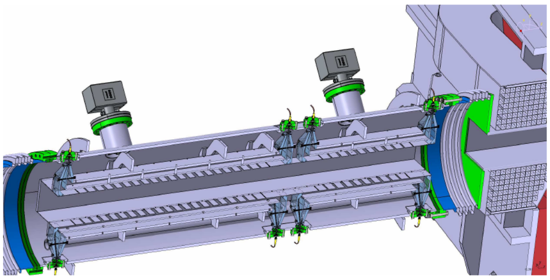

Figure 1: Cross sectional preliminary drawing of the full Palmer pickup tank(2 m installation length).

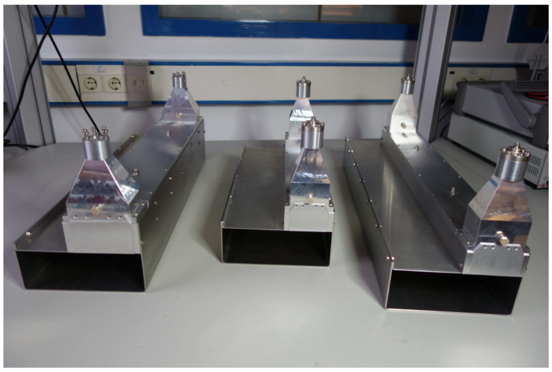

Figure 2: Three Faltin prototypes of one quarter of the pickup.

Simulations

Several unwanted modes which interfere with beam cooling were discovered and simulations with lossy ferrite material were conducted in order to damp these modes. Ferrite or some other lossy material will definitely be necessary within the pickup tank to maintain beam cooling performance. In 2014 a program was written which takes impedance and phase data of these waveguide pickups and adds signals from several of these pickups using delay lines of specific length to produce a flat impedance and linear phase over a desired band. This process was optimised using a genetic algorithm. This will be used for further optimisation of the pickup.

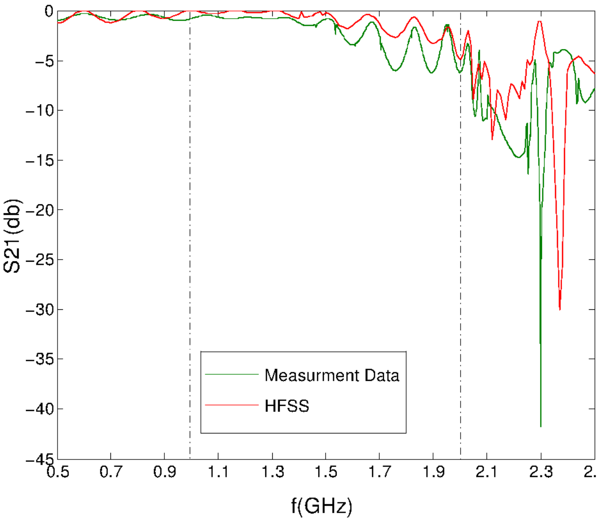

Figure 3: Comparison of measurements of S21 using a network analyser and S21 data from HFSS simulations.

References

[1] CR Technical Design Report 2014 and C.Dimopoulou et al., this report.

[2] D. Barker et al., JACoW Proc. COOL'13, WEPPO21.

DOI:10.15120/GR-2015-1-FG-GENERAL-35

Developments for the CR stochastic cooling system

C. Dimopoulou[1], *D. Barker*[1], *R. Böhm*[1], *M. Bräscher*[1], *M. Dolinska*[2], *R. Hettrich*[1], *M. Kelnhofer*[1], *J. Krieg*[1], *W. Maier*[1], *R. Menges*[1], *C. Peschke*[1], *J. Roßbach*[1], *A. Stuhl*[1], *L. Thorndahl*[3], *and S. Wunderlich*[1]

[1]GSI, Darmstadt, Germany; [2]Frankfurt University; [3]CERN, Geneva, Switzerland

The pertinent CR stochastic cooling system in the frequency bandwidth 1-2 GHz has been reviewed in [1] in the context of the FAIR project. Further progress was made in 2014 on in-house engineering and testing activities as well as procurements.

Metallised ceramic plates for slotline pick-up electrodes are under development in close interaction with a provider.

The water-cooled linear motor drive units, tested synchronously in the prototype pick-up tank (Fig. 1) at room temperature, fulfill the specifications: (i) their max. range of plunging is 70 mm and (ii) at the end, they move back out to their max. aperture within 200 ms, before a new beam is injected.

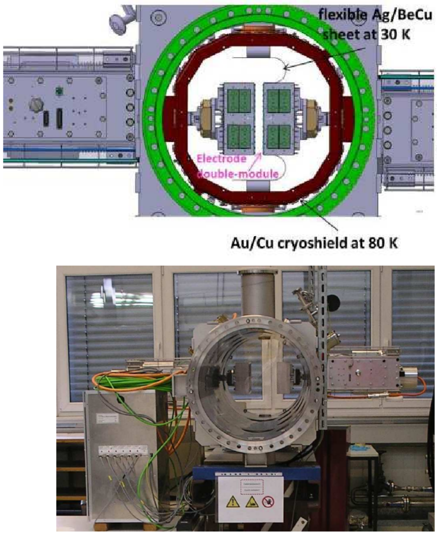

Figure 1: Section of the prototype pick-up tank. The motor units drive synchronously the slotline electrodes.

A special chamber for testing motor drive units under pre-vacuum conditions, at room temperature, was engineered, built and commissioned. It permits long-term tests and improvements of the mechanical concepts in horizontal or vertical orientation in view of the final pick-up tanks. It consists of 1/8 of pick-up tank with Cu-cryoshield dummy and an observation window (Fig. 2). One motor drive unit with electrode module can be mounted so as to slide along the flexible silver-plated copper beryllium sheets.

Simulations with the HFSS code converged to possible designs of the Faltin-type electrodes of the Palmer pick-up. Then, the Palmer cooling performance in the CR with such electrodes has been confirmed in a Fokker-Planck approach. Consequently, demanding prototype electrodes were manufactured, their measured RF poperties confirm the HFSS simulation (see [2] for details).

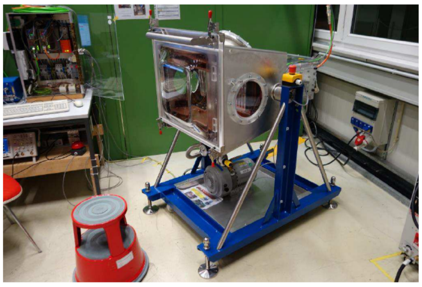

Figure 2: The testing chamber for motor drive units.

The procurement contract for the 1-2 GHz power amplifiers providing a total cw microwave power of 8 kW at the kickers has been awarded. The preseries unit is under development. The 2 optical notch filters (one for antiprotons at v=0.97 c, one for RIBs at v=0.83 c) are finished (Fig. 3), their measured RF properties fulfill the specification i.e. notch depth below -30 dB within 1-2 GHz. In-house design of demanding RF components such as the pick-up module controller as well as the integrated powermeter has started.

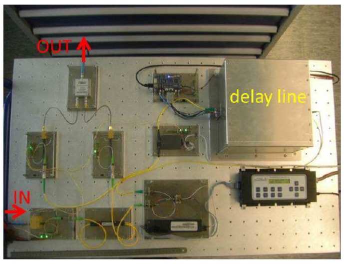

Figure 3: CR optical notch filter layout (0.6 m^2).

The new FAIR-compatible operation program covering the ESR stochastic cooling system has been successfully used with beam in 2014, particularly in demonstrating stochastic cooling of protons at v=0.71 c. This is a major step towards preparing such codes for the CR and gaining benchmarking experience for antiproton cooling in the CR.

A numerical model for simulating stochastic cooling of ions in the time domain is now available, benchmarked against ESR experimental data [3].

References

[1] CR Technical Design Report 2014 and C.Dimopoulou, ICFA Beam Dynamics Newsletter No. 64, p.108 (2014).

[2] D.Barker et al, this report.

[3] M. Dolinska et al., Proc. STORI'14, (in Physica Scripta).

DOI:10.15120/GR-2015-1-FG-GENERAL-36

Fabrication and characterization of Silicon-On-Diamond (SOD) sensors*

S. Sciortino[1,2,#], K. Kanxheri[3,4], S.Lagomarsino[1,2], A. Morozzi[3,4] , G. Parrini[1], D. Passeri[3,4], L. Servoli[4], M. Citroni[5], S. Fanetti[5], E. Berdermann[6], C. J. Schmidt[6], M. Kis[6], M. Träger[6], R. Visinka[6]

[1]Department of Physics, Florence, Italy; [2]INFN, Florence, Italy; [3]University of Perugia, Italy; [4]INFN, Perugia, Italy; [5]LENS, Florence, Italy; 6GSI, Darmstadt, Germany;

We report on the preparation and characterization of integrated diamond detectors implementing the Silicon-On-Diamond (SOD) concept [1]. They have been fabricated by thinning (5×5 mm2) CMOS Monolithic Active Pixel Sensors (MAPS) down to 25 µm and bonding them to polycrystalline Chemical Vapour Deposited (pCVD) diamond plates (5×5×0.5 mm3), by a laser technique [2]. This class of devices exploits the capability of the charges generated in the diamond by ionizing radiation to cross the silicon-diamond interface and to be collected by the MAPS photodiodes. We have assessed that the charge induced in diamond by Minimum Ionizing Particles is collected by the MAPS electronics with an efficiency of about 20 %, depending on the quality of the SOD bonding process and on the silicon-diamond interface. The aim is to prepare low-noise, low material budget integrated radiation hard detectors with a new technique of bonding at the atomic level. Two SOD devices have been implemented (SOD-40 and SOD-43) in this study. The adhesion at the silicon-diamond interface turned out to be better for the SOD-43 device due to technical reasons discussed in [3]. First the CMOS MAPS have been calibrated with monochromatic X-rays, then the device have been tested with charged particles (electrons) either with and without biasing the diamond substrate, to compare the amount of signal collected, We analysed for both SOD prototypes a matrix of 32x32 small photodiode (2x2 µm^2) pixel. The two SOD devices response to X-rays fluorescence has been studied and the calibration relations are very similar. The two calibration factors for the 32x32 small photodiode pixel matrices are: 10.12 ± 0.31 ADC/keV for SOD-40 and 10.43 ± 0.30 ADC/keV for SOD-43. SOD-40 was tested with a ^{90}Sr/Y electron source while SOD-43 was exposed to an electron beam at Beam Test Facility of Frascati, Italy, with beam energy of 345 MeV. The signal collected by the MAPS will have always the component due to the ionization in the silicon layer, while the component due to the diamond should appear only when it is polarized. The carriers created into diamond drift along the applied field toward the silicon-diamond interface and diffuse in the silicon material to be collected by the MAPS. We found that the collected charge remains spatially localized, i.e., almost all the collected charge is inside the 5x5 matrix, centered around the pixel with the maximum signal. By increasing the cluster size we do not add other contributions to the total signal. To evaluate the maximum allowable diamond contribution to the signal we assume that there is no loss in crossing the interface. From a previous work [4] we derive that only a 37% of the charges located at the interface, i.e. at a 25 µm depth in the silicon, will be collected by the MAPS. Assuming a Most Probable Signal (MPS) in the range 7000-8000 e, at 500 V, for the diamond material used for our devices, the maximum signal to be expected from our MAPS is in the interval 2600-3000 e. Figure 1 shows a difference in ADC counts of about 20 for both devices when they are polarized. This amounts to about 540 e injected by diamond, i.e., an efficiency of about 20 % in crossing the silicon-diamond bonding interface. We note that the response due to diamond has an offset voltage of about 250 V which most likely depends on the defective interface. The signal of SOD-43 is higher at 400 V than that of SOD-40. This is tentatively ascribed to the better adhesion between silicon and diamond verified a posteriori in SOD-43, by optical microscopy. We could not verify this hypothesis at higher voltages, due to a high superficial current drawn by the silicon layer.

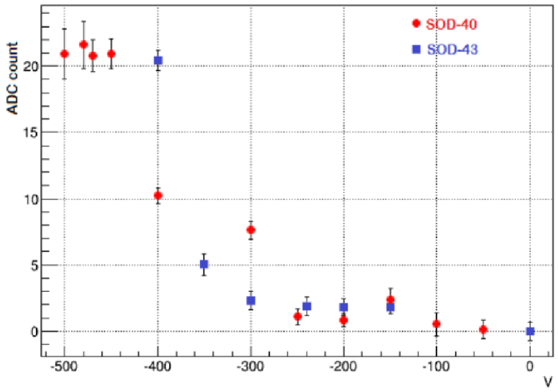

Figure 1: Bias scan for both fully polarized SOD-40 (circles) and not fully polarized SOD-43 in (squares).

References

[1] S. Lagomarsino et al., New perspectives for the Silicon-On-Diamond material, PoS(RD09)029

[2] S Lagomarsino et al., Silicon-on-diamond material by pulsed laser technique, Applied Phys. Lett. 96 (2010) 031901

[3] K. Kanxheri et al., First result on biased CMOS MAPs-on-diamond devices, Nucl. Instr. Meth. A, in press, corrected proofs, 10.1016/j.nima.2015.02.054

[4] S. Meroli, et al. Measurement of charge collection efficiency profiles of CMOS active pixel sensors. Journ. Of Instr. (2012) 07 P09011

---

* Work supported by EU (HadronPhysics3 project No. 283286) and GSI (Detector Technology and Systems Platform) and INFN Italy (experiment 3D_SOD)

#silvio.sciortino@unifi.it

DOI:10.15120/GR-2015-1-FG-GENERAL-37

Fabrication and characterization of efficiency and radiation tolerance of 3D diamond detectors*

S. Sciortino[1,2,#], S.Lagomarsino[1,2], M. Bellini[3], C. Corsi[1,4], V. Cindro[5], K. Kanxheri[6,7], A. Morozzi[6,7], D. Passeri[6,7], L. Servoli[7], E. Berdermann[8], C. J. Schmidt[8], M. Kis[8], M. Träger[8], R. Visinka[8], M. Schreck[9], S. Gsell[9], M. Fischer[9]

[1]Department of Physics, Florence, Italy; [2] INFN, Florence, Italy; [3]INO-CNR Florence, Italy; [4]LENS, Florence, Italy; [5]Jožef Stefan Institute, Ljubljana, Slovenia; [6]University of Perugia, Italy; [7]INFN, Perugia, Italy; [8]GSI, Darmstadt, Germany; [9]University of Augsburg, Germany;

3D diamond detectors combine the intrinsic properties of radiation tolerance of diamond with the advantages of the 3D architecture: a shorter inter-electrode distance and, consequently, lower trapping probability and operating voltage bias. 3D diamond electrodes can be fabricated by laser irradiation [1]. Femtosecond laser irradiation is required, because with longer laser widths, at least in the nanosecond range, a more defective modified material is obtained [2]. We have previously reported [1] on 3D monocrystalline Chemical Vapour Deposited (scCVD) diamond detectors, which exhibited a full collection to beta Minimum Ionizing Particles (MIP) at a voltage bias of a few volts, i.e., one order of magnitude lower than the bias level required for a two 2D sensor prepared with the same material. Since scCVD diamond are presently only obtained in very small areas, usually less than 1 cm^2, we decided to investigate the performances of 3D detectors fabricated on polycrystalline (pCVD) diamond, before and after neutron irradiation up to the highest fluence ever reported for diamond. From our results 3D diamond detectors seem the most radiation-hard detectors available at present. Heteroepitaxial growth of Diamond On Iridium (DOI) seems a very promising technique to obtain a high quality material, more homogeneous in its electronic properties than the pCVD one and not limited in surface area. A 3D sensor implemented on DOI material has also been tested and reported in this work.

Sample preparation ant tests

3D radiation sensors have been implemented on four pCVD samples (5×5×0.5 mm^3) by laser irradiation. Bulk electrodes were fabricated with an 800 nm Ti:Sa 30 fs laser with an energy density of 12 J/cm^2. The columns were started from one of the 5×5 mm2 faces and terminated about 80 μm away from the opposite one. They were connected by graphitic combs written on the surfaces with a Nd:YAG ns laser (schematics in Fig. 1). Two 3D sensors and a 2D reference sensor have been fabricated in each of the four sample as shown in Figure 1. The 3D electrodes are patterned by repeating two elementary cells of sizes 100×160 μm^2 ($3D_{100\times160}$ sensors) or 70×114 μm^2 ($3D_{70\times114}$ sensors). The CCE has been measured by means of a ^{90}Sr beta source, producing 18000 electron-hole pairs per MIP in the sample. The saturation collected charge was evaluated as 8700±300, 7200±300, and 7100±200 for the $3D_{70x114}$, the $3D_{100x160}$ and the 2D sensor, respectively.

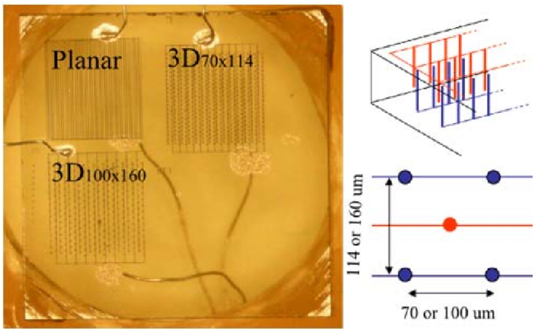

Figure 1: One pCVD sample with the 2D reference sensors and the two 3D sensors. On the right: the unit cell.

The 90% of these values were reached at 45 V, 60 V and 450 V, respectively. Hence, we assessed also for pCVD diamond, that the required bias voltage is an order of magnitude lower for the 3D than for the 2D sensors. The maximum signal for the $3D_{100x160}$ and the 2D sensor have about the same value, but the $3D_{70x114}$ sensors yield a collection efficiency about 20% higher. The CCE vs. voltage bias has been fitted by use of the following expression for the mean free path of the carriers:

$$\frac{1}{\lambda} = \frac{1}{\lambda_g} + \frac{1}{v\tau} \qquad (1)$$

where τ is the lifetime of the carriers, limited by the intra-grain defects, v is the drift velocity, which depends on the applied electric field (the bias voltage), λ_g is a mean path limited by the grain boundaries. The parameter values resulting from the fit of the 2D sensors data are $\tau = 4.3$ ns and $\lambda_g = 160$ μm. We assumed the same value of τ for the 3D sensors and evaluated numerical the CCE, by means of a three-dimensional finite element simulation of the electric field. The resulting values for λ_g were 29 and 25 μm for $3D_{100x160}$ and $3D_{70x114}$, respectively. The above values correlate well with the structure of the grains of the samples, which exhibit a truncated cone shape along the

---

* Work supported by EU (HadronPhysics3 project No. 283286) and GSI (Detector Technology and Systems Platform) and INFN Italy (experiment 3D_SOD)

[#] silvio.sciortino@unifi.it

DOI:10.15120/GR-2015-1-FG-GENERAL-38

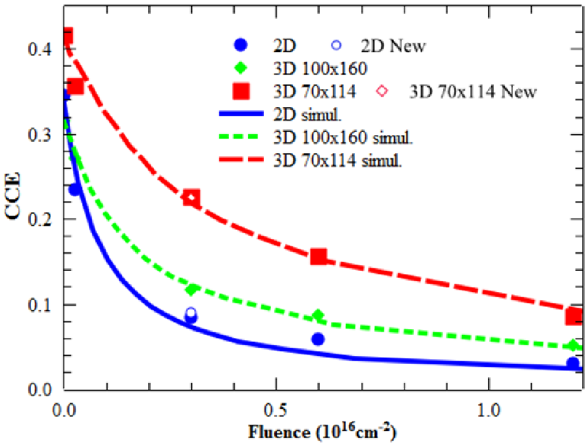

Figure 2: CCE vs, neutron irradiation fluence, 1 MeV equivalent.

diamond thickness, as evidenced by a morphological analysis carried out by optical profilometry. In the case of the 2D sensors the carriers drift almost parallel to the grain boundaries while in the case of 3D sensors they are strongly limited by the polycrystalline material in their path between the columnar electrodes.

Radiation Tolerance of the 3D sensors

We irradiated the four diamond samples at the experimental nuclear reactor of the Jožef Stefan Institute of Ljubljana, with fast neutron (neutrons of energy greater than 100 keV) at fluences ranging from 2.2×10^{14} cm^{-2} to 10^{16} cm^{-2}. Figure 2 shows the variation of the CCE with the equivalent fluence of 1 MeV neutrons, for the 2D and the 3D sensors. In order to prove that the all-carbon electrodes are not degraded by the neutron irradiation, we have also fabricated a new 2D sensor and new 3D $3D_{70x114}$ sensor, on the sample irradiated at 3×10^{15} cm^{-2} 1MeV-eq. neutrons. These new sensors exhibited the same response as the older ones after irradiation (see Fig. 2). The results from the planar sensors allow the immediate evaluation of the hardness factor K of the material, defined by the following relation:

$$\frac{1}{CCE}=\frac{1}{CCE_0}+KL\phi \qquad (2)$$

where ϕ is the fluence and L = 500 μm the thickness of the material. The result, K= (4.7±0.2) 10^{-18} μm^{-1} cm^{2}, is in good agreement with that previously reported in [3]. The data represented in Fig. 2 have been fitted by use of a modification of expression (1):

$$\frac{1}{\lambda}=\frac{1}{\lambda_g}+\frac{1}{v}\left(\frac{1}{\tau}+k\phi\right) \qquad (3)$$

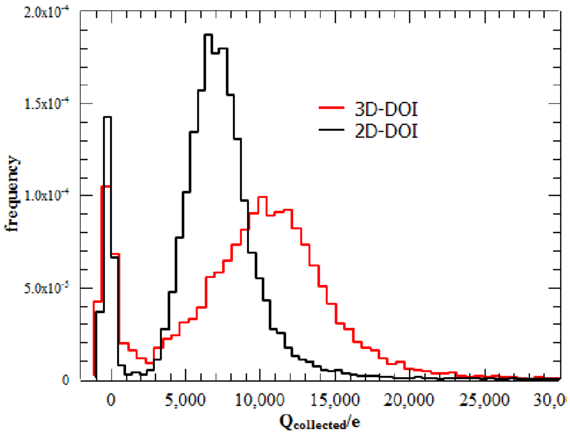

Figure 3: Pulse height spectrum of DOI 2D (at 600 V) and 3D (at 140 V) sensors.

A k value of about 1.5 10^{-6} cm^{2} Hz can be used to fit consistently the three curves. The factor 3 in efficiency gained by the irradiated 3D detectors with the smaller pitch can be explained by the assumption that neutron damage results in the introduction of new intra-bandgap levels reducing the bulk mean lifetime of the charge carriers in the conduction and in the valence band, leaving unaffected the grain boundaries-limited mean free path λ_g.

Diamond On Iridium 3D sensors

A 3D sensor of the type $3D_{70\times114}$ has been implemented on a DOI plate together with a reference planar 2D sensor. The sample is about 500 μm thick, hence the overall generated charge from a MIP beta source is 18000 electrons. The collected charge was 7600 e corresponding to a CCE=42% for the 2D sensor at a bias voltage of 600 V. The 3D sensor yielded a mean value of 11000 e, corresponding to a CCE of 61%, at a bias voltage of 140 V. The relative gain from 2D to 3D is quite high. Figure 3 shows the pulse high spectrum for the two sensors at maximum collection. The DOI sample exhibits relevant pumping effect and polarization. The above results correspond to the pumped state (>100 Gy beta-irradiation). The 2D signal before pumping was 4000 e (21 % CCE). The study of the radiation tolerance of these sensors is under way.

References

[1] S. Lagomarsino et al., Diamond Relat. Mater. 43 (2014) 23.
[2] S. Lagomarsino et al., Appl. Phys. Lett. 103 (2013) 233507.
[3] G. Kramberger, Radiation damage in diamond detectors, September 2012, Vertex 2012, Jeju, Korea

Imaging of dislocation bundles by micro-Raman line width mapping to assess the structural quality of heteroepitaxial diamond for detector applications*

M. Mayr[1], M. Fischer[1], S. Gsell[1], C. Stehl[1], M. Schreck[1#], and E. Berdermann[2] for the ADAMAS collaboration

[1]Universität Augsburg, Augsburg, Germany; [2]GSI, Darmstadt, Germany

Within the ADAMAS collaboration, the role of the diamond group at the University of Augsburg is to develop and manufacture large-area high-quality single crystal diamond suitable for the construction of detectors for heavy ions and minimum ionising particles. In contrast to current samples grown by homoepitaxy on substrates with maximum lateral dimensions of ~10 mm, the heteroepitaxial deposition is done on the Ir/YSZ/Si(001) multilayer system that is available in 100 mm wafer size. As a consequence, these samples that are often known as "Diamond on Iridium" (DoI) offer a realistic chance for a scaling to large areas as required for tracking applications.

Major challenges, however, are the occurrence of polarization effects and an incomplete charge collection with charge collection efficiencies (CCE) varying from sample to sample. These effects are mainly attributed to properties of the bulk, namely lattice defects like dislocations and point defects, generating both deep and shallow charge carrier traps. Being able to control and further reduce the density of these defects is compulsory for future application of DoI material not only in particle physics.

Imaging and quantification of dislocations

A controlled optimization of material synthesis requires efficient concepts for a visualization and quantitative evaluation of threading dislocations. A standard technique for the assessment of dislocation densities uses preferential etching with subsequent counting of the etch-pits. Furthermore, inside the bulk dislocations create inhomogeneous strain fields which broaden XRD- and Raman line profiles. We recently revealed that the density of dislocations as derived from etching experiments shows a characteristic correlation with film thickness [1] and with the width of the diamond Raman line (see Fig. 1).

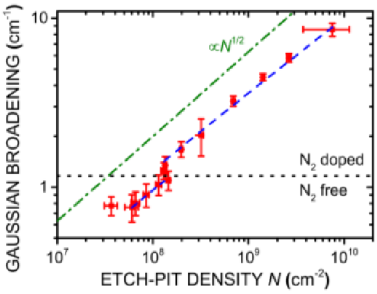

Figure 1: Broadening of the Raman peak vs. etch-pit density. The continuous variation of the dislocation density was achieved by growth of a thick film. The blue fit curve uses the relationship given by Eq. (1). The displaced green curve describes a simple $\sqrt{N}$ behaviour. [1]

The relationship between the mean square strain and the dislocation density N (in cm^{-2}) is described by (1):

$$\overline{\varepsilon_N^2} \propto N \cdot ln \frac{10^7}{2 \cdot \sqrt{N}} \tag{1}$$

Using this approach, it is possible to image the spatial distribution of dislocations by mapping the Raman line width. The stripe pattern in the cross section map (see Fig. 2) is interpreted in terms of bundles of threading dislocations which are tilted away from the surface normal by several degrees. Tilting is attributed to lateral step flow during growth on off-axis substrates [2]. Understanding the interaction between dislocations and surface features is important for a further reduction of defect densities.

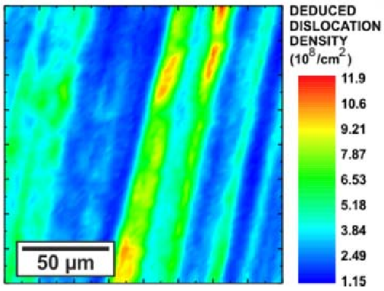

Figure 2: Cross-sectional dislocation density map of a DoI sample grown with 100 ppm N$_2$ on a (001) substrate with [100] off-axis direction, as derived from high-resolution Raman-line width measurements using the calibration curve in Fig. 1.

DoI: state of the art

In the meantime, continuous improvement in heteroepitaxial diamond growth and post-processing (lapping, polishing) has yielded DoI samples with lateral dimensions up to 2 x 2 cm^2 (see Fig. 3) and thin membranes down a thickness of 80 µm. For further thinning and also removing of polishing defects, reactive ion etching (RIE) was successfully applied.

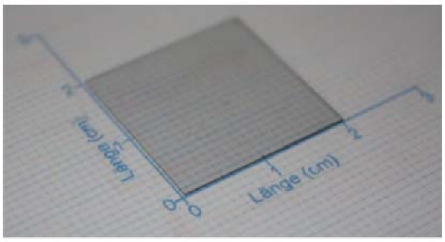

Figure 3: 2 x 2 cm^2 DoI sample supplied to GSI for measurements of the detector properties.

References

[1] C. Stehl et al., Appl. Phys. Lett. **103**, 2013.
[2] M. Mayr et al., Phys. Status Solidi A **211**, 2014 .

---

* Work supported by EU (HadronPhysics3 project No. 283286) and GSI (Platform for Detectors and Systems).

[#]matthias.schreck@physik.uni-augsburg.de

DOI:10.15120/GR-2015-1-FG-GENERAL-39

Project status of the new setting generation system for GSI and FAIR

D. Ondreka, I. Kraus, H. Liebermann, and B. R. Schlei
GSI, Darmstadt, Germany

The progress made on the new setting generation system for FAIR and GSI regarding machine modeling and application development is reported.

In 2014, the main activities were related to benchmarking tests of the SIS18 machine model and support for other technical groups during machine experiments. In this context, the new settings generation system proved extremely useful. In fact, it was essential for the realization of several machine development studies, which required operation schemes impossible to achieve with the present settings generation software SISMODI. In particular, the following machine experiments depended on the use of the new settings generation system: (i) Commissioning of the first module of the new MA cavity with beam and (ii) bunch merging studies using different merging times and amplitudes (both conducted by PBRF); (iii) multi-turn injection studies using a variable angle of the orbit bump at the electrostatic septum and (iv) resonance compensation studies employing a tune ramp with captured beam on the injection or extraction plateau (latter two conducted by PBBP). In all cases, the settings generation system excelled in providing control over the machine as requested by the respective experimentators. Below, a detailed report is given about the bunch merging and resonance compensation experiments.

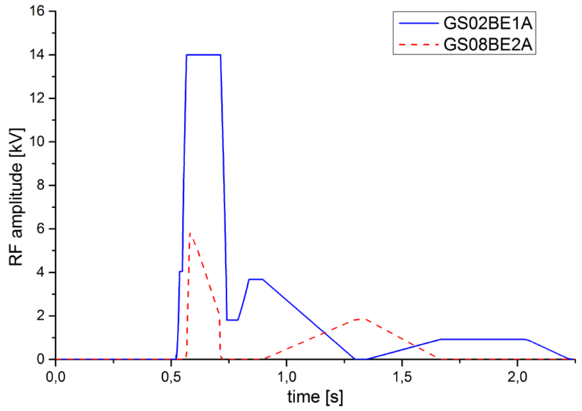

Figure 1: RF amplitudes of the two ferrite cavities in SIS18 for a cycle with two merging steps (4 → 2 → 1).

Because the cavities can be switched on and of sequentially with the new settings generation system, it is possible to combine ramping at full speed and bunch merging (see figure 1). Thus, at the end of the ramp one cavity is always available for the first bunch merging step. Also, the merging times are freely adjustable. This flexibility was extensively used to allow the RF department to test the performance of the bunch merging procedure as a function of the merging times.

The new system was also very helpful for resonance compensation measurements. Using the generic Java interface to the settings, it was possible to perform semi-automated parameter scans of tune and sextupole strengths. Up to 100 settings per hour were established. For each setting, the beam current was read out and saved for analysis. Figure 2 shows some of the recorded current readings, each curve corresponding to a different sextupole setting for a fixed tune. The current drop is a measure for the degree of compensation of the resonance.

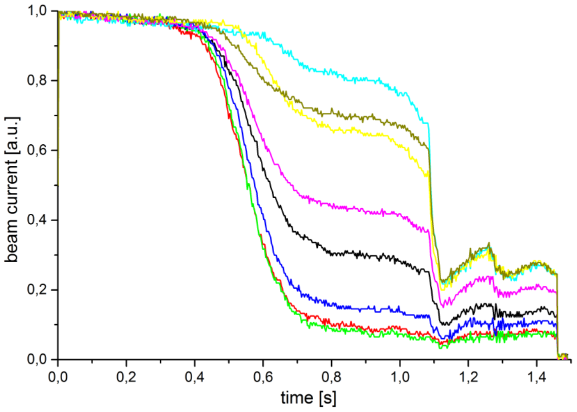

Figure 2: Beam current for different degrees of resonance compensation through variation of the sextupole strengths.

Besides the extensive support of the machine experiments, several development activities were pursued. Especially the work on the machine model for the CRYRING was continued with the main focus on the injector. Particular emphasis was put on modeling the RFQ structure, serving as a prototype for a generic cavity in linear accelerators.

Regarding applications, the development of the LSA version of the ion optics code MIRKO was continued. A satisfactory integration into the control system development environment was established. Concerning the steering and orbit correction program YASP, a collaboration with CERN was established to realize the integration into the FAIR control system.

References

[1] G. Franchetti et al., “Recent development in mitigation of long term beam loss”, HB2014.

DOI:10.15120/GR-2015-1-FG-GENERAL-40

Status of the CS framework and its successor CS++

H. Brand, D. Neidherr
GSI, Darmstadt, Germany

The *CS* framework is a LabVIEW based framework for developing event driven, multi-threaded control systems using an artificial object oriented approach. *CS* was upgraded to version 3.4 based on LabVIEW 2014. Upgrade experience is summarized.

CS++ **will become the successor of *CS* and is based on NI's Actor Framework which is using the native object oriented programming approach consequently following the data-flow paradigm.**

Motivation

The *CS* framework is in use since a couple of years at about 15 experiments at 10 institutes. A detailed description of *CS* is given in [1]. This text aims at describing the enhancements by the most recent version 3.4 and upgrade experience to LabVIEW 2014.

CS framework is using an artificial approach to object oriented programming in LabVIEW. Many features rely on convention and cannot be enforced since the support of the development environment is missing. Therefore we are working on its successor **CS++,** based on NI's Actor Framework [2], to be used for FAIR experiment control systems. The Actor Framework provides some simple base classes for active objects (threads) and well defined communication mechanism. The AF implements a much simpler design than the HGF Class Library [3], so it is much easier for newcomers to learn. In addition we can profit from NI support and community developments, so that for example the migration of the core components within the **CS++** is already done by NI.

Status of CS framework

Last year the *CS* framework had its 10 year anniversary. Since 2004 the core of the framework has been migrated to the most recent LabVIEW versions every three to four years. For the developers of experiment specific *CS* classes this normally means upgrading to the new LabVIEW version. They just have to copy the new core system and recompile their executables. The *CS* upgrade to 3.4 need more work.

For an unknown reason NI changed the way references are compared with each other. This leads not only to important changes in the core system of the *CS* but also to changes in the source code of each class. For this reason we wrote a tool using *VI-Scripting* methods to modify parts of the class specific source code automatically.

NI found a security issue which they closed in newer LabVIEW versions. For the *CS* this leads to several small changes for example in the way how an executable has to be built.

HITRAP @ GSI as well as ISOLTRAP @ CERN and LEBIT @ MSU migrated their systems to *CS* 3.3 (LV 2012). The PHELIX experiment @ GSI has already migrated to *CS* 3.4 (LV 2014). The step from *CS* 3.3 to 3.4 is marginal.

Status CS++

CS++ follows the recommendations of the Actor Framework. It provides base classes of common interest for objects to be used as entities, *CS++Base.lvclass*, and derived actor classes *CS++BaseActor.lvclass*.

- *CS++MessageLogger* client for DSC and Syslog
- *PVConnection* and *PVMonitor* for Shared Variables or DIM communication.
- *CS++DeviceActor* and *CS++DeviceGUI* e.g. CS++DCPwr, CS++DMM, CS++Fgen, CS++Osci, etc. Concrete implementation classes wrapping the IVI-Driver are already available.
- *CS++Factory* provides the methods to create initialized objects of such classes at runtime reading initialization data from configuration file.
- *CS++Reference* can be used to maintain object references respecting data-flow.
- More passive data classes are available providing new datatypes such as PV- or Alarm&Event data.
- *CS++DSCAlarmViewer* and *CS++DSCTrendViewer* connecting to the historical DSC database.

Status & outlook

The *CS* framework 3.4 is stable and in good shape. It will be maintained in future since many experiments rely on it and it cannot be easily replaced.

The **CS++** class libraries are still under development, but already available under the terms of the European Union Public Licence (EUPL) on Github [4]. Some simple demo applications to illustrate the usage and extension of the base classes are available. **CS++** will become the base for the serial test-stand sequencer for the SIS-100 dipole magnets. **CS++** applications can easily connect to *CS* Framework applications using DIM [5].

References

[1] D. Beck et al., Nucl. Instr. Meth. A 527 (2004) 567-579, http://wiki.gsi.de/cgi-bin/view/CSframework,
[2] https://decibel.ni.com/content/groups/actor-framework-2011?view=overview
[3] F.Berck "Prototyp für ein mobiles Agentensystem in NI LabVIEW", Hochschule Darmstadt University of Applied Science, FB EIT, 2010
[4] https://github.com/HB-GSI/CSPP
[5] http://www.cern.ch/dim

DOI:10.15120/GR-2015-1-FG-GENERAL-41

GPU Programming - Speeding Up the 3D Surface Generator VESTA

B. R. Schlei[*]
GSI, Darmstadt, Germany

Abstract

The novel “Volume-Enclosing Surface exTraction Algorith” (VESTA) generates triangular isosurfaces from computed tomography volumetric images and/or three-dimensional (3D) simulation data. Here, we present various benchmarks for GPU-based code implementations of both VESTA and the current state-of-the-art Marching Cubes Algorithm (MCA). One major result of this study is that VESTA runs significantly faster than the MCA.

Introduction

NVIDIAs toolkits (*cf., e.g.,* Ref. [1]) for the development of CUDA®-based software contain, among many other things, example code for an extended version [2] of the original MCA [3]. Here, we compare the performance of this code with our CUDA®- and ANSI-C-based implementation of VESTA [4] on a Linux-based (*i.e.,* openSUSE 13.1) PC with a GeForce GTX 750 Ti graphics card.

In particular, the times that we have measured (*cf.,* Table 1) are averages over 1000 runs each. The measurements start after the data sets have been loaded into texture memory, and they stop after all point coordinates and triplets of point IDs (*i.e.,* triangles) have been computed on the GPU.

Technique	Extended MCA	Marching VESTA	
Mode	**DCED / L**	**DCED / L**	**Mixed / H**
(a) Points	19, 218	12, 814	15, 292
Triangles	6406	6406	11, 362
Time (ms)	**1.43(5)**	**1.28(5)**	1.37(4)
(b) Points	6, 128, 724	4, 085, 840	4, 852, 644
Triangles	2, 042, 908	2, 042, 908	3, 576, 516
Time (ms)	**98.5(1)**	**71.3(1)**	75.9(4)
(c) Points	5, 566, 998	3, 699, 086	4, 346, 120
Triangles	1, 855, 666	1, 855, 666	3, 147, 604
Time (ms)	**23.0(1)**	**18.7(1)**	22.4(1)
(d) Points	33, 240	22, 208	25, 894
Triangles	11, 080	11, 080	18, 350
Time (ms)	**0.82(4)**	**0.63(4)**	0.74(4)
(e) Points	13, 859, 304	9, 267, 824	11, 178, 649
Triangles	4, 619, 768	4, 619, 768	8, 441, 610
Time (ms)	**111.2(1)**	**84.4(1)**	94.6(6)

Table 1: Benchmarks for various processed tomographic data sets: for (a) – (c), *cf.,* Ref. [4] and Ref.s therein, (d) Bucky.raw data is a portion of [1], and (e) Happy Buddha VRI file [5]. For the selected isovalues, *cf.,* Fig. 1.

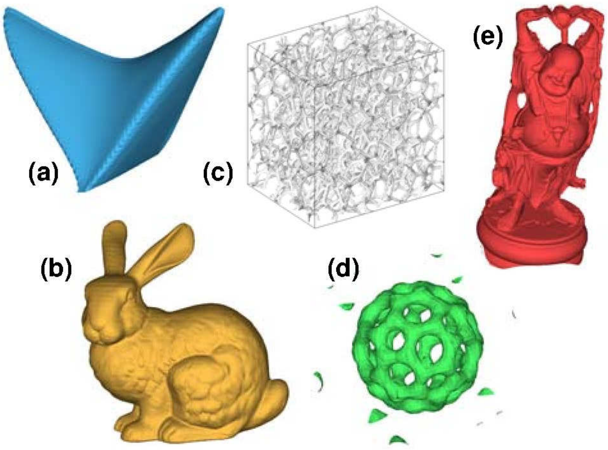

Figure 1: VESTA high resolution “mixed” mode (Mixed/H) isosurface renderings, where the isovalues are equal to (a) 139, (b) 150, (c) 135, (d) 128, and (e) 150, respectively.

Results

For the here considered data sets [1, 4, 5], the extended MCA is about (a) 12%, (b) 38%, (c) 23%, (d) 30%, and (e) 32%, *slower* than the marching variant of VESTA [4], when the latter is executed in its low resolution “disconnect” mode (DCED/L). Furthermore, VESTA is also faster even if higher resolution isosurfaces are computed (*cf.,* Fig. 1), which have about twice the number of triangles (*cf.,* Table 1).

Note that the current code implementation of VESTA does *not* yet use parallel streaming, *nor* it does call device kernels from within kernels. As a consequence, further GPU-based code optimisations may result in an even faster VESTA code.

References

[1] NVIDIA® CUDA® Toolkit 6.5; for more detail, *cf.,* https://developer.nvidia.com/cuda-toolkit/

[2] P. Bourke, “Polygonising a scalar field”, May 1994; for more detail, *cf.,* http://paulbourke.net/geometry/polygonise/

[3] W. E. Lorenzen and H. E. Cline, “Marching Cubes: A High Resolution 3D Surface Construction Algorithm”, Comput. Graph. 21 (1987), p. 163.

[4] B. R. Schlei, “Volume-Enclosing Surface Extraction”, Computers & Graphics 36 (2012) p. 111, doi: 10.1016/j.cag.2011.12.008.

[5] http://graphics.stanford.edu/software/volfill/

---

[*] b.schlei@gsi.de

DOI:10.15120/GR-2015-1-FG-GENERAL-42

CUPID: new system for scintillating screens based diagnostics

B. Walasek-Höhne[1], *D. Acker*[1], *C. Andre*[1], *M. Bevcic*[1], *H. Bräuning*[1], *A. Bräuning-Demian*[1], *T. Brühne*[1], *E. Dierssen*[1], *C. Dorn*[1], *R. Fischer*[1], *H. Graf*[1], *F. Hagenbuck*[1], *M. Hartung*[1], *R. Haseitl*[1], *T. Hoffmann*[1], *K. Höhne*[2], *C. Kleffner*[1], *R. Lonsing*[1], *T. Milosic*[1], *I. Pschorn*[1], *A. Petit*[1], *A. Reiter*[1], *H. Rödl*[1], *U. Scheeler*[3], *C. Schmidt*[1], *M. Schwickert*[1], *K. Steiner*[1], *C. Wetzel*[1], *J. Wiessmann*[1], *J. Wohlers*[1], *D. Varentsov*[1], *and R. Vincelli*[1]

[1]GSI, Darmstadt, Germany; [2]FAIR, Darmstadt, Germany; [3]MIT, Marburg, Germany

The Facility for Antiproton and Ion Research (FAIR) with its wide range of beam parameters poses new challenges for standard beam instrumentation like precise beam imaging. To cover a wide range of foreseen applications, a new technical solution was required for diagnostics upgrades for the PRIOR Experiment, CRYRING and between the Experimental Storage Ring (ESR) and Cave A as a precursor to the FAIR High Energy Beam Transport lines.

The new system (see Figure 1), including digital image acquisition, remote controllable optical system and mechanical design, was set up and commissioned during 2014 beam time. CUPID (Control Unit for Profile and Image Data) is based on the Front-End Software Architecture (FESA) to control beam diagnostic devices.

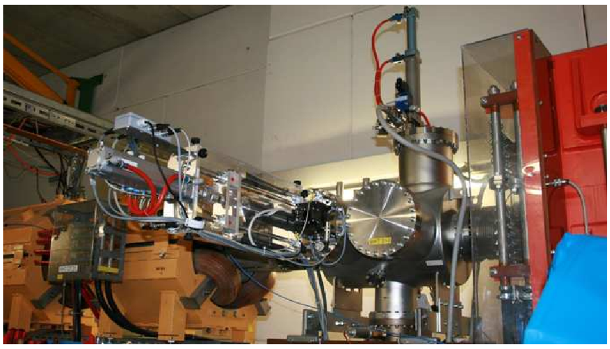

Figure 1: Scintillating Screen installation at High Energy Beam Transport Lines.

The FESA class for the digital GigE camera (IDS uEye UI-5240SE-M, CMOS type) acquires the images and preprocesses the optical data as required by the geometry of the setup (rotation, stretching). It calculates the projections and the intensity histogram and converts pixel number into a position in millimeters, which results in absolute beam position and width. The performance of the system reached more than 15 frames per second with one connected client.

Additionally, dedicated FESA classes access industrial Programmable Logic Controllers (PLCs) for a reliable slow control solution. A Siemens PLC (main unit and satellites) handles control of lens focus and iris motors (LINOS MeVis-Cm 16), read and set by a PID controller (FM355C). PLC digital outputs (SM322) switch the LED to illuminate the target for calibration issues. Camera control and timing, as well as, power supply and reset options for up to eight digital cameras are realized by the in-house developed Camera Power Supply controller CPS8 with network access.

For basic operation the camera controls are reduced to changing the opening of the iris and switching on or off the LED. An expert mode provides more detailed control like changing the exposure time or the binning of the image for low beam intensities. The CUPID system provides three acquisition modes. In the 'free run' mode suitable for slow beam extraction, the camera continuously acquires images with the specified exposure time and frame rate. The acquired images are displayed in the GUI as they arrive in real time. In the 'triggered' mode for fast extraction, the image acquisition is triggered by a machine event of the accelerator. At the time of the trigger, a single image is acquired by the FESA class and displayed by the GUI (see Figure 2). An extension of the 'triggered' mode is the 'sequence' mode, which acquires a predefined number of images with the specified frame rate after a trigger is received.

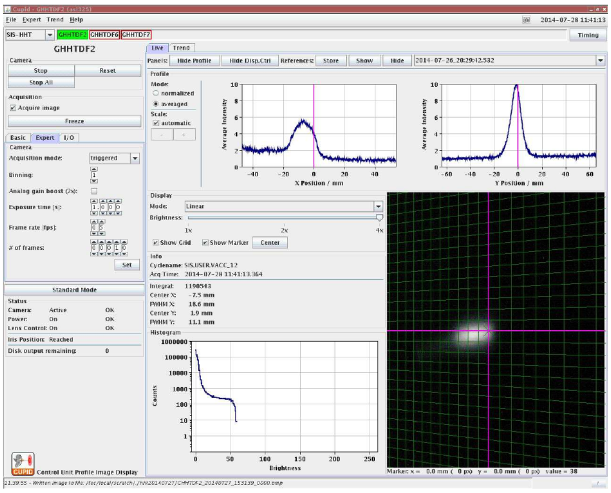

2014-07-28 11:41:13

SIS-HHT | GHHTDF2 | GHHTDF6 | GHHTDF7

2014-07-26_20:29:42.532

☑ Acquire image

Mode: ○ normalized ● averaged

Scale: ☑ automatic

Acquisition mode: triggered

Binning: 1

Analog gain boost (2x): ☐

Exposure time [s]: 1.000

Frame rate [fps]: 05

# of frames: 00010

Mode: Linear

Brightness: 1x 2x 4x

☑ Show Grid ☑ Show Marker

Info
Cyclename: SIS.USER.VACC_12
Acq Time: 2014-07-28 11:41:13.364

Integral: 1190543
Center X: -7.5 mm
FWHM X: 18.6 mm
Center Y: 1.9 mm
FWHM Y: 11.1 mm

Status
Camera: Active OK
Power: On OK
Lens Control: On OK
Iris Position: Reached
Disk output remaining: 0

Marker: x = 0.0 mm (0 px) y = 0.0 mm (0 px) value = 38

11:39:55 - Written image to file: /fec/local/scratch/./hht20140727/GHHTDF2_20140727_153139_0000.bmp

Figure 2: CUPID GUI with an image of 7×10^9 protons at 4 GeV on Chromox screen.

The CUPID system is currently running successfully at 16 different points in the GSI high energy beam transport lines. In daily operation it was used to image several beams from protons up to uranium with various beam energies and intensities. The generally positive feedback by the operating team highlights the simple usage of the GUI and the advanced features of the new system. The work experience gathered so far, confirms CUPID as a standard for scintillating screen based beam instrumentation at GSI and FAIR.

DOI:10.15120/GR-2015-1-FG-GENERAL-43

Optical spectra from Beam Induced Fluorescence (BIF) profile monitor*

Y. Shutko[1#], *D.H.H. Hoffmann*[1], *P. Forck*[2,3], *P. Boutachkov*[2], *R. Haseitl*[2], *T. Sieber*[2], *B. Walasek-Höhne*[2], *V. Lavrik*[3], *S. Udrea*[3], *J. Wieser*[4], *A. Ulrich*[4]
[1]TUD, Darmstadt, Germany, [2]GSI, Darmstadt, Germany; [3]Goethe-Universität, Frankfurt am Main, Germany,[4]TUM, München, Germany.

The development of non-interceptive beam diagnostics methods is of high relevance for the future FAIR accelerator facilities. One of these methods is based on Beam Induced Fluorescence (BIF), based on photons detection emitted by residual gas molecules, e.g. Nitrogen, excited and ionized by the ion beam. Such monitors are already in operation at GSI's LINAC since a few years [1]. However, further BIF-monitor developments are required for applying this method to high energy beams, as those to be delivered by FAIR's SIS100 synchrotron.

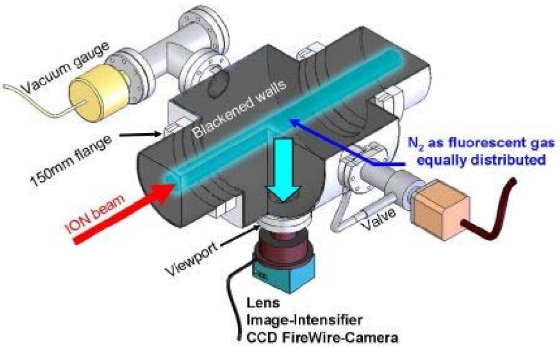

Figure 1: Typical set-up of a BIF profile monitor [2].

For this purpose beam profile and spectroscopic investigations have been performed with different gases in the pressure range from $1\cdot10^{-3}$ to 2 mbar. Heavy ion beams at energies between 100 and 900 MeV/u for slow and fast extraction mode could be used.

A typical experimental set-up is shown in Figure 1. The gas chamber is mounted on the beam line and has blackened inner walls to avoid light reflections. The chamber can be filled by different gases through a needle valve regulated by a vacuum gauge. Single photons emitted by the excited gas molecules are detected by image intensified cameras, either by an ICCD equipped with MCPs in Chevron geometry (Proxivison) or an emCCD (Princeton Instruments ProEM+:512B).

During the experiments performed in 2014 three different set-ups have been used: beam transverse profile set-up with the ICCD camera, beam transverse profile set-up with the emCCD camera and spectroscopy set-up with a CP140-202 spectrograph coupled to the ICCD camera. The grating of the spectrograph operates in the 190-800 nm wavelength range with 50 nm/mm dispersion. The ICCD camera has at least 40% of its peak sensitivity in the 200 to 600 nm wavelength range. To increase the light throughput of the system, the spectrometer's entrance slit has been set to 400 µm which resulted in a spectral resolution of about 12 nm.

As shown in Figure 2, in the case of nitrogen the measurements reveal no significant differences between the slow and fast extraction mode. Moreover, the spectra are consistent with previous results obtained at low ion energies [3].

The measured spectra obtained with Argon at pressures between 0.1 and 1 mbar showed different spectral compositions for the slow and fast extraction mode. This is shown in Figure 3 for measurements performed at 0.4±0.1 mbar N_2 equivalent. The additional, strong emission at 285 and 310 nm, significant only in the case of slow extraction, may be attributed to OH radicals excited by Ar* atoms [4].

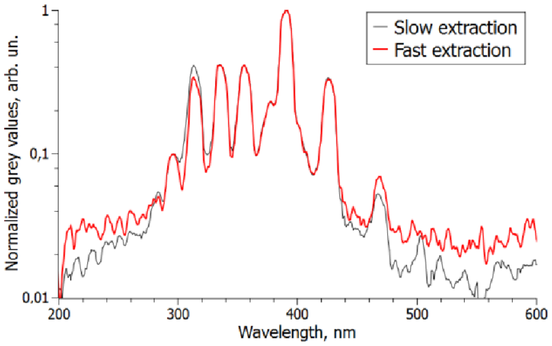

Figure 2: Nitrogen spectra for slow and fast extraction at 0.45±0.02 mbar, U^{73+} 300MeV/u beam.

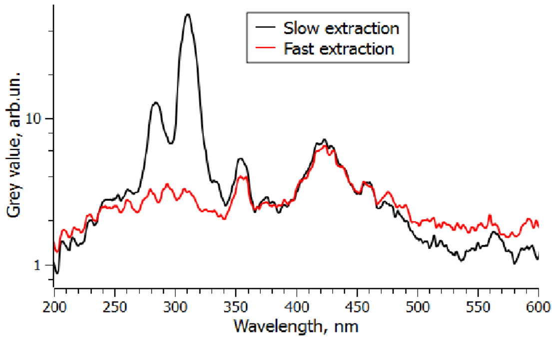

Figure 3: Argon spectra for slow and fast extraction at 0.4±0.1 mbar N_2 equivalent, U^{73+} 300MeV/u beam.

References

[1] C.A. Andre, et al, DIPAC2011 proc., p.185
[2] P. Forck et al, HB2010 proc., p. 497
[3] F. Becker, et al, IPAC2012 proc., p. 798
[4] A. Morozov, et al, Appl. Phys. Lett., **86**, 011502, (2005)

---

* Work supported by BMBF project No. 05P12RDRBN and Graduate School of Excellence ESE TU- Darmstadt.
[#]y.shutko@gsi.de

DOI:10.15120/GR-2015-1-FG-GENERAL-44

Beam induced fluorescence monitor development: Comparison of image intensified CCD and electron multiplying CCD cameras*

Y. Shutko[1#], *D.H.H. Hoffmann*[1], *P. Forck*[2,3], *T. Sieber*[2], *S. Udrea*[3], *V. Lavrik*[3]

[1]TUD, Darmstadt, Germany, [2]GSI, Darmstadt, Germany; [3]Goethe-Universität, Frankfurt am Main, Germany.

Beam Induced Fluorescence (BIF) monitors offer the possibility for non-interceptive beam profile diagnostics and are therefore highly relevant for the future FAIR facility. Several BIF monitors are already in operation at the UNILAC accelerator [1] and are based on Image Intensified CCD (ICCD) cameras. However, recent technological developments of electron multiplying CCD (emCCD) cameras offer an alternative to the ICCD.

During the GSI beam time in 2014 profile measurements have been performed both with an ICCD (Proxivison/Basler) [2] and an emCCD (Princeton Instruments ProEM512B) camera [3]. These two cameras have different working principles: the ICCD camera uses electron multiplication within a microchannel plate (MCP) due to the high voltage applied between photocathode and phosphor screen. The emCCD camera achieves signal amplification by avalanche diode-like electronics in the extended portion of the serial readout register [3].

The goal of the experiments was to compare the performance of the two cameras under similar conditions. A typical experimental set-up is shown in Figure 1.

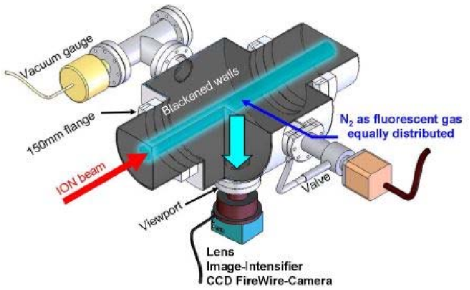

Figure 1: Typical set-up of a BIF profile monitor [2].

The measurements have been performed with 300 MeV/u ^{238}U ion beams in slow extraction mode, pulse duration 500 ms, beam widths 7.2 and 10.7 mm for ICCD and emCCD measurements, respectively. Nitrogen has been used as working gas at pressures of $5 \cdot 10^{-3}$, 10^{-2}, $2 \cdot 10^{-2}$ (ICCD) and $3.5 \cdot 10^{-2}$(emCCD) mbar. To increase the S/N ratio, averages over a few hundred acquisitions have been computed both for background and beam images. Figure 2 and Figure 3 show the transverse profiles obtained with the ICCD and emCCD cameras and also for comparison the profiles from a scintillating screen placed 1 m downstream of the BIF diagnostic chamber.

The magnitude of the ICCD profiles is basically proportional to the N_2 pressure (p). This is not the case for the emCCD. The profile taken at $3.5 \cdot 10^{-2}$ mbar shows a not expectable stronger increase in magnitude than at $5 \cdot 10^{-3}$ and 10^{-2} mbar. The proportionality of the intensity of the N_2 emission at 337 nm to p^2 may cause this behaviour.

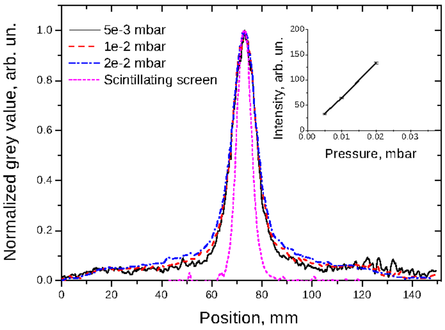

Figure 2: ICCD transverse profiles at different pressures.

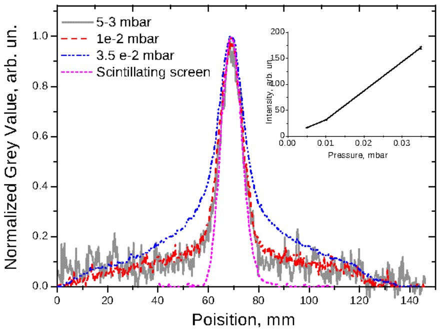

Figure 3: emCCD transverse profiles at different pressures.

The central part of the emCCD low pressure profiles is comparable to the one from the scintillating screen, while the ICCD profiles are systematically broadened. This behaviour can be explained by the fact that single photons produce wide spots in the ICCD acquired image. The effect can be mitigated by proper image processing. The tails of the BIF profiles and the strongly increased width at $3.5 \cdot 10^{-2}$ mbar are most probably due to the N_2 emission at 337 nm, known to give rise to wide profiles, which also are pressure dependent [4]. Filtering this line out should help to improve the profile width accuracy.

References

[1] C.A. Andre et al., DIPAC2011 proc., p.185
[2] P. Forck et al., HB2010 proc., p. 497
[3] David Dussault, Paul Hoess, Proceedings of SPIE Vol. 5563, pp.195-204 (2004)
[4] P. Forck et al., OPAC Workshop 2014

---

* Work supported by BMBF project No. 05P12RDRBN and Graduate School of Excellence ESE TU Darmstadt.

[#]y.shutko@gsi.de

DOI:10.15120/GR-2015-1-FG-GENERAL-45

In-beam tests of PMTs and voltage dividers for particle detectors at FAIR[*]

P. Boutachkov[1], *A. Reiter*[1], *C. Andre*[1], *H. Bräuning*[1], *C. Dorn*[1], *P. Forck*[1,2], *E-M. Glück*[1], *H. Graf*[1], *T. Hoffmann*[1], *V. S. Lavrik*[2], *A. Lieberwirth*[3], *Y. Shutko*[3], *and B. Walasek-Höhne*[1]
[1]GSI, Darmstadt, Germany; [2]Goethe University, Frankfurt, Germany; [3]IKP, Darmstadt, Germany

Scintillation counters are used for beam intensity, beam loss and spill structure measurements at GSI, they will be utilized at FAIR too, see [1] and the references therein. The presented study was started due to the phase out of the Photonis XP2972 photomultiplier, which is presently used in the beam diagnostic counters at GSI. Possible replacement photomultipliers (PMTs) and active voltage dividers (AVDs) were selected based on their characteristics and laboratory tests [1]. From the tested PMTs, Hamamatsu R6427 had the largest gain variation, while the ET Enterprises and the GSI in-house developed AVDs demonstrated stable operation at counting rates above 10 MHz. The response of the selected PMT and AVDs to the modulated spill structure of slowly extracted SIS beam was investigated.

Measurements and Results

The tested PMT and AVD was coupled to a 1 mm thick BC400 scintillator, in a configuration illustrated in Fig. 1 of Ref. [2]. Three scintillators were placed behind each other. The heavy ion beam penetrates the 3 mm plastic, depositing similar energy in the three detectors. The generated signals were recorded with a broad band oscilloscope, which was triggered at a programmable delay relative to the beginning of the spill extraction. A representative measurement is shown in Fig. 1, demonstrating the better performance at high counting rates of the GSI-AVD. Operating at these rates is advantageous for applications where an integrating detector, as an ionization chamber, is calibrated relatively to a scintillator counter.

The amplitude spectra shown in Fig. 2 illustrates two typical cases which can lead to inaccurate measurements: a radiation damaged scintillator and irregular spill structure. An amplitude measurement or a comparison of the counting rates above two different thresholds will provide a criteria of the measurement reliability, as shown in the inset of Fig. 2.

In conclusion, based on the tests described in this contribution and in Ref. [1], the optimum PMT-AVD combination for the future counters at FAIR and GSI is a Hamamatsu R6427 PMT powered by the GSI-AVD. In spite of the better PMT-AVD performance, a reliable measurement with the scintillation counters at instantaneous rates above 13 MHz would require amplitude information.

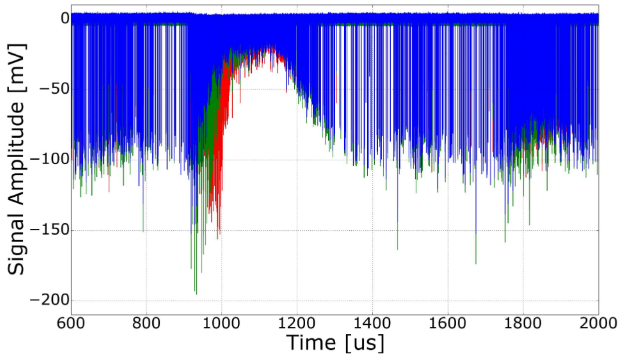

Figure 1: Pulses from ^{238}U ions at 300 MeV/u and average in spill intensity of 1 MHz. At Time∼1 ms, the signal amplitude grows and falls down as the instantaneous beam intensity increases above 13 MHz. Signals from R6427 PMT powered by: GSI-AVD (in red), E220BFN2-01 (in green) and H7415MOD-AVD (in blue). The GSI-AVD withstand higher counting rates compared to the other AVDs.

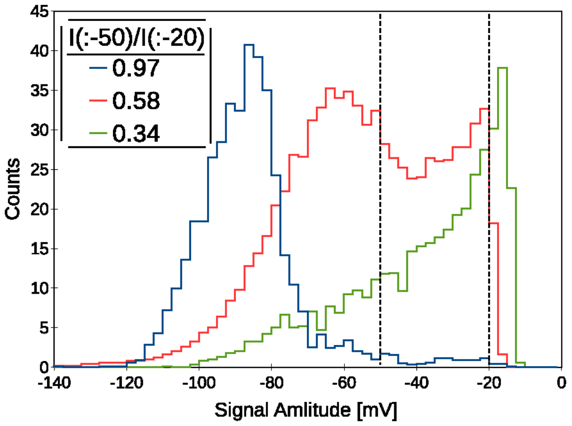

Figure 2: Signal amplitudes for normally operating PMT-AVD in blue, overloaded detector during parts of the spill in red and radiation damaged scintillator in green. The ratio of counts with amplitudes larger than 50 mV and 20 mV is shown in the inset.

References

[1] P. Boutachkov, *et al.*, “Bench Tests of PMTs and Voltage Dividers for Counting Applications at FAIR”, GSI Scientific Rep. (2014)

[2] P. Forck, T. Hoffmann, DIPAC01, Grenoble, p. 129 (2001)

---

[*] It is pleasure to acknowledge the members of the GSI operating team for their support during the experiments.

DOI:10.15120/GR-2015-1-FG-GENERAL-46

Bench tests of PMTs and voltage dividers for counting applications at FAIR

P. Boutachkov, C. Andre, A. Reiter, and T. Hoffmann
GSI, Darmstadt, Germany

This contribution presents selected results from tests of Photomultipliers (PMT) and active voltage dividers (AVD) with a laser diode.

At FAIR, plastic scintillator counters will be used for beam intensity and beam loss measurements [1]. Furthermore, the Photonis company phased out the production of the XP2972 PMT, which is presently used in the beam diagnostic counters at GSI [2,3]. Commercially available PMTs from Hamamatsu and ET Enterprises were selected, based on photo-cathode area, gain, signal rise time and transit time spread. The gain variation and the maximum counting rate were determined for combinations of the selected PMTs and AVDs at various luminances. These parameters determine the scintillator thickness necessary for detection of an ion accelerated by SIS18/100, and the instantaneous beam intensity which can be measured by the counters.

Measurements and Results

Measurements were performed with the Hamamatsu R6427, ET Enterprises 9442B and Photonis XP2972 PMTs. They were biased by a Hamamatsu-H7415MOD, ET Enterprises E220BFN2-01 and an in-house developed active voltage divider.

The PMTs and AVDs were tested with a fast switched laser diode by PicoQuant (FSL500 with a LDH-S-C-405 laser head). This light source emits at wavelength of 405 nm, matching the 420 nm wavelength of maximum emission for a BC400 plastic scintillator.

The full active area of the tested PMTs was illuminated by light pulses of a fixed duration, of approximately 3 ns. Their intensity was varied by changing the FSL500 power setting and by neutral glass filters. The laser was triggered by a white noise generator. The trigger frequency was measured by a rate meter, while the PMT minimum anode amplitude and average anode charge were determined by a 50 Ohm terminated broadband oscilloscope.

The tested PMTs were illuminated by the same light intensity at different repetition rates. For each series of measurements the AVDs high voltages were adjusted in order to observe signals with similar amplitude at 10-100 Hz trigger rate. Data from three measurements are shown in Fig. 1. Before reaching the maximum counting rate for a given PMT-AVD combination the signal amplitude increases, due to the higher voltage drop between the last dynodes.

In the GSI AVD the last 6 dynode voltages are stabilized. The stabilization is done by a voltage follower based on the BSS125 SIPMOS transistor. In comparison, the Hamamatsu divider has 3 stabilized dynodes, while in the ET Enterprises divider all dynodes are stabilized. The measurements showed that the ET Enterprises and the GSI AVDs can withstand counting rates above 10 MHz. Further in-beam tests [4] favored the GSI-AVD, due to better performance at higher counting rates.

Measurements with different neutral glass filters showed more than 10 times larger gain variation for the Hamamatsu R6427 PMT, compared to the ET 9442B and XP2972 PMTs. Based on the tests described in this contribution and in Ref. [4], one can conclude that the optimum PMT-AVD combination for the future counters at FAIR and GSI is a Hamamatsu R6427 PMT powered by the GSI AVD.

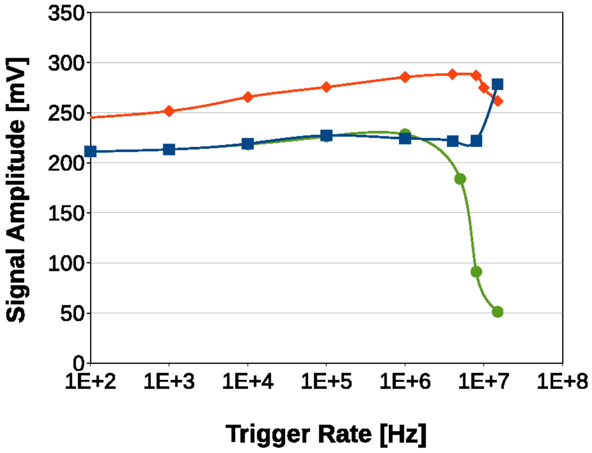

Figure 1: The solid curves follow the evolution of the signal amplitude of different PMT-AVD combinations as a function of the trigger rate. Blue-squares: Plots for the Hamamatsu R6427 PMT powered by GSI AVD. Orange-diamonds: ET 9442B PMT powered by E220BFN2-01. Green-circles: Hamamatsu R6427 PMT powered by Hamamatsu AVD.

References

[1] FAIR Technical Design Report (TDR) – High Energy Beam Transport, GSI, December 2008

[2] P. Forck, T. Hoffmann, DIPAC01, Grenoble, p. 129 (2001)

[3] T. Hoffmann, D. A. Liakin, P. Forck, Proc. 10th Beam Instrumentation Workshop, Upton, New York, p. 329 (2002)

[4] P. Boutachkov, *et al.*, "In-beam Tests of PMTs and Voltage Dividers for Particle Detectors at FAIR", GSI Scientific Rep. (2014)

DOI:10.15120/GR-2015-1-FG-GENERAL-47

Transverse beam shape measurements of intense Uranium beams using optical transition radiation

B. Walasek-Höhne[1], *C. Andre*[1], *H. Bräuning*[1], *C. Dorn*[1], *R. Fischer*[1], *P. Forck*[1], *H. Graf*[1], *F. Hagenbuck*[1], *R. Haseitl*[1], *K. Höhne*[2], *A. Lumpkin*[3], *R. Lonsing*[1], *A. Reiter*[1], *C. Schmidt*[1], *M. Schwickert*[1], *and R. Singh*[1]

[1]GSI, Darmstadt, Germany; [2]FAIR, Darmstadt, Germany; [3]FermiLab, Batavia, USA

Particle-beam diagnostic techniques based on Optical Transition Radiation (OTR) have been demonstrated at a number of facilities with relativistic electron and proton beams [1]. Optical transition radiation is generated when an ion of charge q and velocity β crosses the interface between two media with different dielectric constants. This radiation is emitted over the visible spectrum and standard optical imaging techniques can be used to acquire the OTR signal and then reconstruct beam size and position. Since OTR is a surface phenomenon, thin foils can be used as the converter to reduce beam scattering and minimize heat deposition. The OTR method can be used to measure beam properties as transverse profiles and 2-D shape, transverse position, divergence, emittance and intensity.

The OTR signal of a non-relativistic ion beam has been shown for the first time in 2011 with a pilot OTR experiment at the UNILAC [2]. During the 2014 beam time, usability of the OTR method to obtain profiles of high energetic ion beams was successfully demonstrated and first images were taken. Measurements were performed with 600 MeV/u Uranium beams from SIS18 of intensities up to around 2×10^8 particles per pulse (ppp) and 300 ms pulse length on a stainless steel target. In order to detect the low number of photons a standard CCD Camera (Prosilica GC650) with additional image intensifier (Lambert Instruments I187) was used.

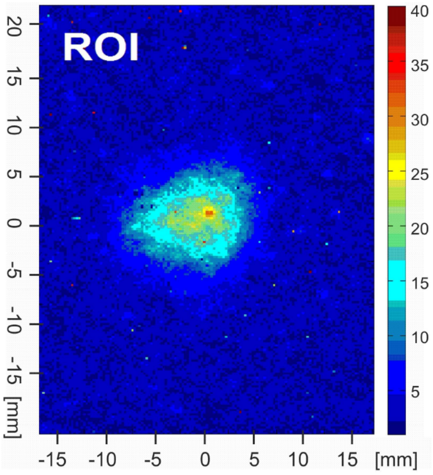

Figure 1: False colour OTR images of beam cross-section during irradiation with 1.5×10^8 U^{92+} ions. The beam energy was 600 MeV/u (pulse length 300 ms).

Various experiments have been performed to estimate the signal strength, to determine the imaging qualities and to evaluate the working regime of the OTR technique. Figure 1 shows a false colour OTR image from 1.5×10^8 U^{92+} ions impinging on the target.

For beam imaging OTR has the advantage that it is expected to show perfect linearity to the number of incident particles without the risk of saturation. In Figure 2 the integral OTR signal is displayed for different particle numbers per pulse. The beam current was measured with a Secondary Electron Monitor (SEM). In our studies the OTR signal shows a linear behaviour with respect to the incident particle number. For U^{92+} ions reasonable beam distributions were acquired down to 2×10^7 ppp.

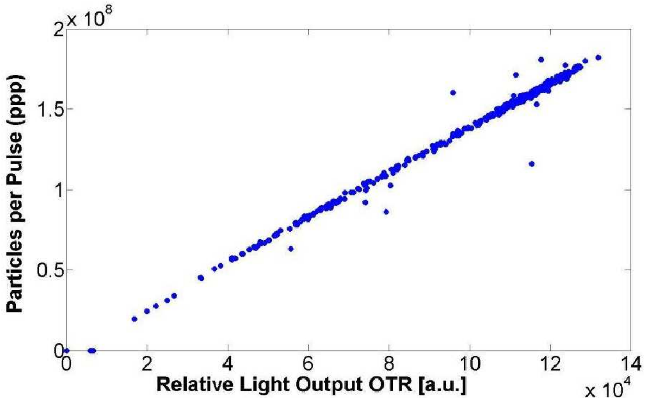

Figure 2: The OTR signal strength as a function of the particle number for the U^{92+} beam.

To determine the imaging qualities of the OTR method, additional profile measurements with a MWPC have been made. The beam profiles obtained with MWPC and OTR are in good agreement. OTR has an advantage of directly obtaining two dimensional beam shape.

The usage of OTR monitoring as a minimally intercepting method can be considered as an alternative to scintillators or BIF monitors.

References

[1] V. E. Scarpine et al., "OTR imaging of intense 120 GeV protons in the NuMI beamline at FNAL" PAC 2007 `http://www.JACoW.org/`

[2] B.Walasek–Höhne et al., "Optical Transition Radiation for non-relativistic ion beams" HB 2012 `http://www.JACoW.org/`

DOI:10.15120/GR-2015-1-FG-GENERAL-48

APD-photosensor serial characterization laboratory for FAIR experiments established

A.Wilms[1]*, the FAIR@GSI division RBDL*[1,#]

[1]GSI, Darmstadt, Germany.

For the readout of the electromagnetic calorimeters of PANDA [1] and R3B [2] Avalanche Photodiodes (APDs) will be used. To this end the individual sensors need to be characterized before installation in the final detector systems. Therefore a screening laboratory has been established October 2014.

The new APD screening facility at GSI

The main part of the newly established APD laboratory inside the Heck hall is the mass screening room in which 100 devices can be characterized simultaneously inside fife climate cabinets. Each cabinet is humidity and temperature controlled and allows the temperature dependent full characterization of the sensors in nearly completely automatized procedures (see Figure 1).

Figure 1: Installation of 5 climate cabinets inside one room of the APD laboratory.

To reach the envisaged screening capacity of 2000 APDs per month, the APD laboratory of the RBDL division is operated in shift mode. For the PANDA EMC, all APDs need to be characterized twice, once before and once after gamma irradiation.

APD screening & results

In addition to the optical parameters measured at given wavelengths, the temperature dependence of the gain-bias characteristics may be measured. Further, the quantum efficiency at different temperatures, the electrical properties like capacitance and excess noise may be measured at the facility in the future, as soon as the ongoing validation of the respective apparatuses is done.

Approx. 4600 APDs have been characterized so far for the PANDA EMC with respect to their parameters at 20°C and at their nominal manufacturer-given gain of M = 100. The distributions for the voltage values to be applied to reach a gain of M = 100 as well as the breakdown voltages of approx. 3800 APDs are shown in Figure 2 and Figure 3 respectively.

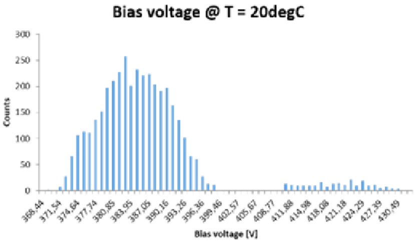

Figure 2: Bias voltage distribution for validated APDs at 20°C for M = 100.

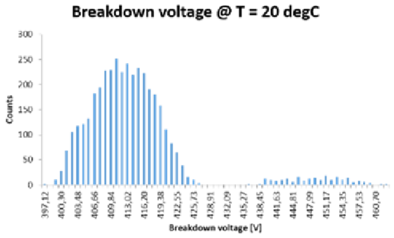

Figure 3: Distribution of breakdown voltage for the same APDs: Two groups of devices can clearly be identified. Both groups are still found within specifications.

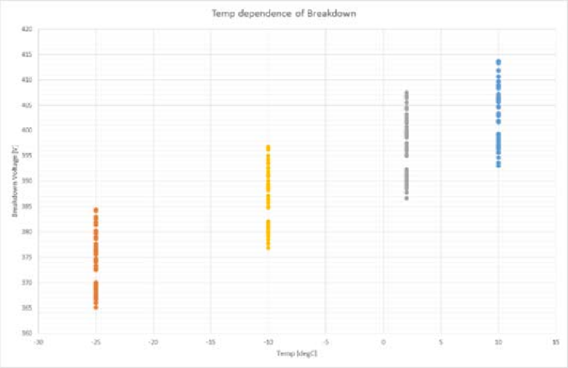

Figure 4 First preliminary data of a sample of 60 APDs showing the temperature dependence of the breakdown voltage. Each device shows a strictly linear behaviour.

Up to now only around 1‰ of the devices did not match the required technical specifications defined by the collaboration.

References

[1]: Technical Design Report for PANDA Electromagnetic calorimeter (2008) arXiv:0810.1216

[2]: Technical Report for the Design, Construction and Commissioning of the CALIFA Barrel (November 2011)

DOI:10.15120/GR-2015-1-FG-GENERAL-49

DOI:10.15120/GR-2015-1-FG-GENERAL-49

SIS100 status report 2014

P. Spiller, U. Blell, L. Bozyk, J. Ceballos Valesco, T. Eisel, E. Fischer, H.G. König, V. Kornilov, P. Kowina, J.P. Meier, A. Mierau, C. Mühle, C. Omet, D. Ondreka, H. Ramakers, N. Pyka, P. Rottländer, C. Roux, P. Schnizer, S. Wilfert, and D. Winters

GSI, Darmstadt, Germany

Introduction

SIS100 is the main accelerator of the FAIR project. It is a worldwide unique heavy ion synchrotron dedicated to accelerate highest intensities of intermediate charge state heavy ion and proton beams up to 100 Tm. From the technical point of view, most challenging issues are the fast ramped superconducting magnets and the acceleration of intense, intermediate charge state heavy ions beams. The latter required a unique lattice design (charge separator lattice) in combination with an ultra-high vacuum system based on distributed cryopumping with actively cooled magnet chambers, adsorption pumps and dedicated cryocatchers for local suppression of gas desorption.

Procurement status

The year 2014 was very much loaded with completing, reviewing and finishing specifications and drawings for all kind of components. Finally, shortly after end of 2014, all contracts for the major SIS100 components and the large series have been closed (i.e. Milestone "M4" has been reached), which is a major step ahead. This corresponds to a bound value of 50% of the SIS100 costbook value. The last large in-kind contract regarding the quadrupole unit production has been successfully negotiated and closed with the Joint Institute for Nuclear Research (JINR, Dubna, Russia) and signed by JINR, GSI and FAIR management at an official ceremony at JINR at 2015/02/20, see fig. 1.

Besides the major series with long production times, many other components have been tendered or contracted, e.g. the injection kicker system, the resonance sextupole magnets (awarded to DANFYSIK, Denmark) and the cryocatcher system. The local cryogenics system will be delivered by the Wroclaw University of Technology (WrUT, Poland) and the manufacturing design review took place for the first bypass line segment. The contract for the production of the bypass line as been awarded to the company KRIOSYSTEM, Poland.

Building planning

Detailed planning for the accelerator tunnel and the supply area (K0923A/T110) complex, including 3D DMU models of the accelerator and its technical infrastructure, has matured and is transitioning to execution planning, which will take place in 2015, see fig. 2. This will allow the creation of the necessary building tendering documents in late 2015.

Figure 1: Signature of quadrupole unit production contract at JINR (l.t.r with the contract in their hands: B. Sharkov / FAIR and V. Matveev / JINR.

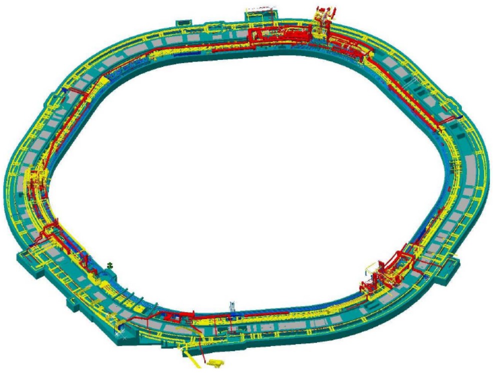

Figure 2: T110 design with cable trays (yellow), cooling water supply lines (blue) and venting (red).

Progress on component tendering and delivery

The first of the 109 s.c. 1.9 T dipole series magnets (FoS) has already been delivered in June 2013 and thoroughly tested under warm and cryogenic conditions. Although, the FOS dipole has a completely new coil design and is being operated at twice the electrical current as the prototype, the quench training showed excellent behavior. Nevertheless, the planned high current operation allows only minimum mechanical errors in the yoke production. Therefore, together with the manufacturer and external experts, the production and welding process has been review and optimized. A mechanically further improved FoS yoke will be produced and delivered until Q3/2015. After a short test period the series production will be released. The FoS thin wall, actively cooled dipole vacuum chamber has been

DOI:10.15120/GR-2015-1-FG-SIS100-01

delivered by the company PINK and tested at warm and cold conditions. The manufacturing has been done with excellent results and the specified UHV properties were achieved. However, the cryogenic pumping properties of the He cooling circuit has to be improved.

The s.c. quadrupole modules (83 pcs, see fig. 3) are very demanding due to their technical complexity and the international structure of the project. The quadrupole units (quadrupole magnet + corrector magnets) will be built at JINR, Dubna, whereas other components (vacuum chambers, cryocatcher, BPM's, local current leads, cryostats, ...) will be tendered by GSI. Currently, 80% of the specification work of the units and all manufacturing drawings for the quadrupole module type 2.5 FoS units are finished and are finally reviewed at JINR; the remaining 20% will be done when the external (industrialized) design work has been completed. The yoke steel (323 t in total) has been ordered at C.D. Wälzholz, Germany and the first lot will be delivered to JINR 04/2015. The cryocatcher tendering is nearly completed, bids do exist. Finally, smaller standardized components like voltage breakers and temperature sensors for the full quadrupole module series has been ordered by GSI in 2014, too.

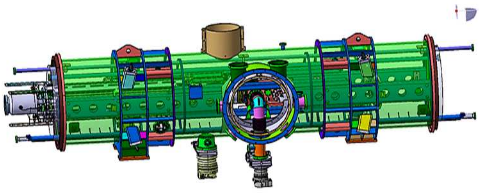

Figure 3: Design of the type 2.5 quadrupole module.

The RF acceleration system (14 pcs, 1.1...3.2 MHz, 20 kV$_p$, 30 kW beam power, see fig. 4) has been tendered by FAIR GmbH and awarded to a consortium of RI/AMPEGON in 11/2014. Preparation of the manufacturing concept is currently done by the consortium, the conceptual design review (CDR) will take place Q1/2015. Driver amplifier and LLRF procurement has been started, too.

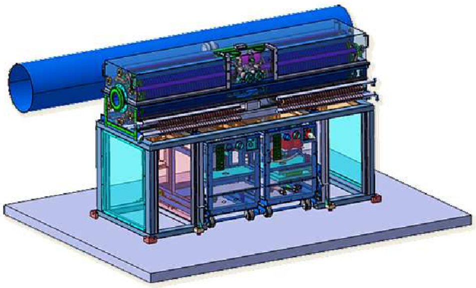

Figure 4: Design of the acceleration cavitiy.

The RF Bunch compression system (9 pcs) has been tendered by GSI and awarded to the company AURION (Germany) in 04/2014. The conceptual design review has been successfully concluded. As last step before the start of production a final design review (FDR) is foreseen, which will take place in 03/2015 - the 1st device will be delivered in 07/2015.

The design of the SIS100 injection straight section (sector 6) has been detailed; as a result, the injection kicker system (6 modules, 130 ns rise time, 7.5 mrad deflection angle) procurement has been started.

S.c. test facilities

The prototype test facility (PTF) has been equipped in 2014 with all missing infrastructure, 13 kA HTS current leads, power supplies, etc. to upgrade it for the testing of the dipole FoS tests. Fig. 5 shows the team after the first dipole cold test.

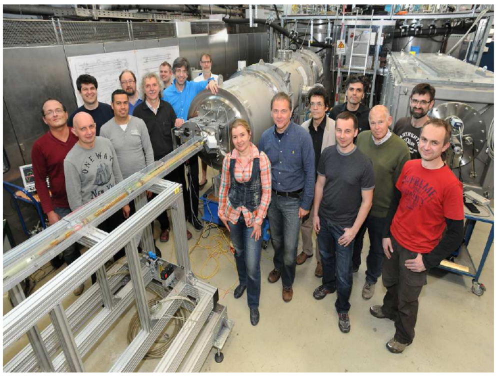

Figure 5: The test team at the PTF with the FoS dipole.

For the series dipole magnet test facility (STF), a dedicated building has been constructed at GSI (Bldg. SH5). The cryogenic system, including feed boxes and test benches is currently commissioned. The power converter for ramping the s.c. dipole magnets with 29 kA/s will be delivered in 04/2015. High precision magnetic field measurement equipment is currently built in a collaboration with CERN. This subproject runs smooth and is profiting a lot from the experience gained during the FoS dipole testing, where high precision mechanical measurement devices has been developed.

The quadrupole unit testing will be done at JINR, Dubna. Here, an R&D contract between GSI and JINR has been closed in 12/2013. The cryoplant at JINR has already been commissioned; measurement equipment will be designed by JINR in parallel to the construction of the first quadrupole units.

Finally, the SIS100 stringtest will comprise two dipoles, one quadrupole module, the cryogenic bypass line, feedbox and current lead box. The space is preserved at the STF and the layout has been completed. The contract for the bypass line has been closed (WrUT) and the FDR will take place in 02/2015. Specifications for the remaining items are 50% finished.

DOI:10.15120/GR-2015-1-FG-SIS100-01

Status of the superconducting magnets for FAIR*

E. Fischer[†], V. Bezkorovaynyy, A. Bleile, J. Ceballos, E. J. Cho, W. Freisleben, N. Joshi, B. Körber, V. Maroussov, F. Marzouki, J. P. Meier, S. Meyer, A. Mierau, H. Müller, H. Raach, C. Roux, P. Schnizer, F. Seifert, A. Stafiniak, K. Sugita, P. Szwangruber, and H. Weiss
GSI, Darmstadt, Germany

Introduction

Within this paper we report shortly on all the many different activities of the group which now is mainly focused on procuring the magnets and associated systems for the FAIR project. While many activities were pursued the successful tests of the SIS100 dipole magnet stick clearly out.

Superconducting magnets

Rapidly cycling magnets for SIS100

Dipoles – production status and first tests The First of Series SIS100 main dipole was delivered last year and its testing campaign has been conducted since December 2013 with a successful cool down, measurement of the virgin field curve, required for field optimisation calculations, and finished with a successful training.

The coil structure was found to provide an insulation of 3 kV already at the factory test. During the first run the magnet quenched slightly below the nominal current with the second quench already above nominal field and reached up to now a maximum current of 15.7 kA and thus shows sufficient operation margin.

The AC losses produced by the SIS100 main dipole magnet are one of the main loads on the cyroplant. are well below the expected value of 70 W for a triangular cycle of 1 Hz. This is considered explainable by the choice of iron (M600-100A silicon steel), the superconducting low loss wire with a CuMn matrix and extra inserts at the magnet ends, foreseen for optimising the end field quality.

The magnetic field was measured using: a hall probe mounted on a mapper, a single stretched wire system, and rotating coil probes at different locations [1, 2]. The field measured with these different systems gave results which were matching each other with sufficient accuracy and second the soundness of the measurement system design.

So the overall tests of the magnets were successful: quench behaviour, magnetic field strength, AC losses. The magnetic field was however a bit deteriorated. The mechanical accuracy of the yoke assembly was investigated with appropriate gauges, which showed that the yoke mechanics was slightly out of specifications. Based on these measurements mitigation actions were discussed with the manufacturer and will be tested and incorporated in the production beginning next year.

Quadrupole modules Aside of the dipoles the main quadrupoles together with all corrector and steerer magnets are assembled into so called units consisting of a main quadrupole and up to two correctors. These quadrupole units will be produced and tested at cold temperature at **J**oint **I**nstitute for **N**uclear **R**esearch (JINR). The collaboration contract for production of quadrupole-, corrector- and steering magnets as well as the integration into units at JINR are finalised and will be signed in January 2015. The units are located within 83 quadrupole doublet modules split in 11 configurations and four basic classes with modules located in the arc, the end of the straight section of the SIS100 machine. All these modules are currently designed in interaction with Babcock Noell Gmbh Würzburg / Germany. The integration of the modules has to fulfill demanding stability criteria of ± 125 μm for the main quadrupoles, which makes the design challenging. The tendering process for the involved components and the integration of modules is in preparation and will be established also in 2015.

Rapidly cycling magnets for SIS300

After manufacturing of a first dipole magnet in collaboration with INFN, Italy, a second collared coil was built together with INFN and CERN in frame of the EU-CRISP project. Ongoing is also the design work on wide aperture quadrupoles for FAIRs HEDgeHOB experiment by IHEP in Protvino, who had already successfully built SIS300 quadrupole and corrector prototypes.

Magnets of the Super-FRS

The specifications of the SuperFRS magnets were released and the tender launched. The dipoles design has been finalised by CEA/Saclay. The multiplets have been thoroughly negotiated and the contract will be awarded soon.

Testing

Prototype test facility activities

While the magnet was produced in parallel the test facility was upgraded so that all parameters of the magnet could be derived including an upgrade of the power converter and procurement of HTS current leads.

---

* We acknowledge the support of the European Community-Research Infrastructure Activity under the FP7 program CRISP (Grant agreement no: 283745) Work Package 5. We acknowledge the support through the JINR–BMBF contract.

[†] e.fischer@gsi.de

DOI:10.15120/GR-2015-1-FG-SIS100-02

The measurements of the field quality were made with the mole, i.e. a rotating coil probe system with a motor operating inside the magnetic field. For series measurements a measurement shaft will be used with cold coil probes as their cores. Together with CERN a system was adapted for measuring the magnetic field in cold conditions in vacuum and successfully tested. A shaft based on this principle will be tested beginning next year.

Series test facility activities

The seres test facility is being built up which is currently mainly dedicated for testing the SIS100 dipoles. The cryoinfrastructure including also the feed boxes have been procured supervised by our colleagues of the cryo group and are currently being tested. It will provide 4 test benches organised in 2 clusters and allow testing the SIS100 string.

At the beginning of the SIS100 series dipole testing all four benches will be used for the tests of the dipole magnets. When the first of series quadrupole doublet will be delivered to GSI one of the test benches will be used to operate the string test [3].

SIS100 quadrupole tests

The test facility at JINR for these magnets is currently being built up. The first power converter is being assembled and will be commissioned soon. Each test bench is equipped with a satellite refrigerator for cooling down and operating of the magnets. This concept simplifies the parallel operation of the test benches. Two satellite refrigerators have already been produced.

Testing Super-FRS magnets at CERN

The cold tests of Super-FRS will be done at CERN under a collaboration agreement between CERN and GSI. Three test benches, suitable for dipole magnets and multiplets respectively, will be available. This allows a continuous operation with one bench being cooled down, one cold and the measurements running, and the third being warmed up. Given that these choices have been made now the hardware can be procured. CERN is already refurbished the necessary cryogenic infrastructure and setting up the other necessary test equipment as, for example, power converters, quench detection systems, and systems for magnetic measurements.

Current leads

The successful test of the first pair of HTS current of last year gave the green light to produce the second pair which was delivered this year and successfully tested. So the series production of the current leads for the series test station and the SIS100 machine was launched. Along with this high current current low current leads have been designed. A prototype has been procured that will be tested beginning next year. For the γ_t-Jump-Quadrupole, a cold normal conducting magnet within a quadrupole doublet module, the design of current leads has been started. For the Hedgehob collaboration 4 pairs of 6 kA HTS current leads shall be procured. A specification is in preparation.

Electrical systems and magnet protection

The quench detection systems for the series test facility have been procured. While these systems could detect a quench reliably in the SIS100 machine, the required cables would create too large parasitic capacitance. Therefore an alternative based on transducers is currently under development.

Conclusion

After the procurement of the different superconducting magnets has been started in 2013, the first SIS100 dipole was tested thoroughly in 2014 and a new built chromaticity sextupole is ready now for testing as a first corrector type magnet. The dipole tests results proved that the magnet design is sound and the requested operation parameters are achievable. In-depth technologic investigations of the yoke production process, supporting the manufacturer, have shown that the remaining problems can be solved by improving the welding technology so that the specified tolerances of the yoke geometry can be achieved. Thus a second yoke will be produced and the corrected first dipole is expected to provide the required magnetic field accuracy. This will allow us launching the series production still in 2015. The production of the other magnets was also prepared in 2014. The telegraphic style of this paper reflects the many activities that are undertaken to realise the FAIR project within the given scope and schedule.

References

[1] P. Schnizer, E. Fischer, P. Akishin, J. P. Meier, A. Mierau, and A. Bleile. Advanced magnetic field description and measurements on curved accelerator magnets. In *Proceedings of IPAC2014, Dresden, Germany*, 2014.

[2] E. Fischer *et al.*, Fast ramped superconducting magnets for FAIR – production status and first test results. *IEEE T. Appl. Supercon.*, 2014. submitted for publication.

[3] K. Sugita *et al.*, String test preparation for the superconducting SIS100 accelerator of FAIR. *IEEE T. Appl. Supercon.*, 24(3):1–4, June 2014.

[4] A. Bleile *et al.* Thermodynamic properties of the superconducting dipole magnet of the SIS100 synchrotron. *Physics Periodica*, 2014. submitted for publication.

[5] E. Fischer *et al.* WEPRI083 IPAC2014, Dresden, Germany, 2014.

[6] H. Raach *et al.* 14 kA HTS current leads with one 4.8 K helium stream for the prototype test facility at GSI. *Physics Periodica*, 2014. submitted for publication.

[7] P. Schnizer *et al.* Low temperature test capabilities for the superconducting magnets of FAIR. *IEEE T. Appl. Supercon.*, 2014. submitted for publication.

DOI:10.15120/GR-2015-1-FG-SIS100-02

The SIS100 laser cooling facility*

D. Winters†1, *T. Beck*2, *G. Birkl*‡2, *M. Bussmann*3, *V. Hannen*4, *Th. Kühl*1,5, *X. Ma*§6, *U. Schramm*‡3,7, *M. Siebold*3, *Th. Stöhlker*1,5,8, *Th. Walther*‡2, *W. Wen*§¶3,6,7, *and P. Spiller*1

1GSI Helmholtzzentrum, Darmstadt, Germany; 2Technical University Darmstadt, Germany; 3Helmholtz-Zentrum Dresden-Rossendorf, Germany; 4Münster University, Germany; 5Helmholtz Institute Jena, Germany; 6Institute of Modern Physics-CAS, Lanzhou, China; 7Technical University Dresden, Germany; 8Jena University, Germany

High-quality, stored ion beams can be obtained by means of electron cooling and/or stochastic cooling. At intermediate kinetic energies ($\gamma\approx1$), these methods work very well. But at very high kinetic energies ($\gamma>5$), they become less effective. For instance, to reach electron cooling at $\gamma=12$, a very sophisticated (voltage up to 6 MV) and thus expensive electron cooling system is required. Therefore, another method was considered for the FAIR heavy-ion synchrotron SIS100: Laser cooling of bunched ion beams. Based on successful experiments with stored, relativistic heavy-ion beams at the ESR [1], it was (2013) decided to set up a laser cooling facility at the SIS100. Within the 3rd term of the Programme Oriented Funding (POFIII) of the Helmholtz Society, we wrote a proposal for this facility as part of accelerator research and development (ARD) within "Matter and Technologies" [2]. Early 2014, the proposal was approved and received the highest marks ('highlight').

Within FAIR@GSI primary beams, a special project group 'SIS100 laser cooling' (PSP-code 2.8.10) was formed, which tasks are to specify, design, order, construct, setup, and test the SIS100 laser cooling facility. (*Note*: The planned laser cooling facility can serve both the SIS100 and the future SIS300.) The project group consists of scientists from SPARC 'laser cooling' [3], which come from GSI and the collaborating partner universities and research centers in Dresden-Rossendorf, Darmstadt, Jena, Münster, and Lanzhou (China).

For laser cooling at the SIS100, the setup must be similar to that used at the ESR, and at least contain a laser system with a beamline (incl. optics and diagnostics), a set of scrapers, a buncher (exciter), and a dedicated fluorescence detection system. The facility will be located 20 m underground (see Fig. 1). The laser light will be transported from the laser lab in the (inner) service tunnel to the (outer) accelerator tunnel, passing through concrete walls and a thick layer of soil between the two tunnels. This laser beamline (length 25 m, diameter 20 cm) should be made out of stainless steel vacuum tubes. Vacuum conditions are required to transport the laser light, which covers a very broad spectrum ranging from the IR ($\lambda\sim\mu$m) down to the XUV range ($\lambda\sim$nm). The laser lab (180 m^2) will contain a special cleanroom (50 m^2) to operate the laser systems. There will also be a detector cave (45 m^2) in which special detector systems for x-ray measurements can be installed (SIS300). Detectors for the IR- to the XUV-range are still compact enough to fit into the SIS100 tunnel. To couple the laser light in and out of the accelerator, special vacuum chambers with optics and diagnostics will be used. Spatial overlap (about 25 m) between laser and ion beam needs to be adjusted using scrapers and reference points.

First tests of the facility will use Li-like ions and laser systems provided by the groups in Darmstadt and Dresden. Once the facility has passed all the tests, and first laser cooling has been demonstrated, other ion species and/or laser systems could be used as well. We emphasize that also laser spectroscopy experiments can be performed! Once the cooling transition is found, it can also precisely be measured. Ultracold beams are also of great interest by themselves. Last, but not least, it will be attempted to extract the laser-cooled ions from the SIS100 and uniquely deliver very cold and very short ultra-relativistic ion bunches to experiments.

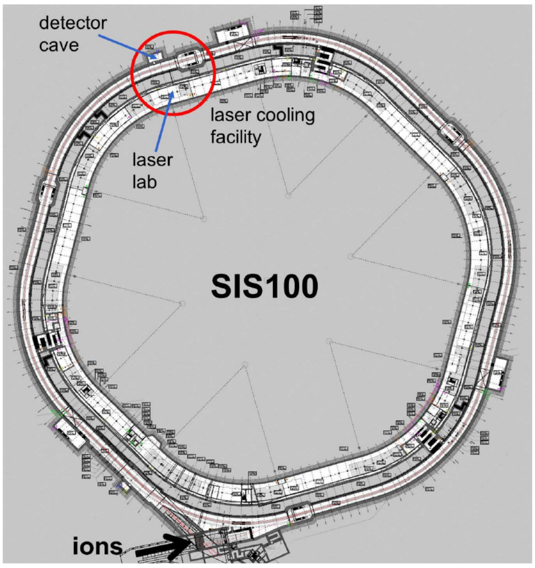

Figure 1: The FAIR heavy-ion synchrotron SIS100. The planned laser cooling facility is indicated by the red circle.

References

[1] U. Schramm *et al.*, Prog. Part. Nucl. Phys. **53** 583 (2004).

[2] https://www.helmholtz-ard.de/e25/

[3] https://www.gsi.de/sparc

---

* Work supported by HGF POFIII ARD-ST2.

† d.winters@gsi.de

‡ Work supported by BMBF.

§ Work supported by BMBF-WTZ.

¶ Work supported by DAAD.

DOI:10.15120/GR-2015-1-FG-SIS100-04

Simulation of laser cooling of heavy ion beams at high intensities

L. Eidam[*][†][1,2] *and O. Boine-Frankenheim*[1,2]
[1]GSI, Darmstadt, Germany; [2]TEMF, TU Darmstadt, Germany

Abstract

In the past the principle of Doppler laser cooling was investigated and verified in low energy storage rings. In the SIS100 laser cooling will be applied to intense ion beams in the high energy regime for the first time. Laser cooling leads to an increase of the longitudinal phase space density and to non-Gaussian bunch distributions. In order to optimize the cooling process and ensure stable operation laser cooling has to studied numerically.

Principle of Laser Cooling

Laser cooling produces very cold beams by intersecting laser light anti parallel with the ion beam. The wavelength of the laser in the particle frame has to fit to an atomic transition with a short lifetime. The absorbed photons always give a kick in the same direction whereas the emitted photons kick the ions in any direction. This results in a net force pointing in the direction of the laser beam. The narrow force only interacts with particles with a momentum deviation of approximately $\Delta p/p \approx 10^{-7}$. The cooling of a hot ion beam is feasible by sweeping the laser frequency to interact with all particles in the bucket [1].

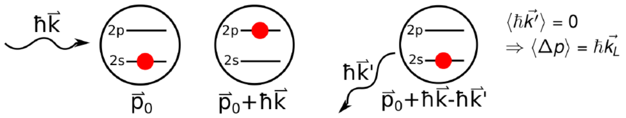

Figure 1: Schematic explanation of directional force for multiple scattering events during the laser cooling process.

Numerical Model

For the studies of the cooling process the simulation considers only the longitudinal phase space because the photon-particle interaction only affects the longitudinal motion. The tracking code contains different RF bucket configurations, intra beam scattering (IBS), space charge (SC) and the laser forces.

The laser forces are modelled statistically to take care of the so called 'random walk' [2]. This concept clarifies that the probability of absorbing the next photon changes after each scattering event. Therefore the assumption of an averaged force is not valid in general. For the simulation the laser interaction region is divided into slices. For each simulated particle in each slice the probability of a scattering event is calculated and statistically applied. The momentum change of a scattering event is given by:

$$\delta_j' = \hbar\vec{k}_{pf} \cdot (1 + \cos(\pi \cdot U_j)) \tag{1}$$

where $\hbar\vec{k}_{pf}$ is the momentum of the photon in the particle frame and U_j a random number. The therm $\cos(\pi \cdot U_j)$ describes the projection on the longitudinal axes of the randomly emitted photon. The probability of this momentum change is given by:

$$\rho(S, \Delta v) = \frac{L_{\text{intersec.}}}{n_{\text{slices}}\beta c_0 \gamma} \frac{\Gamma_L}{2} \frac{S}{1 + S + (2\Delta v/\Gamma_L)^2} \tag{2}$$

where the first factor describes the time interval of each slice and the rest is given by the well known probability of a spontaneous emission of a two level system with the saturation parameter S [2].

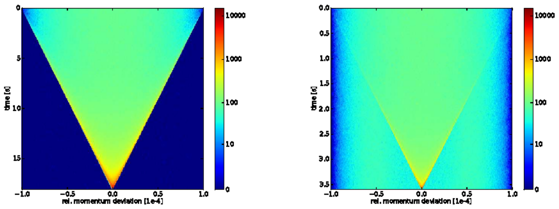

Figure 2: Momentum deviation over time during the cooling process for two different speeds of the laser sweep.

Figure 2 shows the simulated momentum deviation during the cooling process in a regular RF-bucket. In the second plot the sweep of the laser is too fast and some particles get lost behind the laser force and consequently for the cooling process.

Outlook

In the future the laser force and the IBS rates of possible transitions of different ion species will be analysed to find ions for a fast cooling process. Besides different cooling schemes with different RF configurations have to be analysed to optimize the cooling process.

References

[1] M. Bussmann et al, J. Phys.: Conf. Ser. 88, 012043 (2007)

[2] H.J. Metcalf, P. van der Straten, "Laser Cooling and Trapping of Atoms and Ions", Springer (1999)

---

[*] leidam@gsi.de

[†] Work supported by HGShire

DOI:10.15120/GR-2015-1-FG-SIS100-05

Investigation of thin-sheet approaches to simulate beam tube losses*

J. Trommler†1 *and T. Weiland*2
1, 2Institut für Theorie Elektromagnetischer Felder, TU Darmstadt, Germany

Introduction

The beam tube in acceleration facilities is often made of very thin metal. During the switch-on or switch-off process of the dipole-magnets, the fast change in the magnetic field lead to eddy currents in the conductive beam tube. Applying a standard finite-element method (FEM) in order to simulate the parasitic effects results often in inappropriate meshes and high computational effort. Thin sheet approaches improve the mesh quality and speed up the calculations, like shown in Fig. 1. In our report of 2013, existing thin-sheet approaches were studied and compared, and the approach of [1] and [2] were selected to be most efficient for the calculation of beam tube losses. In this report our new algorithm, which was already introduced in the report of 2012 for simple 1D test scenarios, is applied to higher spacial dimensions to be able to compare its performance to the competitive methods.

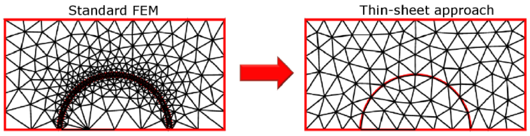

Figure 1: Mesh quality advantage of a thin-sheet approach.

Modified Bases in Higher Dimension

In taking the condition number of the system matrix into account, we developed in 2012 a new method [3] that outperforms the existing approaches according to this measure with respect to the accuracy. The basis functions of mesh elements that are directly connected to the interface are modified in order to account for the variation in thickness direction. But these modified bases are non-conform from one sheet adjacent element to the next. A penalization surface term has to be added to the weak formulation like also known from the discontinues Galerkin method or Raviart-Thomas elements.

A Two-dimensional Test Case

An electro-quasistationary test scenario was chosen to show the performance of our novel algorithm in higher spacial dimensions: A conductor excited by a harmonic voltage source of $U = 2\text{V}$ and $f = 50\text{Hz}$ and a small crack line with less conductivity in its center, see Fig. 2. The results

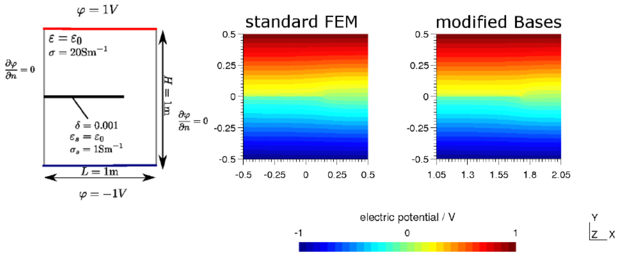

Figure 2: Geometry and result of test scenario.

of our thin-sheet approach are qualitatively comparable to standard FEM. Also the power loss is in good agreement with $P_{\text{el}} \approx 188.3\text{W}$. Fig. 3 shows the condition number of the final system matrix for different sheet thicknesses.

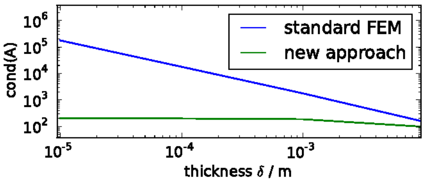

Figure 3: Conditioning with respect to sheet thickness.

Conclusion and Outlook

The promising approach of 2012 using modified bases is successfully applied to higher spacial dimensions, without loosing the advantageous properties. In a next step, the performance will be compared to the competitive methods of [1] and [2] in a beam tube simulation.

References

[1] Mayergoyz, I.D. and Bedrosian, G., “On calculation of 3-D eddy currents in conducting and magnetic shells”, IEEE Trans. Magn. 1995, vol. 31, no. 3, p. 1319–1324

[2] Schmidt, K. and Chernov, A., “A unified analysis of transmission conditions for thin conducting sheets in the time-harmonic eddy current model”, SIAM J. Appl. Math. 2013, vol. 73, no. 6, p. 1980–2003

[3] Trommler, J. and Koch, S. and Weiland, T., “A finite-element approach in order to avoid ill-conditioning in thin-sheet problems in frequency domain - Application to magneto-quasistatics”, JCAM 2012, vol. 236, no. 18, p. 4671–4680

---

[*] Work supported by GSI cooperation with university TU Darmstadt.

[†] trommler@temf.tu-darmstadt.de

DOI:10.15120/GR-2015-1-FG-SIS100-06

Transverse BTF of bunched beams with Gaussian charge density at high energy

P. Görgen[1] *and O. Boine-Frankenheim*[1]
[1]TEMF, TU-Darmstadt, Germany

The transverse beam transfer function (BTF) is a widely-used diagnostic tool used in synchrotrons and storage rings. BTFs are commonly used for measurement of the machine tune and of stability diagrams. They can also be used to quantify transverse tune spread due to octupoles [1] or space charge [2] in coasting beams.

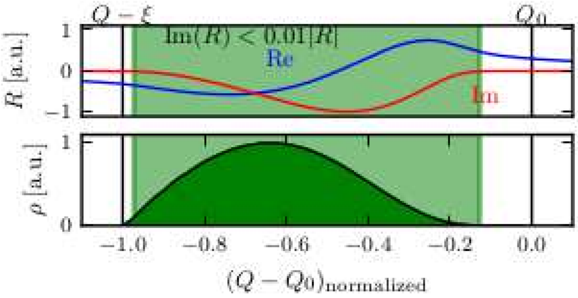

Figure 1: Analytic example BTF R with tune distribution ρ and the recovered tune spread (shaded green).

In this work the diagnostic power of beam transfer functions (BTF) with respect to bunched beams under the influence of a transverse nonlinearity was investigated in collaboration with Brookhaven National Laboratory (BNL). The work was motivated by the desire to recover the incoherent tune spread introduced by an electron lens such as the one recently installed at BNL for compensation of the incoherent beam-beam tune spread [3] directly via a BTF measurement. At GSI the tune spread caused by incoherent space charge in SIS 100 would be of interest. Building on the work by Berg and Ruggiero [1], transverse BTFs were investigated close to coasting beam conditions. In absence of coherent modes, it could be shown that while the exact distribution of incoherent tunes cannot be recovered from BTFs, the total width of the tune spread can be recovered [4]: In BTFs dominated by transverse tune spread such as BTFs of beams interacting with an electron lens in an otherwise very linear machine, the Landau damping arising from such a transverse nonlinearity dominates the beam transfer function and as a result the width of the peak in the imaginary part of the BTF allows determination of the incoherent tune spread. The recovery of tune spread from analytic BTF is shown in Figure 1.

To apply the analytic coasting beam results to bunched beams, it had to be shown that for the investigated working conditions, the effect of bunching is negligible. Beams in RHIC at high energy show nearly frozen synchrotron motion (synchrotron tunes of 10^{-3} and below). Synchrotron frequencies for SIS 100 proton operation are comparable. The transverse nonlinearity arising from the electron lens acts on particles in a bunch and a coasting beam alike. The assumption was validated in simulation for typical operating conditions. The simulations showed that the BTF did not change notably as a function chromaticity or synchrotron frequency. The recovery of the tune spread introduced by the electron lens works on bunches in simulation. The width of the peak in the imaginary part of the BTF still gives good estimate of the tune spread accurate to about 10-20% when applied to simulated BTF. The uncertainty is primarily caused by noise. The tune spread recovery method can be trivially automatized.

A validation measurement was carried out using the beam-beam effect to replicate the transverse fields of an electron lens while avoiding effects particular to the beam-beam effect. The tune spread recovered by the aforementioned method showed good agreement with the results obtained indirectly from the distance between coherent beam-beam modes in strong bunches and from emittance and beam current measurements.

A generalized theory incorporating conditions for space charge in SIS 100 with protons at high energy is currently under development. The shape of the transverse fields giving rise to the tune spread is identical for a Gaussian electron lens and the self-fields of a transversely Gaussian proton beam. However, while an electron lens acts both on the center of charge of the beam and individual particles and thus also gives rise to a coherent tune shift, this is not the case with space charge: With space charge, the nonlinearity stays spatially aligned with the center of charge of the beam. As a result, space charge is not directly measurable in the BTFs of beams with space charge as the sole source of tune spread. In combination with chromaticity, a characteristic deformation of the BTF was observed for coasting beams [2]. In bunched beams with non-negligible synchrotron motion, a characteristinc pattern of head-tail modes is observed. We are validating the assumption that for near-frozen synchrotron motion, a middle regime exists, where the BTF of bunched beams resemble a superposition of BTF of coasting beams of different currents. In this case, the incoherent space charge tune shift could be obtained by means of a fit against measured BTF data.

References

[1] J. Berg, F. Ruggiero, CERN SL-AP-96-71

[2] S. Paret et al., `doi:10.1103/PhysRevSTAB.13.022802`

[3] W. Fischer et al., *Construction Progress of the RHIC Electron Lenses*, Proceedings of IPAC 2012

[4] P. Görgen et al., `doi:10.1016/j.nima.2014.11.105`

DOI:10.15120/GR-2015-1-FG-SIS100-07

Computation and bench measurements of beam coupling impedance

U. Niedermayer [*1], *L. Eidam*[1], *and O. Boine-Frankenheim*[1,2]
[1]Institut für Theorie Elektromagnetischer Felder, TU-Darmstadt, Schlossgartenstr. 8 64289 Darmstadt; [2]GSI Helmholtzzentrum für Schwerionenforschung

Introduction

Beam coupling impedance can cause excessive heat load and coherent beam instabilities in high intensity synchrotrons. Therefore, a quantification of the beam coupling impedance for the components in SIS100 is outlined. We describe the development of a 2D Finite Element (FEM) frequency domain solver for longitudinal and transverse beam coupling impedances for arbitrary relativistic beam velocity. This solver can compute space charge and resistive wall impedances on a triangular mesh. It is based on the open source FEM package FEniCS [1] and mesh generator GMSH [2] and it is available for download at [3].

The beam coupling impedance of different components was also measured by the wire method. The wire method is based on emulating the electromagnetic fields of a particle beam by a TEM mode, i.e. it corresponds only to an ultra-relativistic beam. In the following we show a comparison for a ferrite ring, which is also analytically accessible.

A Ferrite Ring as Example

A ferrite ring of outer diameter 3.05cm and length 2.54cm was chosen for the validation of both measurement technique and our simulation code. The measurement results, together with a 3D reference simulation in time domain by CST Particle Studio®[4] for relativistic velocity $\beta = 1$ can be seen in Fig. 1 (top). The discrepancy visible in the plot originates mostly from the error in the applied material data as given in the frequency domain by the manufacturer of the ring[5], and the fit of these data on a impulse response function, necessary to perform time domain computations. The measurement was performed with a Vector Network Analyzer, where the longitudinal impedance is obtained from the measured S_{21}-parameter by [6]

$$Z_{\parallel}(f) = 2Z_0 \ln \frac{S_{21}^{\mathrm{REF}}(f)}{S_{21}^{\mathrm{DUT}}(f)}, \tag{1}$$

with Z_0 being the characteristic impedance and S_{21}^{REF} being the transmission in the empty measurement housing.

A 2D simulation with our code, compared to 2D analytic calculations is depicted in Fig. 1 (bottom). Such a simulation in frequency domain allows arbitrary relativistic velocity. The 2D calculations are valid for distributed impedances, i.e. above a certain length, see [7].

Details about our FEM frequency domain solver can be found in [8], and a detailed analysis of the wire measurement method is available in [7]. The wire measurement method was also applied to a SIS18 kicker magnet, see [9].

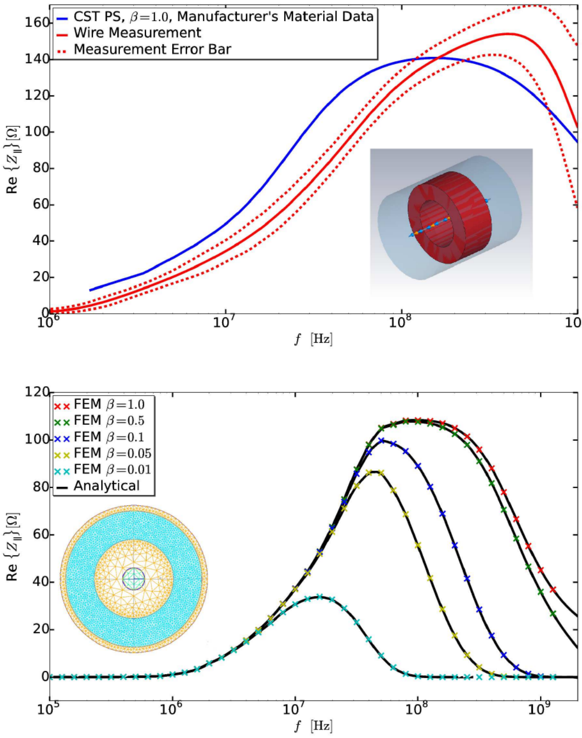

Figure 1: Top: impedance measurement using the wire method [7] vs. 3D numerical computation in the time domain. Bottom: 2D analytical and numerical calculation with the newly developed FEM code [8]. All computations rely on the manufacturer's material data [5], which is specified with 20% error range.

References

[1] FEniCS, www.fenicsproject.org, 2014

[2] C. Geuzaine and J.-F. Remacle, GMSH, www.geuz.org/gmsh, 2014

[3] https://bitbucket.org/uniederm/beamimpedance2d/src, 2015

[4] CST Studio Suite 2013, www.cst.com

[5] http://www.amidon.de/contents/de/d542.html, accessed 2013

[6] L. S. Walling et al., NIM-A 281, 433, 1989

[7] U.Niedermayer et al., NIM-A 776, 129-143, 2015

[8] U.Niedermayer et al., accepted for pub. in PR-STAB, 2015

[9] L. Eidam, Master Thesis, TU-Darmstadt, 2014

---

[*] u.niedermayer@gsi.de

DOI:10.15120/GR-2015-1-FG-SIS100-08

Emittance growth in bunches with space charge due to damping of transverse oscillations

I. Karpov[*][1], *V. Kornilov*[2], *and O. Boine-Frankenheim*[1,2]
[1]TEMF TU Darmstadt, Germany; [2]GSI, Darmstadt, Germany

An emittance growth is an important issue in synchrotrons, which can reduce machine performance. One of the main sources of the transverse emittance blow-up is damping of coherent oscillations appearing after the bunch-to-bucket transfer between synchrotrons. The damping can be passive (decoherence due to chromaticity, octupoles and residual nonlinearities [1,2] and active (transverse feedback system). This process is strongly modified by space charge and rf nonlinearities, which is important for the SIS18, SIS100 synchrotrons of the FAIR project. Decoherence in long bunches due to chromaticity with space charge has been studied using measurements at the SIS18 heavy-ion synchrotron and particle tracking simulations in [3].

Recent measurements at the SIS18 were dedicated to study the influence of transverse nonlinearities and moderate space charge on the decoherence process. Bunches of Ni_{58}^{26+} ions were stored at the energy of 100 MeV/u and kicked transversally with a kick duration of one turn. The resulting transverse oscillations have been recorded with the help of beam position monitors. At the same time, the time evolution of the transverse emittance (using an ionization profile monitor) and the beam current has been stored. In order to model the effect of transverse nonlinearities (because of absence of octupoles magnets at the SIS18) the closed orbit was optimized or distorted for different measurements.

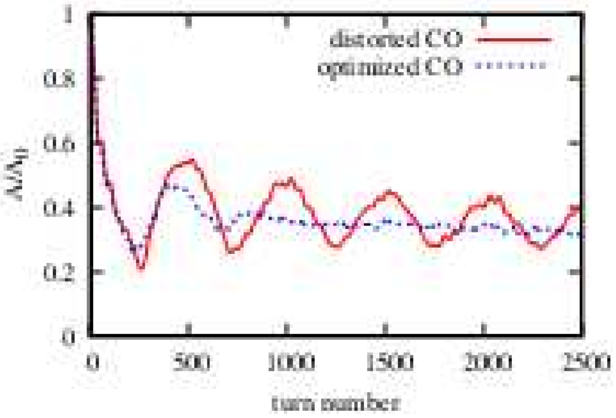

Figure 1: The time evolution of the bunch offset amplitude

As an example figure 1 shows the evolution of the bunch offset amplitude A normalized by the initial value A_0 extracted from the measured signals for two closed orbit settings. Figure 2 produced by plotting the bunch vertical traces and subtracting the total bunch offset, thus reducing the contribution of the head-tail $k = 0$ mode, shows a clear one-knot structure of the mode $k = 1$ which was not damped in the case of induced transverse nonlinearity. For this case the stronger emittance blow-up and beam losses were observed. The goal of theses studies is a detailed understanding of the interplay of the different effects.

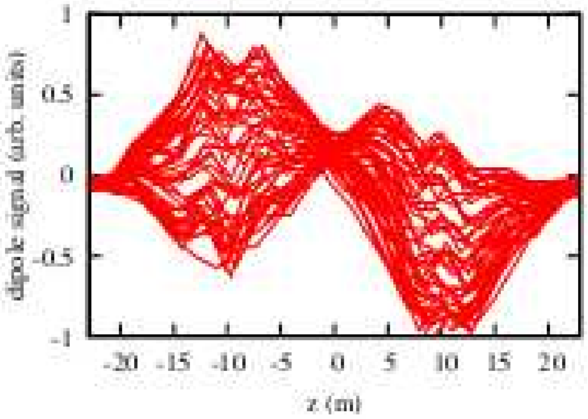

Figure 2: Traces of the transverse bunch signal for 50 consecutive turns. This result proves that the $k = 1$ remains during the process of bunch decoherence in the case of strong transverse nonlinearity.

For the SIS100 synchrotron the resulting bunch decoherence and beam blow-up is due to a combination of the lattice settings (like chromaticity), nonlinearities (residual or imposed by octupole magnets), strong space-charge, and the transverse feedback system. The next step is to study these effects for the SIS100 parameters using particle tracking simulations with the objective of correct combinations for a controlled beam blow-up. The results will be used for determination of requirements for the active and passive damping of coherent bunch oscillations at the SIS100.

References

[1] R.E. Miller, A.W. Chao, J.M. Peterson, S.G. Peggs, M. Furman, SSC Report SSC-N-360 (1987).

[2] M.G. Minty, A.W. Chao, W.L. Spence, Proceedings of PAC95, Dallas, Texas, USA, p. 3037 (1995).

[3] V. Kornilov, O. Boine-Frankenheim, Transverse decoherence and coherent spectra in long bunches with space charge Phys. Rev. ST Accel. Beams 15, 114201 (2012).

---

[*] karpov@temf.tu-darmstadt.de

DOI:10.15120/GR-2015-1-FG-SIS100-09

Verification of the longitudinal feedback topology in SIS18[*]

K. Groß[†][1], *U. Hartel*[2], *H. Klingbeil*[1,2], *U. Laier*[2], *D. Lens*[2], *K.-P. Ningel*[2], *S. Schäfer*[2], *and B. Zipfel*[2]
[1]TEMF, TU Darmstadt, Germany; [2]GSI, Darmstadt, Germany

Introduction

To damp oscillations of bunched beams, SIS100 will be equipped with a bunch-by-bunch (BxB) longitudinal feedback system (LFB). This helps to stabilize the beam, to keep longitudinal emittance blow up low and to minimize beam losses. The proposed LLRF topology of the closed loop system is, in some aspects, similar to the beam phase control system [1]. The difference and challenge is mainly the BxB signal processing followed by the generation of a correction voltage in dedicated feedback cavities. The adapted topology was verified at SIS18 during a beam time in 2014 using LLRF prototype subsystems and the two ferrite acceleration cavities.

Experimental Setup

Instead of applying the frequency correction Δf to the group DDS, i.e. to *all accelerating cavities*, the phase correction $\Delta\varphi$ is converted into an additional, phase shifted RF signal Δu and fed into *dedicated feedback cavities* resulting in an I/Q modulation of the total voltage u_{total} seen by the beam (Fig. 1, bottom right). Copies of the setups shown in Fig. 1 are used to determine the excitation and the required correction voltage for each bunch (and mode). The gray-shaded paths were cut to length to reach all interaction points with the same time delay. During acceleration, the phase $\varphi(f)$ has to be set according to the frequency-dependent phase response of LLRF components and cavity system.

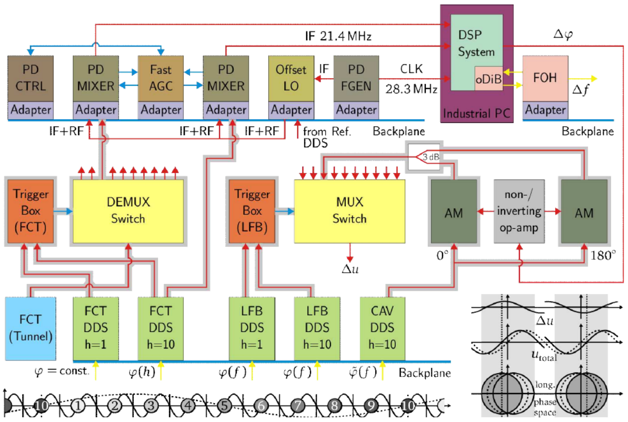

Figure 1: Sketch of LLRF of beam phase control system [2, 3] (top) with modifications for the LFB system (center) and principles of operation (bottom).

Measurement Results

In 2014 individual bunches have been tracked several times over complete SIS cycles at harmonic number $h = 2$ and $h = 4$. In particular, coupled bunch oscillations (Fig. 2), as intentionally excited on Oct. 16th, can now be detected using the DDS-triggered demultiplexing of the beam signal (Fig. 1, bottom left).

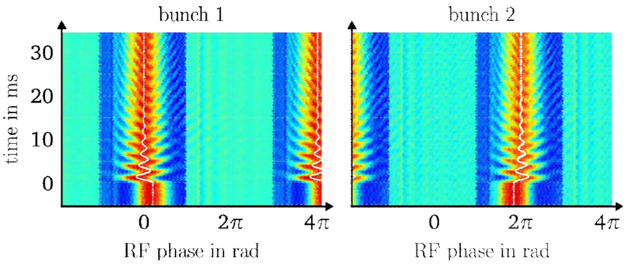

Figure 2: Waterfall plot of single bunches at $h = 2$ with BxB phase detection $\Delta\varphi$ (white lines) using one DSP system per bunch for an out-of-phase excitation.

A triggered LLRF signal (Fig. 3, left) providing the correction voltage for an individual bunch (cf. Fig. 2, left) at flattop was generated for the first time on Oct. 18th. The achieved damping of dipolar bunch oscillations shown in Fig. 3 (right) is a *proof of principle* for the proposed topology of the longitudinal feedback system.

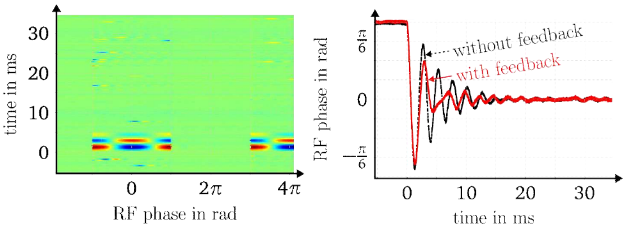

Figure 3: BxB LLRF correction signal Δu (left). Damping of dipole oscillations in SIS18 on Oct. 18th, 2014 (right).

The authors would like to thank D. Ondreka and H. Liebermann for the support and the customized machine setup which allowed to use one of the two main ferrite cavities as dedicated feedback cavity.

References

[1] Klingbeil et al., IEEE Trans. Nuc. Sci., Vol. 54, No. 6 (2007).
[2] Klingbeil, Laier, Regelsystemtopologie SIS18, internal note, revision 1.00, GSI (2009).
[3] Laier, SIS HF Phasen Synchronisationstopologie, internal note, revision 1.50, GSI (2011).

---

[*] Work supported by the German Federal Ministry of Education and Research (BMBF) under the project 05P12RDRBF.
[†] gross@temf.tu-darmstadt.de

DOI:10.15120/GR-2015-1-FG-SIS100-10

A novel DC current transformer using magneto-resistance sensors for FAIR

E. Soliman[1, 2], *H. Reeg*[1], *M. Schwickert*[1], *K. Hofmann*[2]
[1]GSI, Darmstadt, Germany; [2]IES Institute, TU Darmstadt, Germany.

A Novel DC Current Transformer (N-DCCT) for FAIR SIS100 is under development at GSI Beam Diagnostic department in collaboration with IES Institute of TU Darmstadt. DCCTs are used as non-intercepting standard tools for online beam current measurement in synchrotrons and storage rings. The working principle of commonly used DCCTs is well known [1]. However, at certain bunch frequencies in ring accelerators inaccurate readings are observed due to inter-modulation distortion. The N-DCCT senses the magnetic field created by the ion beam current, using Tunneling Magneto-Resistance (TMR) sensors. Also a closed-loop N-DCCT is currently under development.

TMR Sensor for N-DCCT

Currently a N-DCCT based on TMR sensors is under development at GSI. The N-DCCT open-loop structure is shown in Figure 1 [2]. The main measurement principle is precise detection of the ion beam DC magnetic field by TMR sensors. In the present setup the TMR sensors from MultiDimension Company [3] are placed inside an air gap of a high permeability ferromagnetic ring core with 10 mm width (VITROVAC '6025F'). The value of the magnetic field inside the air gap is calculated according to the following formula:

$$B_{gap} = \frac{\mu_o}{d} I_P \tag{1}$$

Where B_{gap} is the magnetic field inside the air gap in Tesla, µo is the permeability of vacuum in Tm/A, I_P is the beam current and d is the air gap width in m.

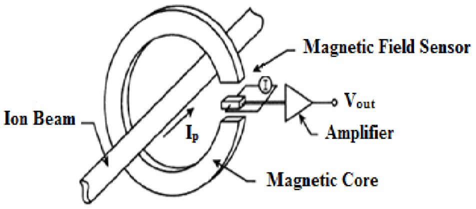

Figure 1: N-DCCT Open Loop Structure.

The TMR's output voltage is directly proportional to the ion beam current. A voltage amplifier is added to enhance the N-DCCT resolution. Printed circuit boards were fabricated to compare the performance of different MR sensors. A test setup has been prepared for the N-DCCT as shown in Figure 2. A mechanical support was manufactured to hold the flux concentrator. In addition a µ-metal box for shielding covers the whole N-DCCT test setup.

A DC current is generated in a conducting wire at the center of the core using a power amplifier and a signal generator. The value of the produced voltage from the power amplifier is ±32V. This will produce a ±0.32A in the wire. The value of the magnetic field intensity in the air gap of the core will be ±0.04mT. The output voltage of the TMR sensors is amplified with a voltage amplifier of gain 10.

Tests were carried out for two different TMR sensors, MMLH45F and MMLP57F. Figure 3 shows the output voltage of the N-DCCT versus input current for the MMLH45F. The slope of transfer characteristic is the sensitivity of the N-DCCT. The measured value from the experimental test is 0.566V/A, while the theoretical value is 0.75V/A. The sensitivity of the TMR sensor to the magnetic field is 0.453V/mT from the measurements and 0.6V/mT from the sensor's datasheet. Measurements with the sensor type MMLP57F yielded a sensitivity of 0.275 V/A, compared to 0.31V/A (datasheet). The noise analysis for the system is currently under investigation.

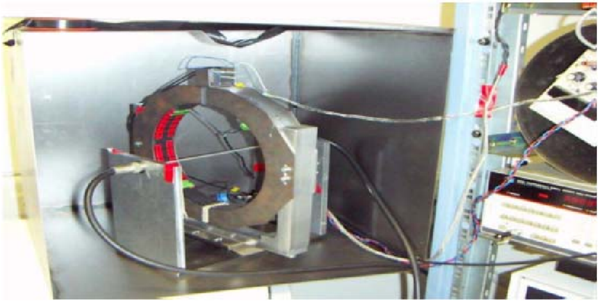

Figure 2: N-DCCT Test Setup.

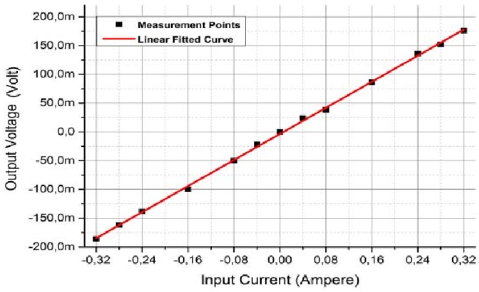

Figure 3: Output Voltage of the N-DCCT.

References

[1] K. Unser, "A Toroidal DC Beam Current Transformer with High Resolution", IEEE Trans. Nuclear Science, NS-28 No. 3, June 1981
[2] M. Häpe et al., "High Dynamic Magnetic Beam Current Measurements ...", DIPAC'05, May 2005, p. 102; http://www.JACoW.org
[3] MultiDimension Technology Co., Ltd., (CN)
[4] VACUUMSCHMELZE GmbH & Co. KG, (D).

---

* Work supported BMBF project ID: 05P12RDRBG.
#pt@desy.de

DOI:10.15120/GR-2015-1-FG-SIS100-11

Heavy ion induced desorption measurements on cryogenic targets *

Ch. Maurer† [1,2], *L.H.J. Bozyk*[1], *P.J. Spiller*[1], *and D.H.H. Hoffmann*[2]
[1]GSI, Darmstadt, Germany; [2]TU Darmstadt, Institut für Kernphysik, Germany

Introduction

Heavy ion impact induced gas desorption is a key process that drives beam intensity limiting ionization losses in heavy ion synchrotrons. Minimizing this effect, by providing low desorption yield surfaces, is an important issue for maintaining a stable ultra high vacuum during accelerator operation with medium charge state heavy ions. At room temperature the desorption yield per incident ion η is known to scale with the electronic energy loss at the surface [1]. Nevertheless, measurements with the prototype cryocatcher for SIS100 showed a different scaling [2], which needs to be understood. An experiment to systematically examine this behaviour is presented. The cryogenic beam-induced desorption yields at different temperatures and for different beam parameters are investigated.

Experimental Setup

The experiment described in this article has been set up at the SIS18 at GSI. Its UHV system is connected to the accelerator's beamline via a differential pumping line, containing a conductance limiting pipe with small diameter. In the target area a pressure in the 10^{-10} mbar regime has to be reached in order to clearly resolve the desorption peaks. Therefore, the setup is partially baked. The cryogenic target has the geometry of the SIS100 cryocatcher's front part and is cooled by a coldhead. It gets hit by a fast extracted 1μs beam pulse. Gas desorbed by the beam impact spreads in the diagnostic volume which is well defined by the pipe mentioned above. The pressure evolution is measured an extractor gauge. A more detailed description of the setup is given in [3].

Methodology of the measurements

The extraction of the beam from the synchrotron triggers a fast pressure measurement of 10 s duration. It allows a fine resolution of pressure rise and relaxation, out of which the amplitude of the pressure peak is determined. By using the ideal gas law and the number of beam particles a desorption yield is obtained. The temperature of the target is varied by a heater and by activating and deactivating the coldhead. Measurements at intermediate temperature levels were taken with a thermally drifting target.

Results

The determined desorption yield η is plotted in figure 1 against the beam energy for different experimental parameters. At or close to room temperature the known scaling with the electronic energy loss at the surface could be observed. However, at cryogenic temperatures the scaling looks different than at room temperature, which is not yet understood. An accordance with earlier measurements with the cryocatcher protoype [2] could not yet be found.

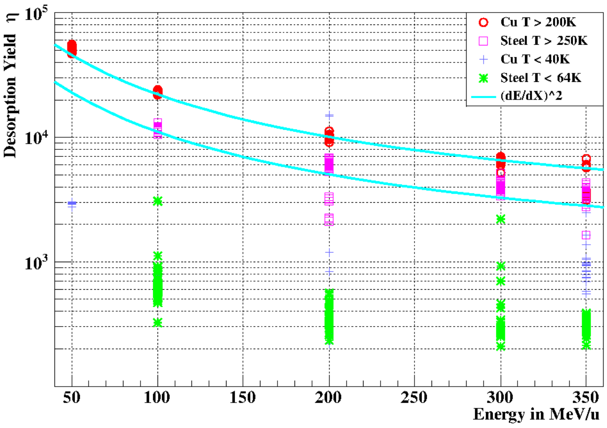

Figure 1: Comparison between the energy dependance of η for different experimental parameters.

Outlook

Data obtained from this experiment is still undergoing analysis, so no concluding statement can yet be made. A central part of this analysis will be a gas dynamic simulation to better understand the influence of de/adsorption on the setup's other cold/warm surfaces. Different experimental geometries are also bound to factor into the results, which will also be investigated by this method.

References

[1] H. Kollmus et al., "Measurements of Ion-beam Loss Induced Desorption at GSI", in AIP Conf. Proc. **773**, p. 207 (2005)

[2] L.H.J. Bozyk, H. Kollmus, P.J. Spiller, "Development of a Cryocatcher-System for SIS100", in Proc. of IPAC 2012, p. 3239

[3] Ch. Maurer et al., "Heavy Ion Induced Desorption Measurements on Cryogenic Targets," in Proc. of IPAC 2014, p. 867

---

* This project is funded by the german ministry for education and research (FKZ 06DA7031)

† C.Maurer@gsi.de

DOI:10.15120/GR-2015-1-FG-SIS100-12

Systematic measurement of the pumping properties of a cryogenic surface

F. Chill[1,2], *L. Bozyk*[2], *O. Kester*[1,2], *and P. Spiller*[2]
[1]Goethe-Universität, Frankfurt, Germany; [2]GSI, Darmstadt, Germany

Introduction

The residual gas density in the beam vacuum system of a heavy ion synchrotron is a crucial factor for stable and reliable beam operation at highest intensities. The Interaction of the beam particles with the residual gas may cause severe beam loss. In combination with ion impact stimulated gas desorption from the beam pipe, this can lead to a reduced beam lifetime and transmission of the acceleration cycle. Therefore, beam induced pressure rise must be suppressed by the pumping system.

To achieve proper vacuum conditions, the vacuum chambers of SIS100 will act as cryogenic surface pumps. Cryogenic surfaces are able to pump gases according to their saturated vapor pressure (SVP) curves. This process is called *cryocondensation*. The reachable pressures for all heavy gases are sufficiently low for stable beam operation. The SVP of hydrogen is too high even at a temperature of 4.2 K. If the surface coverage is sufficiently low, hydrogen can be pumped to lower pressures by so called *cryosorption* [1]. This effect can be characterized by two parameters: The *sticking coefficient* which is the probability of a gas particle impacting on the surface to be bound. It is directly linked to the pumping speed provided by the cryogenic walls. The *mean sojourn time* describes how long a particle remains bound to a surface. Both parameters together determine the equilibrium pressure. This pressure as a function of the surface coverages at a specific temperature is called *isotherm*.

Measurements at cryogenic temperatures

An UHV experiment (see Figure 1) to determine these parameters has been set up. The cold surface is provided as a small stainless steel chamber which is cooled by a cryocooler. So far, measurements in the temperature range from 7.2 to 23 K have been conducted. The lower corner valve remains closed once the cryostat reaches its target temperature. It is adjusted by resistive counter heating of the inner chamber. Subsequently, hydrogen is let into the cryostat through the copper orifice. The gas flow is monitored by two extractor gauges. Its magnitude equals the pumping speed of the cold surface. Its value suggests, that all the particles entering the inner chamber are bound and do not reflect back through the Cold-Warm-Transition. In this case, the sticking coefficient is close to one and seems to be mostly independent of temperature and surface coverage within the examined range. The gas flow is stopped from time to time by closing the gate valve until an equilibrium pressure is reached. Integration of the gasflow over time yields the currently accumulated surface coverage. This value and its corresponding equilibrium pressure results in one point on the isotherm. The resulting isotherms for different temperatures are shown in Figure 2.

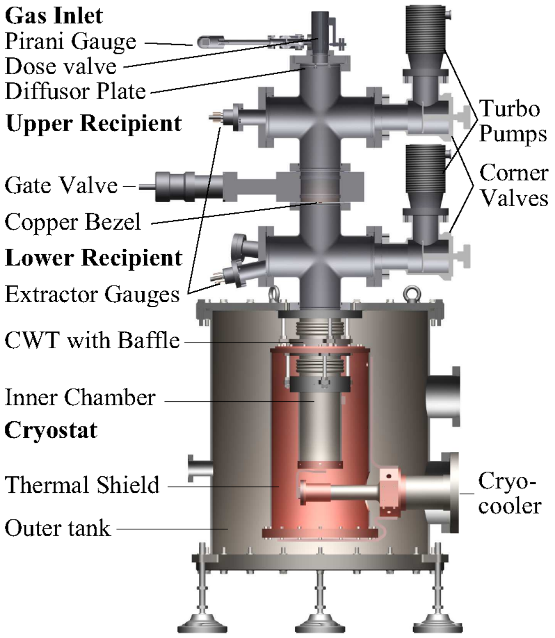

Figure 1: Measurement setup for cryosorption.

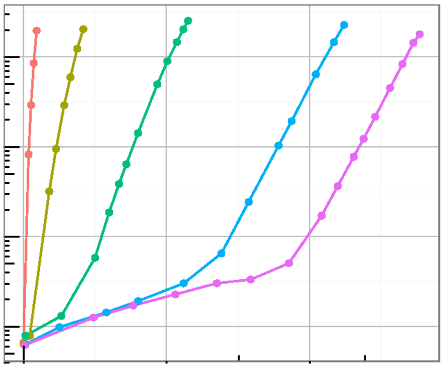

Figure 2: Preliminary isotherms for H_2 on stainless steel. A coverage of $\approx 2.2 \cdot 10^{15}\,\mathrm{cm}^{-2}$ equals one monolayer [2].

References

[1] E. Wallén, J. Vac. Sci. Technol., A 14, 1996, p. 2916

DOI:10.15120/GR-2015-1-FG-SIS100-13

[2] K. Jousten, Wutz Vakuumtechnik, Springer 2013, p. 236

DOI:10.15120/GR-2015-1-FG-SIS100-13

FLUKA study of beam loss monitors for SIS100: General diagnostics and quench prevention of superconducting magnets

S. Damjanovic[1]

[1]GSI, Darmstadt, Germany

In view of the planned coverage of the synchrotron SIS100 with beam loss monitors (BLMs), FLUKA studies were performed aiming at two goals: to evaluate the sensitivity of these detectors to the expected beam losses at SIS100, and to estimate the BLM quench prevention thresholds via the correlation between the energy deposition inside the superconducting coils and the BLM active volume. A large number of ion species and energies were considered. The results of these studies, described in detail elsewhere [1], very much support the use of the BLMs for quench prevention (protection of magnets) via an interlock generation, as used at the LHC.

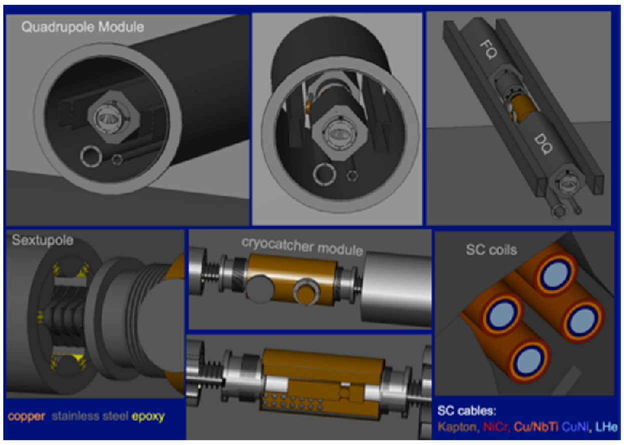

Figure 1: FLUKA geometry of a quadrupole module.

The goal as described required a precise modelling of the geometry of a SIS100 quadrupole module, the SIS100 extraction straight section and the SC coils including the cable details (Fig.1).The results on the response of the LHC-IC type BLMs to the beam losses within the warm quadrupole doublet of the SIS100 extraction straight section show a great sensitivity of these monitors. Instantaneous radiation caused by 0.1% beam loss at injection- and 0.0001% at extraction energy will be detected if BLMs are placed close to the source.

The different aspects of machine protection are usually based on a variety of systems. Quench prevention of SC magnets can only be ensured by a BLM system, the only active system in case of fast losses with time scales between 100 μs and 10 ms. While the total energy and therefore the overall damage potential is very much larger at the LHC, certain accidental scenarios can be equally severe at SIS100, due to the Z^2 dependence of the initial energy deposition. The responsible quantity for the quenching of SC coils is the local energy deposition, and as little as 1mJ/cm^3 quenches a magnet. Quenching would cause a downtime of more than hour, while real damage of a single magnet would cause much longer downtimes at very high costs. All this suggests that the protection of the SIS100 machine should also be strict.

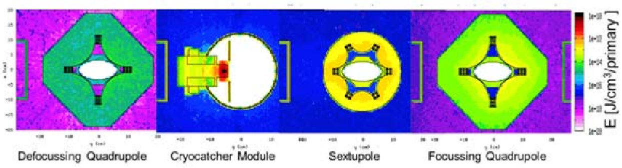

Figure 2: Energy deposition in the region of the SC coils.

The possibility of quench prevention of the SIS100 SC magnets by the planned BLM system has been studied with FLUKA simulations. As a representative example for a source of beam loss at SIS100, the losses due to charge exchange of U^{28+} beams were examined. The corresponding special distribution of the energy deposition within the individual components of a quadrupole module is shown in Fig.2. The LHC-IC type BLMs were found to be sensitive both to the quench prevention thresholds and to the loss rates expected due to these losses. In addition, a number of other ion species and energies including protons were considered to demonstrate a comparable sensitivity for all other beams to be accelerated with SIS100.

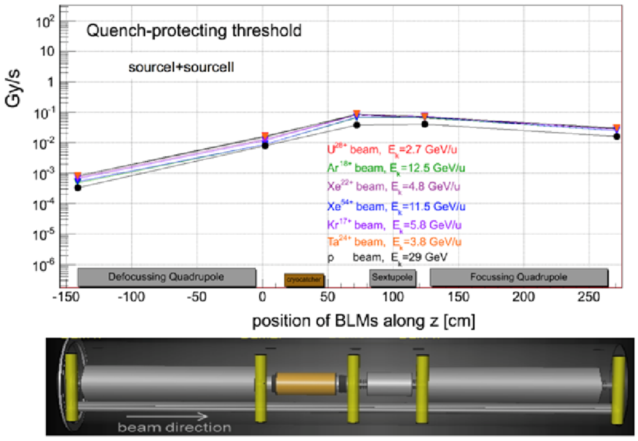

Figure 3: BLM quench prevention threshold along a quadrupole module for p and ions beams of different E.

An interesting finding of this study (Fig.3) was that, for the same beam loss location, the quench-prevention thresholds were almost identical for all ion species/energies including protons. In the future, a systematic investigation of all possible failures at SIS100 is required to optimally integrate the BLM system into the beam interlock system.

References

[1] S. Damjanovic, EDMS Note, Document FAIR-1SBDX-ER-0001, Id 1473055 (2015).

DOI:10.15120/GR-2015-1-FG-SIS100-14

FLUKA simulation of LHC BLMI response functions for different particles

V. S. Lavrik^{1,2} *and A. Reiter*^{1}

^{1}GSI, Darmstadt, Germany; ^{2}Goethe University Frankfurt am Main, Frankfurt, Germany; GSI, Darmstadt, Germany

LHC-type beam loss monitors based on ionization chamber (LHC BLMI) are planned as beam loss detector for SIS 100 operation. This type of beam loss monitor has different response functions for various particle types. In this contribution FLUKA[1] simulations of the response functions for different types of particles are presented. In order to simulate a response function of the beam loss monitor, the model of BLMI was implemented in the Monte Carlo code FLUKA.

The BLMI consists of 60 parallel plate ionization chambers packed in a stainless steel cylindrical vessel with a 2 mm wall and covered on top and bottom by two stainless steel plates 5 mm and 4 mm thick respectively. The signal is created by collecting electron-ion pairs on a pile of 61 parallel aluminum electrodes with a thickness of 0.5 mm, diameter 75 mm and equally spaced by 5.75 mm. Electrodes are held by 6 stainless steel rods which are in turn fixed by insulating ceramic pieces. The volume of a detector is filled with nitrogen gas with overpressure of 100 mbar.

An ionizing particle deposits energy into the volume of BLMI and creates electron-ion pairs which are collected by electrodes. The minimum energy, which a particle needs in order to create an electron-ion pair, the so called W-factor, is 35 eV for nitrogen. The energy deposition was calculated by FLUKA in a sensitive volume between the electrodes and then converted into charge per primary simulated particle. The result is compared with simulations performed in Geant4 (version 8.0 patch-01) by CERN BLM group[2].

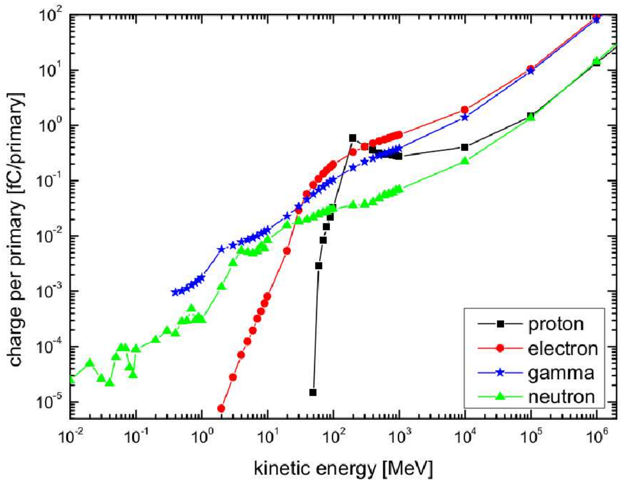

Figure 1: Response of the ionization chamber for particles impacting longitudinally to the detector axis.

Two series of simulations were performed depending on the impact direction of the beam: a longitudinal impact direction (the beam is uniformly distributed, parallel to the detector axis and has a circular cross section with a diameter of the detector) and transversal (the beam is uniformly distributed and has a rectangular cross section which is matched with a detector cross section). The response function was obtained for 4 types of particles: protons, electrons, gammas and neutrons in the range of 10KeV up to 1TeV.

The result of simulations is presented in Figures 1 and 2. The behavior of corresponding curves is similar for two different simulations. But the amplitude of the response functions in case of longitudinal irradiation is higher, because the large amount of material, traversed by the beam, generates a higher number of secondary particles. Both figures match the Geant 4 simulations which were cross checked with the experiment. These results are the base for further optimizations of the future SIS 100 Beam Loss Monitoring System.

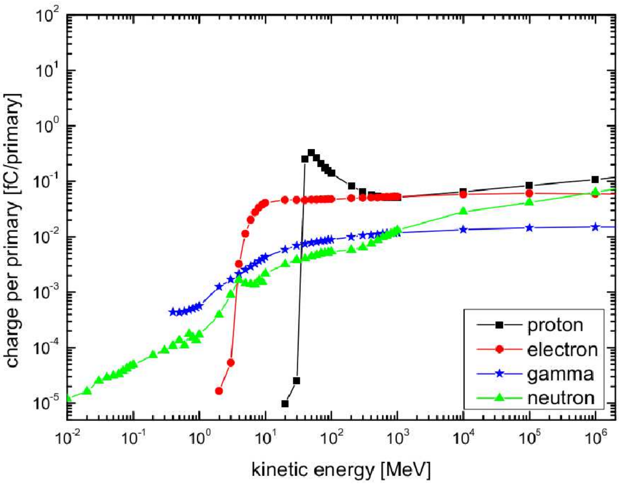

Figure 2: Response of the ionization chamber for particles impacting transversally to the detector axis.

References

[1] "The FLUKA Code: Developments and Challenges for High Energy and Medical Applications" T.T. Böhlen, F. Cerutti, M.P.W. Chin, A. Fassò, A. Ferrari, P.G. Ortega, A. Mairani, P.R. Sala, G. Smirnov and V. Vlachoudis, Nuclear Data Sheets 120, 211-214 (2014)

[2] M.Stockner et. all, CERN-AB-2006-086 BI

DOI:10.15120/GR-2015-1-FG-SIS100-15

Laboratory tests of beam loss monitor detectors for SIS 100*

V.S. Lavrik[1,2], *P. Boutachkov*[1], *S. Damjanovic*[1], *and B. Voss*[1]
[1]GSI, Darmstadt, Germany; [2]Goethe University Frankfurt am Main, Frankfurt, Germany

A main source of primary beams at FAIR will be the SIS 100 synchrotron. SIS 100 will deliver ion beams with more than two orders of magnitude higher intensity than SIS 18 and will be operated in a range of 18-100 Tm rigidity. During the machine operation beam losses are unavoidable. In order to achieve quantitative determination of beam losses LHC-type beam loss monitor (BLMI) are foreseen[1]. This detector is robust, easy to maintain and has a well understood response. This contribution describes the bench test and characterization of BLMI.

The CERN LHC beam loss monitor consists of parallel plate ionization chambers, packed in a cylindrical stainless steel vessel with a wall thickness of 2 mm. The volume of a detector is filled by nitrogen gas under overpressure of 100 mbar. The standard operation point for the detectors is 1.5 kV.

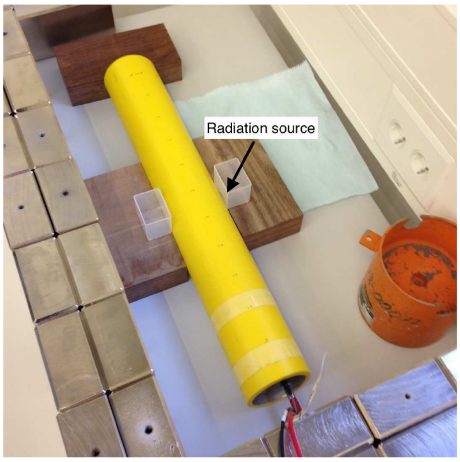

Figure 1: Testing bench of a BLMI characterization

Characterization of BLMI was performed in the detector laboratory of GSI. The test bench is shown in Figure 1. BLMI (yellow tube) was placed in a location which was surrounded by iron bricks in order to prevent unnecessary irradiation to the personnel. ^{60}Co γ source with activity of 2.3 MBq was placed on the detector surface as indicated in Figure 1. The ionization current was measured by a Keithley 6485 picoampermeter.

Two series of measurements were done: without a radiation source and with a radiation source. The results are shown in Figure 2. The black squares represent an ionization current with a subtracted leakage current for the corresponding detector. According to the experimental data all detectors have the same efficiency within the error bars.

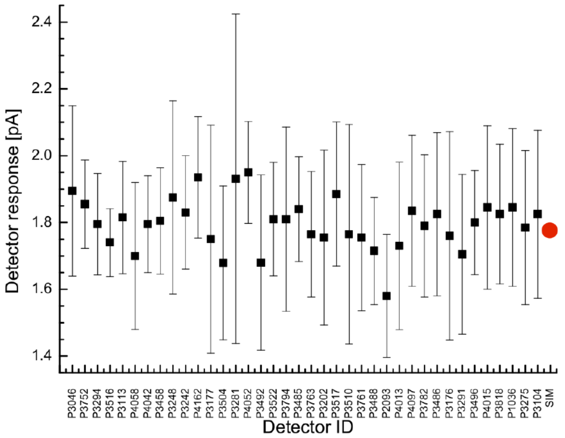

Figure 2: Black squares: ionization current in a ^{60}Co radiation field (leakage current is subtracted); red circle: FLUKA simulation

The model of BLMI was implemented in FLUKA Monte-Carlo code[2]. The response function of a detector was calculated in an isotropic ^{60}Co radiation field and compared with a measured ionization current (Figure 2 red circle). Simulated response matches with measured ionization current within the error bar.

A testing bench for BLMI acceptance test was established and 38 BLMIs were characterized in the detector laboratory of GSI. The acceptance test shows that all the detectors have uniform response and can be integrated into the SIS 100 beam loss monitoring system. Also FLUKA simulations were done and match measured response within the error bars.

References

[1] Measurements and Simulations of Ionization Chamber Signals in Mixed Radiation Fields for the LHC BLM System M.Stockner et. all, CERN-AB-2006-086 BI

[2] ”The FLUKA Code: Developments and Challenges for High Energy and Medical Applications” T.T. Böhlen, F. Cerutti, M.P.W. Chin, A. Fassò, A. Ferrari, P.G. Ortega, A. Mairani, P.R. Sala, G. Smirnov and V. Vlachoudis, Nuclear Data Sheets 120, 211-214 (2014)

---

* Work supported by BMBF-Projekt 05E12CD1

DOI:10.15120/GR-2015-1-FG-SIS100-16

Survey and alignment of the synchrotron SIS18

V. Velonas[1], *I. Pschorn*[1], *T. Miertsch*[1], *K. Knappmeier*[1]
GSI, Darmstadt, Germany

To fulfil the intensity requirement of the GSI Facility as well as projects and conceptions of the future facility of FAIR, a number of high precise geometrical 3D measurements as well as conceptual work have been carried out during the past year. Responsible for these activities was the survey and alignment (S&A) group of GSI, which is assigned to the project division *Engineering* within *FAIR@GSI*. The S&A team is involved in many projects like i.e. CryRing, EMTEX, SIS100 "first-of-series"(FOS) dipole and others for the different FAIR and GSI machines. This short report focusses on the realignment of the SIS18 synchrotron, which was carried out completely in one go, what was never done since the first installation.

A low grade of quality of the circling beam in the SIS18 made the commissioning in February 2014, after a 1 year lasting shutdown period, very difficult. This fact and the hypothesis that the construction activities for the future FAIR facilities, including piling and lowering the ground water level, will have an impact in the current position of the machine, lead to a total survey of the actual position of all SIS18 magnets, BPM and adjacent machine parts by 3D measurements.

Measuring the 3D point network, a Laser Tracker and a level instrument were used. The surveying of SIS18 was carried out within four days. All fiducials on the components just like the temporary points on the wall and pillars as well as the Laser Tracker stations were included in the network adjustment. Parts of the transfer line to the synchrotron (TK) as well as the HEBT area behind the SIS18 were surveyed in order to supervise these transit areas of the beam. The accuracy of the network points after the free adjustment, which was done to define the inner geometry of the network (minimal constraints), was between 0.02mm to 0.05mm in all three directions. For the geodetic datum only the fiducials on the dipoles were used. After the final adjustment calculation it turned out that the new coordinates had a huge variation regarding to the nominal coordinates. The relative deviation between the components in the lateral and in the vertical position was up to 4mm and 5mm respectively [1].

A major realignment of the whole area was needed from the analyses of the results.

All components of the SIS18 should be aligned, as well as four quadrupoles in TK9 area. The TASA-point system requires for alignment the use of a Laser Tracker to measure the two fiducial points on the magnets together with inclinometers that are needed to determine the precise lateral inclination of the components. In contrast to the magnets BPM chambers have up to now no fiducial points with a precise reference to the internals. Thus, the specified actual position of BPM internals and their alignment was based on assumptions.

The alignment tolerances for magnets and BPM in lateral and vertical direction were defined as better than 0.2mm; in a few cases up to 0.5mm was acceptable. The remaining lateral tilt after alignment should not exceed 0.1mrad.

Some problems appeared during the alignment which was relative with the number of the adjustment feet of the components. It was confirmed again that the alignment of a three-feet-component is much friendlier and faster compared to a component with four feet.

With few exceptions - caused by mechanical reasons - all magnets could be aligned within tolerance (fig. 1, 2). The complete alignment was carried out within four weeks.

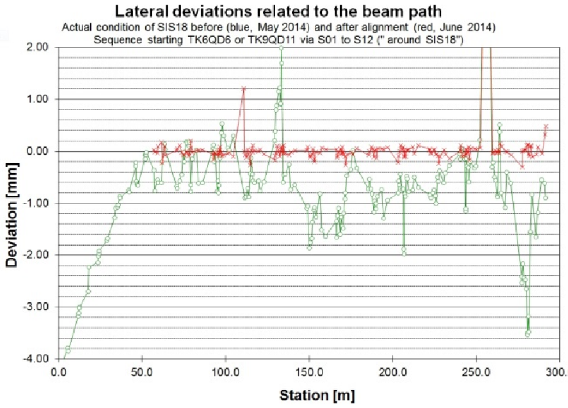

Figure 1: Beam plot for synchrotron SIS18. Lateral deviation before (green) and after (red) alignment

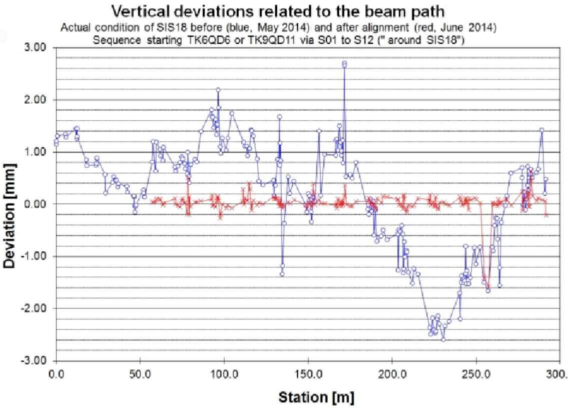

Figure 2: Beam plot for synchrotron SIS18. Vertical deviation before (blue) and after (red) alignment

References

[1] I. Pschorn, T. Miertsch, K. Knappmeier, V Velonas, „SIS18 Netz und Justage – interne Reports"

---

[1] alignment@gsi.de

DOI:10.15120/GR-2015-1-FG-SIS18-01

Observation of dynamic transverse emittance exchange in SIS-18

R. Singh, P. Forck, G. Franchetti, T. Giacomini, and P. Kowina
GSI, Darmstadt, Germany

The theory of linear coupling and the consequent dynamic emittance exchange is well known [1]. Transverse beam emittance exchange due to linear coupling was observed in SIS-18 during regular accelerator operation. Skew-quadrupoles are installed at GSI SIS-18 to control and utilize the linear coupling e.g. for optimization of the injection efficiency [2]. However, these skew-quadrupoles are not used during the normal operations, and any linear coupling due to misaligned magnets is usually neglected. Careful measurements were performed to verify the role of tune crossing on this exchange process. Preliminary attempts for compensation of linear coupling were made, using the emittance exchange as a diagnostic observable.

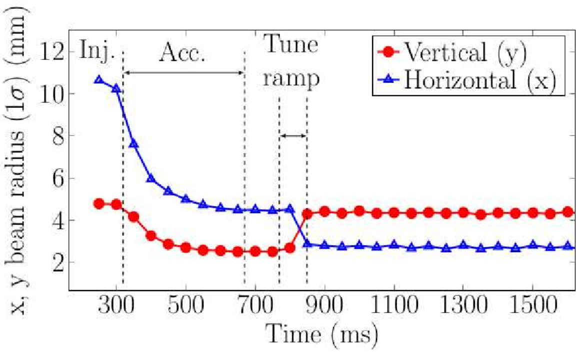

Figure 1: Evolution of the beam radii during the acceleration cycle during the high intensity operations at SIS-18.

Figure 1 shows the evolution of horizontal and vertical beam dimensions measured using an Ionization profile monitor (IPM) during the acceleration cycle for a high intensity (10^{10} stored particles) N^{7+} beam in the slow extraction mode. The high intensity working point at injection is $Q_x = 4.16$ and $Q_y = 3.29$. On the extraction flattop, the horizontal tune was ramped from $Q_x = 4.16$ to $Q_x = 4.33$ in ≈ 100 ms for the resonant slow extraction. Simultaneous transverse Schottky measurement established that the tune crossing and thus the linear coupling was the cause of this exchange. Figure 2 (top) shows the time evolution of the transverse beam profile before and after the exchange.

In follow-up measurements during summer 2014, emittance exchange was regularly observed due to tune crossing. This emittance exchange due to "residual" linear coupling is undesired since it led to beam losses when the vertical aperture could not accommodate the larger vertical beam due to emittance exchange. Therefore, first attempts for compensation of linear coupling were performed. The emittance exchange served as an online diagnostic for linear coupling. A scan of relative strengths of the two skew-quadrupoles was made such that, a compensation vector opposite to the natural skew error was constructed. Figure 2 shows a comparison of transverse beam profile evolution with (bottom) and without (top) compensation. The plot shows the emittance exchange and a partial compensation of linear coupling. The reasons for partial compensation of linear coupling are unclear. Perhaps, the minimum strength of skew quadrupoles was too strong for construction of appropriate compensation vector. Linear coupling has been utilized beneficially at several synchrotrons and a better control of linear coupling is foreseen at SIS-18.

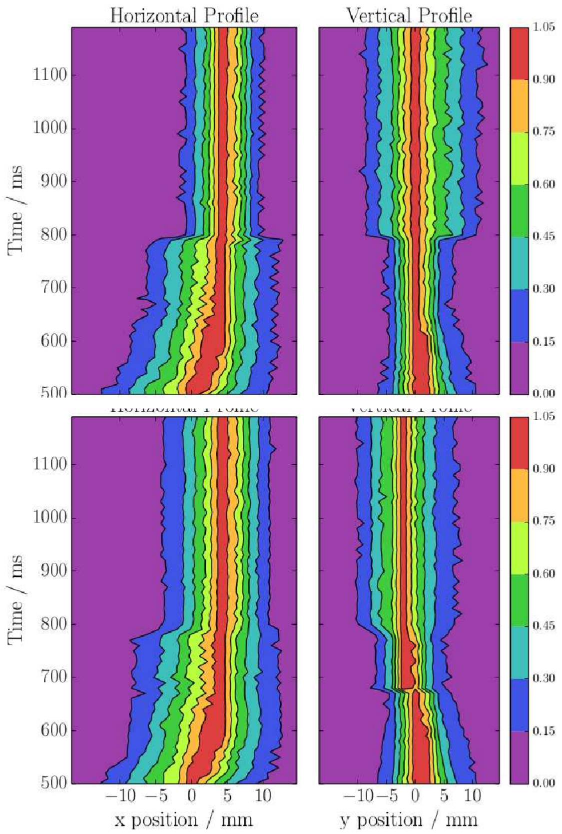

Figure 2: Horizontal and vertical beam profile evolution during the emittance exchange process for uncompensated (top) and compensated (bottom) linear coupling.

References

[1] A. Franchi et al., "Emittance sharing and exchange driven by linear betatron coupling in circular accelerator", PRST-AB 10, 064003 (2007)

[2] W. Daqa et al., "Linear Coupling With Space Charge in SIS18", Proceedings of IPAC10, Kyoto, Japan (2010)

DOI:10.15120/GR-2015-1-FG-SIS18-02

Space charge effects on quadrupolar oscillations in SIS-18

R. Singh, P. Forck, and P. Kowina
GSI, Darmstadt, Germany

Quadrupolar or beam envelope oscillations give valuable information about the injection matching and the incoherent space charge tune shift. The shift in quadrupolar mode oscillation frequency with respect to beam intensity gives a direct estimate of space charge tune shift. An asymmetric pick-up [1] is installed in SIS-18 to observe the quadrupolar moment oscillations.

Figure 1 shows the quadrupolar pick-up installed in SIS-18 along with an ion beam with horizontal and vertical displacement of $(\bar{x}, \bar{y})$ with respect to pick-up center and transverse dimensions of (σ_x, σ_y) . Let U_R, U_L, U_T and U_B be the voltages induced on right, left, top and bottom electrodes by the beam.

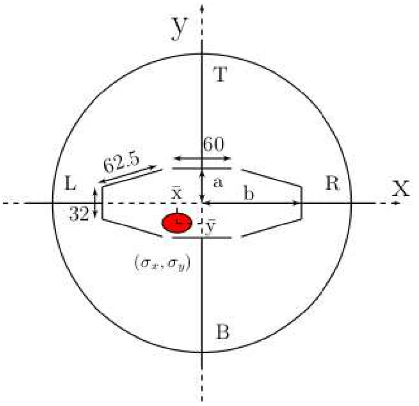

Figure 1: Front view of the pick-up design; a = 35.3 mm, b = 100.3 mm, length of the electrodes in longitudinal plane l = 216 mm. All the lengths are given in mm units.

The electrodes are connected in the "quadrupolar" configuration, i.e. $\Xi_q = (U_R + U_L) - (U_T + U_B)$ such that the quadrupolar moment of the beam $({\sigma_x}^2 - {\sigma_y}^2 + \bar{x}^2 - \bar{y}^2)$ is extracted as the first order signal component.

$$\Xi_q \propto Z \cdot I_{beam} \cdot m \cdot \left({\sigma_x}^2 - {\sigma_y}^2 + \bar{x}^2 - \bar{y}^2\right) \quad (1)$$

where Ξ_q is the quadrupolar signal, Z is the transfer impedance of the pick-up and m is the quadrupolar sensitivity of the pick-up. Z and m are determined by electromagnetic simulations [1].

The frequency of quadrupolar oscillations is directly affected by the incoherent space charge tune shift as discussed in references [2, 3]. For an elliptic beam with a uniform transverse distribution, the space charge dependence of quadrupolar mode frequency is given by,

$$Q_{coh,1,2} = 2Q_{x,y} - (1.5 - 0.5\frac{\bar{\sigma}_{x,y}}{\bar{\sigma}_x + \bar{\sigma}_y})\Delta Q_{sc,x,y} \quad (2)$$

where ΔQ_{sc} is the incoherent tune shift, Q_x, Q_y are the horizontal and vertical tunes and $Q_{coh,1,2}$ represent the normalized quadrupolar mode frequencies. At low intensities, $Q_{coh,1,2}$ is twice the tune frequency $2 * (Q_x, Q_y)$.

Due to the absence of any suitable quadrupolar exciter in SIS-18, quadrupolar oscillations were excited using the injection beta mismatch from UNILAC to SIS-18. The beam conditions were kept similar except the injected beam current was varied from the UNILAC to increase the incoherent tune shift ΔQ_{sc}, while the quadrupolar signal Ξ_q, the mean transverse beam profile over several turns $(\bar{\sigma}_x, \bar{\sigma}_y)$ and the beam current I_{beam} was recorded.

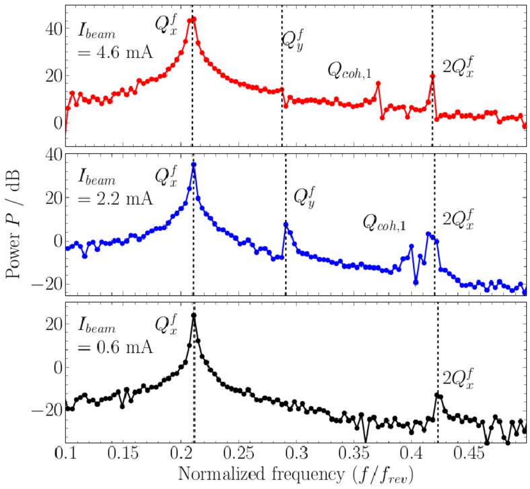

Figure 2: Shift of quadrupolar mode $Q_{coh,1}$ with respect to beam current. Q_x^f denotes the fractional part of Q_x.

Figure 2 shows the quadrupolar signal spectrum at three beam current levels. A strong mismatch was only induced in horizontal plane, and therefore only $Q_{coh,1}$ is visible in the spectrum. There was a clear dependence of $Q_{coh,1}$ on beam current in accordance to Eq. 2, as it moves away from $2Q_x^f$ as the beam current or ΔQ_{sc} is increased. Detailed report on these measurements can be found in [4].

References

[1] J. A. Tsemo Kamga et al., "Calculation of the quadrupole moment ${\sigma_x}^2 - {\sigma_y}^2$ for an asymmetrical Pick-up", GSI scientific report 2013.

[2] W. Hardt, "On the incoherent space charge limit for elliptic beams", CERN/ISR/Int. 300 GS/66.2.

[3] I. Hofmann, "Stability of anisotropic beams with space charge", Physical Review E 57 (4), 4713.

[4] R. Singh et al., "Observations of the quadrupolar oscillations at GSI SIS-18", Proc. of IBIC'14 (2014)

DOI:10.15120/GR-2015-1-FG-SIS18-03

Eigenmode computation for the GSI SIS 18 ferrite cavity*

K. Klopfer[†1], *W. Ackermann*[1], *and T. Weiland*[1]
[1]Technische Universität Darmstadt, Institut für Theorie Elektromagnetischer Felder (TEMF), Schlossgartenstraße 8,
64289 Darmstadt, Germany

Introduction

In the heavy-ion synchrotron SIS 18 two identical cavities are operated, which are loaded with the Ferroxcube 8C12m ferrite material. The permeability of the ferrites exhibits a characteristic dependence both on frequency and bias magnetic field strength. The latter is of particular importance for the tuning of the resonance frequency of the resonator system. Due to the extension of the existing facility to the FAIR, new interest in a better understanding of ferrite cavities of the SIS 18 type has aroused. As the aim of the presented study, a tool for the numerical simulation of the lowest eigenmodes of such resonators was developed. Clearly, its application to the SIS 18 cavity requires accurate material data. Hence, designated measurements were carried out at GSI.

Permeability measurement

The dependence of the permeability of the Ferroxcube 8C12m material on frequency and bias magnetic was determined using a reflection as well as a transmission measurement approach. The obtained values for low RF levels are fully compatible with each other within their estimated error margins up to moderate frequencies. A detailed discussion of the measurement results can be found in [1].

Computational approach

A dedicated solver was developed, implemented and successfully verified. It is able to efficiently handle nonlinear complex eigenvalue problems even on distributed memory machines, which arise in the context of the tensor material modeling. Furthermore, the distribution of the magnetic field excited by the bias current is precisely taken into account. For more details on the employed numerical methods we refer to [2, 3].

Analysis of the fundamental mode

The computational model used in the numerical simulation of the GSI SIS 18 cavity is depicted in Fig. 1. The simulation results for the resonance frequency of the fundamental mode are shown in Fig. 2. Also, additional results obtained with an alternative equivalent circuit model taking into account the radial dependence of the bias field are included. The simulation results are discussed in more detail in [3].

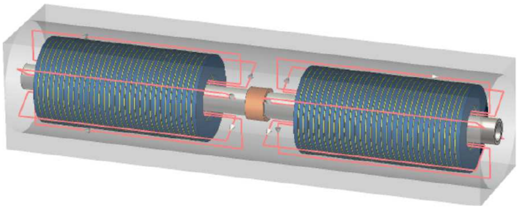

Figure 1: CAD model used for the numerical simulation of the GSI SIS 18 cavity. It consists of ferrite ring cores as well as copper discs. The coupling windings are represented by thin wires.

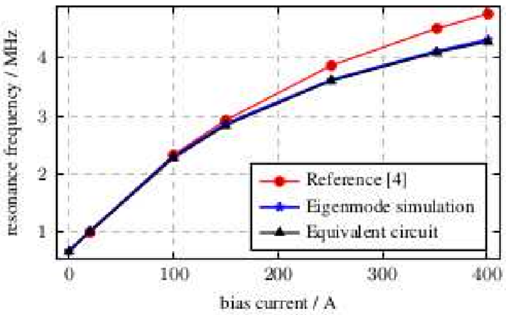

Figure 2: Resonance frequency as a function of the bias current for the prototype cavity with 29 cores on each side of the gap for small RF levels.

Summary

The computation of the fundamental mode of the GSI SIS 18 ferrite cavity has successfully been demonstrated.

References

[1] Klaus Klopfer, Uwe Niedermayer, Harald Klingbeil, Wolfgang Ackermann, Hans Günther König, and Thomas Weiland, "Measurement of the magnetic material properties and simulation and modeling of ferrite-loaded cavities", Phys. Rev. ST Accel. Beams, vol. 18, issue 1, 2015.

[2] Klaus Klopfer, Wolfgang Ackermann, and Thomas Weiland, "Computation of Complex Eigenmodes for Resonators Filled With Gyrotropic Materials", IEEE Trans. Magn., vol. 51, no. 1, 2015.

[3] Klaus Klopfer, "Computation of Complex Eigenmodes for Resonators Filled With Gyrotropic Materials", PhD thesis, TU Darmstadt, tuprints: 4210, 2014.

[4] Uta Hartel, "Modellierung des Regelungs- und Steuerungssystems einer Beschleunigungseinheit für Synchrotrons", Diploma thesis, TU Darmstadt, 2011.

---

* Work supported by GSI.

[†] klopfer@temf.tu-darmstadt.de

DOI:10.15120/GR-2015-1-FG-SIS18-04

Simulations of a quadrupolar pick-up at GSI SIS-18*

Joel Alain Tsemo Kamga†1, *Wolfgang F.O. Müller*1, *and Thomas Weiland*1

1Technische Universität Darmstadt, Institut für Theorie Elektromagnetischer Felder (TEMF), Schlossgartenstrasse 8, 64289 Darmstadt, Germany

Introduction

This report presents the simulation results for an asymmetrical capacitive pick-up installed at GSI SIS-18. In the past, it was used as BPM (Beam Position Monitor) and is planned to be used for measuring the transverse beam size oscillations at SIS-18. The main goal of this project consists in estimating the properties of the pick-up and evaluating its usage as a quadrupole signal monitor. Due to the fact that the bunch for the SIS-18 operation is long compared to the pick-up electrode, first simulations have been performed with the electrostatic solver of the simulation software CST EM Studio to estimate the pick-up properties [1]. Now, to study the pick-up behavior in the frequency range of insterest for GSI, some simulations have been performed using the PIC solver of CST PS (Particle Studio) [2] and the results are presented in this report.

Simulations and Results

The pick-up design used for the simulations is shown below in Fig. 1

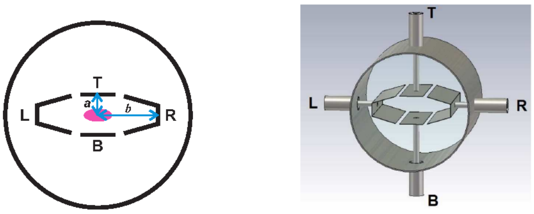

Figure 1: **Left**: front view of the pick-up design, b = 100.3 mm, a = 35.3 mm; **right**: perspective view of the pick-up from CST PS.

The quadrupolar signal Ξ for the traditional diff-over-sum method is given by $(U_R+U_L-U_T-U_B)/(U_R+U_L+U_T+U_B)$, where U_R, U_L, U_T and U_B are the amplitudes of the FFT signal voltages induced on the respective pick-up plates. Since the frequency range of interest for a typical SIS-18 opetration is between 10 kHz and 10 MHz, a high terminating resistor of 1 MΩ was connected at the output of each electrode to obtain a low 3 dB cutoff frequency of the plate. The simulation was carried out, as mentioned in the introduction, using CST PS, with a PIC solver in the frequency range of DC $\leq f \leq$ 200 MHz.

On the above diagram in Fig. 2, one can see that, the greater the horizontal beam size σ_x, the greater the quadrupolar signal in the whole frequency range, as expected. Furthermore, one can see that, in the frequency range of interest (10 kHz $\cdots$ 10 MHz) the quadrupolar signal is almost constant; the maximal deviation of $\Xi(f)$ (10 kHz $\leq f \leq$ 10 MHz) from the value of Ξ at 10 MHz is in the order of around 0.21%. The lower picture in the above figure shows the quadrupolar signal at 10 MHz for different values of σ_x/σ_y. One can state a good agreement between both solvers; the maximal relative deviation of the PIC solver results from the electrostatic ones is around 0.4%.

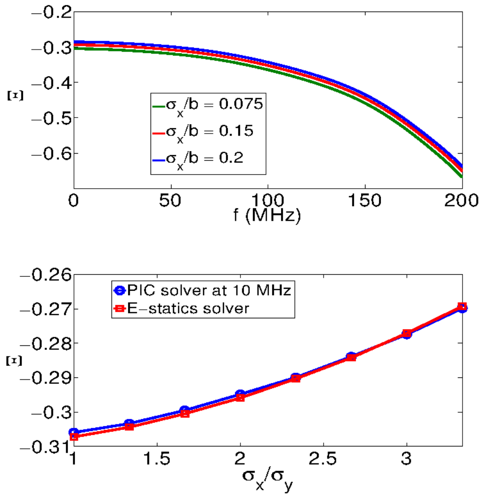

Figure 2: Quadrupolar signal Ξ for a centred beam; **above**: Ξ as a function of frequency; **below**: Ξ as a function of the horizontal beam size σ_x; σ_y/b = 0.075, b = 100.3 mm

Conclusions

The simulations for an asymmetrical pick-up have been investigated in this project. One has seen that, in the frequency range of interest for GSI, the pick-up behaves capacitiv. Moreover, there was a good agreement between the PIC und electrostatic results. In conclusion, one can say that, for beams, whose longitudinal extent is much larger that the electrode length, the pick-up properties, like for instance the sensitivity, can be estimated very good electrostatically; this has the advantage that the simulation time is very low compared to that of the PIC solver.

References

[1] Joel A. Tsemo Kamga, et al., *GSI Scientific Report 2013.*

[2] CST AG, "CST Particle STUDIO", ww.cst.com

---

[*] Work supported by GSI

[†] tsemo@temf.tu-darmstadt.de

DOI:10.15120/GR-2015-1-FG-SIS18-05

Streak camera as a new diagnostic tool for SIS18 ion beams*

L. Bozyk, M. Schwickert, R. Singh, P. Spiller, and B. Walasek-Höhne
GSI, Darmstadt, Germany

Streak cameras are typically used in electron accelerator facilities or plasma physics experiments to record processes with high time resolution. In 2014 a streak camera has been installed behind SIS18 at GSI. The streak camera will be used to study and optimize bunching and extraction of heavy ion beams from the synchrotron by measuring simultaneously in one spacial and in the time domain.

The extracted beam is observed with a BC400 plastic scintillator which is widely used in beam diagnostics. It has a rise time of 0.9 ns and decay time of 2.4 ns. It emits light with a maximal emission at 420 nm (violet/blue). Two scintillators are mounted in 45° with respect to the beam axis on a target ladder, which can be moved by a stepper motor. The scintillator is observed from below the beam axis. An optical system, consisting of four lenses and four mirrors, guides the emitted light to the streak camera. The optical system images 30 mm of the scintillator onto the 10 mm wide entrance slit of the streak camera, which observes the horizontal plane. Black moleton covering the setup enhances the contrast by excluding ambient light.

The installed streak camera is an "Universal Streak Camera", model C10910 by Hamamatsu. It allows streak times between 1 ns and 120 ms and has a motorized slit to be fully remote operable. Sensitive components, as the control PC, are placed in a measurement room, USB and firewire connections are extended via optical fibre. The whole system can be operated from the main control room of GSI via remote desktop access. In the fast extraction mode, the streak camera is triggered by the same signal, as the kicker modules of SIS18. It is generated in the electronics room by the Rf-system and has a jitter of 10 ns to 20 ns. By means of a delay generator one can account for trigger delays and time-of-flight of the beam. The long streak time of 120 ms is used to observe slow extracted beams. In this mode, the setup is triggered by timing events.

In autumn 2014 the streak camera system has been commissioned with different heavy ion beams from SIS18. Figure 1 shows the time-evolution of the horizontal profile of four bunches U^{28+} hitting the scintillator. The bunches hit at the same position, but obviously have different intensities. In Figure 2 the projection of streak data of an U^{29+}-beam onto the time axis is compared with the signal of the fast beam current transformer in the extraction line. In figure 3 the flattop voltage was chosen to low. The streak camera system also allows to resolve the spill structure and movements of the extracted beam during slow extraction .

First test with the streak camera in the SIS18 extraction line look very promising and show good capabilities to observe dynamics within the bunches.

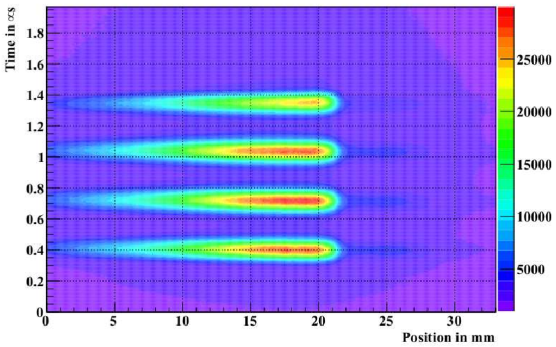

Figure 1: Streak picture of fast extracted U^{28+} beams at 200 MeV with four bunch operation (1H4). 30 pictures have been averaged.

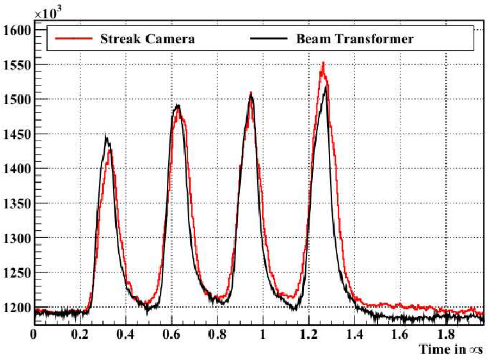

Figure 2: Comparison between the signal recorded with the beam transformer in the extraction beam line and the projection of a single streak picture onto the time axis for a U^{29+}-beam in arbitrary units.

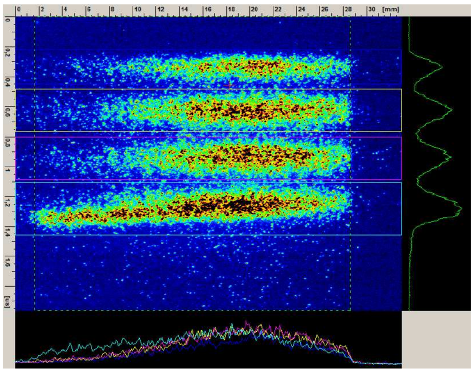

Figure 3: Screenshot from the online-display with U^{29+}-beam at 210 MeV: The flattop voltage (1 kV) is chosen slightly to low. The deformed bunch can not be recognized on the beam transformer.

---

* Work supported by BMBF, projectt 05E12CD1

DOI:10.15120/GR-2015-1-FG-SIS18-06

Recent improvements in TOPOS

R. Singh, K. Lang, and P. Kowina
GSI, Darmstadt, Germany

TOPOS is the digital Tune, Orbit and POSition measurement system which is currently under operation at GSI SIS-18 [1]. TOPOS provides bunch-by-bunch position from all 12 beam position monitors (BPMs) during the full acceleration cycle. It can also provide digitized raw BPM signal from all 48 pick-up electrodes (4 per BPM) at 125 MSa/s for ≈ 300 ms. TOPOS is designed to operate under a high dynamic range (90 dB) of beam currents in SIS-18.

TOPOS has been extensively utilized for SIS-18 optimisation and operation as well as for studying beam dynamics [2, 3, 4] in the past years. The widespread usage of TOPOS brought out the following technical issues:

1. An amplifier gain dependent closed orbit position variation of up-to 2 mm was observed as shown in Fig. 1 for 20 and 30 dB gains.
2. Erroneous position data for periods much longer than the set acquisition time was acquired by TOPOS system. This occured randomly for several BPMs.
3. Beam-based bunch detection for short bunches (with $< 7-8$ ADC samples) failed during the high energy proton beam operation.

Several beam-based tests were performed with TOPOS in response to the recurring operational issues mentioned above. The conclusions as well as the resulting upgrades to the TOPOS are reported in the next section.

Tests and Conclusion

Amplification dependent position variation was suspected to be an error in the present position calculation algorithm (i.e. weighted mean) due to its reliance on a complicated baseline restoration procedure described in [5]. Therefore, an alternate and simpler method for position calculation based on regression fitting was implemented. Figure 1 shows the comparison of the calculated horizontal position along the acceleration ramp between both algorithms. The amplifier gain dependence of beam position remains the same irrespective of the algorithms used. A small systematic bias (≤ 0.1 mm) between the positions calculated by both algorithms is due to the difference in their noise suppression characteristics. On further investigation it was found, that the calibration of the distinct amplifier chains connected to the 4 BPM electrodes were performed by a fixed amplitude signal generator. This calibration configuration allowed calibration only in a small range of amplification (i.e 10 to 20 dB). A new front-end electronics will be installed in SIS-18 where a calibration method based on varying input amplitude will be used to correct this error.

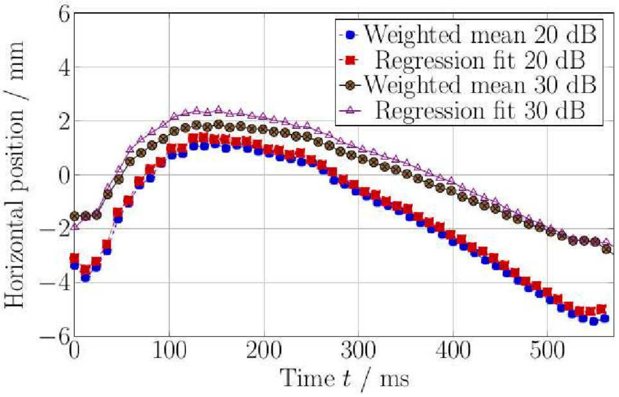

Figure 1: Comparison of measured horizontal beam position during the acceleration at two separate gain settings with both algorithms.

The problem with the erroneous acquisition length was related to the storage of the RF synchronous time-stamp generated for each bunch in the Libera FPGA. The error occurred when the time-stamp was not reset after the measurement cycle was finished. This happened in special conditions such as, when the end of measurement cycle coincided with the read strobe signal responsible for reading and clearing the time-stamp. This issue is resolved.

The issue of short bunch detection was studied by applying FPGA simulations. It was found that the bunch detection worked well for Gaussian shaped bunches with a sufficiently high amplitude even for a bunch length down to three samples. Offline simulations with recorded beam data with short bunches (upto 6 samples) also worked fine. Thus, the problem could not be reproduced during the investigations and is probably linked to the erroneous acquisition length issue.

References

[1] K. Lang, "TOPOS: A new tool for beam position measurements at SIS-18", GSI scientific report 2010 (2010)

[2] V. Kornilov et al., "Transverse decoherence and coherent spectra in long bunches with space charge", Phys. Rev. ST Accel. Beams 15, 114201 (2012)

[3] R. Singh et al., "Interpretation of transverse tune spectra in a heavy-ion synchrotron at high intensities", Phys. Rev. ST Accel. Beams 16, 034201 (2013)

[4] G. Franchetti et al., "Recent development in the mitigation of long term high intensity beam loss at FAIR", Proc. of HB 2014 (2014)

[5] R. Singh, "Tune measurements at SIS-18: Methods and Applications", TU Darmstadt (2013)

DOI:10.15120/GR-2015-1-FG-SIS18-07

Commissioning of a sensitive tune monitoring system in SIS-18

R. Singh, T. Hoffmann, and P. Forck
GSI, Darmstadt, Germany

The front-end hardware of the baseband tune measurement system (BBQ) [1] has been routinely used for sensitive tune measurements at SIS-18 with real time spectrum analyser as the acquisition component [2]. The new TUne MEasurement system (TUME) integrates the BBQ front-end hardware with a FESA [3] based data acquisition and control element, and a Java based graphical user interface. The first operational results of the new TUME system at SIS-18 are presented.

The TUME system is designed to fulfil the following requirements :

- Monitor the tunes during the whole acceleration cycle or the time specified by the user. It should be possible to use different time-scales for calculating tunes.
- Provide facilities to filter and store the measurement data via a simple user interface.

Figure 1 shows the various components of the tune monitoring system. The pick-up signal is connected to the BBQ front-end hardware which consists of peak detectors and an amplifier chain. The output of BBQ front-end is connected to a VME based front end controller (FEC) which consists of the 8 channel, 16-bit, 100 MSa/s SIS-3302 ADC module. Two channels are used for the digitization of the output of the BBQ front-end for horizontal (x) and vertical (y) planes. The ADC module is clocked by the SIS-RF signal followed by a rate divider to control the clock rate. This is required to support the various harmonic operational modes of SIS-18. The GSI machine timing events are converted to CERN timing events which are fed to the TUME FESA class via the CERN timing receiver VME (CTRV) module.

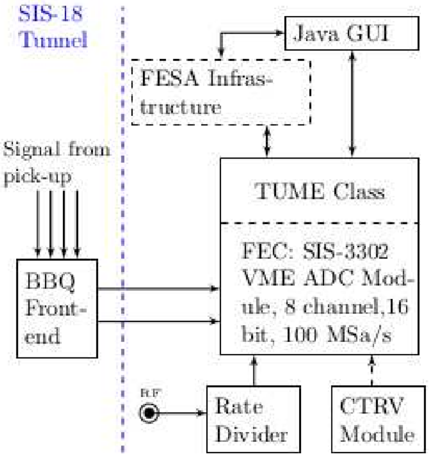

Figure 1: The data acquisition scheme for the tune measurement system.

A TUME FESA class performs an FFT on the acquired samples based on user preferences to obtain the tune spectrum. A peak search routine extracts the tune value from the spectrum. Clients can subscribe to the properties of this FESA class to obtain the tune spectrum and tune values throughout the acceleration cycle. A Java based GUI (shown in Fig. 2) was developed to display the evolution of tune spectrum during the whole cycle. It provides further options for FEC settings, filtering the data, storage of data and advanced techniques for frequency spectra estimation.

The first beam based tests were performed in Autumn 2014 with 10^9 U^{28+} particles accelerated from 11.4 to 300 MeV/u. The BBQ front-end was connected to a pick-up in the quadrupolar configuration. Therefore, both x and y tunes are visible in channel 1 as shown in Fig. 2.

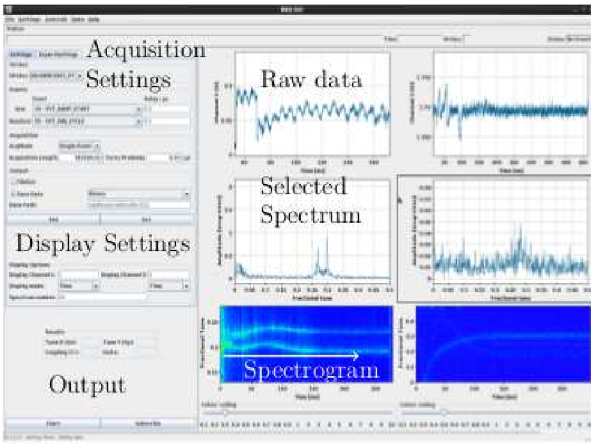

Figure 2: The TUME GUI shows the evolution of tune spectrum and tune over time.

The top plot shows the raw time domain data from the BBQ front-end. The middle plot shows the spectrum for a selected time window (from display settings). The lowest plot shows the tune spectra over time for the specified duration in acquisition settings. The FESA class and GUI are still under development, and will be brought into regular operation at the beginning of next SIS-18 run.

References

[1] M. Gasior, “High sensitivity tune measurement using direct diode detection”, Proc. of BIW’12 (2012)

[2] R. Singh, “Tune measurements at GSI SIS-18: Methods and applications”, PhD Thesis, TU Darmstadt (2012)

[3] T. Hoffmann, “FESA - The front end software architecture at FAIR”, Proc. of PCaPAC08, Ljubljana, Slovenia (2008)

DOI:10.15120/GR-2015-1-FG-SIS18-08

Spill time-structure and main dipole power converter ripple in SIS-18

M. Kirk, D. Ondreka, H. Welker, C. Kleffner, P. Kowina, R. Singh and P. J. Spiller
GSI, Darmstadt, Germany

Tracking studies were carried out with an in-house code in order to estimate the severity of the power converter induced ripple in the dipoles as concerns its influence on the roughness of the spill when undergoing transverse RF "Knock-Out" (KO) excitation. The excitation comes from a strip-line exciter. In addition, a lattice resonance at Q_x=13/3 is created by sextupole magnets which were powered to provide an amplitude of K_2L=0.03 m^{-2}. The working point's tunes were Q_x=4.3296 and Q_y=3.27. With the longitudinal RF off, the reference $^{12}C^{6+}$ DC beam had a Half-Width in its relative momentum spread of $\delta_{p,2\sigma}$=0.04%. A Hardt condition was imposed on the optics to minimize ions lost to the first extraction septum by adding the offset K_2L=0.206 m^{-2} to each of the 1C-sextupoles and setting K_2L=-0.369 m^{-2} to each 3C-sextupole, producing losses at the septum's wires ≈3.5% of the initially stored ions, with ripple in the dipoles taken from Fig. 1. This loss is close to the simulated loss of 3.3% in the absence of the dipole magnet B-field ripple. It is therefore assumed that the ripple in the spill in Fig. 2, is not caused by septum collisions to a large extent.

A single power converter is connected in series to the dipoles. Fig. 1 taken from [1] shows the dipole circuit ripple at the nominal direct current of I_n=1190 A which was (partially) reconstructed from the discrete Fourier transform of an 8-bit oscilloscope trace of the difference between the set-point and actual current. With identifiable components in the range 100 to 1100 Hz (including the anticipated 300 and 600 Hz) added together to give Fig. 1 and implemented in the simulation, Fig. 2 was produced.

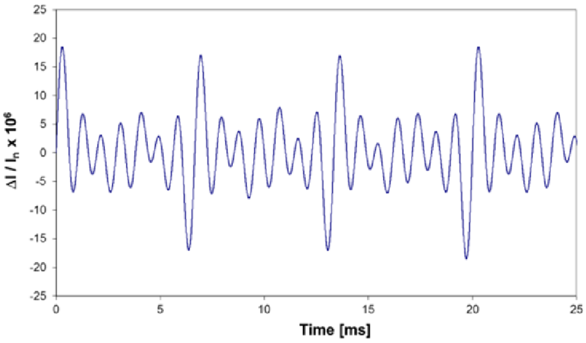

Figure 1: Partially reconstructed dipole current ripple. Maximum relative deviation in current is ca. 1.8x10^{-5}.

Each of the stored ions received, per transit through the exciter, a perturbation in its horizontal trajectory angle made with the design orbit, the magnitude of which was sampled randomly (per ion) from a Gaussian distribution cut at ±3σ, thereby allowing the contribution to the spill from just the dipole current to be determined. In Fig. 2 which shows the induced spill-ripple, the regularly spaced strong peaks occurring at 150 Hz are suspected to be directly correlated to the power converter ripple's signal envelope.

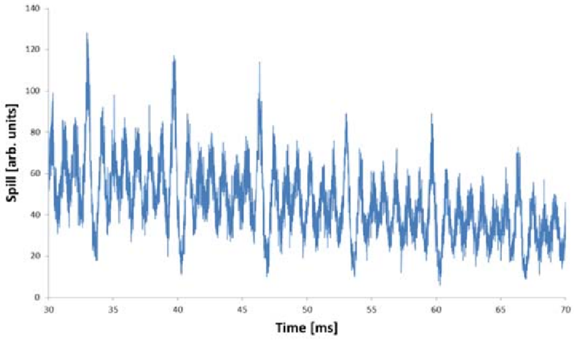

Figure 2: Simulated spill with dipole ripple.

In Fig. 3, which shows the distribution of the spill's Maximum-to-Average current from a 100-bin window (10 µs bins) moving over the spill of Fig. 2, one sees a clear degradation in spill smoothness. However, with nominal operation (K_2 offsets zero) for which the amplitude was raised to K_2L=0.064 m^{-2}, to permit a potential closed orbit bump of ~20 mm, no spill-ripple was observed.

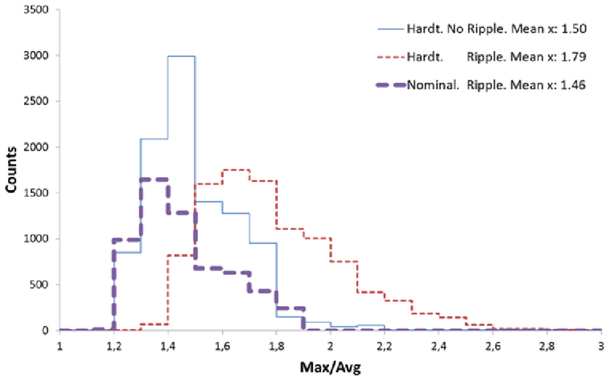

Figure 3: Simulated spill "roughness" distribution.

Measured spill-ripple, due to magnets, is considered excessive. Ions crossing the separatrix faster should reduce it. To this end, a recent prototype modification to the KO system, capable of delivering a new KO voltage form and higher maximum voltage, may achieve this.

References

[1] M. Kirk et al., "SIS-18 RF Knock-Out Optimisation Studies", IPAC'13, Shanghai, May 2013, MOPFI007, http://www.jacow.org .

DOI:10.15120/GR-2015-1-FG-SIS18-09

Super-FRS design status report*

M. Winkler[†1], *S. Althoff*[1], *F. Amjad*[1], *K.-H. Behr*[1], *A. Bergmann*[1], *T. Blatz*[1], *A. Brünle*[1], *E.J. Cho*[1], *W. Freisleben*[1], *H. Geissel*[1,2], *M. Gleim*[1], *C. Karagiannis*[1], *B. Kindler*[1], *H. Kollmus*[1], *E. Kozlova*[1], *A. Krämer*[1], *A. Kratz*[1], *J. Kurdal*[1], *H. Leibrock*[1], *H. Müller*[1], *G. Münzenberg*[1], *C. Mühle*[1], *I. Mukha*[1], *C. Nociforo*[1], *L. Orona*[1], *S. Pietri*[1], *A. Prochazka*[1], *S. Purushotaman*[1], *M.V. Ricciardi*[1], *C. Scheidenberger*[1,2], *F. Schirru*[1], *C. Schlör*[1], *P. Schnizer*[1], *H. Simon*[1], *C. Schlör*[1], *P. Szwangruber*[1,3], *F. Wamers*[1], *H. Weick*[1], *A. Wiest*[1], *C. Will*[1], *J.S. Winfield*[1], *Y. Xiang*[1], *and FAIR@GSI division*[1]

[1]GSI, Darmstadt, Germany; [2]JLU Giessen, Germany

System design

The revised layout of the Energy Buncher Spectrometer [1] has been finalized. It consists of two dipole stages deflecting the beam in opposite direction, forming a S-shape system. The new layout allows for a much simplified rectangular geometry of the required LEB cave. The ion-optical design includes an intermediate focus between the two dipole stages keeping the overall dispersion in limits. Details of the ion-optics are given at [2].

Magnets

CEA Saclay took over the design revision of the superconducting dipole magnets for Super-FRS. Although the existing prototype dipole fulfilled the magnetic parameters it required a revision of the cryostat including the cold mass. The FDR on the revised design (see Fig.1) was already held. CEA is now finalizing the design and preparing the tendering documents including the necessary specification. The magnets will then be tendered by FAIR.

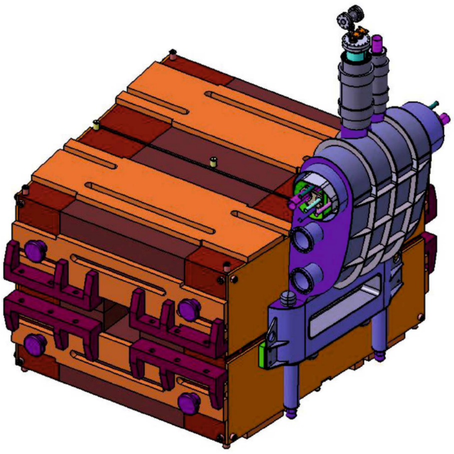

Figure 1: Revised design of SC the dipole magnet.

Unfortunately the tendering of the superconducting multiplets needed to be paused in September2014 due to formal reasons. The already qualified companies were asked to submit new offers. Contract negotiations are ongoing at the moment of writing this report and awarding is expected now for Q2/2015.

A handling test was performed for the existing radiation resistant dipole magnet. Later this 95 ton device must be installed in several parts in the highly shielded target area by means of the overhead crane in the target building of Super-FRS. The installation procedure was simulated with the help of a truck-mounted crane.

Moreover we needed to revise the adjustment support. The alignment of the magnet as well as other components in the target area can only be done remotely without any interivisibility. It turned out that the existing support unit does not satisfy the very high demand on reliability which requires the design of a new adjustment unit.

Figure 2: Simulation of the NC dipole installation.

Local cryogenics

For the planning of the Super-FRS magnet testing at CERN, several important topics related to the cryogenic safety have been investigated by CSCY together with the colleagues at CERN. Those include the final settle-down of the set pressure for the safety devices of the Super-FRS magnets according to the Pressure Equipment Directive (PED), the non-symmetrical forces on the multiplet cryostat in case of sudden loss of insulation vacuum to air, and the vacuum tank protection in case of a possible breakdown of the cryogenic piping in the multiplet cryostat. In addition, the dynamic forces on the magnet support struc-

---

* Work supported by EU, CRISP contract No. 283745/CEA-IRFU/KVI-CART/FAIR@GSI PSP code: 2.4

† m.winkler@gsi.de

DOI:10.15120/GR-2015-1-FG-SFRS-01

tures for the test facility in the testing hall 180 have been checked for the case of helium gas release during worst-case quench. The results coming out of the investigations have been evaluated by the Safety Department at CERN and the submitted documents provide the basis to get the approval for the design and the operation of the test facility at CERN. Furthermore, the physical interfaces have been finalized between the cryogenic infrastructures, i.e., the jumper-connection, and the magnet cryostats, which is one of the most important interfaces through the magnet design and fabrication, the magnet testing at CERN and the final installation and operation at FAIR/GSI. Based on the cryogenic parameters including the heat loads of the magnet cryostat, the pressure drops, the flow rates and the cooldown time estimation provided by the CSCY, a preliminary cryogenic design of the test facility has been done at CERN in summer 2014.

Beam instrumentation

The development and production of the slit systems for Super-FRS was contracted as the first project within the framework of the Collaboration Agreement between GSI and KVI-CART. Altogether 18 slit pairs (horizontal as well as vertical) will be installed in the Super-FRS. Most of the slit-jaws will consist of Densimet blocks having dimensions of up to 200x180x250 mm^3. The overall weight of the heaviest slit-systems will be close to 1 ton. The preliminary design could already be finished including aspects like remote handling capability (in the Pre-Separator). Special care was taken on thermal effects which could arise in the Pre-Separator due to high beam/fragment intensities [3].

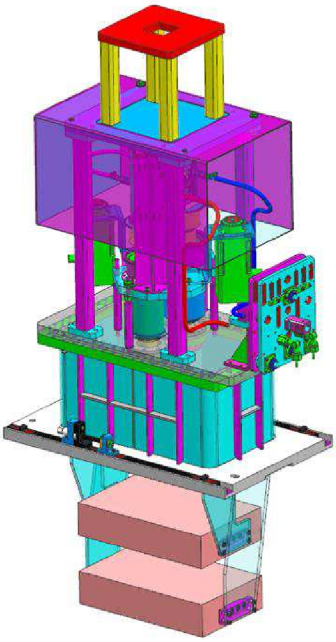

Figure 3: Daesign proposal of the y-slit system including remote controlled media pannel.

Target area / handling system

A Hot-Cell mock-up was installed on the ESR roof (see Fig.4). It consists of a metallic frame and two master-slave manipulators. The frame simulates the front area/shielding window of the future Super-FRS Hot Cell [4] and serves as the support for the manipulators. The manipulators are double telescopic systems with a load capacity of 20 kg and a maximum slave extended length of 3270 mm. The arms are completely equilibrating in all operational positions (with no load). It is foreseen to transfer and install these manipulators to the future Hot-Cell.

Figure 4: Hot-Cell mock-up mounted on the ESR roof

The main purpose of the mock-up is to validate the concepts of the equipment which is under development now and must be designed for remote-handling (target, beam catcher, etc., but also equipment used at the pbar separator). Another important aspect is the training of personnel in advance of 'hot' operation. Partially we collaborate here with SPIRAL2 in the framework of the EU CRISP project and remote handling tests with our French colleagues could be performed.

References

[1] H. Geissel et al., "Dispersion-matched spectrometer in the low-energy branch of Super-FRS", NIM B 317 (2013) 227

[2] J. Winfield et al., "Status of Ion-Optics for the Super-FRS", this report

[3] J. Gellanki et al., "Super-FRS Slit System and Possible Passive Cooling Techniques", this report

[4] M. Winkler et al., "Super-FRS Design Status Report", GSI Scientific Report 2010 (2011) 133

DOI:10.15120/GR-2015-1-FG-SFRS-01

Super-FRS slit system and possible passive cooling techniques

J. Gellanki[1], *C. Douma*[1], *N. Kalantar-Nayestanaki*[1], *O. J. Kuiken*[1], *M. F. Lindemulder*[1], *H. Moeini*[1], *C. Nociforo*[2], *C. Rigollet*[1], *H. A. J. Smit*[1], *H.J. Timersma*[1], *K. H. Behr*[2], *C. Karagiannis*[2], *M. Gleim*[2], *C. Schlör*[2], *H. Simon*[2], *and M. Winkler*[2]

[1a]KVI-CART, University of Groningen, NL-9747 AA, Groningen, The Netherlands; [2b]GSI, D-64291 Darmstadt, Germany

X− and Y− position slit systems will be used to stop the unwanted charge states of the primary beam and fragments produced at the reaction target of the Super-FRS at the FAIR facility, GSI. In the case of the most frequently used fission reaction of ^{238}U beam at 1.5 GeV/u on ^{12}C target (2.5 g/cm^2), one of the lowest charge states of ^{238}U fragments produced at the target may reach one of the X-slits with an energy of about 1.3 GeV/u with a maximum power of 500 W. The basis of the Super-FRS X− and Y− slit systems are two DENSIMET®185 (97% Tungsten, 2% Nickel and 1% Iron) metal blocks, which have to move in a vacuum chamber in horizontal direction ($0 - 400$ mm) and in vertical direction ($0 - 200$ mm), respectively. Due to the highly radioactive environment, some of the slits are designed to allow for robot handling. Overview of Super-FRS slit system is shown in the Fig. 1. NX advanced thermal simulations Ref. [1] are carried out to estimate the maximum and minimum temperature values on the slits and on the apparatus in the neighborhood of the slits. Several cooling methods have been simulated on a block of DENSIMET with a proposed dimensions of $200 \times 180 \times 250$ mm^3, and which will be used in the pre-separator of the Super-FRS beam line. The present results from the thermal simulations suggest two new possible passive cooling techniques to lower the temperature of the block by substantial amounts without any water cooling during experiments.

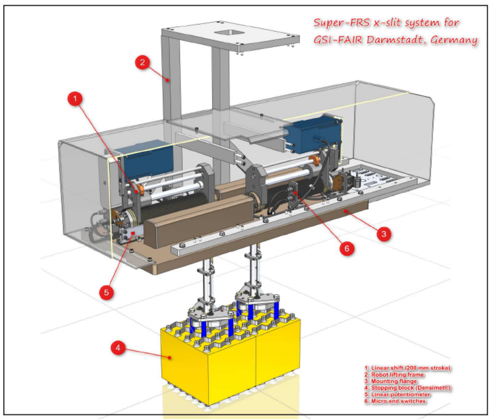

Figure 1: Schematics of the Super-FRS slit system which is under construction at KVI-CART, is shown.

Simulations and the new passive cooling techniques have been tested by a test run at the AGOR beam line at KVI-CART. In this run, three different densimet blocks: 1) pure densimet (emissivity ∼ 0.07; as per literature), 2) densimet block with welded stainless steel (SS) strips as radiators (SS emissivity ∼ 0.65) and 3) densimet block with cerablack coating Ref. [2] of thickness 0.15 mm (cerablack emissivity ∼ 0.9) have been used. The pure block and the block with SS strips having the same dimensions of $30 \times 30 \times 50$ mm^3 and the coated block is of $25 \times 25 \times 50$ mm^3. Each block has been exposed with ^{20}Ne beam of power Q = 21 W for about four hours. Preliminary results of this test run are shown in the Fig. 2. As seen from the figure, the densimet block with the cerablack coating radiates out the heat much faster than the other two blocks. Further details can be found in Ref. [3].

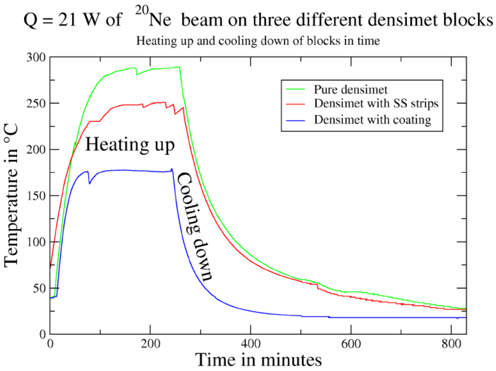

Figure 2: Preliminary results of test run with ^{20}Ne beam are shown. Heating and cooling responses of the pure densimet block are shown in green. The same is shown for the block with stainless steel welded strips and cerablack coating by the red and the blue solid lines, respectively. As seen in the picture, each densimet block was exposed to a beam (heating up) for about four hours. The decrease in temperature of each curve represents the cooling down of the corresponding block. For more details see text.

References

[1] Siemens NX (NX Thermal and Flow) software.

[2] http://atfinet.com/index.php/applications/thermal-management/high-emissivity-coatings.

[3] J. Gellanki et al., *To be submitted to Nucl. Instr. Meth. Phys. Res. A.*

DOI:10.15120/GR-2015-1-FG-SFRS-02

Profile monitors for the Super-FRS*

C. Nociforo[1], *J. Adamczewski-Musch*[1], *K.H. Behr*[1], *A. Brünle*[1], *J. Frühauf*[1], *N. Kurz*[1], *S. Löchner*[1], *A. Reiter*[1], *K. Rytkönen*[2] *and M. Witthaus*[1] and the FAIR@GSI division
[1]GSI, Darmstadt, Germany; [2]University of Jyväskylä, Department of Physics, 40014 Jyväskylä, Finland

Profile monitors providing precision measurement of horizontal and vertical beam profiles are essential for transport and targeting of Super-FRS beams.

Introduction

At GSI the beam monitoring technique based on Secondary Electron EMission (SEM) is routinely used for the high power UNILAC beams. When charged particles hit a metallic surface, secondary electrons are liberated, escaping from it forming a measurable signal. Wire SEM grids are widely used as device to measure the profile of the ion beams. While the yield probability of secondary electron emission is low, these devices can produce signal up to 10nC/wire in case of SIS beam. At FAIR beam intensities, e.g. 4.5x10^{11} ^{238}U/spill, beam passing through the wire, undergoes to a significant energy loss (few GeV) even if the particle are not stopped, and wires can be damaged by the temperature rise. Presently, SEM-grids of different material and geometry satisfying the Super-FRS beam parameters are under investigation.

Beam test

A standard GSI monitor DG1010 [1] designed with wire spacing and diameter of 1.5 mm and 0.1 mm, respectively, was installed in vacuum at the first focal plane F1 of the FRS and irradiated with U beam. The number of horizontal and vertical W wires was 16. To simulate an experimental condition similar to that of the Super-FRS, the wire signals were transported over a long cable (length >50 m). A current-to-frequency converter QFW POLAND [2] was used to measure the profile of the beam. The electronics was triggered by the start of extraction TTL pulse delivered by the accelerator timing system.

The response of the detector was studied with slow-extracted ^{238}U^{73+} beam at 300 MeV/u and fast-extracted ^{238}U^{29+} beam at 125 MeV/u. At higher energy the beam intensity did not exceed 2.8x10^{8} ions/s. At lower energy the maximum intensity delivered by the SIS18 was equal to 10^{10} ions/spill. Due to the small area of the detector one single charge state distribution per time could be measured by the grids. The intensities of the different charge states of the beam were simulated and compared with the measured ones. The horizontal profile of ^{238}U^{90+} beam reaching F1 with a magnetic rigidity of 8.085 Tm corresponded to a measured charge of 0.19 nC. The U charge state distribution produced in 40 μm of Ti material inserted at the FRS target position was estimated by using the GLOBAL code [3]. The emission of secondary electrons from the W surface was calculated by the Sternglass formula [4]. Under the assumption that 7% of the beam crossed the wires, the estimated charge was 1.46 times the measured one.

The response of the detector to fast-extracted beam was tested after adding a capacitance of 4.7 nF to stretch the pulse.

The 3D measurement of a time-resolved beam profile of ^{238}U^{88+} at about 125 MeV/u, reaching F1 after impinging a 10 μm Ti foil, is shown in Figure 1. The ratio between measured and simulated charges decreased up to 0.36 for the maximum intensity (assuming no losses up to the FRS target).

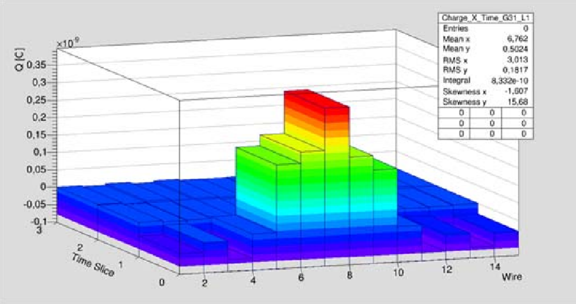

Figure 1: ^{238}U^{88+} profile at 125 MeV/u (fast extraction).

Further analysis of the test results will add constraints to the mechanical design of the Super-FRS SEM-grids. Effects of off-axis charge states hitting the frame and return wires were noted. Although a larger geometric coverage is required at the Super-FRS, present results ensure a standard operation along the separator.

Outlook

Further optimization, not only for the emission yield but also to increase precision of measured position and width of the beam, are foreseen. At the Super-FRS target, because of the high power absorption, different SEM material will be tested.

References

[1] P. Strehl, “Beam Instrumentation and Diagnostics”, Springer (2006), p.105.
[2] http://wiki.gsi.de/cgi-bin/view/EE/POLAND.
[3] C. Scheidenberger et al., Nucl. Instr. Meth. B142 (1998) 441.
[4] E. J. Sternglass, Phys. Rev. 108 (1957) 1.

---

[*] PSP code: 2.4.6.1.4

DOI:10.15120/GR-2015-1-FG-SFRS-03

In-Beam Test of the TwinTPC at FRS*

A. Prochazka[1], *M. Pikna*[2], *B. Sitar*[2], *P.Strmen*[2], *I.Szarka*[2], *C. Nociforo*[1], *S. Pietri*[1], *and FAIR@GSI Division*[1]
[1]GSI, Darmstadt, Germany; [2]Comenius University, Bratislava, Slovakia

One of the crucial requirement for the future tracking detector at the Super-FRS [1] is a high efficiency tracking at particle intensities around 1 MHz. To improve the efficiency at high rates of the standard TPC [2] and future GEMTPC detector [3] so called Twin design is proposed.

The main idea of the Twin design is to use two independent drift volumes with electric fields of opposite direction. This allows to calculate a Control Sum which is in principle sum of the drift times from the drift volumes. As the sum should be a constant it can be used for for pile-up and noise rejection and for multi-hit track reconstruction.

The TwinTPC prototype was built at Comenius University Bratislava. The TwinTPC drift volumes were filled with P10 gas at normal temperature and pressure and were operated at electric field of $400V/cm$. Each drift space was read by two anode wires and a delay line. The anode wires were used to calculate drift time (y-coordinate) and delay line was used to measure x-coordinate. For the future the single-strip readout with multi-hit digital electronics is foreseen for x-coordinate measurement. The signals were processed by conventional electronics (pre-amplifiers, shaping amplifier, discriminator) and time was measured by multi-hit TDC (Caen V1290) with $25ps$ time resolution. All times were measured relative to reference times derived from the hits of a plastic scintillator. The Control Sum was calculated as $t_{CS} = t_1 + t_2 - 2 \cdot t_t$, where t_1 and t_2 are drift timed from the two drift spaces and t_t is the reference time coming from scintillator. All times are measured in multi-hit mode.

The test was done using Au beam at $700MeV/u$ at the FRS. The particle rate was estimated from the number of hits registered by the plastic scintillator which were sent to scaler unit and the mutli-hit TDC. The efficiency was measured at different beam intensities and was estimated from the number of events for which we can unambiguously assign drift times fulfilling the control sum condition. The typical distribution of the control sum is shown in Fig 1. The width of the control sum is partially determined from the time resolution of the drift time measurement. The achieved time resolution (RMS) of the single drift volume was around $1ns$ for rates below 100kHz, corresponding to about $50\mu m$ position resolution for P10 gas. At higher rate (700kHz) the time resolution dropped to $3ns$.

The measured efficiency of the drift time reconstruction using the Twin design at different rates is shown in Fig. 2. The obtained results are compared with the efficiency of the single-volume TPC with single-hit readout and with simulation as described in [4]. The results conclude the Twin design works and show possible areas for improvement.

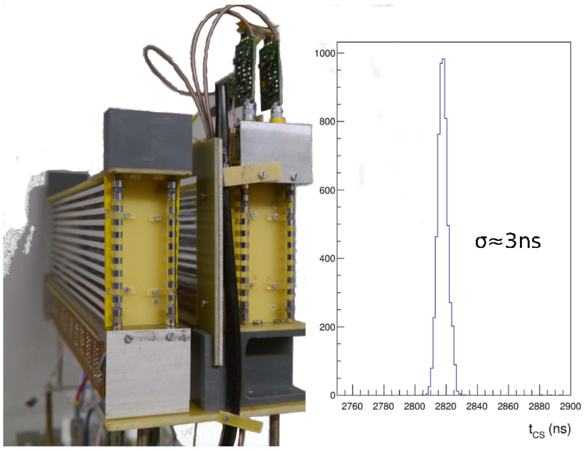

Figure 1: Left: TwinTPC prototype photo showing two drift volumes. Right the distribution of the Control Sum

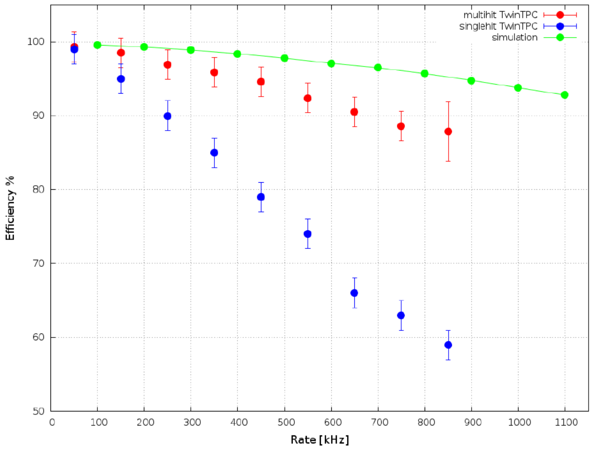

Figure 2: The TwinTPC drift time reconstruction efficiency (red points) as a function of rate. The blue points are efficiency of the single drift volume with single-hit electronics, the green points are simulation.

References

[1] H. Geissel et al.,Nucl. Instr. and Meth. B204(2003)71-85
[2] R. Janik et al.,Nucl. Instr. and Meth. A640(2011)54-57
[3] F. Garcia et al.,GSI Scientific Report 2012(2013)173
[4] A. Prochazka et al., GSI Scientific Report 2012(2013)174

---

* PSP code: 2.4.6.1.3

DOI:10.15120/GR-2015-1-FG-SFRS-04

On the Crystal Structure of Intrinsic CVD Diamond-on-Iridium Sensors*

E. Berdermann[1#], M. Kiš[1], C. J. Schmidt[1], M. Träger[1], R. Visinka[1], K. O. Voss[1], M. Fischer[2],
S. Gsell[2], M. Mayr[2], M. Schreck[2], K. Afanaciev[3], and M. Ciobanu[4]
[1]GSI, Darmstadt, Germany; [2]Universität Augsburg, Germany; [3]NC PHEP, Minsk, Belarus; [4]ISS, Bucharest, Romania

Ion Beam Induced Current (IBIC) experiments were performed with high-quality Diamond-on-Iridium (DOI) sensors aiming to visualize shape and spatial distribution of crystal dislocations in this new detector-grade diamond type. For the first time, DOI samples were irradiated with ^{12}C microbeams of 3.6 and 11.4 AMeV kinetic energy in two crystallographic directions, the [001] (i.e. along the surface normal) and the [110] (lateral) direction. Different ion energies enable the imaging of the Collected Charge (CC) in diverse crystal planes lying in depths corresponding to the Bragg maxima (here: 25µm and 170µm, respectively). Stopped, mono-energetic ions generate the same amount of electron - hole (e-h) pairs in intrinsic single crystal sensors - independent of the point or angle of the ion incidence. Ideal detectors have a CC efficiency (CCE) equal unity showing uniform maps, whereas real sensors reveal reduced CC and maps modified by crystal defects.

Sample Preparation and Mounting

A sensor of 265µm thickness and (5x5) mm² area [1] was re-metallized with six edgeless stripe electrodes connected in parallel to an SMA connector used for biasing and readout (Fig. 1, left). Edgeless contacts are difficult but indispensable in lateral IBIC tests. They produce occasionally abnormal leakage currents disturbing bias stability and energy resolution. Figure 1 (right) shows two sensors mounted for lateral experiments.

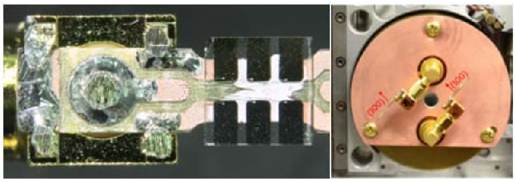

Figure 1:(left) Edgeless DOI sensor mounted on an SMA. (right) Two sensors aligned for lateral IBIC tests.

First IBIC Results

In Figures 2 and 3, examples of top-view (001) and lateral (110) maps are presented, obtained from layers in 25µm (at 3.6 AMeV) and 170µm depth (at 11.4AMeV) behind the corresponding diamond surface. In each case, areas of (288 x 232) µm² have been irradiated.

The selected pulse-height conditions used are indicated in the right spectra. The X-axes of the CC distributions are calibrated in energy values, assuming 13.4 eV per ion-induced charge carrier in diamond. The 3.6 AMeV data are presented in the range 0 - 45 MeV in 1keV/ch and the 11.4 AMeV in the range 0 - 290 MeV in 100 keV/ch, respectively. Note that, the colour values (i.e. the CC plotted on the Z-axis of the 3D maps) do not represent pure signal amplitudes, since these are generated by weighting each pulse height with the number of events at that place. However, considering the strict homogeneous irradiation performed with the micro-beam facility, the maps confirm predominantly areas of high, rather homogeneous CCE.

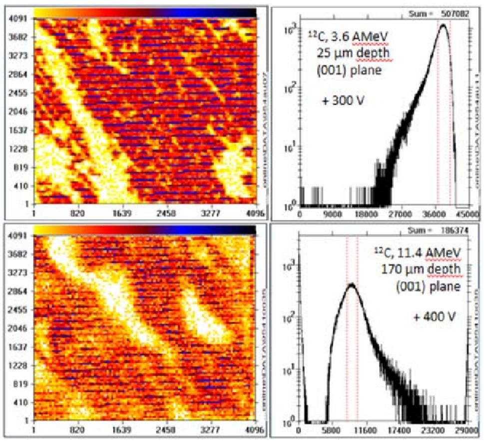

Figure 2: (001) IBIC maps (left) obtained with the conditions shown in the spectra (right). The data correspond to layers below the contact in a depth of 25µm (top) and 170µm (bottom), respectively.

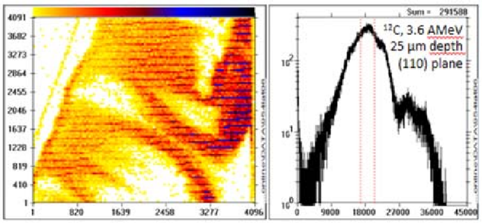

Figure 3: (110) Lateral IBIC maps and spectra (s. text).

Preliminary Conclusions

Top-view and cross-section maps differ significantly in the CC pattern. In top view, granular structures are visible with a characteristic length of 50 -100 µm. In contrast, the cross-section maps are dominated by stripes along the growth direction of a slightly tilted angle. Both observations show intriguing similarities to the shape and alignment of threading dislocations bundles observed by mapping the Raman-line widths [2]. Further studies are required to establish the preliminary results and to elucidate the influence of the contacts on the CCE patterns.

References

[1] E. Berdermann et al., GSI Scientific Report (2011)
[2] M. Mayr et al., Phys. Status Solidi A **211** (2014)

---

* Work supported by EU, HadronPhysics3, contract No. 283286

#e.berdermann@gsi.de

DOI:10.15120/GR-2015-1-FG-SFRS-05

Development of large area diamond detectors for time-of-flight measurements of heavy ions

F. Schirru[1], C. Nociforo[1], M. Kiš[1], M. Ciobanu[1,2], J. Fruehauf[1], M. Träger[1], R. Visinka[1], K. Behr[1], A. Brünle[1], I. Dillmann[1,3], C. Karagiannis[1], A. Kratz[1], N. Kurz[1], M. Marta[1], A. Prochazka[1], S. Pietri[1], S. Perushothaman[1], B. Szczepanczyk[1], H. Weick[1], M. Winkler[1]

[1]GSI, Darmstadt, Germany, [2]ISS, Bucharest, Romania, [3]TRIUMF, Vancouver, Canada

A few experiments have been carried out in order to assess the Time-of-Flight (ToF) performances of radiation detectors based on diamond material.

In early 2014, two diamond devices of 0.3 and 0.6 mm thickness, respectively were irradiated at JINR (Dubna, Russia) using an ^{40}Ar beam at 40.5 MeV/u. Amplification of the induced signal was performed by broadband pre-amplifiers (DBA-IV) [1]. In this case, the sensors, mounted a couple of cm away from each other, showed a resolution of $_{tof}$ ~ 80 ps per detector pair.

In August 2014, another experiment was performed with the FRS at GSI. This time, large-area radiation detectors based on two 20x20x0.3 mm^3 polycrystalline CVD diamonds have been developed. Electrodes were fabricated in house in a 16-strips geometry by depositing on both sides of the diamond samples Cr/Au layers of 50/100 nm thickness, respectively. Each device was then mounted on a board (Fig. 1) which has an integrated amplification stage [2] and is able to provide LVDS signals as output. The novelties of this experiment were: the use of integrated electronics, a distance between the diamond detectors of more than 30 m, and experimental conditions similar to those expected at the Super-FRS [3].

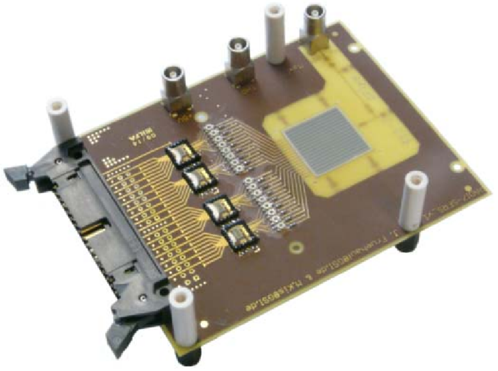

Figure 1: Diamond detector and its integrated electronics.

In this experiment at GSI, the diamond detectors have been irradiated with a ^{197}Au beam at 1 GeV/u. ToF measurements were performed in two ways: i) placing the detectors only 2 cm apart (S4 case) and ii) placing them more than 30 m apart (S2-S4 case).

As for the S4 case, first the effect of the threshold and bias voltage on the ToF resolution of the sensors was studied. It was observed that the best performances could be achieved with a voltage of -200 V. In this case, σ_{tof} =39.8 ps has been found between two strips of the front and back diamond detector. This value has shown also no dependence on the beam rate in the range of 1 – 10 kHz. For the S2-S4 case with 30 m flight path, the diamond sensors showed a resolution of σ_{tof} =52.7 ps. Taking advantage of the Time Projections Chambers (TPCs) [4] mounted along the beam line, a position correction was applied which led to an excellent resolution of σ_{tof} =45.7 ps (Fig. 2). No dependence on the beam rate over the range 10 – 80 kHz was found.

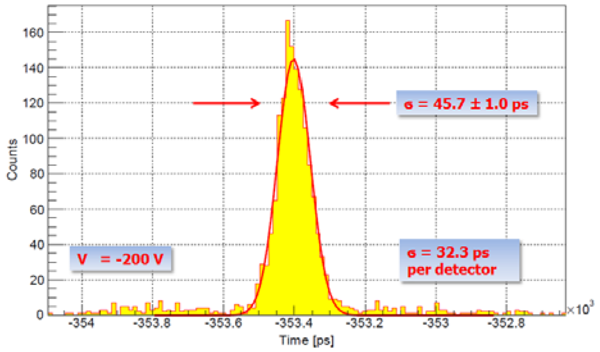

Figure 2: Diamond ToF resolution (S2-S4 case).

The new developed diamond detectors have shown excellent timing properties making this material an attractive solution for the next generation of experiments foreseen at the FRS and Super-FRS. It has to be mentioned that the ToF resolution of the diamond detectors can be further improved once a correction for the deposited energy will be done.

References

[1] P. Moritz et al., Diam. Relat. Mater. 10, p. 1765, (2001).

[2] M. Ciobanu et al., IEEE Transactions on Nuclear Science, vol. 58, n. 4, 2073, (2011).

[3] M. Winkler et al., Nucl. Instr and Meth. B 266, 4183, (2008).

[4] R. Janik et al., Nucl. Instr and Meth. B 640, 54, (2011).

---

* This work has been supported by the German Helmholtz Association via the Young Investigators Grant "LISA - Lifetime Spectroscopy for Astrophysics" (VH-NG627).

DOI:10.15120/GR-2015-1-FG-SFRS-06

Proposal of an RF-only double-funnel system for ions extraction from a cryogenic stopping cell for the Super-FRS at FAIR

Victor Varentsov[1, 2,*]

[1]Facility for Antiproton and Ion Research in Europe (FAIR GmbH), Darmstadt, Germany; [2]Institute for Theoretical and Experimental Physics, Moscow, Russia

In 2001 we proposed [1] an idea to replace a radio-frequency quadrupole (RFQ) or sextupole (SPIG) rod structure, which are conventionally used for an ion beam extraction from stopping gas cells into vacuum, by an RF-only ion funnel. Later we suggested [2] the using this technique for production of focused ion beams. Recently this RF-only ion funnel concept has been successfully checked [3] at Stanford University, USA in measurements of ions extraction into vacuum from a high-pressure (10 bar) noble-gas environment.

Here we propose the RF-only double-funnel system for ions extraction from a cryogenic stopping cell for the Super-FRS at FAIR, which prototype device is described in details in [4]. A schematic representation of this double-funnel system is shown in Fig. 1.

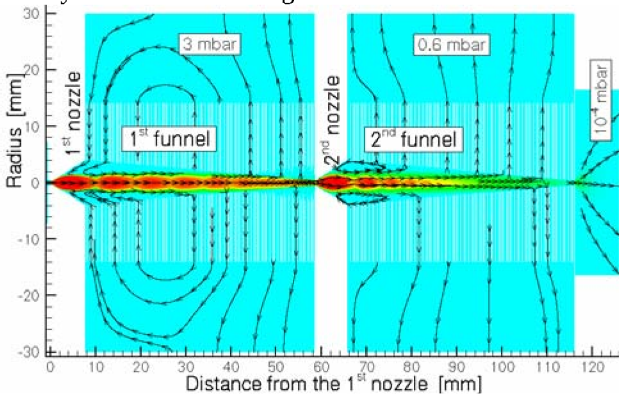

Figure 1: (color online) Schematic design of the RF-only double-funnel system for ions extraction from a cryogenic stopping cell for the Super-FRS at FAIR. The simulated velocity field for helium buffer gas at the stagnation pressure of 2 bar and temperature of 75 K in the gas cell is shown in addition. See text for explanation.

The ions are extracted from gas cell (not shown in the Fig.1) via supersonic He buffer gas flow through the 1st converging-diverging nozzle that has the following dimensions: the subsonic converging cone has the entrance diameter of 1.3 mm, the length of 1 mm; nozzle throat diameter is 0.3 mm; the supersonic diverging cone has the length of 7.7 mm and the exit diameter of 8.0 mm. The funnels are connected through the 2nd diverging nozzle having the throat diameter of 0.8 mm, the length of 7.2 mm and the exit diameter of 8.0 mm. The both funnels have the same following geometry: the number of ring electrodes is 144, they have the same outer diameter of 28 mm and the inner diameter decreasing from 8.0 mm at the funnel entrance to 0.8 mm at the funnel exit; ring electrodes made from 0.1 mm thick stainless steel sheets; the gap between electrodes is 0.25 mm. It should be notice, that the design of these funnels is identical (except of the length and the number of ring electrodes) to funnel that has been used in the Stanford's apparatus [3].

RF-voltages applied to the funnels (in such a way that phase shift between adjacent ring electrodes is 180°) confine the ions inside the funnels while the most part of the buffer gas flow out through the gaps between funnel rings and pumped. No any DC field is applied to the funnel electrodes and the ions are transported through this double funnel system only under a combined action of RF field and the buffer gas flow. The both nozzles have a ground potential.

The operation of this double-funnel system we have explored by means of detailed computer simulations. First, we made gas dynamic simulations for the buffer gas flow. Then the results of these simulations (flow fields of gas density, temperature and velocity) we used as input for ion-trajectory Monte-Carlo simulations. A detailed description of the similar computer simulations one can find elsewhere ([2, 3] and references inside). Notice that the measurements in [3] are in a good agreement with these computer simulations.

The results of gas dynamic simulation for the helium buffer gas velocity field at the stagnation pressure of 2 bar and temperature of 75 K in the gas cell is shown in the Fig. 1 for illustration. A complex gas flow barrel shock-wave structures inside the funnels are clear visible. The gas flow rate through the 1st nozzle is 123.7 mbar l/s (at the room temperature of the vacuum pumps). At the background gas pressures in the 1st and the 2nd vacuum chamber, which are maintained by pumping, of 3.0 mbar and 0.6 mbar, the gas flow rates through these chamber are 99.5 mbar l/s and 24 mbar l/s, correspondingly. The gas flow rate into the next vacuum chamber (downstream the 2nd funnel exit) is only 0.19 mbar l/s that allows extracting ions into the high-vacuum conditions ($2\cdot10^{-4}$ mbar) with the use of 1000 l/s turbo molecular pump.

Some results of the ion-trajectory simulations are shown in next figures. Fig. 2 shows the ion transmission as function of ion mass at fixed RF frequency and funnel RF voltages. The influence of the 1st funnel RF voltage on the ion transmission for ion masses m = 20 and m = 100 at fixed RF frequency and the 2nd funnel RF voltage is shown in the Fig. 3. The effect of the 2nd funnel RF voltage on the ion transmission for ion masses m = 20 and m = 100 at fixed RF frequency and the 1st funnel RF voltage is shown in the Fig. 4. The influence of the RF frequency on the ion transmission for ion masses m = 20 and m = 100 at fixed 1st funnel RF voltage 20 V_{pp} and 2nd funnel RF voltage 10 V_{pp} is shown in the Fig. 5.

DOI:10.15120/GR-2015-1-FG-SFRS-07

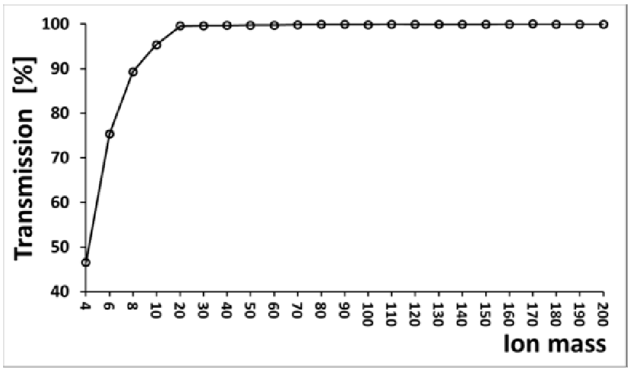

Figure 2: Ion transmission as function of ion mass at fixed 1st funnel RF voltage 20 V_{pp} and 2nd funnel RF voltage 10 V_{pp} and RF frequency 5 MHz.

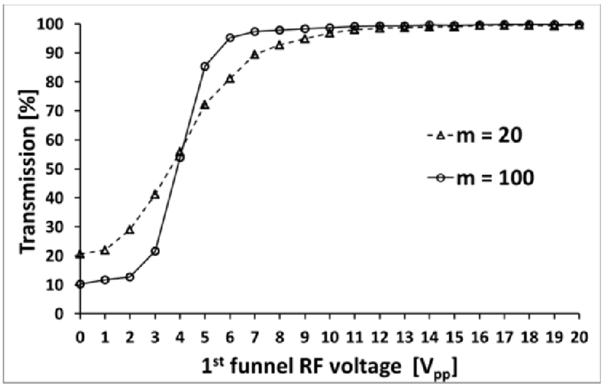

Figure 3: Ion transmission for ion masses m = 20 and m = 100 as function of the 1st funnel RF voltage at fixed 2nd funnel RF voltage 10 V_{pp} and RF frequency 5 MHz.

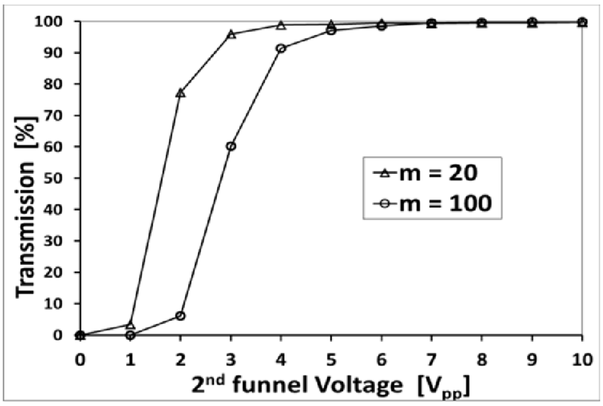

Figure 4: Ion transmission for ion masses m = 20 and m = 100 as function of the 2nd funnel RF voltage at fixed 1st funnel RF voltage 20 V_{pp} and RF frequency 5 MHz.

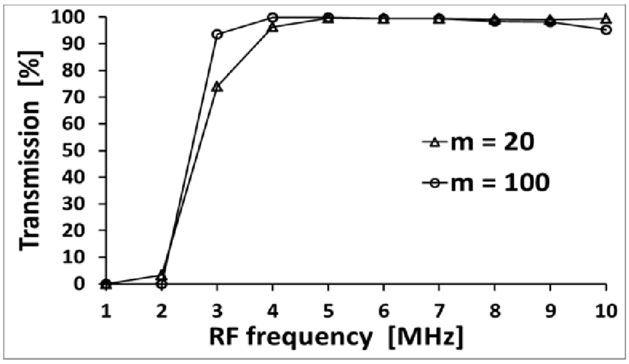

Figure 5: Ion transmission for ion masses m = 20 and m = 100 as function of RF frequency at fixed 1st funnel RF voltage 20 V_{pp} and 2nd funnel RF voltage 10 V_{pp}

The presented results make it apparent that our proposal of the RF-only double-funnel system looks very promising and can be used for ions extraction from a cryogenic stopping cell for the Super-FRS at FAIR. It has the extraction efficiencies of more than 99% for ions in a wide range of masses, it is compact, has relatively simple design and do not require big vacuum pumps for the buffer gas evacuation. Moreover, it has big advantage over the present prototype device [4] because it allows the gas cell operation at much higher stagnation pressure (2 bar). The design pressure in [4] is only 0.3 bar that corresponds to a stopping cell length of 100 cm for the required gas thickness of 20 mg/cm^2. It means that the gas cell can be made much shorter (15 cm) and will allow, in addition, for a smaller time of ions transportation through the stopping gas cell by applying a higher longitudinal DC potential gradient.

References

[1] V.L. Varentsov, “A new approach to the extraction system design”, SHIPTRAP Collaboration Workshop, Mainz, Germany, March 19-20, 2001, unpublished.

[2] V.L. Varentsov, Proc. SPIE 7025 (2008) 702509-12. doi:10.1117/12.802356.

[3] T. Brunner, et al., Int. J. Mass Spectrom. 379 (2015) 110. doi: 10.1016/j.ijms.2015.01.003.

[4] M. Ranjan, et al., Nucl. Instr. and Meth. A 770 (2015) 87.

DOI:10.15120/GR-2015-1-FG-SFRS-07

Eddy current effect of quadrupole and CR dipole magnet beam chambers

S. Y. Shim, K. Dermati, S. Wilfert, A. Dolinskii, O. Gorda, and R. Fuchs
GSI, Darmstadt, Germany

In order to keep the stable particle operation, beam chamber needs to have the high-quality vacuum state and thermal stability from external influence. The time-dependent magnetic field produces the secondary effects of heating and stray magnetic field, which can disturb the quality of the inside vacuum and the magnetic field. We present here the numerical simulation results for the recent issues related to the vacuum beam chambers of SIS100 quadrupole magnets and the current ripple effect of CR dipole magnet for the field stability optimization.

QP Star shaped beam chamber

The rib distance of the star-shaped beam chamber for quadrupole (QP) magnet has been changed from 17 mm to 7 mm. More number of ribs increase mechanical stability and the heat conduction between cooling pipe and beam chamber surface. The opposite effect is that it reduces electric resistance on the beam chamber which can be a cause of increasing eddy current. Therefore, we need to confirm the results of this design modification. The eddy loss depends on magnetic field operation scenario and we consider the 2c and triangular cycle which have higher operation load compared to other scenarios. Considering the planned boundary and initial conditions, we could find the effect of changing rib distance. Compared to previous design, the 7 mm rib distance shows small increasement of heat loss and temperature. The magnitude of increments are ΔT = 0.17 K, ΔW = 0.3 W/m at 2c and ΔT = 0.23 K, ΔW = 0.7 W/m at triangular cycle. These opposite effects are compensated and not considerably high.

Jump QP beam chamber

Jump QP has an operation scenario with ramping rate of 1600 T/s. It is the ramping rate of the integral field of the field gradient in QP magnet. After considering the real magnet dimensions, we found the ratio of 13.333 between the effective length and reference radius. With this dimensional ratio, we can interpret 1600 T/s to the value of 120 T/s at the reference radius and the corresponding maximum field is 300 G. Even though it is not extreme operation condition, this high ramping rate initiates us to confirm the effect of this operation. The simulation result shows that the time delay is $\sim 22.4\mu$s between driving current and magnetic field. Figure 1 shows the maximum temperature on the beam chamber as a function of time. Each cycle corresponds to the ramping cycles. Due to the short duty cycle with high field ramping rate, it has dynamic temperature variation. The conversed maximum temperature is estimated $\sim$ 7.5 K after infinite operation. The influence of Jump QP magnet operation on beam chamber is less than SIS100 main QP magnet.

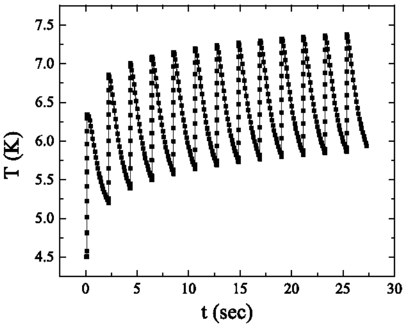

Figure 1: Maximum temperature on the beam chamber with respect to operation time.

CR dipole beam chamber

The magnet for the Collector Ring (CR) is designed to keep constantly accurate magnetic field. Therefore, the stability of the applied electric current is an important parameter for the field stability. The maximum tolerance of field variation is $\Delta B_{max}/B_0 \cong 10^{-6}$. The reported maximum current ripple is $\Delta I_{max}/I_0 \cong 10^{-4}$ considering all magnet circuits. Based on these parameters, we simulate the frequency dependence of the magnetic field from 10 Hz to 10 kHz. The maximum normalized field variation is found to be $\sim 6.3 \times 10^{-5}$ at 10 Hz. This value shows exponential decay with increasing the ripple frequency. Through the simulation procedure, we found that the reason of this field shielding effect was the secondary magnetic field by eddy current in the beam chamber. The field tolerance less than 10^{-6} have been found around 2 kHz and 5.5 kHz in the middle of magnet and the beam space inside the beam chamber, respectively.

References

[1] A. Dolinskii, et.al. Proceedings of IPAC'11 Conference, San-Sebastian, 2011, WEPC054

[2] S. Y. Shim, The Influence of Driving Current Ripple on CR Dipole Magnet, 6th BINP-FAIR-GSI workshop, 2014

DOI:10.15120/GR-2015-1-FG-CS-01

Status of the SIS100 local cryogenics*

B. Streicher[1], *T. Eisel*[1], *J. C. Velasco*[1], *M. Chorowski*[2], *A. Iluk*[2], *P. Duda*[2], *M. Kauschke*[1], *J. Polinski*[2], *A. Täschner*[1], *F. Wamers*[1], *and H. Kollmus*[1]

[1]GSI, Common Systems: Cryogenics, Darmstadt, Germany; [2]Wroclaw University of Technology, Poland

Introduction

The cryogenic system for the FAIR (Facility for Antiproton and Ion Research) superconducting (SC) SIS100 synchrotron and its first specified components were described in [1]. The design progress, project evolution as well as newly specified components are described in the following sections.

By-Pass Line

By-pass Lines (BPLs) pass each of the six straight warm sections of SIS100 to supply liquid helium and cold electrical connections to the SC quadrupole doublets within these sections. Detailed technical specification [2] concerning the BPL system was prepared and approved at GSI in 2013. Based on this, the in-kind contract was signed between FAIR and the Wroclaw University of Technology (WrUT). In conjunction with the cryogenic group CSCY, the WrUT has worked out a detailed technical design of the first BPL part connecting the cryogenic feed-in point at SIS100 directly to the cold arc magnet (see Fig. 1). The design details and interfaces were settled during the Final Design Review held at GSI in February 2015. It includes the design of process pipes, bus-bars, vacuum vessel, supports and instrumentation. The production of this first component will start during first quarter of 2015 and is supposed to be finished and delivered to GSI before the end of 2015. This component will be a part of the SIS100 String Test set-up tested at Serial Test Facility connecting first dipole and quadrupole. Moreover, a new clamping system to fix the bus-bar pairs was developed at WrUT and is currently being tested at GSI. This clamping system shall be used in the SIS100 BPLs.

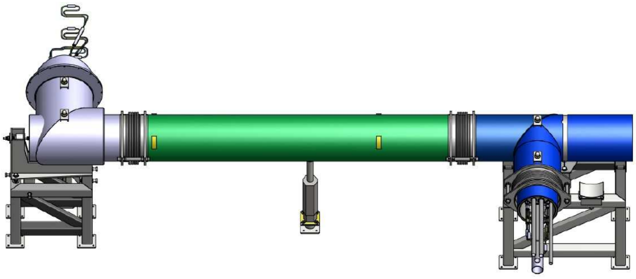

Figure 1: 3D model representation of the final design for BPLP50 (see [2]) made by WrUT.

Current Lead Box (CLB)

In order to supply the electrical connections for 4 types of SC magnets, in total 8 electrical circuits have to be cooled from normal conducting state to the SC state entering the SIS 100 accelerator ring. Devices called Current Lead Boxes perform this duty. The detailed specification of this particular component for the local cryogenic system of SIS100 was finished and submitted to the EDMS system in October 2014 (see [3]). An elaborated 3D model (see Fig. 2) was already prepared at GSI as well as flow scheme and control and instrumentation including basic P&ID. Based on this document, WrUT together with GSI shall prepare this component's design till the end of 2015. The in-kind contract concerning this component is currently being prepared at GSI.

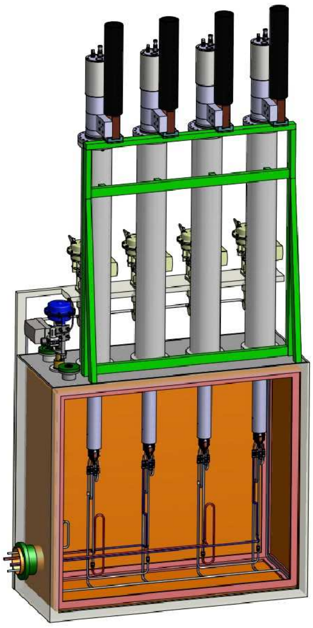

Figure 2: Schematic representation of a SIS100 current lead box specified at GSI (see [3]).

References

[1] B. Streicher et.al., Cryogenics for SIS100 Accelerator, GSI Preprint (http://repository.gsi.de/record/68024)

[2] Detailed Specification of the Local Cryogenic By-Pass System for SIS100 (https://edms.cern.ch/document/1261140/8)

[3] Current Lead Boxes for SIS100 (https://edms.cern.ch/document/1174196/1)

---

* FAIR@GSI PSP code: 2.8.12 and 2.14.8.1.6

DOI:10.15120/GR-2015-1-FG-CS-02

Status and commissioning of the Helium Supply Plant (HeSu) and the Series Test Facility (STF)

A. Breidert[1], *C. Schroeder*[1], *A. Beusch*[1], *M. Kauschke*[1], *B. Streicher*[1], *F. Walter*[1], *and H. Kollmus*[1]
[1]GSI, Common Systems: Cryogenics, Darmstadt, Germany

The Helium Supply Plant (HeSu)

For the FAIR Project a standard helium liquefier with a capacity of approx. 20 l/h has been installed at GSI. The liquefied helium is stored in 3000 l stationary Dewar vessel and transferred to mobile vessels using a decant station. A recovery line has been installed connecting the testing hall via the UHV lab to a 20 m^3 storage balloon. The HeSu will be used for LHe consumers on laboratory scale. At a later stage of the FAIR project the whole liquefier plant will be used for experiments with no direct connection to the campus distribution system.

The contract with Air Liquide was signed in 2013. The installation on site was performed in summer 2014 and the commissioning started in September and was successfully completed in November 2014. The first users appeared already in the same year. Main customers in the next years are supposed to be the CW-Linac, beam diagnostics, and the UHV group.

Figure 1: The HeSu plant. From right to left: purifier cold box and LHe storage

The Series Test Facility (STF)

In order to test the 108 fast-ramped superconducting dipole magnets of the SIS100, a cryogenic test facility has been specified by GSI and manufactured and installed by Linde KT. It is currently under commissioning at GSI with a site acceptance test (SAT) in late spring of 2015.

The overall cooling capacity of the cryo plant is about 1.5 kW (4.5 K equivalent) and can be distributed to four test benches individually. The capacity of the cryogenic system is designed to simultaneously cool down one magnet while another one is being operated at cold state for the cryogenic and magnetic measurements. The other two test benches serve for warming up and for magnet exchange, respectively. Beyond the SIS 100 dipoles, the high flexibility of the setup allows also the testing of other FAIR magnets, like the SIS100 quadrupole modules, the operation of a string configuration or even SuperFRS magnets. The plant is designed for subcooling to 4.4 K at 1.8 bar. The overall capacity is divided into 690 W cooling power at 4.4 K, a liquefaction rate of 6 g/s, and 2 kW cooling power at 50 K to 80 K for shield cooling.

The magnet is placed between feed and end box. The magnet and the end box are moveable on a rail system. The magnet extends into the feed and end box. By using large flanges on both sides of the boxes easy access to the interface area is guaranteed. This design saves space and avoids bellows for the insulation vacuum cryostats.

The magnet is fixed in space on the rail system, while feed and end box have to be flexible to compensate the mechanical tolerances. This is realized by rubber compensators, such as normally used for compressors. Also the jumper line to the feed box is flexible.

The planning started already in early 2012, after the tendering process the kick-off with the contractor took place mid of 2013. After finishing the new annex building SH5 all components were delivered during spring to summer 2014. The first component was the helium cycle compressor with an electrical power consumption of 465 kW, followed by the oil removal system, the gas management panel and the main cold box together with a 3000 l liquid helium Dewar. All this components were placed in the annex building. In front of SH2/SH5 3 buffer tanks were installed, one 100 m³ gaseous helium storage tank for the helium inventory, one 50 m³ gaseous helium storage tank for quench gas and one 40 m³ liquid nitrogen tank for the precooling of the helium in the cold box. In SH2 the cold end of the cryo plant was installed. On a 2nd floor two distribution boxes and the so called string box were placed, left and right hand side two test benches on a rail system with feed and end boxes, see figure 2. In December 2014 all installation work was finished and the point of mechanical readiness was reached and the commissioning phase was started. In spring 2015 the commissioning will be complete and it will end with the side acceptance tests (SAT).

Figure 2: Ground floor: The two right-hand test benches. First floor: The two distribution boxes and the multipurpose terminal.

DOI:10.15120/GR-2015-1-FG-CS-03

THttpServer and JavaScript in ROOT[*]

J. Adamczewski-Musch[1], *B. Bellenot*[2], *S. Linev*[1], *and the FAIR@GSI project*[1]
[1]GSI, Darmstadt, Germany, [2]CERN, Geneva, Switzerland

Introduction

The ROOT [1] software framework is widely used in most HEP experiments. ROOT is also often applied for monitoring and control at different stages of data taking and online analysis. Many such online tasks could be solved with web technologies – http protocols for data exchange, and powerful JavaScript/HTML graphics to implement user interfaces.

JavaScript ROOT

The prominent functionality of JavaScript ROOT (JSROOT) library is the ability to read binary ROOT files and provide interactive ROOT-like graphics in web browsers (Figure 1). Many significant changes and improvements have been implemented in 2014 compared to original JSRootIO [2] code.

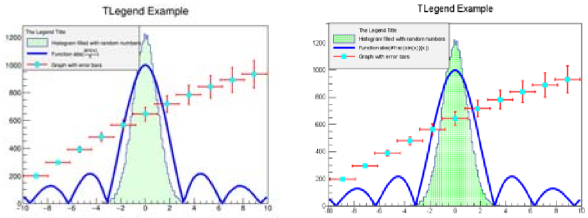

Figure 1: Same canvas, displayed with native ROOT graphics (left) and JSROOT (right)

The I/O part of JSROOT has been organized modular and structurally similar to native ROOT I/O functionality. Most objects stored in binary ROOT files now can be read from the web-browser, using meta-information provided within ROOT files (so-called “streamer-infos”). Several special cases of custom streamers (like TCanvas or TList) are treated in a central place, making it much easier to maintain and extend functionality in the future. It is possible to display and overlay data from different ROOT files in the same browser window.

The graphical part of JSROOT code has been fully rewritten and decoupled from I/O part of the JSROOT library. The main focus was put on flexibility – now JSROOT graphics can be inserted in any webpage, and one can update graphics interactively. Many new features have been implemented, e.g. context menu, statbox update, comfort zooming.

JSROOT code, documentation and examples are available online [3] and with ROOT distribution.

THttpServer class

The new THttpServer class of ROOT implements http protocol by means of embeddable Civetweb [4] server. With simple http requests syntax one could obtain object data from application in different form. (binary, xml, json, png). The TBufferJSON class has been developed to convert ROOT objects into JSON (JavaScript Object Notation), which can be directly evaluated in web browsers.

The user interface for THttpServer has been implemented with JSROOT (Figure 2). One could browse, display, and monitor objects registered to the server. In addition one could execute registered commands (like start/stop analysis or clear histograms) in the server application. There is also the possibility to perform TTree::Draw() on the server and display results in the browser.

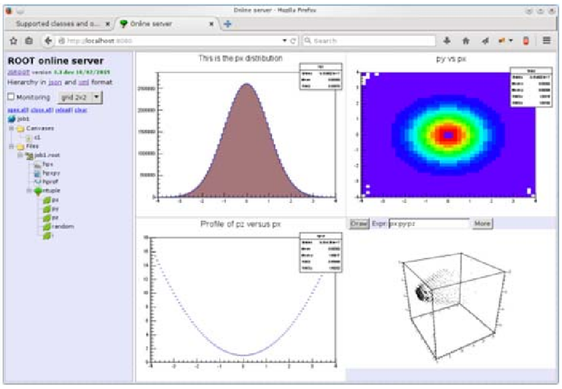

Figure 2. Browser with objects available from httpserver.C macro. The objects hierarchy is on the left side, several displayed objects are on the right. Also tree draw functionality is shown.

Source code, documentation, and several examples for THttpServer are included into the ROOT distribution.

Conclusions and outlook

THttpServer together with JSROOT provide a powerful tool set to create ROOT-based online applications. JSROOT functionality is also used to implement web interface for DABC, MBS and Go4 frameworks [5].

References

[1] ROOT project homepage http://root.cern.ch
[2] B.Bellenot, S.Linev, “ROOT I/O in JavaScript”, Journal of .Physics: Conference Series, vol 513, Proceedings of CHEP 2013, http://iopscience.iop.org/1742-6596/513
[3] JSROOT homepage https://root.cern.ch/js/jsroot.html
[4] Civetweb embeddable webserver, project homepage https://github.com/bel2125/civetweb
[5] S. Linev, “Web interface in DABC”, GSI scientific report 2013, doi:10.15120/GR-2014-1-FG-CS-12

---

[*] PSP codes: SFRS 2.4, ILIMA 1.2.2.4, R3B 1.2.5.1.4, 1.2.6.6, 1.2.5.1.2, HADES 1.1.2.4

DOI:10.15120/GR-2015-1-FG-CS-04

Status and developments for DAQ system MBS v6.3[*]

J. Adamczewski-Musch[1], N. Kurz[1], S. Linev[1], and the FAIR@GSI project[1]
[1]GSI, Darmstadt, Germany

Introduction

The software framework MBS (Multi Branch System) has been established as common DAQ system at GSI for more than 20 years [1]. Various experiments apply MBS for data taking. Besides supporting the users when setting up the experiment, the MBS framework is continuously being improved and developed due to changed requirements. This article reports the most recent experiences and ongoing developments of MBS.

MBS installation update

In 2014 19 new MBS systems (12 VME based, 7 PC/PCI Express based) have been installed and came into operation at GSI and worldwide. In addition 9 MBS systems have been upgraded to the MBS production version or to new operating system versions. Furthermore three travel MBS systems for experiments outside of GSI have been set up.

Developments

Improved PCI Express (PCIe) readout

The MBS driver software for PEXOR/KINPEX PCIe optical receiver boards has been improved for x86 Linux platforms [2]. This consists in a new kernel module *mbspex* with corresponding C library. Additionally, a command line tool *gosipcmd* allows front-end configuration and controls concurrently to running MBS DAQ. If the MBS user readout function calls *mbspex* library functions only, a safe read-out will be possible simultaneous with external control system access. However, backward compatibility to existing readout code is provided by the new driver.

White rabbit timing system

In the GSI test beam campaign 2014 synchronisation with White Rabbit timing receivers (WTR) [3] has been introduced successfully at the experiment Land/R3B for the first time. With the help of the VETAR (VME) and PEXARIA (PCI Express) WTRs several independent MBS systems running with global triggers systems have been synchronised.

In addition a prototype of the R3B silicon tracker (SITR) could be included in the White Rabbit time stamp scheme. The SITR is designed to run without global, but with individual detector input signal triggers (local triggers). It provides for each signal over threshold a charge (energy) and a White Rabbit time stamp.

To accomplish synchronisation with the MBS systems running with global triggers, two LVDS signal lines have been sent from a VETAR WTR into the SITR: 1) White Rabbit controlled 200 MHz for time counting; 2) A 100 KHz pulse train, phase stable with the 200 MHz clock. The 64 bit White Rabbit time reference is sent serially encoded in each ten microsecond interval of consecutive pulses.

MBS systems running with global triggers and a system running with local triggers could be successfully synchronised. This serves as blueprint for FAIR data acquisition setups, where these conditions will be standard.

Controls with DABCs

Control and monitoring MBS nodes via tcp/ip socket from remote is since long time possible: a status server would deliver run state and rate information to monitoring clients like Go4, and multiple MBS nodes would receive commands via prompter socket. Additionally, for DABC controls two new channels have been introduced for MBS v6.3: a remote log server ("logrem") sending log output to the control client; and a remote command channel ("cmdrem") in the MBS dispatcher process that inserts client commands beside the local MBS console input. These new channels may be started from the beginning by command line argument ("*mbs -dabc*"), or started from running dispatcher session by new commands ("*start logrem*", "*start cmdrem*"). DABC library offers modules to connect these channels. The DABC executable *mbscmd* can either control the MBS dispatcher process via *cmdrem* socket, or the MBS prompter process via the already existing multi-node control socket.

Webserver GUI

The MBS control sockets may be accessed by a separate DABC process running an http web server [4]. The DABC web server will forward http command requests via the *cmdrem* channel to MBS dispatcher. It will retrieve log messages from MBS *logrem* channel and DAQ status from MBS status socket, and may export this information to the web. This allows remote control of each single node dispatcher from web browser. In addition to the default DABC tree display of these web objects, a dedicated MBS control GUI has been developed for this DABC web server using JavaScript with the *jQuery UI* environment.

---

[*] PSP codes: SFRS 2.4, ILIMA 1.2.2.4, R3B 1.2.5.1.4, 1.2.6.6, 1.2.5.1.2.5, SPARC 1.3.1.3.11,, SD-SEM 2.3.6.5.1.6.30

DOI:10.15120/GR-2015-1-FG-CS-05

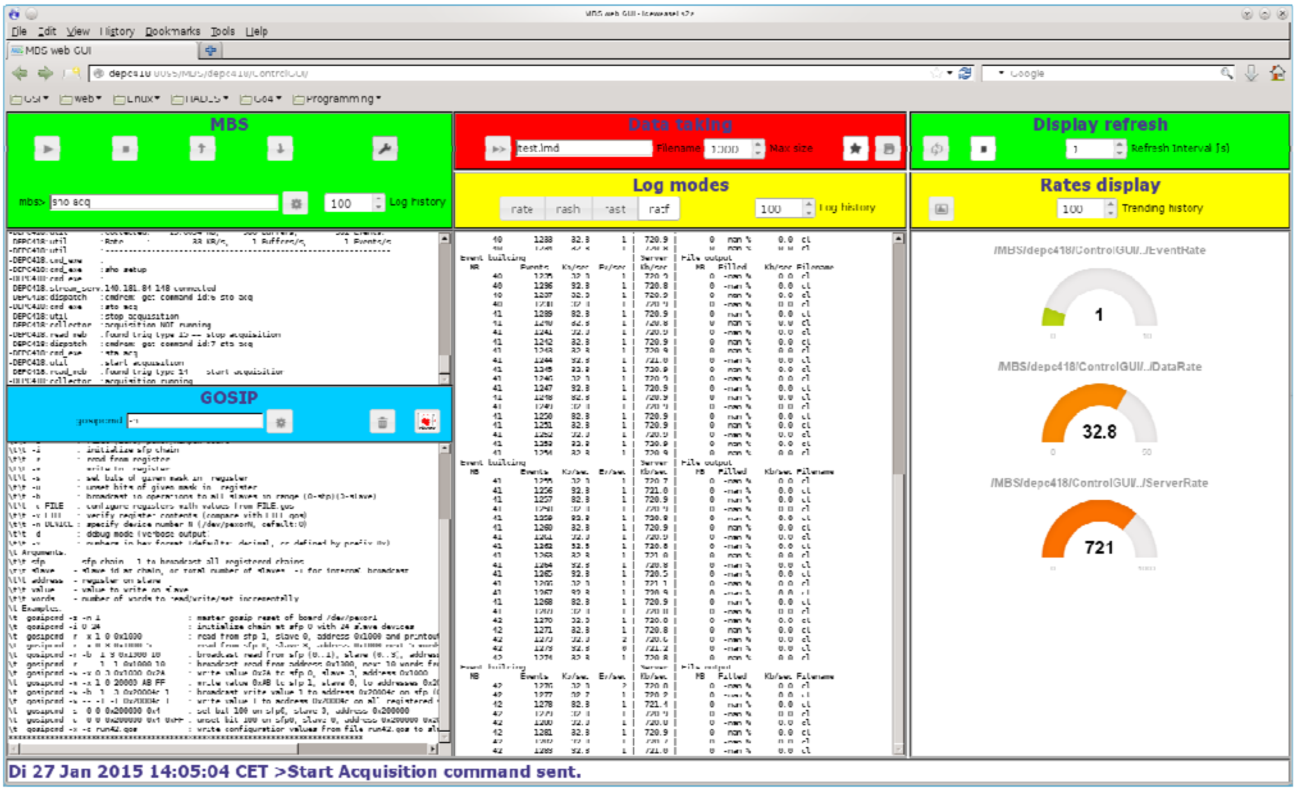

Di 27 Jan 2015 14:05:04 CET >Start Acquisition command sent.

Figure 1: The MBS web browser control GUI

Figure 1 shows a screenshot of such a GUI. The dispatcher interactive command line appears in the browser and offers additional shortcut buttons for mostly used commands, like start/stop acquisition, *@startup*, *@shutdown*. Data taking commands and status is shown in a separate tile with control buttons for open/close file, file mode and RFIO/local disk set up. The run or file status of the acquisition is visualized by red or green background colours of the control tiles. Data rates are displayed both as graphical gauge or trending rate meters, and as text terminal output of the previously known *rate*, *rash*, *rast*, or *ratf* shell commands of MBS. Automatic refresh frequency of the browser display can be set in a dedicated box. Moreover, when running on MBS Linux PC, the DABC web server also offers to call the frontend configuration tool *gosipcmd* [2], so a command line and output box for this tool can optionally be shown in the browser. Additionally, a dedicated frontend configuration GUI, like POLAND setup [2], may be started by a button in a different browser window.

Outlook

The new features described above are partially already installed at GSI as development version 6.x (“mbslogin deve”) and can be tested. They will be part of the future production version MBS 6.3 to be released in 2015. Moreover, adjustments to new PC hardware and 64bit Linux are currently under work and will be available with this release.

References

[1] Multi Branch System home page: *http://www.gsi.de/mbs*

[2] J. Adamczewski-Musch, N. Kurz, S. Linev, “mbspex driver software for PEXOR/KINPEX readout boards”, this report

[3] D. Beck et al., “Paving the Way for the FAIR General Machine Timing System”, GSI scientific report 2013, doi:0.15120/GR-2014-1-FG-CS-08

[4] S. Linev, “Web interface in DABC”, GSI scientific report 2013, doi:10.15120/GR-2014-1-FG-CS-12

DOI:10.15120/GR-2015-1-FG-CS-05

mbspex driver software for PEXOR/KINPEX readout boards[*]

J. Adamczewski-Musch[1], N. Kurz[1], S. Linev[1], and the FAIR@GSI project[1]
[1]GSI, Darmstadt, Germany

Introduction

The GSI PEXOR/KINPEX (“PEX family”) PCIe boards were designed for data read out from various detector front-ends via optical SFP connections to an X86 PC host [1]. Communication between PEX and front-end hardware is handled via the *gosip* protocol [2]. For triggered data acquisition, the trigger module TRIXOR can be connected to PEX. The PEX boards have been applied for many years with the data acquisition framework MBS [3]. An improved Linux kernel module driver *mbspex.ko* has been implemented such that concurrent access from MBS and separate control processes is now possible. The new application library *libmbspex* provides higher level functionality to user space. Moreover, a command line tool *gosipcmd* allows inspection and configuration of any front-end register from an interactive shell, GUI, or remote web server. Fig. 1 shows these *mbspex* software components in a typical Linux host PC with MBS DAQ and several control applications.

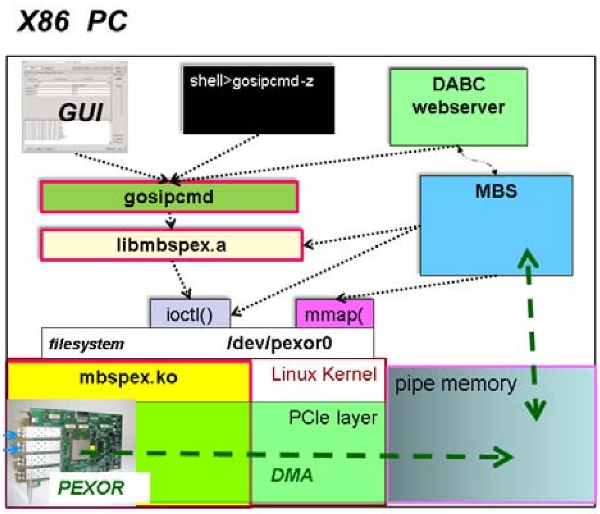

Figure 1: Overview of *mbspex* software components on an X86 Linux node

Linux device driver

Access of any user program to PEX and the connected front-end hardware requires device driver software, usually consisting of a kernel module and optionally a corresponding user space library.

Kernel module

The *mbspex* kernel module merges the previous simple driver *pexormbs* for MBS data acquisition with the larger *pexor* driver for DABC and FESA frameworks [4]. It implements all basic *gosip* protocol functionalities, like initialization of chains, front-end field bus access, and “token” data request, as *ioctl()* functions. Additionally, there are DMA operations to send data to any destination pointer in physical memory (MBS "pipe", see Fig.1). All these *ioctl()* calls are protected by a kernel mutual exclusive semaphore. This allows concurrent access to the PEX device without crashing the system.

Since the kernel module keeps track of all initialized devices at the sfp chains, a “broadcast” i/o is possible: with one *ioctl()* the same value can be written to the same address on all devices of a chain, or of all chains. Furthermore, several registers of each frontend can be configured at once from a single *ioctl()* data bundle. This can be combined with broadcast mode and allows in principle to safely reconfigure all frontends at once while data acquisition read out is running.

On the other hand, all *ioctl()* calls of *pexormbs* driver are remained in *mbspex* driver with the same key values. So any legacy MBS code may ignore the “locked” *ioctl()* features and still work directly on the PEX board control registers. For this purpose file operation *mmap()* is still implemented to map the PEX board memory to virtual addresses of the MBS process. Alternatively, *mmap()* can map any physical PC memory to user space. MBS is using this to access the reserved “pipe” memory for subevent buffering.

Finally, *mbspex.ko* exports some PEX and TRIXOR registers via the kernel sysfs feature. The properties can be inspected by reading corresponding file handles under directory */sys/class/mbspex/*.

User library

The *libmbspex* user space library is written in C language and uses the file system handle */dev/pexor0* with *ioctl()* calls as interface to the kernel module (see Fig.1). It provides high level functions for register i/o with the PEXOR board, with any single front-end, or with all configured front-end boards in a “broadcast” mode. Additionally, *gosip* “token mode” data transfer from the front-end buffers and DMA transfer to PC host memory can be initiated by simple function calls. All these functions are protected against concurrent access already in the kernel module. So different control applications like *gosipcmd* may link and use *libmbspex* simultaneously. Moreover, MBS user readout code can be based on *libmbspex* function calls only.

Application for MBS DAQ

The MBS DAQ framework does not operate the front-end hardware directly, but just ensures that user read-out functions are called whenever module TRIXOR receives a trigger signal. It does not require *libmbspex* functionali-

---

[*] PSP code: SD-SEM 2.3.6.5.1.6.30.

DOI:10.15120/GR-2015-1-FG-CS-06

ty, but interacts with *mbspex.ko* by means of *ioctl()* and *mmap()* file operations. They are merely applied to wait for next trigger, and to map the pipe buffer physical memory (Fig. 1). These calls have been kept compatible with the previous kernel module *pexormbs.ko*, so no modifications to MBS framework have been needed. Also any legacy user readout code will work with *mbspex.ko*, since memory mapped access to PEX control registers is still supported.

However, to provide safe concurrent frontend access between MBS and external control tools, adjustments in MBS user readout code are necessary. Here any token data request must use primitive function calls of *libmbspex*. An example of such readout code has been provided for POLAND/QFW front-ends of FAIR beam diagnostic projects [5].

Command line tool gosipcmd

The command line tool *gosipcmd* works as shell application on top of *libmspex* (Fig.1). It provides interactive command access to PEX board and the SFP-connected frontend registers via gosip protocol. The resulting values are printed to terminal. The main functionalities cover:

- reset PEX board, initialize SFP chains
- read/write any address on frontend slave
- incremental read/write from start address
- register bit manipulation
- broadcast mode: read/write same register at all connected frontends
- configure / verify with script files *.gos
- plain or verbose, hex or decimal output mode

A more complete list of available options can be printed using “gosipcmd -h”. At GSI *gosipcmd* is already provided at X86 Linux installations (hosts “X86L-nn”) for MBS v6.2.

Frontend control GUI

Since *gosipcmd* uses *stdin*/*stdout* as plain text data interface, it can serve as base for any special front-end configuration script, or graphical user interface (GUI) application.

POLAND GUI

An example of such frontend GUI has been developed for configuration of POLAND charge to frequency converters of beam diagnostics [5]. It is designed with Qt4 graphics library and shown as screenshot in Fig.2. Since it uses *gosipcmd* calls only, it is decoupled from the actual *mbspex* library version and may work both with *mbspex* and *pexor* driver installations, i.e. with MBS or FESA read out. The *stdout* of *gosipcmd* is redericted to an embedded text window which allows verbose register inspection, and dumping of event data buffers. PEX board and SFP chains may be initialized on click. Each POLAND frontend device can be selected and the meaningful registers displayed and manipulated. Moreover, it is possible to broadcast same register settings to all devices, as this is already supported at kernel module level. Also configuration scripts of *gosipcmd* (*.gos) may be selected and applied from the GUI.

The POLAND GUI is installed at GSI for MBS v6.2 on X86 Linux and available via alias “poland”.

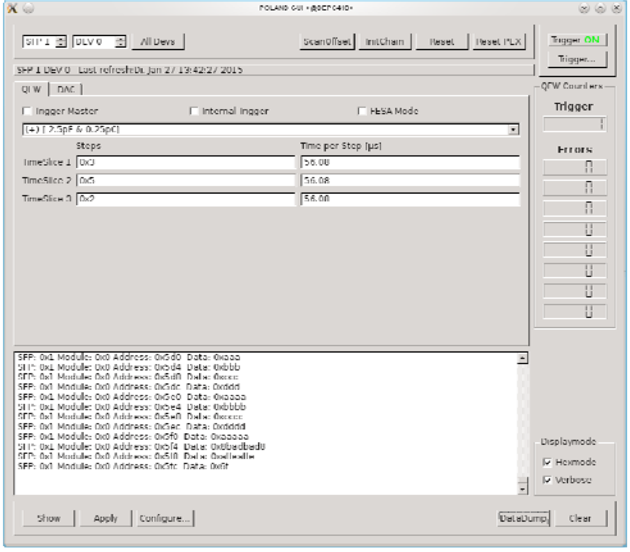

SFP 1 DEV 0 Last refresh:Di Jan 27 13:42:27 2015

☐ Trigger Master ☐ Internal Trigger ☐ FESA Mode

(+) [2.5pF & 0.25pC]

	Steps	Time per Step [µs]
TimeSlice 1	0x3	56.08
TimeSlice 2	0x5	56.08
TimeSlice 3	0x2	56.08

```
SFP: 0x1 Module: 0x0 Address: 0x5d0  Data: 0xaaa
SFP: 0x1 Module: 0x0 Address: 0x5d4  Data: 0xbbb
SFP: 0x1 Module: 0x0 Address: 0x5d8  Data: 0xccc
SFP: 0x1 Module: 0x0 Address: 0x5dc  Data: 0xddd
SFP: 0x1 Module: 0x0 Address: 0x5e0  Data: 0xaaaa
SFP: 0x1 Module: 0x0 Address: 0x5e4  Data: 0xbbbb
SFP: 0x1 Module: 0x0 Address: 0x5e8  Data: 0xcccc
SFP: 0x1 Module: 0x0 Address: 0x5ec  Data: 0xdddd
SFP: 0x1 Module: 0x0 Address: 0x5f0  Data: 0xaaaaa
SFP: 0x1 Module: 0x0 Address: 0x5f4  Data: 0x0badbad0
SFP: 0x1 Module: 0x0 Address: 0x5f8  Data: 0xdeadbeef
SFP: 0x1 Module: 0x0 Address: 0x5fc  Data: 0x6f
```

☑ Hexmode
☑ Verbose

Figure 2: POLAND Qt4 GUI using *gosipcmd* interface

DABC webserver GUI

Besides such local control GUI, a remote control of *gosipcmd* has been implemented as gosip plug-in for the webserver of software framework DABC [6]. This webserver runs as independent DABC process on the MBS Linux node (Fig.1) and provides a full interface to the local *gosipcmd* via HTTP request and response. A web browser version of the POLAND GUI has been implemented for this mechanism, using JavaScript with *jQuery UI* plug-ins (Fig.3).

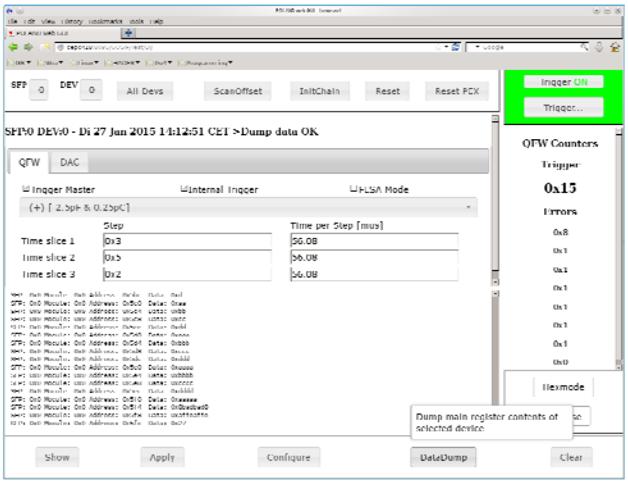

SFP:0 DEV:0 - Di 27 Jan 2015 14:12:51 CET >Dump data OK

☐ Trigger Master ☐ Internal Trigger ☐ FESA Mode

(+) [2.5pF & 0.25pC]

	Step	Time per Step [mus]
Time slice 1	0x3	56.08
Time slice 2	0x5	56.08
Time slice 3	0x2	56.08

Trigger 0x15

Errors 0x8 0x1 0x1 0x1 0x1 0x1 0x1 0x0

Dump main register contents of selected device

Figure 3: POLAND web GUI at DABC web server

Additionally, a generic *gosipcmd* browser command line GUI will be available as part of the DABC webserver controls for MBS v6.3 [7].

DOI:10.15120/GR-2015-1-FG-CS-06

References

[1] J. Hoffmann, N. Kurz, S. Minami, W. Ott, and S. Voltz, “PCI-express Optical Receiver”, GSI scientific report 2008, p 258.

[2] S. Minami, J. Hoffmann, N. Kurz, and W. Ott, “Design and Implementation of a Data Transfer Protocol via Optical Fibre“, presented at the 17th IEEE Real-Time Conference, Lisboa 2010, Paper PDAQ-31

[3] Multi Branch System (MBS) home page: http://www.gsi.de/mbs

[4] J. Adamczewski-Musch, H.G.Essel, S. Linev, “The DABC Framework Interface to Readout Hardware”, IEEE TNS Vol.58, No.4, August 2011, pp. 1728-1732

[5] S. Löchner, J. Adamczewski-Musch, H. Bräuning, J. Frühauf, N. Kurz, S. Linev, S. Minami, M. Witthaus, “POLAND - Low Current Profile Measurement Readout System”, GSI Scientific Report 2013, doi:10.15120/GR-2014-1-FG-CS-13

[6] Data Acquisition Backbone Core (DABC) home page: http://dabc.gsi.de

[7] J. Adamczewski-Musch, N. Kurz, S. Linev, “Status and developments for DAQ system MBS v6.3”, this report

DOI:10.15120/GR-2015-1-FG-CS-06

Applications of the TRB3 and Associated Front End Electronics in Recent Beam Times*

Michael Traxler[1], *Joern Adamczewski-Musch*[1], *Matthias Hoek*[2], *Marcin Kajetanowicz*[3], *Grzegorz Korcyl*[3], *Sergey Linev*[1], *Ludwig Maier*[4], *Jan Michel*[5], *Andreas Neiser*[2], *Marek Palka*[3], *Manuel Penschuck*[5], *Pawel Strzempek*[3], *Cahit Ugur*[1], *and FAIR@GSI Division*[1]

[1]GSI, Darmstadt, Germany; [2]Institute for Nuclear Physics, Johannes Gutenberg-Universität Mainz, Germany; [3]Institute of Physics, Jagiellonian University, Poland; [4]Physik Department E12, Techn. Univ. München, Germany; [5]Institut für Kernphysik, Goethe-Universität Frankfurt, Germany

The TRB3 platform [1] with its associated Front-End-Electronics has been proven in the recent years to be very useful for many applications and has been successfully used by several experiments/groups in 2014.

The HADES collaboration performed a pion test beam experiment in May 2014 and two production pion beam runs in July and August/September 2014, where the TRB3 was used by several detector systems. The HADES pion tracker (see [2]) located in the NE5 area in front of the HADES experiment was used to determine the momentum of each pion. The FEE, based on the n-XYTER ASIC, was read out by the TRB3 and seamlessly integrated in the HADES DAQ, where the TRB3 had a pure digital task.

The pion hodoscope used the Padiwa-AMPS FEE board together with the TRB3 (see [3]) for precise TDC and QDC measurements. The diamond start detector employed the TRB3 for the precise T0 time determination.

The CBM-TOF collaboration used a large setup of 7 TRB3 boards together with 14 TOF-FEE (detector specific strip-down of the TRB3) modules to perform RPC-detector test beam times in April and October 2014. The PADI-FEE delivered the LVDS signals to the TRB3 based system for digitisation. The desired time precision as well as the required DAQ-event rates have been reached during the second beam time.

The PANDA-Barrel-DIRC group set up a system of 20 MCP-PMTs (each 64-channel) with PADIWAs as FEE and 24 TRB3s for test beams in April and July/September 2014 to test the DIRC optics in beam together with the readout electronics.

The CBM-RICH group set up a RICH-detector prototype at CERN with 16 64-channel MA-PMTs with a Padiwa + TRB3 (18 were used) based readout. An online display of the RICH rings is shown in fig. 1. Preliminary analysis results show good efficiency for RICH rings.

Additional to these experiments and test beams the TRB3 has been used in other production experiments like the DIRC-Detector in the WASA experiment in Jülich.

Furthermore, a larger number of test setups of various groups exists, who used the TRB3 platform in 2014 to read out their detectors and plan to use the TRB3 in their final setups. Just to have some of these groups mentioned: PANDA STT, CBM-MVD, HADES-ECAL, MUSE collaboration, A1 Neutron detector, Coimbra-PET, Cracow-PET, etc.

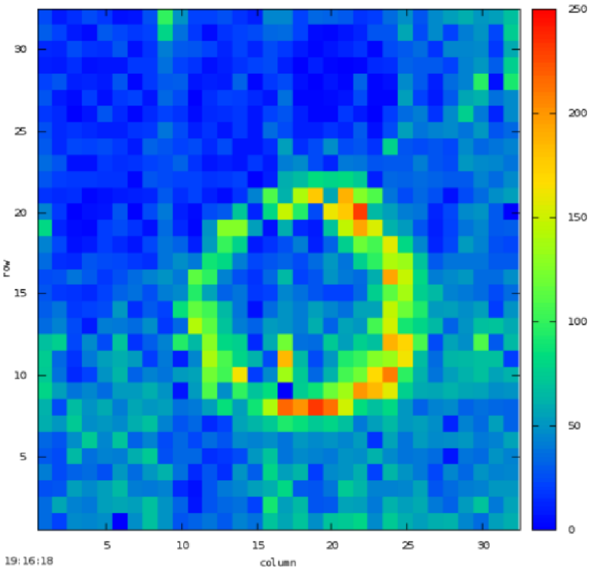

Figure 1: Online heat map of hits measured in the the array of 1024 MA-PMT channels of the CBM-RICH detector. The ring is visible during spills from the SPS beam.

All these experiences, together with the users, improved the platform substantially. The lessons learned jointly with new developments on the TDC side (see [4] will also lead to developments like a crate based TRB3 system "TRB3SC" and the joint effort for an optimized FEE+TDC+DAQ electronics "DIRICH" for PANDA-DIRC, CBM-RICH and HADES-RICH.

References

[1] All information about the TRB3 can be found here: http://trb.gsi.de

[2] L. Fabbietti et al., "Integration of the Pion-Beam Tracker into the HADES DAQ", GSI-SR2013-NQM-HADES-10, GSI Scientific Report 2013

[3] M. Traxler et al., "A Precise Multi-Channel QDC FEE utilizing FPGAs as Discriminators and Delay Elements Based on the TRB3 as TDC and Readout Platform", GSI-SR2013-NQM-HADES-13, GSI Scientific Report 2013

[4] C. Ugur et al., "FPGA Based Multi-Channel TDC Development", GSI Scientific Report 2014

---

* Work supported by FAIR@GSI PSP codes: 1.4.1.5, 1.1.2.4

DOI:10.15120/GR-2015-1-FG-CS-07

Numerical simulations of a field emitter-based extractor gauge for pressure measurements in cryogenic vacuum systems

M. Lotz[1,2], St. Wilfert[1], A. Krämer[1], and O. Kester[1,2]
[1]GSI, Darmstadt, Germany, [2]Goethe University of Frankfurt, Germany

Pressure measurement in the UHV and XHV range in cryogenic vacuum environments has always been considered a metrological problem. However, especially for the cryogenic beam vacuum sections of the SIS100 a pressure measurement would be useful since local pressure rises caused by dynamic vacuum can lead to self-amplifying beam loss effects.

In general, conventional hot-filament ionization gauges can be used in cryogenic vacuum systems. However, during operation they generate a huge heat load causing numerous disadvantages in low temperature systems. Therefore, an ionization gauge was developed where the heat-generating filament was replaced by a non-thermal cathode. The electron release mechanism of this cathode type is based on field emission. It has been shown in a previous study [1] that it is possible to read pressures under cryogenic vacuum conditions using this type of gauge. Unfortunately, the lower pressure measuring limit of the used gauge is too high to measure the low pressures expected in the future SIS100. This was caused inter alia by the low electron current relative to the current used in a commercial extractor gauge with thermionic filament. To increase the current, the carbon nanotube-type (CNT) field emitter will be replaced by a field emitter array (FEA), which is developed at the Paul Scherer Institute (PSI) in Switzerland.

The FEA consists of an array of micro-structured molybdenum tips and has an integrated micro grid for electron extraction at a very short distance. Therefore, even small extraction voltages between 100-150 V are sufficient to generate an emission current in the range of mA. These emitters were repeatedly tested at PSI and showed promising emission properties [2].

Numerical simulations on the previously studied CNT-based gauge have been carried out using the program suite *AMaze*. The results showed that in this gauge configuration many electrons directly hit the anode grid end closure without the typical oscillation within the ionization volume, i.e. the volume inside the anode grid (Figure 1).

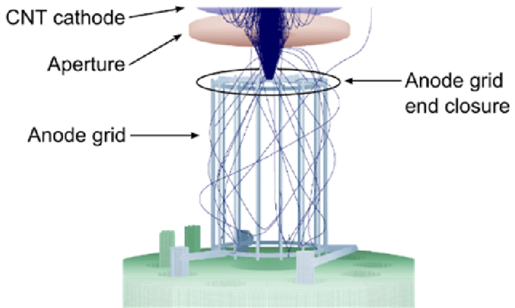

Figure 1: Electron trajectories in the CNT-based extractor gauge.

Since ions generated outside the ionization volume do not reach the ion collector electrode, the detectable pressure dependent ion current is very low. In order to increase the ion current signal the electrons must run on elongated paths through the ionization volume. This can be facilitated by a change of the cathode position. Therefore, an improved gauge design is developed in which three individual field emitter spots are arranged as a ring around the anode grid. This geometry is similar to that of conventional extractor gauges with ring-shaped thermionic cathodes. Numerical simulations on this improved gauge design have confirmed the considerations on the electron trajectories within the gauge (Figure 2). As a result, the gauge sensitivity should be substantially increased relative to the CNT-based extractor gauge previously investigated.

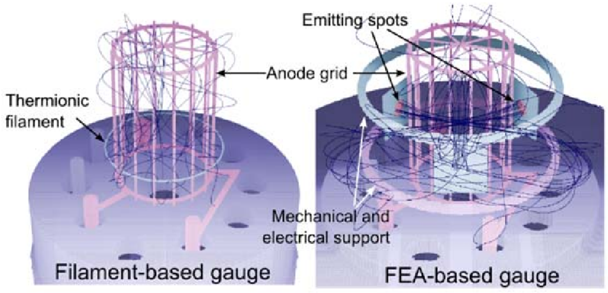

Figure 2: Comparison of electron trajectories in a FEA-based and a filament-based extractor gauge.

The improved gauge design, as shown in Figure 3, will be realized and studied extensively in terms of its operating performance in both room temperature and cryogenic vacuum environments. The experimental investigations will provide information on whether the lower pressure measuring limit is shifted to significantly lower pressures by the modifications made.

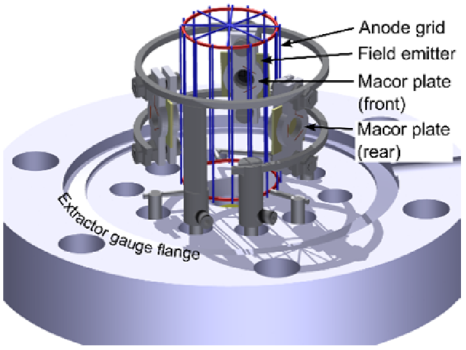

Figure 3: The improved FEA-based extractor gauge.

References

[1] Lotz, M. *et al.*, GSI Report 2013-1, 263 p. (2013)
[2] Kirk, E. *et al.*, J. Vac. Sci. Technol. B 27, 1813 (2009)

DOI:10.15120/GR-2015-1-FG-CS-08

New tests of large area Continuous Position Sensitive Diamond Detector

M. Ciobanu[1], M. Pomorski[2], E. Berdermann[3], C. Bunescu[1], H. Comisel[1], V. Constantinescu[1], M. Kiš[3], O. Marghitu[1], M. Träger3, K-O.Voss[3]and P.Wieczorek[3]

[1]ISS, Bucharest, Romania; [2]CEA, Saclay, France; [3]GSI, Darmstadt, Germany

The first Continuous Position Sensitive Diamond Detector (CPSDD) was made on a single crystal (sc) based material [1]. The high efficiency of sc provides a high enough Signal to Noise ratio (S/N) to fully test the CPSDD with alpha particles.

The first Large Area CPSDD (LACPSDD) was made on a 30 x 30 mm^2 polycrystalline (pc) diamond plate [2], obtained by chemical vapor deposition. In beam tests with ^{54}Ni 1.7AGeV particles it shows an ion rate limitation due to the detector time constant.

We made two new pc LACPSDD, one having 10 x 10 mm^2 (x 110 μm) and the second one (Fig. 1) having 20 x 20 mm^2 (x 180 μm). On each detector side a DLC layer is deposited, equipped with two metallic charge collection electrodes. The relative impact position can be obtained by charge division measurement. Each detector is connected to four charge sensitive amplifiers (CSA).

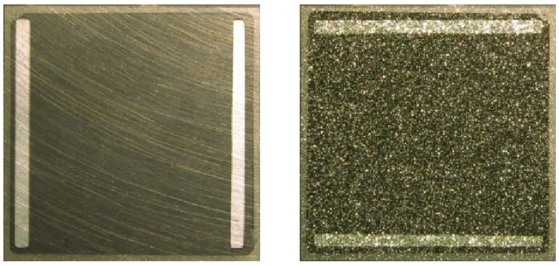

Figure 1: The 20 x 20 mm^2 LACPSDD. Left: view of the substrate side. Right: view of the growth side. On each side there are visible the DLC layer (dark) and the metallic electrodes for charge collection (light). The two pairs of metallic electrodes are oriented at 90°. The DLC layer has $R_D \sim 30$ KΩ/□, and capacitance between layers $C_D \sim 100$ pF.

Tests with alpha particles highlighted that the induced signal delay depends on particle impact position: it is maximal in the centre of the detector and minimal near the electrode. Since the peaking time of the CSA must be greater than the maximal delay, we have modified all the used CSAs [3] to have a 1.5 μs peaking time thus minimizing the ballistic deficit. We obtained a very good correlation between the total collected charges by the two layers and found that the main limitation is due to the small value of the S/N i.e. maximum of 16 in case of alpha particles (the energy lost by an alpha particle is 5.486 MeV, equivalent to an induced signal charge of approx. 67 fC). In addition, the pc material has a broad dispersion of the detection efficiency.

Detector was also tested in ^{12}C micro-beam at 11.4 MeV/A beam energy [4], which provides approx. 25 times larger S/N ratio for stopped particles. We have manually positioned the beam into 62 discrete positions and used the automatic beam micro-sweeps in small rectangles of 280 x 230 μm^2. Subsequently, the data were processed as follows:

1. Electrical calibration by using a pulse and 4 ways distributor; offsets and different gains were corrected.
2. For each position, the median centre (x.y) and standard deviation $\sigma_{x,y}$ were obtained. Data outside the centre $\pm 4\sigma_{x,y}$ and outside collecting strips were ignored.
3. The remaining points were fitted to 2D Gaussian distributions, providing higher accuracy for estimates of the measured centres.
4. For each of the 62 micro-beam positions, an error vector is derived, based on the known micro-beam focus and on the fitted actual position of the centre.
5. The x and y components of the error vectors are fitted by series expansions of 2D Legendre polynomials of 5th degree, which provides a continuous 2D coverage.
6. All data points that were not filtered out at step 2 were corrected by continuous 2D error vector (Fig. 2).

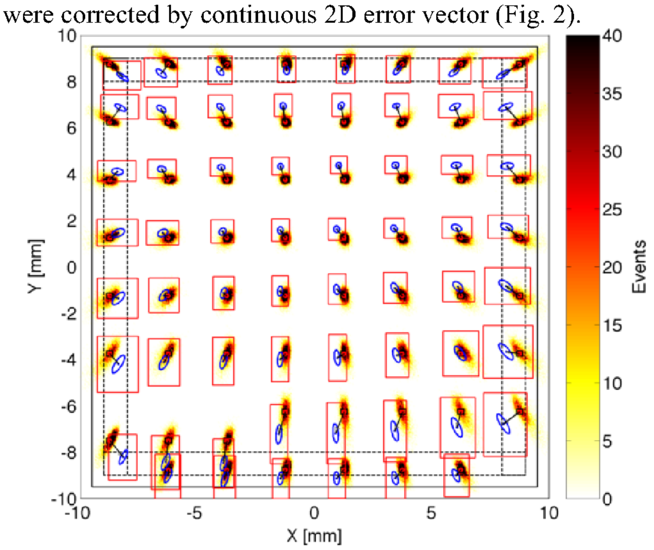

Figure 2: The original (blue contours), micro-beam injection frames (red) and reconstructed spots, after electrical calibration, data filtering (red rectangle contours) and geometrical calibration.

After correction, the 62 measured distributions agree very well with the micro-beam injection frames.

References

[1] M. Pomorski et al., Phys. Stat. Sol. A, 206, pp. 2109-2114, (2009).
[2] M. Ciobanu et al., GSI-Sci. Rep. 2012, pp. 213.
[3] M. Ciobanu et al., IEEE NSS Conf. Rec., N30-20, pp. 2028-2032, (2008).
[4] M. Ciobanu, Large Area Continuous Position Sensitive Diamond Detector Tests (2014), http://www-adamas.gsi.de/index.php?mgid=6#ADAMAS03

DOI:10.15120/GR-2015-1-FG-CS-09

Femtosecond laser enhanced transient current technique*

S. Sciortino[1,2,#], *S.Lagomarsino*[1,2], *C. Corsi*[1,3], *M. Bellini*[4], *T. Apostolova*[5], *E. Berdermann*[6], *C. J. Schmidt*[6], *M. Kis*[6], *M. Träger*[6], *R. Visinka*[6]
[1]Department of Physics, Florence, Italy; [2] INFN, Florence, Italy; [3]LENS, Florence, Italy; [4]INO-CNR Florence, Italy; [5]INRNE, Sofia, Bulgaria; [6]GSI, Darmstadt, Germany

The aim of this work is to understand the processes involved in laser irradiation of diamond below and close to the graphitization threshold. The study is performed under the same conditions of the experimental procedure used to produce 3D diamond detectors [1], in order to improve the technique of preparation of 3D diamond sensors with optimal performances.

To this purpose a Transient Currents Technique (TCT) has been used to measure laser-induced current signals in a diamond detector, in a wide range of laser intensities, from low fields up to the diamond graphitization threshold, at different bias voltages.

The current transients vs. time and the overall charge collected have been recorded to be compared with theoretical simulations.

Transient currents were produced by laser irradiation in a 500 μm thick monocrystalline diamond detector, biased at different voltage values, from 0 to 600 V.

A Ti:Sa mode-locked laser source has been used for excitation, with central wavelength 800 nm, pulse width 30 fs, repetition rate 1000 Hz. The energy densities at a focus of 8 μm diameter are in the range of 0-8 J/cm^2, i.e., the maximum energy per pulse was 4 μJ.

The current vs. time was acquired by a broadband (6 GHz) oscilloscope.

At low laser fields a 2.5 GHz, 40 dB amplifier was used. In this way it was possible to span on four order of magnitude of current intensity. The lower current signal detectable was 0.4 μA and the highest current 3 mA.

The current transients are observed in a time window increassing from 25 ns to 1.2 μs as the energy per pulse goes from 0.1 μJ to 4 μJ. This increase is due to the high density of the plasma generated by the field and the mutual attraction of holes and electrons.

A semi-quantitative model which accounts for these two processes has been developed to fit the current lineshapes.

Figure 1 shows the plot of the collected charge vs. the energy per pulse I at a 500 V bias voltage. This has been determined from the collected charge by integrating the current transients. The slope of the curve up to 1 μJ is fitted with a power trend $Q \propto I^m$, with an exponent m = 4.4, pointing out that the excitation is a mixed non-linear effect involving four and five photon ionizations.

This is consistent with the fact that the frequency emission of the laser corresponds to a broad photon energy range centered at 1.55 eV and the direct bandgap of diamond is about 7 eV, so that at least four photons are required to excite free carriers. We also observe a flattening of the curve at higher laser intensity. This is probably due to the electron-hole recombination occurring during the very long transients, typical of the high energy irradiation pulses.

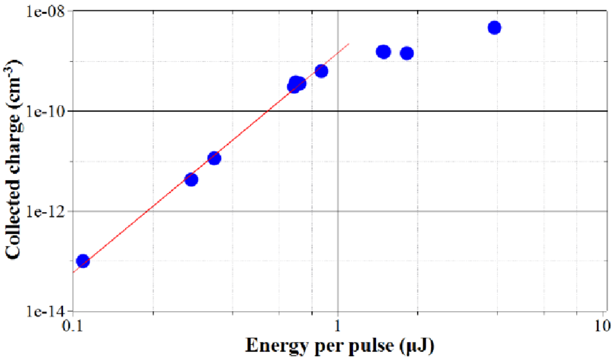

Figure 1: Collected charge vs. energy per pulse

Further measurement aimed to reach the graphitization threshold are under way.

Theoretical modeling aimed to simulate the experimental conditions of excitation and graphitization is also in progress.

References

[1] S. Lagomarsino, M. Bellini , C. Corsi , F. Gorelli , G. Parrini, M. Santoro, and S. Sciortino, Appl. Phys. Lett. 103 (2013) 233507.

---

* Work supported by EU (HadronPhysics3 project No. 283286) and GSI (Detector Technology and Systems Platform) and INFN Italy (experiment 3D_SOD)

#silvio.sciortino@unifi.it

DOI:10.15120/GR-2015-1-FG-CS-10

DOI:10.15120/GR-2015-1-FG-CS-10

JCR publications to the programme matter and universe published in 2014

See http://repository.gsi.de for more information.

[1] B. Abelev et al. Performance of the ALICE experiment at the CERN LHC. *International journal of modern physics / A*, 29(24):1430044, 2014.

[2] B. Abelev et al. Measurement of charged jet suppression in Pb-Pb collisions at $\sqrt{s_{NN}}$ = 2.76 TeV. *Journal of high energy physics*, 1403(3):13, 2014.

[3] B. Abelev et al. Multiparticle azimuthal correlations in p-Pb and Pb-Pb collisions at the CERN Large Hadron Collider. *Physical review / C*, 90(5):054901, 2014.

[4] B. Abelev et al. Suppression of ψ(2S) production in p-Pb collisions at $\sqrt{s_{NN}}$ = 5.02 TeV. *Journal of high energy physics*, 2014(12):73, 2014.

[5] B. Abelev et al. Measurement of visible cross sections in proton-lead collisions at $\sqrt{s_{NN}}$ = 5.02 TeV in van der Meer scans with the ALICE detector. *Journal of Instrumentation*, 9(11):P11003 – P11003, 2014.

[6] B. Abelev et al. Suppression of γ(1S)at forward rapidity in Pb-Pb collisions at $\sqrt{s_{NN}}$=2.76TeV. *Physics letters / B*, 738:361 – 372, 2014.

[7] B. Abelev et al. Beauty production in pp collisions at $\sqrt{s} = 2.76 TeV$ measured via semi-electronic decays. *Physics letters / B*, 738:97 – 108, 2014.

[8] B. Abelev et al. Production of charged pions, kaons and protons at large transverse momenta in pp and Pb–Pb collisions at $\sqrt{s_{NN}} = 2.76$ TeV. *Physics letters / B*, 736:196 – 207, 2014.

[9] B. Abelev et al. Azimuthal anisotropy of D meson production in Pb-Pb collisions at $\sqrt{s_{\mathrm{NN}}} = 2.76$ TeV arXiv. *Physical review / C*, C90(3):034904, 2014.

[10] B. Abelev et al. J/ψ production and nuclear effects in p-Pb collisions at $\sqrt{S_{NN}}$ = 5.02 TeV. *Journal of high energy physics*, 1402(2):73, 2014.

[11] B. Abelev et al. Measurement of quarkonium production at forward rapidity in pp collisions at $\sqrt{s} = 7$ TeV. *The European physical journal / C*, C74(8):2974, 2014.

[12] B. Abelev et al. Neutral pion production at midrapidity in pp and Pb-Pb collisions at $\sqrt{s_{\mathrm{NN}}} = 2.76$ tev. *The European physical journal / C*, C74(10):3108, 2014.

[13] B. B. Abelev et al. Centrality, rapidity and transverse momentum dependence of J/ψ suppression in Pb-Pb collisions at $\sqrt{s_{\mathrm{NN}}}$=2.76 TeV. *Physics letters / B*, B734:314 – 327, 2014.

[14] B. B. Abelev et al. Corrigendum to 'Multi-strange baryon production at mid-rapidity in Pb-Pb collisions at $\sqrt{s_{NN}} =$ 2.76 TeV' [Phys. Lett. B 728 (2014) 216-227]. *Physics letters / B*, 734:409 – 410, 2014.

[15] B. B. Abelev et al. Event-by-event mean p_{t} fluctuations in pp and Pb-Pb collisions at the LHC. *The European physical journal / C*, 74(10):3077, 2014.

[16] B. B. Abelev et al. Exclusive J/ψ photoproduction off protons in ultra-peripheral p-Pb collisions at $\sqrt{s_{\mathrm{NN}}} = 5.02$ TeV. *Physical review letters*, 113(23):232504, 2014.

[17] B. B. Abelev et al. Freeze-out radii extracted from three-pion cumulants in pp, p–Pb and Pb–Pb collisions at the LHC. *Physics letters / B*, 739:139 – 151, 2014.

[18] B. B. Abelev et al. Measurement of prompt D-meson production in $p-Pb$ collisions at $\sqrt{s_{NN}}$ = 5.02 TeV. *Physical review letters*, 113(23):232301, 2014.

[19] B. B. Abelev et al. Multiplicity Dependence of Pion, Kaon, Proton and Lambda Production in p-Pb Collisions at $\sqrt{s_{NN}}$ = 5.02 TeV. *Physics letters / B*, B728:25 – 38, 2014.

[20] B. B. Abelev et al. Transverse momentum dependence of inclusive primary charged-particle production in p-Pb collisions at $\sqrt{s_{NN}} = 5.02 TeV$. *The European physical journal / C*, 74:3054, 2014.

[21] B. B. Abelev et al. Two- and three-pion quantum statistics correlations in Pb-Pb collisions at $\sqrt{s_{NN}} = 2.76$ TeV at the CERN Large Hadron Collider. *Physical review / C*, 89(2):024911, 2014.

[22] B. Abelev et al. Technical Design Report for the Upgrade of the ALICE Inner Tracking System. *Journal of physics / G*, G41(8):087002, 2014.

[23] M. Ablikim et al. Observation of $e^+e^- \rightarrow \pi^0\pi^0 h_c$ and a Neutral Charmoniumlike Structure $Z_c(4020)^0$. *Physical review letters*, 113(21):212002, 2014.

[24] M. Ablikim et al. Search for C-parity violation in $J = \psi \rightarrow \gamma\gamma$ and $\gamma\phi$. *Physical review / D*, 90(9):092002, 2014.

[25] M. Ablikim et al. Search for the weak decays $j/\psi \rightarrow d_s^{(*)} e^+ \nu_e + c.c.$ *Physical review / D*, 90(11):112014, 2014.

[26] M. Ablikim et al. Observation of $J/\psi \rightarrow p\overline{p}a_0(980)$ at BESIII. *Physical review / D*, 90(5):052009, 2014.

[27] M. Ablikim et al. Measurement of the branching fraction for ψ (3686) $\rightarrow \omega K^+ K^-$. *Physical review / D*, 89(11):112006, 2014.

[28] M. Ablikim et al. Precision measurement of the mass of the τ lepton. *Physical review / D*, 90(1):012001, 2014.

[29] M. Ablikim et al. Observation of $\eta' \rightarrow \pi^+\pi^-\pi^+\pi^-$ and $\eta' \rightarrow \pi^+\pi^-\pi^0\pi^0$. *Physical review letters*, 112(25):251801, 2014.

[30] M. Ablikim et al. Search for the radiative transitions ψ (3770) $\rightarrow \gamma\eta_c$ and $\gamma\eta_c(2S)$. *Physical review / D*, 89(11):112005, 2014.

DOI:10.15120/GR-2015-1-ANNEX-01

[31] M. Ablikim et al. Search for the rare decays $J/\psi \longrightarrow D_s^- \rho^+$ and $J/\psi \longrightarrow \overline{D}^0 \overline{K}^{*0}$. *Physical review / D*, 89(7):071101, 2014.

[32] M. Ablikim et al. Measurement of χ_{cJ} decaying into $\eta' K^+ K^-$. *Physical review / D*, 89(7):074030, 2014.

[33] M. Ablikim et al. Amplitude Analysis of the $D^+ \longrightarrow k_s^0 \pi^+ \pi^0$ Dalitz Plot. *Physical review / D*, 89(5):052001, 2014.

[34] M. Ablikim et al. Study of $e^+e^- \longrightarrow p\overline{p}\pi^0$ in the vicinity of the ψ(3770). *Physical review / D*, 90(3):032007, 2014.

[35] M. Ablikim et al. Observation of electromagnetic Dalitz decays $j/\psi \rightarrow pe^+e^-$. *Physical review / D*, 89(9):092008, 2014.

[36] M. Ablikim et al. Observation of $e^+e^- \longrightarrow \gamma X(3872)$ at BESIII. *Physical review letters*, 112(9):092001, 2014.

[37] M. Ablikim et al. Precision measurements of $b(d^+ \longrightarrow \mu^+ \nu_\mu)$, the pseudoscalar decay constant f_{D^+}, and the quark mixing matrix element $|V_{cd}|$. *Physical review / D*, 89(5):051104, 2014.

[38] M. Ablikim et al. Observation of a Charged $(dd^{-*})^{\pm}$ Mass Peak in $e^+e^- \longrightarrow \pi d\overline{D}^*$ at $\sqrt{s}$= 4.26 GeV. *Physical review letters*, 112(2):022001, 2014.

[39] M. Ablikim et al. Observation of a Charged Charmonium-like Structure in $e^+e^- \longrightarrow d^* \overline{D}^{\pm} \pi^{\pm}$ at $\sqrt{s}$ = 4.26 GeV. *Physical review letters*, 112(13):132001, 2014.

[40] M. Ablikim et al. Study of $e^+e^- \longrightarrow pp^-$ in the vicinity of ψ(3770). *Physics letters / B*, 735:101 – 107, 2014.

[41] P. Achenbach et al, and A. Hypernuclear Collaboration. Recent Studies of Hypernuclei Formation with Electron Beams at MAMI. *Few-body systems*, 55(8-10):887 – 892, 2014.

[42] J. Adamczewski et al. The CBM-RICH detector. *Journal of Instrumentation*, 9(06):C06002 – C06002, 2014.

[43] J. Adamczewski et al. Event reconstruction in the RICH detector of the CBM experiment at FAIR. *Nuclear instruments & methods in physics research / A*, 766:250 – 254, 2014.

[44] J. Adamczewski-Musch et al. Determination of tolerances of mirror displacement and radiator gas impurity for the CBM RICH detector. *Nuclear instruments & methods in physics research / A*, 766:221 – 224, Feb 2014.

[45] J. Adamczewski-Musch et al. Wavelength shifting films on multianode PMTs with UV-extended window for the CBM RICH detector. *Nuclear instruments & methods in physics research / A*, 766:180 – 182, 2014.

[46] J. Adamczewski-Musch et al. The CBM RICH project. *Nuclear instruments & methods in physics research / A*, 766:101 – 106, Feb 2014.

[47] C. Adolph et al. Transverse target spin asymmetries in exclusive ρ^0 muoproduction. *Physics letters / B*, 731:19 – 26, 2014.

[48] G. Agakishiev et al. Lambda hyperon production and polarization in collisions of p(3.5 GeV)+Nb. *The European physical journal / A*, 50(5):81, 2014.

[49] G. Agakishiev et al. Associate k^0 production in $p + p$ collisions at 3.5 GeV: The role of $\delta(1232)^{++}$. *Physical review / C*, 90(1):015202, 2014.

[50] G. Agakishiev et al. Medium effects in proton-induced K^0 production at 3.5 GeV. *Physical review / C*, 90(5):054906, 2014.

[51] G. Agakishiev et al.Searching a dark photon with HADES. *Physics letters / B*, 731:265 – 271, 2014.

[52] G. Agakishiev et al.. Baryon resonance production and dielectron decays in proton-proton collisions at 3.5 GeV. *The European physical journal / A*, 50(5):82, 2014.

[53] S. Altstadt et al. ^{13,14}Be(n, γ) via Coulomb dissociation for nucleosynthesis towards the r-process. *Nuclear data sheets*, 120:197 – 200, 2014.

[54] H. Alvarez-Pol et al. Performance analysis for the CALIFA Barrel calorimeter of the R^3B experiment. *Nuclear instruments & methods in physics research / A*, 767:453 – 466, 2014.

[55] A. N. Andreyev et al. α decay of ^{176}Au. *Physical review / C*, 90(4):044312, 2014.

[56] A. Andronic. An overview of the experimental study of quark–gluon matter in high-energy nucleus–nucleus collisions. *International journal of modern physics / A*, 29(22):1430047, 2014.

[57] A. Andronic. Experimental results and phenomenology of quarkonium production in relativistic nuclear collisions. volume 931, pages 135 – 144, Amsterdam, 2014. Quark Matter, Darmstadt (Germany), 19 May 2014 - 24 May 2014, North-Holland Publ. Co.

[58] A. Arcones Segovia and J. Bliss. Nucleosynthesis of elements between Sr and Ag in neutron- and proton-rich neutrino-driven winds. *Journal of physics / G*, 41(4):044005, 2014.

[59] Y. Ayyad et al. Proton-induced fission of ^{181}Ta at high excitation energies. *Physical review / C*, 89(5):054610, 2014.

[60] B. Özel-Tashenov et al. Low-energy dipole strength in Sn 112 , 120. *Physical review / C*, 90(2):024304, 2014.

[61] C. Böhm et al. Evolution of nuclear ground-state properties of neutron-deficient isotopes around Z=82 from precision mass measurements. *Physical review / C*, 90(4):044307, 2014.

[62] F. V. Böhmer et al. First measurement of dE/dx with a GEM-based TPC. *Nuclear instruments & methods in physics research / A*, 737:214 – 221, 2014.

[63] W. Barth et al. Carbon stripper foils for high current heavy ion operation. *Journal of radioanalytical and nuclear chemistry*, 299(2):1047 – 1053, 2014.

[64] M. Beard, E. Uberseder, R. Crowter, and M. Wiescher. Comparison of statistical model calculations for stable isotope neutron capture. *Physical review / C*, 90(3):034619, 2014.

[65] T. Beisitzer, R. Stiele, and J. Schaffner-Bielich. Equation of state with an extended SU(3) quark-meson model under conditions prevailing in core collapse supernovae. *Physical review / D*, 90(8):085001, 2014.

[66] O. Beliuskina et al. On the synthesis of neutron-rich isotopes along the N = 126 shell in multinucleon transfer reactions. *The European physical journal / A*, 50(10):161, 2014.

[67] J. Benlliure et al. Fission in Lead on Proton and Deuteron Reactions at 500 A MeV. *Nuclear data sheets*, 119:277 – 279, 2014.

[68] N. Benouaret et al. Photoexcitation of the Stable Tl Isotopes Below the Neutron Separation Energy. *Acta physica Polonica / B*, 45(2):193 – 198, 2014.

[69] W. Bentz, A. Arima, A. Richter, and J. Wambach. Analytic approach to nuclear rotational states and the role of spin: A minimal model. *Physical review / C*, 89(2):024314, 2014.

[70] M. Birch et al. First Compilation and Evaluation of Beta-Delayed Neutron Emission Probabilities and Associated Half-Lives for A $\leq$ 72 Nuclei. *Nuclear data sheets*, 120:66 – 69, 2014.

[71] S. Bogner et al. Nonperturbative Shell-Model Interactions from the In-Medium Similarity Renormalization Group. *Physical review letters*, 113(14):142501, 2014.

[72] N. Brambilla et al. QCD and strongly coupled gauge theories: challenges and perspectives. *The European physical journal / C*, 74(10):2981, 2014.

[73] P. Braun-Munzinger, B. Friman, and J. Stachel. Preface [Quark Matter 2014, Darmstadt]. *Nuclear physics / A*, 931:vii – viii, 2014.

[74] S. E. Brunner, L. Gruber, J. Marton, H. Orth, and K. Suzuki. Time resolution below 100 ps for the SciTil detector of PANDA employing SiPM. *Journal of Instrumentation*, 9(03):C03010 – C03010, 2014.

[75] R. Caballero-Folch et al. β-decay and β-delayed Neutron Emission Measurements at GSI-FRS Beyond N=126, for r-process Nucleosynthesis. *Nuclear data sheets*, 120:81 – 83, 2014.

[76] M. Cardinali et al. Frontend electronics for high-precision single photo-electron timing using FPGA-TDCs. *Nuclear instruments & methods in physics research / A*, 766:231 – 234, Feb 2014.

[77] M. Ciobanu et al. PADI, an Ultrafast Preamplifier - Discriminator ASIC for Time-of-Flight Measurements. *IEEE transactions on nuclear science*, 61(2):1015 – 1023, 2014.

[78] M. L. Cortés, R. Hoischen, K. Eisenhauer, J. Gerl, and N. Pietralla. BC404 scintillators as gamma locators studied via Geant4 simulations. *Journal of Instrumentation*, 9(05):C05049 – C05049, 2014.

[79] D. Cortina-Gil et al. CALIFA, a Dedicated Calorimeter for the $R^3B/FAIR$. *Nuclear data sheets*, 120:99 – 101, 2014.

[80] L. P. Csernai and H. Stöcker. Global collective flow in heavy ion reactions from the beginnings to the future. *Journal of physics / G*, 41(12):124001 –, 2014.

[81] L. P. Csernai, D. J. Wang, M. Bleicher, and H. Stöcker. Vorticity in peripheral collisions at the Facility for Antiproton and Ion Research and at the JINR Nuclotron-based Ion Collider fAcility. *Physical review / C*, 90(2):021904, 2014.

[82] S. Dababneh, J. Görres, M. Heil, F. Käppeler, R. Reifarth, and M. Wiescher. A compact Ge-BGO coincidence array for ultra-sensitive in-beam gamma spectroscopy. *Nuclear instruments & methods in physics research / A*, 737:135 – 141, 2014.

[83] V. Derya et al. Isospin properties of electric dipole excitations in ^{48}Ca. *Physics letters / B*, 730:288 – 292, 2014.

[84] I. Dillmann, et al. The Karlsruhe Astrophysical Database of Nucleosynthesis in Stars Project – Status and Prospects. *Nuclear data sheets*, 120:171 – 174, 2014.

[85] C. Droese et al. The cryogenic gas stopping cell of SHIPTRAP. *Nuclear instruments & methods in physics research / B*, 338:126 – 138, 2014.

[86] A. K. Dubey et al.. Testing of triple-GEM chambers for CBM experiment at FAIR using self-triggered readout electronics. *Nuclear instruments & methods in physics research / A*, 755:62 – 68, 2014.

[87] M. Dutra et al. Relativistic mean-field hadronic models under nuclear matter constraints. *Physical review / C*, 90(5):055203, 2014.

[88] A. A. Dzhioev, A. I. Vdovin, J. Wambach, and V. Y. Ponomarev. Inelastic neutrino scattering off hot nuclei in supernova environments. *Physical review / C*, 89(3):035805, 2014.

[89] R. Dzhygadlo et al.. Simulation and reconstruction of the PANDA Barrel DIRC. *Nuclear instruments & methods in physics research / A*, 766:263 – 266, 2014.

[90] K. Eberhardt, J. Greene, B. Kindler, B. Lommel, and A. Stolarz. Targets for accelerator-based research. *Journal of radioanalytical and nuclear chemistry*, 299(2):909 – 912, 2014.

[91] A. Echler et al. Application of calorimetric low temperature detectors for precise stopping power measurements of heavy ions in matter. *Journal of low temperature physics*, 176(5-6):1033 – 1039, 2014.

[92] M. Eibach et al. Direct high-precision mass measurements on ^{241,243}Am, ^{244}Pu , and ^{249}Cf. *Physical review / C*, 89(6):064318, 2014.

[93] S. Eliseev et al. A phase-imaging technique for cyclotron-frequency measurements. *Applied physics / B*, 114(1-2):107 – 128, 2014.

[94] J. Even et al. In-situ formation, thermal decomposition, and adsorption studies of transition metal carbonyl complexes with short-lived radioisotopes. *Radiochimica acta*, 102(12):1093 – 1110, 2014.

[95] J. Even et al. Synthesis and detection of a seaborgium carbonyl complex. *Science*, 345(6203):1491 – 1493, 2014.

[96] L. Fabbietti et al. Corrigendum to "The PANDA GEM-based TPC prototype" [Nucl. Instrum. Methods Phys. Res. A 628 (1) (2011) 204–208]. *Nuclear instruments & methods in physics research / A*, 735:659, 2014.

[97] E. Fischer et al. Status of the Superconducting Magnets for FAIR. *IEEE transactions on applied superconductivity*, 24(3):1 – 7, 2014.

[98] B. Friman. Probing the QCD phase diagram with fluctuations. *Nuclear physics / A*, 928:198 – 208, 2014.

[99] T. Gaitanos and H. Lenske. Production of multi-strangeness hypernuclei and the YN-interaction. *Physics letters / B*, 737:256 – 261, 2014.

[100] T. Gasenzer, L. McLerran, J. M. Pawlowski, and D. Sexty. Gauge turbulence, topological defect dynamics, and condensation in Higgs models. *Nuclear physics / A*, 930:163 – 186, 2014.

[101] L. Gastaldo et al. The Electron Capture ^{163} Ho Experiment ECHo. *Journal of low temperature physics*, 176(5-6):876 – 884, 2014.

[102] A. Gezerlis et al. Local chiral effective field theory interactions and quantum Monte Carlo applications. *Physical review / C*, 90(5):054323, 2014.

[103] P. Ghosh. Systematic characterization and quality assurance of silicon micro-strip sensors for the Silicon Tracking System of the CBM experiment. *Journal of Instrumentation*, 9(07):C07001 – C07001, 2014.

[104] L. Ghys et al. Evolution of fission-fragment mass distributions in the neutron-deficient lead region. *Physical review / C*, 90(4):041301, 2014.

[105] J. Glorius et al. Experimental cross sections of ^{165}Ho (α, n) ^{168}Tm and ^{166}Er$(\alpha, n)^{169}$Yb for optical potential studies relevant for the astrophysical γ process. *Physical review / C*, 89(6):065808, 2014.

[106] A. Gottardo et al. Isomeric decay spectroscopy of the ^{217}Bi isotope. *Physical review / C*, 90(3):034317, 2014.

[107] E. Grodner et al. newblock Hindered Gamow-Teller Decay to the Odd-Odd $N = Z^{62}$Ga : Absence of Proton-Neutron T=0 Condensate in A=62. *Physical review letters*, 113(9):092501, 2014.

[108] L. Groening et al. Experimental Proof of Adjustable Single-Knob Ion Beam Emittance Partitioning. *Physical review letters*, 113(26):264802, 2014.

[109] M. Haas, L. Fister, and J. M. Pawlowski. Gluon spectral functions and transport coefficients in Yang-Mills theory. *Physical review / D*, 90(9):091501, 2014.

[110] H.-W. Hammer and S. König. Constraints on a possible dineutron state from pionless EFT. *Physics letters / B*, 736:208 – 213, 2014.

[111] M. Heil et al. Stellar neutron capture cross sections of ^{20,21,22}Ne. *Physical review / C*, 90(4):045804, 2014.

[112] A. Hennig et al. Mixed-symmetry octupole and hexadecapole excitations in the N=52 isotones. *Physical review / C*, 90(5):051302, 2014.

[113] Y. Heo and M. F. M. Lutz. On kinematical constraints in the hadrogenesis conjecture for the baryon resonance spectrum. *The European physical journal / A*, 50(8):130, 2014.

[114] M. Hoek et al. The PANDA Barrel DIRC detector. *Nuclear instruments & methods in physics research / A*, 766:9 – 13, Feb 2014.

[115] E. Jäger et al.. High intensity target wheel at TASCA: target wheel control system and target monitoring. *Journal of radioanalytical and nuclear chemistry*, 299(2):1073 – 1079, 2014.

[116] Z. Kalaninová et al. Decay of $^{201-203}$Ra and $^{200-202}$Fr. *Physical review / C*, 89(5):054312, 2014.

[117] G. Kalicy et al. Status of the PANDA Barrel DIRC. *Journal of Instrumentation*, 9(05):C05060 – C05060, 2014.

[118] K. Kamikado, N. Strodthoff, L. von Smekal, and J. Wambach. Real-time correlation functions in the O(N) model from the functional renormalization group. *The European physical journal / C*, 74(3):2806, 2014.

[119] S. König and H.-W. Hammer. Precision calculation of the quartet-channel scattering length. *Physical review / C*, 90(3):034005, 2014.

[120] J. Khuyagbaatar et al. ^{48}Ca+^{249}Bk Fusion Reaction Leading to Element Z=117: Long-Lived α-Decaying ^{270}Db and Discovery of ^{266}Lr. *Physical review letters*, 112(17):172501, 2014.

[121] B. Kindler et al. Self-supporting isotopic chromium thin films. *Journal of radioanalytical and nuclear chemistry*, 299(2):1141 – 1143, 2014.

[122] T. Kodama, H. Stöcker, and N. Xu. 40 years of collective flow in relativistic heavy ion collisions - the barometer for primordial hot and dense QCD matter. *Journal of physics / G*, 41(12):120301, 2014.

[123] E. M. Kozulin et al. Shell effects in damped collisions of ^{88}Sr with ^{176}Yb at the Coulomb barrier energy. *Physical review / C*, 89(1):014614, 2014.

[124] T. Kurtukian-Nieto et al. Production cross sections of heavy neutron-rich nuclei approaching the nucleosynthesis r -process path around A = 195. *Physical review / C*, 89(2):024616, 2014.

[125] M. Laatiaoui et al.. Perspectives for laser spectroscopy of the element nobelium. volume 227, pages 69 – 75, Dordrecht [u.a.], 2014. Proceedings of the 9th International Workshop on Application of Lasers and Storage Devices in Atomic Nuclei Research "Recent Achievements and Future Prospects", Poznan (Poland), 13 May 2013 - 16 May 2013, Springer Science + Business Media B.V.

[126] M. Laatiaoui et al. On laser spectroscopy of the element nobelium (Z = 102). *The European physical journal / D*, 68(3):71, 2014.

[127] K. Langanke and G. Martínez-Pinedo. The role of electron capture in core-collapse supernovae. *Nuclear physics / A*, 928:305 – 312, 2014.

[128] C. Langer et al. Thermonuclear reaction ^{30}S$(p, \gamma)^{31}$Cl studied via Coulomb breakup of ^{31}Cl. *Physical review / C*, 89(3):035806, 2014.

[129] C. Lederer et al. ^{62}Ni (n, γ) and ^{63}Ni (n, γ) cross sections measured at the n_TOF facility at CERN. *Physical review / C*, 89(2):025810, 2014.

[130] A. Lehmann et al. Improved lifetime of microchannel-plate PMTs. *Nuclear instruments & methods in physics research / A*, 766:138 – 144, Feb 2014.

[131] H. Leibrock, C. Mühle, A. Kalimov, and P. Nalimov. Optimization of the Quadrupoles for the Collector Ring of FAIR. *IEEE transactions on applied superconductivity*, 24(3):1 – 4, 2014.

[132] H. Leibrock, P. Rottländer, C. Mühle, and F. C. Ozturk. Solenoid Development for an Emittance Transfer Experiment With a Design Environment System. *IEEE transactions on applied superconductivity*, 24(3):1 – 4, 2014.

[133] P. M. Lo, B. Friman, and K. Redlich. Polyakov loop fluctuations and deconfinement in the limit of heavy quarks. *Physical review / D*, 90(7):074035, 2014.

[134] B. Lommel et al. Reduction of isotopically enriched ^{50}Ti-dioxide for the production of high-intensity heavy-ion beam. *Journal of radioanalytical and nuclear chemistry*, 299(2):977 – 980, 2014.

[135] C. Louchart et al. The PRESPEC liquid-hydrogen target for in-beam gamma spectroscopy of exotic nuclei at GSI. *Nuclear instruments & methods in physics research / A*, 736:81 – 87, 2014.

[136] M. Lutz, R. Bavontaweepanya, C. Kobdaj, and K. Schwarz. Finite volume effects in the chiral extrapolation of baryon masses. *Physical review / D*, 90(5):054505, 2014.

[137] M. Lutz, D. Samart, and Y. Yan. Combined large-N_c and heavy-quark operator analysis for the chiral Lagrangian with charmed baryons. *Physical review / D*, 90(5):056006, 2014.

[138] J. Lynn, J. Carlson, E. Epelbaum, S. Gandolfi, A. Gezerlis, and A. Schwenk. Quantum Monte Carlo Calculations of Light Nuclei Using Chiral Potentials. *Physical review letters*, 113(19):192501, 2014.

[139] J. Marganiec et al. Study of the $^{15}\mathrm{O}(2p,\gamma)^{17}$Ne Cross Section by Coulomb Dissociation of ^{17}Ne for the rp Process of Nucleosynthesis. *Acta physica Polonica / B*, 45(2):229 – 234, 2014.

[140] A. Marin. Neutral meson production in pp and Pb–Pb collisions measured by ALICE at the LHC. volume 931, pages 438 – 443, Amsterdam, 2014. Quark Matter, Darmstadt (Germany), 19 May 2014 - 24 May 2014, North-Holland Publ. Co.

[141] G. Marquínez-Durán et al. GLORIA: A compact detector system for studying heavy ion reactions using radioactive beams. *Nuclear instruments & methods in physics research / A*, 755:69 – 77, 2014.

[142] G. Martínez-Pinedo, T. Fischer, and L. Huther. Supernova neutrinos and nucleosynthesis. *Journal of physics / G*, 41(4):044008 –, 2014.

[143] G. Martínez-Pinedo, Y. H. Lam, K. Langanke, R. G. T. Zegers, and C. Sullivan. Astrophysical weak-interaction rates for selected A = 20 and A = 24 nuclei. *Physical review / C*, 89(4):045806, 2014.

[144] N. Martin. Light (hyper-)nuclei production at the LHC measured with ALICE. volume 931, pages 1103 – 1107, Amsterdam, 2014. Quark Matter, Darmstadt (Germany), 19 May 2014 - 24 May 2014, North-Holland Publ. Co.

[145] F. Matteucci, D. Romano, A. Arcones, O. Korobkin, and S. Rosswog. Europium production: neutron star mergers versus core-collapse supernovae. *Monthly notices of the Royal Astronomical Society*, 438(3):2177 – 2185, 2014.

[146] B. Mei et al. Origin of odd-even staggering in fragment yields: Impact of nuclear pairing and shell structure on the particle-emission threshold energy. *Physical review / C*, 89(5):054612, 2014.

[147] O. Merle et al. Development of an Endcap DIRC for PANDA. *Nuclear instruments & methods in physics research / A*, 766:96 – 100, 2014.

[148] A. Morales et al. Half-Life Systematics across the N = 126 Shell Closure: Role of First-Forbidden Transitions in the β Decay of Heavy Neutron-Rich Nuclei. *Physical review letters*, 113(2):022702, 2014.

[149] A. I. Morales et al. β-decay studies of neutron-rich Tl, Pb, and Bi isotopes. *Physical review / C*, 89(1):014324, 2014.

[150] K. Morita, V. Skokov, B. Friman, and K. Redlich. Net baryon number probability distribution near the chiral phase transition. *The European physical journal / C*, 74(1):2706, 2014.

[151] I. Mukha. Neutron Radioactivity. *Acta physica Polonica / B*, 45(2):321 – 330, 2014.

[152] D. A. Nesterenko et al. Direct determination of the atomic mass difference of ^{187}Re and ^{187}Os for neutrino physics and cosmochronology. *Physical review / C*, 90(4):042501, 2014.

[153] C. Nociforo. Time-of-flight measurements at the Super-FRS. *Journal of Instrumentation*, 9(01):C01022 – C01022, 2014.

[154] B. Nowak, J. Schole, and T. Gasenzer. Universal dynamics on the way to thermalization. *New journal of physics*, 16(9):093052 –, 2014.

[155] A. Ozawa et al. Charge-changing cross sections of ^{30}Ne , ^{32,33}Na with a proton target. *Physical review / C*, 89(4):044602, 2014.

[156] P. S. Pagala, M. Ferre, and L. M. Orona Dominguez. Evaluation of modular robot system for maintenance tasks in hot cell. *Fusion engineering and design*, 89(9-10):2309 – 2313, 2014.

[157] J. M. Pawlowski and F. Rennecke. Higher order quark-mesonic scattering processes and the phase structure of QCD. *Physical review / D*, 90(7):076002, 2014.

[158] V. Perschina-Nägele, A. Borschevsky, and M. Iliaš. Theoretical predictions of properties and volatility of chlorides and oxychlorides of group-4 elements. I. Electronic structures and properties of MCl_4 and $MOCl_2$ (M = Ti, Zr, Hf, and Rf). *The journal of chemical physics*, 141(6):064314, 2014.

[159] T. Petrovic, M. Vencelj, M. Lipoglavsek, R. Novak, and D. Savran. Efficient Reduction of Piled-Up Events in Gamma-Ray Spectrometry at High Count Rates. *IEEE transactions on nuclear science*, 61(1):584 – 589, 2014.

[160] B. Pfeiffer, K. Venkataramaniah, U. Czok, and C. Scheidenberger. Atomic mass compilation 2012. *Atomic data and nuclear data tables*, 100(2):403 – 535, 2014.

[161] J. Pietraszko, T. Galatyuk, V. Grilj, W. Koenig, S. Spataro, and M. Träger. Radiation damage in single crystal CVD diamond material investigated with a high current relativistic ^{197}Au beam. *Nuclear instruments & methods in physics research / A*, 763:1 – 5, 2014.

[162] M. Röder et al. Efficiency determination of resistive plate chambers for fast quasi-monoenergetic neutrons. *The European physical journal / A*, 50(7):112, 2014.

[163] C. Rappold et al. On the measured lifetime of light hypernuclei $^{3}_{\Lambda}$H and $^{4}_{\Lambda}$H. *Physics letters / B*, 728:543 – 548, 2014.

[164] P. Rau, J. Steinheimer, S. Schramm, and H. Stöcker. Conserved charge fluctuations in a chiral hadronic model including hadrons and quarks. *Physics letters / B*, 733:176 – 182, 2014.

[165] R. Rescigno et al. Performance of the reconstruction algorithms of the FIRST experiment pixel sensors vertex detector. *Nuclear instruments & methods in physics research / A*, 767:34 – 40, 2014.

[166] I. Rinaldi, S. Brons, O. Jäkel, B. Voss, and K. Parodi. A method to increase the nominal range resolution of a stack of parallel-plate ionization chambers. *Physics in medicine and biology*, 59(18):5501 – 5515, 2014.

[167] J. L. Ripley, B. D. Metzger, A. Arcones, and G. Martinez-Pinedo. X-ray decay lines from heavy nuclei in supernova remnants as a probe of the r-process origin and the birth periods of magnetars. *Monthly notices of the Royal Astronomical Society*, 438(4):3243 – 3254, 2014.

[168] B. Roberts, Y. Stadnik, V. Dzuba, V. Flambaum, N. Leefer, and D. Budker. Parity-violating interactions of cosmic fields with atoms, molecules, and nuclei: Concepts and calculations for laboratory searches and extracting limits. *Physical review / D*, 90(9):096005, 2014.

[169] I. Rodríguez, P. O. Hess, S. Schramm, and W. Greiner. Neutron stars within pseudo-complex general relativity. *Journal of physics / G*, 41(10):105201 –, 2014.

[170] J. L. Rodríguez-Sánchez et al. Proton-induced fission cross sections on ^{208}Pb at high kinetic energies. *Physical review / C*, 90(6):064606, 2014.

[171] S. Rosswog, O. Korobkin, A. Arcones, F.-K. Thielemann, and T. Piran. The long-term evolution of neutron star merger remnants - I. The impact of r-process nucleosynthesis. *Monthly notices of the Royal Astronomical Society*, 439(1):744 – 756, 2014.

[172] D. Rudolph et al. Alpha-Photon Coincidence Spectroscopy Along Element 115 Decay Chains. *Acta physica Polonica / B*, 45(2):263–272, 2014.

[173] J. Runke et al. Preparation of actinide targets for the synthesis of the heaviest elements. *Journal of radioanalytical and nuclear chemistry*, 299(2):1081 – 1084, 2014.

[174] A. Sanchez Lorente. Hypernuclear physics studies of the PANDA experiment at FAIR. *Hyperfine interactions*, 229(1-3):45 – 51, 2014.

[175] N. Sato et al.. Production of ^{256}Lr in the ^{249,250,251}Cf +^{11}B, ^{243}Am + ^{18}O, and ^{248}Cm + ^{14}N reactions. *Radiochimica acta*, 102(3):211–219, 2014.

[176] A. Sauerwein et al. Determination of the ^{142}Ce(γ, n) cross section using quasi-monoenergetic Compton backscattered γ rays. *Physical review / C*, 89(3):035803, 2014.

[177] M. Saxena et al. Rotational behavior of $^{120,122,124}Te$. *Physical review / C*, 90(2):024316, 2014.

[178] F. Schirru, D. Chokheli, and M. Kiš. Thin single crystal diamond detectors for alpha particle detection. *Diamond and related materials*, 49:96 – 102, 2014.

[179] S. Schmidt et al. Behavior of a trapezoid-based data acquisition system up to 100kHz and beyond. *Nuclear instruments & methods in physics research / A*, 768:192 – 196, 2014.

[180] C. Schmitt, K.-H. Schmidt, and A. Kelić-Heil. SPACS: A semi-empirical parameterization for isotopic spallation cross sections. *Physical review / C*, 90(6):064605, 2014.

[181] L. Schnorrenberger et al. Characterization of γ-ray detectors using the photon tagger NEPTUN for energies up to 20MeV. *Nuclear instruments & methods in physics research / A*, 735:19 – 23, 2014.

[182] C. Schwarz et al. Prototyping the PANDA Barrel DIRC. *Nuclear instruments & methods in physics research / A*, 766:32 – 35, Feb 2014.

[183] V. M. Shapoval, P. Braun-Munzinger, I. A. Karpenko, and Y. M. Sinyukov. Femtoscopy correlations of kaons in Pb+Pb collisions at LHC within hydrokinetic model. *Nuclear physics / A*, 929:1 – 8, 2014.

[184] P. G. Sharov, I. A. Egorova, and L. V. Grigorenko. Anomalous population of ^{10}He states in reactions with ^{11}Li. *Physical review / C*, 90(2):024610, 2014.

[185] C. Simon, I. Deppner, N. Herrmann, P. A. Loizeau, and J. Frühauf. Performance test of a fully differential float-glass multi-strip MRPC prototype for the CBM ToF wall with cosmic rays. *Journal of Instrumentation*, 9(09):C09028 – C09028, 2014.

[186] G. Simpson et al. Yrast 6^+ Seniority Isomers of ^{136,138}Sn. *Physical review letters*, 113(13):132502, 2014.

[187] M. Singla, S. Chatterji, W. F. J. Müller, V. Kleipa, and J. M. Heuser. Finite element simulations of low-mass readout cables for the CBM Silicon Tracking System using RAPHAEL. *Nuclear instruments & methods in physics research / A*, 735:366 – 373, 2014.

[188] D. Siwal et al. Pulse shape analysis of a two fold clover detector with an EMD based new algorithm: A comparison. *Nuclear instruments & methods in physics research / A*, 741:108 – 116, 2014.

[189] J. Steinheimer, J. Auvinen, H. Petersen, M. Bleicher, and H. Stöcker. Examination of directed flow as a signal for a phase transition in relativistic nuclear collisions. *Physical review / C*, 89(5):054913, 2014.

[190] H. Stoecker and C. Sturm. FAIR – Cosmic matter in the laboratory. *Astronomische Nachrichten*, 335(6-7):581–586, 2014.

[191] O. Svoboda et al. Electromagnetic calorimeter for the HADES@FAIR experiment. *Journal of Instrumentation*, 9(05):C05002 – C05002, 2014.

[192] T. Szücs, I. Dillmann, R. Plag, and Z. Fülöp. KADoNiS-p: The Astrophysical p-Process Database. *Nuclear data sheets*, 120:191 – 193, 2014.

[193] J. Taprogge et al. $1p_{3/2}$ Proton-Hole State in ^{132}Sn and the Shell Structure Along N = 82. *Physical review letters*, 112(13):132501, 2014.

[194] J. Taprogge et al. Identification of a millisecond isomeric state in ^{129}Cd$_{81}$ via the detection of internal conversion and Compton electrons. *Physics letters / B*, 738:223 – 227, 2014.

[195] A. Toia. Centrality dependence of particle production in p–A collisions measured by ALICE. volume 931, pages 315 – 319, Amsterdam, 2014. Quark Matter, Darmstadt (Germany), 19 May 2014 - 24 May 2014, North-Holland Publ. Co.

[196] R.-A. Tripolt, J. Braun, B. Klein, and B.-J. Schaefer. Effect of fluctuations on the QCD critical point in a finite volume. *Physical review / D*, 90(5):054012, 2014.

[197] R.-A. Tripolt, N. Strodthoff, L. von Smekal, and J. Wambach. Spectral functions for the quark-meson model phase diagram from the functional renormalization group. *Physical review / D*, 89(3):034010, 2014.

[198] R.-A. Tripolt, L. von Smekal, and J. Wambach. Flow equations for spectral functions at finite external momenta. *Physical review / D*, 90(7):074031, 2014.

[199] A. Trzcińska et al. Barrier Height Distributions - the Influence of Weak Channels. *Acta physica Polonica / B*, 45(2):383 – 390, 2014.

[200] A. Tumino et al. New determination of the ^{2}H(d , p) ^{3}H and ^{2}H(d , n) ^{3}He reaction rates at astrophysical energies. *The astrophysical journal / 1*, 785(2):96, 2014.

[201] S. Typel. Neutron skin thickness of heavy nuclei with α-particle correlations and the slope of the nuclear symmetry energy. *Physical review / C*, 89(6):064321, 2014.

[202] S. Typel, H. H. Wolter, G. Röpke, and D. Blaschke. Effects of the liquid-gas phase transition and cluster formation on the symmetry energy. *The European physical journal / A*, 50(2):17, 2014.

[203] E. Uberseder et al. First Experimental Constraint on the ^{59}Fe$(n,\gamma)^{60}$Fe Reaction Cross Section at Astrophysical Energies via the Coulomb Dissociation of ^{60}Fe. *Physical review letters*, 112(21):211101, 2014.

[204] Z. Vajta et al. Excited states in the neutron-rich nucleus ^{25}F. *Physical review / C*, 89(5):054323, 2014.

[205] A. Vascon et al. Fundamental aspects of molecular plating and production of smooth crack-free Nd targets. *Journal of radioanalytical and nuclear chemistry*, 299(2):1085 – 1091, 2014.

[206] F. Wamers et al. First Observation of the Unbound Nucleus ^{15}Ne. *Physical review letters*, 112(13):132502, 2014.

[207] M. Wang et al. NUBASE2012 Evaluation of Nuclear Properties. *Nuclear data sheets*, 120:6 – 7, 2014.

[208] H. Watanabe et al. Monopole-Driven Shell Evolution below the Doubly Magic Nucleus ^{132}Sn Explored with the Long-Lived Isomer in ^{126}Pd. *Physical review letters*, 113(4):042502, 2014.

[209] S. Watanabe et al. Ground-state properties of neutron-rich Mg isotopes. *Physical review / C*, 89(4):044610, 2014.

[210] D. Weber, H. Feldmeier, H. Hergert, and T. Neff. From nucleon-nucleon interaction matrix elements in momentum space to an operator representation. *Physical review / C*, 89(3):034002, 2014.

[211] A. Wendt et al. Isospin symmetry in the sd shell: Transition strengths in the neutron-deficient sd shell nucleus ^{33}Ar. *Physical review / C*, 90(5):054301, 2014.

[212] M.-R. Wu, T. Fischer, L. Huther, G. Martínez-Pinedo, and Y.-Z. Qian. Impact of active-sterile neutrino mixing on supernova explosion and nucleosynthesis. *Physical review / D*, 89(6):061303, 2014.

[213] C. Xiao, L. Groening, and O. K. Kester. Collimation and decoupling of ECR source beams for brilliance optimization. *Nuclear instruments & methods in physics research / A*, 738:167 – 176, 2014.

[214] Z. Xu et al. β-Decay Half-Lives of ^{76,77}Co, ^{79,80}No, and ^{81}Cu: Experimental Indication of a Doubly Magic ^{78}No. *Physical review letters*, 113(3):032505, 2014.

[215] A. Yakushev et al. Superheavy Element Flerovium (Element 114) Is a Volatile Metal. *Inorganic chemistry*, 53(3):1624 – 1629, 2014.

[216] V. Zinyuk et al. Azimuthal emission patterns of K$^+$ and of K$^-$ mesons in Ni+Ni collisions near the strangeness production threshold. *Physical review / C*, 90(2):025210, 2014.

JCR publications to the programme from matter to materials and life published in 2014

See http://repository.gsi.de for more information.

[1] B. Afra, M. Lang, T. Bierschenk, M. D. Rodriguez, W. J. Weber, C. Trautmann, R. C. Ewing, N. Kirby, and P. Kluth. Annealing behaviour of ion tracks in olivine, apatite and britholite. *Nuclear instruments & methods in physics research / B*, 326:126 – 130, 2014.

[2] B. Afra, K. Nordlund, M. D. Rodriguez, T. Bierschenk, C. Trautmann, S. Mudie, and P. Kluth. Thermal response of nanoscale cylindrical inclusions of amorphous silica embedded in α-quartz. *Physical review / B*, 90(22):224108, 2014.

[3] M. Ali, P. Ramirez, S. Nasir, Q.-H. Nguyen, W. Ensinger, and S. Mafe. Current rectification by nanoparticle blocking in single cylindrical nanopores. *Nanoscale*, 6(18):10740, 2014.

[4] M. Ali, P. Ramirez, S. Nasir, Q.-H. Nguyen, W. Ensinger, and S. Mafe. Nanoparticle-induced rectification in a single cylindrical nanopore: Net currents from zero time-average potentials. *Applied physics letters*, 104(4):043703 –, 2014.

[5] P. Y. Apel, I. V. Blonskaya, O. L. Orelovich, B. Sartowska, and R. Spohr. Radiation effects of swift heavy ions in polymers: Determination of nanoshapes from electroconductivity. *Nuclear instruments & methods in physics research / B*, 326:158 – 162, 2014.

[6] B. Aurand, B. Elkin, L.-O. Heim, B. Lommel, B. Kindler, M. Tomut, C. Rödel, S. Kuschel, O. Jäckel, and T. Kuehl. Ultra-thin polymer foils for laser-ion acceleration. *Journal of radioanalytical and nuclear chemistry*, 299(2):965 – 968, 2014.

[7] D. Bernhardt, A. Becker, M. Grieser, M. Hahn, C. Krantz, M. Lestinsky, O. Novotný, R. Repnow, D. W. Savin, K. Spruck, A. Wolf, A. Müller, and S. Schippers. Absolute rate coefficients for photorecombination and electron-impact ionization of magnesiumlike iron ions from measurements at a heavy-ion storage ring. *Physical review / A*, 90(1):012702, 2014.

[8] T. Beyer, K. Blaum, M. Block, C. E. Düllmann, K. Eberhardt, M. Eibach, N. Frömmgen, C. Geppert, C. Gorges, J. Grund, M. Hammen, S. Kaufmann, A. Krieger, S. Nagy, W. Nörterhäuser, D. Renisch, C. Smorra, and E. Will. An RFQ cooler and buncher for the TRIGA-SPEC experiment. *Applied physics / B*, 114(1-2):129 – 136, 2014.

[9] T. Bierschenk, B. Afra, M. D. Rodriguez, R. Giulian, C. Trautmann, S. Mudie, M. C. Ridgway, and P. Kluth. Effect of electronic energy loss on ion track formation in amorphous Ge. *Nuclear instruments & methods in physics research / B*, 326:113 – 116, 2014.

[10] A. Bondarevskaya, E. A. Mistonova, K. N. Lyashchenko, O. Y. Andreev, A. Surzhykov, L. N. Labzowsky, G. Plunien, D. Liesen, F. Bosch, and T. Stöhlker. Method for the production of highly charged ions with polarized nuclei and zero total electron angular momentum. *Physical review / A*, 90(6):064701, 2014.

[11] A. Borschevsky, V. Pershina-Naegele, E. Eliav, and U. Kaldor. Relativistic coupled cluster study of diatomic compounds of Hg, Cn, and Fl. *The journal of chemical physics*, 141(8):084301 –, 2014.

[12] B. Botermann, D. Bing, C. Geppert, G. Gwinner, T. W. Hänsch, G. Huber, S. Karpuk, A. Krieger, T. Kühl, W. Nörtershäuser, C. Novotny, S. Reinhardt, R. Sánchez, D. Schwalm, T. Stöhlker, A. Wolf, and G. Saathoff. Test of Time Dilation Using Stored Li^+ Ions as Clocks at Relativistic Speed. *Physical review letters*, 113(12):120405, 2014.

[13] A. Bret, A. R. Piriz, and N. A. Tahir. Imprint reduction in rotating heavy ions beam energy deposition. *Nuclear instruments & methods in physics research / A*, 733:200–202, 2014.

[14] S. Busold, A. Almomani, V. Bagnoud, W. Barth, S. Bedacht, A. Blažević, O. Boine-Frankenheim, C. Brabetz, T. Burris-Mog, T. E. Cowan, O. Deppert, M. Droba, H. Eickhoff, U. Eisenbarth, K. Harres, G. Hoffmeister, I. Hofmann, O. Jaeckel, R. Jaeger, M. Joost, S. Kraft, F. Kroll, M. Kaluza, O. Kester, Z. Lecz, T. Merz, F. Nürnberg, H. Al-Omari, A. Orzhekhovskaya, G. Paulus, J. Polz, U. Ratzinger, M. Roth, G. Schaumann, P. Schmidt, U. Schramm, G. Schreiber, D. Schumacher, T. Stoehlker, A. Tauschwitz, W. Vinzenz, F. Wagner, S. Yaramyshev, and B. Zielbauer. Shaping laser accelerated ions for future applications - The LIGHT collaboration. *Nuclear instruments & methods in physics research / A*, 740:94–98, 2014.

[15] S. Busold, K. Philipp, A. Otten, and M. Roth. Image plate characterization and absolute calibration to low kilo-electron-volt electrons. *Review of scientific instruments*, 85(11):113306 –, 2014. ISI:000345646000258.

[16] S. Busold, D. Schumacher, O. Deppert, C. Brabetz, F. Kroll, A. Blazevic, V. Bagnoud, and M. Roth. Commissioning of a compact laser-based proton beam line for high intensity bunches around 10 MeV. *Physical review / Special topics / Accelerators and beams*, 17:031302, 2014.

[17] W. Chen, G. Vorobyev, D. Guo, F. Herfurth, P.-M. Hillenbrand, U. Spillmann, S. Trotsenko, A. Gumberidze, and T. Stöhlker. Metal vapor target for precise studies of ion-atom collisions. *Review of scientific instruments*, 85(5):053513, 2014.

[18] J.-M. Costantini, C. Trautmann, W. J. Weber, and T. Wiss.

DOI:10.15120/GR-2015-1-ANNEX-02

[Editorial] EMRS 2013 syposium M. *Nuclear instruments & methods in physics research / B*, 327:1, 2014.

[19] T. Döppner, A. L. Kritcher, P. Neumayer, D. Kraus, B. Bachmann, S. Burns, R. W. Falcone, S. H. Glenzer, J. Hawreliak, A. House, O. L. Landen, S. LePape, T. Ma, A. Pak, and D. Swift. Qualification of a high-efficiency, gated spectrometer for x-ray Thomson scattering on the National Ignition Facility$^{a)}$. *Review of scientific instruments*, 85(11):11D617 –, 2014.

[20] A. Dauletbekova, K. Schwartz, M. V. Sorokin, A. Russakova, M. Baizhumanov, A. Akilbekov, M. Zdorovets, and M. Koloberdin. F center creation and aggregation in LiF crystals irradiated with $^{14}N,^{40}Ar$, and ^{84}Kr ions. *Nuclear instruments & methods in physics research / B*, 326:311 – 313, 2014.

[21] D. Denis-Petit, M. Comet, T. Bonnet, F. Hannachi, F. Gobet, M. Tarisien, M. Versteegen, G. Gosselin, V. Méot, P. Morel, J.-C. Pain, F. Gilleron, A. Frank, V. Bagnoud, A. Blazevic, F. Dorchies, O. Peyrusse, W. Cayzac, and M. Roth. Identification of X-ray spectra in the Na-like to O-like rubidium ions in the range of 3.8–7.3a^o. *Journal of quantitative spectroscopy & radiative transfer*, 148:70 – 89, 2014.

[22] S. Depierreux, V. Yahia, C. Goyon, G. Loisel, P. E. Masson-Laborde, N. Borisenko, A. Orekhov, O. Rosmej, T. Rienecker, and C. Labaune. Laser light triggers increased Raman amplification in the regime of nonlinear Landau damping. *Nature Communications*, 5:4158, 2014.

[23] C. Deutsch, N. A. Tahir, M. Barriga-Carrasco, V. Ceban, P. Fromy, D. Gilles, D. Leger, G. Maynard, B. Tashev, and L. Volpe. Multiple scattering in electron fluid and energy lossin multi-ionic targets. *Nuclear instruments & methods in physics research / A*, 733:39–44, 2014.

[24] A. Estradé, R. Kanungo, W. Horiuchi, F. Ameil, J. Atkinson, Y. Ayyad, D. Cortina-Gil, I. Dillmann, A. Evdokimov, F. Farinon, H. Geissel, G. Guastalla, R. Janik, M. Kimura, R. Knöbel, J. Kurcewicz, Y. Litvinov, M. Marta, M. Mostazo, I. Mukha, C. Nociforo, H. Ong, S. Pietri, A. Prochazka, C. Scheidenberger, B. Sitar, P. Strmen, Y. Suzuki, M. Takechi, J. Tanaka, I. Tanihata, S. Terashima, J. Vargas, H. Weick, and J. Winfield. Proton Radii of $^{12-17}B$ Define a Thick Neutron Surface in ^{17}B. *Physical review letters*, 113(13):132501, 2014.

[25] S. Faik, A. Tauschwitz, M. Basko, J. A. Maruhn, O. Rosmej, T. Rienecker, V. G. Novikov, and A. S. Grushin. Creation of a homogeneous plasma column by means of hohlraum radiation for ion-stopping measurements. *High energy density physics*, 10:47 – 55, 2014.

[26] C. Florica, E. Matei, A. Costas, M. E. Toimil Molares, and I. Enculescu. Field Effect Transistor with Electrodeposited ZnO Nanowire Channel. *Electrochimica acta*, 137:290 – 297, 2014.

[27] X. Gao, Y.-J. Yuan, J.-c. Yang, S. Litvinov, M. Wang, Y. Litvinov, W. Zhang, D.-Y. Yin, G.-D. Shen, W.-p. Chai, J. Shi, and P. Shang. Isochronicity corrections for isochronous mass measurements at the HIRFL-CSRe. *Nuclear instruments & methods in physics research / A*, 763:53 – 57, 2014.

[28] S. Granville, E. Matei, I. Enculescu, and M. E. Toimil Molares. Cu codoping control over magnetic precipitate formation in ZnCoO nanowires. *Applied physics letters*, 105(25):252403, 2014.

[29] J. Gunst, Y. Litvinov, C. H. Keitel, and A. Pálffy. Dominant Secondary Nuclear Photoexcitation with the X-Ray Free-Electron Laser. *Physical review letters*, 112(8):082501, 2014.

[30] M. Hahn, N. R. Badnell, M. Grieser, C. Krantz, M. Lestinsky, A. Müller, O. Novotný, R. Repnow, S. Schippers, A. Wolf, and D. W. Savin. Electron-ion recombination of Fe^{12+} forming Fe^{11+} : labratory measurements and theoretical calculations. *The astrophysical journal / 1*, 788(1):46 –53, 2014.

[31] A. G. Hayrapetyan, O. Matula, A. Aiello, A. Surzhykov, and S. Fritzsche. Interaction of Relativistic Electron-Vortex Beams with Few-Cycle Laser Pulses. *Physical review letters*, 112(13):134801, 2014.

[32] P.-M. Hillenbrand, S. Hagmann, D. Atanasov, D. Banaś, K.-H. Blumenhagen, C. Brandau, W. Chen, E. De Filippo, A. Gumberidze, D. L. Guo, D. H. Jakubassa-Amundsen, O. Kovtun, C. Kozhuharov, M. Lestinsky, Y. Litvinov, A. Müller, R. A. Müller, H. Rothard, S. Schippers, M. S. Schöffler, U. Spillmann, A. Surzhykov, S. Trotsenko, N. Winckler, X. L. Yan, V. A. Yerokhin, X. L. Zhu, and T. Stöhlker. Radiative-electron-capture-to-continuum cusp in $U^{88+} + N_2$ collisions and the high-energy endpoint of electron-nucleus bremsstrahlung. *Physical review / A*, 90(2):022707, 2014.

[33] P.-M. Hillenbrand, S. Hagmann, A. B. Voitkiv, B. Najjari, D. Banaś, K.-H. Blumenhagen, C. Brandau, W. Chen, E. De Filippo, A. Gumberidze, D. L. Guo, C. Kozhuharov, M. Lestinsky, Y. Litvinov, A. Müller, H. Rothard, S. Schippers, M. S. Schöffler, U. Spillmann, S. Trotsenko, X. L. Zhu, and T. Stöhlker. Electron-loss-to-continuum cusp in $U^{88+} + N_2$ collisions. *Physical review / A*, 90(4):042713, 2014.

[34] U. H. Hossain, V. Lima, O. Baake, D. Severin, M. Bender, and W. Ensinger. On-line and post irradiation analysis of swift heavy ion induced modification of PMMA (polymethyl-methacrylate). *Nuclear instruments & methods in physics research / B*, 326:135 – 139, 2014.

[35] U. H. Hossain, F. Muench, and W. Ensinger. A comparative study on degradation characteristics of fluoropolymers irradiated by high energy heavy ions. *RSC Advances*, 4(91):50171 – 50179, 2014.

[36] U. H. Hossain, T. Seidl, and W. Ensinger. Combined in situ infrared and mass spectrometric analysis of high-energy heavy ion induced degradation of polyvinyl polymers. *Polymer chemistry*, 5(3):1001 – 1012, 2014.

[37] L. M. Innes, C.-H. Chen, M. Schiel, M. Pevarnik, F. Haurais, M. E. Toimil Molares, I. Vlassiouk, L. Theogarajan, and Z. S. Siwy. Velocity Profiles in Pores with Undulating Opening Diameter and Their Importance for Resistive-Pulse Experiments. *Analytical chemistry*, 86(20):10445 – 10453, 2014.

[38] P. Jagodziński, M. Pajek, D. Banaś, H. Beyer, M. Trassinelli, and T. Stöhlker. Ray-tracing simulations of spherical Johann diffraction spectrometer for

in-beam X-ray experiments. *Nuclear instruments & methods in physics research / A*, 753:121 – 130, 2014.

[39] T. Jahrsetz, S. Fritzsche, and A. Surzhykov. Inelastic Raman scattering of light by hydrogenlike ions. *Physical review / A*, 89(4):042501, 2014.

[40] D. Jakubaßa-Amundsen, R. Müller, A. Surzhykov, and V. Yerokhin. Relativistic theory for radiative forward electron emission in heavy ion-atom encounters. *The European physical journal / D*, 68(12):367, 2014.

[41] C. Jean, L. Belliard, T. W. Cornelius, O. Thomas, M. E. Toimil Molares, M. Cassinelli, L. Becerra, and B. Perrin. Direct Observation of Gigahertz Coherent Guided Acoustic Phonons in Free-Standing Single Copper Nanowires. *The journal of physical chemistry letters*, 5(23):4100 – 4104, 2014.

[42] M. Kühnel, J. M. Fernández, F. Tramonto, G. Tejeda, E. Moreno, A. Kalinin, M. Nava, D. E. Galli, S. Montero, and R. Grisenti. Observation of crystallization slowdown in supercooled parahydrogen and orthodeuterium quantum liquid mixtures. *Physical review / B*, 89(18):180201, 2014.

[43] A. V. Kantsyrev, A. A. Golubev, A. V. Bogdanov, V. S. Demidov, E. V. Demidova, E. M. Ladygina, N. V. Markov, V. S. Skachkov, G. N. Smirnov, I. V. Rudskoy, A. P. Kuznetsov, A. V. Khudomyasov, B. Y. Sharkov, S. V. Dudin, S. A. Kolesnikov, V. B. Mintsev, D. N. Nikolaev, V. Y. Ternovoi, A. V. Utkin, D. S. Yuriev, N. S. Shilkin, V. E. Fortov, V. I. Turtikov, V. V. Burtsev, M. V. Zhernokletov, N. V. Zavialov, S. A. Kartanov, A. L. Mikhailov, A. V. Rudnev, M. V. Tatsenko, D. Varentsov, and L. Shestov. TWAC-ITEP proton microscopy facility. *Instruments and experimental techniques*, 57(1):1 – 10, 2014.

[44] Y. S. Kozhedub, V. M. Shabaev, I. I. Tupitsyn, A. Gumberidze, S. Hagmann, G. Plunien, and T. Stöhlker. Relativistic calculations of x-ray emission following a $Xe - Bi^{83+}$ collision. *Physical review / A*, 90(4):042709, 2014.

[45] S. Kraft-Bermuth, V. Andrianov, A. Bleile, A. Echler, P. Egelhof, P. Grabitz, C. Kilbourne, O. Kiselev, D. McCammon, and P. Scholz. Precise Determination of the Lyman- α 1 Transition Energy in Hydrogen-like Gold Ions with Microcalorimeters. *Journal of low temperature physics*, 176(5-6):1002 – 1008, 2014.

[46] K. Kreim, M. L. Bissell, J. Papuga, K. Blaum, M. De Rydt, R. F. Garcia Ruiz, S. Goriely, H. Heylen, M. Kowalska, R. Neugart, G. Neyens, W. Nörtershäuser, M. M. Rajabali, R. Sánchez Alarcón, H. H. Stroke, and D. T. Yordanov. Nuclear charge radii of potassium isotopes beyond. *Physics letters / B*, 731:97 – 102, 2014.

[47] S. Kreim, D. Beck, K. Blaum, C. Borgmann, M. Breitenfeldt, T. E. Cocolios, A. Gottberg, F. Herfurth, M. Kowalska, Y. Litvinov, D. Lunney, V. Manea, T. M. Mendonca, S. Naimi, D. Neidherr, M. Rosenbusch, L. Schweikhard, T. Stora, F. Wienholtz, R. N. Wolf, and K. Zuber. Competition between pairing correlations and deformation from the odd-even mass staggering of francium and radium isotopes. *Physical review / C*, 90(2):024301, 2014.

[48] B. Kuttich, M. Engel, C. Trautmann, and B. Stühn. Tailored nanochannels of nearly cylindrical geometry analysed by small angle X-ray scattering. *Applied physics / A*, 114(2):387 – 392, 2014.

[49] M. Lang, M. Toulemonde, J. Zhang, F. Zhang, C. L. Tracy, J. Lian, Z. Wang, W. J. Weber, D. Severin, M. Bender, C. Trautmann, and R. C. Ewing. Swift heavy ion track formation in $Gd_2Zr_{2-x}Ti_xO_7$ pyrochlore: Effect of electronic energy loss. *Nuclear instruments & methods in physics research / B*, 336:102 – 115, 2014.

[50] M. Lang, F. Zhang, J. Zhang, C. L. Tracy, A. B. Cusick, J. VonEhr, Z. Chen, C. Trautmann, and R. C. Ewing. Swift heavy ion-induced phase transformation in Gd_2O_3. *Nuclear instruments & methods in physics research / B*, 326:121 – 125, 2014.

[51] K. Li, B. Borm, F. Hug, D. Khaghani, B. Löher, D. Savran, N. A. Tahir, and P. Neumayer. Developments toward hard X-ray radiography on heavy-ion heated dense plasmas. *Laser and particle beams*, 32(04):631 – 637, 2014.

[52] W. Li, P. Kluth, D. Schauries, M. D. Rodriguez, M. Lang, F. Zhang, M. Zdorovets, C. Trautmann, and R. C. Ewing. Effect of orientation on ion track formation in apatite and zircon. *American mineralogist*, 99(5-6):1127 – 1132, 2014.

[53] Y. Litvinov, M. Palczewski, E. A. Cherepanov, and A. Sobiczewski. Ilustration of accuracy of presently used nuclear-mass models. *Acta physica Polonica / B*, 45(10):1979 – 1991, 2014.

[54] M. Lochmann, R. Jöhren, C. Geppert, Z. Andelkovic, D. Anielski, B. Botermann, M. Bussmann, A. Dax, N. Frömmgen, M. Hammen, V. Hannen, T. Kühl, Y. A. Litvinov, R. López-Coto, T. Stöhlker, R. C. Thompson, J. Vollbrecht, A. Volotka, C. Weinheimer, W. Wen, E. Will, D. Winters, R. Sánchez, and W. Nörtershäuser. Observation of the hyperfine transition in lithium-like bismuth $^{209}Bi^{80+}$: Towards a test of QED in strong magnetic fields. *Physical review / A*, 90(3):030501, 2014.

[55] B. Marx, K. S. Schulze, I. Uschmann, T. Kämpfer, O. Wehrhan, H. C. Wille, K. Schlage, R. Röhlsberger, E. Weckert, E. Förster, T. Stöhlker, and G. G. Paulus. High precision measurement of undulator polarization in the regime of hard x-rays. *Applied physics letters*, 105(2):024103, 2014.

[56] O. Matula, A. G. Hayrapetyan, V. G. Serbo, A. Surzhykov, and S. Fritzsche. Radiative capture of twisted electrons by bare ions. *New journal of physics*, 16(5):053024 –, 2014.

[57] R. Miletich, K. S. Scheidl, M. Schmitt, A. P. Moissl, T. Pippinger, G. D. Gatta, B. Schuster, and C. Trautmann. Static elasticity of cordierite I: Effect of heavy ion irradiation on the compressibility of hydrous cordierite. *Physics and chemistry of minerals*, 41(8):579 – 591, 2014.

[58] F. Muench, S. Bohn, M. Rauber, T. Seidl, A. Radetinac, U. Kunz, S. Lauterbach, H.-J. Kleebe, C. Trautmann, and W. Ensinger. Polycarbonate activation for electroless plating by dimethylaminoborane absorption and subsequent nanoparticle deposition. *Applied physics / A*, 116(1):287 – 294, 2014.

[59] F. Muench, A. Eils, M. E. Toimil-Molares, U. H. Hossain, A. Radetinac, C. Stegmann, U. Kunz, S. Lauterbach, H.-J. Kleebe, and W. Ensinger. Polymer activation by reducing agent absorption as a flexible tool for the creation of metal films and nanostructures by electroless plating. *Surface and coatings technology*, 242:100 – 108, 2014.

[60] F. Muench, T. Seidl, M. Rauber, B. Peter, J. Brötz, M. Krause, C. Trautmann, C. Roth, S. Katusic, and W. Ensinger. Hierarchically porous carbon membranes containing designed nanochannel architectures obtained by pyrolysis of ion-track etched polyimide. *Materials chemistry and physics*, 148(3):846 – 853, 2014.

[61] S. Nasir, M. Ali, P. Ramirez, V. Gómez, B. Oschmann, F. Muench, M. Nawaz Tahir, R. Zentel, S. Mafe, and W. Ensinger. Fabrication of Single Cylindrical Au-Coated Nanopores with Non-Homogeneous Fixed Charge Distribution Exhibiting High Current Rectifications. *ACS applied materials & interfaces*, 6(15):12486 – 12494, 2014.

[62] A. Osipowicz and B. Zipfel. Electron optical imaging properties of the KATRIN high field solenoid chain. *Nuclear instruments & methods in physics research / A*, 760:68 – 72, 2014.

[63] J. Papuga, M. L. Bissell, K. Kreim, C. Barbieri, K. Blaum, M. De Rydt, T. Duguet, R. F. Garcia Ruiz, H. Heylen, M. Kowalska, R. Neugart, G. Neyens, W. Nörtershäuser, M. M. Rajabali, R. Sánchez, N. Smirnova, V. Somà, and D. T. Yordanov. Shell structure of potassium isotopes deduced from their magnetic moments. *Physical review / C*, 90(3):034321, 2014.

[64] S. Park, M. Lang, C. L. Tracy, J. Zhang, F. Zhang, C. Trautmann, P. Kluth, M. D. Rodriguez, and R. C. Ewing. Swift heavy ion irradiation-induced amorphization of $La_2Ti_2O_7$. *Nuclear instruments & methods in physics research / B*, 326:145 – 149, 2014.

[65] A. R. Piriz, Y. B. Sun, and N. A. Tahir. Rayleigh-Taylor linear growth at an interface between an elastoplastic solid and a viscous liquid. *Physical review / E*, 89(6):063022, 2014.

[66] J. Prokůpek, J. Kaufman, D. Margarone, M. Krůs, A. Velyhan, J. Krása, T. Burris-Mog, S. Busold, O. Deppert, T. E. Cowan, and G. Korn. Development and first experimental tests of Faraday cup array. *Review of scientific instruments*, 85(1):013302, 2014.

[67] R. Reifarth and Y. Litvinov. Measurements of neutron-induced reactions in inverse kinematics. *Physical review / Special topics / Accelerators and beams*, 17(1).

[68] M. D. Rodriguez, W. X. Li, F. Chen, C. Trautmann, T. Bierschenk, B. Afra, D. Schauries, R. C. Ewing, S. T. Mudie, and P. Kluth. SAXS and TEM investigation of ion tracks in neodymium-doped yttrium aluminium garnet. *Nuclear instruments & methods in physics research / B*, 326:150 – 153, 2014.

[69] D. Schauries, B. Afra, T. Bierschenk, M. Lang, M. D. Rodriguez, C. Trautmann, W. Li, R. C. Ewing, and P. Kluth. The shape of ion tracks in natural apatite. *Nuclear instruments & methods in physics research / B*, 326:117 – 120, 2014.

[70] K. S. Scheidl, G. D. Gatta, T. Pippinger, B. Schuster, C. Trautmann, and R. Miletich. Static elasticity of cordierite II: effect of molecular CO_2 channel constituents on the compressibility. *Physics and chemistry of minerals*, 41(8):617 – 631, 2014.

[71] R. Schmidt, J. Blanco Sancho, F. Burkart, D. Grenier, D. Wollmann, N. A. Tahir, A. Shutov, and A. R. Piriz. First experimental evidence of hydrodynamic tunneling of ultra–relativistic protons in extended solid copper target at the CERN HiRadMat facility. *Physics of plasmas*, 21(8):080701, 2014.

[72] H. M. Scholz-Marggraf, S. Fritzsche, V. G. Serbo, A. Afanasev, and A. Surzhykov. Absorption of twisted light by hydrogenlike atoms. *Physical review / A*, 90(1):013425, 2014.

[73] K. S. Schulze, B. Marx, I. Uschmann, E. Förster, T. Stöhlker, and G. G. Paulus. Determination of the polarization state of x rays with the help of anomalous transmission. *Applied physics letters*, 104(15):151110, 2014.

[74] J. Schwartz, S. Aloni, D. F. Ogletree, M. Tomut, M. Bender, D. Severin, C. Trautmann, I. W. Rangelow, and T. Schenkel. Local formation of nitrogen-vacancy centers in diamond by swift heavy ions. *Journal of applied physics*, 116(21):214107, 2014.

[75] L. Senje, M. Yeung, B. Aurand, S. Kuschel, C. Rödel, F. Wagner, K. Li, B. Dromey, V. Bagnoud, P. Neumayer, M. Roth, C.-G. Wahlström, M. Zepf, T. Kuehl, and D. Jung. Diagnostics for studies of novel laser ion acceleration mechanisms. *Review of scientific instruments*, 85(11):113302, 2014.

[76] B. Sharkov and D. Varentsov. Experiments on extreme states of matter towards HIF at FAIR. *Nuclear instruments & methods in physics research / A*, 733:238 – 241, 2014.

[77] P. Shuai, H. S. Xu, X. L. Tu, Y. H. Zhang, B. H. Sun, M. Wang, Y. Litvinov, K. Blaum, X. H. Zhou, J. J. He, Y. Sun, K. Kaneko, Y. J. Yuan, J. W. Xia, J. C. Yang, G. Audi, X. L. Yan, X. C. Chen, G. B. Jia, Z. G. Hu, X. W. Ma, R. S. Mao, B. Mei, Z. Y. Sun, S. T. Wang, G. Q. Xiao, X. Xu, T. Yamaguchi, Y. Yamaguchi, Y. D. Zang, H. W. Zhao, T. C. Zhao, W. Zhang, and W. L. Zhan. Charge and frequency resolved isochronous mass spectrometry and the mass of ^{51}Co. *Physics letters / B*, 735:327 – 331, 2014.

[78] V. Sivakov, E. Y. Kaniukov, A. V. Petrov, O. V. Korolik, A. V. Mazanik, A. Bochmann, S. Teichert, I. J. Hidi, A. Schleusener, D. Cialla, M. Eugenia Toimil-Molares, C. Trautmann, J. Popp, and S. E. Demyanov. Silver nanostructures formation in porous Si/SiO$_2$ matrix. *Journal of crystal growth*, 400:21 – 26, 2014.

[79] C. Smorra, K. Blaum, K. Franke, Y. Matsuda, A. Mooser, H. Nagahama, C. Ospelkaus, W. Quint, G. Schneider, S. Van Gorp, J. Walz, Y. Yamazaki, and S. Ulmer. Towards a high-precision measurement of the antiproton magnetic moment. *Hyperfine interactions*, 228(1-3):31 – 36, 2014.

[80] A. Sobiczewski and Y. Litvinov. Accuracy of theoretical descriptions of nuclear masses. *Physical review / C*, 89(2):024311, 2014.

[81] A. Sobiczewski and Y. Litvinov. Predictive power of nuclear-mass models. *Physical review / C*, 90(1):017302, 2014.

[82] M. V. Sorokin, K. Schwartz, C. Trautmann, A. Dauletbekova, and A. S. El-Said. Modeling of defect accumulation in lithium fluoride crystals under irradiation with swift ions. *Nuclear instruments & methods in physics research / B*, 326:307 – 310, 2014.

[83] T. Stöhlker, Y. A. Litvinov, A. Bräuning-Demian, M. Lestinsky, F. Herfurth, R. Maier, D. Prasuhn, R. Schuch, and M. Steck. SPARC collaboration: new strategy for storage ring physics at FAIR. *Hyperfine interactions*, 227(1-3):45 – 53, 2014.

[84] N. A. Tahir, F. Burkart, A. Shutov, R. Schmidt, D. Wollmann, and A. R. Piriz. Simulations of beam-matter interaction experiments at the CERN HiRadMat facility and prospects of high-energy-density physics research. *Physical review / E*, 90(6):063112, 2014.

[85] N. A. Tahir, V. Kim, B. Schlitt, W. Barth, L. Groening, I. Lomonosov, A. Piriz, T. Stöhlker, and H. Vormann. Three-dimensional thermal simulations of thin solid carbonfoils for charge stripping of high current uranium ion beams at a proposed new heavy-ion linac at GSI. *Physical review / Special topics / Accelerators and beams*, 17(4):041003, 2014.

[86] S. Tashenov, D. Banaś, H. Beyer, C. Brandau, S. Fritzsche, A. Gumberidze, S. Hagmann, P.-M. Hillenbrand, H. Jörg, I. Kojouharov, C. Kozhuharov, M. Lestinsky, Y. Litvinov, A. Maiorova, H. Schaffner, V. Shabaev, U. Spillmann, T. Stöhlker, A. Surzhykov, and S. Trotsenko. Observation of Coherence in the Time-Reversed Relativistic Photoelectric Effect. *Physical review letters*, 113(11):113001, 2014.

[87] D. Tiedemann, K. E. Stiebing, D. Winters, W. Quint, V. Varentsov, A. Warczak, A. Malarz, and T. Stöhlker. A pulsed supersonic gas jet target for precision spectroscopy at the HITRAP facility at GSI. *Nuclear instruments & methods in physics research / A*, 764:387 – 393, 2014.

[88] C. L. Tracy, J. McLain Pray, M. Lang, D. Popov, C. Park, C. Trautmann, and R. C. Ewing. Defect accumulation in ThO_2 irradiated with swift heavy ions. *Nuclear instruments & methods in physics research / B*, 326:169 – 173, 2014.

[89] X. L. Tu, Y. Sun, Y. H. Zhang, H. S. Xu, K. Kaneko, Y. A. Litvinov, and M. Wang. A survey of Coulomb displacement energies and questions on the anomalous behavior in the upper fp-shell. *Journal of physics / G*, 41(2):025104 –, 2014.

[90] A. E. Velasco, C. Yang, Z. S. Siwy, M. E. Toimil Molares, and P. Taborek. Flow and evaporation in single micrometer and nanometer scale pipes. *Applied physics letters*, 105(3):033101, 2014.

[91] M. Vogel, H. Häffner, K. Hermanspahn, S. Stahl, J. Steinmann, and W. Quint. Resistive and sympathetic cooling of highly-charged-ion clouds in a Penning trap. *Physical review / A*, 90(4):043412, 2014.

[92] F. Wagner, S. Bedacht, A. Ortner, M. Roth, A. Tauschwitz, B. Zielbauer, and V. Bagnoud. Pre-plasma formation in experiments using petawatt lasers. *Optics express*, 22(24):29505 –, 2014.

[93] F. Wagner, C. P. João, J. Fils, T. Gottschall, J. Hein, J. Körner, J. Limpert, M. Roth, T. Stöhlker, and V. Bagnoud. Temporal contrast control at the PHELIX petawatt laser facility by means of tunable sub-picosecond optical parametric amplification. *Applied physics / B*, 116(2):429 – 435, 2014.

[94] T. White, N. Hartley, B. Borm, B. Crowley, J. Harris, D. Hochhaus, T. Kaempfer, K. Li, P. Neumayer, L. Pattison, F. Pfeifer, S. Richardson, A. Robinson, I. Uschmann, and G. Gregori. Electron-Ion Equilibration in Ultrafast Heated Graphite. *Physical review letters*, 112(14):145005, 2014.

[95] R. Zabels, I. Manika, K. Schwartz, J. Maniks, and R. Grants. MeV–GeV ion induced dislocation loops in LiF crystals. *Nuclear instruments & methods in physics research / B*, 326:318 – 321, 2014.

[96] V. A. Zaytsev, A. V. Maiorova, V. M. Shabaev, A. V. Volotka, S. Tashenov, G. Plunien, and T. Stöhlker. Parity-nonconservation effect in the dielectronic recombination of polarized electrons with heavy He-like ions. *Physical review / A*, 89(3):032703, 2014.

[97] W. Zhang, X. L. Tu, M. Wang, Y. H. Zhang, H. S. Xu, Y. Litvinov, K. Blaum, R. J. Chen, X. C. Chen, C. Y. Fu, Z. Ge, B. S. Gao, Z. G. Hu, W. J. Huang, S. Litvinov, D. W. Liu, X. W. Ma, R. S. Mao, B. Mei, P. Shuai, B. H. Sun, J. W. Xia, G. Q. Xiao, Y. M. Xing, X. Xu, T. Yamaguchi, X. L. Yan, J. C. Yang, Y. J. Yuan, Q. Zeng, X. Y. Zhang, H. W. Zhao, T. C. Zhao, and X. H. Zhou. Time-of-flight detectors with improved timing performance for isochronous mass measurements at the CSRe. *Nuclear instruments & methods in physics research / A*, 756:1 – 5, 2014.

[98] W. Zhang, X. L. Tu, M. Wang, Y. H. Zhang, H. S. Xu, Y. Litvinov, K. Blaum, X. C. Chen, Z. G. Hu, W. J. Huang, X. W. Ma, R. S. Mao, B. Mei, P. Shuai, B. H. Sun, T. Yamaguchi, J. W. Xia, G. Q. Xiao, X. Xu, X. L. Yan, J. C. Yang, Y. J. Yuan, X. H. Zhou, H. W. Zhao, and T. C. Zhao. A timing detector with pulsed high-voltage power supply for mass measurements at CSRe. *Nuclear instruments & methods in physics research / A*, 755:38 – 43, 2014.

[99] N. A. Zubova, Y. S. Kozhedub, V. M. Shabaev, I. I. Tupitsyn, A. V. Volotka, G. Plunien, C. Brandau, and T. Stöhlker. Relativistic calculations of the isotope shifts in highly charged Li-like ions. *Physical review / A*, 90(6):062512, 2014.

DOI:10.15120/GR-2015-1-ANNEX-02

JCR publications to the programme cancer research published in 2014

See http://repository.gsi.de for more information.

[1] V. Batista, D. Richter, S. Combs, and O. Jäkel. Inter- and Intra-fractional Motion Robustness for Pancreatic Patients Treated With Scanned Carbon Ion Therapy. 56th Annual Meeting of the American-Society-for-Radiation-Oncology, San Francisco (California (USA)), 14 Sep 2014 - 17 Sep 2014, 2014.

[2] M. Beck, C. Rombouts, M. Moreels, A. Aerts, R. Quintens, K. Tabury, A. Michaux, A. Janssen, M. Neefs, E. Ernst, B. Dieriks, R. Lee, W. De Vos, C. Lambert, P. Van Oostveldt, and S. Baatout. Modulation of gene expression in endothelial cells in response to high LET nickel ion irradiation. *International journal of molecular medicine*, 4:1124–32, 2014.

[3] A. Becker, M. Durante, G. Taucher-Scholz, and B. Jakob. ATM Alters the Otherwise Robust Chromatin Mobility at Sites of DNA Double-Strand Breaks (DSBs) in Human Cells. *PLoS one*, 9(3):e92640, 2014.

[4] C. Bert and M. Durante. Particle radiosurgery: A new frontier of physics in medicine. *Physica medica*, 30(5):535 – 538, 2014.

[5] C. Bert, C. Graeff, M. Riboldi, S. Nill, G. Baroni, and A. Knopf. Advances in 4D Treatment Planning for Scanned Particle Beam Therapy – Report of Dedicated Workshops. *Technology in cancer research & treatment*, 13(6):485–95, 2014.

[6] G. Bertrand, M. Maalouf, A. Boivin, P. Battiston-Montagne, M. Beuve, A. Levy, P. Jalade, C. Fournier, D. Ardail, N. Magné, G. Alphonse, and C. Rodriguez-Lafrasse. Targeting Head and Neck Cancer Stem Cells to Overcome Resistance to Photon and Carbon Ion Radiation. *Stem cell reviews and reports*, 10(1):114 – 126, 2014.

[7] J. Deperas-Standylo, E. Gudowska-Nowak, and S. Ritter. Stochastic modelling for biodosimetry: Predicting the chromosomal response to radiation at different time points after exposure. *The European physical journal / D*, 68(7):204, 2014.

[8] J. G. Eley, W. D. Newhauser, R. Lüchtenborg, C. Graeff, and C. Bert. 4D optimization of scanned ion beam tracking therapy for moving tumors. *Physics in medicine and biology*, 59(13):3431 – 3452, 2014.

[9] G. Fattori, M. Riboldi, E. Scifoni, M. Krämer, A. Pella, M. Durante, S. Ronchi, M. Bonora, R. Orecchia, and G. Baroni. Dosimetric effects of residual uncertainties in carbon ion treatment of head chordoma. *Radiotherapy and oncology*, 113(1):66 – 71, 2014.

[10] G. Fattori, N. Saito, M. Seregni, R. Kaderka, A. Pella, A. Constantinescu, M. Riboldi, P. Steidl, P. Cerveri, C. Bert, M. Durante, and G. Baroni. Commissioning of an Integrated Platform for Time-Resolved Treatment Delivery in Scanned Ion Beam Therapy by Means of Optical Motion Monitoring. *Technology in cancer research & treatment*, 13(6):517 – 528, 2014.

[11] K. Frey, J. Bauer, D. Unholtz, C. Kurz, M. Krämer, T. Bortfeld, and K. Parodi. TPS PET —A TPS-based approach for in vivo dose verification with PET in proton therapy. *Physics in medicine and biology*, 59(1):1 – 21, 2014.

[12] T. Friedrich, M. Durante, and M. Scholz. Comments to the paper “Modelling of cell killing due to sparsely ionizing radiation in normoxic and hypoxic conditions and an extension to high LET radiation” by A. Mairani et al., Int. J. Radiat. Biol. 89(10), 2013, 782–793. *International journal of radiation biology*, 89:782–793, 2014.

[13] T. Friedrich, M. Durante, and M. Scholz. Modeling Cell Survival after Irradiation with Ultrasoft X Rays using the Giant Loop Binary Lesion Model. *Radiation research*, 181(5):485 – 494, 2014.

[14] T. Friedrich, U. Scholz, M. Durante, and M. Scholz. RBE of ion beams in hypofractionated radiotherapy (SBRT). *Physica medica*, 30(5):588 – 591, 2014.

[15] J. Friess, A. Heselich, S. Ritter, P. G. Layer, and C. Thielemann. Electrophysiologic and molecular characteristics of cardiomyocytes after heavy ion irradiation in the frame of the ESA IBER-10 program. *Journal of radiation research*, 55(suppl 1):i40 – i41, 2014.

[16] J. Golak, R. Skibiński, K. Topolnicki, H. Witała, E. Epelbaum, H. Krebs, H. Kamada, U.-G. Meißner, V. Bernard, P. Maris, J. Vary, S. Binder, A. Calci, K. Hebeler, J. Langhammer, R. Roth, A. Nogga, S. Liebig, and D. Minossi. Low-energy neutron-deuteron reactions with N^3LO chiral forces. *The European physical journal / A*, 50(11):177, 2014.

[17] C. Graeff. Motion mitigation in scanned ion beam therapy through 4D-optimization. *Physica medica*, 30(5):570 – 577, 2014.

[18] C. Graeff, A. Constantinescu, R. Lüchtenborg, M. Durante, and C. Bert. Multigating, a 4D Optimized Beam Tracking in Scanned Ion Beam Therapy. *Technology in cancer research & treatment*, 13(6):497 – 504, 2014.

[19] L. Herr, T. Friedrich, M. Durante, and M. Scholz. A Model of Photon Cell Killing Based on the Spatio-Temporal Clustering of DNA Damage in Higher Order Chromatin Structures. *PLoS one*, 9(1):e83923, 2014.

[20] S. Hild, C. Graeff, J. Trautmann, M. Kraemer, K. Zink, M. Durante, and C. Bert. Fast optimization and dose calculation in scanned ion beam therapy. *Medical physics*, 41(7):071703, 2014.

DOI:10.15120/GR-2015-1-ANNEX-03

[21] C. P. Karger, M. Scholz, P. E. Huber, J. Debus, and P. Peschke. Photon and Carbon Ion Irradiation of a Rat Prostate Carcinoma: Does a Higher Fraction Number Increase the Metastatic Rate? *Radiation research*, 181(6):623 – 628, 2014.

[22] A. Knopf, S. Nill, I. Yohannes, C. Graeff, S. Dowdell, C. Kurz, J.-J. Sonke, A. K. Biegun, S. Lang, J. McClelland, B. Champion, M. Fast, J. Wölfelschneider, C. Gianoli, A. Rucinski, G. Baroni, C. Richter, S. van de Water, C. Grassberger, D. Weber, P. Poulsen, S. Shimizu, and C. Bert. Challenges of radiotherapy: Report on the 4D treatment planning workshop 2013. *Physica medica*, 30(7):809 – 815, 2014.

[23] M. Krämer, E. Scifoni, F. Schmitz, O. Sokol, and M. Durante. Overview of recent advances in treatment planning for ion beam radiotherapy. *The European physical journal / D*, 68(10):306, 2014.

[24] S. Luft, D. Pignalosa, O. Arrizabalaga, E. Nasonova, A. Helm, M. Durante, and S. Ritter. The effect of X-rays and C-ions on pluripotent embryonic stem cells. *Journal of radiation research*, 55(suppl 1):i55 – i56, 2014.

[25] S. Luft, D. Pignalosa, E. Nasonova, O. Arrizabalaga, A. Helm, M. Durante, and S. Ritter. Fate of D3 mouse embryonic stem cells exposed to X-rays or carbon ions. *Mutation research / Genetic toxicology and environmental mutagenesis*, 760:56 – 63, 2014.

[26] L. Piersanti, F. Bellini, F. Bini, F. Collamati, E. De Lucia, M. Durante, R. Faccini, F. Ferroni, S. Fiore, E. Iarocci, C. L. Tessa, M. Marafini, I. Mattei, V. Patera, P. G. Ortega, A. Sarti, C. Schuy, A. Sciubba, M. Vanstalle, and C. Voena. Measurement of charged particle yields from PMMA irradiated by a 220 MeV/u ^{12}C beam. *Physics in medicine and biology*, 59(7):1857 – 1872, 2014.

[27] M. Prall, R. Kaderka, N. Saito, C. Graeff, C. Bert, M. Durante, K. Parodi, J. Schwaab, C. Sarti, and J. Jenne. Ion beam tracking using ultrasound motion detection. *Medical physics*, 41(4):041708, 2014.

[28] D. Richter, C. Graeff, O. Jäkel, S. E. Combs, M. Durante, and C. Bert. Residual motion mitigation in scanned carbon ion beam therapy of liver tumors using enlarged pencil beam overlap. *Radiotherapy and oncology*, 113(2):290 – 295, 2014.

[29] D. Richter, N. Saito, N. Chaudhri, M. Härtig, M. Ellerbrock, O. Jäkel, S. E. Combs, D. Habermehl, K. Herfarth, M. Durante, and C. Bert. Four-Dimensional Patient Dose Reconstruction for Scanned Ion Beam Therapy of Moving Liver Tumors. *International journal of radiation oncology, biology, physics*, 89(1):175 – 181, 2014.

[30] B. Roth, C. S. Gibhardt, P. Becker, M. Gebhardt, J. Knoop, C. Fournier, A. Moroni, and G. Thiel. Low-dose photon irradiation alters cell differentiation via activation of hIK channels. *Pflügers Archiv*, 1:1, 2014.

[31] M. Saager, C. Glowa, P. Peschke, S. Brons, M. Scholz, P. E. Huber, J. Debus, and C. P. Karger. Carbon Ion Irradiation of the Rat Spinal Cord: Dependence of the Relative Biological Effectiveness on Linear Energy Transfer. *International journal of radiation oncology, biology, physics*, 90(1):63 – 70, 2014.

[32] F. S. B. Subtil, J. Wilhelm, V. Bill, N. Westholt, S. Rudolph, J. Fischer, S. Scheel, U. Seay, C. Fournier, G. Taucher-Scholz, M. Scholz, W. Seeger, R. Engenhart-Cabillic, F. Rose, J. Dahm-Daphi, and J. Hanze. Carbon ion radiotherapy of human lung cancer attenuates HIF-1 signaling and acts with considerably enhanced therapeutic efficiency. *The FASEB journal*, 28(3):1412 – 1421, 2014.

[33] C. L. Tessa, T. Berger, R. Kaderka, D. Schardt, S. Burmeister, J. Labrenz, G. Reitz, and M. Durante. Characterization of the secondary neutron field produced during treatment of an anthropomorphic phantom with x-rays, protons and carbon ions. *Physics in medicine and biology*, 59(8):2111 – 2125, 2014.

[34] V. Tschachojan, H. Schroer, N. Averbeck, and W. Mueller-Klieser. Carbon ions and X-rays induce pro-inflammatory effects in 3D oral mucosa models with and without PBMCs. *Oncology reports*, 32(5):1820–1828, 2014.

[35] C. Wälzlein, M. Krämer, E. Scifoni, and M. Durante. Advancing the modeling in particle therapy: From track structure to treatment planning. *Applied radiation and isotopes*, 83:171 – 176, 2014.

[36] C. Wälzlein, M. Krämer, E. Scifoni, and M. Durante. Low-energy electron transport in non-uniform media. *Nuclear instruments & methods in physics research / B*, 320:75 – 82, 2014.

[37] C. Wälzlein, E. Scifoni, M. Krämer, and M. Durante. Simulations of dose enhancement for heavy atom nanoparticles irradiated by protons. *Physics in medicine and biology*, 59(6):1441 – 1458, 2014.

DOI:10.15120/GR-2015-1-ANNEX-03

Doctoral theses 2014 supparted by the GSI

See http://repository.gsi.de for more information.

[1] H. Al-Omari. *Measurement and interpretation of laser accelerated protons at GSI.* Dr., Univ. Frankfurt/M, Darmstadt, 2014.

[2] S. Altstadt. $^{13,14}B(n,\gamma)$ *via Coulomb Dissociation to Constrain the Astrophysical r-Process.* Dr., Goethe Universität Frankfurt/M, 2014.

[3] A. Arend. *Optimization of a transition radiation detector for the Compressed Baryonic Matter experiment.* Dr., JWGU Frankfurt, 2015.

[4] T. Balog. *Development of Detector Systems for CBM and SFRS at FAIR.* Dr., Comenius University Bratislava, 2014.

[5] A. Becker. *Influence of repair proteins and chromatin modifiers on mobility of DNA double-strand breaks induced by heavy ion irradiation.* Dr., TU Darmstadt, 2014.

[6] M. Bendel. *Entwicklung einer neuartigen Nachweismethode hochenergetischer Teilchen im CALIFA-Kalorimeter.* Dr., Technische Universität München, München, 2014.

[7] C. Brabetz. *Development of specially shaped laser beams for the optimized acceleration of particles.* Dr., University of Frankfurt, 2014.

[8] D. Bremer. *Measurements and simulations on position dependencies in the response of single PWO crystals and a prototype for the PANDA EMC.* Dr., JLU Giessen, Giessen, 2014.

[9] S. Busold. *Construction and characterization of a laser-driven proton beamline at GSI.* Dr., Darmstadt Technical University, Darmstadt, 2014.

[10] G. Colucci. *Relativistic effective models for dense nuclear matter at non-zero temperature and magnetic field.* Dr., JWGU Frankfurt, Frankfurt am Main, 2014.

[11] A. Constantinescu. *Planning studies for a non-invasive treatment of atrial fibrillation with acanned beams.* Dr., TU Darmstadt, Darmstadt, 2014.

[12] A. Echler. *E-TOF Messungen mit kalorimetrischen Tieftemperatur-Detektoren zur Bestimmung spezifischer Energieverluste und zur Massenidentifikation niederenergetischer Schwerionen.* Dr., Uni Mainz, Mainz, 2013.

[13] S. El-Mousatti. *Elektronenstrahl-Diagnostik zur Bestimmung vom transversalen Profil intensiver Ionenstrahlen.* Dr., Darmstadt Technical University, Darmstadt, 2014.

[14] D. Gelfand. *Lattice theory of nonequilibrium Fermion production.* Dr., Ruperto-Carola Univ. Heidelberg, Heidelberg, 2014.

[15] M. Grahl. *Low-energy effective models for two-flavor quantum chromodynamics and the universality hypothesis.* Dr., JWGU Frankfurt, Frankfurt, 2014.

[16] R. Grün. *Impact of tissue specific parameters on the prediction of the biological effectiveness for treatment planning in ion beam therapy.* Dr., Philipps-Universität Marburg, Marburg, 2014.

[17] G. Guastalla. *Shell structure in the vicinity of the doubly magic* ^{100}*Sn via Coulomb excitation at PreSPEC.* Dr., TU Darmstadt, Darmstadt, 2014.

[18] T. Habermann. *Fast pulse shape analysis for AGATA.* Dr., JWGU Frankfurt, Frankfurt, 2014.

[19] S. Höfer. *Zeitaufgelöste Röntgenbeugung an einkristallinem Indiumantimonid.* Dr., University of Jena, Jena, 2015.

[20] A. Hayrapetyan. *Angular momentum representation of laser-driven matter waves: twisted electrons and atoms.* Dr., Heidelberg, Heidelberg, 2014.

[21] M. Heide. *Measurement of semi-electronic beauty-hadron decays via their impact parameter in pp collisions in ALICE.* Dr., Westfälischen Wilhelms-Universität Münster, Münster, 2014.

[22] M. Heine. *Measurement of (n,g)-Rates of Light Neutron-Rich Nuclei for the r-Process Nucleosynthesis.* Dr., TU Darmstadt, Darmstadt, 2015.

[23] A. Heinz. *QCD under extreme conditions: Inhomogeneous condensation.* Dr., JWGU Frankfurt, Frankfurt am Main, 2014.

[24] M. Herrlitz. *Elucidation of DNA methylation changed in response to ionizing radiation induced double strand breaks.* Dr., TU Darmstadt, Darmstadt, 2014.

[25] G. Hoffmeister. *Influencing laser-accelerated ions by femtosecond-laser desorption.* Dr., Darmstadt Technical University, Darmstadt, 2014.

[26] M. Holl. *Quasi-Free Scattering from Relativistic Neutron-Deficient Carbon Isotopes.* Dr., TU Darmstadt, Darmstadt, 2014.

[27] U. H. Hossain. *Swift Heavy Ion Induced Modification of Aliphatic Polymers.* Dr., Darmstadt Technical University, Darmstadt, 2015.

[28] L. Huther. *Nucleosynthesis in Neutrono Driven Winds.* Dr., TU Darmstadt, Darmstadt, 2013.

[29] M. Köhler. *Dielectron production in proton-proton collisions with ALICE.* Dr., TU Darmstadt, Darmstadt, 2014.

[30] M. Kühnel. *Time-resolved crystallization of deeply cooled liquid hydrogen isotopes.* Dr., University of Frankfurt, Frankfurt, 2014.

DOI:10.15120/GR-2015-1-ANNEX-04

[31] M. L. Knichel. *Transverse momentum distributions of primary charged particles in pp, p-Pb and Pb-Pb collisions measured with ALICE at the LHC.* Dr., TU Darmstadt, Darmstadt, 2014.

[32] J. Kopfer. *Development of a prototype camera and Monte Carlo studies for the optimisation of the CBM-RICH detector.* Dr., Bergische Universitaet Wuppertal, Wuppertal, 2014.

[33] B. Löher. *Probing the Decay Characteristics of the Pygmy Dipole Resonance in the Semi-Magic Nucleus ^{140}Ce with Gamma-Gamma Coincidence Measurements.* Dr., Johannes Gutenberg-Universität Mainz, Mainz, 2014.

[34] P.-M. Lang. *Aufbau und Test des Protonenmikroskops PRIOR.* Dr., Darmstadt Technical University, Darmstadt, 2014.

[35] J.-F. Martin. *Coulex fission of ^{234}U, ^{235}U, ^{237}Np, and ^{238}Np studied within the SOFIA experimental program.* Dr., Université Paris Sud, Paris, 2014.

[36] D. Müssig. *Re-scanning in scanned ion beam therapy in the presence of organ motion.* Dr., TU Darmstadt, Darmstadt, 2014.

[37] O. Matula. *Atomic Processes with Twisted Particles: Photoionization and Radiative Recombination.* Dr., University of Heidelberg, Heidelberg, 2014.

[38] J. Mendoza. *Nuclear masses and their imapct in r-process nucleosynthesis.* Dr., TU Darmstadt, Darmstadt, 2014.

[39] M. A. Najafi. *Quasi-free proton and neutron knockout reactions in ^{20}O.* Dr., University of Groningen, Groningen, 2013.

[40] S. Nasir. *Stimuli-Triggered Ionic and Molecular Transport through Track-Etched Nanopores.* Dr., Darmstadt Technical University, Darmstadt, 2014.

[41] N. Petridis. *The internal multiphase target for storage ring experiments.* Dr., University of Frankfurt, Frankfurt, 2014.

[42] P. Piasecki. *Strongly interacting matter in a finite volume.* Dr., TU Darmstadt, Darmstadt, 2014.

[43] C. Pinke. *Lattice QCD at finite temperature with Wilson fermions.* Dr., JWGU Frankfurt, Frankfurt am Main, 2014.

[44] D. Rohr. *On development, feasibility, and limits of highly efficient CPU and GPU programs in several fields.* Dr., JWGU Frankfurt, Frankfurt am Main, 2014.

[45] C. Romig. *Investigation of nuclear structure with relative self-absorption measurements.* Dr., TU Darmstadt, Darmstadt, 2014.

[46] B. Roth. *Exposure to sparsely and densely ionizing irradiation results in an immediate activation of K^+ channels in A549 cells and in human peripheral blood lymphocytes.* Dr., TU Darmstadt, Darmstadt, 2014.

[47] C. Schuy. *Fragmentation of 400 meV/u ^{12}C on a thin graphite target.* Dr., TU Darmstadt, Darmstadt, 2015.

[48] E. Seel. *Effective theories of QCD at non-zero temperature.* Dr., JWGU Frankfurt, Frankfurt, 2014.

[49] R. Singh. *Tune Measurement At GSI SIS-18: Methods And Applications.* Dr., TU Darmstadt, Darmstadt, 2014.

[50] M. Singla. *The Silicon Tracking System of the CBM experiment at FAIR : development of microstrip sensors and signal transmission lines for a low-mass, low-noise system.* Dr., JWGU Frankfurt, Frankfurt am Main, 2014.

[51] I. Sorokin. *Characterization of silicon microstrip sensors, front-end electronics, and prototype tracking detectors for the CBM experiment at FAIR.* Dr., JWGU Frankfurt, Frankfurt am Main, 2014.

[52] F. Tommasino. *DNA damage induction and processing following exposure to low and high LET radiation : the role of micrometer-scale clustering in higher-order chromatin structures.* Dr., TU Darmstadt, Darmstadt, 2014.

[53] J. Uphoff. *Open Heavy Flavor and Other Hard Probes in Ultra-Relativistic Heavy-Ion Collisions.* Dr., JWGU Frankfurt, Frankfurt, 2014.

[54] F. Wagner. *Kontrolle des zeitlichen Kontrastes am Lasersystem PHELIX.* Dr., Darmstadt Technical University, Darmstadt, 2014.

[55] X. Yan. *Precision mass measurements of neutron-deficient nuclei in storage rings.* Dr., Grad. University of CAS, 2014.

Experiments performed at the GSI accelerators in 2014

Compiled by Burkhard Kolb[1], beam time coordinator 2014

[1]GSI, Darmstadt, Germany

In all tables 1 shift represents 8 hours of beam delivered to an experiment including necessary accelerator tuning time.

Exp	Short title	Spokesperson	Area	Ion	Shifts
U182	CO chemistry with Sg	Kratz/ Düllmann/ Even	X8	^{22}Ne	13
U207	Laser spectroscopy of Nobelium	Backe/ Block	Y7	^{48}Ca	25
U249	R&D on advanced diamond detectors	Kis	X0	C	14
U259	Chemistry Z=114	Düllmann	X8	^{48}Ca, ^{50}Ti	59
U263	Study of shell effects in the system U+U	Heinz	Z7	U	20
U275	Plasmastripper	Xu Jacoby	Z6	Bi, Au	23
U277	Reaction Studies	Heinz	Y6	Xe	25
U278	Decay properties of Db-258	Andersson/ Heßberger	Y7	^{50}Ti	48
U279	Single Event Transient Measurements in Asynchronous Logic for project FATAL	Schweiger/ Zimmermann/ Voss	X0	Ti	32
U280	Heavy Ion Stopping in Laser-Plasmas	Rosmej	Z6	Ti, Ca	17
U281	Ion energy loss at maximum stopping power in a laser-generated plasma	Cayzac/ Blazevic	Z6	N	20
U282	Interaction of heavy ions with dense plasma	Ortner/ Blazevic	Z6	Ca	22
UBIO	RadBio Experiments	Friedrich/ Scholz	X0, X6	C, Au, U	28
UMAT	Material science	Severin/ Trautmann	X0, M1, M3	C. Sm, Bi, Au, U	443

E082	beta decay	Litvinov	ESR	^{152}Sm	36
E098	Channeling in Cave A	Bräuning-Demian	ESR/HTA	U	13
E101	Hyperfine-splitting of Be-like Bismuth	Nörtershäuser	ESR	BI	38
E103	Towards the Observation of Quasi-Molecular Radiation	Gumberidze	ESR	^{132}Xe	30
E108	ESR (p,gamma)	Reifarth/Heil	ESR	^{124}Xe	9

DOI:10.15120/GR-2015-1-ANNEX-05

E111	Measurement of Breit interaction	Trotsenko	ESR	Au	31
E120	HITRAP commissioning	Herfurth/Steck	ESR	N, Ne	56

S333	HADES pion beam	Salabura	HAD	N (pions)	64
S386	PANDA-DIRC	Schwarz	HTC	p, N (pions)	10
S401	CBM-detectortests	Heuser/Kis	HAD/HTC	Ca, Ni	10
S417	SFRS development	Nocifo-ro/Simon	FRS	Ni, Au, U	12
S419	Umbrella test for DESPEC	Algora	FRS	Xe	6
S426	AGATA 85Br	Pietralla/Gerl	FRS	^{86}Kr	14
S431	Agata campaign	Gerl	FRS	U	13
S434	Agata campaign	Gerl	FRS	Ni	24
S436	tensor force	Tanihata	FRS	p, C	35
S437	eta prime	Itahashi/Fujioka	FRS	p	12
S438	Test R3B GLAD	Aumann / Simon	FRS/HTC	U	40
S439	PRIOR	Varentsov	HHT	p	27
SBIO	Investigations on therapy of atrial fibrillation	Durante	HTM	C, Fe	51
SESA	Space related radiation biophysics	Durante	HTA/HTM	Xe	1
SMAT	Material science	Trautmann	HTA	Bi, Sm, Au, U	53

Statutory organs and scientific advisory committees of GSI (2014)

Compiled by K. Füssel

Supervisory Board / Aufsichtsrat (AR):

Staatssekretär Dr. G. Schütte [chair],
Bundesministerium für Bildung und Forschung, Bonn/Berlin (Germany),
as representative of the Federal Republic of Germany

Dr. B. Vierkorn-Rudolf,
Bundesministerium für Bildung und Forschung, Bonn/Berlin (Germany),
as representative of the Federal Republic of Germany

Ministerialdirigent Dr. R. Bernhardt [vice-chair],
Hessisches Ministerium für Wissenschaft und Kunst, Wiesbaden (Germany),
as representative of the State of Hesse in Germany

Ministerialdirigentin I. Schäfer,
Ministerium für Bildung, Wissenschaft, Weiterbildung und Kultur, Mainz (Germany),
as representative of the State of Rhineland-Palatinate in Germany

Ministerialrat D. Klein,
Thüringer Kultusministerium für Bildung, Wissenschaft und Kultur, Erfurt (Germany),
as representative of the State of Thuringia in Germany

Prof. Dr. K.-H. Kampert,
Bergische Universität Wuppertal (Germany),
as representative of the Scientific Council of GSI

Prof. Dr. U. Steigenberger,
ISIS Rutherford Appleton Laboratory, Oxfordshire (United Kingdom),
as representatives from the fields of science and economy

Prof. Dr. R. Heuer,
European Organization for Nuclear Research CERN, Geneva (Switzerland),
as representatives from the fields of science and economy

Dr. B. Lommel,
GSI Helmholtzzentrum für Schwerionenforschung,
as spokesperson of the Scientific-Technical Council of GSI

Directors' Board / Geschäftsführung (GF):

Prof. Dr. H. Stöcker, U. Weyrich
Prof. Dr. K. Langanke (assoc.), Prof. Dr. O. Kester (assoc.)

Scientific Council / Wissenschaftlicher Beirat (WBR):

https://www.gsi.de/work/organisation/wissenschaftliche_gremien/wr.htm
K.-H. Kampert [chair], Bergische Universität Wuppertal (Germany);
A. Bracco, University of Milano (Italy); *P. Chomaz*, CEA/Saclay, Gif-sur-Yvette (France); *R. Hayano*, University of Tokyo (Japan); *B. Jacak*, Stony Brook University, Stony Brook, New York (USA); *S. Jacquemot*, LULI, Palaiseau (France); *T. Roser*, BNL, Upton (USA); *E. Tomasi-Gustafsson*, CEA/Saclay, IRFU/SPhN, IN2P3/IPN Orsay (France); *A. Warczak*, Jagiellonian University, Warsaw (Poland);
Secretary: K.-D. Groß

DOI:10.15120/GR-2015-1-ANNEX-06

Scientific and Technical Council / Wissenschaftlich-Technischer Rat (WTR):

https://www.gsi.de/work/organisation/wissenschaftliche_gremien/wtr.htm
B. Lommel (Spokesperson); *D. Ackermann; R. Bär; W. Barth; W. Bayer; P. Braun-Munzinger; A. Bräuning-Demian; M. Durante; R. Fuchs; M. Gorska; F. Herfurth; Y. Leifels* (Vice-Spokesperson)*; V. Lindenstruth; Y. Litvinov;P. Malzacher; F. Maas; D. Ondreka; K. Peters; H. Reich-Sprenger; C. Scheidenberger; L. Schmitt; M. Schwickert; P. Senger; H. Simon; P. Spiller; J. Stadlmann; M. Steck; T. Stöhlker; C. Trautmann; G. Walter; U. Weinrich;*

Scientific Programme Advisory Committees of GSI

https://www.gsi.de/work/organisation/wissenschaftliche_gremien.htm

General Program Advisory Committee G-PAC:

P. Giubellino[chair], INFN Turin, Turin (Italy);
B. Blank, CEN Bordeaux-Gradignan, Gradignan (France); *Y. Blumenfeld*, CERN, Geneva (Switzerland); *W. Catford*, University of Physics, Guilford (UK); *R. Hoekstra*, KVI Groningen, Groningen (The Netherlands); *S. Leupold*, Uppsala University, Uppsala (Sweden); *N. Pietralla*, Technische Universität Darmstadt, Darmstadt (Germany); *H. Schatz*, Michigan State University, East Leasing (USA); *R. Schuch*, Stockholm University, Stockholm (Sweden); *A. Türler*, Paul Scherer Institut, Villigen (Switzerland); *M. Wada*, RIKEN, Saitama (Japan); *M. Weidemüller*, Ruprecht-Karls-Universität Heidelberg, Heidelberg (Germany).

PHELIX Committee:

https://www.gsi.de/work/organisation/wissenschaftliche_gremien/pac/ppac.htm
V. Fortov [chair], JIHT, RAS, Moscow (Russia);
D. Gericke, University of Warwick, Coventry (UK); *A. Golubev*, ITEP, Moscow (Russia); *D. Schneider [vice-chair]*, LLNL-PAT/NIF, Livermore, California (USA); V. *Tikhonchuk*, University of Bordeaux 1, Talence (France); *O. Willi*, Heinrich Heine Universität, Düsseldorf (Germany).

Biophysics & Radio-Biology Program Advisory Committee (Bio-PAC):

G. Reitz [chair], Deutsches Zentrum für Luft- und Raumfahrt (DLR), Cologne (Germany);
F. A. Cucinotta, NASA Johnson Space Center, Houston, Texas (USA); D. *Goodhead*, Emeritus Director of the Med. Res. Council Rad. and Genome Stability Unit, Oxford (United Kingdom); *T. Haberer*, HIT Betriebs GmbH am Universitätsklinikum Heidelberg, Heidelberg (Germany); *A. Kronenberg*, Lawrence Berkeley National Laboratory, Berkeley, California (USA); *L. Sabatier*, Institute of Cell. & Mol. Radiation Biology, Fonteney-aux-Roses (France).

Materials Research Program Advisory Committee (Mat-PAC):

P. Apel, JINR, Dubna (Russia); *S. Bouffard*, CEA-CNRS-ENSICAEN, Caen (France);
K. Hjort, University of Uppsala, Uppsala (Sweden); *W. Wesch*, Friedrich-Schiller-Universität Jena, Jena (Germany).

GSI Users' Group Executive Committee (UEC):

https://www.gsi.de/work/user/gsi_users_group.htm

Nuclear Structure:
T. Faestermann (Germany); M. Pfutzner (Poland); D. Cortina (Spain); A. Jungclaus (Spain);
P. Regan [past chair], (UK)

Nuclear Collision:
P. Salabura (Poland); T. Matulewicz (Poland); Nicole Bastid (France)

Atomic Physics:
D. Dauvergne (France); A. Müller (Germany)

Plasma Physics:

J. Jacoby (Germany); T. Kühl (Germany)
Heavy Elements:
J. Kratz (Germany); A. Türler (Germany)
Theory:
W. Cassing (Germany)
Biophysics:
M. Löbrich (Germany)
Materials Research:
W. Ensinger [chair], (Germany)
Students:
B. Schuster (Germany)

DOI:10.15120/GR-2015-1-ANNEX-06

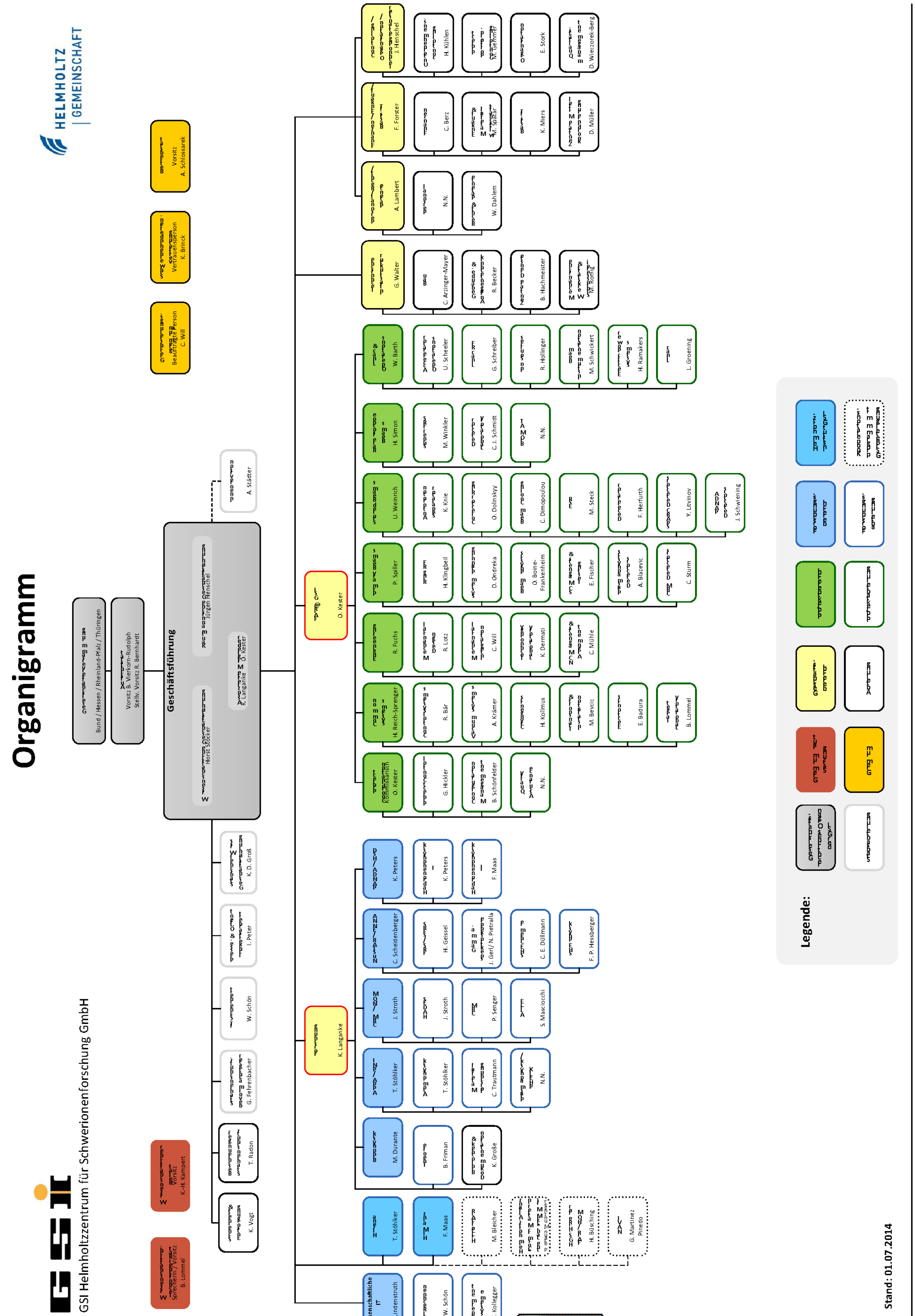

DOI:10.15120/GR-2015-1-ANNEX-07

List of Authors